M8.069-ACD

PROPULSION ENGINEERING | MANUAL

DEVELOPMENT ENGINEERING

MCDONNELL DOUGLAS ASTRONAUTICS COMPANY-WEST

MCDONNELL DOUGLAS CORPORATION

CHANGE SUMMARY

This change package issues new material for Section 10, Preliminary Rocket Vehicle Design. Included are a part of Subsection 10-2, Rocket Flight Performance and all of Subsection 10-3, Vehicle Sizing Analysis.

CHANGED PAGE LIST

REMOVED	ADDED	
	FRONT	BACK
CHANGE SUMMARY/CHANGE PAGE LIST		
A	A	BLANK
TABLE OF CONTENTS		
3 4A	3* 4A	4 4B
12A —	12A 12C	12B 12D
17	17*	18
SECTION 10		
10-23 10-87	10-23* 10-87	10-24 10-88*
10-97 THRU 10-107	10-97 THRU 10-193	10-98 BLANK

*Unrevised reprints from previous issues

A3-250-ADOO-DDH-74036
July 5, 1974

MEMORANDUM

Subject: REQUIRED PROPULSION & MECHANICAL DESIGN PROCEDURE FOR VERIFYING FLEXIBLE ELEMENT MARGINS AGAINST FLOW RESONANCE

To: Propulsion & Mechanical Supervision and Group Engineers

Copies to: A. P. O'Neal, A3-250; Holders of Propulsion Engineering Manual (PA-1); File

This memorandum documents a Propulsion & Mechanical design requirement whenever flexible elements, such as bellows and flex hoses, are used in a fluid system. It is required that the flexible element be analytically checked using the attached methodology to verify it is within the safe operating range. This screening will verify the initial acceptability of the flexible element; i.e., a stress indicator below 11,000 psi. Following this, it is required that VS&A do a detailed analysis including the acoustic modes which this screening procedure does not cover.

Finally, it is required that you have from VS&A, documented agreement that the flexible element is not susceptable to flow induced resonance for your specified application. The VS&A documentation can be implemented either by memo or their signature on the specification control drawing.

This memorandum is to be placed in Section 10.0, "Rocket Propulsion System Constraints," of the Propulsion Engineering Manual (PA-1).

D. D. Hofferth
Chief Engineer - Propulsion & Mechanical

JDS:l
Attachment: Noted

ANALYSIS NOMENCLATURE

VARIABLE		DIMENSIONS
A	Bellows Flow Area	ft^2
BOP	Bellows Operational Parameter (See Figure 1)	lb_f/in^2
C_E	Upstream Geometry Factor	Dimensionless
C_F	Vortex Force Coefficient	Dimensionless
D	Bellows Inside Diameter	in
D_M	Bellows Convolution Mean Diameter	in
g_c	Gravitational Constant	$ft\text{-}lb_m/lb_f\text{-}sec^2$
h	Bellows Convolution Height	in
K_A	Bellows Longitudinal Spring Rate	lb_f/in
N_C	No. of Bellows Convolutions	Dimensionless
N_P	No. of Bellows Convolution Plies	Dimensionless
P_D	Flow Dynamic Pressure	lb_f/in^2
Q	Dynamic Amplification Factor	Dimensionless
SI	Stress Indicator (See Figure 3)	lb_f/in^2
SSR	Specific Spring Rate (See Table I)	lb_f/in^2
t	Bellows Convolution Ply Thickness	in
V	Maximum Flow Velocity	ft/sec
$\dot{W}$	Maximum Flowrate	lb_m/sec
λ	Bellows Convolution Pitch	in
ρ	Density	lb_m/ft^3
σ	Convolution Tip Width	in
E	Modulus of Elasticity	lb_f/in^2

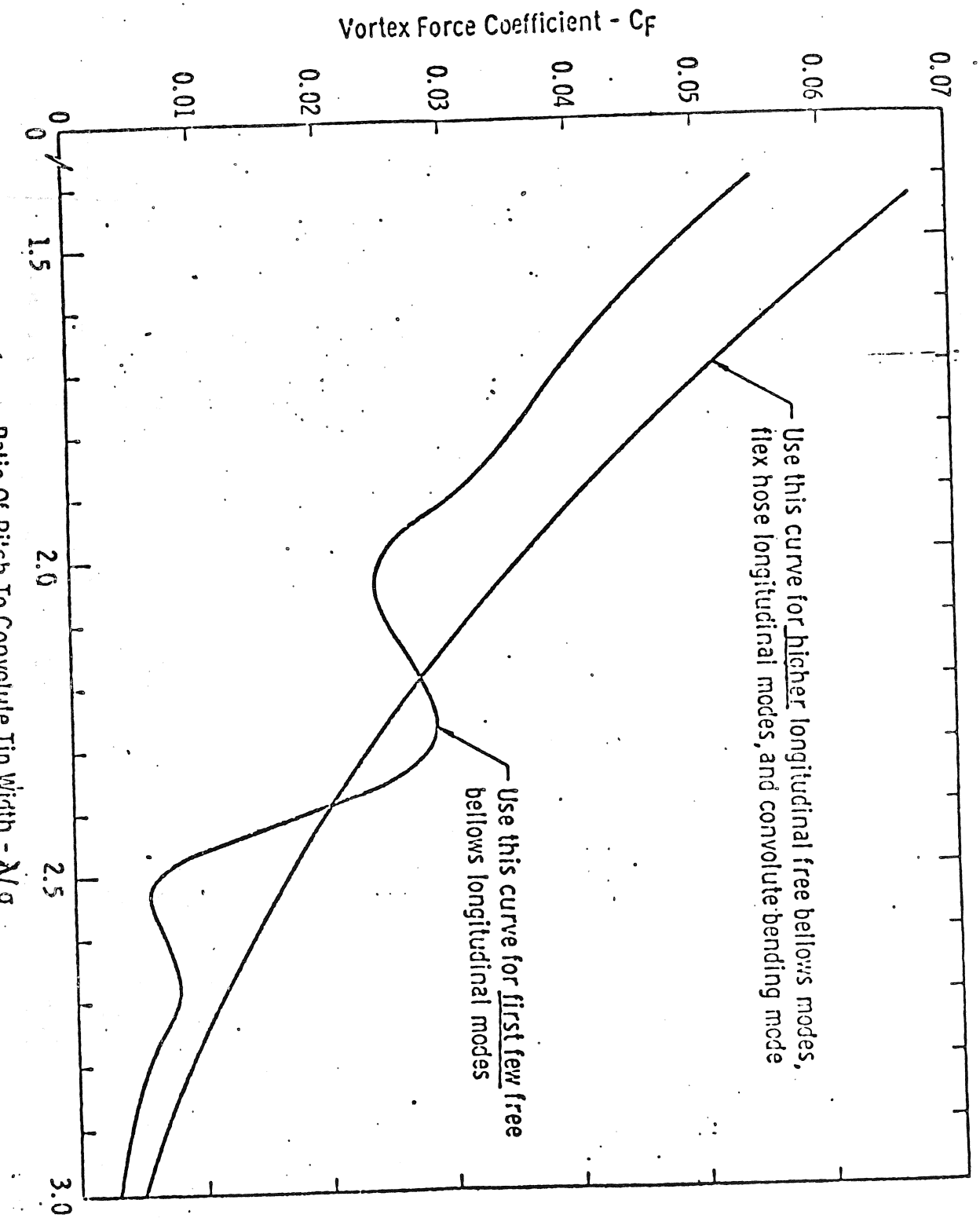

Figure 1. Summary Of Bellows Vortex Force Coefficient Experimental Data

Specific Spring Rate (see Note 1)	Number Plies	Internal Media (see Note 2)	Curve No.
all ranges	1	low pressure gases	1
over 2000 lb/in^2	1	high pressure gases, light liquids	1
over 2000	1	water, dense liquids	2
under 2000	1	high pressure gases, light liquids	2
under 2000	1	water, dense liquids	3
over 3000	2	all	3
2000-3000	2	all pressure gases	4
under 2000	2	all pressure gases	5
2000-3000	2	all liquids	5
under 2000	2	all liquids	6
over 3000	3	all	4
2000-3000	3	all	5
under 2000	3	all pressure gases	5
under 2000	3	all liquids	6

Use of Table - To use table, first calculate bellows specific spring rate, then look up application curve number corresponding to this specific spring rate, number of plies, and internal media.

Note 1: The specific spring rate is here defined as

$$S.S.R. = \frac{K_A N_c}{D_m N_p}$$

or is the spring rate per convolute, per ply, per unit of diameter.

Note 2: Low pressure gases will be defined here as being those gases below 150 psia. Light liquids will be defined as having a density, relative to water, of less than 0.2.

TABLE I

Applications Information for Use with Q Values
Data in Figure 2

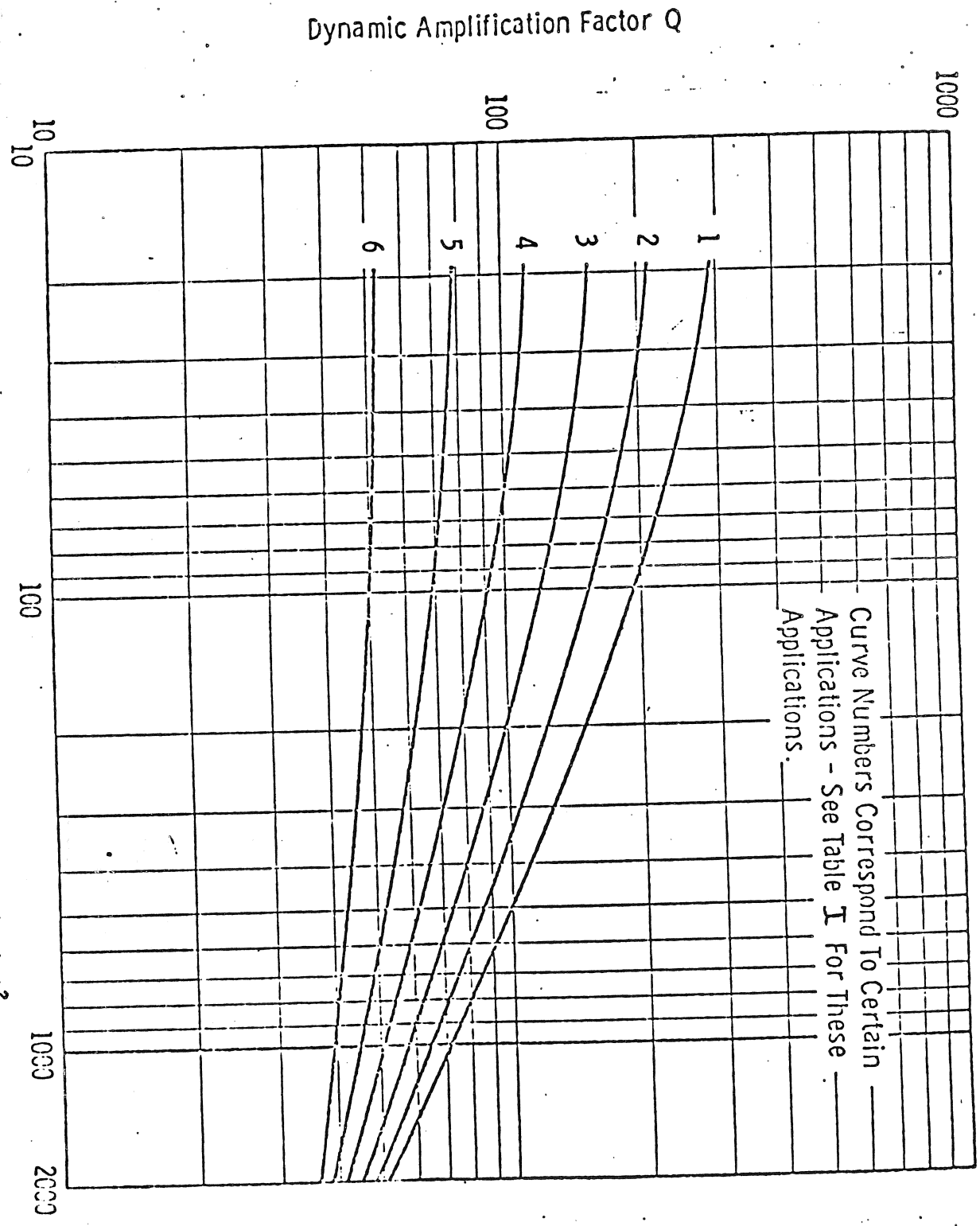

Figure 2. Dynamic Amplification Factors For Various Bellows Applications.

PRELIMINARY SCREENING FOR FLEXIBLE ELEMENT FLOW RESONANCE

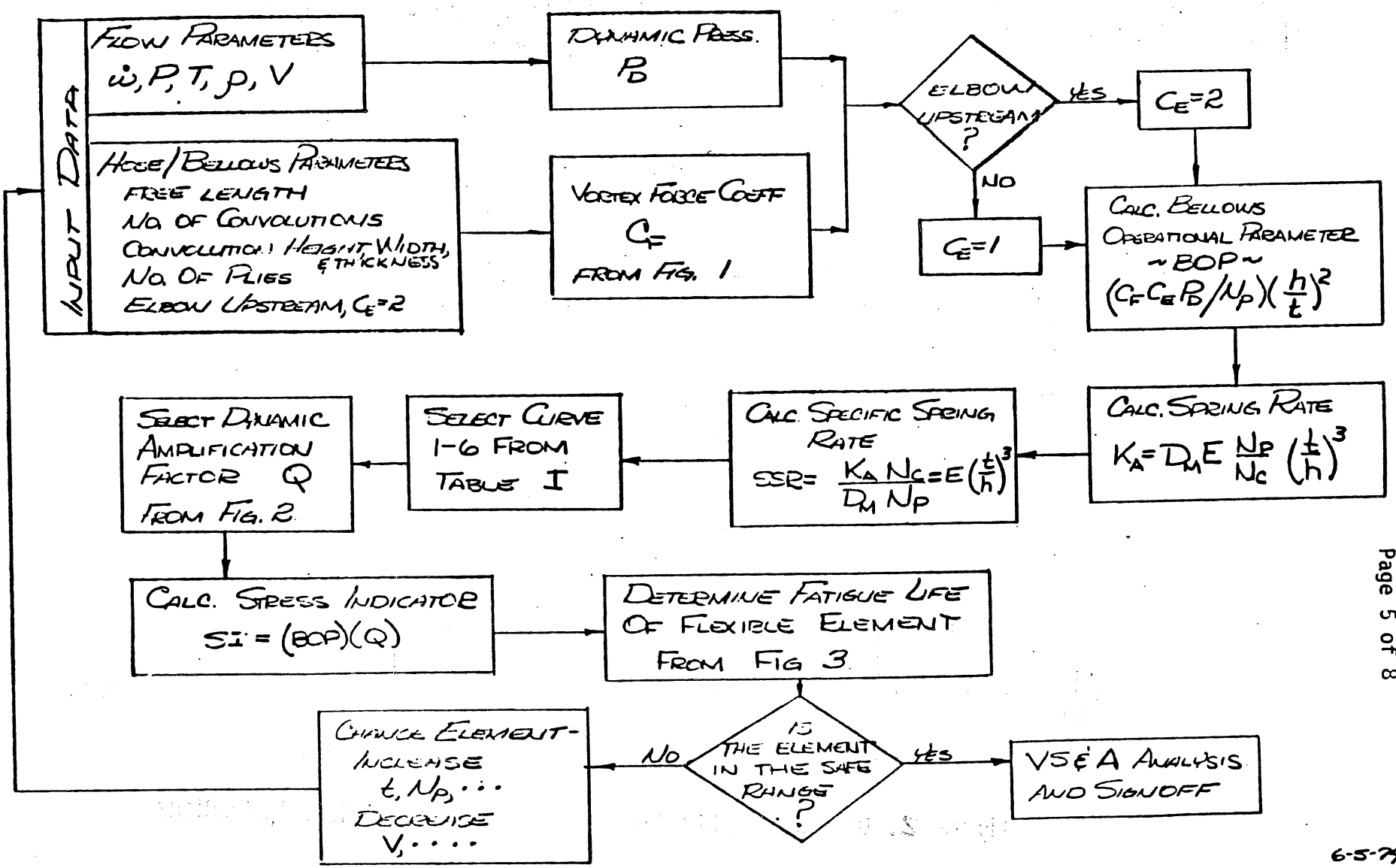

6-5-74

NO PAGE
#6

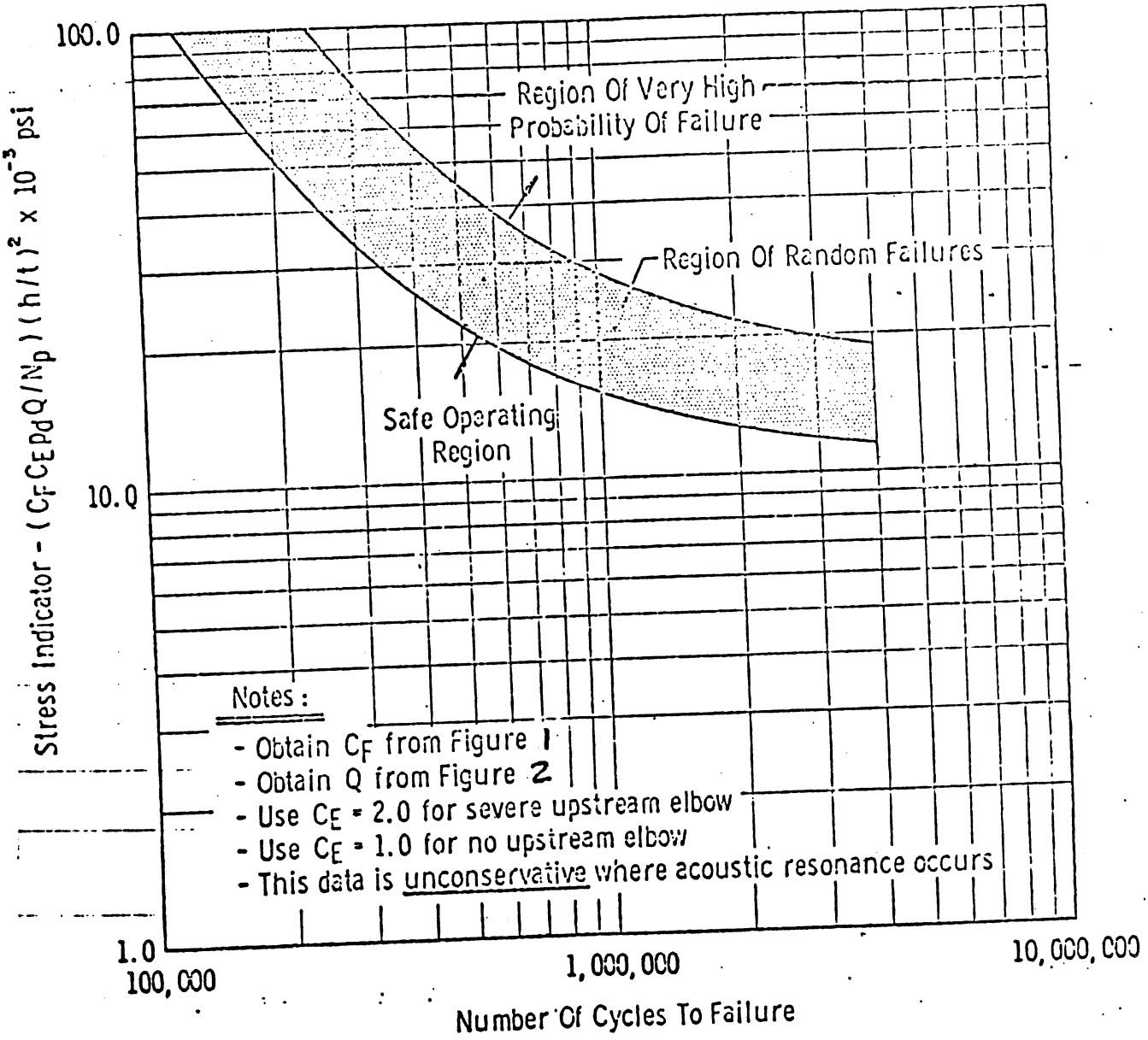

Figure 3. Preliminary Bellows Fatique Life Data

LIST OF REFERENCES

(A) "Solar LOX Feed Duct-Deletion of Flow Testing Portion of Qualification Test Program," M. L. Joy, Saturn Analysis Report 4B-1919.

(B) "Study of Minimum Pressure Loss in High Velocity Duct Systems," C. R. Gerlach, E. C. Schroeder, Quarterly Report No. 5, Contract No. NAS8-21133, August 5, 1968

(C) Letter - Southwest Research Institute to NASA (MSFC), C. R. Gerlach, Quarterly Progress Report - "Minimum Pressure Loss in High Velocity Flow Duct Systems," August 1, 1969

PREFACE

This manual is an official document of the Development Engineering Division and is authorized by SP 1.045-ACD, Development Engineering Manuals – Authority for Issuance and Control.

MEMORANDUM

A3-250-ADA2-D/M-25
July 5, 1974

Subject: PROPULSION & MECHANICAL DEPARTMENTAL DESIGN REVIEW CHECKLIST

To: H. R. Beemer, W. A. Gaubatz, R. R. Shaffer, Propulsion & Mechanical Supervision, A3-253

Copies to: All Holders of Propulsion Design Manuals PA-1 and PC-1, and Fluid Power Manual AJ-1; File

In order to insure that all propulsion and mechanical designs consistently reflect the experience gained in all present or past programs, the attached departmental design review checklist has been created. It is intended that a copy of the checklist will be completed by the responsible design engineer and submitted to the appropriate propulsion and mechanical supervision for approval along with the engineering paper implementing each new design. Propulsion and mechanical supervision are responsible to insure that the checklist is implemented to an appropriate level of detail and that adequate files are maintained.

The present checklist is not considered to be the ultimate document. Due to the scope of the propulsion and mechanical design responsibility, this checklist can cover only the minimum acceptable departmental requirements. The use of more detailed checklists in specific design areas to supplement the departmental checklist is highly recommended. In addition, all suggestions for improving the effectiveness of the departmental checklist are welcomed and should be directed to G. C. Coleman.

Until the departmental design review checklist can be formally incorporated into the propulsion and mechanical design manuals (PA-1, PC-1, and AJ-1), all manual holders are instructed to reproduce and insert a copy of this memo and attached checklist into each manual.

R. R. Shaffer for
D. D. Hofferth
Chief Engineer - Propulsion & Mechanical

GCC/awd
Attachment (Noted)

CHECKLIST FOR PROPULSION AND MECHANICAL DESIGN REVIEW

	YES*	NO*	N/A*	REMARKS*
A. External Considerations				
1. Inputs				
Externally generated line pressure surges?				
Human factors - handling, protection?				
Electrical requirements?				
Thermal inputs, thermal distortion, insulation requirements?				
Mechanical loads and distortion?				
Interface compatibility?				
Motion envelope (external interferences, clearances) thermal, dynamic?				
2. Coordination				
Electronics (power input, control logic, redundancy, EMI)				
Other Propulsion/Mechanical sections (Prop/Ordnance/Hydraulics)				
Effectiveness (reliability, FMEA)				
Thermo - (heat input, output, etc.)				
VS&A - (vibration, acoustics, etc.)				
Flight Dynamics & Control (performance requirements, etc.)				
Structures (attachments, locations, etc.)				
Strength (stresses, safety factors, etc.)				
M&P (material properties, compatibility, etc.)				
Manufacturing (fabrication, schedules)				

* The responsible designer must initial the appropriate column.
, - signifies the item has been considered and the effort is complete.
No - the item has not been thoroughly considered. Further justification is required to be noted in the remarks column as a result of a "no" response.
N/A - not applicable or no impact despite a "no" response.

7/3/74

	YES*	NO*	N/A*	REMARKS*
A. 3. Environment (qual, pre-flight, flight)				
Ambient pressure (positive/vacuum)?				
Acceleration (+, -, zero g)?				
Vibration?				
Temperature (+, -, thermal shock)?				
Shock?				
Humidity? (rain? snow? hail?)				
Salt?				
Sand?				
Purge required?				
Acoustic?				
Nuclear radiation?				
Sun exposure?				
B. Internal Considerations				
1. Performance requirements cost				
Comprehensive review of requirements complete?				
Design requirements defined/checked by analysis?				
2. Reliability				
Failure effects analysis (component/system)?				
Failure research on problems with similar systems/components? (alerts, experience storage program, GIDEP)				
Component interaction?				
Sneak circuits (pneumatic, fluid, or electrical)?				
Redundancy requirements?				
Protective devices? Overload protection? No trapped cryogenics? Pressure relief provision? Relief valve flow capacity vs. input?				
Human factors (inadvertent connection/ assembly error susceptibility? Effects?)?				
Fail safe?				
Effect of inadvertent operation/ (Pre-flight? Flight?)				

	YES	NO	N/A	REMARKS
B. 3. Design				
Design manual review (Propulsion Engineering Manual PA-1, Solid Prop. Manual PC-1, Fluid Power Manual AJ-1, Safety Manual)				
Previous experience with similar designs?				
Seal loads (adequate/excessive?)?				
Cleanliness requirements? Contamination generation/tolerance?				
Cryogenic pumping? Moisture? Vacuum? Pressure collapse?				
Bellows restraint? Liners?				
Filtration (inlets/outlets)?				
Heaters not allowed?				
Multiply bellows provided?				
Flexure accommodation provided (thermal/dynamic)?				
Insulation requirements, materials? (Avoid vacuum jacketing?)				
Weight?				
Propulsive venting/leakage effects?				
No bulkhead fittings?				
Internal tolerance control (static, dynamic, temp.)?				
Pressure connections - brazed, welded?				
Static seals - seal welds where possible?				
Dynamic seals - bellows; O-ring cutting, etc.)				
Design simple as possible?				
4. Materials				
Compatibility of operational and test media; cleaning fluids				
No structural solder?				
No dip brazing?				
Lubrication effects (over/adequate/under lubricated; threads?)				
Steel tubing material?				
Material compatibility - LOX/GOX; titanium; hydrogen embrittlement?				
Corrosion/stress corrosion susceptibility?				
Flow decay in N_2O_4?				
Heat treat?				

	YES*	NO*	N/A**	REMARKS
B. 4. (continued)				
No mercury contamination?				
Fatigue sensitivity?				
Dissimilar metals?				
Corrosive protection?				
Cold flow effects?				
Static electrical build-up/discharge?				
Outgassing effects?				
5. Margins - stress, impact loads, mechanism forces, performance				
Material properties from M & P?				
Allowable leakage margins?				
Stress margin?				
Safety factors?				
Component cycle or operational cycle life (including checkout)?				
Fracture mechanics check?				
Fatigue stresses?				
Continuous duty solenoids?				
Force/actuation margins?				
Personnel safety (1/4 burst)?				
Collapse pressure (internal/external)?				
Pre-load check?				
Torque values?				
Growth potential?				
Allowable performance degradation?				
Analytical verification of margins? Margins realistic? (Leakage, tolerances, etc.)				
6. Dynamics				
Response time?				
Flow/ΔP?				
Internal pressure surges (closing dynamics)?				
Flow resonance?				
Operational stability (chatter)?				
Geysering?				
Thermal movement?				
Flexure accommodation?				

	YES	NO	N/A	REMARKS
B. 6. (continued)				
Pump ripple?				
"Organ pipe" effects? (resonant coupling)				
7. Operations and Test				
Test requirements (Adequate? Damaging?)				
Development test				
Qual test				
PAT test				
Field test				
Maintainability?				
Repair? In place?				
Storage requirements? Shelf life?				
Checkability? Disassembly of flight configuration required? Able to test adequately?				
Handling (protection, minimum wall gages?)				
Accessibility (for checkout, maintenance, inspection?)				
Safety?				
Adequate provisions for instrumentation and checkout?				

CONTENTS

Section 1 INTRODUCTION (To be added)

Section 2 PROPULSION OPERATIONS (To be added)

Section 3 TECHNICAL DOCUMENTATION (To be added)

Section 4 ROCKET PROPULSION PRINCIPLES 4-1

4-1 Definitions 4-1
4-1.1 Chemical Rockets 4-1
4-1.2 Non-Chemical Thermal Rockets 4-3
4-1.2.1 Cold Gas Systems 4-3
4-1.2.2 Nuclear Rockets 4-4
4-1.2.3 Electrothermal Thrusters 4-4
4-1.3 Electric Acceleration Rockets 4-4
4-1.3.1 Electrostatic Thrusters 4-4
4-1.3.2 Electromagnetic Thrusters 4-5
4-2 Rocket Performance 4-5
4-2.1 Thrust 4-6
4-2.2 Thrust Coefficient 4-6
4-2.3 Characteristic Exhaust Velocity 4-8
4-2.4 Specific Impulse 4-8
4-2.5 Total Impulse 4-9
4-2.6 Impulsive Velocity 4-9
4-2.7 Thrust-To-Weight Ratio 4-9
4-2.8 Propulsion System Performance 4-11
4-3 Propulsion System Applications 4-14
4-3.1 Primary Thrust 4-15
4-3.2 Propulsive Maneuvering 4-16
4-4 Bibliography 4-21

Section 5 LIQUID PROPULSION SYSTEMS 5-1

5-1 Monopropellant Systems 5-1
5-2 Bipropellant Systems 5-2
5-2.1 Pressure-Fed Propulsion Systems 5-8
5-2.2 Pump-Fed Propulsion Systems 5-9

5-3 Rocket Engine 5-11
5-3.1 Thrust Chamber Assembly 5-11
5-3.1.1 Injector Design 5-15
5-3.1.2 Combustion Chamber 5-20
5-3.1.3 Nozzle 5-38
5-4 Feed System 5-40
5-4.1 Tankage 5-40
5-4.1.1 Tank Configurations 5-40
5-4.1.2 Propellant Expulsion 5-41
5-4.2 Ducts 5-41
5-4.3 Propellant Management 5-41
5-4.4 Propellant Pumps 5-44
5-4.4.1 Pump Selection Criteria 5-45
5-4.1.2 Turbine Selection 5-54
5-5 Pressurization System 5-57
5-6 Valves 5-63
5-6.1 Valve Classification 5-63
5-6.2 Valve Pressure Drop 5-65
5-6.3 Valve Leakage 5-66
5-6.4 Valve Actuators 5-68
5-7 Bibliography 5-68

Section 6 SOLID PROPULSION SYSTEMS 6-1

6-1 Solid Propellant Grains 6-1
6-1.1 Composite Propellants 6-1
6-1.1.1 Chemical Composition 6-2
6-1.1.2 Performance 6-5
6-1.1.3 Manufacturing Processes 6-5
6-1.2 Double-Base Propellants 6-9
6-1.3 Composite-Modified Double-Base Propellants 6-9
6-2 Internal Ballistics of Solid-Propellant Rockets 6-9
6-2.1 Mass Balance Equations 6-11
6-2.2 Temperature Sensitivity 6-11
6-2.3 Erosive Burning 6-12
6-3 Grain Geometry 6-12
6-3.1 End-Burning Grains 6-13
6-3.2 Rod Grains 6-13
6-3.3 Shell Grains 6-14
6-3.4 Star Grains 6-14
6-4 Solid Propellant Motor Design 6-16
6-4.1 Motor Case 6-16
6-4.2 Nozzle 6-17
6-4.3 Igniter 6-17
6-5 Thrust Control 6-20
6-5.1 Thrust Termination 6-20

6-5.2 Thrust Vector Control 6-21
6-5.3 Thrust Variation 6-22
6-5.3.1 Pintle Concept 6-22
6-5.3.2 Mass Excitation Concept 6-22
6-5.3.3 Vortex Valve Motor 6-24
6-5.3.4 Pulse Motor 6-24
6-6 Hybrid Propulsion Systems 6-24
6-7 Bibliography 6-26

Section 7 COLD GAS PROPULSION SYSTEMS 7-1

7-1 Effective Specific Impulse 7-3
7-2 Performance Analysis 7-4
7-3 Nozzle Performance Effects 7-7
7-4 Bibliography 7-17

Section 8 NUCLEAR PROPULSION THRUSTERS 8-1

8-1 Nuclear Reactor Rockets 8-1
8-1.1 Nuclear Reactor Theory 8-3
8-1.1.1 Nuclear Fission 8-4
8-1.1.2 Reactor Control 8-7
8-1.1.3 Shielding 8-7
8-1.2 Solid-Core Nuclear Rockets 8-8
8-1.2.1 Reactor Design 8-8
8-1.2.2 Reactor Materials 8-9
8-1.2.3 Rocket Performance 8-10
8-1.3 Liquid-Core Nuclear Rockets 8-11
8-1.4 Gaseous-Core Nuclear Rockets 8-11
8-2 Radioisotope Rockets 8-12
8-3 Bibliography 8-14

Section 9 ELECTRIC PROPULSION THRUSTERS 9-1

9-1 Electrothermal Thrusters 9-3
9-1.1 Resistojet Thrusters 9-3
9-1.2 Arc-jet Thrusters 9-6
9-2 Electrostatic Thrusters 9-7
9-2.1 Ion Thrusters 9-7
9-2.1.1 Contact Ion Thrusters 9-7
9-2.1.2 Electron Bombardment Ion Thrusters 9-8
9-2.2 Colloid Thrusters 9-9
9-2.2.1 Configuration 9-9
9-2.2.2 Application 9-11
9-3 Electromagnetic Thrusters 9-13
9-4 Bibliography 9-13

Section 10 PRELIMINARY ROCKET VEHICLE DESIGN 10-1

10-1 Vehicle Sizing and Selection Methodology 10-1
10-1.1 Mission Requirements and Performance 10-1
10-1.2 Vehicle and Subsystem Sizing and Selection Procedures 10-1
10-1.3 Automated Sizing Methods 10-19
10-1.3.1 General Missile Sizing Program 10-19
10-1.3.2 Missile Synthesis/Analysis Program (MSAP) 10-21
10-2 Rocket Flight Performance 10-21
10-2.1 General Performance Considerations 10-21
10-2.1.1 Basic Equation of Motion 10-24
10-2.1.2 Mass characteristics 10-24
10-2.1.3 Velocity Characteristics 10-27
10-2.1.4 Earth Rotation 10-31
10-2.1.5 Burn Time 10-31
10-2.1.6 Altitude 10-32
10-2.1.7 Thrust/Weight Ratio 10-32
10-2.1.8 Range 10-33
10-2.1.9 Effect of Parameters on Vehicle Performance . . .10-33
10-2.2 Space Launch Vehicles 10-39
10-2.2.1 Space Launch Vehicle Performance 10-41
10-2.2.2 Orbital Missions 10-67
10-2.2.3 Lunar Missions 10-74
10-2.2.4 Space Missions 10-76
10-2.2.5 System Considerations 10-85
10-2.3 Free Flight Rockets 10-91
10-2.3.1 Direct Fire Systems 10-96
10-2.3.2 Sounding Rockets 10-97
10-2.3.3 Surface-to-Air Rockets 10-100
10-2.3.4 Surface-to-Surface Indirect-Fire Systems 10-102
10-2.3.5 Numerical Example 10-105
10-3 Vehicle Sizing Analysis 10-110
10-3.1 General Sizing Relationships 10-110
10-3.1.1 Structure Factor 10-111
10-3.1.2 Growth Factor 10-111
10-3.1.3 Vehicle Mass Ratio 10-114
10-3.2 Optimum Staging Critieria — General 10-131
10-3.3 Optimum Sizing — General 10-135
10-3.3.1 Constant Structure Factor 10-136
10-3.3.2 Variable Structure Factor 10-137
10-3.4 Propulsion System Selection Criteria 10-137
10-3.4.1 Space Launch Vehciles 10-137
10-3.4.2 Maneuvering Missiles 10-138
10-3.5 Optimum Sizing of Launch Vehicles 10-138
10-3.6 Maneuvering Missiles (Air-to-Air, Surface-to-Air, and Air-to-Surface) 10-141

10-3.6.1 Velocity Staging 10-141
10-3.6.2 Range Staging 10-147
10-3.6.3 Parametric Studies 10-148
10-3.6.4 Air-to-Surface Missile Design System 10-159
10-3.7 Generalized Exchange Ratio Analysis 10-170
10-3.7.1 Analytical Relationships (Fixed Velocity) . . . 10-171
10-3.7.2 Graphical Presentation (Fixed Velocity) 10-173
10-3.7.3 Numerical Example (Fixed Velocity) 10-173
10-3.7.4 Exchange Ratio Chart (Effects on Velocity) . . 10-173
10-4 Propulsion System Preliminary Design (To be added)
10-5 Solid Motor Preliminary Design (To be added)
10-6 Liquid Propulsion System Preliminary Design (To be added)
10-7 Nomenclature 10-184
10-8 References and Bibliography 10-184

Section 11 ROCKET PROPULSION SYSTEM TESTING (To be added)

SEctio 12 THERMODYNAMICS 12-1

12-1 Definitions 12-1
12-1.1 Stored Energy 12-1
12-1.2 Energy in Transition 12-2
12-1.3 Enthalpy 12-3
12-1.4 Entropy 12-3
12-1.5 Specific Heat 12-3
12-2 Thermodynamic Laws 12-3
12-2.1 General Energy Equation 12-4
12-2.2 Simple Energy Equation 12-5
12-3 Thermodynamic Properties 12-5
12-3.1 Pressure-Temperature Diagram 12-5
12-3.2 Pressure-Specific Volume Diagram 12-5
12-3.3 Temperature-Entropy Diagram 12-7
12-4 Perfect Gas Relationships 12-7
12-4.1 Process Equations for Perfect Gas 12-7
12-4.2 Work for Non-Flow Process 12-9
12-4.3 Specific Heat, Internal Energy, and Enthalpy Relationships 12-11
12-4.4 Enthropy Relations 12-13
12-5 Real Gas Relationships 12-13
12-6 Mixtures of Gases 12-15
12-6.1 Volumetric Analysis to Gravimetric Analysis 12-21
12-6.2 Gravimetric Analysis to Volumetric Analysis 12-21
12-6.3 Dalton's Law of Partial Pressures 12-22
12-6.4 Molecular Weight and Gas Constant for Mixture 12-22
12-7 Thermodynamic Cycles 12-22
12-7.1 Ideal Cycles 12-23

12-7.1.1 Liquid Compression Cycles 12-26
12-7.1.2 Gaseous Compression Cycles 12-26
12-7.2 Real Cycles 12-27
12-7.2.1 Real Liquid Compression Cycles 12-27
12-7.2.2 Real Gaseous Compression Cycles 12-35
12-7.3 Refrigeration Cycles 12-38
12-8 Bibliography 12-41

Section 13 FLUID MECHANICS (To be added)

Section 14 HEAT TRANSFER 14-1

14-1 Basic Laws of Heat Transfer 14-1
14-1.1 Fundamentals of Conduction 14-1

14-1.2 Fundamentals of Radiation 14-2
14-1.3 Fundamentals of Convection 14-3
14-1.4 Combined Heat Transfer 14-4
14-1.5 Dimensional Analysis 14-4
14-2 Conduction 14-5
14-2.1 Steady-State One-Dimensional Conduction 14-5
14-2.1.1 Walls of Simple Geometrical Configuration 14-9
14-2.1.2 Composite Structures 14-11
14-2.1.3 Systems with Heat Sources 14-12
14-2.1.4 Heat Transfer from Extended Surfaces 14-12
14-2.2 Two-Dimensional and Three-Dimensional Steady-State Conduction 14-14
14-2.2.1 Potential-Field Plotting 14-15
14-2.2.2 Analogical Methods 14-18
14-2.2.3 Numerical Methods 14-18
14-2.3 Transient Heat Conduction 14-22
14-2.3.1 Negligible Internal Resistance 14-22
14-2.3.2 Measurable Internal Resistance 14-24
14-2.3.3 Graphical Method 14-29
14-2.3.4 Numerical Methods 14-33
14-3 Radiation 14-37
14-3.1 Radiation Laws 14-37
14-3.1.1 Stephan-Boltzman Law 14-37
14-3.1.2 Planck's Law 14-37
14-3.1.3 Wein's Displacement Law 14-42
14-3.1.4 Lambert's Cosine Law 14-44
14-3.1.5 Kitchoff's Law 14-44
14-3.2 Radiation from Real Bodies 14-45
14-3.3 Irradiation of Real Bodies 14-46
14-3.4 Radiant Heat Exchange Between Black Bodies 14-48
14-3.5 Radiant Heat Exchange Between Gray Bodies 14-51
14-3.6 Radiation from Gases 14-54
14-3.7 Solar, Terrestrial, and Atmospheric Radiation 14-56
14-3.8 Configuration Factors 14-63
14-3.8.1 Numerical Values 14-63
14-3.8.2 Configuration Factor Catalogue 14-70
14-4 Convection 14-97
14-4.1 Fluid Flow 14-97
14-4.2 Dimensionless Parameters for Convective Heat Transfer 14-97
14-4.3 Basic Equations 14-98
14-4.4 Convective-Heat-Transfer Coefficients 14-99
14-4.5 Forced Convection Over Flat Plates 14-99
14-4.5.1 Laminar Flow 14-99
14-4.5.2 Turbulent Flow 14-105
14-4.6 Free Convection 14-106
14-4.6.1 Flat Plates 14-106

14-4.6.2 Cylinders, Spheres and Ducts 14-107
14-4.6.3 Free Convection Caused by Centrifugal Forces . 14-109
14-4.6.4 Rotating Bodies 14-110
14-4.6.5 Combined Forced and Free Convection 14-111
14-4.7 Forced Convection Inside Pipes, Ducts, and Nozzles 14-111
14-4.7.1 Effect of Reynolds Number 14-111
14-4.7.2 Entrance Effects 14-112
14-4.7.3 Log Mean Temperature Difference 14-113
14-4.7.4 Laminar Flow in Pipes 14-113
14-4.7.5 Turbulent Flow in Pipes 14-115
14-4.7.6 Forced Convection Inside Nozzles 14-116
14-4.7.7 Liquid Metals 14-117
14-4.8 Forced Convection Over Exterior Surfaces 14-119
14-4.8.1 Cylinders 14-120
14-4.8.2 Spheres 14-120
14-5 Heat Transfer with Phase Change 14-120
14-5.1 Fundamentals of Boiling Heat Transfer 14-120
14-5.1.1 Regimes of Boiling 14-120
14-5.1.2 Nucleation 14-123
14-5.1.3 Bubble Growth and Motion 14-123
14-5.1.4 Pool Boiling Heat Transfer 14-125
14-5.2 Correlation of Boiling Heat Transfer Data 14-126
14-5.2.1 Nucleate Pool Boiling 14-126
14-5.2.2 Maximum Heat Flux 14-131
14-5.2.3 Film Pool Boiling 14-132
14-5.2.4 Minimum Heat Flux 14-133
14-5.2.5 Boiling With Forced Convection 14-133
14-5.3 Fundamentals of Condensation 14-138
14-5.4 Heat-Transfer Coefficients for Filmwise Condensation . . . 14-138
14-5.4.1 Equation for Laminar Flow 14-138
14-5.4.2 Effect of Turbulence 14-139
14-5.4.3 Effect of High Velocity Vapor 14-140
14-5.4.4 Effect of Superheated Vapor 14-151
14-6 Mass Transfer 14-141
14-6.1 Definitions 14-141
14-6.2 Mass Transfer Coefficients 14-141
14-6.3 Molecular Diffusion 14-143
14-6.3.1 Diffusion Through Solids 14-143
14-6.3.2 Diffusion in Binary Gas Mixtures 14-145
14-6.4 Interphase Mass Transfer 14-146
14-6.5 Simultaneous Heat and Mass Transfer 14-147
14-7 Heat Transfer in High-Speed Flow 14-148
14-7.2 Continuum Regime 14-149
14-7.2.1 Laminar Flow 14-150
14-7.2.2 Turbulent Flow 14-150

14-7.3 Free Molecule Flow 14-151
14-7.4 Transition and Slip Flow Regimes 14-151
14-7.5 Ablation 14-152
14-8 Heat Exchangers 14-153
14-8.1 Types of Heat Exchangers 14-154
14-8.2 Heat Transfer Rate 14-154
14-8.2.1 Overall Heat Transfer Coefficient 14-154
14-8.2.2 Reference Area 14-154
14-8.2.3 Log Mean Temperature Difference 14-157
14-8.2.4 Temperature Correction Factor 14-157
14-8.2.5 Core Pressure Drop 14-159
14-8.3 Heat-Exchanger Effectiveness 14-160
14-8.4 Fouling Factors 14-161
14-9 Applications 14-162
14-9.1 Application No. 1 — Liquid/Gas Heat Exchanger Design 14-162
14-9.1.1 Design Requirements 14-162
14-9.1.2 Nomenclature 14-162
14-9.1.3 Given Data 14-163
14-9.1.4 Assumptions 14-163
14-9.1.5 Procedure 14-164
14-9.1.6 Calculations 14-165
14-9.2 Application No. 2 — Tank Vent Duct Heater Requirements 14-168
14-9.2.1 Design Requirements 14-168
14-9.2.2 Nomenclature 14-168
14-9.2.3 Given Data 14-169
14-9.2.4 Assumptions 14-169
14-9.2.5 Procedure 14-169
14-9.2.6 Calculations 14-172
14-9.3 Application No. 3 — Rocket Motor Throat Transient Temperature Calculation 14-173
14-9.3.1 Design Requirements 14-174
14-9.3.2 Nomenclature 14-174
14-9.3.3 Given Data 14-174
14-9.3.4 Assumptions 14-174
14-9.3.5 Procedure 14-174
14-9.3.6 Calculations 14-176
14-9.4 Application No. 4 — Rocket Nozzle Heat Transfer Computer Solution 14-177
14-9.4.1 Design Requirements 14-177
14-9.4.2 Nomenclature 14-177
14-9.4.3 Given Data 14-178
14-9.4.4 Assumptions 14-178
14-9.4.5 Procedure 14-178
14-9.4.6 Calculations 14-183

14-10 Nomenclature 14-185
14-11 Bibliography 14-187

Section 15 STRUCTURAL MATERIAL PROPERTIES (To be added)

Section 16 REFERENCE DATA (To be added)

FIGURES

4-1	Rocket Propulsion Energy Sources	4-2
4-2	Thrust Coefficient versus Area Ratio	4-7
4-3	Optimum Thrust Coefficients	4-8
4-4	Impulsive Velocity Increment Data	4-11
4-5	Potential Performance of Various Propulsion Systems	4-13
4-6	Impulsive Velocity versus Mass Ratio	4-14
4-7	Payload Weight versus Burnout Velocity	4-15
4-8	Propulsion Maneuvering Methods	4-16
4-9	Thrust Requirements for Typical Applications	4-17
4-10	Stored Gas Attitude Control Rocket System	4-20
4-11	Attitude Control Systems Weight Comparison	4-21
4-12	Typical Pulse Pressure History	4-21
5-1	Liquid Propulsion System Functional Schematic	5-1
5-2	Monopropellant Rocket Engine	5-2
5-3	Hydrazine Performance Curves	5-3
5-4	Freezing Point and Vacuum Specific Impulse (at 20% NH_3 Dissociation) of Hydrazine – Nitrate – Water	5-4
5-5	Performance vs Mixture Ratio	5-8
5-6	Typical Specific Impulse and Density Specific Impulse Ranges	5-8
5-7	Pressure-Fed System	5-9
5-8	J-2 Engine Schematic	5-10
5-9	J-2 Engine Installation in the S-IVB Stage	5-12
5-10	Thrust Chamber Assembly Parameters	5-13
5-11	Schematic Diagrams of Representative Injector Configurations	5-16
5-12	Complex Injector Pattern	5-17
5-13	Transverse Mode Pressure Distributions	5-19
5-14	Propellant Humped Mass Distribution	5-20
5-15	Typical Baffle Configurations	5-20
5-16	Typical Heat Transfer Rate Variation	5-21
5-17	Typical Temperature Gradient at the Thrust Chamber Wall	5-21
5-18	Values of the Properties Variation Parameter δ	5-23
5-19	Nomograph for Combustion Gas Heat Transfer Coefficient	5-24
5-20	Heat Transfer Capabilities of Thrust Chamber Cooling Methods	5-30
5-21	Minimum Weight Thrust Chamber Cooling Methods	5-30
5-22	Regimes of Heat Transfer from a Hot Wall to a Flowing Coolant	5-32
5-23	Ablative Nozzle Design	5-36
5-24	Flow Effects for Typical Nozzle Configurations	5-39

5-25	Length Comparisons of Nozzle Configurations	5-40
5-26	Applicability of Typical Propellant Expulsion Techniques	5-42
5-27	Typical Pump-Fed Liquid Engine Schematic	5-44
5-28	Typical Turbopump Regenerative Cycle	5-45
5-29	Schematic of a Typical Centrifugal Pump	5-46
5-30	Chart for Determination of Specific Speed	5-47
5-31	Pump Selection Chart	5-48
5-32	Efficiencies of Pump Configurations	5-48
5-33	Definition of Pump Suction Heads	5-49
5-34	Nomogram for Required Pump Suction Head	5-50
5-35	Nomogram for Suction Parameter	5-51
5-36	Nomogram for Specific Speed	5-52
5-37	Disassembled View of the Fuel Pump for the Thor MB-3 Engine	5-54
5-38	J-2 Engine Oxidizer Turbopump	5-55
5-39	J-2 Engine Fuel Turbopump	5-55
5-40	Exploded View of the J-2 Fuel Pump	5-56
5-41	Impulse Turbine Configurations	5-56
5-42	Reaction Turbine Configuration	5-57
5-43	Turbine Efficiency Data	5-58
5-44	Pressurization System Schematics	5-59
5-45	Cold-Gas Pressurization System	5-63
5-46	Solid-Propellant Gas-Generator Pressurization System	5-63
5-47	Functional Comparison of Several Valve Types	5-64
5-48	Typical Shutoff Valve Arrangements	5-65
5-49	Selection Criteria for Shutoff Valves	5-66
5-50	Valve Flow Resistance Comparison	5-67
5-51	Leakage Rate Comparison Chart	5-67
5-52	Typical Helim Leak Rate as a Function of Closure Surface Roughness	5-69
6-1	Specific Impulse Versus Composition	6-7
6-2	Chamber Temperature Versus Composition	6-8
6-3	Burning Rate for a Typical Composite Propellant	6-10
6-4	Effect of Burning-Surface-to-Throat-Area Ratio on Chamber Pressure	6-11
6-5	End-Burning Grain	6-13
6-6	Rod Propellant Grain	6-13
6-7	Shell Propellant Grain	6-14
6-8	Rod and Shell Propellant Grain	6-14
6-9	Development of the Star Propellant Grain	6-14
6-10	Design Parameters of Star Grains	6-15
6-11	Grain Partitions in the Star Design	6-15
6-12	Typical Solid Propellant Motor	6-16
6-13	Conventional Convergent-Divergent Nozzle	6-17
6-14	Typical Rocket-Type Ingiter	6-19
6-15	Typical Basket Igniter	6-19
6-16	Typical Perforated Tube Igniter	6-19
6-17	Methods of Thrust Termination and Thrust Reversal	6-20

6-18	Pressure and Thrust Decay Phenomena During Fore-End Thrust Reversal Event	6-20
6-19	Typical Thrust Vector Control Systems	6-21
6-20	Rotating Nozzle	6-22
6-21	Controllable Thrust Solid Motor Concepts	6-23
6-22	Schematic Design of a Hybrid Rocket	6-24
7-1	Reaction Control System Weight Comparison	7-1
7-2	Basic Stored Gas System	7-2
7-3	Specific Impulse versus Gas Temperature	7-3
7-4	Compressibility Factors	7-4
7-5	Parahydrogen Specific Heat Ratio (γ) Data	7-8
7-6	Helium Specific Heat Ratio (γ) Data	7-9
7-7	Nitrogen Specific Heat Ratio (γ) Data	7-10
7-8	Compressibility Chart	7-11
7-9	High Pressure Compressibility Chart	7-12
7-10	Tank Blowdown Pressure Versus Prediction	7-13
7-11	Calculated and Actual Bottle Temperature History	7-14
7-12	Calculated and Actual Bottle Pressure History	7-14
7-13	Vacuum Thrust Coefficients	7-15
7-14	Critical Isentropic Flow Function	7-15
7-15	Pressure-Temperature Relationships for Nitrogen	7-15
7-16	Gas Viscosities	7-16
7-17	Critical Temperature Ratio	7-16
8-1	Flight Configuration of NERVA Engine	8-3
8-2	Fission Cross-Section for Uranium-235	8-5
8-3	Neutron Production Ratios for Nuclear Fuels	8-6
8-4	Typical Vehicle Shielding Configuration	8-8
8-5	Schematic Diagram of a Solid-Core Nuclear Rocket	8-8
8-6	Solid-Core Reactor Configuration	8-8
8-7	Vaporization Rate of Solid-Core Reactor Materials	8-10
8-8	Thrust-to-Engine-Weight Ratios	8-11
8-9	Radioisotope-Heated Thruster Configuration	8-12
8-10	Theoretical Performance of Heated Propellants	8-12
9-1	Nuclear-Electric Propulsion System Mass	9-3
9-2	Typical Resistojet Thruster	9-4
9-3	Heated Gas Propulsion System Schematic	9-5
9-4	Schematic Diagram of Radiation Cooled Arc-jet	9-7
9-5	Schematic of Contact Ion Engine	9-8
9-6	Sastrugi Ionizer	9-8
9-7	Schematic of Electron Bombardment Ion Thruster	9-9
9-8	Colloid Thruster Schematic	9-10
9-9	Colloid Propulsion System Schematic	9-10
9-10	Colloid Propulsion System Assembly Drawing	9-11
9-11	Colloid Propulsion System Weight	9-12
9-12	Colloid Propulsion System Power Requirements	9-12

10-1	Launch Vehicles Performance Available in 1971 – 1975	10-4
10-2	TAT(3C)/Delta(TSE)/TE364(1440) Orbital Capability, 90° Launch From ETR	10-6
10-3	Vehicle Cost Versus Payload Weight	10-13
10-4	Typical Missile or Space Launch Vehicle Configuration	10-14
10-5	Typical Missile System Design Procedure	10-16
10-6	GMSP Block Diagram	10-20
10-7	Forces Acting on a Rocket	10-24
10-8	Drag Coefficient of a Typical Surface-to-Surface Rocket	10-29
10-9	D/F for Large Rocket (≈2500 lb/ft^2 Vehicle Weight/Frontal Area)	10-30
10-10	Ideal Velocity Increment Data	10-34
10-11	Effort of Growth Factor on Ideal Burnout Velocity	10-35
10-12	Rocket Vehicle Design Relationships	10-36
10-13	Rocket Vehicle Payload Fraction versus Velocity Relationship	10-37
10-14	Space Payload Capabilities of Launch Vehicles	10-38
10-15	Exchange Ratio Curves for $\Delta I_{SP}/\Delta_S$ (Zero g Flight In Vacuume) – Single Stage	10-39
10-16	Thrust Curve Adjustment	10-41
10-17	Spherical Trigonometric Coordinates of Launch Trajectory	10-42
10-18	Typical Trajectory Profile in Launch Plane	10-42
10-19	Kick Angle – Vertical Rise Time Ratio (Low Orbit Mission)	10-43
10-20	Vehicle Vertical Rise Times	10-44
10-21	First Stage Burnout Angle Nomograph	10-45
10-22	Cursory First-Stage Velocity Losses	10-46
10-23	Cursory First-Stage Velocity Losses	10-46
10-24	Cursory First-Stage Velocity Losses	10-46
10-25	Cursory First-Stage Velocity Losses	10-46
10-26	Cursory First-Stage Velocity Losses	10-47
10-27	Cursory First-Stage Velocity Losses	10-47
10-28	Cursory First-Stage Velocity Losses	10-47
10-29	Average Upper-Stage Flight-Path Angle (Single Upper-Stage)	10-48
10-30	Average Upper-Stage Flight-Path Angle (Two Upper-Stages)	10-48
10-31	Change in First-Stage Losses Due to Altitude Variation of Gravity	10-49
10-32	First-Stage Gravity – Loss Constant	10-50
10-33	First-Stage Gravity – Loss Constant	10-51
10-34	First-Stage Mass Ratio Correction Factor	10-52
10-35	First-Stage Mach Number at Peak Drag	10-53
10-36	First-Stage Drag – Loss Constant	10-53
10-37	First-Stage Thrust Atmospheric Losses	10-54
10-38	First-Stage Burnout Altitude Constant	10-55
10-39	First-Stage Range-Angle Nomograph	10-56
10-40	Earth Rotational Effect on Launch Velocity	10-56
10-41	Powered Flight Coordinate System	10-57
10-42	Drage Curve	10-62
10-43	Effect of Pitch Rate Iteration	10-66

10-44 Elliptical Orbital Satellite Velocity 10-69
10-45 Circular Orbital Satellite Velocity 10-70
10-46 Circular Orbital Satellite Velocity 10-70
10-47 Circular Orbital Satellite Velocity 10-71
10-48 Circular Orbital Satellite Velocity 10-72
10-49 Elliptical Orbital Satellite Period 10-73
10-50 Circular Orbital Satellite Period 10-74
10-51 Circular Orbital Satellite Period 10-74
10-52 Circular Orbital Satellite Period 10-75
10-53 Circular Orbital Satellite Period 10-75
10-54 Circular Orbital Satellite Period 10-76
10-55 Circular Orbital Satellite Period 10-76
10-56 Hohmann Transfer Ellipse 10-77
10-57 Initial Hohmann Transfer Injection Requirements 10-77
10-58 Hohmann Transfer Velocity Requirements 10-78
10-59 Lunar Mission Requirements 10-79
10-60 Lunar Mission Requirements 10-80
10-61 Paths of Objects Under Influence of Central Body 10-81
10-62 Hyperbolic Excess Speed vs Initial Speed 10-81
10-63 Earth to Solar Orbit Transfer 10-82
10-64 Effects of Low Acceleration from Earth Orbit 10-83
10-65 Effect of Acceleration Level on Impulsive Energy Loss 10-83
10-66 Planetary Landing Characteristics 10-84
10-67 Rendezvous Mission Techniques 10-84
10-68 Rendezvous Terminal Phase Maneuver 10-85
10-69 Earth's Rotation Velocity Increment at Launch Site 10-86
10-70 Axial Acceleration at Burnout (Vacuum Conditions) 10-87
10-71 Dynamic Pressure During Stage Operation 10-88
10-72 Pressure Ratio for Standard Atmosphere 10-89
10-73 Maximum Dynamic Pressure Nomograph 10-90
10-74 Maximum Dynamic Pressure Nomograph 10-91
10-75 Time at Maximum Dynamic Pressure 10-92
10-76 Axial Acceleration During Stage Operation (Vacuum Atmosphere) 10-93
10-77 Mach Number at Maximum Dynamic Pressure 10-94
10-78 Maximum Heat Rate Parameter Nomograph 10-95
10-79 Direct Fire – Boost/Sustain; Effect of Impulse Ratio on Time to Target 10-97
10-80 Direct Fire – All-Boost; Effect of Growth Factor on Minimum Time to Target 10-98
10-81 Direct Fire – All-Boost; Effect of Ballistic Coefficient on Growth Factor 10-98
10-82 Direct Fire – All-Boost; Effect of Propellant Mass Fraction on Growth Factor 10-98
10-83 Summit Altitude of a Rocket in Drag Free Vertical Flight 10-99
10-84 Range R on a Spherical Nonrotating Earth, and Optimum Angle of Elevation γ_{bo} at Burnout as a Function of Burnout Velocity V_{bo} 10-99
10-85 Sounding Rocket – All Boost/Sustain; Effect of Growth Factor on Summit Altitude 10-100

10-86 Sounding Rocket – All Boost; Effect of Propellant Weight Fraction on Growth Factor 10-101
10-87 Sounding Rocket – All Boost; Effect of Balistic Coefficient on Growth Factor 10-101
10-88 Surface-to-Air – All Boost; Effect of Time to Altitude on Growth Factor 10-102
10-89 Surface-to-Air – All Boost; Effect of Propellant Mass Fraction on Growth Factor 10-103
10-90 Surface-to-Air – All Boost; Effect of Ballist Coefficient on Growth Factor 10-103
10-91 Effects of Ballistic Coefficient on Burnout Velocity 10-104
10-92 Indirect Fire – All Boost; Effect of Thrust-to-Weight Ratio on Optimum Launch Quadrant Elevation 10-105
10-93 Indirect Fire – Boost/Sustain; Effects of Impulse Ratio on Optimum Launch Quadrant Evaluation 10-105
10-94 Indirect Fire – All Boost; Effect of Range on Growth Factor 10-106
10-95 Boost/Sustain Engine; Variation of Specific Impulse with Thrust 10-106
10-96 Indirect Fire – Boost/Sustain; Effects of Range on Impulse Ratio 10-107
10-97 Indirect Fire – Boost/Sustain; Effect of Range on Growth Factor 10-107
10-98 Indirect Fire – All Boost; Effect of Propellant Weight Fraction on Growth Factor 10-108
10-99 Indirect Fire – All Boost; Effect of Ballistic Coefficient on Growth Factor 10-108
10-100 Flow Diagram 10-109
10-101 Growth Factor vs Ideal Velocity Ratio (Single-Stage Vehicle) 10-112
10-102 Growth Factor vs Ideal Velocity Ratio (Single-Stage Vehicle) 10-113
10-103 Growth Factor for Like Parameters (Multiple Stage) 10-115
10-104 Growth Factor for Like Parameters (Multiple Stage) 10-116
10-105 Growth Factor for Like Parameters (Multiple Stage) 10-117
10-106 Growth Factor for Like Parameters (Multiple Stage) 10-118
10-107 Growth Factor for Like Parameters (Multiple Stage) 10-119
10-108 Growth Factor for Like Parameters (Multiple Stage) 10-120
10-109 Growth Factor for Like Parameters (Multiple Stage) 10-121
10-110 Growth Factor for Like Parameters (Multiple Stage) 10-122
10-111 Growth Factor for Like Parameters (Multiple Stage) 10-123
10-112 Growth Factor for Like Parameters (Multiple Stage) 10-124
10-113 Growth Factor for Unlike Structure Factors (Two-Stage Vehicles) 10-125
10-114 Comparison of Vehicle Performance for a Launch Vehicle with Propulsive Stages 10-131
10-115 Effects of Stage Sizing on Vehicle Weight 10-132
10-116 Payload vs Launch Weight 10-133
10-117 Stage Mass Ratio for Like Parameters (Multiple-Stage Vehicles) 10-134
10-118 Curve Fits for the Approximation of the Structure Factor Variations 10-135
10-119 Optimum Sizing Nomograph for Stages with Unlike Parameters (Constant Structure Factor vs Step Weight) 10-139
10-120 Structure Factor Selection Data 10-140
10-121 Typical Step Mass Fraction vs Propellant Weight 10-142
10-122 Typical Specific Impulse vs Propellant Weight Plot 10-143
10-123 Typical Velocity Losses Versus Stage Mass Ratio 10-143
10-124 Interceptor Performance for Two Velocity Staging Ratios (V_{bo} = C) 10-144

10-125 Interceptor Performance for Two Velocity Staging Ratios ($R_T = C$) 10-144
10-126 Typical Required Burnout Velocity vs Staging Ratio 10-145
10-127 Typical Gross Weight vs Staging Ratio 10-145
10-128 Typical Inert Weight vs Propellant Weight 10-146
10-129 Typical Missile Gross Weight vs Staging Ratio 10-149
10-130 Typical Required Burnout Velocity vs Staging Ratio 10-150
10-131 Effect of Staging Criteria 10-151
10-132 Typical Trajectory Parameterization Data Presentation 10-152
10-133 Typical Trajectory and Thrust Histories for Air-Launch Missile Systems 10-153
10-134 Sizing Sequence for Packaging Liquid Propulsion System 10-155
10-135 Sizing Sequcne for Solid Propellant Motors 10-157
10-136 Motor – Structural Modules 10-158
10-137 Typical Parametric Study Procedure Flow Chart (Liquid Propellant System) . . . 10-160
10-138 Total Impulse vs Motor Length – TASM 10-161
10-139 Gross Weight vs Range Low Altitude Launch (1000 ft) 10-163
10-140 Missile Sizing Procedure 10-164
10-141 Missile Sizing Resutls 10-165
10-142 Effects of Specific Impulse and Density Impulse on Missile Performance 10-167
10-143 Effects of Diameter and Length on Missile Performance 10-168
10-144 Effects of Propellant Burning Time on Missile Performance 10-169
10-145 Benefits of Air-Augmentation 10-169
10-146 Benefits of Altitude – Compensating Nozzles – Cruise Flight Mode 10-170
10-147 Stage Payload Weight – Specific Impulse Ratio 10-174
10-148 Stage Payload Weight – Stage Initial Gross Weight Exchange Ratio 10-175
10-149 Stage Payload Weight – Propellant Weight Exchange Ratio (Fixed Structural Weight) 10-176
10-150 Stage Payload Weight – Propellant Weight Exchange Ratio (Variable Structural Weight) 10-177
10-151 Stage Payload Weight – Thrust Exchange Ratio 10-178
10-152 Stage Gross Weight – Specific Impulse Exchange Ratio 10-179
10-153 Stage Gross Weight – Inert Weight Exchange Ratio 10-180
10-154 Stage Gross Weight – Thrust Exchange Ratio 10-181
10-155 Exchange Ratios Derived From $V_{bo} = I_{sp}\, g_o \ln r_v$ 10-183

12-1	Pressure/Specific-Volume/Temperature Surface for a Material That Contracts on Freezing	12-6
12-2	Pressure/Specific-Volume/Temperature for a Material That Expands on Freezing	12-8
12-3	Temperature-Enthropy Diagram	12-9
12-4	Perfect Gas Process Paths on the Pressure-Volume Diagram	12-9
12-5	Non-Flow Process With Work Output	12-10
12-6	Values of Specific Heats and Gammas for Common Gases	12-12
12-7	Ideal Gas Process Paths on the Temperature-Entropy Diagram	12-13
12-8	Nelson-Obert Generalized Compressibility Chart (High-Pressure Region)	12-18
12-9	Nelson-Obert Generalized Compress ility Chart (Medium-Pressure Region)	12-19
12-10	Nelson-Obert Generalized Compressibility Chart (Low-Pressure Region)	12-20
12-11	Open Loop Heat Engine Cycle	12-22
12-12	Closed Loop Heat Engine Cycle	12-23
12-13	Liquid Compression Cycle	12-26
12-14	Gaseous Compression Cycle	12-27
12-15	Regenerative Cycle	12-27
12-16	T-S Diagrams of Fluid Properties	12-28
12-17	Rankine Cycle – Type A Fluid	12-29
12-18	Rankine Cycle with Dry Expansion	12-29
12-19	Rankine Cycle Thermal Efficiency	12-30
12-20	Rankine Cycle Diagram Efficiency	12-30
12-21	Rankine Cycle – Type B Fluid	12-31
12-22	Thermal Decomposition Rates of Organic Fluids	12-31
12-23	Regenerator Analysis for Biphenyl Rankine Cycle	12-32
12-24	Thermal and Diagram Efficiencies for Type B Rankine Cycle (Biphenyl)	12-32
12-25	Regenerative Rankine Cycle	12-32
12-26	High Pressure Regenerative Ranking Cycle Efficiency	12-33
12-27	Low Pressure Regenerative Rankine Cycle Efficiency	12-33
12-28	Supercritical Rankine Cycle	12-33
12-29	Feher Cycle	12-34
12-30	Supercritical Rankine Cycles for Type A and B Fluids	12-34
12-31	Supercritical Rankine Cycle Efficiency	12-34
12-32	Feher Cycle Efficiency	12-35
12-33	Brayton Cycle	12-35
12-34	Brayton Cycle Efficiency	12-36
12-35	Regenerative Brayton Cycle	12-36
12-36	Brayton Cycle – With Regeneration	12-37
12-37	Stirling Cycle	12-37
12-38	Regenerative Ericsson Cycle	12-38
12-39	Comparison of Power and Refrigeration Systems	12-28
12-40	Comparison of Power and Refrigeration Cycles	12-39
12-41	Ideal Vapor/Compression Refrigeration Cycle	12-39
12-42	Air Refrigeration System	12-40
12-43	Ammonia-Water Absorption Refrigeration System	12-40
12-44	Cascade Refrigeration System	12-41

14-1	Conduction Heat Flow	14-2
14-2	Order-of-Magnitude of Thermal Conductivity	14-2
14-3	Heat Transfer System	14-4
14-4	Nomenclature for Conduction Through a Hollow Cylinder	14-9
14-5	Nomenclature for Conduction Through a Hollow Sphere	14-11
14-6	Nomenclature for Conduction Through a Composite Slab	14-11
14-7	Nomenclature for Conduction Through a Composite Cylinder	14-11
14-8	Nomenclature for Heat Conduction in Plane Wall with Internal Heat Generation	14-12
14-9	Nomenclature for Heat Conduction in a Long Circular Cylinder with Internal Heat Generation	14-12
14-10	Nomenclature for 3-Dimensional Heat Conduction in Cartesian Coordinates	14-15
14-11	Nomenclature for Heat Conduction in Cylindrical Coordinates	14-15
14-12	Nomenclature for Heat Conduction in Spherical Coordinates	14-15
14-13	Isotherms and Heat Flow Lines in a Potential Field	14-16
14-14	Arrangement of the Analog Field Plotter	14-18
14-15	One-Dimensional Nodal Network	14-19
14-16	Two-Dimensional Nodal Network	14-19
14-17	Three-Dimensional Nodal Network	14-19
14-18	Two-Dimensional Nodal Point Boundary Conditions	14-21
14-19	Nodal Nomenclature at an Irregular Boundary	14-22
14-20	Dimensionless Temperature Ratio versus Product of Biot and Fourier Moduli (Bi)(Fo)	14-24
14-21	Central Temperature Histories in Various Solids	14-25
14-22	Dimensionless Temperature Distribution in a Wall Subjected to a Sudden Change in Environmental Temperature	14-26
14-23	Dimensionless Heat Flow to or from a Wall Subjected to a Sudden Change in Environmental Temperature	14-26
14-24	Dimensionless Temperature Distribution in a Long Circular Cylinder Subjected to a Sudden Change in Environmental Temperature	14-27
14-25	Dimensionless Heat Flow to or From a Long Circular Cylinder Subjected to a Sudden Change in Environmental Temperature	14-27
14-26	Dimensionless Temperature Distribution in a Sphere Subjected to a Sudden Change in Environmental Temperature	14-28
14-27	Dimensionless Heat Flow to or from a Sphere Subjected to a Sudden Change in Environmental Temperature	14-28
14-28	Central Temperature History in an Infinite Plate	14-30
14-29	Position Correction Chart for an Infinite Plate	14-30
14-30	Central Temperature History in an Infinite Cylinder	14-31
14-31	Position Correction Chart for an Infinite Cylinder	14-31
14-32	Central Temperature History for Spheres	14-32
14-33	Position Correction Chart for Spheres	14-32
14-34	Gaussian Error Integral	14-33
14-35	Dimensionless Temperature Distribution in a Semi-Infinite Slab Subjected to a Sudden Change in Environmental Temperature	14-34
14-36	Dimensionless Temperature Ratio in a Semi-Infinite Solid with Convection at the Surface	14-35

14-37	Semi-Infinite Solid with Constant Heat Flux at the Surface	14-36
14-38	Transient Temperature Rise of a Fin	14-37
14-38A	Cylindrical Shell – Internal Surface Insulated	14-38.2
14-38B	Cylindrical Shell – External Surface Insulated	14-38.8
14-38C	Spherical Shell – Internal Surface Insulated	14-38.14
14-38D	Spherical Shell – External Surface Insulated	14-38.20
14-39	Schmidt Plot in an Infinitely Thick Wall	14-39
14-40	Schmidt Plot for a Time-Dependent Boundary Condition	14-40
14-41	Three-Dimensional Network for the Numerical Method	14-40
14-42	Subdivision of a Plate for a Transient-Numerical Solution	14-40
14-43	Heat Balance on an Exterior Nodal Point with Convection and Radiation	14-42
14-44	Spectral Distribution of Emissive Power	14-42
14-45	Maximum Monochromatic Emissive Power versus Temperature	14-43
14-46	Emissive Power Ratio versus Wavelength Ratio	14-43
14-47	Fraction of Total Emissive Power versus Wavelength Ratio	14-43
14-48	Nomenclature for Intensity of Radiation	14-45
14-49	Variation of Monochromatic Absorptance of Emittance with Wavelength for an Electrical Conductor	14-45
14-50	Variation of Monochromatic Absorptance or Emittance with Wavelength for an Electrical Nonconductor	14-45
14-51	Directional Variation of Emittance for Electrical Nonconductors	14-46
14-52	Directional Variation of Emittance for Electrical Conductors	14-46
14-53	Ratio of Hemispherical Emittance to Normal Emittance	14-47
14-54	Transmission Factor for Various Transparent Areas	14-48
14-55	Variation of Average Absorptance with Emitter Temperature	14-48
14-56	Geometrical Shape-Factor Notation	14-51
14-57	Equivalent Black Body Thermal Radiation Networks	14-52
14-58	Equivalent Gray Body Thermal Radiation Networks	14-53
14-59	Water Vapor Emittance at One Atmosphere Total Pressure and Zero Partial Pressure	14-54
14-60	Emittance Correction Factor for Water Vapor to Values Other than One Atmosphere and Zero Partial Pressure	14-55
14-61	Carbon Dioxide Emittance at One Atmosphere Total Pressure	14-55
14-62	Emittance Correction Factor for Carbon Dioxide to Values Other Than One Atmosphere Total Pressure	14-56
14-63	Correction to Gas Emittance Due to Spectral Overlapping of Carbon Dioxide and Water Vapor	14-57
14-64	Variation of Solar Energy with Altitude	14-58
14-65	Combination Nomogram for Solar Altitude and Azimuth	14-59
14-66	Equilibrium Temperature of Various Surfaces	14-60
14-67	Spectral Distribution Curves Related to the Sun	14-62
14-68	Configuration Factor – Basic Geometries	14-63
14-69	Configuration Factors for Geometry 1	14-64
14-70	Configuration Factors for Geometry 2, Φ = 30 and 60°	14-64
14-71	Configuration Factors for Geometry 2, Φ = 90 and 120°	14-65
14-72	Configuration Factors for Geometry 3	14-65
14-73	Configuration Factors for Geometry 4	14-66

14-74 Configuration Factors for Geometry 8 14-66
14-75 Configuration Factors for Geometry 9 14-67
14-76 Configuration Factors for Geometry 10 14-67
14-77 Configuration Factors for Geometry 11 14-67
14-78 Velocity and Temperature Profiles for Laminar Boundary Layer In Flow Over a Flat Plate 14-103
14-79 Dimensionless Velocity and Temperature Profiles in Laminar Boundary Layer for Flow Over a Flat Plate at Constant Temperature 14-104
14-80 Velocity Profiles for Laminar and Turbulent Boundary Layers in Flow Over a Flat Plate 14-105
14-81 Velocity and Temperature Profiles Near a Vertical Heated Plate 14-106
14-82 Free-Convection Heat Transfer From Two Parallel Vertical Plates Spaced a Distance b Apart 14-108
14-83 Correlation of Data for Free-Convection Heat Transfer From Horizontal Cylinders in Gases and Liquids 14-108
14-84 Free-Convection Heat Transfer From the Interior Surfaces of Vertical Ducts Having Various Cross-Sectional Geometries 14-109
14-85 Free-Convection-Cooled Gas-Turbine Blade 14-110
14-86 Velocity and Boundary Layer Profiles for a Disk Rotating in an Infinite Environment 14-111
14-87 Velocity Distributions, Temperature Profiles and Variation of the Unit-Convective Conductance Near the Inlet of a Tube for Air Being Cooled in Laminar Flow 14-112
14-88 Velocity Distribution and Variation of Unit-Convective Conductance Near the Entrance of a Tube for a Fluid in Turbulent Flow 14-114
14-89 Temperature Distribution for a Fluid Heated by a Pipe at Constant Temperature 14-114
14-90 Comparison of Convective Heat Transfer Coefficients 14-118
14-91 Velocity Distributions Indicating Flow Separation on a Cylinder in Cross Flow 14-119
14-92 Local Nusselt Number for Heat Transfer From a Cylinder in Cross Flow 14-119
14-93 Typical Boiling Curves for a Pool of Water at Atmospheric Pressure 14-222
14-94 Characteristics of Forced-Convection Vaporization — Heat-Transfer Coefficients Versus Quality and Types of Flow Regimes 14-124
14-95 The Effect of Surface Wettability on the Bubble Contact Angle 14-125
14-96 Heat Flux Versus Degree of Superheating for Nucleate Boiling of Water 14-126
14-97 Predicted Nucleate and Film Pool Boiling Correlations for Oxygen 14-127
14-98 Predicted Nucleate and Film Pool Boiling Correlations for Nitrogen 14-128
14-99 Predicted Nucleate and Film Pool Boiling Correlations for Hydrogen 14-129
14-100 Predicted Nucleate and Film Pool Boiling Correlations for Helium 14-130
14-101 Reynolds Number Factor, F 14-135
14-102 Suppression Factor, S 14-136
14-103 Peak-Heat-Flux Correlation for Forced-Convection Boiling and Vaporation 14-137
14-104 Effect of Turbulence in Film on Heat Transfer With Condensation 14-140
14-105 Concentratin Boundary Layer on a Flat Plate 14-142
14-106 Partial Pressure Gradients in Equimolar Counterdiffusion of Two Gases 14-145

14-107	Partial Pressure Gradients in the Diffusion of Gas A Through a Stationary Gas B	14-145
14-108	Flow Regimes of Gas Dynamics	14-149
14-109	Boundary Layer Temperature Profiles During High-Velocity Flow	14-150
14-110	High-Speed Stanton Number for Free Molecule Flow	14-152
14-111	Recovery Factor for Free Molecule Flow	14-152
14-112	Stanton Number for Slip Flow Over a Flat Plate	14-153
14-113	Representative Types of Heat Exchangers	14-155
14-114	Heat Transfer in Flow Normal to a Staggered Tube Bank	14-156
14-115	Heat Transfer in Flow Normal to an In-Line Tube Bank	14-156
14-116	Heat Transfer in Flow Through Plain Plate-Fins	14-156
14-117	Heat Transfer in Flow Transverse to Finned Circular Tubes	14-156
14-118	Comparison of f/j Ratios for Various Heat Exchanger Geometries	14-157
14-119	Correction Factor to Counterflow LMTD for Heat Exchanger with One Shell Pass and Two, or a Multiple of Two, Tube Passes	14-158
14-120	Correction Factor to Counterflow LMTD for Heat Exchanger with Two Shell Passes and a Multiple of Two Tube Passes	14-158
14-121	Correction Factor to Counterflow LMTD for Crossflow Heat Exchangers, Fluid on Shell Side Mixed, Other Fluid Unmixed, One Tube Pass	14-159
14-122	Correction Factor to Counterflow LMTD for Crossflow Heat Exchanger, Both Fluids Unmixed, One Tube Pass	14-160
14-123	Heat-Exchanger Effectiveness for Parallel Flow	14-161
14-124	Heat-Exchanger Effectiveness for Counterflow	14-161
14-125	1-2 Parallel-Counterflow Exchanger Performance	14-161
14-126	Heat-Exchanger Effectiveness for Crossflow with Both Fluids Unmixed	14-161
14-127	Heat-Exchanger Effectiveness for Crossflow with One Fluid Mixed, the Other Unmixed	14-162
14-128	Heat Exchanger Configuration	14-163
14-129	Pool Boiling Hydrogen Heat Transfer Coefficient	14-164
14-130	Heat Transfer Nomenclature	14-164
14-131	Helium Cooling Data	14-166
14-132	Computer Program Flow Chart	14-167
14-133	Orbital Workshop Waste Tank Configuration	14-169
14-134	Water Ice Separation Temperature	14-170
14-135	Thermal Model Waste Tank Vent Duct	14-171
14-136	Duct Dimensionless Temperature Profile	14-173
14-137	Duct Temperature Profile	14-173
14-138	Ullage Rocket Motor Nozzle Assembly	14-175
14-139	Film Coefficient Parameter vs Ratio of Specific Heats	14-175
14-140	h_c Crossplot	14-176
14-141	Temperature Ratio Crossplot	14-177
14-142	Nozzle Assembly (TE-364-4)	14-178
14-143	TE-364-4 Nozzle Pressure	14-181
14-144	TE-364-4 Nozzle Temperature Profiles	14-181
14-145	Nozzle Convective Heat Transfer Coefficients (h_c)	14-182
14-146	Nozzle Backside Convective Heat Transfer Coefficient Profile	14-183
14-146A	Nozzle Temperature Distribution at Axial Station 7.1	14-183
14-146B	Predicted Nozzle Liner – Glass Phenolic Interface Temperatures	14-183
14-147	Nozzle Finite Element Model for Thermal Analysis	14-184

TABLES

4-1	Characteristics of Principal Rocket Propulsion Systems	4-3
4-2	Rocket Engine Formulas	4-10
4-3	Typical Performance Parameters for Rocket Propulsion Systems	4-12
4-4	Velocity Requirements for Several Missions	4-13
4-5	Performance Requirements for Primary Thrusters	4-18
4-6	Thrust Vector Control Methods for Rocket Engines	4-19
4-7	Attitude Control Thruster Operational Combinations	4-20
5-1	Theoretical Rocket Engine Propellant Summary	5-5
5-2	Liquid Rocket Oxidizer Properties	5-6
5-3	Liquid Rocket Fuel Properties	5-7
5-4	Types of Combustion Instability	5-14
5-5	Cooling Method Screening Chart	5-26
5-6	Thrust Chamber Cooling Methods	5-27
5-7	Influence of Engine Design Parameters on Coolant Temperature	5-31
5-8	Coolant Characteristics for Liquid-Rocket Propellants	5-33
5-9	Recommended Values for Bulk Temperature Factor, Φ_1, For Hydrogen	5-34
5-10	Properties of Various Metal Refractory Materials	5-35
5-11	Room Temperature Properties of Ablative Materials	5-38
5-12	Typical Design Point Pump Performance Data	5-53
5-13	Pressure Vessel Safety Factors	5-60
5-14	State-of-the-Art Characteristics of Candidate Pressurization Systems	5-60
5-15	Pressurization System Investigation Summary	5-61
6-1	Current Composite Oxidizers	6-2
6-2	Properties of Composite Propellant Binders	6-3
6-3	Composite Propellant Performance Data	6-6
6-4	Double-Base and Composite-Modified Double-Base Propellant Performance Data	6-10
6-5	Typical Properties of Nozzle Materials	6-18
6-6	Theoretical Performance of Several Hybrid Rocket Propellant Combinations	6-25
7-1	Characteristics of Typical Propellant Gases	7-5
7-2	Ideal Cold Gas System Venting Equations	7-7
8-1	Nuclear Rocket Program Testing Highlights	8-2
8-2	NERVA Engine Performance	8-3
8-3	Properties of Reactor Materials	8-9
8-4	Characteristics of Radioisotope Heat Sources	8-13
9-1	Electric Propulsion Systems	9-2
9-2	Properties of Gaseous Propellants	9-4

9-3	Properties of Vaporizing Liquid Propellants	9-4
10-1	Burnout Velocities Required for Various Missions	10-2
10-2	U.S. Space Launch Vehicles	10-7
10-3	Typical U.S. Missiles	10-8
10-4	Typical U.S. Research Rockets	10-10
10-5	Typical U.S. Rocket Motors	10-11
10-6	Missile Subsystem Characteristics	10-18
10-7	Vehicle Preliminary Design and Analysis and Technical Interfaces	10-18
10-8	Typical GMSP Intermodule Data Flow	10-22
10-9	Stage and Step Mass Characteristics	10-25
10-10	Stage and Vehicle Velocity Characteristics	10-28
10-11	First and Second Stage Vehicle Parameters	10-61
10-12	Input Parameters From Results for Stage 1	10-63
10-13	Tabular Values of the Sine and Cosine Integrals	10-64
10-14	Comparison of Computed Trajectory Parameters	10-67
10-15	Comparison of Results	10-68
10-16	Exchange Ratio Analysis	10-182
10-17	Nomenclature for Section 10	10-184
10-18	List of Acronyms	10-193
12-1	Process Exponents for a Perfect Gas	12-9
12-2	Equations for Reversible Nonflow Ideal Gas Processes, Assuming a Constant Specific Heat	12-14
12-3	Van der Waals Constant	12-15
12-4	Critical Constants	12-16
12-5	Beattie-Bridgeman Equation Constants	12-17
12-6	Comparison of Common Thermodynamic Cycles	12-24
12-7	Variations of the Rankine Cycle	12-25
12-8	Refrigeration Data	12-39
14-1	Order-of-Magnitude of Convective Heat-Transfer Coefficients	14-3
14-2	Dimensionless Groups	14-6
14-3	One-Dimensional Steady-State Heat Conduction Equations	14-10
14-4	Equations for Steady-State Heat Transfer From Extended Surfaces	14-13
14-5	Selected Magnitudes of Modified Bessel Functions	14-14
14-6	Conduction Shape Factor S for Various Systems	14-17
14-7	Analogical Systems Comparisons	14-18
14-8	Transient One-Dimensional Heat Conduction Equations	14-23
14-9	Transient Temperature Distribution in Two- and Three-Dimensional Systems	14-38
		14-38.1
14-9A	Schneider Chart Application Summary	14-41
14-10	Thermal Radiation Laws	14-44
14-11	Radiation Functions	14-49
14-12	Total Emittance Data	14-55
14-13	Average Lengths of Radiant Beams in Various Gas Shapes	14-61
14-14	Solar-Spectral-Irradiance Data	14-71
14-15	Table of References for Configuration Factors	14-100
14-16	Convective Heat Transfer Coefficients	14-120
14-17	Coefficients for Calculating Nu_D for a Circular Cylinder in Cross Flow	14-120
14-18	Coefficients for Calculating Nu_D for Noncircular Cylinders in Cross Flow	14-120

14-19 Heat Transfer Coefficients for Boiling and Condensation 14-121
14-20 Values of the Coefficient Csf in Equation 213 for Various Liquid-Surface Combinations 14-131
14-21 Mass Diffusivities for Gases and Liquids 14-143
14-22 Atomic Volumes 14-144
14-23 Henry's Law Constants for Various Gases in Water at Moderate Pressures $m \times 10^{-4}$, atm/(lb mole/cu ft) 14-146
14-24 Thermal Accommodation Coefficient, α 14-151
14-25 Normal Fouling Factors 14-162
14-26 Values of A_c and a 14-172
14-27 Values of b and b/a at O.D. = 1.75 in. 14-173
14-28 Values of $(T - b/a)/(T_o - b/a)$ at q_H = 17 Btu/hr 14-173
14-29 Duct Temperature T, °R at O.D. = 1.75 in. 14-173
14-30 FM-5063 Carbon Phenolic Thermal Properties 14-179
14-31 FM-5064 Graphite Phenolic Thermal Properties 14-179
14-32 FM-5044 and FM-5045 Glass Phenolic Thermal Properties 14-180
14-33 FM-5046 Glass Phenolic Thermal Properties 14-180
14-34 FM-5039 Asbestos Phenolic Thermal Properties 14-181

Section 4
ROCKET PROPULSION PRINCIPLES

This section presents an overview of the field of rocket propulsion by defining terms, identifying the most important rocket performance parameters, and describing the general propulsion system selection criteria. The principal categories of rocket propulsion are identified and defined in paragraph 4-1. The basic rocket equations and the conditions for their use are described in paragraph 4-2. Paragraph 4-3 discusses applications for rocket propulsion systems, and introduces criteria for selecting the appropriate systems for specific applications. Subsequent Sections 5 through 9 of this manual expand on material which is introduced in this section.

4-1 DEFINITIONS

Propulsion is defined as the act of changing the natural state of motion of a mass, and the device that provides this change is called the propulsion system. The most important categories of propulsion systems that have practical application to missiles and space are those utilizing jet propulsion.

A jet propulsion system provides useful thrust as a reaction to the change of momentum of ejected mass in the form of a jet. Jet propulsion systems are usually categorized as either rockets or ducts. Duct propulsion systems include all propulsion devices that obtain mass from the surrounding environment, and eject this mass to produce thrust. Rockets are defined to include all jet propulsive devices which carry within themselves all the reactive mass to be ejected.

All rockets can be divided into two categories, based upon the mechanism they employ to accelerate the jet of ejected mass. These two categories are thermal and electrical. Thermal rockets provide thrust by the thermodynamic process of converting the heat energy of the mass to be ejected into kinetic energy. Purely electrical rockets accelerate the jet of ejected mass by means of electrostatic or electromagnetic fields. (Some of the so-called electrical rockets make use of combinations of the two categories of acceleration.)

Figure 4-1 presents a schematic classification of rockets in terms of their propulsive energy sources. It presents a fundamental classification of rockets in terms of the method of acceleration of the propellants: i.e. thermal acceleration, or electric acceleration. Thermally accelerated rockets are subclassified, in terms of the heat source, as either chemical or non-chemical. Chemical reaction rockets consist of solid propulsion and liquid propulsion categories. Non-chemical thermal rockets are divided into three categories: cold gas, nuclear heated, and electrically heated. Electrically heated rockets consist of resistojets and arc-jets. Electrically accelerated rockets utilize charged propellants which are accelerated by the application of an electrostatic or electromagnetic field.

Table 4-1 provides a list of the principal rocket propulsion systems and their basic characteristics. These characteristics include the kind of working fluid which provides the mass to be ejected, the energy source, the means of transmitting the energy to the working fluid, and the means of accelerating the working fluid to develop thrust. It is the differences in these basic characteristics that distinguish the various types of rocket systems, and that cause wide variations in the size, performance, and application range of the rocket propulsion systems. Each of the propulsion system types listed in the table are described briefly in the following paragraphs.

4-1.1 Chemical Rockets

The majority of rockets fall into the category of chemical rockets. In a chemical rocket, the propellants furnish both the mass and the energy required for propulsion. The chemical energy contained in the propellants is liberated by a reaction which may be in the form of a monopropellant decomposition, or the combustion of two or more propellants.

The earliest rockets were the solid-propellant chemical rockets. In these devices, the solid propellant, called the grain, is contained in a pressure vessel equipped with a nozzle at its aft end. When the solid grain is ignited, its chemicals react to produce heated gas. The propellant is reacted at a pressure higher than ambient, and the resultant gases are expanded and accelerated through the nozzle to produce thrust.

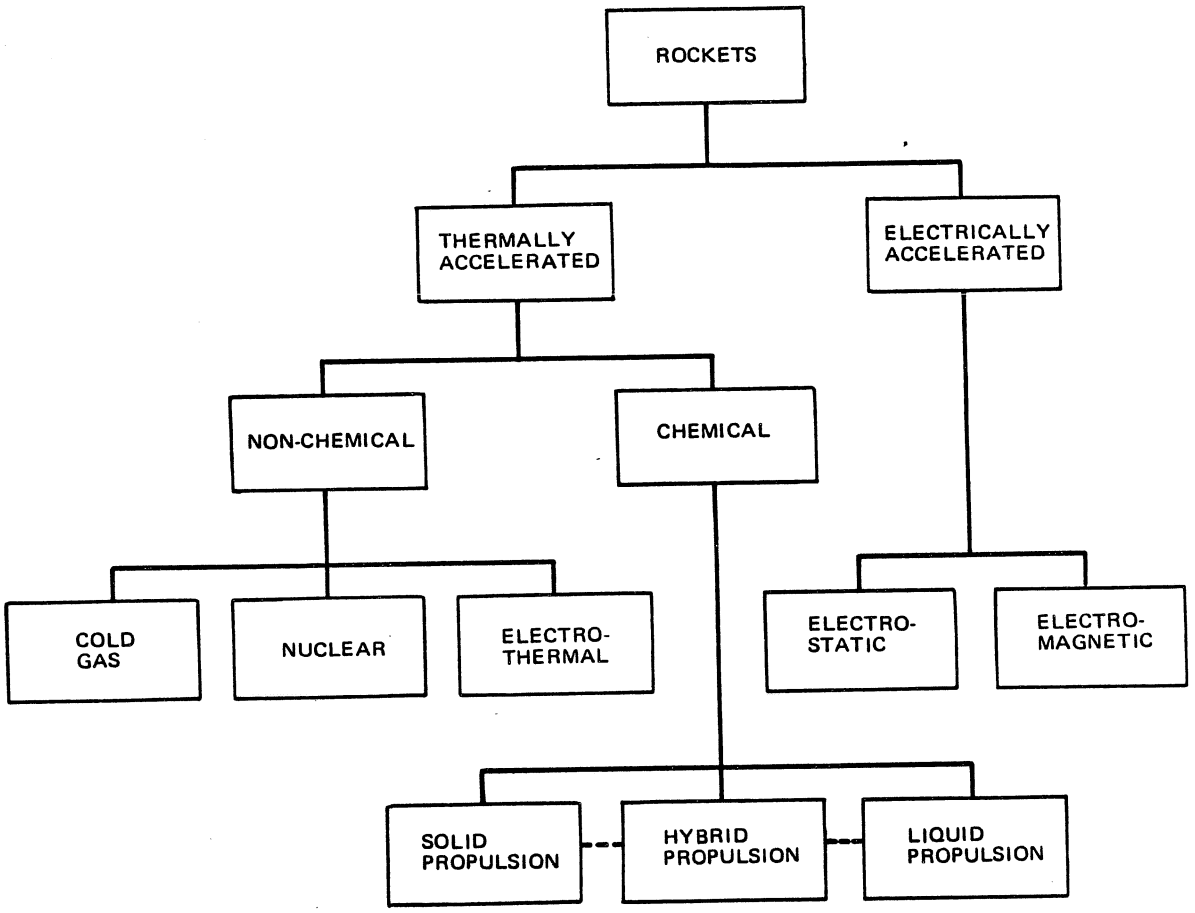

Figure 4-1. Rocket Propulsion Energy Sources

The liquid-propellant rocket is similar to the solid propellant rocket in principle, but differs in that usually two propellants are carried in separate storage tanks. During operation, the liquid propellants are introduced into a combustion chamber, where they react to produce (as in the solid rocket) heated gaseous products, which are expanded rearward through a nozzle. Liquid propellant systems contain a number of important subcategories, the most important of which relate to the character of the propellants used.

Monopropellant systems utilize the chemical energy released during the thermal decomposition of a single liquid, such as hydrogen peroxide, or hydrazine. Decomposition of the monopropellant is usually initiated by passing the propellant through a catalyst bed.

Bipropellant systems make use of two liquid propellants which release energy during combination. This exothermic combination is a mutual oxidation-reduction of the two propellants, and the propellants normally consist of a fuel and an oxidizer. Ignition of the fuel and oxidizer will occur spontaneously upon contact if the propellant combination is hypergolic. (Fuels which ignite spontaneously in air are said to be pyrophoric). If the propellants are not hypergolic, additional energy will have to be added to the propellant mixture in the combustion chamber by an igniter in order to initiate combustion.

Work has been accomplished on the use of more than two propellants in a liquid propellant system. To improve performance, these systems frequently include a metal, such as berylium, lithium, or boron.

Liquid propellant combinations are commonly classified as earth-storable, space-storable, or cryogenic. Cryogenic propellants are those that are liquid only at very low temperatures. A cryogenic propellant is usually defined as a liquid whose normal boiling point is less than 222°R (123°K). A storable propellant is defined as a fluid

which remains in its liquid state after it attains thermal equilibrium with its environment. This definition allows that the propellant tank may be insulated, and that any increase in propellant vapor pressure will be restricted to some reasonable value below its critical pressure. Under this definition, some cryogenic propellants are considered space storable.

A chemical rocket that combines a solid fuel with a liquid oxidizer is called a hybrid rocket. Hybrid rockets have some of the advantages of a liquid engine, such as stop, restart, and throttling capability; and some of the advantages of a solid motor, such as reduced complexity. Conversely, they have some of the disadvantages of a liquid engine, such as reduced reliability, and propellant positive expulsion requirements in zero-g environment; and some of the disadvantages of a solid motor, such as grain storage temperature limitations.

Additional information on chemical rockets is included in Section 5, Liquid Propulsion Systems, and Section 6, Solid Propulsion Systems.

4-1.2 Non-Chemical Thermal Rockets

Thermally accelerated rockets include several types of rockets which obtain propulsive energy from sources other than chemical combination of the propellants. The most common of these non-chemical thermal rockets are cold-gas, nuclear-heated, and electrothermal rockets. In the cold-gas rocket, thermal energy is stored in the gaseous propellant in the form of pressure energy; in the nuclear rocket, thermal energy is added to the propellant in the form of heat from a nuclear energy source; and in the electrothermal rocket, heat is added to the propellant from an electrical energy source.

4-1.2.1 Cold Gas Systems

Cold gas systems are rocket propulsion systems that develop reaction thrust by expanding a pressurized cold gas through a nozzle. A cold gas, loosely defined as any gaseous material utilized at room temperature or below, furnishes both the mass and the energy required for propulsion. Energy is stored in the cold gas in the form

Table 4-1. Characteristics of Principal Rocket Propulsion Systems

Rocket Propulsion System	Working Fluid	Energy Source	Means of Transmitting Energy to Working Fluid	Means of Accelerating Working Fluid
CHEMICAL SYSTEMS (Liquids and Solids)	Hot gaseous products of reacted chemical propellants	Chemical Energy of unreacted propellants	Conduction and radiation in the combustion chamber	Thermal expansion
COLD GAS SYSTEMS	Inert cold gas	Potential Energy of gas stored at high pressure	None required	Thermal expansion
NUCLEAR ROCKETS	Heated low molecular weight gas	Heat from nuclear reactor or decay of radioactive isotope	Conduction and radiation in the reactor	Thermal expansion
ELECTRICAL ROCKETS Resistojet	Heated low molecular weight gas, or biowaste gases	Electrical energy from solar cells or fuel cells	Resistive heating element	Thermal expansion
Arc-jet	Heated low molecular weight gas	Heat from nuclear reactor converted to electrical energy	Electrical arc	Thermal expansion
Plasma Thruster	Plasma (high temperature, electrically neutral gas containing electrons, ions, and neutral species)	Same as arc-jet	Electromagnetic field, plus electrical arc	Electromagnetic compression and acceleration, plus thermal expansion
Ion Thruster	High temperature gaseous ions (usually of alkaline metals)	Same as arc-jet	Electrostatic field	Electrostatic acceleration
Colloid Thruster	Cold liquid spray of charged particles	Same as arc-jet or resistojet	Electrostatic field	Electrostatic acceleration

of potential energy due to compression of the gas. Nitrogen and helium are the most common cold gases now in use.

This category of propulsion system also includes the liquified gases and subliming solids that have been proposed to optimize gas storage. These liquids and solids change to the gaseous state at the temperature and pressure at which they are used. The operating temperature of a cold-gas system is generally at, or lower than, 530°R. Heating of the propellant by the ambient environment occurs only if the propellant temperature drops significantly below ambient.

Additional information on cold-gas systems is included in Section 7, Cold Gas Propulsion Systems.

4-1.2.2 Nuclear Rockets

In a nuclear rocket, heat energy from a nuclear power source is transmitted to a working fluid by means of a heat exchanger. The working fluid is heated to a high temperature at high pressure, and is then ejected through a nozzle, as in the chemical rocket. However, nuclear energy has far more potential than the energy of chemical propellants. For example, the fission of uranium-235 releases 10^7 times the energy of a chemical reaction from the same mass of propellant. Even though much of this energy is not usuable, nuclear rockets are capable of significantly higher performance than chemical rockets.

The major category of today's nuclear rockets utilizes the heat generated by fission in a reactor to raise the temperature of a working fluid such as hydrogen. The reactor is of the solid core type, with the fissionable material embedded in a matrix of graphite. Other concepts, not yet proven, include the use of tungsten as the solid core material, and the use of liquid and gaseous core reactors.

Nuclear reactors are capable of heating propellants to very high temperatures, but, in practice, propellant temperature must be limited to avoid exceeding the safe working temperature of the structural elements of the reactor. Since heat always flows from a hotter to a cooler region, the heat-transfer surface must always be at a higher temperature than the gaseous propellant. This limits the gas temperature attainable to less than the melting point of the most refractory solid suitable for the purpose, and therefore limits the performance that can ultimately be developed by the rocket.

Another type of nuclear rocket is the radioisotope rocket. Radioisotope rockets utilize the energy released by the decay of radioactive isotopes to heat the working fluid. Radioisotope systems are currently under development for use as auxiliary propulsion and power devices.

Additional information on nuclear rockets is included in Section 8, Nuclear Propulsion Thrusters.

4-1.2.3 Electrothermal Thrusters

In electrothermal systems, the working fluid is heated electrically at high pressure, and accelerated by thermal expansion through a supersonic nozzle. The principal electrothermal thrusters are the resistojet and the arc-jet. The resistojet uses a resistive heating element to heat the working fluid, and the arc-jet utilizes an electric arc.

Electrothermal thrusters obtain the energy for heating of the propellants from an external electrical power source. Since such power sources are heavy, the use of electrothermal rockets may be limited to applications which require an electric power supply for other purposes, and which can make this power supply available to the rocket when required.

The resistojet and the arc-jet are generally limited to thrusts of less than one pound. The resistojet may be used with a variety of propellants including stored gas, vaporized liquids, and biowaste products. Its specific impulse is about 800 sec for hydrogen, and less for denser propellants. Arc-jets are capable of somewhat higher specific impulse but have larger power requirements than resistojets. Arc-jet development is currently inactive.

Additional information on electrothermal rockets is included in Section 9, Electric Propulsion Thrusters.

4-1.3 Electric Acceleration Rockets

Electric acceleration rockets use electrical, rather than thermal, energy to accelerate the propellant. There are two general categories of electric acceleration rockets: electrostatic, and electromagnetic thrusters.

4-1.3.1 Electrostatic Thrusters

Electrostatic thrusters are characterized by the use of an electrostatic field, or direct-current potential, to accelerate the working fluid. There are two important categories of propulsion systems that use electrostatic acceleration, i.e., the ion propulsion system, and the colloid thruster.

The ion propulsion system has three basic elements:

a. The ionizer, consisting of a device to ionize neutral matter and separate the positive ions from the electrons for subsequent separate acceleration.

b. The accelerator, which accelerates the ions produced by the emitter to the velocity required by the mission specific impulse requirements.

c. The beam neutralizer, which recombines the positive ions and the electrons to insure that the net charge of the propellant leaving the vehicle is neutral. This minimizes the build-up of space charge on the vehicle which would reduce propulsion system performance.

The prototype ion propulsion systems are further distinguished by the type of ionizer used as either electron-bombardment thrusters, or contact-ion thrusters.

The second general category of electrostatic propulsion systems is the colloid system, or charged-particle electrostatic thruster. This device uses a cold charged liquid spray as the working fluid, and electrostatically accelerates the fluid particles to produce thrust. The electrical colloid system provides light-weight auxiliary propulsion for spacecraft applications. Colloid thrusters are in an earlier stage of development than ion thrusters. Colloid thrusters have a lower thrust level and lower performance, but they are simpler, operate at low temperature, and have smaller power requirements than ion thrusters.

4-1.3.2 Electromagnetic Thrusters

Electromagnetic thrusters achieve acceleration by the interaction of magnetic fields on propellant plasma. A plasma is a high-temperature, electrically neutral gas containing electrons, ions, and neutral species. When a conductor located in a magnetic field carries a current, a force is exerted on the conductor at right angles to both the conductor and to the magnetic field. By utilizing a plasma as the conductor, it is possible to accelerate the plasma and thus attain very high gas velocities.

There are three mechanisms by which the plasma engines produce thrust:

a. Arc heating of the gas, followed by an adiabatic expansion to convert the heat energy to direct kinetic energy.

b. Electromagnetic compression of the gas by a radially inward directed electromagnetic pinch force, followed by an expansion and acceleration in the axial direction.

c. Direct acceleration of the gas in the thrust direction by the axial components of the electromagnetic forces acting on the gas.

Research and development is currently under way on several variations of electromagnetic thrusters, most of which make use of all three of these mechanisms in varying proportions. These systems are called plasma thrusters, magnetoplasmadynamic (MPD) thrusters, magnetohydrodynamic (MHD) thrusters, magnetogasdynamic (MGD) thrusters, and pinch effect thrusters.

Electromagnetic thrusters offer much promise for low thrust, high performance space propulsion due to their potentially high efficiency and relatively low power requirements. However, these systems are still in the early stages of development.

Additional information on electric acceleration rockets is included in Section 9.

4-2 ROCKET PERFORMANCE

Nearly all of the rockets currently in operation, or available in the near future, employ thermal expansion to develop thrust. These include cold gas, all chemical, nuclear, and electrothermal rockets. The basic equations for ideal rocket performance that follow are, in general, only applicable to thermal engines. Performance analysis relationships for the electrical acceleration rockets have been included in Section 9.

The ideal rocket equations are derived based upon several assumptions:

a. The working fluid is a homogeneous gas, obeying the perfect gas laws, throughout the chamber and nozzle.

b. There is no friction, and no heat transfer across the walls. The flow is therefore isentropic.

c. The flow is one-dimensional through the chamber and nozzle.

The performance calculated from these relationships reproduces actual rocket performance within 1 to 10 percent.

The symbols used in the equations are:

Symbols:

A	Area, in^2
c	Effective exhaust velocity, ft/sec
c^*	Characteristic velocity, ft/sec
C_F	Thrust coefficient
F	Thrust, lb
g	Gravitational acceleration, ft/sec^2
I_{sp}	Specific impulse, lb-sec/lb, or sec
I_t	Total impulse, lb-sec
$\dot{m}$	Mass flowrate, lb-sec/ft
M	Molecular weight, lb/mole
P	Pressure, lb/in^2 absolute
R	Gas constant, ft-lb/lb-°R
r	Vehicle mass ratio
T	Temperature, °R
t	Time, sec

v	Velocity, ft/sec
w	Weight, lb
$\dot{w}$	Weight rate of flow, lb/sec
γ	Ratio of specific heats
ϵ	Nozzle expansion ratio
λ	Propellant loading factor

Subscripts:

a	Ambient
c	Chamber outlet (nozzle inlet)
e	Nozzle exit
t	Nozzle throat

The system of physical units used is discussed in Section 16.

4-2.1 Thrust

The equation for thrust of a rocket engine is derived by integration of the pressure forces acting over the internal and external surfaces of the thrust chamber, which results in the equation:

$$F = \dot{m}v_e + (P_e - P_a)\,A_e \qquad (1)$$

The first term is usually referred to as the momentum thrust since it is the net momentum increase of the exhaust gases accelerated and exhausted from the nozzle.

The second term, the pressure thrust, consists of the product of the cross-sectional area of the exhaust jet leaving the nozzle, and the difference between the exhaust pressure and the ambient pressure.

When the ambient pressure is equal to the exhaust pressure, the pressure thrust term is zero, and the thrust is expressed as:

$$F = \dot{m}v_e = \frac{\dot{w}}{g}\,v_e \qquad (2)$$

This condition gives the maximum thrust for a given ambient pressure. A nozzle expansion ratio designed to allow the expansion of the propellant products to the exact pressure of the surrounding fluid is referred to as the optimum expansion ratio.

The effective exhaust velocity is defined by the equation:

$$c = \frac{Fg}{\dot{w}} = v_e + \frac{(P_e - P_a)A_e g}{\dot{w}} \qquad (3)$$

and can be determined from thrust and propellant-flow measurements. When $p_e = p_a$, the effective exhaust velocity, c, is equal to the exhaust velocity of the propellant gases, v_e.

4-2.2 Thrust Coefficient

A useful equation for the thrust of a rocket engine may be expressed as a function of throat area, effective chamber pressure, and the important performance parameter, thrust coefficient

$$F = P_c A_t C_F \qquad (4)$$

The thrust coefficient, C_F, defined by this equation represents the performance augmentation due to the nozzle. The values of C_F are usually greater than one and less than two. Thrust coefficient can be evaluated theoretically by the expression:

$$C_F = \sqrt{\frac{2\gamma^2}{\gamma-1}\left(\frac{2}{\gamma+1}\right)^{\frac{\gamma+1}{\gamma-1}}\left[1-\left(\frac{P_e}{P_c}\right)^{\frac{\gamma-1}{\gamma}}\right]} + \frac{P_e - P_a}{P_c}\,\frac{A_e}{A_t} \qquad (5)$$

The first term represents the contribution of the momentum thrust, and the second term the pressure thrust.

The ratio of nozzle exit area to throat area is usually referred to as the nozzle expansion ratio, or area ratio:

$$\epsilon = A_e/A_t \qquad (6)$$

The nozzle expansion ratio is of particular importance because it determines the exit pressure ratio, P_e/P_c, of the nozzle for a given specific heat ratio. Thus, thrust coefficient is seen to be a function of the ratio of the specific heats, γ, the expansion ratio, ϵ, and the ambient pressure ratio, P_a/P_c.

Figure 4-2 shows the variation of thrust coefficient with respect to area ratio and ambient pressure ratio for a γ of 1.2. From this figure it can seen that at a fixed ambient pressure ratio ($0 < P_a/P_c < 1$), the value of thrust coefficient as a function of expansion ratio has a single maximum. This maximum point is called the optimum thrust coefficient for the given ambient pressure ratio. The optimum thrust coefficient corresponds to the optimum expansion ratio, where exit pressure equals ambient pressure, and the second term of the C_F equation 5 vanishes.

Vacuum thrust coefficient results when the ambient pressure is equal to zero. From Figure 4-2 it can be seen that C_F increases as ambient pressure decreases, approaching the vacuum thrust coefficient ($P_a/P_c = 0$) as a limit. For any finite expansion ratio, vacuum C_F is greater than optimum C_F, since optimum C_F, by definition, is based upon an ambient pressure greater than zero.

As the expansion ratio is increased, optimum C_F approaches vacuum C_F. As expansion ratio approaches infinity, both optimum C_F and vacuum C_F approach a limit, sometimes called C_F ultimate, which consists of the first two terms under the radical in equation 5. For either optimum or vacuum conditions, the thrust coefficient equation can be reduced to a function of nozzle expansion ratio, ϵ, and ratio of specific heats, γ, facilitating nozzle performance trade-off analyses.

In Figure 4-3, values of optimum thrust coefficient are shown plotted as a function of exit pressure ratio for a range of nozzle expansion ratios and specific heat ratios. Nozzle expansion ratio is fixed by the physical nozzle geometry, which is often limited by packaging and weight constraints of the rocket engine in the vehicle. Specific heat ratio, γ, is a function of the combustion gas properties only, and is determined by the propellant combination selected, and by the state of completion of the combustion process. Values of γ for combustion gases range from about 1.2 for most solid propellants, to 1.3 for most liquid propellants. For cold gases, representative specific heat ratios are about 1.1 for butane and propane, 1.4 for air and nitrogen, and 1.66 for helium and argon.

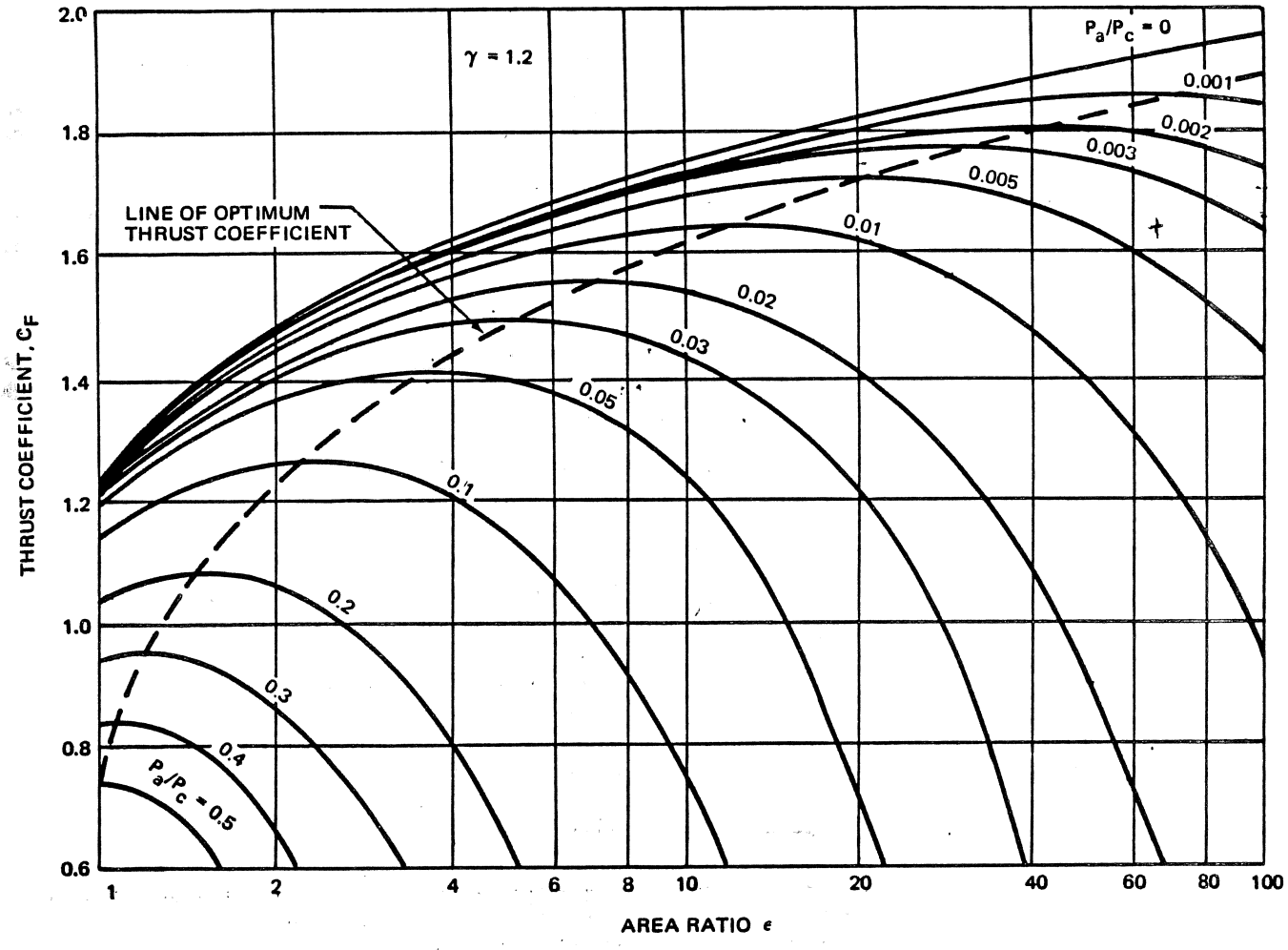

Figure 4-2. Thrust Coefficient versus Area Ratio

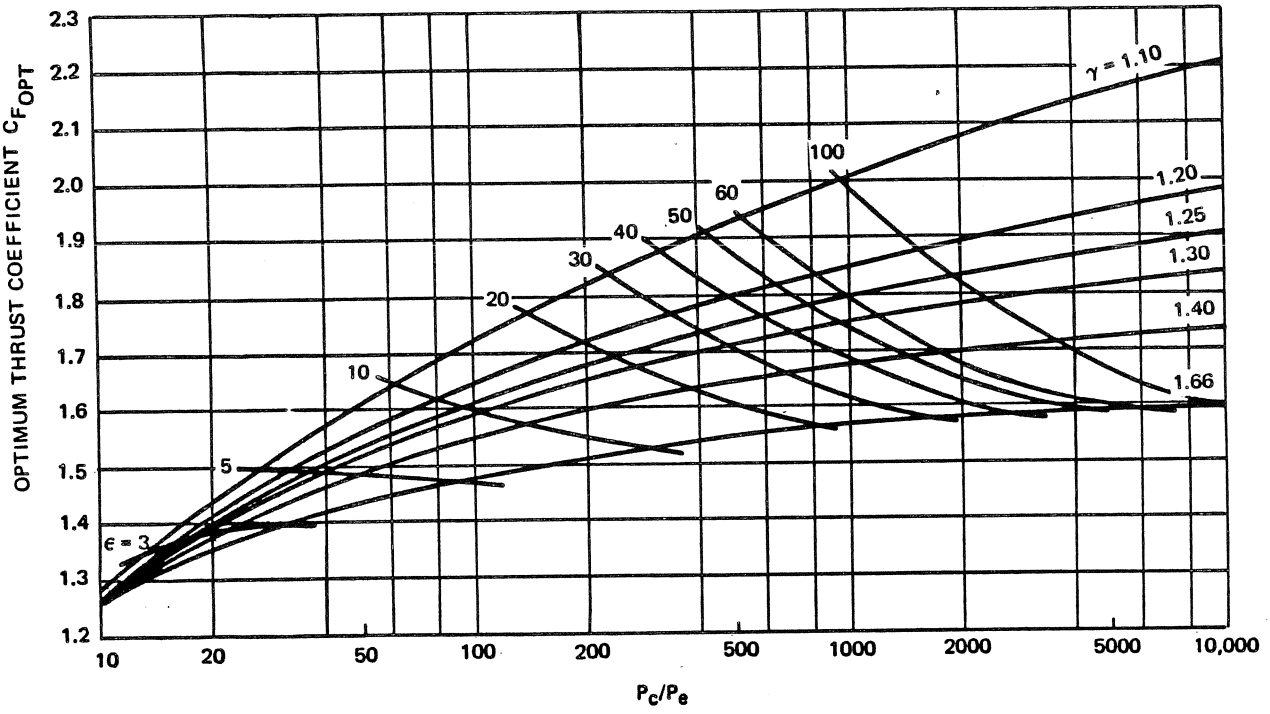

Figure 4-3. Optimum Thrust Coefficients

4-2.3 Characteristic Exhaust Velocity

Characteristic exhaust velocity is defined by the expression:

$$c^* = \frac{P_c A_t g}{\dot{w}} \tag{7}$$

The weight flowrate, $\dot{w}$, through the combustion chamber and nozzle can be calculated from:

$$\dot{w} = P_c A_t \sqrt{\frac{\gamma g}{RT_c}\left(\frac{2}{\gamma+1}\right)^{\frac{\gamma+1}{\gamma-1}}} \tag{8}$$

For given gas properties and chamber temperature, the flow through a supersonic nozzle is a function of two parameters: it varies directly with the throat area and the chamber pressure at the nozzle inlet. As long as the flow in the nozzle throat remains sonic, an increase or decrease in downstream pressure will not affect the flowrate, and the nozzle is referred to as being chocked. Substituting equation 8 into equation 7, c^* can be evaluated theoretically as:

$$c^* = \sqrt{\frac{gRT_c}{\gamma\left(\frac{2}{\gamma+1}\right)^{\frac{\gamma+1}{\gamma-1}}}} \tag{9}$$

From equation 9, characteristic exhaust velocity is seen to be a function only of the gas properties and the temperature at the nozzle inlet. In chemical rockets, propellant combinations producing high combustion temperatures and low values of molecular weight are necessary to achieve high values of c^*. Thus c^* is often used as a measure of effectiveness for the combustion process.

4-2.4 Specific Impulse

The overall performance of a rocket engine is most commonly expressed by a term called the specific impulse which is the thrust delivered for each pound per second of propellant expended. It is defined by the equation:

$$I_{sp} = F/\dot{w} = c/g \tag{10}$$

A theoretical expression for specific impulse can be developed from equation 10 as:

$$I_{sp} = \sqrt{\frac{RT_c}{g}\left(\frac{2\gamma}{\gamma-1}\right)\left[1-\left(\frac{P_e}{P_c}\right)^{\frac{\gamma-1}{\gamma}}\right]} + \frac{P_e - P_a}{\dot{w}} A_e \qquad (11)$$

At optimal expansion, the right-hand term vanishes.

Recall that the gas constant, R, can be expressed as the universal gas constant divided by the molecular weight, M, of the exhaust products. Also the exit pressure ratio, P_e/P_c, is determined by the nozzle geometry. Thus, as a rough approximation, the specific impulse is proportional to $\sqrt{T_c/M}$.

As a measure of the overall performance of the rocket engine, specific impulse is a function of the performance of both combustion chamber and the nozzle. Thus specific impulse may be expressed in terms of the product of c^* and C_F as:

$$I_{sp} = c^* C_F/g \qquad (12)$$

4-2.5 Total Impulse

Total impulse is the integral of the thrust over the operating time. It can also be defined as a function of specific impulse:

$$I_t = \int_o^t F dt = \int_o^t I_{sp}\,\dot{w} dt \qquad (13)$$

In solid-propellant rockets, the flowrate is difficult to determine. Therefore, the total impulse is usually determined by integrating the area under the thrust-time curve from the motor firing record.

For convenience, the most often used rocket equations are listed in Table 4-2, arranged to facilitate evaluation of the specific parameters in the left-hand column, given the values of the various parameters listed in the top row.

4-2.6 Impulsive Velocity

The importance of specific impulse to vehicle performance can be evaluated in terms of its effect on impulsive velocity. Impulsive velocity is defined as the ideal velocity increase, Δv, that would be realized if all the propulsive impulse were converted into vehicle velocity. The relationship between impulsive velocity and specific impulse is obtained by integrating the reaction thrust equation, neglecting the effects of gravitational attraction and aerodynamic drag. This integration results in equation 14.

$$\Delta v = g\, I_{sp} \log_e\left(\frac{w_{Launch}}{w_{Burnout}}\right) \qquad (14)$$

where:

Δv = Impulsive velocity increment, ft/sec

w_{Launch} = Vehicle initial or launch weight, lb

$w_{Burnout}$ = Vehicle final or burnout weight, lb

The ratio of vehicle launch-to-burnout weight is also known as the vehicle mass ratio, or:

$$r = w_{Launch}/w_{Burnout} = \frac{1}{1-\lambda} \qquad (15)$$

where:

λ = Vehicle mass fraction, the ratio of propellant weight (available to produce thrust) to vehicle launch weight.

From equation 14 it can be seen that impulsive velocity is more sensitive to change in specific impulse than it is to change in mass ratio. Figure 4-4 is a plot of stage Δv as a function of specific impulse and mass ratio.

4-2.7 Thrust-To-Weight Ratio

The thrust-to-weight ratio of a rocket is defined by the expression

$$F/w = \frac{F}{w_{pl} + w_p + w_s + w_{ps}} \qquad (16)$$

where:

F = Engine thrust, lb

w_{pl} = Payload weight, lb

w_p = Weight of propellant, lb

w_s = Weight of structure and miscellaneous, lb

w_{ps} = Propulsion system dry weight, lb

Table 4-2. Rocket Engine Formulas

	A_t Throat Area in^2	c Exhaust Velocity ft/sec	c^* Characteristic Exhaust Velocity ft/sec	C_F Thrust Coefficient	F Thrust lb	I_{sp} Specific Impulse sec	P_c Chamber Pressure psia	$\dot{w}$ Weight Flowrate lb/sec
$A_t =$	—	$\frac{c\dot{w}}{P_c C_F g}$	$\frac{c^*\dot{w}}{P_c g}$	$\frac{F}{P_c C_F}$	$\frac{F}{P_c C_F}$	$\frac{I_{sp}\dot{w}}{P_c C_F}$	$\frac{F}{P_c C_F}$	$\frac{c^*\dot{w}}{P_c g}$
$c =$	$\frac{P_c A_t C_F g}{\dot{w}}$	—	$c^* C_F$	$c^* C_F$	$\frac{F g}{\dot{w}}$	$I_{sp} g$	$\frac{P_c A_t C_F g}{\dot{w}}$	$\frac{F g}{\dot{w}}$
$c^* =$	$\frac{P_c A_t g}{\dot{w}}$	$\frac{c}{C_F}$	—	$\frac{c}{C_F}$	$\frac{F g}{C_F \dot{w}}$	$\frac{I_{sp} g}{C_F}$	$\frac{P_c A_t g}{\dot{w}}$	$\frac{F g}{C_F \dot{w}}$
$C_F =$	$\frac{F}{P_c A_t}$	$\frac{c}{c^*}$	$\frac{c}{c^*}$	—	$\frac{F}{P_c A_t}$	$\frac{I_{sp} g}{c^*}$	$\frac{F}{P_c A_t}$	$\frac{F g}{c^* \dot{w}}$
$F =$	$P_c A_t C_F$	$\frac{c\dot{w}}{g}$	$\frac{c^* C_F \dot{w}}{g}$	$P_c A_t C_F$	—	$I_{sp}\dot{w}$	$P_c A_t C_F$	$I_{sp}\dot{w}$
$I_{sp} =$	$\frac{P_c A_t C_F}{\dot{w}}$	$\frac{c}{g}$	$\frac{c^* C_F}{g}$	$\frac{c^* C_F}{g}$	$\frac{F}{\dot{w}}$	—	$\frac{P_c A_t C_F}{\dot{w}}$	$\frac{F}{\dot{w}}$
$P_c =$	$\frac{F}{A_t C_F}$	$\frac{c\dot{w}}{A_t C_F g}$	$\frac{c^*\dot{w}}{A_t g}$	$\frac{F}{A_t C_F}$	$\frac{F}{A_t C_F}$	$\frac{I_{sp}\dot{w}}{A_t C_F}$	—	$\frac{c^*\dot{w}}{A_t g}$
$\dot{w} =$	$\frac{P_c A_t g}{c^*}$	$\frac{F g}{c}$	$\frac{F g}{c^* C_F}$	$\frac{F g}{c^* C_F}$	$\frac{F}{I_{sp}}$	$\frac{F}{I_{sp}}$	$\frac{P_c A_t g}{c^*}$	—

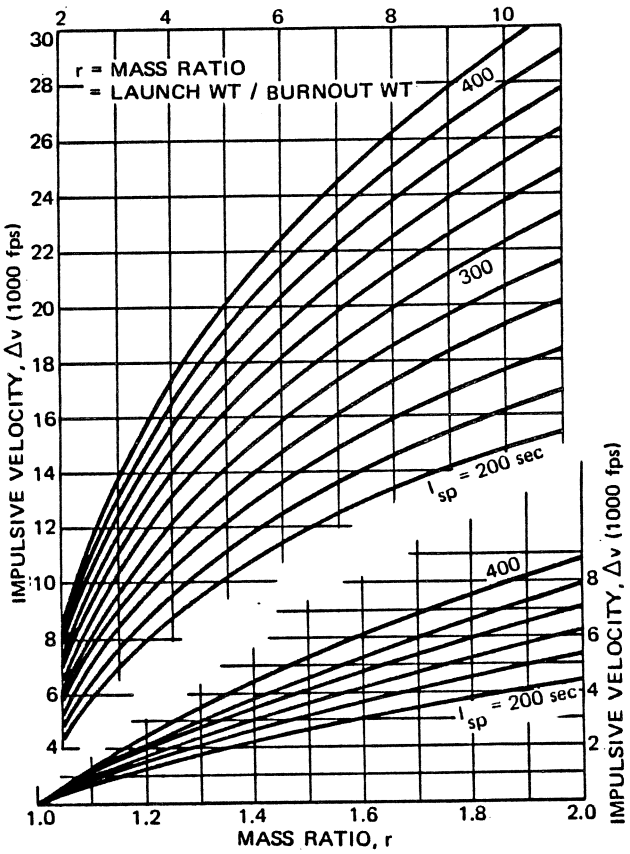

Figure 4-4. Impulsive Velocity Increment Data

The thrust-to-weight ratio is the parameter which describes the acceleration capability of a rocket. This ratio generally increases during the operation of a propulsive stage, because the vehicle weight decreases as the propellant is expended and the engine thrust remains essentially constant.

The thrust-to-weight ratio is particularly useful in evaluating vehicle performance in a strong gravitational field. For example, the thrust of the first stage must be greater than the weight of the total vehicle (thrust-to-weight ratio greater than one) for the vehicle to rise off the ground. When the vehicle has entered a trajectory that has a tangential velocity component, the resultant centrifugal force tends to counteract the gravitational force acting on the vehicle. Therefore the thrust-to-weight ratio of an upper stage may be less than one, and is usually based on acceleration requirements.

The thrust-to-weight ratio of a space vehicle, which operates in a very low gravity field, is generally considerably less than one. Specific impulse and total impulse are generally more significant design parameters for this type of application.

4-2.8 Propulsion System Performance

The net performance of a propulsion system is measured by the thrust, the specific impulse, and the thrust-to-weight ratio of the system. The typical ranges of thrust, specific impulse, and thrust-to-weight ratios for different types of rocket engines are listed in Table 4-3, and are shown graphically in Figure 4-5.

From Figure 4-5 it can be seen that the chemical rockets, and to some extent the nuclear rockets, have relatively low values of specific impulse. On the other hand, these systems offer relatively low propulsion system weights and high thrust capabilities, and therefore have high thrust-to-weight ratios. At the other end of the scale, the electrical propulsion devices have very high specific impulses, but low thrust-to-weight ratios. These devices require heavy electrical power sources to deliver the energy needed for high expulsion velocities.

Specific impulse is an important propulsion system design parameter because it provides a measure of the efficiency with which propellant mass is ejected. The usefulness of a rocket propulsion system is limited by its efficient expenditure of propellant mass, because the rocket must carry within itself all the mass needed to develop propulsive reaction.

Since the specific impulses of the advanced electrical rocket engines are appreciably higher than those of chemical or nuclear rockets, they expend relatively small quantities of propellant to develop thrust. However, the low acceleration potential of the electrical propulsion systems dictates a long period of time for acceleration, and relegates these engines to missions with long flight times in weak gravitational fields.

Typical impulsive velocity requirements for a range of missions are listed in Table 4-4. Figure 4-6 shows the effects of mass ratio variations on impulsive velocity for a range of specific impulses. For comparative purposes, the various categories of propulsion systems have been listed on this curve at their approximate specific impulse values. Included for reference are typical ranges of impulsive velocity versus mass ratio for the SIVB stage of the Saturn launch vehicle, and for the second stage of the Delta launch vehicle. For each of these stages, an increase in mass ratio (decrease in payload) results in an increase in impulsive velocity. For a given mass ratio, the SIVB stage delivers a higher impulsive velocity than the Delta second stage because it has a higher specific impulse.

The theoretical curves of Figure 4-6 represent families of single-stage, constant-specific-impulse vehicles. In practice, when large impulsive velocities are required, multistage vehicles are used. After the propellant is consumed in each stage, the empty stage is discarded,

Table 4-3. Typical Performance Parameters for Rocket Propulsion Systems

Rocket Propulsion System	Thrust (lb)	Specific Impulse (sec)	Thrust-to-Weight Ratio	Duration	State-of-the-Art
CHEMICAL ROCKETS	<1 to $>10^6$	200 to 500	10^{-2} to 100	Seconds to Hours	Off-the-Shelf
COLD GAS SYSTEMS	0.1 to 10	50 to 180	10^{-2} to 1	Seconds	Off-the-Shelf
NUCLEAR ROCKETS					
Fission	10^4 to 10^6	500 to 1,000	10^{-2} to 30	Seconds to Hours	Flight Prototype
Radioisotope	<1	500 to 1,000	10^{-5} to 10^{-3}	Days	Flight Prototype
ELECTRICAL ROCKETS					
Resistojet	<1	300 to 1,000	10^{-4} to 10^{-1}	Days	Flight Prototype
Arc-jet	10^{-1} to 10^{0}	750 to 2,500	10^{-4} to 10^{-2}	Days	Experimental
Ion Thruster	10^{-3} to 10^{-2}	4,000 to 25,000	10^{-5} to 10^{-3}	Months	Flight Prototype
Colloid Thruster	10^{-4} to 10^{-3}	1,000 to 8,000	10^{-4} to 10^{-2}	Months	Experimental
Plasma Thruster	10^{-3} to 10^{-1}	1,000 to 15,000	10^{-5} to 10^{-3}	Weeks	Advanced Concept/ Experimental

and operation of the succeeding stage is initiated. Staging the vehicles permits adding the impulsive velocity increments of each successive stage to the payload to attain the required velocity with a lighter weight vehicle.

In theory, maximum performance is achieved with an infinite number of stages, but the performance gain obtained by adding additional stages decreases rapidly after the first few stages. In practice, vehicles rarely have more than three or four stages because the small additional performance achievable by adding one more stage is not justified by the added complexity and cost.

The vehicle burnout velocity is equal to the sum of the velocity increments imparted by each stage:

$$v_{Burnout} = \Delta v_1 + \Delta v_2 + \cdots + \Delta v_{final} \qquad (17)$$

The ideal impulsive velocity increment of each stage is determined by its mass ratio and the specific impulse of its propulsion system as described in equation 14. The selection of the specific impulse and mass ratio for each stage is dependent on many factors, including the availability of existing hardware. If each of the stages has the same mass ratio and the same specific impulse, each stage will contribute equally to the burnout velocity.

If the stage mass ratios are equal, a given percentage increase in specific impulse of the propulsion system of any one of the stages will result in the same increase in payload burnout velocity. However, if the stage mass ratios are not equal, the greatest increase in burnout velocity will be obtained if the specific impulse improvement is applied to the stage with the highest mass ratio.

If the specific impulse is the same for the propulsion system of each stage, a given improvement in mass ratio of any one of the stages will result in the same increase in burnout velocity. However, if the stage specific impulses are not equal, the greatest increase in burnout velocity will be achieved if the mass ratio improvement is applied to the stage with the highest propulsion specific impulse.

Upper stages usually have higher specific impulses than lower stages when both use the same propellants because the upper stages operate in a vacuum. Therefore, if an

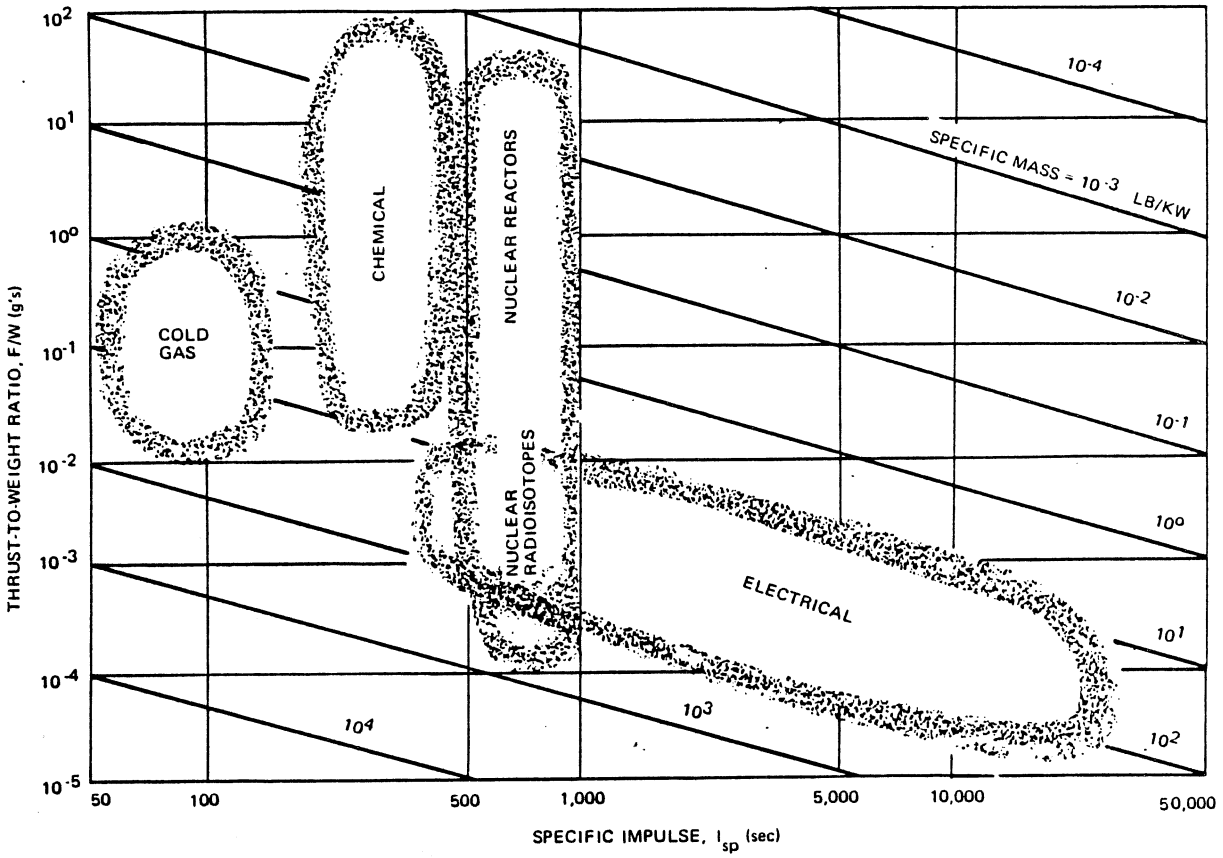

Figure 4-5. Potential Performance of Various Propulsion Systems

Table 4-4. Velocity Requirements for Several Missions

Mission	Total Velocity (fps)
IRBM (1000 NM range)	12,000
ICBM (5000 NM range)	24,000
Earth Satellite (300 NM orbit)	26,000
Earth Escape, or Lunar Impact	36,000
Mars or Venus Rendezvous	38,000
Lunar Excursion	53,000
Venus Excursion	76.000

increase in burnout velocity is sought, it is generally attractive to evaluate an upper stage first, for potential improvement in mass ratio, or for the use of more energetic (higher c*) propellants.

A desired change in stage mass ratio can be achieved with a smaller reduction in inert weight of an upper stage than a lower stage. For example, a decrease of one pound of inert weight of the final propulsive stage permits an increase of one pound in payload weight without change in burnout velocity; but a one-pound reduction of inert weight in the next lower stage permits a one pound weight increase in the final stage, which theoretically must be shared by propellant, structure, and the payload. If the propulsive performance of the final stage is to be unchanged, the fraction of this added pound which can be assigned to increased payload is $1/r_{final}$, where r_{final} is the mass ratio of the final stage.

For a given vehicle impulse level, a trade can be made between payload weight and burnout velocity, as shown by the curves in Figure 4-7. For example, at the constant impulse level represented by curve A, the payload can be increased, with a resulting decrease in burnout velocity, by moving from the design point to point 1. Conversely, burnout velocity can be increased to point 2 for the indicated decrease in payload weight.

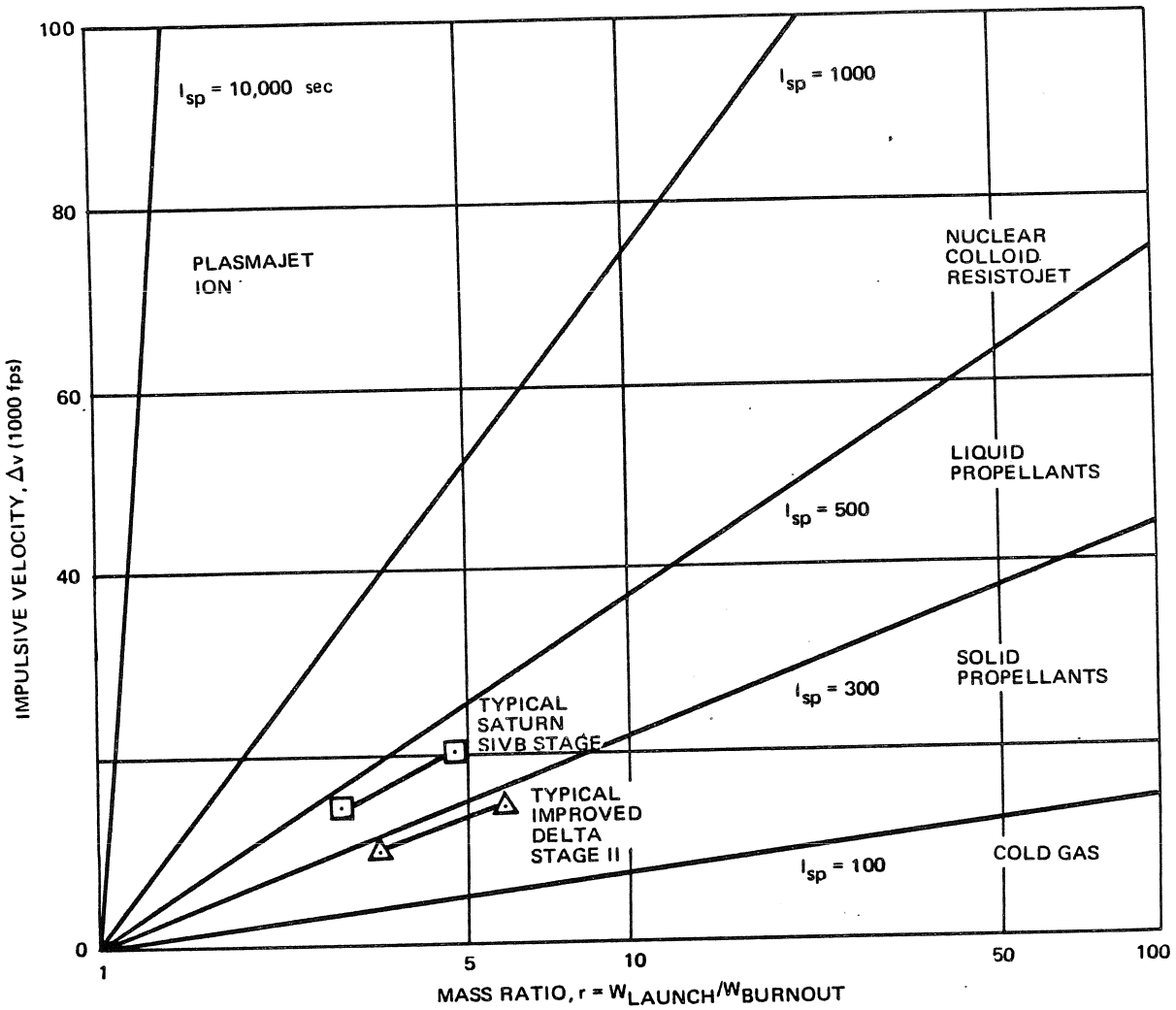

Figure 4-6. Impulsive Velocity versus Mass Ratio

The vehicle impulse level can be increased to the condition described by curve B by increasing mass ratio or specific impulse, or both. Payload weight can then be increased without change in burnout velocity, as indicated by point 3, burnout velocity can be increased without change in payload, point 4, or any other payload and burnout velocity combination which lies on curve B can be achieved.

The foregoing discussion of vehicle performance is based on the impulsive velocity equation 14 which excludes gravity and aerodynamic drag effects. This equation is useful for understanding the relative effects of changing mass ratio and specific impulse. However, in the evaluation of real vehicles, gravitational and aerodynamic drag effects must also be included in determining the payload burnout velocity achievable on a given launch vehicle. These effects are most pronounced on the first stage. Thrust level and initial propellant weight also affect performance because they modify the shape of the optimum trajectory and thus influence the magnitude of the gravity effect.

4-3 PROPULSION SYSTEM APPLICATIONS

Propulsion system applications can be divided into two broad categories: primary thrust, and attitude control. Primary thrust is concerned with imparting a net velocity change, and steering, to the vehicle. Attitude control is concerned with maintaining a selected vehicle orientation.

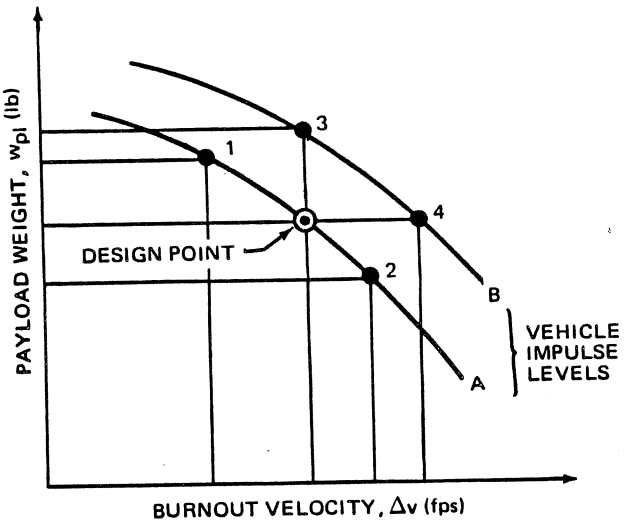

Figure 4-7. Payload Weight versus Burnout Velocity

Primary thrust generally is held constant. However, in some applications it is necessary to vary primary thrust over a wide range. The method selected to vary the thrust level, or throttle the rocket engine, is dependent on the type of propulsion system used. For example, chemical rockets usually have constant throat areas, and throttling of an individual thruster is accomplished by control of its combustion pressure. The combustion pressure of a chemical rocket is a function of the mass rate of propellant combustion. In liquid rockets, propellant mass flowrate into the combustion chamber is generally controlled by throttle valves in the propellant feed system. In solid rockets, the rate of propellant combustion may be varied by tailoring the grain design to provide the desired variation in burning surface, or by the use of layers of propellant that have different burning rates at the pressures being produced.

Steering consists of controlling the direction of the vehicle velocity vector. During operation of the primary propulsion system, steering is usually accomplished by actuation of auxiliary devices which deflect the primary exhaust, and the thrust vector, with respect to the vehicle centerline, thus producing turning forces and a change in the direction of the vehicle. This is called thrust vector control. When the primary propulsion system is not operating, aerodynamic control surfaces may be used if the vehicle is within the atmosphere. Outside the atmosphere, a secondary propulsion system must be used to provide any necessary steering.

Figure 4-8 presents a typical arrangement of an attitude control system (ACS), and means of increasing or decreasing vehicle velocity. During powered flight, pitch and yaw control is obtained by gimballing the primary thruster, and roll control is obtained by operating the ACS roll thrusters. When the primary thruster is not operating, pitch, yaw, and roll control is obtained by operating the appropriate ACS thrusters. In this arrangement, the roll thrusters are operated in pairs to produce rotation without translation. The pitch and yaw thrusters are operated individually, which causes some translation as well as rotation. However, the translation will be small if the distance between the thruster and the vehicle center-of-gravity is large, particularly if the thrust-to-weight ratio is small. If pure rotation is also required on the pitch and yaw axes, additional thrusters must be provided for paired operation.

Two other relatively low thrust applications involve a small increase or decrease in vehicle velocity along the vehicle axis, without rotation. Thrusters for these applications are identified in Figure 4-8 as Δv and retro. The retro function may be used to separate a spent stage from the upper stages or the payload. The retro function in decreasing vehicle velocity may also be used for midcourse correction or to decrease orbital altitude. The Δv function can be used for midcourse correction or to increase orbital altitude. Usually the Δv, retro, and ACS thrusters are mounted in fixed positions. A combination of the Δv and ACS thrusters can be used to provide secondary propulsion if the required thrust level is quite low. Generally the thrust of an ACS thruster does not exceed 100 lb, although applications as large as 600 lb have been considered.

Figure 4-9 identifies thrust ranges and critical operational requirements for typical applications of primary and secondary thrust propulsion systems. In any given vehicle, the thrust level required for attitude control is several orders of magnitude lower than the primary thrust.

4-3.1 Primary Thrust

In general, the primary requirements of the first stage are high-thrust and low-cost propellants; specific impulse and mass ratio are less critical than for upper stages. The upper stage primary requirements are high specific impulse and high mass ratio; thrust and propellant cost are less critical. Therefore, it is attractive to use low-cost, low I_{sp}, propellants (e.g. liquid oxygen and kerosene) on the first stage, and more expensive but higher I_{sp} propellants (e.g. liquid oxygen and liquid hydrogen) on the upper stages, particularly for large liquid boosters such as Saturn.

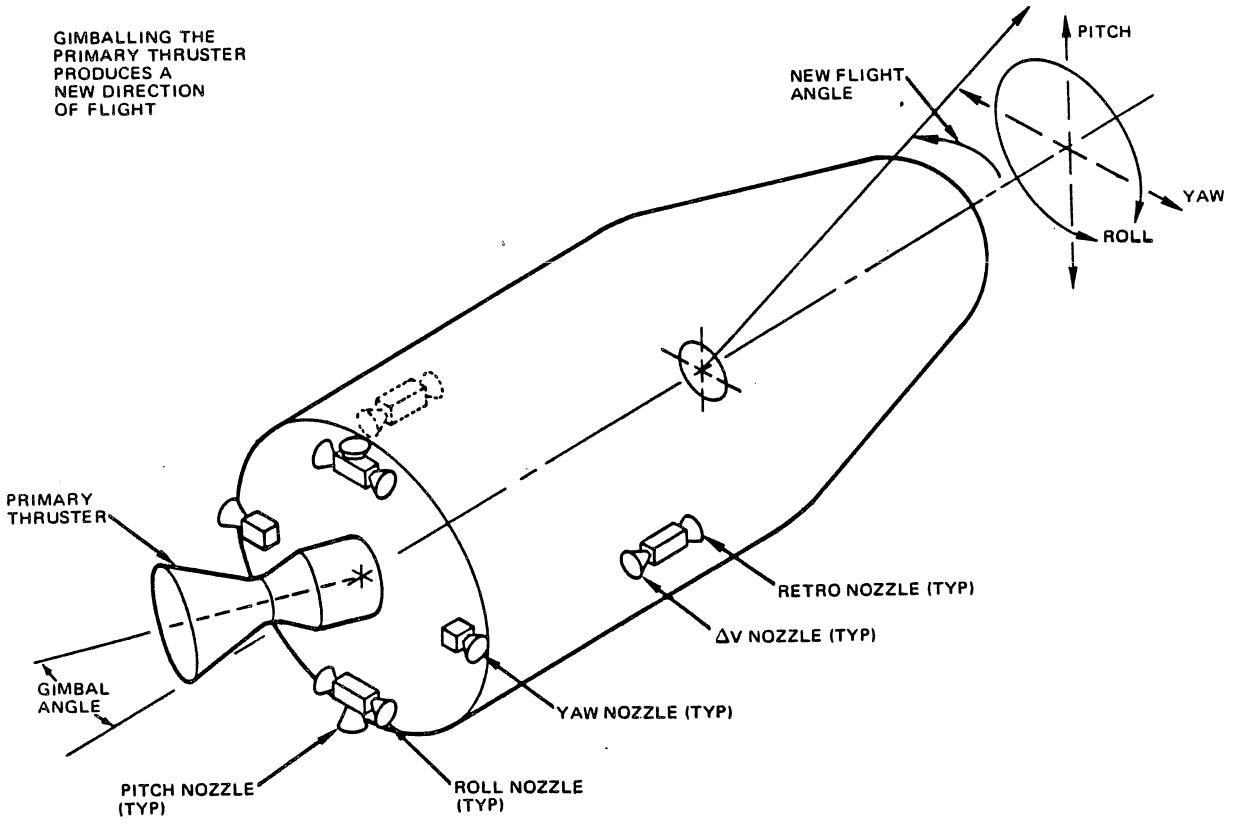

Figure 4-8. Propulsion Maneuvering Methods

Table 4-5 describes general performance requirements of primary thrusters which influence the selection of a particular type of propulsion system for specific applications. Chemical propulsion systems are used for all of these applications, and are most attractive for nearly all. Nuclear and electric propulsion systems become attractive for space missions which require very high burnout velocities, such as trips to the outer planets or very close approach solar probes. Even for these cases, however, chemical propulsion is preferred for the first stage of the launch vehicle.

Liquid propulsion systems generally are best suited to space applications which require high Δv performance, and may require thrust throttling or restart capability. Solid propulsion systems generally are best suited to missile applications which require long time storage in an operational condition, very short launch-readiness time, and insensitivity to high-g maneuvering loads. Storable liquid propulsion systems are also used in missile applications.

Thrust-vector direction control using the primary propulsion system can be accomplished with a movable or a fixed nozzle. Nozzle swivelling can be accomplished through the use of hinges or gimbals. For fixed nozzles, thrust vector direction may be varied by moving external devices, such as jet vanes or jetavators, into the rocket exhaust, or by injecting a fluid into the nozzle downstream of the throat to produce an unsymmetrical pressure distribution. Thrust vector control methods for liquid and solid propulsion systems are shown in Table 4-6 which also indicates the principal advantages and disadvantages of each method.

4-3.2 Propulsive Maneuvering

An important propulsive maneuvering application is concerned with controlling the attitude of a booster or space vehicle. Attitude control rocket systems, which are reaction control devices, provide thrust about the vehicle pitch, yaw, and roll axes. Figure 4-10 is a schematic diagram of an attitude control system. It consists of a

propellant (stored gas in this illustration), plumbing, control valves, and a number of fixed thrusters which are oriented about the vehicle in a specific configuration. Desired rotational or translational motion is obtained by operation of appropriate combinations of these thrusters as described in Table 4-7.

During operation of the primary propulsion system, motion about the pitch and yaw axes can be obtained by operation of the primary thrust vector control system. With a single primary thruster, roll axis control usually requires operation of the roll thrusters of an attitude control system. During times when the primary propulsion system is not operating, the pitch and yaw thrusters of an attitude control system are required to provide motion about these axes.

Usually the thrust requirements for an attitude control system are very much smaller than those of a primary propulsion system, so that its thrust chamber assemblies are quite small. The total impulse requirements vary over a wide range depending on mission requirements. Propellants used for attitude control systems include: stored gas, monopropellants, bipropellants, and solid propellants. Each of these types of propellants is applicable for some requirements. Figure 4-11 illustrates the effect of each of these types of propellants on the weight of an attitude control system, as a function of total impulse requirements. The trends are shown as broad bands to emphasize that design requirements, the propellants selected, and design ingenuity also have a major effect on system weight.

Although Figure 4-11 suggests that cold gas is lightest for total impulses up to 1,000 lb-sec, and monopropellants are lightest between 1,000 and 10,000 lb-sec, design studies for specific applications may shift the weight cross-over points significantly. For example, even though the Titan-III Transtage ACS required 32,000 lb-sec total impulse, a monopropellant system selected to improve reliability was only 5 percent heavier than the bipropellant system it replaced.

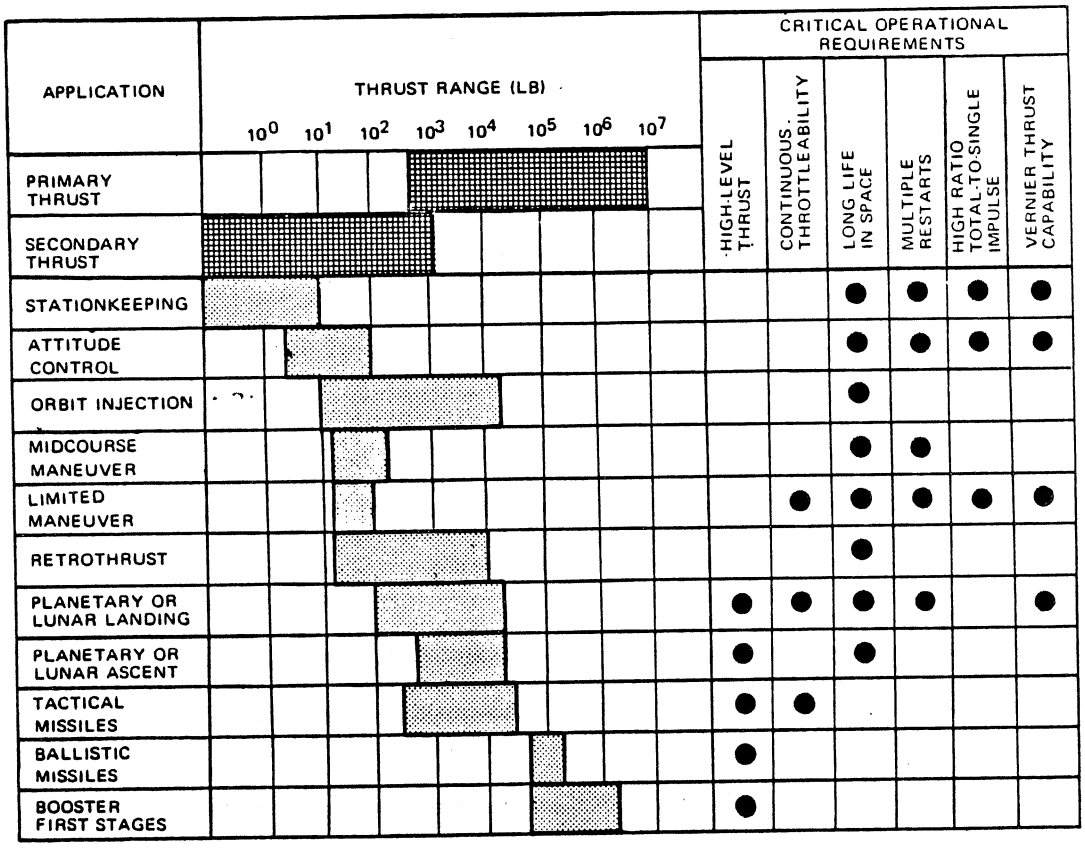

Figure 4-9. Thrust Requirements for Typical Applications

Table 4-5. Performance Requirements for Primary Thrusters

Applications \ Requirements		Operational Time			Volume Constraints	Manuevering g-Loads	Zero-g Operation	Δv Performance	Restart	Throttling
		Storage	Readiness	Use						
Missiles	Tactical	Years	Seconds	Seconds	Critical	High	No	Low to Medium	Some	Some
	Ballistic Booster	Years	Seconds	Minutes	Some are Critical	Low	No	Medium	No	No
	Reentry	Years	Seconds	Seconds	Critical	High	Yes	Low	Some	Some
Space	Expendable Booster First Stage	Not Applicable	Days	Minutes	Not Critical	Low	No	Medium	No	No
	Upper Stages	Not Applicable	Days	Hours	Not Critical	Low	Some	High	Some	No
	Space Vehicles	Not Applicable	Days	Months	Not Critical	Most are Low	Yes	High	Yes	Yes

Stored gas has been used most extensively, and it has the highest demonstrated reliability. Further, since it is used in a gaseous state it is insensitive to zero-g or large lateral g-loads. However, because gases have low specific impulses and require pressure vessels for storage, the weight of stored gas systems becomes unattractive when total impulse requirements exceed 1,000 lb-sec.

Monopropellant attitude control systems became attractive when low temperature catalysts were developed. These systems have demonstrated high reliability, and they are weight competitive in applications with total impulse requirements as large as 30,000 lb-sec. However, monopropellant systems require positive expulsion in zero-g and high lateral-g environments.

Bipropellant systems have somewhat lower reliability, and they require positive expulsion in zero-g and high lateral-g environments. However, bipropellant systems are generally lightest for total impulse requirements greater than 15,000 lb-sec.

Solid propellant attitude control systems are attractive for vehicles with volume constraints and intermediate total impulse requirements. They are also attractive for long time storage before use, and they are relatively insensitive to g-loads. However, they are not practical for stop-start operation, and, once initiated, their energy is expended according to the design duty cycle.

The monopropellant, bipropellant, and solid propellant reaction control systems obtain their energy by chemical reaction of the propellants. This reaction can occur as required in each individual thrust chamber assembly, or it can occur in a remote gas generator. In the latter case, the warm combustion products are ducted to each nozzle.

A promising variation of reaction control within the atmosphere consists of ejecting the propellants transverse to the direction of flight in such a manner as to create a shock wave on the skin of the vehicle. The high pressure area behind the shock produces a force which augments, or amplifies, the basic reaction force. There are two control system concepts currently used to obtain force amplification, external burning (EB) and jet interaction (JI). External burning occurs when a pyrophoric fuel is injected into the surrounding atmosphere. Jet interaction occurs when completely reacted propellants are injected into the surrounding atmosphere. If the reacted propellants ejected are fuel

Table 4-6. Thrust Vector Control Methods for Rocket Engines

TYPE	GIMBALLED OR HINGED THRUST CHAMBER	GIMBALLED OR HINGED NOZZLE	GIMBALLED SMALL CONTROL THRUST CHAMBERS	GIMBALLED TURBINE EXHAUST GAS	SECONDARY LIQUID OR GAS INJECTION	JET VANES	JETAVATOR
CONFIGURATION			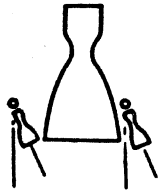	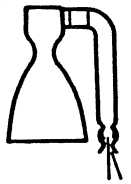		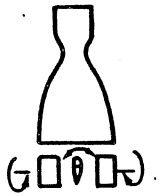	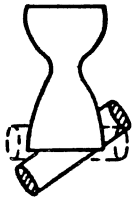
DESCRIPTION	UNIVERSAL JOINT SUSPENSION	FLEXIBLE SHEAR SEAL JOINT HINGE OR GIMBAL	TWO OR MORE GIMBALLED AUXILIARY THRUST CHAMBERS	GIMBAL ON TURBINE EXHAUST NOZZLE	FLUID INJECTION IN NOZZLE - ONE SIDE AT A TIME	TWO OR MORE AERO-DYNAMIC VANES IN NOZZLE EXHAUST	ROTATING AIRFOIL SHAPED COLLAR NEAR NOZZLE EXIT
ADVANTAGES	VERY LOW DRAG LOSS-SIMPLE AND RELIABLE	VERY LOW DRAG LOSS - LINEAR CONTROL	PROVIDES VERNIER AND INDEPENDENT CONTROL	RECOVERY OF USEFUL THRUST	LIGHT WEIGHT NOZZLE - RAPID RESPONSE	PROVIDES HIGH SIDE FORCES	LOW DRAG LOSSES - LOW TORQUE - LESS EROSION THAN JET VANE
DISADVANTAGES	NO ROLL CAPABILITY	HIGH ACTUATION TORQUE	EXPENSIVE AND COMPLEX	THRUST LIMITED BY TURBINE REQUIREMENTS	LARGE SIDE FORCES REQUIRE EXCESSIVE AMOUNT OF SECONDARY FLUID	HIGH DRAG AT ALL DEFLECTIONS - VANE EROSION - NON LINEAR VARIABLE SHAFT TORQUE	HEAVY
PROPULSION SYSTEM USAGE	LIQUID SYSTEMS	SOLID SYSTEMS	LIQUID SYSTEMS	PUMP FED LIQUID SYSTEMS	SOLID AND LIQUID SYSTEMS	SOLID AND LIQUID SYSTEMS	SOLID SYSTEMS

Table 4-7. Attitude Control Thruster Operational Combinations

THRUSTER NO.	PITCH		YAW		ROLL	
	UP	DOWN	LEFT	RIGHT	CW	CCW
1			X			
2		X				
3				X		
4	X					
5				X		
6	X					
7			X			
8		X				
9						X
10					X	
11						X
12					X	

rich, the force amplification may be due partly to EB and partly to JI. EB and JI are attractive because they increase the effective specific impulse of the propellants. EB is more effective than JI within the atmosphere, but EB is ineffective outside the atmosphere. JI can be used inside or outside the atmosphere, but it is more effective within the atmosphere.

An attitude control system is required to provide small impulse bits to correct small position or attitude errors. When generating small impulse bits, it is customary to maintain the thrust level constant, and vary the pulse duration to obtain the required magnitude of the impulse bit. The time duration of thrust application is called the pulse width. The minimum impulse bit obtainable in a given system is determined by the minimum achievable pulse width. Pulse widths as short as 5 milliseconds have been achieved. It is desirable to limit the pulse width to provide only the corrective impulse bit required, in order to avoid over-correction and to minimize the total impulse requirements of the system. When the pulse width is very short, some decrease in I_{sp} occurs because of start and stop transient conditions. Figure 4-12 shows a typical pulse pressure-time history.

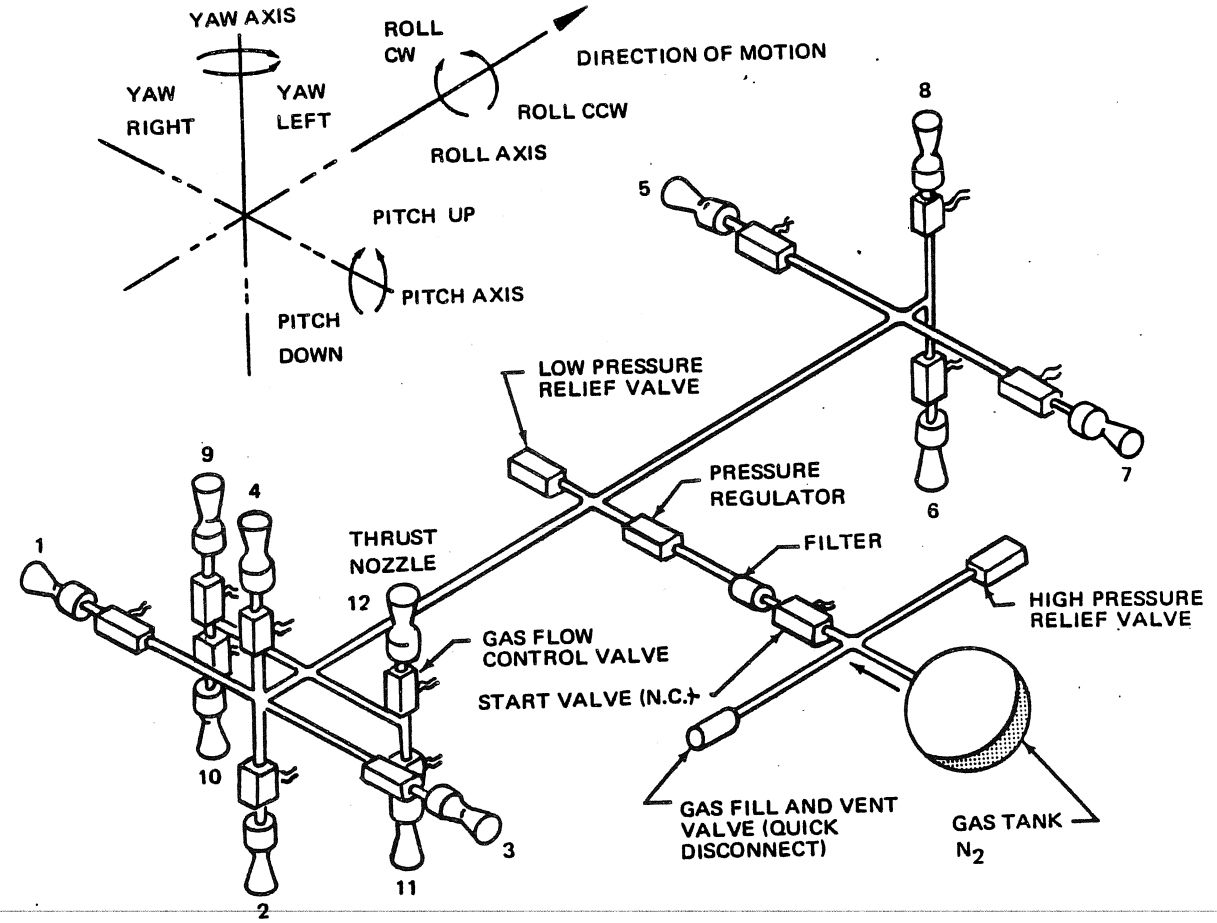

Figure 4-10. Stored Gas Attitude Control Rocket System

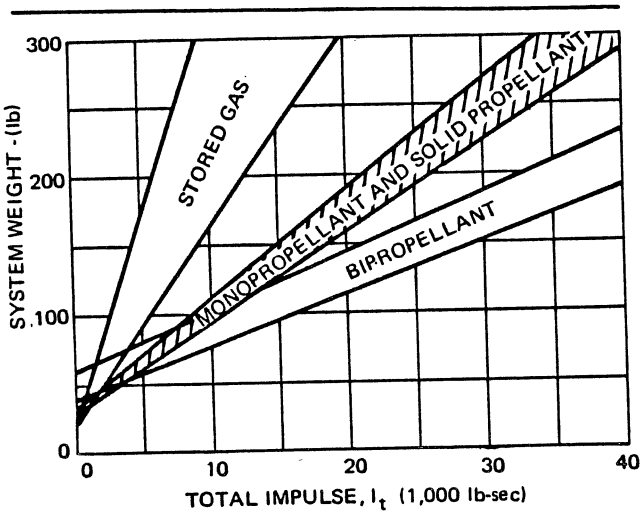

Figure 4-11. Attitude Control Systems Weight Comparison

4-4 BIBLIOGRAPHY

1. *Space Data,* TRW Systems, Redondo Beach, California, 1965

2. M. Barrere, et al., *Rocket Propulsion,* Elsevier Publ. Co., Amsterdam 1960.

3. R. W. Bussard and R. D. DeLauer, *Nuclear Rocket Propulsion*, McGraw-Hill Book Co., New York, 1958.

4. W. R. Corliss, *Propulsion Systems for Space Flight*, McGraw-Hill Book Co., New York, 1960

5. R. D. Heitchue, *Space Systems Technology*, Reinhold Book Corp., New York, 1968.

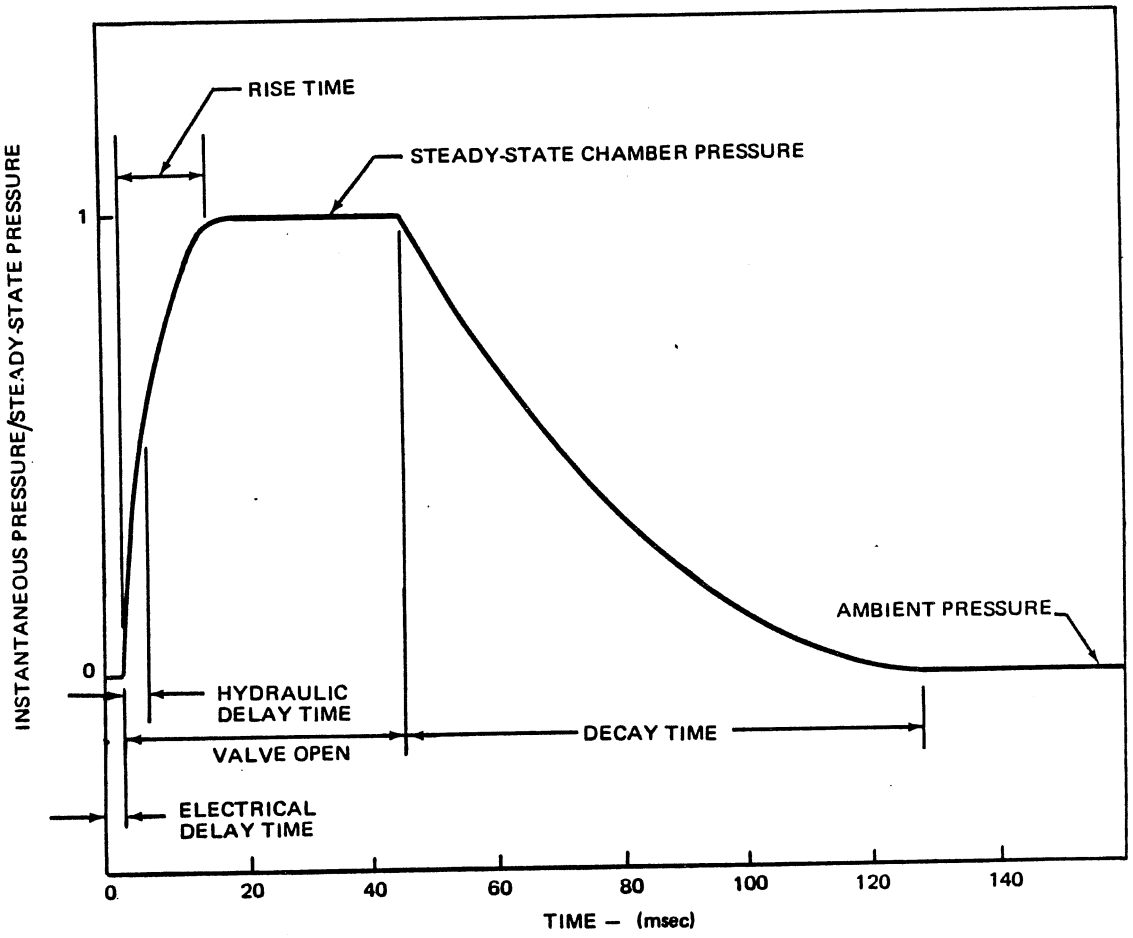

Figure 4-12. Typical Pulse Pressure History

6. G. W. Howell and T. M. Weathers, *Aerospace Fluid Component Designers Handbook*, Vol I and II, RPL-TDR-64-25, TRW, Inc., 1967.

7. H. H. Koelle, *Handbook of Astronautical Engineering*, McGraw-Hill Book Co., New York, 1961.

8. O. E. Lancaster, *Jet Propulsion Engines*, (Vol XII, High Speed Aerodynamics and Jet Propulsion). Princeton University Press, Princeton, 1959.

9. H. S. Seifert, *Space Technology*, John Wiley and Sons, New York, 1959.

10. E. Stuhlinger, *Ion Propulsion for Space Flight*, McGraw-Hill Book Co., New York, 1964.

11. G. P. Sutton, *Rocket Propulsion Elements*, John Wiley and Sons, New York, 1963.

12. M. J. Zucrow, *Aircraft and Missile Propulsion*, Vol I and II, John Wiley and Sons, New York, 1958

Section 5
LIQUID ROCKET PROPULSION SYSTEMS

This section describes the different kinds of liquid propulsion systems and discusses the configurations and selection criteria of the subsystems and components which constitute these systems. The design of liquid rocket propulsion systems will be the subject of the Liquid Propulsion Systems Manual (PB1). The properties of liquid propellants will be covered in the Propellants Manual (PD1).

A liquid propulsion system consists of three basic subsystems: Pressurization system, propellant feed system, and the rocket engine, (Figure 5-1). Liquid propulsion systems are classified as pressure-fed or pump-fed, depending on whether or not a pump is included in the propellant feed system. Liquid rocket propulsion systems are also commonly classified according to the types of propellants used as monopropellants or bipropellants. Monopropellants are liquids which can be made to decompose chemically and release heat. Bipropellants release heat when they combine chemically. Bipropellant systems are also classified according to the operating temperature of the propellants, e.g. earth-storable or cryogenic.

5-1 MONOPROPELLANT SYSTEMS

A monopropellant is a liquid which contains all of the ingredients required to produce an exothermic chemical reaction. In monopropellants of current interest, such as hydrazine, this reaction is a chemical decomposition. The decomposition rate increases with increase in temperature. When a monopropellant is heated above a critical temperature, called the autodecomposition temperature, the decomposition rate is fast enough that the resultant heat release rate can maintain, or exceed, the autodecomposition temperature without an external heat source.

The temperature of the system upstream of the decomposition chamber must be held below the autodecomposition temperature to avoid explosions. Conversely, monopropellants must be chemically stable at the maximum system temperature in order to avoid uncontrolled decomposition and heat release. Therefore, the system design must include a means of initiating decomposition when required. Initiation of the reaction can be accomplished by an igniter which produces a high

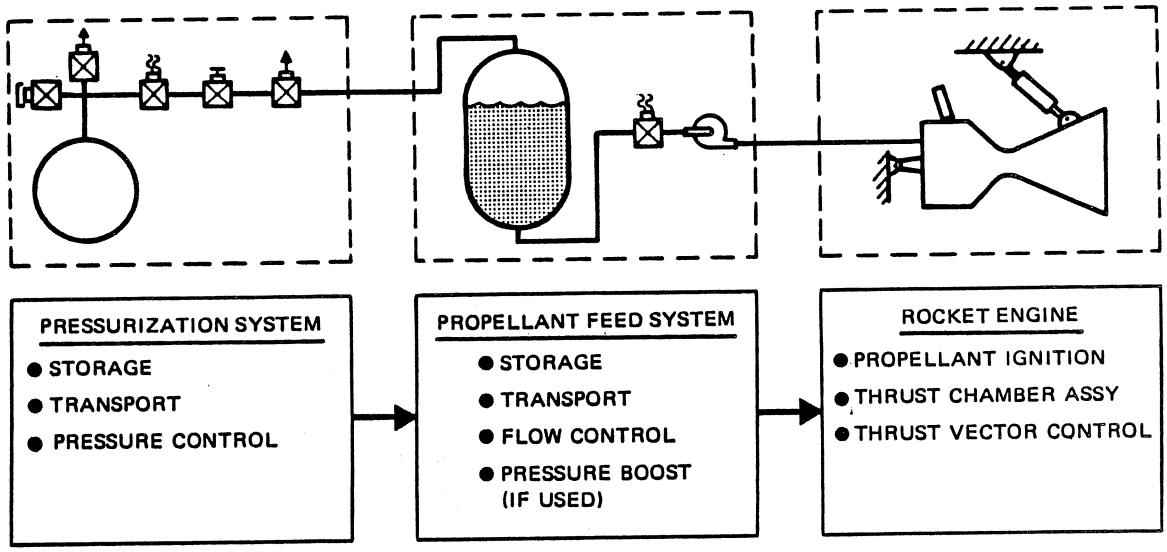

Figure 5-1. Liquid Propulsion System Functional Schematic

temperature in the decomposition chamber. Reaction can also be initiated by a catalyst placed in the decomposition chamber.

Since a monopropellant system handles only one propellant, it requires relatively few components. Therefore, the system hardware weight is relatively light and reliable. The specific impulse of monopropellants is considerably lower than that of bipropellants. Thus, proportionately more weight of monopropellant, than bipropellant, is required for the same total impulse. The higher reliability of monopropellant systems makes them attractive for many applications, particularly if the total impulse requirement is low.

Figure 4-11 in Section 4 shows that monopropellant propulsion systems generally are lighter than bipropellant systems for total impulse requirements below about 5,000 lb-sec, because of the lower hardware weight of the simpler system. However, when the total impulse exceeds 15,000 lb-sec, monopropellant systems are usually heavier than bipropellant systems, because the weight of the additional monopropellant required more than offsets the lesser hardware weight.

Figure 5-2 is a sketch of a typical monopropellant engine. This sketch shows that a monopropellant engine differs from a conventional bipropellant engine in that a single propellant is injected into a catalyst bed which occupies a significant portion of a decomposition chamber. The design of the catalyst bed controls the extent of decomposition which, in turn, determines the specific impulse of the monopropellant.

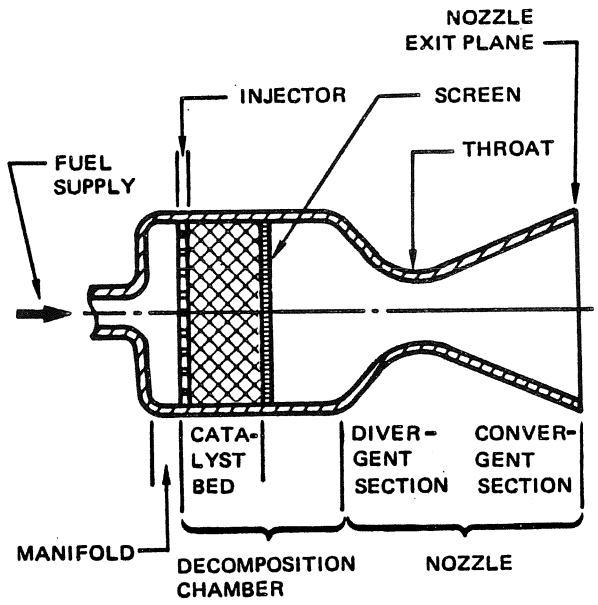

Figure 5-2. Monopropellant Rocket Engine

Hydrazine, hydrogen peroxide, and ethylene oxide are typical monopropellants. Recent improvements in catalysts have made hydrazine the most attractive of the monopropellants for most applications because it now combines good performance with ease of handling.

Anhydrous hydrazine decomposes according to the following consecutive reactions

$$3\,N_2H_4 \xrightarrow{cat} 4\,NH_3 + N_2 + 144,300\ BTU$$

$$4\,NH_3 \xrightarrow{\Delta\ cat} 2\,N_2 + 6\,H_2 - 79,200\ BTU$$

The first reaction generally is complete. The degree of completion of the second reaction, ammonia decomposition, is determined by the catalyst bed design. Since the decomposition of ammonia is endothermic, a catalyst bed design which provides the least ammonia decomposition provides the highest heat release, and hence, the maximum specific impulse. If no ammonia decomposition occurs, a theoretical specific impulse of 260 sec is achievable.

Anhydrous hydrazine boils at 236°F and freezes at 36°F. This relatively high freezing temperature limits the applicability of anhydrous hydrazine. Blends of hydrazine with other liquids have been developed that reduce the freezing point, but usually they decrease the specific impulse. Typical additives are water and hydrazine nitrate. The addition of water depresses the freezing point and the specific impulse. The addition of hydrazine nitrate increases the specific impulse slightly, but it also increases shock sensitivity.

Figure 5-3 presents performance curves for a blend of 50 percent hydrazine-20 percent hydrazine nitrate-30 percent water, as a function of the percent of ammonia dissociated. For this blend, a maximum I_{sp} of about 206 sec is achievable.

Figure 5-4 is a ternary diagram for hydrazine, hydrazine nitrate, and water, which shows the effect of composition on freezing temperature and specific impulse. The specific impulse values are based on 20 percent ammonia dissociation at an expansion ratio of 50. For the 50 percent hydrazine-20 percent hydrazine nitrate-30 percent water composition, Figure 5-4 shows that the freezing temperature is –85°F (375°R) and the specific impulse is 200 sec.

5-2 BIPROPELLANT SYSTEMS

Bipropellants are frequently classified according to their liquid storage temperature ranges. The most common temperature categories are cryogenic and earth-storable. Propellants are termed cryogenic if they are liquid at very low temperatures, i.e., below 222°R. Propellants are earth-storable if they are liquid at earth surface temperatures, e.g., 395°R to 620°R.

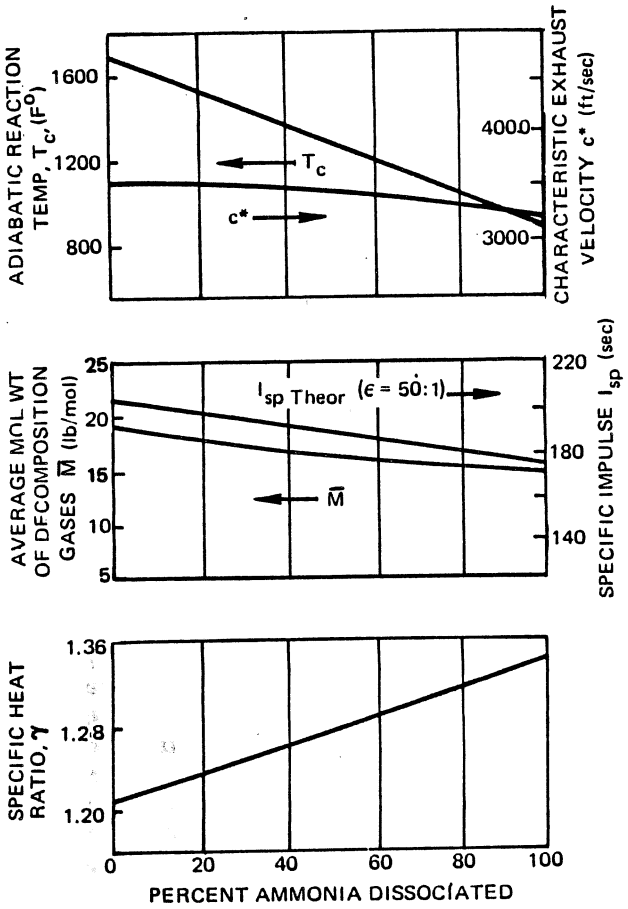

Figure 5-3. Hydrazine Performance Curves

A propellant is storable if it can attain thermal equilibrium with its environment and remain a liquid. Generally, this definition of storability allows the use of thermal insulation and a reasonable increase in propellant vapor pressure, but it excludes the input of power to provide refrigeration or heating. Within this definition, most cryogenic and earth-storable propellants are considered storable in space for many applications.

Table 5-1 lists typical sea level and vacuum performance values for many bipropellant combinations of current interest. These values, based on the mixture ratio, r, shown for each propellant, are: propellant bulk specific gravity, δ_p; combustion temperature, T_c; characteristic exhaust velocity, c*; and specific impulse, I_{sp}.

The propellant bulk specific gravity, δ_p, is the ratio of the weight of the combined propellants to the weight of an equal volume of water at a specified temperature. In the metric system of units, specific gravity has the same numerical value as density, in gm/cc. However, in the English system of units, which is used in this manual, density is given in lb/ft^3 and is equal to specific gravity multiplied by the density of water (62.4 lb/ft^3).

The mixture ratio, r, is the ratio of the weight flow rate of the oxidizer to the weight flow rate of the fuel. Tables 5-2 and 5-3, which present physical properties of oxidizers and fuels, show that the densities of oxidizers are considerably higher than the fuels with which they are used. Thus, for a given propellant combination, the bulk density and specific gravity increase as the mixture ratio increases.

Specific impulse, which also varies with r, reaches a maximum at a value of r which is less than the stoichiometric mixture ratio. The stoichiometric mixture ratio is the unique weight ratio of oxidizer to fuel which corresponds to complete combustion; i.e., to the formation of saturated molecules in the combustion process. At values of r which are less than the stoichiometric mixture ratio, an increase in r increases the combustion temperature, T_c, and the molecular weight of the combustion products, M. As r approaches the stoichiometric ratio from the fuel rich side, M continues to increase at the same rate, but the rate of increase of T_c slows because of dissociation and reversal of the chemical reactions. Dissociation not only reduces the effective heat release but also adds fuel and oxidizer diluents that further reduce the average combustion temperature.

Since specific impulse is proportional to $\sqrt{T_c/M}$, it is apparent that the maximum I_{sp} occurs when T_c reaches the dissociation temperatrue. Dissociation occurs at a fuel-rich mixture ratio so that the lower density fuel is the unreacted diluent. This results in a lower average value of M at the maximum combustion temperature, further increasing the maximum value of specific impulse. Figure 5-5 illustrates the rate of change in T_c, M and I_{sp} as a function of mixture ratio for a typical propellant combination.

An ideal propellant would have high values of δ_p and I_{sp}. However, higher I_{sp} propellants generally have lower values of δ_p. The product $\delta_p \cdot I_{sp}$, sometimes called the density specific impulse, is frequently used as a measure of propellant performance, although $I_{sp} \cdot \log \delta_p$ would be a more accurate representation. Figure 5-6 presents variations in I_{sp} and $\delta_p \cdot I_{sp}$ for several cryogenic and earth-storable propellant combinations as a function of mixture ratio. Note that the earth-storable propellant combinations generally are denser, have lower specific impulses and utilize lower propellant mixture ratios than the cryogenic propellant combinations.

The curves in Figure 5-6 should not be interpreted to suggest that propellant combinations with high density and intermediate specific impulse are preferable to combinations with low density and high specific impulse. The selection of a particular propellant combination is dependent on many factors including: Δv requirements, storability, envelope constraints, and total system weight. When Δv is the dominant requirement, such as for upper stages, the low density, high I_{sp} cryogenic propellants usually are selected. Earth-storable propellants usually are selected when long storage time or envelope restriction requirements are dominant, such as for missiles.

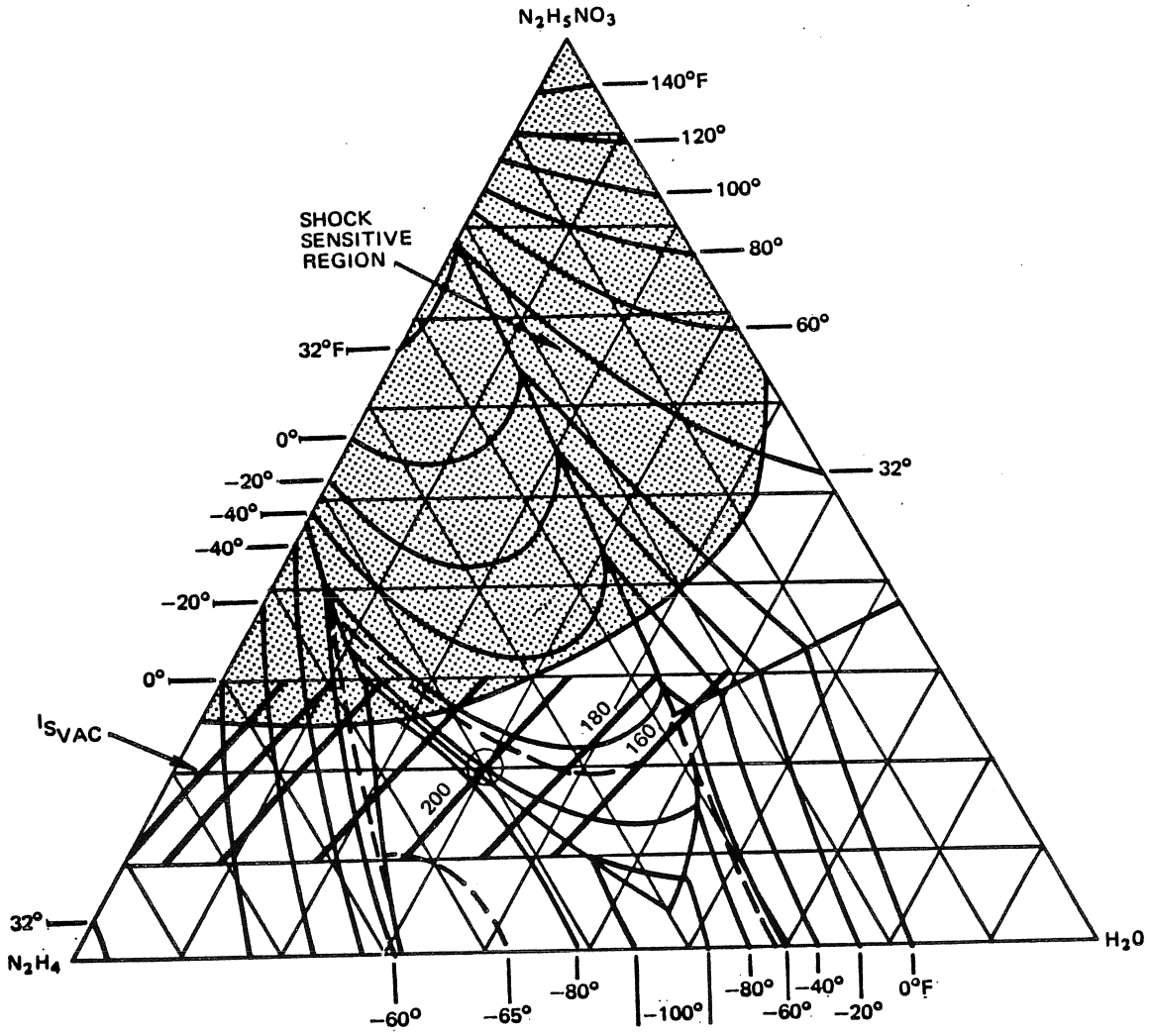

Figure 5-4. Freezing Point and Vacuum Specific Impulse (at 20% NH_3 Dissociation) of Hydrazine – Hydrazine Nitrate – Water

Table 5-1. Theoretical Rocket Engine Propellant Summary

OXIDIZER	FUEL	P_c = 1000 psia, Optimum Sea Level Expansion Shifting Equilibrium					P_c = 100 psia, ϵ = 40, Shifting Equilibrium				
		r	δ_p	T_c (°R)	c* (ft/sec)	I_{sp} (sec)	r	δ_p	T_c (°R)	c* (ft/sec)	$I_{sp_{vac}}$ (sec)
O_2	H_2	4.0	0.284	5330	7950	388	4.5	0.325	5610	7840	454
	CH_4	3.15	0.811	6350	6120	310	3.25	0.817	5840	5960	365
	C_2H_6	2.95	0.898	6480	6050	307	2.95	0.896	5930	5880	362
	C_3H_8	2.75	0.911	6500	6020	305	2.82	0.912	5960	5860	359
	C_2H_2	1.6	0.857	7460	6590	330	1.65	0.867	6690	6390	384
	C_2H_4	2.45	0.885	6850	6100	312	2.5	0.887	6170	5945	365
	RP-1	2.55	1.00	6590	5900	299	2.6	1.01	6030	5730	351
	N_2H_4	0.90	1.065	6120	6220	313	0.95	1.066	5680	6060	367
	UDMH	1.67	0.975	6490	6120	310	1.67	0.975	5940	5960	364
	NH_3	1.41	0.833	5580	5880	295	1.41	0.833	5260	5790	347
F_2	H_2	8.0	0.468	7120	8370	410	10.2	0.538	6820	8050	475
	B_2H_6	5.45	1.09	8980	7370	371	5.5	1.12	7920	7110	431
	B_5H_9	4.6	1.20	9120	7130	360	4.6	1.2	8000	6860	417
	CH_4	4.35	1.021	7620	6770	345	4.45	1.027	7050	6680	408
	N_2H_4	2.25	1.31	8420	7290	364	2.25	1.33	7580	7070	422
	CN_2H_6	2.38	1.24	8200	6840	347	2.43	1.246	7400	6650	408
	UDMH	2.45	1.192	7770	6610	339	2.45	1.192	7030	6440	400
	N_2H_4–UDMH(2)	2.50	1.26	8150	6940	349	2.50	1.264	7330	6740	409
	NH_3	3.3	1.18	8240	7210	360	3.3	1.18	7450	7000	417
O_3	H_2	3.8	0.284	5830	8580	423	4.1	0.298	5650	8390	493
OF_2	H_2	5.75	0.374	6300	8390	411	6.0	0.384	6000	8180	474
	CH_4	5.0	1.06	7960	7080	356	5.1	1.07	7200	6880	414
	C_2H_6	4.4	1.15	8180	7100	355	4.6	1.15	7380	6870	413
	C_3H_8	4.35	1.17	8250	7050	354	4.4	1.18	7450	6860	412
	B_2H_6	3.67	0.993	8350	7350	372	3.67	0.993	7410	7130	434
	N_2H_4	1.62	1.272	7340	6850	345	1.62	1.272	6610	6650	403
	CN_2H_6	2.4	1.25	7850	6950	350	2.4	1.25	7050	6730	407
	N_2H_4-UDMH(2)	2.1	1.24	7700	6940	350	2.18	1.24	6970	6730	407
H_2O_2 (100%)	B_2H_6	1.84	0.795	4880	6460	333	1.86	0.807	4610	6260	391
	N_2H_4	2.27	1.27	5270	5770	288	2.32	1.276	5010	5700	338
N_2O_4	N_2H_4	1.33	1.21	5870	5860	292	1.36	1.23	5500	5740	342
	CN_2H_6	2.17	1.20	6110	5730	288	2.26	1.21	5660	5570	338
	UDMH	2.6	1.166	6190	5680	287	2.7	1.17	5720	5520	336
	N_2H_4-UDMH(2)	2.0	1.20	6050	5560	287	2.0	1.2	5620	5570	339
HNO_3 15% N_2O_4	RP-1	5.0	1.329	5670	5180	263	5.1	1.33	5300	5070	309
	UDMH	3.1	1.255	5680	5410	272	3.2	1.26	5320	5290	320
ClF_2	N_2H_4	2.80	1.495	7010	5970	293	2.85	1.498	6460	5840	339
	UDMH	3.0	1.365	6430	5550	278	3.05	1.369	6060	5460	325
ClO_3F	N_2H_4	1.45	1.2115	6220	5910	295	1.5	1.215	5760	5770	345

(1) Specific impulse is at mixture ratio for maximum I_{sp}, Ammonia, chlorine trifluoride, and perchloryl fluoride are taken to be liquids at 77°F. All other propellants are taken to be liquids at 77°F or at the normal B.P. whichever is lower.

(2) Equal parts by weight of Hydrazine and UDMH.

Table 5-2. Liquid Rocket Oxidizer Properties

OXIDIZER	CHEMICAL FORMULA	B. P. °F	F. P. °F	δp @ 77°F	SP. HEAT Btu/lb °F @ 77°F	CRITICAL TEMP °F	CRITICAL PRESS. psia	VAPOR PRESS. @ 77°F, psia	VAPOR PRESS. @ 160°F, psia	VISCOSITY CENTIPOISE @ 77°F	COST $/lb	TOXICITY
Oxygen	O_2	−297.4	−361.1	1.143(2)	0.406(2)	−182	731	(1)	(1)	0.190(2)	0.03	Nontoxic
Fluorine	F_2	−306.6	−363.3	1.510(2)	0.367(2)	−200	808	(1)	(1)	0.24(2)	3.50	High
Ozone	O_3	−169.6	−315.0	1.46(2)	0.354(2)	10.2	802	(1)	(1)	1.55(3)		High
Oxygen Difluoride	OF_2	−228.6	−371	1.521(2)		−72	719	(1)	(1)	0.283(2)	5.50	High
100% Hydrogen Peroxide	H_2O_2	302.4	31.2	1.443	0.63	855	3145	0.038	0.58	1.156	1.00	Low
90% Hydrogen Peroxide	90% H_2O_2, 10% H_2O	285.5	11.3	1.387	0.66			0.052	0.76	1.156	0.50	Low
Nitrogen Tetroxide	N_2O_4	70.1	11.8	1.433	0.374	316.4	1470	17.2	111	0.393	0.075	High
Inhibited Red Fuming Nitric Acid	83% HNO_3, 2% H_2O 15% N_2O_4	150	−63.4	1.555	0.419	520		2.57	19	1.29	0.055	Medium
Chloride Trifluoride	ClF_3	53.2	−105.4	1.809	0.309	308	837.7	24.9	118	0.41	2.40	High
Perchoryl Fluoride	ClO_3F	−52.2	−230.8	1.412	0.263	203.3	778.9	172	501	0.384(2)	8.50	Medium
Bromide Pentafluoride	BrF_5	105.4	−76.9	2.46		387		8.38	43.0		4.50	High
Tetranitro-methane	$C(NO_2)_4$	258.8	56.8	1.63	0.297			0.213	2.28	1.76		Medium

(1) Above critical point.
(2) Value taken at the normal B. P. rather than 77°F.
(3) Value taken at −297.5°F.

Table 5-3. Liquid Rocket Fuel Properties

FUEL	CHEMICAL FORMULA	B. P. °F	F. P. °F	δp @ 77°F	SP. HEAT Btu/lb-°F @ 77°F	CRITICAL TEMP °F	CRITICAL PRESS. psia	VAPOR PRESS. @ 77°F psia	VAPOR PRESS. @ 160°F psia	VISCOSITY CENTIPOISE @ 77°F	COST $/lb	TOXICITY
Hydrogen	H_2	−423	−434.4	0.071(2)	2.22(2)	−399.8	188.1	(1)	(1)	0.0139(2)	0.50	Nontoxic
Diborane	B_2H_6	−134.5	−265.9	0.437(2)	0.669(2)	62.1	581	(1)	(1)	0.133(2)	40.00	High
Pentaborane	B_5H_9	140	−52	0.618	0.573	456	557	4.0	21	0.3	10.00	High
Methane	CH_4	−258.7	−296.5	0.424(2)	0.822(2)	−117	673	(1)	(1)	0.115(2)	0.20	Low
Ethane	C_2H_6	−127.5	−277.6	0.546(2)	0.581(2)	89.8	708	600	(1)	0.162(2)	0.006	Low
Propane	C_3H_8	−43.7	−305.8	0.585(2)	0.534(2)	206	617	130	368	0.205(2)	0.006	Low
Ethylene	C_2H_4	−154.7	−272.5	0.566(2)		49.3	742	(1)	(1)	0.26(2)	0.05	Low
Acetylene	C_2H_2	−119.2	−115.2	0.612(2)	0.35(2)	96.8	91.1		(1)			Medium
RP-1	$(CH_{1.97})_n$	10% Evap @ 390°F	−76.0	0.81	0.48	758	315		0.7	2.0	0.02	Low
Hydrazine	N_2H_4	236.3	34.7	1.004	0.737	716	2135	0.28	2.85	0.90	1.60	Medium
Monomethyl-hydrazine	CN_2H_6	189.5	−62.3	0.874	0.70	609	1195	1.0	9.0	0.781	2.05	Medium
Unsymmetrical Dimethyl-hydrazine (UDMH)	$C_2N_2H_8$	146	−71.0	0.786	0.653	482	786	3.03	18.5	0.509	0.85	Medium
50% Hydrazine & 50% UDMH	50% N_2H_4 50% $C_2N_2H_8$	158	18.8	0.898	0.694	634	1696	2.75	15.1	0.817	1.225	Medium
Anhydrous Ammonia	NH_3	−28.0	−107.9	0.604	1.09	270	1639	150	516	0.135	0.045	Medium
Triethyl-aluminum	$(C_2H_5)_3$ Al	367.9	−50	0.832	0.52	603	550	Nil	0.15	2.58		

(1) Above critical point
(2) Values are taken at the normal B. P. rather than 77°F.

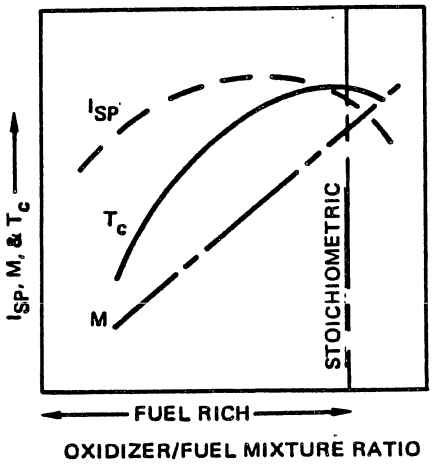

Figure 5-5. Performance vs Mixture Ratio

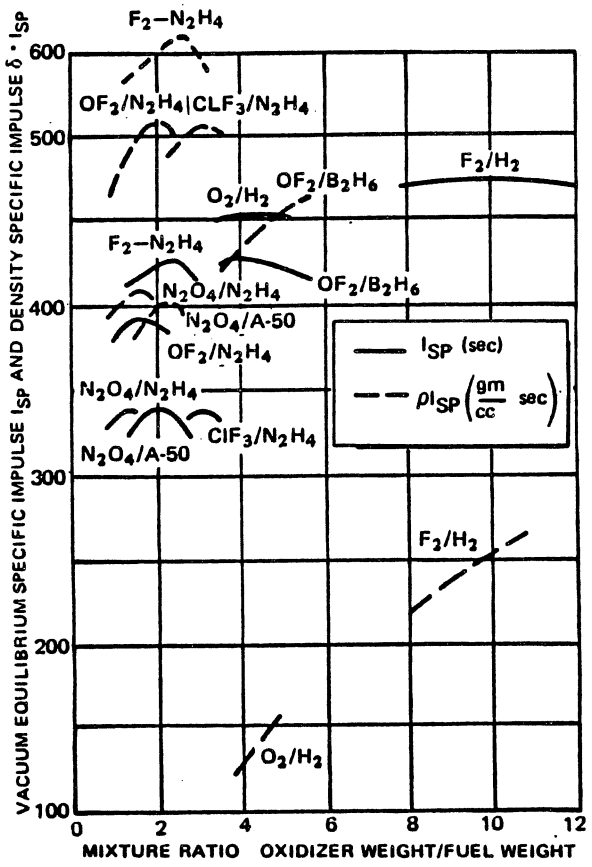

Figure 5-6. Typical Specific Impulse and Density Specific Impulse Ranges

In addition to the properties already discussed, the following qualities are generally desired in a propellant:

a. Good ignition characteristics.

b. High combustion efficiency.

c. Stable combustion.

d. Good thermal and chemical stability.

e. Low risk of explosion.

f. Good storage quality.

g. Good compatibility with materials.

h. Easy transport and handling.

i. Low toxicity.

j. Low cost.

It is not possible to find a propellant combination which possesses all these desired qualities; therefore, all qualities must be compared and evaluated for the particular propulsion system and mission. This results in the selection of a propellant combination based on the qualities which are considered best for a specific propulsion system and mission, and with the remaining qualities still being acceptable even though not as good as desired.

5-2.1 Pressure-Fed Propulsion Systems

A liquid propulsion system is pressure-fed when the propellants are transferred from the propellant tanks to the engine entirely by the pressure in the tanks. Figure 5-7 is a schematic of a pressure-fed propulsion system used on tthe Apollo service module. The system consists of three subsystems: Pressurization, propellant feed, and the engine. The pressurization subsystem includes the helium pressurant bottle, pressure regulators, check valves, and relief valves. The propellant feed subsystem includes the tanks, and the lines and valves between the tanks and the engine. These subsystems contain the propellants and control their flow to the engine. The propellants react in the engine and are expelled through the engine nozzle to produce thrust.

In a pressure-fed system the propellant tank pressure should be about 75 psi higher than the combustion chamber pressure, P_c, to transfer the propellants and to decouple the engine from the feed system dynamics. In order to avoid excessive propellant tank weight, total impulse should be limited to a few million pound seconds, and P_c should not exceed about 300 psia. In order to avoid excessive engine weight and envelope at chamber pressures this low, the thrust level of pressure-fed engines is usually limited to about 10,000 lb.

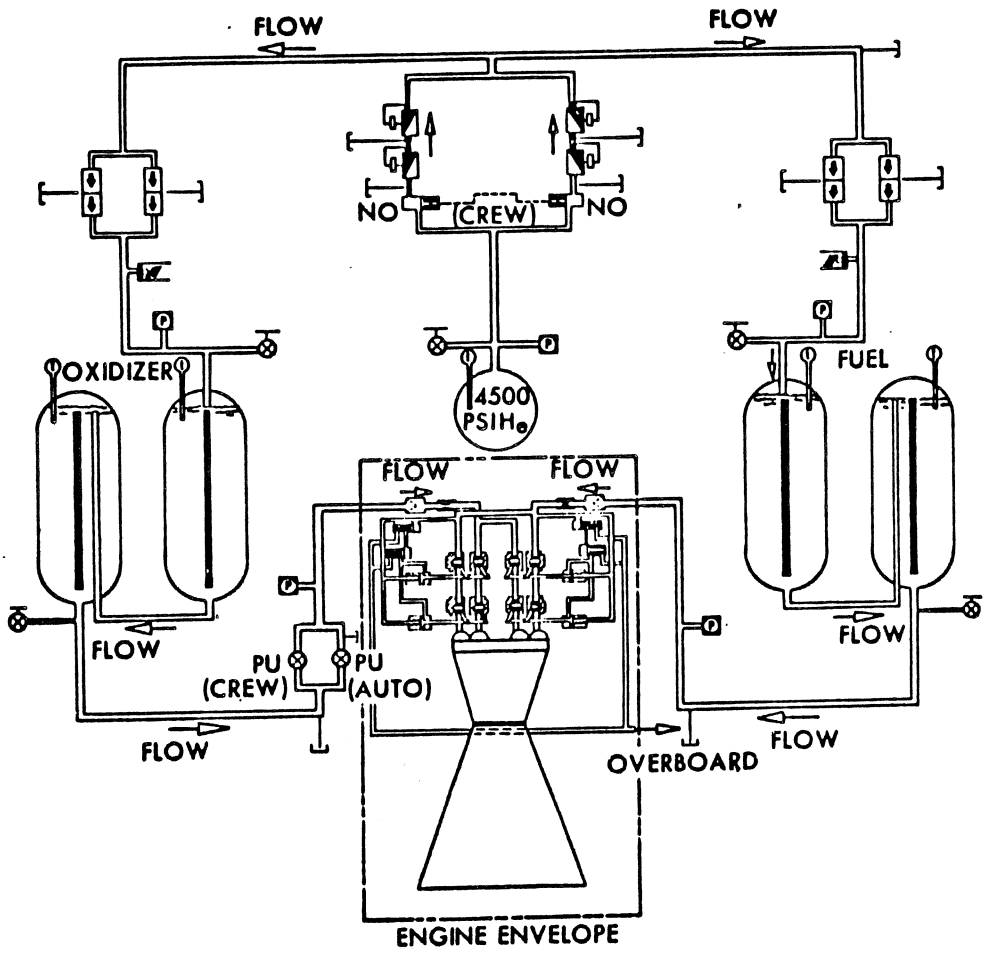

Figure 5-7. Pressure-Fed System

Pressure-fed systems are invariably heavier than pump-fed systems for comparable total impulse and thrust requirements. However, pressure-fed systems are simpler and, therefore, tend to be more reliable and less expensive. Because of this higher reliability, a pressure-fed system is often selected for critical applications in preference to a lighter-weight pump-fed system. For example, the Apollo service module propulsion system, shown in Figure 5-7, has a total impulse of about 12 million lb-sec, and a thrust level of about 20,000 lb. Based on these considerations, some bipropellant systems are pressure-fed. However, monopropellant systems, because of their small total impulse requirements and because of their emphasis on simplicity, are always pressure-fed.

5-2.2 Pump-Fed Propulsion Systems

A pump-fed system may be considered to be a pressure-fed system which has had a pressure-boost pump inserted in the propellant feed subsystem. In a pump-fed system, the propellant tank pressure can be reduced to a level which assures the minimum acceptable entrance pressure to the pump. This lower pressure permits a reduction in tank wall thickness which results in significantly lighter tanks. A boost pump can deliver the propellants to the engine at much higher pressure than a pressure-fed system, thus permitting reduction in engine envelope and weight for a given thrust level. In a pump-fed system, such as in the Saturn S-IVB, tank pressure is about 40 psia, and combustion pressure is about 800 psia. The propulsion system has a thrust of 230,000 lb and a total impulse of about 90 million lb-sec.

Figure 5-8 is a schematic of the J-2 engine system including propellant turbo-pumps. The LO_2 and LH_2 pumps are driven by direct drive turbines which are powered by the combustion products of an oxygen-hydrogen gas generator. The pump output pressures are about 1,200 psia, and most of the pressure drop to the combustion pressure occurs through the

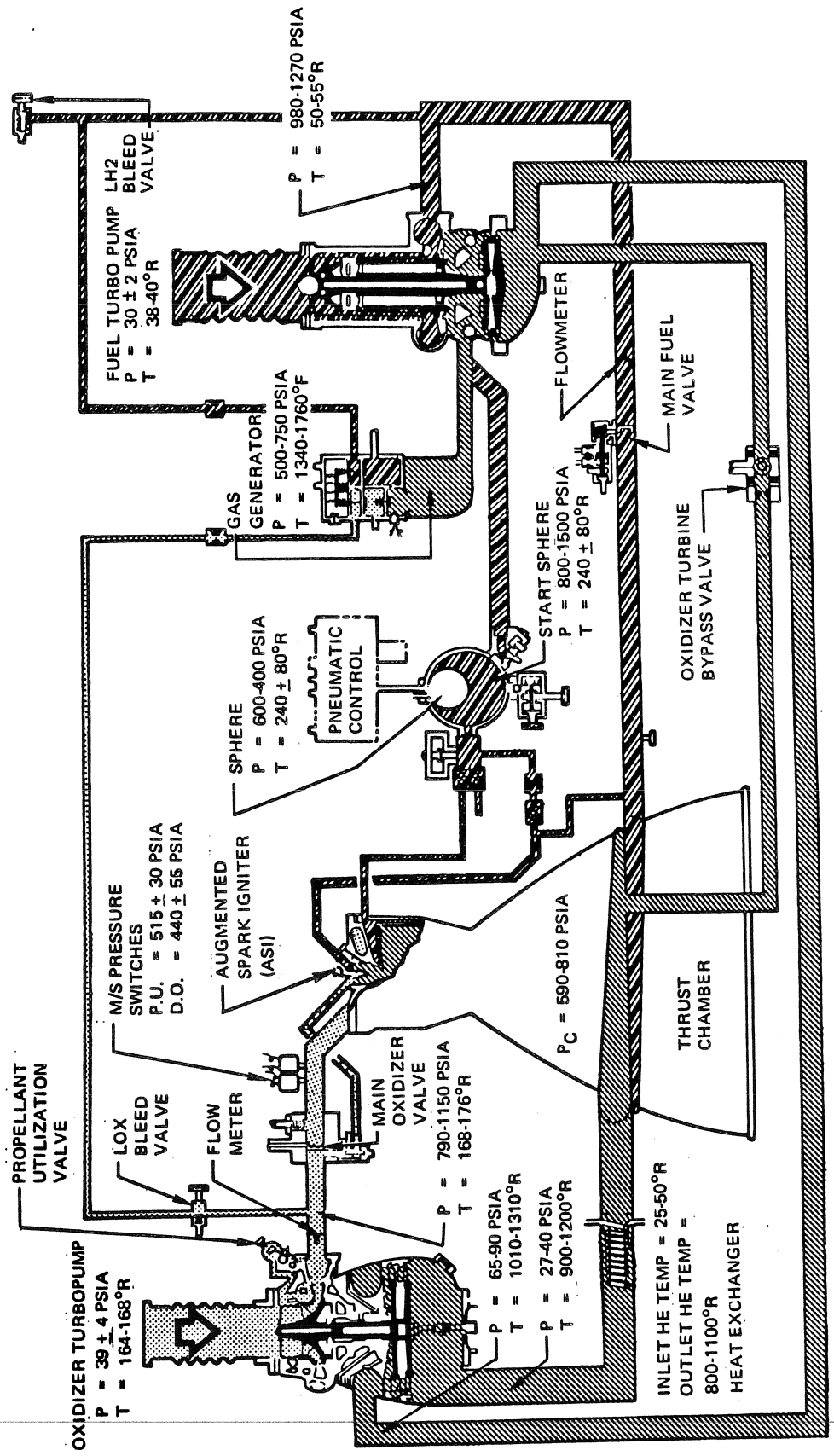

Figure 5-8. J-2 Engine Schematic

injector. The pressurization system and the propellant feed system are not shown, but the feed system lines connect to the oxygen and hydrogen turbopump inlet ducts. Figure 5-9 is an illustration of the J-2 engine installation which shows the manner in which the components are packaged in the S-IVB stage.

5-3 ROCKET ENGINE

The rocket engine consists of a thrust chamber assembly which generates thrust, and a thrust vector control system which directs the thrust.

5-3.1 Thrust Chamber Assembly

The purpose of the thrust chamber assembly (TCA) is to facilitate release of chemical energy from the propellants, and to convert this energy to thrust for a defined operating life. The efficiency of energy release and conversion to thrust is described by the specific impulse. The achievement of a desired operating life of the TCA is promoted by limiting the temperature of the chamber walls to values which are compatible with their structural capability, and by limiting the magnitude of pressure oscillations caused by combustion instability.

The principal components of the TCA are: The injector, the thrust chamber, and the nozzle. Additional components frequently considered to be part of the TCA include: The propellant valves, the igniter (if required), and the pressure-boost pump, if the propulsion system is pump-fed. The oxidizer and fuel are mixed and atomized by the injector, and the mixture reacts chemically in the combustion chamber. The resulting combustion products are accelerated in the nozzle and exhausted to the ambient at high velocity to produce a net thrust in the opposite direction.

As discussed in Section 4, paragraph 4-2, the specific impulse, I_{sp}, can be expressed in terms of c^* and C_F as:

$$I_{sp} = \frac{c^* C_F}{g}$$

where:

c^* = Characteristic exhaust velocity, ft/sec

C_F = Thrust coefficient

g = Acceleration of gravity, 32.17 ft/sec^2

The characteristic exhaust velocity, c^*, is a measure of the chemical energy in the propellants which is available for release. The magnitude of c^* depends primarily on the combustion temperature and the molecular weight of the combustion products. Each propellant combination has a unique value of c^* which is based on complete combustion of the propellants. Well designed rocket engines achieve values of c^* which are about 90 to 95 percent of the ideal value of c^*. The efficiency of combustion is controlled by the design of the injector and the combustion chamber.

The thrust coefficient, C_F, is a measure of the conversion of the released energy to thrust. The magnitude of C_F is determined primarily by the exit pressure ratio and the specific heat ratio of the combustion products. The efficiency of conversion of the energy of the combustion products to thrust is controlled by the design of the nozzle.

Figure 5-10 illustrates variations which occur in significant parameters as the propellants pass through the thrust chamber assembly. The oxidizer and the fuel are distributed in the manifold to appropriate injector locations before injection into the combustion chamber.

The supply pressure drops about 25 percent as the propellant flows through the orifices in the injector. The pressure remains essentially constant in the combustion chamber, decreases to about 50 percent of the chamber pressure in the nozzle convergent section, and then decreases to a very low pressure in the nozzle divergent section. The exit pressure is a function of the expansion ratio, $\epsilon = A_e/A_t$, where A is the cross-section area of the nozzle, and the subscripts refer to the exit-plane, e, and the throat-plane, t, respectively.

The propellant temperature rises rapidly in the combustion chamber to the combustion temperature. The temperature decreases about 15 percent in the nozzle convergent section and then decreases through the divergent section to about 25 percent of the combustion temperature at the nozzle exit, depending on the expansion ratio.

Combustion of the propellants occurs essentially at stagnation conditions. The combustion products accelerate to sonic velocity at the throat and then continue to accelerate supersonically in the divergent section of the nozzle. The Mach number at the exhaust plane is a function of ϵ.

a. Combustion Transients – The starting of a thrust chamber has to be controlled so that a timely and even ignition of propellants is achieved and that the chamber pressure and thrust are built up smoothly and quickly to their rated values. The *initial propellant flow is less than full flow*, and the *starting mixture ratio* is different from the *operating mixture ratio*. A low initial flow prevents an excessive accumulation of unignited propellants in the chamber and tends to assure a smooth buildup of chamber pressure.

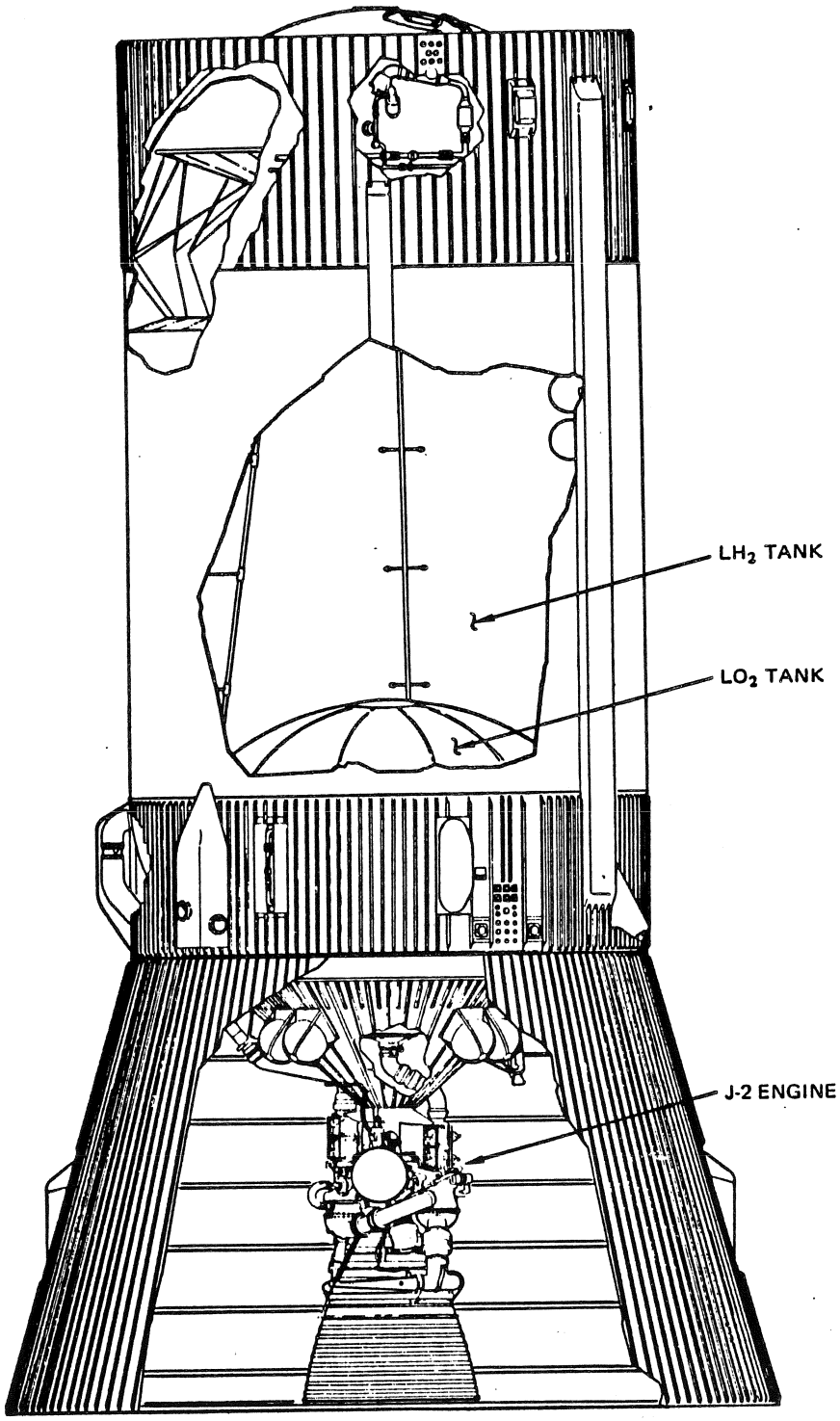

Figure 5-9. J-2 Engine Installation in the S-IVB Stage

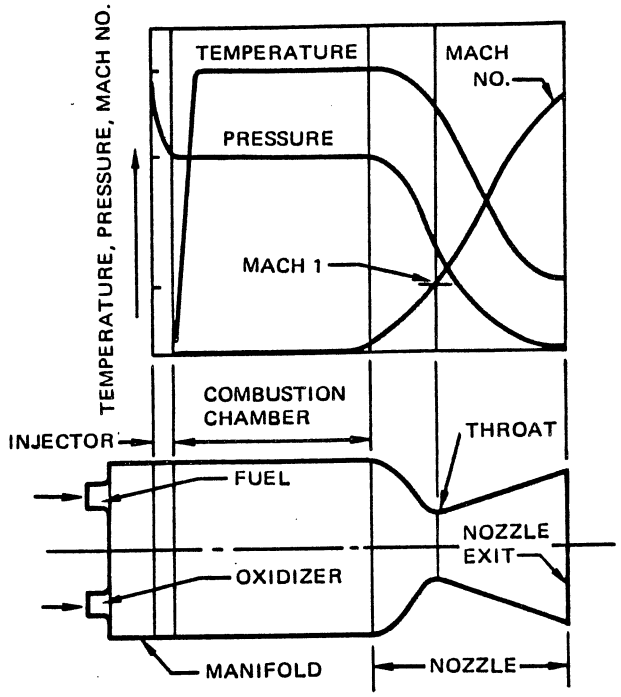

Figure 5-10. Thrust Chamber Assembly Parameters

The starting injection velocity is low, the initial vaporization and mixing of propellants in a cold combustion chamber is incomplete, and there will be local regions of lean and rich mixtures. The optimum starting mixture is, therefore, only an average of a range of mixture ratios, all of which are readily ignited. Mixture ratios near the stoichiometric mixture ratio have a high heat release per unit of propellant and therefore permit bringing the chamber and the gases up to equilibrium faster than would be possible with other mixtures.

Each propellant has a certain *ignition delay*, which is the time necessary to bring an ignitable mixture from the initial condition in the thrust chamber to the temperature at which rapid burning takes place. This delay has been measured and is usually less than 0.05 sec; this delay increases at lower liquid propellant ambient temperatures. During this interval, a quantity of unburned propellant accumulates in the chamber. If the delay is unduly long, or if the starting propellant flow is excessive, explosions may result which may be servere enough to cause the destruction of the complete rocket engine.

In starting a thrust chamber one propellant always reaches the chamber a very short time ahead of the other. It is almost impossible to synchronize the fuel and oxidizer feed systems exactly so that the propellants reach the chamber simultaneously at all injection holes. Frequently, a more reliable ignition is assured when one of the propellants is intentionally made to reach the chamber first. For a fuel-rich starting mixture the fuel is admitted first, while for a fuel-lean starting mixture the oxidizer is given the lead.

The propellant valves are, therefore, often so controlled that they operate in a definite sequence, thereby assuring an intentional lead of one of the propellants and a controlled buildup of flow and mixture ratio. Often the valves are only partially opened, avoiding an accumulation of hazardous unburned propellant mixture in the chamber. Once combustion is established, the valves are fully opened and full flow may reach the thrust chamber assembly. The initial reduced flow burning period is called the *preliminary stage*. Opening of the fuel and oxidizer valves is so sequenced and controlled that an orderly buildup of chamber pressure, flow, and thrust and an orderly transition to the rated operating mixture ratio are achieved without entering a regime of potential combustion instability.

Propellants that do not ignite spontaneously need to be activated by the addition of energy supplied by an igniter. The igniter is located near the injector, so that it can ignite the starting mixture, but out of the main flow stream so that it does not obstruct steady state combustion. At least four different types of successful propellant igniters have been used.

Spark plug ignition has been used successfully on liquid oxygen-liquid hydrogen thrust chambers. The spark plug is usually located in a region where initial fuel and oxidizer vapors will form an ignitable mixture. This method seems to be particularly applicable to rocket engines which need to be restarted in flight. The spark plug is often built into the injector. Many of the early rocket thrust chamber designs used this ignition method, and it is currently used on the J-2 engine.

Pyrotechnic ignition makes use of a solid propellant squib or grain with a burning duration of a few seconds. The solid propellant charge is electrically ignited by a hot wire or other means and burns with a hot flame within the combustion chamber. Almost all solid propellant rockets (reference Section 6) and many liquid rocket chambers are ignited in this fashion. The igniter container may be designed to fit directly onto the injector or the chamber, or may be held in the chamber from outside through the nozzle. A pyrotechnic igniter can only be used once. The charge must be replaced before another ignition can be accomplished.

Another method of ignition is called precombustion chamber ignition. In precombustion chamber ignition a small starting chamber is connected to the main combustion chamber through an orifice. This starting chamber is similar to the precombustion chambers used on some internal combustion engines. A small amount of fuel and oxidizer is injected into the precombustion chamber and ignited by a spark plug, catalyst, or other means. The burning mixture exhausts into the main combustion chamber in a torch-like fashion and ignites the main propellant flow which is injected into the main chamber. This ignition procedure permits repeated starting of variable thrust engines and has proved successful with oxygen-gasoline, oxygen-alcohol and acid-kerosene thrust chambers.

Auxiliary fluid ignition is a method whereby some liquid or gas, in addition to the regular fuel and oxidizer, is injected into the combustion chamber for very short periods during the starting operation. This fluid is hypergolic with either the fuel or the oxidizer so that it produces spontaneous combustion. The combustion of nitric acid and some organic fuels can, for instance, be initiated by the introduction of a small quantity of aniline at the beginning of the rocket operation. Liquids, such as triethyl aluminum (TEA) and triethyl boron (TEB) can accomplish a hypergolic ignition when preloaded in the fuel piping. A mixture of TEA and TEB is used to ignite the Thor engines.

b. Combustion Instability – Some nominal fluctuation of combustion pressure occurs during normal combustion. When the magnitude of this cyclic pressure variation becomes significant, the combustion process is described as unstable. If the pressure fluctuations become very large, structural failure of the thrust chamber assembly may occur.

Combustion instability can occur over a range of frequencies from a few cycles per second to ultrasonic. Three distinct types of instability occur within this frequency spectrum, as shown in Table 5-4. At frequencies below about 1,000 cycles per second, combustion instability is usually caused by fluctuations in the feed system pressure. At higher frequencies, the combustion process itself is the source of the disturbance. Generally, the higher frequencies are more damaging to the chamber and are more difficult to control.

Combustion instability is controlled primarily by the injector design. The injector promotes smooth combustion by providing a finely atomized, intimate mixture of the propellants in the proper mass ratio, a short distance from the injector face. Incorporation of a significant pressure drop across the injector effectively decouples the combustion process from the propellant feed system dynamics which are the principal source of low frequency instability. A well designed injector also minimizes the tendency towards high frequency combustion instability by control of the propellant mass distribution across the combustion chamber diameter.

Table 5-4. Types of Combustion Instability

FREQUENCY RANGE	COMPARATIVE WAVE LENGTH	TERMINOLOGY	MODE
LOW <100 CPS	LONGER THAN THE LONGEST DIMENSION OF THE ENGINE SYSTEM	FEED SYSTEM COUPLED; CHUG, SURGE, ETC.	LONGITUDINAL
INTERMEDIATE 100 TO 1,000 CPS	SHORTER THAN PROPELLANT FEED LINES, BUT LONGER THAN THRUST CHAMBER ACOUSTIC MODES.	FEED SYSTEM COUPLED MODE; BUZZ, ENTROPY WAVE, ETC.	USUALLY LONGITUDINAL
HIGH >1,000 CPS	ORDER OF THRUST CHAMBER ACOUSTIC MODES	COMBUSTION INSTABILITY, ACOUSTIC, INTRINSIC, SCREAMING, ETC.	USUALLY TRANSVERSE (RADIAL OR CIRCUMFERENTIAL)

The magnitude of combustion instability increases as its frequency approaches the natural acoustic frequencies of the combustion chamber. These natural frequencies are determined by the physical dimensions of the thrust chamber. When the thrust chamber design does not reduce the higher frequency combustion pressure fluctuations to within acceptable limits, baffles are incorporated in the combustion chamber usually as part of the injector, to attenuate the pressure spikes by shifting natural frequencies.

The thrust chamber wall temperature is dependent on the temperature of the combustion gas, the heat transfer rate between the gas and the interior wall surface, and the rate of rejection of heat absorbed at this surface. The gas temperature is determined by the combustion process. The unit heat transfer rate to the interior wall surface is dependent on the temperature difference between the gas and the wall, and on the coefficient of convective heat transfer.

This coefficient is dependent upon the velocity of the gas flow, the system geometry and the thermal properties of the gas. For normal combustion, the heat transfer rate increases rapidly in the nozzle convergent section, reaches a maximum at the throat and decreases rapidly in the expansion section. Thus, the portions of the thrust chamber adjacent to the nozzle throat are most susceptible to premature failure due to heating, and the design of this section frequently incorporates special high-temperature materials or added capability for conducting the heat away from this area. When combustion instability occurs, the heat transfer rate in all sections of the thrust chamber assembly increases significantly.

5.3.1.1 Injector Design

An injector is designed to control the flow of propellants to the combustion chamber to achieve efficient and stable combustion, and to control the temperature of the thrust chamber walls. Normally, an injector consists of two propellant distribution manifolds and an orifice plate. The manifolds distribute the oxidizer and the fuel to desired locations across the thrust chamber diameter. The plate contains orifices at these locations to meter and direct the flow of the propellants into the combustion chamber.

The injector design controls: The pressure drop across the injector at the required propellant flowrate, the propellant mass distribution, the local oxidizer-to-fuel mixture ratio, and the fineness of the propellant atomization in the combustion chamber. The pressure drop across the injector should be about 25 percent of the supply pressure in order to assure that the low frequency variations in the feed system pressure do not cause combustion instability.

The propellant mass distribution should be concentrated at a cross-sectional diameter which is equal to the combustion chamber radius, in order to minimize the contribution of the combustion process to combustion instability. The mixture ratio at all locations should be equal to the overall desired mixture ratio, and the drop sizes of the atomized propellants should be small to promote complete combustion.

Injectors are frequently designed to provide a fuel-rich propellant mixture adjacent to the chamber walls to maintain their temperature below some critical value. This distribution results in increased operating life, but decreases the efficiency of combustion.

5-3.1.1.1 Injector Configuration

Many different injector configurations have been used in rocket engines. The configurations can be categorized according to the method used to atomize the propellants, such as: Impinging jets, impinging sheets, nonimpinging jets or sheets, and combinations of the first three categories. Figure 5-11 illustrates some typical injector configurations in each of these categories. The configurations shown are repeated in a pattern around the injector face to achieve a desired mass distribution of the propellants.

Selection of a particular injector configuration is usually based on performance considerations. When performance is not critical, or when several alternate configurations meet the performance requirements, cost usually becomes the dominant selection criterion. Because the development of new configurations increases cost, engine manufacturers tend to use injector categories and configurations that have proven satisfactory in previous designs.

An injector may contain more than one configuration in order to achieve special performance characteristics, such as a fuel-rich mixture near the chamber walls, or a variation in propellant mass distribution across the chamber diameter. Figure 5-12 shows the injector pattern for a version of the LEM descent engine which uses several injector configurations in different density distributions. This varied pattern was selected to achieve stable and efficient combustion with relatively cool chamber walls.

Injector effectiveness is usually measured by the c^* efficiency achieved in the engine. However, most engines can achieve a relatively high c^* efficiency if the combustion chamber is large because the propellants will remain in the combustion chamber a longer time, permitting vaporization and reaction of poorly atomized propellants. The characteristic length, L^*, is a measure of the time that the propellants remain in the combustion chamber. The propellants must be mixed and atomized very quickly in order to achieve complete combustion in a small L^* combustion engine. Therefore, it is appropriate to measure injector effectiveness in terms of the c^* efficiency achieved in a given L^*.

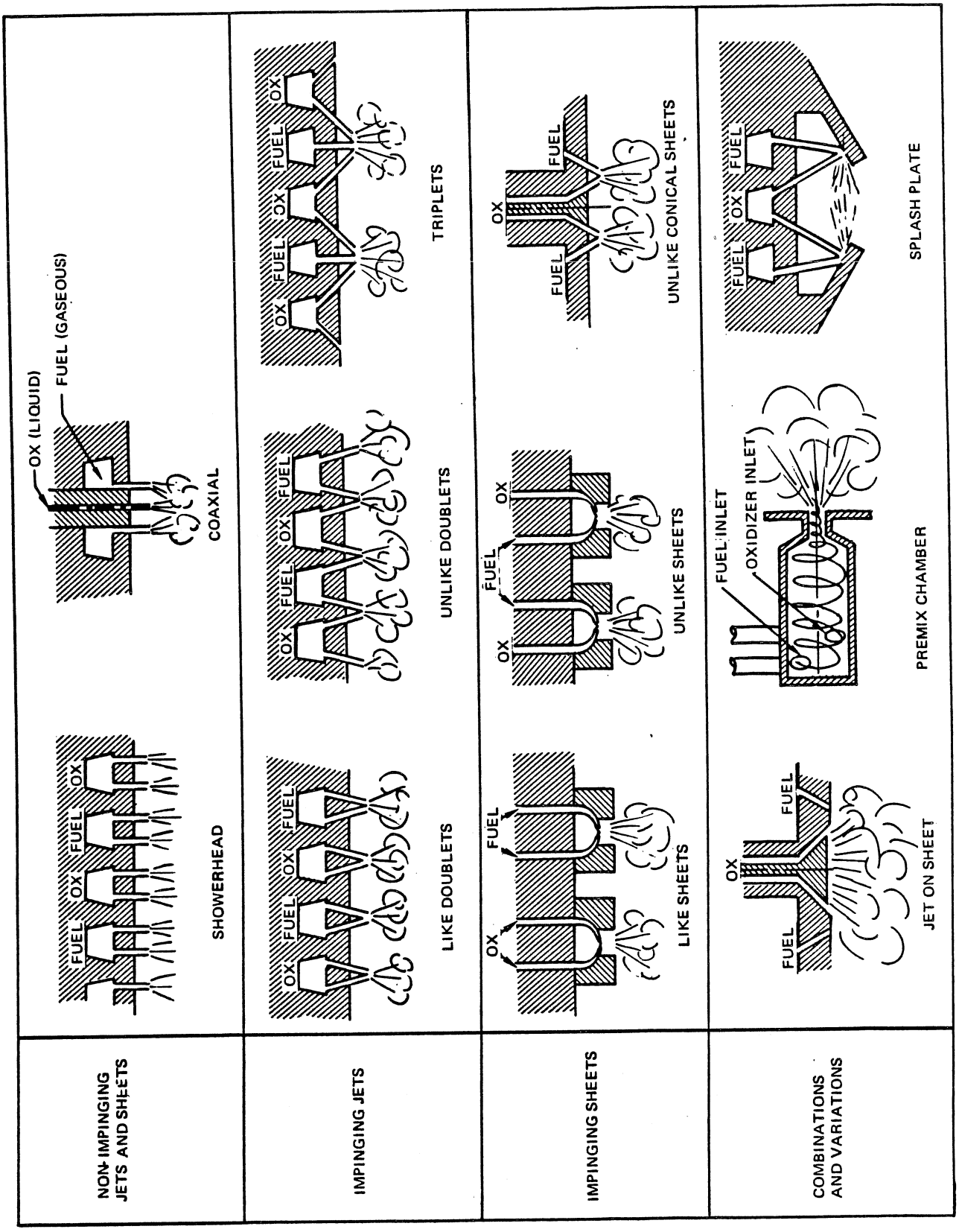

Figure 5-11. Schematic Diagrams of Representative Injector Configurations

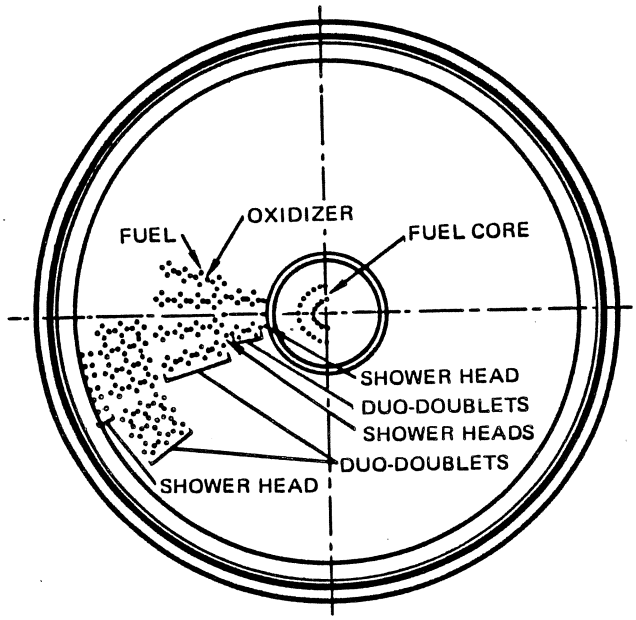

Figure 5-12. Complex Injector Pattern

Impinging-jet injector configurations are most frequently used because they provide good performance at a reasonable cost. The selection of doublets, triplets, or larger numbers of jets intersecting at a common point is based on design considerations such as the propellant characteristics, the mixture ratio, and the thrust per injector cluster. Engines which use liquid oxygen and kerosene base propellants, such as those on Thor, Atlas, and Saturn IC boosters, use impinging-jet configurations.

Aerojet has developed an injector design, called the Hyperthin injector in which the impinging-jets are so small that very high c^* efficiency is achievable in low thrust, low L^* engines. A like-impinging doublet Hyperthin injector has been used successfully with storable hybergolic propellants in a very low L^* engine in the jet interaction control system of an experimental MDAC flight vehicle. Impinging sheet injectors have delivered very high c^* efficiencies in low L^* experimental engines, using earth storable hypergolic propellants, up to 5,000 lb thrust.

In the nonimpinging jet and sheet category, shower heads and coaxial configurations are most commonly used. The shower head injector is inexpensive but gives only moderate c^* efficiency and requires larger values of L^*. It is used sometimes in conjunction with other configurations as shown in Figure 5-12. The coaxial injector is of interest when one of the propellants enters the combustion chamber as a gas. The relatively high gas velocity shears the liquid thus promoting atomization and mixing. The coaxial configuration is used in the Saturn J-2 engines which use liquid hydrogen and liquid oxygen as the propellants. The hydrogen enters the combustion chamber as a gas in the annular ring which surrounds the liquid oxygen stream.

The jet-on-sheet configuration shown in Figure 5-11 is used as a single element with hypergolic earth storable propellants in the TRW 1,050- to 10,500-lb variable thrust LEM descent engine. This configuration has been successfully tested in a 250,000-lb fixed thrust design, still using a single element and the same propellants, in the minimum cost booster design program which was sponsored by USAF Rocket Propulsion Laboratory. This injector provides high c^* efficiency in fairly large L^* engines.

The use of premix chambers and splash plates has diminished in recent years with the development of the higher performance injector configurations described in the preceeding paragraphs.

5-3.1.1.2 Injector Control of Combustion Stability

Although the injector is intended primarily to promote efficient combustion, its design also exerts a significant influence on the stability of combustion. Table 5-4 lists the principal causes of combustion instability in terms of the frequency range of pressure fluctuations. The low frequency range is readily eliminated by providing a pressure drop across the injector of about 25 percent of the propellant supply pressure.

The intermediate frequency range combustion instability is generally caused by mechanical vibrations of the structure of the engine, and by miscellaneous other causes including flow disturbances caused by high heat-transfer rates. The intermediate frequency range of instability is difficult to eliminate when it occurs. Fortunately, the pressure amplitude fluctuations generally do not exceed 5 percent of the chamber pressure, so that this category of instability rarely causes significant damage to the engine.

High frequency combustion instability is most frequently encountered in liquid propellant engines, and it is this type of instability which causes the major engine damage attributed to combustion instability. Therefore, a significant portion of injector design effort is concerned with minimizing the occurrence and magnitude of high-frequency combustion instability.

High-frequency combustion instability is considered to be a forced oscillation of the combustion chamber gases, which is driven by the interaction of the resonance properties of the combustion process and the resonance properties of the chamber geometry. Therefore, this instability can be treated as a phenomenon which is not influenced directly by feed-system effects. The chemical reaction of the propellants supplies the energy to

support the pressure oscillations, and the combustion chamber geometry causes amplification of the pressure at frequencies which correspond closely to the acoustic resonances of the combustion chamber.

High frequency instability occurs in both longitudinal and transverse modes. The longitudinal mode propagates in the chamber axial direction. For this mode, the injector face plate and the converging section of the nozzle act as boundaries which reflect the pressure waves without phase reversal. The frequency of longitudinal instability is a function of acoustic velocity and chamber length.

$$\text{Frequency} = \frac{a}{2L} \qquad (1)$$

where:

a = Acoustical velocity, ft/sec

L = Chamber length, ft

The frequency of longitudinal instability generally is higher than 500 cycles per second and increases as the chamber length decreases. This type of instability usually is not damaging and it can be minimized by incorporating an annular cavity baffle on the face of the injector.

The transverse modes of instability propagate in the direction which is normal to the chamber axis. These modes are tangential or radial. The transverse modes are predominant in large, high-performance rocket engines and can be very destructive because they are capable of causing pressure fluctuations that exceed 100 percent of the rated chamber pressure in the region near the injector face. These large amplitude, high frequency pressure changes can produce an increase of the heat transfer rate for steady-state combustion. Such an increase can cause a burnout of the injector or of tube-wall combustion chambers in time periods as short as 100 milliseconds.

Figure 5-13 shows the pressure distributions, at several time intervals, for several transverse modes of instability in a chamber of cylindrical cross-section. The solid lines represent pressures greater than the mean pressure throughout the cavity, and the dotted lines represent pressures lower than the mean. Two different types of wave forms have been observed for tangential modes. One is the standing mode which can be considered to have a wave form that remains fixed in position while the amplitude fluctuates. The other wave form is the spinning tangential wave, in which the amplitude remains constant while the entire wave form rotates.

Transverse modes of instability are sloshing modes. During steady-state combustion, the chamber pressure can be represented by a mean value. If the chamber is excited into the first tangential standing mode, the pressure starts off high on one side of the chamber and low on the other side. A quarter of a cycle later the pressure is uniform and conforms to the mean chamber pressure. A half cycle after the initial condition, the pressure is high on the side of the chamber where it was low originally, and vice versa. In the standing mode of instability, the line of mean pressure remains fixed and the gas moves with respect to the line.

The first tangential mode of instability has a region of uniform pressure (node) at the center, and regions of maximum pressure fluctuation (anti-nodes) at the walls of the chamber. To minimize tangential instability modes, the propellants should be concentrated near the center of the chamber where pressure fluctuations are small.

The first radial mode has maximum pressure fluctuations at the walls and the center of the chamber. The minimum pressure fluctuation occurs at 63 percent of the maximum radius. Thus, to minimize radial modes of instability, the propellants should be concentrated in a ring at 63 percent of the chamber diameter.

To minimize instability caused by both radial and tangential modes, the propellant mass should be concentrated in a ring at about 50 percent of the chamber diameter. This mass distribution, shown in Figure 5-14, is known as the humped distribution. The humps should be high and narrow to minimize combustion instability most effectively.

Upon initiation of a radial mode of instability, the gas motion causes the pressure to be high at the center line of the combustion chamber, and low at the chamber wall. One half cycle later, the pressure becomes low at the center line where it had been high, and vice versa.

Higher harmonics of transverse waves are more difficult to visualize. For example, in the second standing tangential mode there are two waves sloshing simultaneously in the chamber, each having its own corresponding high and low pressure positions.

The high-frequency tangential mode of combustion instability occurs more frequently than the radial mode in a combustion chamber of circular cross-section. The spinning tangential mode occurs more frequently than the standing tangential mode in combustion chambers that do not have baffles.

Baffles are incorporated in the combustion chamber when combustion instability cannot be reduced to acceptable limits by control of the injector design. Figure 5-15 illustrates two commonly used baffle configurations. The radial ridges on the injector face diminish tangential instability, and the concentric ring ridges on the injector face reduce radial instability. Longitudinal instability is decreased by the inclusion of a small annular volume at the juncture of the injector and the chamber walls.

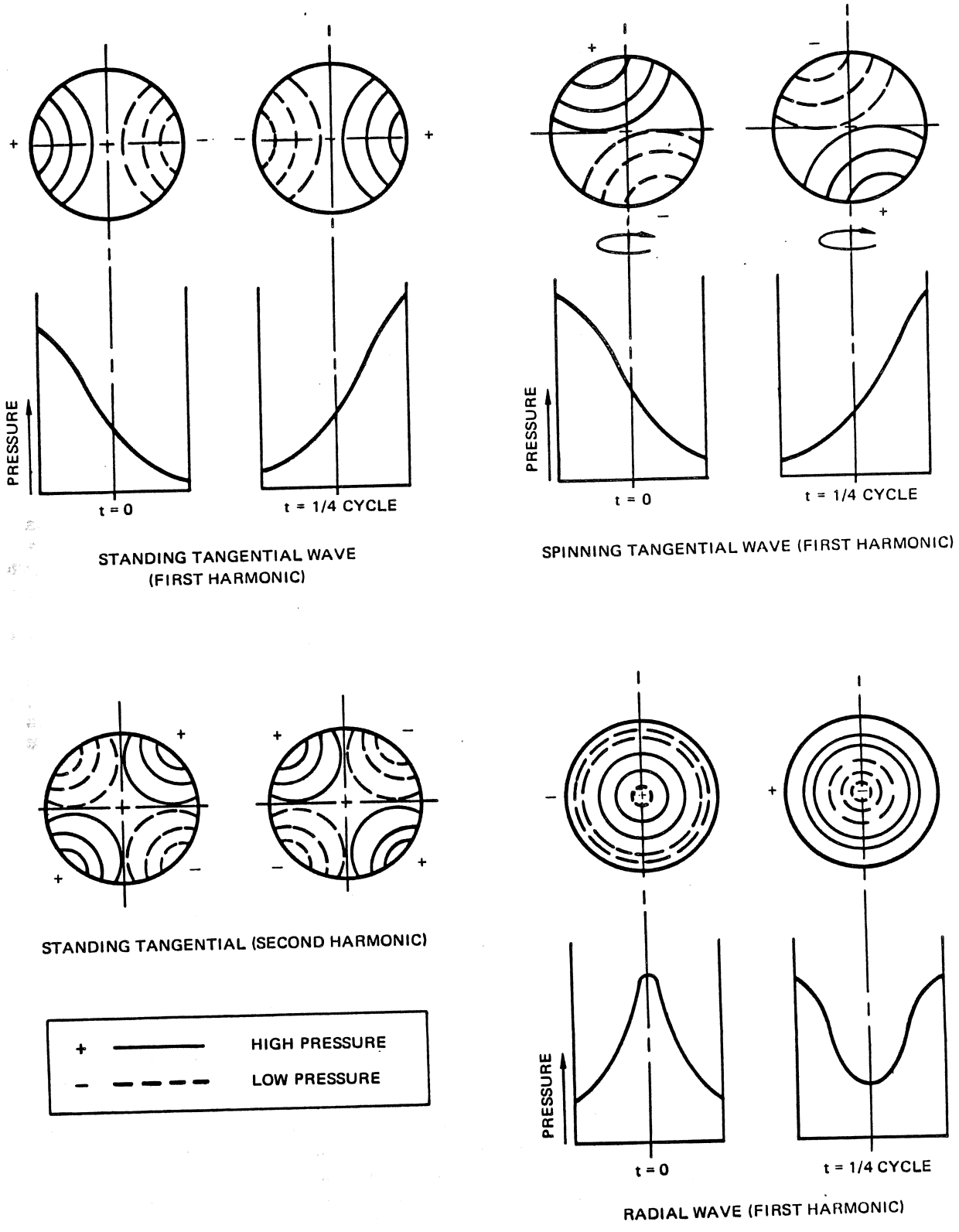

Figure 5-13. Transverse Mode Pressure Distributions

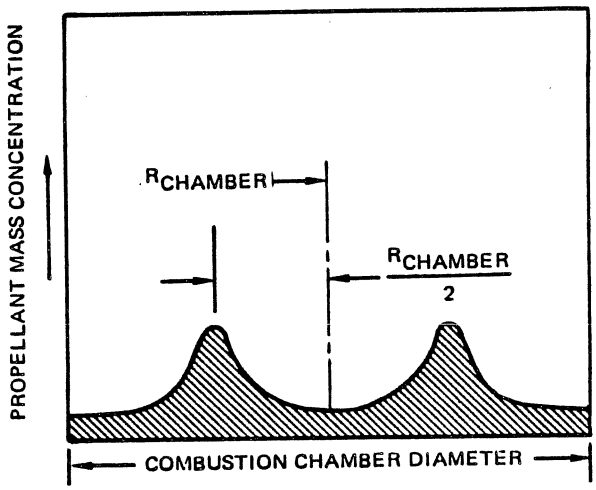

Figure 5-14. Propellant Humped Mass Distribution

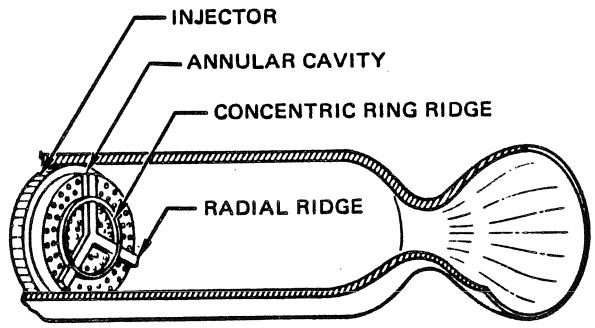

Figure 5-15. Typical Baffle Configurations

Perforated accoustic liners in the combustion chamber are also used to damp combustion instability. All of these devices change the combustion chamber geometry to shift the natural frequencies of the chamber and thus attenuate the amplitude of the acoustic pressure waves at the operating frequencies.

5-3.1.2 Combustion Chamber

The combustion chamber is a pressure vessel with an injector on one end and a nozzle on the other end. Most combustion chambers have a circular cross-section to minimize weight and facilitate economical fabrication. A well designed chamber promotes efficient combustion of the propellants and minimizes heat loss through the walls. The ideal rocket equations presented in Section 4 are based on the assumption that combustion is completed in the combustion chamber, and that the hot gas products are expanded and accelerated in the nozzle.

The combustion process consists essentially of three steps: Propellant mixing to form droplets, vaporization of the droplets, and chemical reaction of the vapor. Since the chemical reaction occurs very quickly, the time required for the mixing and vaporization processes determines how long the propellants must remain in the combustion chamber for the chemical reaction to be completed. The characteristic length, L^*, is a measure of the stay-time of the propellants in the combustion chamber. The parameter L^* is defined as:

$$L^* = \frac{V_c}{A_t} \qquad (2)$$

where:

V_c = Combustion chamber volume, ft^3

A_t = Nozzle throat cross-section area, ft^2

The value of L^* should be kept to a minimum, consistent with efficient combustion, to minimize envelope, weight, heat losses, and the time for thrust to build up and decay. The injector design controls propellant mixing and the size of the drops that are formed. The rate of vaporization is a characteristic of the propellants. Thus, for a given propellant combination, the injector design controls the magnitude of L^*.

Rate of heat transfer to the walls is a function of the gas temperature and the coefficient of heat transfer. Figure 5-16, which shows the variation of the heat transfer rate in a typical engine, emphasizes that this rate is greatest in the vicinity of the nozzle throat, even though the gas at this location is significantly cooler than the maximum combustion temperature. Thus, any evaluation of heat lost from the engine must include consideration of the nozzle as well as the combustion chamber.

5-3.1.2.1 Thrust Chamber Heating

In a rocket engine, the energy lost to the walls of the thrust chamber by heat transfer causes an increase in the wall temperature. The engine design must include provisions for dissipating this heat to a thermal sink to prevent excessive wall temperatures. Heat is transferred by convection and radiation from the hot combustion gases to the thrust chamber wall. This raises the temperature of the wall on the hot gas side, T_{w_1}, as shown in Figure 5-17, and causes heat to flow by conduction through the wall, thus raising the temperature of the wall and its outer surface, T_{w_2}. Heat from the outer surface is then transferred to the cooler thermal sink, or ambient environment, T_s, by convection and radiation. The wall temperature continues to increase until equilibrium conditions are established, at which time the heat transfer rates from the hot gas to the wall, through wall, and from the wall to the thermal sink are all equal.

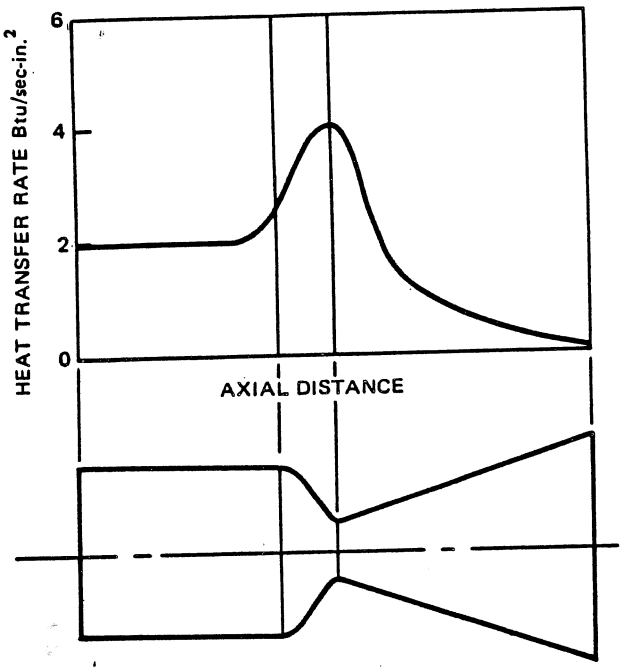

Figure 5-16. Typical Heat Transfer Rate Variation

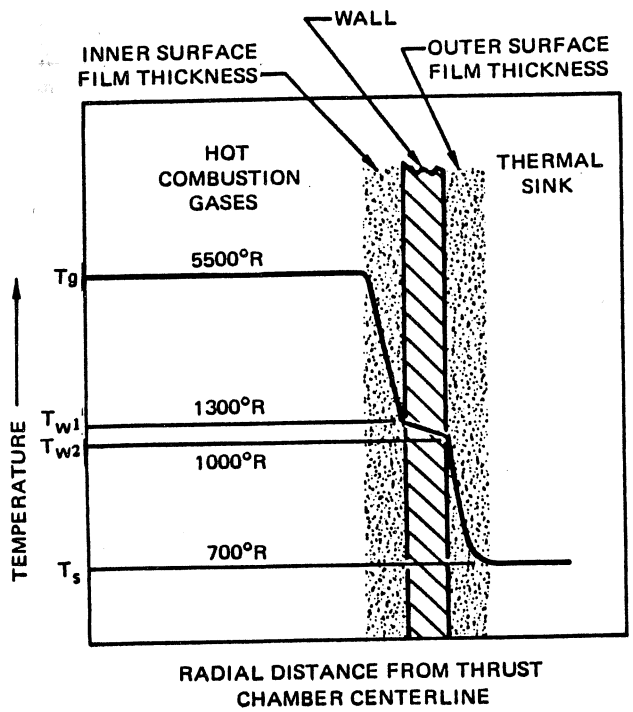

Figure 5-17. Typical Temperature Gradient at the Thrust Chamber Wall

It is desirable to minimize the transfer of heat from the combustion gases to the thrust chamber walls in order to maximize propulsion efficiency and minimize wall cooling problems.

Generally, less than 5 percent of the total energy generated during combustion is transferred as heat to the chamber walls. For a typical rocket of 10,000-lb thrust, the heat rejection to the wall may be between 700 and 3000 Btu/sec, depending on the exact conditions. Most of the lost heat is transferred to the chamber wall by means of convection. The portion of lost heat transferred by radiation varies from about 5 percent for small engines to as much as 25 percent for large engines. The products of combustion, such as CO, CO_2 and H_2O, which emit and absorb radiation, are the source of the radiation loss. If metals are added to the fuels, such as in slurries, radiation losses may be significantly greater.

The steady-state heat transfer rate, q, through the thrust chamber wall can be approximated by:

$$q = q_{c_1} + q_{r_1} = q_k = q_{c_2} + q_{r_2} \qquad (3)$$

Equation 3 can be restated in terms of the temperature distribution shown in Figure 5-17 as:

$$\begin{aligned} q &= (\bar{h}_{c_1} + \bar{h}_{r_1})\, A_1 (T_g - T_{w_1}) \\ &= \frac{kA}{L}(T_{w_1} - T_{w_2}) \\ &= (\bar{h}_{c_2} + \bar{h}_{r_2})\, A_2 (T_{w_2} - T_s) \end{aligned} \qquad (4)$$

If the thrust chamber wall is thin, equation 4 can be approximated by:

$$\begin{aligned} q &= (\bar{h}_{c_1} + \bar{h}_{r_1})(T_g - T_{w_1}) \\ &= \frac{k}{L}(T_{w_1} - T_{w_2}) = (\bar{h}_{c_2} + \bar{h}_{r_2})(T_{w_2} - T_s) \end{aligned}$$

where:

q/A = Total heat transfer rate, Btu/hr

q_c = Convective heat transfer rate, Btu/hr

q_r = Radiative heat transfer rate, Btu/hr

q_k = Conductive heat transfer rate, Btu/hr

$\bar{h}_c$ = Average convective heat transfer coefficient, Btu/hr-ft²-°R

$\bar{h}_r$ = Average radiative heat transfer coefficient, Btu/hr-ft²-°R

k = Thermal conductivity, Btu/hr-ft-°R

L = Wall thickness, ft

A = Heat transfer area, ft^2

T_g = Gas temperature, °R

T_w = Wall temperature, °R

T_s = Sink temperature, °R

q/A = Heat transfer rate per unit area, $Btu/hr\text{-}ft^2$

Subscript 1 refers to conditions on the hot gas side of the wall and subscript 2 refers to conditions on the cool sink side of the wall.

The heat loss, q, is determined primarily by the value of $\bar{h}_{c_1}$ and, to a lesser extent by the value of $\bar{h}_{r_1}$. The equilibrium temperature T_{w_2} of the outer surface of the thrust chamber wall is determined primarily by $\bar{h}_{c_2}$ if the ambient environment consists of a fluid, or by $\bar{h}_{r_2}$ if the ambient is a vacuum. The equilibrium temperature T_{w_1} of the inner surface of the thrust chamber is determined primarily by T_{w_2} and k.

The combustion gas convective heat transfer coefficient, h_{c_1}, is a function of the fluid flow, thermal properties of the fluid, and system geometry. The Bartz equation following, which frequently is used to calculate the value of h_{c_1}, has been shown to correlate fairly well with limited experimental data.

$$h_{c_1} = \frac{0.026}{D_t^{0.2}} \left[\left(\frac{\mu^{0.2} C_p}{Pr^{0.6}}\right)_o \left(\frac{P_c g}{c^*}\right)^{0.8}\right] \left(\frac{A_t}{A}\right)^{0.9} \sigma \quad (5)$$

where:

$\bar{h}_{c_1}$ = Convective heat transfer coefficient, $Btu/sec\text{-}in^2\text{-}°R$

A = Local cross-section area of flow, in^2

A_t = Throat cross-section, area, in^2

C_p = Specific heat at constant pressure, Btu/lb-°R

c^* = Characteristic exhaust velocity, ft/sec

D_t = Throat diameter, in

g = Gravitation acceleration, ft/sec^2

k = Thermal conductivity, Btu/sec-in-°R

P_c = Chamber pressure, lbs/in^2

Pr = Prandtl number = $\mu C_p/k$

μ = Viscosity, lb/in-sec

σ = Boundary layer correction factor

The factor σ, which contains corrections for gas property variations across the boundary layer, can be determined from the curves in Figure 5-18. It should be noted that some of the units used in the Bartz equation differ from conventional heat transfer units. The subject of convective heat transfer is covered in greater detail in Section 14, Heat Transfer.

The factor within the brackets in equation 5 is constant throughout the nozzle, since the evaluation is made at stagnation conditions, so that only (A_t/A) and σ need to be evaluated at each station. Typically, σ has a value close to unity. Equation 5 shows that, for a given application, h_c reaches its maximum value at the throat $(A = A_t)$. Furthermore, at any given position in the thrust chamber, h_c increases rapidly as P_c increases, and h_c decreases slowly as D_t increases. The value of P_c in present engines generally does not exceed 1,000 psia, with resultant values of q/A of less than 20 $Btu/sec\text{-}in^2$, or about 10^6 $Btu/hr\text{-}ft^2$.

Future engine requirements call for higher values of P_c to improve performance in a compact configuration. This will increase both h_c and q/A. The resulting increased cooling problems may be solved by use of advanced cooling techniques such as film or transpiration cooling. However, if these advanced cooling methods prove to be impractical in specific applications, it will be necessary to decrease P_c and increase D_t until the required thrust is achieved with an acceptable heat transfer rate.

Figure 5-19 is a nomograph which permits rapid estimation of h_{c_1}. Its use requires estimation of the specific heat ratio, γ the gas thermal conductivity, k, and the Reynolds number (Re) of the combustion gas. A value of γ of 1.2 may be used for solid propellants, and 1.3 for liquid propellants. The value of k is a function of the composition of the exhaust products, and it increases with increase in temperature. At 3500°R, k typically has a value of 0.06 Btu/hr-ft-°R for oxides of carbon and nitrogen, and has a value of 0.114 for steam.

A value of h_{c_1} can be obtained from Figure 5-19 by using the following procedure:

a. Estimate values of γ and k.

b. Calculate Reynolds number.

c. Draw a straight line between these values of Re and γ. The intersection of this line with the right index line establishes the right index point.

d. Draw a straight line between the estimated value of k and the hydraulic diameter D_H. The intersection of this line with the left index line establishes the left index point. Since D_H is 4 times the flow cross-sectional area divided by the wetted perimeter, D_H is the inside diameter for circular cross-sections.

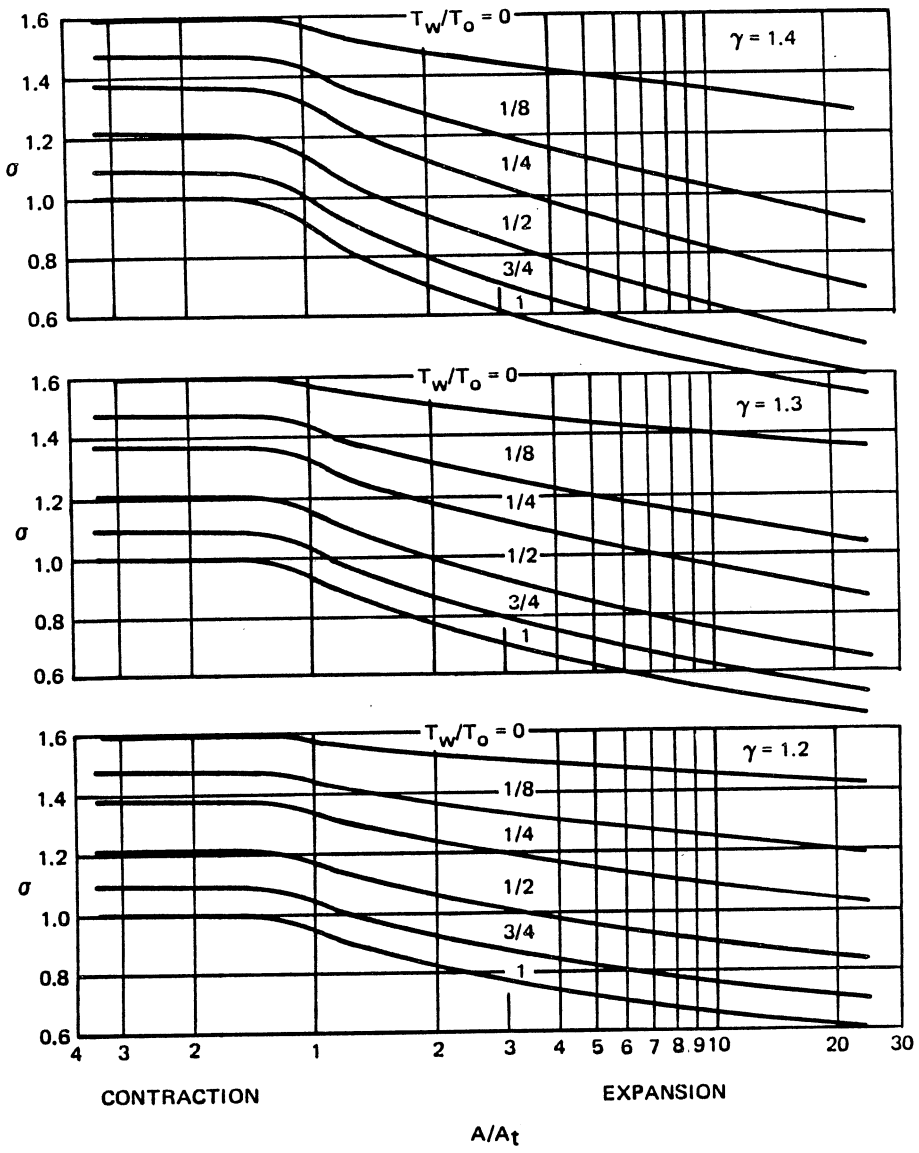

Figure 5-18. Values of the Properties Variation Parameter σ

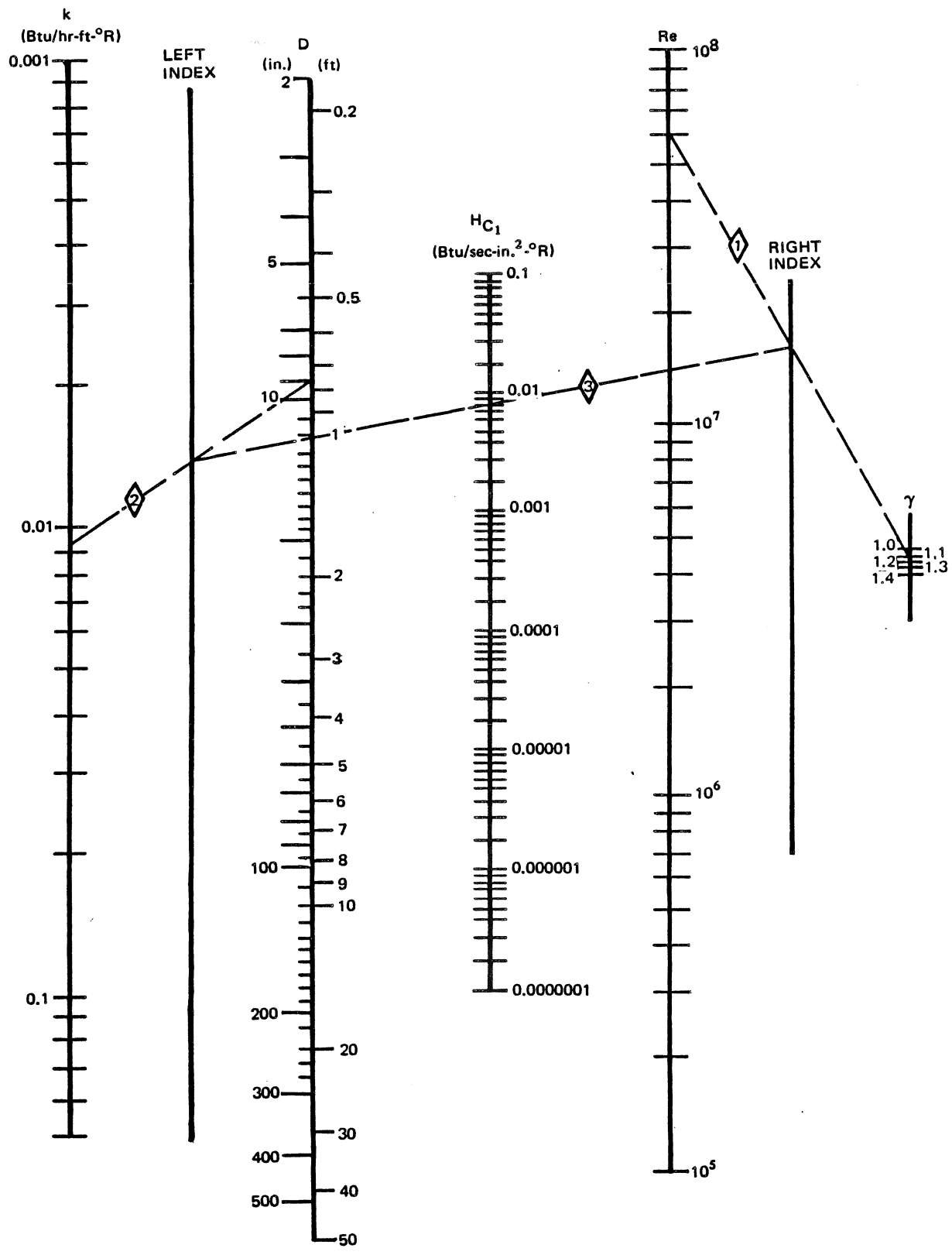

Figure 5-19. Nomograph for Combustion Gas Heat Transfer Coefficient

e. Draw a straight line between the right and left index points. This line intersects the h_c line at the desired value of h_c.

Reynolds number is a dimensionless parameter which can be calculated from:

$$Re = \frac{VD\rho}{\mu} \quad (6)$$

where:

Re = Reynolds number

V = Local combustion gas velocity, ft/sec

D = Local thrust chamber diameter, ft

ρ = Local combustion gas density, lb/ft^3

μ = Local combustion gas viscosity, lb/ft-sec

Reynolds number is typically greater than 10^6 in the nozzle throat region of rocket engines.

5-3.1.2.2 Thrust Chamber Cooling

The thrust chamber's heat rejection rate determines its cooling requirements. The heat rejection rate is dependent on several engine design parameters including thrust, throat area, chamber pressure, and nozzle area ratio, and on the propellant parameters of mixture ratio and specific impulse. The time duration of this heat transfer rate also influences the selection of the method of cooling the thrust chamber.

Table 5-5 presents broad screening criteria for determining the applicability of several cooling methods to a variety of operational requirements.

Table 5-6 describes the principal methods used to cool thrust chambers, and identifies the appropriate application for each method. Combinations of two or more methods of cooling can be used to cool critical sections of the thrust chamber. Also, different cooling methods may be used in various locations, such as regenerative cooling of the combustion chamber and part of the nozzle, and then radiation cooling of the rest of the nozzle.

Figure 5-20 indicates the heat transfer rate capabilities of the principal cooling methods. The nominal heat transfer rates shown in this figure are based on operating times exceeding one minute.

Figure 5-21 shows the influence of thrust and operating time on the selection of a cooling method for a minimum weight liquid propellant engine. The figure indicates that regenerative cooling should be used for nearly all main propulsion applications. Although the conclusions are based on the use of a particular propellant combination, they are generally applicable to all engines which use liquid propellants.

Table 5-7 summarizes the changes in coolant temperature which result from changes in the principal engine design parameters. The table shows that cooling requirements usually increase with increase in thruster performance.

Exceptions to the rule occur if thrust is increased by increasing propellant flowrate. In this case, thrust can be increased by increasing the throat area, or by holding the throat area constant and allowing the chamber pressure to increase. For either of these conditions, the increased coolant flowrate results in a decrease in the final temperature of the coolant. A greater decrease in coolant temperature is achieved if the throat area, rather than the chamber pressure, is increased to obtain the desired increase of thrust.

5-3.1.2.3 Regenerative Cooling

The propellant used in regenerative cooling should not corrode or clog the coolant passages, and it should have a high value of specific heat, a measure of its ability to absorb heat. Tables 5-2 and 5-3, which list physical properties of several liquid rocket oxidizers and fuels, show that fuels generally have higher values of specific heat than oxidizers. For this reason, and because oxidizers usually are less compatible with coolant system materials, a fuel generally is used as the coolant.

The specific heats of most propellants are much higher when they are in the liquid, rather than in the gaseous, state. Hydrogen, which has the highest specific heat, is an exception to this rule. Thus, for most coolants, it is important that the heat absorbed does not cause vigorous boiling in the coolant passages. If boiling should occur, the engine wall might burn through because both the specific heat and the coolant density, and weight flowrate would decrease, greatly reducing the heat absorption capability of the coolant.

The rate of heat transfer between the thrust chamber wall and the coolant is a function of the temperature difference, and the coefficient of heat transfer across the coolant film. Figure 5-22 shows the heat transfer rate as a function of this temperature difference. The slope of the solid curve is a measure of magnitude of the coefficient of heat transfer. This figure discloses that there are four distinct categories of heat transfer coefficients i.e., forced convection, nucleate boiling, unstable gas film, and radiation. If the nucleate boiling regime is exceeded, a sharp increase in wall temperature will occur which may cause engine failure.

Table 5-5. Cooling Method Screening Chart

COOLING METHOD →	REGENERATIVE	RADIATION	ABLATION	FILM	TRANSPORTATION	OPEN TUBE	INERT HEAT SINK	ENDOTHERMIC HEAT SINK
APPLICABLE TO SPACE RESTART OF MOTOR	Applicable	Applicable	Applicable	Limited	Limited	Applicable	Applicable	Limited
APPLICABLE TO SHORT PULSE MOTOR	Not Applicable	Applicable	Applicable	Not Applicable	Not Applicable	Limited	Applicable	Limited
APPLICABLE TO THROTTLEABLE MOTOR	Limited Range	Applicable	Applicable	Possibly Limited	Possibly Limited	Applicable	Applicable	Limited
RUN TIME LIMIT	No Limit	Hours	5 to 20 Min	No Limit	Limited by Source of Coolant	No Limit	Less than 2 Min	Limited by Source of Coolant
EFFECT ON PROPELLANT CHOICE	H_2, RJ-1, N_2H_4, A-50	Compatibility with Walls and Coating Critical	Limits Run Time	Cooling Properties Important	Cooling Properties Important	H_2 Best	Compatibility with Walls and Coating Critical	Flame Temperature Important
CHAMBER PRESSURE LIMITS	Affected by Coolant Passage Design	50 psia or Less, to 90 psia for Low Thrust	Limits Run Time for Throat Application	No Limit	No Limit	No Limit	Limits Run Time	Limits Run Time
VACUUM OPERATION	Residual Thrust	Possible Limit on Coating Life	Some Residual Thrust	Residual Thrust	Residual Thrust	No Limit	No Limit.	Residual Thrust
ATTITUDE WITH RESPECT TO SUN	Trapped Coolant Affected by Soak	No Effect	Soak Temperatures Limited to 500°F	No Effect	No Effect	No Effect	No Effect	Soak Temperatures Limited
METEOROIDS	May Puncture Tubes	May Erode Coating	No Effect	No Effect	No Effect	May Puncture Tubes	No Effect	No Effect
HEAT TRANSFER TO VEHICLE	Minimum	Maximum	Minimum	Minimum	Minimum	Coolant Temperature May be > 1500°F	Function of Time and Soak Transients	Can be Limited
ADVANCED NOZZLE GEOMETRY	Limited by Passage Sizes	Limited by Pressure and Configuration	Throat Erosion Critical	Applicable	Applicable	Applicable Limited by Passage Sizes	Time Limited	Time Limted
EXTERIOR ENGINE TEMPERATURE	Approaches Coolant Temperature 500° to 1000°F	3500°F Maximum	500° to 800°F Maximum	Can be Controlled	Can be Controlled	May Approach 1500°F	Can be Limited. May be > 4000°F.	Can be Limited
PROPULSION SYSTEM PENALTIES	Pressure Losses	Large Chamber Size Due to Low P_c	Chamber Weight and Run Time Limited	I_{sp} Loss	I_{sp} Loss	Affects Optimum O/F	Time Limit Versus Chamber Weight	Time Limited

Table 5-6. Thrust Chamber Cooling Methods

NAME	DESCRIPTION	TEMPERATURE DIAGRAM	APPLICATION
REGENERATIVE COOLING 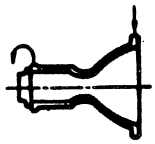	One of propellants (fuel) circulated in wall cooling jacket and passed into injector for combustion; most commonly used method	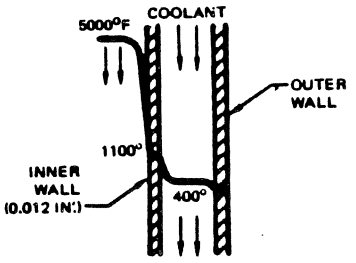	Most liquid-propellant applications; low and high thrust to moderate chamber pressure; used on Atlas, Titan, Thor, Saturn, etc.
INJECTOR DESIGN MODIFICATION	Alteration in main chamber gas core mixture ratio to produce low temperature at wall periphery and reduce wall heat input	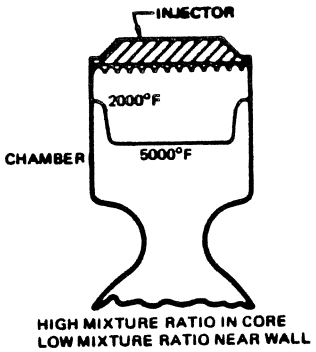	Most current large-thrust liquid-propellant designs employ reduced mixture ratio conditions at the injector periphery
RADIATION COOLING 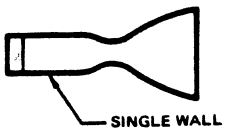	High-temperature, lightweight, refractory-metal pressure vessel which glows white hot and rejects heat by thermal radiation. (Reaches thermal equilibrium)	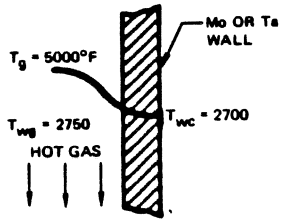	Low-thrust, low chamber-pressure unit for attitude control (e.g., Apollo Service Module) Uncooled nozzle exit skirt extensions
HEAT-SINK COOLING	Heavy-walled metal shell. (Does not reach thermal equilibrium)	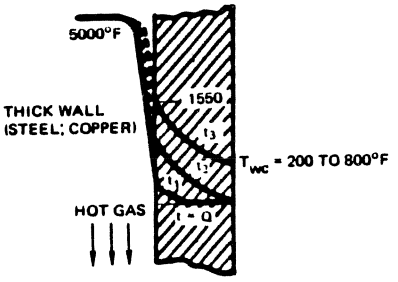	Short-duration, low-thrust, low-pressure units. (Typical experimental unit for evaluating propellants or feed-system features, JATO's, or retro-rockets)
ABLATIVE COOLING	Progressive endothermic decomposition of wall surface, forming insulating char for passage of prolysis gases	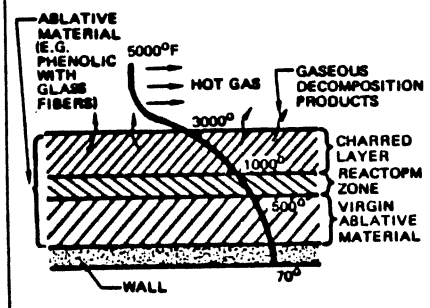	Liquid or solid-propellant, moderate- and low-pressure, limited-duration design for combustion chamber and nozzle, skirt extensions; throttleable space engines; attitude-control space engines

Table 5-6. Thrust Chamber Cooling Methods (Continued)

NAME	DESCRIPTION	TEMPERATURE DIAGRAM	APPLICATION
TURBINE EXHAUST-GAS COOLING 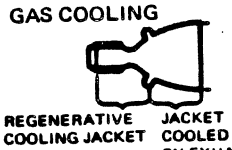	Turbine exhaust gas (900 to 1500 F) is used as coolant in cooling jacket and/or as film-cooling fluid	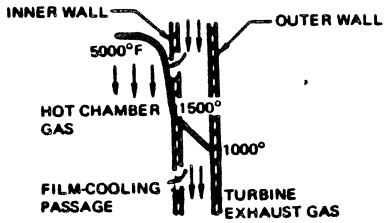	Limited to nozzle exit skirt extensions because of small amount of available gas and heat capacity.
LOW FLAME-TEMPERATURE	Inside wall temperature achieves temperature of combustion; equilibrium condition	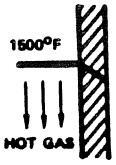	Low-performance propellants with low flame temperature. (Nitrate solid propellant or H_2O_2)
FILM COOLING	Coolant film injected as heat-absorption boundary between combustion gas and wall surface	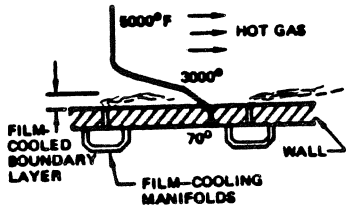	Very high-pressure and large-thrust applications
DUMP COOLING 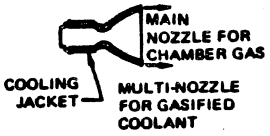	Fraction of propellant is used as coolant in cooling jacket and eventually dumped overboard for performance gain	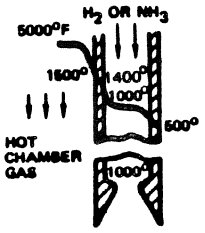	Generally, H_2 or NH_3 fuels
INSULATION COOLING	Low conductivity coating or layer on wall surface for heat flux reduction	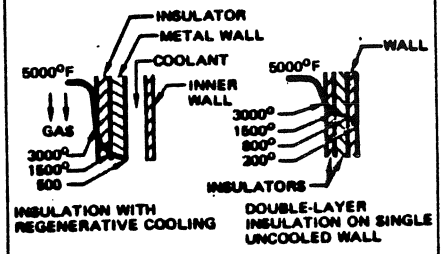	High-pressure, high-performance solid or liquid propellants for high heat-flux conditions
SELF-COOLING 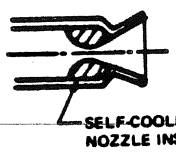	Porous refractory metal matrix filled with vaporizing material which transpires through to the gas surface	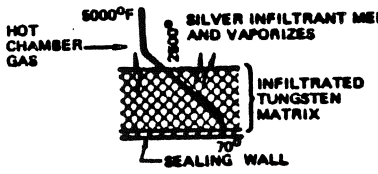	Liquid or solid-propellant designs where heat fluxes are severe or where shear or char erosion is large; throat inserts

Table 5-6. Thrust Chamber Cooling Methods (Continued)

NAME	DESCRIPTION	TEMPERATURE DIAGRAM	APPLICATION
TRANSPIRATION COOLING	Diffusion of mass transfer coolant through thick porous or mesh wall with low velocity; absorption of heat through wall and blockage on surface	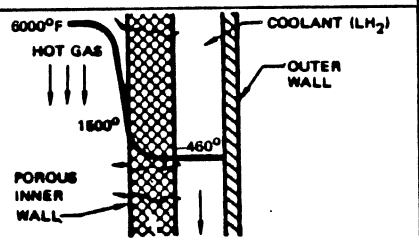	Nuclear, F_2-H_2 O_2-H_2 fueled designs for ultra-high heat-flux application with low performance loss
SACRIFICAL SOLID-PROPELLANT COOLING	Solid-propellant grain composition of low combustion temptera-ture forms gas film coolant layer	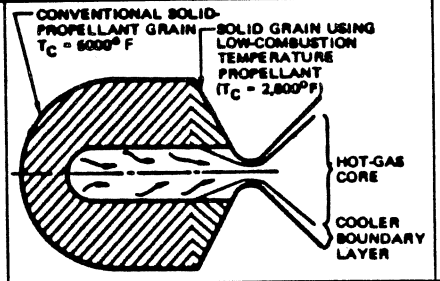	Solid-propellant nozzle protection for high heat flux; large-thrust, high-pressure designs
COMBINED METHODS	Use of two or more methods to reduce cooling pressure drop, increase performance, duration, reduce weight, etc.	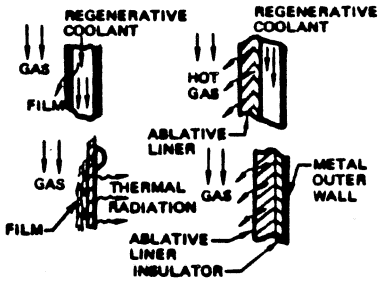	High- and low-pressure-thrust, etc., special applications for heat-transfer optimization

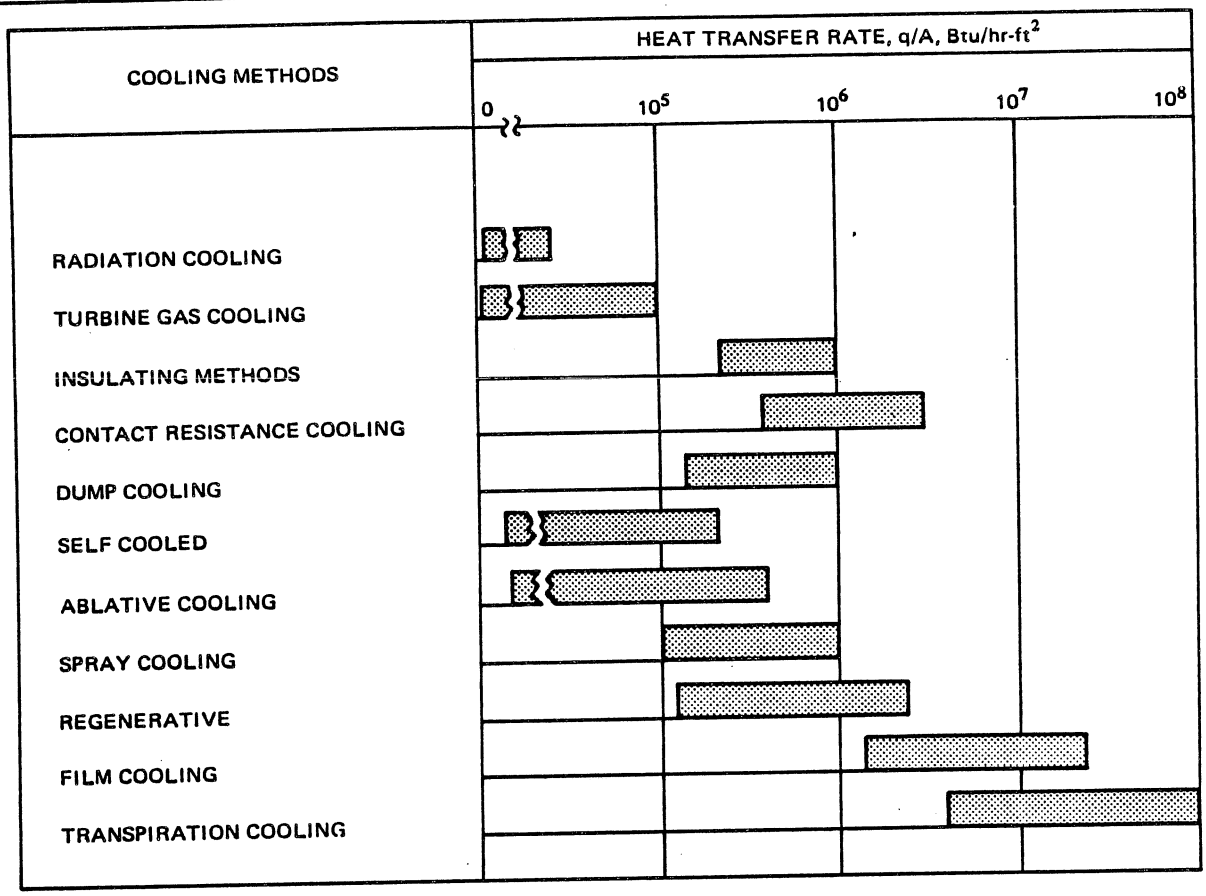

Figure 5-20. Heat Transfer Capabilities of Thrust Chamber Cooling Methods

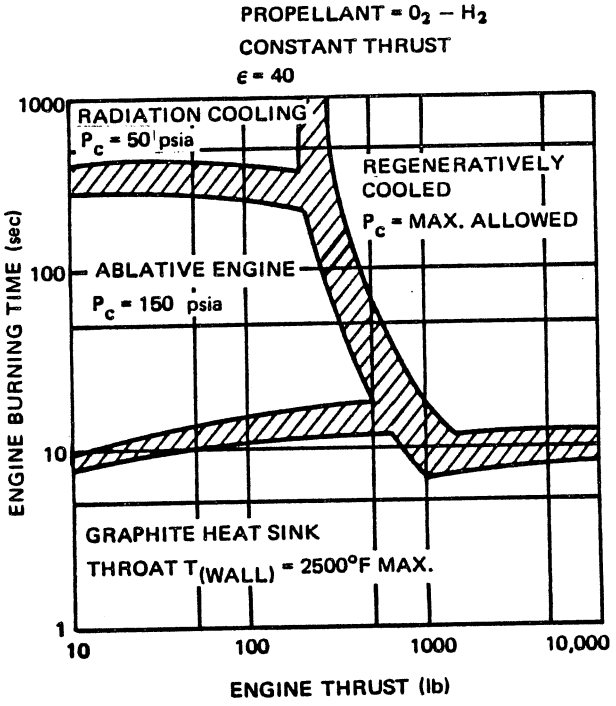

Figure 5-21. Minimum Weight Thrust Chamber Cooling Methods

The normal forced convection region at low heat flux, region A-B in Figure 5-22, has a liquid boundary layer of predictable characteristics. Here the wall temperature is usually below the boiling point of the liquid at the cooling jacket pressure, and the liquid film coefficient can be calculated from:

$$h_l = 0.023\,\bar{c}\,(\dot{w}/A)\,Re^{-0.2}\,Pr^{-0.67} \qquad (7)$$

where:

h_l = Liquid film coefficient of heat transfer, Btu/hr-ft²-°R

Re = Reynolds number = $\rho v D_H/\mu$

Pr = Prandtl number = $\bar{c}\mu/k$

$\dot{w}$ = Coolant flow rate, lb/hr

$\bar{c}$ = Average specific heat of the coolant, Btu/lb-°R

A = Coolant cross-section flow area, ft²

D_H = Hydraulic diameter = 4 A/P

Table 5-7. Influence of Engine Design Parameters on Coolant Temperature

INCREASING PARAMETER	CONSTANT PARAMETERS	BULK COOLANT-TEMPERATURE CHANGE	REMARKS
P_c	$F, \epsilon, r, I_{sp}, \dot{w}$	Increase*	Effect of h_{c_1} increase exceeds area decrease.
$P_c, F, \dot{w}$	ϵ, r, I_{sp}	Slight Decrease	Effect of increased heat flux offset by increased coolant flow.
r	$F, \epsilon, I_{sp}, \dot{w}, P_c$	Increase	Reduced fuel coolant flow and increased gas temperature.
ϵ	$F, r, I_{sp}, \dot{w}, P_c$	Increase	Increased surface area dominates.
$F, \dot{w}$	ϵ, r, I_{sp}, P_c	Decrease	Increased coolant flow and decreased h_{c_1} exceed area increase effect.
I_{sp}	$F, \epsilon, r, \dot{w}, P_c$	Increase	Reduced coolant flow and increased T_w.

*A gas-side deposit having a low thermal conductance, which dominates the gas-side film coefficient, may cause a decrease in coolant temperature rise with P_c.

Parameters:

P_c = Chamber Pressure
F = Thrust
ϵ = Nozzle Expansion Ratio
r = Mixture Ratio
I_{sp} = Specific Impulse
w = Propellant Flowrate

P = Wetted perimeter of coolant flow area, ft

v = Coolant velocity, ft/hr

μ = Coolant absolute viscosity, lb/ft-hr

k = Coolant conductivity, Btu/hr-ft-°R

ρ = Coolant density, lb/ft^3

The propellant vapor pressure increases with temperature and, when the vapor pressure exceeds the local propellant pressure in the coolant passage, small vapor bubbles begin to form on the hot wall. This phenomenon, known as nucleate boiling, induces turbulence which increases the heat transfer rate without a proportional increase in wall temperature. This increase is shown by the steeper slope region B-C in Figure 22, where $(q/A)_{max}$ is the limiting value of the heat transfer rate at C.

During nucleate boiling, some of the propellant may remain in the vapor phase. However, as long as liquid wets the coolant passage wall, the heat transfer coefficient can be approximated by the empirical equation:

$$h_l = 0.06 \frac{k_l}{D_H} \left(\frac{\rho_l}{\rho_v}\right)^{0.28} \left(\frac{D_H G X}{\mu_l}\right)^{0.87} Pr_l^{0.4} \qquad (8)$$

where:

$G = \rho v$ = Mass velocity, lb/hr-ft^2

X = Vapor mass fraction

and the subscripts l and v refer to liquid and vapor, respectively.

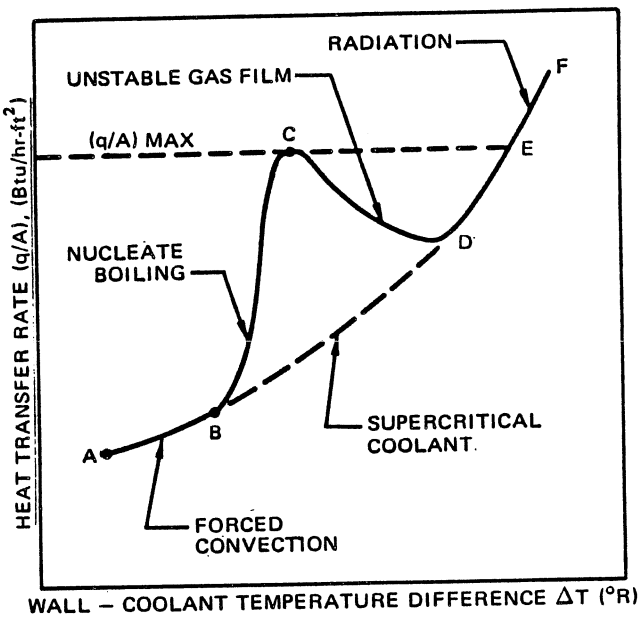

Figure 5-22. Regimes of Heat Transfer from a Hot Wall to a Flowing Coolant

As the heat transfer rate is increased beyond C, the rate of bubble formation becomes so great that a gas film intermittently separates the coolant from the hot wall. This region, shown as C-D in Figure 5-22 is characterized by an unstable gas film which causes the wall temperature to increase even with a decrease in heat transfer rate. In practice, the heat transfer rate does not decrease and, when a value greater than $(q/A)_{max}$ is reached, the heat transfer characteristic jumps from C to E with the indicated large rise in wall temperature.

In the region from E to F a stable gas film continuously separates the coolant from the hot wall and heat is transferred primarily by radiation. Operation in this region increases the probability of adverse chemical changes in the coolant, and burnout of the thrust chamber wall, because of the high temperature.

Regeneratively cooled thrust chambers generally are designed to operate in the nucleate boiling regime at a heat transfer rate which is less than $(q/A)_{max}$. Cooling can also be accomplished by a fluid which is above its critical pressure and critical temperature. In this case there is no nucleate boiling and heat transfer is accomplished by radiation and gas convection, as shown by the broken line B-D in Figure 5-22. Coolants which operate in this regime should have large values of specific heat in order to minimize the resulting rise in wall temperature for a required heat transfer rate.

Table 5-8 lists heat transfer characteristics of several propellants which have been used as coolants in regeneratively cooled thrust chambers. Each has a relatively high specific heat and relatively low viscosity and low vapor pressure. Hydrogen and ammonia, which have the highest specific heats and the lowest viscosities and vapor pressures of the listed propellants, normally operate in the supercritical heat transfer regime. The other listed propellants are used in the nucleate boiling region.

The heat rejected raises the coolant temperature according to the equation:

$$q = \dot{w}\,\bar{c}\,(T_1 - T_2) \qquad (9)$$

where:

q = Heat rejection rate, Btu/hr

$\dot{w}$ = ρ v A = Coolant flow rate, lb/hr

T_1 = Coolant initial bulk temperature, °R

T_2 = Coolant final bulk temperature, °R

In nucleate boiling, T_2 must be less than the coolant bulk boiling temperature at the cooling jacket pressure in order to avoid the occurrence of an unstable gas film condition.

From equation 4 it follows that the rate of heat transfer from the hot wall to the coolant is determined by:

$$\frac{q}{A} = h_l\,(T_{w_2} - T_1) \qquad (10)$$

where the heat transfer coefficient h_l is determined by equation 7 or 8 and the coolant temperature varies from T_1 to T_2. For design purposes, the coolant-side wall temperature T_{w_2} may be assumed to be 50°R higher than T_2.

The magnitude of h_l increases with increase of the propellant velocity flowing through the coolant passages. However, since the required coolant weight flow rate is established by equation 9, an increase in coolant velocity is accomplished by reduction of the coolant passage cross-sectional area with a resultant increase in pressure drop of the coolant. To avoid an excessive pressure drop through the cooling jacket, reduction of the coolant passage cross-sectional area frequently is limited to the throat region of the thrust chamber nozzle where the maximum heat rejection from the combustion gases occurs.

Coolants which operate in the supercritical region are in the gaseous state and are not concerned with boiling heat transfer. Hydrogen is most commonly used in the supercritical condition as a coolant. Hydrogen is particularly effective as a coolant because it has a large value of specific heat in the liquid state which becomes significantly larger in the gaseous state.

Table 5-8. Coolant Characteristics for Liquid-Rocket Propellants

LIQUID COOLANT	BOILING CHARACTERISTICS		CRITICAL TEMPERATURE, °F	CRITICAL PRESSURE, psia	SPECIFIC HEAT, Btu/lb-°F	THERMAL CONDUCTIVITY Btu/hr-ft-°F	VISCOSITY lb/hr-ft	HEAT OF VAPORIZATION Btu/lb	NUCLEATE BOILING CHARACTERISTICS			
	PRESSURE, psia	BOILING TEMPERATURE, °F							TEMPERATURE, °F	PRESSURE, psia	VELOCITY, fps	q_{ul} Btu/sec-in^2
AMMONIA	14.7 100 500 1000	−28 56 161 221	271	1670	1.07	0.29	0.55	596.2	40 140	500 500	30 60 30 60	5.3 7.9 2.6 3.0
HYDRAZINE	14.7 100 500 1000	237 360 512 598	714	2130	0.74	0.29	2.3	540.0	120 270	600 600	30 60 30 60	13.5 18.0 8.7 13.0
KEROSENE	14.7 100 200	423 627 712	760	290	0.45	0.09	5.2	125.0	75 75	100 200	3.0 27.6 3.0 27.6	1.5 3.9 1.4 3.8
N_2O_4	14.7 100 600	70 155 250	316	1470	0.75	0.06	1.0	178.2	60 120 200	600	60	7.0 5.7 3.8
RFNA	14.7 100 500	159 274 405	.....	.....	0.42	.....	3.2	247.0	90 210	500 500	30 48 30 48	6.7 7.1 4.8 9.5
UDMH	14.7 100 500	145 260 420	480	880	0.65	0.12	1.3	250.7	80 80	300 800	30 60 30 60	3.0 4.4 2.9 4.0
HYDROGEN	14.7 100	−436 −408	−400	188	3.7	0.078	0.017	195.3				

NOTE: Specific heat, thermal conductivity, and viscosity values are given for 70°F, except (1) ammonia at −28°F and (2) hydrogen at −410°F.

The coefficient of heat transfer, h_c, for supercritical cooling is a function of wall and coolant temperature, of coolant passage geometry, and of the coolant velocity and physical properties. The heat transfer rate can be determined from equation 11 which correlates well with experimental data for supercritical hydrogen cooling.

$$h_c = 0.25 \frac{k}{D_H}\left[Re^{0.8}\, Pr^{0.4}\left(\frac{T_w}{T_b}\right)^{-0.55}\right] \Phi_1\, \Phi_2 \quad (11)$$

where:

Φ_1 = A correction factor for the critical temperature region where the physical properties of hydrogen change drastically with temperature. Values of Φ, as a function of temperature are contained in Table 5-9.

Φ_2 = A correction factor for the entrance region where the thermal boundary layer is not yet established.

$$\Phi_2 = 0.865\left[\frac{Re^{0.25}}{x/D_H}\right]^{0.22}$$

T_w = Wall temperature, °R

T_b = Coolant bulk temperature, °R

k = Thermal conductivity, Btu/hr-ft°R

x = Distance into the coolant passage, ft

The decrease in pressure as the coolant flows through the cooling section can be calculated from the equation:

$$\Delta p = f \frac{L}{D_H} \frac{\rho v^2}{2g\ 144} \quad (12)$$

where:

Δp = Pressure drop, lb/in^2

f = Friction factor

L = Tube length, ft

D_H = Coolant passage hydraulic diameter, ft

ρ = Coolant density, lb/ft^3

v = Coolant velocity, ft/sec

g = Acceleration of gravity, ft/sec^2

Table 5-9. Recommended Values for Bulk Temperature Factor, Φ_1, For Hydrogen

T_b (°R)	Φ_1
40	1.0
50	1.0
60	0.38
70	0.51
80	0.70
90	0.80
100	0.92
110	0.96
120	1.00

The friction factor can be estimated from:

$$f = 0.184\, Re^{-0.2} \quad (13)$$

The design of a cooling system often involves a compromise between desirable but conflicting characteristics. For example, equation 9 shows that an increase in coolant velocity permits a linear decrease in cross-section area of the coolant passage, and equation 11 reveals that the heat transfer coefficient increases nearly linearly with an increase in coolant velocity. However, equation 12 indicates that the pressure drop through the cooling section increases with the square of the coolant velocity. Thus, the selection of coolant design velocity involves a trade between improved heat transfer and decreased envelope, versus increased supply pressure.

Methods of reducing the severity of thrust-chamber heat-transfer conditions by lowering wall temperature, increasing the upper nucleate-boiling limit, or reducing the bulk coolant-temperature rise, may be categorized as gaseous-side and coolant-passage modifications.

On the gas side, four methods of influencing the hot-gas-to-chamber-wall heat flow are:

a. Bonding a solid insulating material, having high-temperature strength and low thermal conductivity (see Table 5-10), to the gas side of the metal wall.

b. Providing for gas-side deposition, during firing, by utilizing additives in the liquid propellants.

Table 5-10. Properties of Various Metal Refractory Materials

Material	Melting Temp °F	Coefficient of Thermal Expansion, X 10^{-6} in./in.-°F		Thermal Conductivity, Btu/hr-ft-°F		Specific Heat Btu/lb-°F		Temp °F	Strength, psi		Modulus of Elasticity, X 10^{6}
		Ref Temp °F	Coefficient	Ref Temp °F	Conductivity	Ref Temp °F	Specific Heat		Ultimate	Yield	
Copper	1981	68	8.93	68	221	75	0.092	75	33,000	10,000	16.0
		392	10.09	392	214	392	0.096				
		1112	14.15	1112	199	1112	0.104				
Aluminum 24S-T	1200	68-212	12.90	64	130	64-212	0.212	75	68,000	45,000	10.3
		68-392	13.30					400	53,000	35,000	9.27
		68-572	13.70					700	7,500	6,500	
Carbon Steel SAE 1020	2780	68-212	6.50	32	30	68	0.115	85	62,400	42,000	29.2
		68-752	7.40	752	25	752	0.140	900	45,500	23,500	16.9
		68-1292	8.20	1472	15	1472	0.153	1200	20,000	10,200	12.5
Alloy Steel SAE X4130	2700	32-212	7.04	32	25	212	0.114	75	98,300	74,000	29.5
		32-752	7.68	752	22	752	0.142	400	94,200	73,600	24.5
		32-1292	8.24	1472	15	1472	0.211	1000	65,000	53,400	15.5
Stainless Steel AISI Type 302	2550	32-212	8.23	32	9	212	0.122	75	93,000	37,000	
		32-752	9.78	752	11	752	0.136	400	75,000	23,400	
		32-1292	10.43	1472	15	1472	0.153	1200	52,000	15,500	20.7
Nickel Alloy Inconel	2540	100	6.00	86	10	78-212	0.109	75	85,000	36,000	31.0
		500	8.40	392	11			400	78,000	28,000	29.5
		900	9.80	1472	16			1200	71,000	22,000	23.0
Alumina	3720	60-1850	4.00	2000	14	70-3100	0.29				
Magnesia	4900	60-2700	8.50	2000	15	60-3270	0.29				
Zirconia	4600-4700	30-2000	4.50	2000	0.5	60-2550	0.175				
Silicon Nitrate	3450†	1650	1.45								
Carbon	6402††	60-220	1.6-2.9	2000	1-9	60-1850	0.29				
Graphite	3681	60-220	1.0-2.4	2000	20-87	60-1850	0.29				
Silicon Carbon	4010†	60-2750	3.70		9						

† Decomposes
††Sublimates

c. Reducing the gas temperature, either uniformly across the chamber flow area, or locally in the vicinity of the chamber wall, by altering the effective propellant mixture ratio.

d. Providing a protective layer of gas or liquid along the wall by injection cooling.

On the liquid side of the thrust-chamber wall, modifications tending to reduce the severity of the heat-transfer problem include:

e. Increasing the coolant velocity by reducing coolant-passage cross-sectional flow area.

f. Increasing the heat conduction from the locally heated region by employing a fin effect within the coolant passage.

g. Increasing the coolant subcooling in high heat-flux regions (throat) by coolant-passage design, providing for relatively low coolant temperatures at the critical sections.

Methods e and g are directed toward increasing the upper nucleate-boiling limit thereby providing a greater margin of operational safety for chamber cooling, while the fin effect results in more efficiently utilizing the coolant-passage wall-coolant interface for heat transfer.

5-3.1.2.4 Ablative Cooling

Ablative cooling involves the use of wall materials which undergo endothermic thermal degradation and consequent mass removal, but leave enough material to preserve structural integrity. Char-forming plastics reinforced with organic or inorganic fibers have proved to be superior for thrust chamber applications.

Commonly used materials include phenolic and epoxy resins reinforced with high-silica glass, carbon, or graphite fibers. Figure 5-23 illustrates an ablative nozzle design which utilizes these materials. A tungsten insert is included at the throat to minimize change in throat area due to erosion.

Initially, a resin-based ablative wall acts as an ordinary heat sink, but low thermal conductivity causes the surface temperature to rise very rapidly. At about 1000°F, the resin decomposes endothermically into a porous carbonaceous char and pyrolysis gases. As the char increases in depth and temperature, the pyrolysis gases may undergo additional endothermic thermal cracking as they percolate through the char and into the combustion gas boundary layer.

With silica reinforcement, as the surface temperature approaches 3000°F, a highly endothermic reaction with carbon in the char may take place, providing additional

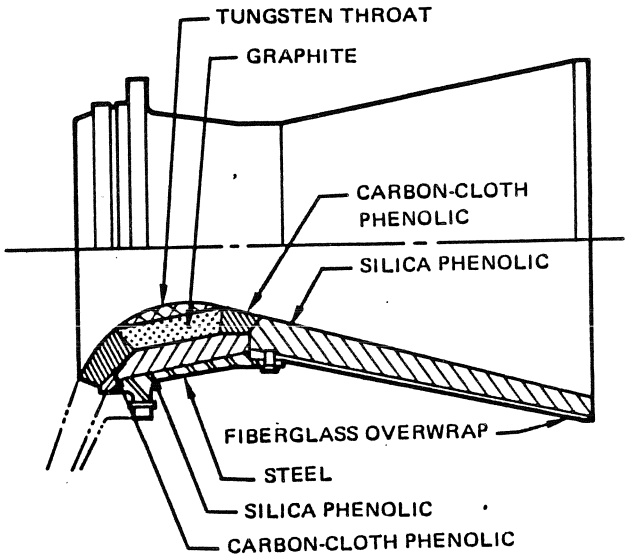

Figure 5-23. Ablative Nozzle Design

thermal protection. Above this temperature, the silica will melt to provide a very viscous film which may protect the char from chemical erosion, but which itself may eventually be subject to surface erosion by viscous shear. At even higher temperatures, additional silica reactions and vaporization may take place.

With carbon and graphite fibers, melting does not occur. In this case, oxidizing atmospheres can cause rapid surface erosion. The relatively low thermal conductivity of the char layer restricts the transfer of heat to the virgin ablative material. Heat soak-back effects can continue after engine shutdown.

In rocket-engine applications, where regenerative cooling cannot be easily applied and where limited dimensional changes are tolerable, the use of ablative materials is quite attractive. Thus, in low-thrust space engines, where insufficient fuel coolant is available for regenerative cooling, ablative materials are used in the combustion chamber and exit-cone regions. With relatively nonoxidizing or low combustion temperature propellants, suitable ablative materials can even be used in the throat region without affecting performance adversely. They are also used as liners for exit cones of solid-rocket motors, and, in high-thrust liquid-propellant engines, may be used for skirt extensions.

The self-regulating thermal protection afforded by ablative cooling makes this method particularly suitable for throttleable engines. Ablative chambers have been particularly useful for pulsing or cycling operations, where individual pulses may be of very short duration, approaching a few milliseconds.

A number of problems must be considered when ablative cooling is to be used. It has sometimes been difficult to control the fabrication process and to obtain reproducible properties for the char and virgin material. Relatively minor variations in the manufacturing process may cause severe performance degradation due to thermal stresses which spall or tear apart the ablative materials. Other problems include outgassing of the binder after engine shutdown, the effects of long-term exposure to vacuum, uneven erosion of combustion chamber liners due to injector nonuniformities, and severe flow of molten glass.

The required thickness of an ablative material to withstand a given environment depends mainly on the char rate and the surface erosion rate. These rates are strongly dependent upon the thermal conductivity of the char layer and the density of the virgin material. The lightest design may involve a composite wall consisting of a high-density ablative as thick as the erosion loss, backed up by a low-density ablative with the best possible charring properties.

In the absence of appreciable surface erosion, the char rate for a given ablative material is mainly dependent on the propellant combination and to a much lesser extent on local combustion gas pressure. Correlation of a large amount of experimental data has been satisfactorily achieved with proportionality of char depth to square root of time.

Surface erosion rates depend strongly on surface temperature and combustion-gas composition and pressure. Erosion for high flame-temperature propellant systems appears to be controlled mainly by melting and partial vaporization of silica for refrasil phenolic. For phenolic-nylon with Lox/RP-1, erosion is controlled mainly by surface combustion of the char. With the F_2/H_2 propellant system, surface erosion appears negligible for carbonaceous chars from phenolic-nylon and carbon or graphite-reinforced phenolics.

The capabilities of ablative thrust chambers are continually being extended by:

a. Development of new resin-reinforcement combinations tailored for specific applications.

b. Better fabrication methods and quality control.

c. Development of improved throat inserts.

d. Use of auxiliary film cooling to reduce ablative surface temperature and auxiliary regenerative cooling to minimize wall thickness. In some cases, pre-charred ablative liners appear particularly attractive.

The time required for liner material to reach its ablation temperature can be estimated by the relationship:

$$\frac{T_s - T_i}{T_{aw} - T_i} = 1 - \exp\left[\frac{h^2 \alpha t}{k^2}\right] \operatorname{erfc}\left[\frac{h}{k}\sqrt{\alpha t}\right] \qquad (14)$$

where:

T_s = Ablating surface temperature, °R

T_i = Initial temperature, °R

T_{aw} = Adiabatic wall temperature, °R

h = Film heat transfer coefficient, Btu/hr-ft²-°R

α = $k/\rho c_p$ = Thermal diffusivity

t = Time, hr

erfc[Z] = Complimentary error function

$$= 1 - \frac{2}{\pi}\int_0^Z e^{-z^2}\, dz$$

$$T_{aw} = T_\infty \left[1 + Pr\left(\frac{\gamma - 1}{2}\right) M^2\right] \qquad (15)$$

where:

T_∞ = Free stream temperature, °R

γ = Specific heat ratio

M = Mach number

The wall temperature and the ablation rate are related by the equation:

$$\frac{T - T_i}{T_s - T_i} = \exp\left[\frac{-q_m Z}{\alpha \rho Q^*}\right] \qquad (16)$$

where:

q_m = Quasi-steady state heat flux

Z = Semi-infinite slab thickness, in

Q^* = Effective heat of ablation

$$Q_m = \upsilon \rho Q^* \qquad (17)$$

where:

υ = Ablation rate, in/sec

Table 5-11 presents typical values of appropriate properties of two common ablative materials.

Table 5-11. Room Temperature Properties of Ablative Materials

PROPERTY	REFRASIL	MAGNESIUM OXIDE
THERMAL DIFFUSIVITY α, ft^2/hr	3.23×10^{-3}	3.85×10^{-2}
THERMAL CONDUCTIVITY k, Btu/hr-ft-°R	0.142	1.90
SPECIFIC HEAT c, Btu/lb-°R	0.38	0.22
DENSITY ρ, lb/ft^3	112.	225.
ABLATION TEMPERATURE T_s, °R	3,860	5,700
EFFECTIVE HEAT OF ABLATION Q*, Btu/lb	3,000 TO 10,000	>10,000

5-3.1.3 Nozzle

The thrust chamber nozzle consists of convergent, throat, and divergent sections. In addition to the nozzle heat transfer problems discussed above, the propulsion engineer is concerned with the design of the nozzle geometry to obtain the highest possible thrust coefficient C_F within the constraints of other design requirements such as dimensions and weight.

There are several factors which must be taken into consideration in nozzle design. Some are peculiar to the nozzle itself and others must be considered as part of the overall vehicle design. An ideal nozzle is designed on the assumption of isentropic expansion of the exhaust gases with no losses. The flow process in real nozzles differs from that of an ideal nozzle because of friction effects, heat transfer, imperfect gases, non-axial flow, and non-uniformity of the working substance and flow distribution. The nozzle shape is of considerable concern because of its effect on the following parameters:

a. Wall friction losses are a function of the surface area of the nozzle.

b. Vehicle structural weight is a function of the nozzle length and expansion ratio.

c. Heat transfer to the nozzle wall is a function of the nozzle surface area.

d. Radial velocity losses are a function of the nozzle divergence angle.

e. Rocket installation weight and vehicle design problems increase with larger nozzles.

f. Separation and turbulence losses are also a function of the divergence angles at any one point.

g. Dissociation and recombination, which have come to play an important role in rocket engine performance, are also affected by the nozzle contour.

The nozzle contour should therefore be designed for the maximum thrust-to-surface area ratio with the consideration of all the preceding parameters.

Rocket nozzles can be divided into two categories, non-adaptive and adaptive, or altitude compensating nozzles. Non-adaptive nozzles are those that contain the expanding gases in a fixed geometry, such as conical and bell configurations, and adaptive nozzles are those that permit the expanding gases to vary their geometry as a function of the ambient pressure, such as plug and aerospike nozzles. The non-adaptive nozzles, achieve the optimum thrust coefficient at only one value of ambient pressure, while the adaptive nozzles achieve the optimum thrust coefficient over a range of altitudes.

Figure 5-24 lists several different nozzle configurations and shows the variations in gas flow patterns at sea level and altitude ambient pressures. Nearly all rocket nozzles are non-adaptive conical or bell nozzles. Although the adaptive plug and expansion-deflection nozzle configurations offer potentially larger values of C_F over a range of altitude operation, structural and heat transfer considerations have limited their use. The aerospike configuration is less sensitive to heat transfer problems, and its truncated spike geometry provides a very short nozzle length. Figure 5-25 shows the relative nozzle lengths required for each configuration.

There are many different materials which can be utilized in nozzle design, depending on the type of cooling to be employed. Radiation cooling, ablation cooling, and regenerative cooling are the primary methods currently being employed.

Regenerative cooling is normally limited by the coolant which restricts the nozzle area ratio at which this method can be used. For this type of cooling, however, the same type of metals can be used in nozzle fabrication as was mentioned previously for thrust chambers.

Ablation cooling is a method that can be used for a nozzle on an ablative chamber, or for nozzle extensions for regeneratively-cooled chambers. Materials such as high-silica phenolics, silica epoxies, and carbon-cloth phenolics are only a few materials of this type. They are usually backed with an insulation material such as asbestos-phenolic and then wrapped with fiberglass for longitudinal and hoop strength.

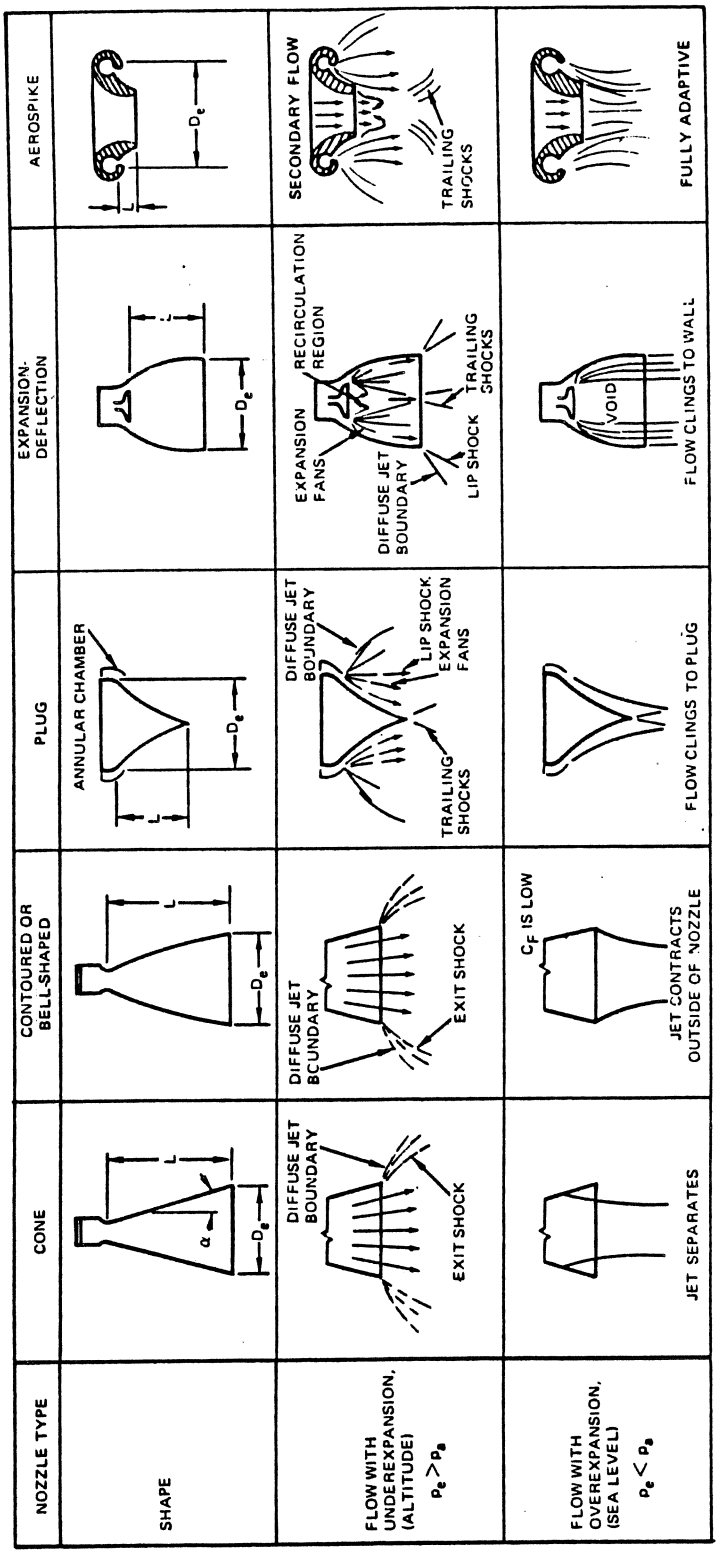

Figure 5-24. Flow Effects for Typical Nozzle Configurations

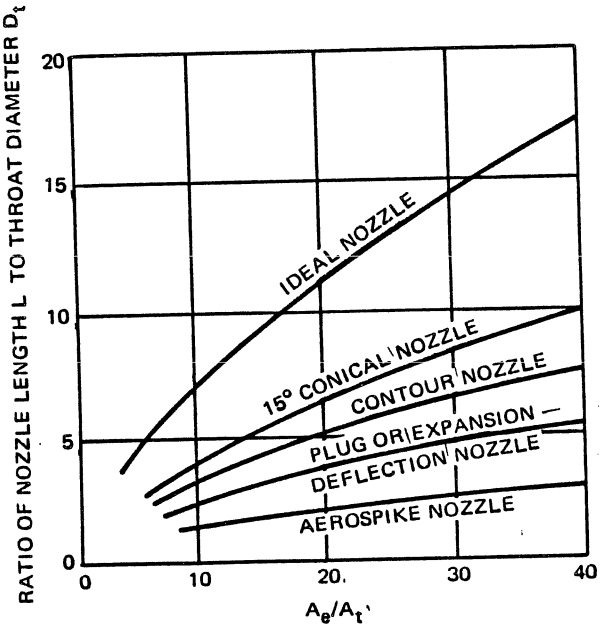

Figure 5-25. Length Comparisons of Nozzle Configurations

Radiation-cooled nozzle extensions can be used for ablatively-cooled and regeneratively-cooled thrust chambers. Radiation cooling depends on the use of a thin wall which is heated by the combustion gases to an equilibrium temperature at which the heat radiated to space from the wall is equal to the heat transferred to the wall from the combustion gases. Materials which are suitable for use under such conditions are tungsten, molybdenum, columbium, titanium, and cobalt-based materials such as Haynes 25. The refractory metals tungsten, molybdenum, and columbium are rapidly oxidized by liquid-rocket exhaust containing water vapor, carbon dioxide, or any free oxygen, unless the surfaces are protected by suitable coatings. These coatings are usually the limiting factors in the use of refractory metals.

5-4 FEED SYSTEM

The feed system for a rocket engine consists of tanks to store the propellants, ducts to transport the propellants, and means of controlling the propellant flowrates and mixture ratio. The design of each of these elements is influenced by the interactions among the elements and by the overall propulsion system requirements. The major aim in the design of the propellant feed system is to obtain the simplest, most reliable, and lightest system possible to perform the desired function.

5-4.1 Tankage

The propellant tanks must be structurally adequate and, in many applications, are also required to provide control of the temperature and orientation of the propellants. Structural adequacy is achieved by selection of the appropriate combination of tank shape, material, thickness, and reinforcement.

Control of propellant temperature is facilitated by the use of insulation to minimize heat flow to or from the propellants, and mixing devices which minimize temperature variations within the propellants.

Control of propellant orientation is of concern in the determination of vehicle dynamics, prediction of heat transfer, and propellant venting and expulsion. Slosh baffles, propellant settling devices, positive expulsion devices, and start tanks are used to control propellant location.

5-4.1.1 Tank Configurations

Spherical tanks are the lightest for a given propellant volume. However, if a large volume of propellant must be stored, the spherical tanks cannot be arranged satisfactorily to eliminate unused volume for the overall vehicle configuration. In this case, the overall vehicle weight may be greater than if a more compact, but heavier, tank arrangement is utilized. Also, the weight advantage of a sphere diminishes for low pressure applications, such as in pump fed systems, because the allowable skin thickness based on internal pressure requirements may be less than needed to satisfy handling requirements.

Cylindrical tanks with hemispherical or ellipsoidal ends are generally used when spherical tanks cannot be packaged compactly. Toroidal tanks can usually be packaged compactly; however, it is difficult to keep the propellants over the discharge port at all times, especially when the tanks are partially full and the vehicle is being reoriented or the vehicle direction is being changed. Fabrication problems also tend to be greater with the toroidal tank.

A single tank with an internal bulkhead which separates the fuel and oxidizer is also utilized and can be packaged compactly. However, extreme care must be taken to insure that the bulkhead is leakproof, especially if the propellants are hypergolic.

There are other factors which affect tank and vehicle weights in addition to the shape of the tanks. The tank materials must be compatible with the propellants and must be as light and strong as possible. Materials usually used for tanks are aluminum, titanium, and stainless steel. Tank insulation must also be carefully designed because sufficient insulation must be applied to keep the

propellants within required temperature limits, but improper insulation selection or too much insulation,will result in unnecessary weight. Meteoroid protection for the tanks may also be needed, requiring additional design effort to assure minimum weight.

5.4.1.2 Propellant Expulsion

Expulsion devices provide assurance that the propellant will be positively expelled from the storage tanks when required. These devices are used when environmental g-loads tend to displace the liquid from the tank outlet. Tanks subject to zero-g conditions, or to large maneuvering loads, are candidates for positive expulsion devices. Figure 5-26 shows schematically several typical propellant expulsion techniques, and lists the advantages and disadvantages of each technique, and the limitations of each under zero-g, or maneuvering load conditions.

The last five expulsion techniques illustrated in Figure 5-26 are positive expulsion devices. They rely on positive movable barriers to keep the pressurant gas separated from the liquid to be expelled. The barriers used are piston, bellows, diaphragm, and bladder. All of these barriers are susceptible to damage in at least one operational mode, as noted in the table. The barriers are generally made of metals which are compatible with the gas and the liquid. For some applications, however, the barrier can be made of a compatible elastomeric or plastic material. These lower modulus materials are more permeable than metals, but less susceptible to creasing and tearing.

5-4.2 Ducts

Propellant ducts consist of rigid and flexible members. The rigid duct members consist of both straight and curved elements joined to comply with envelope restrictions, which usually require an irregular path between the storage tanks and the engine. The flexible members are included to facilitate duct installation, to compensate for small thermal and structural duct deflections, and to comply with engine gimballing requirements.

The propellant ducts must be structurally adequate and should minimize pressure drop and heat transfer. Structural adequacy is achieved by the selection of appropriate materials, wall thicknesses, and attachment fittings. Materials are selected on the basis of weight, cost, and compatibility with the propellants and the environment. Stainless steel and aluminum alloys are most frequently used. Wall thicknesses are selected based on the material used and on the combined static and dynamic stresses imposed.

The static stresses include circumferential tension due to internal pressure, axial compression and tension due to bending between supports, and buckling due to thermally induced axial compression. The causes of dynamic stresses include internal pressure surges, vibrations induced by fluid flow perturbations, and vibrations induced by vehicle vibrations. The pressure surges include continuous minor surges caused by flow control, and infrequent major surges, or water hammer, caused by rapid opening or closing of shutoff valves.

Fluid flow across discontinuties in the duct causes relatively high-frequency, low-amplitude pressure variations as a function of fluid velocity. When this driving frequency approaches the natural frequency of a flexible duct, large stresses may be induced in the duct. Vehicle induced vibrations are influenced by the attitude and location of the duct in the vehicle, the method of duct support, and the distance between supports.

5-4.3 Propellant Management

Propellant management consists of controlling the supply and use of propellants in a rocket propulsion system during operation. The quantity of propellant on board at launch is controlled to meet requirements established by the mission objectives. The rate of use of these propellants during flight is tailored to achieve a desired mixture ratio, and to minimize the amount of one of the propellants remaining after the other propellant is exhausted.

In an ideal case, the weight of oxidizer and fuel loaded into the vehicle propellant tanks would be just enough to achieve the performance objectives of a given mission. In practice, some propellant must be added to this minimum amount to compensate for the quantity that will be trapped in the feed system because of its geometry, and thus is not available for the generation of thrust. Some additional propellant is also provided to allow for the normal variations in the performance of the system components, and in the case of cryogenic propellants, to allow for overboard venting. Frequently propellant is also added for non-thrust-producing purposes such as heating, auxiliary power and pressurization.

The weight of propellant loaded into the vehicle tanks can be controlled accurately by several different methods. Propellant may be transferred from a calibrated ground tank, as is done for Titan II. Loading may be made through an integrating flowmeter, as is done for the Thor fuel tanks and for Titan III. The flow of propellant into the vehicle tanks may be continued until an onboard measuring device, such as a liquid level sensor or a capacitance probe, signals that the desired quantity has been loaded.

All of these measuring methods are applicable to earth storable propellants, but only the techniques employing onboard measuring devices are feasible for cryogenic propellants because some of the cryogen supplied to the vehicle boils and must be vented overboard to prevent buildup of tank pressure.

EXPULSION TECHNIQUES	SCHEMATICS	ZERO-G START	MANEUVERING LOADS
DIRECT PRESSURIZATION	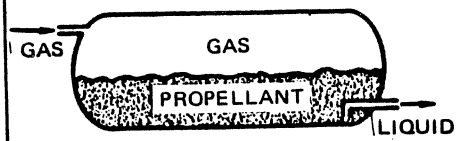	Yes, if used with a propellant settling device.	DON'T USE
TRAP	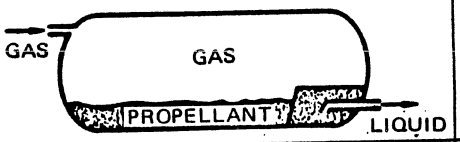	YES	DON'T USE
SPINNING	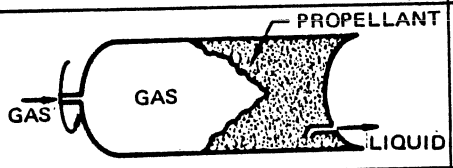	YES	Applicable to low loads only.
SURFACE TENSION	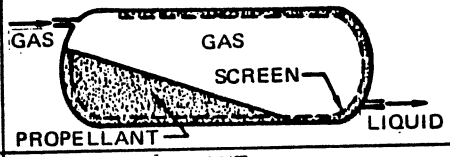	YES	Applicable to moderate loads only.
PISTON	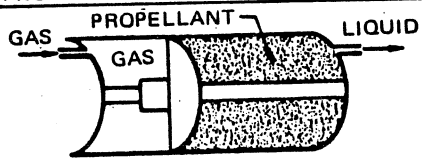	YES	Applicable and reusable. Some leakage past piston will occur. Heavy weight. Short pistons may cock. Low volumetric efficiency.
BELLOWS	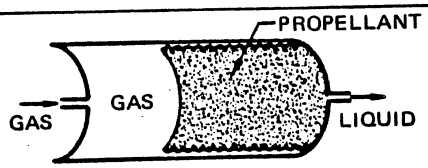	YES	Applicable and reusable. Heavy weight. Subject to vibration damage. Low volumetric efficiency.
COLLAPSING BLADDER	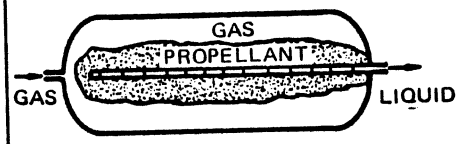	YES	Applicable to moderate loads. Elastomeric bladder is reusable. Susceptible to damage during sloshing.
EXPANDING BLADDER	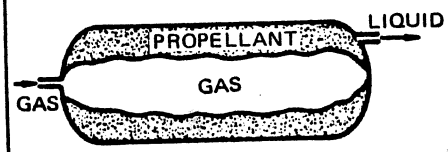	YES	Applicable for moderate loads. Elastomeric bladder is reusable. Susceptible to damage during sloshing.
ROLLING DIAPHRAGM	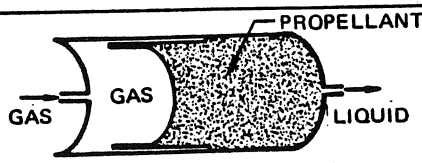	YES	Applicable. May tear or cock. Elastomeric diaphram is reusable.

Figure 5-26. Applicability of Typical Propellant Expulsion Techniques

A typical liquid level sensor is the float switch. When the propellant reaches a prescribed level in the tank, the float switch is actuated and it provides a signal which can be used to shut off the propellant supply, as in the Thor liquid oxygen tank. Since this device provides a measure of propellant volume only, density which is a function of temperature, must also be known to determine the propellant weight. The propellant bulk temperature can be sensed by temperature transducers. Cryogenic propellants can be held at a desired temperature until shortly before launch by controlling the tank pressure by means of a vent valve.

Passive devices, such as capacitance probes, are also used to determine the weight of propellant in tanks. The propellant liquid or vapor fills the space between the capacitor plates, depending on capacitor location, and acts as a dielectric. The capacitance of the probe is a function of its surface area and the value of the dielectric constant. Because the propellant's dielectric constant varies with its density, the capacitance of the probe is proportional to the local propellant density.

The capacitance probe output can be calibrated in terms of propellant weight, if the capacitor samples average density conditions in the tank. A tubular capacitor (such as used in the S-IVB fuel and oxidizer tanks), which is nearly as long as the tank and which is oriented substantially vertically near the tank centerline, will give an accurate weight readout.

If all of the usable propellants were burned, the propellant utilization would be 100 percent. In practice, engines frequently are shut down when a performance objective, such as a desired velocity, is achieved, leaving residual quantities of both propellants in the tanks.

When maximum total impulse is desired, one of the propellants is inevitably depleted before the other. The residual propellant at engine shutdown is equivalent to an unusable dead weight carried by the stage which reduces the weight of useful payload that can be carried. Therefore it is desirable to achieve a high percentage of propellant utilization.

Propellant utilization is a quantitative measurement of the effective use of the propellants. The effectiveness of propellant utilization is evaluated by:

$$\eta_{PU} = \left(\frac{P_C}{P_T}\right) \times 100\% = \left(1 - \frac{P_R}{P_T}\right) \times 100\% \qquad (18)$$

where:

η_{PU} = Propellant utilization efficiency, %

P_C = Propellant consumed (at propellant depletion shutdown), lb

P_R = Residual propellant (at propellant depletion shutdown, lb

P_T = Total propellant at launch, lb

Residual propellant is frequently defined as the usable propellant remaining after depletion of either the usable oxidizer or the usable fuel. Residual propellant may also be defined as the total remaining propellant, including the unusable propellant at depletion. The unusable propellant may be defined as the quantity trapped because of system geometry, or the definition can also include the propellant bias. The bias is the quantity of one propellant, usually fuel, which is added to the required loading to assure that the other propellant will be depleted first.

If thrust is terminated prior to propellant depletion, the residual propellant may be estimated by simulating the performance of the propulsion system to a propellant depletion shutdown. Total propellant may be defined as all of the usable propellant, or as all of the onboard propellant, including the unusable propellant. In general these variations in the definition of residual and total propellant have a negligible effect on the propellant utilization efficiency.

To maximize propellant utilization, it is necessary to control the weight of oxidizer and fuel loaded into the vehicle tanks, and to control their mixture ratio during combustion. The propellant utilization system, which consists of procedures and hardware, may be either an open-loop or a closed-loop system.

The open-loop system procedures consist of determining the propellant loading required, and then loading that weight of propellant on board. The propellant loading, weight of oxidizer and fuel, required is based on the mission total impulse requirements, and the predicted inflight engine mixture ratio. The weight of the propellants loaded is determined by volume and density measurements. The open-loop hardware consists of fixed mixture ratio controls built into the propellant feed system. Typically this fixed control consists of flow-limiting orifices in the fuel and oxidizer feed lines which are used in conjunction with a tank-top pressure regulator to produce the desired mixture ratio.

The closed-loop propellant utilization system may use essentially the same propellant loading procedure. However, the closed-loop system includes hardware which continuously measures the weight of oxidizer and fuel remaining in the propellant tanks, and by means of throttle valves, varies the propellant flowrates to adjust the engine mixture ratio to comply with the residual propellant ratio, thus approaching simultaneous depletion of the oxidizer and the fuel.

Many factors can cause random in-flight variations in the mixture ratio of a propulsion system, such as pressure

variation in the tanks, changes in feed system pressure drop due to filter clogging, off-nominal-position throttle valves, and unequal shifts in propellant density due to changes in propellant tank temperature. If the magnitudes of these variables are small and predictable, an open-loop system will provide a high propellant utilization efficiency; otherwise a closed loop system may be required.

5.4.4 Propellant Pumps

Pumps are used in rocket propellant feed systems to deliver the propellants from the vehicle tanks to the thrust chamber assembly at the required pressure. The pumps are usually located in the feed lines close to the thrust chamber to obtain additional pump inlet pressure from the fluid elevation head, and to minimize the length of high pressure ducting required. Positive displacement or centrifugal propellant pumps generally are used, and the energy required to drive the pumps may be obtained from a separate source or from the propellants which are being pumped. The selection of the type of device used to drive the pump is dependent on the type of energy that is available.

Separate energy sources include electrical power, and liquid or solid propellant gas generators. Because of weight considerations, electrical power is used only if the energy requirements are small, and an onboard electrical power supply, required for other purposes, is available when it is needed to pump the propellants. A separate gas generator frequently is used to provide all of the energy for a small total-impulse system. In a large total-impulse system, a separate gas generator usually provides the energy to accelerate the pump to operating speed, and then some of the propellant is diverted from the pump discharge to provide subsequent pump energy requirements. This energy is usually obtained by burning the propellants in a gas generator and exhausting the combustion products through a gas turbine.

Figure 5-27 is a schemetic diagram of a typical pump-fed engine. In this configuration, a gas generator burns a small portion of the propellants to power a turbine which drives the propellant pumps through a gear reduction. Additional energy may be extracted from the turbine exhaust by the use of a heat exchanger and an exhaust nozzle, as shown. The amount of gear reduction required is dependent on the design of the turbine and

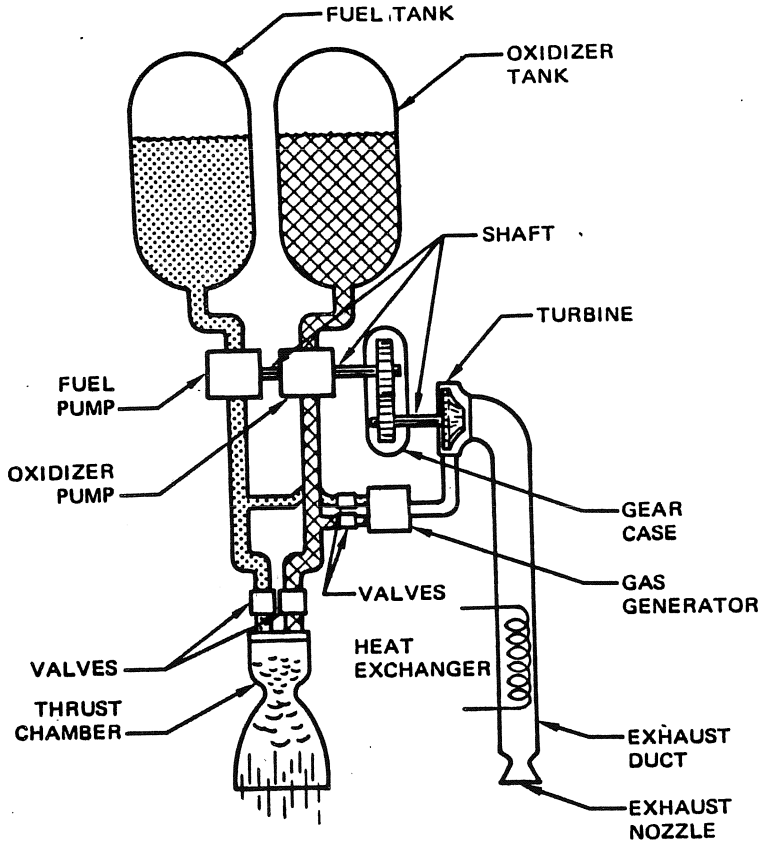

Figure 5-27. Typical Pump-Fed Liquid Engine Schematic

the pumps. For example, the RJ-1 and liquid oxygen pumps for the Thor MB-3 engine are on a common shaft and are driven by the turbine through a 4.885:1 gear reduction. On the other hand, the liquid hydrogen and liquid oxygen pumps for the S-IVB J-2 engines are directly coupled to separate turbines with no speed reduction.

Figure 5-28, a schematic of the RL 10A-3 engine, illustrates another method of using propellant to drive the propellant pumps. This method, called the regenerative cycle, can be used when liquid hydrogen is one of the propellants and is used to regeneratively cool the thrust chamber. The hydrogen is heated and vaporized in the coolant passages, and then expanded through the turbine to supply power for the pumps before being injected into the thrust chamber. In the RL 10A-3 engine, the hydrogen pump is coupled directly to the turbine and the oxygen pump is driven through a gear reduction. The turbine power and speed can be regulated by diverting some of the hydrogen around the turbine.

Since hydrogen is cryogenic, there is usually sufficient heat capacity in the thrust chamber walls before engine ignition to vaporize enough hydrogen to supply the initial required power to bring the pumps up to operating speed. Thus this method does not require a gas generator for starting or for continuous operation.

5-4.4.1 Pump Selection Criteria

Pumps are generally divided into positive displacement and steady flow categories. Positive displacement pumps, running at constant speed, can deliver a constant flow of fluid against a wide range of pressures. The flowrate is a direct function of the pump displacement and speed. Typical positive displacement configurations include piston, valve, gear, wobble plate and diaphragm. This category generally is used for low-flow high-pressure requirements which represent only a small portion of the total pumping applications for rockets.

Most rocket pumping applications require delivery of propellants at large flowrates and relatively high pressures. These requirements are met efficiently by steady-flow centrifugal pumps. Figure 5-29 is a sketch which shows that the principal elements of a centrifugal pump are the stationary housing, containing the inlet and outlet ports and the volute passage, and the rotating impeller and shaft.

The working fluid enters the eye of the impeller around the shaft centerline, is accelerated radially outward in the impeller channels and enters the volute at high velocity and low pressure. The fluid velocity decreases and its pressure increases as it passes through the volute, which increases in cross-sectional area as it approaches the pump outlet port. Internal leakage is minimized

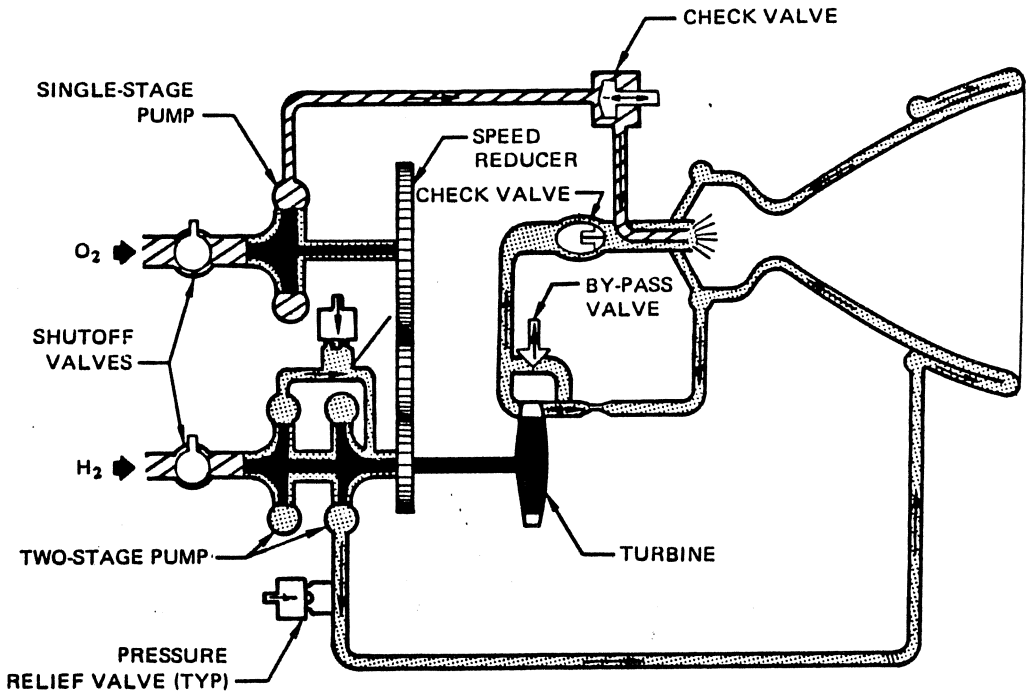

Figure 5-28. Typical Turbopump Regenerative Cycle

between the high pressure pump discharge and the low pressure inlet impeller locations by maintaining close clearances between the rotating and stationary parts at the wearing surfaces. External leakage along the shaft is prevented by the shaft seals.

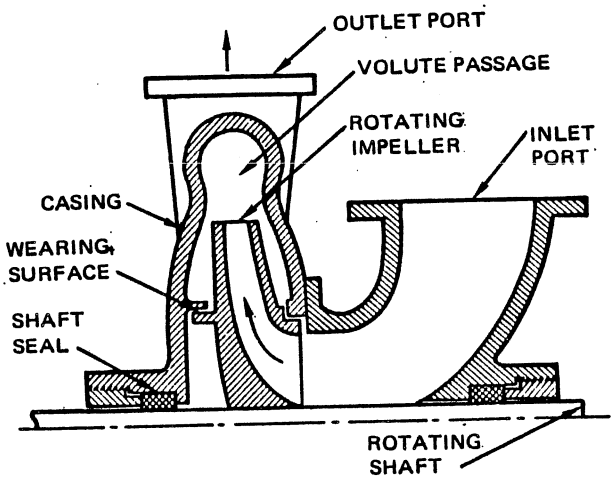

Figure 5-29. Schematic of a Typical Centrifugal Pump

5-4.4.1.1 Specific Speed

For a given centifugal pump design, the fluid flowrate is porportional to rotational speed, the delivered fluid pressure is proportional to the square of speed, and the power required to drive the pump is proportional to the cube of speed. From these relationships it is possible to derive a parameter, or type number, called specific speed

$$N_s = \frac{N\sqrt{Q}}{(\Delta H)^{3/4}} \qquad (19)$$

where:

N_s = Specific speed

N = Actual speed, rpm

Q = Capacity, gpm

ΔH = Fluid pressure head rise, ft

The specific speed is calculated for the best efficiency point. It is constant for all similar pumps, and does not change with speed for the same pump.

The specific speed is used to classify impellers, on the basis of their performance and proportions, independently of their actual size or the speed at which they operate. Figure 5-30 can be used to calculate the specific speed for a particular set of requirements. The example shown in this chart shows that the specific speed is 3,300 for a pump running at 3,500 rpm that delivers 1,250 gpm at 125 ft of fluid head.

5-4.4.1.2 Pump Power Requirements

The horsepower required to deliver a fluid at a given weight flowrate and pressure can be calculated from the relationship:

$$P = \frac{\eta \dot{w} \Delta H}{550} \qquad (20)$$

where:

P = Shaft power input to the pump, hp

η = Pump efficiency, %

$\dot{w}$ = Fluid flowrate, lb/sec

ΔH = Head rise delivered by the pump, ft

The pump efficiency, η, increases as internal leakage, turbulance, and friction decrease.

Figure 5-31 is a chart which can be used to calculate shaft horsepower for water which has a specific gravity of unity. The horsepower required to pump any fluid can be determined if the solution for water is multiplied by the specific gravity of the fluid being pumped. This chart also indicates the type of pump which should be used for a particular capacity and head rise. Figure 5-32 describes the different kinds of centrifugal pumps in terms of specific speed, and indicates the pump efficiency, η, each pump type can achieve as a function of volume flowrate. Figure 5-32 also indicates the range of values of the pump suction parameters, which can be obtained with each of these pump configurations. The pump suction parameter is a measure of the tendency of a pump to cavitate.

The efficiency curves in Figure 5-32 show that pump efficiency increases as the flowrate increases, and that the maximum efficiency at any flowrate occurs at a specific speed of about 2,500 rpm, which is in the range of the Francis impeller configuration. The efficiency curves are representative of single and multistage pumps, although multistage units tend to be slightly less efficient.

The efficiency of pumps falls off rapidly for specific speeds less than about 1,000, because low specific speed impellers have long narrow vane passages which result in large fluid friction losses and greater disk friction losses. In addition, leakage is proportionally greater because the leakage area is a greater percentage of the passage area for small flows, and the pressure differential is greater. For a given head and capacity, it is desirable to use as large a specific speed as possible, since this results in a smaller-diameter impeller and hence a smaller and lighter pump. In general the efficiency will also be higher at a higher specific speed.

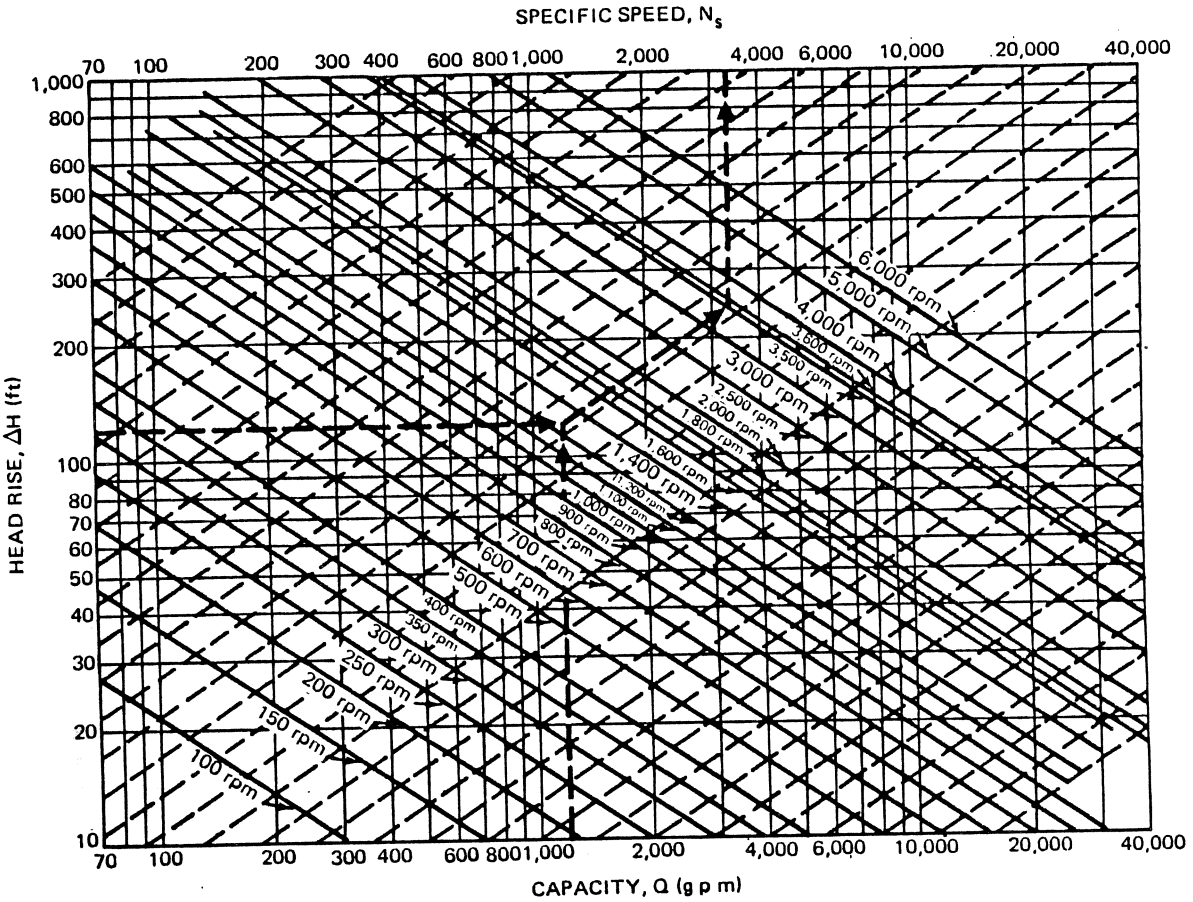

Figure 5-30. Chart for Determination of Specific Speed

5-4.4.1.3 Cavitation

Pump performance is limited by cavitation, a phenomenon which occurs when the static pressure at any point in a fluid flow passage becomes less than the fluid vapor pressure, allowing the formation of vapor bubbles, or cavities, in the fluid. These cavities collapse suddenly when the fluid static pressure again exceeds the vapor pressure, and the surrounding liquid rushes in to fill the void. In centrigugal pumps, cavitation is most likely to occur in the inlet to the pump impeller because this is the location where the lowest absolute pressure is encountered. Excessive cavitation can damage the impeller and may cause fluctuation of the pump discharge which, in turn, can cause erratic combustion and severe thrust chamber vibrations.

To avoid cavitation, the suction head above vapor pressure which is required by the pump must always be less than the available net positive suction head, (NPSH), delivered by the feed lines to the pump. As shown in Figure 5-33, the available net positive suction head is the sum of the tank pressure, and the elevation head of the propellant surface above the pump inlet, minus the friction losses in the line between the tank and pump, and the vapor pressure of the fluid. When the vehicle is undergoing acceleration during flight, the head due to elevation must be corrected accordingly.

The net positive suction head required by the pump can be determined from the pump suction parameter and the suction specific speed.

$$\sigma = \frac{H_s}{\Delta H_e} \tag{21}$$

$$S = \frac{N_s}{\sigma^{3/4}} = \frac{N\sqrt{Q_e}}{H_s^{3/4}} \tag{22}$$

where:

σ = Pump suction parameter

H_s = Required pump suction head, ft

S = Suction specific speed

and the subscript e refers to maximum efficiency conditions.

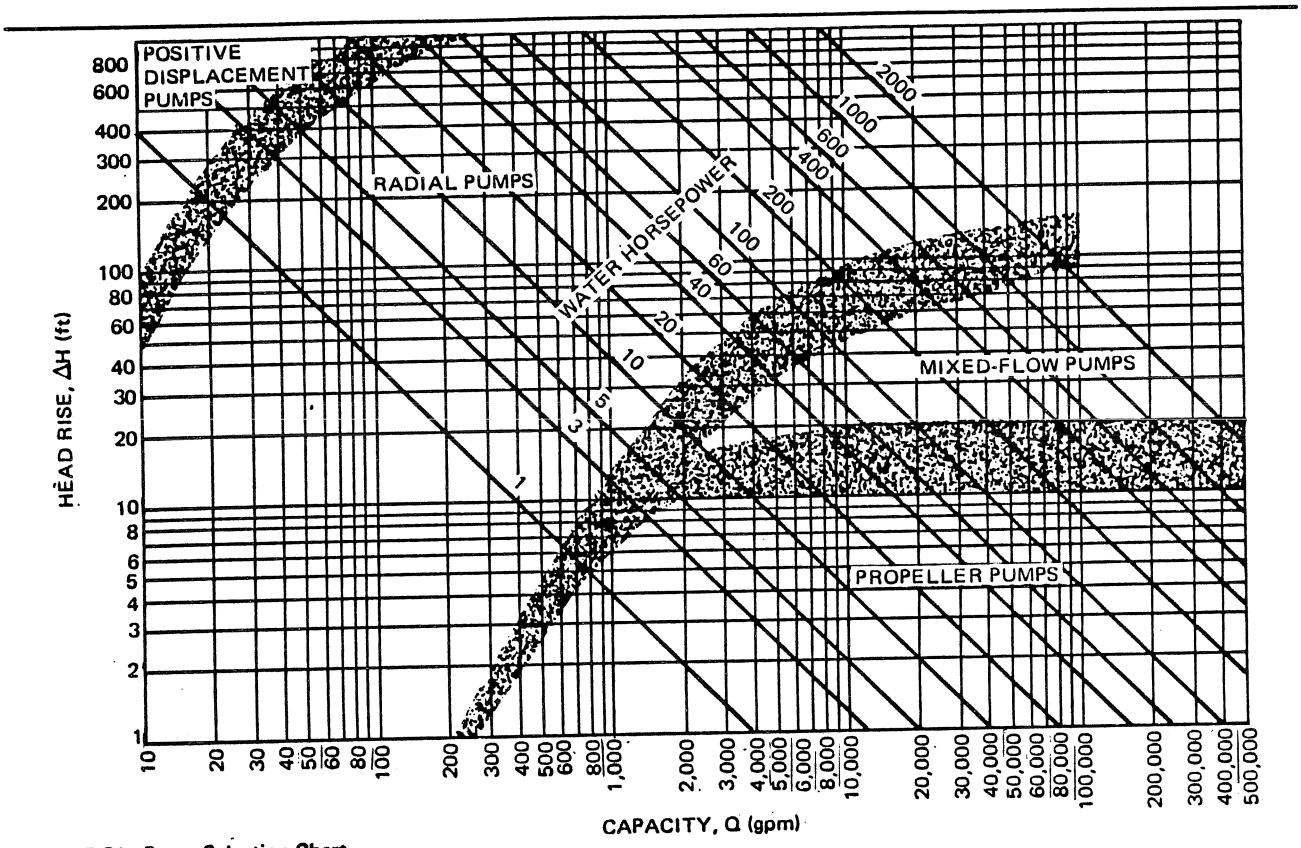

Figure 5-31. Pump Selection Chart

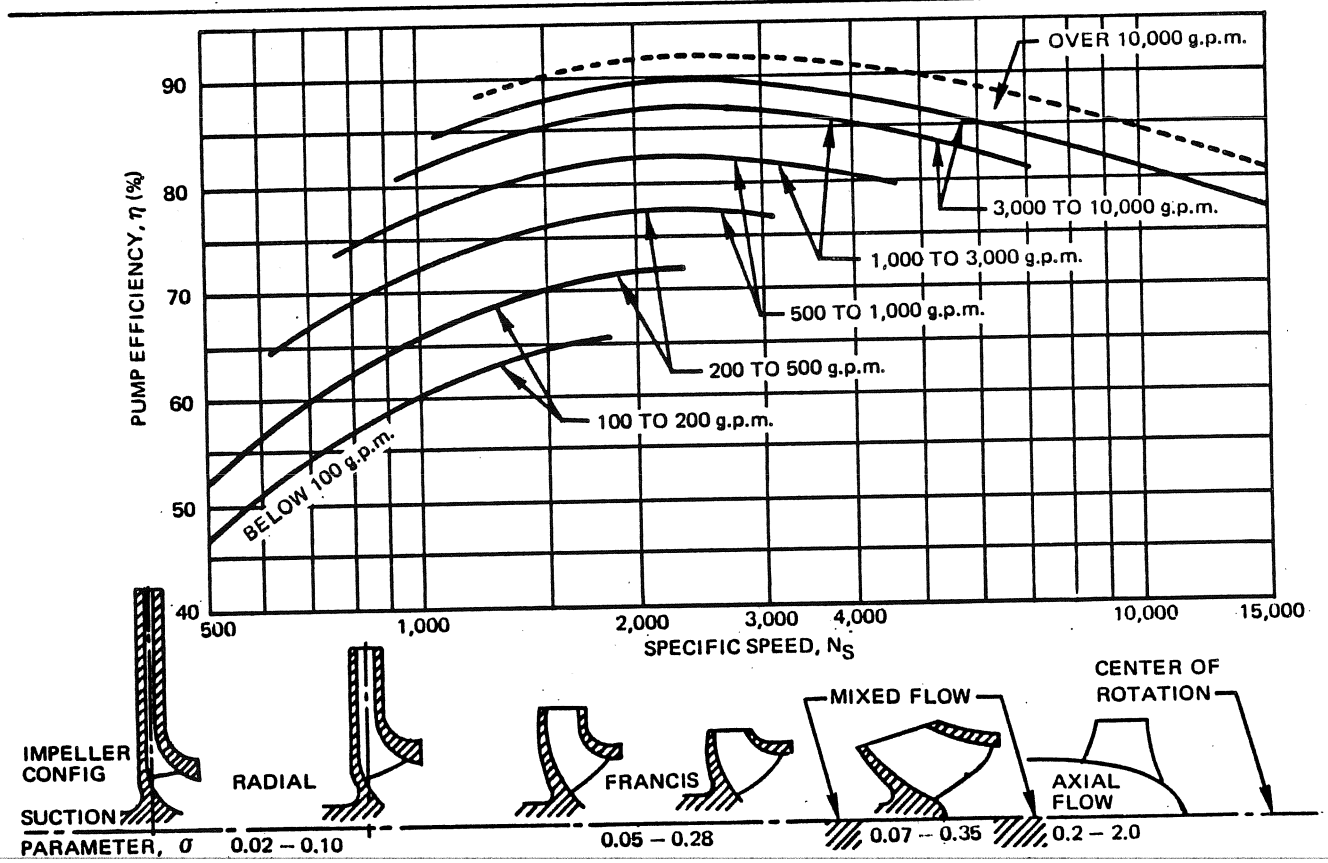

Figure 5-32. Efficiencies of Pump Configurations

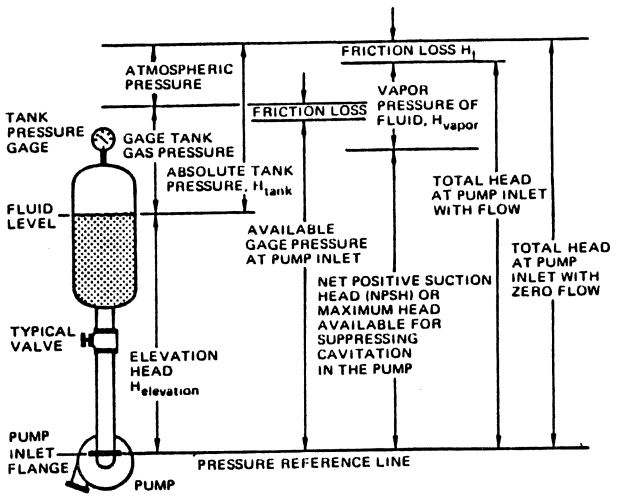

Figure 5-33. Definition of Pump Suction Heads

Figure 5-32 lists ranges of values N_S and σ for the basic centrifugal impeller configurations. The pump suction parameter, σ, depends on the quality of the pump design and its specific speed, N_S.

The cavitation limits of a new pump design must be determined experimentally. These cavitation characteristics can then be described by the calculated magnitude of the pump suction parameter, σ. The cavitation limits of other pumps of the same hydraulic design, but different sizes and speeds can be predicted by determining their values of σ.

The magnitude of the delivered head, ΔH, tends to decrease as the pump design approaches the axial flow configuration, but the magnitude of the required pump suction head, H_S, is dependent primarily on the inlet velocity and the smoothness of the pump inlet geometry. Therefore the magnitude of σ tends to increase as the impeller design approaches an axial configuration. However, within a given category of impeller design, an increase in σ represents an increasing tendency towards cavitation.

The suction specific speed, S, a function of N_S and σ, also is used to evaluate the cavitation characteristics of pumps. Pumps that have good suction characteristics have suction specific speeds near 15,000 rpm. Pumps which are subject to local cavitation usually have values of suction specific above 30,000 rpm.

Nomograms which facilitate calculation of required pump suction head, H_S, pump suction parameter, σ, and pump specific speed N_S are presented in Figures 5-34, 5-35, and 5-36 respectively. Values of N_S can be determined by the nomogram in Figure 5-36 if Q is stated in Ft^3/sec or by the chart in Figure 5-30 if Q is stated in gpm. When the suction specific speed, S, has not been determined previously, the pump suction parameter may be selected by the impeller configuration, as shown in Figure 5-32, and a value of S may be chosen in the average range, to determine a preliminary specific speed for initial design purposes.

5-4.4.1.4 Pump Applications

High speed rotating configurations typically are used in rocket applications to minimize pump envelopes and weights. These pumps generally are driven by turbines which are powered by combustion of a portion of the main engine propellants as illustrated in Figure 5-28. These light weight systems are capable of efficiently delivering a large flowrate of propellant at relatively high pressures.

Figure 5-37 is a disassembled view of the centrifugal pump which delivers the earth-storable fuel, RJ-1, to the Thor MB-3 engine. This pump is similar to the liquid oxygen pump on the same engine. They are both driven by a common turbine through a gear reduction system. Installation geometry requires that the fuel enter the pump through an inlet elbow which causes an additional pressure drop and thus increases the required pump suction head. However, the pump contains a rotating inducer which compensates somewhat for this drop by increasing the pressure of the propellant at the inlet to the impeller. This inducer is an axial flow propeller which has a low required suction head because it is submerged in the propellant. The use of the inducer reduces the overall required pump suction head, H_S. The impeller has a radial configuration with typical values of specific speed, N_S, and pump suction parameter, σ, as described in Figure 5-32. Table 5-12 contains values of significant parameters for this pump and several other rocket propellant pumps.

Figure 5-38 presents a cross-section of the turbopump that delivers liquid oxygen to the J-2 engine on the S-IVB stage of the Saturn rocket. In this design, entrance losses to the pump impeller are minimized because the propellant inlet to the inducer is coaxial with the pump centerline. The pump has a Francis configuration impeller with values of N_S and σ listed in Table 5-12. These values are typical of the range shown in Figure 5-32. This pump is coupled directly to a two-stage impulse turbine.

Figure 5-39 contains a cross-section of the turbopump that delivers liquid hydrogen to the J-2 engine. Fuel enters the impeller through a multistage rotating inducer. The impeller has a multistage axial flow configuration with values of N_S and σ listed in Table 5-12. These values are typical for the axial flow range shown in Figure 5-32. Figure 5-40 is a cutaway view of this pump showing the shape of the stator and rotor blades.

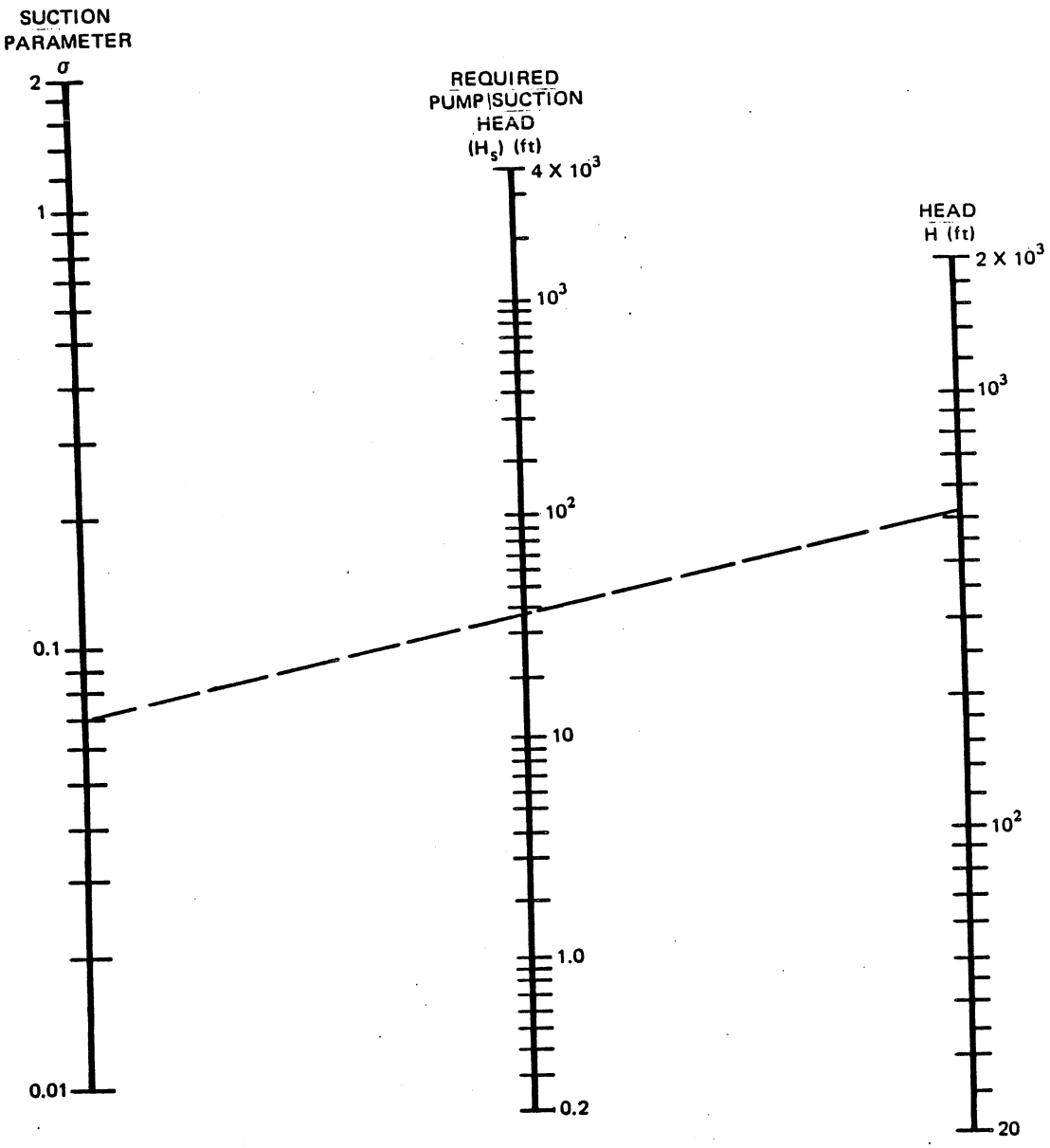

Figure 5-34. Nomogram for Required Pump Suction Head

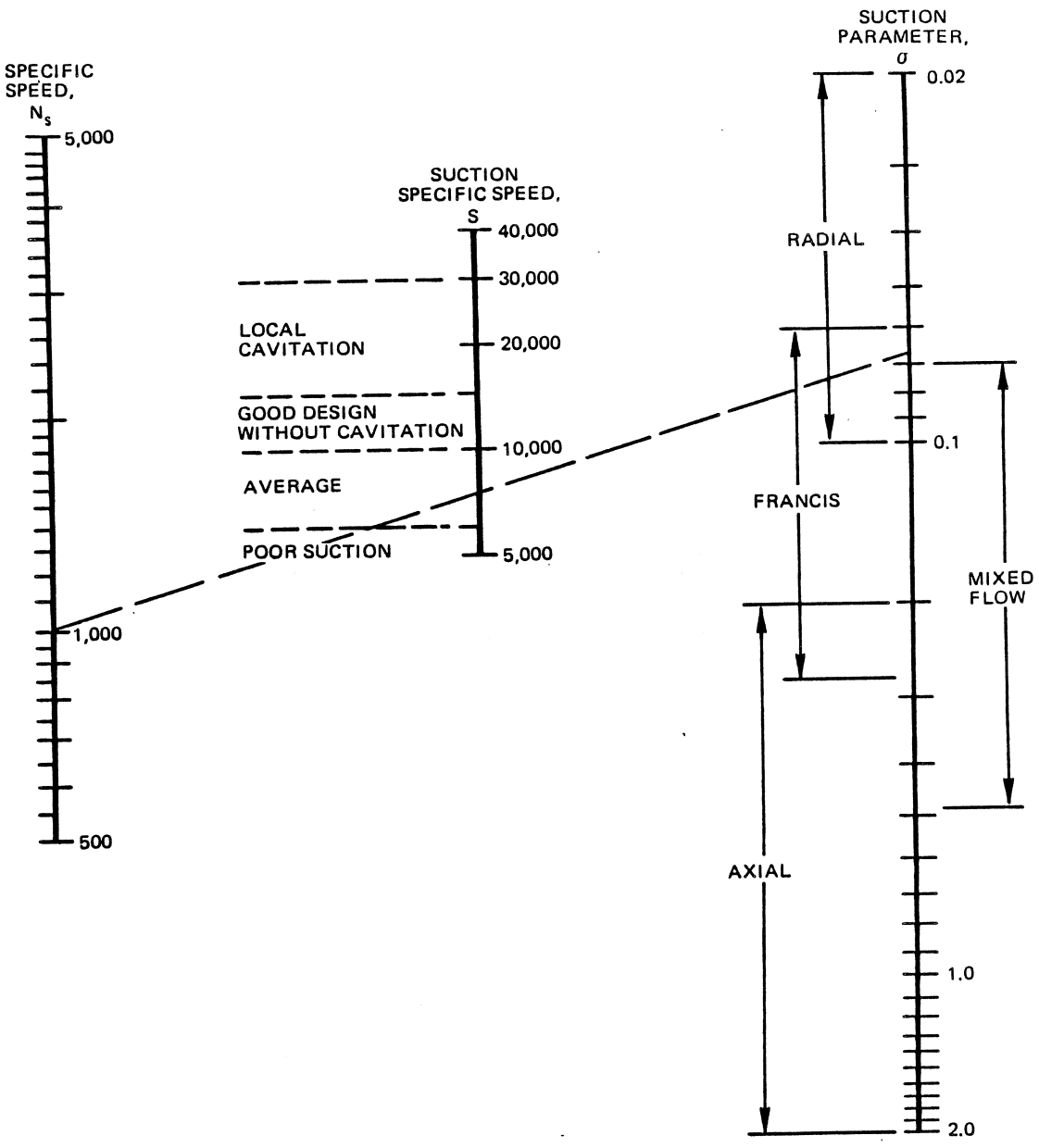

Figure 5-35. Nomogram for Suction Parameter

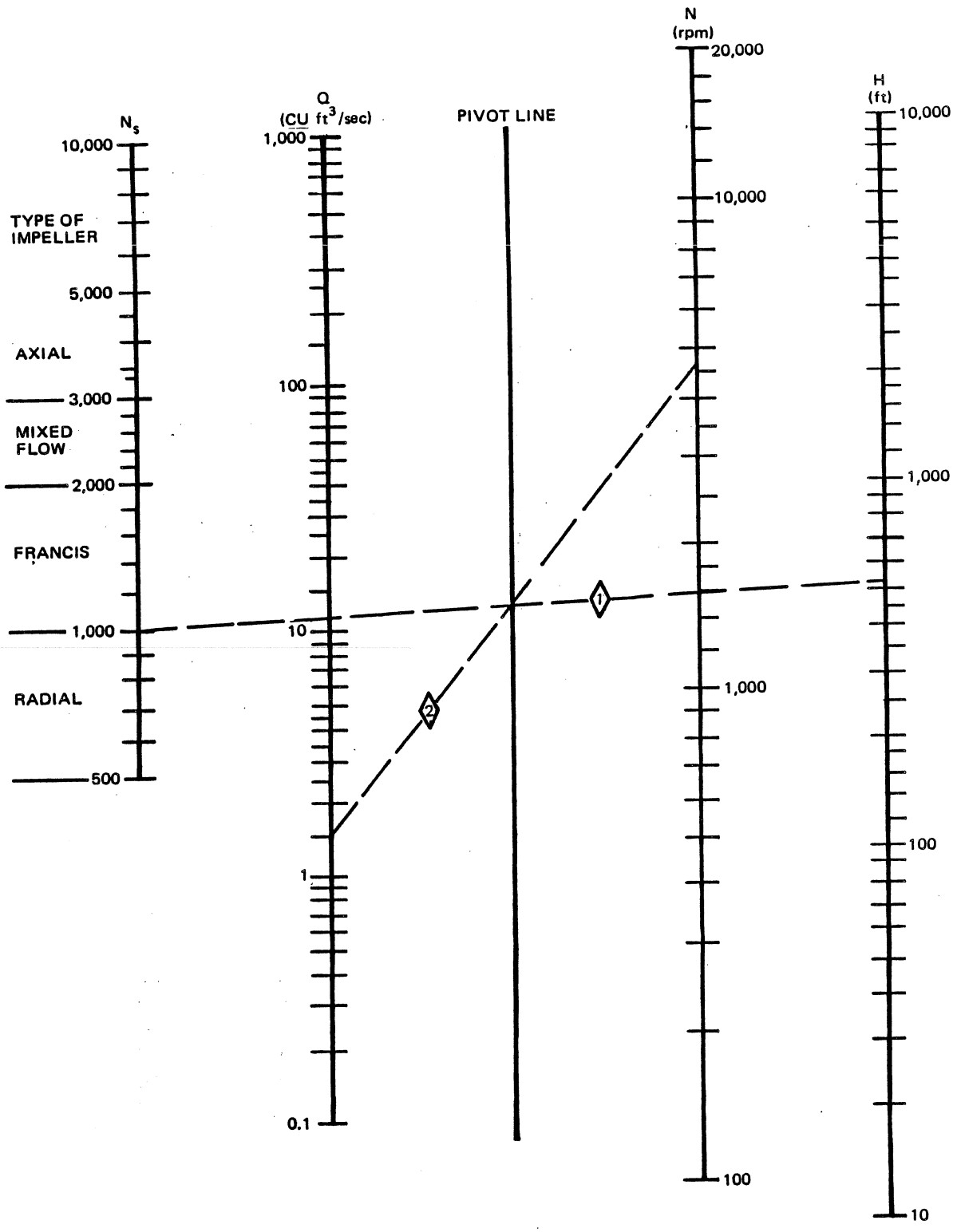

Figure 5-36. Nomogram for Specific Speed

Table 5-12. Typical Design Point Pump Performance Data

VEHICLE/ENGINE	THOR/MB-3		SIVB/J2	
PROPELLANT	RJ-1	LO_2	LO_2	LH_2
TEMPERATURE, °R	520	164	164	37
DENSITY, lb/ft^3	53.2	70.8	70.8	4.40
PUMP CONFIGURATION	RADIAL	FRANCIS	FRANCIS	AXIAL
N = SPEED, rpm	6311	6311	8600	26,750
Q = FLOWRATE, gpm	1838	2962	2640	8450
ΔH = DEVELOPED HEAD, ft	2397	1666	2125	37,500
H_r = REQUIRED PUMP SUCTION HEAD, ft	32.4	54	30.5	162
SUPPLIED NPSH, ft	130	108	45.8	370
P = SHAFT POWER, HP	1325	1804	2220	7713
η = EFFICIENCY, %	71.6	79.1	80.2	73.2
N_s = SPECIFIC SPEED, rpm	800	1320	1410	9100
σ = SUCTION PARAMETER	0.013	0.032	0.029	0.018
S = SUCTION SPECIFIC SPEED, rpm	20,000	17,000	20,000	18,000

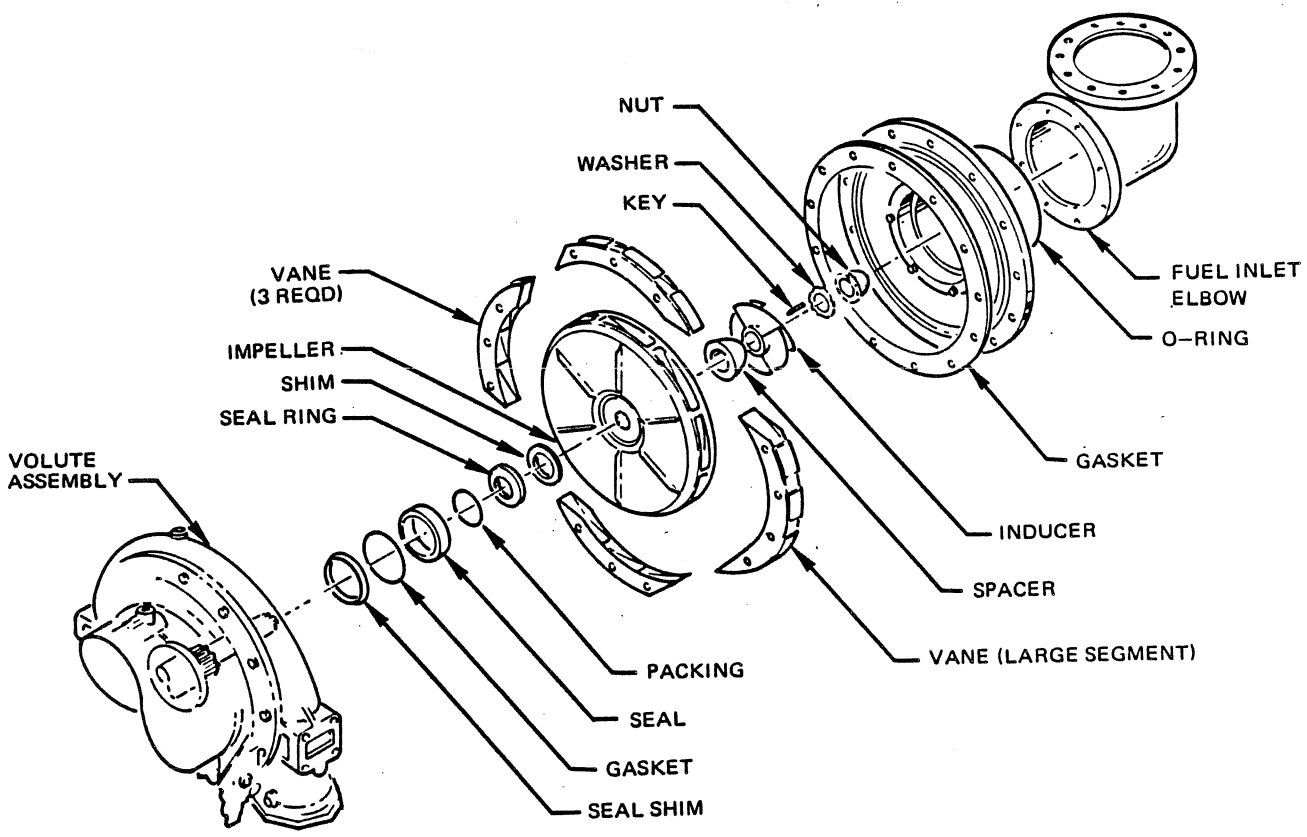

Figure 5-37. Disassembled View of the Fuel Pump for the Thor MB-3 Engine

5-4.4.2 Turbine Selection

A turbine is a device which transfers energy from a flowing fluid to a rotor when the fluid is passed through blades which are attached to the rotor. The two basic categories of turbines are impulse turbines and reaction turbines.

In an impulse turbine the working fluid, usually a hot gas, is fed through divergent nozzles to the rotor, as shown in Figure 5-41. The gas pressure is decreased, and its velocity is increased, as it passes through the nozzle, and the pressure remains constant, but the velocity decreases as the gas passes through the rotor blades. The decrease in the momentum of the gas, caused by its velocity decrease, imparts a force to the rotor blades. This force, multiplied by the duration of its application, produces an impulse on the rotor which is equal to the change in gas momentum.

In a reaction turbine, some of the gas pressure drop occurs across the rotor blade as shown in Figure 5-42. The gas enters the rotor through stationary nozzles formed by the stator blades which are similar to the rotor blades. Gas velocity increases in the stator and decreases in the rotor. Both impulse and reaction rotors are driven by a change in gas momentum, but in a reaction turbine part of the driving force is derived from an acceleration of the gas relative to the blade. Additional driving force is derived from the change of direction of the absolute velocity, which accelerates the rotor.

A reaction turbine must be designed to minimize internal leakage because a pressure drop occurs across the rotor blades. To limit leakage, stator nozzles are placed all around the periphery, the clearance between the rotor blade tips and the housing is held to a minimum, and several stages are used to keep the pressure drop per stage low. Because of the pressure drop across the moving blades, the rotor is subjected to an axial force which may be very large. To compensate for this axial force, a reaction turbine is sometimes designed with balanced double flow, that is, the gas enters midway from the ends and expands axially in both directions.

On the other hand, an impulse turbine is insensitive to leakage because there is no gas pressure drop across the rotor blades. Thus an impulse turbine does not require close clearances, and can accept relatively large pressure drops per stage.

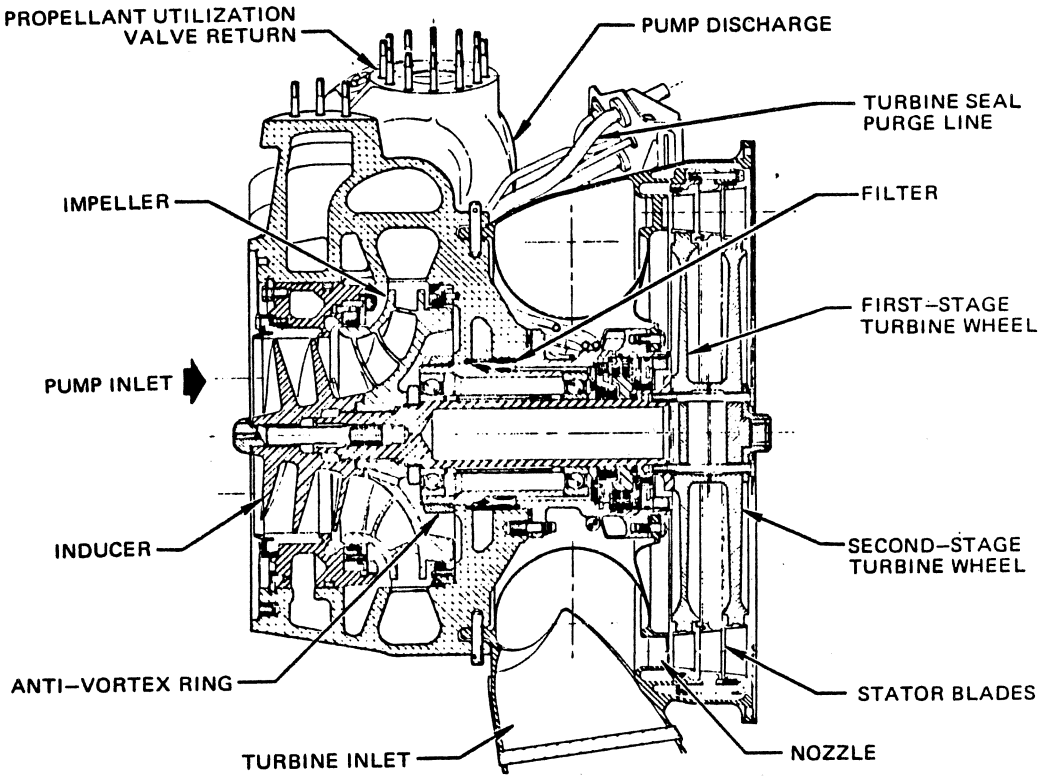

Figure 5-38. J-2 Engine Oxidizer Turbopump

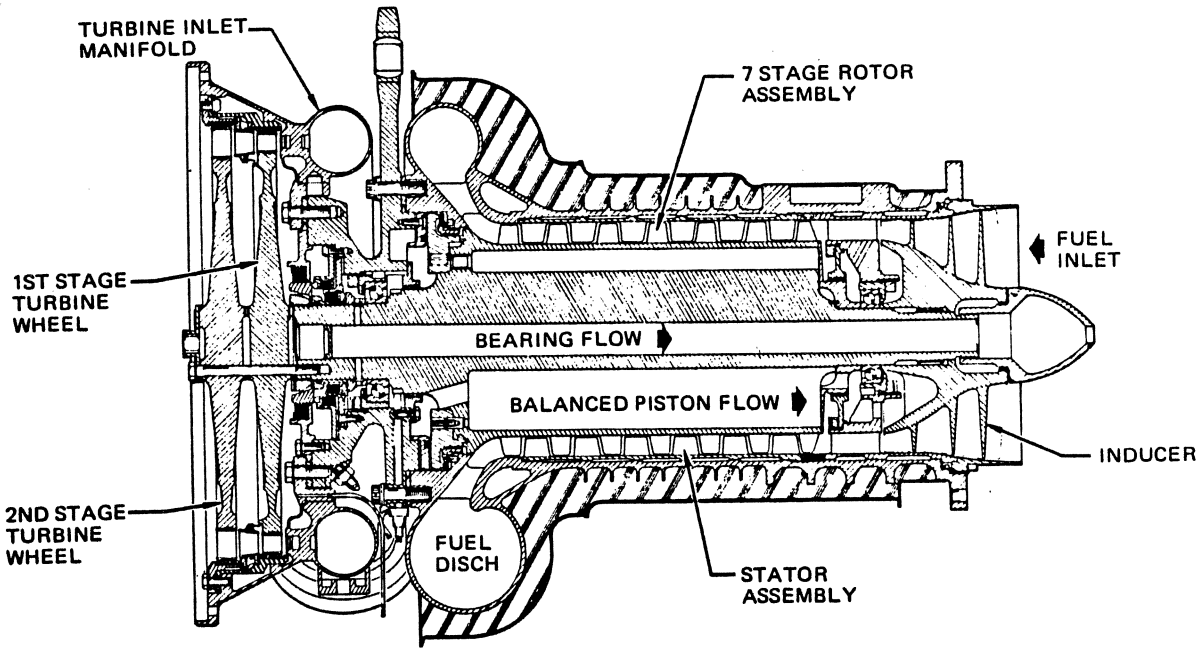

Figure 5-39. J-2 Engine Fuel Turbopump

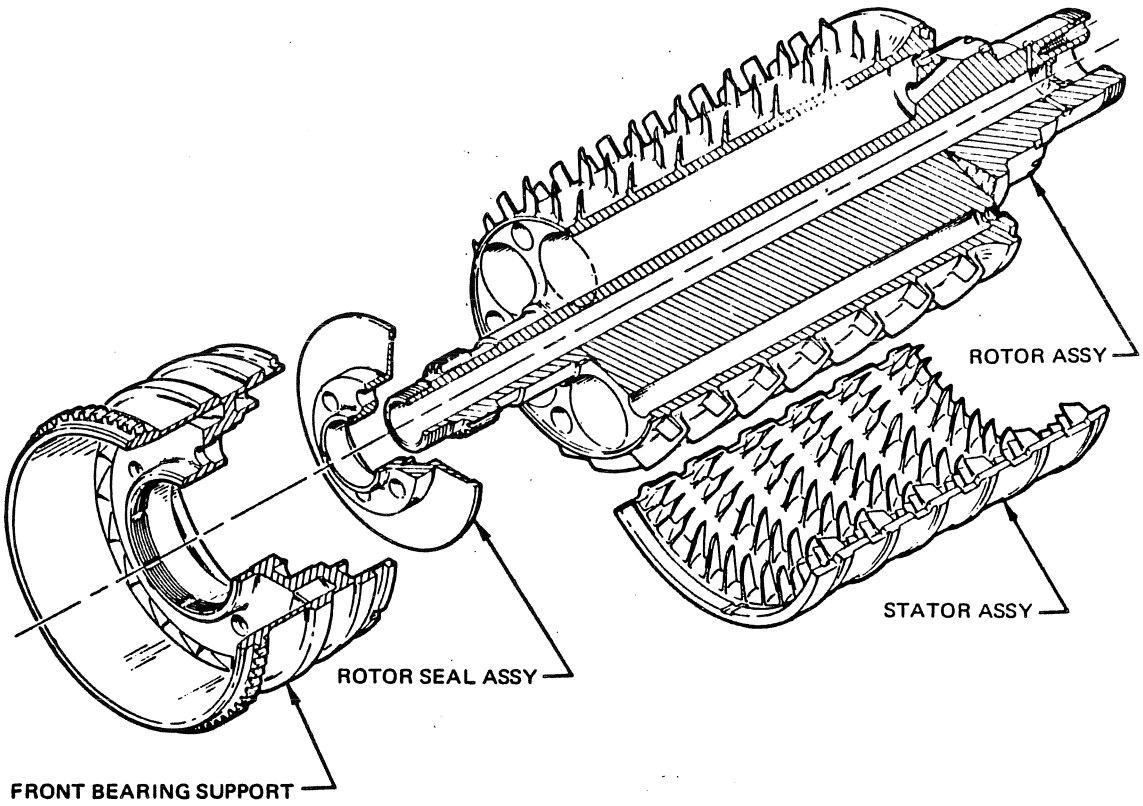

Figure 5-40. Exploded View of the J-2 Fuel Pump

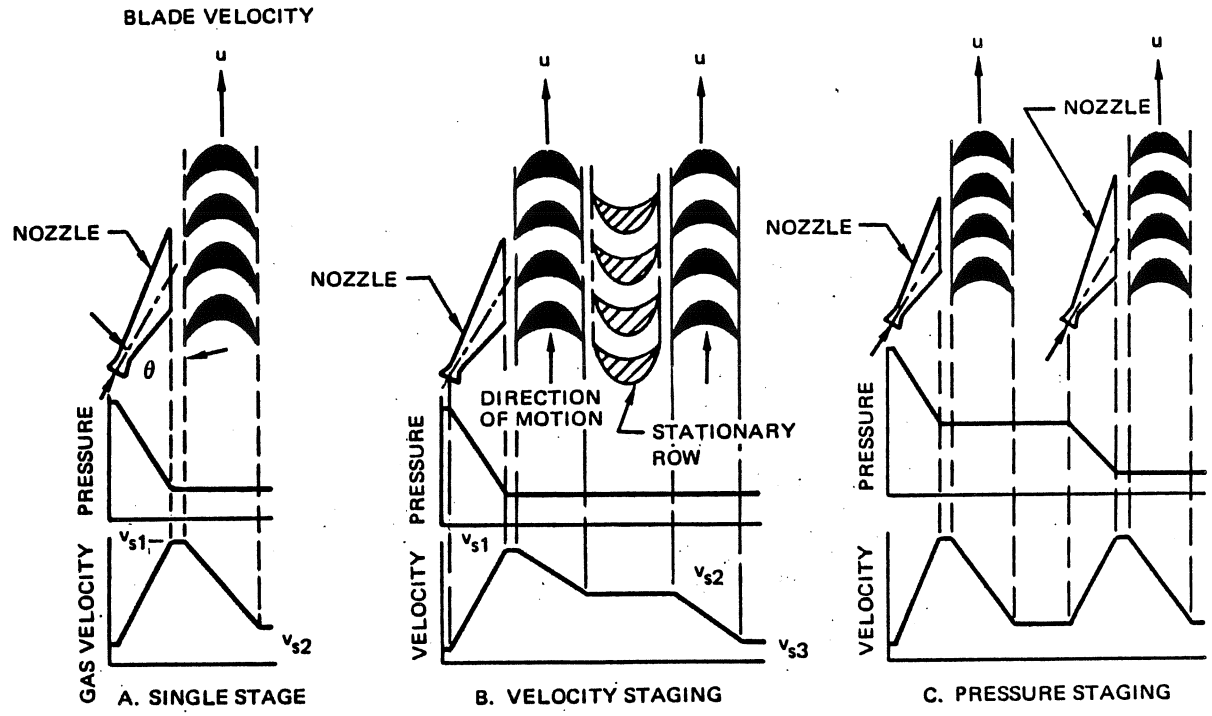

Figure 5-41. Impulse Turbine Configurations

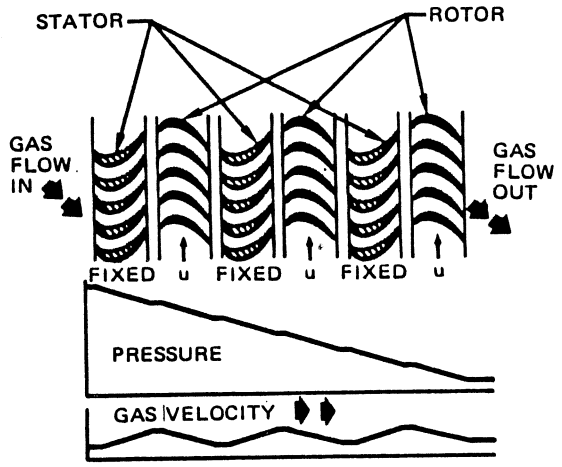

Figure 5-42. Reaction Turbine Configuration

The power supplied by a turbine is proportional to the decrease in the enthalpy of the gas and the turbine efficiency, and can be calculated from:

$$P_t = \eta_t \dot{w} c_p T_1 J \left[1 - \left(\frac{P_2}{P_1}\right)^{(\gamma-1)/\gamma}\right] \qquad (23)$$

where:

P_t = Turbine power, ft-lb/sec

η_t = Turbine efficiency, %

$\dot{w}$ = Gas flowrate, lb/sec

c_p = Gas specific heat at constant pressure, Btu/lb-°R

T_1 = Inlet temperature, °R

J = Joule's Constant, 778 ft-lb/Btu

P_1 = Gas inlet pressure, psia

P_2 = Gas outlet pressure, psia

Since there is no pressure drop across its rotor blades, an impulse turbine theoretically requires only one stage to absorb the power available in the combustion products. In practice, the stage pressure ratio P_1/P_2 is limited to about 4:1. The efficiency of a single stage impulse turbine generally does not exceed 80 percent and efficiency decreases with an increasing number of stages.

When more than one impulse stage is required, the staging may be accomplished by decreasing the velocity partially in each stage, as shown in Figure 5-41b, or by decreasing the pressure partially in each stage, as shown in Figure 5-41c. The turbines shown in Figures 5-38 and 5-39 are two-stage impulse turbines with velocity staging.

The efficiency of a reaction turbine can exceed 90 percent. However, it requires many more stages than an impulse turbine for a given pressure ratio. Therefore, although a reaction turbine is more efficient, most rockets use impulse turbines because of their design simplicity, smaller envelope, and lighter weight.

Figure 5-43 presents efficiency data for reaction and impulse turbine as a function of the velocity ratio μ/v_{s1}, where u is the blade velocity and v_{s1} is the gas velocity entering the blades as shown in Figure 5-41a. Each turbine configuration has an optimum efficiency and a corresponding specific velocity ratio. The envelope of these optimum points is the maximum efficiency curve.

5-5 PRESSURIZATION SYSTEM

A pressurization system applies sufficient pressure to the propellants in the storage tanks to assure that the propellant is delivered to the rocket engine at the pressure required for proper engine operation. This is accomplished by controlling the pressure of the gas space, or ullage, in the propellant tanks which increases as the propellants are used.

For pressure-fed engines, the ullage pressure must exceed the engine combustion chamber pressure by about 25 percent to allow for pressure losses in the propellant ducts and the injector. Chamber pressures for pressure-fed engines commonly range from 100 to 300 psia. Ullage pressure requirements for pump-fed engines are determined by pressure losses in the propellant ducts and by the required suction head of the pump. For pump-fed systems, the ullage pressure is usually in the range of 10 to 50 psia, even though the chamber pressure may exceed 1,000 psia.

The weight of a pressurization system consists of the sum of the weights of the pressurant, the pressurant tank, and the lines and valves between the pressurant tank and the propellant tank. The weight of the lines and valves is a function of the installation geometry, and is relatively small. The tank weight and pressurant weight are related by the expression:

$$\frac{W_T}{W_{PR}} = 18\frac{\rho}{s} K z R T \qquad (24)$$

where:

W_T = Tank weight, lb

W_{PR} = Pressurant weight, lb

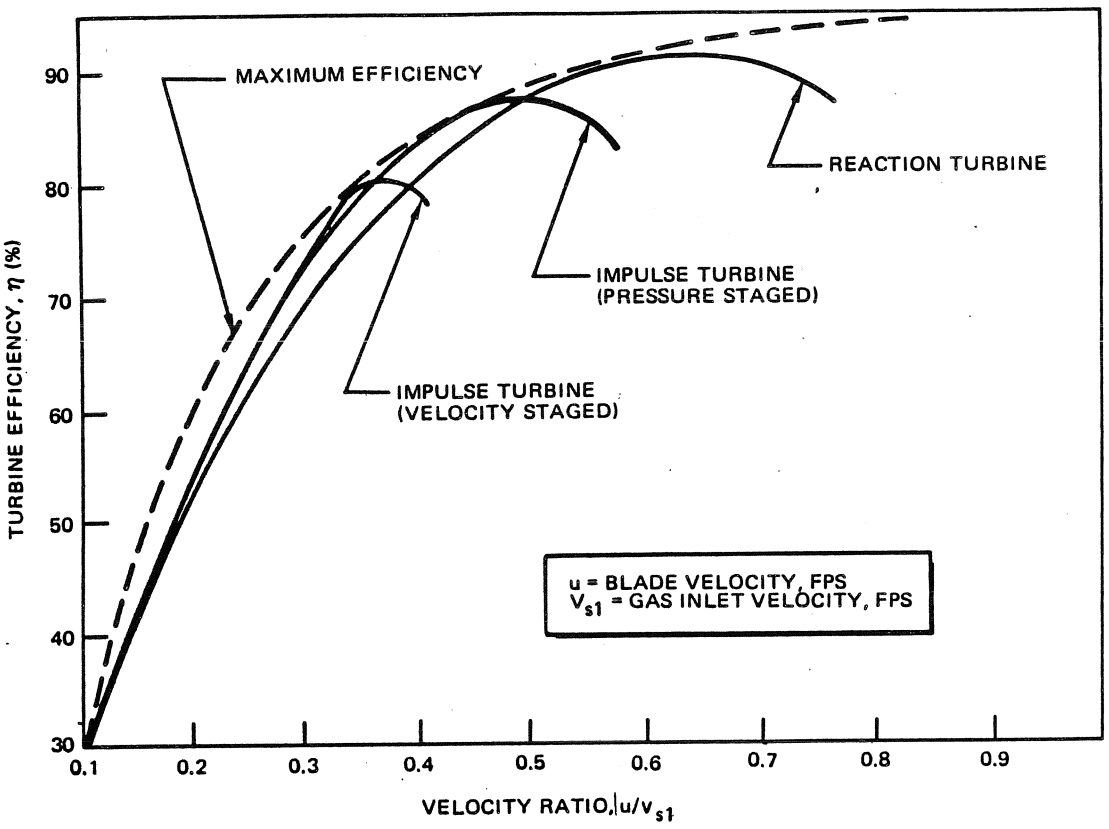

Figure 5-43. Turbine Efficiency Data

ρ = Tank material density, lb/in^3

s = Tank material ultimate stress, lb/in^2

K = Factor of safety

z = Compressibility factor of the gas in the pressurant tank

R = Gas constant, ft-lb/lb-°R

T = Gas temperature, °R

Table 5-13 lists pressurant tank materials and factors of safety selected for several MDAC program applications. At room temperature, using a titanium 6 AL-4V pressurant tank with a factor of safety of 2.0, equation 24 reduces to:

$$W_T/W_{PR} = 3.6 \times 10^{-5} zRT$$

For a given set of requirements, the pressurization system weight will be less for a pump-fed, than for a pressure-fed, propulsion system, because the lower ullage pressure requirement reduces the required weight of pressurant and pressurant tank. This subject is also discussed in Section 7.

Figure 5-44 illustrates several types of pressurization systems, and Table 5-14 identifies the relative advantages and disadvantages of each of these systems. Table 5-15 provides design and use data for each of these pressurization systems. From Table 5-15 it is apparent that stored gas and solid propellant gas generator systems have been used most frequently.

The basic hardware for each of these pressurization systems includes a pressure vessel, a means of isolating the pressurant source from the propellant tanks, and a means of controlling the ullage pressure. Figures 5-45 and 5-46 illustrate specific hardware for these functional requirements for two representative types of pressurization systems.

The cold gas system shown in Figure 5-45 uses a pressurant tank, a solenoid valve, and a pressure regulator to achieve the basic functions. Also included are check valves, to prevent back-migration of the propellants, and relief valves to protect the propellant tanks from over-pressurization.

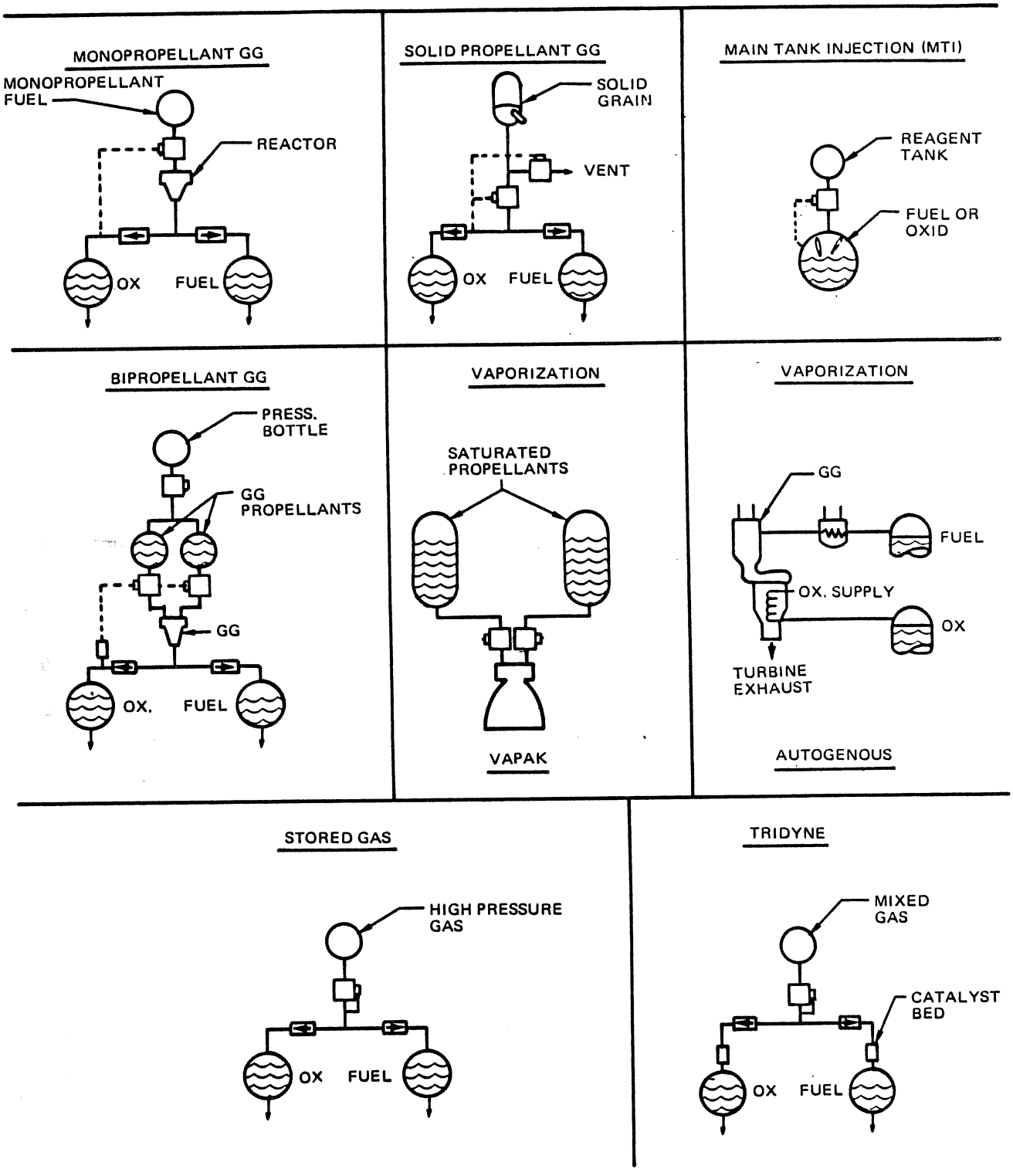

Figure 5-44. Pressurization System Schematics

Table 5-13. Pressure Vessel Safety Factors

PROGRAM USE	SAFETY FACTORS		MATERIAL	MISSION
	PROOF	BURST		
MLV	1.32	1.55	4130 STEEL	UNMANNED
IMPROVED DELTA	1.10	1.25	6AL-4V TITANIUM	UNMANNED
S-IVB CRYOGENIC TEMP. TANKS @ – 412 ± 12°F	1.67	2.22	6AL-4V TITANIUM	MANNED
S-IVB AMBIENT TEMP. TANKS	1.9	2.5	6AL-4V TITANIUM	MANNED
S-IVB/V APS	1.9	2.5	6AL-4V TITANIUM	MANNED
S-IVB/IB APS	1.5	2.5	AM355 STEEL	UNMANNED
MARCAS	1.5	2.0	6AL-4V TITANIUM	UNMANNED
MOL	1.5	2.0	6AL-4V TITANIUM	MANNED

Table 5-14. State-of-the-Art Characteristics of Candidate Pressurization Systems

Pressurization System Types	Pressurant		System					
	Contaminant Content	Reactability With Propellant	Pressure	Volume	Weight	Stop-Restart Capability	Development Risk	Cost
Monopropellant Gas Generator	Medium	Medium	Low	Medium	Medium	Good	Low-To-Medium	Medium-To-High
Solid Propellant Gas Generator	High	Medium	Low	Small	Light	Poor	Low	Low
Bipropellant Gas Generator	Medium	Medium	Low	Medium	Medium	Good	Medium	High
Stored Gas	Low	Low	High	Large	Heavy	Good	Low	Medium
Main Tank Injection	Low	High	Low	Small	Light	Good	High	High
Liquid Vaporization	Low	Low	Low	Small	Light	Poor	Low	High
Catalyzed Mixed Gas Tridyne	High	Medium	High	Large	Heavy	Good	High	High

Table 5-15. Pressurization System Investigation Summary

PRESSURIZATION SYSTEM	STATE-OF-THE-ART	APPLICATIONS	DESIGN CRITERIA	DESIGN LIMITATIONS
1. Monopropellant Gas Generator (MPGG)	A. Single-burn N_2H_4 is state-of-the-art B. Supply on demand MPGG being developed for N_2H_4 and MHF fuels.	A. Single-burn, thermal bed N_2H_4 MPGG test flown on Corporal missile. B. Hamilton Standard developing bootstrap, 2-stage N_2H_4 MPGG for Aerojet Post Boost Propulsion System (PBPS) program. C. N_2H_4 MPGG proposed for NASA ALPS program.	A. Decomposition products reactive with most oxidizers B. Gas temperature and molecular weight variable for N_2H_4 C. Clean gas D. Long self life and packaging flexibility. E. Spontaneous startup and restartable (N_2H_4 with Shell 405 catalyst). F. I_2O_5 powder being tested by NOTS for initiating thermal catalyst bed. G. Molecular weight 7-13 for N_2H_4 products.	A. 1 lb/sec highest single reactor flowrate demonstraded with N_2H_4 and Shell 405 catalyst. B. Shell 405 catalyst expensive. C. Anhydrous N_2H_4 freezing PT. $\approx 34^{\circ}F$. D. I_2O_5 powder may not be storable for 5 years. E. Injector plugging with catalyst dust could be problem. F. Condensables in decomposition products.
2. Solid Propellant Gas Generator (SPGG)	A. Single-burn units with positive expulsion and $P_c < 2000$ are state-of-the-art	A. Bullpups A and B; Prestage; Upstage; Minuteman Stage II LITVC tank. B. Army developing SPGG for Gun-Launched Rocket. C. GD/C delivered 7 storable prepackaged propellant systems with SPGG's to AFRPL.	A. Must design for burnrate at lowest predicted temperature. B. Some stop-start capability can be attained by manifolding multiple grains. C. Molecular weight 19 to 25.	A. Does not basically possess stop-restart capability. B. Exhaust products reactive with many oxidizers. C. High pressure ($>$ 2500 psi) performance not characterized.
3. Bipropellant Gas Generator	A. Continuous burn, storable propellant GG's are state-of-the-art. B. Cryogenic propellant GG's have not been used for direct propellant tank pressurization. C. GG for heating stored gas is state-of-the-art.	A. Early Bomarc fuel and oxidizer tanks; Corporal test vehicle oxizer tank; Titan II fuel tanks.	A. Generally operated at off-optimum mixture ratio to obtain low temperature. B. Generally consider fuel-rich and oxidizer-rich GG's for fuel and oxizizer tanks respectively. C. L/D $\approx$ 4.5 yields good GG designs. D. Molecular weight 16-23 for fuel-rich, approximately 30 for oxidizer-rich, storable propellant GG's.	A. Reactive with propellants. B. Condensables present in combustion products. C. Restart not demonstrated. D. Uncooled GG limited to approximately 1650°F.

Table 5-15. Pressurization System Investigation Summary (Continued)

PRESSURIZATION SYSTEM	STATE-OF-THE-ART	APPLICATIONS	DESIGN CRITERIA	DESIGN LIMITATIONS
4. Stored Gas	A. Regulated, blowdown and bang-bang systems are state-of-the-art and flight demonstrated. B. Cascade and other special types are state-of-the-art but have not been demonstrated.	A. Stored gas system used on majority of missiles and spacecraft flown to date. B. Minuteman III PBPS is latest application using regulated helium system.	A. Has high reliability, low technical risk features. B. Helium and nitrogen most used gases. C. Cryogenic storage reduces system inert weight. D. Molecular weight = 4 for H_e, 28 for N_2.	A. Helium has leakage tendencies. B. High residual weight if expansion approaches adiabatic process. C. System weight becomes high for storage pressure $>$ 5000 psi.
5. Main Tank Injection (MTI)	A. Demonstrated but not flight qualified.	A. No system operational (test only) B. Titan II pre-pressurization test.	A. Reagent must be hypergolic with propellant pressurized. B. Molecular weight approximately the same as bipropellant GG.	A. Must have free surface for reaction and release of gases. B. MTI of ClF_5 may be impossible.
6. Vaporized Propellant-Vapak	A. Basic concept is state-of-the-art but very limited operational use.	A. Titan II, Stage II oxidizer tank.	A. Accurate temperature or composition control necessary for accurate pressure. B. Generally best to use low expulsion pressure. C. Wide variation in molecular weight.	A. Limited to critical pressure of propellant. B. Most storable propellants limited to ~ 400 psia. C. Mixture ratio variations. D. Large residual gas weight possible.
7. Vaporized Propellant-Autogenous	A. State-of-the-art used on several operational systems.	A. Titan II, Stage I oxidizer tank; Thor LOX tank; S-IV and S-IVB LH_2 tanks.	A. Energy source and heat exchanger required to vaporize propellants. B. Wide variation of molecular weight.	A. No general limitations – most are configuration dependent (e.g., materials, pressure, temperature, etc.).
8. Tridyne (Catalyzed Gas)	A. State-of-the-art, but never used operationally.	A. Being developed for an advanced space application.	A. O_2/H_2 or $O_2/H_2/CH_4$ are reactive constituents. B. Molecular weight $\approx$ 4 when H_e inert gas used.	A. 1500°F present upper limit on catalyst bed temperature. B. Significant quantities of H_2O generated causing pressure collapse and/or propellant contamination.

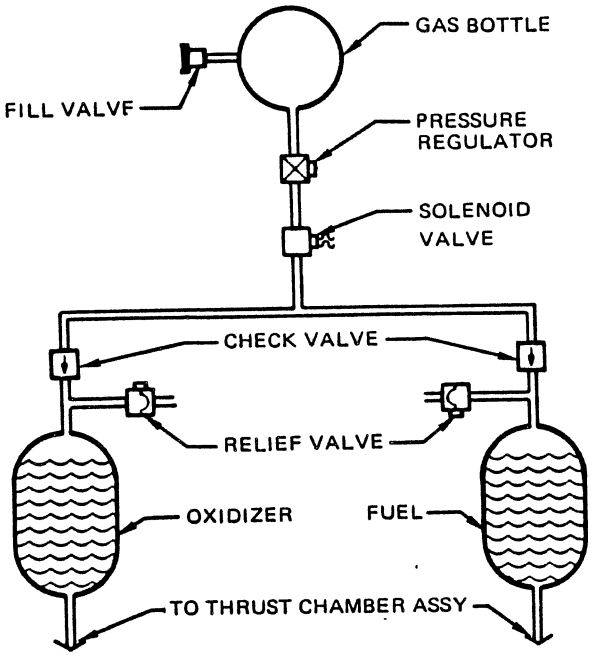

Figure 5-45. Cold-Gas Pressurization System

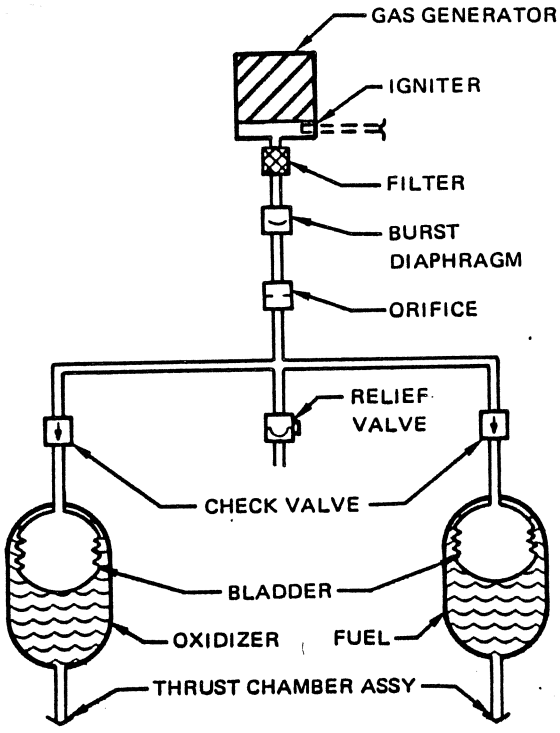

Figure 5-46. Solid-Propellant Gas-Generator Pressurization System

The system shown in Figure 5-46 uses a gas generator, a burst diaphragrm, and an orifice to perform the basic function. This system also includes check valves to prevent excessive pressure in the gas generator. Figure 5-46 also illustrates a positive method of propellant expulsion.

A gas generator provides a supply of fuel-rich gas at approximately 2000°F, which can be used to pressurize propellant tank ullage. Because the extent of the propellant reaction is difficult to control, and because of the elevated temperature of the pressurant, a barrier is usually maintained between the pressurant and the propellant. The barrier may be an expandible barrier as shown in Figure 5-46 or it may be another positive expulsion device as shown in Figure 5-26.

5-6 VALVES

A valve is a fluid system component device that stops, starts, or regulates the flow of fluid in a system by means of a movable element which opens or obstructs a flow passage. The movable valve element is operated by an actuator which may be attached to, or be integral with, the valve body. Valves are included in propellant feed systems to provide on-off and flow control capability, and are included in pressurization systems to provide on-off and pressure control capability.

Propulsion system valves must comply with a wide range of requirements, and maintain a high degree of operational reliability. A cost constraint may be included in addition to typical specification requirements such as: propellant compatibility, envelope, port sizes and locations, weight, temperature, pressure, vibration, acceleration, shock loads, pressure drop at design flowrate, response time, allowable leakage, and operating life. The configurations and materials of the valve and the actuator can be varied to achieve the requirements of specific applications.

5-6.1 Valve Classification

Figure 5-47 illustrates schematically the functional elements of several kinds of valves used in propellant feed systems and pressurization systems. Each of these valves contains a spring loaded closure element which, to facilitate comparison, is shown in a poppet configuration. The relative arrangement of the spring with respect to the closure and the valve body determines whether the valve functions as a relief, regulator, check, or shutoff valve.

For example, in the shutoff valve illustration, the poppet is held against the seat by a spring force that is greater than the opposing fluid force caused by the upstream pressure acting on the poppet area. The poppet is lifted off the body seat by an actuator force which opposes, and is greater than, the spring force. The actuator shown

VALVE TYPE	FUNCTION	SCHEMATIC ARRANGEMENT
SHUTOFF VALVE	SPRING CLOSES POPPET AND STOPS FLOW. ACTUATOR PRESSURE OPENS POPPET AND STARTS FLOW	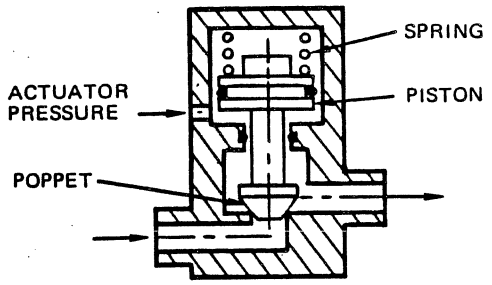
PRESSURE REGULATOR	MAINTAINS CONSTANT DOWNSTREAM FLUID PRESSURE. SPRING IS OPPOSED BY DOWNSTREAM PRESSURE ACTING ON THE PISTON, THEREBY CONTROLLING POPPET POSITION	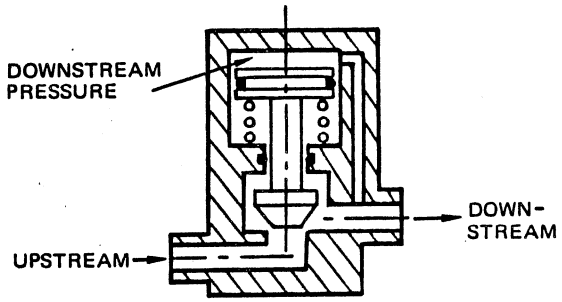
PRESSURE RELIEF VALVE	LIMITS UPSTREAM PRESSURE. SPRING OPPOSED BY FLUID UPSTREAM PRESSURE ACTING ON THE POPPET	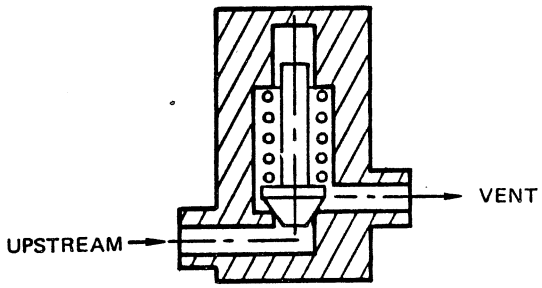
CHECK VALVE	PERMITS FLOW IN ONE DIRECTION ONLY REVERSE PRESSURE INCREASES POPPET SEAL	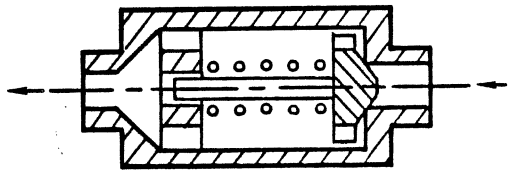
QUICK DISCONNECT COUPLING	PERMITS SEPARATION OF DUCTS WITHOUT LOSS OF FLUID, WHEN COUPLING IS RECONNECTED, PROBE OPENS BOTH POPPETS	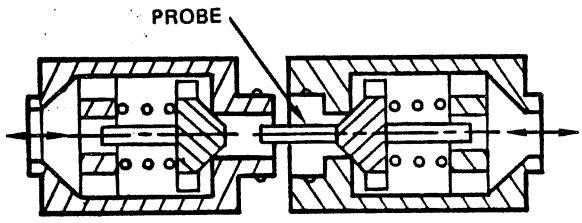

Figure 5-47. Functional Comparison of Several Valve Types

is a piston, and the force is obtained by the application of external fluid pressure to the under side of the piston. In small valves a solenoid frequently is used to provide the actuation force.

The regulator shown is similar to the shutoff valve except that the spring force tends to hold the poppet open, the vent port position is reversed, the actuation port position is reversed, and actuation is achieved by system pressure downstream of the poppet.

The relief valve illustrated in Figure 5-47 is equivalent to a shutoff valve without an actuator. The relief valve poppet opens when the upstream fluid pressure rises above some critical value at which the resulting force acting on the poppet exceeds the spring force. The fluid is vented external to the system until the upstream pressure decreases sufficiently so that the spring force exceeds the opposing net fluid force and the valve closes.

The check valve in effect is a low pressure relief valve which vents internally. However, its primary function is to prevent reverse fluid flow, and the inherent relief action is usually kept to a low pressure value to minimize the added system pressure drop. The quick-disconnect coupling consists of two opposing check valves which prevent flow when the coupling is separated, and which are opened by the probe during engagement of the coupling.

The valves in Figure 5-47 are shown in simplified form. In practice, more complex arrangements are often used to reduce valve response time, to increase valve accuracy, or to produce a smaller and lighter package. Figure 5-48 presents two shut-off valve arrangements, a simple solenoid-operated valve which has a fast response, but is flow limited, and a solenoid-pilot fluid-operated valve which has a slower response with increased flow capacity.

Propulsion system valves may also be classified in terms of the type of closure used to control flow. The closure is the subassembly of a valve, consisting of two components, usually a stationary seat and a movable element, which produce a sealing interface when they are forced together. Most rocket propulsion flight system valves have a ball, blade, butterfly or poppet closure.

Each type of valve closure can be made in several configurations. Figure 5-49 illustrates a typical configuration of each of these categories, and identifies general characteristics that influence its selection for a specific application. Generally, poppet valves are preferred for low leakage and long life. Butterfly valves are attractive when pressure drop is critical in relatively large diameter lines. Ball valves and blade valves produce minimum disturbance of the flowing fluid and have a very low pressure drop for any line size.

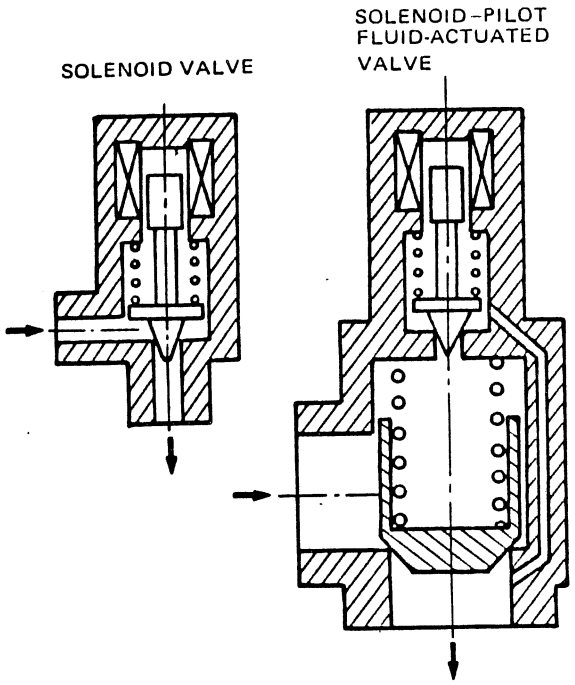

Figure 5-48. Typical Shutoff Valve Arrangements

A special group of devices that is of interest for long-term storage applications is the hermatically sealed, one-shot category of valves. This group is dominated by the explosive valves, which are designed in both normally open (actuates closed) and normally closed (actuates open) configurations. These valves are actuated by the ignition of an explosive charge, and they are limited to a single actuation. If repeated on-off capability is needed, series-parallel groupings of normally open and normally closed explosive valves are sometimes used. Burst diaphragms and diaphragm-cutter valves also fall in this general category.

5.6.2 Valve Pressure Drop

Flow resistance is a major factor to be considered in the selection of the valve type. A comparison of the relative resistance of several types of closures is shown graphically in Figure 5-50. This comparison is based on data published by the valve industry. The resistance coefficient, or K-factor shown in Figure 5-50 is a measure of the pressure loss through a component of a fluid-flow system in terms of velocity head. The K-factor is defined by the relationship:

$$K = \frac{h_L}{v^2/2g} = 0.447\,\rho\Delta P\left(\frac{A}{\dot{w}}\right)^2 \qquad (25)$$

VALVE CONFIGURATION	TYPICAL VALVE CHARACTERISTICS			
	INTERNAL LEAKAGE	PRESSURE DROP	WEIGHT	ENVELOPE–INCLUDING ACTUATOR
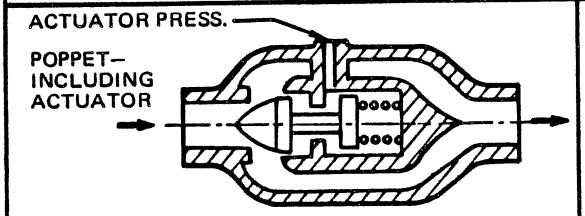	LOW	MEDIUM	MEDIUM	SMALL
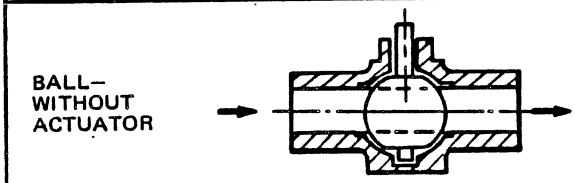	LOW	LOW	HEAVY	LARGE
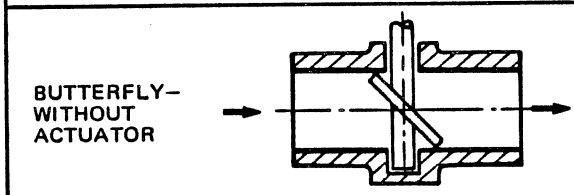	MEDIUM	MEDIUM	LIGHT	MEDIUM
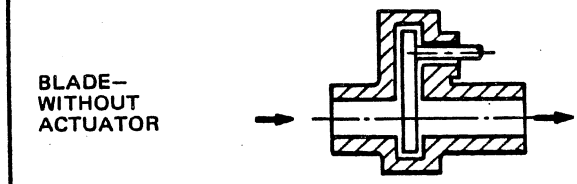	LOW	LOW	HEAVY	LARGE

Figure 5-49. Selection Criteria for Shutoff Valves

where:

h_L = Head loss, ft

v = Average fluid velocity, ft/sec

g = Gravitational constant, 32.17 ft/sec^2

ρ = Fluid density, lb/ft^3

ΔP = Pressure loss, lb/in^2

A = Flow area, in^2

$\dot{w}$ = Weight flowrate, lb/sec

The values of the resistance coefficients plotted in Figure 5-50 are for wide-open valves only. As indicated, a great variation in flow resistance is possible with any given valve type. For this reason, the values should be considered comparative only. Where pressure loss is critical, flow test data should be acquired for particular configurations and specific fluid-flow conditions before precise performance estimates are attempted.

5-6.3 Valve Leakage

Leakage restrictions are imposed on propulsion system valves because of safety and performance requirements. Leakage of energetic propellants can result in fires and explosions, or in the dangerous accumulation of toxic or corrosive materials. For long-term storage, leakage can significantly reduce the amount of useable propellant.

Valve leakage is of two kinds, internal and external. Internal leakage occurs across the closure from upstream to downstream. External leakage escapes from the flow system. The external leak paths consist of static seals, and the permeability of the valve materials. The internal leak paths consist of the closure seal and any internal static seals included in the design.

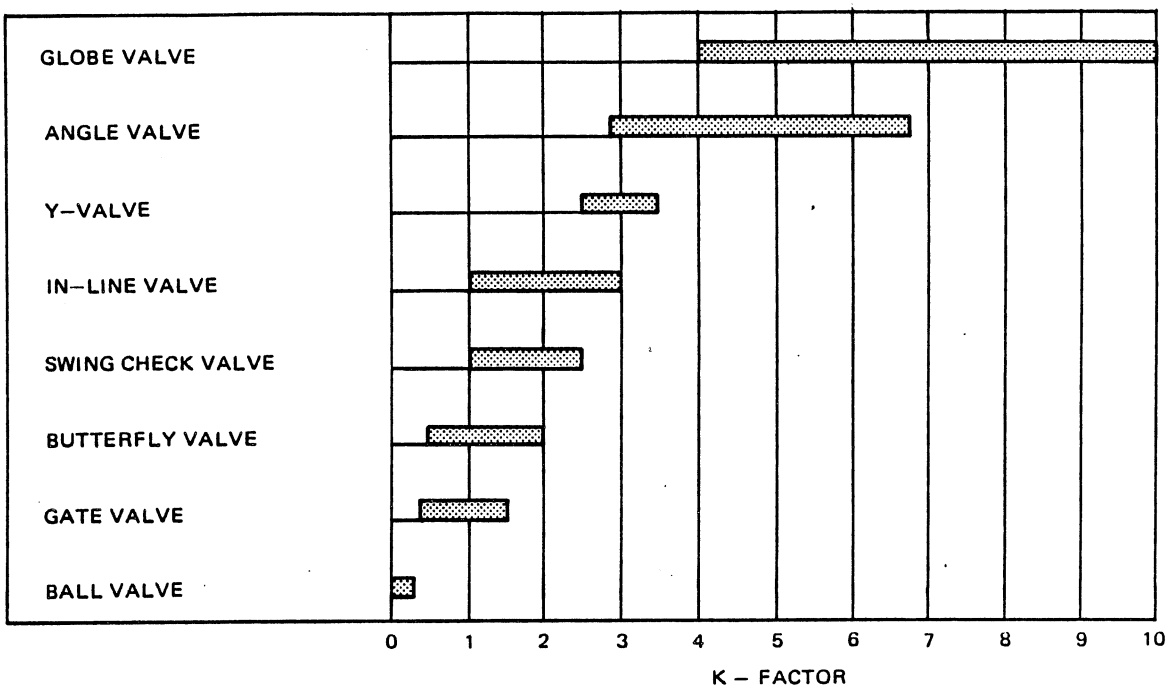

Figure 5-50. Valve Flow Resistance Comparison

Leakage is generally measured at room temperature in terms of standard cubic centimeters per second (sccs) of a test fluid, usually helium. Typical state-of-the-art leakage capabilities are: 10^{-9} sccs per square inch of valve body surface; 10^{-7} sccs per linear inch of static seal perimeter; and 10^{-3} sccs per linear inch of closure seal perimeter. A comparison of leakage rate information for several volume and equivalent weight standards is given in Figure 5-51.

Valve seal materials generally are made of elastomeric or plastic materials. However, since these materials have a limited temperature range and are not compatible with all propellants, metal-to-metal seals are also used for valves.

The leak rate of metal-to-metal seals is dependent primarily on the surface roughness of their contacting surfaces. The total leakage across a valve seat can be estimated from the empirical equation:

$$Q = 1.539 \times 10^{-11} \left(\frac{L}{W}\right) \frac{(P_1^2 - P_2^2)\, h^3}{\mu\, T\, (S)^{2/3}} \qquad (26)$$

where:

Q = Volumetric leakage flowrate, sccs

L = Seal length (circumferential), in

W = Seal width, in

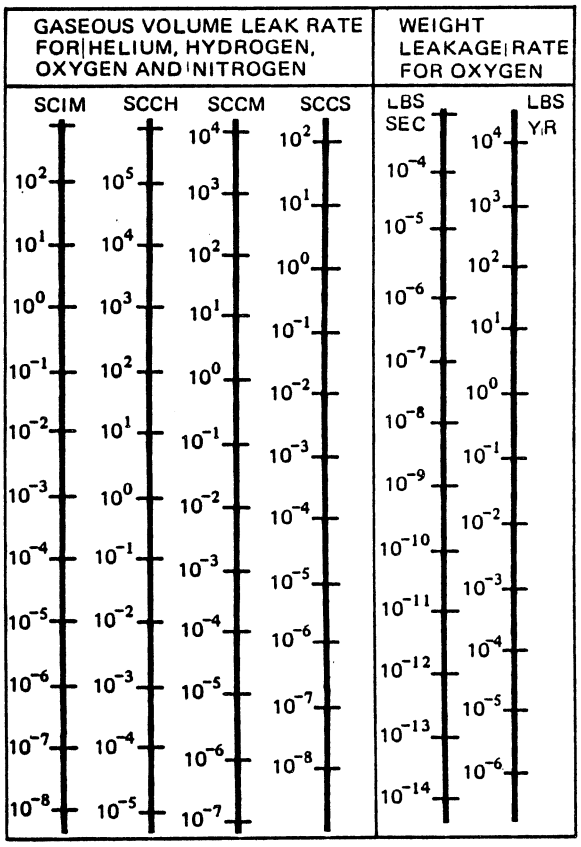

Figure 5-51. Leakage Rate Comparison Chart

P_1 = Upstream pressure, psia

P_2 = Downstream pressure, psia

h = Surface roughness height, μin AA

μ = Gas viscosity, lb-sec/ft^2

T = Gas temperature, °R

S = F/A = Apparent seat stress, psi

Leak rates estimated with equation 26 are in good agreement with test results of flat-faced poppet and seat combinations which have a multi-directional lay surface roughness. Figure 5-52 is a plot of leak rate versus surface roughness, based on equation 26, for a 3-inch diameter poppet valve. A valve of this size with a surface roughness of less than 1 μin AA, had a measured helium leakage of less than 10^{-2} sccs, which is about 10^{-3} sccs per inch of seal.

5-6.4 Valve Actuators

Most aerospace valves are powered by remotely controlled, or automatic actuators. The actuator may be either an integral part of the valve, or a separate device mechanically linked to the valve. Solenoids, diaphragms, bellows, piston-cylinders, and servo torque motors are usually made an integral part of the valve. Electric motors are commonly linked to the valve through a speed reducer.

Typical mechanical factors considered in the design and selection of a valve actuator include length of stroke, speed of travel and magnitude of force required, as well as limitation of weight and envelope size. If a long stroke is required, a solenoid is automatically eliminated. If a fast response time is required, a solenoid or explosive charge should be considered. If large forces must be overcome, an electric motor or a fluid power actuator may be required.

5-7 BIBLIOGRAPHY

1. *Investigation of Cooling Problems at High Chamber Pressures*, Report No. R-3999 (Contract NAS 8-4011) Rocketdyne, May 1963.

2. *Liquid-Propellant Propulsion Systems*, Handbook of Astronautical Engineering, H. H. Koelle, ed., McGraw-Hill Book Co. New York, 1961.

3. D. Altman, et al., *Liquid Propellant Rockets*, Princeton University Press, Princeton, 1960.

4. M. Barrere, et al., *Rocket Propulsion*, Elsevier Publ. Co., Amsterdam, 1960.

5. D. R. Bartz, *A Simple Equation for Rapid Estimation of Rocket Nozzle Convective Heat Transfer Coefficients*, Jet Propulsion, January 1957.

6. A. H. Church, *Centrifugal Pumps and Blowers*, John Wiley & Sons, New York, 1944.

7. V. M. Faires, *Thermodynamics*, 4th Ed., Macmillan, New York, 1965.

8. G. W. Howell and T. M. Weathers, *Aerospace Fluid Component Designers Handbook*, Vol. I, RPL-TDR-64-25, TRW, Inc. 1967.

9. F. Kreith, *Principles of Heat Transfer*, 2nd Ed. International Textbook Co., Scranton, 1966.

10. P. E. Purser, et al., *Manned Spacecraft: Engineering Design and Operation*, Fairchild Publications, New York, 1964.

11. H. D. Samuel, *Liquid Fluorine Shutoff Valve Development Program* USAF Report No. AFRPL-TR-69-41, McDonnell Douglas Astronautics Co., April, 1969.

12. A. J. Stepanoff, *Centrifugal and Axial Flow Pumps*, 2 Ed. John Wiley & Sons, New York, 1957.

13. G. P. Sutton, *Rocket Propulsion Elements* John Wiley and Sons, New York, 1964.

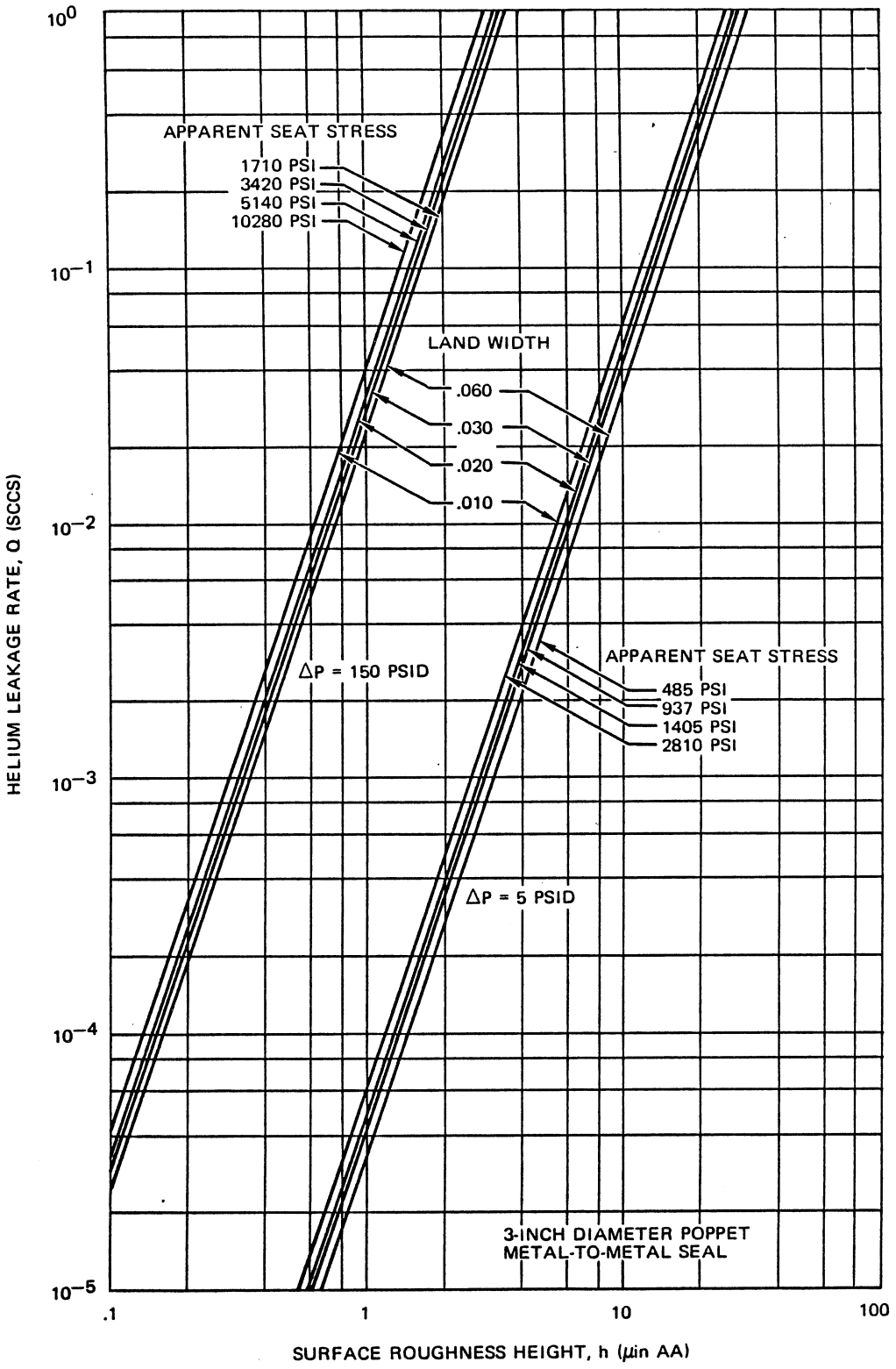

Figure 5-52. Typical Helium Leak Rate as a Function of Closure Surface Roughness

Section 6
SOLID PROPULSION SYSTEMS

The primary element of any solid propulsion system is the solid propellant motor. The motor is an internal combustion device consisting of a combustion chamber, a nozzle through which the combustion products are expelled, the propellant charge, and an ignition system. The most attractive characteristic of the system is its inherent simplicity due to the lack of moving parts such as valves and pumps. Generally, internal insulation is required to protect the motor case from the hot combustion gases, except on very short duration motors.

The basic difference between a solid propellant motor and any other chemical propulsion system is that the fuel and oxidizer are stored in a pre-mixed state with a predetermined expulsion rate, based on the grain geometry, propellant burn rate, and nozzle area. That is, the thrust versus time curve is predetermined.

When a solid propellant motor is ignited, the combustion generally proceeds until all of the propellant is expended. However, a considerable amount of development effort is being expended on thrust modulation and start-stop methods for solid propellant systems. Thrust modulation is possible by varying the throat diameter which, in turn, varies the chamber pressure and thus the thrust and duration. Start-stop capability is possible due to the fact that solid propellants can be extinguished by several methods such as rapid depressurization of the combustion chamber, water quench, barriers, etc. The inclusion of the mechanisms necessary to provide these capabilities, however, diminishes the inherent characteristic of simplicity, adds a weight penalty and reduces the system reliability.

6-1 SOLID PROPELLANT GRAINS

The propellant charge or grain, as a minimum, is a mixture of a suitable fuel and an oxidizer. Usually the propellant will contain additives that enhance processing and increase the burn rate and other performance characteristics. Certain fuel components also act as binders which form a matrix that holds the mixture together, providing structural strength. The propellant is capable of sustaining combustion equally well in a vacuum or in air at sea level. When the propellant charge is ignited, the heat generated causes decomposition of the chemical compounds in its structure to produce combustible gases on the grain surface. The gases are burned and the process proceeds in a predictable fashion. The products of the combustion process are high-temperature gases and, in some cases, solids in suspension in the gases.

Propellant grains may be produced in a large variety of compositions and shapes. The grains may be cast directly into the motor case or may be molded or cast into a separate container and loaded into the motor case as a cartridge or in segments. Grain compositions and configurations are selected to provide desirable operational and physical characteristics. Propellant strength should be fairly uniform over a wide range of temperature, and its density and specific volume should remain as constant as possible despite temperature change. The designer is concerned with obtaining the highest possible density and energy per unit weight since these factors will provide the least weight and size of motor to do a specific job.

Solid propellants may be classified into three general categories: composite or heterogeneous, double base or homogeneous, and composite-modified double-base. The selection of a particular propellant category is dependent on the requirements of the application. Double base propellants tend to be unstable, possessing high energy and a sensitivity to detonation. Composites are more widely used because they combine a wide range of performance capabilities with ease of handling. The composite-modified double-base propellants have properties intermediate to the other two categories.

6-1.1 Composite Propellants

In a composite propellant, the oxidizer and fuel are separate compounds intimately mixed together. In general, the oxidizer is in a crystalline form and is dispersed in some form of binder-fuel matrix. Metal particles ranging in size from 3 to 50 microns diameter are frequently added as fuel.

In most cases, the propellant is made by adding the finely ground oxidizer crystals (and metal-fuel) to a

liquid fuel, thoroughly mixing them, casting the mixture into appropriate molds, and allowing the mixture to solidify or cure. Some formulations require catalysts and/or curing agents to be added to the mix to accomplish the curing process. In other cases, the mixture of fuel and oxidizer powder is mixed under pressure and then extruded to give the desired shape of grain. The castable propellants have the advantage that very large grains (with diameters ranging up to 260 inches) have been made, whereas there is a much smaller practical limit to the size of grain which can be extruded.

6-1.1.1 Chemical Composition

a. Oxidizers – Table 6-1 lists several oxidizers used in composite propellants. Ammonium perchlorate, NH_4ClO_4, is the most commonly used medium burn-rate oxidizer because it gives good performance and is easy to handle. Its good performance is due to its high oxidizing potential, and its hydrogen content which reduces the average molecular weight of the exhaust gases. Easy handling characteristics include: low solubility in water, and relative insensitivity to detonation.

Nitronium perchlorate NO_2ClO_4 has a higher oxidizing potential but it is more sensitive to detonation.

Ammonium nitrate, NH_4NO_3, has a lower oxidizing potential hence a low burning rate. It is used for gas generator applications because it has a low flame temperature as well as a low burn rate, is relatively smoke free, and produces a relatively non-toxic exhaust.

b. Binder-fuels – Many different organic fuels have been used in composite propellants. They are selected in part for their ability to be oxidized, for adding desirable physical properties to the mixtures, and for their desirable fabrication characteristics. Table 6-2 lists several composite propellant binder-fuels with their physical properties. During

Table 6-1. Current Composite Oxidizers

OXIDIZER	FORMULA	MOLECULAR WEIGHT	OXYGEN CONTENT (wt %)	DENSITY (lbs/in^3)	CHARACTERISTICS
LITHIUM PERCHLORATE	$LiClO_4$	106.4	60.2	0.0877	HIGH AVAILABLE OXYGEN HYGROSCOPIC HIGH FLAME TEMPERATURE
SODIUM PERCHLORATE	$NaClO_4$	122.5	52.3	–	HYGROSCOPIC HIGH FLAME TEMPERATURE
POTASSIUM PERCHLORATE	$KClO_4$	138.6	46.2	0.0910	HIGH BURNING RATE NONHYGROSCOPIC POOR LOW-PRESSURE BALLISTICS HIGH FLAME TEMPERATURE LOW TEMPERATURE SENSITIVITY
AMMONIUM PERCHLORATE	NH_4ClO_4	117.5	34.0	0.0704	LOW BURNING RATE LOW BURNING RATE-EXPONENT LOW COST
LITHIUM NITRATE	$LiNO_3$	68.9	58.0	0.0860	HIGH AVAILABLE OXYGEN HYGROSCOPIC
SODIUM NITRATE	$NaNO_3$	89.0	47.0	0.0815	HYGROSCOPIC LOW COST LOW PERFORMANCE
POTASSIUM NITRATE	KNO_3	101.1	39.6	0.0762	LOW COST LOW PERFORMANCE
AMMONIUM NITRATE	NH_4NO_3	80.0	20.0	0.0625	VERY LOW COST MEDIUM PERFORMANCE LOW FLAME TEMPERATURE LOW BURNING RATE

Table 6-2. Properties of Composite Propellant Binders

PROPERTY	POLYVINYL CHLORIDE	POLY-STYRENE	POLY-ETHYLENE	POLY-SULFIDE	NATURAL RUBBER	ARTIFICIAL RUBBER
DENSITY (g/cm^3)	1.16–1.35	1.04–1.06	0.94	1.15–1.25	0.96	0.94
ULTIMATE TENSILE STRENGTH (psi)	1,400–3,500	4,900	1,400–4,300	2,000–10,000	3,300	4,000
ULTIMATE TENSILE ELONGATION (%)	200–450	1–2.5	50–300	0–300	470	550
MODULUS OF ELASTICITY (psi)	LOW	400,000–560,000	85,000–170,000	284,000	LOW	LOW
THERMAL CONDUCTIVITY (Btu/hr-ft°F)	42×10^{-4}	3.4×10^{-4}	1.4×10^{-3}	– –	– –	– –
HEAT CAPACITY (cal/g)	0.3–0.5	0.32	0.55	0.25–0.40	0.37	0.47
THERMAL EXPANSION COEFFICIENT (in/in-°F)	$5–6 \times 10^{-5}$	$6–8 \times 10^{-5}$	$15–20 \times 10^{-5}$	$2–10 \times 10^{-5}$	17×10^{-5}	15×10^{-5}

fabrication, many fuels are mixed with a crystalline oxidizer while the fuel is in the liquid state and often at elevated temperature. Thereafter, the fuel undergoes a chemical or physical change as it cools to harden the grain.

Many kinds of polymerized organic compounds have been used as the binder-fuel in composite propellants. The fuel is chemically and physically transformed by polymerization (which is induced by chemical reagents or cross-linkers and heat) after it has been mixed with its oxidizer and additives. This class of fuel includes vinyl-polyesters, polysulfides, polyurethanes, vinyl pyridines, butadiene polymers, and various types of synthetic rubbers.

Generally, these binder-fuels retain some of their rubbery properties in the cured state and thus are adaptable to adjusting to internal strains without inducing excessive stresses. These vulcanized organic compounds are used extensively in high performance solid propellants. The most commonly used solid propellant fuel binders are polysulfide, polybutudiene, and polyurethane. Depending on the fuel-binder nature, and the amount of curing agent and plasticizer used, the physical properties of composite propellants can range from hard and brittle to soft and resilient.

Polyvinyl chloride, together with a plasticizer, has been used successfully with ammonium perchlorate and ammonium nitrate oxidizers. In very small particle sizes, it does not react with its plasticizer and it can be mixed readily. When cured at 300°F, it absorbs or dissolves the plasticizer and forms the hard matrix of the grain. The high curing temperature causes shrinkage and thermal stresses which limit the size of the grain that can be case bonded.

The polysulfides were the first of the modern polymers to be used as fuel-binders. These polymers demonstrated the ability to bond the propellant grain to the motor case which resulted in simplification of process and manufacturing, and improved reliability of motor operation. Polysulfides have good physical properties at low temperature but have relatively low I_{sp}.

Polyurethane binder-fuels have good physical properties and better I_{sp} than the polysulfides, but moisture must be excluded during processing to avoid the formation of gaseous products that result in porosity and variations in the burning rate.

Three types of binder-fuels based on polybutadiene polymers have been developed which are widely used because they have good physical properties, I_{sp} and processing characteristics. They are, in the order of their development:

1. Polybutadiene-acrylic acid copolymers, PBAA.
2. Polybutadiene-acrylic acid – acrylonitrile terpolymers, PBAN.
3. Carboxyl-terminated polybutadienes, CTPB.

PBAA has a low tear resistance. PBAN has improved tear resistance but has lower physical properties at low temperature. CTPB has excellent low temperature and high temperature physical properties which permit higher solids loading (oxidizer and powdered-metal fuel) than can be used for PBAA or PBAN polymers.

Recent developments indicate that hydroxyl-terminated polybutadiene (HTPB) may be an even more attractive fuel-binder than CTPB. If the HTPB polymerization process is initiated with small quantities of molecular lithium to tie the polymer chains together, the physical properties of HTPB will be significantly better than those of CTPB with no increase in propellant cost.

For example, elongations of 60-80 percent at room temperature have been achieved with HTPB compared to about 40 percent with CTPB. This superior physical characteristic permits the solids loading (Al and NH_4ClO_4) of HTPB to approach 90 percent, compared to about 87 percent for CTPB, resulting in some increase in I_{sp} and density.

If HTPB polymerization is initiated with free radicals, rather than with lithium, the propellant cost will be reduced to about half of the cost of CTPB, and the HTPB performance and physical properties will be comparable to those of CTPB.

c. Metal-Fuels – Most modern composite propellants contain finely-ground metal particles, usually aluminum, as part of the fuel. The addition of small metal particles in a uniform dispersion improves performance in three ways:

1. Increases combustion temperature, thus increasing the specific impulse slightly.
2. Increases grain density, thus allowing more propellant weight to be placed in a given volume.
3. Reduces combustion instability.

On the adverse side, addition of metal particles to the fuel tends to increase the rate of erosion and the radar attenuation properties.

Many of the high-energy fuels under development incorporate fluorinated organic binders and/or difficult-to-handle metals. The use of metal hydrides, such as aluminum hydride (AlH_3), introduces hydrogen, thus lowering the gas molecular weight. However, most hydrides tend to react with the other propellant ingredients during storage, and therefore, techniques are being developed to encapsulate the hydrides. Beryllium is attractive because it is lighter than aluminum, and causes an even greater reduction in the gas molecular weight. However, beryllium is considered only for upper stages because it is extremely toxic. Magnesium and boron have also been considered as fuel additives. Of the two, boron is more energetic but complete combustion is difficult to achieve.

d. Additives – The most direct way of varying the propellant burning rate of a composite propellant is by controlling the oxidizer particle size. However, small amounts of additives have also been found to be effective in enhancing the burning rate of both composite and double base propellants. The nature of the additive and its effectiveness depend on the composition of the propellant with which it is used. Powders of iron oxides, ammonium dichromate, copper chromite, titanium dioxide and magnesium oxide are used to increase the burning rate of composite propellants.

It has also been found that the shape of the aluminum fuel particles influences the propellant burning rate. The burning rate of high energy composities has been increased to as much as 2 inches per second at 1000 psia, with stable operation, by replacing some of the powdered aluminum with small wires or flat strips of aluminum. Other metal fuels, such as zirconium have produced good results in this application. The wires or strips are commonly called staples.

Small amounts of other chemicals are added to propellants to facilitate fabrication and storage. Examples include:

1. Plasticizers such as castor oil or butanediol.
2. Stabilizers such as benzyl mercaptan.
3. Curing catalysts such as ferric acetylacetonate, sulfur, zinc oxide or diphenylguanidine.
4. Anti-foaming agents such as silicone oil.

5. Wetting agents such as lecithin.

6. Antioxidants such as N-phenyl-B-napthylamine.

7. Surfectants such as polygylceryl oleate.

Carbon black is frequently added to inhibit the radiant heat transfer from the flame front to the bulk propellant.

6-1.1.2 Performance

Composition, processing techniques, and performance characteristics of most contemporary solid propellants are considered proprietary by the manufacturers, and many of them are classified for national security reasons. However, sufficient unclassified information is available to illustrate the relative importance of propellant selection on performance. Table 6-3 presents performance data for several typical composite propellants.

For each propellant, the weight percentage and chemical composition of the fuels and oxidizer are listed. The weight percent, only, of the additive is included. The theoretical specific impulse is listed for standard conditions; i.e., 1000 psia chamber pressure, 14.7 psia ambient pressure, and optimum expansion ratio. Propellant density and adiabatic flame temperature (or C^*, which is a function of temperature) are also listed. Since the specific heat ratio, γ, is approximately 1.2 for the exhaust gases of all of these propellants, flame temperature can be determined from equation 8 in Section 4, if C^* is known.

Table 6-3 illustrates that solid propellants, relative to liquid propellants, tend to have; lower specific impulse, higher density, and comparable combustion temperature. Specific impulse is controlled by the choice of oxidizer and fuel (organic binder and metal additive), and by the weight percentage of each. An increase of as much as 30 seconds of specific impulse can be obtained by the addition of metal particles as fuel.

The effects of composition on the performance of composite propellants are usually presented in a ternary diagram. Figures 6-1 and 6-2 show the specific impulse and chamber temperature versus composition for a typical metallized composite propellant. These ternary diagrams represent all possible mixtures of metal additives, oxidizer, and binder. Superimposed on the diagram of Figure 6-1 are equal specific impulse contours, showing that for this propellant combination, a specific impulse plateau of 266 seconds exists in a region bounded by 65 to 70 percent oxidizer, 9 to 15 percent fuel binder, and 18 to 25 percent metal particle fuel. Similarly, equal chamber temperature lines are plotted on the ternary diagram of Figure 6-2.

6-1.1.3 Manufacturing Processes

Composite propellants can be cast, moulded, extruded, and in some cases pressed. Since casting is the primary method used today for large grains, only this method will be discussed. In this process, the oxidizer crystals are ground to proper size in a controlled atmosphere. Several batches of oxidizer crystals, ground to various sizes, are blended with each other to obtain the desired particle size distribution. A premix is prepared by mixing the fuel binder with the necessary curing agents, inert additives and ballistic modifiers in a double motion paddle mixer. The syrupy liquid fuel premix and the oxidizer blend are mixed in a sigma-blade mixer to form a thick substance very similar to dough. The other materials are gradually added during this process. Temperature and viscosity are carefully controlled. When all of the other ingredients have been thoroughly mixed, the curing agent is then added and mixed. The propellant is then transferred from the mixer to the casting facility by a casting pot. The propellant is then pumped under pressure, or cast under vacuum, into the insulated and lined motor case. Detailed steps in this process vary among the propellant manufacturers.

Composite propellants may be either vacuum-cast or pressure-cast. In the vacuum process, the mixture is poured from the mixer into a casting can and transferred to the site at which it is to be cast into the motor or mold. The propellant is then pulled from the casting can, through piping, and into the motor by applying a vacuum to the motor. In the process of flowing from the casting can into the motor, the propellant is forced through a plate perforated with slits or holes. Use of this slit plate facilitates the escape of entrapped air from the thin streams of propellant that ensue.

In the pressure casting process, the mix is poured into a funnel and pulled through a slit plate into the casting can by means of a vacuum. The de-aerated propellant is then forced from the casting can into the motor with gas pressure. The propellant flows into the motor through a bayonet, the tip of which is maintained in a position just below the surface of the propellant already in the motor.

The details of the casting process depend on the configuration of the motor being manufactured. Internal geometry of the motor may dictate the use of multiple casting bayonets in order to avoid folds, or flow discontinuities, particularly if a complex internal star geometry is used. Other geometries may necessitate the use of bottom casting, in which the propellant enters the motor from the bottom (the forward end) or by casting through a hollow perforated mandrel.

Important considerations from the standpoint of the finished product are that the casting process eliminate voids from the propellant, and that it avoid the formation of polymer-rich flow discontinuities, either of which adversely affect the structural integrity of the motor.

Table 6-3. Composite Propellant Performance Data

FUEL – (wt %)		OXIDIZER (wt %)	ADDITIVES (wt %)	DENSITY (lbs/in^3)	c^* (ft/sec)	COMBUSTION TEMP (°R)	I_{sp} (sec)
BINDER	METAL						
PS (23.7)	–	$LiClO_4$ (73.4)	(3.9)	0.068		5310	221
PS (17.4)	–	NH_4NO_3 (78.6)	(4.0)	0.055		3620	205
PS (22)	–	AP (74)	(4.0)	0.062	4950		226
PS (19)	–	AP (74)	(7.0)	0.063	4600		218
PS (18)	–	AP (63)	(19.0)	0.060	4250		206
PS (19.3)	Al (2)	AP (77)	(1.7)	0.062		5230	238
PS (15.3)	Al (5)	AP (73)	(6.7)	0.061		5400	249
PVC (11)	–	AP (74.5)	(14.5)	0.060		5470	225
PVC (8.6)	Al (21)	AP (59)	(11.4)	0.064		6060	242
PU (15.9)	–	AP (82)	(2.1)	0.062		5250	243
PU (22.4)	Al (7.8)	AP (69.8)	–	0.060		5160	247
PU (8.1)	Al (13)	AP (69)	(9.9)	0.062	5168		247
PU (24.1)	Al (15)	AP (60)	(0.9)	0.060		4870	254
PU (13)	Al (16)	AP (66)	(5.0)	0.062	5222		271
POLYESTER-CARBORANE (14.4)	Al (14.4)	AP (70)	(1.2)	0.063		6030	266
PBAA (14.2)	Al (2)	AP (80)	(3.8)	0.059	4987		246
PBAA (15)	Al (8)	AP (74)	(3.0)	0.058	5200		249
PBAA (13.7)	Al (13)	AP (69)	(4.3)	0.061	5224		256
PBAA (11)	Al (16)	AP (70)	(3.0)	0.064		6010	264
PBAA (10.6)	Al (20)	AP (65)	(4.4)	0.064	4964		265
CTPB (10.4)	Al (16)	AP (71)	(2.6)	0.064		6295	263

CODE: PS – POLYSULFIDE
PVC – POLYVINYL CHLORIDE
PBAA – POLYBUTADIENE – ACRYLIC ACID COPOLYMER
PU – POLYURETHANE
CTPB – CARBOXYL-TERMINATED POLYBUTADIENE
AP – AMMONIUM PERCHLORATE

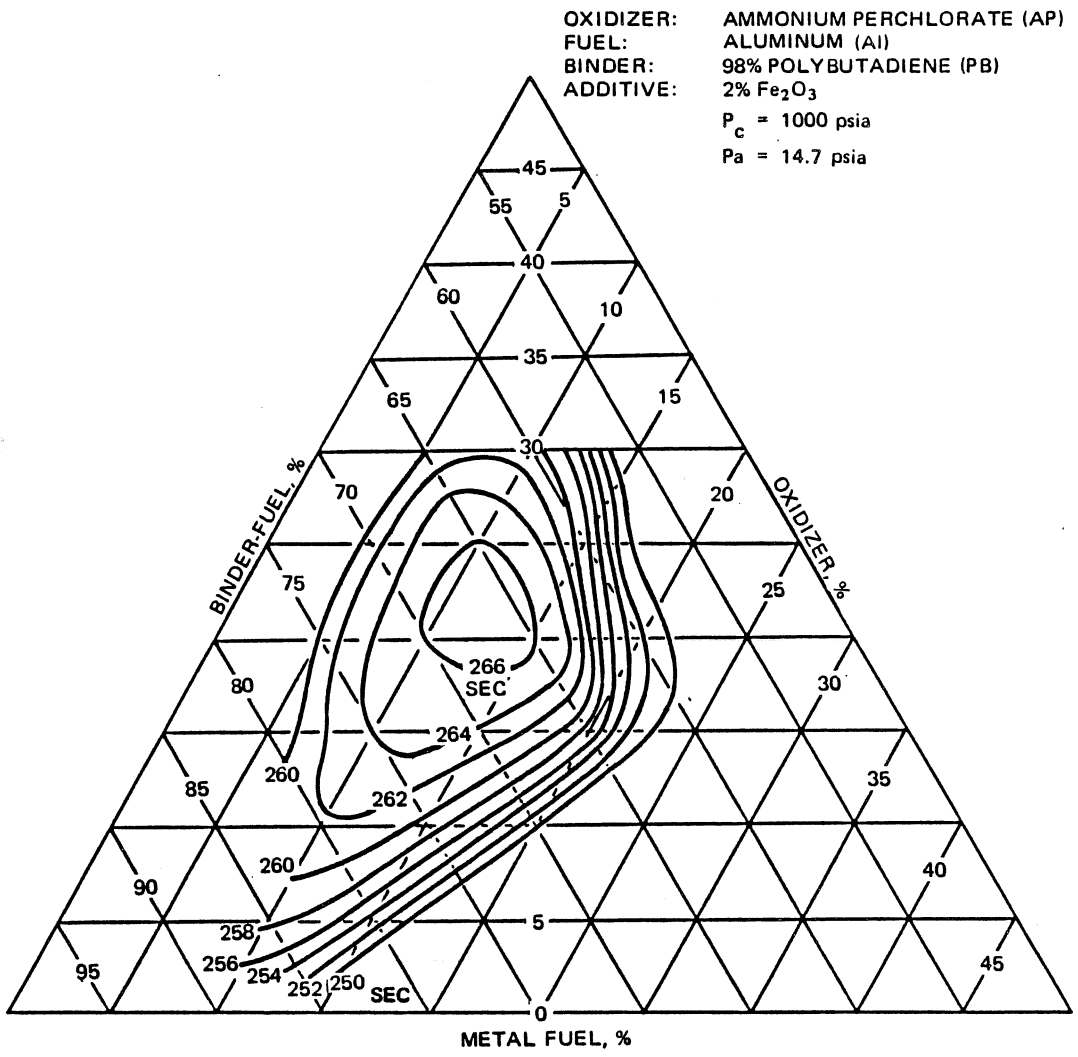

Figure 6-1. Specific Impulse Versus Composition

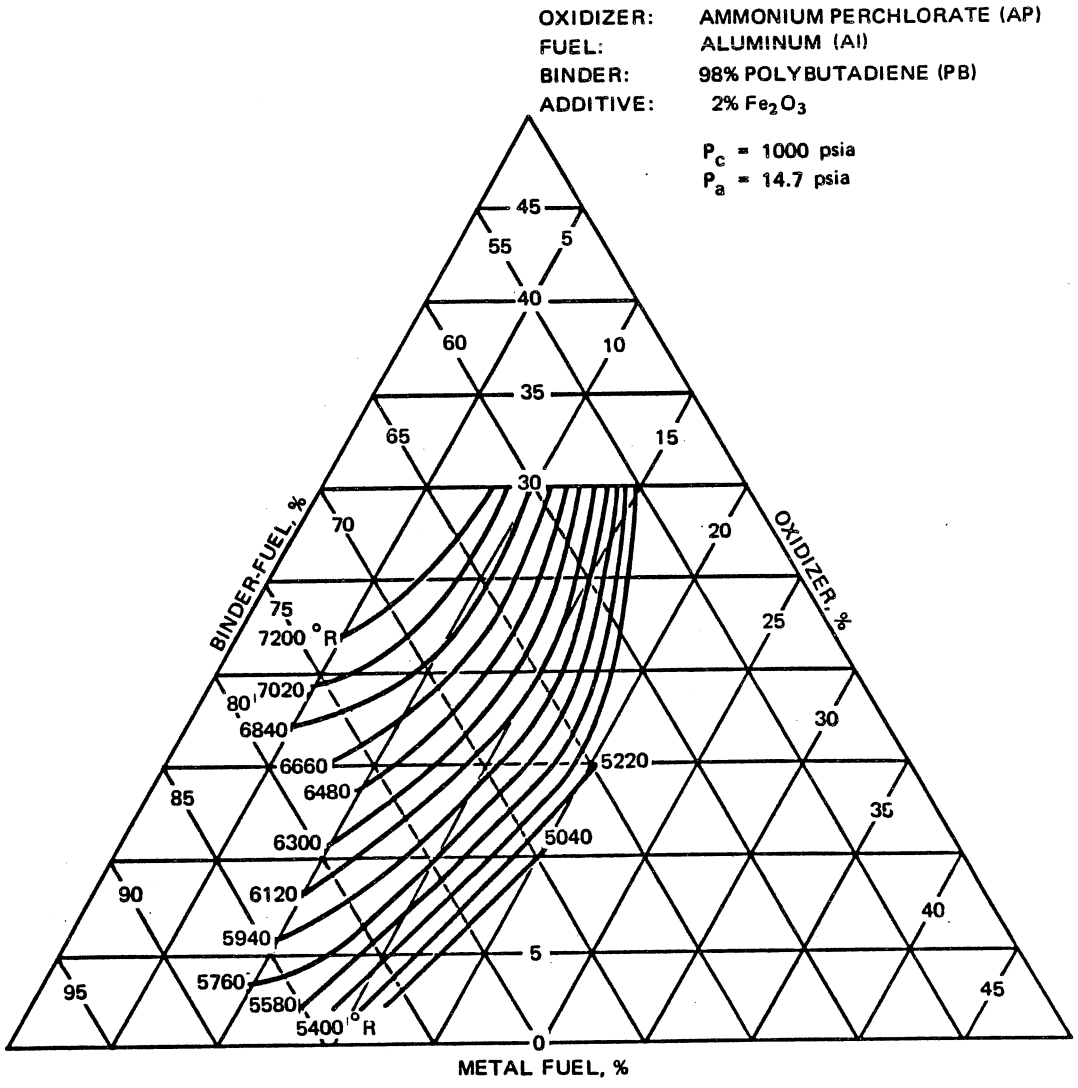

Figure 6-2. Chamber Temperature Versus Composition

Cure time and temperature have pronounced effects on the physical properties of propellants, particularly composites using elastomeric fuel-binders. Elevated temperatures are used for cure. The length of time the propellant is subjected to the cure temperature varies considerably. Polysulfide fuel-binders generally require 24 to 36 hours; carboxyl-terminated hydrocarbons, 100 to 150 hours. During this time, the temperature must be controlled to within about 5°F, and moisture must be excluded from the propellant.

If the cure reaction is exothermic, the propellant mass, if large, may actually have to be cooled. Therefore, one criterion for application of a propellant to very large motors is that it have little or no cure exotherm, a criterion which is met by hydrocarbon fuel-binder propellant.

As the cure proceeds, the viscosity of the propellant increases, gradually at first and then very rapidly, approaching a very high value at times corresponding to gel time for the binder system. Ideally, the physical properties of the propellant reach a constant level when cure is complete. The tendency on the part of some propellants to continue to get harder if they are subjected to cure temperature for periods of time longer than the time at which the physical properties reach their optimum values (termed "post-cure") is considered highly objectionable in that it limits the high-temperature application of the propellant. Post-cure is not a problem with most modern propellants, having been eliminated during the development of new binder materials.

The presence of moisture during cure has an adverse effect on hydrocarbon fuel-binder propellants, although the effect is not as pronounced as it is on the polyurethans. The symptoms are similar to those of an undercured propellant; the material is quite soft and tacky and lacks adequate tensile strength.

The important processes which take place during cure of a composite propellant with an elastomeric fuel-binder are chemical. They consist of linking the prepolymer chains together into a cross-linked molecular network by the formation of chemical bonds between the reactive groups of the curing agent and those present in the prepolymer chain. Some shrinkage occurs as a result of this process, and also due to absorption of the liquids present by the solids, particularly by the inorganic salts used as oxidizers. If the material is sufficiently cross-linked at the time that shrinkage occurs so that it can no longer flow, the shrinkage builds stresses into the propellant grain. Fortunately, most of the volume change in composite propellants takes place during mixing and shortly therafter and can be relieved by flow of the uncured propellant.

6-1.2 Double-Base Propellants

Double-base propellants are propellants in which oxidant and fuel are contained in the same molecule. The name double-base refers to the fact that the propellants are generally based on colloidal mixtures of nitrocellulose and nitroglycerin. Ballistite and cordite propellants, widely used during World War II, belong to this category.

Nitrocellulose (or Cellulose hexanitrate, $C_{12}H_{14}(ONO_2)_6O_4$) is the chief constituent of guncotton. It is an amorphous material which ignites at about 320 to 340°F. It is under-oxidized by approximately 30.2 percent and could therefore be regarded as a fuel even though it contains oxygen. Nitroglycerin (gylcerol trinitrate, $C_3H_5(ONO_2)_3$) is a high-energy explosive in the form of an oily liquid which explodes at 500°F. It is overoxidized by approximately 3.5 percent. The stoichiometric mixture of these two compounds should therefore contain about 8.6 parts of nitroglycerin to 1 part of nitrocellulose.

Unfortunately, to obtain reasonable physical characteristics of the solid colloid, the amount of nitroglycerin must be limited. With suitable plasticizers and stabilizer, the amount of nitroglycerin used may range as high as 40 to 45 percent, but the necessity of attaining good stability during storage generally dictates a considerably smaller amount of nitroglycerin, on the order of about 25 percent. Pure double-base propellants are therefore generally underoxidized, and yield specific impulses of about 200 to 230 seconds, as shown in Table 6-4.

6-1.3 Composite-Modified Double-Base Propellants

The addition of a solid oxidizer to double-base propellants, results in a third category of solid propellant which is really a combination of the two basic propellant types. This third category has acquired the name composite-modified double-base propellant. The same considerations govern selection of oxidzer for these materials as for composite propellants. As seen in Table 6-4, specific impulse values of about 260 seconds can be attained with composite-modified double-base propellants, coupled with good physical properties.

6-2 INTERNAL BALLISTICS OF SOLID-PROPELLANT ROCKETS

The combustion of a solid propellant is entirely localized near the exposed surface of the grain; the burning surface regresses by burning parallel layers in a direction perpendicular to the surface itself. The rate at which the burning surface recedes normal to the surface is known as the linear burning rate. It is a characteristic of the propellant, and for a given composition is dependent only on the initial propellant temperature and the chamber pressure.

Table 6-4. Double-Base and Composite-Modified Double-Base Propellant Performance Data

PROPELLANT COMPOSITION (wt %)	ADDITIVES (wt %)	DENSITY (lbs/in^3)	COMBUSTION TEMP (°R)	I_{sp} (sec)
NITROGLYCERIN (34.2) AND NITROCELLULOSE (50)	15.8	0.056	4230	206
NITROGLYCERIN (19), NITROCELLULOSE (20) AND NITROGUANIDINE (54.7)	5.4	0.060	3730	224
NITROGLYCERIN (49.7) AND NITROCELLULOSE (38.5)	11.8	---	5250	236
NITROGLYCERIN (34.1), NITROCELLULOSE (19.7), ALUMINUM PERCHLORATE (9.8) AND ALUMINUM (18.1)	18.3	0.063	---	267

At any given initial temperature, the empirical relationship between pressure and burning rate may be written:

$$r = a P_c^n \quad (1)$$

where:

- r = Propellant burning rate, in/sec
- a = Burning rate coefficient
- P_c = Chamber pressure lb/in^2, absolute
- n = Burning rate exponent

The burning rate coefficient a is a parameter which is dependent upon the propellant and the initial temperature. The exponent n, called the combustion index, is considered independent of temperature for simplicity in correlating data. It should be noted that the independence of the combustion index with respect to temperature has not been established by either theoretical or experimental methods. Equation 1 is normally used for convenience in the form:

$$r = a (P_c/1000)^n \quad (2)$$

in which case the pressure is normalized to the standard combustion pressure of 1000 psia, and the coefficient a is equivalent to the linear burning rate at 1000 psia. Use of this equation simplifies comparison of data.

Figure 6-3 shows the burning rate of a typical composite propellant as a function of pressure for several values of inital grain temperature.

The burning rate equation is valid only within well-specified ranges of pressures and temperatures. For instance, below a certain pressure the combustion of a propellant may become unstable and possibly stop completely. The burning rate of a solid propellant is generally determined by using a strand burner, also called Crawford bomb, containing a pressurized neutral atmosphere such as nitrogen. The strand burner utilizes a small piece of propellant, shaped like a cigarette, with several small electrical wires passing crosswise through the propellant at measured positions. As the propellant burns, the wires are burned out thus giving an accurate measurement of burning rate.

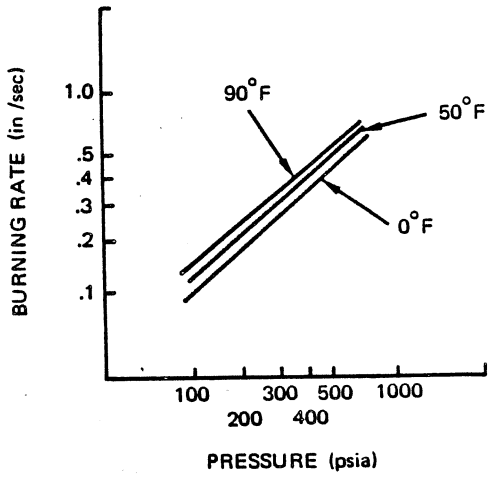

Figure 6-3. Burning Rate for a Typical Composite Propellant

In applications where a more accurate prediction of motor burn rate is required, small motors, commonly called batch test-motors, which are end-burning and contain from two to five pounds of propellant are used. These motors give a more accurate determination of propellant burn rate than the strand burner.

6-2.1 Mass Balance Equations

Using equation 1 to represent the burning rate, the mass burning rate or mass flowrate (neglecting erosion) becomes:

$$\dot{w} = A_s \rho r = A_s \rho a P_c^n \quad (3)$$

where:

A_s = Burning surface area, in^2

ρ = Propellant density, lb/in^3

For stable operation, the mass flow rate must be the same at the propellant surface and at the nozzle exit. The mass burning rate must equal the mass discharge rate which is:

$$\dot{w} = P_c A_t g/c^* \quad (4)$$

where:

A_t = Nozzle throat area, in^2

g = Gravitational constant, 32.17 ft/sec^2

c^* = Characteristic exhaust velocity, ft/sec

Therefore, equating the mass flowrate expressions, the requirement for stable operation is:

$$A_s \rho a P_c^n = P_c A_t g/c^* \quad (5)$$

and the equilibrium chamber pressure will be:

$$P_c = [A_s \rho a c^*/A_t g]^{1/(1-n)} \quad (6)$$

from which it can be seen that the exponent, n must be less than unity for stable operation. Should the exponent approach unity, the pressure will continue to rise until the case bursts or the propellant is all burned.

In solid propellant engineering, the ratio of the propellant burning surface area to the nozzle throat area is an important quantity and is denoted by the symbol K_n, or:

$$K_n = \frac{A_t}{A_s} \quad (7)$$

Equation 6 can be expressed in terms of propellant area ratio, as:

$$P_c = [K_n \rho a c^*/g]^{1/(1-n)} \quad (8)$$

Figure 6-4 shows the effect of propellant area ratio on chamber pressure at several propellant temperatures for a typical composite propellant.

6-2.2 Temperature Sensitivity

The temperature sensitivity of a solid propellant is expressed as the percent change in performance per degree Fahrenheit. The performance parameters affected are burning rate and chamber pressure.

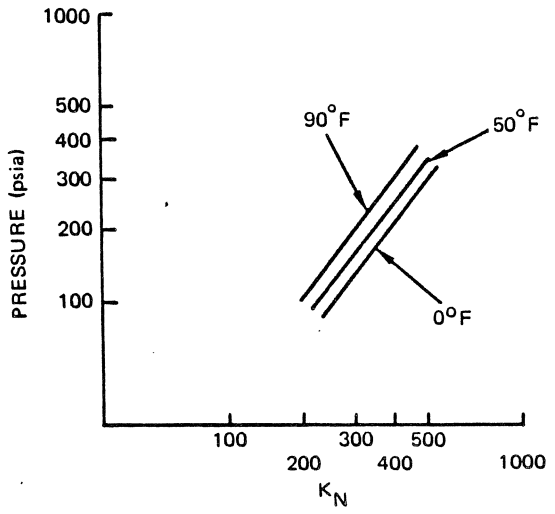

Figure 6-4. Effect of Burning-Surface-to-Throat-Area Ratio on Chamber Pressure

It was assumed in equations 1 and 2 that burning rate is temperature dependent through the coefficient a. (The burning rate exponent n is assumed to be independent of temperature.) Empirical data indicates that this temperature dependency relationship can be expressed as:

$$a = \frac{a_o}{(T_o - T_p)} \quad (9)$$

where:

a_o = An empirical constant

T_o = Spontaneous ignition temperature of propellant, °F

T_p = Temperature of propellant prior to ignition, °F

In practice, T_o is evaluated empirically. As the temperature of the propellant grain (T_p) approaches the spontaneous ignition temperature of the propellant, the burning rate can be seen to approach infinity.

The temperature dependence of the burning rate can be defined as:

$$\pi_r = \frac{1}{r}\left(\frac{\partial r}{\partial T_p}\right)_p \quad (10)$$

where:

π_r = Burning rate temperature coefficient, $°F^{-1}$

$\left(\frac{\partial r}{\partial T_p}\right)_p$ = Rate of change of burning rate with respect to propellant temperature at constant chamber pressure, in/sec/°F

Substituting equations 1 and 9 into equation 10 and performing the indicated differentiation yields:

$$\pi_r = \frac{1}{T_o - T_p} \quad (11)$$

The temperature sensitivity of chamber pressure can be difined as:

$$\pi_p = \frac{1}{P_c}\left(\frac{\partial P_c}{\partial T_p}\right)_k \quad (12)$$

where:

π_p = Temperature sensitivity of chamber pressure, $°F^{-1}$

$\left(\frac{\partial P_c}{\partial T_p}\right)_k$ = Rate of change of chamber pressure with respect to propellant temperature at constant propellant area ratio, psia/°F

Substituting equations 1 and 9 into equation 12, and performing the indicated differentiation leads to the relationship:

$$\pi_p = \frac{\pi_r}{(1-n)} \quad (13)$$

It is now possible to express the variation in burn rate as a function of temperature by integrating equation 10, giving:

$$r = r_o \exp\left[\pi_r(T_p - T_{p_o})\right] \quad (14)$$

where:

r_o = Reference burning rate (at T_{p_o}), in/sec

T_{p_o} = Reference propellant temperature (corresponding to r_o), °F

Similarly, integrating equation 12 yields the variation in chamber pressure with respect to propellant temperature:

$$P_c = P_{co} \exp\left[\pi_p(T_p - T_{po})\right] \quad (15)$$

where:

P_{co} = Reference chamber pressure (at T_{po}) psia

For modern propellants, π_p generally is less than 0.3 percent $°R^{-1}$.

6-2.3 Erosive Burning

The term erosive burning is used to indicate the increased burning rate (usually localized) of a solid propellant as the result of high velocity gas flow parallel to the burning surface. It is generally accepted that erosive burning is caused by an increase in the rate of heat transfer to the solid propellant resulting from the presence of a gas flow parallel to the burning surface. The heat transfer rate increases with increase of gas velocity which causes a decrease in the boundary layer thickness. Impingement of the hot gas flow stream on the propellant surface would also cause erosive burning. A fast burning propellant tends to exhibit a relatively small erosion effect because the rapid evolution of gas, normal to the burning surface, produces a thicker boundary layer than would occur in a slow burning propellant.

On the basis of limited experimental data, a quasi-theoretical equation has been developed to calculate the increase in the burning rate due to erosive effects. This equation is:

$$r = r_o (1 + K_G G) \quad (16)$$

where:

r = Burning rate, in/sec

r_o = Burning rate when the gas velocity is zero, in/sec

G = Mass velocity, lb/in^2-sec

K_G = . Erosive burning constant, in^2-sec/lb

Values of K_G vary over the range of 0.4 to 3.0 for solid propellants. The lower values of K_G are associated with faster burning rate propellants.

6-3 GRAIN GEOMETRY

Since the thrust of a solid propellant rocket is a function of the mass flow rate and effective exhaust velocity, and the amount of propellant surface area and burning rate determine the mass flow rate, it becomes apparent that propellant surface area is one of the controlling factors in solid-rocket performance. The propellant surface area is controlled by the design of the grain. Many grain designs with varying characteristics are available. Propellant grains are generally classified as internal-burning, external-burning, or end-burning. The internal-burning grain burns on the interior exposed surface of the grain perforation; the external-burning grain burns on the exposed exterior surface; and the end-burning grain burns in a direction parallel to the longitudinal axis.

Rocket motors are usually designed to achieve a high volumetric loading, and a constant thrust-time history. The reason for high volumetric loading is quite evident. Since in a solid-propellant rocket all of the propellant is contained within the combustion chamber, the higher the volumetric loading, the smaller the rocket case and inert weight. This results in a higher mass ratio (propellant weight/total rocket weight) and, hence improved performance (ΔV) of the rocket as shown in equation 14 in Section 4.

The lowest motor case design pressure will be achieved for any given set of requirements if the combustion pressure is maintained at a constant level. This permits the minimum weight case design to be used and results in the highest possible propellant mass fraction. Futhermore, since specific impulse increases slightly with increase in combustion pressure, some improvement in average specific impulse will also be obtained. Thus, if mission requirements permit, a constant thrust-time history is a design goal.

There are instances when other factors will have an overriding influence on the type of thrust-time curve required. Therefore in the design of a solid rocket, the particular mission and requirements for the rocket must be established before the grain design may be initiated.

Basically, grain design consists of the study of the geometric characteristics of the grain. For this reason, the parameters used in grain analysis are based on definite mathematical concepts. The design of end-burning and rod grains is relatively straightforward. However, there are two items in the design of an internal burning grain which must be considered.

a. The width of any small passages in the grain must be sufficiently large to allow the combustion gases to flow through the passages at a fairly low velocity.

b. Cross-sectional area of the gas stream at the exit end of the grain should be at least 1.5 times the cross-sectional area of the nozzle throat in order to keep erosive burning at the aft-end of the grain to a minimum.

Erosive burning increases the burning rate of the propellant, which for a specific motor design, results in an increase in chamber pressure.

6-3.1 End-Burning Grains

The end-burning grain is normally free-standing and inhibited on its exterior wall. It fills the chamber cylinder as completely as possible, and exposes only the aft end of the grain to burning (Figure 6-5). This design meets the two requirements set forth earlier, since the volumetric loading approaches 100 percent and the propellant surface area is theoretically constant. Its main advantage is that very long burn times can be achieved.

The end-burning design has two serious deficiencies, however. The first is that it is a relatively low-thrust motor. The thrust may be increased by increasing the radius of the chamber. However, aerodynamic drag then becomes significant and usually intolerable. The second limitation is that as the grain burns, the chamber walls are exposed to the high propellant flame and gas temperatures. To compensate for the increased heat transfer to the chamber wall, a weight penalty must be incurred in the form of insulation or an extra-heavy chamber wall design.

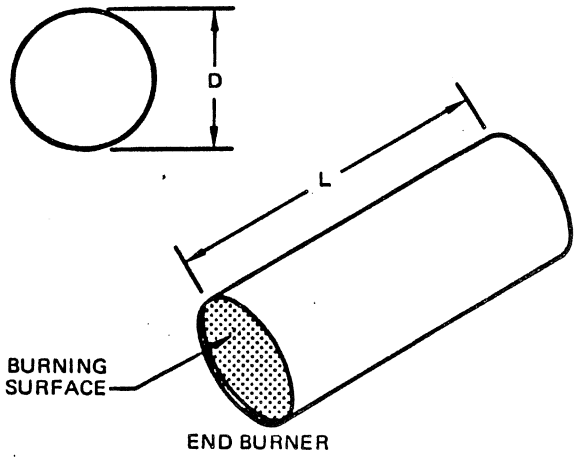

Figure 6-5. End-Burning Grain

6-3.2 Rod Grains

The rod design is a simple external-burning rod of propellant attached at the fore-end of the chamber, as shown in Figure 6-6.

The rod design has the advantage of greater propellant surface area than in an end-burning design in a given motor size, and thus increases the thrust of the motor. However, this design also has limitations. The chamber is exposed to the propellant flame and gas temperature; the propellant surface area decreases linearly with time, and the rod has a tendency to sag or slump before it is ignited, and to waver during burning. The rod may also break up near the end of burning.

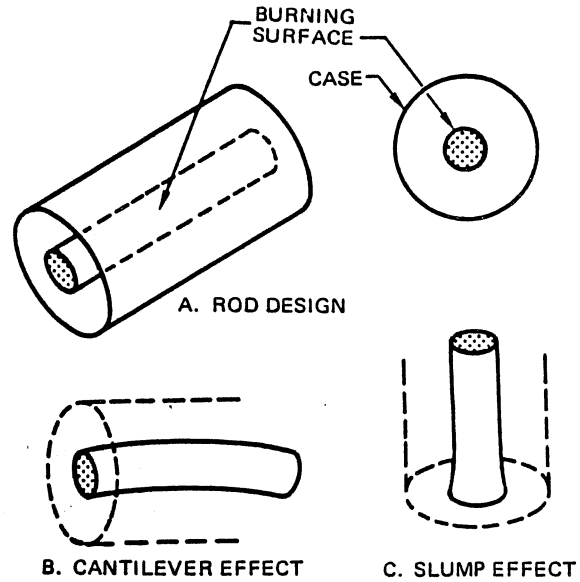

Figure 6-6. Rod Propellant Grain

6-3.3 Shell Grains

The shell or hollow cylinder design eliminates the problem of grain sagging and chamber exposure encountered with the rod design. The shell design (Figure 6-7) is an internally-burning configuration. It has the same maximum duration and loading capabilities as does the rod design. The burning is assumed to take place in a radial direction only, thus the design can be analyzed by a cross-section normal to the cylinder center-axis. With this analysis, the performance of the shell design is linearly progressive. This design eliminates the problems of case exposure and support for the rod design, but it still is inefficient because the case must be designed to withstand the maximum chamber pressure which corresponds to the maximum surface area.

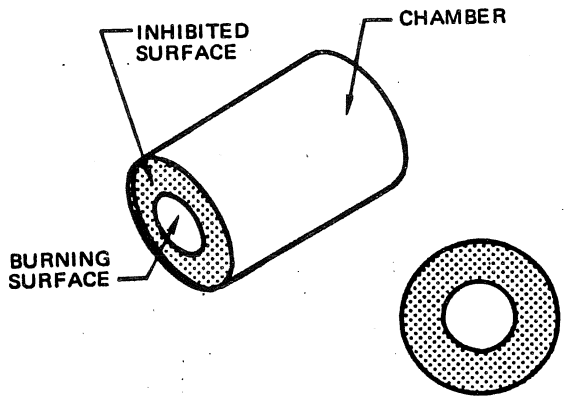

Figure 6-7. Shell Propellant Grain

Since the rod design is regressive by the same amount that the shell design is progressive, a combination of the two, as shown in Figure 6-8, will give a neutral or constant thrust-time curve.

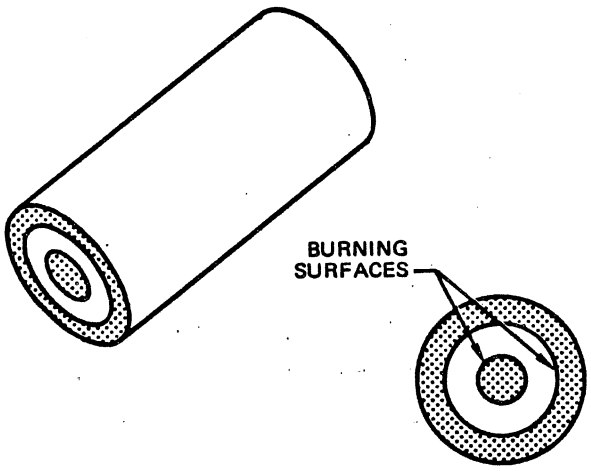

Figure 6-8. Rod and Shell Propellant Grain

In addition to the neutral thrust curve, the rod and shell design has approximately twice the propellant surface area of either the rod or shell designs alone, and consequently, for a given motor has approximately twice the thrust. This design, however, still has the problem of support for the rod.

6-3.4 Star Grains

To counteract the progressivity of the shell, and to avoid the problems of rod support, the next step is to add a piece or pieces of propellant to the shell in such a way that the added propellant will be regressive at approximately the same rate that the shell is progressive. Consider a sector of propellant which has an inherently regressive effect by itself, and add this to the shell design, as shown in Figure 6-9. This resultant design eliminates the rod support problems; however, a new problem, that of stress concentrations at the point of attachment, arises. Stress concentration in a grain occurs whenever there are abrupt changes in the cross-section. Stress-relieving fillets are introduced to avoid these stress concentrations.

Since the design is symmetrical, only a half-sector of the cross-section has to be examined to determine the geometrical performance. Because the sector is symmetric, the angle of such a half-sector can be generalized by π/N, where N is the symmetry number. In this type of design, two additional parameters are important; web thickness and sliver. The web thickness

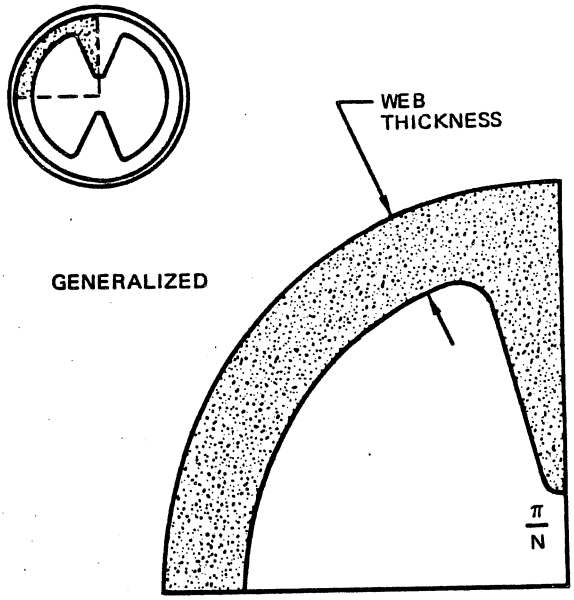

Figure 6-9. Development of the Star Propellant Grain

is defined as the shortest distance between the propellant-grain internal surface and the rocket case. When the propellant burns a distance equal to the web thickness, the main body of the propellant is consumed, and then the pressure and thrust tail-off. Consequently the web thickness is a direct indication of the effectiveness performance duration.

A sliver is a small amount of propellant still to be burned immediately after the main body of the propellant grain burns out. A sudden drop in propellant area takes place at web burn-out, causing the initiation of tail-off conditions. The amount of sliver should be held to a minimum because it burns at a lower pressure, and releases less usable energy than the main body of the propellant. It is possible for a grain to have more than one web; in which case the thickest web is considered the primary web, in that true tail-off cannot begin until it burns out. Burn-out of a minor web will usually be marked by the pressure-time trace becoming regressive.

The design of a star-perforated grain begins with the web, as shown in Figure 6-10. The web thickness, w, is known before the design is initiated since it is determinied by the mission requirements and is calculated by the equation:

$$w = r \cdot t \qquad (17)$$

where r is the propellant burning rate and t is the motor burning time. The web is generally 0.7 times the chamber radius, which allows maximum propellant loading for a star grain design.

Since the design is not a shell design, the arc (length of the web) is determined by the angle Φ. At the end of the arc describing the web, the arc of the stress-relieving fillet begins. The center of this arc falls on the dotted line terminating the angle Φ. The fillet radius is labeled Y_a and the angle of the fillet arc is called alpha (α). Next, the side of the triangular portion of the design is joined tangentially to the fillet arc. This side, called the ray side and defined by L, goes toward the side of the sector. It can be continued to meet the sector side, or it can be stopped and terminated with an outside round as shown.

Arcs at the propellant tips of a grain are termed inside or outside round depending on whether they are concave away from the propellant or concave toward the propellant, respectively. The sector design is now complete and the independent parameters or degrees of freedom are R_c, w, α, Φ, Y_a, L and N.

Mathematical analysis of the burning grain cross-section shown in Figure 6-11 appears difficult. However, if the sectors are partitioned into portions having the same geometric characteristics, each partition may be considered separately, and the performance characteristics of each area can be determined and added together to determine the sector performance. The performance of the grain cross-section can then be determined by multiplying the sector performance by 2N.

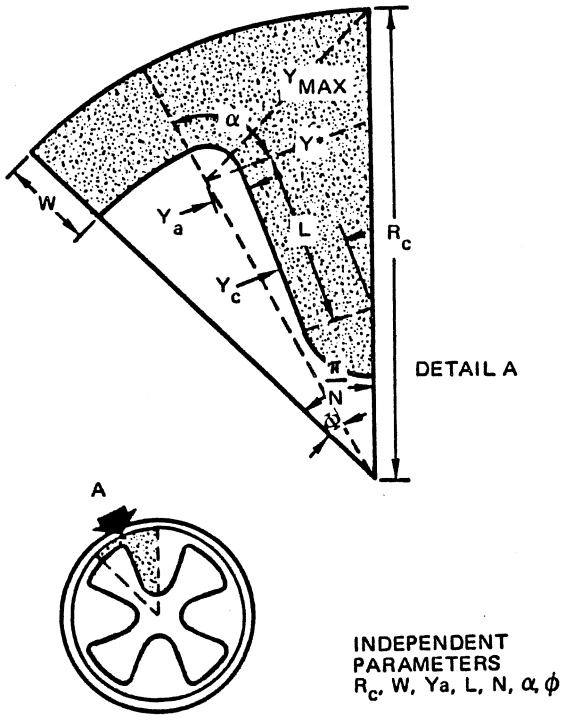

Figure 6-10. Design Parameters of Star Grains

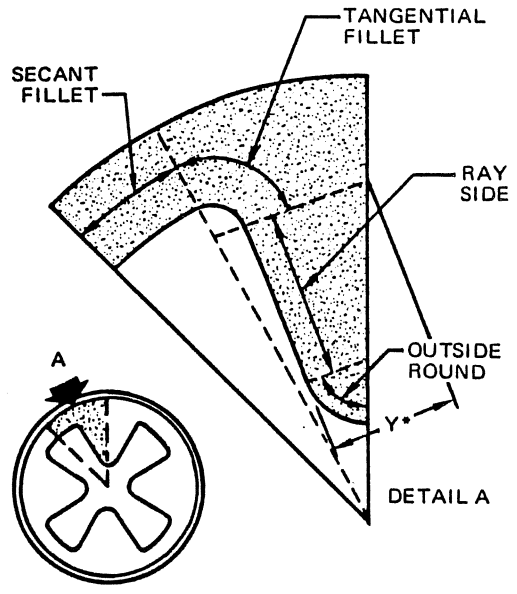

Figure 6-11. Grain Partitions in the Star Design

Figure 6-11 defines the four principal portions or areas of the star design. Each of these areas has a definite geometric performance. Outside rounds always have regressive burning characteristics, and inside rounds are always progressive unless the burning is subject to inerference from another surface. Straight-line portions of the periphery can be considered as neutral burning until interference occurs from another burning surface. The secant fillet can be seen to be slightly progressive. The tangential fillet is progressive until the periphery burns a distance equal to the web thickness.

6-4 SOLID PROPELLANT MOTOR DESIGN

Figure 6-12 shows a typical solid propellant motor design. The principal components of this motor are the motor case, the propellant grain (which is bonded to the case), the nozzle, and the igniter. The most important considerations in the design of the motor hardware are the high temperatures and the erosive gas flows that must be endured. In most motor designs, the length of the motor case is insulated by the case-bonded propellant grain during the motor operating time, prior to web burn-out. A liner is used primarily to provide an optimal bond between the propellant and the case wall. The liner consists of a thin layer of fuel polymer, without oxidizer or metallic additives, that is applied to the chamber wall prior to casting the propellant.

Additional insulation is normally required in the forward and aft domes of the motor case to protect the domes from the hot combustion gases. The insulation is usually a rubber-base material, filled with asbestos or ceramic to provide a better thermal barrier. Because of the progressive burning away of the propellant, the duration of exposure of the domes to high-temperature is also progressive. Therefore, it is usual to taper the forward and aft insulation so that it is thickest near the motor centerline, thinning as it approaches the motor circumference. Motors that must withstand low-temperature handling and storage environmental exposure commonly incorporate a boot, as shown in Figure 6-12. The boot is a flap in the dome insulation that allows the propellant to contract without breaking the bond of the insulation between the propellant and the motor case dome.

6-4.1 Motor Case

The motor case of a solid propellant rocket serves two important functions: it houses the propellant grain, and it acts as the combustion chamber for the motor. The motor case is usually a cylindrical, thin-walled pressure vessel, and is subjected to normal motor chamber pressure, pressure surges, or spikes, and often severe heating.

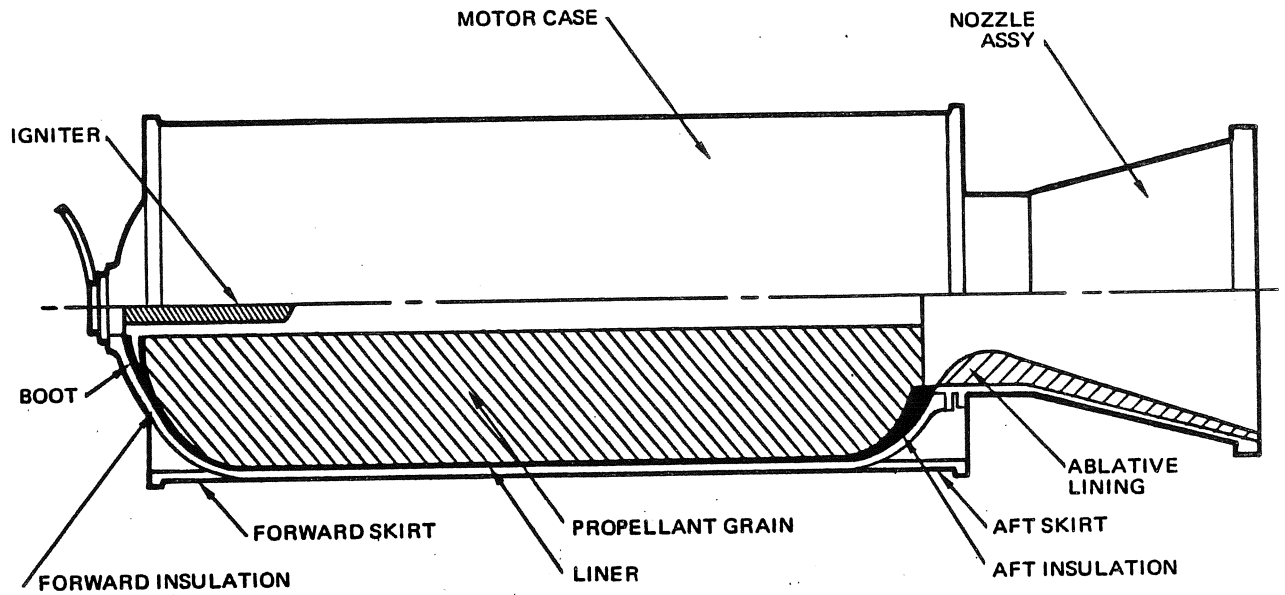

Figure 6-12. Typical Solid Propellant Motor

Solid propellant motor cases are constructed of several types of materials, of which the most commonly used are steel alloys, titanium, or fiberglass-reinforced plastic. The temperature of the chamber wall, which carries the pressure load, determines the physical properties of the stress bearing members, and thus largely determines the chamber design. By reducing the heating of the chamber walls it is possible to reduce the required wall thickness.

The chamber design must also provide for loading of the propellant grain, attachment of the nozzle, and mounting and handling supports.

6-4.2 Nozzle

The function of a solid rocket nozzle is to produce thrust by converting a part of the heat generated by propellant combustion into kinetic energy. The efficiency with which the nozzle performs this function is dependent on the nozzle design. The design of an efficient nozzle requires application of knowledge from a wide variety of technical areas. These include gas dynamics, material technology, heat transfer and stress analysis.

Motor parameters that govern a nozzle design are:

a. Performance characteristics such as exhaust gas composition and temperature, chamber pressure, motor burning duration, thrust level, nozzle throat diameter and expansion ratio.

b. Nozzle envelope and weight limitation.

c. Vehicle mission profile as it affects thrust vector control requirements and flight loads.

These parameters are interdependent in their influence on the selection of the nozzle configuration, materials and structure.

The conventional solid rocket nozzle is the de Laval-type with a convergent entrance section, a minimum area or throat section, and a divergent exit section, as shown in Figure 6-13. The simplest nozzle configuration has conical entrance and exit sections. In more sophisticated designs, both the entrance and exit sections have rounded or contoured shapes and, occasionally, the throat is submerged in the motor chamber to obtain a large expansion ratio within a limited length.

Unconventional techniques, such as annular flow nozzles and expandable exit cones are undergoing development for application to solid rocket motors. These are not currently considered to be state-of-the-art.

The suitability of a nozzle material for a specific application is determined by internal environmental factors such as exhaust gas pressure and temperature, the presence of reactive species in the gas and the solid or liquid-particle phases in the exhaust. The major failure mechanisms of nozzle materials are considered to be corrosion, erosion, thermal ablation, and mechanical spallation. Table 6-5 lists some typical properties of nozzle materials.

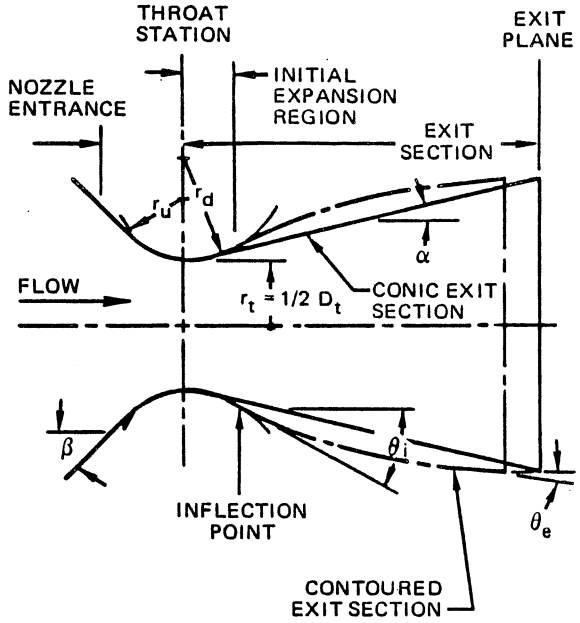

θ_i = INITIAL EXPANSION ANGLE
α = EXPANSION HALF ANGLE
β = CONVERGENT HALF ANGLE
θ_e = EXIT EXPANSION ANGLE
D_t = THROAT DIAMETER
r_t = THROAT RADIUS
r_u = UPSTREAM WALL RADIUS
r_d = DOWNSTREAM WALL RADIUS

Figure 6-13. Conventional Convergent-Divergent Nozzle

6-4.3 Igniter

Combustion of the solid propellant motor is initiated by means of an igniter, which is usually activated by an electric signal. The igniter pressurizes the combustion chamber and raises the temperature of the surface of the propellant grain until the autoignition temperature is reached and local combustion occurs.

Igniters fall into three general categories according to their degree of containment: totally confined, ballistic nozzle, and unconfined.

Table 6-5. Typical Properties of Nozzle Materials

PROPERTY	HEAT SINK MATERIALS**			PLASTIC COMPOSITE MATERIALS***		
	GRAPHITE (AT3)	TUNGSTEN (FORGED)	PYROLYTIC GRAPHITE	CARBON CLOTH (MX-4926)	GRAPHITE CLOTH (FM-5064)	SILICA CLOTH (MX-2600)
DENSITY, gm/cc	1.73	19.0	1.80–2.26	1.43	1.45	1.75
THERMAL CONDUCTIVITY, Btu-ft/hr-ft^2-°F						
WITH GRAIN OR PLY	70–16	96–60	100–40	0.83–0.93	2.29–2.90	0.35–0.38
ACROSS GRAIN OR PLY	40–15		1.2–0.3	0.48–0.58	0.69–0.92	0.30–0.32
SPECIFIC HEAT, Btu/lb-°F	0.25–0.6	0.033–0.047	0.22–0.5	0.20–0.36	0.24–0.39	0.24–0.30
THERMAL EXPANSION, (in/in-°F) X 10^6						
WITH GRAIN OR PLY	1.5	2.5	1.33	3.8	5.3	3.9
ACROSS GRAIN OR PLY	2.2		20	5.3–31.0	17.6	16.5
ULTIMATE TENSILE STRENGTH, psi X 10^{-3}						
WITH GRAIN OR PLY	4.5–7.0	160–10	10–15	18.0–10.5	10.5–7.2	12.0–7.6
ACROSS GRAIN OR PLY	3.0–5.0		1.0	0.90–0.30	0.74–0.33	0.72–0.39
TENSILE MODULUS, psi X 10^{-6}						
WITH GRAIN OR PLY	0.75–0.80	59	4–2.5	2.64–1.60	1.57–1.23	2.62–1.99
ACROSS GRAIN OR PLY	0.90–1.25			1.80–0.05	0.44–0.08	0.48–0.06
COMPRESSIVE STRENGTH, psi X 10^{-3}						
WITH GRAIN OR PLY	9.0–11.0	---	---	36.1–13.5	13.0–3.98	16.2–8.13
ACROSS GRAIN OR PLY	10.0–12.0			62.9–42.5	33.0–21.6	49.1–21.3
COMPRESSIVE MODULUS, psi X 10^{-6}						
WITH GRAIN OR PLY	0.9–1.1	---	---	2.34–1.73	1.50–0.89	3.50–1.95
ACROSS GRAIN OR PLY	0.8–1.0			1.85–0.75	1.05–0.37	2.07–0.78

*ALL VALUES SHOWN ARE ROOM TEMPERATURE PROPERTIES EXCEPT AS NOTED.
**THE SECOND VALUE SHOWN FOR HEAT SINK MATERIALS REFERS TO PROPERITES AT 4000°F.
***THE SECOND VALUE SHOWN FOR PLASTIC COMPOSITE MATERIALS REFERS TO PROPERTIES AT 750°F.

Totally confined igniters include:

a. Bag-igniter consisting of black powder and a squib in a cloth or plastic bag.

b. Powder-can consisting of a container, weakened on one side by scoring or coining, filled with propellant strips and metal-oxidant particles, and initiated by a squib.

c. Jellyroll, which is essentially a hollow roll of cloth, plastic or paper that is coated inside with a pyrotechnic and also initiated by a squib.

Ballistic nozzle igniters include the basket igniter, the perforated tube igniter and the pyrogen igniter. The pyrogen igniter is a miniature high-pressure rocket motor which exhausts into the main motor chamber. The igniter charge is usually a cast-composite propellant contained in a high-strength pressure vessel with a rocket nozzle at one end, as shown in Figure 6-14. A high igniter chamber pressure is desirable in order to maintain a high burning rate of the igniter charge.

In basket or perforated tube igniters, combustion of the igniter charge takes place in a basket or perforated tube which is vented directly into the main motor case. The igniter charge usually consists of discrete pellets or tablets of pressed oxidant/fuel powder, which ignite and burn over their entire surface areas. The pressure-time curve of this type of igniter is more difficult to tailor for a given application than that of the pryogen igniter. Typical ballistic nozzle igniters are shown in Figures 6-14, 6-15, and 6-16.

Unconfined igniters are those ingiters that do not rely on a chamber, other than the rocket motor for confinement during ignition. They are, in fact, nozzled by the rocket motor nozzle.

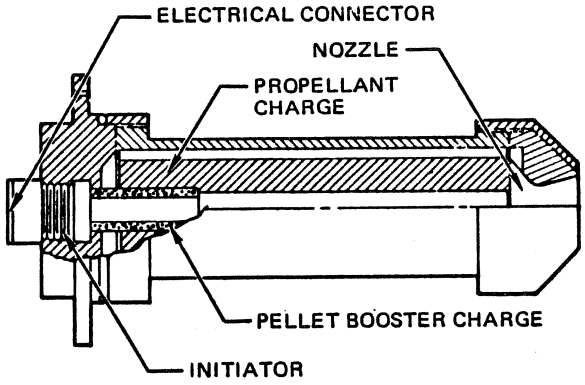

Figure 6-14. Typical Rocket-Type Igniter

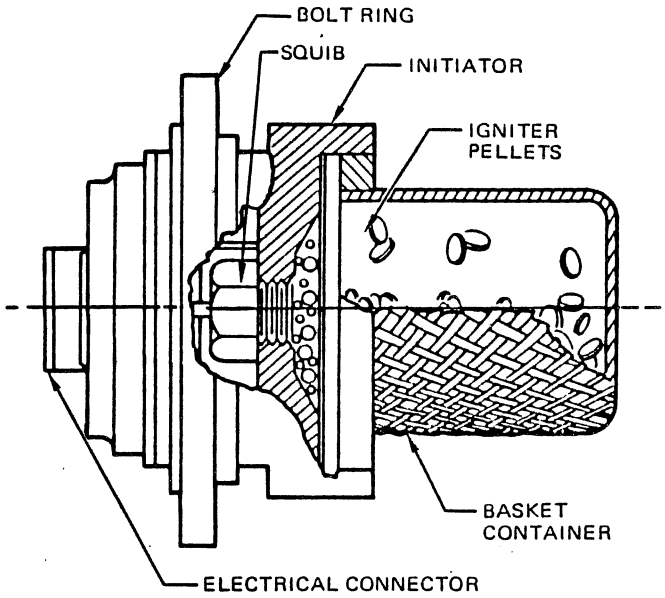

Figure 6-15. Typical Basket Igniter

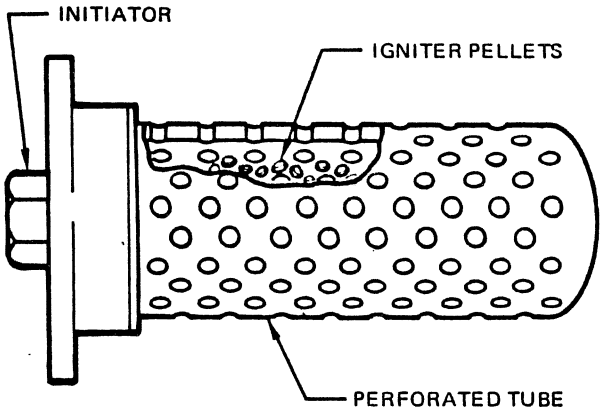

Figure 6-16. Typical Perforated Tube Igniter

Examples of this type of igniter are film igniters and conductive film igniters. Film igniters consist of an ignitable fuel-oxidizer-binder mixture painted directly onto the propellant surface. The film is actuated by a conventional low output totally confined igniter, such as the powder-can igniter. Conductive film igniters consist of a thin strip of conductive pyrotechnic with an overlay of printed-circuit leads applied directly to the propellant.

Successful ignition of the solid propellant rocket motor is generally the result of a series of ignitions, called an ignition train. Elements of this ignition train, which are included within the igniter, may functionally be desribed

as: the initiator, the booster charge, and the sustainer or main charge. In practice, the actual number of stages in the ignition train varies from igniter to igniter. Also, there is some variation in the terminology used to describe these stages.

The initiator is generally an electrically initiated cartridge or squib, containing a heat sensitive charge that produces high-temperature gas and particles. Initiation of the squib results when an electric current is passed through a resistance wire or bridgewire, which heats the surrounding charge to a temperature above the autoignition tempterature. The squib charge decomposes rapidly, producing the energy output necessary to ignite the next stage in the train. The next stage in the ignition train may be the booster charge, or it may be a second initiator stage if the igniter contains many stages.

Safe-and-arm devices are used to prevent the application of an electric current to the initiator prematurely, and also to block and divert the initiator output if inadvertent ignition occurs. Initiators are also subject to premature ignition by induced currents in the firing circuitry. The most common hazards result from test equipment, radio frequency electromagnetic pickup, and power line inductive pickup. This problem has been reduced by designing initiators with a minimum no-fire current and voltage level, and by proper shielding and grounding of the electrical circuits.

Exploding bridgewire (EBW) squibs have been developed to reduce the problems associated with safe-and-arm techniques. These squibs must be initiated by a high voltage source which discharges through the bridgewire. The discharge causes the wire to vaporize rupturing a seal between it and a pyrotechnic charge, and igniting the charge. A firing unit is used to convert a standard low-voltage input signal into a high-voltage output and then release the signal to the EBW squib. By using the EBW system, it is possible to reduce the requirement for a mechanical safe-and-arm system on the igniter. This usually results in a weight reduction, since the safe-and-arm system is replaced by a system of electrical switches to control the arming-and-firing sequence.

One or more stages of booster charges are used in the igniter to reduce the overall time delay of the ignition train. The booster charges are energetic (high burning rate) large relative surface area materials, which quickly pressurize the igniter and activate the main charge of the igniter. It is the main charge of the igniter that supplies the energy to ignite the main motor propellant grain.

6-5 THRUST CONTROL

Many applications of solid propellant rocket engines require that the thrust be controlled. Thrust control includes: thrust termination, thrust vector control, and variation in thrust level.

6-5.1 Thrust Termination

Figure 6-17 illustrates some of the concepts which have been considered to achieve precise thrust termination at will. Any of these concepts may be useful for a particular application. In general, however, destruction of the engine case, separation of the engine and closures, or rapid increase of nozzle throat area can disturb the payload trajectory or result in the application of severe transient accelerations to the vehicle.

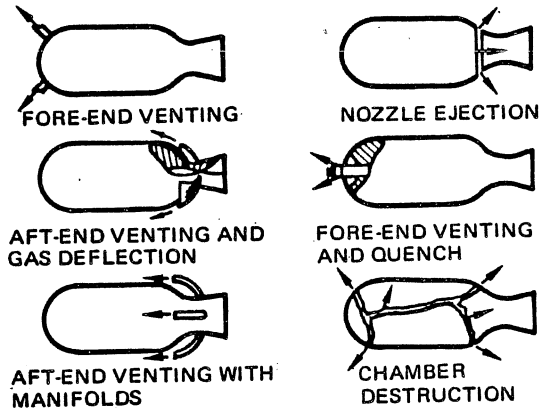

Figure 6-17. Methods of Thrust Termination and Thrust Reversal

Of the many concepts available for impulse control, some form of thrust reversal accompanied by simultaneous separation of the payload is most readily adaptable to a wide range of rocket engine sizes and configurations. Figure 6-18 presents pressure-versus-time and thrust-versus-time curves for a typical thrust reversal system. It shows that this arrangement permits thrust to be terminated much more quickly than a configuration that relies on decay of chamber pressure, even if the propellant combustion is terminated instantly.

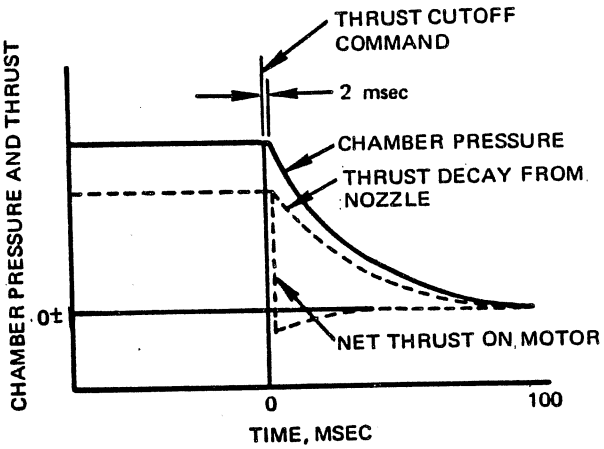

Figure 6-18. Pressure and Thrust Decay Phenomena During Fore-End Thrust Reversal Event

6-5.2 Thrust Vector Control

Many methods of deflecting the nozzle exhaust system of solid rockets to provide thrust vector control (TVC) have been investigated, including jet vanes, jetavators, gimballed nozzles and secondary fluid injection. These methods are illustrated in Section 4, Table 4-6. Figure 6-19 illustrates in some detail three advanced solid propellant TVC methods. The first two are variations of the fluid injection technique.

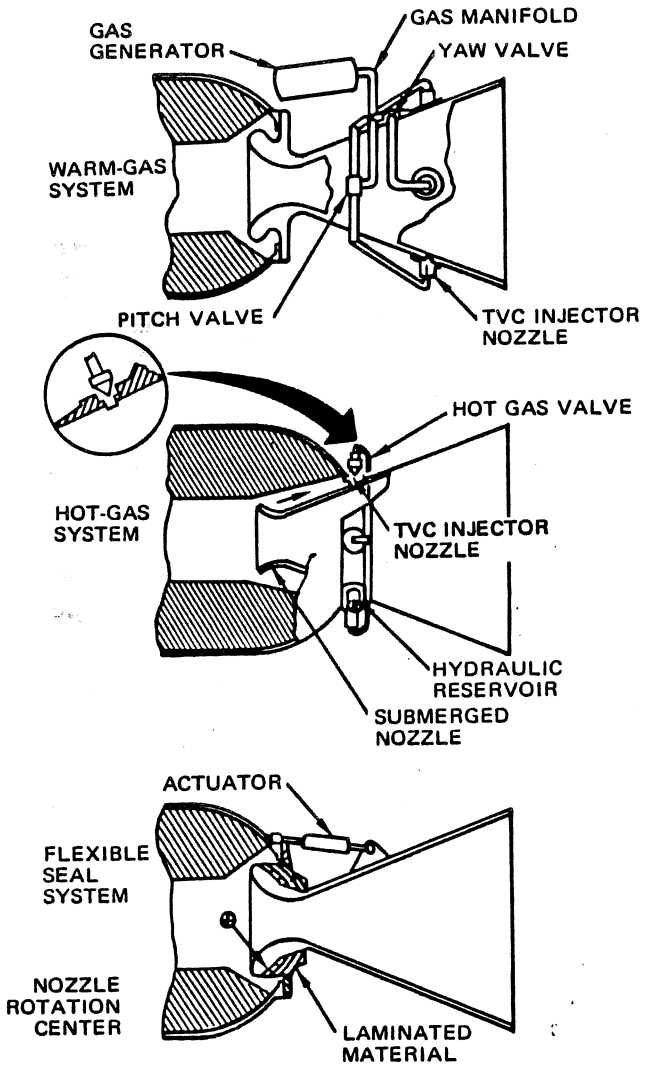

Figure 6-19. Typical Thrust Vector Control Systems

In the warm-gas system TVC, injection impulse is supplied independently of the main motor by a solid propellant gas generator. The relatively low temperature (2000°F) injected gas flows from the gas generator continuously through the manifolds to the pitch and yaw valves. This low combustion temperature, as compared to main motor combustion temperature, considerably eases the design and material problems encountered with the valves.

In the simplest type of warm gas system, a single pitch valve and a single yaw valve each feed two opposing injector nozzles. Flow through the valves from the gas generator is maintained constant by a sonic orifice in the valve inlet. A modulating spool (the heart of the two-stage pressure feedback valves) turns the flow and divides it between the opposing outlets. In the null position, flow is divided equally between the outlets, and the net thrust vector deflection produced by the opposing injector nozzles is zero. When a pitch or yaw command is given, the appropriate valve spool is repositioned pneumatically by an electrical input to the actuator, which increases the flow to one port and reduces the flow to the other, thereby imparting a net deflection to the thrust vector. This is a continuous flowing system, that is, the total gas flow from the generator remains constant and is always ejected through the motor nozzles.

The hot gas or chamber bleed secondary injection TVC system uses main motor high-temperature combustion gases that are bled off the main chamber and injected through metered orifices into the nozzle flow downstream of the throat. Figure 6-19 shows how the high-temperature, highly-erosive, combustion gases flow across the metering pintle and out through the injection orifices. The critical design problems are associated with the pintle-to-seat configuration, pintle cooling, and contaminant buildup. Flowrate is varied as a function of deflection angle demands. The higher the required deflection angle, the further the pintle is backed out of the injection orifice, thereby increasing the flowrate.

In the flexible seal technique, nozzle motion is accomplished by the deflection of a laminated assembly (or doughnut-shaped ring) which consists of alternate layers of an elastomeric material and metal. The assembly is very stiff axially, but is easily deflected in shear for lateral or rotational movement. The seal is bonded to the nozzle on one side and to the chamber mounting flange on the other. When actuators push or pull the nozzle shell, each elastomeric layer moves in a shear mode to accommodate the deflection command. Two critical design problems that require investigation are the life cycle limitations of the laminate material at high temperatures and the axial deflection of the seal under full chamber pressure.

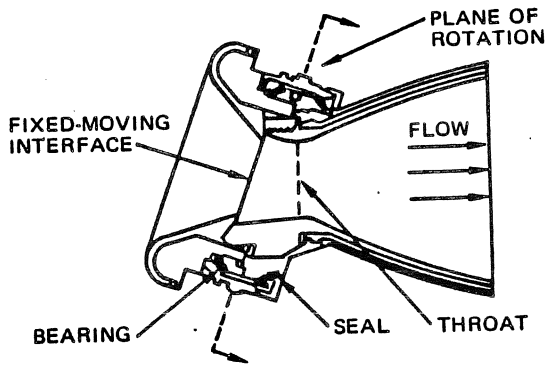

Figure 6-20. Rotating Nozzle

Another method of obtaining thrust vector control is a rotating nozzle which is shown in schematic form in Figure 6-20. The plane of rotation of the nozzle is skewed relative to a plane perpendicular to the axis of the throat. In the neutral position, the thrust axis corresponds to the central axis of the rocket engine. As the nozzle is rotated, however, the plane of the throat gradually approaches an attitude parallel to the plane of rotation of the nozzle.

By shifting the attitude of the throat-exit cone assembly, the jet stream is deflected. The rotating nozzle must always be used in multiple-nozzle sets so that opposite pairs of nozzles can be rotated simultaneously since, for example, as the nozzle rotates to develop a pitch motion, it also develops a yaw misalignment. By rotating a pair of nozzles in opposite directions, the yaw deflections are opposite and cancel each other, while the pitch deflections are mutually additive.

The rotating nozzle has two advantages when compared to a swivel or gimbaled nozzle. The seal system is more nearly a static seal than in the case of the swiveled nozzle, so that the moving fixed interface remains in a constant dimensional relationship. In general, the rotating nozzle can be shorter in over-all length than an equivalent swiveled nozzle. Disadvantages include the lack of linearity in response and the relatively large motion of the nozzle required for a given jet deflection.

Selection of a particular method of thrust vector control depends upon the characteristics of the particular engine and flight vehicle involved. For example, for short-duration engines with relatively large control requirements, jet vanes would be considered a strong candidate. For high-temperature propellant systems operating under vacuum conditions with small total control requirements, studies generally dictate the choice of a secondary-gas injection system. For primary stages with normal control requirements, the swiveled or rotating nozzle would almost certainly be selected.

6-5.3 Thrust Variation

The thrust of solid rocket engines can be varied on-demand or according to pre-established schedules. Thrust variation on-demand can be accomplished with a pintle nozzle, mass excitation, or a vortex valve. Pre-established thrust variation can be accomplished by designing the grain to have specific progressive and/or regressive thrust-time traces. A pulse motor can also be used to obtain pre-established thrust variation or it can be operated on-demand. Figure 6-21 presents schematic illustrations of the on-demand, and the pulse motor, concepts. Descriptions of these concepts are contained in the following paragraphs.

6-5.3.1 Pintle Concept

The pintle concept utilizes a variable throat area device to vary the thrust of a solid propellant motor. This device is a hydraulically actuated plug located in the nozzle throat which translates back and forth thereby varying the throat area. A small percent decrease in throat area increases the chamber pressure a greater percent resulting in a net increase in thrust. Conversely, an increase in throat area causes a decrease in thrust. In order to achieve an adequate thrust modulation range and obtain propellant extinguishment, the solid propellant must have a high burning rate r and a high pressure exponent n of burning rate; as described in equation 1.

6-5.3.2 Mass Excitation Concept

The method of controlling the thrust of a solid motor by injecting a secondary fluid into the combustion chamber is known as mass excitation. The rate of injection regulates the chamber pressure and, hence, the burning rate of the solid propellant. A sudden interruption of the flow of the excitation agent will cause a sudden drop in chamber pressure which, under proper conditions, will cause propellant extinguishment. Thus the method can be used either for continuous thrust modulation or for stop-restart.

Two types of mass excitation system have been developed. These are the liquid/solid system and the solid/solid system. The first system utilizes an energetic liquid for the injectant and the second system uses the combustion products of a solid propellant gas generator for injection into the main solid motor. The liquid/solid system can be shut off completely. The gas generator of the solid/solid system must continue to burn but its combustion products are diverted from the main chamber to decrease thrust. Both of these systems also need a high burning rate, high pressure exponent propellant to provide throttling.

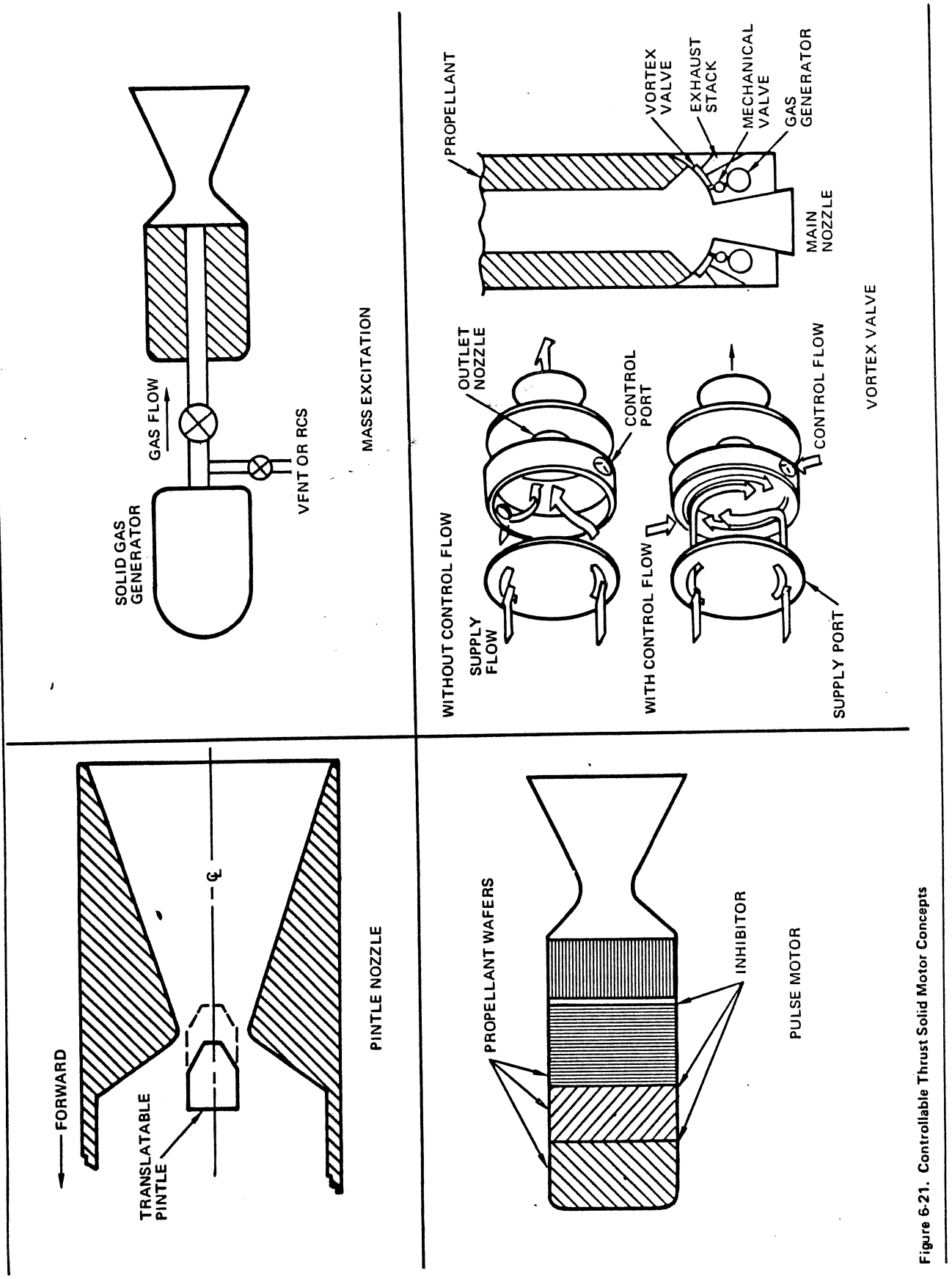

Figure 6-21. Controllable Thrust Solid Motor Concepts

6-5.3.3 Vortex Valve Motor

The vortex valve is a fluidic device used to control the flow of exhaust gases from a solid propellant rocket motor. The valve controls a large stream of hot gas by manipulating a relatively small amount of warm gas. In the process, no moving parts are exposed to the hot, corrosive metal-bearing, exhaust gases.

Fluidic vortex valves are used to control solid propellant rocket motors by presenting a variable impedance to the flow of combustion products out of the combustion chamber. In the usual arrangement, the rocket motor incorporates a conventional fixed-throat nozzle that is supplemented by one or more variable vortex valves. The low modulating capability of vortex valves (when used with a propellant with a high pressure exponent) is sufficient to obtain wide ranges of motor thrust modulation with relatively small valves handling a relatively small fraction of total motor combustion products. At the present time, the vortex valve motor is in the feasibility demonstration stage.

6-5.3.4 Pulse Motor

The pulse motor is a solid rocket motor with the capability of firing individual pulses, either preprogrammed or on command. Both end-burning and radial-burning grains can be used. The time duration between pulses is subject to command control, from complete cutoff for extended periods of time to quasi-continuous burning by sequential ignition of several pulses. This motor, however, has only a stop/restart capability and is limited to missions where preprogrammed thrust levels are needed.

6-6 HYBRID PROPULSION SYSTEMS

Propellants generally chosen for hybrid rockets consist of a solid component plus a liquid component. Customarily, the fuel is the solid component and is placed in a chamber in a manner similar to the usual internal-burning solid propellant rocket charge. The oxidizer is generally handled as a typical liquid propellant. Because many of the characteristics of hybrid rockets are similar to those encountered in solid propellant rockets, hybrids have been included in this section.

The hybrid propulsion system consists of a chamber for the solid component to which is attached a supersonic nozzle at one end, and at the other, an injector to meter and disperse the liquid component properly. In addition, a valve to control the flow of liquid propellant, a tank to contain it, and a propellant pressurization system (presumably stored gas and a pressure regulator) are required. The propellant valve is generally capable of throttling the flow of liquid to the chamber, so that thrust can be varied at will (this also implies the capability of stop-start operation at the desire of the operator). Figure 6-22 is a schematic design of a hybrid rocket in which the liquid oxidizer is sprayed radially from an axial pipe onto a cylindrical solid fuel surface.

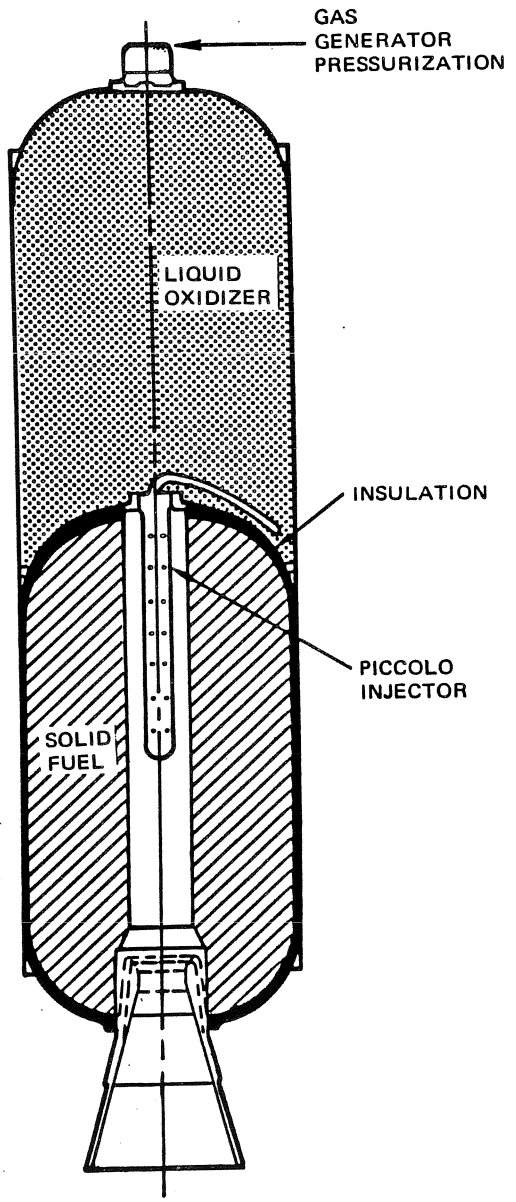

Figure 6-22. Schematic Design of a Hybrid Rocket

In comparison with solid propellant rockets, hybrids offer the possiblity of variable packaging. In other words, greater freedom is available in the selection of the exterior envelope than is possible with a solid propellant system. In comparison with liquid propellant rockets, the hybrid system offers the possibility of decreased complexity (for higher reliability) and higher density (so that less structure is required). Moreover, with both solid and liquid components available, it may be easier to incorporate into the propellant mixture certain elements or compounds, such as beryllium hydride, BeH_2 (a solid), or tetrafluoro-hydrazine, N_2F_4 (a liquid), in order to increase the delivered specific impulse.

On the other hand, containment of highly oxidizing liquids, many of which are toxic, is difficult. Corrosion and contamination can pose serious problems. If throttling of the oxidizer flow is desired, it is unlikely that successful regenerative cooling of the nozzle will be possible, and so nozzle throat erosion may be encountered with resultant thrust malalignment and lower specific impulse.

Finally, in a hybrid rocket the burning rate of the solid component and the flow rate of the liquid component must be nearly equal and uniform over the surface of the solid component. Otherwise, unused propellant remains (thus decreasing the intended velocity increase).

Table 6-6 lists the theoretical performance of several hybrid rocket propellant combinations. It shows that the specific impulse of hybrids is typically higher than that of solids, but lower than that of liquid propellant combinations. The bulk specific impulse of hybrids is competitive with that of liquid propellants.

6-7 BIBLIOGRAPHY

1. M. Barrere, et al., *Rocket Propulsion*, Elsevier Publ. Co., Amsterdam, 1960.

2. R. B. Canright, *Propulsion*, Space Systems Technology, R. D. Heitchue, Ed., Reinhold Book Corp., New York, 1968.

3. R. D. Geckler and K. Klager, *Solid-Propellant Rocket Engines*, Handbook of Astronautical Engineering, H. H. Koelle, Ed., McGraw-Hill Book Co., 1961.

4. C. Huggett, et al., *Solid Propellant Rockets* Princeton University Press, Princeton, 1960.

5. R. B. Kruse, *Solid Propellants*, Modern Materials, Vol. 6, Academic Press, New York, 1968.

6. P. E. Purser, et al., *Manned Spacecraft: Engineering Design and Operation*, Fairchild Publ., New York, 1964.

7. J. I. Shafer, *Solid Rocket Propulsion*, Space Technology, H. Seifert, Ed., John Wiley and Sons, 1959.

8. G. P. Sutton, *Rocket Propulsion Elements*, John Wiley and Sons, New York, 1964.

Table 6-6. Theoretical Performance of Several Hybrid Rocket Propellant Combinations

FUEL	OXIDIZER	MIXTURE RATIO	BULK SPECIFIC GRAVITY δ	COMBUSTION TEMPERATURE °F	SPECIFIC IMPULSE I_{sp}	DENSITY SPECIFIC IMPULSE δI_{sp}
Hydro-carbon $(CH_2)_n$	F_2	2.70	1.78	7430	325	416
	ClF_3	3.34	1.48	5910	257	380
	H_2O_2	6.70	1.34	4940	277	371
	N_2O_4	4.00	1.29	5740	276	356
BeH_2	F_2	4.26	1.53	9136	395	604
BeH_2	ClO_3F	2.12	1.48	7050	339	502
LiH	N_2O_4	2.84	1.20	5250	250	300
LiH	ClF_3	5.25	1.52	6936	293	445
Aluminum 40% $(CH_2)_n$ 60 %	ClF_3	0.55	1.94	6708	259	502

(I_{sp} AND $I_{sp}\delta$ ARE GIVEN AT p_c = 1000 psi AND SEA LEVEL EXPANSION.)

Section 7
COLD GAS PROPULSION SYSTEMS

Cold gas systems develop thrust by expanding a pressurized cold gas through a supersonic nozzle. The gas provides both the accelerated mass and the energy to accelerate this mass. In a basic cold gas propulsion system, all the energy is stored in the cold gas in the form of potential energy due to compression of the gas.

Because of the inherent simplicity of a cold gas reaction system, a high degree of reliability and a relatively low cost can be expected. However, the storage density of the gaseous propellant is low, and the size of the storage tank increases with increased impulse requirements. In addition, cold gas thrusters are relatively inefficient, producing low thrust and low specific impulses. Therefore, this type of system is normally restricted to applications where the energy requirements are small.

Figure 7-1 shows a comparison of the performance of a typical cold gas reaction control system, and typical chemical monopropellant and bipropellant reaction control systems. This figure indicates that cold gas systems are lower in weight than either monopropellant or bipropellant chemical systems for total impulses lower than approximately 1,000 lb-sec, but that for higher total impulse requirements the cold gas system is less desirable than the chemical systems on the basis of system weight. However, because of lower cost and higher reliability, cold gas systems are often attractive for total impulse requirements greater than 1,000 lb-sec.

A typical cold gas propulsion system is shown schematically in Figure 7-2. In this system, a cold gas stored at high pressure is expanded through a regulator to a constant lower pressure, and piped to the nozzles where thrust is to be developed. Several nozzles are used, providing thrust in the pitch, yaw, and roll planes. Each nozzle is provided with a solenoid-actuated valve to control the thrust pulses to the desired plane.

Cold gas propulsion systems are similar to the stored gas systems used to pressurize the propellant tanks in most liquid-propellant rockets. The system hardware for the cold gas propulsion system is identical to that of the stored gas pressurization system except that in the propulsion system, solenoid-actuated nozzles are added to the end of the system. Thus, the design methods for these systems are similar, even though the design objectives are quite different.

Because of the low thrust and total impulse levels of cold gas systems, their use is restricted to secondary propulsion applications, such as attitude control, station keeping, retro-thrust, and limited maneuvering. Impulse control is an important consideration for these applications. The ability of a propulsion system to control impulse is determined by its transient response, and by the minimum impulse bit it can deliver.

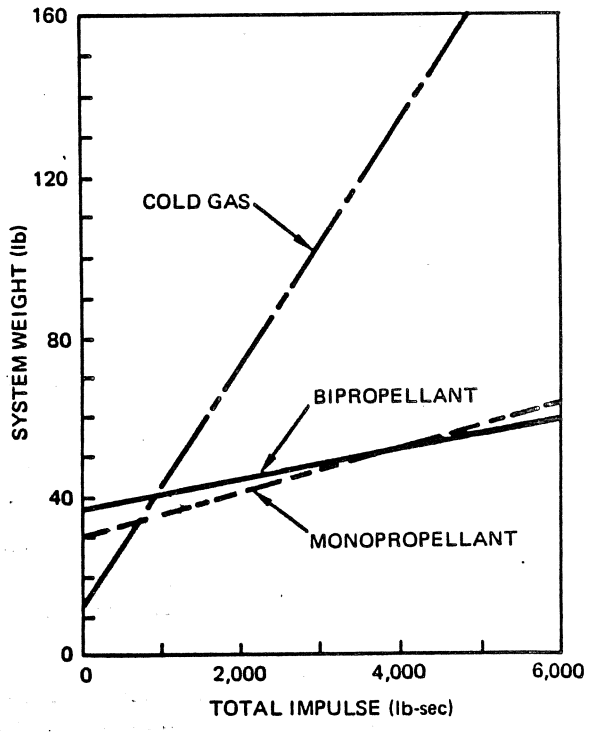

Figure 7-1. Reaction Control System Weight Comparison

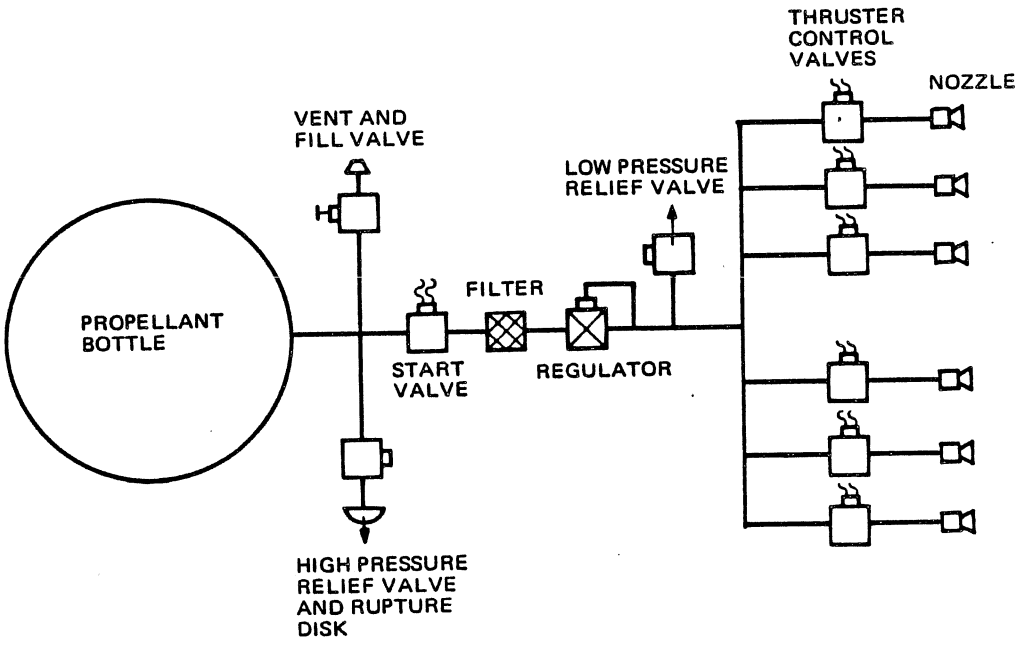

Figure 7-2. Basic Stored Gas System

For a cold gas system, the transient response is determined primarily by the valve characteristics. There is no ignition delay time, as experienced with the chemical systems, and the time required to flow the propellant from the valve to the thruster is low compared to liquid propellant systems. Both rise and decay transients of the thrust are also influenced by the propellant volume between the valve and the nozzle. In the cold gas system, this volume is negligible in most applications, further enhancing transient response.

The minimum impulse bit delivered by a cold gas system is determined by the same factors that determine the system transient response, i.e., valve characteristics, propellant flow time, and system volume. In addition, the density of the propellant trapped in the system volume when the valve closes influences the minimum impulse bit. The relatively low density of the gaseous propellant helps to decrease the minimum bit size of the cold gas system. Thus, the cold gas system provides the smallest impulse bits of the three systems that are compared in Figure 7-1.

Another important consideration for secondary propulsion systems is the degradation of specific impulse that occurs due to pulse operation of the thruster. However, the specific impulse of cold gas systems is relatively independent of pulse width because the only process involved is expansion in the nozzle. For pulse widths of 10 msec or longer, the cold gas thruster will deliver essentially 100 percent of its steady-state specific impulse.

It is possible to improve the performance of the basic cold gas propulsion system (shown in Figure 7-2) in a number of ways. In some applications, the storage density of the pressurized gas may be increased greatly by storing the propellant as either a liquid or a solid. This method of storage is especially attractive in cases where cryogenic fluids are already stored onboard the vehicle, providing a constant low temperature sink in which the propellant gas storage bottles can be immersed. These propellants must be converted to the gas phase prior to introduction to the thruster nozzle. Some heat addition to the propellant supply may be required to accomplish this phase change. However, in some cases, the phase change may be accomplished simply by opening the supply valve so that the high storage pressure is reduced to some lower pressure. In other cases, the heat addition to the propellant supply can be obtained with no significant increase in cost or weight by taking advantage of either waste heat from other systems or the effects of solar heating. These methods are particularly effective for systems with low flowrate demands.

The specific impulse of a cold gas system can be increased significantly by adding heat to the propellant gas prior to expansion through the nozzle. The increase

in specific impulse possible by heating the propellant gas is illustrated by Figure 7-3, which shows specific impulse versus nozzle inlet temperature for hydrogen, helium, and nitrogen. This heating can be accomplished by incorporating a heater in the thruster nozzle assembly. Several types of heaters are possible; the resistojet (discussed in Section 9) makes use of a resistive heater. This system is attractive if excess electrical energy is available from the spacecraft power supply. Another example of a heated gas system is the radioisotope-heated thruster, discussed in detail in Section 8.

7-1 EFFECTIVE SPECIFIC IMPULSE

The performance of a cold gas system can be tailored in a number of ways. Propellant storage density can be increased by reducing the propellant temperature, and system specific impulse can be raised by adding heaters to the thrusters, or by the use of a lower molecular weight propellant gas. To realistically evaluate the effects of these variations on overall system performance, it is desirable to define a measure of effectiveness that relates the total impulse of the system to the weight of the system, as illustrated in Figure 7-1.

The parameter customarily used for this comparison is effective specific impulse, defined by the relationship:

$$I_{sp_{EFF}} = \frac{I_t}{w_{sys}} \qquad (1)$$

where:

$I_{sp_{EFF}}$ = System effective specific impulse, sec

I_t = System total impulse, lb-sec

w_{sys} = System weight, lb

For steady-state conditions,

$$I_t = \bar{I}_{sp}\, w_p \qquad (2)$$

where:

$\bar{I}_{sp}$ = Average specific impulse, sec

w_p = Propellant weight, lb

Also, system weight is defined as:

$$w_{sys} = w_p + w_B + w_{misc} \qquad (3)$$

where:

w_B = Minimum weight of spherical bottle, lb

w_{misc} = Miscellaneous weight (nozzles, valves, lines, fittings, attachments, etc.) lb

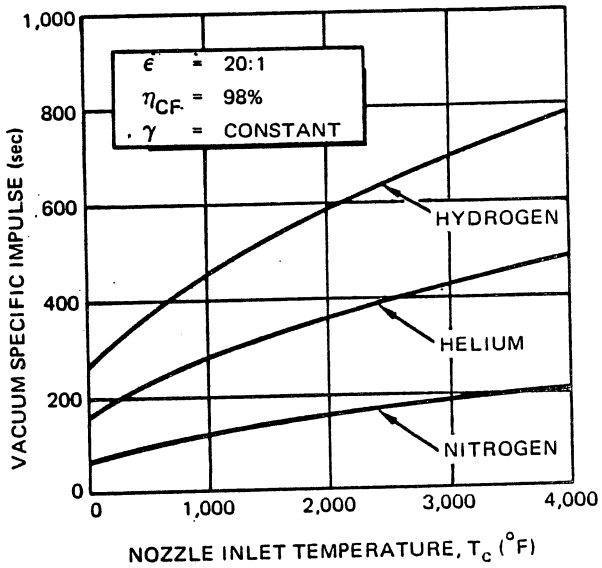

Figure 7-3. Specific Impulse versus Gas Temperature

Substituting equations 2 and 3 into equation 1 yields:

$$I_{sp_{EFF}} = \frac{\bar{I}_{sp}\, w_p}{w_p + w_B + w_{misc}} \qquad (4)$$

In a basic cold gas system, the miscellaneous weight is usually less than 5 to 10 percent of the system weight. For comparison purposes, it is customary to neglect this weight, greatly simplifying the calculations. Thus, neglecting miscellaneous weight, and dividing through by w_p, equation 4 becomes:

$$I_{sp_{EFF}} = \frac{\bar{I}_{sp}}{1 + w_B/w_p} \qquad (5)$$

Since w_B is the weight of a thin-walled spherical bottle, and assuming that the propellant is a perfect gas, effective specific impulse can be expressed as:

$$I_{sp_{EFF}} = \frac{\bar{I}_{sp}}{\left[1 + \dfrac{18\, z_p\, R\, T_p}{(s/\rho)_B}\right]} \qquad (6)$$

where:

z_p = Compressibility factor of propellant gas in bottle

R = Gas constant, ft-lb/lb-°R

T_p = Temperature of propellant gas in bottle, °R

s_B = Allowable bottle skin stress, lb/in^2

ρ_B = Density of bottle material, lb/in^3

Compressibility factors for three candidate propellant gases, hydrogen, helium, and nitrogen, are shown in Figure 7-4 for pressures up to 6,000 psia at room temperature. Compressibility factor is the ratio of the density of a perfect gas to that of a real gas at a given temperature and pressure. Thus, for z-values of less than one, the real gas density is greater than predicted by the perfect gas law, and conversely, high z-values indicate densities less than those given by the perfect gas law. Figure 7-4 shows that for pressures up to 4,500 psia, nitrogen gas can be stored more compactly, in terms of compressibility, than either hydrogen or helium.

At room temperature, using a safety factor of 2, some representative ratios of stress-to-density (s/ρ) for common bottle materials are:

Titanium, 5.0 x 10^5 in.

Aluminum, 3.5 x 10^5 in.

Stainless steel, 1.7 x 10^5 in.

Table 7-1 lists the characteristics of three typical propellant gases: hydrogen, helium, and nitrogen. As a consequence of its low molecular weight, hydrogen has the highest specific impulse of any element. Nitrogen has a specific impulse that is lower than both hydrogen and helium. However, when effective specific impulse is used as a measure of merit, nitrogen is seen to be significantly better than hydrogen or helium.

The values of effective specific impulse given by equation 6 are useful for first-cut comparison. Where detailed system weights are available, or where it is obvious that miscellaneous weights cannot be neglected, the general form of the effective specific impulse formula (equation 4) should be used. Equation 4 should also be used for systems with heat addition, with the weight penalty for the heating system included as part of the miscellaneous weight.

7-2 PERFORMANCE ANALYSIS

Accurate prediction of the performance of a cold gas propulsion system requires analysis of several interdependent transient processes that occur in the system. The propulsion system develops thrust by expelling gas that is withdrawn from the storage bottle. As gas is withdrawn from the bottle, the gas remaining in the bottle goes through an expansion process, which causes a reduction in temperature and pressure of the stored gas. As a consequence of this reduction in temperature, a transfer of heat energy takes place from

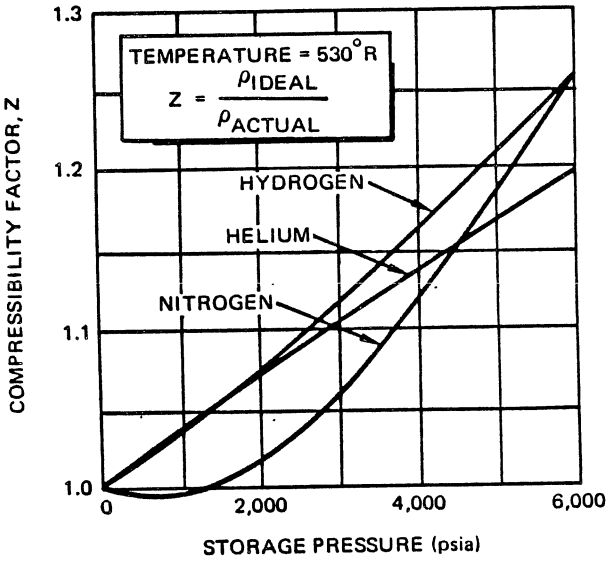

Figure 7-4. Compressibility Factors

the storage bottle and the lines and fittings to the stored gas. The gas that is withdrawn from the storage bottle flows from the supply bottle to the thruster, and is subjected to the effects of friction and heat transfer, both of which vary with the temperature of the gas. Finally, the gas is expanded through the exhaust nozzle, converting the heat energy of the gas into momentum, which results in a reaction thrust.

To predict the interactions of these transient processes, it is first necessary to model the changes in properties of a real gas over the required range of temperatures and pressures. However, the variations in properties of real gases are complex, and models of these properties require families of equations, and often, tables of data. The descriptions of the real processes that occur in the gas system are even more involved, requiring solutions to systems of equations which usually cannot be solved by direct methods, but only by iteration. Because of the complexity of these relationships, their evaluation is usually accomplished by means of an electronic digital computer. One such computer program, G738, developed at MDAC–West for the analysis of cold gas propulsion systems is listed in the Bibliography, Paragraph 7-4.

If ideal conditions are assumed, it is possible to develop a family of cold gas system equations, as given in Table 7-2, which can be solved directly by hand. The ideal cold gas system equations are derived based upon the assumptions:

a. The working fluid is a homogeneous gas, obeying the perfect gas law.

b. Specific heat ratio is constant.

Table 7-1. Characteristics of Typical Propellant Gases

PROPELLANT GAS	SYMBOL	M MOLECULAR WEIGHT	R SPECIFIC GAS CONSTANT (ft-lb/lb-°R)	γ SPECIFIC HEAT RATIO (70°F, 1 atm)	C_F THRUST COEFFICIENT	Z COMPRESS-IBILITY FACTOR	Isp SPECIFIC IMPULSE (sec)	Isp_{EFF} EFFECTIVE SPECIFIC IMPULSE (sec)
HYDROGEN	H_2	2.016	767.0	1.40	1.66	1.160	272	15.2
HELIUM	He	4.000	386.0	1.66	1.53	1.135	163	18.0
NITROGEN	N_2	28.000	55.1	1.40	1.66	1.115	73	33.6

CONDITIONS:
NOZZLE EXPANSION RATIO, ϵ = 20:1
NOZZLE EFFICIENCY, η_{CF} = 98%
PROPELLANT TEMPERATURE, T = 70°F
PROPELLANT PRESSURE, P = 4000 psia
STRESS-TO-DENSITY RATIO, TITANIUM BOTTLE, s/ρ = 5.0×10^5 in.

c. The ambient pressure is zero; nozzle flow is choked.

d. Nozzle flow is frictionless and adiabatic.

e. The regulator throttling process is isenthalpic; thus, for a perfect gas, the process is isothermal.

f. The gas flow through the feed line is subsonic ($M \leq 0.4$).

The equations in Table 7-2 have been developed for two limiting conditions, i.e., adiabatic and isothermal expansion of the gas in the bottle. The expansion of gas in the supply bottle will approach an adiabatic process if the pressure decay is extremely rapid, and the bottle and lines are well insulated. The expansion will approach an isothermal process if the gas flowrates are very low, or if system operation is intermittent, with relatively long periods of non-operation. The operating conditions of real systems will fall somewhere between the conditions defined by these simplified processes. Thus, the values provided by the ideal equations of Table 7-2 are useful in estimating the performance of real systems.

For this analysis, real systems are separated into two categories: those with pressure regulators, and those without regulators. In applications where a constant thrust level is necessary, a pressure regulator must be used. However, when system weight and reliability are more important than a constant thrust level, an unregulated system is usually selected. Therefore, Table 7-2 lists equations for the analysis of both regulated and unregulated systems, with adiabatic or isothermal expansion of the stored gas.

For real gases stored in a supply bottle under pressure, or expanded and cooled during supply bottle blowdown, the specific heat ratio varies appreciably from the nominal (room temperature, one atmosphere) values given in Table 7-1. In addition, the density of a real gas deviates from that predicted by the perfect gas law at high pressures or low temperatures. To compensate for these real gas variations, the value of specific heat ratio which corresponds to the initial supply bottle temperature and pressure should be used with the equations in Table 7-2. Values of specific heat ratio as a function of pressure and temperature are shown in Figures 7-5, 7-6 and 7-7 for hydrogen, helium and nitrogen.

The validity of the equations in Table 7-2 has been verified using computer program, G738, Stored Gas Pressurization and Reaction Control System. A comparison of the results using the equations with the real gas prediction from the computer program shows that the equations predict total impulse to within 5 percent of the value obtained from the computer program for initial bottle pressures up to 6000 psia and initial temperatures in the range of 450°R to 650°R. The error in total impulse is due to compressibility effects which become more significant at the extremes

Table 7-2. Ideal Cold Gas System Venting Equations

PROCESS / PARAMETER	REGULATED SYSTEMS		UNREGULATED SYSTEMS	
	$\eta = \frac{P_C}{P_R}$ $K = f\frac{L}{D}$ 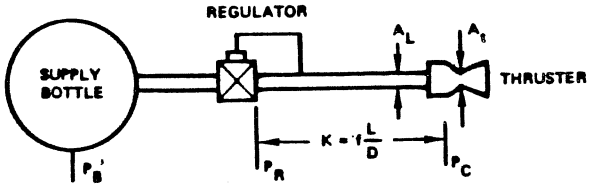		$\eta = \frac{P_C}{P_B}$ $K = f\frac{L}{D}$ 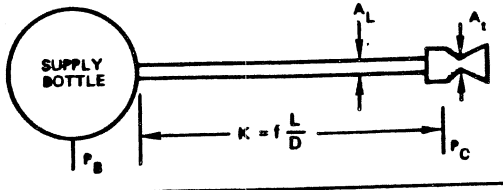	
	ADIABATIC EXPANSION	ISOTHERMAL EXPANSION	ADIABATIC EXPANSION	ISOTHERMAL EXPANSION
CRITICAL FLOW COEFFICIENT, Γ (FIGURE 7-9)	$\Gamma = \sqrt{\gamma\left(\frac{2}{\gamma+1}\right)^{\frac{\gamma+1}{\gamma-1}}}$	$\Gamma = \sqrt{\gamma\left(\frac{2}{\gamma+1}\right)^{\frac{\gamma+1}{\gamma-1}}}$	$\Gamma = \sqrt{\gamma\left(\frac{2}{\gamma+1}\right)^{\frac{\gamma+1}{\gamma-1}}}$	$\Gamma = \sqrt{\gamma\left(\frac{2}{\gamma+1}\right)^{\frac{\gamma+1}{\gamma-1}}}$
FRICTION COEFFICIENT η	$\eta = \frac{P_C}{P_R} = \left[\frac{1+K\Gamma^2}{2}\left(\frac{A_t}{A_L}\right)^2\right]^{-1}$	$\eta = \frac{P_C}{P_R} = \left[\frac{1+K\Gamma^2}{2}\left(\frac{A_t}{A_L}\right)^2\right]^{-1}$	$\eta = \frac{P_C}{P_B} = \left[\frac{1+K\Gamma^2}{2}\left(\frac{A_t}{A_L}\right)^2\right]^{-1}$	$\eta = \frac{P_C}{P_B} = \left[\frac{1+K\Gamma^2}{2}\left(\frac{A_t}{A_L}\right)^2\right]^{-1}$
PROCESS COEFFICIENT a	$a = \eta\Gamma\left(\frac{\gamma+1}{2}\right)\sqrt{gRT_{B_o}} \cdot \frac{A_t P_R}{V_B P_{B_o}}$	$a = \eta\Gamma\sqrt{gRT_{B_o}} \cdot \frac{A_t P_R}{144 V_B}$	$a = \eta\Gamma\left(\frac{\gamma-1}{2}\right)\sqrt{gRT_{B_o}} \cdot \frac{A_t}{144 V_B}$	$a = \eta\Gamma\sqrt{gRT_{B_o}} \cdot \frac{A_t}{144 V_B}$
BOTTLE PRESSURE, P_B (PSIA)	$P_B = P_{B_o}(1-at)^{\frac{2\gamma}{1+\gamma}}$	$P_B = P_{B_o} - at$	$P_B = P_{B_o}(1+at)^{\frac{2\gamma}{1-\gamma}}$	$P_B = P_{B_o} e^{-at}$
BOTTLE TEMPERATURE, T_B (°R)	$T_B = T_{B_o}(1-at)^{\frac{\gamma-1}{2(\gamma+1)}}$	$T_B = T_{B_o}$	$T_B = T_{B_o}(1+at)^{-2}$	$T_B = T_{B_o}$
WEIGHT FLOWRATE, $\dot{w}$ (LB/SEC)	$\dot{w} = \eta\Gamma A_t P_R\sqrt{\frac{g}{RT_{B_o}}} \cdot (1-at)^{-\frac{\gamma-1}{\gamma+1}}$	$\dot{w} = \eta\Gamma A_t P_R\sqrt{\frac{g}{RT_{B_o}}}$	$\dot{w} = \eta\Gamma A_t P_{B_o}\sqrt{\frac{g}{RT_{B_o}}} \cdot (1+at)^{\frac{\gamma+1}{1-\gamma}}$	$\dot{w} = \eta\Gamma A_t P_{B_o}\sqrt{\frac{g}{RT_{B_o}}} \cdot e^{-at}$
THRUST, F (LB)	$F = \eta P_R A_t C_F$	$F = \eta P_R A_t C_F$	$F = \eta P_{B_o} A_t C_F (1+at)^{\frac{2\gamma}{1-\gamma}}$	$F = \eta P_{B_o} A_t C_F e^{-at}$
SPECIFIC IMPULSE, I_{sp} (SEC)	$I_{sp} = \frac{C_F}{\Gamma}\sqrt{\frac{RT_{B_o}}{g}}(1-at)^{\frac{\gamma-1}{\gamma+1}}$	$I_{sp} = \frac{C_F}{\Gamma}\sqrt{\frac{RT_{B_o}}{g}}$	$I_{sp} = \frac{C_F}{\Gamma}\sqrt{\frac{RT_{B_o}}{g}}(1+at)^{-1}$	$I_{sp} = \frac{C_F}{\Gamma}\sqrt{\frac{RT_{B_o}}{g}}$
AVERAGE SPECIFIC IMPULSE, $\bar{I}_{sp}$ (SEC) (1)	$\bar{I}_{sp} = \frac{2}{\gamma+1}\frac{C_F}{\Gamma}\sqrt{\frac{RT_{B_o}}{g}}\left[\frac{1-(P_R/P_{B_o})^{\frac{\gamma+1}{2\gamma}}}{1-(P_R/P_{B_o})^{1/\gamma}}\right]$	$\bar{I}_{sp} = I_{sp}$	$\bar{I}_{sp} = \frac{2}{\gamma+1}\frac{C_F}{\Gamma}\frac{P_{B_o}V_B}{\sqrt{gRT_{B_o}}}\left[\frac{1-(P_{B_f}/P_{B_o})^{\frac{\gamma+1}{2\gamma}}}{1-(P_{B_f}/P_{B_o})^{1/\gamma}}\right]$	$\bar{I}_{sp} = I_{sp}$
TOTAL IMPULSE, I_t (LB-SEC) (1)	$I_t = \frac{V_B}{R}\bar{I}_{sp}\left[\frac{P_{B_o}}{Z_{B_o}T_{B_o}} - \frac{P_{B_f}}{Z_{B_f}T_{B_f}}\right]$	$I_t = \frac{V_B}{RT_{B_o}}\bar{I}_{sp}\left[\frac{P_{B_o}}{Z_{B_o}} - \frac{P_{B_f}}{Z_{B_f}}\right]$	$I_t = \frac{V_B}{R}\bar{I}_{sp}\left[\frac{P_{B_o}}{Z_{B_o}T_{B_o}} - \frac{P_{B_f}}{Z_{B_f}T_{B_f}}\right]$	$I_t = \frac{V_B}{RT_{B_o}}\bar{I}_{sp}\left[\frac{P_{B_o}}{Z_{B_o}} - \frac{P_{B_f}}{Z_{B_f}}\right]$

(1) I_{SP} AND I_T BASED ON EXPANSION TO P_R (REGULATED SYSTEMS) OR P_{B_f} (UNREGULATED SYSTEMS)

Table 7-2. Ideal Cold Gas System Venting Equations (Continued)

SYMBOLS

A_L	FEED LINE (EQUIVALENT) AREA, in^2
A_t	NOZZLE THROAT AREA, in^2
a	PROCESS COEFFICIENT, sec^{-1}
C_F	THRUST COEFFICIENT
D	FEED LINE DIAMETER, in.
e	NATURAL LOGARITHM, BASE, 2.718···
F	THRUST, lb
f	DARCY FRICTION FACTOR
g	GRAVITATIONAL CONSTANT, 32.17 ft/sec^2
K	FRICTION EQUIVALENT LENGTH
L	FEED LINE LENGTH, in.
P_B	BOTTLE PRESSURE, psia
P_c	CHAMBER (NOZZLE INLET) PRESSURE, psia
P_R	REGULATOR OUTLET PRESSURE, psia
R	GAS CONSTANT, ft-lb/lb-°R
T_B	BOTTLE TEMPERATURE, °R
t	TIME, sec
V_b	BOTTLE VOLUME, ft^3
w	WEIGHT FLOWRATE, lb/sec
Z	COMPRESSIBILITY FACTOR
Γ	CRITICAL ISENTROPIC FLOW FUNCTION
γ	SPECIFIC HEAT RATIO, C_p/C_v
η	LINE FRICTION COEFFICIENT

SUBSCRIPTS

B	BOTTLE
c	CHAMBER (NOZZLE INLET)
f	FINAL BOTTLE CONDITION
L	LINE
o	INITIAL CONDITION
R	REGULATOR
t	NOZZLE THROAT

of pressure or temperature. The compressibility factor to be used in the total impulse equation of Table 7-2 may be obtained from a reduced state correlation presented in Figures 7-8 and 7-9.

Since the equations were derived for an ideal gas, those gases, such as helium, which behave in this manner will be characterized reasonably well by these equations as shown in Figure 7-10. For gases such as nitrogen, which deviates markedly from ideal behavior (especially near the critical point), the calculated temperature may be in error by as much as 50 percent in some cases. For this reason, the final temperature to be used in the total impulse equation should never be less than the critical temperature. In fact, the final temperature in a rapid blowdown process will be approximately 50°R to 100°R above the critical value, as evidenced by the data in Figures 7-11 and 7-12 which show the temperature and pressure history in a 415 $in.^3$ nitrogen gas bottle.

The critical temperature is not reached because the natural convection heat transfer process (in small containers undergoing rapid expansion forced convection will also be important) adds heat to the gas and thus lowers the rate of temperature and pressure decay. This process is, of course, no longer adiabatic and is best analyzed with the aid of a computer program.

The thrust coefficients used in the ideal cold gas equations are based on the specific heat ratios given in Table 7-1. Vacuum thrust coefficients for typical values of specific heat ratio are shown plotted as a function of nozzle expansion ratio in Figure 7-13. To further facilitate the use of Table 7-2, a curve of critical isentropic flow function, Γ, is given in Figure 7-14 as a function of specific heat ratio.

7-3 NOZZLE PERFORMANCE EFFECTS

The performance predictions for low-thrust cold gas nozzles are subjected to uncertainties which are generally insignificant in larger chemical rockets. Condensation and boundary layer effects can influence nozzle performance, and the quantitative effects of these phenomena on specific impulse and thrust have been given much attention by cold gas system designers.

Theoretically, the performance of nozzles with condensing fluids cannot be calculated with the same formulas that are used for noncondensing fluids because of the two-phase flow that develops. However, it appears from the experimental data available that, for reasonably well designed nozzles, the effects of condensation are not significant for the commonly used propellant gases, because of the short residence times of the gases in the nozzles.

In the cold gas nozzle expansion process, condensation normally will not develop at the theoretically predicted saturation point due to the absence of suitable surfaces or nuclei to promote it. The short residence times also act to suppress incipient condensation.

The theoretical condensation point can be estimated from a cross-plot of the appropriate vapor-pressure curve with the isentropic process line which passes through the known initial conditions. Figure 7-15 illustrates such a cross-plot assuming nitrogen with nozzle inlet conditions of 10 psia and 530°R. The intersection predicts condensation at 0.02 psia and 90°R, corresponding to an exit pressure ratio (P_e/P_c) of 0.002 and an expansion ratio of 24:1.

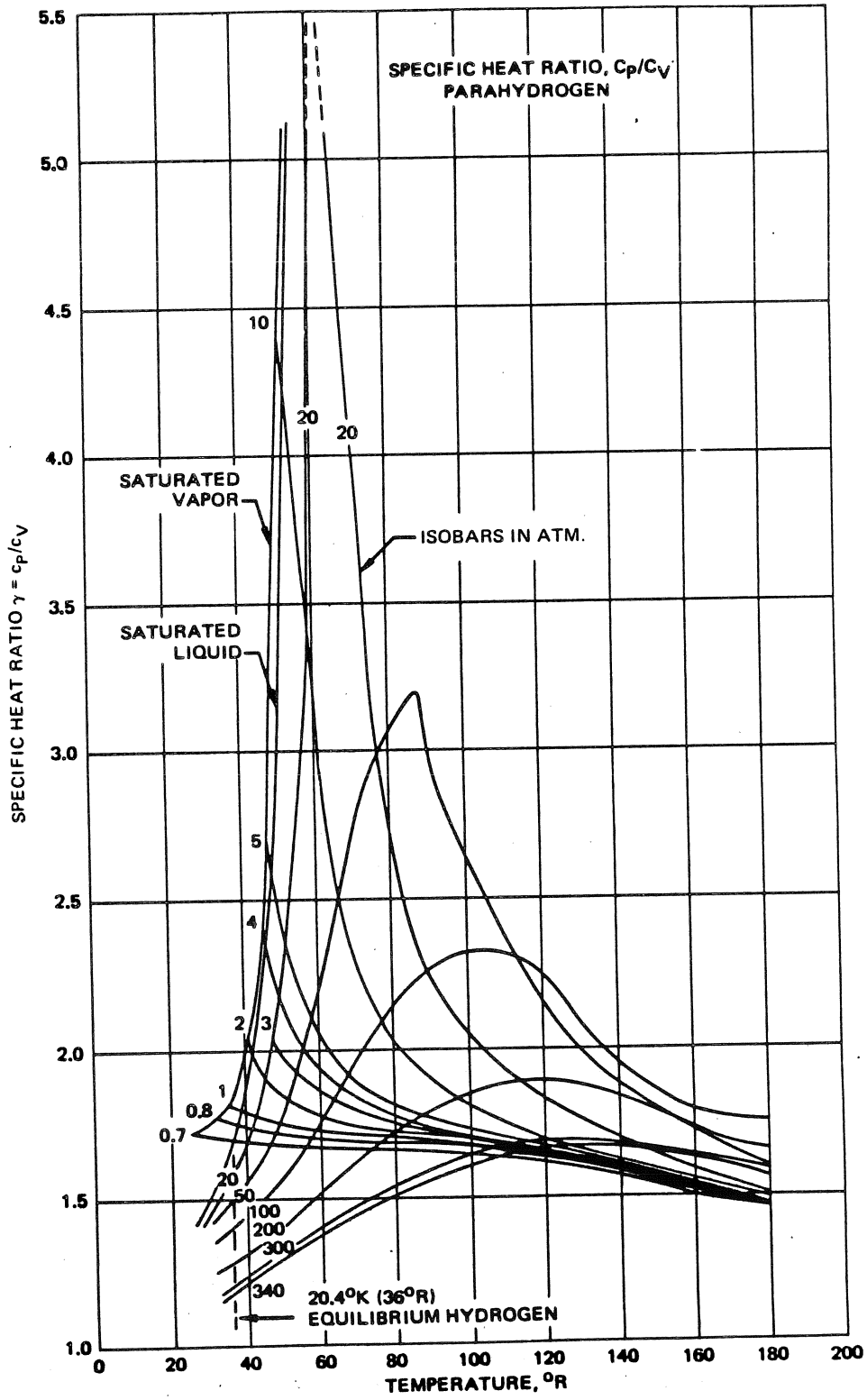

Figure 7-5. Parahydrogen Specific Heat Ratio (γ) Data

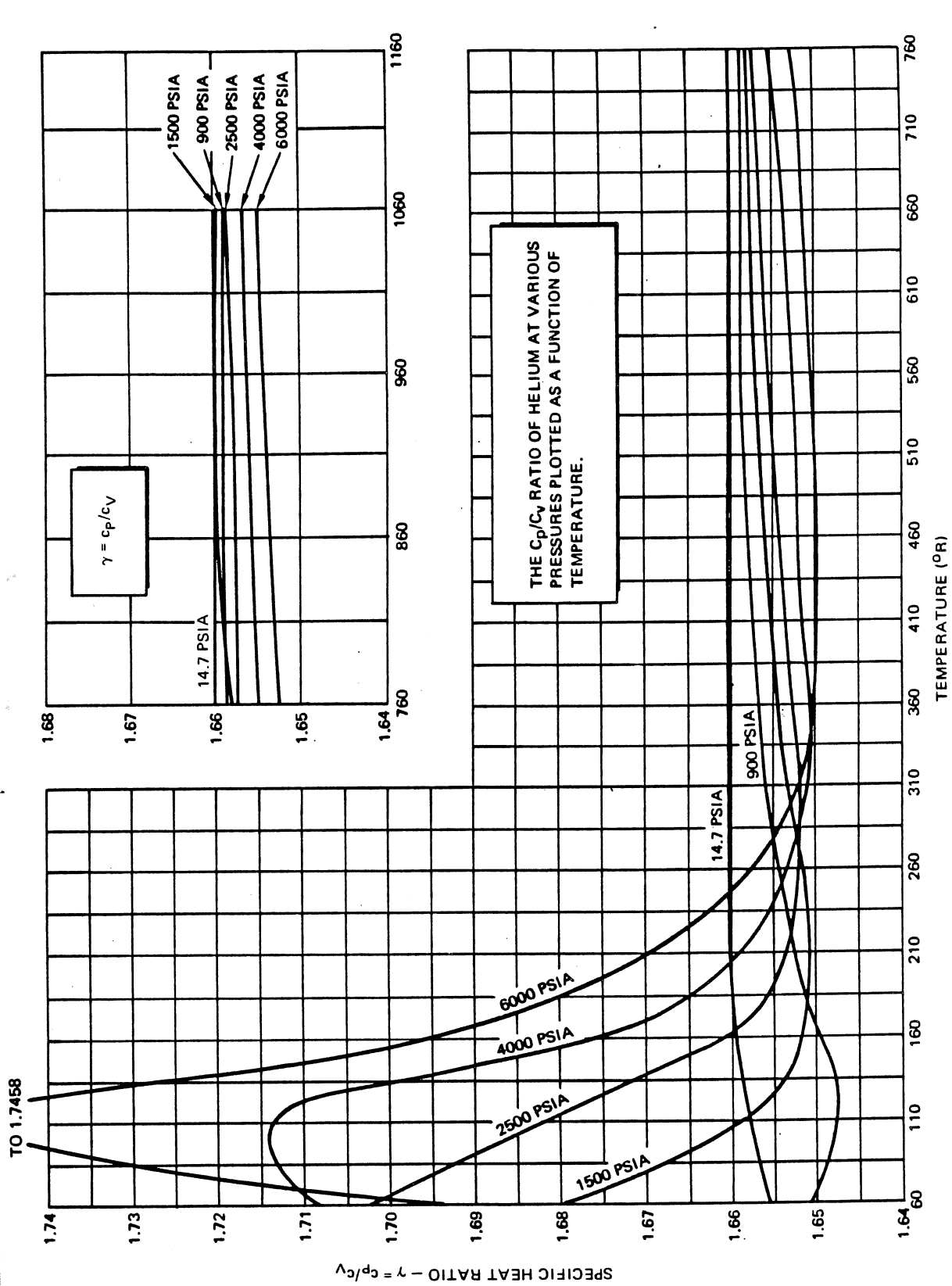

Figure 7-6. Helium Specific Heat Ratio (γ) Data

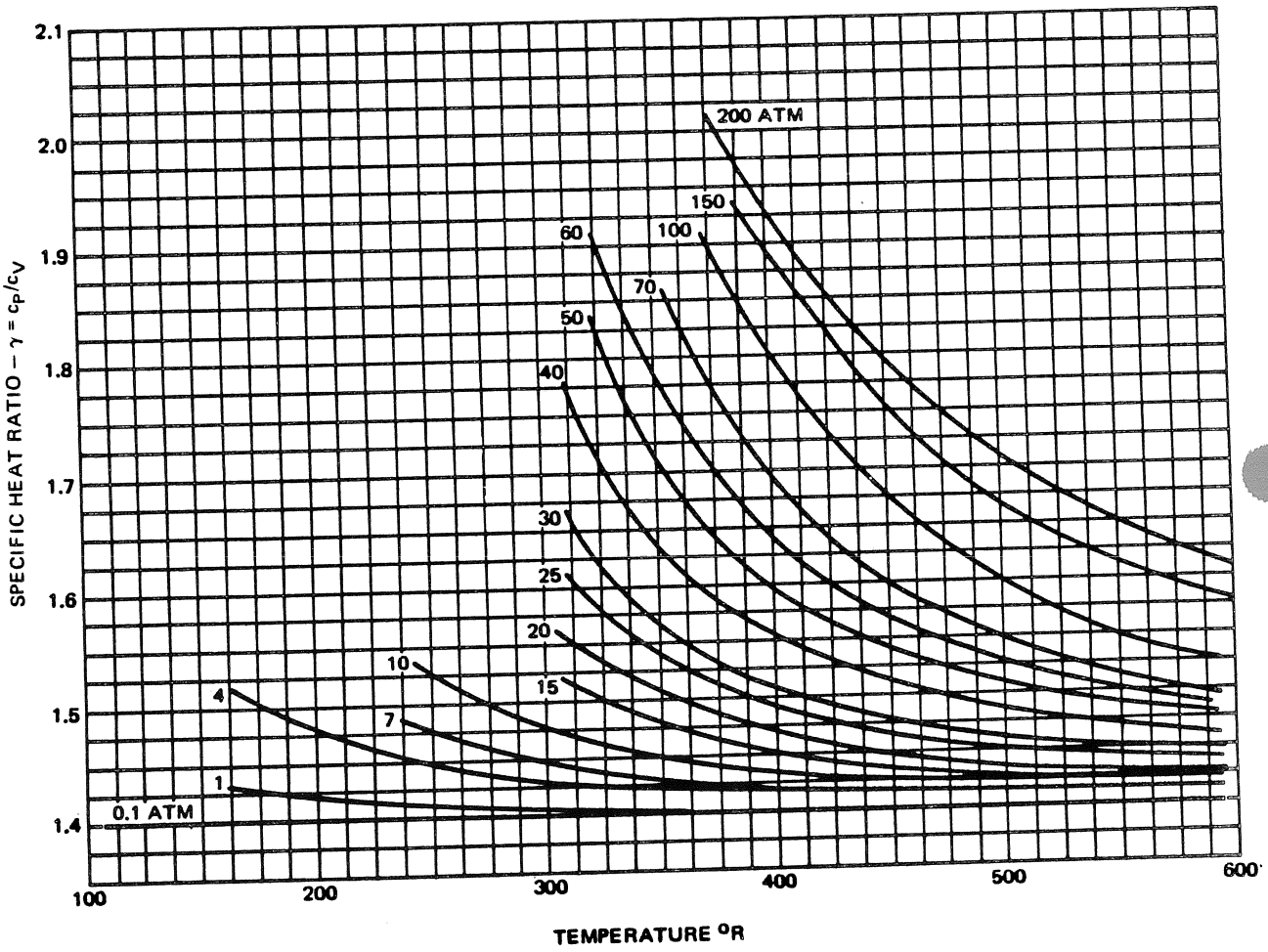

Figure 7-7. Nitrogen Specific Heat Ratio (γ) Data

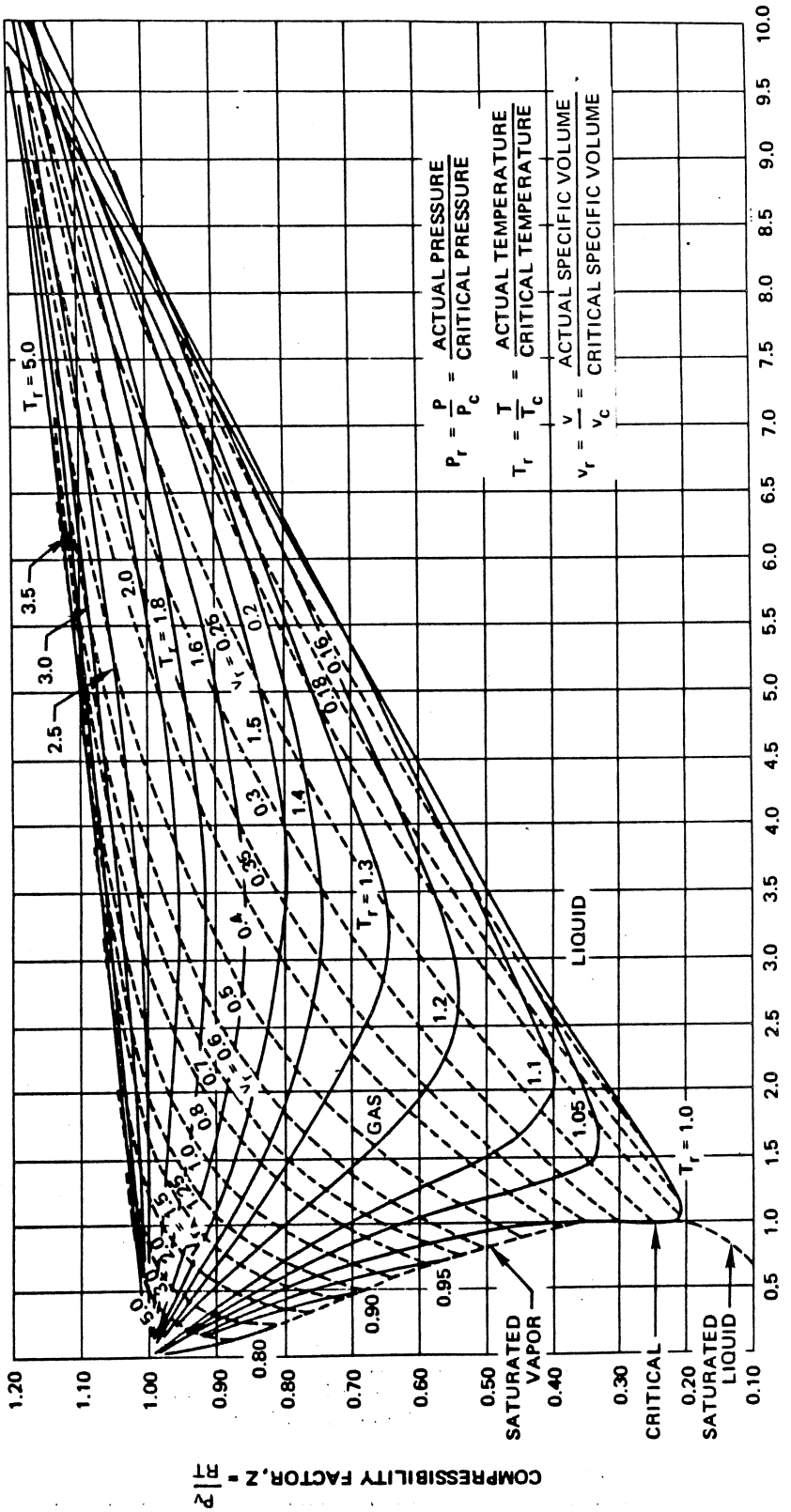

Figure 7-8. Compressibility Chart

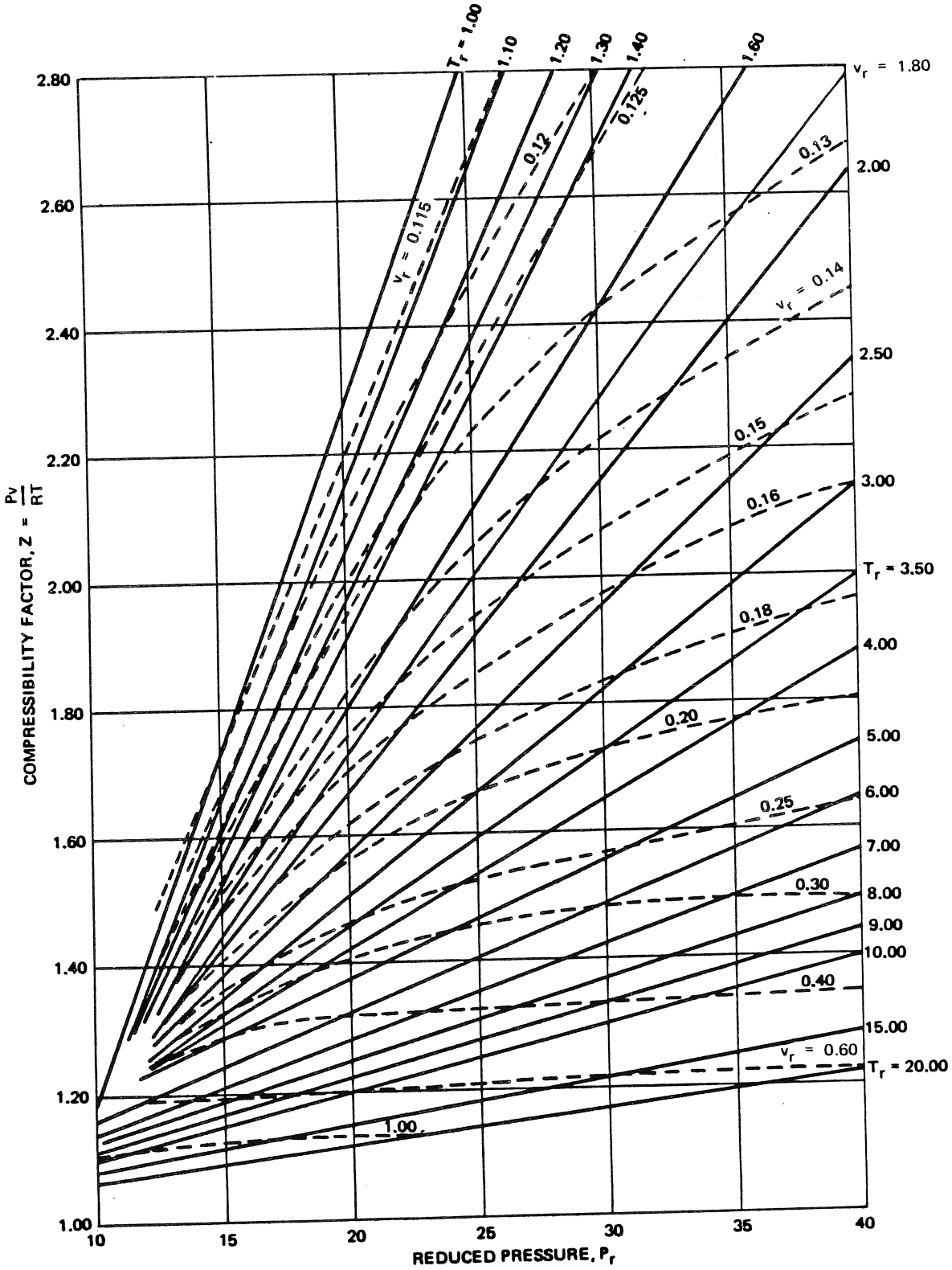

Figure 7-9. High Pressure Compressibility Chart

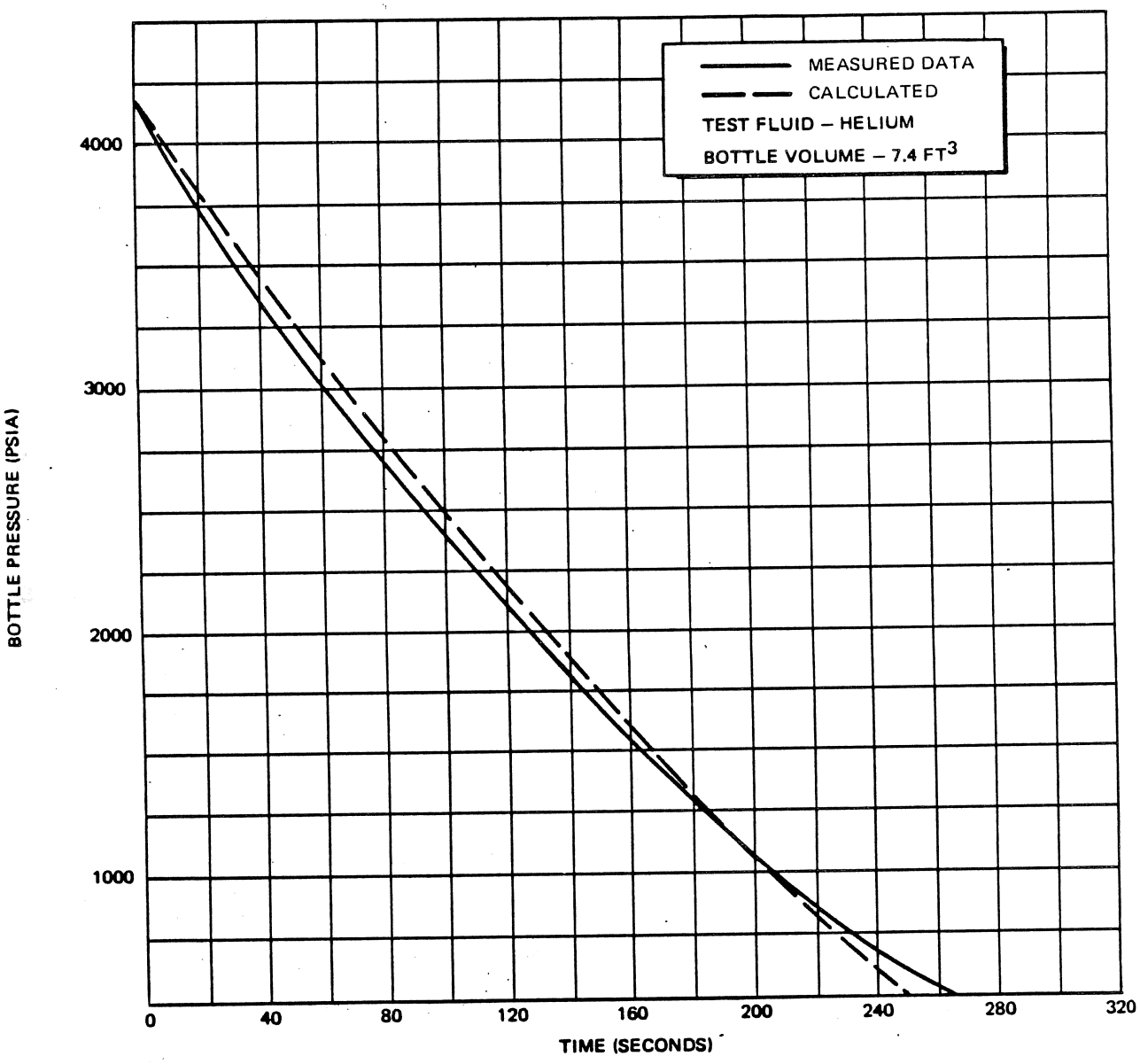

Figure 7-10. Tank Blowdown Pressure versus Prediction

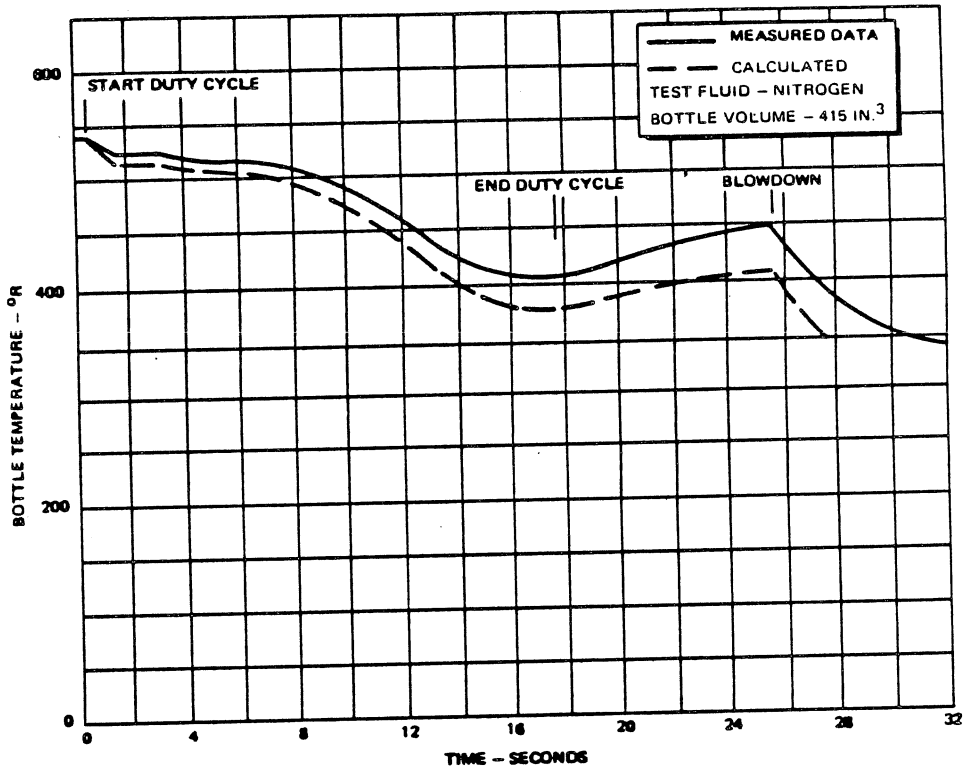

Figure 7-11. Calculated and Actual Bottle Temperature History

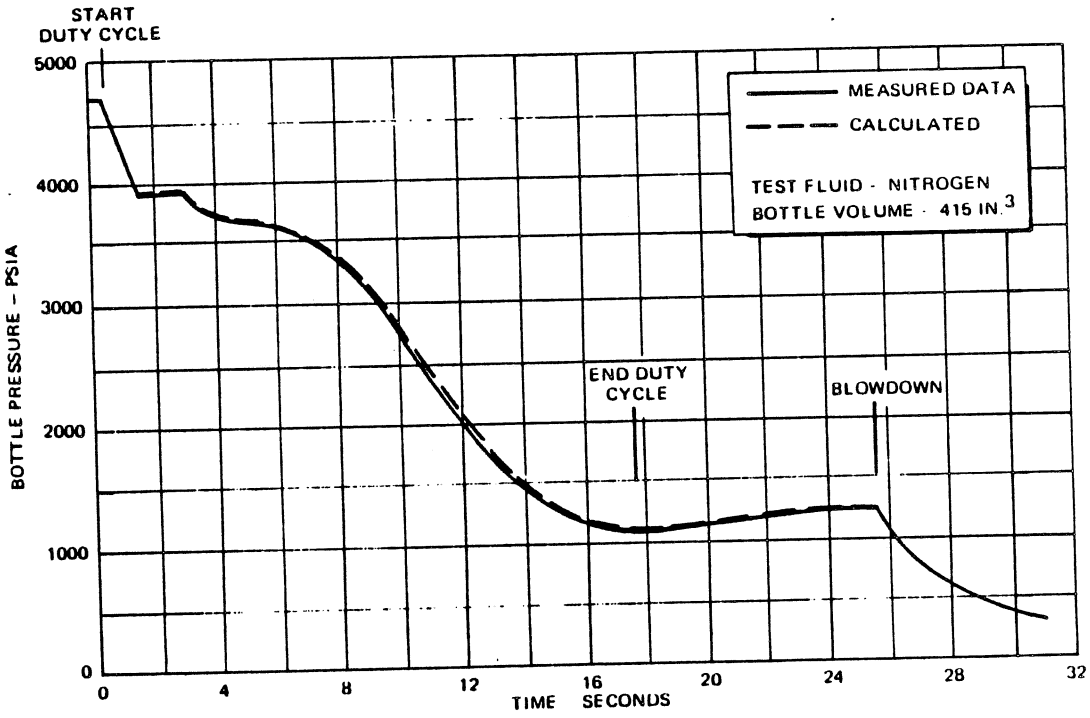

Figure 7-12. Calculated and Actual Bottle Pressure History

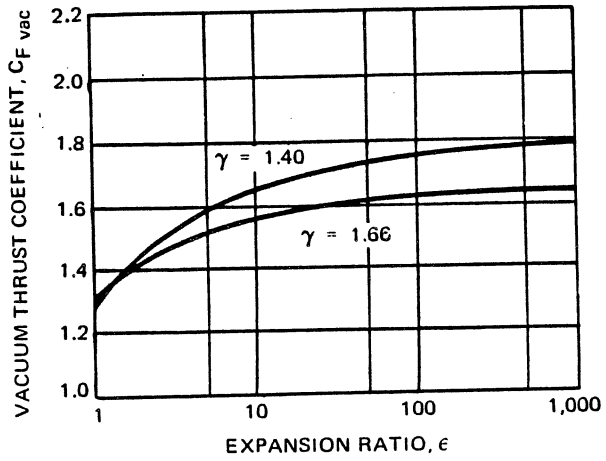

Figure 7-13. Vacuum Thrust Coefficients

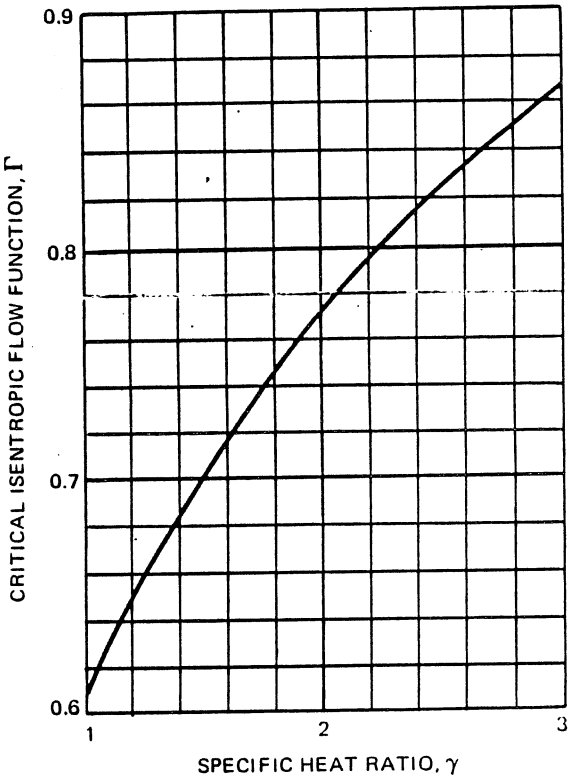

Figure 7-14. Critical Isentropic Flow Function

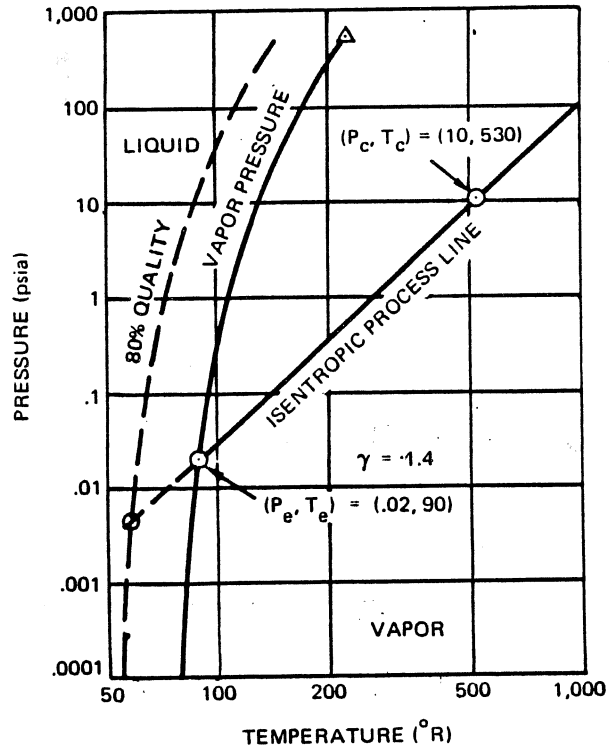

Figure 7-15. Pressure-Temperature Relationships for Nitrogen

In a real nozzle, single phase supersaturated vapor flow will persist past this predicted condensation point until spontaneous formation of nuclei within the flow leads to collapse of the metastable state. This homogeneous condensation can occur only after the small clusters of vapor nuclei exceed a critical radius. Available experimental data indicate this will occur in the 5 percent to 20 percent supersaturated regime. Since the standard formulas for noncondensing flow may be used with good accuracy at least to the point of actual condensation, it follows that the selection of nozzle expansion ratio should be based on criteria other than the theoretical condensation point. Furthermore, there is evidence which shows that an increase in thrust (between 1 percent and 10 percent) may be expected under two-phase flow conditions. Performance predicted by the equations for single phase flow thus is conservative when compared with a real case.

When homogeneous condensation begins to appear, it will form primarily around the nozzle axis away from the nozzle wall and boundary layer. The thrust increase associated with two-phase flow, as compared with ideal gas performance prediction, is due to the energy transferred to the remaining gas by the condensing gas. The release of latent heat from the condensate serves to accelerate the vapor phase and leads to slip flow and

thermal lag between the phases. These effects degrade the specific impulse potentially available, but not below what the ideal gas equations would predict. Thus the nozzle expansion ratio choice may be based on a weight versus thrust coefficient tradeoff without regard to deleterious effects of two-phase flow, at least to the pressure ratio associated with a theoretical predicted 80 percent vapor line, as shown in Figure 7-15.

In small nozzles, boundary layer growth can lead to a significant decrement in specific impulse. Boundary layer losses are most significant for thrust levels below 0.1 lb, but become negligible for thrust levels above 0.5 lb because of Reynolds number effect. An empirical equation for thrust coefficient loss developed by NASA is given as:

$$\delta C_F = \frac{17.6e^{0.003\ 2\epsilon}}{\sqrt{Re_t}} \qquad (7)$$

where:

δC_F = Theoretical C_F – actual C_F

ϵ = Nozzle expansion ratio

Re_t = Reynold's number at nozzle throat

The Reynold's number at the nozzle throat may be computed from:

$$Re_t = \frac{12}{\mu_t} \cdot \frac{\Gamma D_t P_c}{\sqrt{g R T_c}} \qquad (8)$$

$$= 0.05975 \frac{\Gamma P_c}{\mu_t} \sqrt{\frac{M A_t}{T_c}}$$

where

μ_t = Gas viscosity at nozzle throat, lb-sec/ft^2

The gas viscosity at the nozzle throat is obtained from a temperature viscosity curve such as given in Figure 7-16. The temperature of the gas at the throat is computed from nozzle inlet temperature by means of equation 9.

$$T_t/T_c = \frac{2}{\gamma + 1} \qquad (9)$$

For ease in computation, values of the temperature ratio in equation 9 are shown plotted in Figure 7-17.

Experiments conducted with hydrogen, nitrogen and freon flowing at Reynold's numbers from 10,000 to 53,000 showed that the actual thrust coefficient in small nozzles is about 0.39 less that the theoretical value. Viscous losses and changes in the free-stream flow conditions cause an additional 3 percent decrease in actual thrust coefficient.

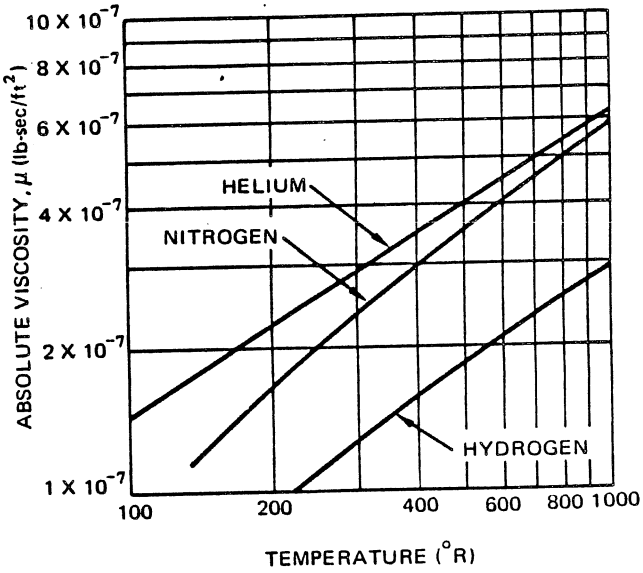

Figure 7-16. Gas Viscosities

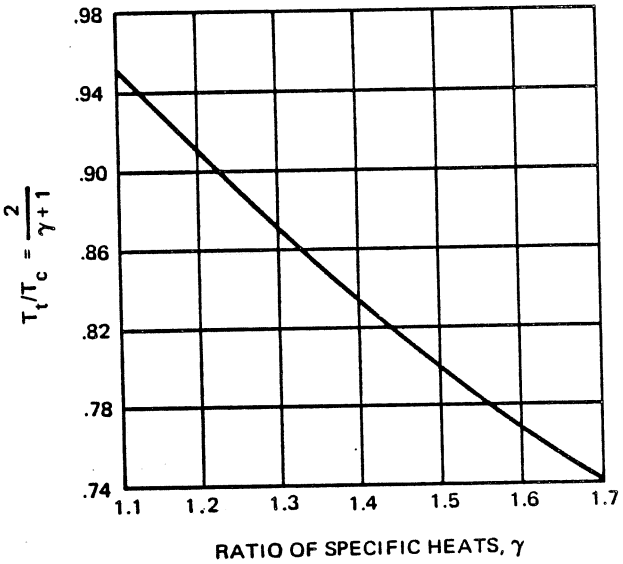

Figure 7-17. Critical Temperature Ratio

7-4 BIBLIOGRAPHY

1. *Electrothermal and Radioisotope Heated Propulsion for Spacecraft Reaction Control*, TRW Systems Group, February, 1968.

2. C. Bonner, *Reaction Control Systems Study*, DAC 61736, McDonnell Douglas Astronautics Co., November, 1968.

3. H. M. Briscoe, "The Choice of Propellant for a Cold Gas Propulsion System for a Satellite," *Journal of the British Interplanetary Society*, Vol 20, 1965-66.

4. H. Greer, "Propulsive Performance of a Cold-Gas Attitude-Control Reaction-Jet System", *Journal of Spacecraft and Rockets* Vol 3 No. 3, March 1966.

5. W. H. Robinson, *Stored Gas Pressurization and Reaction Control Program (G738)*, MDC G0170, McDonnell Douglas Astronautics Co., January, 1970.

6. E. W. Spisz, et al, *Thrust Coefficients of Low-Thrust Nozzles,* NASA TN D-3056, October 1965.

7. P. P. Wegener, *Condensation Phenomena in Nozzles,* Preprint No. 63-509 AIAA Heterogeneous Combustion Conference, December 1963.

8. H. Greer and D. J. Griep, *Dynamic Performance of Low Thrust Cold Gas Reaction Jets in a Vacuum,* Aerospace Report TR-699 (6230-33)-1.

Section 8
NUCLEAR PROPULSION THRUSTERS

The nuclear rocket produces thrust by expelling a high-temperature gas through a supersonic nozzle, just as the chemical rocket. However, instead of producing high-temperature gases by chemical combustion, the nuclear rocket uses heat released from a nuclear energy source to heat the working fluid. No chemical change (except dissociation) takes place in the working fluid. Hydrogen is the preferred working fluid because of its low molecular weight, and consequently, high specific impulse.

There are two important sources of nuclear energy for rocket propulsion: nuclear fission and radioactive isotope decay. In the first, thermal energy is generated by fission in a nuclear reactor. The heat is then transferred to the working fluid, which is heated to a high temperature and expelled through a nozzle. With radioisotope rockets, the working fluid is heated by passing it through a special capsule containing a concentrated radioactive material which, in its decay process, produces heat.

It is anticipated that the nuclear reactor rocket will be the major contender for primary propulsion of future manned interplanetary space vehicles. On the other hand, radioisotope thrusters are best suited for auxiliary propulsion applications such as attitude control and stationkeeping.

8-1 NUCLEAR REACTOR ROCKETS

An important objective of all primary thrust rocket engines is a high specific impulse so that the amount of propellant required to accomplish a mission is minimized. A high specific impulse is achieved by heating a propellant with a low molecular weight to a high temperature. In a nuclear rocket, hydrogen, which has the lowest molecular weight of all the elements, is used as the propellant, and the thermal energy necessary for heating the propellant is provided by a nuclear reactor. The rate of energy release from a nuclear reaction, and therefore the temperature of the reaction that could theoretically be obtained, is almost unlimited. However, at these high temperatures, the reduced strength of the materials used in the reactor limits the maximum temperature to which the propellant can be heated.

There are three types of nuclear reactors theoretically possible for space nuclear propulsion systems: solid-core, liquid-core, and gaseous-core reactors. The core of the reactor is the region containing the fissionable material, or fuel, which reacts to give heat. In a solid-core reactor, the fissionable material is contained in a solid material such as tungsten or graphite. In the case of the liquid- or gaseous-core reactor, the fuel is contained in the core in liquid or gaseous form, respectively.

Solid-core systems will have specific impulses of about 850 seconds, with thrust-to-engine-weight ratios from 2 to 20. A vacuum specific impulse of more than 760 sec, at an exit gas temperature of 4,090°R, and a thrust of about 55,000 lb (with a 40:1 area ratio) have been demonstrated in a solid-core reactor. The ability to restart the system and return to full specific impulse and power has also been demonstrated, as has the ability to control the system over the entire operating range from startup to full power. The technology with which to develop a high thrust (250,000 lb) operational solid core nuclear engine is largely available.

Calculations indicate that liquid-core reactors could perform in the specific impulse range of 1,200 to 1,500 sec. Any thrust level can be obtained depending on the size of the reactor. The thrust-to-engine-weight ratio for these systems would be in the range of 1 to 10. An overriding disadvantage of the liquid-core system is the high fuel-loss ratio anticipated. Loss rates of 0.01 to 0.1 pound of uranium per pound of hydrogen expelled can be expected.

Specific impulses in the range of 1,500 to 2,500 sec are theoretically feasible using gas-core reactors, with thrust-to-engine-weight ratios from 1 to 20. Gas-core reactors tend to be very large, but can have high thrust-to-weight ratios. As in the case of the liquid-core system, the fuel-loss ratio will be high.

The U.S. Nuclear Rocket Program (Project Rover) began in 1955, and the major effort in this program has been devoted to the study of graphite solid-core nuclear engines. Table 8-1 lists the highlights of the testing accomplished on this program. As indicated in the table, testing has been concentrated in the reactor technology program, under Los Alamos Scientific Laboratory

Table 8-1. Nuclear Rocket Program Testing Highlights

CATEGORY	SYSTEM	PURPOSE	DESCRIPTION*	DATE	REMARKS
Reactor Technology Program	Kiwi-A	Initial Feasibility Demonstration	R&D Reactor; P = 100 MW $\dot{w}$ = 7 lb/sec GH_2 T_c = 3200 °R	Jul 1959 to Oct 1960	First rocket reactor power test, Kiwi-A. Kiwi-A-prime, Kiwi-A3: Tests of Kiwi-B core design features; structural weakness of core identified.
	Kiwi-B	Development of Flight Reactor Design	R&D Reactor; P = 1100 MW $\dot{w}$ = 70 lb/sec LH_2 T_c = 3200°R	Dec 1961 to Sep 1964	Major development problem was dynamic instability causing core vibration; 1 1/2 years of development effort required to demonstrate fix. Kiwi-B4D first successful reactor power test at flight power level. Kiwi-B4E demonstrated restart and endurance.
	Kiwi-TNT	Safety Demonstration	R&D Reactor; Same as Kiwi-B, but with large amounts of excess radioactivity inserted in fraction of second.	Jan 1965	Test demonstrated safety of public and launch personnel under worst possible conditions. (Launch abort)
	Phoebus	Advanced Technology Reactor	R&D Reactor; P = 5000 MW I_{sp} = 800 sec T_c = 4500°R	Jun 1965 to Jul 1968	Several design improvements based on Kiwi/NRX core technology. Increased power density, core size, nozzle inlet temperature, and Isp. Fuel corrosion halved by new fuel element design.
	Pewee	Fuel and Core Experiments	R&D Reactor; P = 400 MW Performance may be varied to suit experiment	Nov 1968 (Tests Started)	This small reactor provides a short-turn-around time, relatively inexpensive test bed for fuel element and core support designs.
NERVA Engine Program	NRX-A	Demonstrate Flight Reactor Design	Prototype NERVA Reactor; P = 100 MW I_{sp} = 760 sec T_c = 4090°R	Sep 1964 to Dec 1967	NRX-A series of reactors operated for 1 hour under close control. Fuel element corrosion reduced 80 percent.
	NRX/EST	Demonstrate Flight Engine Hardware	Breadboard Engine; Performance data, same as NRX-A	Dec 1965 to Mar 1966	First operation of nuclear rocket engine system; demonstration of engine control; multiple restarts, and endurance (30 min at rated output)
	XE	Demonstrate Flight Engine	Prototype Flight Engine; Performance data: See Table 8-2	Apr 1968 (Tests Started)	Downward firing NERVA Ground Experimental Engine: engine operational characteristics tests complete NERVA technology program.

*T_c = Nozzle inlet temperature. Core temperatures are appreciably higher.

(LASL), and in the Nuclear Engine for Rocket Vehicle Application (NERVA) program, directed by AEC-NASA Space Nuclear Propulsion Office.

The LASL reactor effort includes the early Kiwi reactor tests, the Phoebus tests, and the Pewee tests. The Aerojet-Westinghouse NERVA engine program has included tests on the prototype flight reactor design (NRX-A), the breadboard engine (NRX/EST), and the prototype flight engine (XE). The flight configuration of the NERVA engine is illustrated in Figure 8-1, and the performance specifications for this engine are given in Table 8-2.

Other significant phases of the Rover program include the development of non-nuclear components by NASA-Lewis, and a contract to Lockheed to design and build a reactor flight test vehicle (Reactor Inflight Test, RIFT: Initiated in May 1962, but subsequently cancelled for lack of funds).

Table 8-2. NERVA Engine Performance

SYMBOL	PARAMETER	VALUE
F	Thrust (lb)	75,000 ± 2000
I_{sp}	Specific Impulse (sec)	825
P_c	Chamber Pressure (psia)	450
ϵ	Expansion Ratio	100:1
Δt	Endurance at Rated Conditions (min)	600
T_c	Nozzle Inlet Temperature (°R)	4500
– –	Propellant	Hydrogen
w_{ps}	Engine Weight, Maximum (lb)	20,000
w_p	Propellant Weight (lb)	180,000 to 290,000

8-1.1 Nuclear Reactor Theory

The source of energy for nuclear power plants is the fission process. An atom, upon absorbing a neutron, becomes unstable and splits into fragments. Some of the matter in the original atom disappears in the process and is converted into heat and other radiant energy. It is this heat that is of interest for the production of power. The highly penetrating, deadly radiation that accompanies the fission can be regarded as something of a nuisance – a nuisance which results in much of the complication in the design of nuclear reactors.

A reactor represents that part of a nuclear power plant where the fission chain reaction is made to occur and where the heat is generated for operating power conversion equipment. The core of the reactor is typically an assemblage of fuel elements, control rods, coolant, and moderator.

The fuel elements are made of plates or rods of uranium metal or ceramic. The plates or rods are usually clad in a thin sheath of refractory metal to provide corrosion resistance, retention of radioactivity and, in some cases, structural support. The coolant, which can be a gas, water, or organic or liquid metal, removes the heat produced in the fuel plates. In a nuclear rocket, the hydrogen propellant acts as the coolant.

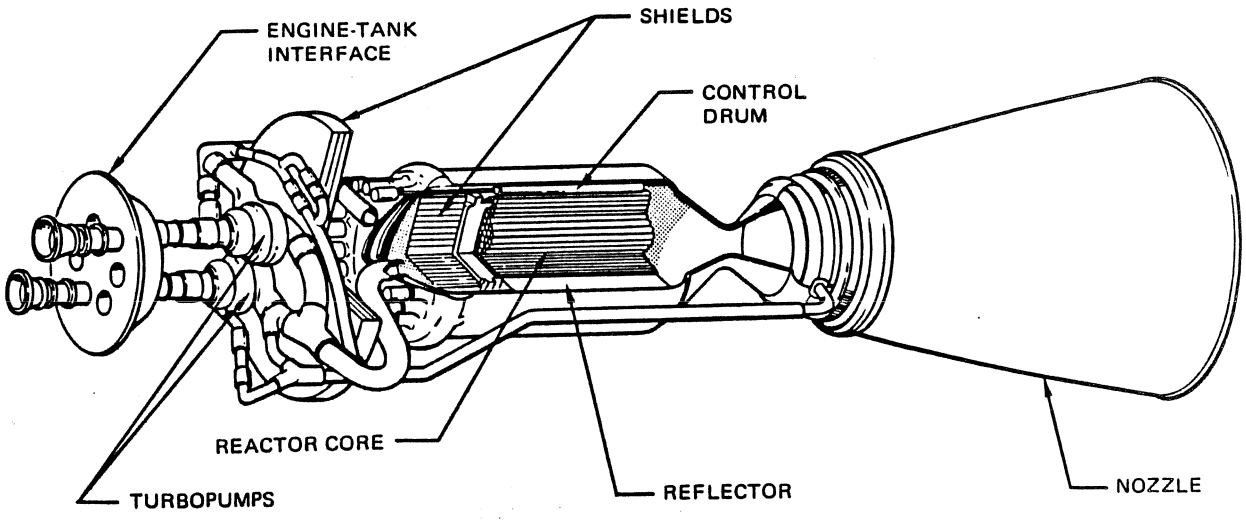

Figure 8-1. Flight Configuration of NERVA Engine

The moderator, commonly water or graphite, is dispersed between the fuel assemblies. It serves to slow down, or moderate, the fast neutrons produced in fission. These lower velocities provide a better opportunity for the neutrons to cause further fission.

The control rods are made of a neutron-absorbing material and, upon movement in or out of the core, vary the number of neutrons available to maintain the chain reaction. The rate of fissioning can thereby be controlled.

A reflector is often placed around the core to reflect back some of the neutrons that leak out from the surface of the core. The reflector is often of the same material as the moderator.

The support structures include the grid plates which position and hold the fuel elements and control rods as well as shrouds and skirts for directing coolant flow.

A biological shield is placed either inside or outside the pressure vessel. This shield, which is made of dense material such as concrete or steel, protects operating personnel from the radiation produced in the core.

8-1.1.1 Nuclear Fission

Some of the isotopes of the heaviest elements, uranium-235, uranium-233, and plutonium-239, can, upon absorbing neutrons, be readily fissioned. This fission of the nucleus produces two, or occasionally three, fragments moving at high speeds, two or three new free neutrons, and considerable radiant energy.

If just one of the two or three neutrons produced in the fission of an atom can be made to fission another atom, and one of the neutrons from this second fission can be made to cause a third fission, and so on, a self-perpetuating chain reaction will result.

The energy resulting from the fission of a uranium-235 atom is distributed among the various products of fission as follows:

	MeV
Kinetic energy of the fission fragments	162
Kinetic energy of the neutrons	6
Instantaneous gamma ray energy	6
Radioactive decay energy	21
Total	195

In order that a chain reaction be maintained, the number of neutrons absorbed by all processes must equal the number produced in fission. At least one of the neutrons produced in each fission must, on the average, cause another fission. The manner in which fission neutrons are distributed among the various absorption processes is termed the neutron economy or the neutron balance.

The kinetic energy of the fission fragments and the radiant energy are ultimately converted into heat in the surrounding material. It is this heat which is transferred to the propellant, and subsequently converted into kinetic energy.

8-1.1.1.1 Fission Fragments

The properties of each of the various products from fission (the fission fragments, the neutrons, and the radiation) are the determining factors in reactor design. The fragments, or atoms, that are formed in the splitting of a heavy nuclide are usually unequal in size, with one fragment considerably larger than the other. Uranium-235 fissions in more than 30 different ways, producing isotopes ranging from zinc, with a mass number of 72, to samarium, with a mass number of 158.

The fission fragments themselves are unstable, especially just upon formation, and they emit radiation, primarily in the form of beta particles and gamma rays. The many different radioisotopes that are formed during fission do not return to a stable, nonradioactive state at the same rate. The radioactivity of some isotopes may disappear within seconds or minutes, whereas that of others may persist for years. Because these radioisotopes continue to emit radiation even after the fission reaction has been stopped, a number of requirements are imposed on the design of reactors.

a. The radioactive fission fragments must be contained, either by an impervious cladding on the fuel elements, or by a tight containment structure around the reactor, to prevent a biological hazard to operators or the public.

b. The continued production of heat due to the absorption of this radiation after a reactor is shut down requires a means for removing this afterglow or decay heat. Immediately after shutdown, this decay heat amounts to some 5 percent of the total reactor power just prior to shutdown, so that a substantial cooling capacity is required.

c. Another effect due to fission fragments, although not related to their radioactivity, is equally important. Some of the fission fragments have high neutron absorption cross-sections and, by removing neutrons from the chain reaction process, tend to shut the reactor down. Since these neutron-absorbing fission fragments accumulate as the chain reaction proceeds, sufficient fuel must be loaded initially, or added subsequently, to compensate for the neutron losses.

8-1.1.1.2 Neutron Moderation

The neutrons from fission are considered to be ejected from the fission fragments immediately after fission and not directly from the original nucleus. About 99 percent of the neutrons are ejected within 10^{-12} sec and are called prompt neutrons. The remainder leave the fragments at a decreasing rate over a period of minutes and are called delayed neutrons.

Most of the neutrons produced in fission are ejected at energies of about 1 MeV, corresponding to velocities of 10,000 miles per second. Neutrons at these energies are termed fast neutrons. Ultimately all these neutrons are absorbed, either by capture by another fissionable atom causing further fission, or by nonfission capture or absorption by fuel, coolant, moderator, or structural materials. Before the neutrons are absorbed, most of them lose some of their energy or are moderated by collisions with the nuclei of atoms. This collision or scattering process occurs by two principal methods: elastic and inelastic scattering.

In elastic scattering, the neutron loses its energy by "billiard ball" type collisions with the nuclei of atoms. The velocity of the neutron after a collision depends upon the mass of the nucleus and the angle of impact. The smaller the target nucleus, the more energy can be transferred to it from the neutron and the slower the resultant neutron velocity. Momentum and kinetic energy are preserved in the elastic scattering process. After many collisions, the neutron slows down to velocities comparable to the velocities that gas molecules have due to thermal effects. The neutrons are then called thermal neutrons and have energies of about 0.025 eV.

In inelastic scattering, a neutron is absorbed by a nucleus with the subsequent emission by the nucleus of another neutron and gamma radiation (fission not occurring). Although the original neutron is captured, a new one takes its place and no net loss of neutrons occurs. A neutron must have a relatively high energy, greater than 0.1 MeV to produce inelastic scattering. Since part of the energy of the incident neutron is given off as gamma radiation, momentum and kinetic energy are not conserved in the inelastic scattering process.

Inelastic scattering is an important process of neutron energy degradation, or moderation, by heavy elements. The coolant in a reactor can also serve as moderator or the moderator can be incorporated as a separate material. From a nuclear standpoint a moderator should have two properties: it should not itself absorb too many neutrons, and it should have a low atomic mass.

8-1.1.1.3 Neutron Absorption

The absorption or capture of neutrons may occur while the neutrons are at high energies (fast), at intermediate energies (epithermal), or at low energies (thermal). The absorption may result in the fission of another atom, it may result in the production of additional fissionable material from fertile material, or the neutrons may be absorbed in structural and other materials in such a way that they make no further contribution to the chain reaction (waste or parasitic absorption).

The ability of a given nuclide to capture or absorb neutrons (or to scatter them) is expressed in terms of its cross-section. Cross-sections are expressed in terms of barns. One barn is 10^{-24} cm^2. Since the diameter of a nucleus is 10^{-12} cm, the barn is roughly the physical area of the nucleus. The term barn is derived from the usual farm variety by a somewhat loose analogy that some elements have cross-sections as big as barns, at least in comparison to other elements. The fission cross-section of uranium-235 is shown in Figure 8-2. Although cross-sections are given as areas and can be considered as the target area which the nuclide presents to the neutron, this target area cannot always be derived from the physical size of the nuclide.

If this target area is visualized as a gravitational field through which the neutron passes, one would expect that the faster the neutron, the shorter the time it will spend in the field and the less likely it is to be captured. For fast neutrons, the cross-sections of nuclides do vary inversely as the neutron velocity, the so-called 1/v rule, as seen in Figure 8-2. However, for slower neutrons, this rule fails. If there is a nuclear process which the nuclide can undergo which requires just that amount of energy possessed by the passing neutron, the probability of neutron capture is much higher. This is analogous to resonance absorption phenomena in nonnuclear processes, and the term resonance absorption is used here as well.

A number of the heavier elements are capable of undergoing fission upon the absorption of a fast neutron. Except for U-235, U-233, and Pu-239, however, the neutrons produced do not have sufficient energy, on the average, to cause further fission. A chain

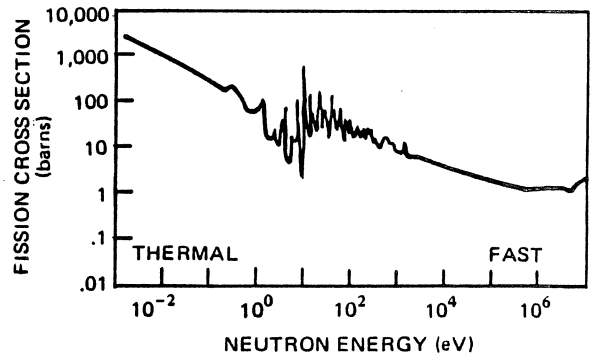

Figure 8-2. Fission Cross-Section for Uranium-235

reaction is not possible, therefore, with other elements. As the neutrons slow down from the fast to the thermal range, the probability of fission of elements other than the three mentioned above becomes very small indeed.

Even for U-235, U-233, and Pu-239, the fission cross sections are small for fast neutrons. In order to sustain a chain reaction with fast neutrons it is necessary, therefore, to keep the probability of fission capture high. In a fast reactor – a reactor where the chain reaction is maintained by fast neutrons – it is necessary to have a high concentration of fissionable atoms with a minimum of extraneous material wastefully absorbing neutrons. Fast reactors are therefore small in size with a high fuel-to-coolant ratio. For the removal of the large amounts of heat from the small volume, very efficient coolants, such as liquid metals, are used.

The fission cross section of U-235 is much higher for thermal than for fast neutrons, e.g., 600 versus 2 barns. Consequently, if the neutrons are slowed down or moderated to thermal energies, the chain reaction is much easier to maintain. A reactor in which the chain reaction is propagated by thermal neutrons is called a thermal reactor.

Uranium-238 and thorium-232, upon absorbing a neutron, can be converted into new fissionable elements, Pu-239 and U-233. Although neutrons absorbed in this way do not assist in the maintenance of the chain reaction, the new fissionable material adds to the fuel supply and contributes subsequently to the chain reaction.

For every neutron absorbed, the fission of U-235 produces an average of 2.5 new neutrons; the fission of U-233, 2.7 neutrons; and the fission of Pu-239, 2.8 neutrons. In Figure 8-3, the ratio of neutrons released per neutron absorbed is shown as a function of the absorbed neutron energy for these fuels. One of these

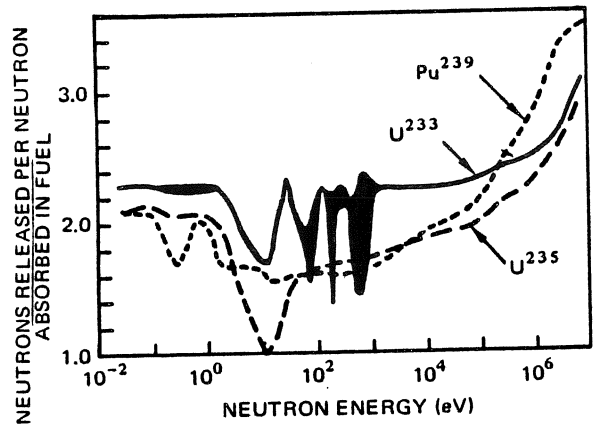

Figure 8-3. Neutron Production Ratios for Nuclear Fuels

neutrons is required to maintain the chain reaction and the rest are available to produce new fissionable material or for waste absorption. If waste absorption can be kept low, it is possible for a reactor to produce more fissionable material than it consumes. Such a reactor is called a breeder reactor. All reactors containing U-238 or Th-232 in their fuel will produce some new fissionable material. The ratio of the number of new fissionable atoms formed to the number consumed is called the conversion ratio. If this ratio is less than one, the reactor is a converter; and if it is one or more, the reactor is, as indicated above, a breeder. In actual practice, most reactors have conversion ratios of 0.5 to 0.7.

The neutrons which are not absorbed in causing fission or the production of new fissionable material are wastefully absorbed in other materials in the reactor. Such materials include structural members, fuel cladding, moderator, control rods, and the coolant. It is desirable, of course, that this wasteful or parasitic absorption be kept to a minimum. Every attempt is made to use materials of low neutron absorption cross-section. Aluminum or zirconium is preferable to stainless steel as fuel cladding or structural material, if temperature and corrosion conditions permit, because of the higher neutron absorption cross-section of stainless steel.

Some types of waste absorption cannot be avoided, such as nonfission capture of a neutron by U-235 (which occurs in addition to fission capture). In a natural uranium reactor, nonfission absorption by U-238 cannot be avoided (natural uranium is 99.3 percent U-238). Since the absorption of neutrons by U-238 occurs mainly at resonances in the intermediate energy range, it is possible to reduce this absorption by separating the fuel elements and interspersing a moderator material that will slow the neutrons down to energies below the resonance energies before the neutron encounters another U-238 atom. It is also possible to reduce the absorption of the neutrons by U-238 by lowering the percentage of U-238 in the fuel – that is, by enriching the fuel with U-235. The use of moderators and fuel enrichment is common practice in reactor design.

Waste absorption of neutrons not only has a deleterious effect on the ability of a reactor to sustain a chain reaction, but also causes materials in the reactor to become radioactive. This radioactivity has three forms. Alpha particles, which consist of two protons and two neutrons, are emitted at high velocities (about 1/10th the speed of light) and carry a positive charge. The massiveness of the particle and its high velocity result in considerable ionization in materials through which it passes. At the same time, its size and charge limit its range to a few inches in air or to the thickness of a few sheets of paper.

Beta particles are electrons emitted from the nucleus at velocities approaching that of light. These particles also cause ionization and have a range of a few feet in air. Gamma rays are a form of electromagnetic radiation similar to X-rays but of shorter wavelength and of very high energies. These rays are highly penetrating and pass through considerable thicknesses of lead or other dense materials before being absorbed.

The rate of radioactive emission from a nucleus decreases or decays exponentially with time. Since the radioactivity never disappears completely, the time taken for the activity to be cut in half, the half-life, is used to indicate the rate of decay.

Both alpha and beta emission change the parent element into a new element, but gamma emission does not. Alpha particle emission leads to a decrease in mass of 4 units and a decrease in atomic number of 2. Beta particle emission causes no change in mass number but increases the atomic number by one.

This induced radioactivity is of special concern in power reactors since it means that materials in and near the reactor core (structural members, coolants, control rods, etc.) may become radioactive. Subsequent handling of these materials is therefore often quite difficult. For example, the oxygen in water absorbs neutrons and produces radioactive N-16. This isotope has a short half-life, 7.6 sec, so that, although shielding is required during reactor operation, the radioactivity quickly decays after reactor shutdown and access is possible. Sodium, on the other hand, becomes activated by neutrons producing Na-24 with a 14.5-hr half-life. Access to primary sodium coolant circuits is therefore limited for some time even after reactor shutdown.

8-1.1.2 Reactor Control

The control system of a nuclear power reactor must provide a means of starting the reactor from a zero rate of fission to the rate corresponding to the desired power level, of keeping this power production at a steady level, and of shutting the reactor down under normal or emergency conditions. This can be accomplished by a number of means, all depending upon a variation in the number of neutrons absorbed in nonfission events. The various control methods include:

a. Addition and removal of fuel.

b. Addition and removal of neutron-absorbing control rods, or the addition and removal of neutron-absorbing salts, such as boron, to the coolant.

c. Addition and removal of moderating materials, thereby changing, for example, the relative number of neutrons absorbed in nonfission capture by U-238.

d. Addition and removal of the reflector, changing the neutron leakage from the reactor.

All these methods require the physical movement of mechanical components, which are activated through a system that detects an increase or decrease in neutron production.

8-1.1.3 Shielding

Virtually all nuclear processes release radiation which is harmful to living tissue and to solid-state electronic components. Hence, if people are to operate or service nuclear equipment, or be served by it, some protective barrier, or shield, must be provided.

There are many sources of hazardous radiation in a nuclear reactor. The escaping neutrons constitute a very serious hazard. Gamma rays are emitted during fission and as a result of fission product decay events. In addition, any material exposed to neutrons may become radioactive; bremsstrahlung activation of some liquid metal coolants by neutron capture gives rise to intense radioactivity. Of the radiations emerging from the reactor, only neutrons and gammas need be considered; charged particles released within the reactor will not escape through the reflector and shield.

Fast neutrons released in fission present some shielding problems. A significant fraction (in the order of 0.1 percent) of the fission neutrons are born with energies of 10 MeV or higher. These high-energy neutrons have fairly long mean free paths and have a tendency to be scattered in a predominantly forward direction. Since neutrons are very damaging biologically, the shield must slow down and capture the fast neutrons, as well as any slower neutrons that escape through the reflector by diffusion.

The most effective gamma shielding materials are those of high mass number. Lead and iron are very effective and are used frequently. Neutron shielding is more complex; the fast neutrons must first be slowed down by elastic or inelastic scattering and then be absorbed. In general, high mass number nuclides are the most effective elastic scatterers and low mass number materials are the most effective inelastic scatterers. To satisfy both gamma and neutron shielding requirements of a reactor, both low and high mass number materials should be included in the shield.

A typical vehicle shielding configuration is shown in Figure 8-4. A disk of high density material which attenuates gamma radiation is placed next to the reactor where the required shadow can be obtained with minimum diameter and weight. Inelastic scattering of neutrons is then accomplished by the low density liquid hydrogen fuel. Also, the radiation flux from the reactor

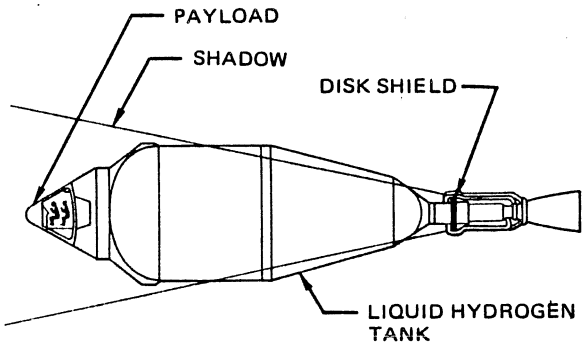

Figure 8-4. Typical Vehicle Shielding Configuration

decreases with the square of the distance, so that increasing the distance between the reactor and the payload reduces the overall shielding requirements.

8-1.2 Solid-Core Nuclear Rockets

The solid-core nuclear rocket is shown schematically in Figure 8-5. In this rocket, hydrogen propellant is heated by flowing through a reactor core which contains fissioning material, and the heated hydrogen is then ejected through a nozzle to produce thrust. The hydrogen is stored as a liquid in the propellant tank, and supplied to the engine by means of a liquid-hydrogen turbopump. The hydrogen is used to cool the nozzle and the reflector before injection into the reactor core.

8-1.2.1 Reactor Design

In nuclear rocket design, the word fuel has a different connotation than in a chemical rocket where it refers to the chemical that is to be oxidized. The fuel is the fissionable material which reacts to provide heat to the propellant. Ordinary uranium contains about 0.7 percent uranium-235. Enriched uranium fuel contains a larger percentage of U-235 (usually about 93 percent). For rocket reactors, U-235, Pu-239, and enriched uranium permit the design of a small lightweight reactor, but they are expensive and difficult to handle.

Fuel elements are discrete assemblies that contain fissionable fuel, usually in the form of a uranium oxide or carbide, in a fuel-bearing material. They may be metal clad assemblies of uranium-containing compounds, or they may be solutions of uranium in other materials.

For thermal reactors, there are two basic arrangements of fuel elements and moderator as shown schematically in Figure 8-6: the homogeneous reactor, and the heterogeneous reactor. In the homogeneous reactor, the fuel elements and moderator are intimately mixed so that the fission heat is generated in the mixture of the two materials. A heat-transfer surface for the hydrogen propellant is provided by passages through the solid

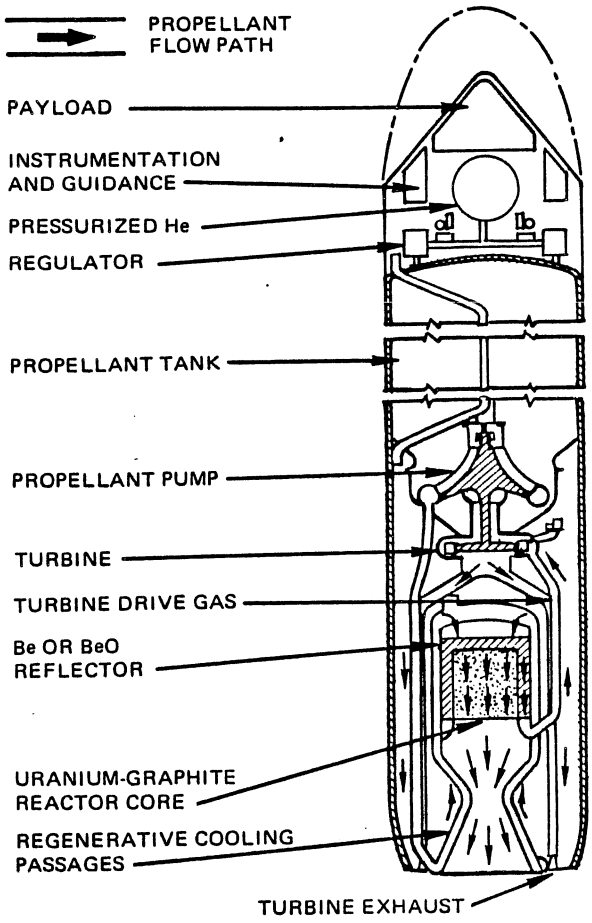

Figure 8-5. Schematic Diagram of a Solid-Core Nuclear Rocket

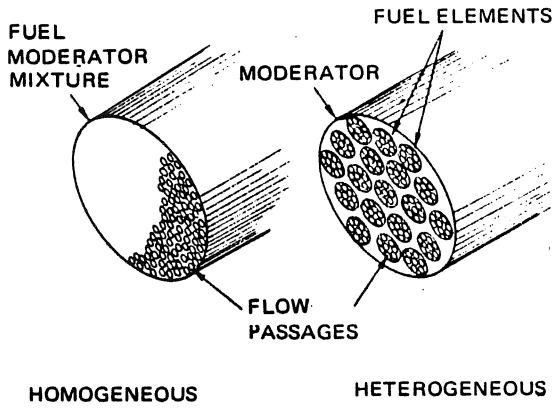

Figure 8-6. Solid-Core Reactor Configuration

core. In the heterogeneous reactor, the fuel elements are separated from the moderator material. As shown schematically in Figure 8-6, the fuel elements of the heterogeneous reactor are in isolated groups surrounded by a matrix of moderating material.

In the case of the homogeneous reactor, the moderator must be a high-temperature material that has good moderator properties. This dual requirement limits the choice of materials available for such a reactor. The virtue of a heterogeneous reactor is that the fuel may be contained in the best high-temperature materials, while the moderator can be made of the best moderator materials.

Another type of solid-core reactor is the fast reactor. It is a homogeneous reactor with no moderator material. The only materials in the core other than the fuel itself are fuel-bearing, high-temperature core materials. Eliminating the moderating material reduces the material selection problems considerably. A major disadvantage of the fast reactor is that more fissionable material is required, which adversely affects the high-temperature properties of the core material.

8-1.2.2 Reactor Materials

The characteristics that are required for suitable fuels and fuel-bearing materials for use in the fuel-element are:

a. High operating temperature (5,500°R)
   1. Low evaporation rate
   2. Adequate strength
b. Compatibility with fissionable material
c. Compatibility with hydrogen
d. Resistance to thermal stress or shock
e. Low neutron absorption cross-section

High-temperature operating capability of the fuel element materials is the most important single requirement. Table 8-3 shows the melting points of typical fuels, and the metals or ceramics that might be used as fuel-bearing materials. It would be desirable to use uranium metal as the fissionable material because of

Table 8-3. Properties of Reactor Materials

Material Type	Material	Symbol	Density (lb/in^3)	Melting Temperature (°R)	Thermal Neutron Absorption Cross-Section (barns)
Fuels	Uranium Nitride	UN	– –	5690*	– –
	Uranium Dioxide	UO_2	– –	5535	– –
	Uranium Carbide	UC	– –	4810	– –
	Uranium	U	0.687	2530	7.68
Metallic Refractories	Tungsten	W	0.695	6580	19.2
	Rhenium	Re	0.738	6200	84.0
	Tantalum	Ta	0.597	5890	21.3
	Molybdenum	Mo	0.367	5170	2.5
Non-Metallic Refractories	Hafnium Carbide	HfC	0.453	7490	105.0
	Tantalum Carbide	TaC	0.515	7480	21.3
	Carbon	C	0.060	7190**	0.003
	Niobium Carbide	NbC	0.279	6790	1.1
	Zirconium Carbide	ZrC	0.245	6210	0.18

* Decomposes
**Sublimes

its high density and low cost. However, the melting point of uranium metal is only 2,530°R compared with the 5,500°R temperature desired.

Uranium nitride (UN) has the highest melting point (5,690°R) of the fuel materials, but it decomposes unless a nitrogen atmosphere is supplied. Therefore, its use must be restricted to special cases where this nitrogen atmosphere can be provided. Uranium dioxide (UO_2) has the next highest melting point (5,535°R). Uranium carbide (UC) has a higher uranium density because there is only one atom diluting the uranium, compared with uranium dioxide, where there are two atoms diluting the uranium.

The melting point of uranium carbide is considerably lower than uranium dioxide, and unless provisions are made to accommodate molten fuel, it is disadvantageous to use uranium carbide. However, uranium carbide and uranium nitride both have the advantage of having a relatively high thermal conductivity compared with uranium dioxide, which is important for minimizing fuel-element thermal stresses.

The choice of the proper fuel-bearing material also requires a compromise between desirable properties. Table 8-3 lists candidate fuel-bearing materials in metallic refractory and nonmetallic refractory categories. Generally the nonmetallics are more desirable because they have higher melting temperatures and smaller thermal neutron absorption cross-sections. However, some of the nonmetallics are unstable in the reactor environment. Hafnium carbide and tantalum carbide tend to lose carbon at high temperature, and they are reduced in the presence of hydrogen. Carbon reacts strongly with hydrogen and must, therefore, be coated with a material that minimizes this reaction. The small cross-sections of niobium carbide and zirconium carbide tend to compensate for their lower melting temperatures.

Another important consideration of high-temperature materials is the rate at which they evaporate at high temperatures. Figure 8-7 shows the vaporization rate of high-temperature materials as a function of temperature. Uranium dioxide has the highest vaporization rate of all the materials shown. The other fuel shown is uranium carbide, which has about a two order-of-magnitude lower vaporization rate than uranium dioxide, but its melting point (represented by the end of the vaporization curve) is almost 1,000°R lower.

Carbon has a high vaporization rate compared with niobium carbide, and tungsten has the lowest vaporization rate of all the materials shown. At 5,500°R, the vaporization rate of carbon is about three orders-of-magnitude greater than that of tungsten, while niobium carbide has about a one order-of-magnitude greater rate of vaporization than tungsten.

Figure 8-7 shows that it would not be practical to make a reactor out of plain uranium dioxide because of its excessive vaporization rate. To reduce the vaporization rate, the uranium dioxide should be completely contained within a material that has a much lower vaporization rate, and that is compatible with hydrogen. A promising selection for the fuel element is uranium dioxide encapsulated within tungsten, as tungsten has the lowest vaporization rate of the materials and also has a high melting point.

If carbon is used as a fuel-bearing material, uranium dioxide fuel cannot be used because it will be converted to uranium carbide in the presence of carbon. Carbon or graphite elements therefore use uranium carbide as a fuel material. Because carbon is attacked chemically by hydrogen, the carbon must be protected. A good protecting material is niobium carbide because it is fairly compatible with carbon.

There are several basic types of fuel element construction. In one type, a uranium compound, such as uranium dioxide, is dispersed in a matrix of a material such as tungsten. This matrix is clad with a layer of pure tungsten so that uranium dioxide is not in direct contact with the hydrogen through the reactor. This minimizes any reaction that would occur between uranium dioxide and hydrogen, and also prevents the loss of uranium dioxide by vaporization.

Another type of fuel element is the solid-solution element. For example, uranium carbide can be dissolved in niobium carbide to make a fuel element. A third type of fuel element is the bulk fuel type. In this case, a tube of refractory material such as tungsten is filled with the uranium compound such as uranium dioxide.

8-1.2.3 Rocket Performance

Predictions of the best thrust-to-engine-weight ratios obtainable from solid-core nuclear rockets are shown plotted as a function of thrust level in Figure 8-8. Values

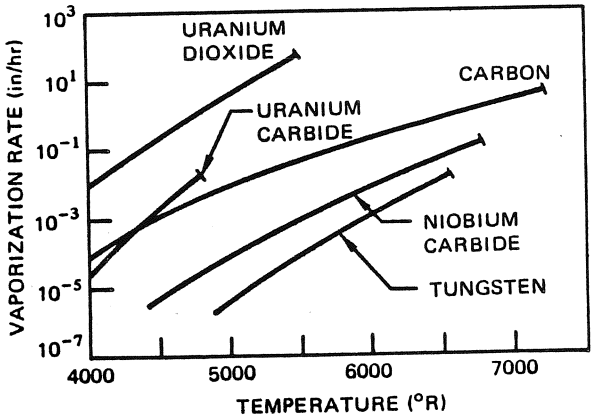

Figure 8-7. Vaporization Rate of Solid-Core Reactor Materials

are plotted for a tungsten-water-moderated reactor, a tungsten fast-neutron reactor, and a graphite-uranium-carbide reactor. Because of the superior moderating properties of water, the engine weight for the tungsten-water-moderated reactor is lower, particularly at the smaller reactor sizes, yielding the relatively high thrust-to-engine-weight ratios shown. Specific impulse is limited to 900 sec.

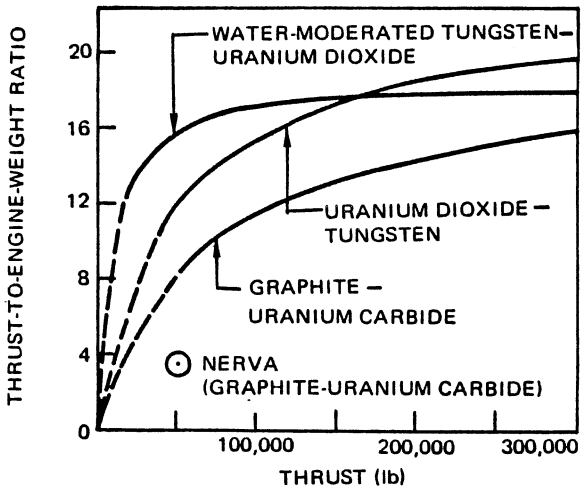

Figure 8-8. Thrust-to-Engine-Weight Ratios

At a thrust level of 50,000 lb, the graphite reactor weighs about twice as much as a tunsten-water-moderated reactor, thus producing one half the thrust-to-weight ratio. However, as the thrust levels increase, the weight of the fuel elements (rather than the moderator) dominate the reactor weight. At thrust levels of 200,000 lb and higher, the thrust-to-weight ratios for all three reactor types are in the range of 14 to 20. The calculated thrust-per-engine weights in Figure 8-8 are anticipated to be the best that could be obtained. The first powerplants built will no doubt fall below the curve. For comparison, the thrust-to-engine-weight of the NERVA engine is also shown on this plot.

8-1.3 Liquid-Core Nuclear Rockets

Liquid-core nuclear-fission rockets have been studied analytically, with some experimental evaluation of critical processes. Specific-impulse limits of 1,300 to 1,500 sec are calculated, with thrust-to-weight ratios of 2 to 10. The specific impulse is limited by increased vaporization of the nuclear fuel with increasing temperature, and the entrainment of the fuel in the expelled hydrogen propellant. The entrainment increases the mean molecular weight of the propellant so that further increases in temperature produce little increase in specific impulse. The large potential fuel loss with liquid-core systems raises major economic and political problems for large rockets, and there is currently little interest in further studies of this system.

8-1.4 Gaseous-Core Nuclear Rockets

For gaseous-core nuclear fission rockets, specific impulses in the range of 1,500 to 2,500 sec seem theoretically feasible, with engine thrust-to-weight ratios greater than one. The limitation of specific impulse arises from the need to transfer heat from the gaseous nuclear fuel to the hydrogen propellant by radiation. Direct heating (i.e., passing the propellant through the fuel) is not feasible, both because of the excessive fuel loss and the difficulty of achieving high specific impulse when heavy fuel particles become a substantial fraction of the propellant.

For radiative heating, the upper limit on temperature, and thus specific impulse, is determined by the absorptivity of hydrogen and the heating of the chamber walls. The absorptivity drops rapidly at temperatures above 100,000°R due to ionization. The need to keep the heat transfer rate to the walls at a reasonable value (less than about 1 kW/cm^2) means that the average temperature of the propellant must be much less than the maximum attained near the fuel core.

Although fuel losses of the order of 1 to 10 percent of the propellant mass flow are anticipated, the prospect of attaining specific impulses of the order of 2,000 sec with high thrust-to-weight ratios makes further research on gas-core reactors desirable.

Gaseous-core fission reactors unfortunately require a quite large minimum critical size at tolerable gas pressures. For a minimum expected thrust level of 250,000 lb at a pressure of 1,000 atm, a minimum reactor mass of over 100,000 lb would be required. This is not too large for the first planetary-transfer stage of a major manned interplanetary mission, but it would be a problem in ground testing, because of the radioactive fission products in the exhaust jet. A thorough exhaust-gas cleaning system would be needed for a gas core fission reactor testing facility.

An early gas-core reactor concept involved heating the hydrogen propellant by diffusion through the hot-fissioning fuel, and containing the fuel by means of centrifugal force. Various vortex arrangements were studied both experimentally and theoretically. The net result of these studies was the conclusion that mixing between propellant and fuel, and the consequent fuel-loss rate, would probably be excessive for specific impulses above 1,500 sec and for reasonable reactor size.

The so-called glow-plug concept studied by McDonnell Douglas Astronautics Co. represents an alternative to the coaxial-flow concept of a gase-core fission reactor. A thin shell, with walls as transparent as possible to radiative energy, contains the fuel. This concept avoids fuel loss and consequent economic and test problems. But the fragility of a shell of the necessary thinness to

avoid melting becomes a major problem. This reactor would have the same minimum size restrictions as the coaxial-flow concept.

Magnetic containment or stabilization of the uranium fuel (which ionizes at a lower temperature than hydrogen) has also been proposed. But the electrical conductivity of uranium plasma at temperatures suitable for a gas-core fission rocket is relatively low. Extensive research is required before the feasibility of these, or other gas-core reactor concepts is determined.

8-2 RADIOISOTOPE ROCKETS

Radioisotopes, when they decay, emit thermal energy at a rate predicted by their half-lives. They represent a compact, reliable source of heat which will continue to function independently of the surrounding environment. Radioisotopes are obtained either as by-products of fission reactor operation or are formed by neutron bombardment of target material in a reactor.

Radioisotope propulsion systems utilize a heated gas expanded through a supersonic nozzle to provide thrust. Heat released from the decay of a radioactive isotope is used to heat the propellant gas. A typical radioisotope thruster is shown in Figure 8-9. This thruster consists of a refractory metal capsule containing the radioactive isotope, surrounded by a propellant flow passage, and thermal insulation. The propellant flow passage terminates at the inlet of a supersonic nozzle through which the heated gases are expanded.

Except for the thruster, the radioisotope system is similar to a cold gas propulsion system. However, heated gas systems realize significant gains in specific impulse over cold gas systems, making these units attractive for many spacecraft applications. Gases, vaporizing liquids, cryogenics, and biowaste products such as carbon dioxide can be used as propellants. Figure 8-10 illustrates the performance increases possible by heating some of these propellants.

A number of considerations that influence the selection of a radioisotope fuel are:

a. Temperature capability of available fuel forms must satisfy mission requirements.

b. Half-life must be adequate for mission requirements.

c. Power density must be sufficient to prevent excessive weight penalties.

d. Isotope must have a potential availability which is compatible with mission requirements.

e. Isotope projected costs must be reasonable.

f. Radiation levels must be compatible with mission limitations.

Table 8-4 lists candidate radioisotopes and pertinent physical characteristics which influence their selection for specific applications. For short missions (5 months or less), both polonium-210 and curium-242 appear very attractive. Their specific power is high and their radiation levels are low, as can be seen in the table. However, for longer missions the power decay may limit their use.

Plutonium-238, which requires little or no shielding, and has a 90-year half-life, appears very attractive for longer missions. Because of its long half-life, Pu-238 has a lower specific power than other alpha sources, is very

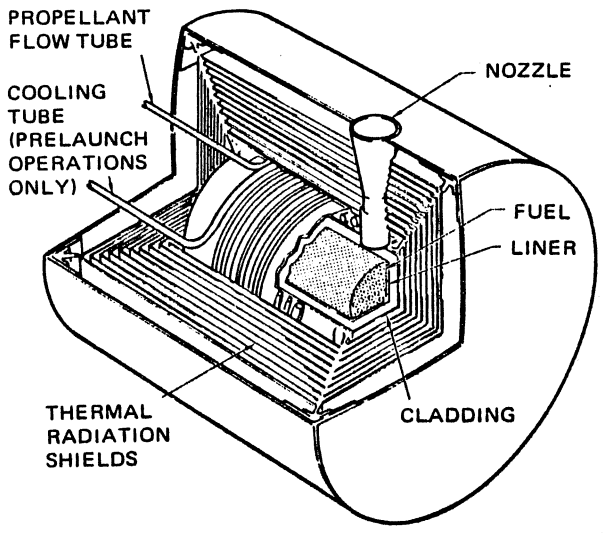

Figure 8-9. Radioisotope-Heated Thruster Configuration

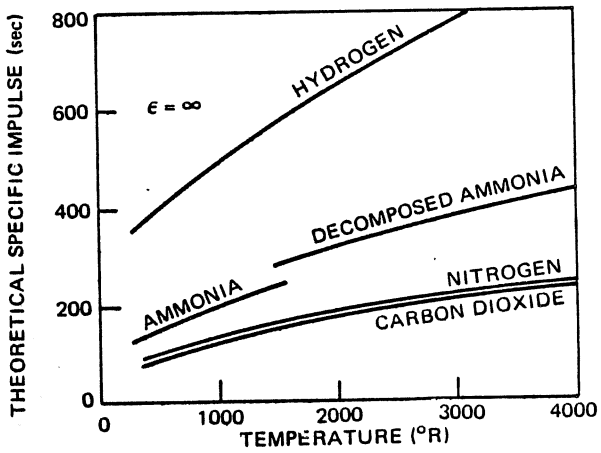

Figure 8-10. Theoretical Performance of Heated Propellants

Table 8-4. Characteristics of Radioisotope Heat Sources

Isotope	Symbol	Half Life (Years)	Power Density (W/g)	Major Radiation Type	Shielding Requirements	Availability	Cost ($/W)
Cobalt-60	Co-60	5.3	17.4	Beta, Gamma	Heavy	Good	33.0
Strontium-90	Sr-90	28.0	0.95	Beta, Bremsstrahlung	Heavy	Good	19.0
Ruthenium-106	Ru-106	1.0	30.6	Beta, Gamma, Bremsstrahlung	Heavy	--	--
Cesium-137	Cs-137	30.0	0.42	Beta, Gamma, Bremsstrahlung	Heavy	Good	21.0
Cerium-144	Ce-144	0.78	25.6	Beta, Gamma, Bremsstrahlung	Heavy	Good	1.0
Promethium-147	Pm-147	2.7	0.361	Beta	Minor	Good	91.0
Polonium-210	Po-210	0.38	141.3	Alpha	Minor	Good	188.0
Plutonium-238	Pu-238	89.0	0.56	Alpha	Minor	Limited	890.0
Curium-242	Cm-242	0.45	120.0	Alpha, Neutron	Minor, except for Neutron Shielding	Potential	17.0
Curium-244	Cm-244	18.0	2.8	Alpha, Neutron		Potential	357.0

expensive (on a per-watt basis) and has limited availability. Hence, it does not appear attractive for use in multi-kilowatt power level propulsion devices, but it does appear attractive for use in low power attitude-control type thrusters which employ storable propellants for their working fluid.

Curium-244, which has a strong surrounding neutron field, appears attractive for longer missions in which high levels of fast neutron radiation can be tolerated. From a radiation level standpoint, it is the worst of the potentially available alpha emitters.

Cerium-144 and ruthenium-106 have good specific powers and may suffice for short or intermediate missions (one year or less); however, the high level of gamma radiation associated with these isotopes present a very severe shielding problem.

Promethium-147, cobalt-60, strontium-90, and cesium-137 are beta-emitting isotopes with relatively long half-lives and could therefore be considered for missions lasting a year or more. The specific powers of these isotopes are relatively low because of their long half-lives. Pm-147, a pure beta emitter, has the lowest accompanying radiation of the beta emitters considered here and is therefore a good prospect for use in radioisotope space systems. However, its low power density and availability preclude its use in multi-kilowatt thrusters, but it does appear quite attractive for use in low-power reaction control engines.

Spacecraft integration and launch handling considerations tend to eliminate those isotopes having significant external radiation fields. Most of the development effort related to radioisotope heat sources for aerospace applications has been performed with Pu-238. Several radioisotope thermoelectric generators powered with Pu-238 are currently in orbit. Others are under development, and extensive aerospace safety qualification testing has been performed with Pu-238 heat sources. An AEC program has been initiated to develop a flight qualified Po-210 heat source.

8-3 BIBLIOGRAPHY

1. *Electrothermal and Radioisotope Heated Propulsion for Spacecraft Reaction Control*, TRW Systems Group, February, 1968.

2. R. W. Bussard, "Nuclear Rocket Propulsion Possibilities," *Space Technology*, H. Seifert, Ed., John Wiley and Sons, New York, 1959.

3. R. W. Bussard and R. D. DeLauer, *Nuclear Rocket Propulsion*, McGraw-Hill Book Co., New York, 2958.

4. R. B. Canright, "Propulsion," *Space Propulsion Technology*, R. D. Heitchue, Ed., Reinhold Book Corp., New York, 1960.

5. F. P. Durhan and J. D. Orndoff, "Nuclear Propulsion," *Handbook of Astronautical Engineering*, H. H. Koelle, Ed., McGraw-Hill Book Co., New York, 1961.

6. S. Glasstone, *Principles of Nuclear Reactor Engineering*, D. Van Nostrand Co., Princeton, 1956.

7. S. Glasstone, M. C. Edlund, *The Elements of Nuclear Reactor Theory*, D. Van Nostrand Co., Princeton, 1963.

8. R. L. Loftness, *Nuclear Power Plants*, D. Van Nostrand Co., Princeton, 1964.

9. W. E. Moeckel, "Propulsion System for Manned Exploration of the Solar System," *Astronautics & Aeronautics*, Vol. 7, No. 8, August, 1969.

10. F. E. Rom, *Nuclear-Rocket Propulsion*, TM X-1685, NASA, Washington, November, 1968.

11. G. P. Sutton, *Rocket Propulsion Elements*, John Wiley and Sons, New York, 1963.

12. R. A. Willaume, et al., *Nuclear, Thermal, and Electric Rocket Propulsion*, Gordon and Breach Science Publishers, New York, 1967.

Section 9
ELECTRIC PROPULSION THRUSTERS

Electric rocket engines are low thrust devices which use electricity to heat or accelerate a propellant to produce specific impulses of 700 to 25,000 sec. Their greatest value will be in space, beyond the influence of planetary gravity, where a small amount of thrust will accelerate heavy objects. In space, the relative weight of an electric propulsion system is small and, owing to its high specific impulse, it will operate on a relatively small amount of propellant.

Because a low thrust, high impulse electric engine will not produce enough thrust to lift itself off the earth's surface, it requires a large, high thrust chemical or nuclear booster rocket to put it into a low-gravity environment. Complete electric rocket engines will consist of propellant feed and metering systems, electric thrusters or accelerators, power sources such as solar cells or nuclear reactors, and power conditioning or conversion equipment.

There are three general categories of electric thrusters: electrothermal, electrostatic, and electromagnetic. Electrothermal engines produce thrust by the expansion of an electrically heated gas through a converging-diverging nozzle. The thrust producing mechanisms and most of the losses are similar to those encountered in chemical rockets.

The electrostatic thrusters produce thrust by accelerating charged particles of propellant by means of an electrostatic field, or direct current potential. Electromagnetic engines produce thrust by both magnetic compression, resulting in pressure forces acting on the thruster, and by direct acceleration of the gas in the thrust direction through the axial components of the electromagnetic forces.

The principal characteristics of these three types of electrical propulsion systems are outlined in Table 9-1, including information about typical working fluids, performance, and development status. The performance parameters listed in Table 9-1 are related by the equation:

$$F = \frac{45.85\,\eta\,P}{I_{sp}} \qquad (1)$$

where:

F = Thrust, lb

η = Overall efficiency, %

P = Input power, kW

I_{sp} = Specific impulse, sec

An expression for the thrust-to-weight ratio of an electrically propelled vehicle can be developed by dividing equation 1 by vehicle weight. Assuming that propulsion system weight dominates the entire vehicle weight, the following approximation can be derived.

$$F/w \approx \frac{45.85\,\eta}{M_{sp}\,I_{sp}} \qquad (2)$$

where:

F/w = Thrust-to-weight ratio

M_{sp} = Propulsion system specific mass, lb/kW

Since specific mass is usually expressed in metric units, this equation may also be written as:

$$F/w \approx \frac{20.80\,\eta}{M_{sp}\,I_{sp}} \qquad (3)$$

where:

M_{sp} = Propulsion system specific mass, kg/kW

Some representative values of propulsion system specific mass are shown in Figure 9-1 as a function of jet power, based upon the use of a nuclear reactor to generate electrical power.

From equations 2 and 3, it is evident that the thrust-to-weight ratio is inversely proportional to the specific impulse. This is a valuable generalization for electrical space engines, and illustrates clearly the trade-off required to achieve high specific impulse.

Table 9-1. Electric Propulsion Systems

Type	Name	Working Fluids: State	Working Fluids: Electric Heating	Working Fluids: Acceleration	Typical Working Fluid	Typical Specific Impulse (sec)	Typical Thrust (lb)	Typical Overall Efficiency (%)	Typical Power Consumption (kW)	Development Status	Remarks
Electro-Thermal	Resistojet	Gaseous	Resistive Heating	Thermal Expansion	Hydrogen, Ammonia	700 to 900	10^{-3} to 0.5	60 to 70	1 to 15	Prototype thrusters have been flight tested.	Optimal for mission times in the order of 100 hours. Any fluid can be used as a propellant. Can operate directly from solar cell output. Jet temperatures to 5000°R.
	Arc-jet	Gaseous	Electric Arc	Thermal Expansion	Hydrogen, Ammonia	1000 to 1200	0.5	30 to 40	30 to 100	Prototype thrusters have been ground tested.	Arc-jets appear to have limited application. Development reached peak in mid-1960's, has since waned. Jet temperatures to 20,000°R.
Electro-Static	Ion	Ionized Atoms	Electric Arc	Electrostatic Field (dc potential)	Cesium, Mercury	5000 to 25,000	10^{-3} to 10^{-2}	50 to 70	0.1 to 5	Prototype thrusters have been flight tested.	Best potential for long-duration (beyond Mars) flights. High efficiency and high specific impulse.
	Colloid	Liquid Spray	Essentially None	Electrostatic Field (dc potential)	Oils, Liquid Metals, Solids	1000 to 8000	10^{-4} to 10^{-3}	40 to 60	.005 to 5	Prototype thrusters have been ground tested.	Simple: No high temperatures; no focussing requirements; small charge relative to accelerated mass. Can operate with biowaste.
Electro-Magnetic	Plasmajet	Plasma	Electric Arc	Magnetic Field	Alkali Metals, Noble Gases, Nitrogen, Hydrogen, Ammonia	1500 to 10,000	10^{-3} to 10	<50	1 to 1000	Performance has been demonstrated by laboratory prototypes.	High specific impluse: Can operate on low voltage power, e.g., directly from solar cell output. Smaller than ion engine for the same thrust. Jet temperatures to 20,000°R.

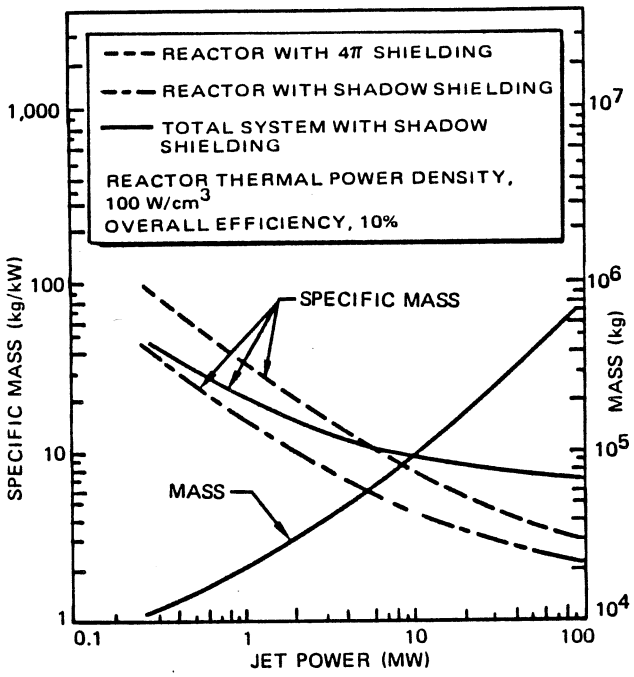

Figure 9-1. Nuclear-Electric Propulsion System Mass

9-1 ELECTROTHERMAL THRUSTERS

Electrothermal thrusters utilize electrical energy to heat a propellant, which is then thermally expanded through a supersonic nozzle to produce thrust. The performance of electrothermal rockets can be computed from the basic equations for ideal rocket performance given in Section 4, together with equations 1 and 2 in this section. Two types of electrothermal thrusters are considered in the following discussion: resistojets, and arc-jets. Resistojets are now in the flight-prototype stage of development, while pure arc-jets are still in the experimental stage of development.

9-1.1 Resistojet Thrusters

The simplest electrical propulsion system is the resistojet (Figure 9-2). Thrust is obtained by passing a propellant gas over an electrical resistance heated element; the high-temperature gas is then expanded through a conventional supersonic nozzle. The major emphasis with resistojets has been on the development of low-power thrusters for auxiliary propulsion. Resistojets are limited to the specific impulse range below 1000 sec, and usually use hydrogen as the propellant gas for best performance. However, a variety of propellants may be considered depending upon the application. These may be categorized as cold gas, vaporizing liquid, cryogenic, and biowaste products.

The conventional resistojet thruster is designed for continuous operation at a given temperature. When thrust is required, electrical power is turned on and the thruster is allowed to reach operating temperature before propellant flow is initiated. High thermal efficiencies ($\approx$ 90 percent) are achieved through the use of thermal insulation and regenerative flow passages. These systems are suitable for stationkeeping or station changing, changes in spacecraft spin rate, drag make up, and other continuous thrust applications.

Resistojets may also be designed for operation in other modes. Two representative modes are the thermal storage mode for pulsed operation, and the fast heat-up mode. For the thermal storage mode, sufficient power is supplied continuously to maintain the thruster at operating temperature. During a pulse, power to heat the propellant is obtained from the thermal capacity of the thruster mass. The thermal capacity of the heater is made large enough to prevent a large drop in thruster temperature at the maximum duty cycle anticipated. The fast heat-up system is designed with a heating element of minimum thermal capacity. When thrust is required, both power and propellant flow are activated simultaneously and maximum temperature is reached very quickly.

Most attitude control thrusters are required to operate in the pulsed mode where buildup and decay time of the chamber pressure may be significant compared to the total pulse length. If this is the case, the performance may be degraded. Specific impulse losses of the order of 5 to 10 percent of steady-state values have been observed for total pulse lengths less than 20 msec. For longer pulses, performance losses are negligible and the delivered specific impulse data of Tables 9-2 and 9-3 apply. The minimum impulse bit attainable without significant specific impulse degradation is about 10^{-6} lb-sec.

Heated gas systems are generally suitable for spacecraft secondary propulsion where thrusts required range from 10^{-4} to 10^{-1} lb. However, systems have been considered for thrust levels up to 1 lb. While there is no theoretical lower limit to thrust levels attainable with heated gas systems, there are practical limitations. The minimum thrust level is determined by the minimum nozzle diameter and chamber pressure deemed practical. Nozzle throats having diameters smaller than 0.010 in. are difficult to manufacture and are subject to plugging. A chamber pressure of 1.0 psia is assumed to be the minimum that can be adequately regulated with commercially available pressure regulators. This combination of chamber pressure and throat diameter corresponds to a thrust level of about 10^{-4} lb.

With the exception of the thruster itself, the resistojet propulsion system is similar to the cold gas and radiosotope systems. A schematic diagram of a typical

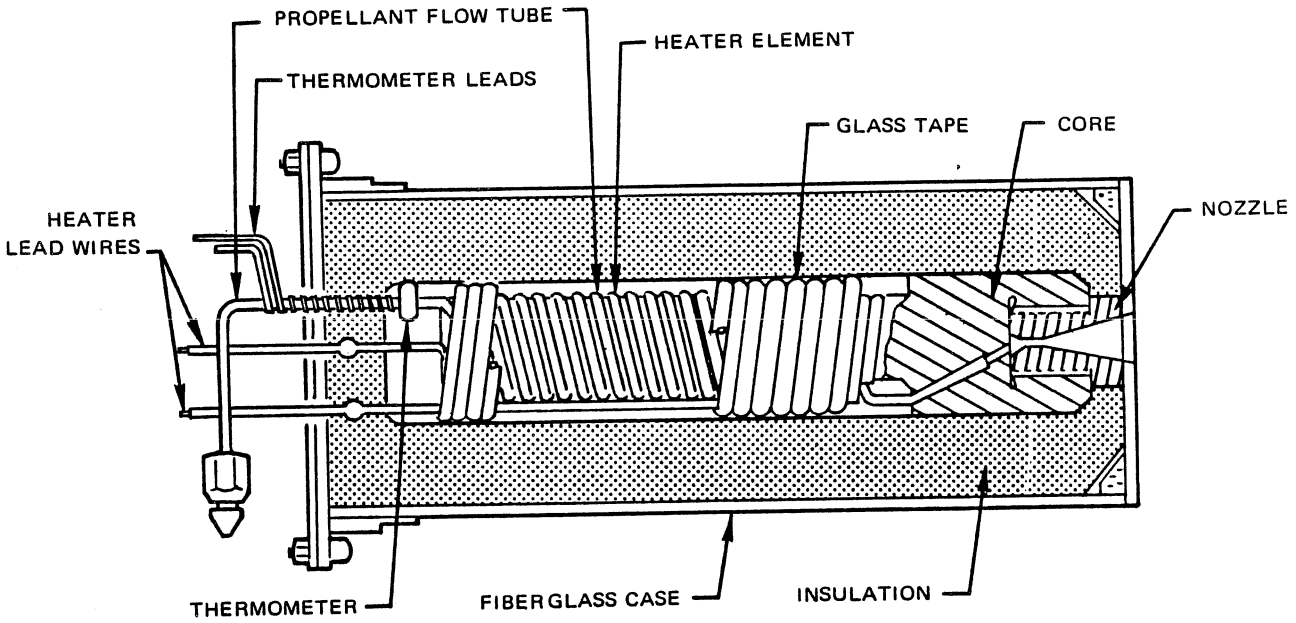

Figure 9-2. Typical Resistojet Thruster

Table 9-2. Properties of Gaseous Propellants

Propellant	Chemical Formula	Molecular Weight	Density at 3500 psia and 32°F (lb/ft³)	Room Temperature Heat Capacity (Btu/lb°F)	I_{sp} Theoretical at 1500°F (sec)	I_{sp} Delivered at 1500°F (sec)	I_{sp} Effective at 1500°F (sec)
Hydrogen	H_2	2.0	1.21	3.42	566	520	22.2
Helium	He	4.0	2.37	1.25	342	316	25.4
Neon	Ne	20.4	11.56		157	143	42.8
Nitrogen	N_2	28.0	17.37	0.247	153	140	54.6
Argon	A	39.9	27.60	0.124	109	99	50.6
Carbon Dioxide	CO_2	44.0	Liquid	0.205	128	117	
Krypton	Kr	83.8	67.20		75	71	50.3
Xenon	Xe	131.3	170.55		59	54	47.1

Table 9-3. Properties of Vaporizing Liquid Propellants

Propellant	Chemical Formula	Molecular Weight	Liquid Density 80°F (lb/ft³)	Heat of Vaporization (Btu/lb)	Heat Capacity (Btu/lb°F)	Vapor Pressure at 80°F (psia)	I_{sp} Theoretical 1500°F (sec)	I_{sp} Delivered 1500°F (sec)	I_{sp} Effective 1500°F (sec)	Vaporization Heat Requirement (W/mlb)*
Ammonia	NH_3	17.0	37.4	499	1.10	153.0	240-280	216-252	198-231	5.4
Water	H_2O	18.0	62.4	1051	1.00	0.5	204	153	138	>12.0
Hydrogen Fluoride	HF	20.1	61.7	648		21.0	180	163	153	8.1
Methanol	CH_3OH	30.5	49.6	473	0.56	2.0	138			>3.0

*For vaporization only.

heated gas system is shown in Figure 9-3. The propellant is stored in the propellant tank at high pressure (1500-4500 psia). A relief valve prevents overpressure of the tank due to filling or because of unexpected temperature rises after the spacecraft is in orbit. A burst disk, set at a pressure slightly higher than the relief valve, is sometimes included downstream of the relief valve to prevent loss of gas caused by a small relief valve leak.

Following launch, the system is activated by opening the start valve which may be squib or solenoid operated or a combination of both. Tank pressure is measured for indications of propellant quantity as a function of time. A filter is commonly employed downstream of the start valve to prevent particulate matter from contaminating the solenoid valves and regulator.

The propellant pressure is reduced to a selected working pressure by the regulator. A working pressure of 50 psia is typical. Solenoid-operated flow control valves control the duration of propellant flow to the propulsive nozzles. A low-pressure relief valve is often used downstream of the regulator to prevent excessive pressure upstream of the flow control valves in the event of regulator leakage.

Most of the gases considered suitable for cold gas systems may be used in heated gas systems with significant increases in performance. Specific impulses for several gases expanded at 1500°F are listed in Table 9-2 along with other pertinent data. Nitrogen is the most commonly used gas since it is readily available at a low cost and its density permits storage within generally accepted spacecraft volumes. Where larger quantities of hydrogen are already on board for other purposes, it is possible to consider using gas that would normally be bled off for storage pressure control.

In specific cases, where gas storage volume rather than weight is at a premium, some of the denser gases such as argon and krypton may be used. Where weight is not of prime concern, substitution of a heavier gas will often permit a growth in total impulse capability, without a change in propellant tankage.

Operation at 1500°F gives approximately two times the specific impulse obtained with cold gas systems, and does so with state-of-the-art materials. However, temperatures are not limited to this value. Hydrogen systems operating at 3600°F have been demonstrated and are under development. Other gases may be used at temperatures higher or lower than 1500°F depending on requirements. For estimating performance at other temperatures, the specific impulse values of Tables 9-2 and 9-3 may be corrected by using the equation:

$$I_{sp} = \sqrt{\frac{T + 460}{1960}} \times I_{sp(1500°F)} \qquad (4)$$

where:

T = Desired operating temperature, °F

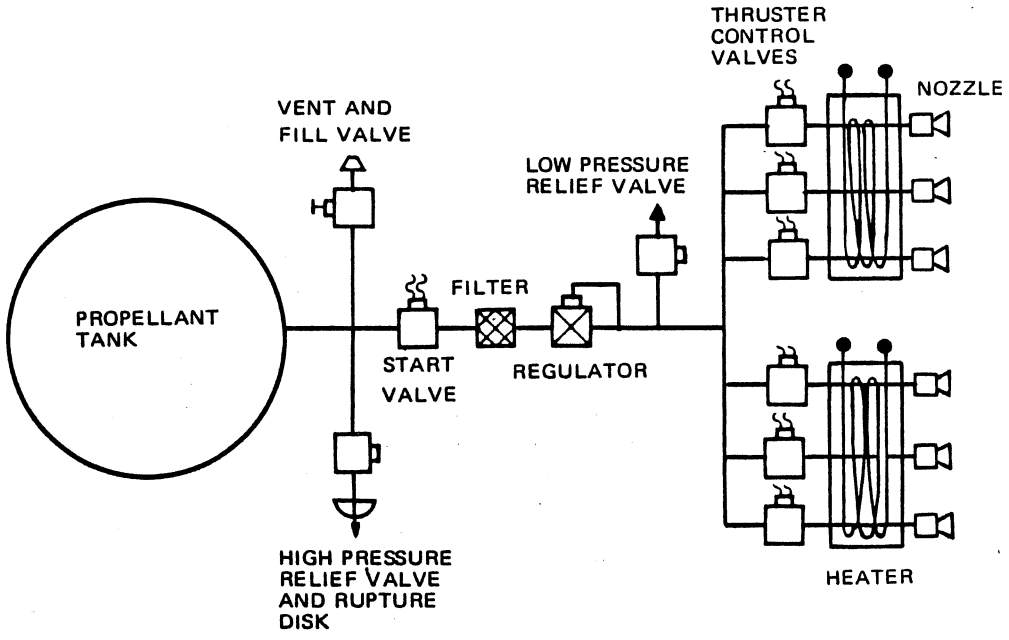

Figure 9-3. Heated Gas Propulsion System Schematic

Although the low molecular weight gases yield the greatest impulse per pound of propellant, they do not necessarily result in the lowest overall system weights. The low molecular weight gases have lower densities at a given pressure and these require larger, heavier tanks than other gases. The heavier gases, such as krypton and xenon, require smaller tankage but yield very low specific impulses. This relationship is usually shown by the defined parameter effective specific impulse, which relates total impulse and system weight. The derivation and use of effective specific impulse is defined by equations 1 to 6 in Section 7.

The weight of the resistojet thruster is very small compared to the weight of the propellant, the propellant storage tank, and the electrical power supply, and may be neglected in a comparison of resistojet system weights. If a source of free electrical energy is available, such as excess energy from the vehicle power supply, then effective specific impulse may be calculated from equation 6. Based on these assumptions, values of effective specific impulse for some of the commonly considered gases are listed in Table 9-2. These values are based on the use of aluminum gas bottles with a safety factor of 2.2.

For greater density and lower tank weight, the propellant may be stored in a liquid phase. There are several criteria for the selection of vaporizing liquid propellants:

a. The vapor pressure should be sufficiently high to allow a supply pressure to the thruster of the order of 10 psia, yet low enough to allow reasonably low storage pressures.

b. The vapor should have a low molecular weight.

c. The propellant should not decompose or crack into products that will deposit on walls of heater tubes, chamber, or nozzles.

d. The propellant should be non-toxic.

e. The propellant should be compatible with the vehicle structural materials.

Although the delivered specific impulse of the storable vaporizing liquid propellant may not always be significantly greater than that stored in gaseous form, the high-density, low-pressure propellant storage results in lighter weight tankage and thus lower total system weights. However, the phase change necessary for vapor expulsion requires the addition of heat. For many systems, the heat of vaporization can be extracted from the propellant itself and its tankage, or from the spacecraft structure and electronic components.

Where excess heat is not available, a separate heat source for vaporization may be required. This would typically draw upon the electrical supply. Table 9-3 lists some propellants considered suitable for heated vaporizing liquid systems. Certain propellants of the hydrocarbon and halogen families which are suitable for cold gas systems are unsuited for heated systems because of decomposition with heat, and the resulting deposition of solid material on system component surfaces. Of the propellants listed, ammonia offers the greatest potential and has been used in a number of systems.

9-1.2 Arc-jet Thrusters

Arc-jet thrusters utilize an electric arc to transmit heat energy to a gaseous propellant. It is possible to obtain much higher propellant temperatures by this means than can be obtained with a heat transfer thruster such as a resistojet, or a solid-core nuclear reactor thruster. With a heat transfer thruster, the propellant temperature is limited by the thermal properties of the heat exchanger structure. With the arc-jet, however, the maximum temperature occurs in the arc.

Arc-jets are usually axisymmetric with a central tungsten cathode inside an annular tungsten anode. The cathode and anode normally form the exhaust nozzle of the thruster. Arc-jet thrusters have been built which are radiation cooled, water-cooled, and regeneratively cooled. A typical radiation-cooled configuration is shown in Figure 9-4.

In order to heat the gas efficiently to high temperatures, the design must accomplish four primary objectives:

a. Deliver maximum power to the propellant.

b. Retain heat in the propellant.

c. Distribute heat evenly throughout the gas.

d. Minimize cooling required for electrodes and insulation.

The first two objectives maximize overall efficiency, and the last two enhance potential for high specific impulse.

Contemporary design arc-jets operate at specific impulses of 1000 to 1200 sec on hydrogen, with an overall efficiency of 30 to 40 percent for the 30 kW sizes and larger. Arc-jets are basically size dependent, and most engines perform best at the highest specific impulse and power levels they can endure. For reasonable operating conditions and currents, the specific impulse of the arc-jet is limited and the efficiencies are low compared to the electrostatic and electromagnetic thrusters. These considerations, together with predicted mission requirements, have tended to relegate pure arc-jets to the area of academic interest only.

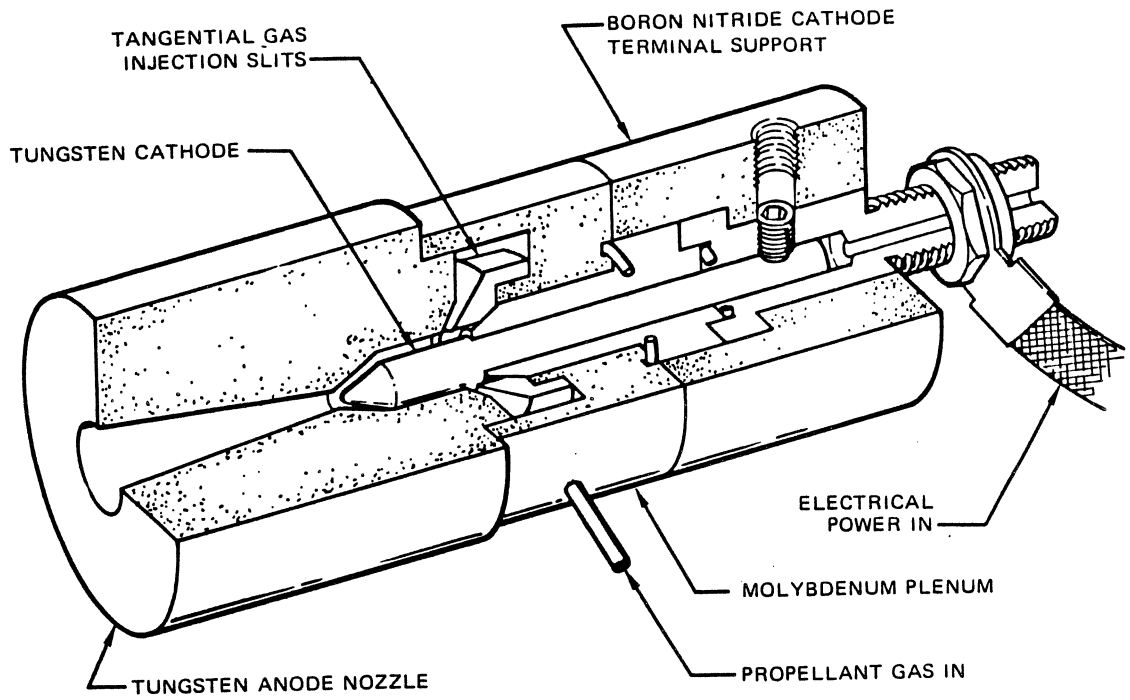

Figure 9-4. Schematic Diagram of Radiation Cooled Arc-jet

9-2 ELECTROSTATIC THRUSTERS

Electrostatic thrusters use an electrostatic field, or direct current potential, to accelerate a working fluid. The two principal categories of propulsion systems using electrostatic acceleration are the ion system and the colloid system. With the ion thruster, propellant is ejected in the form of atomic ions, while the colloid thruster ejects charged particles, each containing many molecules. Several ion propulsion systems are currently in the flight prototype stage of development; colloid propulsion is still in the experimental stage.

9-2.1 Ion Thrusters

For converting atoms to ions, two methods are generally used: contact, or surface, ionization and electron bombardment.

9-2.1.1 Contact Ion Thrusters

The most likely propellant candidates for contact ionization are the alkali metals (lithium, sodium, potassium, rubidium, and cesium), which have low ionization potentials because of their loosely bound valence electrons. Cesium has the lowest ionization potential, and, therefore provides the most efficient source of ions. Further, cesium has a low melting point (83.7°F) and a high vapor pressure at a moderate temperature (600°F), both desirable characteristics for vapor production and feeding. In addition, cesium is the heaviest of the alkali metals, which is also very desirable because the energy increases with mass at any given velocity, and the thrust per unit exhaust area also increases with mass.

Figure 9-5 is a schematic diagram of a contact ion engine using liquid cesium as a propellant. Liquid cesium is stored in the reservoir from which it is fed to a heated vaporizer. Vaporized cesium then flows through the heated delivery tube to the ionizer. The ionizer converts the cesium atoms to ions, which are accelerated through an electrode. As the ions flow downstream from the engine, neutralizing electrons are added to the stream by an electron source, converting the beam to a highly directed plasma.

The heart of the ion engine is the ionizer, where the ions are generated. The ionizer is usually made of porous tungsten which is heated to approximately 2000°F. Gaseous cesium is diffused through the ionizer, emanating as ions from the front surface. For normal operating conditions, about 99 percent of the available atoms are ionized. The efficiency of conversion is a function of the ionizer temperature and the work function of the tungsten surface. Various types of ionizers have been built. Some have used strips, and others used buttons, or disks, of porous tungsten.

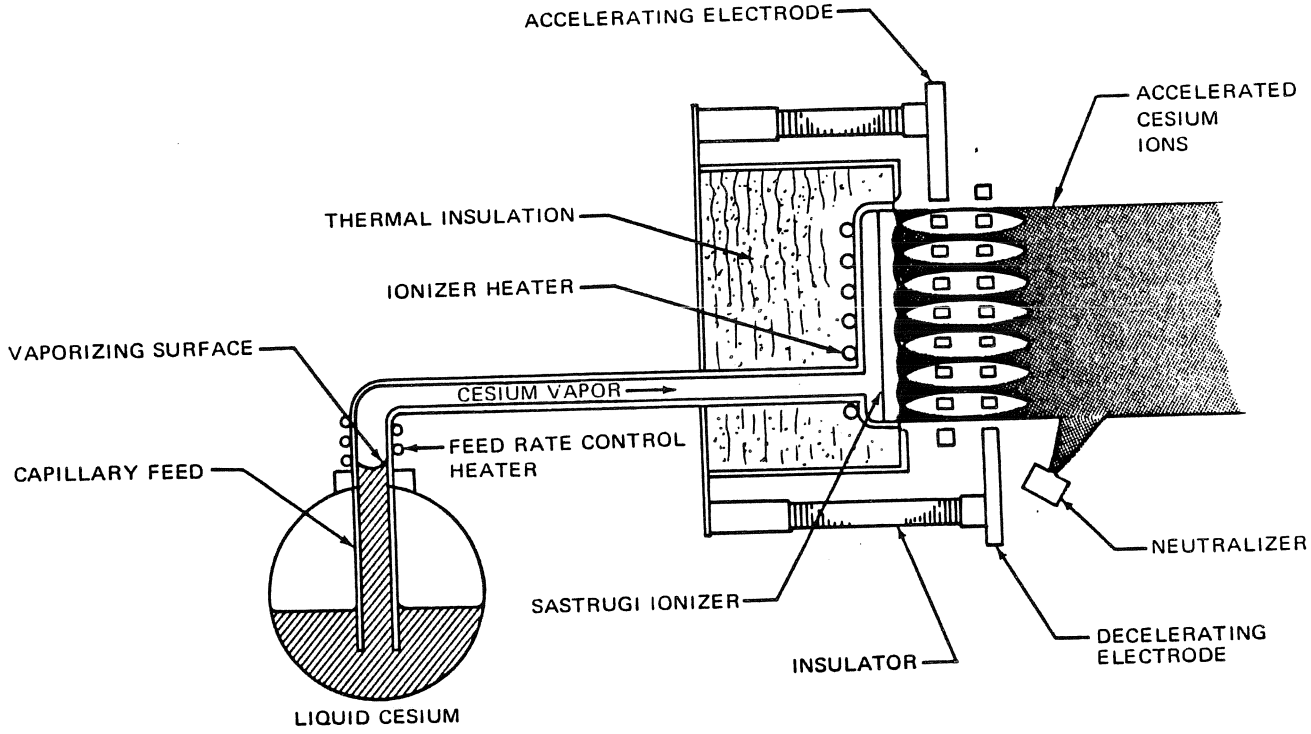

Figure 9-5. Schematic of Contact Ion Engine

As the ions are emitted, they are focused so as to minimize interception and subsequent sputtering of the accelerating electrode. Focusing is accomplished either with a beam-forming electrode or by proper shaping of the emitter surface. The latter is most desirable, but its accomplishment has been impeded by difficulties in obtaining highly refined tungsten powder, and by complex fabrication problems. Intensive ionizer and materials research has overcome most of the difficulties, and led to the development of the Sastrugi ionizer which is the most efficient configuration yet devised. The Sastrugi configuration shown in Figure 9-6, named because of its geometric similarity to the Sastrugi snowfield, is machined from a plate of porous tungsten. The depth and shape of the concave indentations are determined from studies of ion optics. Sastrugi ionizers have provided a current density in excess of 80 mA/cm^2 with 1 percent neutral efflux. However, ionizers are normally run at 16 mA/cm^2 with neutral efflux of 0.6 percent or less.

9-2.1.2 Electron Bombardment Ion Thrusters

Sources of positive ions have been used for many years in high-energy nuclear machines, for various research applications, for mass spectrometers, and for isotope separators. Such sources have almost universally been gas discharge sources, in which the ions are drawn from a plasma generated by ionization of a gas by electrons. Within this category there exists a wide variety of configurations including, for example, electrodeless (radio frequency) discharges, glow discharges, capillary arcs, and oscillating electron sources. A source which appears to offer special advantages for electrostatic propulsion is the low-density, oscillating electron source, sometimes called an electron bombardment, or gas discharge, ion source.

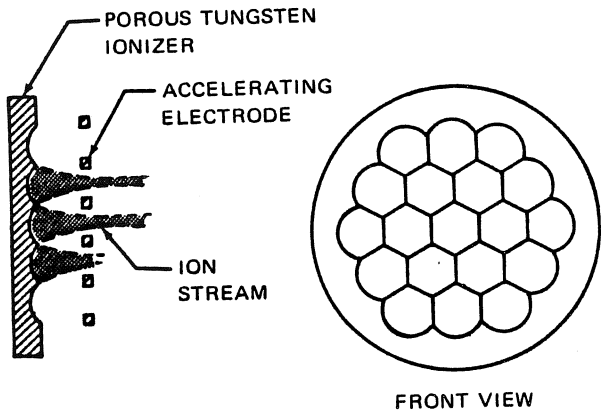

Figure 9-6. Sastrugi Ionizer

A gas discharge, or electron bombardment, ion thruster is shown schematically in Figure 9-7. The ion source is a cylindrical arc chamber with an internal cylindrical anode. A cathode is located on the axis of the system at one of the end plates, and the other end plate is the anti-cathode, or screen electrode, which has apertures in it. The anode is operated at a positive potential with respect to the chamber and end plates which are at cathode potential. A magnetic field is set up parallel to the axis of the device to increase the electron path length. When the plasma is generated, it attaches, or nearly attaches, to the anode and there is a plasma sheath at the ends of the chamber. The entire chamber is operated at a high positive potential, and an accelerator electrode is maintained at a negative potential with apertures that match the apertures in the screen electrode. Ions diffusing to the plasma sheath at the screen electrode are accelerated through the apertures and into beams by fields across the accelerating gap. The beams are then neutralized by the injection of electrons from an emitter at, or close to, ground potential.

Both cesium and mercury are used as propellants for electron bombardment thrusters. Even though the high magnetic fields required for efficient mercury discharges increase engine weights, mercury has several advantages, such as high density, high atomic weight, and ease of handling. However, for long-lifetime engines, mercury ion thrusters have disadvantages which have yet to be surmounted. The two most serious problems are short cathode lifetime and electrode sputtering. Neither of those limitations is a problem in the cesium engine for lifetimes approaching 10,000 hours. The advantages of using cesium as the expellent in a gas discharge source are derived from its unique physical properties. Cesium in the easiest element to ionize and has a large ionization cross section at moderate electron energies. This permits operation of an efficient discharge at arc voltages below the sputtering thresholds of most metals.

9-2.2 Colloid Thrusters

The electrical colloid system provides lightweight auxiliary propulsion for many varieties of spacecraft. The principal advantages of the system are low power and low propellant consumption. Thrust is produced by a stream of charged droplets formed by exposing an electrically conducting liquid to the intense field produced at the tip of a hollow capillary feed tube which is centered within an extractor aperture. Specific impulses of 1,000 sec are achievable with present day state-of-the-art.

9-2.2.1 Configuration

The colloid thruster concept is shown in schematic form in Figure 9-8. Liquid propellant emerging at the tip of

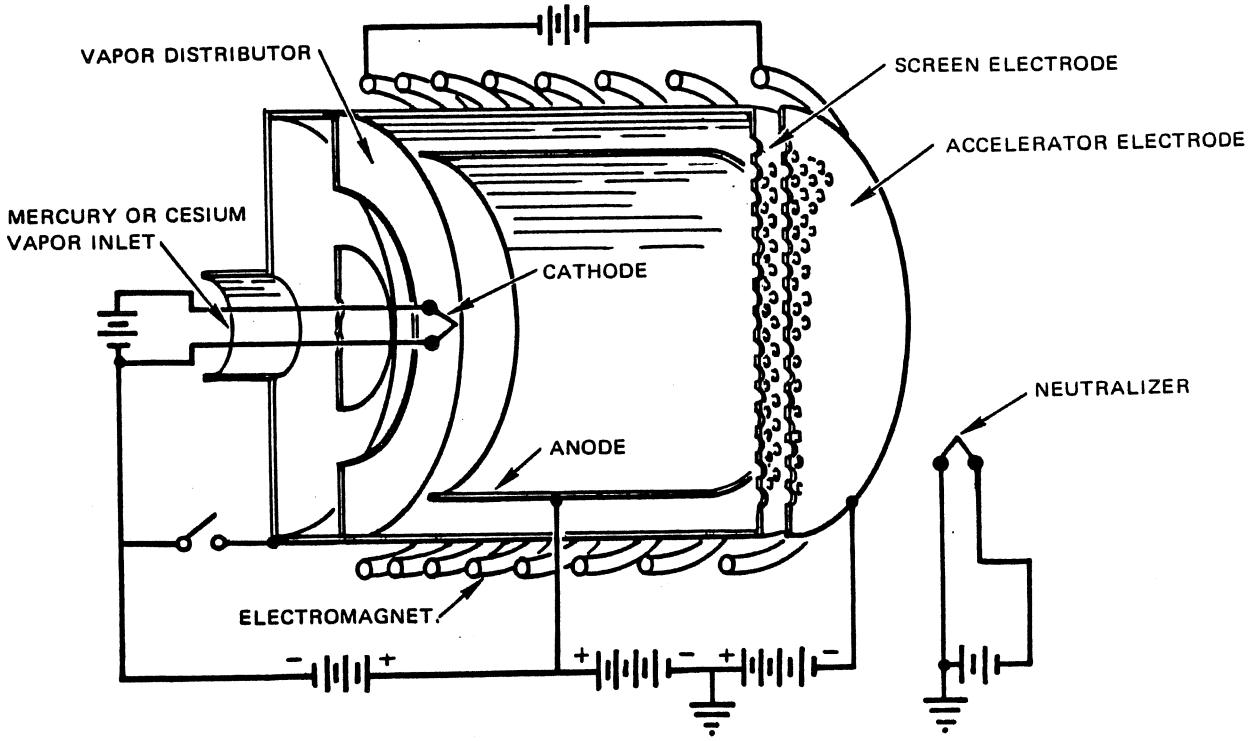

Figure 9-7. Schematic of Electron Bombardment Ion Thruster

the capillary needle is subjected to a strong electrical field. The meniscus at the end of the needle tends to form microscopic jets which accentuate the electrical field pressure, causing a continuous emmision and acceleration of charged droplets, approximately 100 Å or 10^{-6} cm in diameter. The droplets may be either positive or negative, depending on the polarity of the potential applied to the needles. The colloid beam containing the multi-molecular charged particles has a relatively narrow velocity dispersion.

The capillary tube is generally held at a positive potential (nominally 5 to 10 kV). The extractor electrode is kept negative (at about 500 to 1,000 V) in order to produce an electron barrier to the capillary tube.

The peak specific charge of the colloid beam may be varied over a range of 200 to over 300,000 C/kg. For comparison purposes, the specific charge of cesium is fixed at 720,000 C/kg. It is the ability to vary the peak specific charge, by means of adjusting the potential, which enables a variation in thrust and specific impulse of the thruster. This provides the flexibility of optimizing mission and propulsion parameters.

The single needle concept shown in Figure 9-8 typically produces 2.5 to 5 μlb of thrust. Higher thrust levels are easily achieved by going to a multiplicity of needles in modular form.

The most successful colloidal propellant developed to date consists of 19.3 percent by weight solution of sodium iodide in glycerol. The purpose of the sodium iodide is to produce an ionically conducting liquid which is amenable to charging during the spraying process. The charging mechanism is believed to be accomplished by the neutralization of negative iodine ions at the capillary tip, leaving a surplus of positive sodium ions.

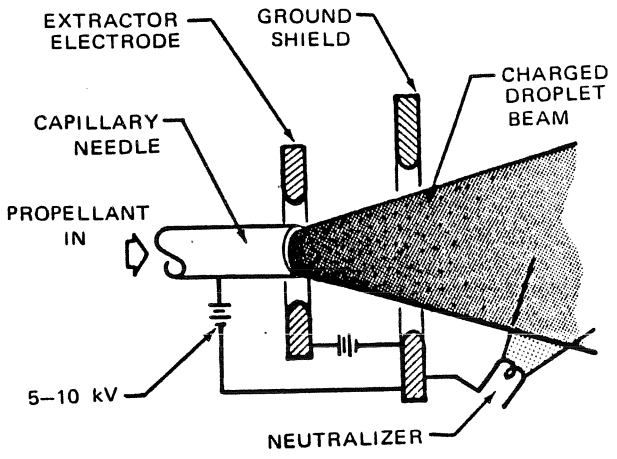

Figure 9-8. Colloid Thruster Schematic

The colloid propulsion system consists of four basic components:

a. Colloid thruster unit

b. Propellant tankage

c. Control valving

d. Power conditioning unit

A typical arrangement of these components is shown in the system schematic diagram, Figure 9-9, and the system assembly drawing, Figure 9-10.

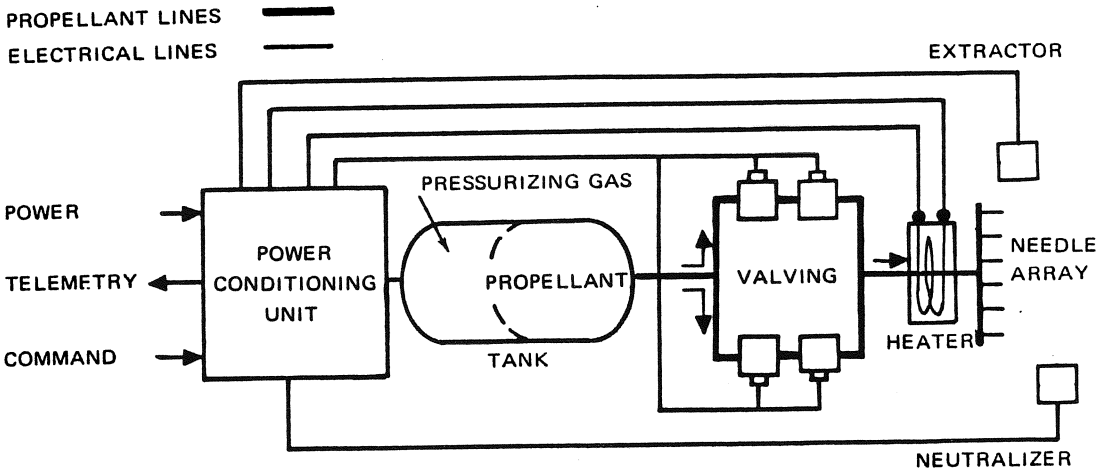

Figure 9-9. Colloid Propulsion System Schematic

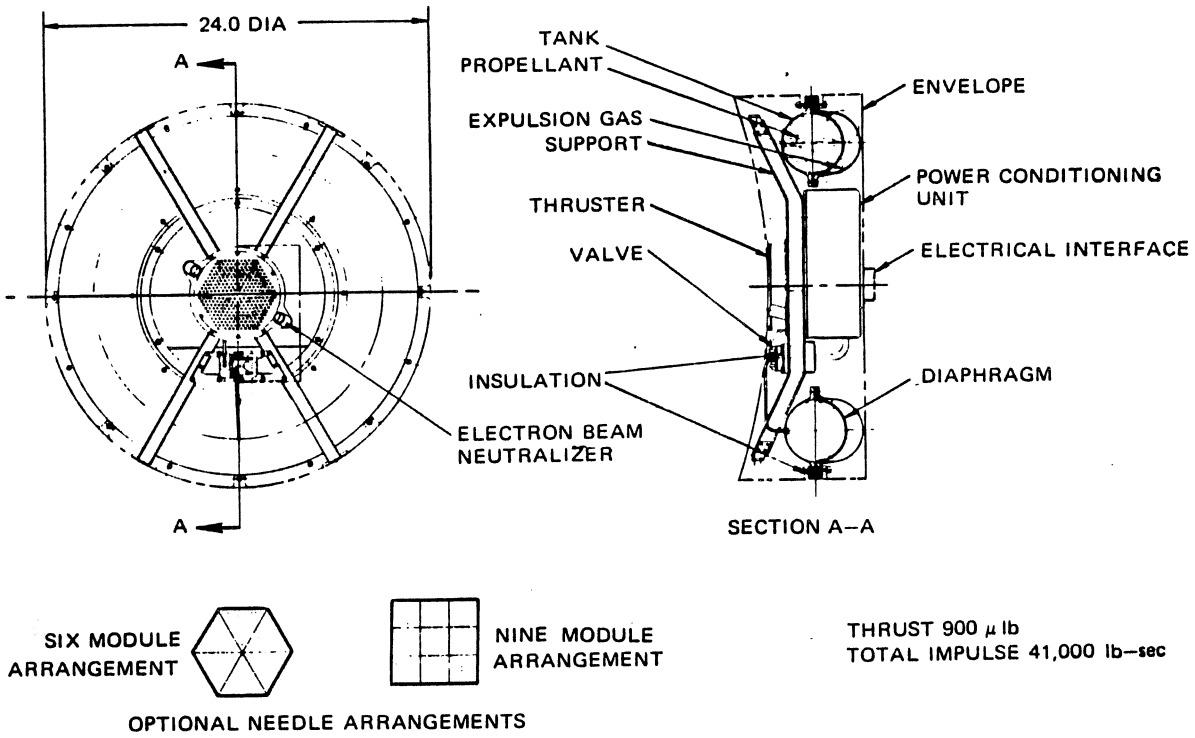

Figure 9-10. Colloid Propulsion System Assembly Drawing

A feed line and plenum assembly of the colloid thruster unit serve the functions of propellant supply and mechanical support for the needle array. Electrically these components are connected to the modular needle array and operate at the same potential as the needles. Each modular array consists of a number of capillary tubes connected to the plenum assembly for propellant supply to the needles. These capillaries provide the proper geometry and electric fields for the production of an electrostatic spray of submicroscopic charged droplets which form the exhaust stream.

The potential for accelerating the droplets is applied between the needles and the extractor. The extractor, which contains apertures concentric with the individual needles, is the accelerating electrode upon which the thrust force is developed and transmitted to the vehicle.

The charged droplet beam is made electrically neutral by the addition of electrons from a thermionic cathode neutralizer. The extractor is biased several hundred volts negative to prevent the electrons from flowing back to the positively charged needles or their supports. The extractor electrodes are mounted on insulators which both electrically isolate and mechanically support the individual components from the support base, which serves as the interface to other parts of the system structure. The thruster components are maintained within their allowable temperature range by thermostatic control.

9-2.2.2 Application

In general, colloid electrical propulsion is attractive for moderate total impulse requirements (up to 50,000 lb-sec) where high specific impulse and low-power penalty are desirable. The thruster range suggested for preliminary selection is between 3 μlb and 1 mlb per thruster. Corresponding power requirements range between 5 and 53 W.

The selection of a particular kind of propulsion system depends heavily upon the overall system weight and electrical power requirements. To aid in the selection of

a system, these two criteria have been generalized in Figure 9-11 and 9-12. Figure 9-11 gives the estimated overall system weight including thruster, power source and conditioner, propellant, and feed system as a function of total impulse for three nominal thrust levels. Weights for intermediate thrust levels may be obtained by cross-plotting at the required total impulse value. Figure 9-12 presents the power requirements as a function of engine thrust. For system studies, the thrust used should be total thrust applicable at one time (for example, simultaneous operation of two or more thrusters).

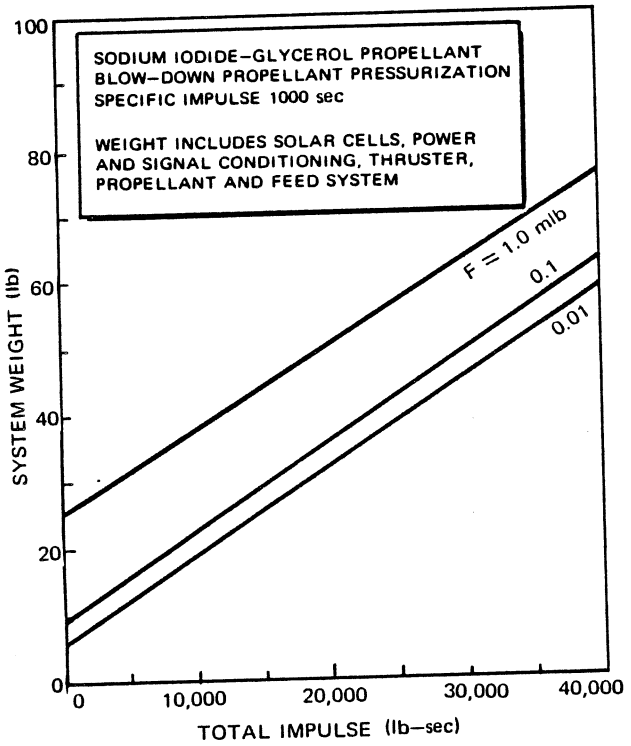

Figure 9-11. Colloid Propulsion System Weight

The following general characteristic data are representative of a typical system and were used in determining the design data.

Propellant	19.3% sodium iodide in glycerol
Propellant density	0.053 lb/in^3
Specific impulse	1,000 sec
Operation life	10,000 hours
Thruster efficiency due to beam divergence	95%
Beam efficiency due to distribution in particle charge to mass ratio	70%
Power conditioning efficiency	75%
Power supply specific weight	0.25 lb/W (typical solar array)
Power conditioner specific weight	0.14 lb/W (at 50 W)
Thruster specific weight	0.85 lb/W
Applied potential	8.5 kV
Needle current	0.5 - 15 μA per needle

Although many of the parameters have been established for this analysis, there are a number of parameters that can be varied to give wide system flexibility. For example, the exhaust velocity or specific impulse is determined by the net applied potential and by the

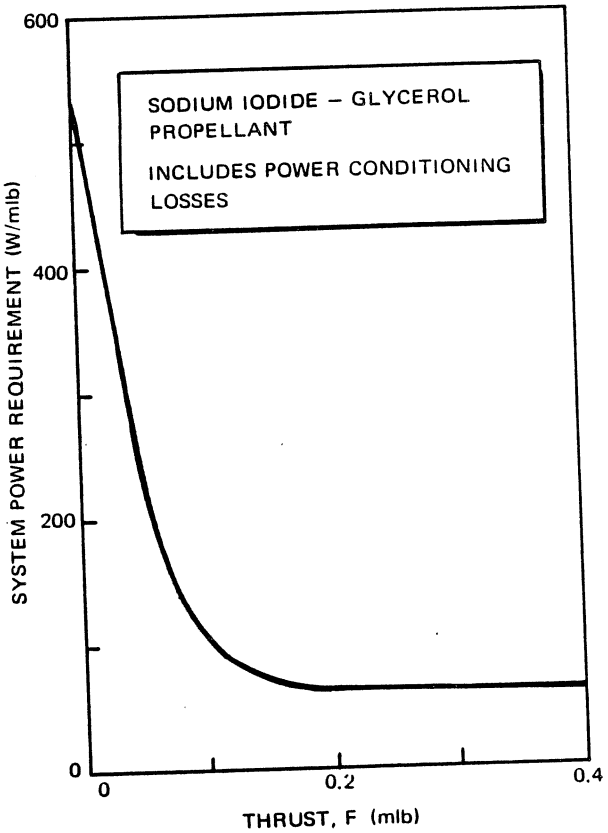

Figure 9-12. Colloid Propulsion System Power Requirements

charge-to-mass ratio of the individual droplets. The charge-to-mass ratio is in turn determined by needle geometry, the electric field, the propellant flowrate and the properties of the propellant.

9-3 ELECTROMAGNETIC THRUSTERS

Electromagnetic thrusters, or plasma jets, are characterized by electromagnetic acceleration of a propellant gas to produce thrust. This is accomplished by heating the propellant gas by means of an arc to produce a plasma consisting of ions, electrons, and neutral particles. When the plasma has been sufficiently ionized to conduct an appreciable current, magnetic forces can be exerted on the gas, accelerating it to high velocities.

In practice, there are three mechanisms by which the electromagnetic thrusters produce thrust. These are:

a. Arc heating of the gas, followed by thermal expansion to convert the heat energy to directed kinetic energy (pure arc-jet).

b. Electromagnetic compression of the gas by a radially inward directed, electromagnetic pinch force, followed by expansion and acceleration in the axial direction.

c. Direct acceleration of the gas in the thrust direction by the axial components of the electromagnetic forces acting on the gas.

Most continuous plasma engines utilize all three of these mechanisms in various proportions.

The plasma ejected by the electromagnetic thruster is electrically neutral, and is not subject to space charge effects. Therefore, the electromagnetic thruster can produce an area density of the jet which is many times greater than that possible with an ion system. For this reason, a plasma motor will always have a much smaller size than an ion motor of the same thrust.

Electromagnetic thrusters offer much promise for low thrust, high specific impulse space propulsion due to their potentially high efficiency and relatively low power requirements. However, these systems are still in the early stages of development.

9-4 BIBLIOGRAPHY

1. *Electrical Colloid Propulsion for Spacecraft Positioning, Stationkeeping, and Attitude Control*, TRW Systems Group, January, 1968.

2. *Electrothermal and Radioisotope Heated Propulsion for Spacecraft Reaction Control*, TRW Systems Group, February, 1968.

3. M. V. Clauser, "Magnetohydrodynamics," *Space Technology*, H. Seifert, Ed., John Wiley and Sons, New York, 1959.

4. W. R. Corliss, *Propulsion Systems for Space Flight*, McGraw-Hill Book Co., New York, 1960.

5. W. R. Mickelsen, *Advanced Concepts in Electric Propulsion*, AIAA Paper 67-426, July 17, 1967.

6. C. Ming Wong, *Advanced Propulsion Systems for Space Applications*, Vol. 1, AIAA, New York, 1966.

7. E. Stuhlinger, "Electric Space Propulsion," *Science Journal*, July, 1969.

8. E. Stuhlinger, "Electrical Propulsion," *Handbook of Astronautical Engineering*, H. H. Koelle, Ed., McGraw-Hill Book Co., New York, 1961.

9. E. Stuhlinger, *Ion Propulsion for Space Flight*, McGraw-Hill Book Co., New York, 1964.

10. G. P. Sutton, "Electrical Propulsion," *Rocket Propulsion Elements*, John Wiley & Sons, New York, 1963.

11. M. L. Yaffee, "Electric Propulsion, Part 1 and 2," *Aviation Week*, 27 January and 3 February, 1964.

Section 10

PRELIMINARY ROCKET VEHICLE DESIGN

10-1 VEHICLE SIZING AND SELECTION METHODOLOGY

10-1.1 Mission Requirements and Performance

The customer (NASA or the Military) usually defines new missile or space system mission requirements. The important considerations in establishing these requirements are related to what the system is and how it is to be used.

During the conceptual and definition phases of the procurement cycle for a new space or missile system, the contractor conducts preliminary design investigations to optimize and select a vehicle concept to meet customer requirements. This is necessary so that a realistic basis can be established for writing design specifications for procurement of the system and all its subsystem elements. In order to efficiently accomplish these tasks, a selection methodology must be established which will quickly lead to the chosen system. Usually this progresses from gross feasibility investigations to successively more complex and detailed examinations of the vehicle and its subsystems. The selection process involves the expertise of a number of interrelated technology disciplines and is based on a multitude of requirements and constraints. Consequently, iterative analysis and selection procedures must be employed.

Several classes of vehicles can be defined based on their mission requirements or applications. Launch vehicles, as defined here, are those used for orbital and interplanetary missions (Space Launch Vehicles) and which generally employ multiple stages. Strategic offensive missiles (ICBM's, IRBM's, etc.) are also in this class but do not reach orbital velocity. Payload weight and velocity at burnout are the important performance considerations for these vehicles. Free-flight rockets are another class of vehicle having velocity and payload as primary mission performance requirements. They follow a ballistic or nonmaneuvering trajectory. Sounding rockets, artillery rockets, unguided tactical missiles, and drones or target missiles are in this category. A third class of vehicles are the maneuvering missiles, i.e., interceptor, guided tactical offensive, and strategic defensive missiles. In addition to burnout velocity and payload weight as primary mission requirements, performance must be optimized for any of four criteria: (1) Minimum time of flight to a space point, (2) Maximum velocity at a space point, (3) Maximum velocity at a given time for a trajectory passing through a given space point, or (4) Maximum velocity at a given time in an open-loop trajectory. Table 10-1[1,4*] summarizes typical performance requirements for the above classes of vehicles and typical current rocket vehicles for each class. More detailed descriptions of mission requirements for each class are described in subsequent subsections.

Since space mission requirements differ widely depending on the combination of weight and burnout velocity requirements for the payload, it is cost-effective to use one launch vehicle for a variety of missions. The performance characteristics for NASA launch vehicles tentatively available in the 1971 to 1975 time period are shown in Figure 10-1. The payload/apogee altitude capability for one Thor-Delta configuration is shown in Figure 10-2.

Tables 10-2 through 10-5 summarize various space launch vehicles, missiles, and research rockets and typical current solid and liquid rocket motors, the important design characteristics for each, and typical performance characteristics and requirements. Figure 10-3 compares the approximate launch vehicle cost per pound of payload for a number of operational space vehicles. It is a current design goal to reduce the costs to $100 per pound of payload to orbit through the use of reusable rocket states, e.g., Space Shuttle, and through simplified design of subsystem elements.

10-1.2 Vehicle and Subsystem Sizing and Selection Procedures

Figure 10-4 is a schematic illustration of a typical missile or space launch vehicle configuration with several subsystems shown and which defines nomenclature for staging used in this manual. Other combinations of liquid and solid motor configurations are frequently used. It should be noted that there is a distinction between a "stage" and a "step." The first stage operation consists of the entire vehicle with the first step motor operating, and so on for the upper stages. The definitions enable straight forward definitions of the mass properties of the system at any time during flight, i.e., mass ratio, step mass fraction, growth factor, etc.

*References listed in Paragraph 10-8.

Table 10-1. Burnout Velocities Required for Various Missions

Mission	Velocity at 100 nm Altitude (non-rotating earth) (ft/sec)	Additional Velocity to Circularize Orbit (ΔV_2)* (ft/sec)	Additional Velocity to Soft Land (ft/sec)	Typical Current Vehicles
Launch Vehicles				
Research Rockets:				Athena, Aerobee
1,000 nm altitude	16,290			
10,000 nm altitude	31,040			
Strategic Offensive Missiles: (surface-to-surface)				Poseidon, Minuteman, Polaris
IRBM (1,000 nm range)	12,240			
ICBM (5,000 nm range)	22,610			
ICBM (10,000 nm range)	25,350			
Space Launch Vehicles:				Long-Tank, Thrust-Augmented Thor-Delta, Atlas/Agena, Titan 3C
Earth Satellite	($V_{100\ nmi} + \Delta V_1$)*			
100 nm orbit	25,581			
300 nm orbit	25,916	350		
1,000 nm orbit	26,990	1,330		
10,000 nm orbit	32,190	4,650		
20,000 nm orbit	33,920	4,850		
100,000 nm orbit	35,580	3,490		
Lunar Missions				Saturn V/Apollo
90 hour transfer	35,850 to 35,910		8,310	
60 hour transfer	35,910 to 36,010		8,700	
50 hour transfer	36,070 to 36,160		9,410	
Interplanetary (minimum energy):				Titan 3D, Atlas/Centaur
Earth Escape	36,178			
Sun	99,900 to 105,700			
Mercury	41,000 to 47,900		15,000	
Venus	37,570 to 39,350		49,100	
Mars	37,370 to 38,860		49,100	
Jupiter	45,700 to 46,800			
Escape Solar System	53,900 to 54,600			
To a Comet	38,000 to 40,000			

**Hohmann Transfer from 100 nmi circular orbit (Sec 10.2.2.2.1)*
where ΔV_1 *= incremental transfer orbit injection velocity, fps*
ΔV_2 *= incremental velocity to circularize new orbit.*

Table 10-1. Burnout Velocities Required for Various Missions (Continued)

Mission	Typical Impulsive Velocity Increment – ft/sec	Typical Current Missiles
Maneuvering Missiles		
Air-to-Air	2,000-5,000	Sidewinder Genie Sparrow Phoenix
Air-to-Surface	1,500-5,000	Harpoon Condor SRAM Bullpup
Surface-to-Air	2,000-10,000	Sprint Spartan Redeye Sam-D Nike-Hercules
Surface-to-Surface		Dragon Subroc Shillelagh
Free-Flight Rockets		
Surface-to-Air	1,000-8,000	Asroc Honest John

TYPICAL DEFINTIONS FOR FIGURES 10-1 AND 10-2.

TAT(9C)/DELTA(TSE)/TE364(2300)(904)
- (909) – NASA MODEL NUMBER DESIGNATION
- (NO. OF CASTOR SRM STRAP-ONS, THRUST-AUGMENTED (THOR), STANDARD LONG TANK)

TAT(6C)/DELTA(TSE)/TE364(2300)(604
TAT(6C)/DELTA(TSE)/TE364(1440)(303)
- (DELTA SECOND STAGE WITH TRANSTAGE ENGINE)
- (SRM WITH 1440 LB OF PROPELLANT)

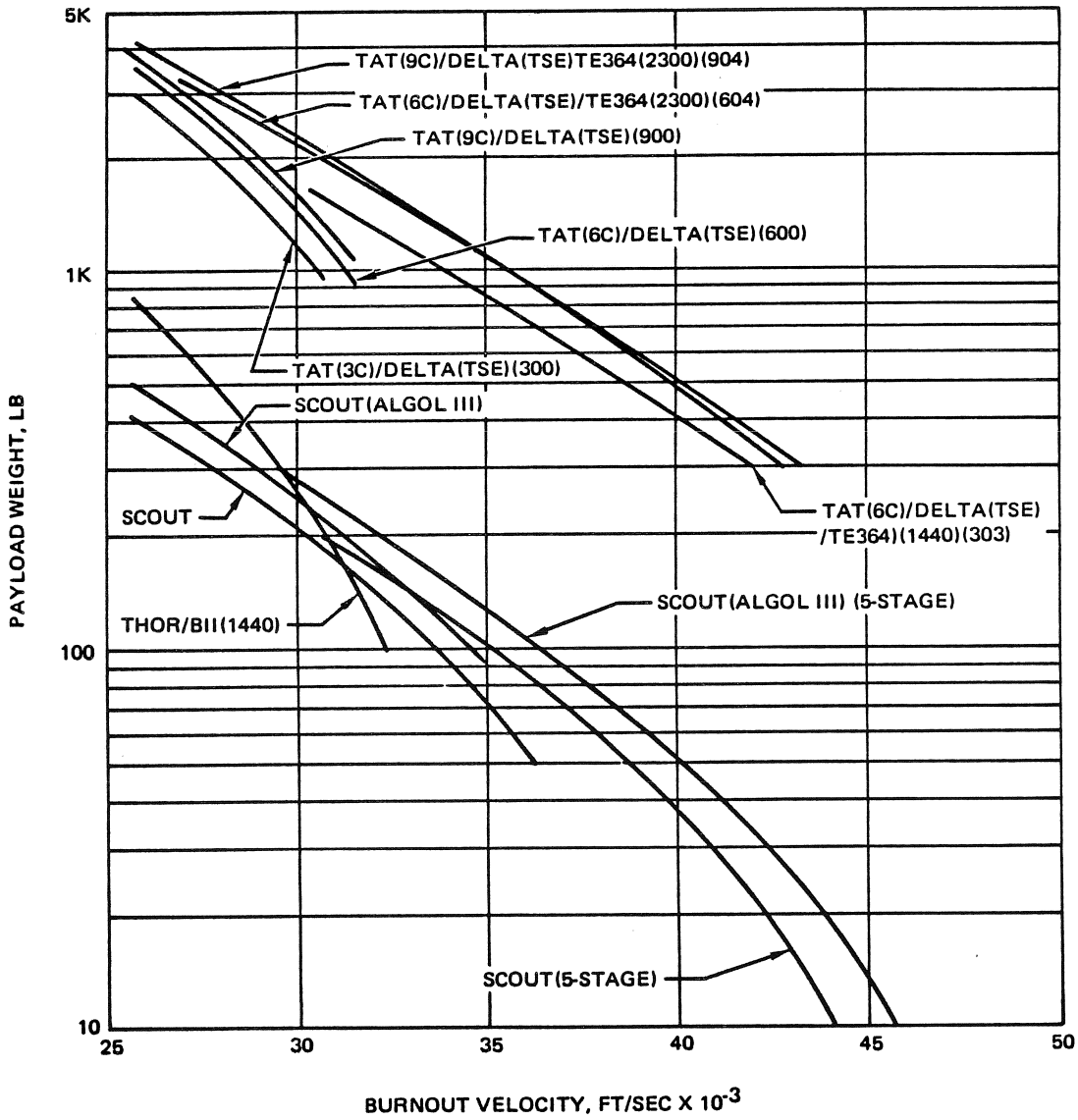

Figure 10-1. Launch Vehicle Performance Available in 1971 – 1975 (Sheet 1 of 2)

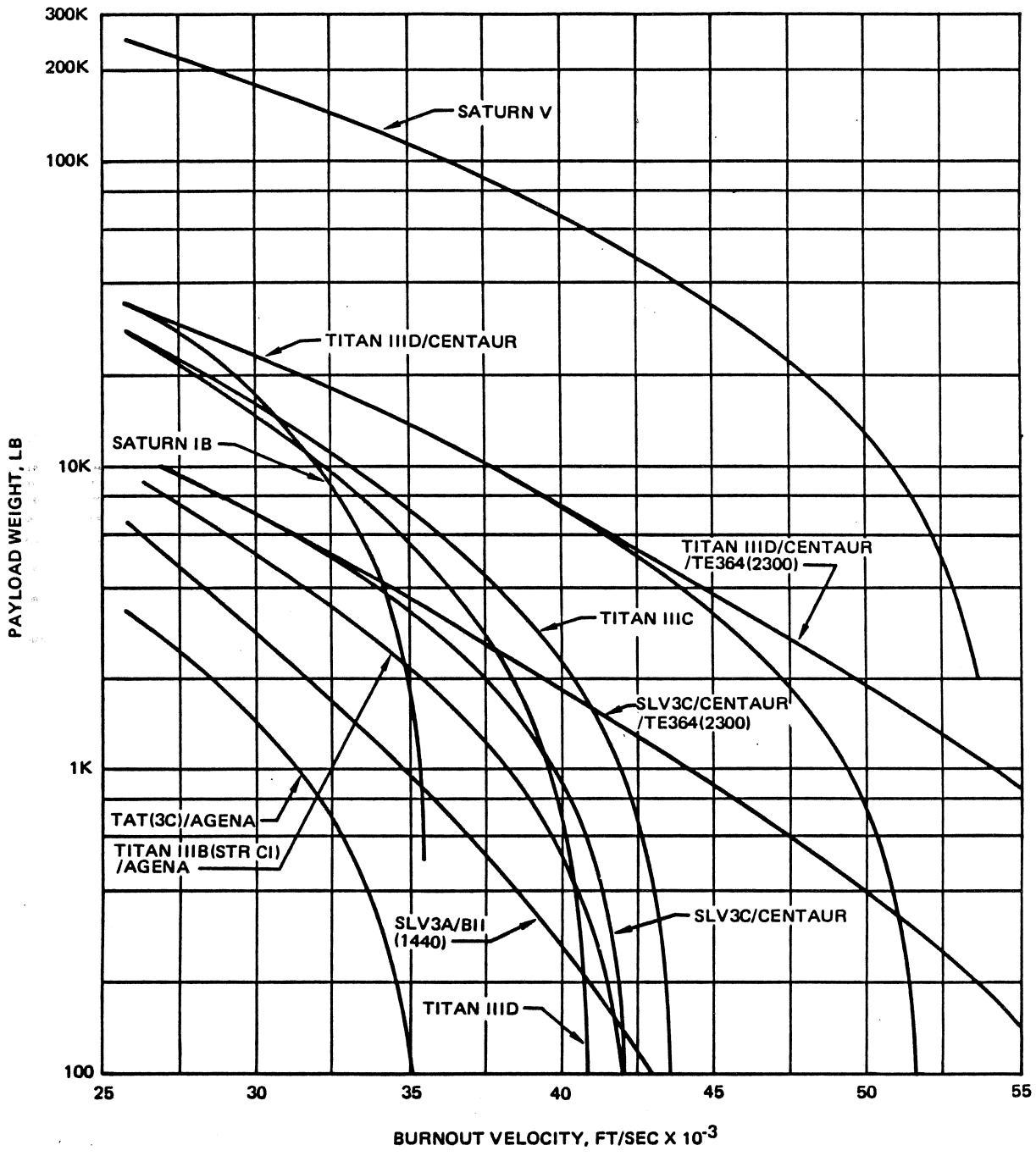

Figure 10-1. Launch Vehicle Performance Available in 1971 – 1975 (Sheet 2 of 2)

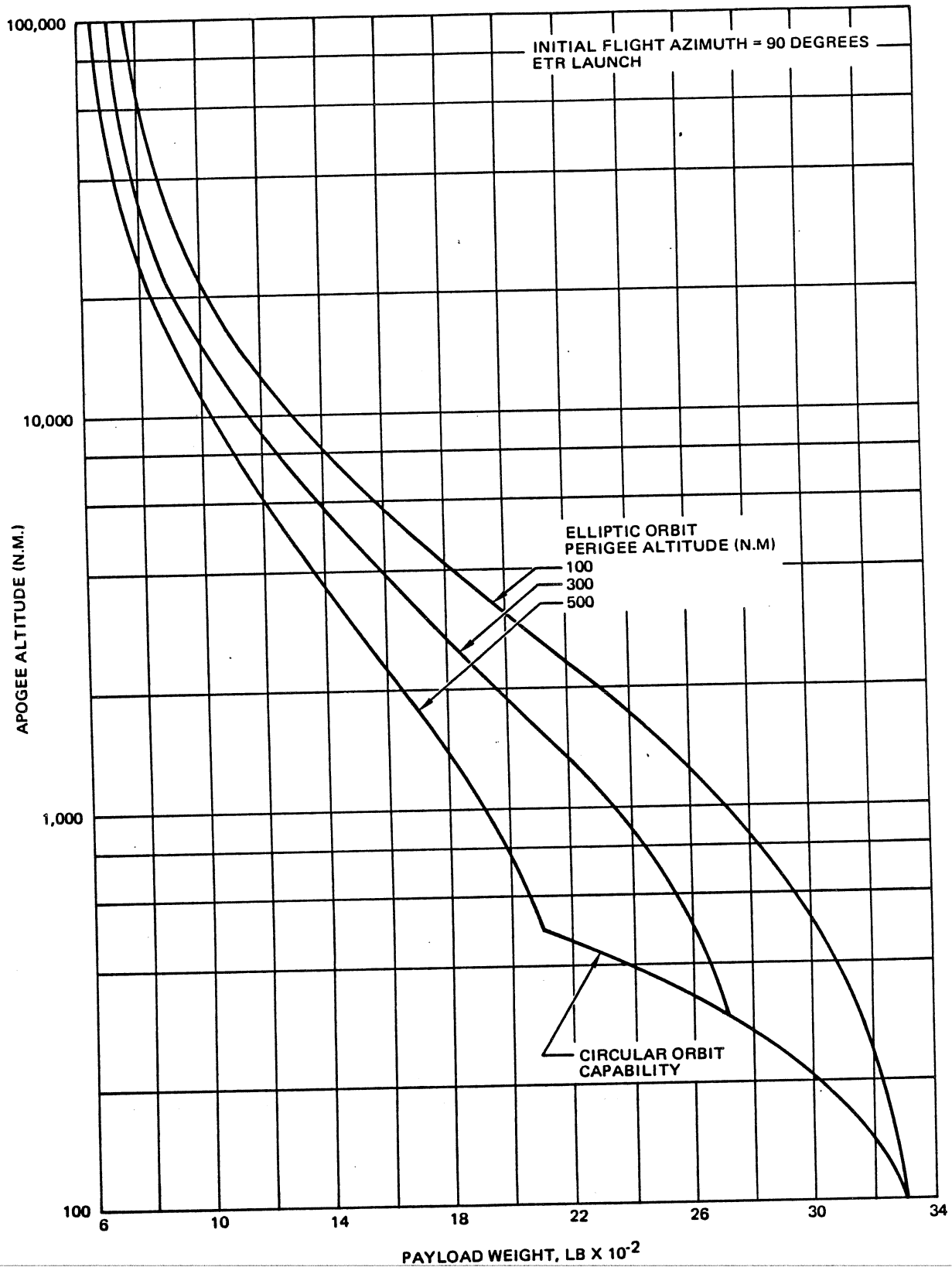

Figure 10-2. TAT(3C)/Delta(TSE)/TE364(1440) Orbital Capability, 90° Launch From ETR

Table 10-2. U.S. Space Launch Vehicles

	Vehicle Name	User Agency	Vehicle Contractor	Propulsion: Stage	Propulsion: Engines	Step Contractor	Step or Motor Designation	Propellant (Oxidizer/Fuel)	Nominal Thrust (lb)[8]	Max. Dia (ft) (Excluding Strap-Ons)	Length (ft) (Excluding Payload)	Launch Weight (lb)	Orbital Payload (lb)
Basic Vehicles	Saturn 1B	NASA	Chrysler	1	8 x Rocketdyne H-1	Chrysler	S-1B	LOX/RP	1,640,000	21.4	80.3	1,290,180	40,000[2]
				2	1 x Rocketdyne J-2	MDAC	S-4B	LOX/LH_2	230,000	21.7	58.4		14,000 (Circumlunar)
	Saturn 5	NASA		1	5 x Rocketdyne F-1	Boeing	S-1C	LOX/RP	7,570,000	33	138	6,262,500	280,000[2]
				2	5 x Rocketdyne J-2	RI	S-2	LOX/LH_2	1,125,000	33	81.5		103,000 (Circumlunar)
				3	1 x Rocketdyne J-2	MDAC	S-4B	LOX/LH_2	230,000	21.8	58.5		
	Long Tank Delta DSV-3P[13]	NASA	MDAC	1	1 x Rocketdyne H-1	MDAC	Thor	LOX/RP-1	209,700	8	73.4	291,000	4,400[1,10]
			MDAC		3,6, or 9 Thiokol TX-354-5	Thiokol	Castor 2	Solid	534,000	2.5	20		1,060 (Escape)[11]
			MDAC	2	1 x Aerojet AJ10-118F	MDAC	Delta	N_2O/Aerozine 50	9,250	8	19.3		1,550[11,12]
				3	1 x TE364-3 or -4	Thiokol		Solid	10,000/15,000	3.2	7.6		
	Scout SLV-1A (Algo) 3-First Stage)	NASA/ Navy/ USAF	LTV	1	1 x UTC Algol 3	LTV	Algol 3	Solid	107,000	3.7	75.1	47,200	300[7]
				2	1 x Thokol TX-354-5	LTV	Castor 2	Solid	61,100				75 (Escape)
				3	1 x ABL X259-B3	LTV	Antares 2	Solid	22,200				
				4	1 x UTC FW-4S	LTV		Solid	5,700				
	Titan 3C[3] SLV-5C	USAF/NASA	Martin Marietta[4]	1	2 x 120-in. UA1205 (strap-on)	UTC		Solid	2,400,000	30 (including strapons)	124	1,400,000	25,000[5]
				2	2 x Aerojet LR-87-AJ-9	Martin		N_2O_4/N_2H_4-UDMH	430,000				5,000 (Escape)
				3	1 x Aerojet LR-91-AJ-9	Martin		N_2O_4/N_2H_4-UDMH	100,000				
				4	2 x Aerojet AJ10-138	Martin	Transtage	N_2O_4/UDMH	16,000				
Upper Steps	Agena D[6]	USAF/NASA	Lockheed		1 x Bell 8096	Lockheed	YLR-81BA-11	IRFNA/UDMH	16,000	5	23.25	15,037	2,300[5,7]
	Centaur	NASA	GDC		2 x P&W RL10A-3	GDC	Centaur	LOX/LH_2	30,000	10	30	37,000	9,900[9]
	Burner 2	USAF	Boeing		1 x TE-M364-2	Boeing	Burner 2	Solid	10,000	5.4	5.8	1,440[9]	3,000[7]
	Burner 2A	USAF	Boeing		1 x TE-M364-2 All	Boeing	Burner 2A	Solid	10,000	5.4	5.8	1,440[9]	5,000[7]
					1 x TE-M-442 Thiokol	Boeing	Burner 2A	Solid	8,000			524[9]	

NOTES: [1]100 nmi orbit; [2]108 nmi orbit; [3]NASA uses Titan 3C for advanced Applications Technology Satelites; [4]Martin is systems integrator, associate contractors are United Technology Center, Aerojet and AC Electronics; [5]from Eastern Test Range; [6]Agena D has two-burn capability; [7]300 nmi orbit circular and polar orbit; [8]SL conditions except for upper stages (vacuum); [9]step motor weight; [10]NASA Model 2910 (First two stages only – nine solids); [11]NASA Model 2914 (3 stages-nine solids); [12]100 x 19,400 nmi, synchronous orbit; [13]The Delta vehicle is undergoing design changes to offer flexible payload capability. Included in current and anticipated modifications are: (1) Extended Long Tank, Thor Booster Tanks, (2) 3, 6, or 9 Castor Strap-on Solid Rocket Motors on the booster, (3) H-1 Rocketdyne booster engine (Model RS-27); (4) modified Transtage Engine (TSE) (AJ-10-aa8F) with N_2O_4/A-50 propellants or a modified Apollo LEM (TRW) engine, (5) Extended cylindrical section on TE-364 motors to increase solid propellant loading, (6) a new Digital Intertial Guidance System (DIGS); Refer to Figure 10-1 and 10-2 for some projected model capabilities.

Table 10-3. Typical U.S. Missiles

Mission Category	Name Designation	Cognizant Service	System Manager Prime Contractor	Status[1]	Assoc Contractor or Manufacturer	Max. Len (ft)	Max. Span, Wings/ Fins (ft)	Body Dia (ft)	Launch Weight (lb)	Assoc Contractor or Manufacturer	No. of Engines Designation, Type	Total Thrust (lb)	Assoc Contractor or Manufacturer and Type	Max. Range (nmi)	Remarks
Air-to-Air	Genie AIR-2A	USAF	McDonnell Douglas	S	McDonnell Douglas	9.57	3.3	1.5	800	Thiokol	1 x spr	36,250	Non Unguided	6	Used on F-101B & F-106; Nuclear Warhead. Also AIR-2B.
	Side-winder-1C AIM-9D	USN	NWC/ Raytheon	P,S	NWC/ Raytheon	9.5	2.1	0.42	185	NAR/Rocketdyne	1 x Mk 36 Mod 5 spr		Raytheon Infrared homing	10	Motorola AIM-9C has semi-active radar homing guidance.
	Sparrow 3 AIM-7E	USN	Raytheon	P,S	Raytheon	12.0	3.3	0.67	450	NAR/Rocketdyne	1 x Mk 38 Mod 4 spr		Raytheon Semi-active CW radar homing	12	Also used by USAF on F-4 F and G models under test.
Air-to-Surface	Bullpup B AGM-12C	USN	Maxson Electronics	P,S	Maxson Electronics	13.6	4.0	1.5	1,785	Thiokol	1 x LR62-RM-2 1 pr	33,000	Maxson Electronics Command	9	1,000 lb conventional warhead; Martin Marietta is making high fragmentation version, AGM-12E, for USAF.
	Hound Dog AGM-28B	USAF	Rockwell International (RI)	S	RI	42.5	9.4	2.4	10,147	Pratt & Whitney	1 x J52-P-3 tj	7,500	NAR/Autonetics Inertial	683	Air-launched from Boeing B-52G/H
	Shrike AGM-45A	USAF	NASC/NWC	P,S	Texas Instruments, SR/Univac	10	3	0.67	390	NAR/Rocketdyne	1 x Mk 39 Mod 7 spr		Texas Instruments, SR/Univac Passive radar homing		Also used by USAF on F105G & F-4C; Aerojet Mk 53 spr is alternate motor.
	SRAM AGM-69A	USAF	Boeing	P,S	Boeing	14		1.46	2,230	Lockheed Propulsion	1 x LPC-415 spr		Singer-General Precision Inertial, DC Power Conditioner	120	Short range attack missile for 13-1 and FB-111 and late model B-52's; nuclear capability; multipulse rocket motor; semi-ballistic or aerodynamic trajectory.
Surface-to-Air	Nike Hercules MIM-14B	Army	Western Electric	S	McDonnell Douglas	41	7.5	2.6	10,000	Thiokol, Hercules	1 x M42A1; 1 x M30A1 spr		BTL/Western Electric Command	75+	Nuclear or conventional warhead; deployed in US and overseas.

[1] D – development P – production R – research S – Service use
tj – turbojet

[2] 1 pr – liquid propellant rocket (Packaged)

[3] spr – solid propellant rocket

[4] AFSC/SAMSO/TRW are program managers; Boeing Company is system integration contractor

Table 10-3. Typical U.S. Missiles (Continued)

Mission Category	Name Designation	Cognizant Service	System Manager Prime Contractor	Status[1]	Assoc Contractor or Manufacturer	Max. Len (ft)	Max. Span, Wings/ Fins (ft)	Body Dia (ft)	Launch Weight (lb)	Assoc Contractor or Manufacturer	No. of Engines Designation, Type	Total Thrust (lb)	Assoc Contractor or Manufacturer and Type	Max. Range (nmi)	Remarks
Surface-to-Air	Safeguard/ Spartan XLIM-49A	Army	BTL/ Western Electric	D,P	McDonnell Douglas	55.2	9.8	3.5		Thiokol Thiokol Thiokol	1 x TX-500 spr 1 x TX-454 spr 1 x TX-239 spr	450,000+	BTL/Western Electric Radar command	100+	High-altitude, anti-ICBM missile; nuclear warhead. Spartan and Sprint are two missiles planned for Safeguard ABM system.
	Safeguard/ Sprint	Army	BTL/ Western Electric	D,P	Martin Marietta	27		4.5		Hercules	2 x spr[3]		BTL/Western Electric Radar command	25	Low-altitude, anti-ICBM missile; nuclear warhead.
Surface-to-Surface	Minuteman 3 LGM-30G	USAF	AFSC/ SAMSO/TRW: Boeing	D,P	Boeing	59.8		6.2	72,810	Thiokol (1st stage) Aerojet (2nd stage) Aerojet & Thiokol (3rd stage)	1 x M55E-1 spr 1 x spr 1 x spr	60,000 34,000	NAA/Autonetics Inertial	7,000+	AVCO MK 11B & C re-entry vehicle and MK 1 & 1A penetration aids. Super hard silos now being developed for ICBM's.
	Polaris A3 UGM-27C	USN	Lockheed MSC	S	Lockheed MSC	31	4.5	4.5	35,000	Aerojet (1st stage) Hercules (2nd stage)	1 x A3 spr 1 x spr		GE, Hughes, MIT, Raytheon Inertial	2,500	First stage – glass filament case.
	Poseidon UGM-73A	USN	Lockheed MSC	P,S	Lockheed MSC	34	6	6	6	Thiokol, Hercules (1st & 2nd stage)	1 x spr 1 x spr		GE, MIT, Raytheon Inertial	2,500	Has double Polaris A3 payload; MIRV warhead; longer range, underwater launched missile (Trident) system (ULMS) under development.
Battlefield Support	Lance XMGM-52A	Army	LTV Aerospace Corp	P,S	LTV Aerospace Corp	20		1.8	3,351	NAA/Rocketdyne	2 x 1 pr[2]		E-Systems, Systron-Donner, Arma Simplified Inertial		Nuclear or conventional warhead.
	Dragon XM-47	Army	McDonnell Douglas	P	McDonnell Douglas	2.5	1.1		13.5	McDonnell Douglas	spr		McDonnell Douglas Wire-guided, Optically tracked		Shoulder-fired, medium assault weapon for use against armor. It will replace 90 mm recoilless rifle. USMC will also use.
	Pershing 1A MGM-31A	Army	Martin Marietta	S	Martin Marietta	34.5		3.3	10,000	Thiokol	2 x spr (XM-105, XM-106)		Bendix/Eclipse Pioneer Inertial	400	Variable range; nuclear warhaed; deployed in Europe.
	Sergeant MGM-20A	Army	SR/Univac	S	SR/UNIVAC	34.5	5.9	2.6	10,000	Thiokol	1 x XM-100 spr	45,000	SR/Univac Federal Systems	75	Deployed in Europe and Pacific; nuclear warhead.

[1] D – development P – production R – research S – Service use
tj – turbojet

[2] 1pr – liquid propellant rocket (Packaged)

[3] spr – solid propellant rocket

[4] AFSC/SAMSO/TRW are program managers; Boeing Company is system integration contractor

Table 10-4. Typical U.S. Research Rockets

General			Airframe					Powerplant							Payload	
Manufacturer or System Manager	Name Designation	Users	Max. Len (ft)	Max. Span (ft)	Body Dia (ft)	Launch Weight (lb)	Assoc Contractor or Manufacturer	Stage No.	No. of Engines	Name/ Designation and Type		Total Thrust (lb)	Weight (lb)	Alt Mi	Remarks
Aerojet Liquid Rocket Corp (ALRC)	Aerobee 170	NASA, Navy	41		1.25	3,010	Hercules, ALRC	1 2	1 1	X216A2/M-5 AJ 11-21	spr 1 pr	48,700 4,880	240	170	Three fins; optional attitude control system.
	Aerobee 350	NASA	50		1.8	6,629	Hercules, ALRC	1 2	1 4	X216A2/M-5 AJ 60-91	spr 1 pr	48,700 16,400	600	202	Developed for NASA/Goddard Space Flight Center.
	Aerobee 1500	NASA	34.2		2.61	11,493	ALRC ALRC	1 2	1 1	28 KS 57000 30 KS 8000	spr spr	57,000 8,000	50	2,000	
Celesco Industries, Inc	Athena	Air Force	50	11.1	2.6	15,900	Thiokol Thiokol Thiokol ALRC Hercules	1 2 3 4	3 1 1 1	1 x TX-33 2 x TX-19 T x 261-4 25KS-10000 BF3-A4	spr spr spr spr spr	54,000 68,000 57,200 10,000 5,000	50-300	100	Powered re-entry at velocities to 24,000 fps used for pen. aid research.
Celesco Industries, Inc	Athena H	USAF, Army	60.2	9	3.3	30,900	Thiokol Hercules AGSRC Hercules	1 2 3 4	5 1 1 	1 x TX-526 4 x TE-29-3 X259A6 23 KS 11000 BE3-A3	spr spr spr spr	95,000 136,000 23,200 10,300 5,900	800 215	200	Powered re-entry up to 30,000 fps used for research on penetration aids. Deployed on Wake Island.
Thiokol Chemical Corp Astro-Met Div	Nike-Tomahawk	NASA, AEC	24		5.4	1.33	1,950	Hercules Thiokol	1 2	1 1	M5-E1 TE-M-416	spr spr	48,700 11,000	100	250	

Table 10-5. Typical U.S. Rocket Motors[1]

General							Physical Data				Remarks
Manufacturer	Vehicle Name	Designation	Type[2]	Fuel	Oxidizer	Cooling[3]	Thrust (lb)	Max. Env Len (in.)	Max. Env Dia (in.)	Weight (lb)	Primary Application
Aerojet-Liquid Rocket Corp (AJLRC)	Aerobee 150	AJ 11-21	L	aniline furfuryl alcohol	IRFNA	R	4,100	190.8	1.5	256	Sustainer motor for Aerobee 150, 150A, 300 and 300A
	Aerobee 350	AJ 60-91	L	aniline furfuryl alcohol	IRFNA	R	16,260	342	22	838	Sounding rocket; four 4,100-lb thrust chambers.
	Delta, Improved Minuteman Motors	AJ 10-118E M-56-E-1	L S	UDMH polyurethane	IRFNA NH_4ClO_4	R	8,087	65.2	33.2	1,454	Second stage for Delta (DSV-3L). Minuteman LGM-30B second stage motor.
		XSR-19-AJ1	S	polyurethane	NH_4ClO_4						Minuteman LGM-30F second stage; titanium case; single submerged nozzle with liquid injection thrust vector control.
	Polaris motors	A2P	S	polyurethane	NH_4ClO_4	A/F		178	54	22,000	Polaris A-2 first stage motor; steel case; four nozzles.
		A3P	S	polyurethane	NH_4ClO_4	A/F		182	54	24,000	Polaris A3 first stage motor; glass filament case; four rotatable nozzles; nitro-plasticizer additive.
	Sparrow 3	MK 65 Mod 0	S	polybutudiene	NH_4ClO_4			61	8	206	Motor for AIM-7F missile.
	Transtage Engines	AJ 10-138	L	Aer 50	N_2O_4	A	8,000	81	48		For use in pairs on Titan 3A third stage and Titan 3C fourth stage. Also used in Thor-Delta 2nd stage (AJ10-118F).
	Titan Engines	LR-87-AJ-5	L	Aer 50	N_2O_4	R	430,000	124	89		Propulsion for Titan 2 first stage. Titan 3 second stage and Titan Gemini first stage. Also -7 and -9.
		LR-91-AJ-5	L	Aer 50	N_2O_4	R	100,000	111	67		Propulsion for second stage Titan 2, Titan 3A and Gemini; third stage Titan 3C. Also -7 and -9.
Bell Aerospace Div of Textron	Agena Engine	8096	L	UDMH	RFNA	R	16,000	84	36	290	Propulsion for Agena.
	LM Ascent Engine	8258	L	N_2H_4	N_2O_4	A	3,500	51	33	203	LM liftoff engine for return to orbiting Apollo spacecraft.
United Aircraft/ Pratt Whitney	RL 10	RL 10A-3-3	L	LH_2	LOX	R	15,000	70.1	39.5	290	Centaur propulsion, Isp = 444 sec
Rocket Research		MR-80A	L	N_2H_4	None	U	60-600	10.7	9.96	17.03	Viking Lander engine.
Hercules, In.	Minuteman	M-57A1	S	double base		A	16,800	85	38		Minuteman third stage
	Polaris A3	X260A3	S	double base		A		88.79	54	9,501	Second stage motor for Polaris A3
	Poseidon C3	PC3-1	S	HC, A1		A		187.96	74.19		Poseidon C3 first stage motor.
	Poseidon C3	PC3-2	S	double base		A		97.26	74		Poseidon C3 missile second stage motor joint venture with Thiokol.
	Sparrow	MK 58 Mod 0	S	CTPB	AP	A					Boost and sustain motor for Sparrow AIM-7F missile.
	Sprint	X265, X271	S	double base		A					Sprint missile first stage (X265); Sprint missile second stage (X271).
Lockheed Propulsion Co	SRAM	SR75-LP-1	S					100.5	17.5	1,459	Motor for AGM-69A SRAM missile.

[1]Does not include data on a number of security classified and unclassified propulsion systems

[2]L-Liquid; S-Solid

[3]R-Regenerative; U-Uncooled; A-Air; F-Fins

Table 10-5. Typical U.S. Rocket Motors[1] (Continued)

General							Physical Data				Remarks
Manufacturer	Vehicle Name	Designation	Type[2]	Fuel	Oxidizer	Cooling[3]	Thrust (lb)	Max. Env Len (in.)	Max. Env Dia (in.)	Weight (lb)	Primary Application
North American Aerospace/ Rocketdyne	Shrike	Mk 39 Mod 7	S					52		8	Shrike missile motor
	Sparrow	Mk 38 Mod 4	S					52		8	Motor for AIM-7E Sparrow missile
	Thor	MB-3	L	RP-1	LOX	R	172,000	141		75.5	2,028 Propulsion for Thor core booster
	Saturn	F-1	L	RP-1	LOX	R	1,522,000	216		144	18,800 Five in Saturn 5 booster
		H-1	L	RP-1	LOX	R	205,000	104		46	1,982 Eight in Saturn 1 and Saturn 1B first stages. Also adapted for Thor core booster
		J-2	L	LH_2	LOX	R	230,000	116		80.5	3,492 Five in S-2 and one in S-4B stages of Saturn 5
	Apollo RCS	SE-6	L	MMH	N_2O_4	A		93	11	5	8.3 Attitude control and stabilization for Apollo command module during re-entry. Two sets of six engine
Thiokol	Burner 2/Delta	TE-364-2, 3	S	hydrocarbon, aluminum	NH4Cl04			9,680	52.2	37.8	1,580 Upper stage motors for Delta and Burner (TE 364-4 adds cylindrical section to spherical design to increase propellant loading).
	Castor 2	TX-354-3, 4, 5	S	hydrocarbon, aluminum	NH_4Cl04			52,150	247	31.0	9,525 Strap-on for Thor/Delta; also Scout and Athena.
	Genie	TU-389	S	hydrocarbon, aluminum	NH_4Cl04			67	15		482 For Genie missile (AIR-2A)

[1] Does not include data on a number of security classified and unclassified propulsion systems

[2] L-Liquid; S-Splid

[3] R-Regenerative; U-Uncooled; A-Air; F-Fins

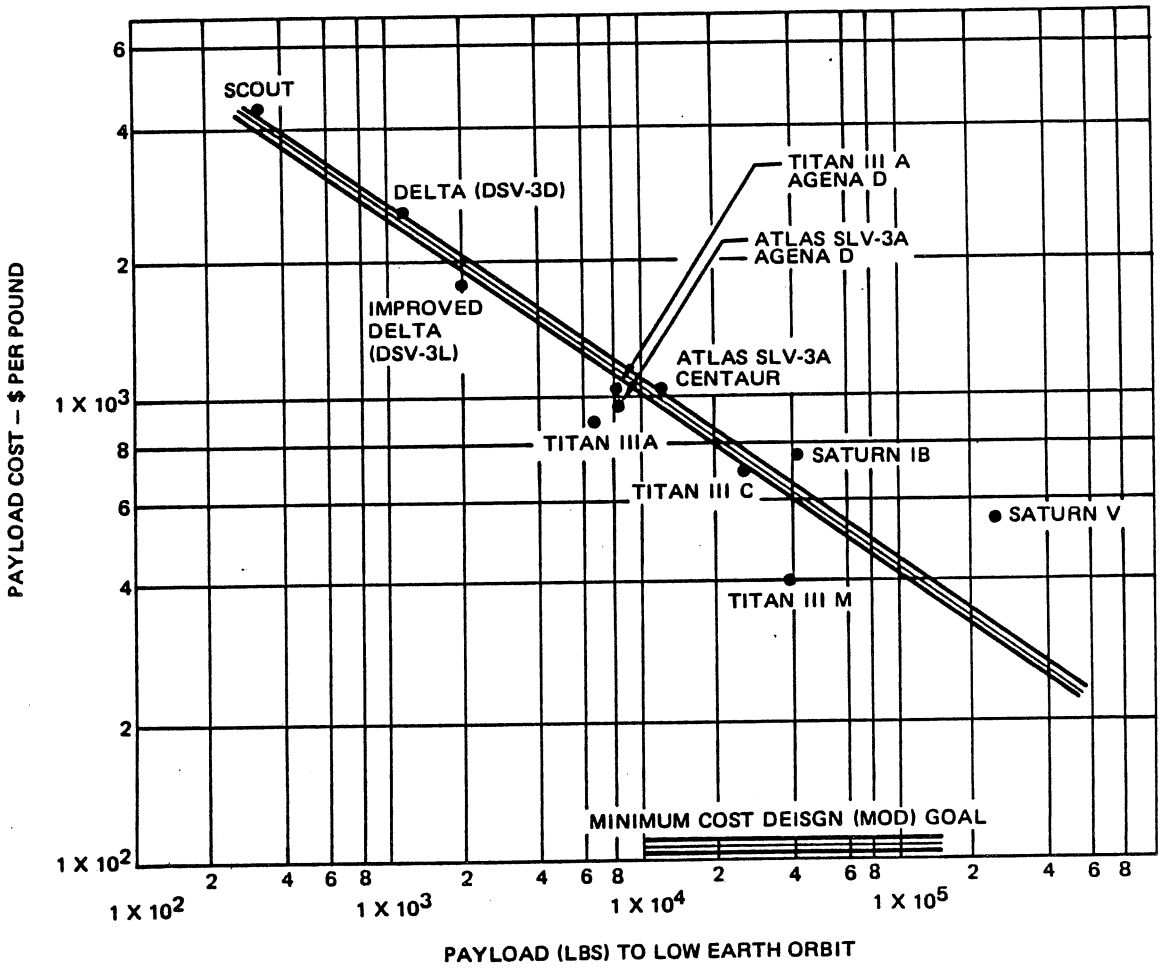

Figure 10-3. Vehicle Cost Versus Payload Weight

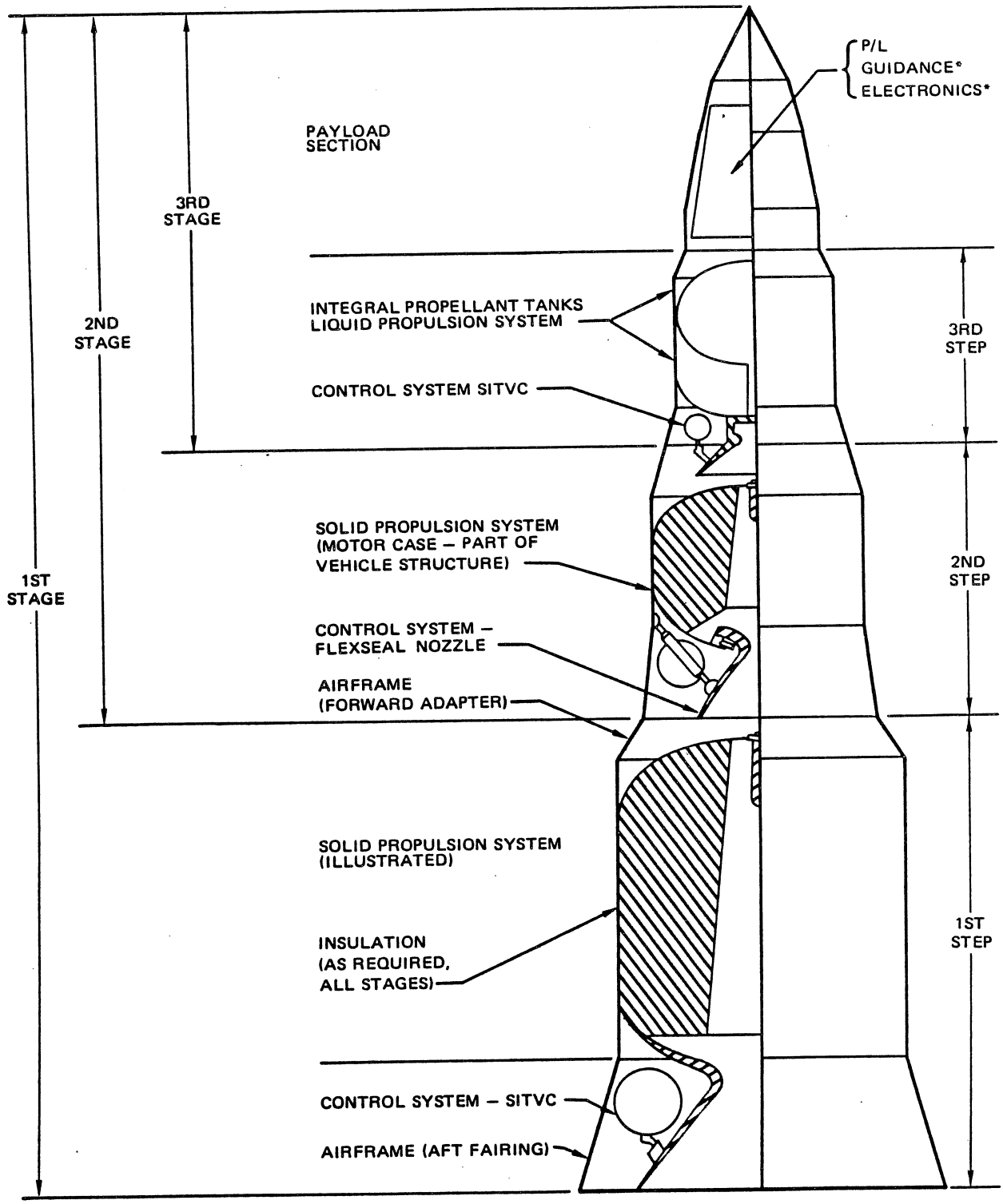

Figure 10-4. Typical Missile or Space Launch Vehicle Configuration

In order to illustrate the sizing and selection procedure for a new vehicle which will meet given mission requirements, the flow diagram for preliminary design of a strategic defense missile system is shown in Figure 10-5. This example differs from considerations for other classes of vehicles primarily in the system analysis area. The vehicle sizing and optimization procedures are similar for the various classes. It should be noted that in the preliminary missile sizing block shown in Figure 10-5, the gross missile characteristics are defined including gross weight, dimensions, number of stages, burnout velocity, velocity staging ratio, total burn time, burn time distribution and subsystem weight and gross dimensions. The subsystem characteristics which must be defined for this example are listed in Table 10-6. The performance of the preliminary design missile (or vehicle) is determined using trajectory analysis and optimization procedures and an iterative procedure which dictates changes to the preliminary design until the mission requirements are satisfied. For this reason, Flight Mechanics personnel are generally responsible for the overall preliminary design sizing and selection and coordinate the inputs of personnel in the other disciplines identified in Table 10-6 and 10-7. The latter table also illustrates parametric and design analysis of typical subsystems.

The System Analysis (Figure 10-5) considerations for a missile design may be further illustrated by the following:

> Suppose that it is desired to design an interceptor which, in combination with a particular set of radar capabilities, produces a given level of effectiveness against a designated group of targets.

The chart below illustrates the major analytical tasks which must be accomplished to arrive at a preliminary design of a "best" configuration to deliver the required performance.

DEFENSIVE MISSILE SYSTEM ANALYSIS TASKS

System Effectiveness Studies

> Intercept Volume-Time Contours
> Single Shost Kill Probability
> Number of Interceptors per Target

Missile Performance Analysis

> Critical Intercept Point
> Interceptor Performance
> Payload Type
> Size

Missile Configuration Trades

> Number of Stages
> Body Shape
> Method of Launch
> Energy Management

Missile Design Trades

> State-of-the-Art
> Subsystem Types
> Subsystem Optimization

Configuration Preliminary Design

The kinds of specific questions which must be answered in the Systems Effectiveness Studies are:

> Should the target be engaged with a large highly effective interceptor or should it be barraged with several small interceptors? Should the interceptor system consist of a two-missile combination, or one missile optimized for short-range capability and another for long-range capability, or should one missile be designed to cover the entire intercept domain?

These are only a few of the questions to be answered but it is clearly difficult to answer these questions without knowing the tradeoffs among missile size, cost, and performance. Usually parametric trade-offs are generated between gross weight and performance. Then the performance variation of a nominal missile across the intercept domain is examined. Finally, the missile performance analysis requires a slightly closer examination of the missile configuration. The selection of the payload necessitiates consideration of packaging constraints, missile weight and cost versus payload weight, and trade-offs between miss distance and warhead yield. The utility of using computer routines to obtain such data with a minimum of foreknowledge of the missile subsystem requirements is apparent from the multiplicity of variables involved.

For many mission applications, both solid and liquid rocket propulsion are logical candidates. Some of the detailed tradeoffs used in selecting one type over another are discussed in paragraphs 10-3, 10-4, and 10-5. However, typical hardware type tradeoffs show that liquid propulsion systems offer:

a. Restart capabilities

b. Less weight for high energy requirements

c. Higher energy systems

and that solid propulsion systems offer

a. Less weight for low energy systems

b. Lower unit costs

c. Lower launch costs

d. Instant readiness for weapon system delivery.

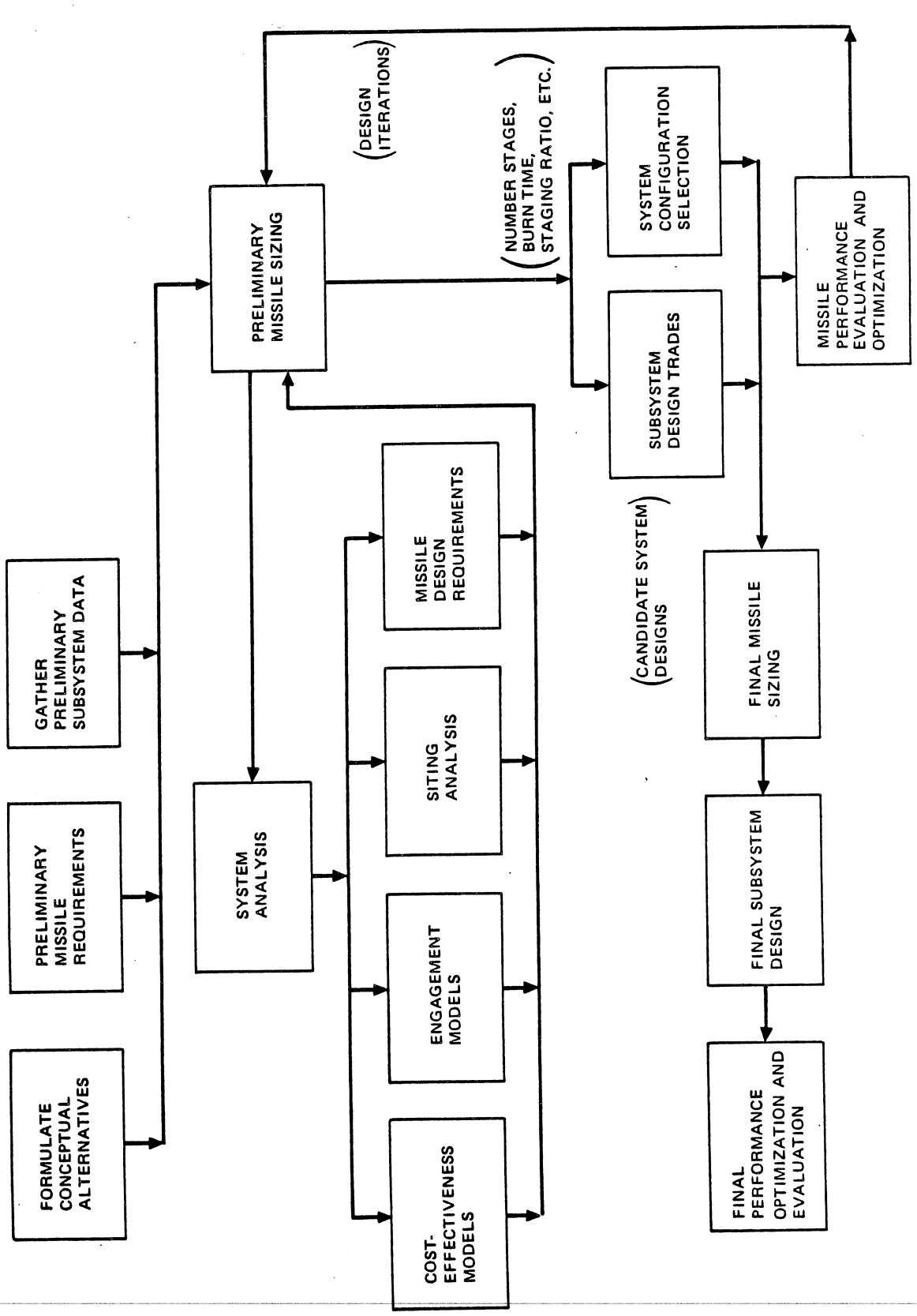

Figure 10-5. Typical Missile System Design Procedure

Table 10-6. Missile Subsystem Characteristics

Propulsion	Control	Airframe	Electronics	Payload
Thrust-time history (nominal and extremes)	Duty cycle force-time history)	Material type(s) and characteristics	Guidance (command homing)	Type
System and engine/ motor chamber pressure-time history	Type (Aero, TVC, RCS)	Construction (shape, size attachment and fabrication, design factors)	Control (sequencing sensing, actuation)	Size and shape
Grain configuration and dimensions(1)	Design features:	Material thickness	Power supply	
Propellant type (solid, liquid, etc.) (physical and ballistic characteristics)	Aero Control Hinge moments	External insulation Type and thickness		
Nozzle design and performance	Aspect ratio			
Motor case or tankage and TCA design	Surface area			
Pressurization subsystem(2) design	Actuation devices			
Thermal protection/ insulation design				

(1) Solid motor only

(2) Liquid propellant subsystem only

Table 10-7. Vehicle Preliminary Design and Analysis and Technical Interfaces

Vehicle Design Analysis	Technical Interface Disciplines	
	Prime	Support*
Number of stages	FM	
Velocity staging ratios	FM	
Stage dimensions and configuration	FM	S&P
Trajectory analysis	FM	
Stage structure factor	FM	S
Propellant type (solid or liquid), energy level and energy management – scheme	FM	P
Thermal protection	A/T	S
Guidance and Control	G&FM	E/E
Separation	FM	MECH
Subsystem performance interfaces	FM	All

Subsystem Parametric and Design Analysis	Technical Interface Disciplines	
	Prime	Support*
Propulsion		
Propellant energy, physical properties	P	FM
Thrust, chamber pressure, and burning time history (performance)	P	FM
TVC and RCS performance	P	FM
Configuration, sizing, cost, weight, materials choice, nozzle (including expansion ratio)		
Tanks and feed system and/or motor cases	P	S
Environmental protection	P	A&T&S
TVC	P	FM-MECH
Reaction control	P	FM
Ignition	P	MECH
TCA	P	
Pressurization systems (liquids)	P	
Propellant loading and utilization (solids and liquids)	P	S
Auxiliary power	P	MECH and FM
Turbo pumps (liquid propellants)	P	
Venting and conditioning (liquid propellants)	P	F
Mechanical		
Configuration sizing, cost, weight, materials choice		
AGE and facilities	M	E/E
Ordnance	M	S
Safety devices	M	E
Ancillary equipment	M	
Environmental control/ life support	M	
Hydraulic and pneumatic power and actuation	M	
Electrical/Electronics		
Configuration, routing, material choice, cost		
Guidance devices	E/E	G&FM
Communications	E/E	
Instrumentation	E/E	
Actuation and sequencing devices	E/E	
Electrical power	E/E	
Structures		
Structural loading (ground and flight)	S	FM
Weight and balance control	S	FM
Configuration, sizing, cost, weight, materials choice		
Airframe	S	F-M-All
Thrust structure	S	P
Aero control	FM	S
Fairings and shroud	S	FM
Attachments and supports	S	All
Payload	S	FM
Interstage	S	FM
Tanks and motor case	S	P
Subsystem integration	S	All
Thermal protection	S	A/T

**Effectiveness Engineering supports all other disciplines. Activity includes reliability, human factors, cost-effectiveness, and safety engineering.*

A/T – Aero Thermo
E/E – Electrical/Electronic
FM – Flight Mechanics
G&FM – Guidance and Flight Mechanics
M – Mechanical
MECH – Mechanics
P – Propulsion
S – Structures
S&P – Structures and Propulsion

It should be noted that a single detailed selection and optimization procedure cannot be used to cover all of the potential system/vehicle requirements of interest. The procedures outlined in the balance of this section must therefore be regarded as broad guidelines for an approach. They should provide the propulsion engineer with an understanding of how this work relates to other disciplines and to the total goal of establishing a rocket vehicle design.

10-1.3 Automated Sizing Methods

Computer routines, for example, the MDAC General Missile Sizing Program (GMSP)[22] and the Missile Synthesis/Analysis Program[23] perform rapid and accurate sizing optimization, and preliminary design of a missile of space configuration and its subsystems for a given performance requirement. The latter program is operational at MDAC-E but has not been adopted at MDAC-W and is not described in detail, since the GMSP is adaptable for general use and contains more detailed subsystem design models.

10-1.3.1 General Missile Sizing Program (GMSP)

A brief discussion of the GMSP is appropriate to further illustrate the methodology of preliminary design. The program is modular in construction and maximizes program flexibility and usefulness such that the individual subsystem modules can be operated separately or in any combination to give the desired results.

It should be noted that the GMSP program is used primarily for sizing ground-to-air systems whereas the Missile Synthesis/Analysis Program is specifically designed for parametric trade studies of advanced tactical air-to-ground and air-to-air missiles. Sizing, as used here, means the process of determining the size, geometry, and weight of a missile based upon the requirement that it deliver a specific payload with a specified level of performance.

The GMSP is written in FORTRAN IV language and is operational on the CDC 6500 Computer. Each major subsystem design and analysis function is included. The sizing approach used is as follows: The program stages a configuration (assigns propellant weights to the respective stages), designs each of the subsystems, establishes the external geometry of the configuration, optimizes the performance, and iterates this process until the missile (1) is staged in a manner which corresponds to the resulting design, (2) is designed to withstand the environment associated with its performance, and (3) delivers the desired performance. Because of the multiplicity of inputs required, and the overall complexity of this program, there are only a small group of specialists who are currently trained to use the program. At MDAC-W, Flight Mechanics personnel should be contacted for help.

10-1.3.1.1 Program Logic and Capabilities

The GMSP represents a coalition of the analysis and design philosophies, techniques and theories of every nonelectrical discipline required to design a missile. Figure 10-6, a block diagram of the program, shows that the technology disciplines represented in the GMSP include propulsion, structures, weights, aerodynamics, thermodynamics, flight mechanics, control analysis, and mechanical systems. These disciplines are executed in separate modules in the program. Each module groups together all the design and analysis functions for a particular subsystem or technology. For example, the propulsion module performs the complete design, optimization, weight and performance analyses for the propulsion system (H218). This includes, for a solid motor, selection of type of grain design, computation of the grain design details to produce the desired thrust versus time shape, three-dimensional ballistic analysis, and nozzle and motorcase design and optimization. A storable liquid propulsion system sizing routine (H834) is also available for pump-fed or pressure fed systems, and several different tankage and pressurization system combinations. Either single or multiple propulsion systems having like or unlike performance characteristics can be accommodated.

Missile Sizing Procedure

The nominal procdure used by the GMSP to size and design a missile configuration is indicated in Figure 10-6. There are three major iterative loops in the program: The initial design loop, the final design loop, and the performance loop. The initial design loop sizes the configuration to produce a specified impulsive velocity. The design of the configuration is based on the trajectory data generated in the preliminary performance module. This loop includes all of the modules except the trajectory and results modules, and is completed only when the configuration's impulsive velocity, computed at the point labeled "velocity check, V_1," is equal to the desired value used in staging the configuration in the staging module.

The final design loop consists of the generation of thermal and structural design trajectories for the initial design configuration and the redesign of the configuration to withstand the resultant environment. The structural design trajectory is used in the design of airframe and control systems. When the design trajectories cause the impulsive velocity of the configuration to change significantly, the configuration is restaged accordingly. Thus, the final design loop is completed only when the configuration (1) is designed to its own design trajectories and (2) possesses the proper impulsive velocity.

At the completion of the final design loop, the trajectory module is again entered — this time to determine the maximum performance of the configuration obtainable through trajectory shaping and to compare that performance to the input sizing

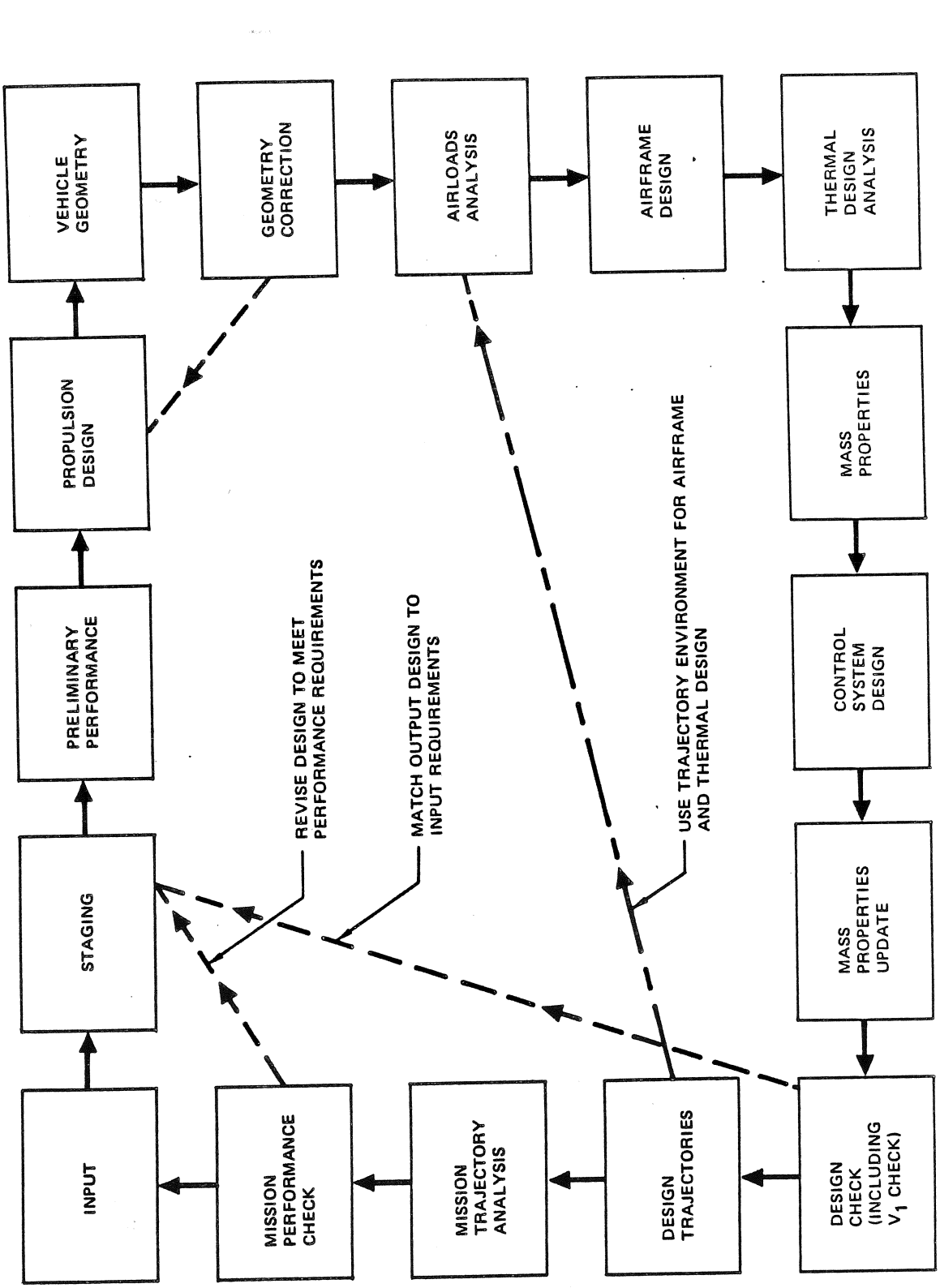

Figure 10-6. GMSP Block Diagram

requirement. When the achieved performance differs from the desired performance, a prediction is made for the impulsive velocity which will result in a configuration design with the correct performance. This loop is iterated until the desired performance is achieved. When the performance loop is complete, the results module is entered to summarize and print out the final configuration characteristics and performance.

A number of variations to this sizing procedure are available as options. For example, in the sizing of several similar configurations, the previously described procedure might be used for the first configuration, and the design trajectories generated for the first configuration would be used to design the subsequent configurations, thus omitting the final design loop. For the generation of a parametric curve of missile gross weight versus performance, the initial design, and possibly the final design, loop would be used. The performance loop would be omitted since the performance resulting from a design configuration would be by definition a point on the desired parametric curve. If the GMSP is used to design and determine performance of a configuration, the final design loop is the only loop required and staging of the configuration can be omitted.

The sizing procedures that have been discussed are normal options provided to cover a variety of applications of the GMSP.[22]

Table 10-8 shows typical input-output data and intermodule data flow within the program.

10-1.3.2 Missile Synthesis/Analysis Program (MSAP)

The Missile/Synthesis/Analysis Program (MSAP) is a relatively compact (10,000 source deck statement) program specifically designed for parametric trade studies of advanced tactical missile configuration. The program is written in FORTRAN IV and is operational on the CDC 6000 series machine. Typical air-to-ground missile configurations are synthesized in less than one minute.

The MSAP capabilities included are as follows:

a. Sizing of lifting surfaces of single-stage missile configurations to satisfy specified maneuvering requirements.

b. Motor sizing iteration logic which exercises the aerodynamic model, the propulsion model and the performance model serially to converge parameters from all three concurrently.

c. Liquid rocket, solid rocket and integral rocket ramjet motor models.

d. Chamber pressure optimization.

e. Linear shaped and conical shaped charge warhead synthesis models.

f. Radar seeker antenna packaging model for blunted, spherical-tipped, tangent ogive configurations.

g. Optional performance envelope definition after missile sizing.

h. Alternative sizing logic to satisfy weight, length, diameter, and range performance constraints.

10-2 ROCKET FLIGHT PERFORMANCE

In the previous subsection, Figure 10-5 illustrates the sizing and selection procedure flow path for a typical rocket. A vitally important part of this process is the determination of missile flight performance for given flight configurations and the subsequent check of this performance against vehicle requirements. Some of the more important configuration and performance parameters are the number of stages, the energy produced by and the burning time of each propulsive stage, and the energy losses associated with the flight trajectory. This section deals primarily with the flight performance aspects for each class of rocket mentioned in subsection 10-1 so that the propulsion design engineer (1) understands the interrelationships between vehicle flight performance and propulsion system design and (2) can perform cursory vehicle performance analysis as a basis for propulsion system preliminary design trade studies without being wholly dependent on other technology inputs. Use of this section should not be construed as a substitute or to by-pass the more precise information which must be obtained from Flight Mechanics or other technology personnel before finalizing a design.

In accordance with these objectives, notably for launch vehicles, specific analytical tools are provided for flight performance predictions. In other cases for example, free-flight rockets, typical parametric data are presented to illustrate tradeoff analysis methodology.

10-2.1 General Performance Considerations

The analysis of a rocket in flight is a particular application of the general theory of the dynamics of rigid bodies in three dimensions.[1,2,12] It is usual in such theory to separate the motion of the center of mass from the motion of the body around the center of mass. For rockets or airplanes the former comprises the theory of flight performance, the latter the theory of stability and control.[3] In this presentation therefore, the rocket appears in the analysis simply as a mass point subject to various forces. As a practical matter, the powered flight path of a ballistic rocket may be intentionally confined

Table 10-8. Typical GMSP Intermodule Data Flow

Module	Output	Input (Source, E = external)
1. Staging	1. Stage Propellant Weights	1. Stage Velocity Distribution (E or 1) 2. Sizing Parameter (Weight or Velocity) (E, 11.5)* 3. Mass Fractions (10.4) 4. Vacuum Isp (2.10) 5. Velocity Losses (11.10)
2. Propulsion	1. Expended Weight Table 2. CG Tables 3. Moments of Inertia Tables 4. Vacuum Thrust Table 5. Inert Weight 6. Inert cg 7. Inert Moments of Inertia 8. External Dimensions 9. Chamber Pressure vs Time 10. Vacuum Isp	1. Stage Propellant Weights (1.1) 2. Acceleration vs Time (11.8) 3. Ambient Pressure vs Time (11.7)
3. Configuration Geometry	1. Vehicle External Geometry 2. Internal Geometry (needed for packaging components) 3. Areas (base, surface, exit, throat, etc.)	1. Subsystem Geometry (2.8, 9.7) 2. Geometry Constraints (E)
4. Geometry Correction	1. Revised External and Internal Geometry with Inconsistencies Eliminated)	1. Vehicle External Geometry (3.1) 2. Internal Geometry (3.2)
5. Preliminary Mass Properties	1. Mass Properties of Propulsion System Only (but in vehicle coordinate system)	1. Propulsion System Mass Properties (2.1, 2.2, 2.3, 2.5, 2.6, 2.7) 2. Propulsion System Dimensions (2.8) 3. Vehicle Geometry (3.1)
6. Airloads	1. Aero Coefficient Tables 2. Airloads	1. Vehicle External Geometry (3.1)
7. Thermal Analysis	1. Insulation Expended Weight vs Time 2. Skin Temperature vs Time 3. Insulation cg Tables 4. Insulation Moments of Inertia Tables	1. Body Attitude vs Time (11.2) 2. Velocity vs Time (11.5) 3. Altitude vs Time (11.6) 4. Vehicle External Geometry (3.1) 5. Areas (3.3)

Source data number corresponds to numbering in Module and Output columns.

Table 10-8. Typical GMSP Intermodule Data Flow (Continued)

Module	Output	Input (Source, E = external)
8. Structures and Airframe	1. Inert Weight 2. Inert cg 3. Inert Moments of Inertia	1. Vehicle Mass Properties (10 or 5) 2. Airloads (6.2) 3. Skin Temperature vs Time (7.2) 4. Geometry (3) 5. Mach Number vs Time (11.1) 6. Body Attitude vs Time (11.2) 7. Reynolds Number vs Time (11.3) 8. Dynamic Pressure vs Time (11.4) 9. Thrust vs Time (11.9)
9. Control Systems	1. Expanded Weight vs Time 2. CG Tables 3. Moments of Inertia Tables 4. Inert Weight 5. Inert cg 6. Inert Moments of Inertia 7. Geometry	1. Aerodynamics (6) 2. Required Duty Cycle (E and 11) 3. Vehicle Geometry (3.1, 3.2) 4. Flowrate Table (2.1) 5. Thrust vs Time (11.9) 6. Chamber Pressure vs Time (2.9) 7. Ambient Pressure vs Time (11.7) 8. Dynamic Pressure vs Time (11.4) 9. Vehicle Mass Properties (5 or 10)
10. Detailed Mass Properties	1. Weight vs Time 2. CG vs Time 3. Moments of Inertia vs Time 4. Mass Fractions	1. Subsystem Mass Properties (2,7, 8, 9)
11. Trajectory Analysis	1. Mach Number vs Time 2. Body Attitude vs Time 3. Reynolds Number vs Time 4. Dynamic Pressure vs Time 5. Velocity vs Time 6. Altitude vs Time 7. Ambient Pressure vs Time 8. Acceleration vs Time 9. Thrust vs Time 10. Velocity Losses	1. Detailed Mass Properties (10) 2. Vehicle External Geometry (3.1) 3. Areas (3.3) 4. Vacuum Thrust Table (2.4) 5. Aero Coefficient Tables (5.1)

to two dimensions, so that the theory of a planar motion is adequate. Further simplification may be achieved by confining the flight path to a straight line (one-dimensional theory). This is useful because it brings out, with a minimum of complication, the significance of several rocket design parameters that are of great importance. The relationship between mass ratio, specific impulse, and thrust-weight ratio on the flight characteristics of a single-stage rocket, and on the performance characteristics of multi-stage rockets are readily understood. The theory of straight-line motion is useful also because it allows rapid estimation of burnout velocity, and hence range, even though the actual powered flight path may be curved. Certain problems of design optimization (e.g., how to minimize the overall rocket mass for a specified payload mass) are discussed. In order to define vehicle performance relationships and to provide a basis for design, rocket propulsion principles are discussed and significant parameters defined.

10-2.1.1 Basic Equation of Motion

As explained above, a rocket in flight can be treated as a particle or mass acted on by the forces of jet reaction, aerodynamic drag and lift, and gravitation. The general equation of power flight can be written vectorially:

$$m \frac{dV}{dt} = F + F_a + F_g \qquad (1)$$

The acceleration (dV/dt) of the instantaneous rocket mass m results from the vector addition of the rocket thrust F, the aerodynamic force F_a, and the gravitational force F_g. Other forces can be introduced if they occur in a particular problem. In general, this equation resolves itself into three scalar equations corresponding to the three components of the acceleration.

For the special case of rectilinear motion in the earth's gravitational field (Figure 10-7) along a path, S, inclined at angle β with respect to the direction of gravity,[1] with the thrust F parallel to the path, the equation takes the scalar form,[4]

$$m \frac{d^2S}{dt^2} = F - D - mg \cos \beta \qquad (2)$$

where S is the distance along the path from an arbitrary reference point, D[2] is the aerodynamic drag,[3] and g[2] is the acceleration of gravity at the location of the rocket. For flight near the earth's surface Equation 2 divided by the vehicle mass, m,[1] becomes

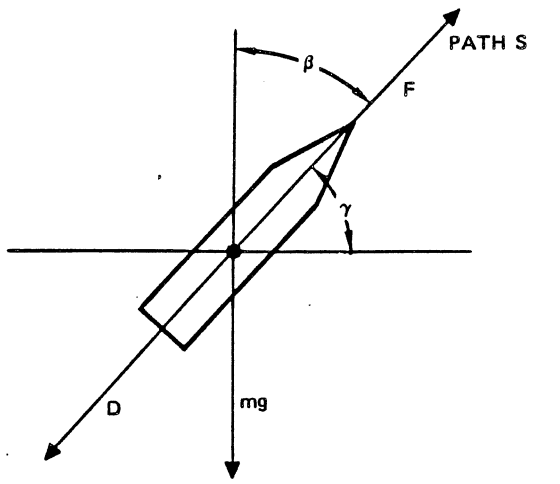

Figure 10-7. Forces Acting on a Rocket

$$\frac{dV}{dt} = g_o I_{sp} m \frac{dm}{dt} - g \cos \beta - \frac{D}{m} \qquad (3)$$

where

$F = g_o I_{sp} \dot{m}$

$m = -dm/dt$[2]

I_{sp} = specific impulse at the altitude of the rocket

In order to integrate Equation 3 to obtain velocity and displacement as functions of time, the individual terms must be examined. These terms are general in nature and cover most vehicle operating conditions. However, there are special cases where unique mass terms are used and these are described as they are encountered.

10-2.1.2 Mass Characteristics

The terms described below pertain to vehicle stages as defined by Figure 10-4 and Table 10-9 and summarize these mass relationships.

10-2.1.2.1 Multistage Vehicle

The mass characteristics are applicable to a vehicle which is comprised of N stages, where the Nth stage includes the Nth step and the payload.

Gross Weight

The gross weight of an individual stage, the nth stage, is indicated by W_{f_n}. The step gross weight is the gross

---

[1] The complimentary angle, γ, is also frequently used as the convention to denote the flight path angle and is referenced from the local horizontal ($Fg = mg \sin \gamma$)

[2] The minus sign indicates mass is leaving the system. Drag and gravity forces act opposite to the thrust force thus are negative quantities. The thrust term when integrated becomes positive.

[3] Note: $D = F_a$ for a point mass in the path of motion.

Table 10-9. Stage and Step Mass Characteristics

	Multiple Stage		Single Stage	
	Stage	Step (s)	Stage	Step (s)
Gross Weight	W_{f_n}	$W_{f_n} - W_{f_{n+1}}$	W_f	$W_f - W_{p\ell}$
Payload	$W_{p\ell}$	$W_{f_{n+1}}$	$W_{p\ell}$	$W_{p\ell}$
Expendable Weight	W_{px_n}	W_{px_n}	W_{px}	W_{px}
Burnout Weight	$W_{bo_n} = W_{f_n} - W_{px_n} \cong W_{f_n} - W_{p_n}$	$W_{bo_n} - W_{f_{n+1}}$	W_{bo}	$W_{bo} - W_{p\ell}$
Usable Propel. Wt.	W_{p_n}	W_{p_n}	W_p	W_p
Mass Ratio	$r_{v_n} = \frac{W_{f_n}}{W_{bo_n}}$	N.A.	$r_v = \frac{W_f}{W_{bo}}$	N.A.
Mass Fraction	N.A.	$\lambda'_{sn} = \frac{W_{p_n}}{(W_{f_n} - W_{f_{n+1}})}$	λ' – N.A.	$\lambda'_s = \frac{W_p}{(W_f - W_{p\ell})}$
Structure Factor	N.A.	$s_{sn} = \frac{(W_{f_n} - W_{f_{n+1}} - W_{p_n})}{(W_{f_n} - W_{f_{n+1}})}$	$s = \frac{(W_f - W_{p\ell} - W_p)}{W_f}$	$s_s = \frac{(W_f - W_{p\ell} - W_p)}{(W_f - W_{p\ell})}$
Growth Factor	$Q_n = \frac{W_{f_n}}{W_{p\ell}}$	N.A.	$Q = \frac{W_f}{W_{p\ell}}$	N.A.
Payload Ratio	$PR_n = \frac{W_{f_n}}{W_{f_{n+1}}}$	N.A.	$PR = \frac{W_f}{W_{p\ell}}$	N.A.
Payload Fraction	$1/PR_n = \frac{W_{f_{n+1}}}{W_{f_n}}$	N.A.	$1/PR = \frac{W_{p\ell}}{W_f} = \frac{1}{Q}$	N.A.

weight of the nth stage minus the gross weight of the n+1 stage. Therefore

$$W_{f_n}(\text{step}) = W_{f_n} - W_{f_{n+1}} \quad (4)$$

The subscript n can have integer values from 1 to N.

It should be noted (Figure 10-4) that the stage gross weights include the payload while the step gross weights do not.

Payload

The vehicle payload weight, $W_{p\ell}$, is nominally defined as the weight which is carried forward of the Nth (or last) step interface.

Expendable Weight

The expendable weight for the nth stage or step in indicated by W_{px_n}. The expendables include all mass expelled from the vehicle during operation of the nth stage (or step). This expelled mass includes propellant, insulation, pressurant, etc. The step and stage expendables are generally identical.

Burnout Weight

The burnout weight of the nth stage is indicated by W_{bo_n}. The stage burnout weight is determined by subtracting the expendables from the gross stage weight:

$$W_{bo_n} = W_{f_n} - W_{px_n} \quad (5)$$

The step burnout weight is determined by subtracting the n+1 stage gross weight from the nth stage burnout weight:

$$W_{bo_n}(\text{step}) = W_{bo_n} - W_{f_{n+1}} \quad (6)$$

Usable Propellant

The usable propellant weight for the nth stage or step is indicated by W_{p_n}. The usable propellant is that propellant which is available in the step or stage to provide vehicle impulsive velocity. The step and stage usable propellant are identical.

Mass Ratio

The mass ratio of the nth stage is indicated by r_{v_n}. This ratio is the stage gross weight divided by the burnout weight. Therefore,

$$r_{v_n} = W_{f_n}/W_{bo_n} \quad (7)$$

A step mass ratio can be defined but has no usefulness in analytical computations.

DELETED (8)

Mass Fraction

The mass fraction of single stage vehicle is indicated by λ' but is not used in calculations given here. This fraction is the ratio of stage usable propellant weight to stage gross weight:

$$\lambda' = W_p/W_f \quad (9)$$

(not applicable for most cases)

The step mass fraction is:

$$\lambda'_{sn} = W_{p_n}/(W_{f_n} - W_{f_{n+1}}) \quad (10)$$

(for nth stage)

Structure Factor

The structure factor of a single stage vehicle is indicated by s. This factor is the gross weight minus the propellant and payload weight divided by the stage gross weight.

$$s = \frac{W_f - W_{p\ell} - W_p}{W_f} \quad (11)$$

The step structure factor for a multiple stage vehicle is determined in the same manner using the step gross weight definitions,

$$s_{sn} = (W_{f_n} - W_{f_{n+1}} - W_{p_n})/(W_{f_n} - W_{f_{n+1}}) \quad (12)$$

Additional structure factor details are presented in Subsection 10-3.

Growth Factor

The weight parameter for a rocket design may be stated in a nondimensional form, as the ratio of rocket gross weight to payload weight. This ratio is designated the growth factor becasue it indicates to the designer how much his rocket must weigh in relation to the payload, or how much the overall weight must "grow" to account for unit increases in payload. The growth factor is

useful, not only as a nondimensional measure of the weight of the rocket, but also as an indicator of the efficiency of the chosen method of delivery; a low growth factor indicates high efficiency.

The growth factor for the nth stage is indicated by Q_n and is calculated as follows:

$$Q_n = W_{f_n}/W_{p\ell} \quad (13)$$

Payload Ratio

The payload ratio is indicated by PR. This parameter is the ratio of the gross weight of a stage to the gross weight of the stage above.

$$PR_n = \frac{W_{f_n}}{W_{f_{n+1}}} \quad (14)$$

The ratio is equal to the growth factor of a single stage vehicle.

$$PR = \frac{W_f}{W_{p\ell}} = Q \quad (15)$$

The growth factor of a multiple stage vehicle, having N stages is the product of the payload ratio for all the individual stages,

$$Q_N = \Pi_{n=1}^{N} PR_n \quad (16)$$

Payload Fraction

The payload and vehicle designer frequently use the term payload fraction which is the inverse ratio of PR

$$\frac{1}{PR_n} = \frac{W_{f_{n+1}}}{W_{f_n}} \text{ (multistage vehicle)} \quad (17)$$

$$\frac{1}{PR} = \frac{W_{p\ell}}{W_f} = \frac{1}{Q} \text{ (single stage vehicle)} \quad (18)$$

10-2.1.2.2 Single Stage Vehicle

The terms described above are applicable to a single stage vehicle except that the subscript n is not meaningful and is dropped. Also, some of the step terms specify an n+1 term which becomes $W_{p\ell}$ for a one stage vehicle. All of the terms are summarized in Table 10-9 for both multiple and single stage vehicles.

10-2.1.3 Velocity Characteristics

In addition to the mass characteristics vehicle velocity characteristics are required in order to determine vehicle performance values. The terms discussed below pertain to multistage and single stage vehicles. They are general in nature and cover most vehicle operating conditions. However there are special cases where unique velocity terms are used.

Table 10-10 summarizes the velocity terms discussed below.

10-2.1.3.1 Multistage Vehicle

The velocity terms are applicable to a vehicle which is comprised of N stages. Stage terms are denoted by the subscript n which can have interger values from 1 to N. Overall vehicle terms are denoted either by the subscript N or by deletion of the subscripts entirely.

a. Initial Velocity – The velocity at which a stage or vehicle is traveling immediately prior to initiation of burning is called initial velocity. For any one stage this is designated V_{o_n} or simply V_o for a single stage vehicle.

b. Ideal Burnout Velocity – The ideal, e.g., impulsive, burnout velocity is that velocity which a stage or vehicle would attain if all of the propulsive impulse were converted to stage or vehicle velocity, plus the initial velocity. For a stage, this is designated $V_{bo_{I_n}}$ and for for the vehicle it is designated $V_{bo_{I_N}}$. In some instances the subscript I refers to inertial conditions and is appropriately noted. Inertial condition refers to the absolute velocity conditions in space. For example, for a vehicle launched in the same direction as the earth's rotation, the earth's rotation velocity is added vectorially to the burnout velocity to obtain the inertial burnout velocity (Paragraph 10-2.2.1.4).

c. Ideal Velocity Increase – The stage or vehicle ideal velocity increase is the velocity increment which would be realized if all the propulsive impulse were converted to velocity. This is designated ΔV_{I_n} for a stage and ΔV_{I_N} for the vehicle. This velocity is similar to the ideal burnout velocity except that it does not include the initial velocity, i.e.,

$$\Delta V_{I_n} = V_{bo_{I_n}} - V_{o_n} = g_o I_{sp_n} \log_e (W_{f_n}/W_{bo_n}) \quad (19)$$

and

$$\Delta V_{I_N} = V_{bo_{I_N}} - V_{o_n} = g_o \sum_{n=1}^{N} I_{sp_n} \log_e (W_{f_n}/W_{bo_n}) \quad (20)$$

In Equations 19 and 20, the specific impulse I_{sp}, is treated as a constant equal to the average I_{sp} over

Table 10-10. Stage and Vehicle Velocity Characteristics

	Multiple Stage		Single Stage
	Stage	Vehicle	
Initial Velocity	V_{o_n}	V_{o_N}	V_o
Ideal or Inertial Burnout Velocity	$V_{bo_{I_n}}$	$V_{bo_{I_N}}$	V_{bo_I}
Ideal Velocity Increment	ΔV_{I_n}	ΔV_{I_N}	ΔV_I
Total Velocity Loss	$\Delta V_{L_n} = \Delta V_{L_{D_n}} + \Delta V_{L_{g_n}} + \Delta V_{L_{T_n}}$	$\Delta V_{L_N} = \sum_{n=1}^{N} \Delta V_{L_n}$	$\Delta V_L = \Delta V_{L_D} + \Delta V_{L_g} + \Delta V_{L_T}$
Drag Loss	$\Delta V_{L_{D_n}}$	$\Delta V_{L_{D_N}} = \sum_{n=1}^{N} \Delta V_{L_{D_n}}$	ΔV_{L_D}
Gravity Loss	$\Delta V_{L_{g_n}}$	$\Delta V_{L_{g_N}} = \sum_{n=1}^{N} \Delta V_{L_{g_n}}$	ΔV_{L_D}
Thrust-Atmospheric Loss	$\Delta V_{L_{F_n}}$	$\Delta V_{L_{F_N}} = \sum_{n=1}^{N} \Delta V_{L_{F_n}}$	ΔV_{L_F}
Actual Burnout Velocity	$V_{bo_n} = V_{bo_{I_n}} - V_{bo_n}$	$V_{bo_N} = V_{bo_{I_N}} - \Delta V_{L_N}$	$V_{bo} = V_{bo_I} - \Delta V_L$
Actual Velocity Increment	$\Delta V_n = \Delta V_{I_n} - \Delta V_{L_n}$	$\Delta V_N = \Delta V_{I_N} - \Delta V_{L_N}$	$\Delta V = \Delta V_I - \Delta V_L$

the powered portion of the flight. The weight terms are defined in Paragraph 10-2.1.2.

d. Velocity Losses – The velocity losses associated with rocket flight are caused by aerodynamic drag, gravity, and thrust-atmospheric effects. If the vehicle thrust vector, F, is not in line with the velocity vector, there is an additional reduction in the available thrust due to the angle of attack, α. The available impulsive thrust is therefore given by F cosα. The relative magnitude of these losses depends on the vehicle physical characteristics and mission requirements (air-to-air, air-to-ground, space, etc.). The aerodynamic and thrust-atmospheric losses are significant for rockets operating under 100,000 feet. None of the individual velocity losses is a major consideration for long range ballistic or orbital missile systems, but typically, may total 3 to 5 percent of the thrust impulse. The total stage losses are indicated by ΔV_{L_n} and the total vehicle losses by ΔV_{L_N}.

e. Drag Losses – It is usual to express the instantaneous aerodynamic drag D of a rocket in terms of a drag coefficient C_D based on the maximum frontal area A of the vehicle, including such attachments as fins, wings, etc.:

$$D = C_D A \frac{1}{2} \rho_a \frac{V^2}{g_o} = C_D A q \qquad (21)$$

C_D = aerodynamic drag coefficient, dimensionless

where

ρ_a = local air density, lb/ft^3

V = magnitude of the instantaneous rocket velocity, fps

A = frontal or reference area, sq ft

q = dynamic pressure, lb/ft^2

The vehicle drag coefficient depends on the configuration, angle of attack, angle of yaw, and, most important for supersonic vehicles, on the flight Mach number, M. The drag characteristics of a representative missile configuation[9] are shown in Figure 10-8 to illustrate the dependence of drag coefficient on Mach number and angle of attack.

It is important to analyze the drag penalty in terms of the above parameters. For example, consider a rocket in atmospheric flight. Substitution of the value of D in Equation 21 in the differential Equation 3 yields:

$$\frac{dV}{dt} = -g_o I_{sp} \frac{dm}{m(dt)} - g \cos\beta - \frac{C_D A \frac{1}{2} \rho_a V^2}{m g_o} \qquad (22)$$

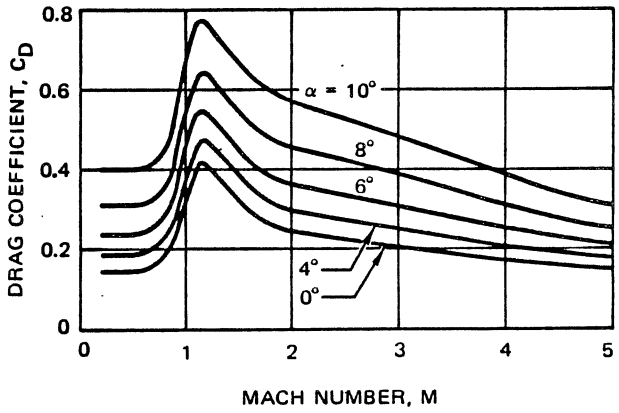

Figure 10-8. Drag Coefficient of a Typical Surface-to-Surface Rocket

Exact integration of this equation is not possible because of the complexity of the last term. Even if C_D were independent of speed, the drag term in Equations 2 or 3 would make it impossible to integrate the equation except under certain artificial restrictions. For example, if the gravity term can be neglected (horizontal flight or very large thrust-to-weight ratio), the equation can be integrated if the product $C_D \rho_a/F$ is expressed simply as a function of velocity.[5] If the drag to thrust ratio quantity $C_D \rho_a/F$ can be taken as a constant, the equation can be integrated without dropping the gravity term.[6] Finally, there is the straight forward method of integrating the equation numerically without any restrictions whatever.[7]

The most useful and also the simplest integration is that for the case of zero drag, i.e., negligible D/m. This corresponds to flight above the atmosphere, e.g., the second and third stages of a three-stage satellite launcher or a rocket launched at high altitude. In addition, the zero drag approximation is quite good for any rocket-propelled vehicle, even in the dense atmosphere, provided that the rocket thrust is very large with respect to the drag force. In a family of similar vehicles of different sizes having the same ballistic properties, D is proportional to the square of a typical dimension and m is proportional to the cube of that dimension, so that D/m varies inversely as the size. Consequently, the effect on drag on the performance of a rocket vehicle may not be significant for a large rocket, especially if the

flight is largely exo-atmospheric. For the purpose of a preliminary design, for which an approximate estimate of burnout velocity is sufficient, a rocket of the size of the Scout, for example, is large enough to allow neglect of the drag.[8] This is shown by a plot of the D/F ratio versus time during the powered portion of a standard flight of a large ballistic rocket (Typically Scout, Thor, and Atlas) (Figure 10-9). The drag penalty in terms of burnout velocity for this type of rocket is about 4 percent.

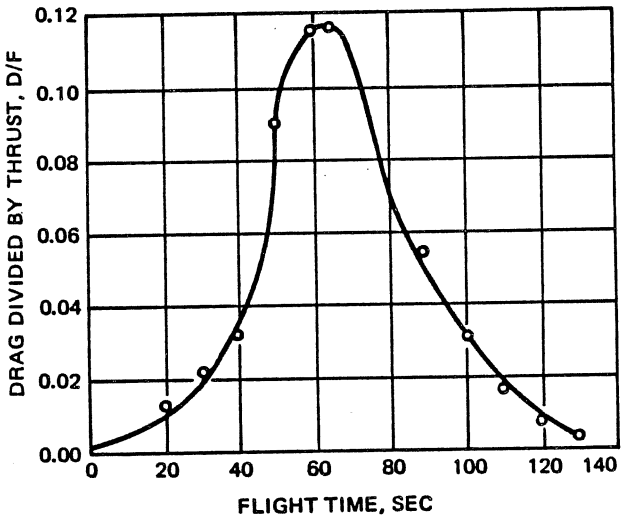

Figure 10-9. D/F for Large Rocket ($\approx$ 2500 lb/ft^2 Vehicle Weight/Frontal Area)

An approximate means of evaluating the drag term is to use the computed no-drag trajectory to provide C_D, ρ_a, V, and M as functions of time and then to compute the integral numerically using the no-drag trajectory parameters. This is acceptable when the correction term is small. For large drag effects, Equation 22 must be integrated numerically. An empirical method for calculating this term for large missiles and launch vehicles is given in Paragraph 10-2.2, and for high speed-missiles is given in Paragraph 10-2.3.

The effects of drag on the trajectory of a vehicle may be expressed in terms of a ballistic coefficient parameter,

$$C = \frac{W_f}{C_D d^2} \qquad (23)$$

where d is the diameter and W_f is the weight of the missile or projectile. This parameter is useful for describing the effects of drag in the post burnout flight phase, particularly for missiles and projectiles. Although the ballistic coefficient is a useful parameter for the determination of drag effects for the post-burnout trajectory phase, it is not useful for the propulsive phase of the trajectory because of the effects of thrust and weight changes. In the compilation of parametric performance data, it is more convenient to work with a modified form of the ballistic coefficient C, defined as

$$C' = W_{p\ell}/id^2 \qquad (24)$$

where

$W_{p\ell}$ = the payload weight in pounds,

i = the drag form factor.

This form of the ballistic-coefficient parameter is more convenient to use, Paragraph 10-2.3.4.1 and Figure 10-91, because the rocket payload is usually specified as an initial condition (as opposed to the situation for artillery projectiles where the weight of the complete projectile is specified).

The velocity loss due to drag during the operation of any stage is indicated by $\Delta V_{L_{D_n}}$. The drag loss for the vehicle is denoted by $\Delta V_{L_{D_N}}$ and is the sum of the stage losses:

$$\Delta V_{L_{D_N}} = \sum_{n=1}^{n} \Delta V_{L_{D_n}} \qquad (25)$$

The equation for determining the drag loss as a function of time is related to Equation 21:

$$\Delta V_{L_{D_n}} = g_o \int_o^{t_b} \frac{\frac{1}{2}\rho_a V^2 C_D A}{W_f\left[1-\frac{r}{I_{sp_{s\ell}}} t\right]} dt \qquad (26)$$

where r = thrust to weight ratio = $\frac{F}{W_f}$

Additional details of drag loss claculations are presented in Paragraphs 10-2.2 and 10-2.3.

f. Gravity Losses — These losses result from rocket flights which have a velocity component opposite the gravitational force of the earth. A simple example of this loss is vertical flight of a rocket to a relatively low altitude such that the earth's gravity can be considered constant:

$$\Delta V_{L_g} = g_o t_b \qquad (27)$$

However, considering the variations of gravity with altitude and of the angle of the vehicle with the local vertical, the gravity loss is given by:

$$\Delta V_{L_g} = g_o \int_o^{t_b} \left(\frac{r_e}{r_e + h}\right)^2 \cos\beta \, dt \qquad (28)$$

where

r_e = the radius of the earth

h = altitude above the reference

However, in this form the variation of h and β must be expressed as a function of time in order to integrate Equation 28. Therefore, specialized approximations or empirical data are generally used to determine gravity losses (Paragraph 10-2.2).

g. Thrust-Atmospheric Losses — These losses are caused by the reduction of the vacuum thrust level by atmospheric pressure during the portion of flight through the atmosphere. Thus, the ratio of sea level specific impluse to vacuum specific impulse, which is determined by the nozzle and propellant characteristics, is the important parameter determining these losses.

Integration of the following equation will give the thrust-atmospheric losses for a single stage rocket[13]:

$$\Delta V_{L_F} = g_o \int_o^{t_b} \frac{r\left(\frac{1}{x} - 1\right)\frac{p_h}{p_{s\ell}}}{1 - \frac{r}{I_{sp_{s\ell}}} t} \, dt \qquad (29)$$

where

r = the liftoff thrust to weight ratio

x = the ratio of seal level and vacuum specific impulses

p_h = atmospheric pressure at altitude

$p_{s\ell}$ = atmospheric pressure at sea-level

However, the variation of p_h must be expressed as a function of time in order to integrate the equation. Approximations of empirical data described in Paragraph 10-2.2 may be used to determine thrust-atmospheric losses.

h. Actual Burnout Velocity — The actual burnout velocity for a rocket is the resultant velocity which has been reduced from the ideal by the velocity losses. In other words, this is the ideal burnout velocity minus the total losses including gravity, drag and thrust atmospheric losses. For a vehicle stage the actual burnout velocity is

$$V_{bo_n} = V_{bo_{I_n}} - \Delta V_{L_n} \qquad (30)$$

and for the overall vehicle the actual burnout velocity equation is:

$$V_{bo_N} = V_{bo_{I_N}} - \Delta V_{L_N} \qquad (31)$$

i. Actual Velocity Increment — The actual velocity increment is the resultant increment which has been reduced from the ideal increment by the velocity losses. For a vehicle stage this can be expressed by

$$\Delta V_n = \Delta V_{I_n} - \Delta V_{L_n} \qquad (32)$$

and for the overall vehicle the expression is

$$\Delta V_N = \Delta V_{I_N} - \Delta V_{L_N} \qquad (33)$$

The numerical values obtained from these expressions are equal to those of Equations 30 and 31, respectively, for burnout conditions (no coast). If coast conditions occur between staging ΔV_{I_N} and ΔV_{I_N} change due to changes in altitude (I_{sp}) and drag, gravity, and thrust-atmospheric losses.

10-2.1.3.2 Single Stage Vehicle

The terms described above are also applicable to a single stage vehicle except that the subscripts n and N are not meaningful and are therefore dropped. All of the terms are summarized in Table 10-10 for multiple and single stage vehicles.

10-2.1.4 Earth Rotation

In order to analyze the performance of some vehicles, it is necessary to transform the flight conditions relative to the launch site into the inertial coordinate system. This requires vectorially adding the rotational velocity of the launch site, V_{rot}, to the vehicle velocity vector. Additional details are presented in Paragraph 10-2.2.

10-2.1.5 Burn Time

Burn time is that period of time when the state or vehicle is providing thrust. This is also called duration of powered flight. For a multistage vehicle, the burn time for a stage is indicated by t_{b_n} and for a single stage vehicle it is indicated by t_b. The most common practical example is the burn time of a single stage vehicle with steady mass flow, i.e., a thrust that varies only as a result

of changing external atmospheric pressure. For this case the burn time is:

$$t_b = \frac{(W_f - W_{bo})\, I_{sp}}{F} \qquad (34)$$

The thrust F and specific impulse I_{sp} values can be either sea level or vacuum. However, they cannot be mixed, i.e., both must be sea level or both must be vacuum values. The term $(W_f - W_{bo})$ in this equation is assumed equal to the weight of propellant burned and does not include any other inert weight loss which does not contribute to total impulse.

10-2.1.6 Altitude

There are several altitude terms generally associated with rocket flight. These are: initial altitude, burnout altitude, maximum altitude, and orbital altitude. Each of these terms will be discussed in the following paragraphs.

10-2.1.6.1 Initial Altitude

The initial altitude, h is the vertical displacement of a rocket vehicle or stage at the start of powered flight. For an air launched vehicle this could be the altitude of the aircraft at launch, for one stage of multistage vehicle this could be the burnout altitude of a preceding stage. For a single stage vehicle initial altitude is indicated by h_o, and for one stage of a multistage vehicle it is indicated by h_{o_n}.

10-2.1.6.2 Burnout Altitude

Burnout altitude is the altitude reached by a vehicle or stage at the end of powered flight. It is calculated by considering the distance along the path of a vehicle as a function of time, and can be obtained by integration of Equation 2 if the variation of m with t, or the equivalent thrust-time curve is specified.

For a single stage vehicle, burnout altitude is indicated by h_{bo}, and for one stage of a multistage vehicle it is indicated by h_{bo_n}. A practical example of burnout altitude is the case of drag-free vertical flight of a single stage vehicle for which the burnout altitude is:

$$h_{bo} = g_o I_{sp} t_b \left[1 - \frac{\log_e r_v}{r_v - 1}\right] - \frac{1}{2} g^* t_b^2 + V_o t_b + h_o \qquad (35)$$

where

$g^* \cong g_o$ near earths surface (several hundred thousand feet).

Other burnout altitude calculations are presented for specific vehicle types in later paragraphs.

10-2.1.6.3 Maximum Altitude

Maximum altitude is the summit altitude achieved by a rocket and is determined by adding to the burnout altitude the altitude gained during coast. This term is associated mostly with sounding rockets and ballistic missiles and is indicated by h_m. For a single stage vehicle the maximum altitude is

$$h_m = h_{bo} + \Delta h_c \qquad (36)$$

where h_c is the coast altitude increment. For a multistage vehicle the maximum altitude is:

$$h_m = h_{bo_N} + \Delta h_{c_N} \qquad (37)$$

where h_{bo_N} is the burnout altitude of the last stage, and Δh_{c_N} = the coast altitude increment after last stage burnout.

The coasting distance for a vertically launched single stage vehicle, considering the variation of gravity with altitude but disregarding aerodynamic drag, is

$$\Delta h_c = \frac{V_{bo}^2}{2 g_o} \cdot \frac{(r_e + h_{bo})^2}{r_e^2 - \frac{V_{bo}^2 (r_e + h_{bo})}{2 g_o}} \qquad (38)$$

For a single stage rocket which reaches a summit altitude that is small compared to the earth's radius, r_e, Equation 38 reduces to

$$\Delta h_c \cong \frac{V_{bo}^2}{2 g_o}$$

where

$$g_o \cong g^*$$

10-2.1.6.4 Orbital Altitude

Orbital altitude values are associated with satellites satellites and space launch vehicles. The orbital altitude is characterized by apogee and perigee, h_a and h_p, altitudes (Paragraph 10-2.2.2).

10-2.1.7 Thrust/Weight Ratio

Vehicle thrust/weight ratio, r, is another term which is generally used in performance calculations. The thrust-to-weight ratio is the parameter which describes the acceleration capabilities of a rocket. This ratio generally increases during the operation of a propulsive

stage, because the vehicle weight decreases as the propellant is expended and the engine thrust remains essentially constant.

The thrust-to-weight ratio is particularly useful in evaluating vehicle performance in a strong gravitational field. For example, the thrust of the first stage must be greater than the weight of the total vehicle (thrust-to-weight ratio greater than one) for the vehicle to rise off the ground. When the vehicle has entered a trajectory that has a tangential velocity component, the resultant centrifugal force tends to counteract the gravitational force acting on the vehicle. Therefore the thrust-to-weight ratio of an upper stage may be less than one, and is usually based on acceleration requirements.

The thrust-to-weight ratio of a space vehicle, which operates in a very low gravity field, is generally considerably less than one. Specific impulse and total impulse are generally more significant design parameters for this type of application.

In general, the liftoff thrust/weight ratio is the most commonly used value. The liftoff thrust/weight ratio equations for a single stage and multistage vehicle are:

$$r = F/W_f \text{ (single stage)} \quad (39)$$

$$r_1 = F_1/W_{f_1} \text{ (multistage)} \quad (40)$$

where F_1 is the thrust of the first stage of the multistage vehicle.

10-2.1.8 Range

The range for a rocket vehicle generally refers to the distance from the launch point to the point of interest (usually a ground or airborne target). For surface-to-surface ballistic missiles the ragne is measured along the surface of the earth whereas the others generally measure the range as a straight line from launch to target. The simplest form of ballistic range equation occurs for a launch angle of 45° in a drag-free environment on a flat earth. This form is

$$R = V_{bo}^2/g_o \quad (41)$$

Other range relationships are unique for the different vehicle classes and will be discussed in those particular sections.

10-2.1.9 Effect of Parameters on Vehicle Performance

In the design of any rocket system, the determination of performance parametrics is a necessary first step since these define the relationship between the performance requirement and physical characteristics. Performance parametrics serve not only as the basis for trade-off considerations among competing requirements and characteristics, but they also show the sensitivity of the rocket's physical characteristics to variations in performance requirement, propulsion system efficiency, aerodynamic characteristics (primarly drag), and energy management technique.

It is not possible, in a handbook of this scope, to present parametric performance data which will cover every conceivable situation. The purposes of this discussion, therefore, will be to call attention to those parameters which affect the performance of a rocket; to illustrate various approximation techniques; and to present a limited amount of parametric performance information.

10-2.1.9.1 Mass and Energy Relationships

The importance of specific impulse to vehicle performance can be evaluated in terms of its effect on ideal velocity.

From Equation 19 it can be seen that ideal velocity is sensitive to changes in mass ratio. Figure 10-10 is a plot of stage ΔV_I as a function of specific impulse and mass ratio.

Similar relationships for growth factor, stage mass fraction (λ'), specific impulse, and ideal velocity capability for a vehicle or stage are illustrated in Figures 10-11, 10-12, 10-13, and 10-14. Information in the latter forms are useful for quickly determining the payload of a single or multistage vehicle depending on the terms used for defining the mass characteristics of the vehicle.

Figure 10-12 is applicable for determining the payload of a one-stage or multistage rocket vehicle, i.e., payload weight = PRx W_f = payload ratio x launch weight. For multistage vehicles, each stage is first considered to originate from V = 0 on the s_s contours, after which the upper stages are translated to their proper positions, as shown by the dotted lines. The latter curves are similar to those shown in Figure 10-13 where the payload-velocity curves are plotted for any combination of specific impulse, I_{sp} and step structure factor, s_s, by interconnecting the corresponding dots in the table. If such curves are traced on vellum, they can be transferred to Figure 10-14 for performance analysis of upper stages. By placing the Index Point of the vellum over the burnout condition for the preceding stage, one may read-off the corresponding values of payload vs velocity. Figure 10-14 also shows typical performance data for several current launch vehicles.

The relationships between the rocket weight (payload, structure, and propellants) and performance (ideal velocity increment and specific impulse) can also be expressed mathematically to provide visibility of sensitive parameters.

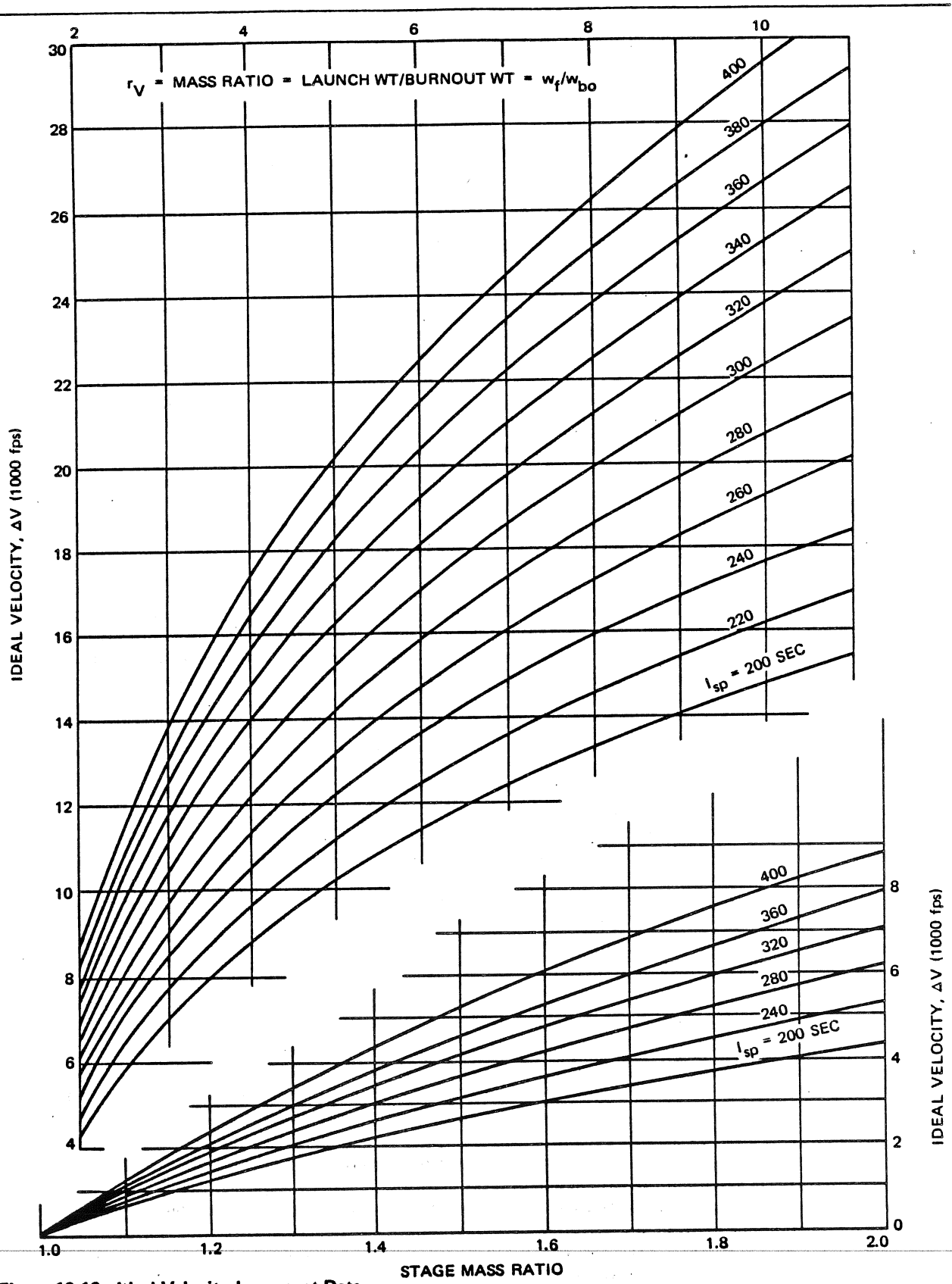

Figure 10-10. Ideal Velocity Increment Data

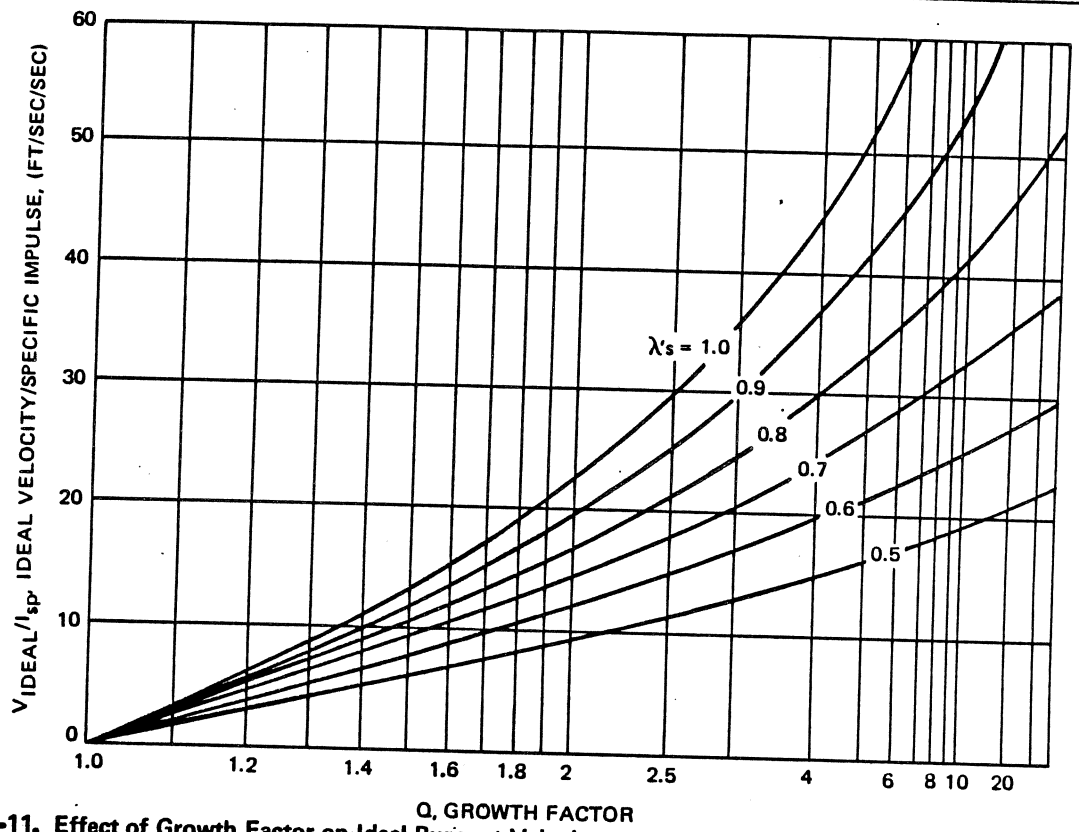

Figure 10-11. Effect of Growth Factor on Ideal Burnout Velocity

The burnout velocity of a single stage vehicle can be obtained by rewriting and integrating Equation 3 without any specification on the variation of the vehicle mass with time or the thrust being held constant (aerodynamic drag neglected).

$$\Delta V = V_{bo} - V_o$$

$$= g_o I_{sp} \log_e \left(\frac{W_f}{W_{bo}}\right) - g\, t_b \cos\beta \qquad (42)$$

By putting r, s, and Q* into Equation 42, it becomes

$$\frac{V_{bo} - V_o}{g_o\ I_{sp}} = \log_e \left(\frac{Q}{sQ+1}\right) - \left(\frac{Q - sQ - 1}{Q\,r}\right) \frac{g\cos\beta}{g_o} \qquad (43)$$

For vertical flight near the earth's surface,

$$\frac{V_{bo} - V_o}{g_o\ I_{sp}} = \log_e \left(\frac{Q}{sQ+1}\right) - \left(\frac{Q - sQ - 1}{Q\,r}\right) \qquad (44)$$

The preceding equation demonstrate that burnout velocity and the range (either vertical or horizontal) of a rocket vehicle depend on (1) the specific impulse or the effective exhaust velocity; (2) the launch to-burnout-mass ratio, and (3) the burning time or the thrust-to-weight ratio. Several significant observations can be made about the effects of these parameters on the flight performance.

The burnout velocity increases linearly with an increase in specific impulse. From this standpoint high specific impulse propellants are to be perferred. However, higher I_{sp} propellants tend to have lower bulk densities. For a given tank volume, lower propellant density results in increased structural factor, s.

The burnout velocity diminishes as the structural factor rises, so that it is not a simple matter to decide whether a particular high specific impulse propellant is superior to one of lower specific impulse. For example, the high I_{sp} might be coupled with a low density, so that the designer might have to accept a larger s along with the high I_{sp}. The net effect of these opposing factors is not always in the direction of high I_{sp}. Moderate increases in velocity and range can be achieved by switching from "ordinary" to "high-energy" propellants. Large increases are possible by reduction of the structural mass fraction: mathematically V_{bo} becomes infinite as s + 1/Q

*NOTE: Q = PR for a single stage vehicle.

DESIGN PARAMETERS

$$\frac{I}{Q} = \frac{1}{PR} = \text{PAYLOAD FRACTION} = \frac{W_{pl}}{W_f} = \frac{\text{PAYLOAD}}{\text{LAUNCH WEIGHT}} = \frac{1-r_V s_s}{r_V(1-s_s)} \quad \text{(eq 10-2/6)}$$

$$s_s = \text{STRUCTURE FACTOR} = \frac{W_{bo} - W_{pl}}{W_f - W_{pl}} = \frac{W_f - W_p - W_{pl}}{W_f - W_{pl}}$$

$$r_V = \text{MASS RATIO} = \frac{\text{LAUNCH WEIGHT}}{\text{BURNOUT WEIGHT}} = \frac{W_f}{W_{bo}} = e^{\frac{\Delta V}{I_{sp} g_o}}$$

$$\frac{\Delta V}{I_{sp} g_o} = \text{VELOCITY RATIO} = \frac{\text{BURNOUT VELOCITY}}{\text{EFFECTIVE EXHAUST VELOCITY}}$$

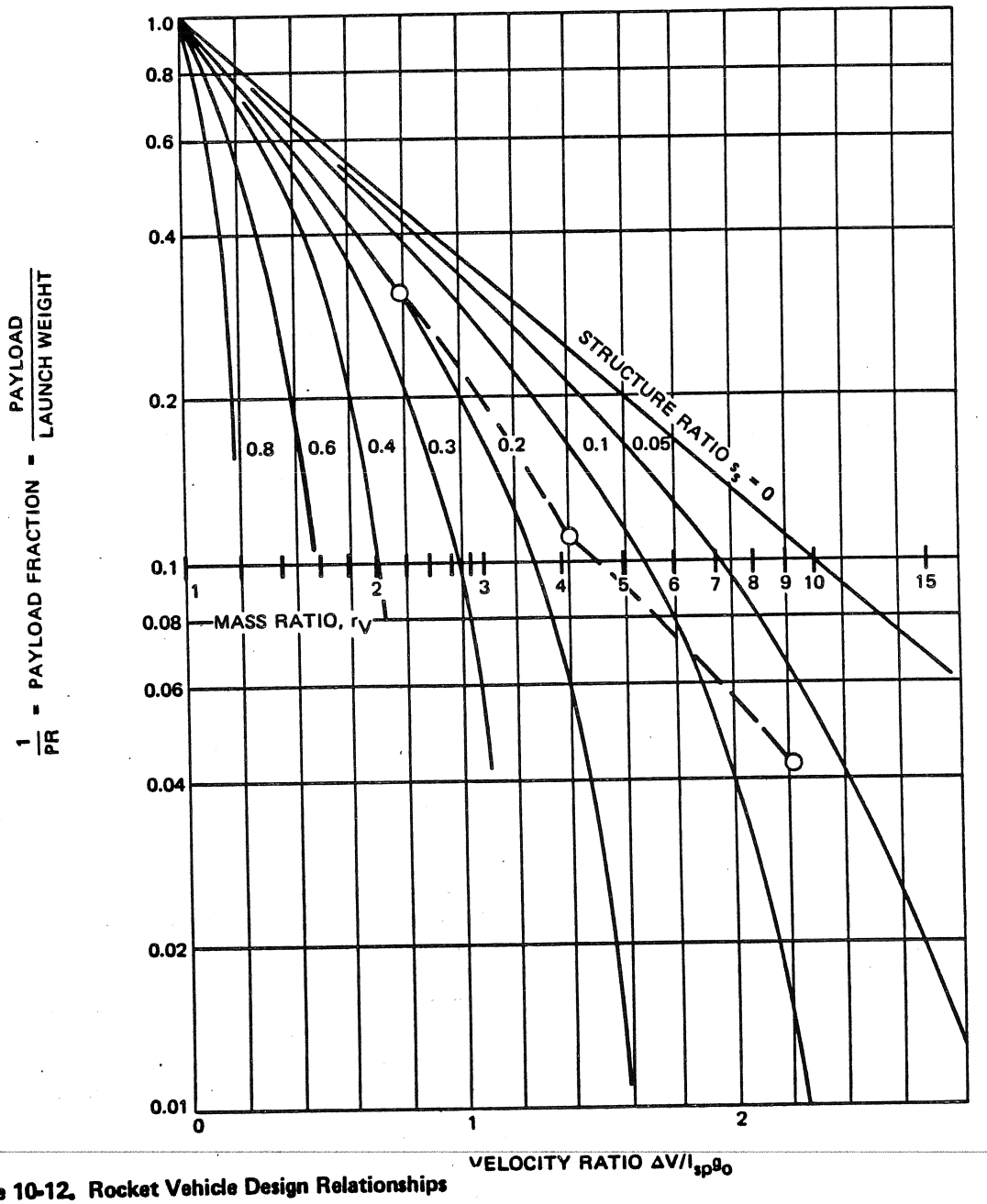

Figure 10-12. Rocket Vehicle Design Relationships

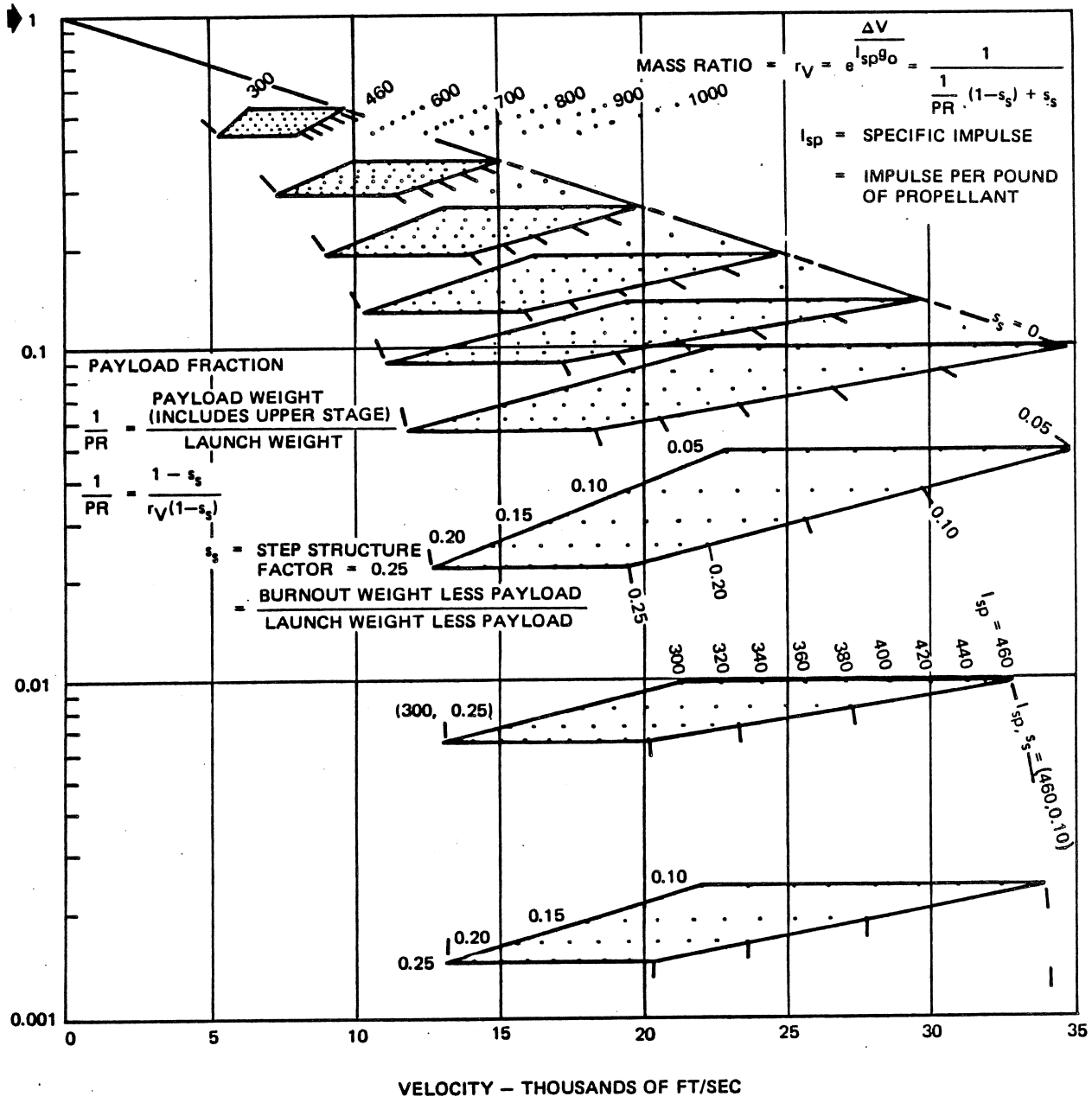

Figure 10-13. Rocket Vehicle Payload Fraction versus Velocity Relationship

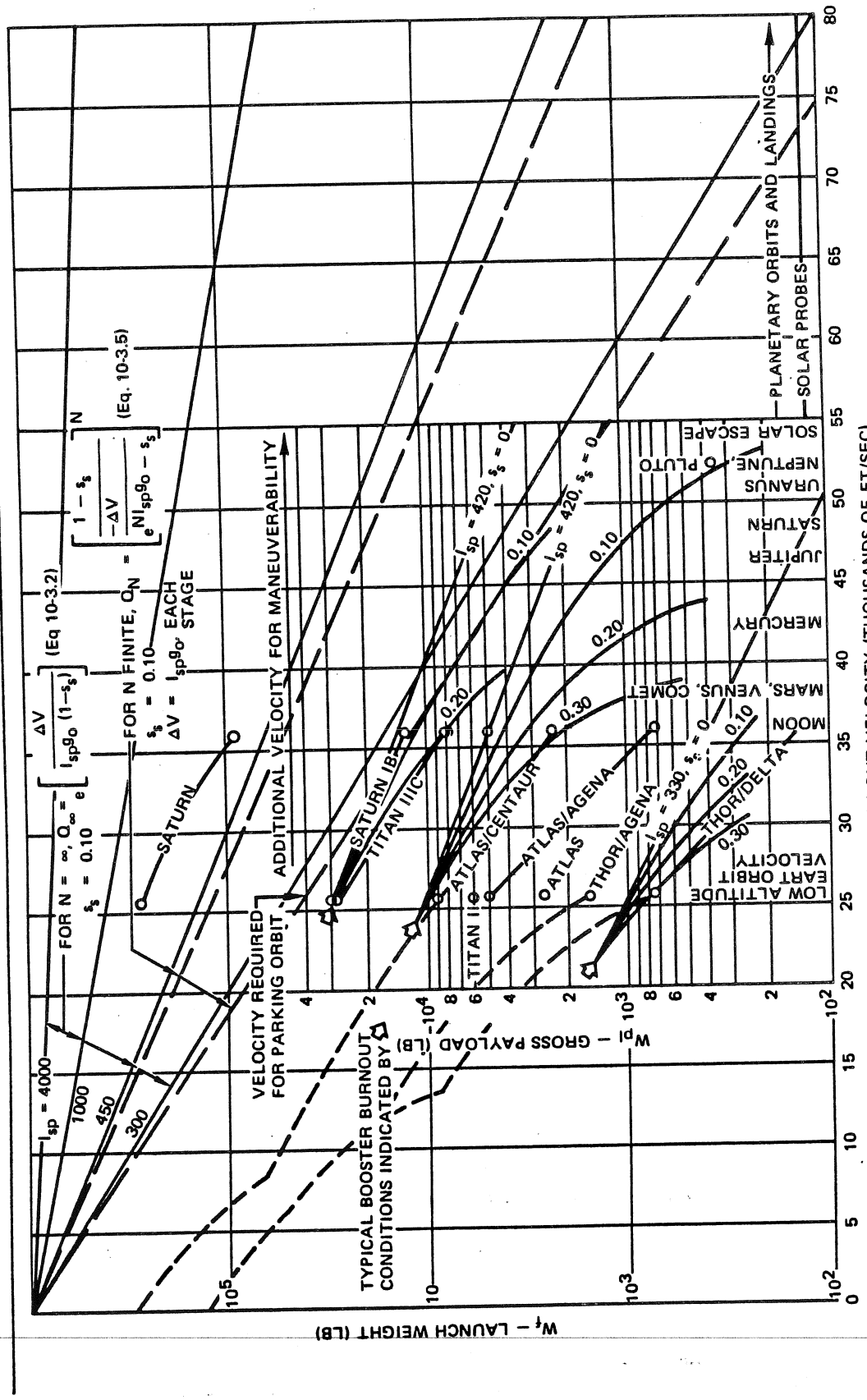

- THE PAYLOAD-VELOCITY DATA POINTS (O) FOR CURRENT LAUNCH VEHICLES HAVE BEEN TAKEN FROM UNCLASSIFIED SOURCES WITHOUT MODIFICATION.
- THE PERFORMANCE OF ADDITIONAL STAGES CAN BE OBTAINED BY USE OF THE ROCKET VEHICLE DESIGN CHART IN FIGURE 10-13. EXAMPLES OF THIS METHOD OF ANALYSIS ARE GIVEN BELOW BY THE "COMET TAIL" CURVES MARKED WITH INDICES ( ).

Figure 10-14. Space Payload Capabilities of Launch Vehicles

approaches zero. From sensitivity parametric analysis it can be shown that

$$\frac{\Delta I_{sp}}{\Delta s} = -I_{sp} \frac{\ln (s + \frac{1}{Q})}{(s + \frac{1}{Q})} \qquad (45)$$

and this relationship is shown in Figure 10-15.

It is seen possible for the structural design engineer to produce performance benefits (by improving s) greater than the propulsion engineer can produce (by improving I_{sp}). The spectacular increase in the range of chemical rockets in recent years, from the 200 mile range of the V-2 to the 5,000-mile-plus range of the ICBM's, has been the result largely of structural improvements rather than of propulsion gains (I_{sp}).

The effect of burning time appears in the negative last term of Equations 43 and 44 mainly through the thrust-to-weight ratio, r. A long burning time (small thrust-to-weight ratio) acts to reduce the burnout velocity for a rocket of fixed full-to-empty mass ratio. This, in turn, reduces the range: although an increase in burning time may extend the powered path, the coasting path is reduced by a much greater amount. Such considerations tend to favor the adoption of a short burning time, i.e., an "impulsive" thrust-time program,

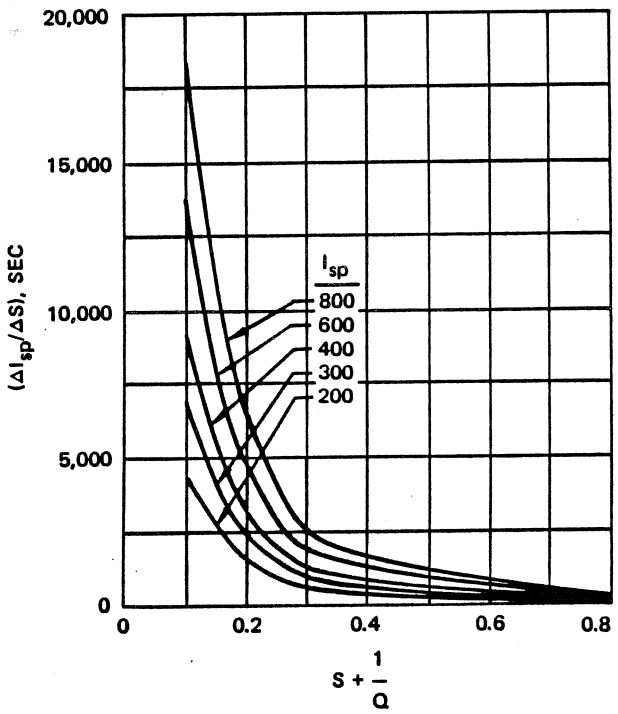

Figure 10-15. Exchange Ratio Curves for $\Delta I_{sp}/\Delta_s$ (Zero g Flight in Vacuum) — Single Stage

to achieve maximum range. However, several additional factors may enter into this optimization analysis.

One of these factors is the effect of atmospheric drag. An implusive thrust-time program produces a short powered path, so that burnout velocity is achieved a short distance from the launching point. For a vehicle launched in the dense regions of the atmosphere, the loss in range due to the resulting drag may outweigh the gain due to short burning time. The computation of burnout velocity with the inclusion of drag is presented in Paragraph 10-2.2.

Another factor is the effect of short burning time on the very important full-to-empty mass ratio, r_V and/or the growth factor, Q. A short burning time results in large accelerations with consequently high g loads in the structure, which in turn requires a heavier structure. Also, for a vehicle launched from a low altitude the severe aerodynamic pressures and aerodynamic heating resulting from rapid attainment of the maximum velocity will require a heavier structure. An obvious effect of the selection of a short burning time for a rocket of specified gross mass is that a large engine is required and less propellant can be carried; again, this impairs the range.

The optimum burning time is thus selected by considering the interplay of r, s, and Q in the last term of Equation 44 for a given V_{bo} and propellant if the drag is negligible. The optimum propulsion system or propellant is selected by considering the interplay of I_{sp}, s, and Q.

Finally, it should be observed that the optimization of rocket gross weight and/or burning time cannot be concluded without considering the trajectory. The final design will be affected by aerodynamic loads, drag, aerodynamic heating, required flight control forces, and the component of g along the flight path, all of which depend on the trajectory.

10-2.2 Space Launch Vehicles

In order to evaluate a vehicle's performance,[12] first the mission requirements need to be defined.[13] In this section, the primary emphasis is placed upon missions that utilize an initial low altitude orbit prior to injection into the transfer trajectory; however, the analyses permit computation of direct ascent trajectories. Mission requirements are defined by a velocity requirement at a particular altitude and flight path angle. In specifying the velocity requirements for the orbital missions, it is assumed that for the low altitude orbits the vehicle flies directly into the orbit, a procedure which is usually found to be optimum. For the higher energy orbits, a Hohmann transfer maneuver (Paragraph 10-2.2.2.2) is performed from the initial parking orbit.

The lunar mission is defined by rather narrow velocity bands. Usually, for preliminary lunar performance evaluations, the earth escape velocity is used. For more critical lunar evaluations the velocity band associated with a peculiar transit time can be used. The interplanetary missions, however, have broader velocity bands. Consistency in payload capability and comparisons of different vehicles necessitates the evaluation of the performance capacility for both the high and low velocity requirements. To be tanken into consideration in defining the velocity requirements are those constraints imposed upon the trajectory by systems considerations and non-nominal vehicle performance.

After the mission requirements have been defined, the vehicle performance capability can be evaluated. The cursory analysis for the booster presented herein is based on empirical data developed for representative parametric vehicles. The upper stage performance is computed by a single analytical approximation. An "approximate" analysis (but more precise method) for the booster (first stage) performance amenable to hand calculation is also presented from empirical data,[13] and categorizes the performance degradations into gravity, drag, and nozzle-atmosphere pressure (thrust-atmoshperic) losses. Precise computations for upper stage performance are based upon very accurate closed-form analytic approximations that generally use either the assumption of a constant pitch rate or constant inertial attitude of the vehicle's thrust axis. This latter analysis can be generalized but is much too complex for presentation here, so only gross procedures are presented. High speed digital computer programs are usually used for solutions. It should be noted that in trajectory analysis it is important to determine the relationships between the velocity vector (magnitude and direction) of the vehicle and its thrust vector during all portions of the powered flight. In the two-dimensional, orbital or vertical launch plane, the history of the angular displacement between these vectors is termed the pitch program.

Graphical and tabular data are presented for use in computing velocity requirements for orbital missions. With respect to performance optimization and system considerations, it may be shown that for interplanetray, lunar and high-energy orbital flights it is usually most efficient to park in a low altitude orbit and, at the proper location, to inject and execute a Hohmann transfer[14,15] to the proper velocity. From many studies done previously, a parking orbit altitude of about 100 nautical miles has been found to be optimum for most vehicle/mission combinations. Parking at lower altitudes may provide greater performance capability, but heating, orbit life time, and tracking become problems. For systems using a radio guidance system, parking orbit altitudes of about 120 nautical miles are sometimes found to be necessary with respect to elevation angles at burnout. For missions requiring orbit rendezvous a parking altitude of about 300 nautical miles is usually found to be optimum with respect to performance and orbit life time. However, even for a parking orbit altitude as low as 300 nautical miles it is often found to be beneficial to park initially at 100 nautical miles and then transfer to the rendezvous parking altitude. With regard to orbit life time, a satellite having a representative ballistic coefficient parameter, $W_{p\ell}/C_D A$ of 10 lb/ft^2 has a predicted life time at 300 nautical miles of 800 days and at 100 nautical miles of only 0.8 day or 12 revolutions.

Either due to specific mission requirements or vehicle constraints, it is sometimes not possible to use a parking orbit. For example, individual solid propellant stages have the problem of short burning times and no restart capability to provide separate impulsive increments for launch and a parking orbit-Hohmann transfer maneuver [or a parking orbit-lunar or interplanetary injection impulse increment (Paragraph 10-2.2.2.2)]. There are techniques which circumvent these problems but the associated payload degradations may not warrant the use of the parking orbit profile. The method usually employed to alleviate the problem is to have a coast phase between stages. This, however, requires attitude stabilization during the coast phase which necessitates a spin table to spin the vehicle, or a reaction cold or hot gas attitude control system.

Respective stage(s) are sized to the exact increment of velocity required for each of the following; launch into orbit, circularizing at a part orbit altitude and finally executing a Hohmann transfer or lunar-interplanetary trajectory. However, this reduces the vehicle's flexibility for use in other missions; it also increases the required performance pad allowance because the dispersions associated with achieving the parking orbit, plus each restart must be added rather than averaged. Therefore, in order to reduce all these problems, it is sometimes more profitable to use a direct-ascent type trajectory. Here the stages are burned sequentially and usually burn out with flight path angles of the order of 70 to 90 degrees. Probably the most severe systems constraint on this type of trajectory is the fact that the launch window for lunar, interplanetary or synchronous orbits is frequently prohibitively short.

In order to clarify the procedure involved in determining the vehicle performance, a listing of the major steps involved is included. These steps essentially follow the time sequence of the actual trajectory mentioned previously. Also, the presentation of the data and methods will be in the order of the following steps. It is assumed that the data defining both the mission and vehicle have been determined.

a. Determine or assume the burnout flight path angle of the first stage.

b. Calculate first-stage burnout velocity for the above flight path angle.

c. Calculate first-stage burnout altitude and range angle.

d. Transform velocity and flight path angle into the inertial system (multiaxis coordinate system).

e. Claculate upper-stage(s) burnout conditions for an assumed pitch program.

f. Compare final conditions with the mission requirements.

g. Repeat steps a through f as many fines as necessary to obtain final mission conditions within reasonable accuracy.

This sequence of analysis is used specifically for the approximate computation of vehicle performance. The cursory analysis eliminates steps d, f, and g, and determines the burnout velocity conditions for rough approximation (≅10 percent). the approximate analysis can be used to determine the performance of a wide range of launch vehicles within an accuracy of 3 percent for assumed average flight path angles obtained from empirical data. In general, the first stage of the vehicle can have an initial thrust-to-weight ratio of >1.0 to 3.0 with a propellant vacuum specific impulse of 250 to 500 pound-seconds per pound. The first-stage burnout flight path angle can vary from 0 to 90 degrees. The physical size or weight of the vehicle is not limited since the analysis is in parametric form. The range of data allows the analysis of booster stages from present-day vehicles up to and including vehicles of advanced state-of-the art design using high-energy liquid propellants. The data are not sufficient for nuclear booster stages, although the method is certainly valid. The balance of Paragraph 10-2.2.1 is devoted to further explanation of the performance estimation techniques.

It must be pointed out that for performance evaluation concerning the distance traveled along a flight path, Equation 2 must be integrated. In order to accomplish the integration in a practical manner, simplified methods are used. These methods are based on vehicles of constant vacuum thrust (Figure 10-16) and certain assumed mass conditions related to the inert and expended weight. For actual vehicles, such as those using solid propellant stages with regressive (or progressive) burning, the vacuum thrust levels must be adjusted to an average constant thrust for use in this analysis. Also, seal-level (or other nominal flight altitude) thrust must be adjusted by the same amount as vacuum thrust to keep the ratio of seal-level (or nominal altitude) specific impulse to vacuum specific impulse constant, as shown in Figure 10-16.

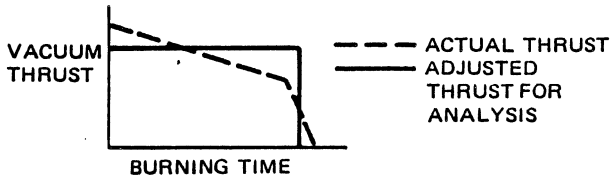

Figure 10-16. Thrust Curve Adjustment

The average vacuum thrust-time history is best found by averaging the vacuum thrust over the burning period prior to tail-off operation, distributing the tail-off portion reactilinearly at average vacuum thrust, and terminating at a time such that the same total tail-off impulse is realized.

For simple trajectory calculations, the burnout mass of each vehicle stage includes all the unexpected mass, i.e., mass of stages above the step of interest, step structure, motor case or tank, unused propellant and fluids.

10-2.2.1 Space Launch Vehicle Performance

10-2.2.1.1 Kick Angle

To develop the cursory analytical performance model, it is necessary to understand the events which occur during flight in the trajectory plane. Figure 10-17 describes, by spherical trigonometry coordinates, the relationships between the flight trajectory and the earth as a reference. The trajectory plane is the earth great circle plane passing through the launch site and the rocket planar flight trajectory (refer to Paragraph 10-2.2.1.4).

In the first-stage portion of the flight (Figure 10-18), a gravity turn or "zero angle of attack" trajectory can be used to reduce the aerodynamic forces acting on the vehicle. In this case, for any impulsive velocity increment, ΔV, the gravitational velocity component V_g combines with it to provide a resultant vehicle velocity vector exactly tangent to the flight path. Because a singularity exists at zero initial velocity, all vehicles following gravity turn trajectories must be launched vertically and programmed for zero pitch for a short period of time, t_v, the length of which is arbitrary but is usually related to the initial thrust-to-weight ratio. After the vertical rise, an artificial "kick angle," β_o, a nearly instantaneous but finite rotation of the vehicle centerline and velocity vector, is given to the vehicle to initiate the gravity turn. The flight path angle, β_o, may also be measured from the local horizontal and defined as α_o. Since β_o and α_o are complimentary angles and

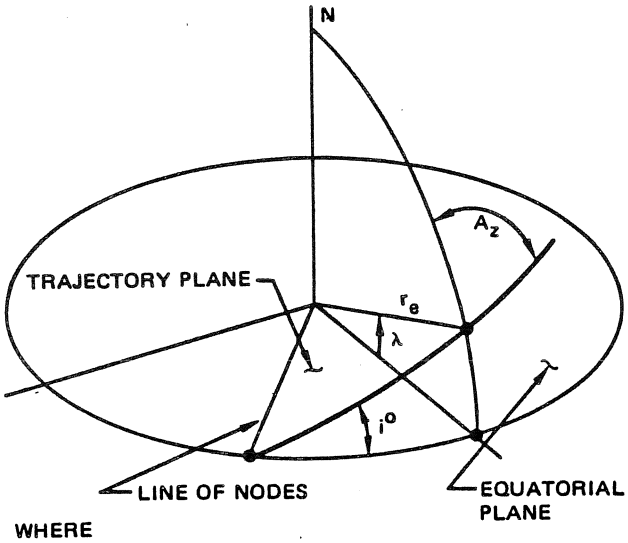

WHERE

i^o = INCLINATION OF THE TRAJECTORY PLANE WITH RESPECT TO THE EQUATORIAL PLANE

λ = LATITUDE OF LAUNCH SITE

A_z = LAUNCH AXIMUTH MEASURED FROM TRUE NORTH

Figure 10-17. Spherical Trigonometric Coordinates of Launch Trajectory

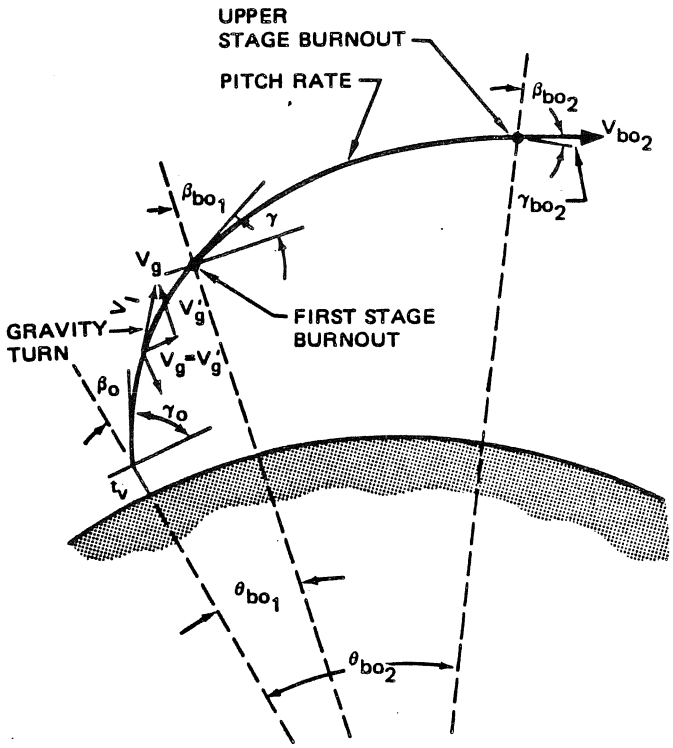

Figure 10-18. Typical Trajectory Profile in Launch Plane

either convention is acceptable, the term β_o is arbitrarily used here. The kick angle is a "tool" used in preliminary trajectory calculations to represent the pitch-over period before gravity turn. The burnout flight path angle β_{bo_1} (or α_{bo_1}) of the first stage is dependent on the magnitude of the kick angle. At first-stage burnout, t_{b_1}, the vehicle is assumed to be sufficiently out of the atmosphere that the second stage can be flown on a pitch program without regard to aerodynamic effects. In some cases this assumption is not altogether valid, but the error realized in terms of performance is usually small. In the case of the thrust-augmented Thor/Delta vehicle, significant performance gains are achieved by starting optimal trajectory shaping earlier, e.g., a gravity turn is initiated early by employing a kick rate (non-instantaneous vehicle turn) and continued for 70 to 80 sec. Once the dynamic pressure on the vehicle falls to 300 to 400 PSF (and after the thrust augmenting solid rocket motors are jettisoned) the vehicle is flown at an angle of attack. This type of flight operation represents a sophistication of trajectory shaping analysis beyond the scope of this text and this simplified method presented is adequate for preliminary calculations and/or for understanding the mechanics of flight.

At first-stage burnout, the increment in velocity due to the earth's rotational effects is vectorally added to the burnout velocity vector. Thus, the upper stage is flown in the relative reference system (coordinates relative to solar space system) while the first stage is flown in the relative reference system (coordinates relative to the launch site position). At this point the upper stages can be coasted or flown with a desired pitch program to burnout. The angle θ_{bo} is the range angle from launch to burnout.

Past experience has indicated that the coast phases between stages for chilldown, ullage control, etc., of a cryogenic liquid propellant vehicle have a significant effect on trajectory shaping and thus on overall performance. Therefore, an analysis is included in this section for determinining coasting characteristics based on the assumption of parabolic motion with constant velocity. This analysis is a fast and simple method for determining changes in trajectory parameters during a short coast period (less than 60 seconds) due to the previously mentioned conditions of chilldown, ullage control, etc. Another method, based on Kepler's equations of motion along conic sections,[13,33] gives a more precise but complicated method of determining

changes in trajectory parameters for long coast phases but is omitted because it is beyond the scope of this presentation.

10-2.2.1.2 Burnout Flight Path Angle and Vertical Rise Time

The determination of first stage performance depends on knowledge of the burnout angle of the first stage. The first-stage burnout angle may be determined from the kick angle used at the end of the vertical rise. Thus, the determination of the burnout angle β_{bo_1} is related to the initial kick angle, β_o. The empirical data in Figure 10-19 indicate the ratio of initial kick angle to vertical rise time required in order to perform a low-orbit mission. The ratio is dependent on the initial thrust-to-weight ratio and the first-stage mass ratio. The shaded area indicates the spread determined by the various vehicles studied. Generally, the low mass ratio first stages (r_v = 2.0 to 3.5) determine the lower limit of the area while those with mass ratios greater than 3.5 determined the upper limit. These data were generated for specific values of vertical rise time, shown in Figure 10-20 as a function of initial thrust-to-weight ratio. It should be noted that for such vehicles as the thrust-augmented Thor/Delta, Figures 10-19, 10-20, and 10-21 are not applicable because the vehicle is flown with a kick rate and the solids are dropped before first stage liquid engine burnout.

Since the kick angle is dependent on the vertical rise time, and thus the velocity at the time of kick, the initial thrust-to-weight ratio in the abscissa of Figures 10-19 and 10-20 is the actual initial value and is not corrected for a varying vacuum and sea-level thrust. These are the only two cases where the actual value of initial thrust-to-weight is used if a correction is necessary.

The nomograph shown in Figure 10-21 presents the first-stage burnout angle as a function of the kick angle, vacuum specific impulse, initial thrust-to-weight ratio, and the first-stage mass ratio. As is shown in the example of Figure 10-21, the initial thrust-to-weight ratio and vacuum specific impulse are used to construct a horizontal line which intersects a vertical line determined by the initial kick angle at the top of the figure. The intersection of the two lines determines the burnout angle. In most cases, the resulting burnout angle will be close to the actual value determined by trajectory calculations.

If the mission of interest is something other than a low altitude orbit, an estimate will have to be made for the burnout angle. Generally, the low orbit mission results in the largest burnout angle and thus other missions would probably require burnout angles somewhat smaller than those given in Figure 10-21.

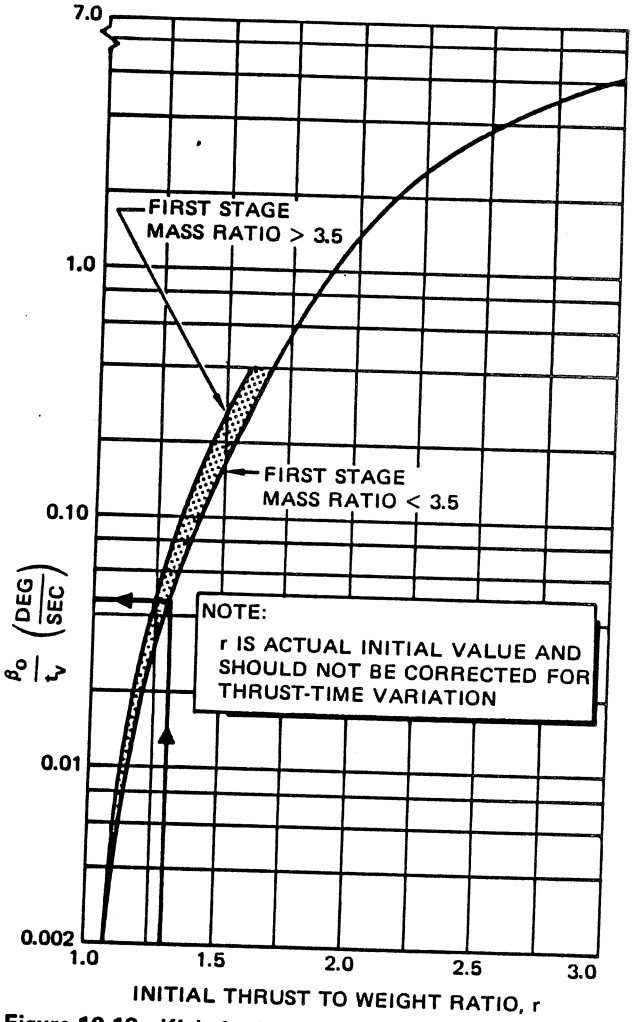

Figure 10-19. Kick Angle – Vertical Rise Time Ratio (Low Orbit Mission)

10-2.2.1.3 Cursory Estimation of Performance

This method of estimating the burnout velocity is a first approximation. The results also indicate trends for a particular vehicle configuration which can be used to roughly optimize various vehicle characteristics and trajectory parameters.

The total ideal velocity required to perform a particular mission must be determined so that a vehicle configuration can be sized to perform the mission. With a minimum of knowledge about the overall configuration and a few estimates of vehicle mass and drag characteristics, the first approximation for the total velocity loss and mission velocity gives the required ideal velocity.

This type of analysis applies even if a single stage is being sized to be used with another stage or stages already

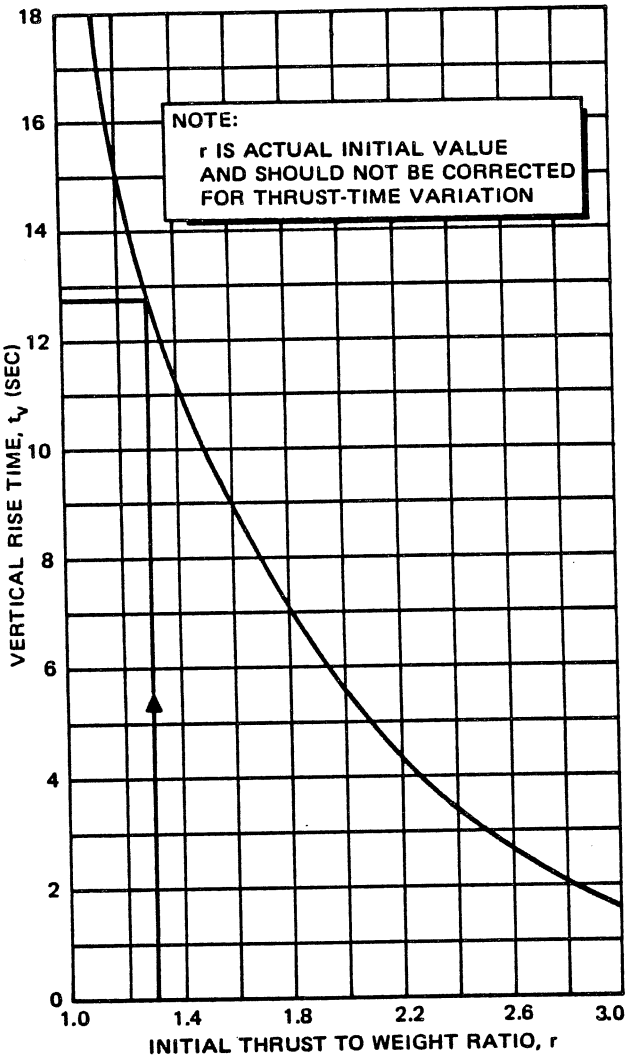

Figure 10-20. Vehicle Vertical Rise Times

available. Special precautions must be exercised, however, if thrust augmented stages are used, e.g, Thor/Delta, where burnout of the first stage varies for the main and strap-on motors. These analyses should consider the first stage as applying until solid motor burnout after which the mass and velocity characteristics of the balance of main motor burning is treated as second stage operation, with appropriate adjustment for losses as calculated below for first stages.

The ideal or total velocity increment ΔV_{I_n}, of a stage operating in a vacuum is expressed by Equation 19, where the I_{sp} is the vacuum value. The velocity increment of a stage thrusting in the atmosphere and a gravitational field is given by Equation 32, where the term ΔV_{L_n} is defined as the sum of the stage velocity losses due to gravity, drag, and thrust-atmospheric effects.

a. First-Stage Losses — An approximate but rapid method for evaluating the first-stage burnout velocity by determining the velocity loss, ΔV_{L_1}, during first-stage flight involves the use of Figures 10-22 through 10-28 which present the total velocity loss, ΔV_L, of a single-stage vehicle as a function of the initial thrust-to-weight ratio, vacuum specific impulse, and first-stage burnout flight path angle. These data were generated for a vehicle with the following characteristics:

$$\frac{I_{sp_{sl}}}{I_{sp_{vac}}} = 0.85, \quad \frac{C_{D_{max}} A}{W_f} = 0.0002, \quad \frac{W_f}{W_{bo}} = 4.0$$

The parameter, $C_{D_{max}}$, is the maximum drag coefficient obtained from the drag coefficient versus Mach number variation. This value usually occurs at a Mach number of approximately 1.0 (refer to Figure 10-8).

If the vehicle of interest has characteristics differenct from those assumed above, the following relations can be used independently to adjust the losses obtained from Figures 10-22 through 10-28.

Drag loss correction:

$$\Delta(\Delta V_L) = 2 \times 10^6 \left(\frac{C_{D_{max}} A}{W_f} - 0.0002 \right) \qquad (46)$$

Thrust-atmospheric loss correction:

$$\Delta(\Delta V_L) = 3780 \left(0.85 - \frac{I_{sp_{sl}}}{I_{sp_{vac}}} \right) \qquad (47)$$

Gravity loss correction:

$$\Delta(\Delta V_L) = 0.85\, g_o \frac{F}{W_f} I_{sp_{vac}} \cos\beta_{bo} \left(\frac{1}{4} - \frac{W_{bo}}{W_f} \right) \qquad (48)$$

After having determined the first-stage burnout velocity, V_{bo_1}, through the use of Equation 30, the component of the launch site rotational velocity along the assumed launch azimuth is vectorially added to V_{bo_1} to obtain the inertial burnout velocity, V_{bo_I}, Paragraph 10-2.2.

b. Upper-Stage Performance — The burnout velocity of a vehicle's upper stages can be expressed in much the

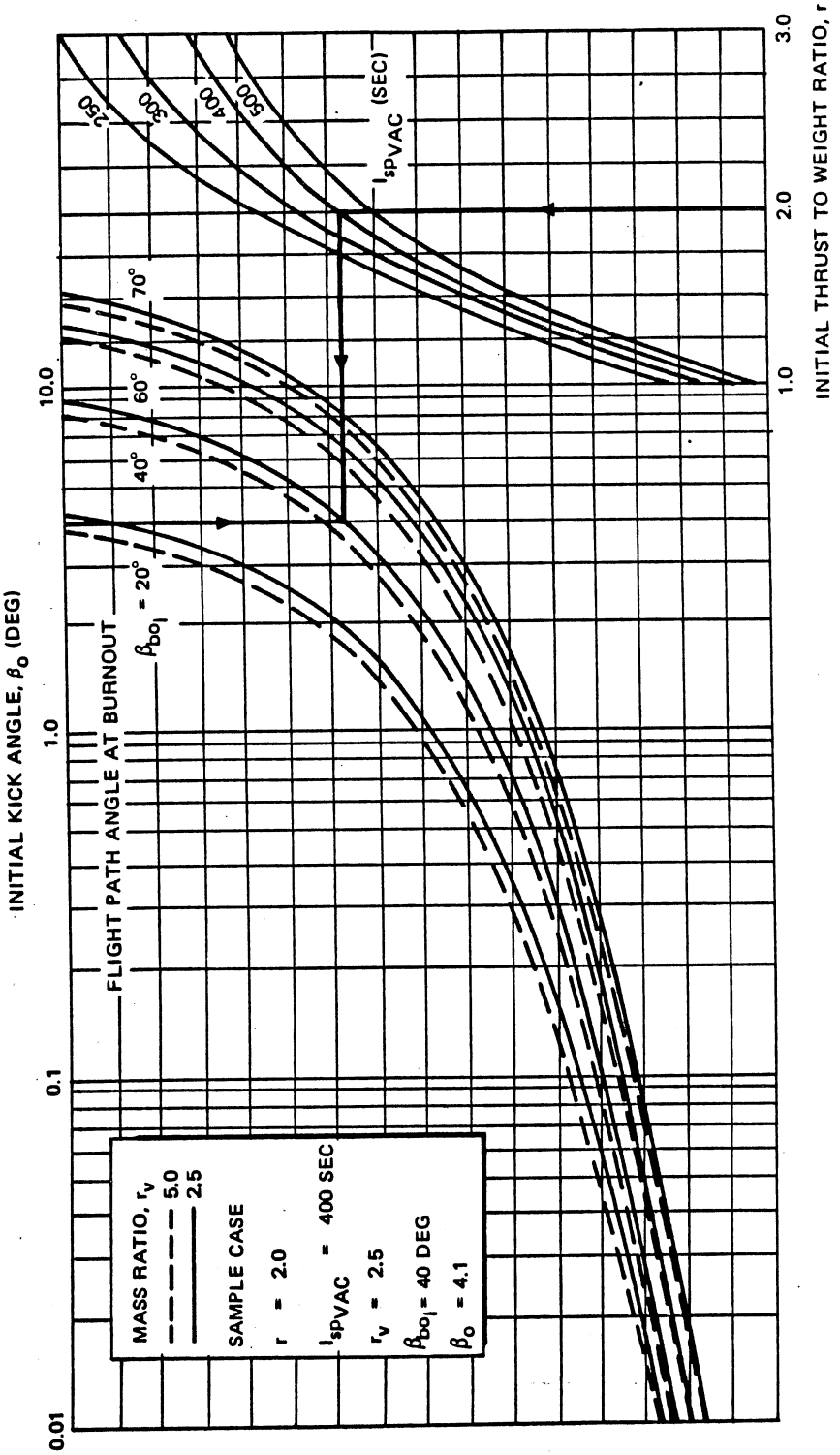

Figure 10-21. First-Stage Burnout Angle Nomograph

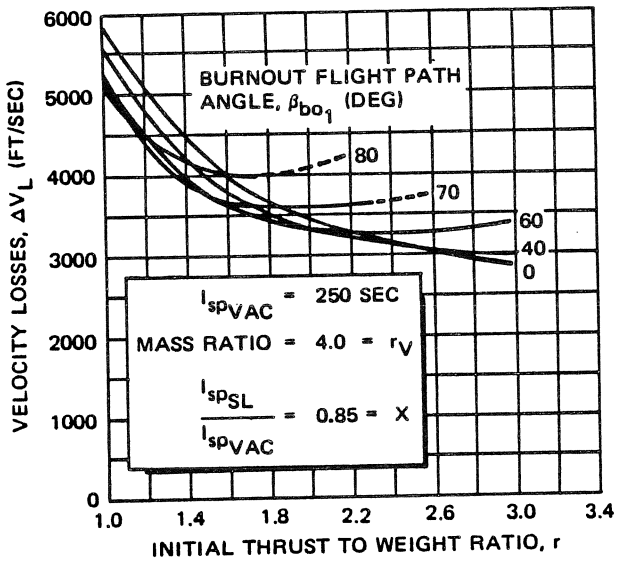

Figure 10-22. Cursory First-Stage Velocity Losses

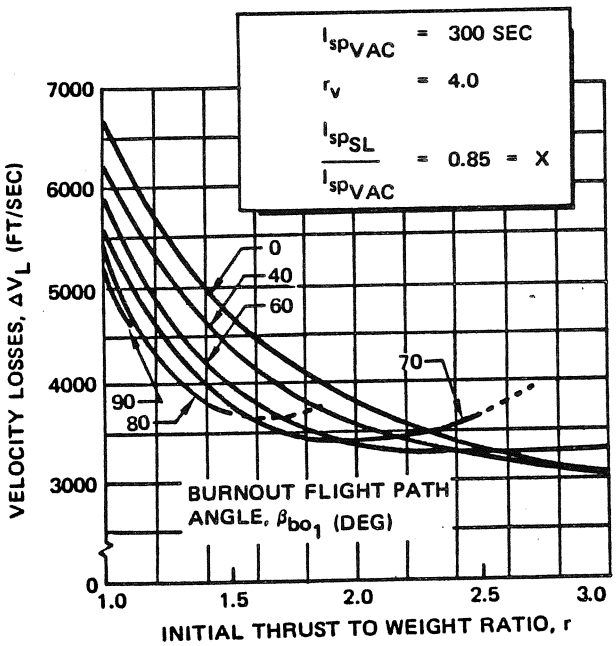

Figure 10-23. Cursory First-Stage Velocity Losses

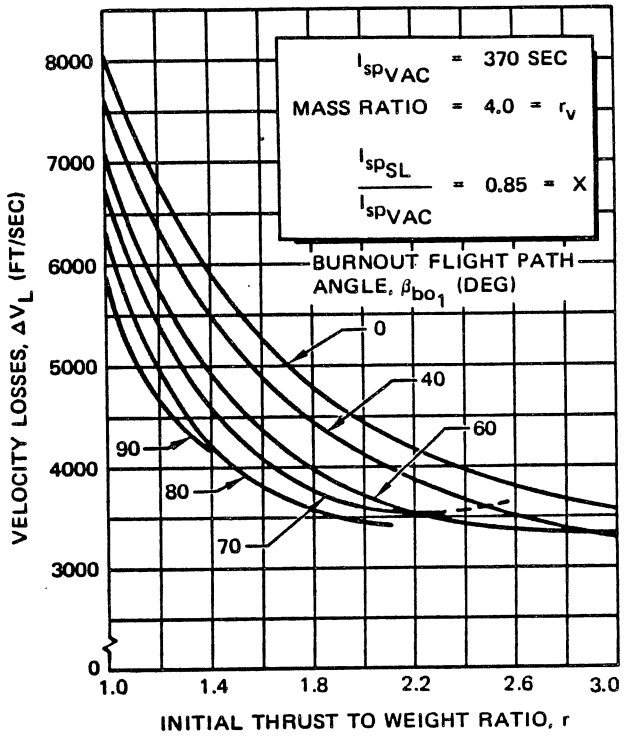

Figure 10-24. Cursory First-Stage Velocity Losses

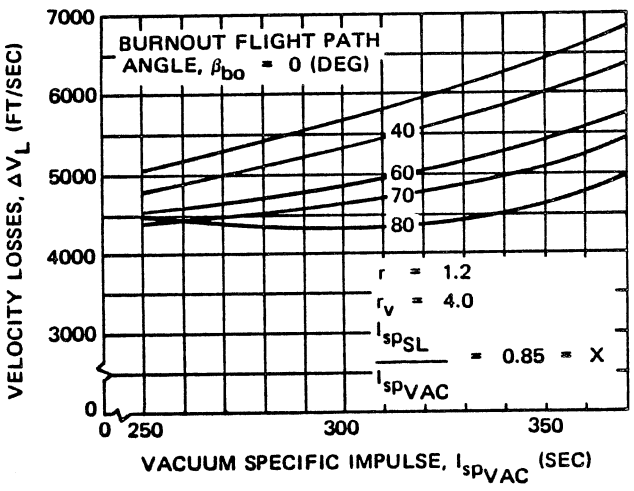

Figure 10-25. Cursory First-Stage Velocity Losses

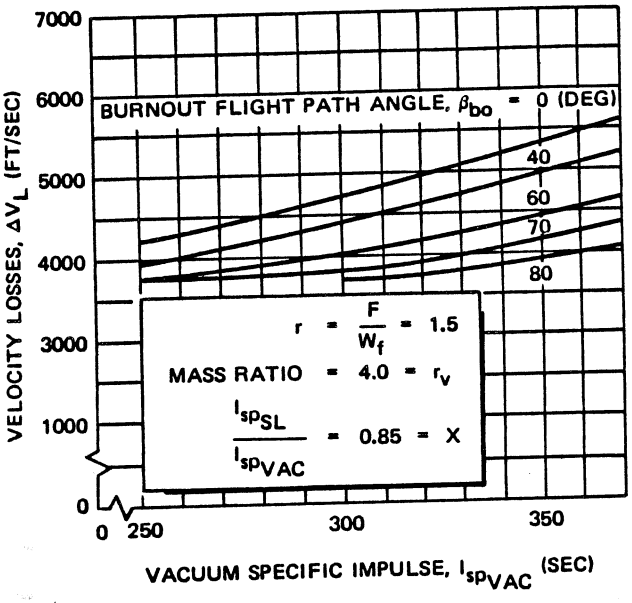

Figure 10-26. Cursory First-Stage Velocity Losses

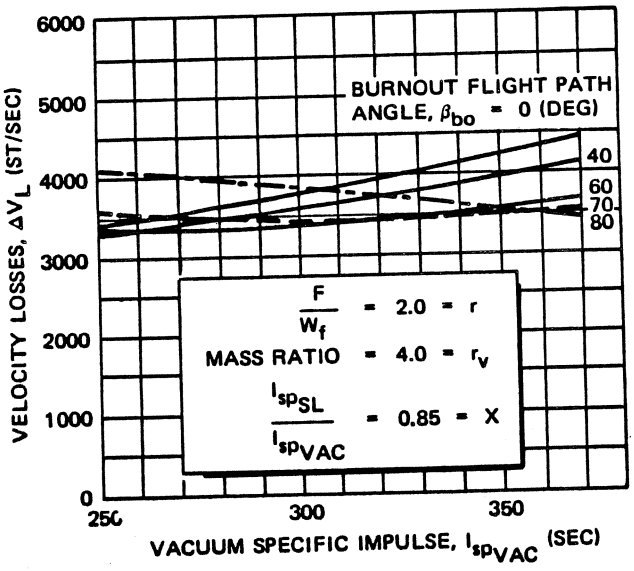

Figure 10-27. Cursory First-Stage Velocity Losses

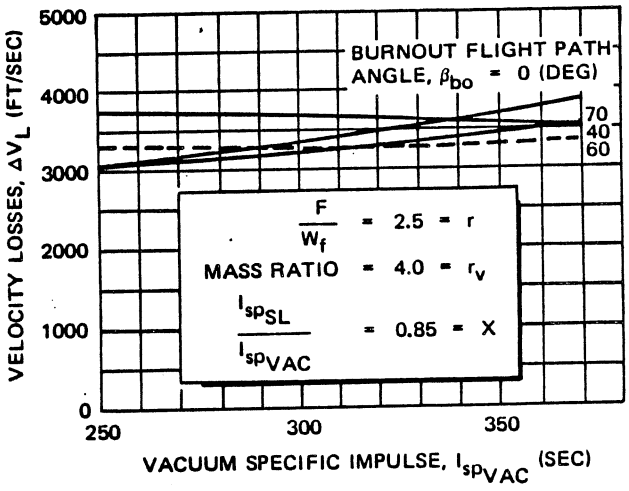

Figure 10-28. Cursory First-Stage Velocity Losses

same manner as that shown in Equation 30 and for N stages, Equation 31:

$$V_{bo_{IN}} = V_{bo_{I_1}} + \sum_{n=2}^{N} \Delta V_{I_n} - \sum_{n=2}^{N} \Delta V_{L_n} \qquad (49)$$

where the losses are due to gravity and angle of attack. The gravity loss is the more significant of these, thus the upper stage losses can be expressed as:

$$\Delta V_L = g^* t_b \cos \bar{\beta} \qquad (50)$$

where $\bar{\beta}$ is an average flight path angle selected between the initial and burnout values of the upper stage flight path angle. The average flight path angle $\bar{\beta}$, is dependent on the thrust-pitch program of the upper stage. The term g^* refers to the acceleration of gravity at the average or effective altitude during the flight. For simplicity, and with little error, $g_o = g^*$ near the earth's surface, up to 100,000 ft.

Typical average flight path angles are shown on Figures 10-29 and 10-30 for one and two upper stages, respectively. These data, which are a function of the initial flight path angle, were generated from trajectory data for low orbit missions and thus the burnout is 90 degrees. Where two upper stages are involved, a dependence on the initial

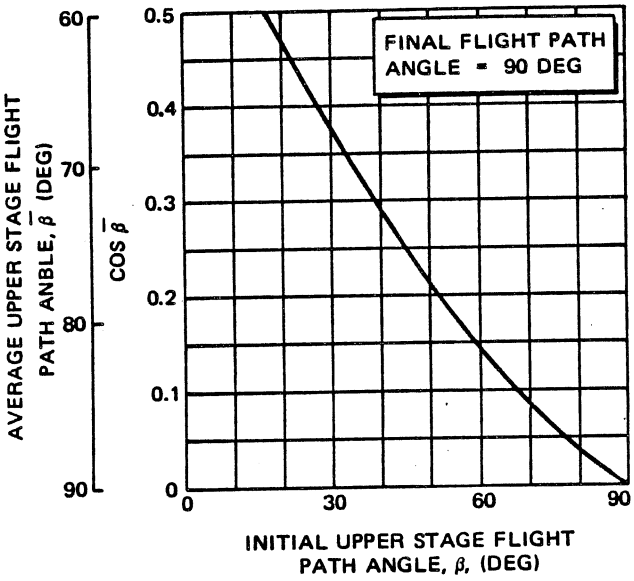

Figure 10-29. Average Upper-Stage Flight-Path Angle (Single Upper Stage)

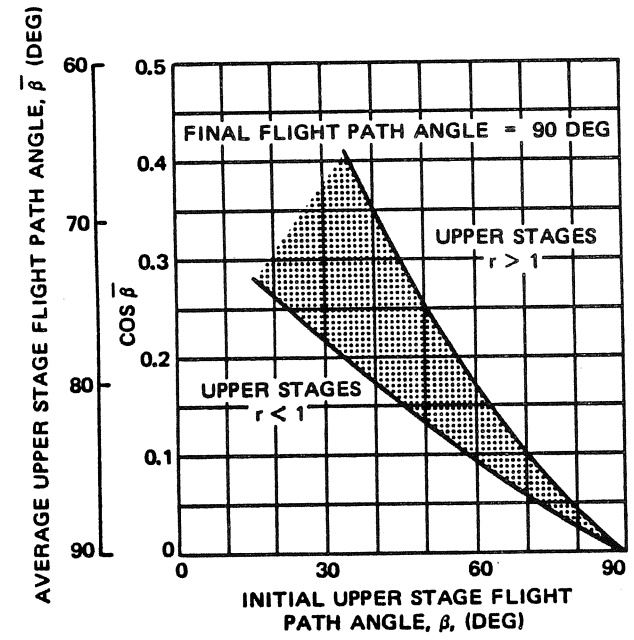

Figure 10-30. Average Upper-Stage Flight-Path Angle (Two Upper Stages)

thrust-to-weight ratio is indicated. This is explained by the fact that stages with a low thrust-to-weight ratio ($r_{vac} < 1.0$) have long burning times and spend a relatively long time near a flight path angle of 90 degrees, which increases the value of $\bar{\beta}$. Stages with a high thrust-to-weight ratio ($r_{vac} > 1.0$) act much the same as a single upper stage. The data (given in Figures 10-29 and 10-30) were determined empirically from several trajectory calculations. Any angle of attack losses due to thrust misalignment were included in the calculations of $\bar{\beta}$. Thus, angle of attack losses have not been neglected.

For missions where the burnout flight path angle is not 90 degrees, the following relationship has been determined for an approximation to $\bar{\beta}$ for use in Equation 50,

$$\bar{\beta} = 0.7\,(\beta_{bo} - \beta_1) + \beta_1 \qquad (51)$$

where β_1 and β_{bo} are the initial and final flight path angles. This relation is at best representative because of the number of variations possible in the upper-stage characteristics and flight profile.

10-2.2.1.4 Approximate Estimation of Performance

a. First-Stage Performance – An approximate determination of first-stage burnout velocity, but more precise than that given for the cursory analysis, is based on Equation 32 except that gravity, drag, and thrust-atmospheric losses are evaluated separately and more accurately. The total losses of the first stage can be expressed by:

$$\Delta V_{L_1} = \Delta V_{L_{g_1}} + \Delta V_{L_{D_1}} + \Delta V_{L_{F_1}} \qquad (52)$$

$\Delta V_{L_{g_1}}$ = gravitational loss

$$= (g_o t_b - K_{gg}) \left[1 - K_g \left(1 - \frac{1}{r_{v_1}}\right)\left(\frac{\beta_{bo}}{90^\circ}\right)^2\right] \qquad (53)$$

$$\Delta V_{L_{D_1}} = \text{drag loss} = K_D \frac{C_{D_{PD}} A}{W_{f_1}} \qquad (54)$$

$$\Delta V_{L_{F_1}} = \text{thrust-atmospheric loss} = K_a \qquad (55)$$

1. Gravitational Loss – The first-stage gravitational loss expressed by Equation 53 is a function of the vehicle design parameters, the burnout angle, and two empirical constants, K_{gg} and K_g. The term $g_o t_b$ in Equation 53, is the gravitational loss expected from vertical flight in a constant gravitation field. However, due to the variation of a gravitational field as the inverse square of the distance from the center of attraction, the

constant, K_{gg}, is needed to correct the over-estimated loss determined by $g_o t_b$. The value of K_{gg} can be determined from the data shown in Figure 10-31. The constant, K_g, is a function of the initial thrust-to-weight ratio, vacuum specific impulse, and mass ratio. This constant can be found in Figures 10-32 and 10-33 for mass ratios of 2.5 and 5.0, respectively. If the first stage has a mass ratio of some value other than 2.5 or 5.0, the correction factor shown in Figure 10-34 should be used to adjust the value of K_g for a mass ratio of 2.5 obtained from Figure 10-33.

2. Drag Losses – The drag losses of a vehicle are shown in Equation 54 to be a function of the ratio, $C_D A/W_f$, where C_D is a representative value of the drag coefficient for the vehicle of interest. In Paragraph 10-2.2.1.3, Cursory Estimation of Performance, it was assumed that the maximum drag coefficient was representative of the vehicle drag characteristics. However, for precise calculations, the drag coefficient at maximum drag force during the trajectory, $C_{D_{PD}}$, was found to be more representative. Determining $C_{D_{PD}}$ requires knowledge of the Mach number at maximum drag, M_{PD}, in order to pick off the correct value from the curve of drag coefficient versus Mach number. The parameter, M_{PD}, is shown in Figure 10-35 as a function of the ratio $\sqrt{Isp_{vac}}$ (r) and burnout flight path angle. The empirical constant, K_D was also found to be a function of $\sqrt{Isp_{vac}}$ (r) and β_{bo} as is shown in Figure 10-36.

   The drag loss obtained by these relations is representative of a first-stage flight that burns out above the atmosphere. If first-stage burnout occurs in the atmosphere, the drag loss obtained by these relations will essentially include any drag loss encountered during the second-stage flight, thus in calculating the second stage performance, it can be assumed to operate in a vacuum.

3. Thrust-Atmospheric Losses – Thrust-atmospheric losses are caused by the reduction of the vacuum thrust level by atmospheric pressure during the portion of flight through the atmosphere. Thus, the ratio of sea level specific impulse to vacuum specific impulse, which is determined by the nozzle and propellant characteristics, is the important parameter determining these losses. Also, the initial thrust-to-weight ratio has a small effect which is included in Figure 10-37 for the determination of K_a.

   The values of K_a shown in Figure 10-37 are representative of conical and DeLaval type nozzles only. Exotic nozzle configurations such as plug (or spike) or expansion-deflection types would have lower losses for the same initial conditions.

4. First-Stage Burnout Altitude – After the burnout velocity and flight path angle have been determined for the first stage, the calculation of burnout altitude remains to complete the description of the first-stage burnout conditions.

$$h_{bo_1} = \left[h_{bo} - \frac{\left(\Delta V_{L_{D_1}} + \Delta V_{L_{F_1}} \right)}{2} t_{b_1} \right] \left[1 - \left(\frac{\beta_{bo_1}}{K_h} \right)^2 \right] \qquad (56)$$

   where h_{bo} is the alitude attainable by the first stage in nonatmospheric vertical flight, from Equation 35. The burnout altitude then is dependent on the vehicle parameters (listed in Equation 56), the atmospheric losses, the burnout flight path angle, and the empirical constant, K_h. The constant, K_h, is a function of initial thrust-to-weight ratio, vacuum specific impulse, and mass ratio. The variation of K_h (in radians) is shown in Figure 10-38 in nomograph form (Note: β_{bo}, is in radians in this equation).

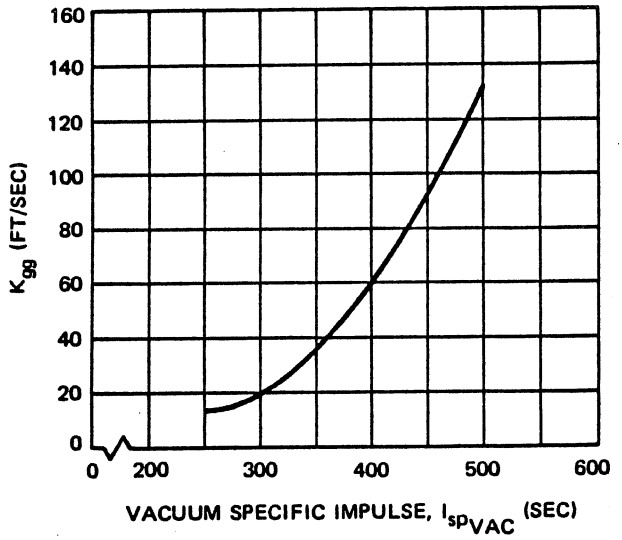

Figure 10-31. Change in First-Stage Losses Due to Altitude Variation of Gravity

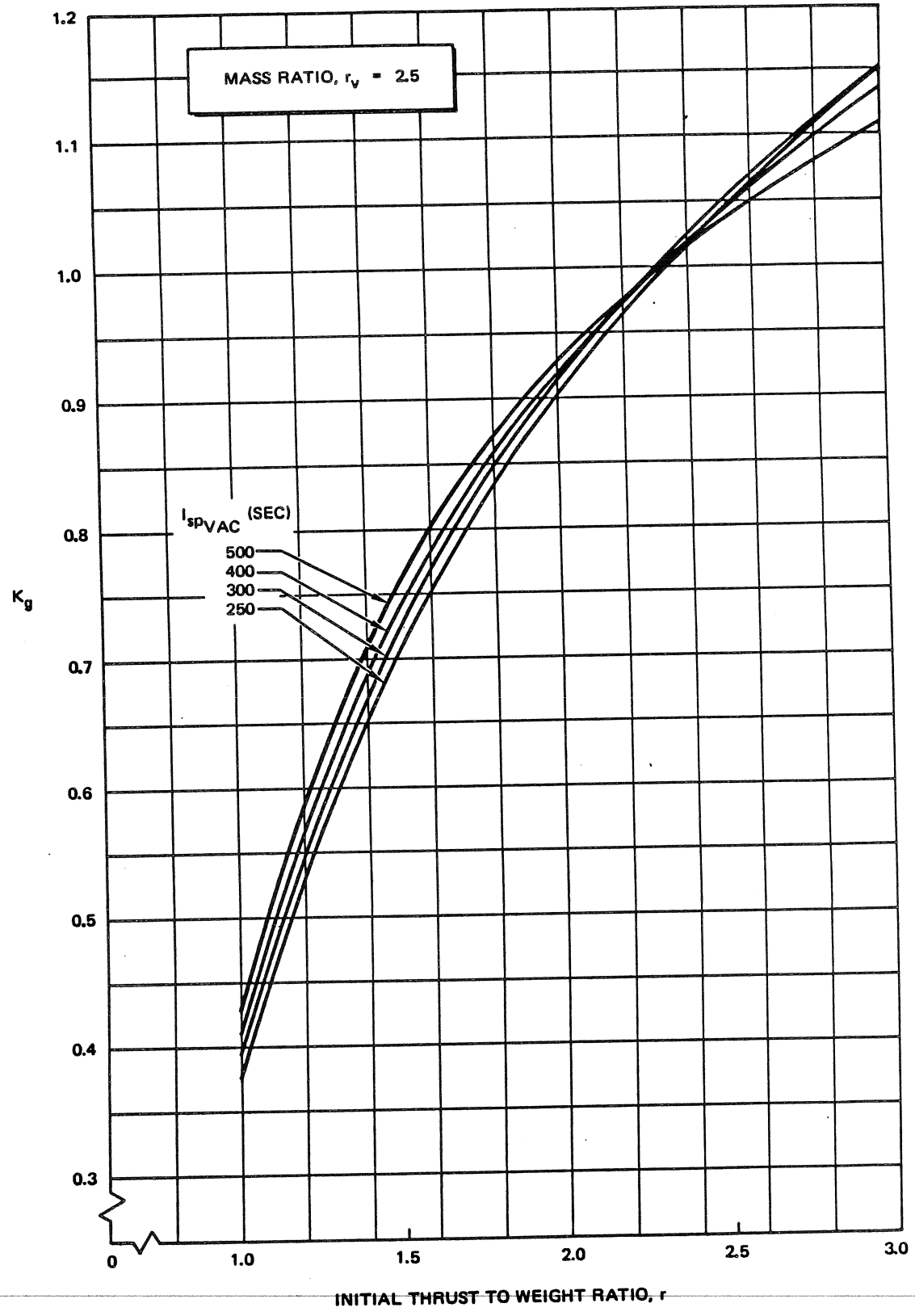

Figure 10-32. First-Stage Gravity – Loss Constant

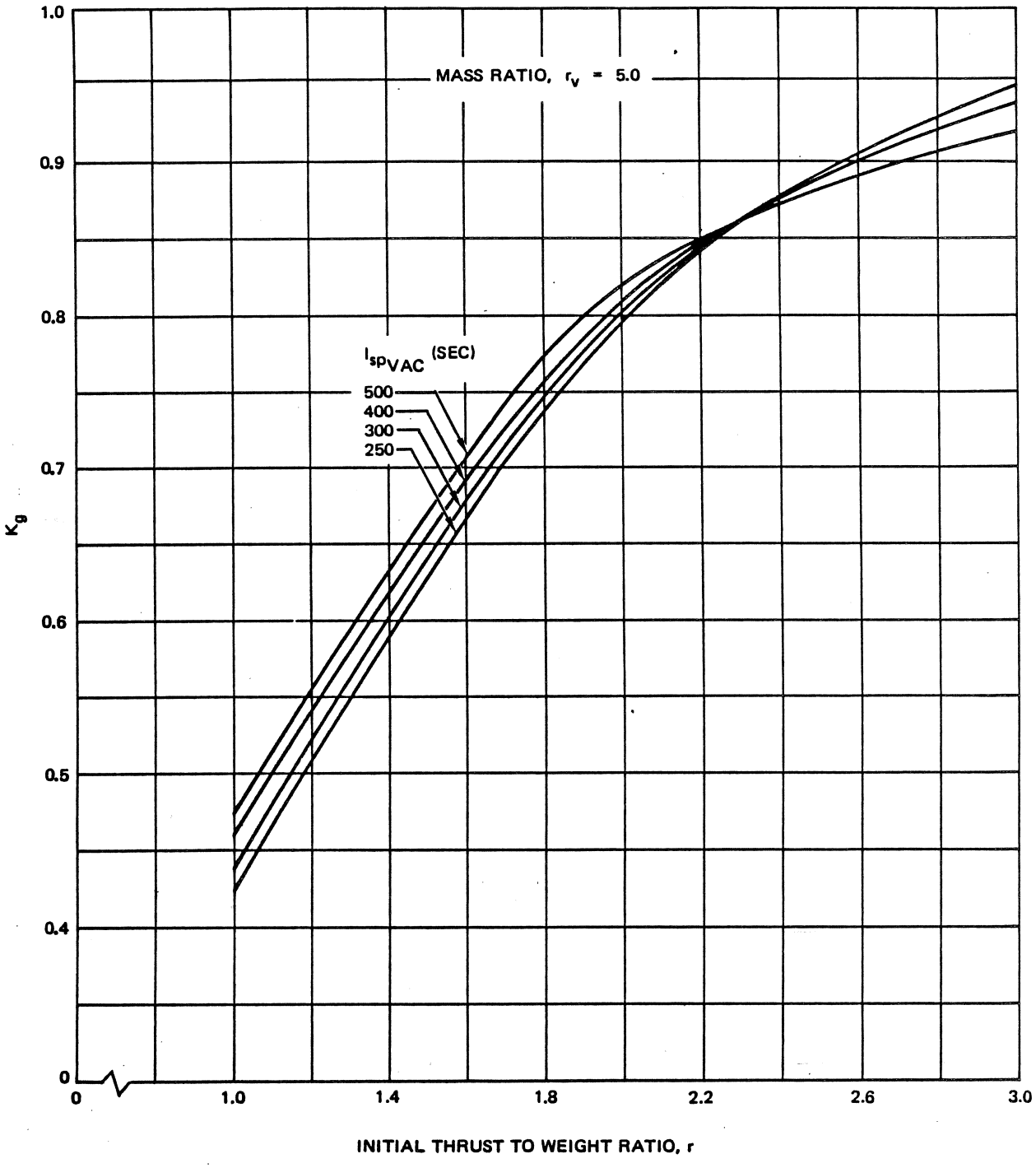

Figure 10-33. First-Stage Gravity – Loss Constant

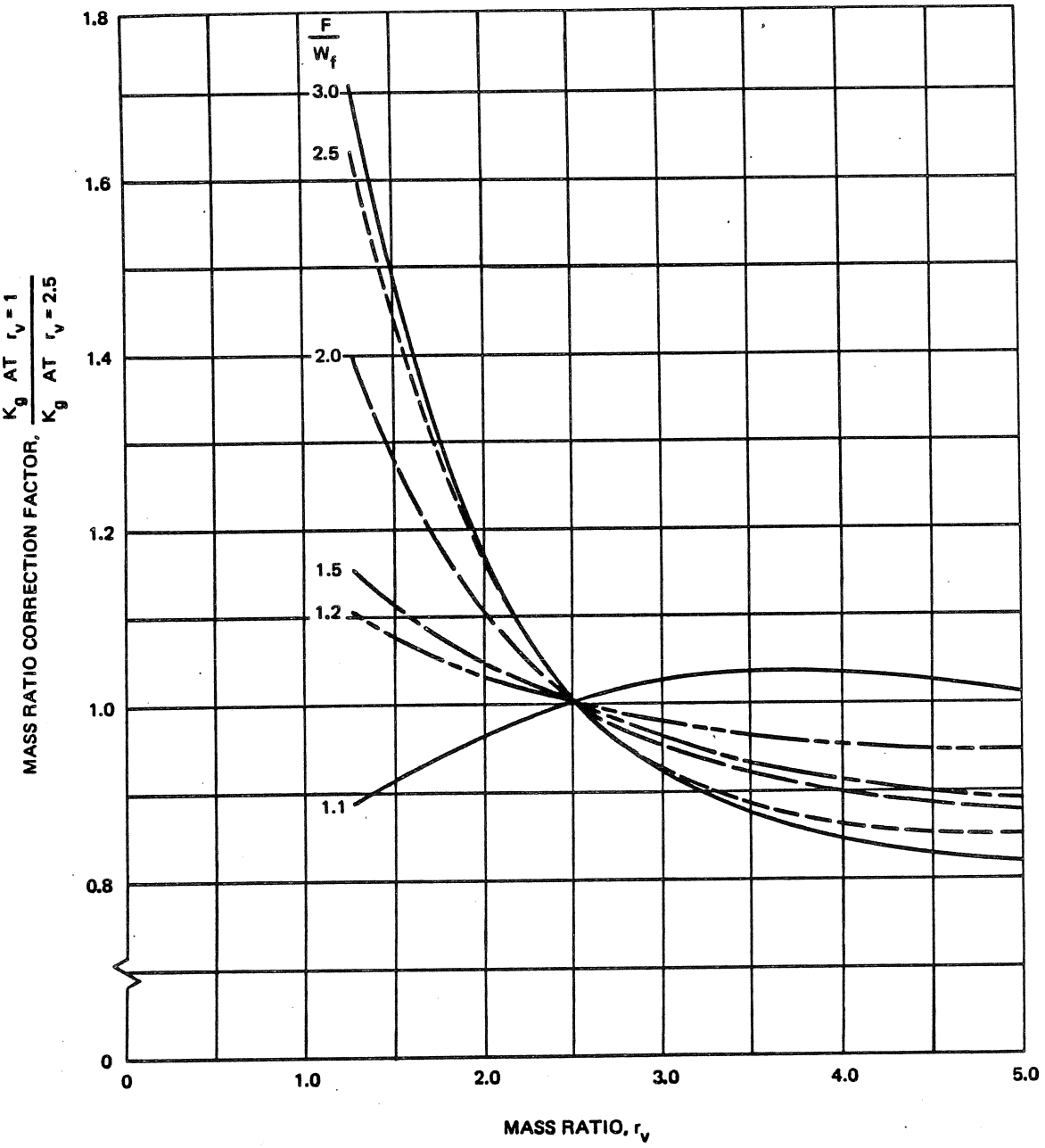

Figure 10-34. First-Stage Mass Ratio Correction Factor

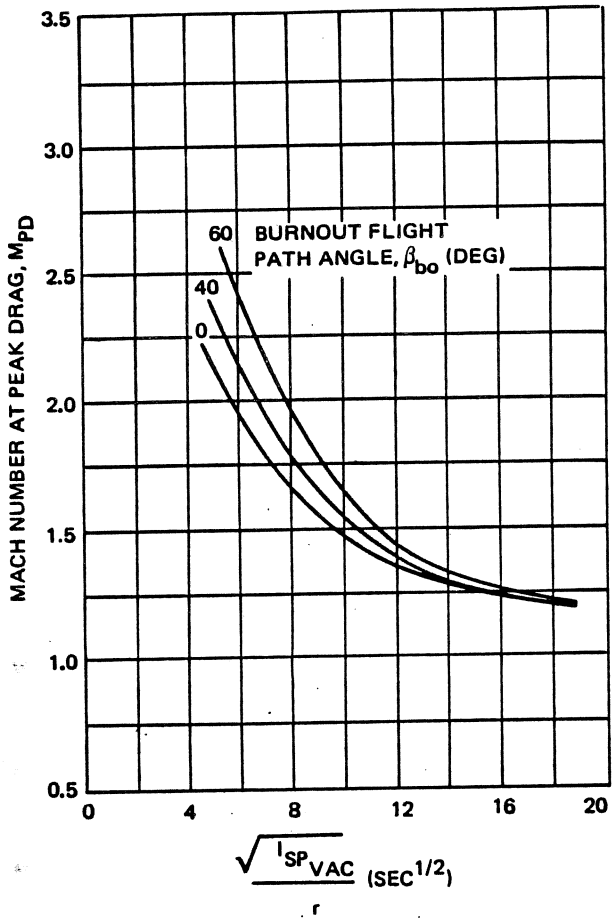

Figure 10-35. First-Stage Mach Number at Peak Drag

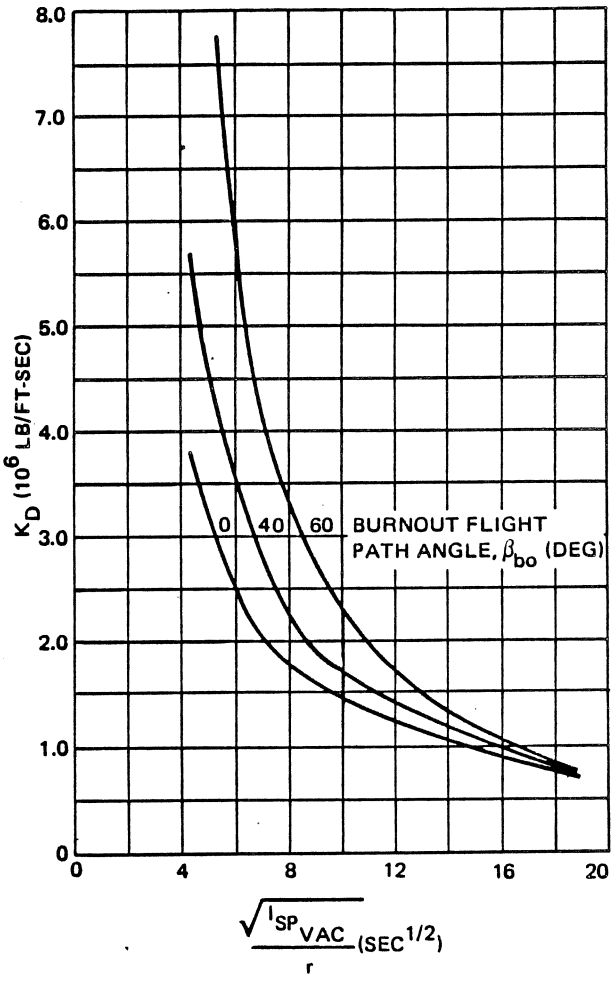

Figure 10-36. First-Stage Drag – Loss Constant

5. First-Stage Range at Burnout – The range angle of the vehicle at first-stage burnout, θ_{bo_1}, defined in Figure 10-18, is necessary to completely define the burnout location. Since the range angle at burnout is small for a vehicle's first stage, an empirical method is used for the representation of range angle. Figure 10-39 presents a nomograph in terms of the first-stage parameters from which the value of burnout range angle can be obtained. It is assumed that rotation of the earth during first-stage burning is a negligible effect.

6. Effects of Earth's Rotation – In order to use the following methods for analyzing upper stage performance, it is necessary to transform the first-stage burnout conditions into the inertial (or solar) coordinate system. This requires vectorially adding the rotational velocity of the launch site to the first-stage velocity vector. The magnitude of the rotational velocity in the launch azimuth plane can be determined from Figure 10-69 in Paragraph 10-2.2.5.1 for the launch site location and launch azimuth of interest (refer to Figure 10-7). It should be noted that an eastward launch increases first-stage velocity and a westward launch decreases velocity. Figure 10-40 shows the vector addition procedure to be used in correcting vehicle position, velocity, etc., to inertial coordinates.

   To calculate the values of the inertial velocity, V_{bo_I} and the inertial flight path angle β_{bo_I}, use the following equations:

$$V_{bo_I} = \sqrt{(V_{bo})^2 + (V_{rot})^2 + 2\,(V_{bo})\,(V_{rot})\sin\beta_{bo}} \qquad (57)$$

$$\beta_{bo_I} = \cos^{-1}\left(\frac{\cos\beta_{bo}}{V_{bo_I}}\right) V_{bo} \qquad (58)$$

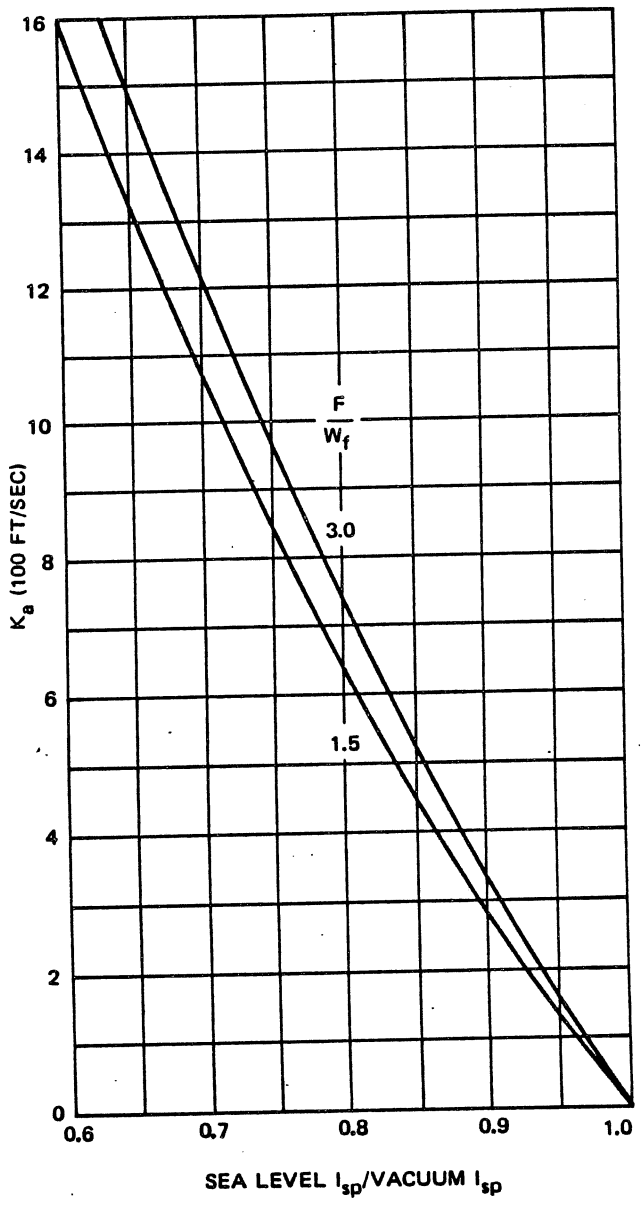

Figure 10-37. First-Stage Thrust Atmospheric Losses

Since the vehicle thrust axis is aligned with the relative velocity vector, V_{bo}, due to the gravity turn, a change in angle of attack, α, results when the transformation is made to inertial coordinates. This change can be evaluated by:

$$\alpha_{bo} = \beta_{bo_I} - \beta_{bo} \tag{59}$$

Angle of attack α, inertial burnout velocity V_{bo_I}, inertial flight path angle at burnout β_{bo_I}, burnout altitude h_{bo}, and the range angle θ_{bo} must be known for the performance analysis of succeeding stages (Figure 10-7).

b. Upper Stage Performance – After calculation of first stage performance for a gravity turn flight within the atmosphere, the performance to low orbit of upper stages in the absence of an atmosphere may be calculated more precisely than by using Equation 49 in the cursory analysis. For this case, it is necessary to specify the initial thrust orientation and initial components of velocity in terms of an inertial rectangular coordinate system, with its vertical axis along the initial local vertical. Thus, where performance is to be computed for more than one stage of a phase of stage operation, the reference axes must in each case be rotated about the center of attraction (the center of the earth) until the vertical axis is the local vertical at that time. Figure 10-41 illustrates schematically the procedure for a typical trajectory profile. It is possible to execute a series of successive evaluations where each separate phase of the analysis provides the initial conditions to succeeding steps. In this way, the time variation of the trajectory elements can be determined for the stages being analyzed.

1. Input Parameters – The input parameters for the calculations include the initial conditions, denoted by subscript i, which are expressed in terms of the initial thrust orientation angle, ϵ_{o_i}, the inertial flight path angle, β_i, and the initial inertial angle of attack, α_i, or,

$$\epsilon_{o_i} = \beta_i - \alpha_i = \epsilon_i - \theta_i \tag{60}$$

The signs of the angles are shown in Figure 10-41. Components of the initial inertial velocity, V_i are:

$$\dot{x}_i = V_i \sin \beta_i \tag{61}$$

$$\dot{y}_i = V_i \cos \beta_i \tag{62}$$

where the initial values are obtained from burnout conditions of the first stage or at the end of a preceding coast period. Parameters which must be specified from stage data are: (1) vacuum specific impulse, $I_{sp_{vac_i}}$, (2) the initial thrust-to-weight ratio, F_{vac}/W_i, (3) the final weight ratio

$$\frac{1}{r_{v_f}} = \frac{W_{final}}{W_{initial}} = \frac{W_{bo_n}}{W_{f_n}} \tag{63}$$

(4) the average radius r^*, between r_i and r_f, and (5) the corresponding effective gravity, g^*, force during the trajectory phase, e.g., at the average radius.

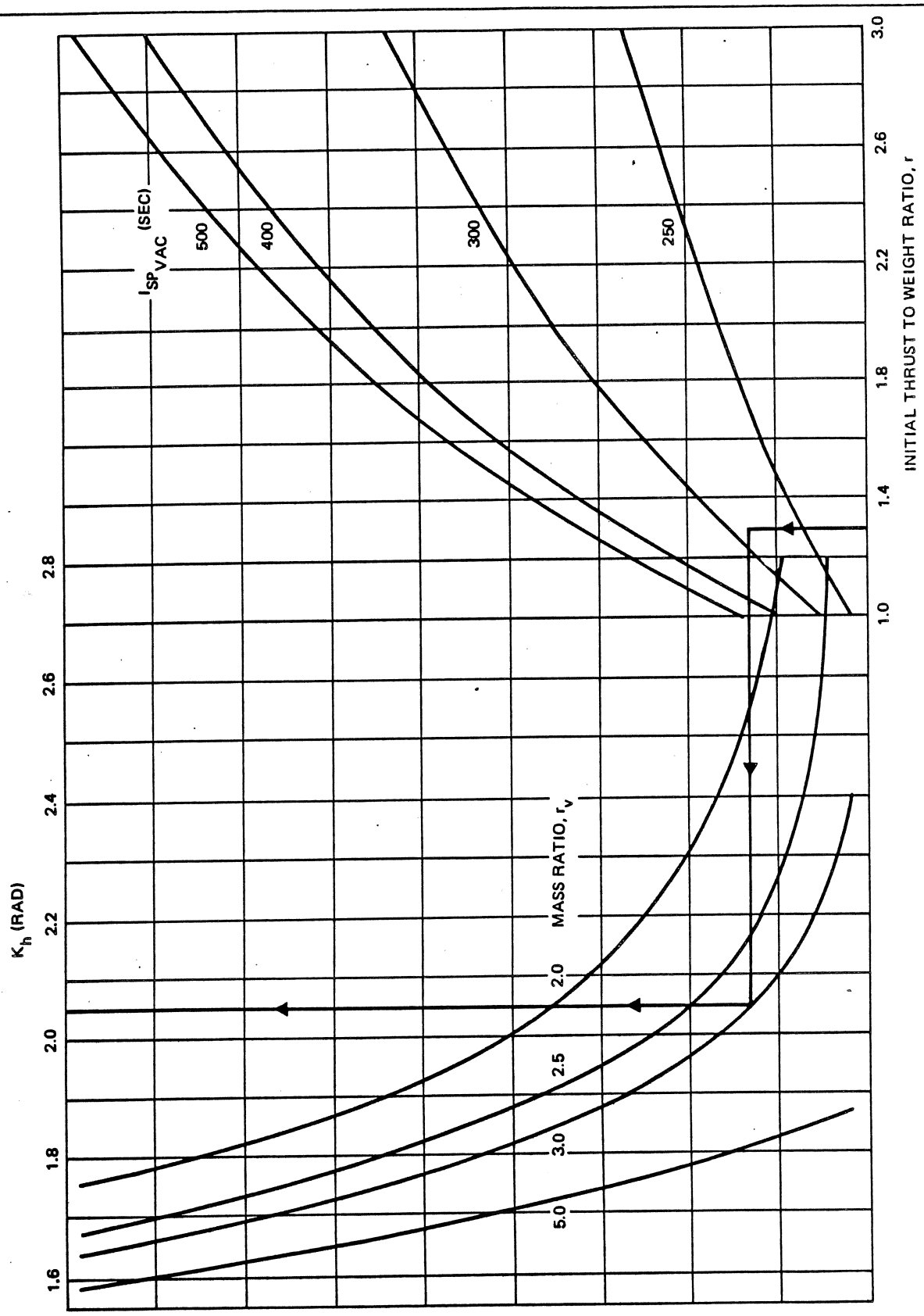

Figure 10-38. First-Stage Burnout Altitude Constant

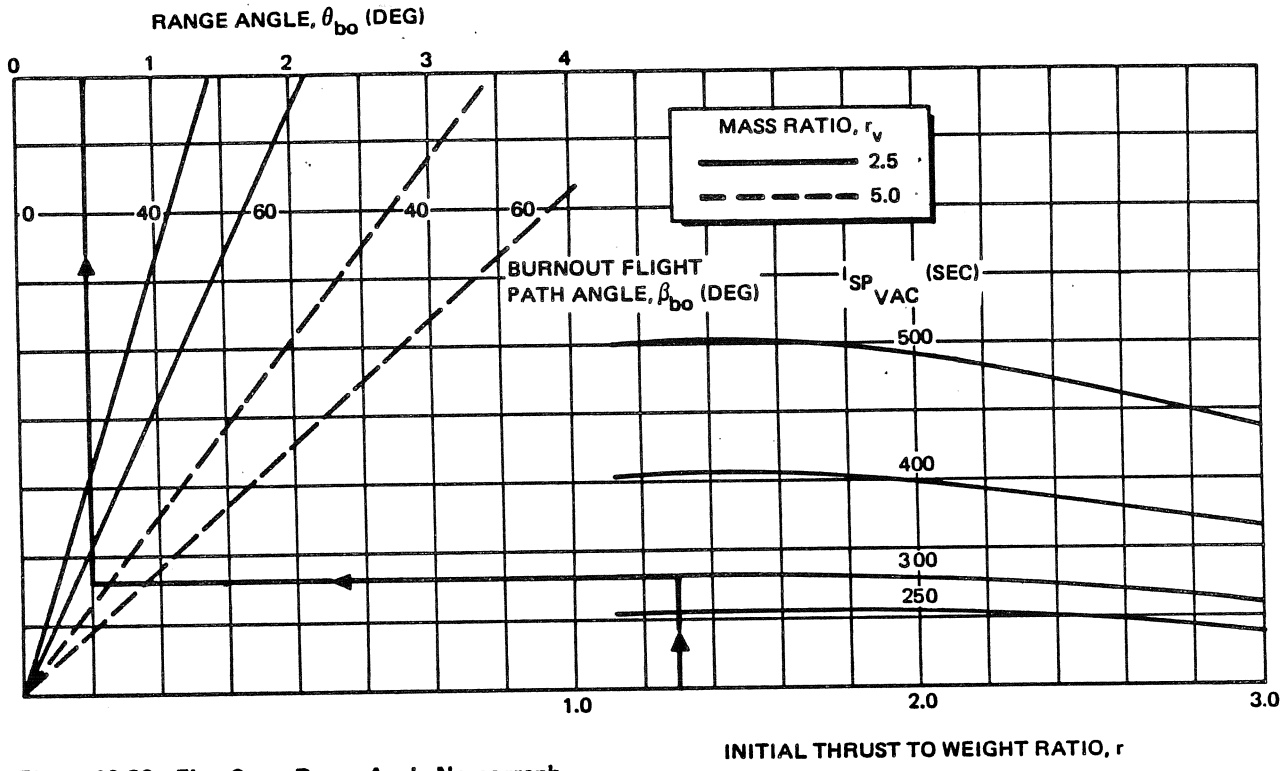

Figure 10-39. First-Stage Range-Angle Nomograph

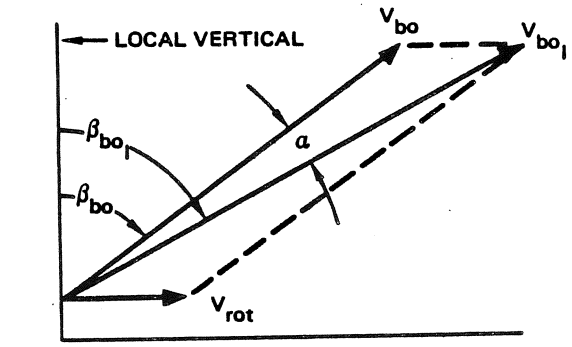

Figure 10-40. Earth Rotational Effect on Launch Velocity

An initial estimate for the constant pitch rate, $\dot{\epsilon}$, must also be given. Generally, the optimal value of $\dot{\epsilon}$ required to achieve the desired final conditions will lie between $\dot{\epsilon} = 0$ and $\dot{\epsilon} = 0.2$ degree per second. For similar performance by the first stages of vehicles, upper stages with relatively high thrust-to-weight ratios tend to have optimal values of $\dot{\epsilon}$ in the upper part of the range, and values of $\dot{\epsilon}$ for those with relatively low thrust-to-weight ratios will be found in the lower part.

With the altitude an initiation, h_i, given, the value of the radial distance from the center of attraction at that time, r_i (i.e., y_i), can be determined. Then a value of the effective radius, r^* may be estimated by the relation

$$r^* = r_i + t_b \left[V_i + g_o I_{sp_{vac}} \left(1 + \frac{\frac{1}{r_{v_f}} \ln \frac{1}{r_{v_f}}}{1 - \frac{1}{r_{v_f}}} \right) - \frac{g_o t_b}{2} \right] K^* \cos \beta_i \qquad (64)$$

where K^* is a constant for a given vehicle following a given trajectory. For typical vehicles and trajectories, approximate values of K^* have been found by use of the empirical relationship

$$K^* \approx \frac{(0.0163) \frac{F_{vac}}{W_i}}{\frac{1}{r_{v_f}} \left[1 - \frac{1}{r_{v_f}} \left(1 - \ln \frac{1}{r_{v_f}} \right) \right]} \qquad (65)$$

based on the assumption that the effective altitude for a period of powered flight motion is that altitude at which the average flight path angle is achieved.

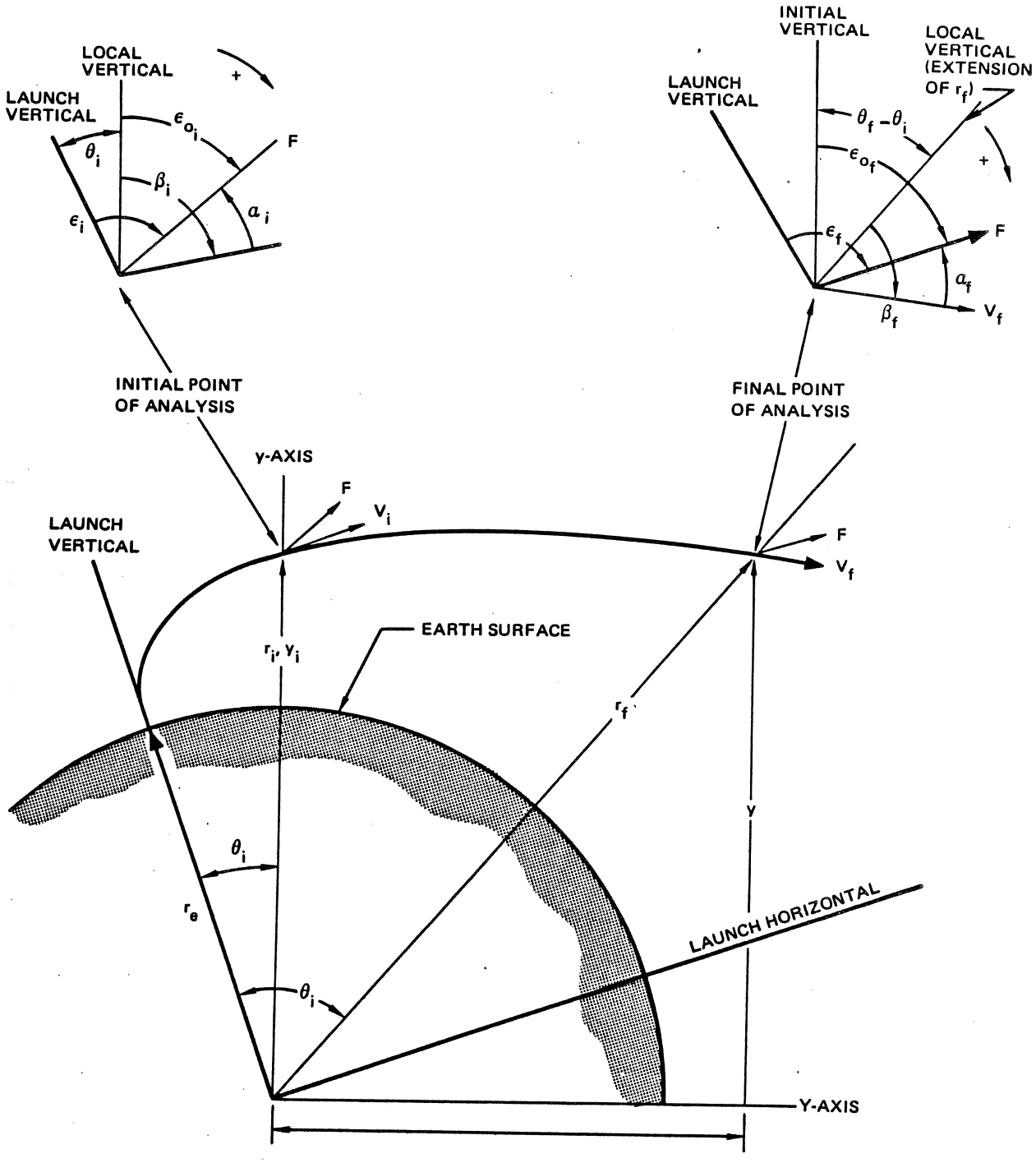

Figure 10-41. Powered Flight Coordinate System

After r^* is computed, the acceleration of gravity at this distance from the attracting body is found by:

$$g^* = g_o \left(\frac{r_e}{r^*}\right)^2 \tag{66}$$

2. Computation of Final Trajectory Parameters – The following definitions are now made:

(a) The effective exhaust velocity is

$$c^* = g_o I_{sp_{vac}} \tag{67}$$

(b) The generalized initial thrust-to-weight ratio is:

$$\eta = \frac{F_{vac}}{W_i} \cdot \frac{g_o}{g^*} \tag{68}$$

where

F_{vac} = Constant;

W_i = the initial weight.

(c) The trust orientation in the new coordinate system is denoted by:

$$\epsilon = \nu + \xi p \tag{69}$$

where

$$\nu = \epsilon_{o_i} + \frac{c^* \epsilon}{\eta g^*}$$

$$\xi = -\frac{c^* \dot{\epsilon}}{\eta g^*} \tag{70}$$

$\dot{\epsilon}$ = rate of change of thrust orientation angle, ϵ

(d) Two constants ζ and χ are defined by:

$$\zeta = \frac{(c^*)^2}{\eta g^*} = \frac{g_o I_{sp}{}^2{}_{vac}}{(F_{vac}/W_i)} \tag{71}$$

and

$$\chi = \frac{\zeta}{c^*}\sqrt{\frac{g^*}{r^*}} = \frac{I_{sp_{vac}}}{(F_{vac}/W_i)}\sqrt{\frac{g^*}{r^*}} \tag{72}$$

Using these new definitions and those given previously, the final retangular components of position and velocity are given at the end of the trajectory phase by the following equations:

$$y = \frac{\zeta}{\chi}\left[\mathrm{Im}(Z) + \frac{v_i}{c^*}\sin\chi\left(1 - \frac{1}{r_{v_f}}\right)\right] + r_i \cos\chi\left(1 - \frac{1}{r_{vf}}\right) \tag{73}$$

$$x = \frac{\zeta}{\chi}\left[\mathrm{Im}\,(\omega) + \frac{\dot{x}_i}{c^*}\sin\chi\left(1 - \frac{1}{r_{vf}}\right)\right] \tag{74}$$

$$\dot{y} = -c^*\left[R(Z) + \frac{r_i \chi}{\zeta}\sin\chi\left(1 - \frac{1}{r_{vf}}\right)\right] + v_i \cos\chi\left(1 - \frac{1}{r_{vf}}\right) \tag{75}$$

$$\dot{x} = -c^* R(\omega) + x_i \cos\chi\left(1 - \frac{1}{r_{vf}}\right) \tag{76}$$

where the following additional definitions hold:

$$\left\{\begin{aligned} \mathrm{Im}(Z) &= A\sin\chi\,\frac{1}{r_{v_f}} - B\cos\chi\,\frac{1}{r_{v_f}} \\ R(Z) &= A\cos\chi\,\frac{1}{r_{v_f}} + B\sin\chi\,\frac{1}{r_{v_f}} \end{aligned}\right\} \tag{77}$$

$$\left\{\begin{aligned} \mathrm{Im}(\omega) &= C\sin\chi\,\frac{1}{r_{v_f}} - D\cos\chi\,\frac{1}{r_{v_f}} \\ R\,(\omega) &= C\cos\chi\,\frac{1}{r_{v_f}} + D\sin\chi\,\frac{1}{r_{v_f}} \end{aligned}\right\} \tag{78}$$

and

$$\begin{aligned} A &= \frac{1}{2}(E\cos\nu - F\sin\nu) \\ B &= \frac{1}{2}(C\sin\nu + H\cos\nu) \\ C &= \frac{1}{2}(E\sin\nu + F\cos\nu) \\ D &= \frac{1}{2}(-G\cos\nu + H\sin\nu) \end{aligned} \tag{79}$$

$$E = \left\{ Ci\left[(\xi+\chi)\frac{1}{r_{v_f}}\right] Ci(\xi+\chi)\right\} + \left\{ Ci\left[(\xi-\chi)\frac{1}{r_{v_f}}\right] - Ci(\xi-\chi)\right\}$$

$$F = \left\{ Si\left[(\xi+\chi)\frac{1}{r_{v_f}}\right] Si(\xi+\chi)\right\} + \left\{ Si\left[(\xi-\chi)\frac{1}{r_{v_f}}\right] - Si(\xi-\chi)\right\}$$

$$G = \left\{ CI\left[(\xi+\chi)\frac{1}{r_{v_f}}\right] Ci(\xi+\chi)\right\} - \left\{ Ci\left[(\xi-\chi)\frac{1}{r_{v_f}}\right] - Ci(\xi-\chi)\right\} \quad (80)$$

$$H = \left\{ Si\left[(\xi+\chi)\frac{1}{r_{v_f}}\right] Si(\xi+\chi)\right\} - \left\{ Si\left[(\xi-\chi)\frac{1}{r_{v_f}}\right] - Si(\xi-\chi)\right\}$$

The functions in Equation 80 are the sine and cosine integrals[27,28,29] which are defined symbolically as:

$$Si(u) = \int_0^u \frac{\sin\sigma}{\sigma}\, d\sigma$$

$$Ci(u) = -\int_u^\infty \frac{\cos\sigma}{\sigma}\, d\sigma \quad (81)$$

where σ is a defined angle for integration, in this case related to ξ and χ.

x Upon finding x, y, $\dot{x}$, and $\dot{y}$ the final values of altitudes, h_f, velocity, V_f, and flight path angle, β_f, are determined by:

$$h_f = \sqrt{x^2+y^2} - y_i + h_i = r_f - r_e \quad (82)$$

$$V_f = \sqrt{\dot{x}^2+\dot{y}^2} \quad (83)$$

$$\beta_f = \cos^{-1}\frac{\dot{x}x+\dot{y}y}{\sqrt{(x^2+y^2)(\dot{x}^2+\dot{y}^2)}} = \cos^{-1}\left(\frac{\dot{x}x+\dot{y}y}{V_f r_f}\right) \quad (84)$$

where $y_i = r_i$ at initiation and $r_i = r_e + h_i$.

The incremental value of range angle traversed by the vehicle during the burning phase under analysis is given by:

$$(\theta_f - \theta_i) = \cos^{-1}(y/r_f) \quad (85)$$

and the true range angle referenced to the launch vertical is

$$\theta_f = \theta_i + \cos^{-1}(y/r_f) \quad (86)$$

where θ_i is the initial range angle.

Given the initial value, ϵ_{oi}, for the thrust attitude referenced to the initial vertical, the final attitude, ϵ, with respect to the same reference is:

$$\epsilon = \epsilon_{o_i} + \dot{\epsilon}\, t_b \quad (87)$$

and the thrust attitude referenced to the launch vertical is:

$$\epsilon_f = \theta_i + \epsilon \quad (88)$$

The final angle of attack is given by:

$$\alpha_f = \beta_f + \theta_f - \epsilon_f \quad (89)$$

with the angles having the algebraic signs indicated in Figure 10-33.

3. Velocity Loss Computation – The velocity losses for the portion of the trajectory under analysis are assumed to be almost wholly composed of losses due to gravity and angle of attack. Therefore, the losses can be found from the relation

$$\Delta V_L = g_o I_{sp_{vac}} \ln\left(\frac{W_i}{W_f}\right) + V_i - V_f \quad (90)$$

4. Iteration on Pitch Rate – If the initial estimate of pitch rate, $\dot{\epsilon}$, used in calculating the performance is too low (in the positive sense), the following deviations from the desired mission requirements will result at termination: (1) the final altitude will be too high; (2) the final flight path angle will be too low; and (3) the final velocity will be too low.

If $\dot{\epsilon}$ is too high, the opposite effect upon these parameters will be observed. In either case, the observation of the effect of $\dot{\epsilon}$ upon these three quantities indicates the direction, and to some degree the magnitude, of the change which is required in $\dot{\epsilon}$ in order that the desired final conditions be achieved. If after adjustment of $\dot{\epsilon}$ in the indicated direction of the results of the second calcuation of parameters do not indicate that this new value is optimal, linear interpolation or short linear extrapolation can be used to closely approximate the optimal value of $\dot{\epsilon}$ to be used in the final iteration. While the relationship between $\dot{\epsilon}$ and the final trajectory parameters is almost linear for small changes in $\dot{\epsilon}$, it may be desirable to obtain a finer approximation for pitch rate; in this case final conditions for three different values of pitch rate can be computed to indicate precisely the value of $\dot{\epsilon}$ which will most nearly achieve the desired orbit conditions simultaneously. Typically, these variations in $\dot{\epsilon}$ will occur within the range mentioned previously, $0 \leq \dot{\epsilon} \leq 0.2$ (although it is possible for vehicles with widely varying characteristics of configuration and powered flight operation to require pitch rates outside this range in accomplishing certain missions).

Although the basic evaluation process is suited to manual computation, the solution of the equations for upper-stage performance evaluation given in this section could be greatly facilitated by the use of a small or medium-sized digital computer. Incorporation of any required iteration processes into the computer program would further simplify the application of the method and reduce the time required for an evaluation.

c. Coasting – In general, there are two reasons for coasting between phases of powered flight. First, a short delay may be necessary to allow reorientation of the vehicle for guidance purposes, completion of the upper-stage ignition cycle, or performance of other similar activities during and after staging. Second, a period of coasting (of varying duration) may be required for achievement for a given mission. Where the period of coasting is relatively short (less than 60 seconds), the changes in trajectory parameters can be approximated by assuming that the vehicle moves along a parabolic arc, with constant acceleration due to gravity. With the conditions at start of coast given as V_1, h_1, β_1, θ_1, α_1, and t_1, and with the time of coasting, t_c, specified, the velocity at the end of the coast period is:

$$V_2 = \sqrt{V_1^2 - 2g_o t_c V_1 \cos\beta_1 + g_o^2 t_c^2} \qquad (91)$$

The expression for altitude is:

$$h_2 = h_1 + t_c V_1 \cos\beta_1 - \frac{1}{2} g_o t_c^2 \qquad (92)$$

The corresponding value of flight path angle is given by:

$$\beta_2 = \tan^{-1}\left(\frac{V_1 \sin\beta_1}{V_1 \cos\beta_1 - g_o t_c}\right) \qquad (93)$$

The range angle at the end of coasting in degrees is:

$$\theta_2 = \theta_1 + \left(\frac{180}{\pi}\right)\frac{t_c V_1 \sin\beta_1}{r_1} \qquad (94)$$

where $r_1 = h_1 + r_e$, and r_e is the radius of earth.

The vehicle angle of attack at the end of coasting, assuming a pitch rate, $\dot{\epsilon}_c$, during coast, is:

$$\alpha_2 = \alpha_1 + (\beta_2 - \beta_1) + (\theta_2 - \theta_1) - \dot{\epsilon}_c t_c \qquad (95)$$

where β_2 and θ_2 are obtained from Equations 93 and 94 respectively.

If the vehicle thrust axis pitches at the same rate as the velocity vector, the angle of attack will remain constant during coast. The vehicle attitude at the end of coast, with respect to the launch vertical, is:

$$\epsilon_2 = \beta_2 + \theta_2 - \alpha_2 \qquad (96)$$

d. Performance Evaluation for a Midcourse Correction – The evaluation of performance for a midcourse correction during the coast phase of a lunar or interplanetary trajectory can be calculated assuming ideal conditions; that is, no velocity losses are encountered during the midcourse burning phase. The increment in velocity added during the midcourse correction is given by Equation 19.

In most cases, the midcourse velocity increment will be added at some angle with respect to the inertial velocity vector. This changes not only the magnitude of the velocity but also its direction. Thus the increment in velocity must be vectorially added to the inertial velocity vector to determine the total change due to the midcourse correction.

10-2.2.1.5 Example of Approximate Performance Estimations

In order to relate the methods for performance estimation, an example two-stage liquid-propellant vehicle is analyzed in the following section for a 100 nautical mile circular earth orbit mission. The analysis follows the basic precise performance evaluation method.

a. Vehicle Parameters — The given first and second stage vehicles parameters are defined in Table 10-11.

b. Determination of First-Stage β_{bo} — Referring to Figure 10-20, the time of vertical rise is found to be 12.8 seconds for $F/W_f = 1.3$. There is no adjustment required for the initial thrust-to-weight ratio because a liquid propellant vehicle has essentially constant thrust when flown at a constant altitude. Since a low orbit mission is of interest, the ratio β_{bo}/t_v may be determined from Figure 10-19. With the first-stage mass ratio of 3.06, the lower portion of the shaded area of Figure 10-19 is used to obtain $\beta_{bo}/t_v = 0.045$ deg/sec, which gives a $\beta_{bo} = 0.57$ degree for $t_v = 12.8$ seconds. The burnout angle obtained from Figure 10-21 for this, β_o, with the first stage Isp_{vac} and F/W_f is 60 degrees.

c. Determination of First Stage Burnout Velocity — The following considerations are applicable:

1. Gravity Loss — The first stage gravity loss is found by solving Equation 53.

$$\Delta V_{L_{g_1}} = (g_o t_b - K_{gg}) \left[1 - K_g \left(1 - \frac{1}{r_{v_1}}\right) \left(\frac{\beta_{bo}}{90^\circ}\right)^2\right] \quad (53)$$

Table 10-11. First and Second Stage Vehicle Parameters

Vehicle Parameter	First Stage	Second Stage
$r = F/W_f$	1.30	0.9205 vac
$I_{sp_{vac}}$ sec	295	425
$\frac{I_{sp_{s1}}}{I_{sp_{vac}}} = X$	0.88	.088
W_f lb	2,309,000	754,000
$W_f/W_{bo} = r_v$	3.06	4.136
t_b sec	133.6	350.07
C_D vs M	Fig. 10-2.30(1)	0 (vac)
Launch	ARM	N.A(2)
Launch Azimuth — deg	110	N A

(1) The drag curve for the vehicle must be supplied from test data, by similarity, or assumed.

(2) N.A — Not applicable.

where K_g and K_{gg} are determined from the data on Figure 10-32 and 10-31, respectively. K_{gg} solely a function of Isp_{vac} is found to be 20 feet per second. K_g, determined from Figure 10-32, represents a mass ratio of 2.5, which requires a correction factor obtained from Figure 10-34 that is used to obtain the proper value for a mass ratio of 3.06.

$$K_{g_{(3.06)}} = (\text{correction factor}) \cdot K_{g_{(2.5)}}$$
$$= (0.97)(0.61)$$
$$= (0.59).$$

Therefore, solving Equation 53 with the above values of K_g, K_{gg}, vehicle parameters, and calculated $\beta_{bo} = 60$ degrees gives:

$\Delta V_{L_g} = 3520$ feet per second.

2. Drag Loss — The drag loss is as defined by Equation 54.

$$\Delta V_{L_{D_1}} = K_D \frac{C_{D_{PD}} A}{W_{f_1}} \quad (54)$$

requires the knowledge of the drag coefficient at maximum drag force, $C_{D_{PD}}$, during the trajectory. This is determined by first finding the Mach number at maximum drag, M_{PD}, from Figure 10-35. M_{PD} depends on β_{bo} and the ratio $\sqrt{Isp_{vac}} / F/W_f$. For

$$\frac{\sqrt{I_{sp_{vac}}}}{\frac{F}{W_f}} = 13.22 \text{ and } \beta_{bo} = 60 \text{ degrees},$$
$$M_{PD} = 1.38$$

Referring to the C_D versus M variation (Figure 10-42, it is seen that the $C_{D_{PD}} = 0.62$. Thus the drag loss is:

$$\Delta V_{L_D} = K_D \frac{(0.62)\,452}{2.309 \times 10^6} = K_D\,(121.5 \times 10^{-6})$$

where $K_D = 1.44 \times 10^6$ as obtained from Figure 10-36. Performing the multiplication gives:

$\Delta V_{L_D} = 175$ ft/sec.

3. Thrust-Atmospheric Effects — The thrust-atmospheric effects are simply obtained

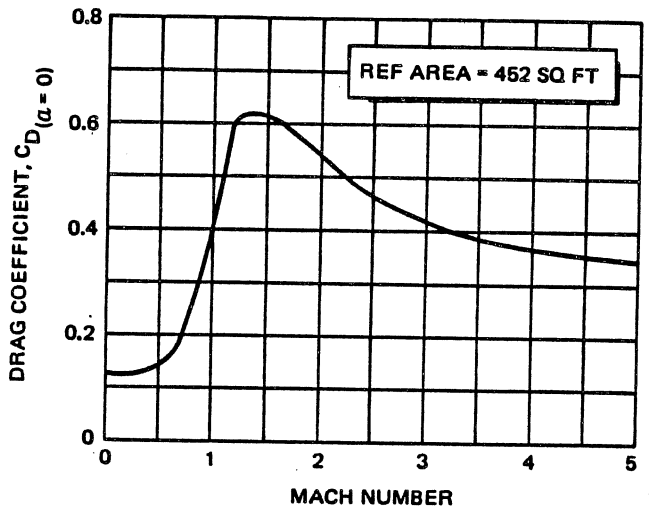

Figure 10-42. Drag Curve

from Figure 10-37 for a value of $I_{sp_{sl}}/I_{sp_{vac}}$ = 0.881. The results is:

$$\Delta V_{L_T} = K_a = 330 \text{ ft/sec.}$$

The first-stage burnout velocity as defined by Equation 32

$$\Delta V = \Delta V_I - \Delta V_L = V_{bo} \qquad (32)$$

where

$$\Delta V_I = g_o I_{sp_{vac}} \ln \left(\frac{W_f}{W_{bo}}\right) \qquad (19)$$

and

$$\Delta V_L = \Delta V_{L_g} + \Delta V_{L_D} + \Delta V_{L_F} \qquad (52)$$

For the stage being analyzed:

$$\Delta V_I = g_o (295) \ln 3.06 = 10{,}610 \text{ ft/sec}$$

The relative (to earth) burnout velocity is:

$$\Delta_{bo_1} = \Delta V_I = 10{,}610 - 3520 - 175 - 330$$

$$= 6{,}585 \text{ ft/sec}$$

for relative burnout angle, β_{bo_1}, of 60.0 degrees.

d. Determination of First-Stage Burnout Altitude – The expression for h_{bo_1} involves h_{bo}, the burnout altitude for nonatmospheric vertical ascent.

$$h_{bo} = g_o I_{sp_{vac}} t_b \left(1 - \frac{\ln \frac{W_f}{W_{bo}}}{\frac{W_f}{W_{bo}} - 1}\right) - \frac{g t_b^2}{2} + V_o t_b + h_o \qquad (35)$$

which gives a value of h_{bo} = 291,500 feet for the first stage of interest ($V_o + h_o = 0$). The expression for the first stage burnout altitude is

$$h_{bo_1} = \left[h_{bo} - \frac{\left(\Delta V_{L_{D_1}} + \Delta V_{L_{F_1}}\right)}{2} t_{b_1}\right] \left[1 - \left(\frac{\beta_{bo_1}}{K_h}\right)^2\right] \qquad (56)$$

where the drag and thrust-atmospheric losses are 175 and 330 feet per second, respectively. K_h is the empirical constant obtained from Figure 10-38:

$$K_h = 2.05 \text{ radians}$$

Evaluation of h_{bo_1} gives

$$h_{bo_1} = \left[291{,}500 - \frac{(505)(133.6)}{2}\right] \left[1 - \left(\frac{60}{(2.05)(57.3)}\right)^2\right] = 187{,}000 \text{ ft.}$$

e. Determination of Range Angle and Vehicle Attitude at First-Stage Burnout – It is of interest to determine the range angle from the launch site to first stage burnout θ_{bo_1}, in order to obtain the angular position of the vehicle centerline with respect to the launch vertical. This value can be determined from the nomograph of Figure 10-39 which gives θ_{bo_1} = 0.5 degrees. The vehicle attitude with respect to the launch vertical is

$$\epsilon_{bo_1} = \beta_{bo_1} + \theta_{bo_1} = 60.5 \text{ degrees}$$

(Figure 10-17 and 10-41, refer to Paragraph 10-2.68).

f. Determination of Earth's Rotational Effects – As previously pointed out, it is necessary to vectorially add the launch azimuth component of the launch site rotational velocity to the first-stage burnout conditions. For a 110-degree launch from AMR (equivalent to 70 degree launch azimuth), the component of velocity, V_{rot}, is 1,262 feet per

second as determined from Figure 10-69, Para. 10-2.2.5.1. The inertial burnout velocity, V_{bo_I}, is shown by:

$$V_{bo_I} = \sqrt{(V_{bo_I})^2 + (V_{rot})^2 + 2\,(V_{bo_I})(V_{rot}) \sin \beta_{bo_I}} \quad (57)$$

which gives V_{bo_I} = 7,703 ft per second.

The inertial burnout angle,

$$\beta_{bo_I} = \cos^{-1}\left(\frac{\cos \beta_{bo_I}}{V_{bo_I}} V_{bo_I}\right) \quad (58)$$

which gives β_{bo_I} = 64.7 degrees.

Since the velocity vector has been rotated, the vehicle centerline has the following inertial angle of attack:

$$\alpha = \beta_{bo_I} - \beta_{bo_I} = 4.7 \text{ degrees} \quad (59)$$

No coast phase was assumed for this example so that the second-stage calculations follow directly.

g. Determination of Second-Stage Burnout Conditions — Assuming that the second stage trajectory is essentially nonatmospheric, the stage burnout conditions can be computed by the method described previously. The first-stage inertial burnout conditions required for computation of the final condtions at second-stage burnout are summarized in Table 10-12.

For the purpose of computation it is assumed that these values, as well as those of other input parameters, are exact, as the accuracy of results depends upon the maintenance of several significant digits throughout.

Table 10-12. Input Parameters From Results for Stage 1

	Symbols			
Parameters	1st Stage Burnout		2nd Stage Initial Conditions	Numerical Value
Inertial Flight Path Angle (degrees)	β_{bo_1}	=	β_i	64.7
Inertial Velocity (ft/sec)	V_{bo_1}	=	V_i	7703
Inertial Angle of Attack (degrees)	α_{bo_1}	=	α_i	4.7
Altitude (feet)	h_{bo_1}	=	h_i	187,000
Range Angle (degrees)	θ_{bo_1}	=	θ_i	0.50

h. Input Parameters — By use of initial conditions in Table 10-12, the initial thrust orientation angle and initial components of velocity can be found. The thrust orientation angle (referenced to the local vertical at the time of second-stage ignition) is:

$$\epsilon_{o_i} = \beta_i - \alpha_i$$
$$= 64.7^\circ - 4.7^\circ$$
$$= 60.0^\circ \quad (60)$$

The initial inertial velocity components are:

$$\dot{x}_i = V_i \sin \beta_i$$
$$= (7{,}703 \text{ ft/sec}) \sin (64.7^\circ)$$
$$= 6{,}964.2 \text{ ft/sec} \quad (61)$$

$$y_i = V_i \cos \beta_i$$
$$= (7{,}703 \text{ ft/sec}) \cos (64.7^\circ)$$
$$= 3{,}291.9 \text{ ft/sec.} \quad (62)$$

The second stage characteristics are given in Table 10-11.

Since the second stage thrust-to-weight ratio, F_{vac}/W_i, does not differ markedly from the norm for similar stages and conditions, it is assumed that the desired value of pitch rate, $\dot{\epsilon}$, lies near the middle of the range $0 \leq \dot{\epsilon} \leq 0.2$ degree/second. Therefore, during second stage burning it is assumed:

$$\dot{\epsilon} = 0.10 \text{ deg/sec.}$$

The altitude at second stage ignition is h_i = 187,000 feet, and the radial distance from the center of the earth at that time is

$$r_i = r_e + h_i$$
$$= 20{,}902{,}900 \text{ ft} + 187{,}000 \text{ ft}$$
$$= 21{,}089{,}900 \text{ ft}$$

where r_e is the mean radius of the earth.

The effective radial distance during burning is estimated from:

$$r^* = r_i + t_b \left[V_i + g_o I_{sp_{vac}} \left(\frac{1 + \frac{1}{r_{vf}} \ln \frac{1}{r_{vf}}}{1 - \frac{1}{r_{vf}}} \right) - \frac{g_o t_b}{2} \right]$$

$$K^* \cos \beta_i \quad (64)$$

where

$$K^* = \frac{(0.0163)\,\frac{F_{vac}}{W_i}}{\frac{1}{r_{vf}}\left[1-\frac{1}{r_{vf}}\left(1-\ln\frac{1}{r_{vf}}\right)\right]} \qquad (65)$$

the approximate value of the constant K^* is found to be $K^* = 0.150$ and the gravitational acceleration at the earth's surface, g_o, is taken as 32.174 ft/sec^2. Using the values of:

t_b = 350.07 sec

$I_{sp_{vac}}$ = 425 sec

$\frac{1}{r_{vf}}$ = 0.2418

β_i = 64.7 deg

V_i = 7,703 ft/sec

r_i = 21,089,900 ft

which were given or computed previously,

r^* = 21,304,320 ft

The acceleration of gravity at a distance of r^* from the earth's center is:

$$g^* = g_o\left(\frac{r_e}{r^*}\right)^2 \qquad (66)$$

$$= (32,174)\left(\frac{20,902,900}{21,304,320}\right)^2 \text{ ft/sec}^2$$

$$= 30.9730 \text{ ft/sec}^2$$

The effective exhaust velocity is:

$$c^* = g_o I_{sp_{vac}} \qquad (67)$$

$$= (32.174)\,(425) \text{ ft/sec}$$

$$= 13,674 \text{ ft/sec}$$

and the generalized thrust-to-weight ratio

$$\eta = \left(\frac{F_{vac}}{W_i}\right)\left(\frac{g_o}{g^*}\right) = (0.9205)\,\frac{32.174}{30.9730} \qquad (68)$$

$$= 0.95619$$

The thrust orientation referenced to the inital local vertical is given by:

$$\epsilon = \nu + \xi P \qquad (69)$$

and the components ν and ξ are (with $\dot{\epsilon} = 0.010$):

$$\nu = \epsilon_{oi} + \frac{c^*\dot{\epsilon}}{\eta g^*} \qquad (70)$$

$$= (60.0 + 46.1707) \text{ degrees}$$

$$= 1.85303 \text{ radians}$$

$$\xi = \frac{c^*\dot{\epsilon}}{\eta g^*} = 0.80583 \text{ radian.}$$

The constants ζ and χ are:

$$\zeta = \frac{(c^*)^2}{\eta g^*} = (6.31334)\,(10^6) \text{ ft} \qquad (71)$$

$$\chi = \frac{\zeta}{c^*}\sqrt{\frac{g^*}{r^*}} = 0.55670 \text{ radian.} \qquad (72)$$

It is now desired to find the quantities E, F, G, and H of Equation 80. The evaluation of the sine and cosine integrals involved can be made through use of existing books of tables. The most extensive tables of sine and cosine integrals are those published or sponsored by the National Bureau of Standards[27,28,29] and these are utilized here. The function arguments and function values required in the equations are given in Table 10-13. In general, it is true that the symbolic relation

$$Si(-u) = -Si(u)$$

holds for negative arguments. For real values of the argument only, the following symbolic relationship also holds true:

$$Ci(-u) = Ci(u)$$

Use of the results of Table 10-13 in Equation 80 gives:

$$E = \left\{Ci\left[(\xi+\chi)\frac{1}{r_{v_f}}\right] - Ci\,(\xi+\chi)\right\} + \left\{Ci\left[(\xi-\chi)\frac{1}{r_{v_f}}\right] - Ci\,(\xi-\chi)\right\}$$

$$= -2.42207$$

Table 10-13. Tabular Values of the Sine and Cosine Integrals

Function Argument u		Cosine Integral Ci(u)	Sine Integral Si(u)
$(\xi + \chi)$	$= -0.24913$	−0.82805	−0.24827
$(\xi + \chi)\frac{1}{r_{vf}}$	$= -0.06024$	−2.23313	−0.06023
$(\xi - \chi)$	$= -1.36253$	+0.45689	−1.22959
$(\xi - \chi)\frac{1}{r_{vf}}$	$= -0.32946$	−0.56011	−0.32748

$$F = \left\{ Si\left[(\xi+\chi)\frac{1}{r_{v_f}}\right] - Si(\xi+\chi)\right\} + \left\{ Si\left[(\xi-\chi)\frac{1}{r_{v_f}}\right] - Si(\xi-\chi)\right\} = +1.09015$$

$$G = \left\{ Ci\left[(\xi+\chi)\frac{1}{r_{v_f}}\right] - Ci(\xi+\chi)\right\} - \left\{ Ci\left[(\xi-\chi)\frac{1}{r_{v_f}}\right] - Ci(\xi-\chi)\right\} = -0.38807$$

$$H = \left\{ Si\left[(\xi+\chi)\frac{1}{r_{v_f}}\right] - Si(\xi+\chi)\right\} - \left\{ Si\left[(\xi-\chi)\frac{1}{r_{v_f}}\right] - Si(\xi-\chi)\right\} = -0.71406$$

The quantities A, B, C, and D are calcuated with $\nu = 1.85303$. The values are

$$A = 1/2\,(E\cos\nu - F\sin\nu) = -0.18624$$
$$B = 1/2\,(G\sin\nu + H\cos\nu) = -0.8693 \qquad (79)$$
$$C = 1/2\,(E\sin\nu + F\cos\nu) = -1.31493$$
$$D = 1/2\,(-G\cos\nu + F\cos\nu) = -0.39695$$

for $\cos\nu = -0.27850$ and $\sin\nu = +0.96044$. The values of A, B, C, and D are in turn used to calcuate the quantities Im (Z), R(Z), Im(ω) and R(ω). The value of:

$\frac{1}{r_{vf}}$ is found to be 0.13461 and $\sin\chi\frac{1}{r_{vf}}$ is found to be 0.13461 and $\sin\chi\frac{1}{r_{vf}} = 0.13420$, $\cos\chi\frac{1}{r_{vf}} = 0.99095$.

$$Im(Z) = A\sin\chi\frac{1}{r_{vf}} - B\cos\chi\frac{1}{r_{vf}} = +0.06115 \qquad (77)$$
$$R(Z) = A\cos\chi\frac{1}{r_{vf}} + B\sin\chi\frac{1}{r_{vf}} = -0.19622$$

$$Im(\omega) = C\sin\chi\frac{1}{r_{vf}} - D\cos\chi\frac{1}{r_{vf}} = +0.21689 \qquad (78)$$
$$R(\omega) = C\cos\chi\frac{1}{r_{vf}} + D\sin\chi\frac{1}{r_{vf}} = 1.35630$$

The rectangular coordinates of the second stage burnout position are given by Equations 73 and 74. The angle

$\chi\left(1-\frac{1}{r_{vf}}\right) = 0.42209$ and $\cos\chi\left(1-\frac{1}{r_{vf}}\right) = +0.91223$ and $\sin\chi\left(1-\frac{1}{r_{vf}}\right) = +0.40967$, where ξ, χ, r_i, $\dot{y}$, $\dot{x}$, and c^* have the values computed previously.

$$y = \frac{\zeta}{\chi}\left[Im(Z) + \frac{\dot{y}_i}{c^*}\sin\chi\left(1-\frac{1}{r_{vf}}\right)\right] + r_i\cos\chi\left(1-\frac{1}{r_{vf}}\right) = 21{,}050{,}860 \text{ ft} \qquad (73)$$

$$x = \frac{\zeta}{\chi}\left[Im(\omega) + \frac{\dot{x}_i}{c^*}\sin\chi\left(1-\frac{1}{r_{vf}}\right)\right] = 4{,}825{,}780 \text{ ft} \qquad (74)$$

The velocity components at second stage burnout are:

$$\dot{y} = -c^*\left[R(Z) + \frac{r_i\chi}{\zeta}\sin\chi\left(1-\frac{1}{r_{vf}}\right)\right] + \dot{y}_i\cos\chi\left(1-\frac{1}{r_{vf}}\right) = -4731 \text{ ft/sec} \qquad (75)$$

$$\dot{x} = -c^* R(\omega) + \dot{x}_i\cos\chi\left(1-\frac{1}{r_{vf}}\right) = 25{,}345 \text{ ft/sec} \qquad (76)$$

Using the computed values of x, y, $\dot{x}$, and $\dot{y}$, the values of the second stage altitude, h_f, burnout velocity V_f, and burout flight path angle, β_f, are calculated:

$$h_f = \sqrt{x^2+y^2} - y_i + h_i = r_f - r_e = 21{,}596{,}910 \text{ feet} - 20{,}902{,}900 \text{ feet} = 694{,}010 \text{ feet} \qquad (82)$$

$$V_f = \sqrt{\dot{x}^2+\dot{y}^2} = 25{,}345 \text{ ft/sec} \qquad (83)$$

$$\beta_f = \cos^{-1}\left(\frac{x\dot{x}+y\dot{y}}{\sqrt{(x^2+y^2)(\dot{x}^2+\dot{y}^2)}}\right) = \cos^{-1}(0.03756) = 87.85 \text{ degrees} \qquad (84)$$

It is now possible to examine whether the assumed value of pitch rate, $\dot{\epsilon}$, can be changed in such a manner that the final conditions will more nearly approximate the parameters required for achievement of the desired orbit. The corresponding parameters for a 100 nautical mile circular earth orbit are approximately:

h_c = 607,610 feet

V_c = 25,581 ft/sec

β_c = 90.00 degrees (or γ_c = 0 degrees)

By comparison, it is evident that the computed value of burnout altitude is too high, and the values for burnout velocity and flight path angle are too low.

Reference to the criteria given leads to the conclusion that the initial value of $\dot{\epsilon}$ = 0.10 deg/sec is too low. However, the parameters obtained through use of this value are sufficiently close to orbital condtions to establish that $\dot{\epsilon}$ is only slightly different from 0.10 deg/sec. Therefore, it is assumed that the difference in pitch rate is $\Delta\dot{\epsilon}$ = +0.01 deg/sec and that the new value of pitch rate is $\dot{\epsilon}$ = 0.11.

Upon recalculating the components of burnout position and velocity with the new value of $\dot{\epsilon}$ = 0.11 and with the other input parameters unchanged, the following results are found:

y = 20,987,940 feet (73)

x = 4,835,850 feet (74)

$\dot{y}$ = 5,446 ft/sec (75)

$\dot{x}$ = 24,930 ft/sec (76)

The new burnout element calculated from these values are:

h_f = 634,950 feet (82)

V_f = 25,517 ft/sec (83)

β_f = 89.35 degrees (or γ_f = 0.65 degrees) (84)

Comparison of the new computer trajectory parameters to the desired conditions indicates, in the same manner as before, that the pitch rate is still too low. This fact is further illustrated by Figure 10-43.

The values of $\beta_f(\gamma_f)$, V_f, and h_f obtained by using the first estimates of $\dot{\epsilon}$ = 0.10 and $\dot{\epsilon}$ = 0.11 can be used to find a final value of $\dot{\epsilon}$ which will most nearly satisfy the most critical condition or conditions. By

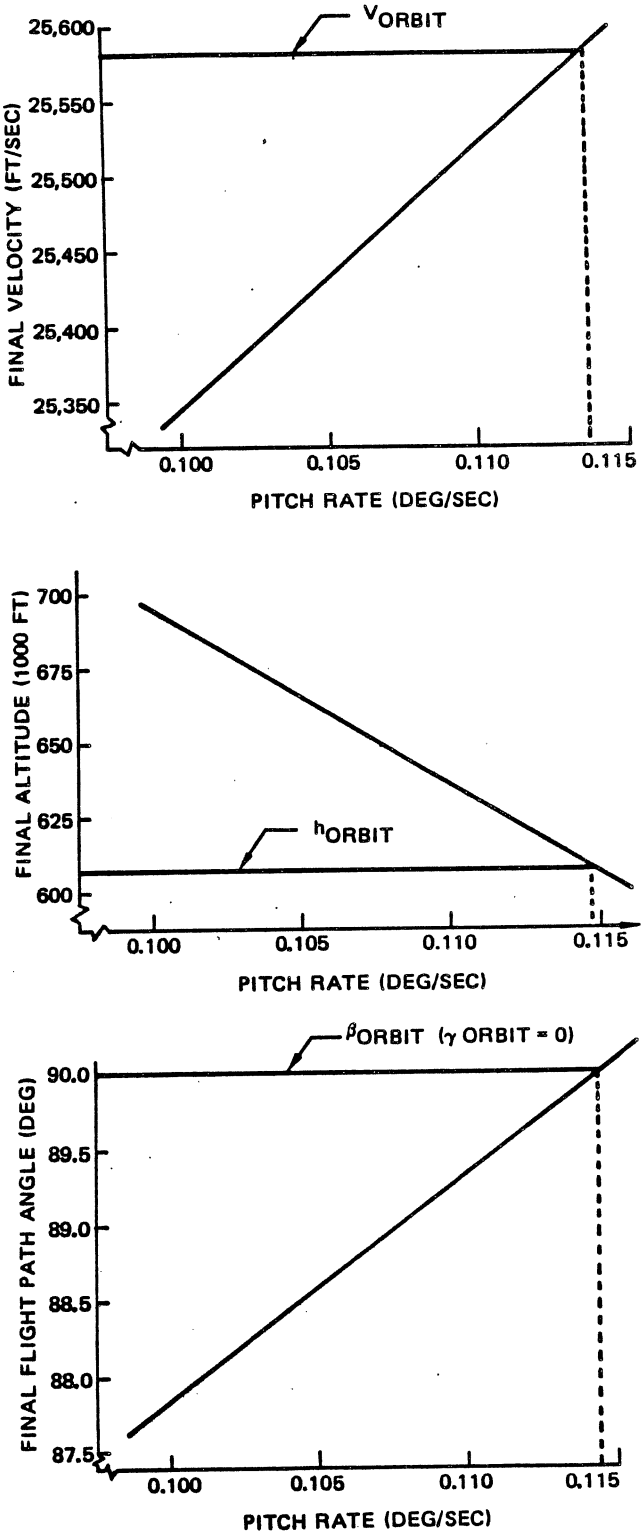

Figure 10-43. Effect of Pitch Rate Iteration

linear extrapolation a value of ϵ can be obtained for each of the three parameters which will result in achievement of that parameter within the error incurred by linear extrapolation. The inability to achieve all orbital conditions simultaneously is largely a result of input inaccuracies from the first-stage analysis, which could be rectified to some extent by iteration upon the flight path angle at first-stage burnout.

In order to provide an idea of the accuracy which can be obtained for this particular case without recourse to iteration upon the first-stage burnout angle, a value of pitch rate is chosen by linearly extrapolating to value $\epsilon = 0.1143$, which will give approximately the desired value of flight path angle (the true relationship between flight path angle and pitch rate is almost linear). Also, this value is intermediate between the extremes of $\epsilon = 0.1137$ (required to achieve the desired velocity) and $\epsilon = 0.1146$ (required to achieve the desired altitude). The results obtained by the same computational procedure followed previously are:

$$y = 20{,}960{,}700 \text{ ft} \quad (73)$$

$$x = 4{,}839{,}700 \text{ ft} \quad (74)$$

$$\dot{y} = -5755 \text{ ft/sec} \quad (75)$$

$$\dot{x} = 24{,}934 \text{ ft/sec} \quad (76)$$

which in turn are used to compute the final parameters. These are given in Table 10-14 together with a summary of the values of the burnout trajectory elements computed for the other values of pitch rate.

The true range angle is

$$\theta_f = \theta_i + \cos^{-1}(y/r_f)$$

$$= \theta_i + \cos^{-1}\left(\frac{y}{\sqrt{x^2+y^2}}\right) \quad (86)$$

$$= 0.50 + 13.05 \text{ degrees} = 13.55 \text{ degrees}$$

Table 10-14. Comparison of Computed Trajectory Parameters

Pitch Rate, ϵ (deg/sec)	Altitude, h_f (ft)	Velocity, V_f (ft/sec)	Flight Path Angle, β_f (deg)
0.10	694,010	25,345	87.85
0.11	634,950	25,517	89.35
0.1143	609,220	25,589	89.99
Burnout elements for 100 nmi circular orbit	607,610	25,581	90.00

for

$$\dot{\epsilon} = 0.1143$$

The thrust orientation angle at second stage burnout is:

$$\epsilon = \epsilon_{o_i} + \dot{\epsilon} t_b$$

$$= 60.0 \text{ degrees} + (0.1143 \text{ deg/sec})(350.07 \text{ sec})$$

$$= 100.01 \text{ degrees} \quad (87)$$

where ϵ is referenced to the local vertical at the time of second-stage ignition. The thrust attitude referenced to the launch vertical is:

$$\epsilon_f = \theta_i + \epsilon = 0.50 + 100.1 \text{ degrees}$$

$$= 100.51 \text{ degrees} \quad (88)$$

The final angle of attack is computed by:

$$\alpha_f = \beta_f + \epsilon_f$$

$$= 89.99 + 13.55 - 100.51 \text{ degrees}$$

$$= 3.53 \text{ degrees} \quad (89)$$

Velocity losses for second stage are given by the relationship:

$$\Delta V_L = g_o I_{sp_{vac}} \ln\left[\frac{W_{f_2}}{W_{bo_2}}\right] + V_i - V_f \quad (90)$$

$$= (13{,}674 \text{ ft/sec})(1.41964) + 7703 \text{ ft/sec} - 25{,}589 \text{ ft/sec (from Figure 10-44)}$$

$$= 1526 \text{ ft/sec}$$

i. Comparison of Results – In order to indicate the validity of the approximate solution and also its accuracy, the trajectory for the example vehicle was simulated with a Two-Dimensional Trajectory Program on a digital computer.[13] Table 10-15 presents the comparison of results.

Since the purpose of the method of analysis demonstrated is primarily the computation of vehicle performance rather than simulation, it is not expected that the pitch rate for the demonstration problem will be identical, but it should be comparable. Likewise, occurence of events along the trajectory are not necessarily expected to coincide, and consequently slightly different results may be produced at intermediate points, as a first-stage burnout in this case. However, the performance results obtained at the final point should be similar.

Table 10-15. Comparison of Results

Parameter	Approximate Solution	Computer Simulation
First Stage		
V_{bo_I} (ft/sec)	7,703	7,705
β_{bo_I} (deg)	64.7	64.45
h_{bo} (ft)	187,000	179,410
θ_{bo} (deg)	0.50	0.52
Second Stage		
V_{bo_I} (ft/sec)	25,589	25,581
β_{bo_I} (deg)	89.99	90.00
h_{bo} (ft)	609,220	607,633
θ_{bo} (deg)	13.55	13.52
ϵ (deg/sec)	0.1143	0.1180

The accuracy of the approximate solution is within the limits expected for closed form techniques. The largest sources of error are realized from the first-stage analysis and the effect of these deviations is noticeable at final burnout. In the example, further iteration involving the first-stage burnout angle and use of a slightly different pitch rate could have been performed to reduce the discrepancies even further. This type of iteration process will most certainly be necessary for missions where an accurate estimate must be made for the first-stage burnout angle (i.e., for missions other than low altitude orbit missions for which the atmospheric portion of flight has been analyzed in this section).

10-2.2.2 Orbital Missions

10-2.2.2.1 Velocity and Orbital Period

a. Velocity – Figure 10-44 shows the perigee velocity required for orbital missions as a function of perigee altitude and orbit eccentricity, for a range in perigee altitudes of 100 to 10,000 nautical miles. The associated apogee altitude may be simply evaluated through use of the following equation:

$$h_a = \left[(h_p + r_e)\frac{(1+e)}{(1-e)}\right] - r_e \qquad (97)$$

where:

e = eccentricity

h_a = apogee altitude (maximum radius altitude)

h_p = perigee altitude (minimum radius altitude)

r_e = radius of the earth (3,440 nautical miles)

Given specific apogee and perigee altitudes, the eccentricity is:

$$e = \frac{h_a - h_p}{(h_a + h_p + 2r_e)} \qquad (98)$$

Circular orbit velocity requirements, as a function of orbit altitude, for altitudes of 0 to 2,000 nautical miles are found in Figures 10-45 through 10-48.

b. Orbital Period – Similar figures of the resulting orbital period as a function of perigee altitude and eccentricity are presented in Figure 10-49, for a range in perigee altitudes of 100 to 10,000 nautical miles.

Circular orbit periods as a function of orbit altitudes for altitude of 0 to 4,000 nautical miles and are found in Figures 10-50 through 10-55.

10-2.2.2.2 Hohmann Transfer

The minimum energy path (Hohmann transfer)[14,15] between two circular coplanar earth orbits is an elliptic segment that is tangent to both of the circular orbits. If the outer orbit has a radius greater than about 15.56 times the original parking orbit, propellant may be saved by going to any radius larger than that desired and then returning to the final orbit by applying a small impulse. This bi-elliptic transfer takes considerably longer than the Hohmann transfer and does not save very much propellant.

The earth Hohmann transfer consists of the addition of an impulsive incremental velocity of magnitude ΔV_1, while parked in a circular orbit, then at apogee of the transfer orbit an incremental impulse velocity of sufficient magnitude, ΔV_2, is added to circularize the orbits as shown in Figure 10-56.

For the Hohman transfer analysis presented here, representative parking orbit altitude of from 100 to 2,000 nautical miles were chosen. It is assumed here that tangential addition of the velocity occurs instantaneously. This is a realistic approximation for acceleration greater than 1/2 g.[16]

a. ΔV_1 – The initial incremental injection velocity, ΔV_1, required at the parking orbit altitude to transfer to an apogee altitude corresponding to the

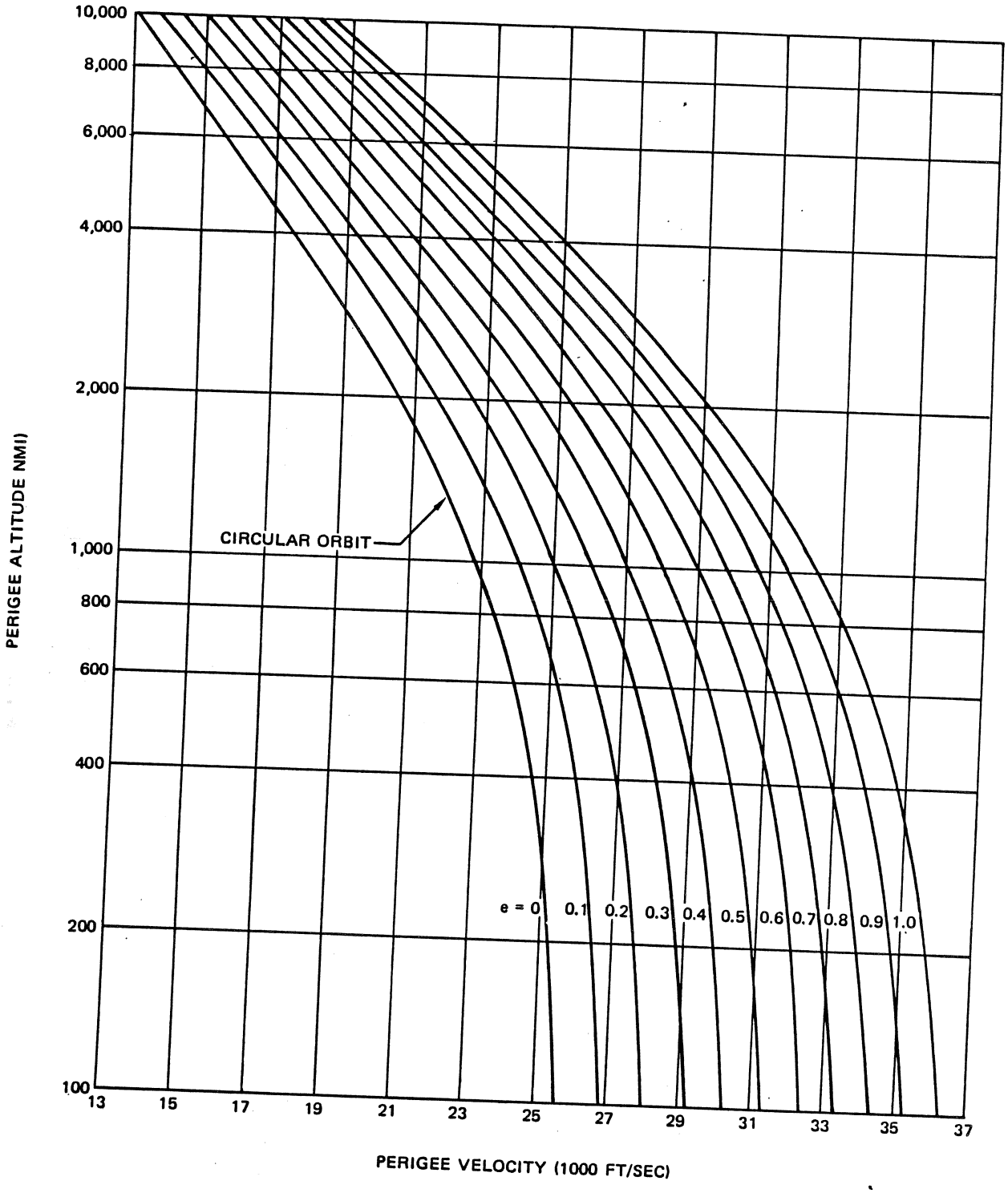

Figure 10-44. Elliptical Orbital Satellite Velocity

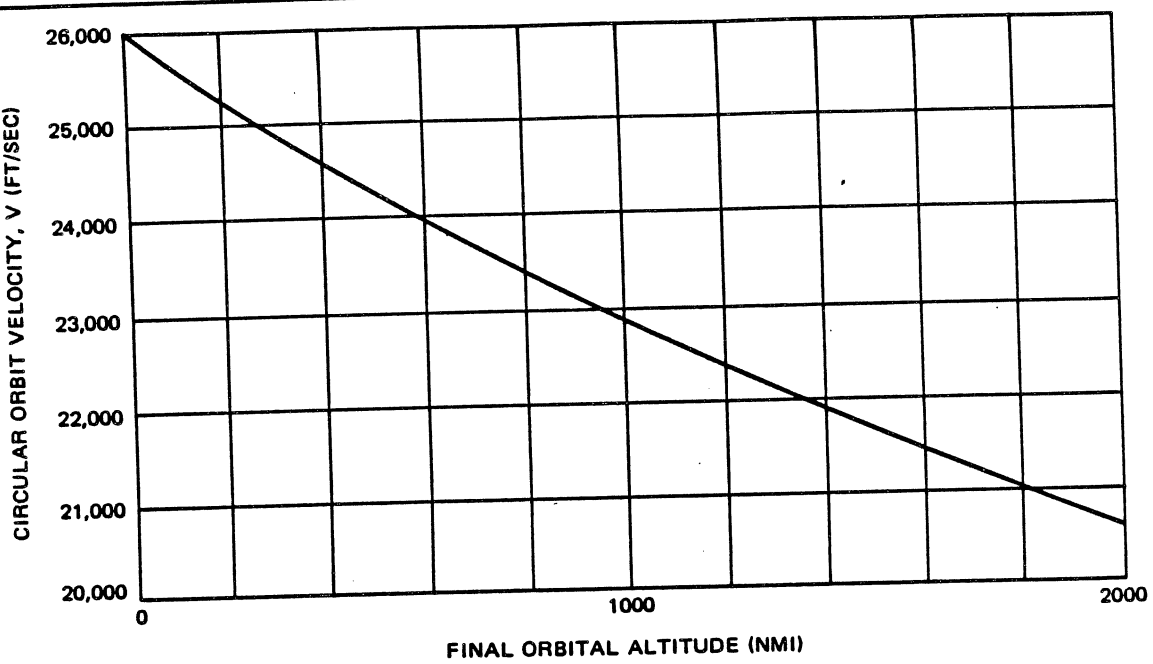

Figure 10-45. Circular Orbital Satellite Velocity

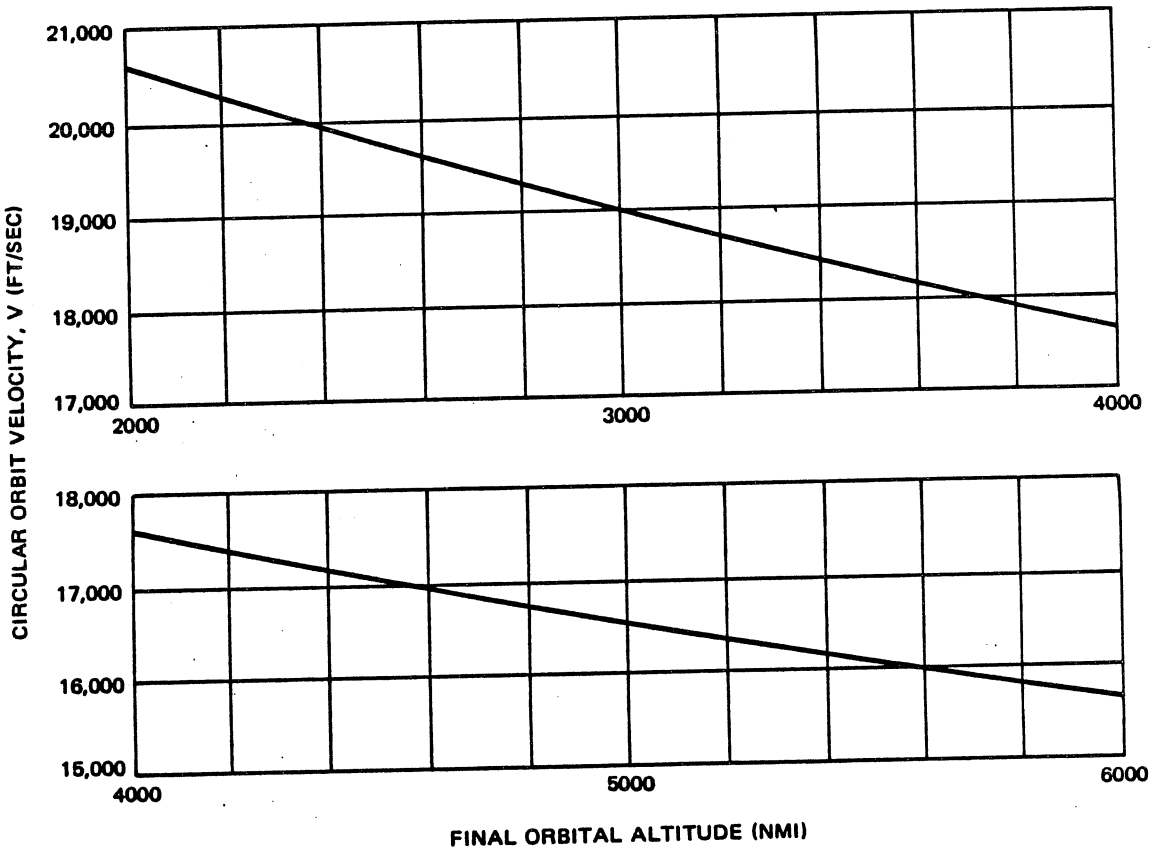

Figure 10-46. Circular Orbital Satellite Velocity

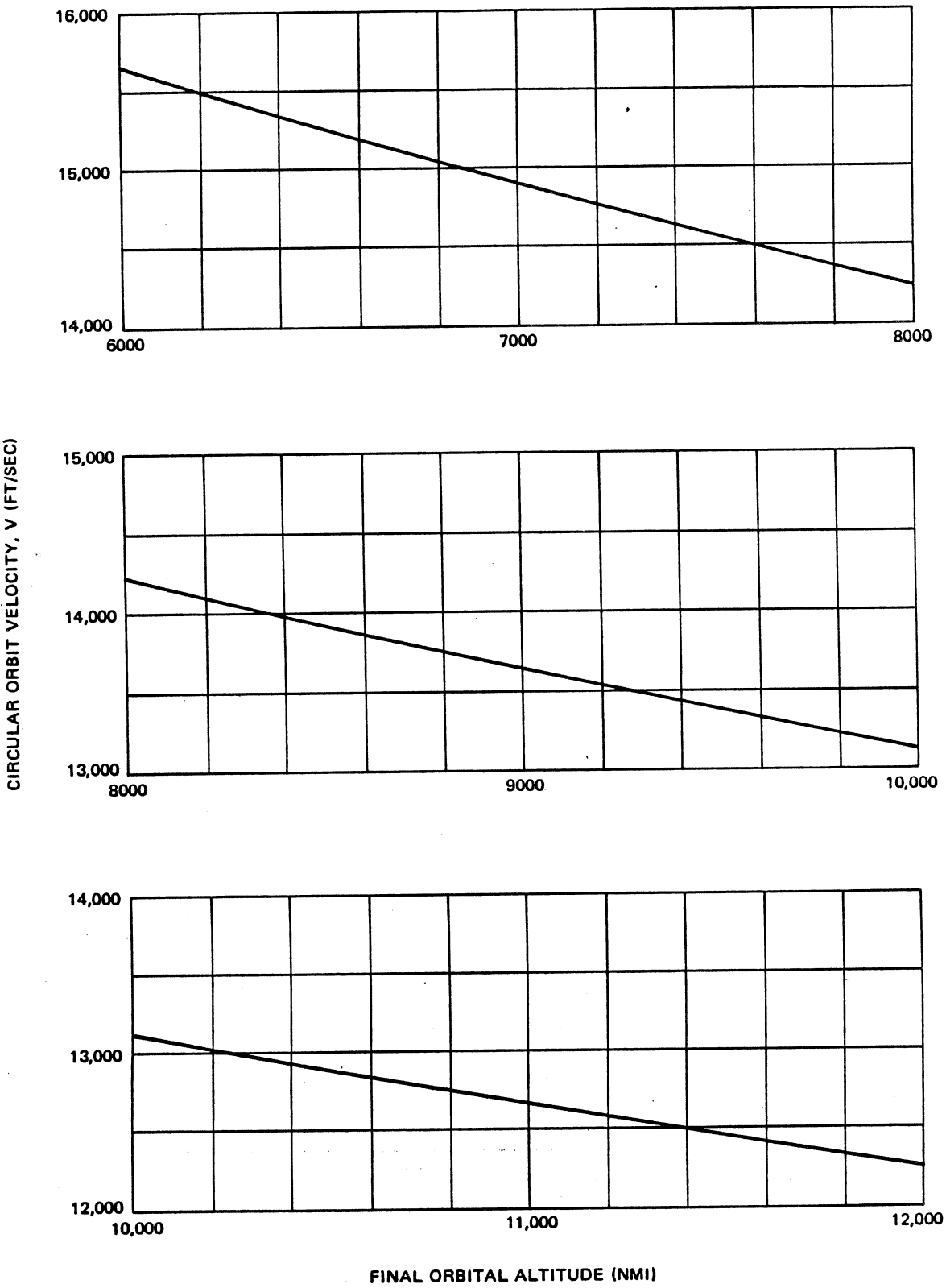

Figure 10-47. Circular Orbital Satellite Velocity

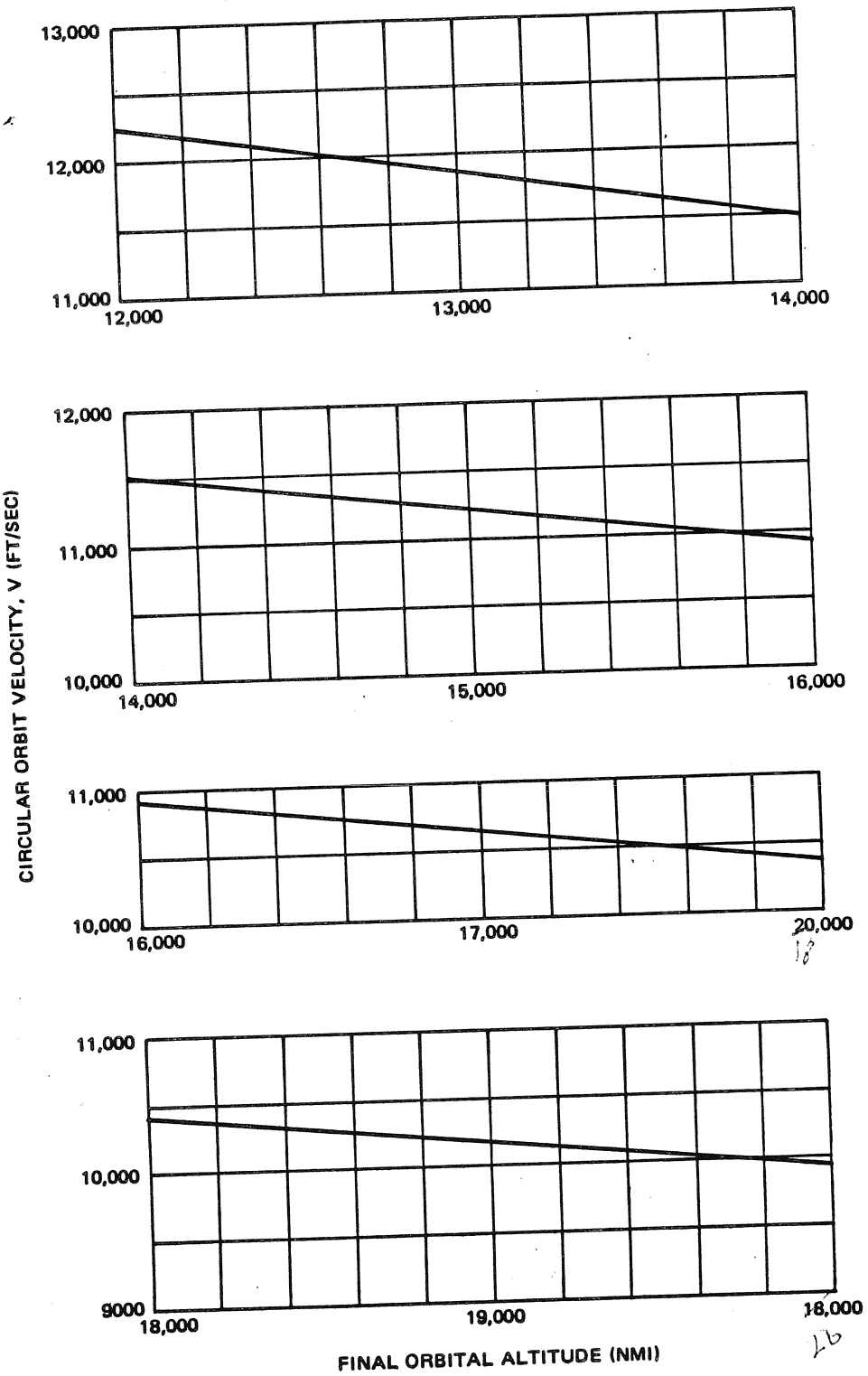

Figure 10-48. Circular Orbital Satellite Velocity

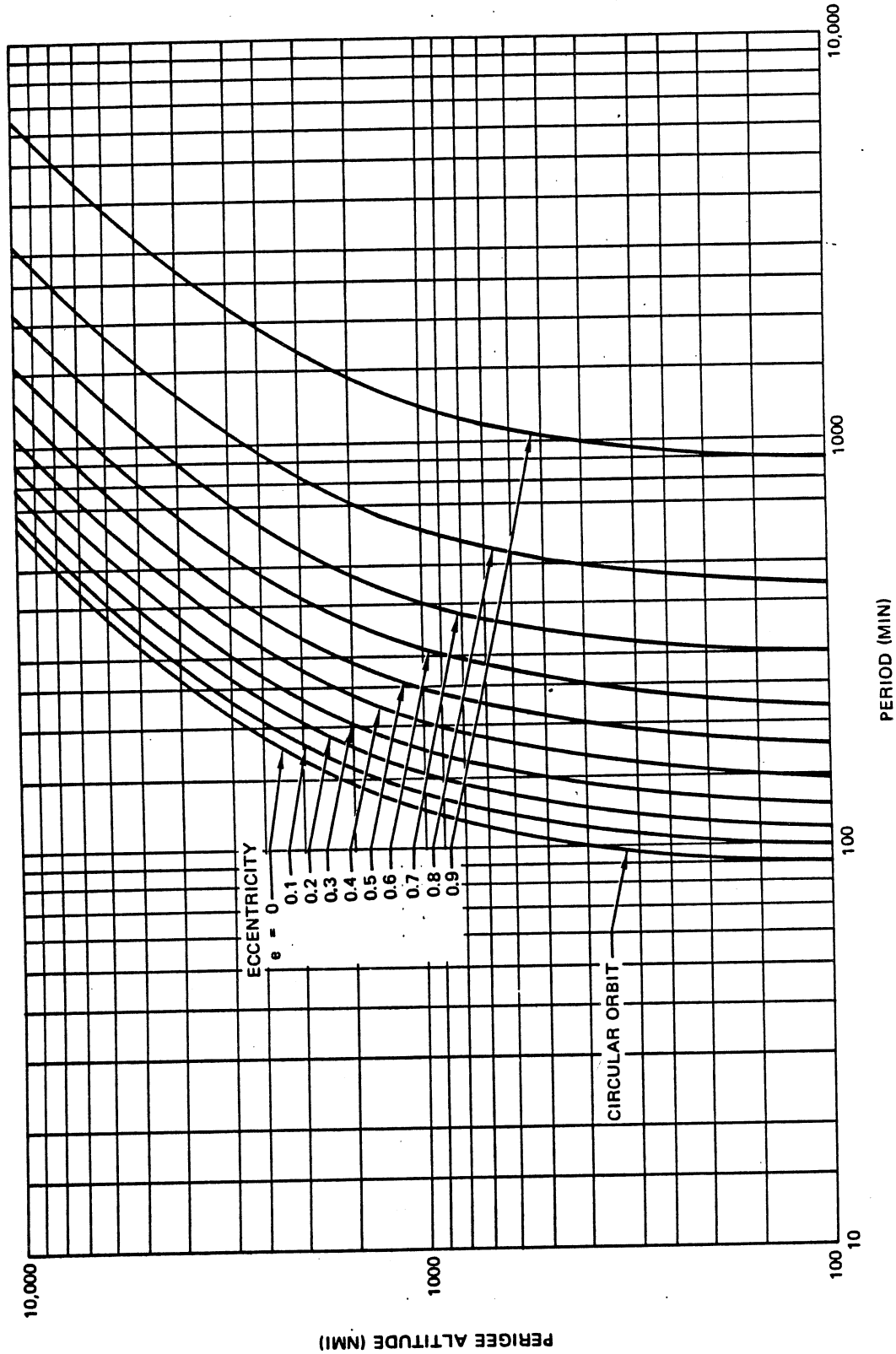

Figure 10-49. Elliptical Orbital Satellite Period

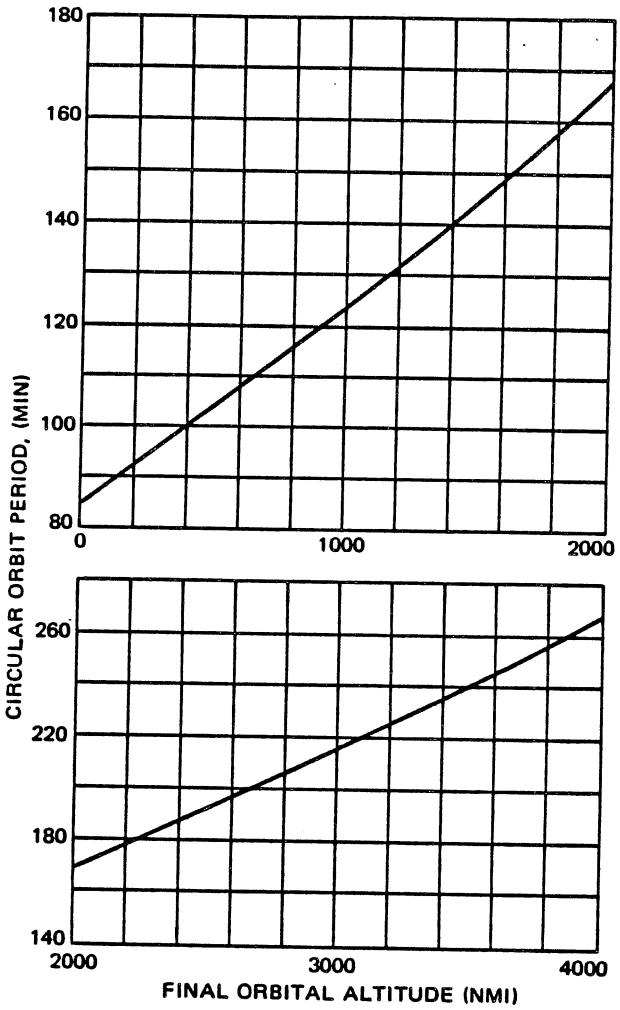

Figure 10-50. Circular Orbital Satellite Period

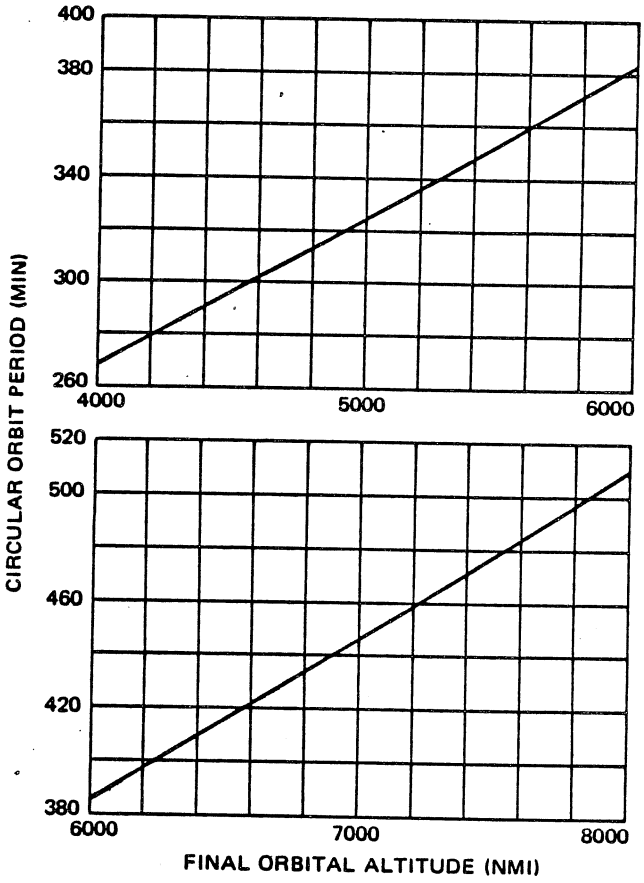

Figure 10-51. Circular Orbital Satellite Period

desired final orbit altitude is presented in Figures 10-57 and 10-58 for altitudes from 0 to 2,000 nautical miles, and 100 to 10,000 NM, respectively.

b. ΔV_2 – Similarily, the incremental velocity, ΔV_2, required to circularize the orbit at the apogee of the transfer orbit is presented in Figure 10-58.

c. ΔV_T – The sum of ΔV_1 plus ΔV_2, is presented in Figure 10-58 for altitude of 100 to 10,000 nautical miles.

10-2.2.3 Lunar Missions

A range of injection velocities for normal lunar missions is presented for use in evaluating and quoting lunar payload capabilities. Figure 10-59 shows the required injection velocity from a parking orbit altitude, r_o, of 100 nautical miles as a function of the time of flight from injection to the moon. At each flight time, a range of velocities is shown corresponding to trajectories which arrive at the moon when the moon is at perigee and apogee in its orbit about the earth. The velocity required at some other parking orbit altitude, r_1 may be computed to yield the same injection energy.

$$V_1^2 = V_o^2 - \frac{2\mu e}{r_o} + \frac{2\mu e}{r_1} \qquad (99)$$

where:

$\mu e = g_o r_e^2 = 1.40766 \times 10^{16}$ ft^3/sec^2 (gravitational parameter)

and:

$r_e = 0.209029 \times 10^8$ ft (radius of earth)

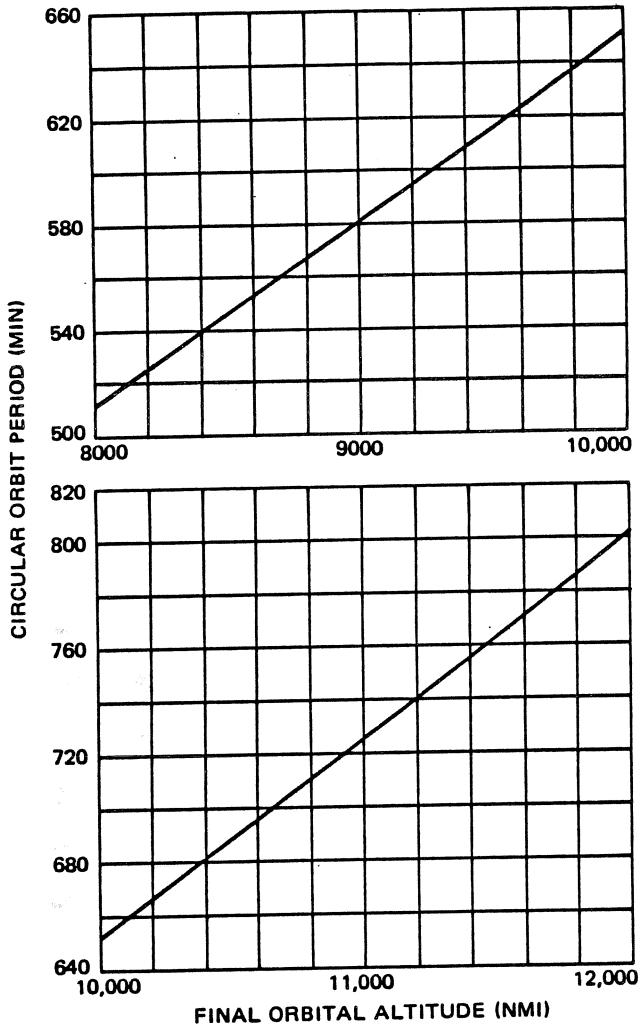

Figure 10-52. Circular Orbital Satellite Period

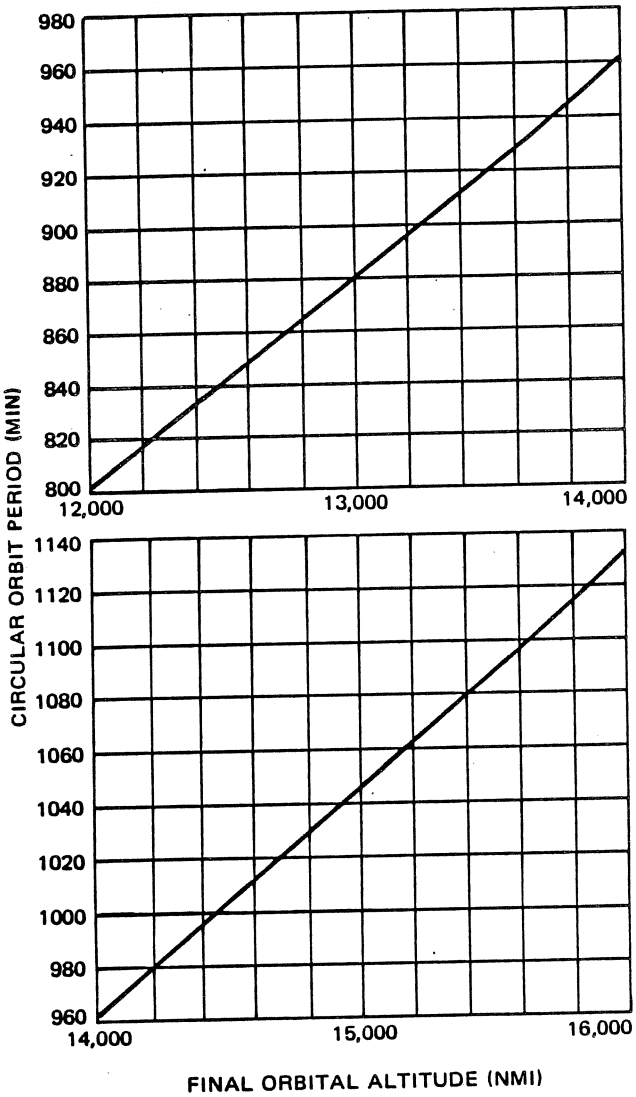

Figure 10-53. Circular Orbital Satellite Period

The velocity required for lunar transfer and escape from earth parking orbits, with altitudes of 80 to 300 nautical miles, is presented in Figure 10-60. The three velocity bands shown in the figure represent lunar transfer times of 50, 66, and 90 hours based on a parking orbit altitude of 100 nautical miles.

The particular velocity (or flight time) to be employed on a mission is usually the result of a comprehensive optimization study considering injected payload weight capability, launch guidance errors, tracking accuracy, tracking station location, midcourse correction, and terminal deboost (if any) fuel requirements. Typically, such analyses for lunar orbiter, soft landing, and circumlunar trajectories have yielded optimum flight times in the range of 60 to 90 hours. Since the total velocity range from 90-hour missions to escape missions is only about 350 ft/sec, and this usually represents a small increment in vehicle payload weight capability, it is common in preliminary launch vehicle studies to represent lunar missions by a single number – the earth escape velocity,*

$$V_{escape} \cong 36{,}180 \text{ ft/sec at 100 nmi}$$

For more exact studies, bands of injection velocities* may be read from Figure 10-60, corresponding to the flight times of interest, such as

V_o = 36,070 → 36,160 ft/sec at 100 nmi for t_f = 50 hr

*Rounded to 10 ft/sec

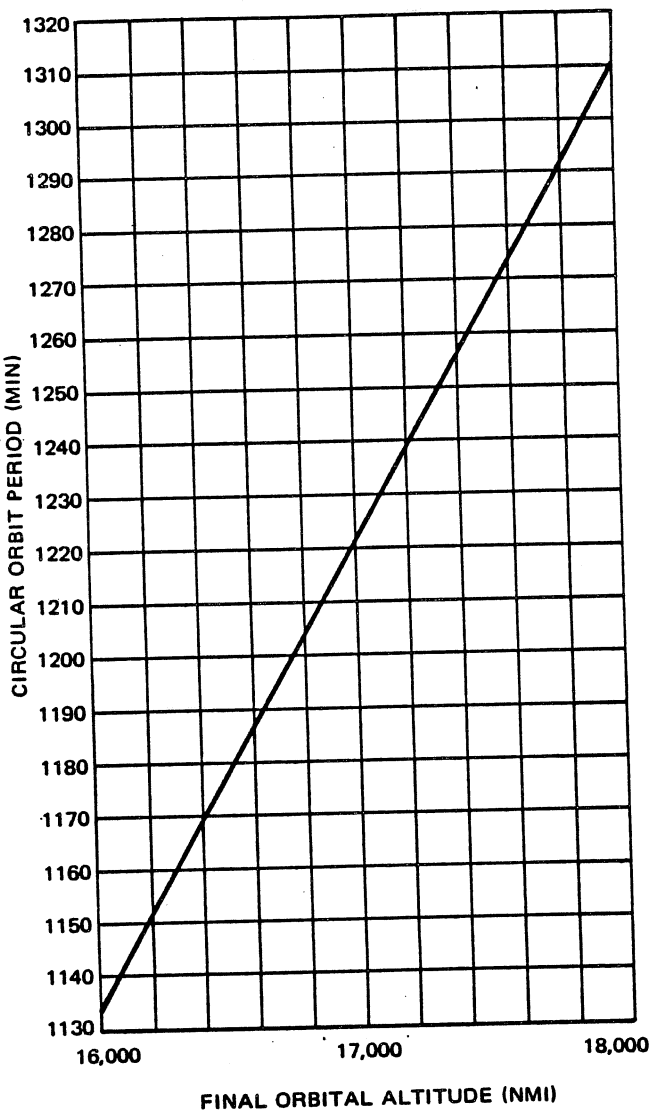

Figure 10-54. Circular Orbital Satellite Period

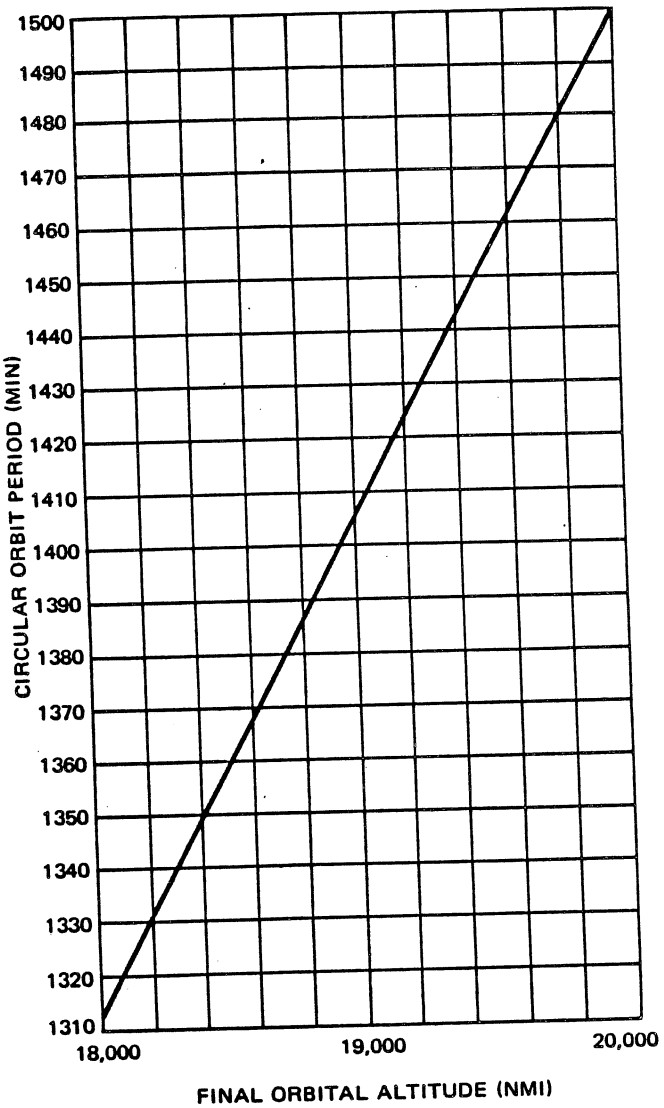

Figure 10-55. Circular Orbital Satellite Period

V_o = 35,910 → 36,010 ft/sec at 100 nmi for t_f = 66 hr

V_o = 35,850 → 35,910 ft/sec at 100 nmi for t_f = 90 hr

The velocity discussed above are inertial velocities and may be partly composed of a component of velocity due to the earth's rotation. Generally, a "launch window" or range of permissible liftoff times on a given day will be mechanized by varying the launch azimuth and parking orbit coast duration in a systematic way with liftoff time. Typically, the launch window obtainable for a launch azimuth range of 85 to 115 degrees (from AMR) will vary from 2.0 to 5.2 hours depending on the lunar declination. The payload loss, or equivalent velocity requirement, due to not firing at a 90-degree launch azimuth can be estimated simply but is not presented here. Interplanetary velocity requirements for Venus and Mars missions may also be calculated using similar methods but are beyond the scope of this presentation.

10-2.2.4 Space Missions

10-2.2.4.1 Basic Principles

The astronomer Johannes Kepler empirically formulated three laws to describe the motion of the planets:

a. The orbit of each planet is an ellipse that has the sun at one focus.

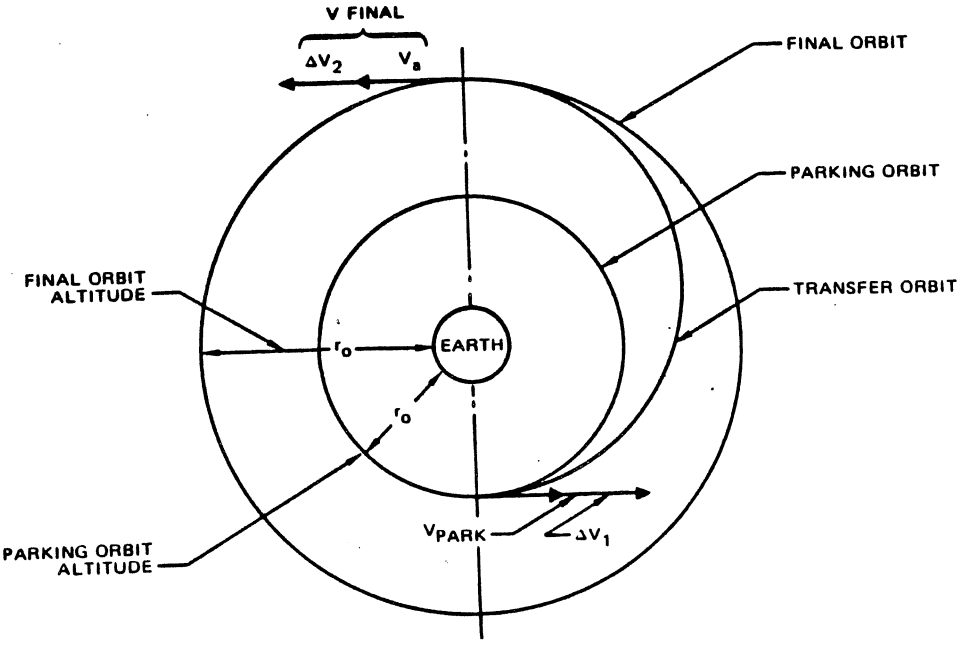

Figure 10-56. Hohmann Transfer Ellipse

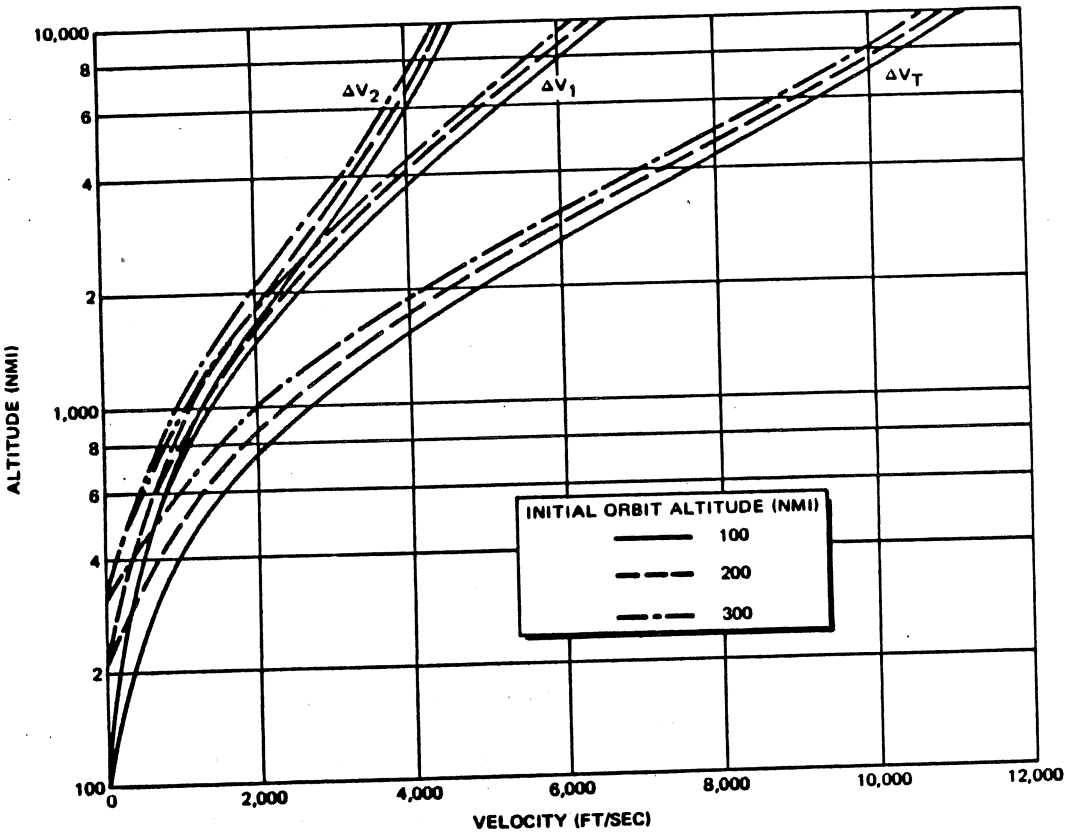

Figure 10-57. Initial Hohmann Transfer Injection Velocity Requirements

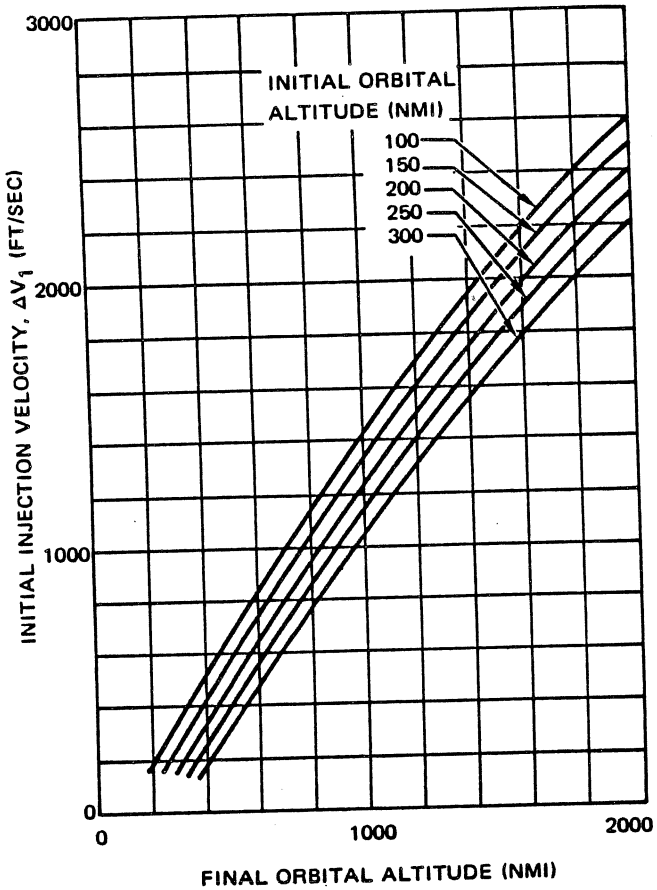

Figure 10-58. Hohmann Transfer Velocity Requirements

b. The line joining a planet and the sun sweeps over equal areas in equal intervals of time. (That is, a planet moves faster when it is close to the sun and slower when it is farther away.)

c. The square of a planet's time of revolution about the sun is proportional to the cube of its mean distance from the sun.

While Kepler's laws are based purely on his observations, Sir Isaac Newton formulated essentially the same laws from his new law of gravitation. (Newton's law of gravitation states that all particles of matter attract all other particles, and that the force of their attraction is proportional to the square of the distance between them.) From this law, Newton found that the planets continually orbit the sun because of the balance between the sun's gravitational attraction and the centrifugal force of their orbital motion. He also ascertained that Kepler's laws apply to any object moving under the influence of a single attraction body, but that the path will be one of the conic sections and not necessarily an ellipse.

Conic sections are mathematically defined curves encompassing ellipses and hyperbolas; the circle is a special case of the ellipse and the parabola is the curve between the ellipse and hyperbola. One can easily demonstrate these curves by directing a flashlight beam at a wall. When the beam is perpendicular to the wall, the spot is a circle. As the beam is titled, the spot becomes elliptical. And as the beam is titled even further, the ellipse disappears at the point where the angle of tilt equals the angle of the beam. Beyond this, the spot is hyperbolic.

Newton derived another law governing the motion of one body about another – called two-body motion. It relates the orbit speed, V, to the distance from the central body, r_c:

$$V^2 = K' \left(\frac{2}{r_c} - \frac{1}{a_x} \right) \qquad (100)$$

The term "a_x" is the semi-major axis of the orbit. K' is the gravitational constant times the sum of the masses of the two bodies. This expression represents a conservation of energy which is constant everywhere on the orbit.

The path of an object moving solely under the influence of a central body is one of the conic sections shown in Figure 10-61. The path is such that the focus of the conic section lies at the center of the central body. An object in orbit follows a circular or elliptical path, whereas one on an escape trajectory follows a parabolic or hyperbolic path.

For a circular orbit r_c equals a_x everywhere on the orbit and therefore $V^2 = K'/a_x$. The orbital speed is inversely proportional to the square root of the orbit's semi-major axis.

From Equation 100, we can also deduce that when an orbit is begun some distance, r_c, from the Earth, the orbit's semi-major axis is determined entirely by inital speed; the higher the speed, the larger the orbit.

A parabolic orbit is one which extends indefinitely. The speed in a parabolic orbit is:

$$V^2 = K' \left[\frac{2}{r_c} - \frac{1}{\infty} \right] = 2K'/r_c$$

Thus, the speed needed to escape from a body is $\sqrt{2}$ times circular orbit speed.

Achieving escape speed does not suddenly free an object from the gravitational force of the parent body. Rather, gravitational force will continually slow it down but it will never fall back. We can think of an object in a parabolic orbit as eventually coming to a stop after traveling a tremendous distance (theoretically infinite).

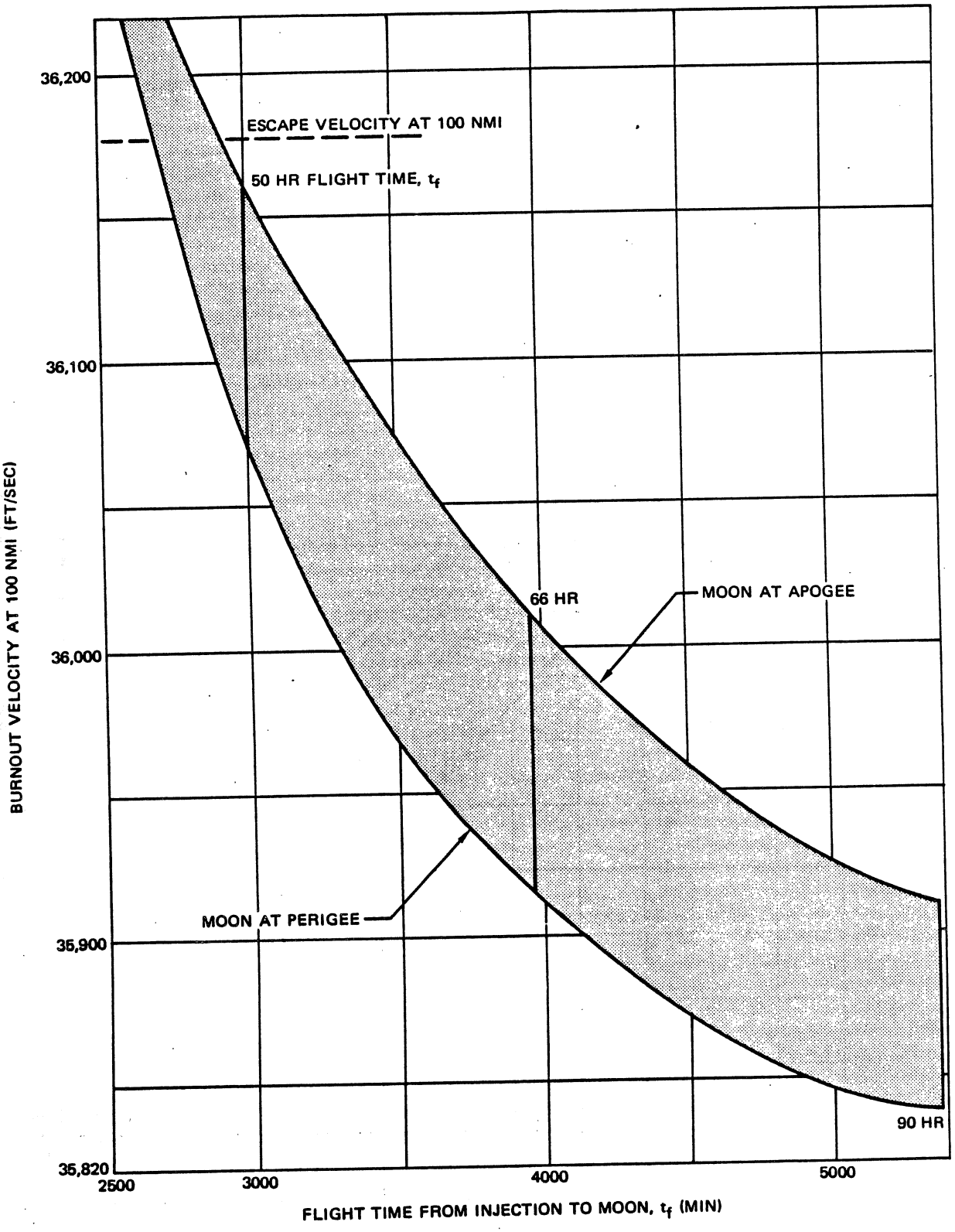

Figure 10-59. Lunar Mission Requirements

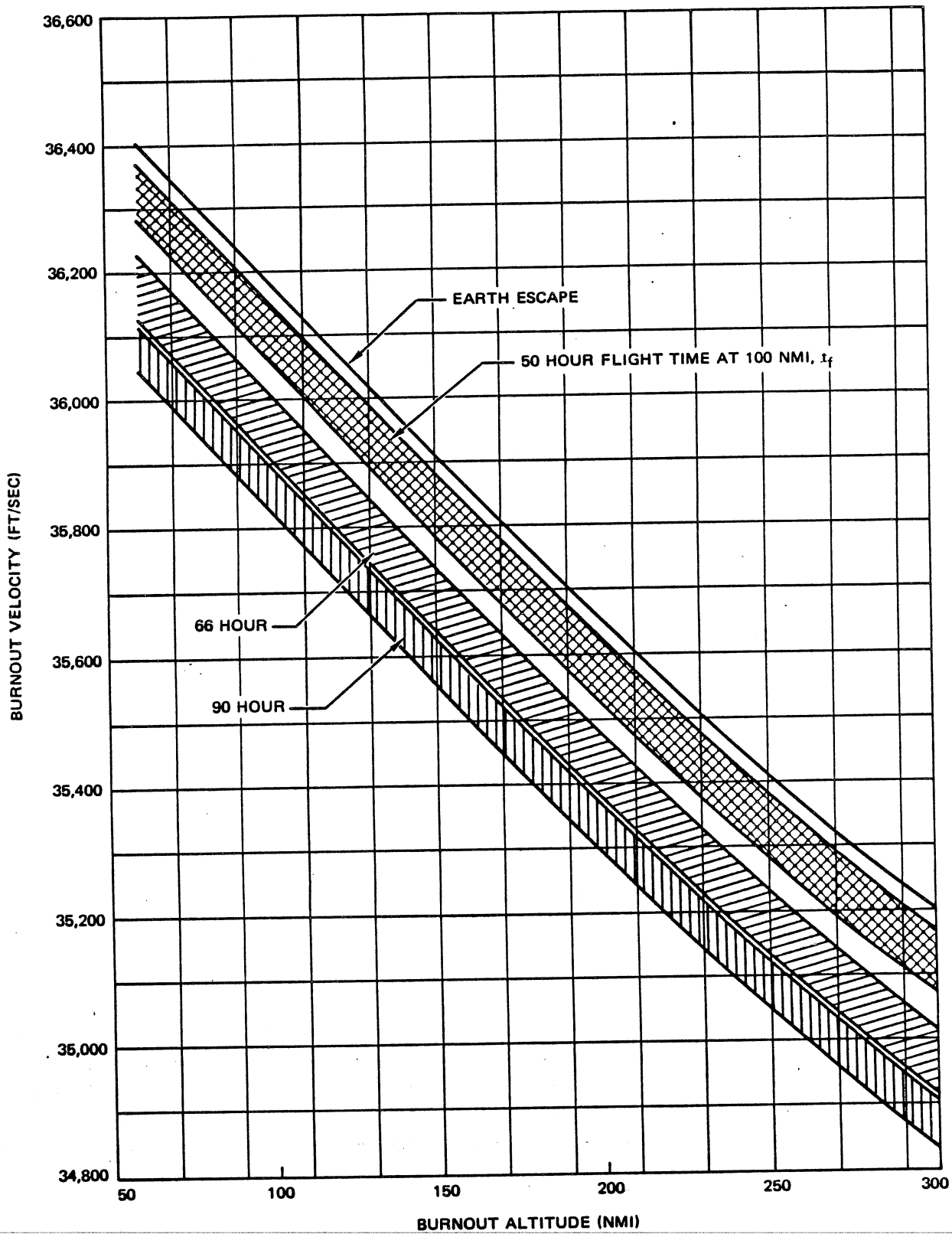

Figure 10-60. Lunar Mission Requirements

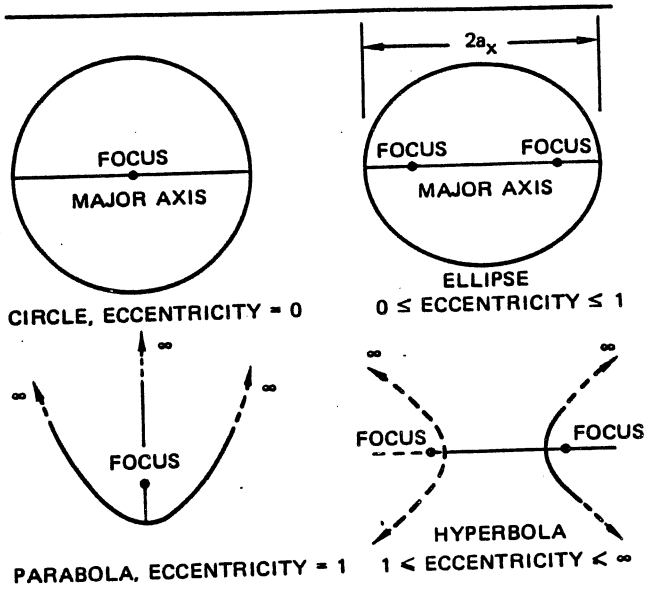

Figure 10-61. Paths of Objects Under Influence of Central Body

If an object is launched with a speed higher than escape speed, it will follow a hyperbolic path. The difference between this orbit and the parabolic one, besides the difference in shape, is that after having traveled a tremendous distance the object is still moving; this is in contrast to the object in a parabolic orbit, which we think of as stopping after a very long distance.

The speed an object has at a very great distance is its hyperbolic excess speed. The speed, V_∞, is obtained from Equation 101:

$$V_\infty^2 = K' \left(\frac{2}{\infty} - \frac{1}{a_x}\right) = -\frac{K'}{a_x} \qquad (101)$$

(a_x is negative for hyperbola)

Since

$$V^2_{escape} = 2K'/r_c, \; V_\infty^2 = V^2 - V^2_{escape}$$

In departing from a celestial body with more speed than the minimum escape speed, a vehicle traverses the gravity field in less time and loses less speed in the process. Thus, any increase in the inital speed beyond escape speed results in a more than equivalent increase in hyperbolic excess speed. At very high inital speeds, the hyperbolic excess speed is nearly equal to the initial speed because very little speed was lost in escaping from the parent body.

The curve in Figure 10-62 shows the hyperbolic excess speed (the theoretical speed an object has after coasting an infinite distance from a body) as a function of initial launch speed from earth. The difference between the initial speed and the hyperbolic excess speed is the speed lost in coasting through the earth's gravitational field. The greater the initial speed, the less the amount lost due to gravity.

Equation 101 is frequently used in mission feasibility calculations. For example, a space station is to be established halfway between the earth and the sun; by Equation 101, the total speed needed to accomplish this mission can be determined. In this mission, the space station starts from the earth but goes into orbit about the sun. Therefore, it is under the simultaneous influence of two celestial bodies.

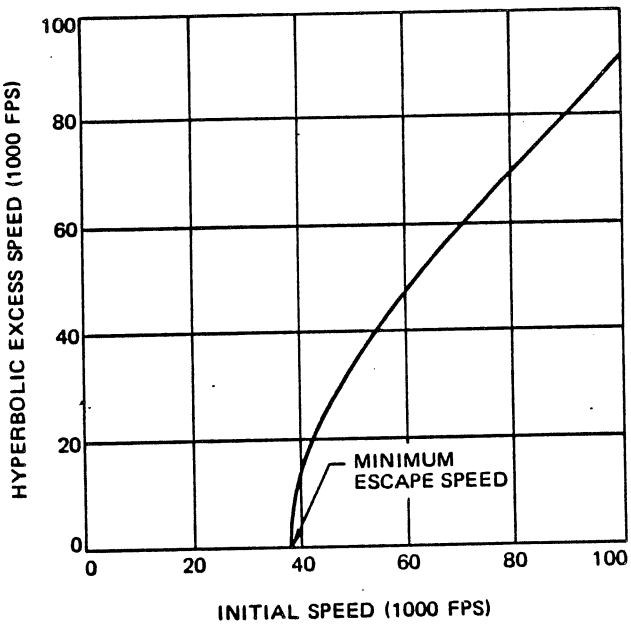

Figure 10-62. Hyperbolic Excess Speed vs Initial Speed

A precision solution to this three-body problem is unknown. For simplicity, however, it may be considered with sufficient accuracy, as a succession of two-body problems. Near the earth, the space station may be thought of as being in an earth orbit only. Further from the earth, the station can be considered to be orbiting the sun, completely divorced from the earth. There are many possible transfer paths between the earth and the final orbit, but the one that is accomplished with the lowest speed is the Hohmann transfer, which is tangent to the initial and final orbits.

In calculating the speed necessary for this mission, a system of characteristic units is employed for simplicity. In this system, the unit of distance for an earth-centered orbit is one equatorial radius. The unit of speed is the speed of a hypothetical satellite at a distance of 1, which is at the earth's surface. This speed is approximately 25,900 fps. For sun-centered, or heliocentric, orbits the

unit of distance is one astronomical unit (A.U.), the mean distance from the earth to the sun, 93,000,000 miles. The heliocentric speed unit is the speed of the earth on its orbit: 97,700 fps. With this set of units, the value of K' in Equation 101 is numerically 1.

Figure 10-63 shows one way a spacecraft can be put into a solar orbit midway between earth and sun. The spacecraft will follow the transfer orbit if its speed is sufficiently reduced below the earth's orbital speed. The spacecraft must then escape the earth with enough speed left to reduce its orbital speed about the sun. When perihelion of the transfer orbit is reaches, another speed reduction is needed to circularize the orbit.

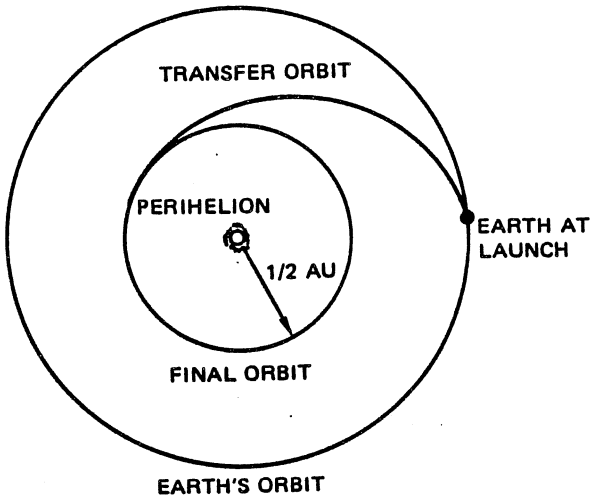

Figure 10-63. Earth to Solar Orbit Transfer

Escape from earth requires a speed of $\sqrt{2}$ units whn ascending from the surface (neglecting drag and gravitational losses), but just escaping from the earth is not enough. There must be enough speed left over after earth escape to reduce the orbital speed about the sun in order for the station to fall towards the sun. The semi-major axis of the transfer orbit is 3/4 heliocentric units. From the earth's orbit, where $r_c = 1$ unit, the initial speed of the transfer orbit is equal to:

$$\sqrt{\frac{2}{1} - \frac{1}{0.75}} = 0.82 \text{ heliocentric units}$$

But the earth's orbital speed is 1 unit so a reduction of 0.18 heliocentric units in speed is required. This is the speed our station must have relative to the earth when it is far from the earth. It is the necessary hyperbolic excess speed. But this speed is in heliocentric units and is corrected to geocentric units by the ratio of characteristics speeds,

$$\frac{97,700}{25,900} = 3.8$$

The total speed to escape the earth and make the transfer can now be obtained as:

$$V = \sqrt{V^2_{\text{escape}} + V^2_{\infty}} = 1.57 \text{ units} \qquad (102)$$

When the perihelion of the transfer orbit, r = 1/2, is reached the vehicle will have a speed of 1.64 units. But circular orbit speed is only 1.41 units, which requires another speed reduction of 0.23 units. In terms of geocentric units, this speed is 0.87.

The total speed required for the mission is therefore 2.44 units. Thus, this mission requires a rocket with a total speed capability of about 63,000 fps, neglecting the losses mentioned earlier.

The time it takes the station to revolve once around the sun is easily found by Kepler's third law, e.g., the square of a planet's time of revolution about the sun is proportional to the cube of its mean distance from the sun. Since the semi-major axis of the final orbit is just half that of the earth's, the station's orbital period is 129 days.

While two-body motions are quite simply described a more precise description of a vehicle's motion in space requires the consideration of numerious additional factors: other celestial bodies, an atmosphere, nonhomogenity of the principal body, solar radition pressures, and thrust forces. These, as well as other factors, cause the vehicle's motion to depart from thay predicted by the two-body laws.

10-2.2.4.2 Effects of Low Thrust

While thrust is applied to a vehicle in space, the vehicle's orbit is not characterized by the two-body laws. For a high-thrust vehicle, the time of thrust application is short and conditions at the end of the thrusting period determine the orbit. On the other hand, low-thrust propulsion devices such as ion or plasma rockets can operate for longer durations. These low-thrust devices can be used by a vehicle in orbit to increase its speed from orbital speed to escape speed. The trajectory during this period of acceleration spirals out from the center, making many revolutions until the required speed is attained. For increasing speed from an initial circular orbit, the thrust force is continually directed approximately along the path of flight, Figure 10-64. A thrust force in the radial direction is not efficient for escaping from a circular orbit but is used to adjust some orbit parameters such as eccentricity. A thrust force applied perpendicular to the orbit plane changes the inclination of the orbit.

Low-acceleration schemes, when used to increase speed rather than to modify an orbit, have the disadvantage of

gaining speed quite slowly. For example, a vehicle, when starting in a circular orbit near earth's surface and accelerating at a constant rate of 1 pound of thrust for every 1,000 lbs of weight (weight at earth's surface), takes about 8.7 days and 39 revolutions to reach escape speed.

Accelerating slowly also requires more impulsive speed than high acceleration. (Impulsive speed is a measure of the total energy output of a rocket and is a measure of total energy output of a rocket and is the ideal speed that would be attained by acceleration in the absence of gravitational and drag forces) (Figure 10-65).

Shown is the impulsive speed a vehicle needs to attain various hyperbolic excees speeds (indicated by V_∞) when starting from a circular orbit near the earth. The difference between the impulsive speed required at a particular acceleration and that required for an infinite acceleration (indicated by dashes, ---) is a measure of the energy loss caused by low acceleration.

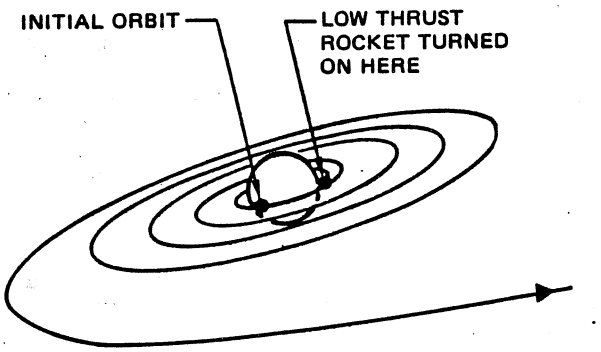

Figure 10-64. Effects of Low Acceleration from Earth Orbit

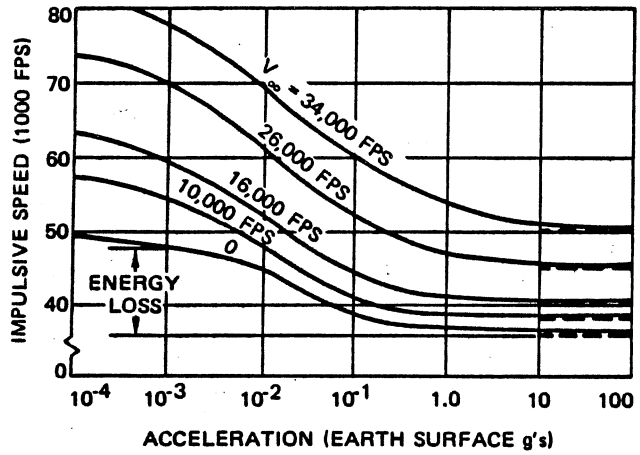

Figure 10-65. Effect of Acceleration Level on Impulsive Energy Loss

Using a thrust of 1 pound per 1,000 pounds of weight to increase speed from circular orbit speed to escape speed requires an impulsive speed of 48,000 fps. For a hypotetical infinite acceleration, the speed requirement would be 36,700 fps. The difference of 11,300 fps is the loss caused by low acceleration and can be explained as follows:

An object coasting in a gravitational field possesses a constant total energy. This energy consists of a potential component, a function of distance from the center of attraction, and a kinetic component. Since the kinetic energy increases as the square of the speed, the greatest increase in total energy, which is the point of lowest potential energy, and hence, closest to the gravitational center. But, a low-acceleration vehicle increases speed from long periods of time, and since its orbit grows in a spiral, its speed is increased at greater distance from the orbital center, on the average, than with a higher-acceleration vehicle.

10-2.2.4.3 Planetary Capture and Braking

An object which comes to a planet from a great distance (for instance, a vehicle returning to earth from Mars) will approach it at least as fast as the speed necessary to escape from the planet. This is because an object that starts falling toward a planet from a great distance has about the same amount of potential energy as the kinetic energy possessed by one launched from the surface with escape speed. And so the object will trade its potential energy for kinetic energy as it falls reaching escape speed at the planet's surface. And the higher the speed the object has at a great distance, the higher its approach speed will be.

To be captured by a planet, a vehicle's approach speed must be cut below escape speed by either rocket or atmospheric braking – or by a collision with the planet. Because the planet has an attraction for the approaching object, the size of the planet in terms of a target is larger than its physical size. This target is sometimes called a planet's effective cross section, virtual diameter, or capture arc. An object approaching the planet within it will be drawn onto a collision course. The effective cross section of a planet is determined by its physical size, the speed of the approaching object, and the mass of the planet. The higher the speed of the approaching body, the nearer the effective cross section is to the physical size of the planet.

The presence of a planetary atmosphere is advantagous for planetary loading because it can be used, within limits, for braking. Without an atmosphere, as in the case of the moon, braking for a low-speed landing must be accomplished with rockets (Figure 10-66).

Where a planet's atmosphere is used for braking, the target for the incoming vehicle is much smaller than it

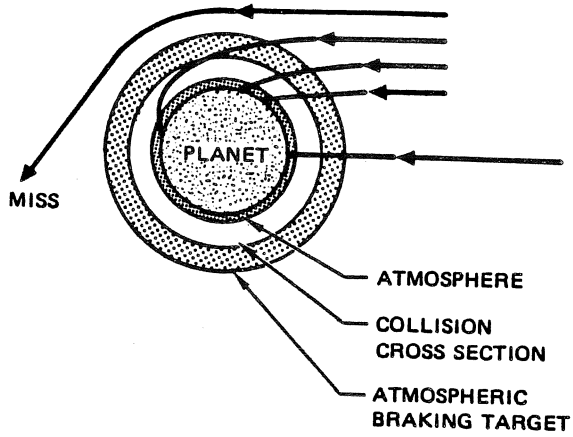

Figure 10-66. Planetary Landing Characteristics

would be for mere collision. The vehicle must fly into a narrow corridor, and if it misses the outer edge of this boundary, its approach to the atmosphere will be too shallow, it will not be slowed enough, and it will not be captured by the target planet (if its approach speed exceeds the planet's escape speed). Missing the inside edge of the corridor will result in too steep a penetration and consequent destruction. Therefore, the target for an atmospheric braking maneuver is a narrow band around the planet.

A body approaching a planetary atmosphere possesses a very large amount of energy – so much, in fact, that if all the energy were converted to heat within the body itself, it would, in most cases, be more than enough to completely vaporize the body. However, much of the energy goes to heat the air or gas around the body, and only part of the energy is transferred to the body as heat.

A slender, low-drag body will penetrate deeply into the dense atmosphere before it is appreciably slowed down, a condition which causes very high aerodynamic heating. A high-drag body, on the other hand, causes the braking to occur at high altitudes, thereby reducing the heating.

In addition to heating, aerodynamic braking results in rapid deceleration. Interestingly, the peak deceleration is practically independent of the drag characteristics of the entry body. It is highly dependent, though, on entry speed, angle of penetration of the atmosphere, and the density distribution of the atmosphere. Penetrating the atmosphere in a steep descent prevents a gradual deceleration in thin air. Instead, the braking is postponed until dense air is reached, which causes high decelerations and aerodynamic heating. An atmosphere whose density increases gradually allows a softer, less severe entry than one whose density increases rapidly.

With a lifting vehicle, aerodynamic heating and deceleration can be less than what they would be for a pure drag vehicle. The lift development by the vehicle can be used to maintain a higher altitude during the initial deceleration. Also, a lifting vehicle can maneuver to a preferred landing site and land conventionally if its low-speed lift-to-drag ratio is high enough. The lift can be developed either by wings with conventional airfoils or by shaping of the vehicle body.

10-2.2.4.4 Rendezvous

The rendezvous mission comprises an ascent phase, a terminal phase, and docking (Figure 10-67).[36] The ascent phase may be accomplished by either of two basic ascent echniques: Direct ascent or waiting orbit. In the direct ascent technique, the chase vehicle is launched when the launch site is close to the orbital plane of the target. The chaser then makes a direct transfer to intercept the target, applying the proper velocity increments to make the plane of its orbit coincident with that of the target and to attain the target's velocity. A problem of the direct ascent technique is that the time interval within which the launch must occur, the launch window, is only a matter of minutes and occurs infrequently.

In the waiting orbit technique, the chaser is put into either a chasing orbit or a parking orbit. It is launched into the orbital plane of the target, irrespective of the target's position. The periods of the chasing and parking orbits are shorter than the period of the target's orbit; therefore, angular deficiencies between target and chaser are made up. Next, at the appropriate time, the chaser is put into coincidence with the target by an impulsive type correction for the chasing-orbit case or an orbital-transfer for the parking orbit case.

In the terminal phase, the chaser is less than about 100 mi from the target and may be guided or driven up to the target. There are two basic terminal phase maneuvers: proportional navigation and orbital mechanics (Figure 10-68).[36] In the proportional navigational maneuver, the intent is to null the angular

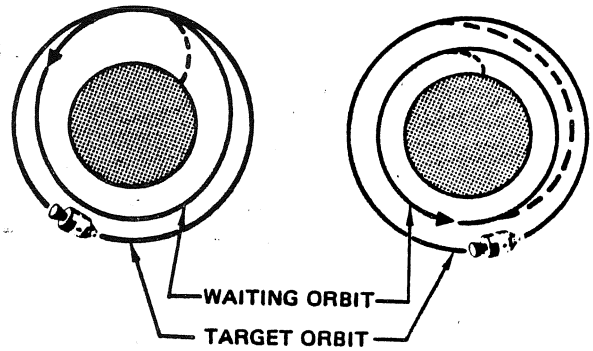

Figure 10-67. Rendezvous Mission Techniques

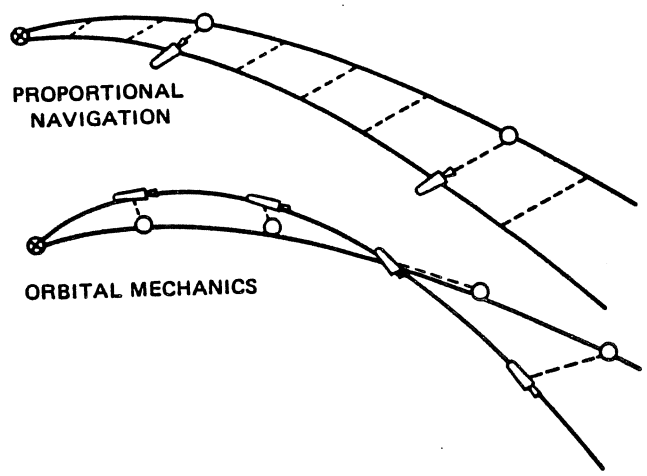

Figure 10-68. Rendezvous Terminal Phase Maneuver

motion of the line of sight so that the approach to the target is then accomplished. In the orbital mechanics maneuver, readings are taken to see whether the coasting paths being followed will lead to interception; if they will not, propulsion is used to correct the coasting orbit of the chaser to an orbit which results in rendezvous. In this latter maneuver, a final velocity correction must of course be applied just before contact to null the velocity of the chaser relative to the target. While the terminal phase control for either maneuver may be accomplished efficiently by either manual or automatic means, it is believed that manual means will ultimately prove superior by far in the actual docking maneuver.

10-2.2.5 System Considerations

There are limiting features of space systems which constrain their design and/or performance. Such constratints include launch location, range safety, maximum allowable acceleration, loads, heating, guidance, and performance dispersions. The vehicle designer must evaluate various constraining parameters and, by knowing the boost vehicle characteristics, derive the value associated with them. However, no attempt is made to show design modifications or trajectory shaping techniques that will relieve the constraint. Usually at this point in a preliminary design, it is best to design the vehicle to the constraint rather than to shape the trajectory to relieve the constraint. Trajectory shaping should be used only to relieve constraints, such as maximum dynamic pressure or total heat input, when a specific vehicle is being used for a mission for which it was not designed.

10-2.2.5.1 Launch Site Limitations

Much work has been done on launch site limitations imposed by geographical location. For preliminary design studies, launch site limitations affecting flight mechanics are functions of latitude, since the longitude of the launch site only affects the time of launch.

The computation of vehicle performance should include the velocity vector component in the plane of a trajectory which is associated with the particular launch site location and the azimuth of the trajectory plane. A curve of this velocity component is presented as a function of its two dependent parameters in Figure 10-69. From the curve it is apparent that the velocity decrement resulting from launch at nonequatorial latitudes is only on the order of 200 ft/sec for the present launch sites (AMR and WTR).

When estimating a vehicle's payload capability, it is convenient to assume the velocity component normal to the launch azimuth plane to be merely an effective dog-leg of the trajectory plane. However, to more precisely determine the required launch azimuth, the launch azimuth angle should be perturbed an amount equivalent to the effective dog-leg angle resulting from the earth's rotational velocity component normal to the trajectory plane. This angle is:

$$\Delta A_z = \frac{87{,}548 \cos\lambda \cos A_z}{V_{bo_I} \sin\beta_{bo}} \text{ degrees} \qquad (103)$$

where:

ΔA_z = increment in launch azimuth angle

V_{bo_I} = inertial burout velocity in launch azimuth plane (ft/sec)

β_{bo} = inertial burnout flight path angle in launch azimuth plane

λ = geocentric latitude of launch site.

10-2.2.5.2 Loads and Aerodynamic Heating

To be considered early in any preliminary design are the maximum anticipated loads and heating parameters. The analysis presented here yields these loads and parameters to a reasonable degree of accuracy so that design criteria studies of staging. In preliminary design studies, the loads at both maximum acceleration and maximum dynamic pressure are determined by the structural engineer, and each piece of structure is designed with respect to the more critical load. The aerothermodynamicist is interested in the maximum heat rate and total heat input experienced by the vehicle during powered flight.

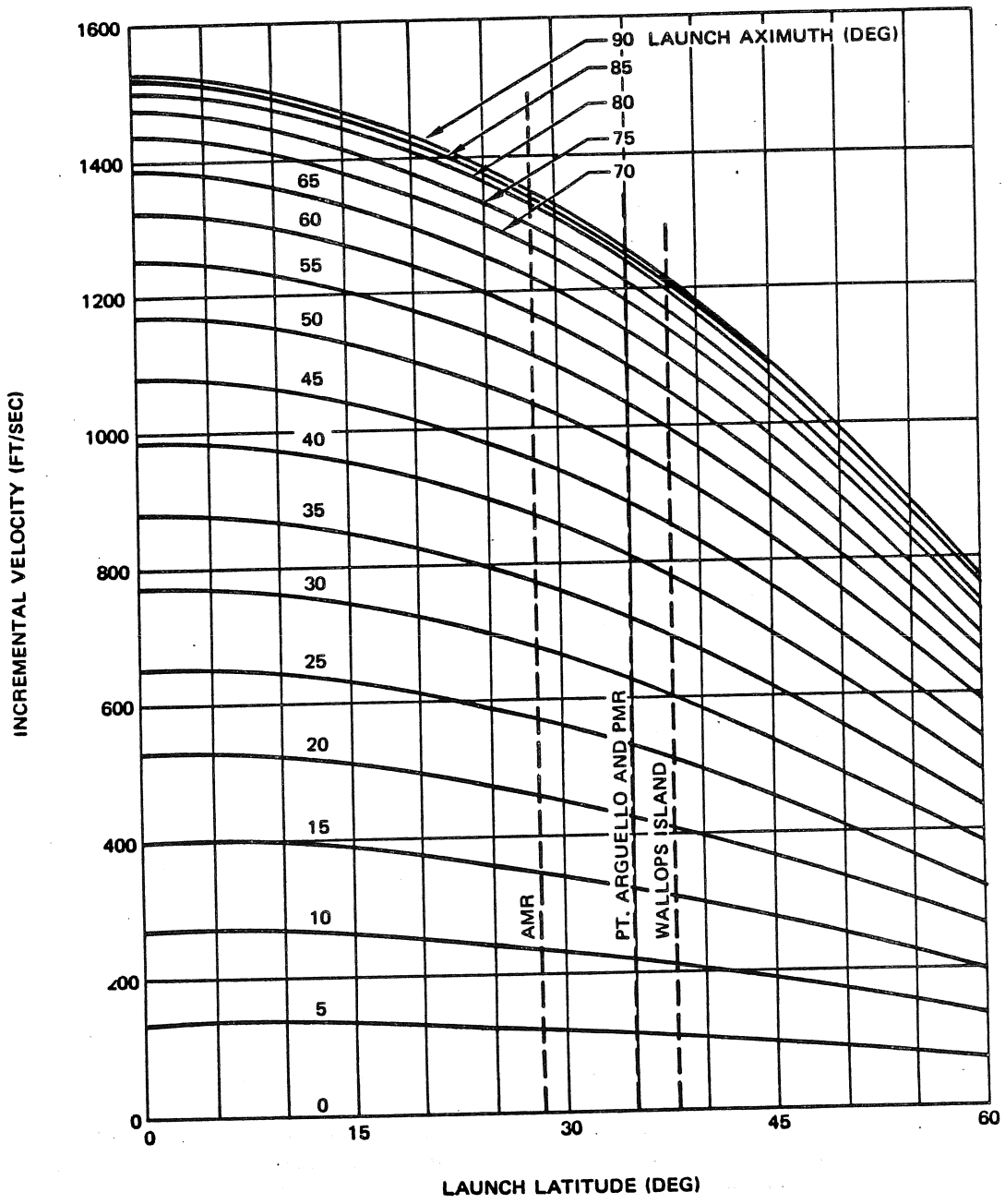

Figure 10-69. Earth's Rotation Velocity Increment at Launch Site

a. Staging – Of interest for structural considerations are axial acceleration and dynamic pressure just prior to staging. Assuming a rectilinear thrust-time curve, maximum acceleration occurs at burnout of each stage. Figure 10-70 provides data for obtaining the maximum acceleration of upper states. It is a plot of axial acceleration at burnout as a function of the initial vacuum thrust-to-weight ratio and the mass ratio. To evaluate the maximum acceleration for atmospheric operation, the following equation is applied:

$$a_{bo} = \left\{\left[1 - (1 - x)\frac{p_{bo}}{p_o}\right] r_{vac} - \frac{q_{bo}}{W_f/C_D A}\right\} r_v \qquad (104)$$

where:

$$r_{vac} = \frac{1}{x} \cdot \frac{F_{sl}}{W_f}$$

$$x = \frac{I_{sp_{sl}}}{I_{sp_{vac}}}$$

and the drag coefficient, C_D, is at the hypersonic value.

The dynamic pressure at burnout, q_{bo}, is found from Figure 10-71 by using the burnout velocity and altitude computed by methods described in the previous section. The atmospheric pressure ratio at burnout, p_{bo}/p_o is plotted against burnout altitude, h_{bo}, in Figure 10-72.

b. Maximum Dynamic Pressure – The maximum dynamic pressure and associated axial acceleration during booster operation are of interest to the designer. The nomograph presented as Figures 10-73 and 10-74 can be used to compute maximum dynamic pressure. This curve was derived empirically and is based on vehicle parameters representative of presently conceived vehicles. In constructing the curve, a rectilinear thrust-time variation was assumed, for other thrust-time variations, an initial thrust-to-weight ratio based on a mean thrust value will give reasonably accurate results.

From experience it has been found that maximum dynamic pressure occurs at altitudes between 30,000 and 35,000 feet. For space shots, maximum dynamic pressure usually occurs at altitudes near the upper limit 35,000 feet. For sounding rockets and highly lofted shots, maximum dynamic pressure occurs nearer the lower limit of 30,000 feet. Also maximum bending loads usually occur in these regions. This is caused by the fact the the greatest wind shears occur at altitudes between 30,000 and 40,000 feet.

To compute the axial acceleration:

$$a_{q_{max}} = \left\{\left[1 - (1 - x)\frac{p_{q_{max}}}{p_o}\right] - \frac{q_{max}}{(r_{vac})\left(\frac{W_f}{C_D A}\right)}\right\} a \qquad (105)$$

To aid in finding acceleration, Figures 10-75 and 10-76 are provided. Time of maximum dynamic pressure, $t_{q_{max}}$, is presented in Figure 10-75. Using $t_{q_{max}}$ for t in Figure 10-76, the parameter a is found. Since no computation of velocity is made in finding q_{max}, a curve of Mach number as a function of q_{max}, Figure 10-77 is included. It can be used to obtain C_D at a q_{max} for computing $W_f/C_D A$. Maximum dynamic pressure for both the upper and lower altitude limits has been plotted.

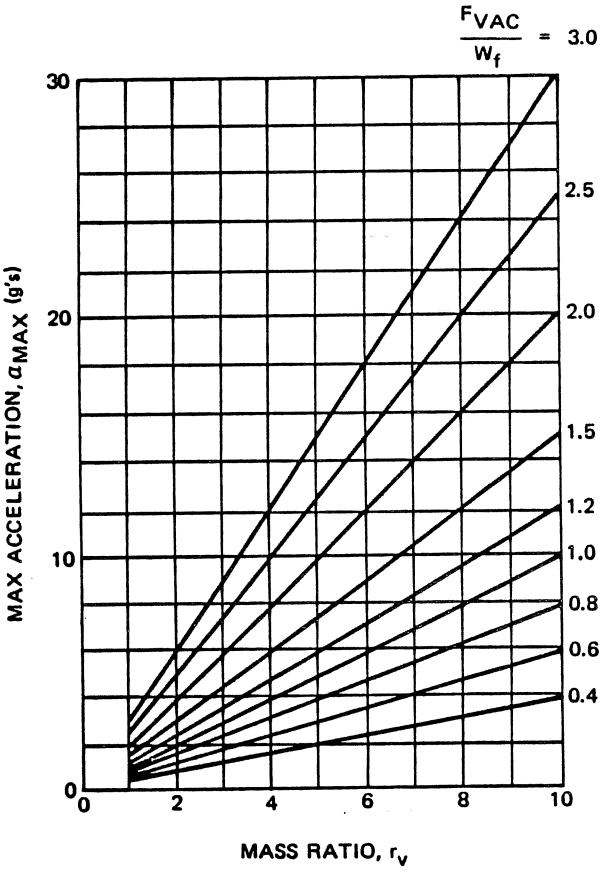

Figure 10-70. Axial Acceleration at Burnout (Vacuum Conditions)

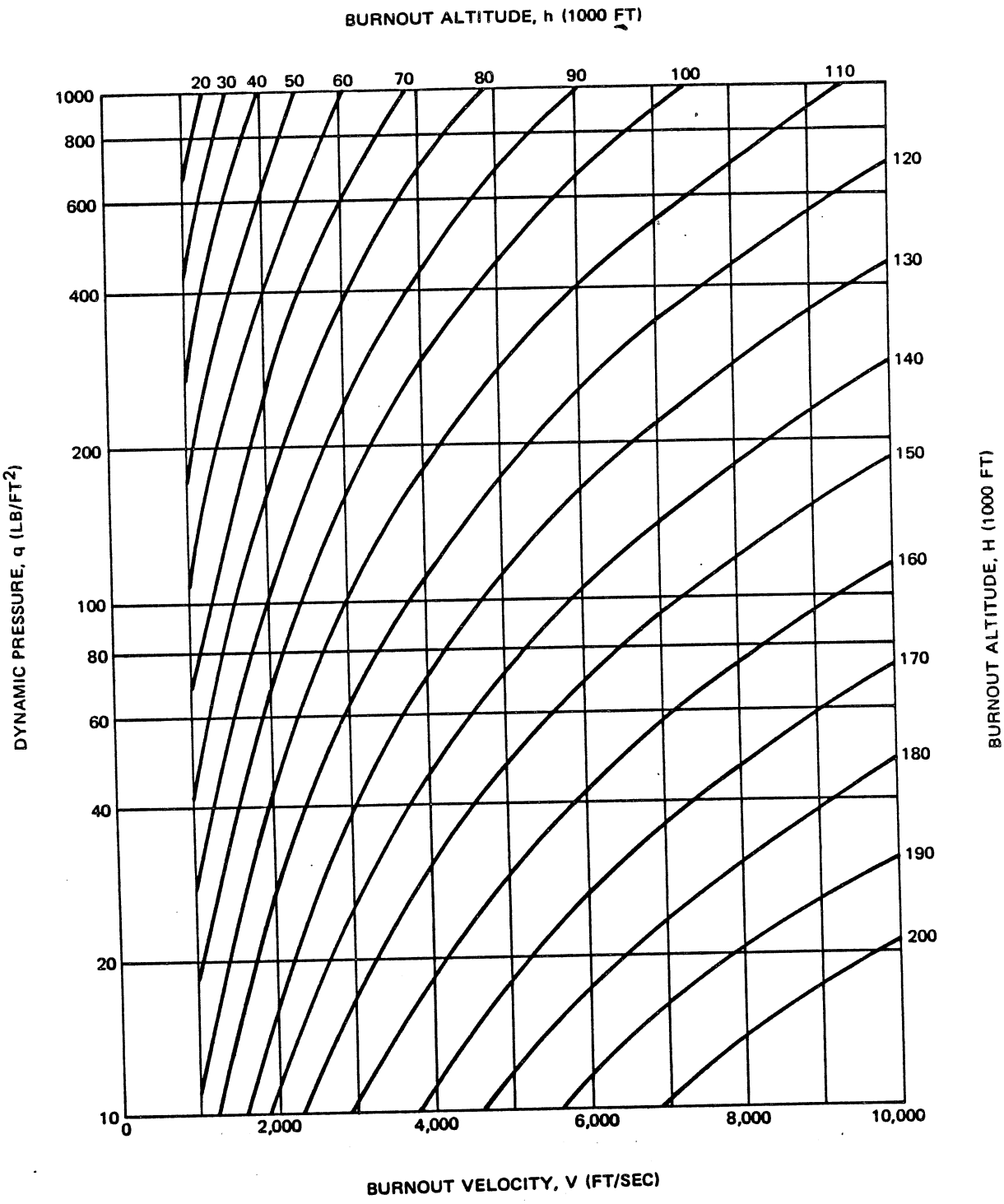

Figure 10-71. Dynamic Pressure During Stage Operation

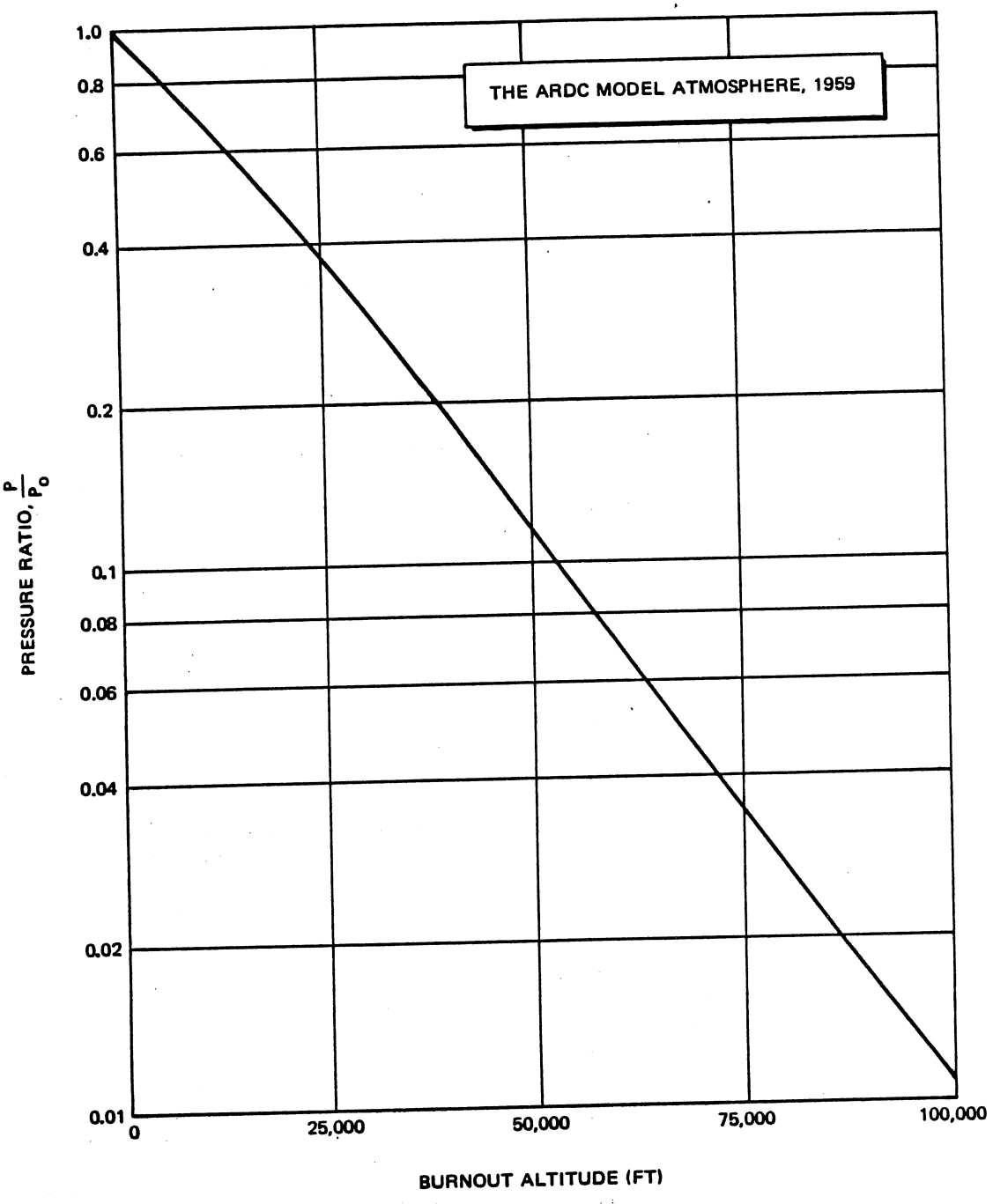

Figure 10-72. Pressure Ratio for Standard Atmosphere

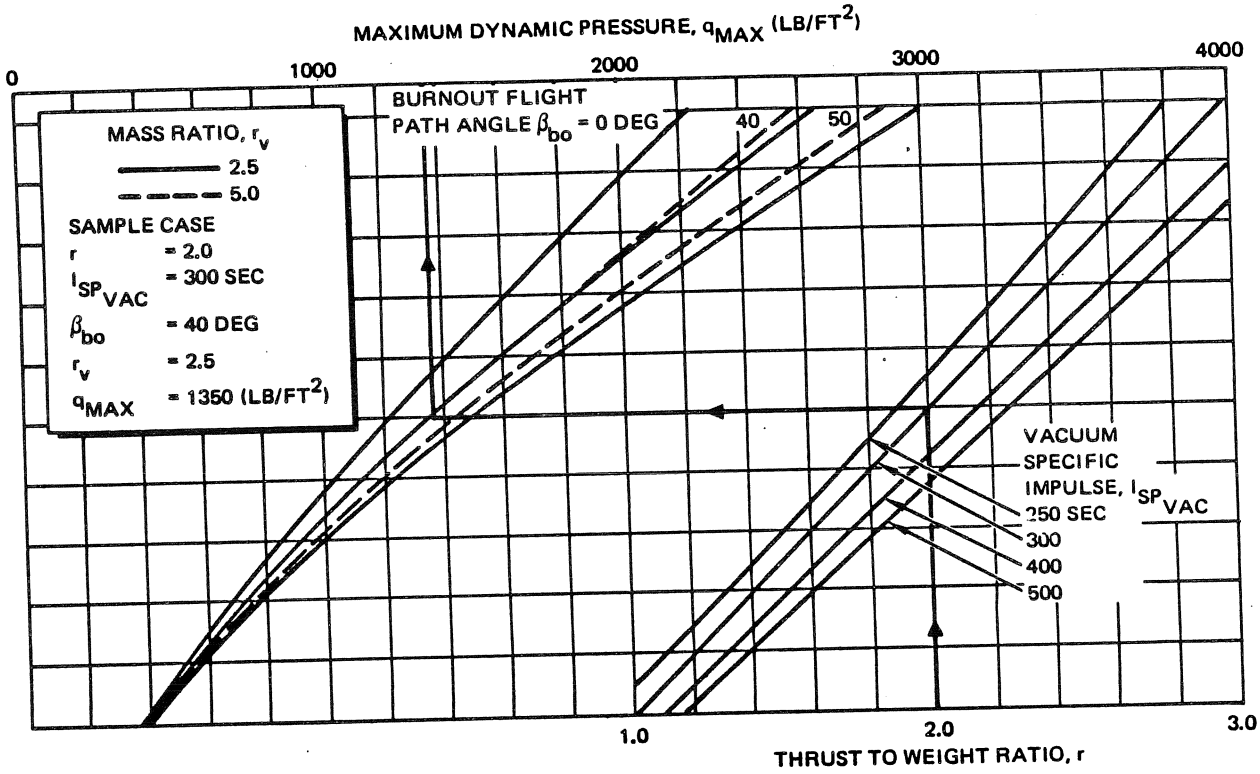

Figure 10-73. Maximum Dynamic Pressure Nomograph

c. Heating – Knowing the maximum heating rate and the total heat input experienced by the vehicle during ascent through the atmosphere, the thermodynamicist can estimate, for instance, the necessity for aerodynamic heating insulation to protect structural elements and also optimize with respect to added insulation weight the boiloff of cryogenic propellants.

The maximum value of the parameter, qV, experienced during booster operation is used as a conventient indicator of the maximum heating rate realized by the vehicle. This parameter has been plotted as a function of the vehicle paramters in nomograph form in Figure 10-78. The q in this parameter is dynamic pressure, not a heat transfer parameter.

The total heat input during booster operation, is approximated by $\int qVdt$. Although the integrated aerodynamic heat input may be proportional to $\int qVdt$, it is still necessary to determine if the temperature rise of the vehicle external skin is also proportional to this parameter. Obviously, it is the skin temperature, and not the aerodynamic heat input, which determines when overheating conditions are approached. Numerous factors, in addition to the convective boundary layer input, determine the temperature rise: namely, the thickness and specific heat of the skin, thermal conductivity and emissivity, the presence of insulation, the proximity of heat sinks such as structural members, heat losses to pressurizing gases inside propellant tanks, etc. It has been generally experienced that the total heating indicator, $\int qVdt$, and the maximum heating rate indication, qV_{max}, must be calibrated for each booster vehicle by actual skin temperature calculations to establish the maximum safe value. Any trajectory involving this booster may then be quickly evaluated from the standpoint of aerodynamic heating solely on the basis of the heating indicator. Current liquid propellant space boosters have total heating parameters on the order of 0.85 to 1.2 x 10^8 ft-lb/ft^2-sec., whereas Saturn and Post Saturn-type vehicles are apt to have total heating parameters on the order of 0.6 and 0.8 x 10^8 ft-lb/ft^2-sec. High initial thrust-to-weight ratio, solid-propellant vehicles are apt to have total heating parameters up to 4 to 6 x 10^8 ft-lb/ft^2-sec. Though heating is experienced

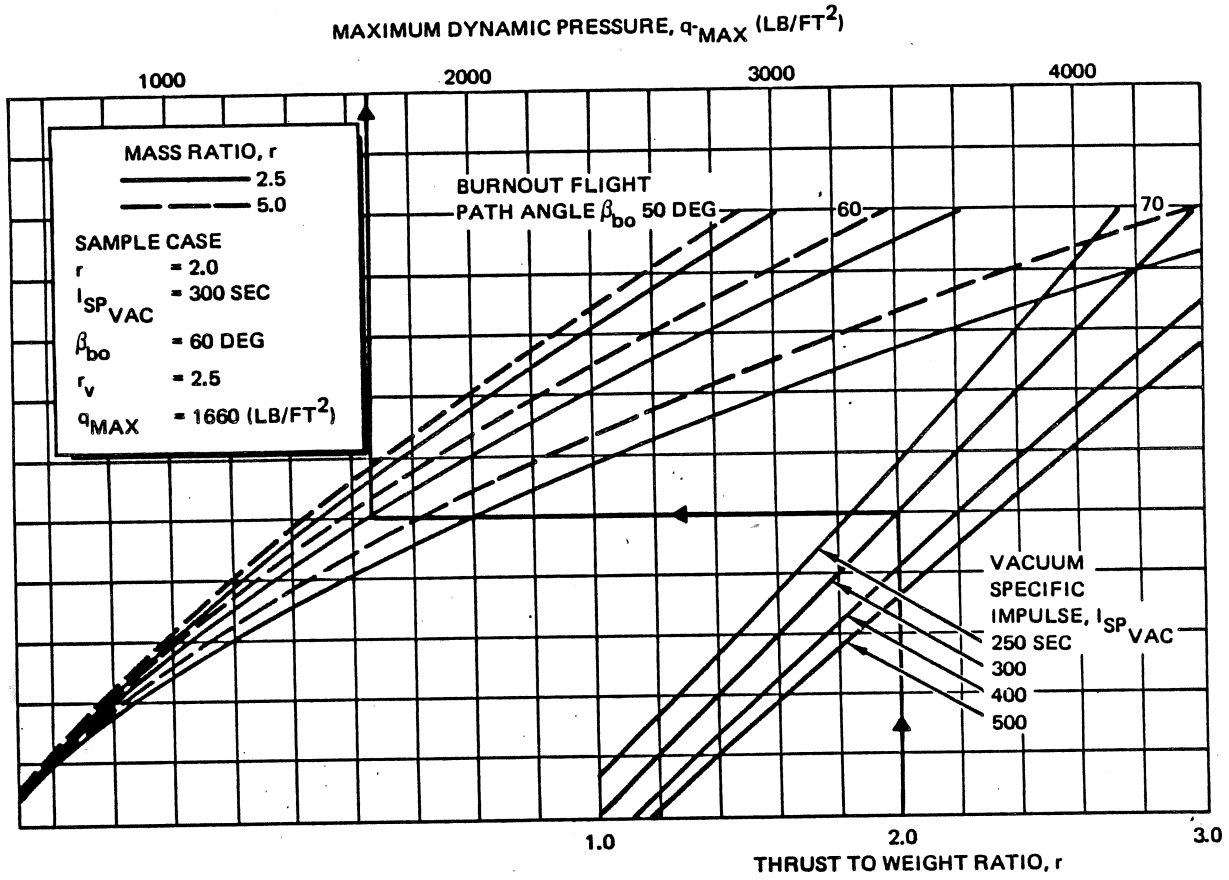

Figure 10-74. Maximum Dynamic Pressure Nomograph

during second-stage operations it is found that the total integral is nearly independent of the second-stage parameters.

10-2.3 Free Flight Rockets

The relationship between performance and physical characteristics for the following types of free flight rockets are discussed in this section:

a. Direct-fire rockets of the type normally employed in antitank or similar roles.

b. Sounding rockets which are launched vertically for the purpose of reaching extreme altitudes.

c. Surface-to-air rockets for an interceptor role (unguided).

d. Indirect-fire surface-to-surface artillery rockets.

e. Air-to-air or air-to-surface rockets (unguided).

Each of these types are discussed separately in the following sections, except Type e, because its performance and characteristics are similar to the other types, a through d, and are described by examining applicable combinations of data.

The parameters, or variables, that are considered in the evaluation of free-flight rocket performance can be divided into three major categories:

a. Factors associated with performance such as payload, velocity, range, altitude, time of flight, and launch angle.

b. Factors associated with the propulsion system such as energy management technique, specific impulse, thrust, burning time, and propellant-weight fraction.

c. Aerodynamic considerations such as shape, means of stablization, drag characteristics, and diameter.

Generally speaking, those factors associated with performance will be specified as fixed conditions for the solution of a given problem, with the possible exception of launch angle (in the case of indirect-fire artillery rockets) and time of flight.[16]

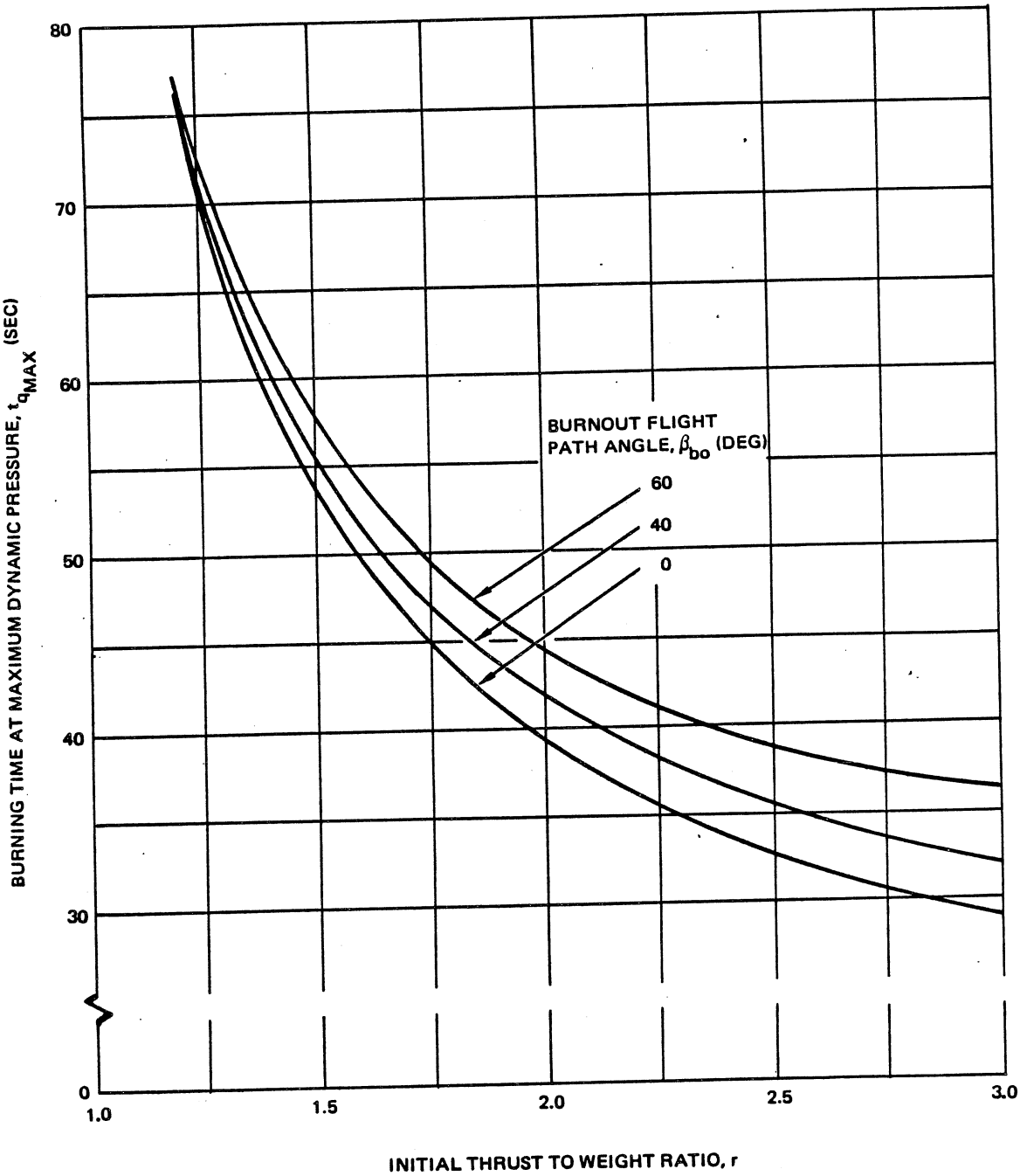

Figure 10-75. Time at Maximum Dynamic Pressure

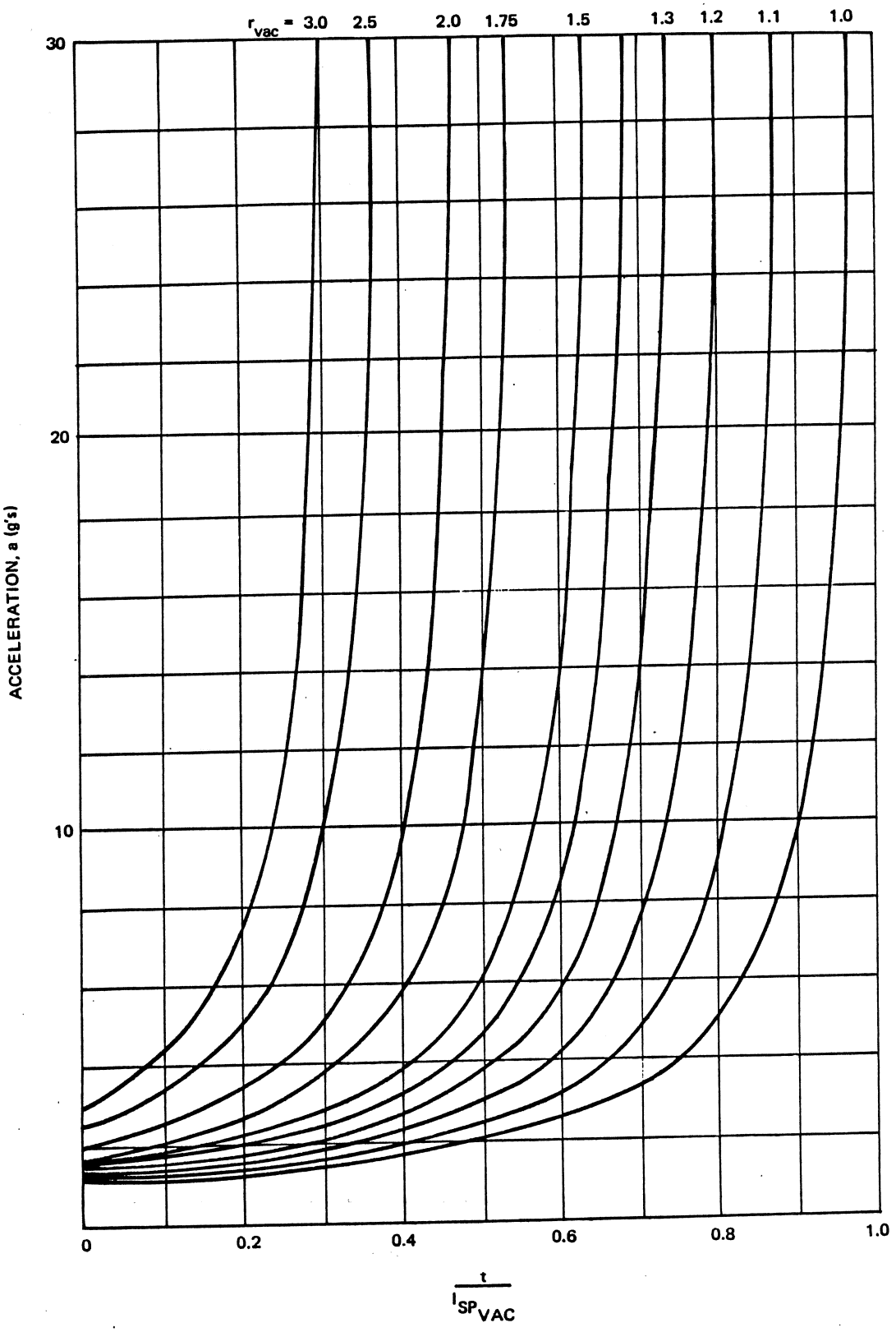

Figure 10-76. Axial Acceleration During Stage Operation (Vacuum Atmosphere)

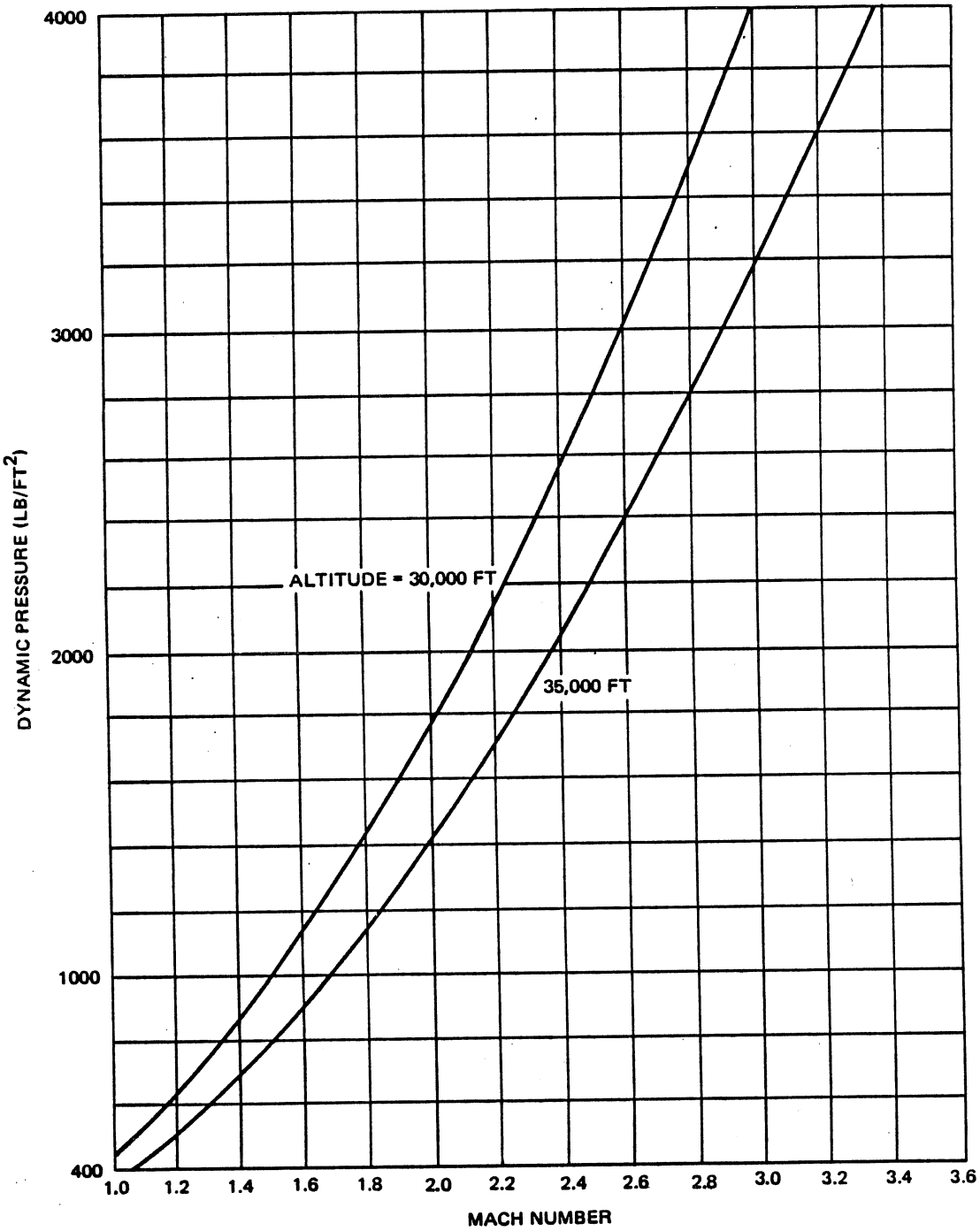

Figure 10-77. Mach Number at Maximum Dynamic Pressure

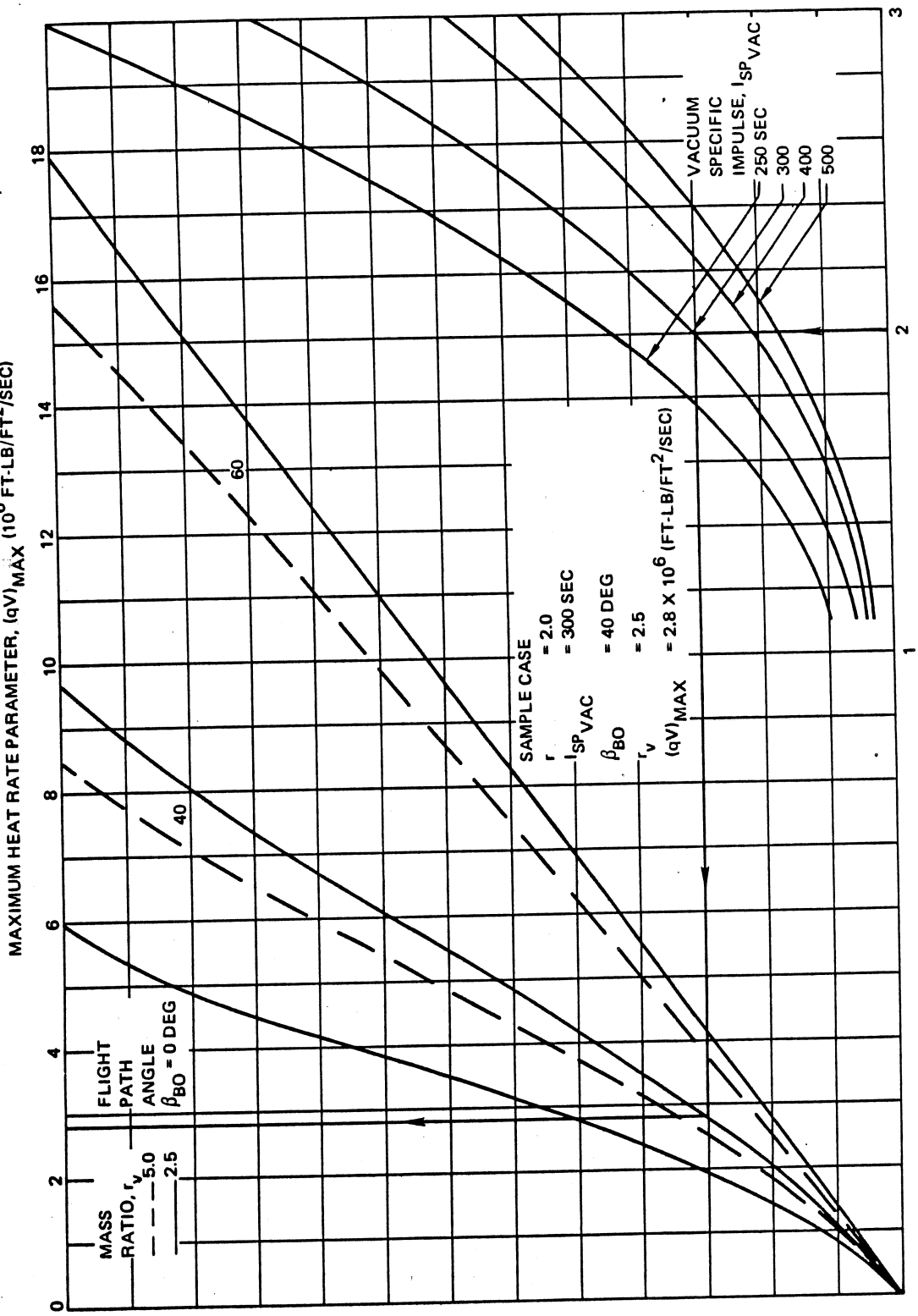

Figure 10-78. Maximum Heat Rate Parameter Nomograph

Determination or selection of optimum values of the propulsion system performance variables for a rocket system is called energy management. Energy management determines the magnitude of the boost and sustainer thrusts, and their duration. It also considers the duration of coast periods. The objective of energy management is to deposit the payload at the target with a minimum expenditure of propulsive energy while meeting performance, cost, and reliability requirements.

Where the effects of drag can be established accurately or neglected without undue effect, it is possible to estimate the velocity increment that the propulsion system must impart to the payload. It is then a simple matter to calculate the size the propulsion system required. There are various methods for estimating the velocity requirement, depending upon the application, and the degree of accuracy desired. The general relationships between performance and physical characteristics of free-flight rockets are essentially identical to those defined for conventional launch vehicles (refer to Paragraph 10-2.2 and Figures 10-11 and 10-15 for example). Specific detailed information is provided in the following paragraphs.

10-2.3.1 Direct Fire Systems

10-2.3.1.1 Velocity Requirements

If we assume that the effects of drag can be accounted for, it is usually a simple matter to determine the velocity requirement for a direct-fire rocket. In the absence of drag, the velocity requirement for a constant-acceleration boost phase is:

$$V_{bo} = \frac{R_T}{t_f - 1/2\, t_b} \qquad (106)$$

Where R_T = range to the target, t_f = desired time of flight and the desired burning distance or time, t_b.

Although this equation neglects the effects of drag and gravity, it is useful for approximation.

10-2.3.1.2 Parametric Performance

Both ballistic and maneuvering types of trajectories have been used for direct-fire systems. Either of these is essentially flat, however, and the degree of maneuver, if used, is generally limited. Therefore, for the purposes of parameterization, no distinction is made between the two types. Generally speaking, it is sufficient for performance calculations to assume a constant-altitude, line-of-sight trajectory.

Among the commonly employed energy management techniques for direct-fire rockets are:

a. Boost

b. Boost/sustain

c. Boost/coast/sustain.

In the boost method, the booster motor fires continuously throughout the flight of the rocket, or until fuel is depleted, and delivers a boost total impulse, I_B. This approach is by far the least complex of the above and has found use generally in the field of simple, unguided, ballistic rockets.

The boost/sustain approach consists of an initial thrust of the booster motor, F_B, for a prescribed burning time, t_{b_B}, and which provides a total impulse segment, I_B, followed by a sustaining thrust of the motor at a lower constant level, F_s, for a time, t_{bs}, with total impulse, I_s. While this approach offers performance advantages over the boost approach for some applications, it requires a more complex and costly motor construction. The boost/coast/sustain method is a variation of the latter technique with a coast period between the boost and sustain phases.

The technique used will depend to some extent on the level of performance required and on the intended method of use. Considering the method of use, we must determine whether burning outside the launch tube can be permitted. In the case of direct-fire infantry weapons, this cannot usually be permitted because of the exhaust plume effects; whereas for weapons to be employed on armored vehicles, there is no problem (aside from accurary considerations) involved in burning outside the launch tube. If burning outside the launch tube is permitted, either the boost or the boost/sustain approaches will apply. When burning outside the tube is not permitted, the choice is between the boost and the boost/coast/sustain approaches, with the boost approach generally limited to low performance systems by the maximum velocity which can be attained within the limits of the tube length and the rocket acceleration.

In defining the relationship between performance and physical characteristics for direct-fire rockets, it is not necessary to separate those rockets which must have a coast phase from those that do not. The reason for this is that, in the usual case, the additional time of flight will be negligible.

Figure 10-79 presents the relationship between target range, time of flight, t_f, and energy management scheme, F_S/F_B, for a given set of missile characteristics. The best energy management scheme is seen to be boost (no sustain) in cases where a minimum time of flight is desired. This is usually the case for systems which allow no control over the missile after launch. However, in cases where command guidance is used, time of flight is a secondary consideration, with the velocity of the

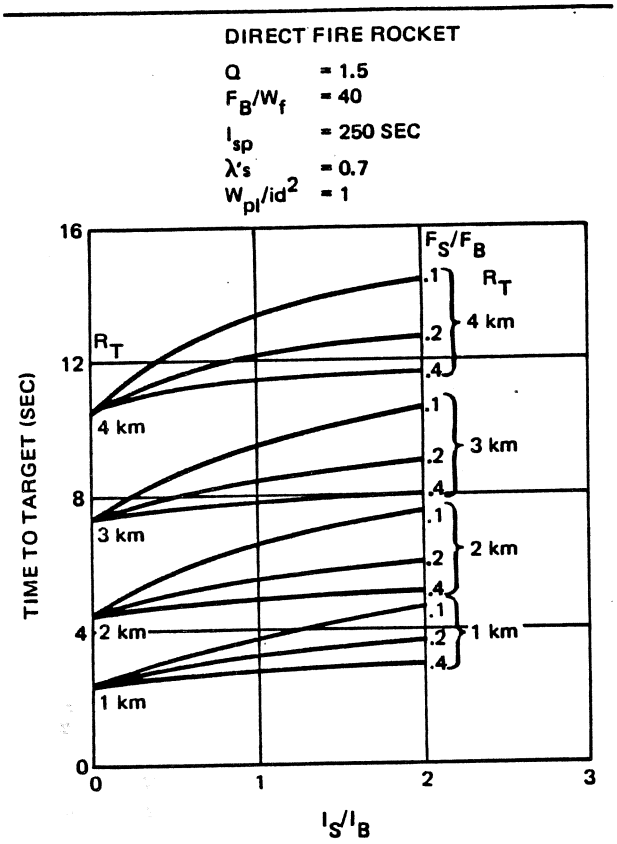

Figure 10-79. Direct Fire – Boost/Sustain; Effect of Impulse Ratio on Time to Target

missile being limited by considerations of gunner capabilities, command data rates, and type of command link. Since the considerations involved in the determination of time of flight (or average velocity) for the command-guided cases are many and varied, it is desirable to concentrate for the remainder of this discussion on the system which yields minimum time of flight, namely, the boost system.

Figure 10-80 presents trade-offs with respect to growth factor, time of flight, range, and boost acceleration. A performance limit appears to be reached at a growth factor of about 3.0 because increases beyond this point reduce the time of flight an insignificant amount. Increasing the boost acceleration reduces the time of flight, but decreases the percentage of powered flight. For example, at a growth factor of 1.7 and F_B/W_f = 20 the burning distance is about 3 km, and we reach 4 km in 9.7 seconds. If we increase F_B/W_f to 80, the burning distance is reduced to about 1 km and we reach 4 km in 8.5 seconds. This illustration points out another of the choices facing the designer, namely, the trade-off between time to target and percentage of powered flight. These parameters, in turn, are directly influenced by the drag and gravity velocity losses associated with the choise of energy management scheme employed (See Paragraph 10-2.1). For example: A long burning time (low F_B/W_f) tends to reduce drag losses but gravity losses are increased and conversely short burning times (high F_B/W_f) reduces gravity losses but increase drag.

Once the designer has examined the trade-offs between range and time of flight, he may wish to determine the effects of various design parameters (Table 10-9) on the missile weight (or growth factor) for a specified performance level. For example, Figure 10-81 shows the trade-off between W_{pl}/id^2 (Equation 24), and growth factor (ratio of rocket gross weight to payload weight) for a specified performance level of 2 km in 3 seconds. Figure 10-82 illustrates the trade-off between step mass fraction (ratio of usable propellant to gross weight), λ'_s, I_{sp} and growth factor for the same performance level. In the final analysis, performance and design selection may be based on the practical considerations of cost, reliability, and availability of state-of-art technology for building the missile.

The preceding paragraphs illustrated the types of trade-offs with which the designer of direct-fire rockets must be concerned. From this discussion, the following conclusions can be drawn:

a. For minimum time to target, the boost system is superior to the boost/sustain system.

b. The choice of boost acceleration must result from a consideration of the trade-off between time to target and percentage of powered flight desired.

c. Increasing λ'_s, I_{sp}, W_{pl}/id^2, or F_B/W_f results in decreased missile weight for a given payload weight and specified performance (time to target).

d. Increasing the growth factor beyond about 3.0 for all-boost systems results in negligible performance increase for the range of parameters studied.

10-2.3.2 Sounding Rockets

10-2.3.2.1 Vertical Ascent and Ballistic Trajectory

For a single stage rocket in vertical flight in drag-free space, the summit altitude, h_m, is plotted in Figure 10-83 as a function of vehicle mass ratio, r_v, and specific impulse, I_{sp}. This figure is based on the use of Equations 35, 36, and 38.

It is possible to compute with fair accuracy the range on the earth's surface of a ballistic rocket by treating the powered portion of the trajectory as vertical and the coasting portion as elliptic. Such a computation ignores, of course, the increment of range achieved during powered flight, which may be small for a single-stage rocket, and it ignores the effect on the burnout velocity of the tilt of the powered flight path (Paragraph 10-2.2). Both effects increase the range beyond the computed value.

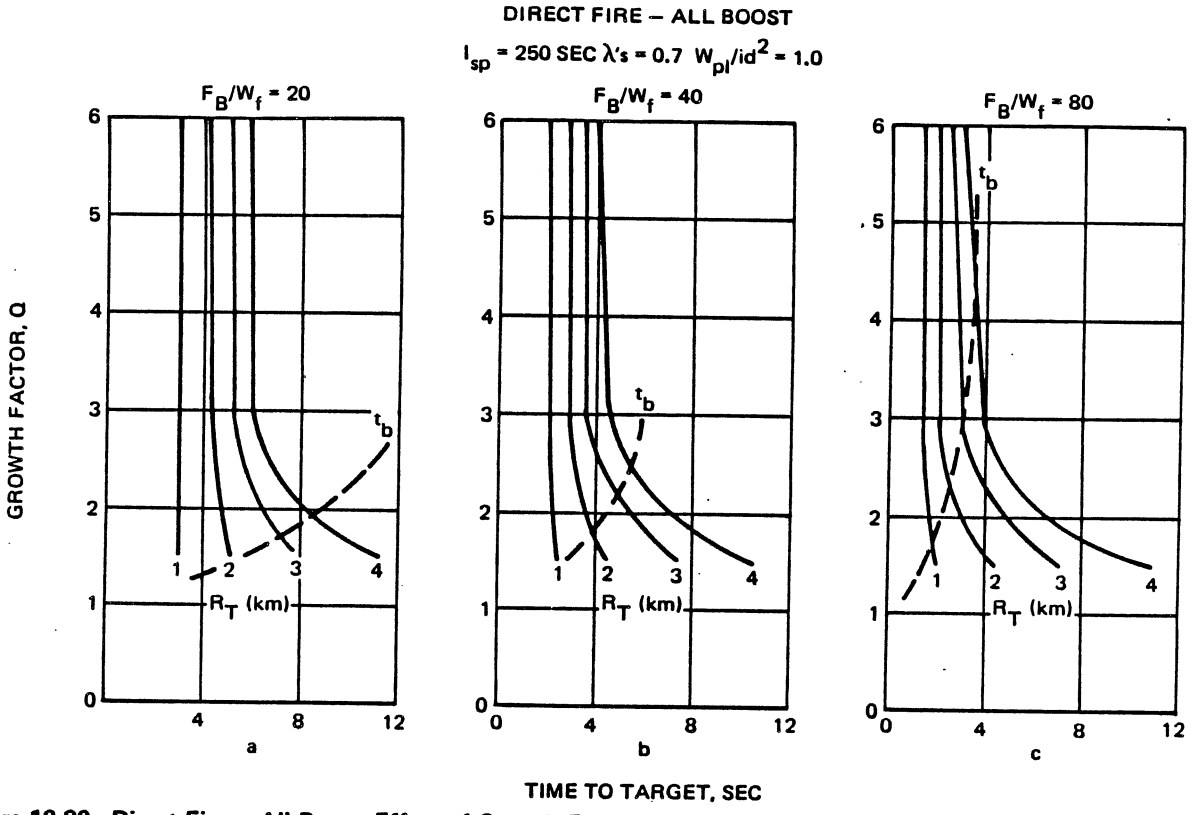

Figure 10-80. Direct Fire – All-Boost; Effect of Growth Factor on Minimum Time to Target

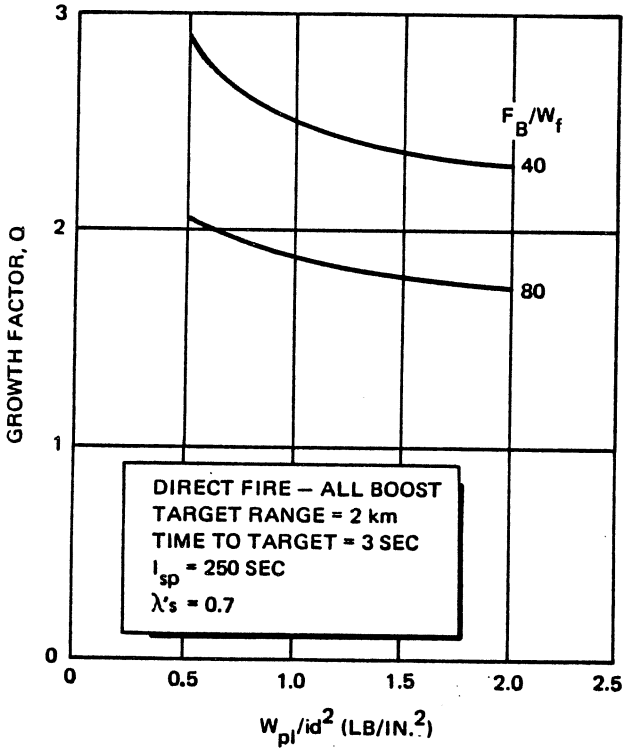

Figure 10-81. Direct Fire – All-Boost; Effect of Ballistic Coefficient on Growth Factor

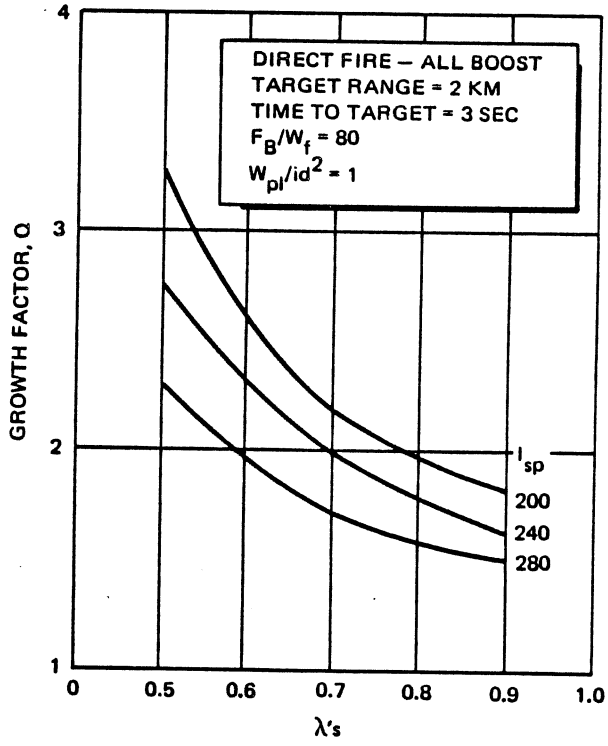

Figure 10-82. Direct Fire – All-Boost; Effect of Propellant Mass Fraction on Growth Factor

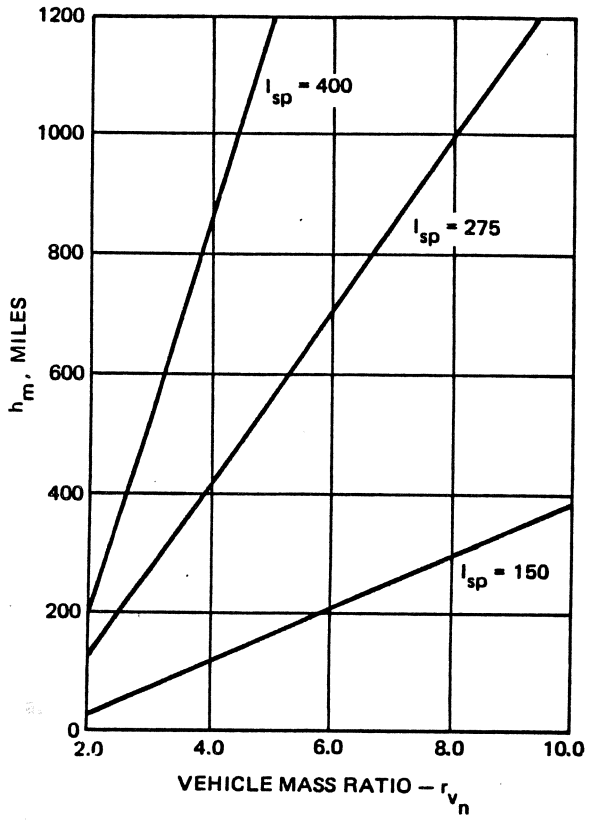

Figure 10-83. Summit Altitude of a Rocket in Drag-Free Vertical Flight

The maximum coasting range, R, along the surface of a nonrotating earth can be determined by application of the theory of elliptic orbits in a central-force inverse-square field.[25,26]

$$R = 2 r_e \sin^{-1} \frac{V_{bo}^2}{2 g_o r_e - V_{bo}^2} \qquad (107)$$

Where the angle is expressed in radians for small V_{bo} this reduces to

$$R = \frac{V_{bo}^2}{g_o} \qquad (41)$$

For V_{bo} large, but less than $\sqrt{2 g_o r_e}$, the denominator of Equation 107 approaches zero and R becomes πr_e; that is, a burnout velocity of $(2 g_o r_e)^{1/2}$ is just sufficient for entry into a circular satellite orbit. The optimum angle of elevation γ, (Figure 10-18) of the trajectory at burnout varies with the intended range, R, as:

$$\tan \gamma_{bo} = \frac{1 - \sin (R/2 r_e)}{\cos (R/2 r_e)} \qquad (108)$$

Note: $\gamma_{bo} = 90 - \beta_{bo}$ (degrees)

For short ranges, γ_{bo} is 45 degrees, which is the familiar result for a parabolic trajectory on a flat earth. For long ranges the right side of Equation 108 is always less than unity, so that γ_{bo} is less that 45 degrees. For the extreme case of a satellite, γ_{bo} is zero. The maximum range and optimum angle of elevation are shown in Figure 10-84 as functions of the burnout velocity, based on Equations 107 and 108.

The range calculation can be corrected for the earth's rotation by permitting V_{bo} in Equation 107 and 41 to represent the vector sum of the relative burnout velocity and the velocity of the launching site, and by adding to the calculated range the distance that the landing point moves in the direction of the flight path of the rocket during flight. These corrections cancel out for the case of a short-range ballistic rocket.

10-2.3.2.2 Parametric Performance

The only trajectory profile to be considered here for the sounding rocket is vertical ascent. In some cases it may be desirable to launch a sounding rocket away from the vertical to ensure impact within a given area, but for purposes of performance parameterization, the vertical ascent is sufficient.

The energy management techniques which are used with sounding rockets are:

a. Boost

b. Boost/sustain

c. Staged boost

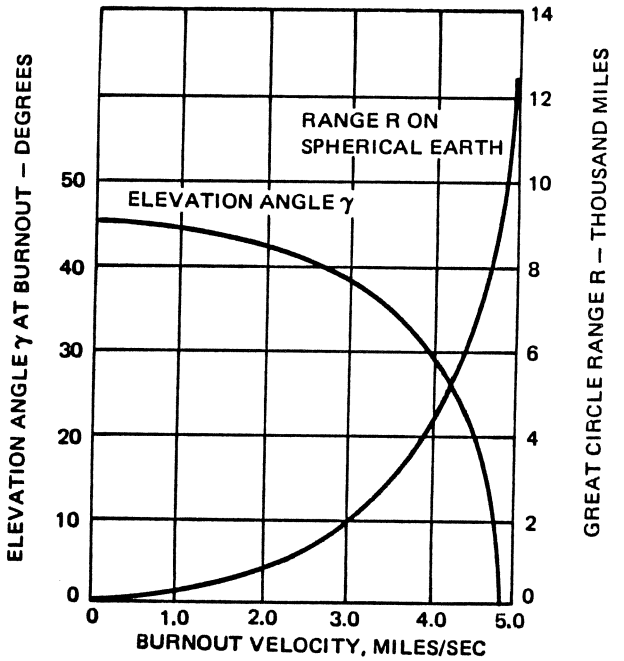

Figure 10-84. Range R on a Spherical Nonrotating Earth, and Optimum Angle of Elevation γ_{bo} at Burnout as a Function of Burnout Velocity V_{bo}

In the staged boost technique, the total thrust is delivered by a series of booster motors, each jettisoned upon burnout. This technique is not used frequently and is not specifically discussed here. In general, performance evaluation for staged boost systems is similar to that for multistaged vehicles which is presented in other sections of the manual.

The choice between these approaches must be the result of a trade-off, considering the boost system to be the simplest, cheapest, most reliable, and least efficient; whereas the staged boost would be the most complex, most expensive, most efficient, and least reliable. Furthermore, the staged boost has the hazards of falling motor cases. The boost/sustain approach would be intermediate in all of the above considerations.

In Figure 10-85 the relationship between growth factor, energy management scheme, boost acceleration, and peak altitude is presented for sounding rockets. It can be seen here that the boost/sustain approach would provide the lowest missile weight for a given altitude. The relationship is shown for a single set of I_{sp}, λ's and W_{pl}/id^2, some shifting of data would occur if these parameters were changed.

For any given maximum altitude, the growth factor will be inversely proportional to λ's, I_{sp}, and W_{pl}/id^2. This is shown in Figures 10-86 and 10-87 for summit altitudes of 150,000 ft and 250,000 ft. These curves are for the all-boost case; however, the boost/sustain curves would be similar. From these curves, we see that the lightest missile results from a high performance motor (high λ's and I_{sp}) and a large payload-to-diameter ratio.

10-2.3.3 Surface-to-Air Rockets

10-2.3.3.1 Trajectory Profile

The unguided surface-to-air rocket flies a ballistic trajectory and may be launched at any quadrant-elevation angle, QE, e.g., elevation angle from the horizontal at the missile longitudinal axis, necessary for intercept of the target. Usually, the rocket will be designed to reach a given altitude in a given time and, therefore, the vertical ascent is of primary concern. For this reason the vertical trajectory is normally used to size the rocket, although it must be kept in mind that the vertical distance traveled in a given time will be slightly less for trajectories other than the vertical.

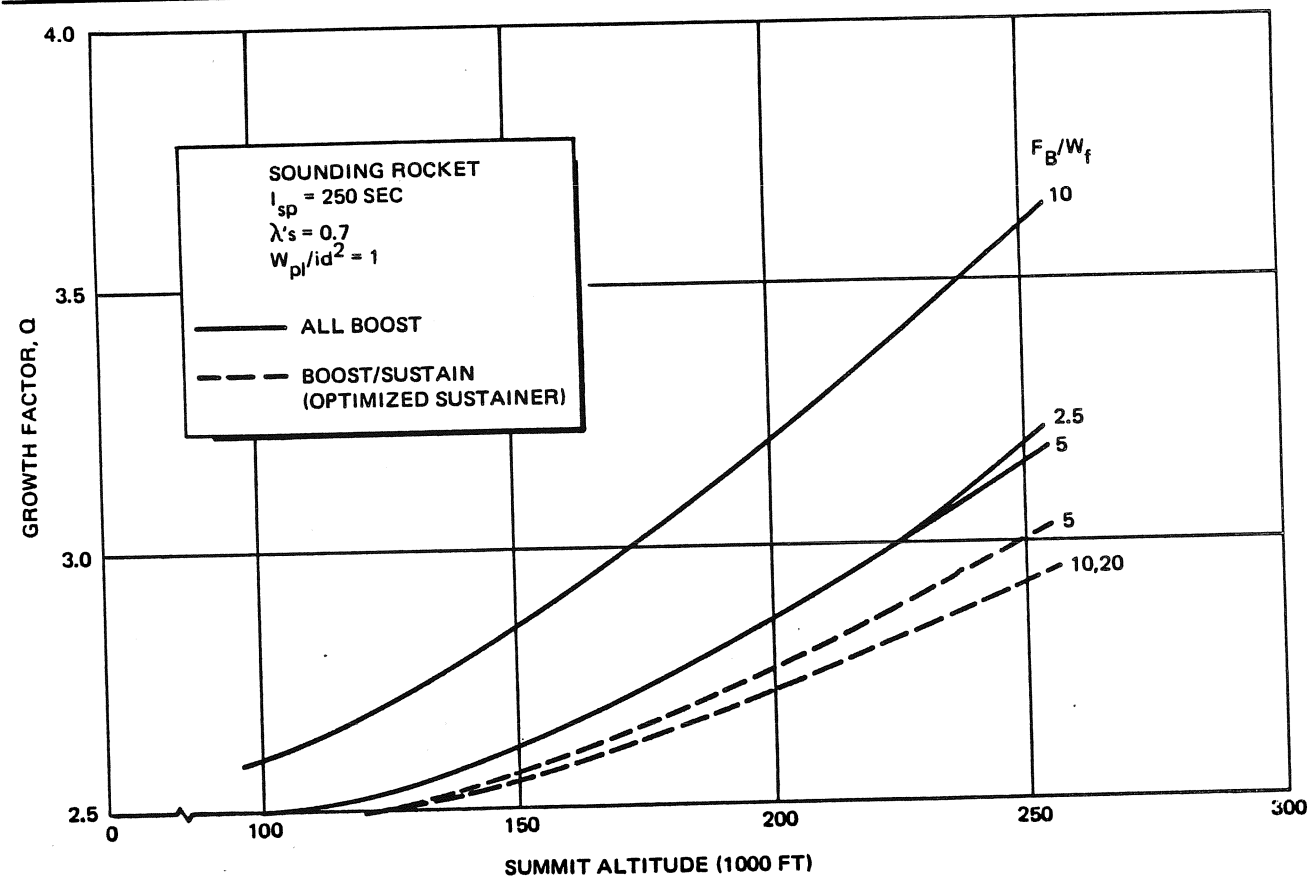

Figure 10-85. Sounding Rocket – All Boost and Boost/Sustain; Effect of Growth Factor on Summit Altitude

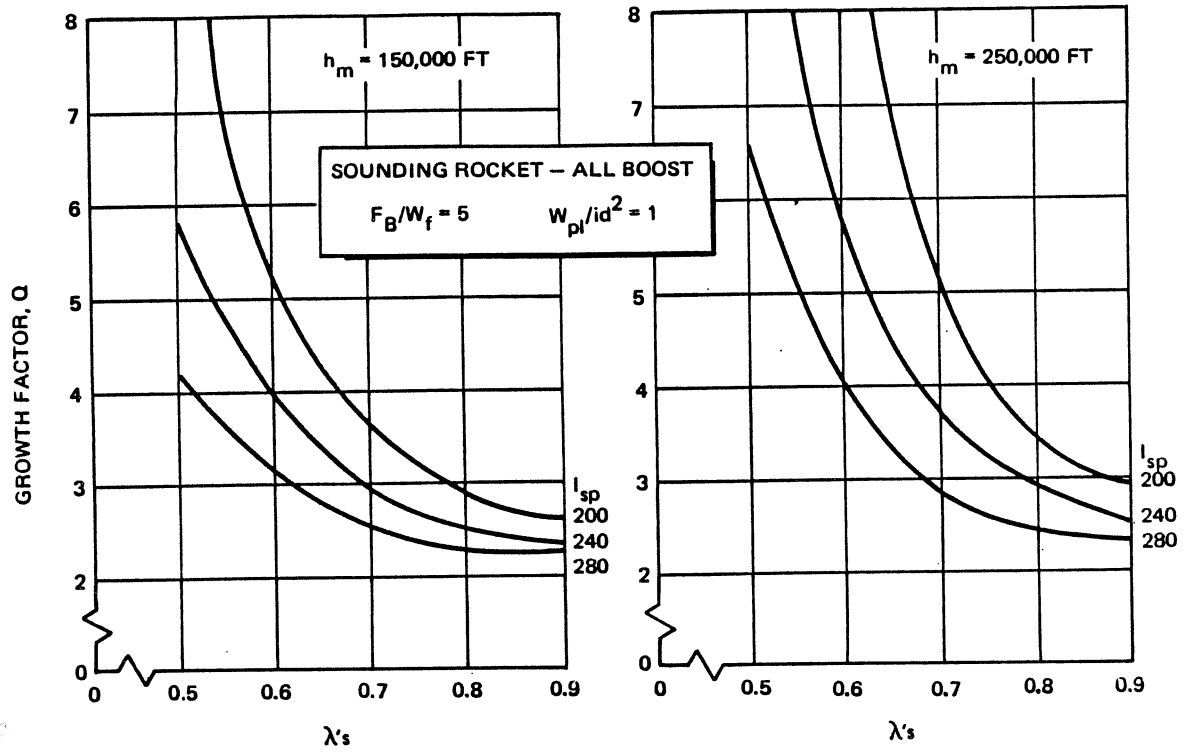

Figure 10-86. Sounding Rocket – All-Boost; Effect of Propellant Weight Fraction on Growth Factor

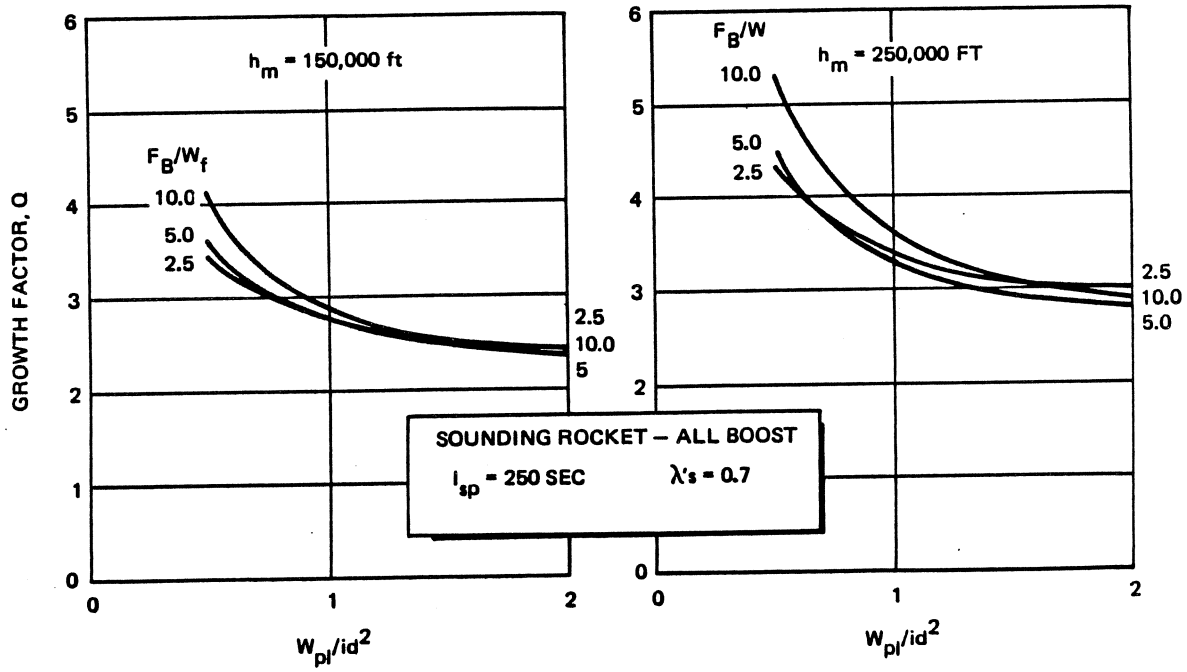

Figure 10-87. Sounding Rocket – All-Boost; Effect of Ballistic Coefficient on Growth Factor

10-2.3.3.2 Energy Management

Energy management techniques applicable to surface-to-air rockets are:

a. Boost

b. Boost/sustain

c. Staged boost

If we consider that minimum time to target will be desired for the surface-to-air rocket, and that achievable accuracy will limit this type of rocket to low altitude application (under 30,000 ft), the boost approach will usually be found to be the most attractive. For this reason, the discussion will be limited to the boost approach.

10-2.3.3.3 Parametric Performance

Figure 10-88 presents the relationship between growth factor, boost acceleration, and time to altitutde for target altitutde of 20,000 ft.

Note that, an increase in boost acceleration reduces the time of altitude. An increase in growth factor above a value of 5 would decrease time to altitude very little.

The trade-off between I_{sp}, λ's, and growth factor for a specified performance level of 20,000 ft in 5 sec is given in Figure 10-89. Figure 10-90 illustrates the trade-off between W_{pl}/id^2, F_B/W_f, and growth factor for the same performance level.

From the previous discussion, the following conclusions may be drawn:

a. Increasing growth factor above 5 results in negligible performance increase for the range of parameters studied.

b. Increasing λs, I_{sp}, and W_{pl}/id^2 results in decreased missile weight for a given payload weight.

10-2.3.4 Surface-to-Surface Indirect-Fire Systems

10-2.3.4.1 Velocity Requirements

A crude approximation of the velocity requirement for the indirect-fire rocket is given by another form of the drag-free range Equation 107:

$$R = \frac{V_{bo}^2 \sin(2QE)}{g_o} \qquad (109)$$

which, for the optimum launch angle of 45 degrees yields the required velocity increment

$$V_{bo} = \sqrt{R\, g_o} \qquad (110)$$

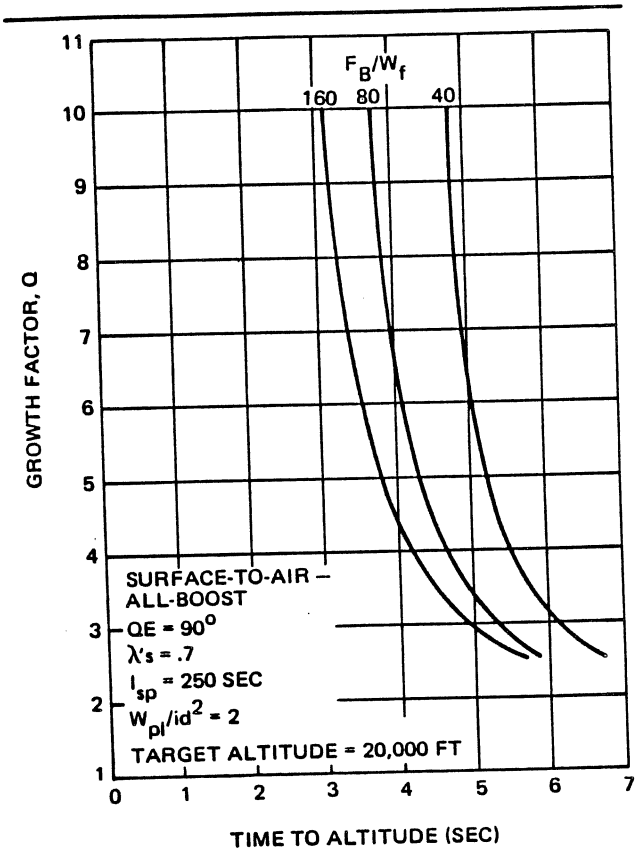

Figure 10-88. Surface-to-Air — All-Boost; Effect of Time to Altitude on Growth Factor

While the drag-free approximations are adequate for preliminary work on most missile systems, the relatively greater effect of drag on the indirect-fire system often requires a more accurate calculation. This can be obtained through use of the ballistic range table[16] which introduces the effect of drag in the form of the ballistic coefficient $W_f/C_D\, d^2$ or W_{pl}/id^2. Figure 10-91 presents the relationship between range, burnout velocity and ballistic coefficient based on range table information. Since the ballistic coefficient is not independent of burnout velocity, the use of Figure 10-91 requires an iterative procedure for any given payload and diameter. However, these data are useful for rapid, accurate estimation of performance parametrics for high acceleration surface-to-surface rockets.

10-2.3.4.2 Energy Management

Among the methods that have been used to impart propulsive energy to indirect-fire rocket systems are:

a. Boost

b. Boost/sustain

c. Staged boost

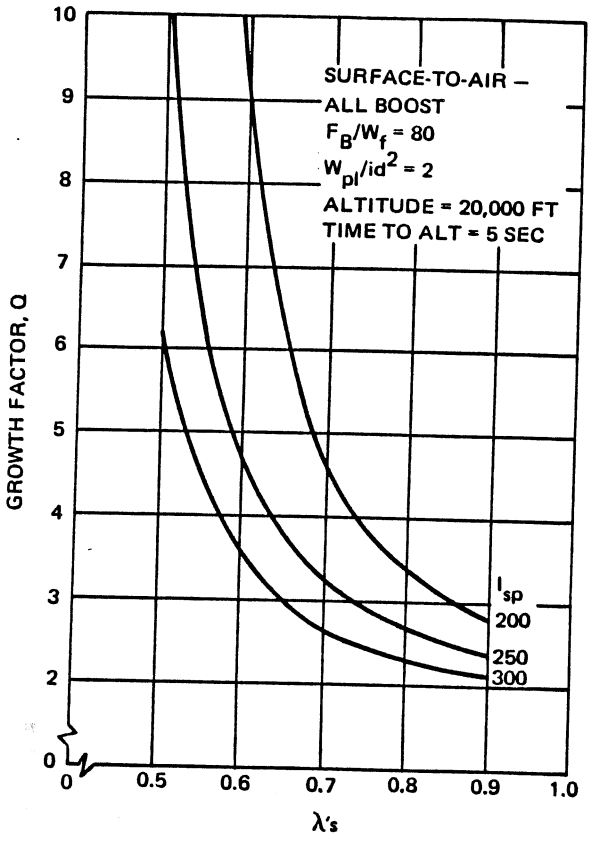

Figure 10-89. Surface-to-Air – All-Boost; Effect of Propellant Mass Fraction on Growth Factor

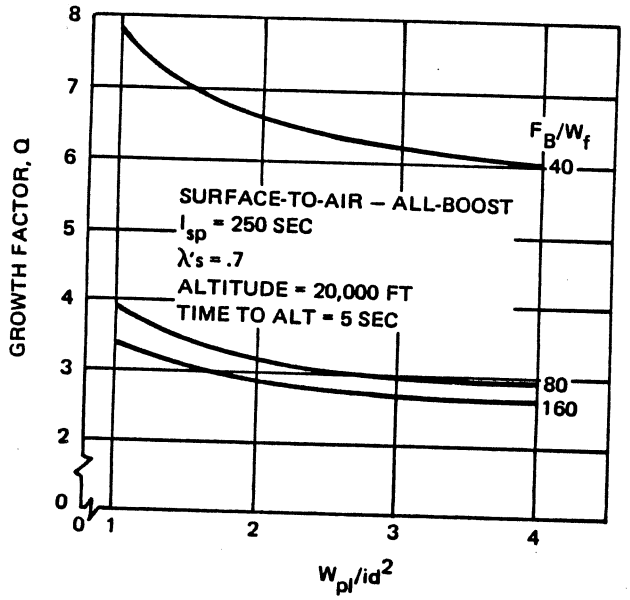

Figure 10-90. Surface-to-Air – All Boost; Effect of Ballistic Coefficient on Growth Factor

In the boost method, the booster motor fires continuously throughout the flight of the rocket, or until fuel is depleted. This approach is by far the least complex of the above and has found use generally in the field of simple, unguided, ballistic rockets.

The boost/sustain approach consists of an initial thrust of the booster motor, followed by a constant sustaining thrust of lesser magnitude. While this approach offers performance advantages over the boost approach for some applications, it requires a more complex and costly motor construction.

In the staged boost approach, the total thrust is delivered by a series of booster motors, each jettisoned upon burnout. This is the most efficient means of energy management but its use is limited to those cases where weight considerations override the cost and reliability penalties of staging, and where the hazards of falling motor cases can be permitted. Since very few rockets within the scope of this section meet these limitations, this discussion will not include the staged boost approach.

10-2.3.4.3 Parametric Performance

The angle at which the rocket must be launched in order to achieve maximum range is of initial interest to the designer. Figure 10-92 presents the effect of boost acceleration F_B/W_f and growth factor Q on the optimum launch angle for an all boost system, with fixed values of I_{sp}, λ's, and W_{pl}/id^2. Although the data would be different if these parameters (I_{sp}, λ's, W_{pl}/id^2) were varied, the trends of the curve are worth noting. Low accelerations require the highest launch angles, with the dependence of launch angle on acceleration being strongest at low accelerations. Higher growth factors indicate higher launch angles because they are equivalent to longer boost burning times at any given level of acceleration.

For a boost/sustain system, the optimum launch angle, QE, will be a little greater than for an all-boost system as shown in Figure 10-93. As the ratio of sustainer thrust to booster thrust is decreased and/or the ratio of sustainer impulse to booster impulse is increased, an increase in optimum launch angle is indicated.

Figure 10-94 presents the relationship between growth factor and range for an all-boost system with QE optimized and λ's, I_{sp}, W_{pl}/id^2 held constant. It is seen that the lower accelerations permit more efficient engergy management schemes since they yield a lower growth factor for any specified range. Although this curve is constructed for only one value each of I_{sp}, λ's, and W_{pl}/id^2, it is indicative of trends. Therefore the growth factor (for a given range) will be inversely proportional to I_{sp}, λ's, and W_{pl}/id^2. Trade-offs between these parameters should be examined as discussed later on in

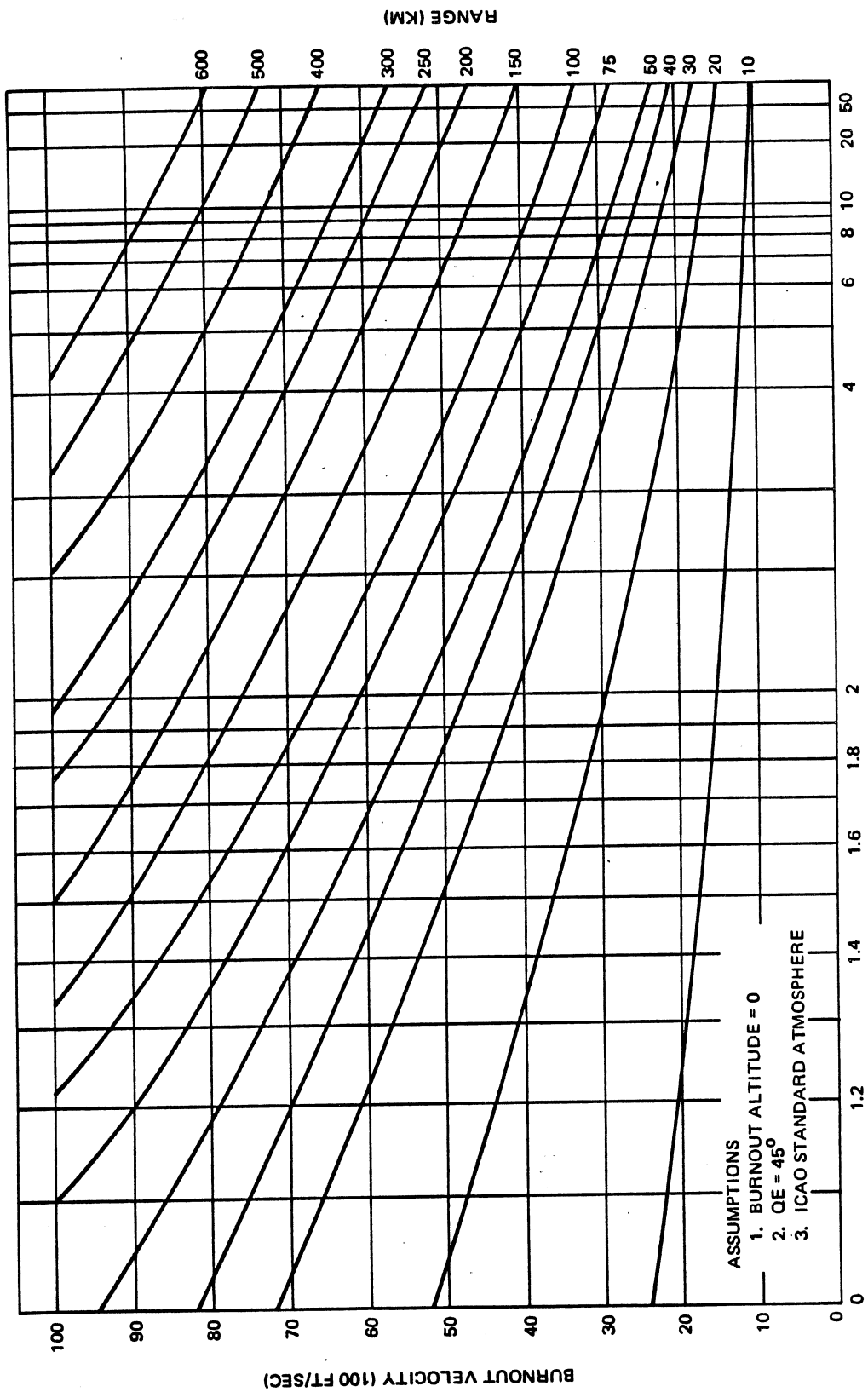

Figure 10-91. Effect of Ballistic Coefficient on Burnout Velocity

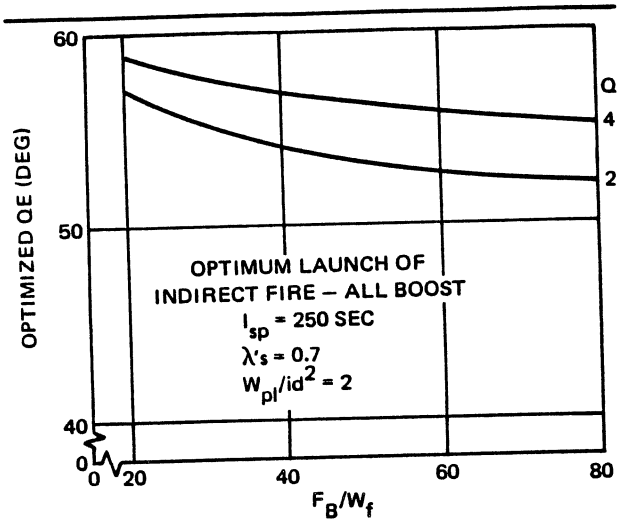

Figure 10-92. Indirect Fire – All-Boost; Effect of Thrust-to-Weight Ratio on Optimum Launch Quadrant Elevation

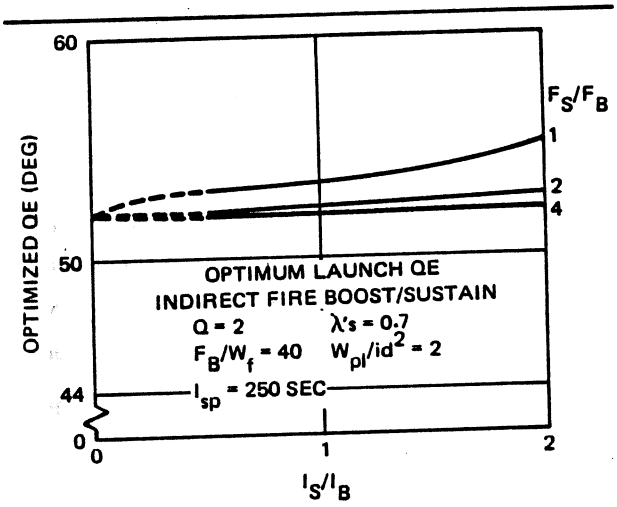

Figure 10-93. Indirect Fire – Boost/Sustain; Effect of Impulse Ratio on Optimum Launch Quadrant Elevation

this section. Examination of Figure 10-94 curve shows that significant range increases can be obtained for relatively minor rocket-weight increases. For example, whereas a growth factor of about 2 is required for a range of 30 kilometers, a 25 percent increase in missile weight (an increase of Q from 2.0 to 2.5) doubles the range (to 60 km).

The relationship between growth factor and range for a boost/sustain system will depend upon the choice of sustainer parameters in addition to the parameters discussed above for the all-boost system. There is no unique method for determining optimum sustainer parameters since the choice will depend upon which characteristics of the rocket the designer is attempting to optimize; for example, weight or accuracy. The designer has a choice of methods for providing the sustainer impulse. This can be done with separate booster and sustainer motors, or by one motor with two thrust levels. In the case of separate motors, it is possible to achieve high specific impulse with each motor, but the propellant weight fraction of the combination is usually lower than for a single motor with two thrust levels. In the latter case of a single motor with two thrust levels, the specific impluse of the sustainer operation will be less than for the booster (due to decreased chamber pressure during the sustainer phase) if a constant-geometry nozzle is used. The motor case hardware must be designed for the booster operation pressure. For this discussion it will be assumed that a single motor with two thrust levels and fixed nozzle geometry is used. The relationship between the ratio of sustainer thrust to booster thrust and the resulting ratio of specific impulse is presented in Figure 10-95.

Figure 10-96 indicates the type of parametric data which should be generated for optimization of sustainer parameters in situations where minimizing weight is the primary concern.

Figure 10-97 presents the relationship between growth factor and range for a boost-sustain system, where the sustainer parameters are assumed to have been fixed by considerations other than minimum weight. A comparison of these data with the data for the all-boost system will show that there are conditions for which the boost/sustain system is heavier than an all-boost system. This results from the reduction in sustainer specific impulse as discussed earlier.

The designer will be interested in knowing the sensitivity of the missile weight to variations in performance parameters. Figure 10-98 presents the effects of I_{sp} and λ's on the growth factor for a specific range, acceleration level, and ballistic coefficient. Figure 10-99 presents a similar trade-off with acceleration and ballistic coefficient as variables.

The data presented here is not intended to cover every situation but provides an indication of trends and serves to illustrate the various trade-offs which the designer must consider.

10-2.3.5 Numerical Example

An indirect fire surface-to-surface missile design problem is presented here to illustrate the steps to be followed in designing a missile when the required performance is specified. The problem is to determine the propulsion system characteristics, weight breakdown, and dimensions of a vehicle that will transfer a given payload over a desired range.

The graphs presented in the preceding paragraphs of this chapter indicate the complexity of the relationships between the performance parameters. Because of these

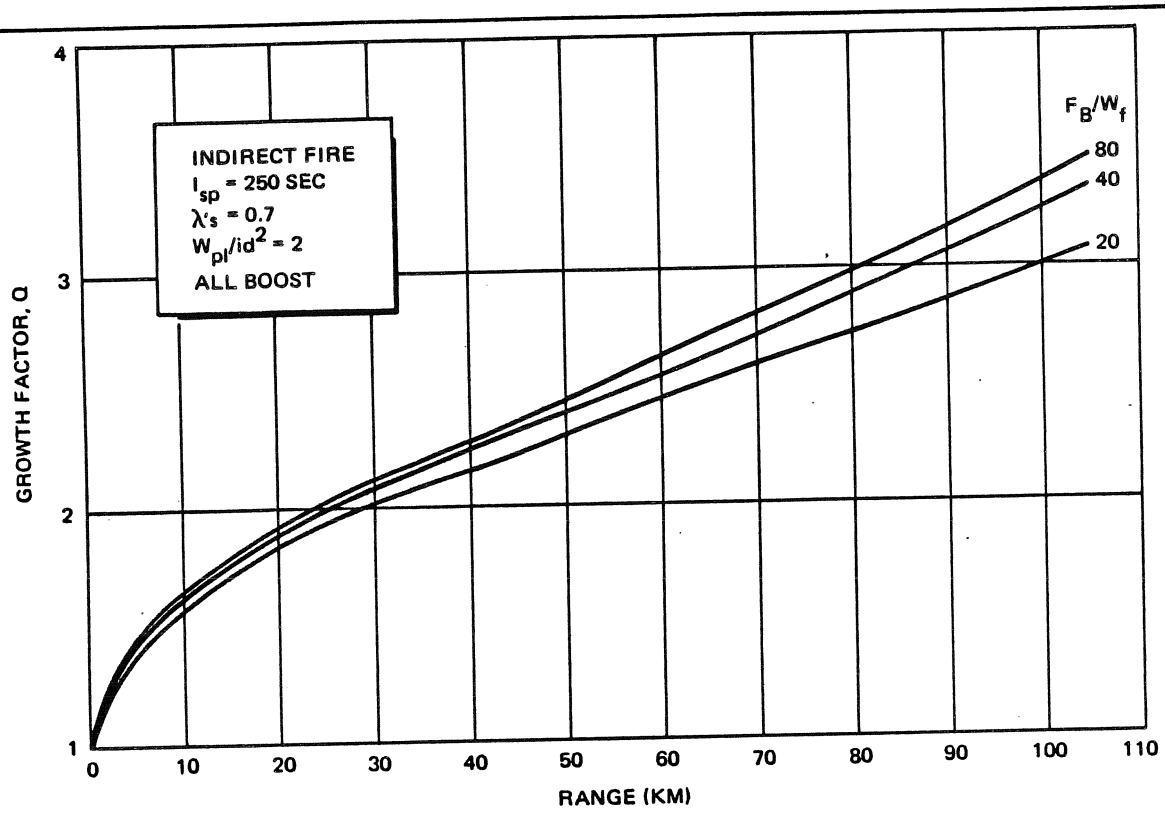

Figure 10-94. Indirect Fire — All-Boost; Effect of Range on Growth Factor

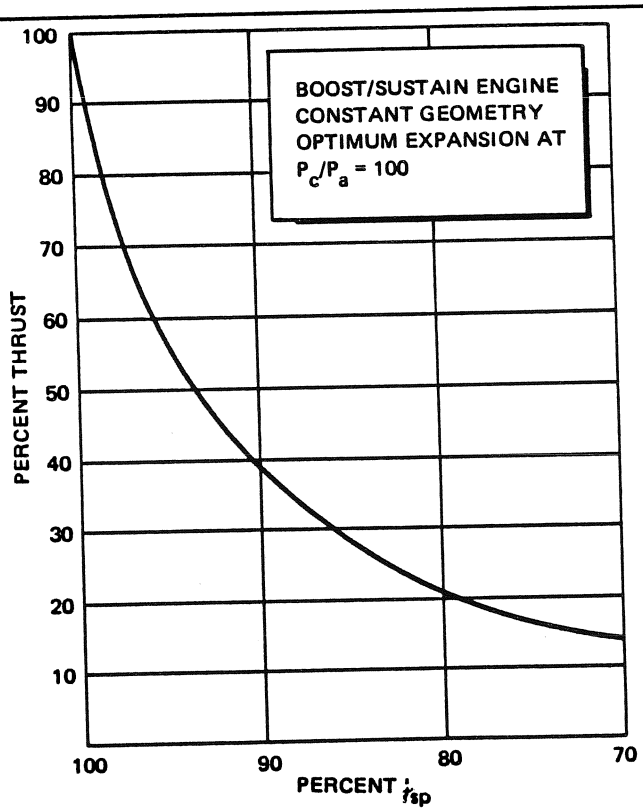

Figure 10-95. Boost/Sustain Engine; Variation of Specific Impulse With Thrust

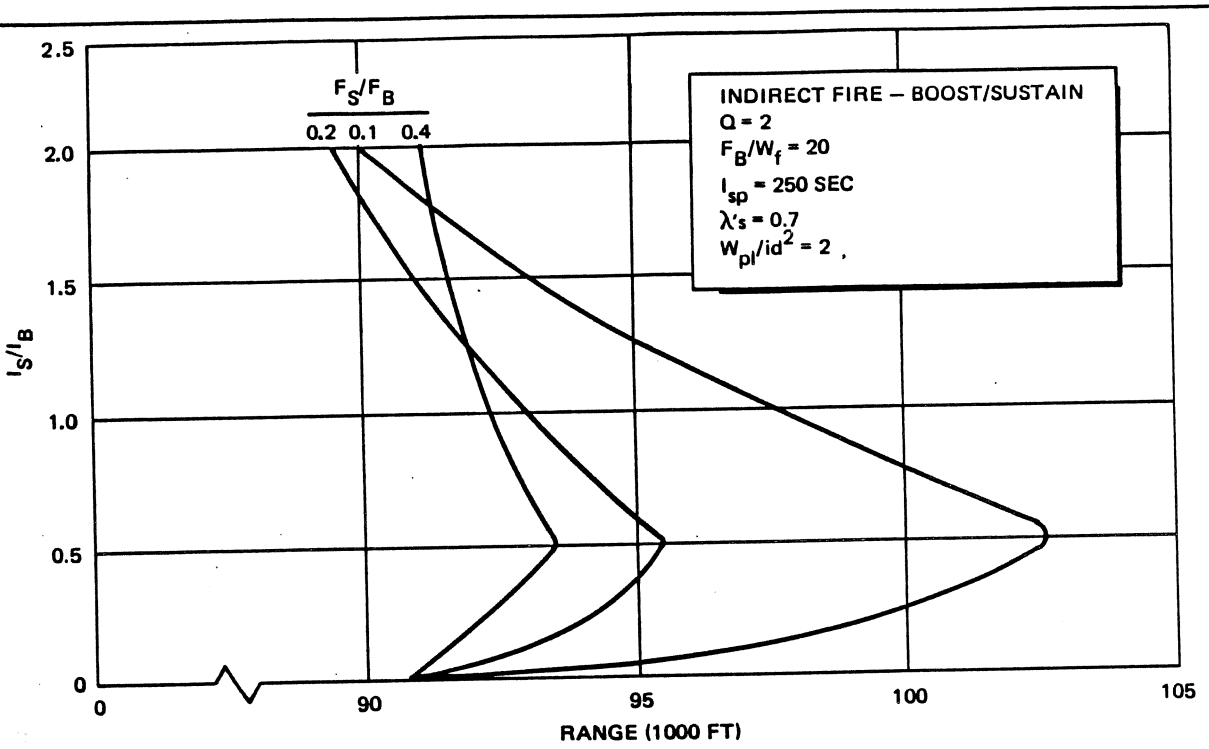

Figure 10-96. Indirect Fire – Boost/Sustain; Effect of Range on Impulse Ratio

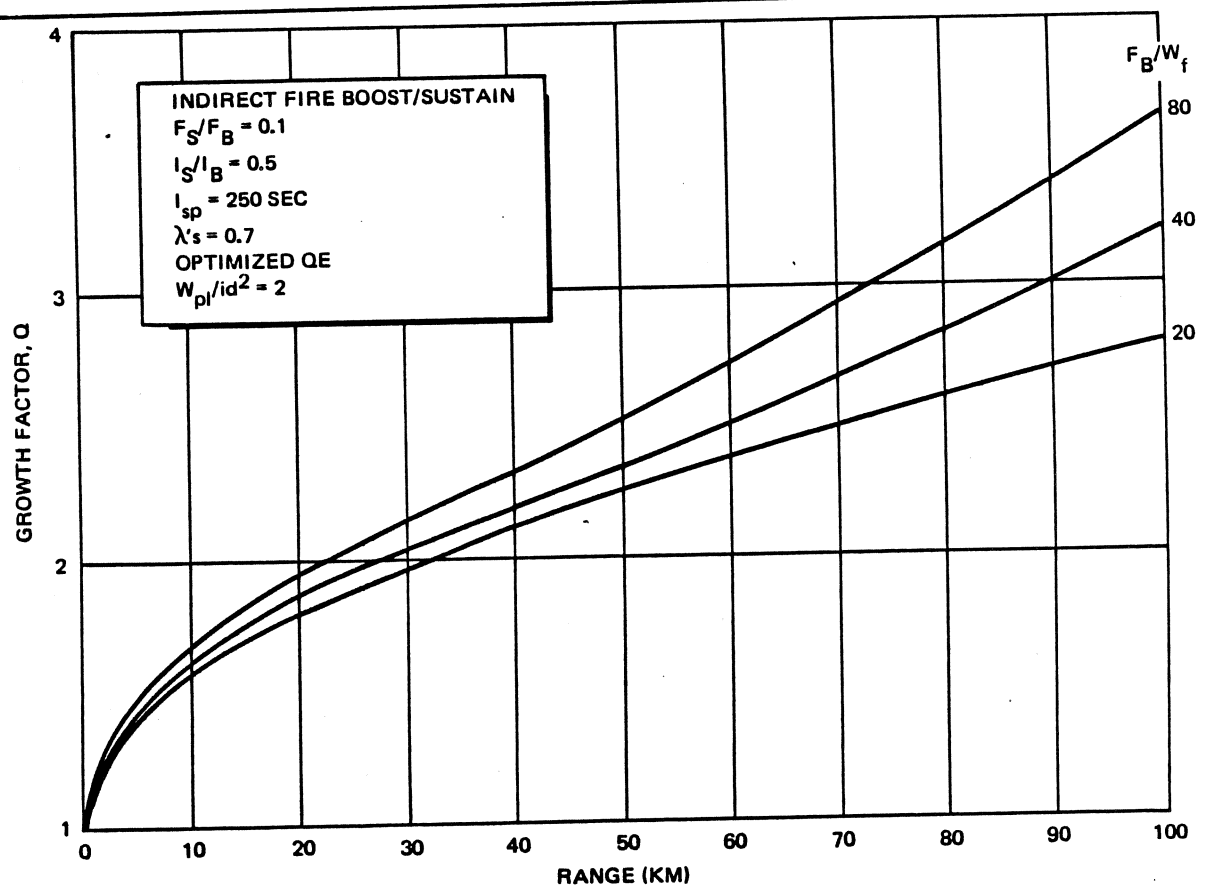

Figure 10-97. Indirect Fire – Boost/Sustain; Effect of Range on Growth Factor

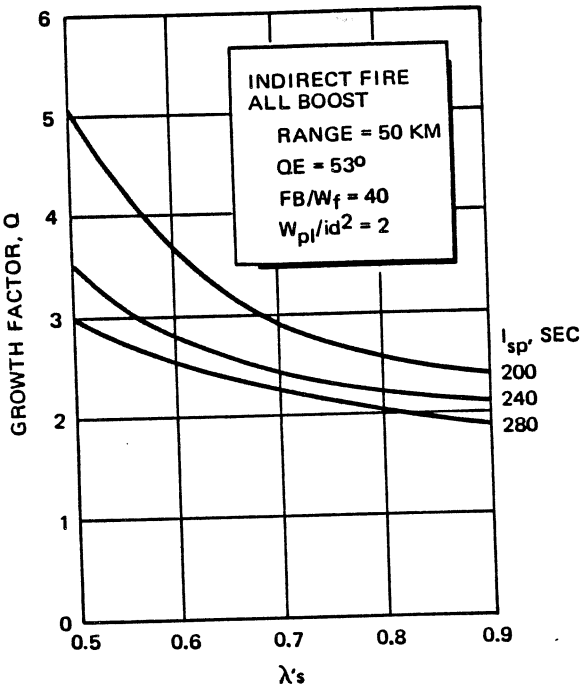

Figure 10-98. Indirect Fire — All-Boost; Effect of Propellant Weight Fraction on Growth Factor

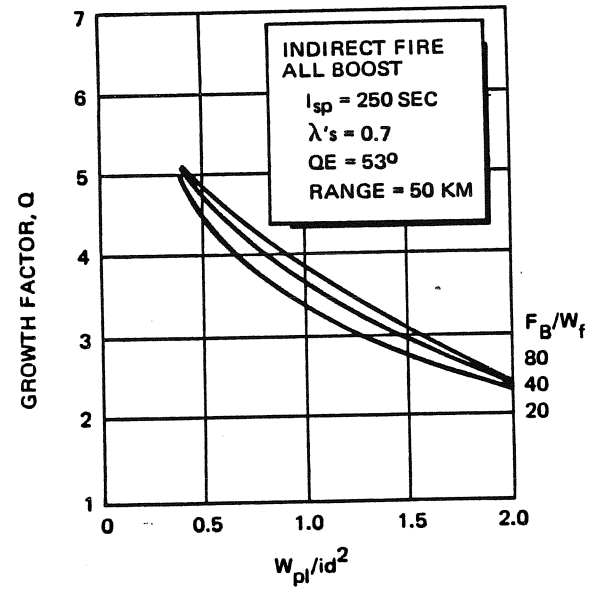

Figure 10-99. Indirect Fire — All-Boost; Effect of Ballistic Coefficient on Growth Factor

complex relationships, there is no easy wasy to arrive at a rocket configuration which will satisfy all the required relationships and still meet the performance requirements. The only alternative is to assume some of the important rocket or motor parameters, such as body diameter and specific impulse, and calculate the performance for these assumed conditions.

The calcuated performance data are compared with the desired values; then the original assumptions are modified and the procedure is repeated until the desired results are obtained. The accuracy of the original assumptions determines the amount of work required to reach the final solution. This is the reason that experience with the design of rocket systems is so important during the preliminary design stage.

Figure 10-100 is a flow diagram illustrating the steps of the design procedures. Block 1 indicates the design performance specification. In this case the rocket range and payload are specified. Blocks 2 and 3 show the parameters whose values are being assumed — that is, the first guess at the design configuration. The next sequence of blocks (4 through 8) illustrates the iterative procedure which must be followed until the initial assumptions are verified. After the iterative process is complete, enough is known about the system to define its performance parameters. This is done in the final Block 11, headed CALCULATE.

A ballistic coefficient is assumed in the first block of the iterative loop (block 3). This fixes the burnout velocity, the booster-mass ratio, the burnout-to-payload-weight ratio, and the payload ballistic coefficient. Notice that the value of the payload ballistic coefficient was assumed in Block 3 and it is necessary that this value be duplicated in Block 8. If this had been satisfied, there are no contradictions and the example can proceed to the defining of values.

If the payload ballistic coefficient value cannot be duplicated and/or the resulting values are not realistic, it will be necessary to make a trade-off study of the parameters in the second block until all criteria are satisfied.

The numerical example which follows utilizes the logic shown in the flow diagram.

a. Start with a specified range R of 30.0 km, and a payload weight of 890.0 lb.

b. From a knowledge of similar rockets, assume a propellant weight fraction, λ's, of 0.77, a specific impulse, I_{sp}, of 250 sec and a payload ballistic coefficient, W_{pl}/id^2, of 4.0 lb/in.^{2}.

c. For the required range, assume a ballistic coefficient, W_{bo}/id^2, of 4.5 lb/in.^{2}. Therefore, a burnout velocity, V_{bo} of 2,700 ft/sec is necessary as shown in Figure 10-91.

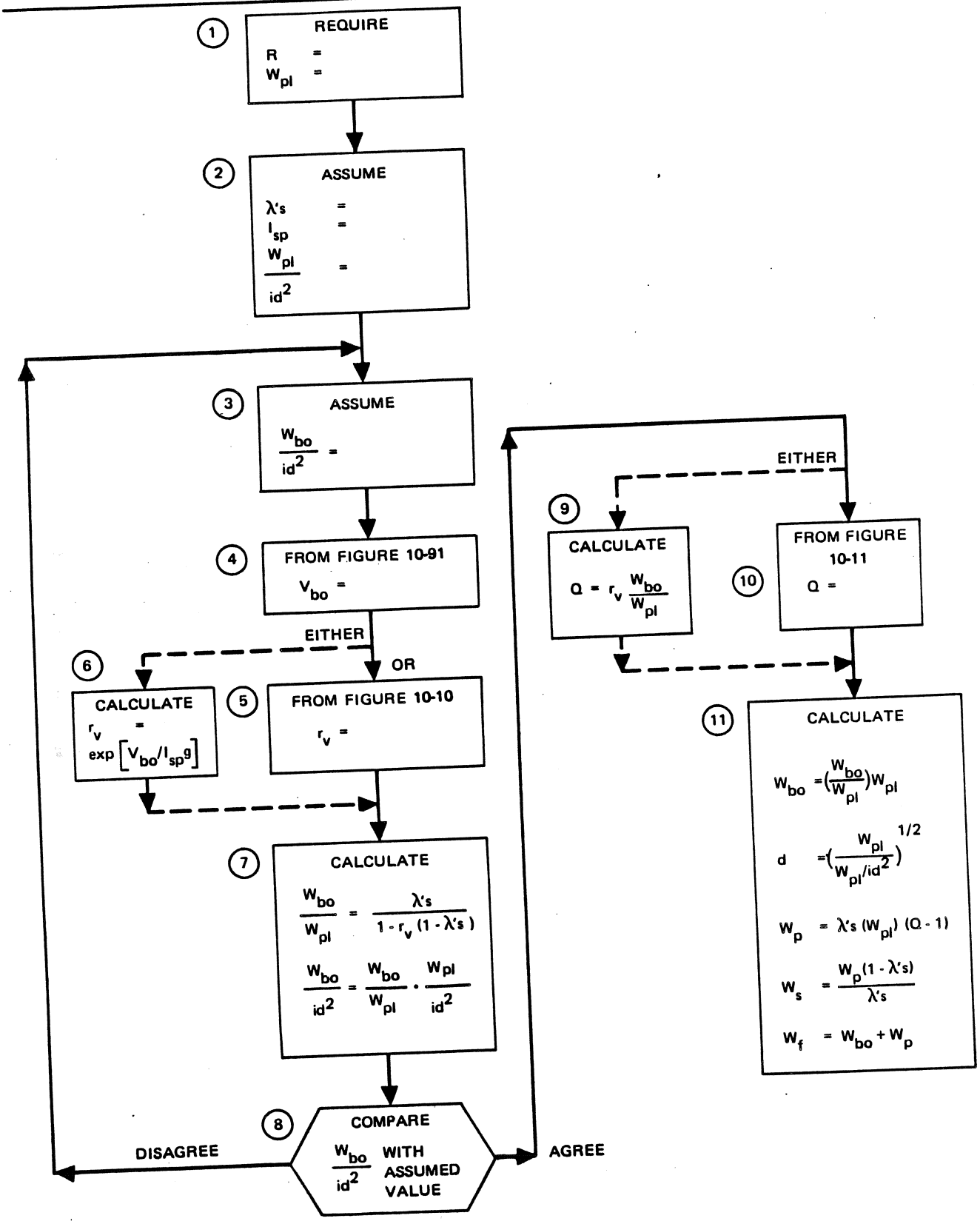

Figure 10-100. Flow Diagram

d. For an I_{sp} of 250 sec, the booster mass ratio, r_v, is determined from Figure 10-10 to be 1.4.

e. For a given λ's of 0.77, calcuate the ratio of burnout weight to payload weight:

$$\frac{W_{bo}}{W_{pl}} = \frac{\lambda's}{1 - r_v(1 - \lambda's)} = \frac{0.77}{1.0 - 1.4\,(0.23)} = 1.138$$

f. Calculate the ballistic coefficient:

$$\frac{W_{bo}}{id^2} = \frac{W_{bo}}{W_{pl}} \cdot \frac{W_{pl}}{id^2} = 1.138\,(4) = 4.552\ \text{lb/in}^2$$

g. A value of W_{bo}/id^2 was assumed in step 3. Match this value with the value calculated in step 6. They are the same within an acceptable error. If they were not the same, then another value of W_{bo}/id^2 should be selected and steps 3 through 7 repeated until they agree.

h. After satisfying step 7, either calculate the growth factor, Q, or read it from Figure 10-11:

$$Q = r_v \cdot \frac{W_{bo}}{W_{pl}} = 1.4\,(1.138) = 1.59$$

i. The burnout weight W_B is calculated:

$$W_{bo} = \frac{W_{bo}}{W_{pl}} \cdot W_{pl} = 1.138\,(890) = 1014\ \text{lb}$$

j. The rocket diameter d can be calculated:

$$d = \left(\frac{W_{pl}}{W_{pl}/id^2}\right)^{1/2} = \left(\frac{890}{4}\right)^{1/2} = 15\ \text{in.}$$

k. Propellant weight W_p is found by:

$$W_p = \lambda's\,(W_{pl})\,(Q - 1)$$

$$= 0.77\,(890)(0.59) = 405\ \text{lb}$$

l. Motor weight, W_{sn}, is:

$$W_{sn} = \frac{W_p\,(1 - \lambda's)}{\lambda's} = \frac{405\,(0.23)}{0.77} = 120\ \text{lb}$$

m. Total weight, W_f, is:

$$W_f = W_{bo} + W_p = 1{,}014 + 405 = 1{,}419\ \text{lb}$$

10-2.4 Maneuvering Missiles

The basic equations previously defined for free-flight missiles are also applicable for predicting gross performance of maneuvering missiles except that corrections must be made to allow for the energy associated with changing direction or altitude during maneuvering. Range, altitude, time to target, V_{bo_1}, and powered flight time are all affected by the maneuvering mission requirements. Since these requirements are quite broad and differ for each application, the missile design is selected at a design point which will optimize a wide range of missions (mission envelope).

Because of the complexity and close interrelationship between design selection and performance this subject is discussed in detail in Paragraph 10-3.6.

10-3 VEHICLE SIZING ANALYSIS

10-3.1 General Sizing Relationships

An engineer in the field of vehicle preliminary design requires a knowledge of the basic relationships between the parameters that determine the vehicle physical size and those that define the mission requirements. Relationships of this type range in complexity from the simple equations for a single stage vehicle, to the complicated equations for the optimization of a multistage vehicle in which each stage involves a different design phiolosphy. It is the object of this section to present these relationships in both analytical and graphical form, such that they may be adapted to preliminary design analysis.

The material presented is intended to aid the designer in determining an optimum vehicle based on design parameters specifying vehicle characteristics. In most cases, the first concern is the minimization of the ratio of vehicle gross weight to payload weight for a specific mission. This type of sizing has been used in the past to determine vehicle sizes for both ballistic missiles and space vehicles. In some cases, maximizing the payload for a given mission while restricting the vehicle size is important (aircraft carried tactical missiles). However, other criteria are often used in determining vehicle size. Particular emphasis is frequently placed on the optimization of vehicles for minimum cost. However, sizing based on a cost criterion is involved with program constraints and is not considered here.

The relationships for vehicle sizing presented are relatively simple because of their basic assumptions and are to be used in cursory investigations where assumptions can be tolerated.

An examination of the performance equations given in Paragraph 10-2 indicates that basic mission definition is in terms of total ideal velocity especially for space launch or ballistic missiles, e.g., Paragraph 10-2.1, Equation 31. A sizing analysis using any criterion usually is related to these fundamental relationships.

10-3.1.1 Structure Factor

Before proceeding with the sizing analysis, an important parameter, step structure factor, should be discussed. The step structure factor, s_s, represents that fraction of the step weight that is not usable propellant and is, therefore, a nondimensional parameter important and most frequently used by the designer in vehicle sizing. It should be noted that it is also the complement of the step mass fraction, λ's. This latter term is frequently preferred by a propulsion engineer in his analysis because it relates in a direct and physical manner to the propulsion system (Paragraph 10-3.6). An examination of vehicles presently in use will indicate a range of step structure factors from 0.05 to 0.30, or higher (λ's = 0.70 to 0.95). It is apparent that the structure factor is also dependent on such parameters as the type of propellant, the step thrust level, the weight supported by the step (including interstage structure) and the size of the step; however, once the design criteria for the step have been defined to the point that the propellant and thrust level have been chosen, the major contributor to the variation of structure factor is step size. In almost all cases, an increase in the size of a given type of step will decrease the step structure factor (indicating that a more efficient container can be built for greater propellant weights). In relation to vehicle sizing, the variation of structure factor with step weight must be included when a sizing analysis is undertaken. However, the use of a constant structure factor with an iterative procedure to include the variation taken directly into account. Not all of the step inert weight is necessarily part of the vehicle structure; however, it is included in the structural inert weight for convenience. Propulsion system inert weight includes motor cases or propellant tanks, ancillary equipment, TVC systems (less expendable fluids), pressurization system, unused propellants, and other nonexpendable fluids (hydraulic oil, etc.). Certain expendable fluids, i.e., reaction control system propellants, pressurization gases, etc., which do not contribute to the axial propulsion force are usually included as inert weight for preliminary sizing analysis, since conservative results will be obtained when using the methods described below.

10-3.1.2 Growth Factor

The ratio of vehicle gross weight to payload weight, previously defined as the growth factor, Q, is another basic parameter of interest in vehicle sizing. A growth factor defines an infinite number of vehicle sizes and corresponding payloads that will perform a particular mission, assuming the number of stages, the structure factors, and the velocity losses remain constant. Thus, it becomes an important tool in preliminary design for comparison purposes since it essentially represents the efficiency of the vehicle configuration for the design mission. After having determined the growth factor, the specific vehicle characteristics, such as propellant and stage weights, can be found for either a specified gross weight or payload weight.

10-3.1.2.1 One Stage

The expression for the growth factor of a one stage vehicle is:

$$Q = \frac{W_f}{W_{pl}} = \frac{1 - s_s}{e^{-\left[\frac{\Delta V_I}{g_o I_{sp}}\right]} - s_s} \qquad (111)$$

where

$\frac{\Delta V_I}{g_o I_{sp}}$ = the nondimensional ideal velocity ratio

The growth factor is presented in graphical form in Figures 10-101 and 10-102 for a range of structure factors from 0.05 to 0.20.

10-3.1.2.2 Infinite Staging

The growth factor for a one stage vehicle represents the maximum value that would ever be required to perform a given mission. On the other hand, the minimum value of growth factor for the same mission is obtained for a vehicle with a large number of stages ($N > 10$) of equal step structure factor and specific impulse will approach the infinte stage value. The growth factor for such an infinitely staged vehicle is:

$$\frac{W_f}{W_{pl}} = e^{\left[\frac{\Delta V_{I_N}}{g_o I_{sp}(1 - s_s)}\right]} \qquad (112)$$

10-3.1.2.3 Mutiple Staging

When considering vehicles of multiple stages, three different classes come to mind and are discussed in subsequent sections:

a. Vehicles with stages of equal structure factor and specific impulse.

b. Vehicles with stages of equal specific impulse but with different structural factors.

c. Vehicles with stages of unlike parameters.

10-3.1.2.4 Stages of Like Parameters

The probability of constructing a vehicle with stages of equal parameters is unlikely. However, analysis of such a vehicle provides information on the effect of increasing

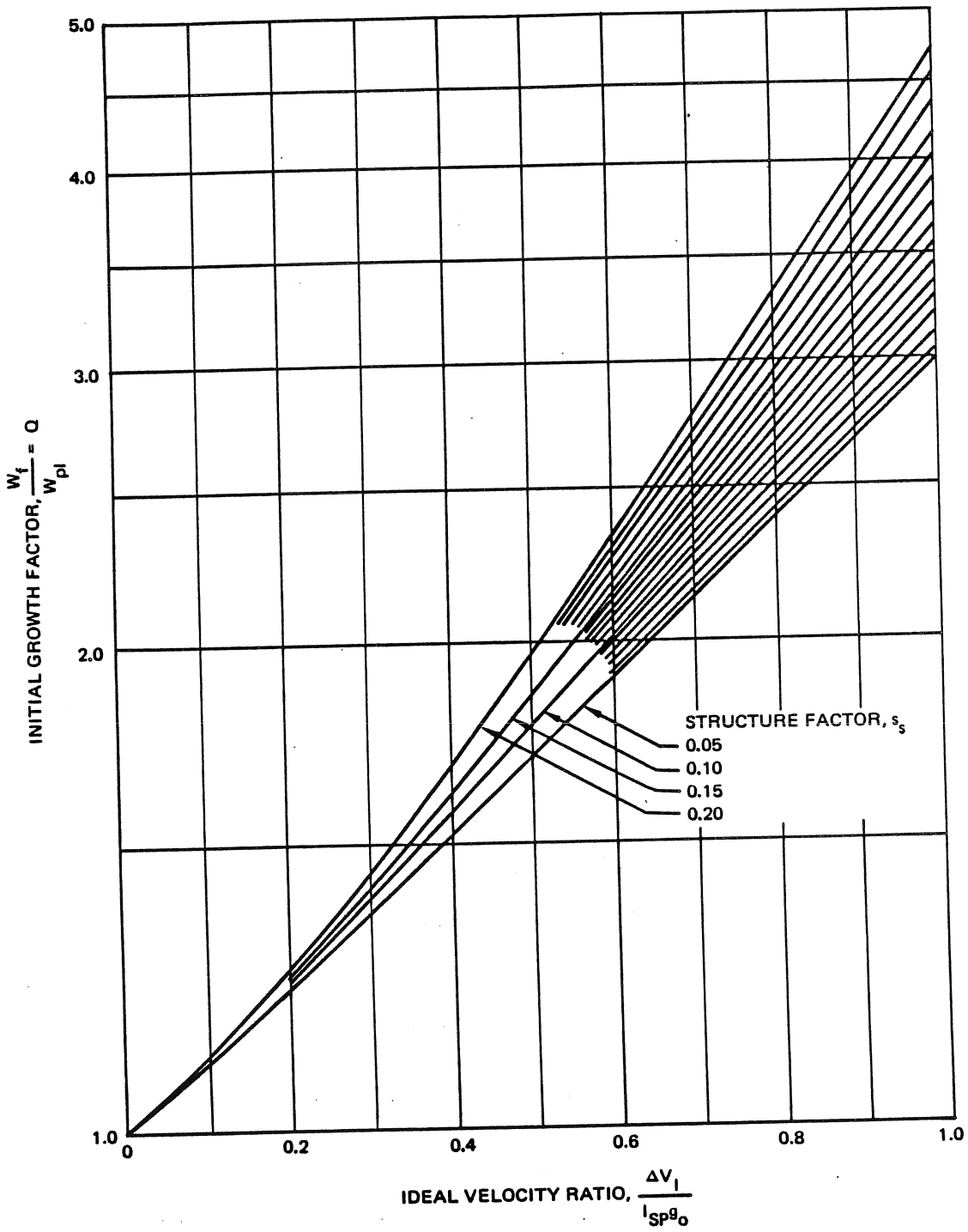

Figure 10-101. Growth Factor vs. Ideal Velocity Ratio (Single-Stage Vehicle)

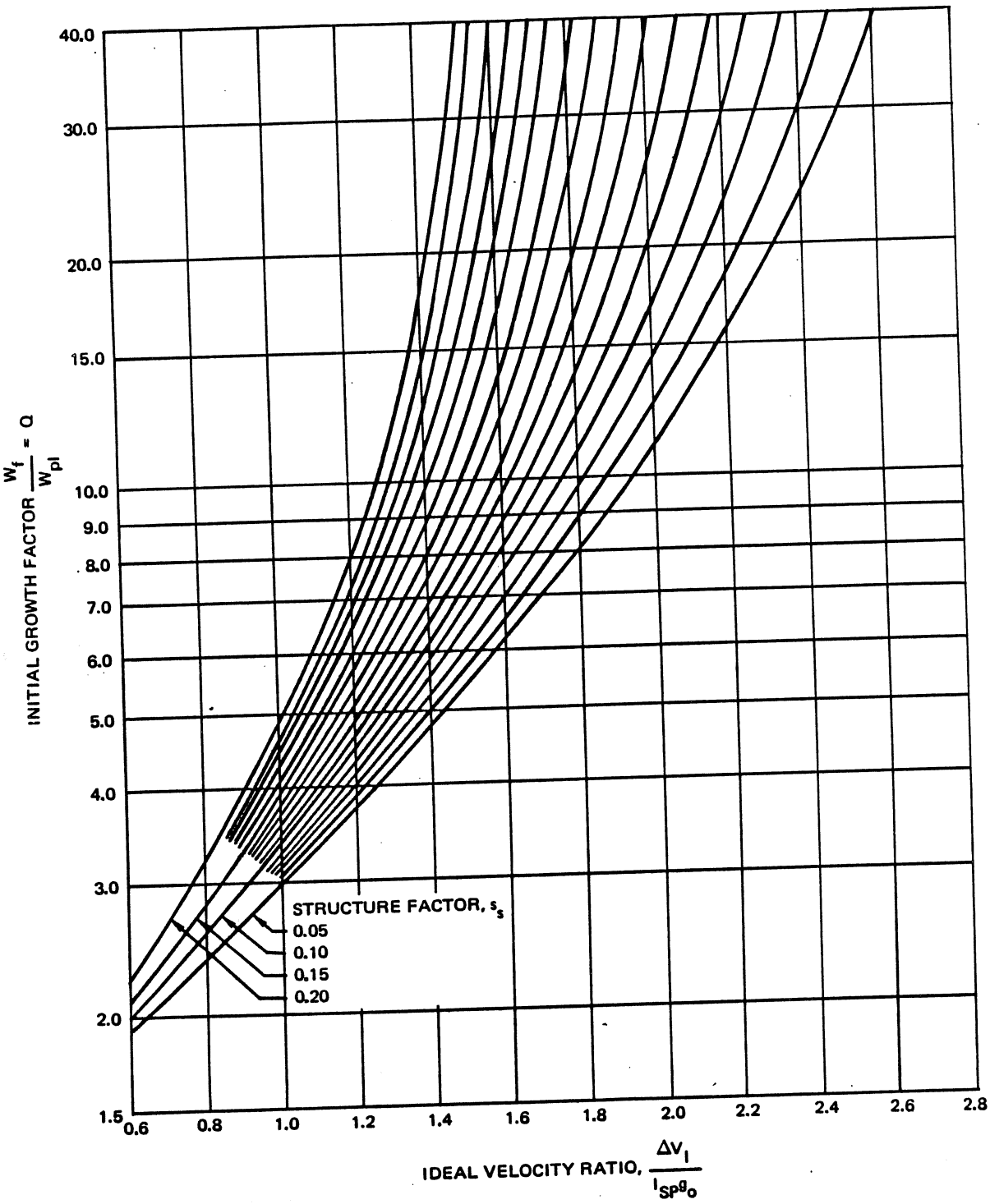

Figure 10-102. Growth Factor vs. Ideal Velocity Ratio (Single-Stage Vehicle)

the number of stages of a vehicle, as well as providing a rapid method of sizing a multi-stage vehicle for preliminary design investigation. The optimum sizing equation developed in this section indicates that a vehicle of like parameters should have equal stage payload ratios for optimum sizing.

$$\frac{W_{f_1}}{W_{f_2}} = \frac{W_{f_2}}{W_{f_3}} = \cdots \frac{W_{f_i}}{W_{f_{i+1}}} = \cdots \frac{W_{f_N}}{W_{pl}} \qquad (113)$$

implying equal ideal velocities per stage such that:

$$\Delta V_{I_N} = N \Delta V_{I_n} \qquad (114)$$

where:

N = number of stages

ΔV_{I_n} = ideal velocity of one stage.

The growth factor for a vehicle with like parameters is:

$$Q = \frac{W_{f_1}}{W_{pl}} = \left(\frac{1 - s_s}{e^{-\left[\frac{\Delta V_{I_N}}{N g_o I_{sp}}\right]} - s_s} \right)^N \qquad (115)$$

This equation is graphically represented in Figures 10-103 through 10-112 for vehicles with one to five stages and with structure factors ranging from 0.05 to 0.20.

10-3.1.2.5 Unlike Structure Factors

The assumption of stages with like specific impulses but unlike structure factors approaches reality when the clustering of solid propellant engines is considered. In such a case, the specific impulse of each stage would remain constant while the structure factor would vary slightly from state to stage due to differing number of clustered engines in each step.

The direct solution of the optimization equation for unlike structure factors becomes involved for vehicles of more than two stages; thus, this analysis will be persented for a two-stage vehicle. The equation for the vehicle growth factor of a two-stage vehicle with like specific impulses but unlike structure factors is:

$$Q = \frac{W_f}{W_{pl}} = \frac{(1 - s_{s1})(1 - s_{s2})}{\left[e^{\left(-\frac{\Delta V_{I_N}}{2 g_o I_{sp}} \right)} - \sqrt{s_{s1} s_{s2}} \right]^2} \qquad (116)$$

The growth factor is shown graphically in Figure 10-113 (Sheets 1 through 5). The growth factor of each individual stage can be determined from the growth factor distribution factor shown in Figure 10-113 (Sheet 6). For vehicles of three or more stages with unlike structure factors, Figure 10-113 (Sheet 6) can be used successively, e.g., by optimally sizing the first stage with respect to the second, the second with respect to the third, and so on.

As a means of illustrating the previous discussion, Figure 10-114 shows the payload-launch weight relationship for various solid and liquid propulsion first stages and with the Saturn S-IVB as a second stage. The differences in payload capability for the various configurations are largely due to step structure factor differences, although the liquid systems have slightly better I_{sp} values. One conclusion is that for the given vehicle combinations, payload capability is relatively insensitive to solid versus liquid propulsion systems. Figure 10-115 shows the impact of stage sizing, using a combination of solid and liquid propulsion stages on vehicle launch weight for a given performance requirement. Figure 10-116 relates payload and launch weight for the same stage combinations. The design point chosen for the vehicle is also illustrated on these figures. The effect of the structural factor for each type of propulsive stage is implicity included in these curves.

10-3.1.3 Vehicle Mass Ratio

In order to define characteristics of stages after having sized a vehicle, analytical and graphical expressions for stage mass ratio are included for the classes of vehicles considered in the preceeding subsection.

10-3.1.3.1 One Stage

The analytical expression for the mass ratio of a single-stage vehicle is:

$$r_v = e^{\left(\frac{\Delta V_I}{g_o I_{sp}}\right)} = \frac{\frac{W_f}{W_{pl}}}{s_s \frac{W_f}{W_{pl}} + (1 - s_s)} = \frac{Q}{1 + s_s(Q-1)} \qquad (117)$$

Equation 117, as a function of the ideal velocity ratio, is shown in graphical form in Figure 10-117 for one-stage through four-stage vehicles with like structure factors for each step.

10-3.1.3.2 Infinite Staging

The vehicle mass ratio for an infinitely staged vehicle is simply equal to the vehicle payload ratio (Note: s=o for infinite staging)

$$r_{v_n} = \frac{W_{f_n}}{W_{f_{n+1}}} \quad (N = \infty) \qquad (119)$$

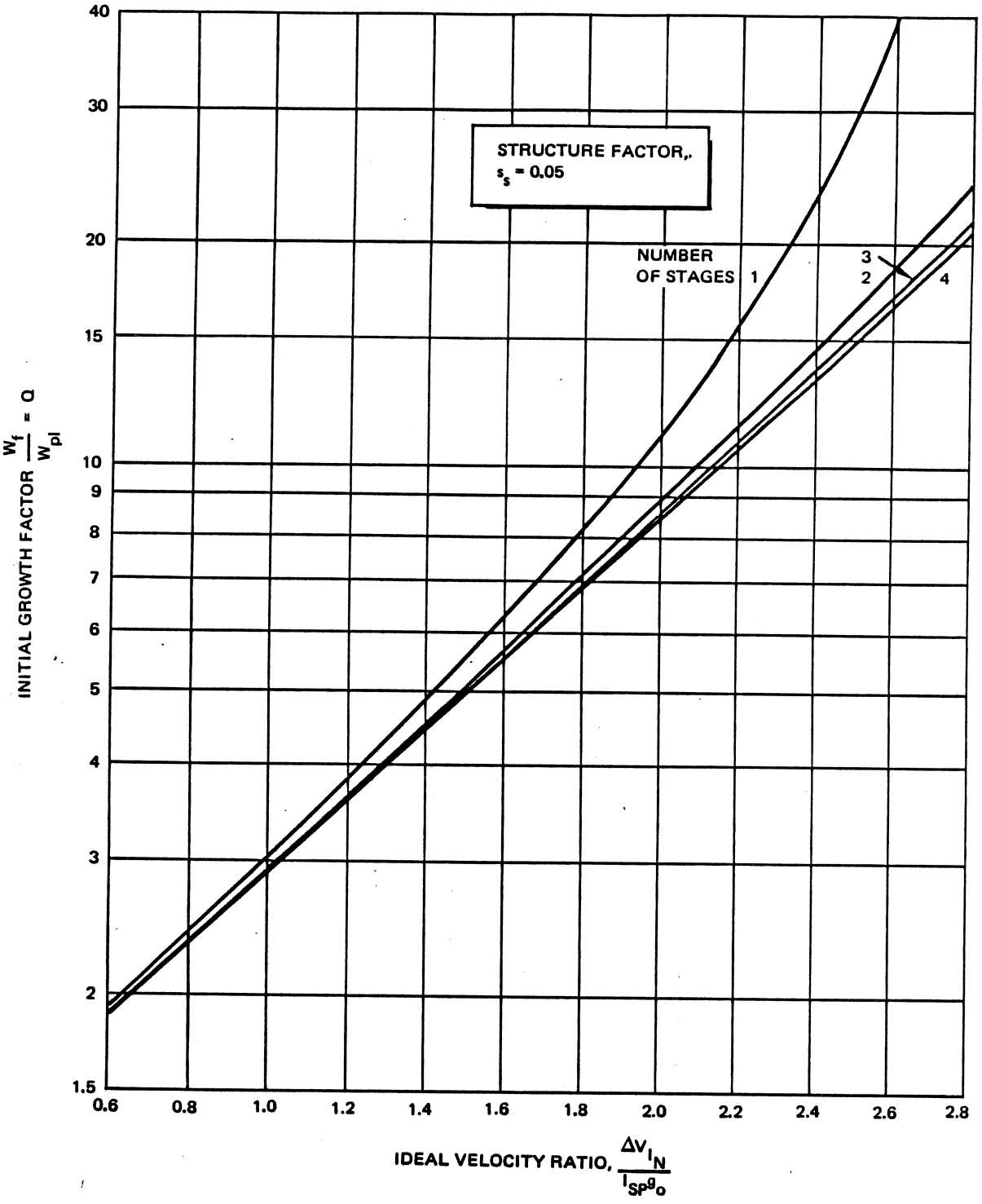

Figure 10-103. Growth Factor for Like Parameters (Multiple Stage)

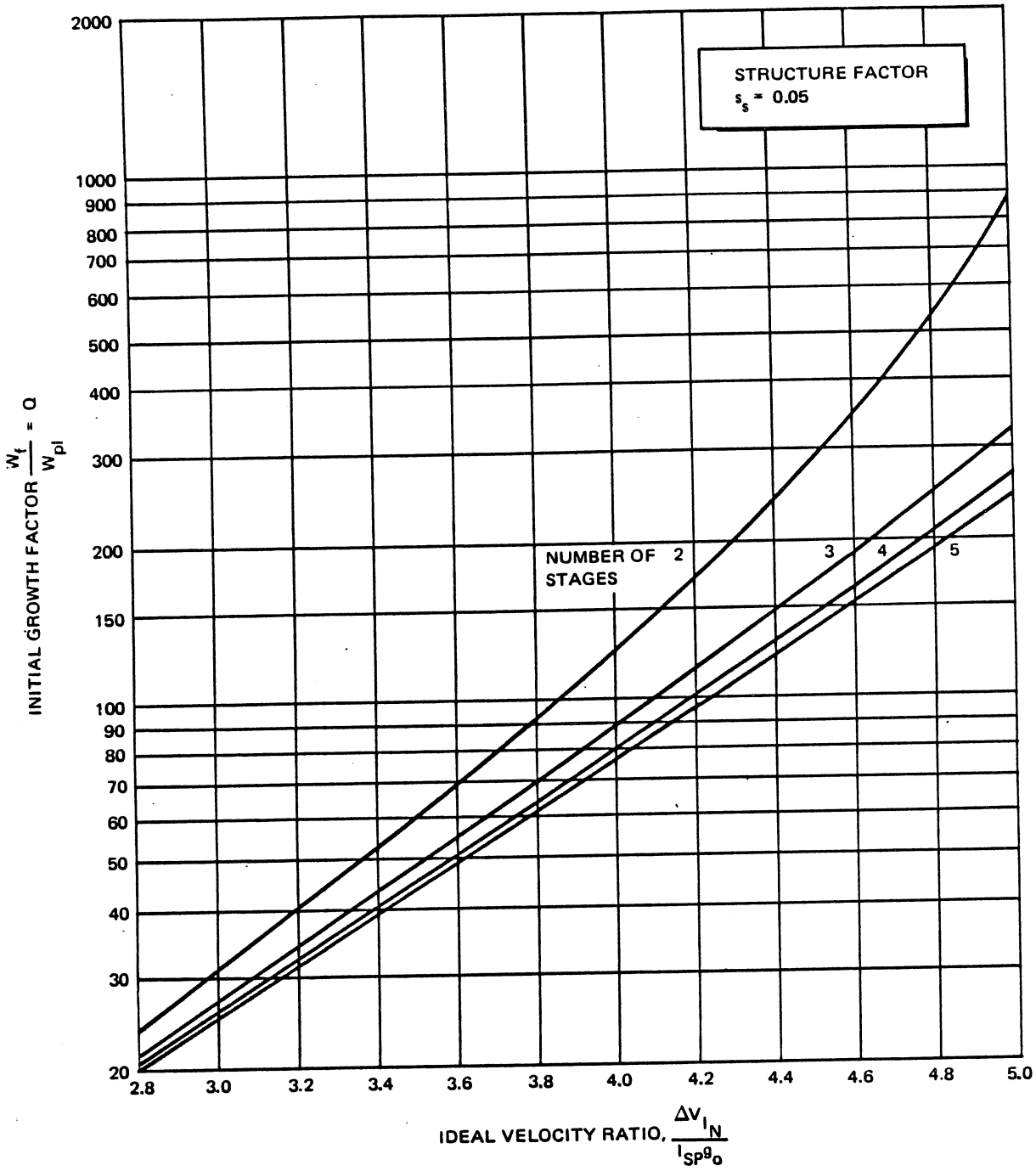

Figure 10-104. Growth Factor for Like Parameters (Multiple Stage)

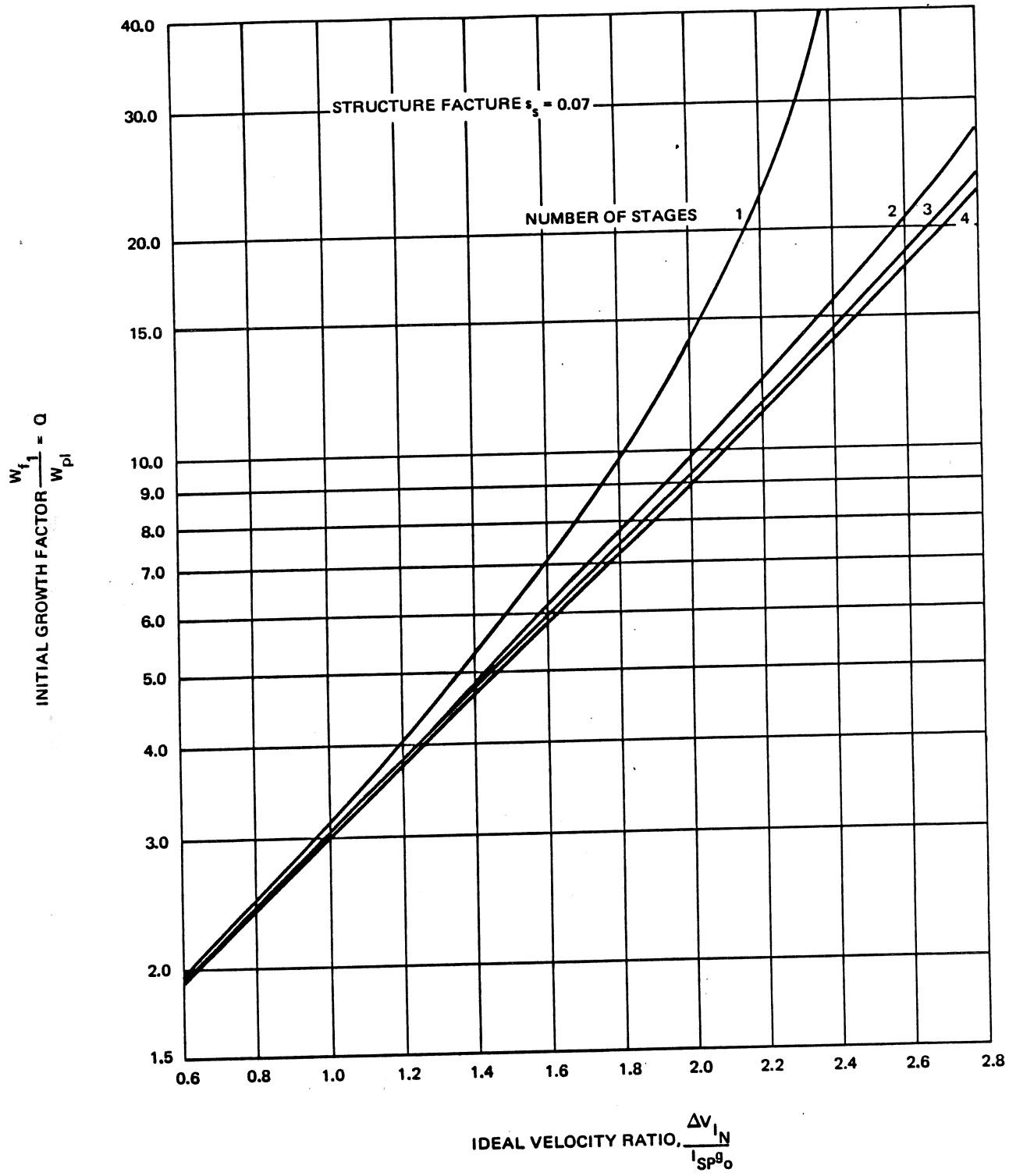

Figure 10-105. Growth Factor for Like Parameters (Multiple Stage)

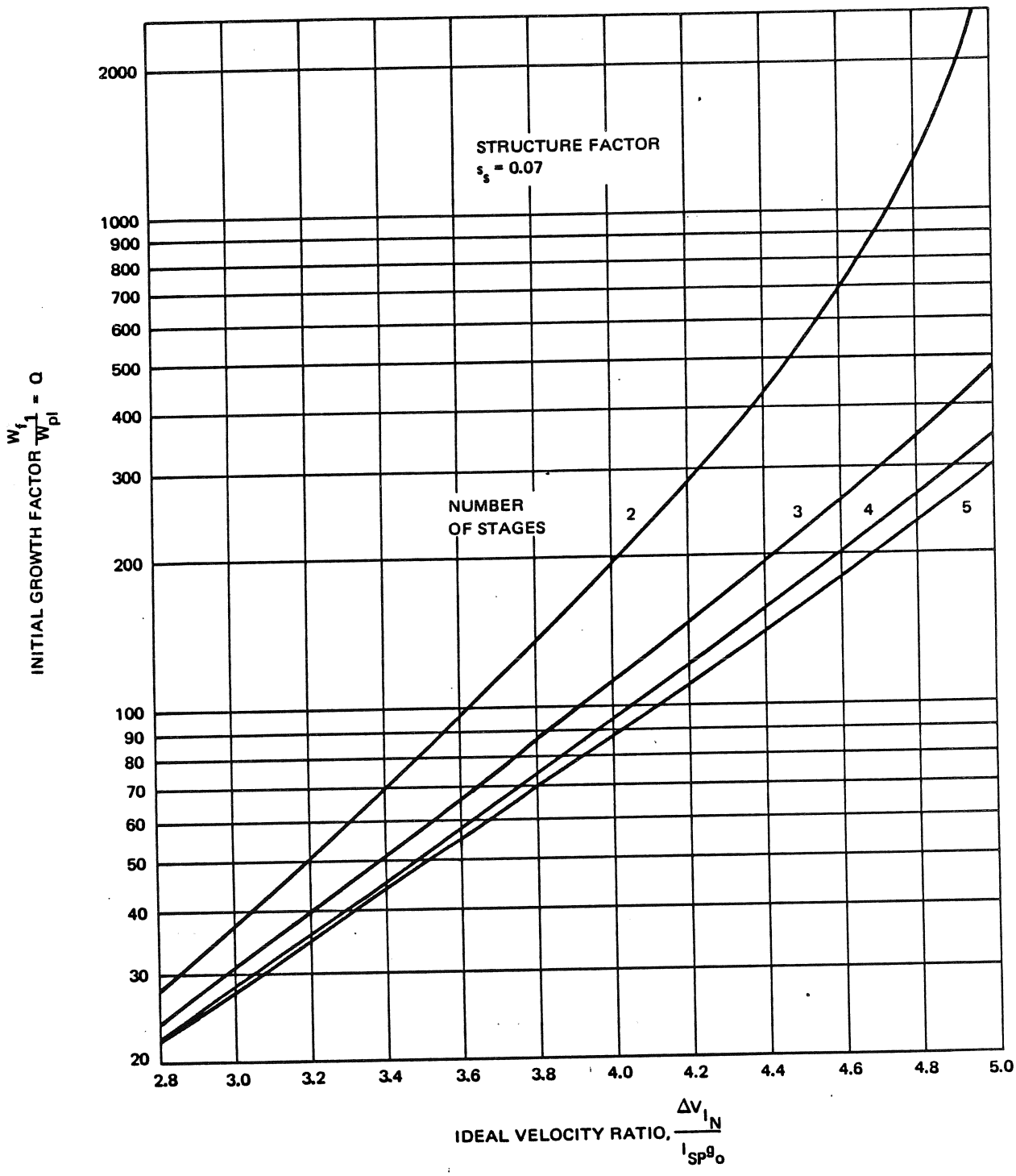

Figure 10-106. Growth Factor for Like Parameters (Multiple Stage)

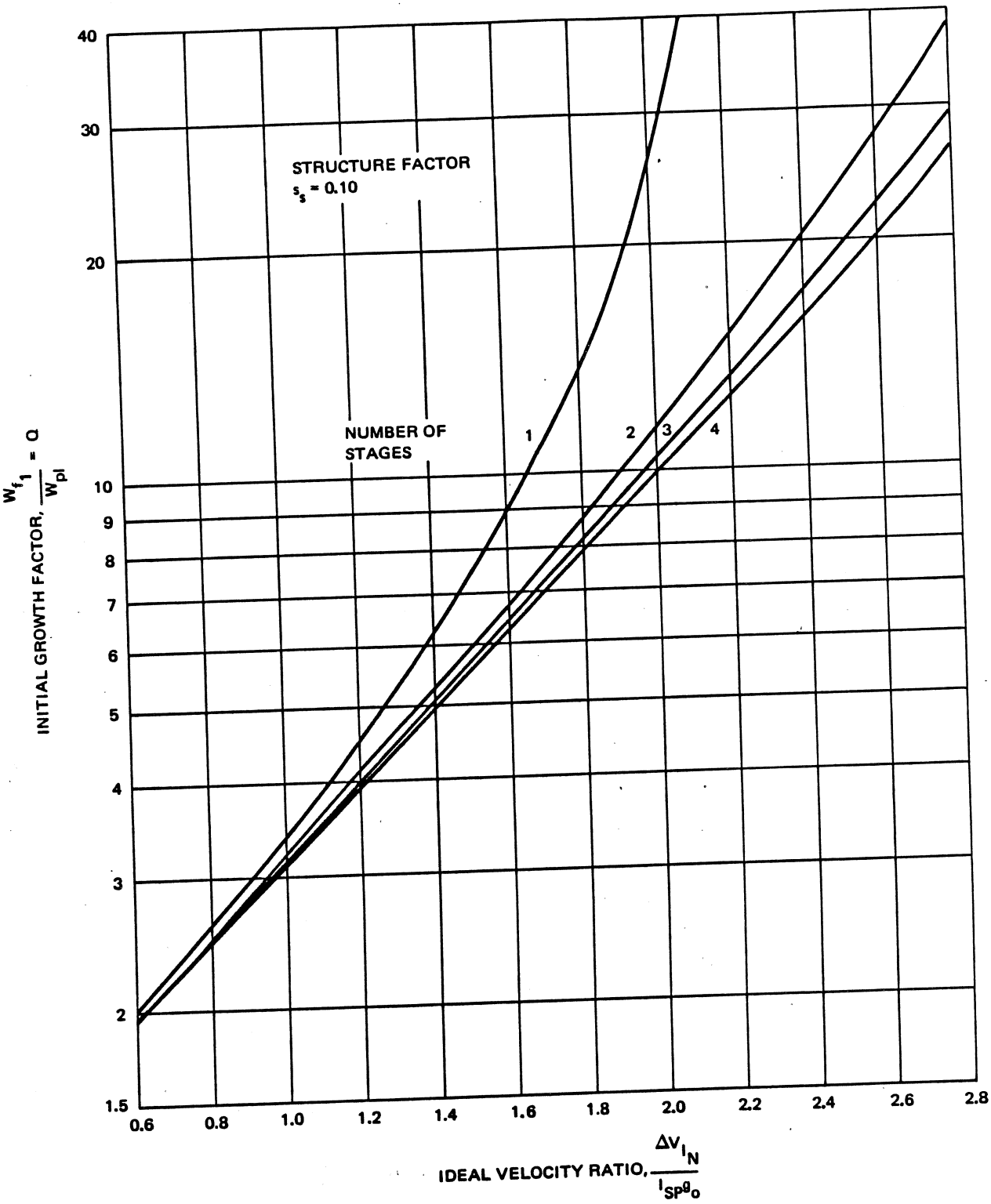

Figure 10-107. Payload Ratio for Like Parameters (Multiple Stage)

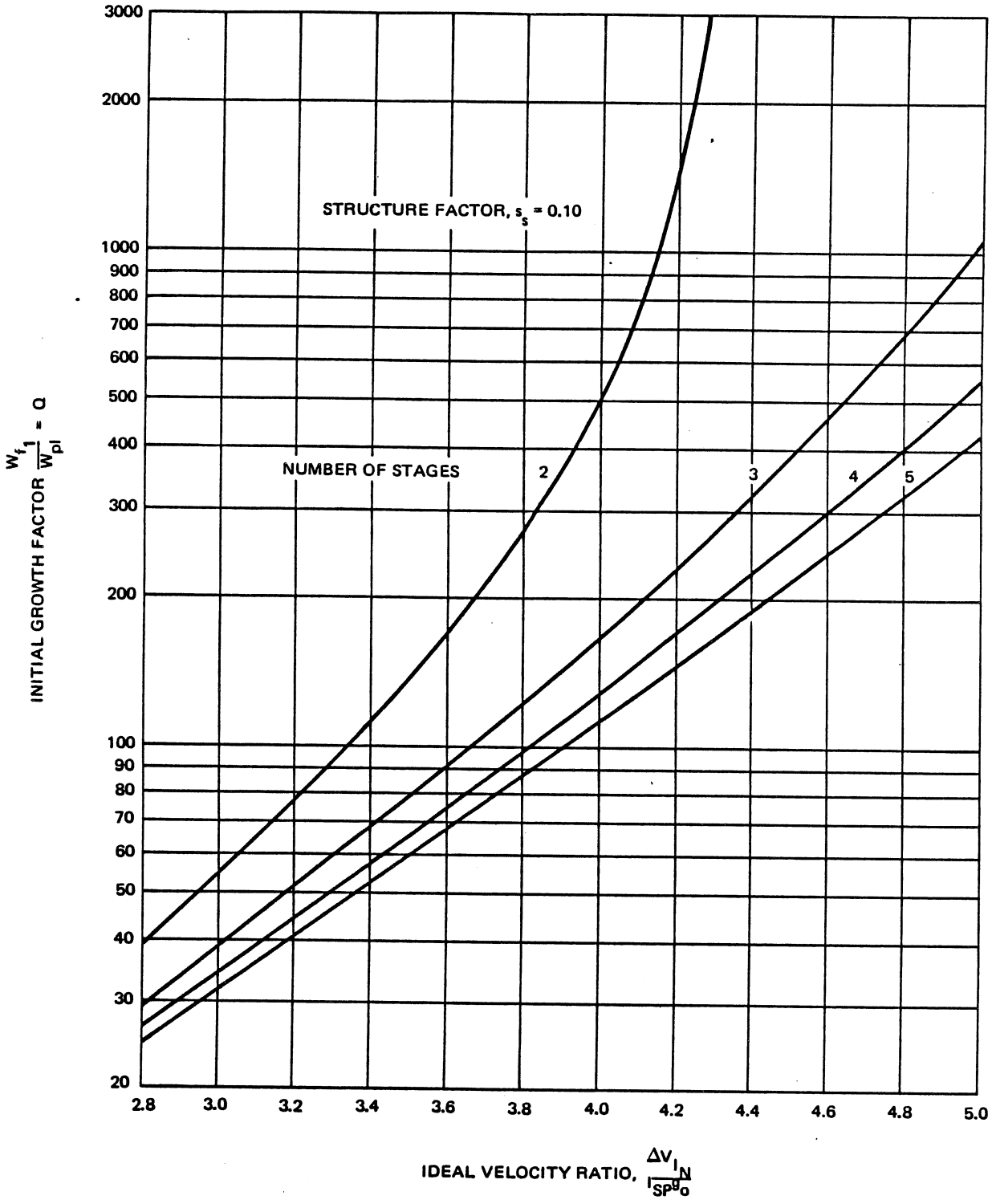

Figure 10-108. Growth Factor for Like Parameters (Multiple Stage)

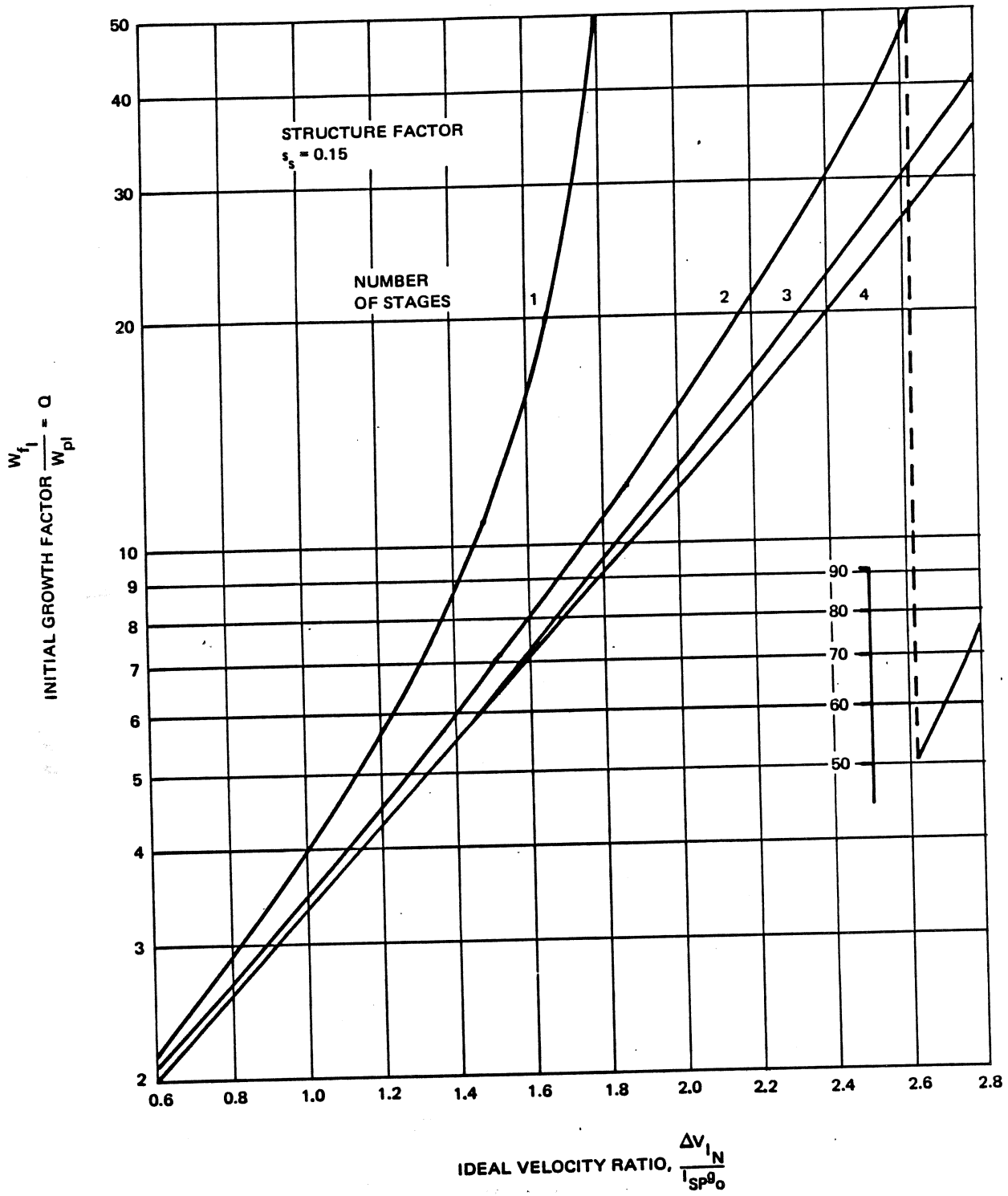

Figure 10-109. Growth Factor for Like Parameters (Multiple Stage)

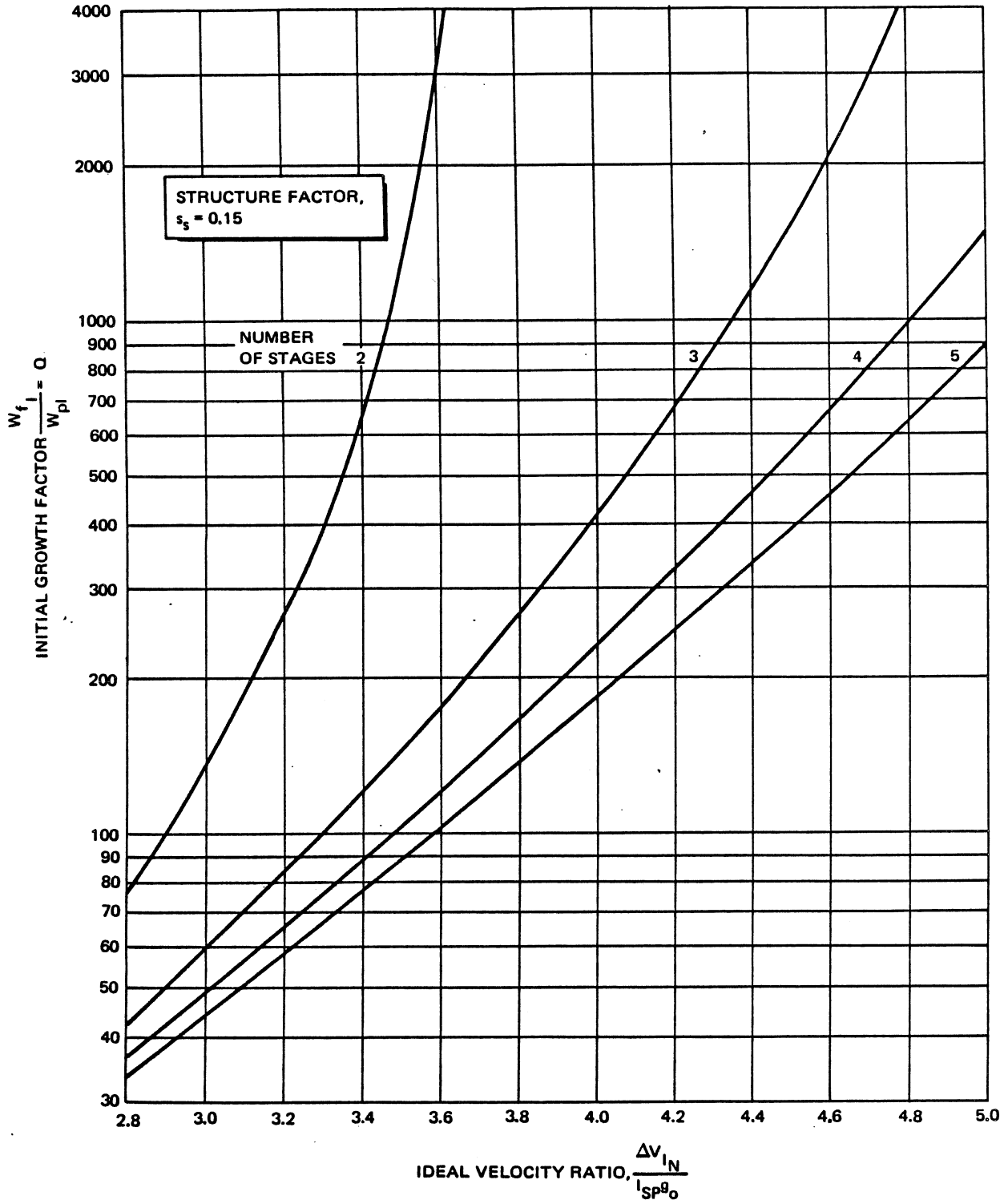

Figure 10-110. Payload Ratio for Like Parameters (Multiple Stage)

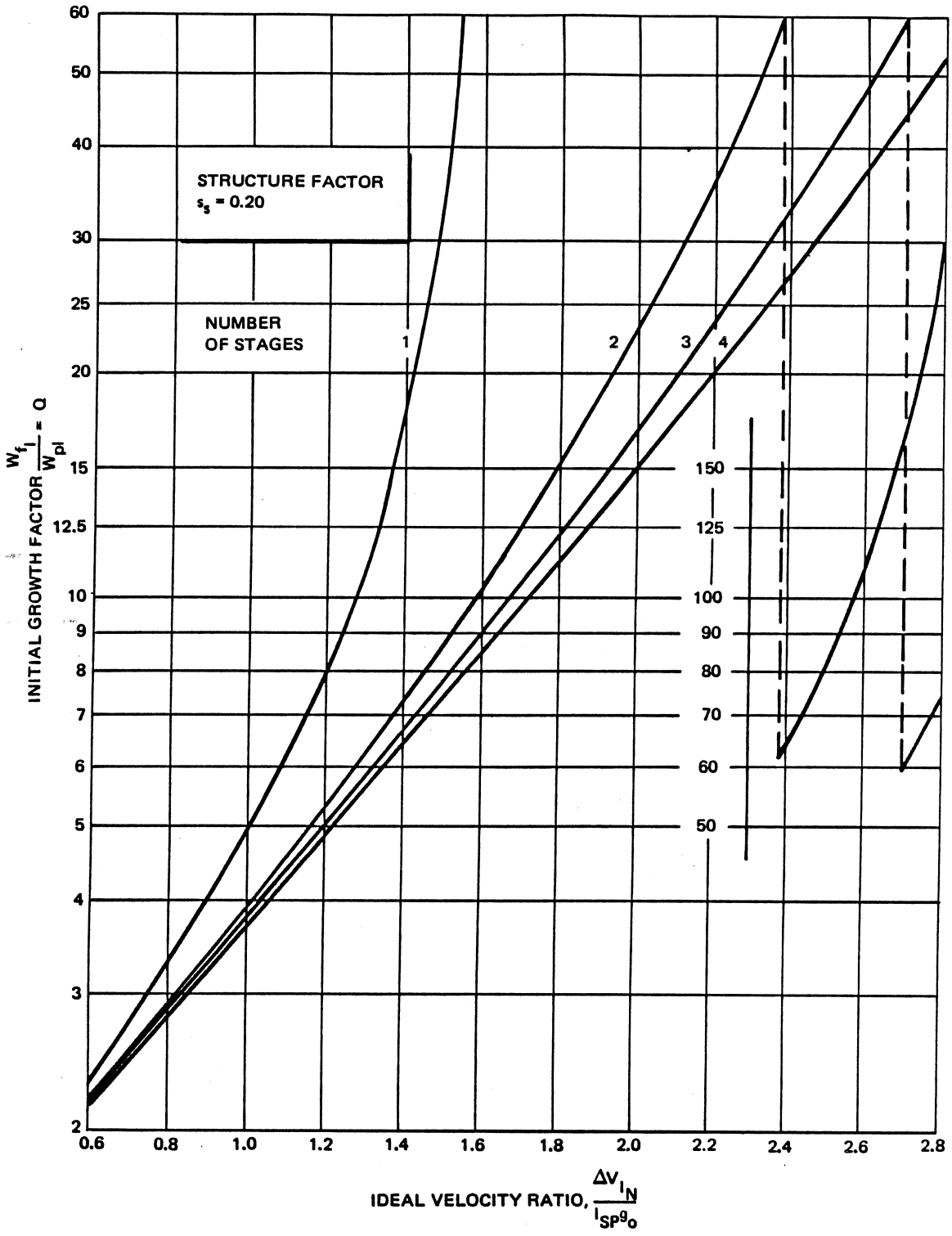

Figure 10-111. Growth Factor for Like Parameters (Multiple Stage)

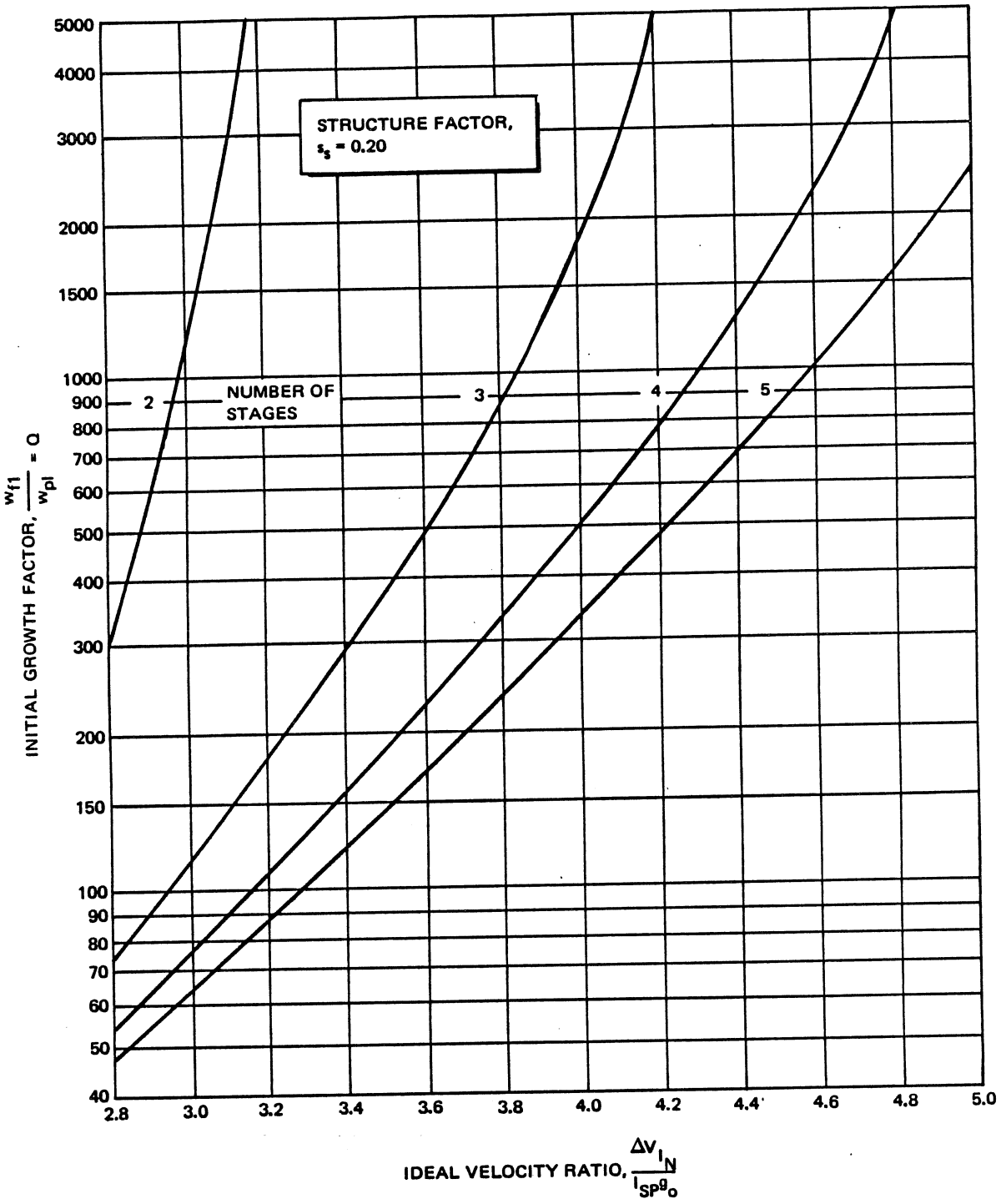

Figure 10-112. Growth Factor for Like Parameters (Multiple Stage)

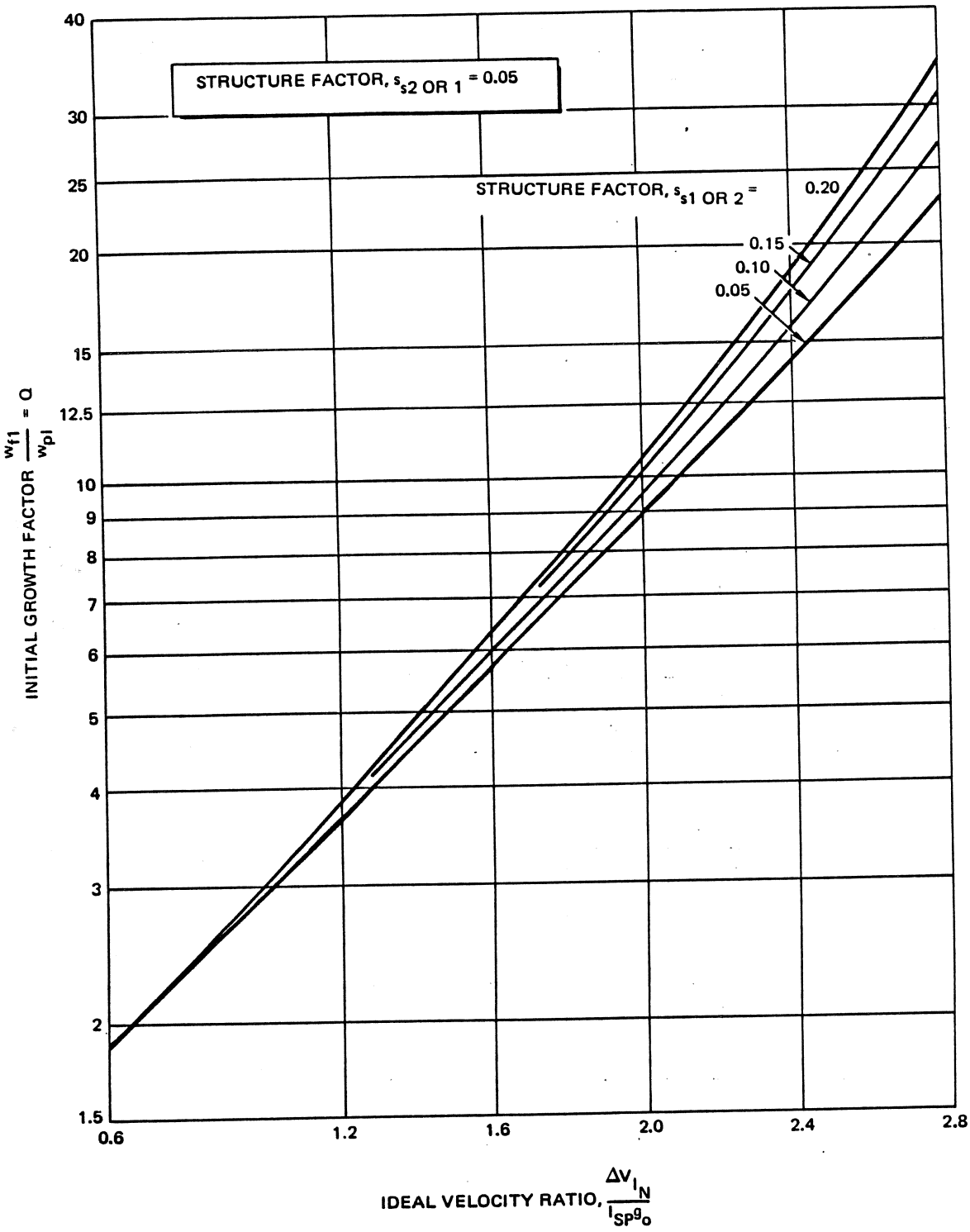

Figure 10-113. Growth Factor for Unlike Structure Factors (Two-Stage Vehicles) (Sheet 1 of 6)

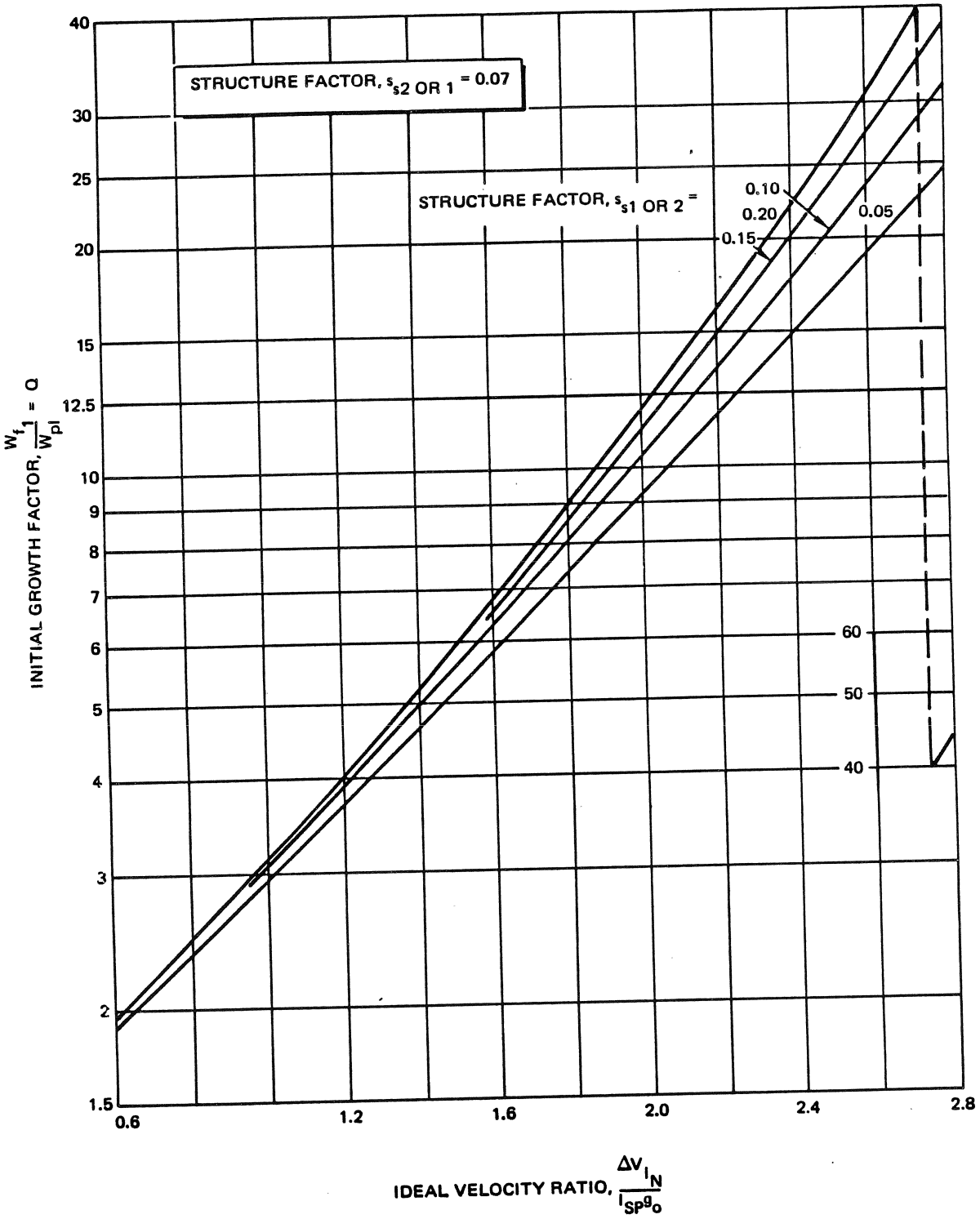

Figure 10-113. Growth Factor for Unlike Structure Factors (Two-Stage Vehicles) (Sheet 2 of 6)

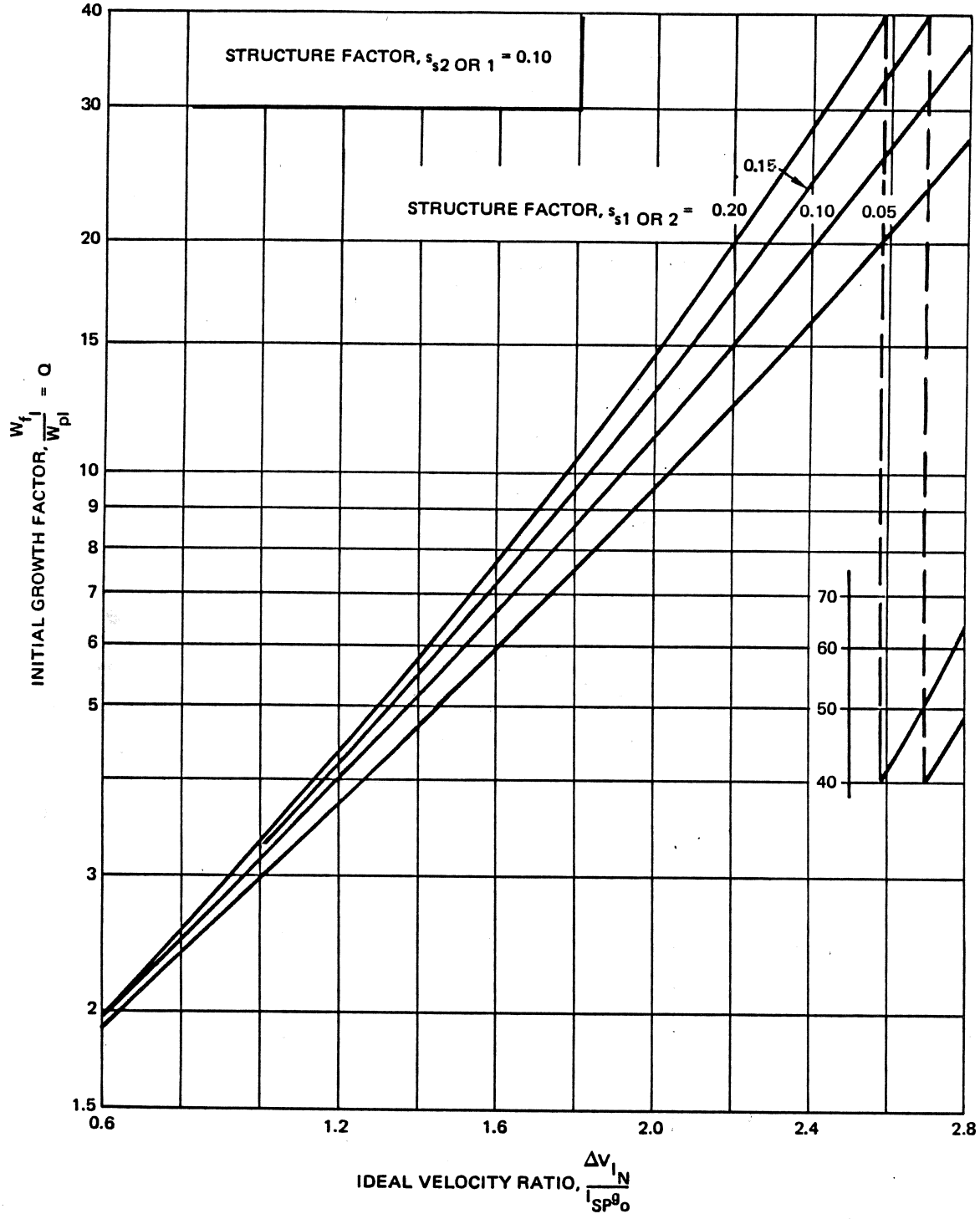

Figure 10-113. Growth Factor for Unlike Structure Factors (Two-Stage Vehicles) (Sheet 3 of 6)

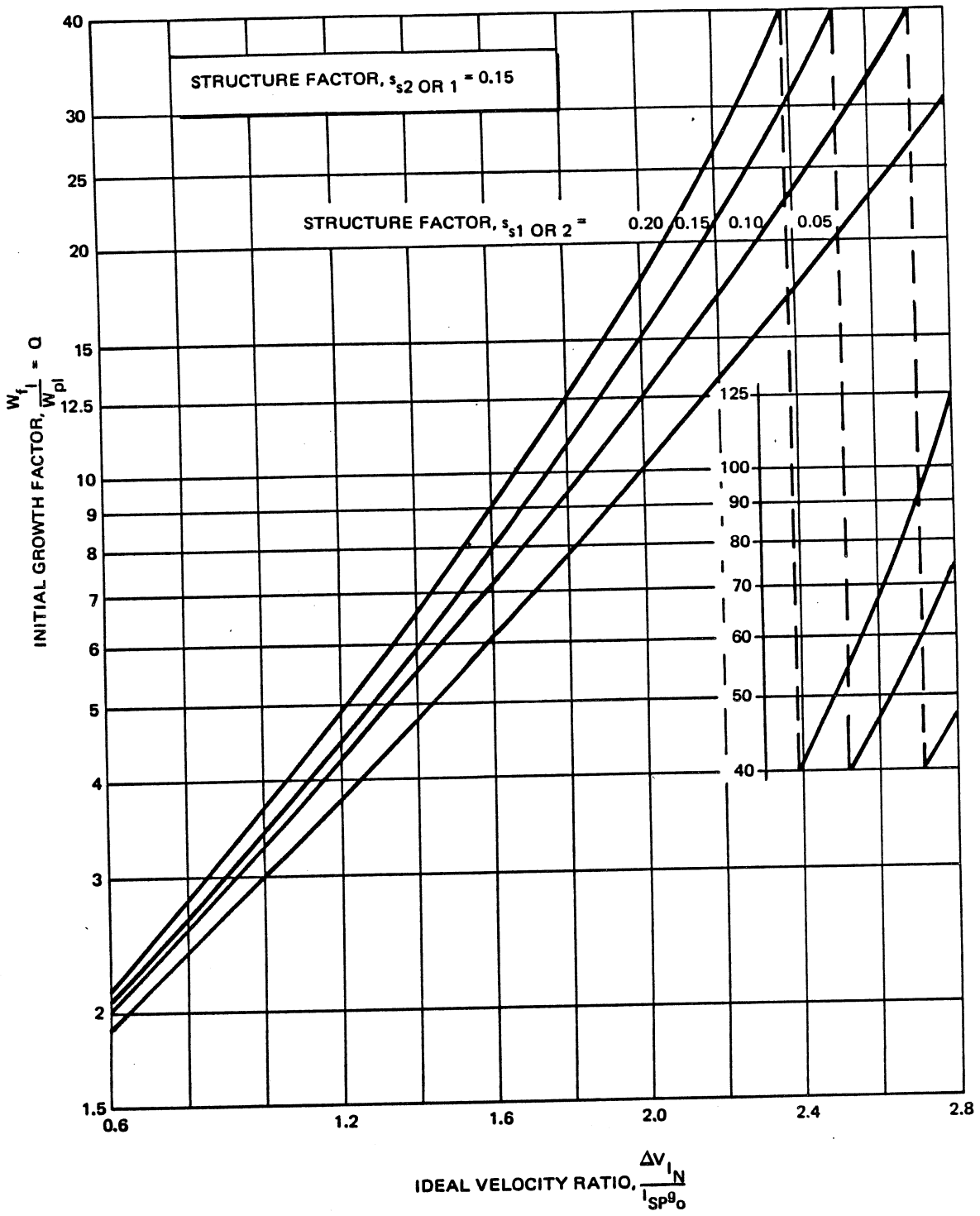

Figure 10-113. Growth Factor for Unlike Structure Factors (Two-Stage Vehicles) (Sheet 4 of 6)

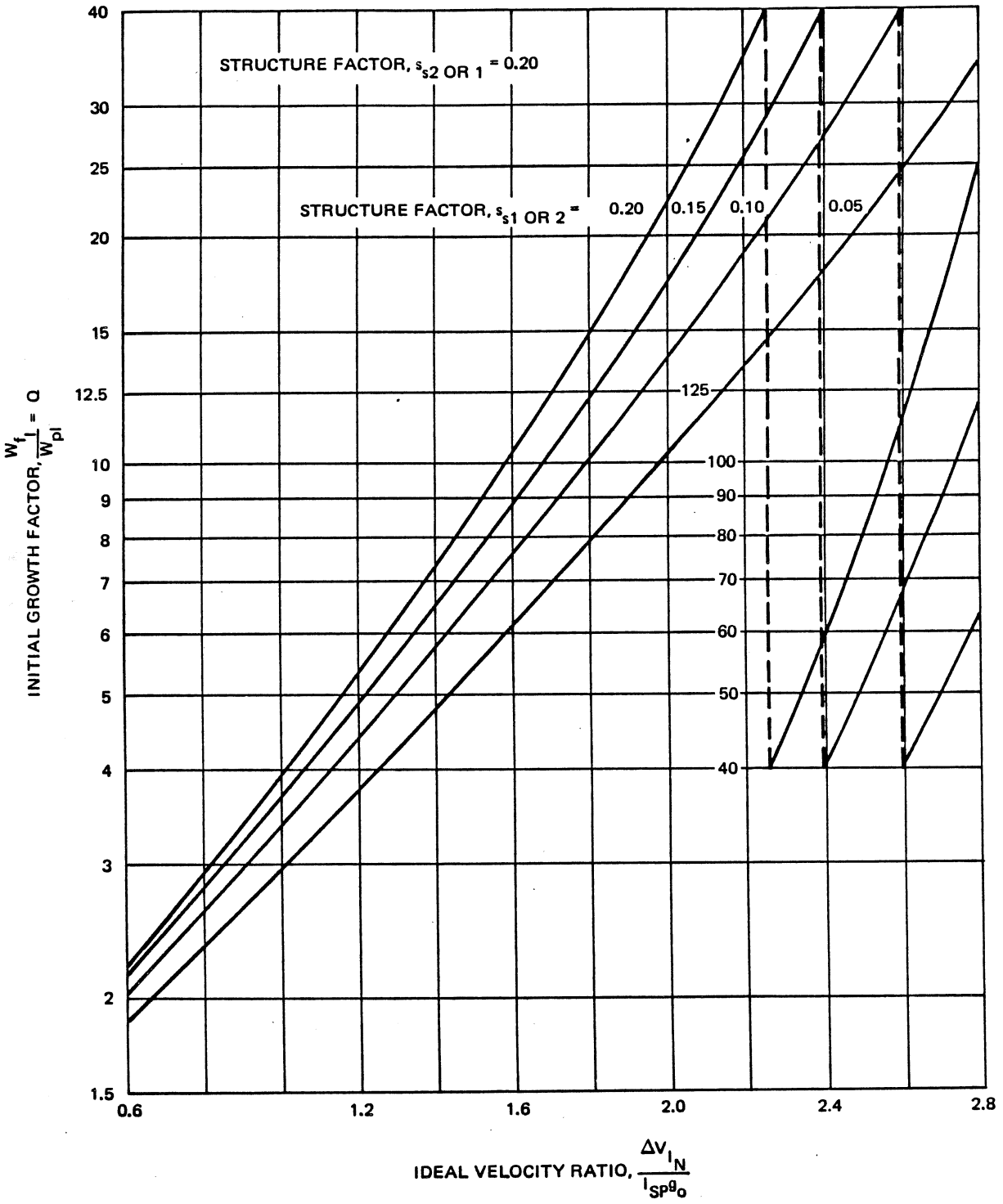

Figure 10-113. Growth Factor for Unlike Structure Factors (Two-Stage Vehicles) (Sheet 5 of 6)

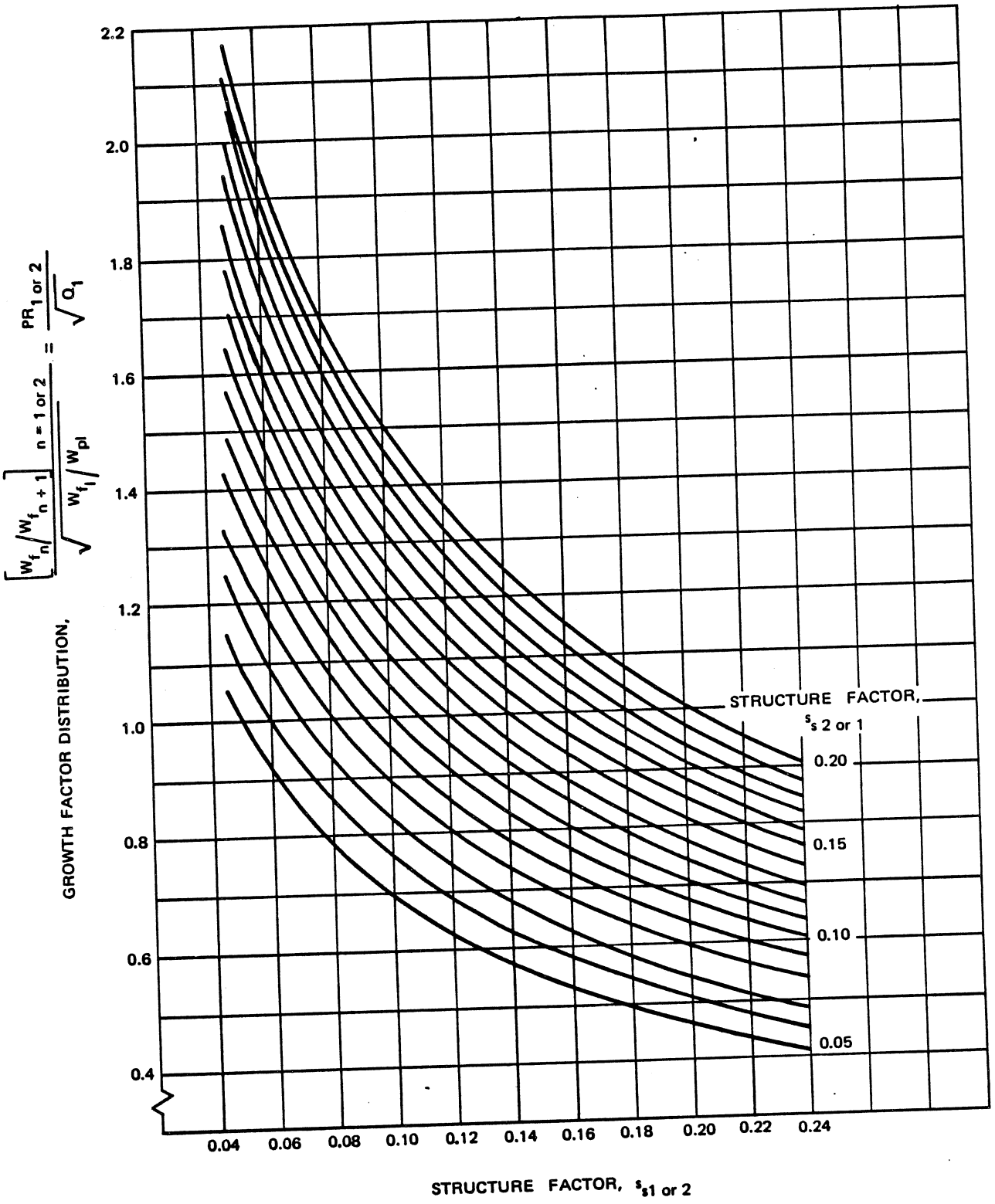

Figure 10-113. Growth Factor for Unlike Structure Factors (Two-Stage Vehicles) (Sheet 6 of 6)

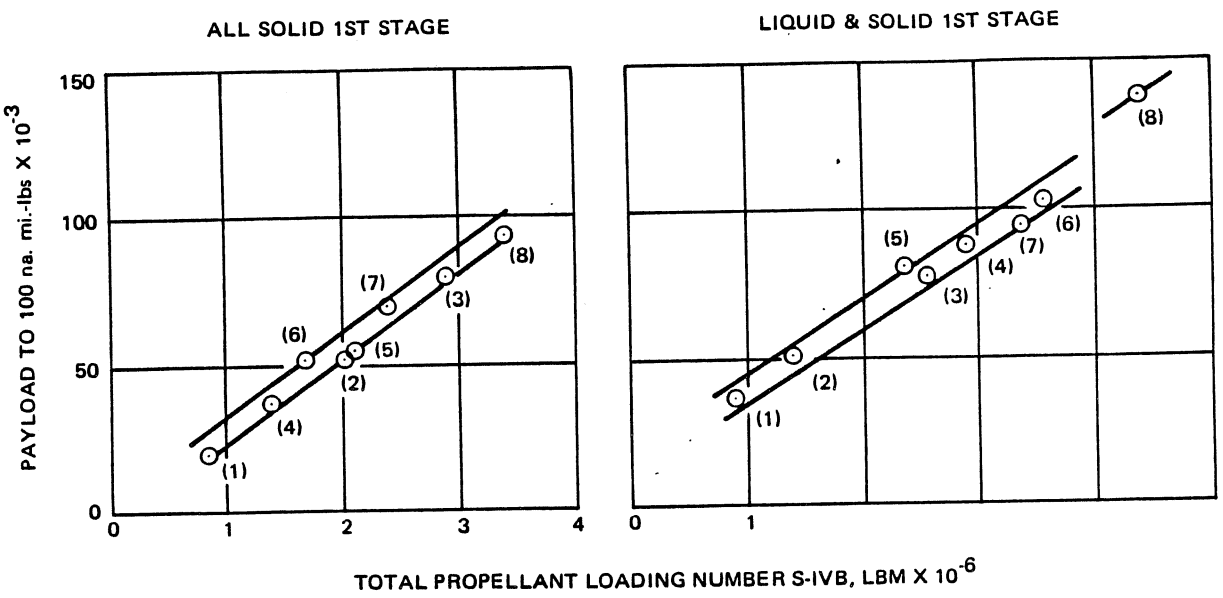

SOLID 1ST STAGE

1. 2-120" (5 SEGMENT) } 120"
2. 5-120" (5 SEGMENT)
3. 5-120" (7 SEGMENT)
4. 2-156" (2 SEGMENT) } 156"
5. 3-156" (2 SEGMENT)
6. 260" } 260"
7. ϕ1-260" - REF. 30
8. ϕ2-260" - REF. 30

LIQUID – SOLID 1ST STAGE

1. SATURN S-IB
2. MODIFIED S-IB
3. S-IB WITH 4-120" (5 SEGMENT STRAP-ONS)
4. MODIFIED S-IB WITH 4-120" (5 SEGMENT STRAP-ONS)
5. MODIFIED S-IB WITH 2-120" (7 SEGMENT STRAP-ONS)
6. MODIFIED S-IB WITH 4-120" (7 SEGMENT STRAP-ONS)
7. ϕ2-260" SOLID MOTOR - REFERENCE 30
8. MS-IC/S-IVB 4–"F-1" LIQUID ENGINES - REFERENCE 30

DUE EAST LAUNCH FROM KSC WITH STANDARD S-IVB SECOND STAGE

Figure 10-114. Comparison of Vehicle Performance for a Launch Vehicle with Different Propulsive Stages[30]

10-3.1.3.3 Multiple Staging

Equation 114 indicated that the total ideal velocity, ΔV_{I_N}, of an optimally sized vehicle with like parameters was divided equally among the stages. Thus the mass ratio of each stage is

$$r_{v_n} = e^{\left[\frac{\Delta V_{I_N}}{N g_o I_{sp}}\right]} \qquad (118)$$

which is shown in Figure 10-117 as a function of the ideal velocity ratio.

For a two stage vehicle with unlike structure factors the mass ratio of any stage can be inferred from Equation 117 to be:

$$r_{v_n} = \frac{W_{f_n}}{W_{bo_n}} = \frac{\frac{W_{f_n}}{W_{f_n+1}}}{s_{sn}\left(\frac{W_{f_n}}{W_{f_n+1}}\right) + (1 - s_{sn})} \qquad (120)$$

After the individual stage growth factors for the vehicle of interest have been determined by Equation 116 and Figure 113, the individual mass ratios can be determined from Equation 120.

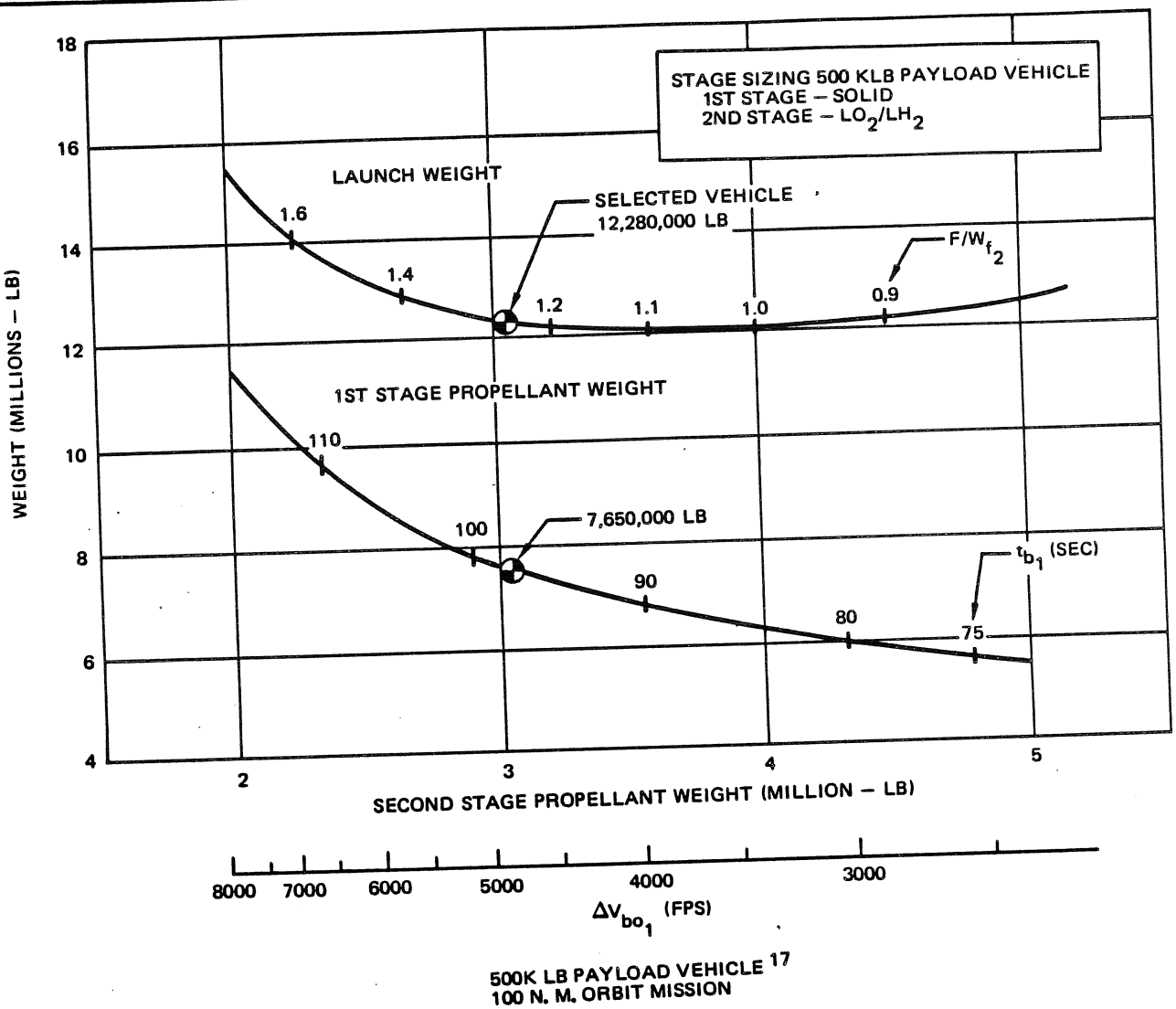

Figure 10-115. Effect of Stage Sizing on Vehicle Weight

10-3.2 Optimum Staging Criteria – General

The purpose of staging analysis is to determine the propellant weight for each step of the vehicle such that the vehicle design satisfies the design requirements. It is also desirable to predict the burnout velocities of the stages which are required for the generation of preliminary trajectory and performance data. Two methods of staging are available – arbitrary staging and optimum staging. For arbitrary staging, the analyst specifies the relative velocities of the stages whereas, for optimum staging the optimum velocity distribution (velocity staging ratio) is determined such that the gross weight required to satisfy the sizing requirement is minimized. For a single stage vehicle no staging optimization is required.

For multiple-stage missiles and space vehicles, three options in optimization criteria are available for optimum staging. These criteria differ depending on vehicle application and are:

a. Optimization of stage velocity distribtuion to establish minimum gross weight for a specified burnout velocity (or maximum burnout velocity for a specified gross weight) for missiles or space launch vehicles.

b. Optimization of stage velocity distribution for maneuvering missiles to establish the particular velocity distribution which results in minimum gross weight to satisfy a desired time of flight to a designated space point (or results in minimum time of flight for the specified gross weight).

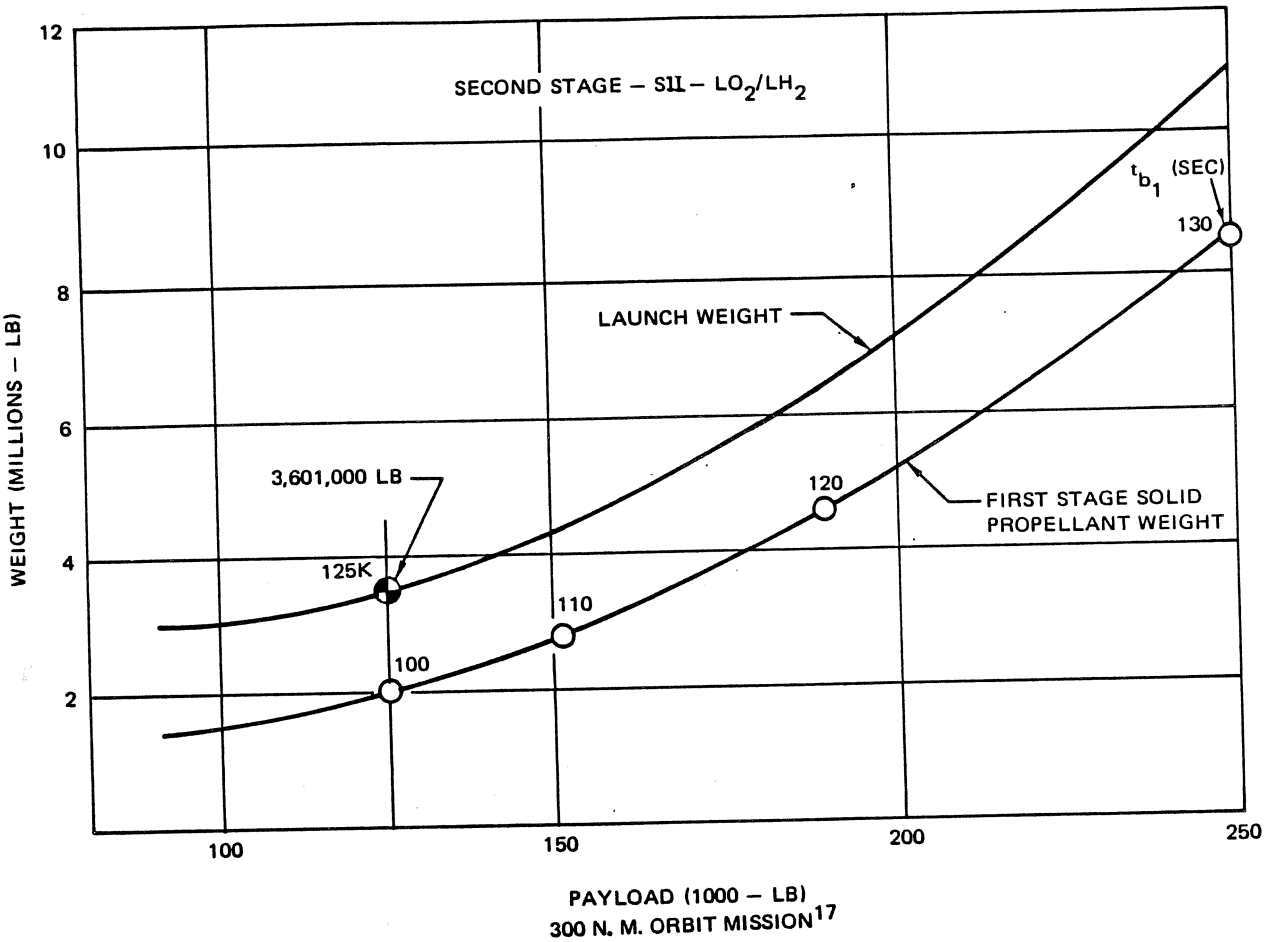

Figure 10-116. Payload vs. Launch Weight

c. Optimization of stage velocity distribution for maneuvering missiles to establish the particular velocity distribution which results in minimum gross weight to satisfy a desired velocity at a designated space point after burnout (or maximizes final velocity for the specified gross weight).

It should be noted that all three criteria apply to missiles but the first is the only one applied to space launch vehicles or ballistic missiles (ICBM's, etc.). These criteria are not to be confused with basic sizing analysis to meet mission performance. Thus, the three staging optimization criteria options listed above are used only to influence the staging ratio selection rather than the burnout velocity of the configuration.

The range, time of flight, or final velocity specified for the latter two options need not correspond to a mission sizing requirement. In the latter, both velocity distribution and total burnout velocity are varied to find values which will minimize gross weight for the range performance requirement. When the optimum velocity distribution is found, the resulting vehicle is scaled in size by scaling the stage velocity requirements to match the input burnout velocity, while maintaining the optimum stage velocity ratios. As a result, vehicles staged according to each of the three optimization criteria will all have the same burnout velocity (when burnout velocity is the design requirement); however, the rocket staged by the first optimization criterion will weigh the least, by definition, and the missiles staged by the latter two criteria will have higher mission performance.

The missile sizing requirement may be stated in terms of the missile performance with respect to a specified space point, evaluated through trajectory simulation and optimization. Burnout velocity is then a design requirement which is used as the design criterion in any particular missile design loop, but which may be

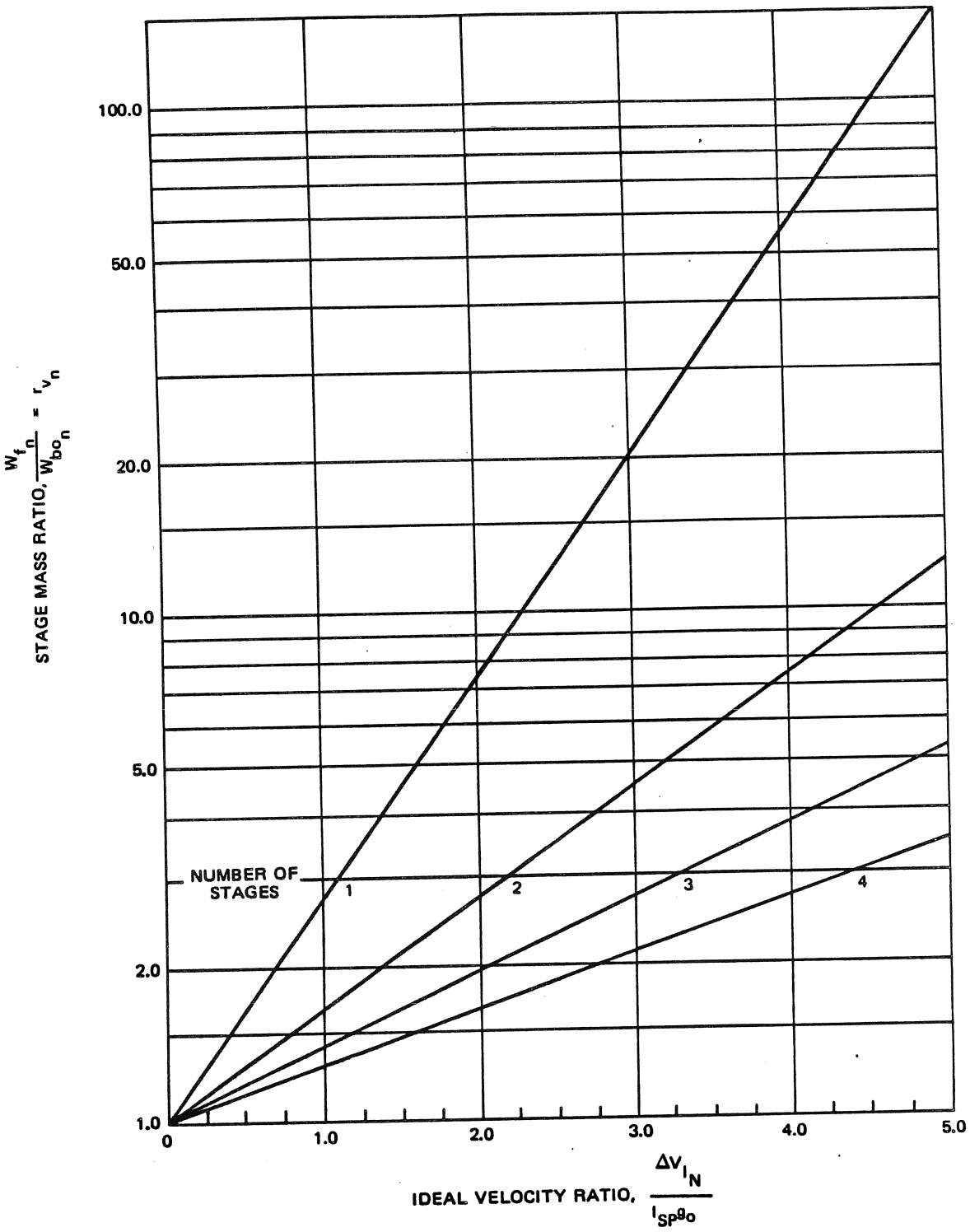

Figure 10-117. Stage Mass Ratio for Like Parameters (Multiple-Stage Vehicles)

modified through performance evaluation, i.e., the burnout velocity requirement is changed for each design iteration as required to satisfy the mission requirement. Therefore, the use of one of the staging optimization criteria to cause staging to be optimized with respect to mission requirements, rather than burnout velocity, will eventually result in a lower missile weight when the sizing requirement is satisfied.

10-3.3 Optimum Sizing – General

The commonly used criterion for optimum sizing of a space launch or large ballistic missile vehicle with respect to the overall system is sizing for maximum payload or, if the payload weight is given, sizing for minimum gross weight (corresponding to a minimum gross-weight payload-weight ratio in both cases). This corresponds to the first staging optimization criterion given in Paragraph 10-3.2. Sizing for maximum payload weight is discussed first in this section; sizing for criteria other than maximum payload is discussed later. For background on the subject of optimum sizing, the reader is referred to the thorough and annotated bibliography of Reference 9; other pertinent sources are found in References 20, 21, and 22.

The sizing method presented here assumes that a given fixed total impulsive velocity means constant gravitational and atmospheric losses. A method including variable losses could be developed using portions of the analyses presented in Paragraph 10-2, but the increased accuracy usually does not warrant the increased complexity. Several different methods for optimally sizing for maximum payload and minimum initial gross weight are available; the differences among them are in the approximations to the representation of the structure-factor/stage-size relationship, s_s, previously defined.

The first and most commonly used method assumes the structure factor to be constant with respect to step weight; in other words, structure factor is constant regardless of step weight. The second method assumes that the structure factor is linearily proportional to step weight. The third and most accurate method assumes the structure factor curve to be fitted by the higher order approximation,

$$s_{sn} = C_n \left(W_{f_n} - W_{f_{n+1}}\right)^{a_n - 1} \qquad (121)$$

The fit of each approximation for a typical structure factor curve is illustrated in Figure 10-118.

Approximations:

Constant =

$$s_{sn} = 0.10$$

Linear =

$$s_{sn} = a_n \left(W_{f_n} - W_{f_{n+1}}\right) + B_n$$

$$= -0.00117 \left(\frac{W_{f_n} - W_{f_{n+1}}}{1000}\right) + 0.15$$

Higher Order =

$$s_{sn} = C_n \left(W_{f_n} - W_{f_{n+1}}\right)^{a_n - 1}$$

$$= 29.5 \left(W_{f_n} - W_{f_{n+1}}\right)^{-0.534}$$

where

$$s_{sn} = \frac{W_{s_n}}{W_{f_n} - W_{f_{n+1}}} \qquad (122)$$

The last two methods are too complex for solution in reasonable time without the aid of a digital computer. The first and easiest method, which assumes a constant structure factor, is readily computable either by hand or with a computer and is discussed below and in Paragraph 10-3.5 where a nomograph solution is presented. The constant structure factor assumption is found to be a reasonable approximation for vehicles of gross weights in the 1,000 to 10,000 pound class.

By using an iterative procedure, a variation of structure factor with stage weight can be simulated to improve the accuracy of the solution. The variable structure factor

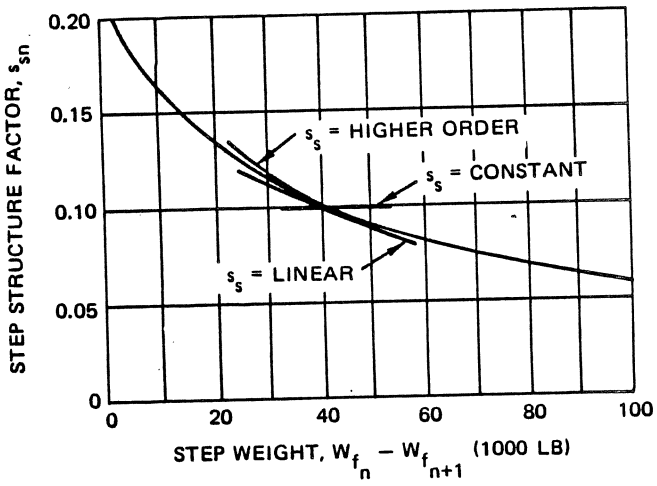

Figure 10-118. Curve Fits for the Approximation of the Structure Factor Variation

method, if programmed on a digital computer, facilitates the computation; however, the increased accuracy results in only a small increase in performance capability, since the optima are rather flat.

An engineer experienced in vehicle design, using the nomograph and evaluating the vehicle performance per the analyses presented in Paragraph 10-3.4, can design a realistically optimum vehicle system in a relatively short time. However, it is desirable, but not necessary, to check the vehicle performance with a two-dimensional trajectory program, which provides much additional information.

10-3.3.1 Constant Structure Factor

Assuming a constant structure factor, s_{sn} = constant, where:

$$s_{sn} = \frac{W_{sn}}{W_{f_n} - W_{f_{n+1}}} \tag{122}$$

The analytical equations for sizing are essentially the same whether the sizing is for minimum gross weight or maximum payload. One first needs an estimation of the total ideal velocity, readily approximated from the analysis presented in Paragraph 10-2.2. The solution is iterative with respect to the ideal velocity; therefore, it is best to plot the optimum distribution as a function of the ideal velocity and iterate, calculating the exact velocity losses for the optimally distributed vehicles per Paragraph 10-2.2 until an estimated ideal velocity is found that matches the computed value.

To optimally size a vehicle, it is necessary to assume a step size; if the vehicle is being sized for minimum vehicle gross weight, a payload ratio is assumed for the first stage; if sizing is for maximum payload, a payload ratio is assumed for the last stage. In either case, if a variable structure factor is not being simulated, it does not matter whether one starts at the first stage or the last. Using the Equation 123, the succeeding or preceding stage ratio is determined.*

$$PR_{n+1} = \frac{\frac{I_{sp_{n+1}}}{I_{sp_n}} (1 - s_{sn+1}) [PR_n s_{sn} + (1 - s_{sn})] - (1 - s_{sn+1})(1 - s_{sn})}{s_{sn+1}(1 - s_{sn})} \tag{123}$$

$(1 \leq n \leq N - 1)$

When starting at the top of the vehicle, all n + 1 and n subscripts are interchanged.

where:

$$PR_n = W_{f_n}/W_{f_{n+1}} \tag{124}$$

$$W_{f_{N+1}} = W_{pl} \tag{125}$$

To approximate a variable structure-factor/step-weight curve, first assume an approximate structure factor of the step being optimized and, having determined its optimum factor; then iterate until they coincide. Next compute all succeeding (or preceding) stage payload ratios, using the previously computed ratio. (It may be desirable, with respect to minimizing the effort for solution, to size all the stages with respect to either the first or last stage payload ratio. This is possible by simply manipulating the subscripts in the following equation.)

$$\Delta V_{I_N} = \sum_{n=1}^{N} I_{sp_n} g_o \ln \left[\frac{PR_n}{PR_n s_{sn} + (1 - s_{sn})} \right] \tag{126}$$

Iterate on the initial assumed stage payload ratio and compute the others until the resulting ideal velocity corresponds to that estimated to be required. Then compute the exact ideal velocity required, compare with the vehicle's actual capability, and iterate again. If necessary, assume a new value for the total ideal velocity required. The vehicle growth factor is then computed from,

$$Q_N = \prod_{n=1}^{N} PR_n = \prod_{n=1}^{N} \frac{W_{f_n}}{W_{f_{n+1}}} \tag{127}$$

The solution sounds tedious, however, with experience and the aid of a small computer or the nomograph presented in Figure 10-119, it is obtained quickly.

In the above analyses, the resultant individual stage gross weights, step gross weights, and step propellant weights can be computed respectively from:

$$W_{f_n} = PR_n W_{f_{n+1}} \tag{128}$$

$$W_{S_n} = W_{f_n} - W_{f_{n+1}} \tag{129}$$

$$W_{p_n} = W_{S_n}(1 - s_{sn}) \tag{130}$$

Should a step, such as a booster, be specified and should maximum payload be desired, sizing proceeds in exactly the same manner as for the upper unspecified steps; however, several gross weights of the upper steps would be assumed and the optimum propellant distribution, as a function of the total ideal velocity capability of the

upper stages would be determined. The burnout velocity capability of the booster would also be determined as a function of its "payload" weight (gross weight of upper stage). The velocity losses associated with the upper stage operation would be calculated for each upper stage gross weight-booster combination and payload corresponding to the desired mission requirements would be determined. The payload capability would then be plotted as a function of the upper stage gross weight, and the maximum payload found. The maximum payload capability vehicle for a specified booster, does not usually provide the minimum growth factor vehicle possible. Minimum growth factor for a vehicle having a specified step is found in the same manner as for a vehicle of all unspecified steps, except that the weight of the specified step is held constant.

10-3.3.2 Variable Structure Factor

The procedure for sizing, assuming a variable structure for each step, is the same as for constant structure factor. There is no necessity to perform an iteration on structure factor if the curve fit is good at the point of optimization. However, the method is too complex for inclusion in this manual.[13]

10-3.4 Propulsion System Selection Criteria

10-3.4.1 Space Launch Vehicles

Space launch vehicle design requirements influence selection criteria and are usually defined by one of the following options:[21]

a. Size to a specified burnout velocity.

b. Size to a specified gross weight.

c. Design to given propellant weights.

d. Design to given step lengths.

The latter two options constrain the design such that the processes of sizing (wherein the vehicle is scaled in size and designed so as to satisfy a performance requirment) and velocity staging (wherein the relative velocity increments of the stages of the vehicle are selected) are not applicable. For these two options the vehicle design is implicitly defined by the given requirements. However, for options 1 and 2, design iteration is required to force the performance or the weight of the vehicle to converge on the sizing requirement. Each iterative design loop consists of the design of a vehicle based on an assignment of propellant weight for each propulsive step and the comparison of the resulting burnout velocity or gross weight to the design requirement.

The design process for each design loop is initiated by examining the stage efficiency parameters — mass fraction and specific impulse — and, based on the values of these parameters and the desired staging criteria, selects the propellant weight to be applied to each propulsive step.

Iterative design loops (considering structures, aero-thermodynamics, propulsion, guidance and control, etc.) are usually required to converge the vehicle design to the design requirement. This is necessary because the efficiency parameters are variables whose values are rarely well-known and must be established independently through evaluation of one or more missile or space vehicle designs.

In addition to the requirements for sizing, propulsion system selection criteria differ for each class of vehicle. For space launch vehicles (1) costs (both nonrecurring and recurring), (2) logistics, and (3) predicted reliability become important selection criteria for propulsion systems. Nonrecurring costs include research (state-of-art improvement) and development (design and test) costs, and facilities cost (test, manufacturing, and launch). Recuring costs include the production, handling, storage, delivery, checkout and launch of each vehicle (including expendable materials). Logistics operations are concerned with safety, checkout and launch. The relative difficulty of these operations greatly influences recurring costs. The predicted reliability of each subsystem of a space launch vehicle is of extreme importance in the selection process. Space payloads are frequently more expensive than launch vehciles and it is therefore necessary to have more reliable launch systems to be cost effective. Of course, for manned systems, the reliability consideration has precedence over all others.

10-3.4.2 Maneuvering Missiles

Air-to-surface (TASM's) air-to-air (AAM's) and surface-to-air (SAM's) satisfy many short-range interceptor or attack mission requirements which inherently include the following considerations:

a. Those related to the performance needed to penetrate a defense and kill the target.

b. Those related to the interface of the propulsion system and other elements of the weapon system.

c. Those imposed by cost.

The first consideration directly influences parameters such as thrust-time history, flight path, exhaust radar signature, and, of course, the tactical situation and enemy defenses. Defense system performance and weapon and aircraft characteristics are interrelated. The effects of missile launch range, aircraft velocity, altitude and radar cross section are major factors in determining the probability of target kill and aircraft survivability. Sufficient data concerning these factors must be utilized

to assure compatibility of the propulsion system characteristics with the scope of performance requirements.

The second consideration includes basic aircraft or launch site compatibility and logistic considerations and is manifested by missile weight and volume restraints, launch and carry conditions, flight and storage environments, weight and balance control, and maintenance requirements. For example, air-launched missile studies have shown that these missiles are primarily volume and length constrained. These system characteristics are significant in defining the advantages and disadvantages of liquid and solid propellants in terms of density, specific impulse, temperature dependence, and packaging.

The cost considerations include the effects of the state of the art of the components making up three major air-launched missile subsystems (propulsion, guidance, and airframe controls), producibility, and production quantity and rate.

Subsequent sections present analytical selection methods in some detail, based on design, cost, and reliability considerations.

10-3.5 Optimum Sizing of Launch Vehicles (Ballistic and Space)

The equations for the optimum sizing of a vehicle for a given mission have been specified in Paragraph 10-3.3. These equations are relatively complicated and require an iterative method for solution. In order to relieve the time-consuming task of straight-forward solution of complex staging equations, a graphic means of solution, in the form of a nomograph, has been developed[13] (Figure 10-119).

Equation 123 representing optimum sizing of a multiple stage vehicle can be rewritten as:

$$I_{sp_1}(1 - r_{v_1} s_{s1}) = I_{sp_n}(1 - r_{v_n} s_{sn}) = I_{sp_{n+1}}(1 - r_{v_{n+1}} s_{sn+1}) = I_{sp_N}(1 - r_{v_N} s_{sN}) \quad (131)$$

since

$$PR_n = \frac{r_{v_n}(1 - s_{sn})}{1 - r_{v_n} s_{sn}} \quad (132)$$

The equation relates the parameters of each step of a vehicle, to facilitate optimum sizing when different constant structure factors, s_s, and different specific impulses, I_{sp}, are assumed in each step. The assumption of a constant structure factor in a step simplifies the sizing equations (Paragraphs 10-3.3.1 and 10-3.3.2). Even though the solution itself allows no variations of a step structure factor, an iterative procedure can be used to include a variation where necessary.

Equation 131 in itself does not provide the complete relationship for vehicle sizing. Since a mission requirement must be met in terms of a total ideal velocity, the following equation must be considered with Equation 131:

$$\Delta V_{I_N} = g_o \sum_{n=1}^{N} I_{sp_n} \ln r_{v_n} \quad (133)$$

The total ideal velocity is the sum of the mission burnout velocity, the velocity losses incurred by the vehicle during flight, and the earth's rotation effects. Generally, the velocity losses can be estimated with reasonable accuracy (Paragraph 10-2) without knowing the size and shape of the vehicle. During the sizing of a vehicle, the payload ratio of each stage, $W_{f_n}/W_{f_{n+1}}$, is of interest to determine the overall vehicle growth factor, W_f/W_{pl}.

Since Equations 132 and 133 are a function of the mass ratio of the stages a nomograph based on that parameter was easily constructed. Examination of Equation 131 indicates that the sizing of all the steps of a vehicle can be referred to the parameters of one particular step, thus reducing the time required for the analysis.

The following example sizing problem is presented to explain the use of the optimum sizing nomograph (Figure 10-119).

Problem. Determine the optimum weight ratio distribution required to put a 4,000 pound payload into a 100 nautical mile circular orbit with a three stage vehicle, assuming an eastward launch from AMR. The specific implulses of the three stages are 250, 300, and 350 lb-sec/lb, respectively. The variation of structure factor with step weight, shown in Figure 10-120, is assumed valid for all three steps.

The ideal velocity for which the vehicle will be sized is:

$$V_{I_N} = V_{bo} - V_{rot} + \Delta V_L \quad (134)$$

where:

V_{bo} = mission burnout velocity (Figure 10-44 and Table 10-1)

V_{rot} = earth's rotational component (Figure 10-69)

ΔV_L = vehicle velocity losses (assumed to be 5,000 ft/sec for illustration of the problem) (Figure 10-30)

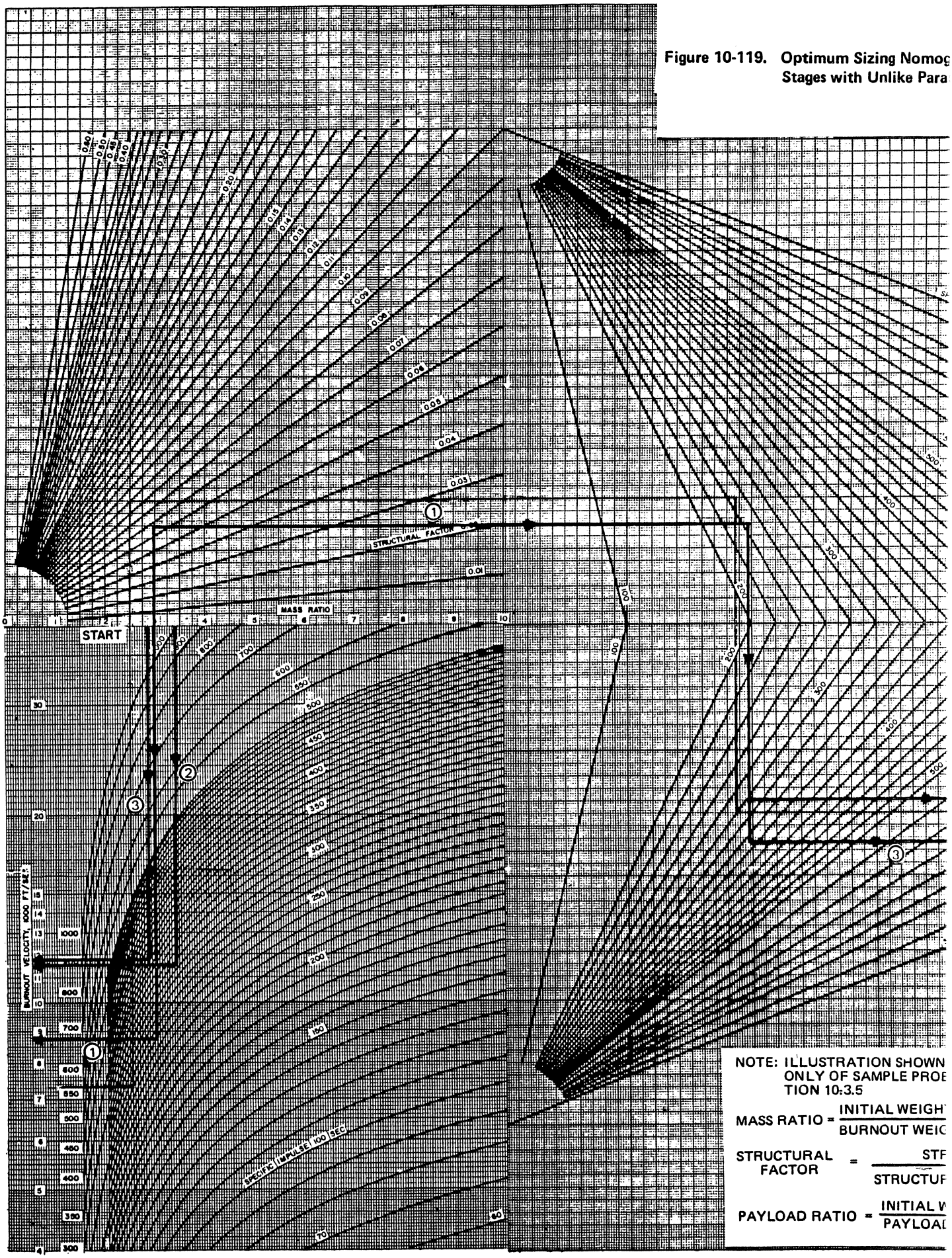

Figure 10-119. Optimum Sizing Nomog
Stages with Unlike Para

Figure 10-119. Optimum Sizing Nomograph for Stages with Unlike Parameters

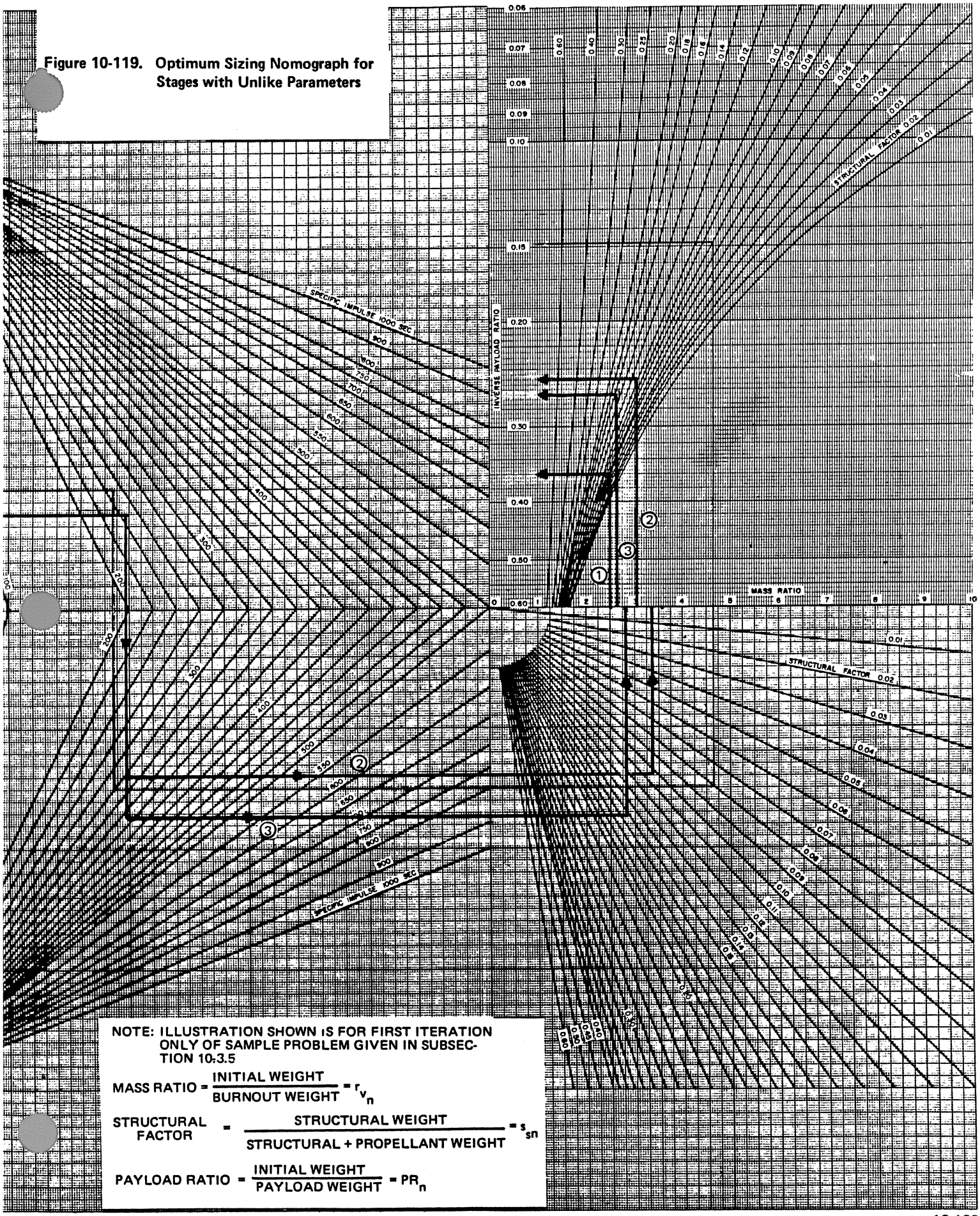

NOTE: ILLUSTRATION SHOWN IS FOR FIRST ITERATION ONLY OF SAMPLE PROBLEM GIVEN IN SUBSECTION 10-3.5

$$\text{MASS RATIO} = \frac{\text{INITIAL WEIGHT}}{\text{BURNOUT WEIGHT}} = r_{v_n}$$

$$\text{STRUCTURAL FACTOR} = \frac{\text{STRUCTURAL WEIGHT}}{\text{STRUCTURAL + PROPELLANT WEIGHT}} = s_{sn}$$

$$\text{PAYLOAD RATIO} = \frac{\text{INITIAL WEIGHT}}{\text{PAYLOAD WEIGHT}} = PR_n$$

Figure 10-119. Optimum Sizing Nomograph for Stages with Unlike Parameters

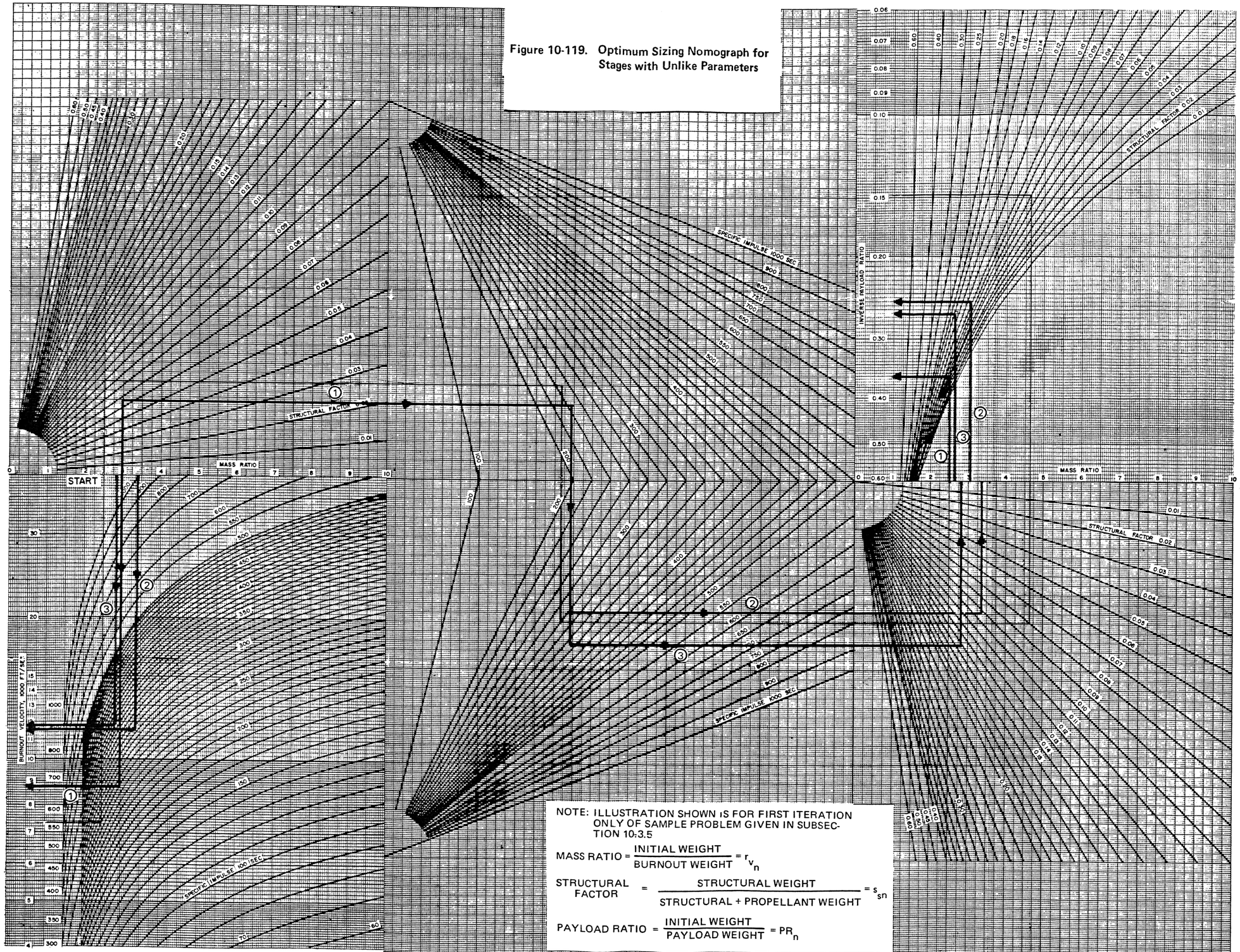

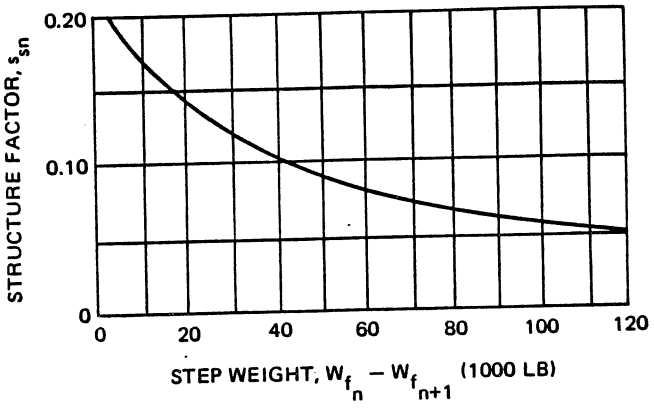

Figure 10-120. Structure Factor Selection Data

which gives:

$$V_{I_N} = 25,581 - 1,342 + 5,000$$
$$= 29,239 \text{ ft/sec}$$

Having once obtained the necessary input parameters, the sizing analysis requires the following steps for solution:

a. Assume a structure factor for each step.

Step	Structure Factor
1	0.07
2	0.10
3	0.15

b. Assume an initial mass ratio for the first stage (r_{V_1} = 3.00).

c. Enter the nomograph at the "start" position at the above mass ratio.

d. Move vertically upward to the first step structure factor (s_{S1} = 0.07).

e. Extend a horizontal line right to the first stage specific impulse (I_{sp_1} = 250 sec).

f. Construct a vertical line downward to the second and third stage specific impulses (I_{sp_2} = 300 sec and I_{sp_3} = 350 sec).

g. From the second stage specific impulse move right horizontally to the second step structure factor (s_{S2} = 0.10).

h. Extend a vertical line upward and read the second stage mass ratio (r_{V_2} = 3.35).

i. Repeat Steps g and h, using the third stage specific impulse and step structure factor (s_{S3} = 0.15 give r_{V_3} = 2.85).

j. Using the specific impulse and mass ratio obtained above for each stage determine the stage ideal velocity from the curve in the lower left hand side of the nomograph. The following velocities were obtained for the example stages:

Stage	Mass Ratio	I_{sp}	Ideal Velocity
1	3.00	250	8,850
2	3.35	300	11,650
3	2.85	350	11,800

The sum of the stage ideal velocities, 32,300 ft/sec, is considerably above that required.

k. Repeat Steps a through j with a different assumption for the initial mass ratio until the desired velocity is reached. For example, the desired velocity is reached with first, second, and third stage mass ratios of 2.48, 3.07, and 2.68, respectively.

l. For the mass ratios and structural factors, find the stage payload ratios from the plot in the upper right hand corner of the nomograph. Note that the value on the ordinate is called the inverse of the payload ratio, (payload fraction). For the example, the payload ratios are given below:

Step/ Stage	Mass Ratio	Structure Factor	Payload Ratio	Ideal Velocity fps
1	2.48	0.07	2.79	7,300
2	3.07	0.10	3.98	10,800
3	2.68	0.15	3.81	11,100
				29,200

m. The total vehicle growth factor is found by Equation 127 which gives:

$$\frac{W_f}{W_{pl}} = \prod_{n=1}^{N} \frac{W_{f_n}}{W_{f_{n+1}}} = (2.79)(3.98)(3.81) = 42.3$$

Thus the vehicle gross weight requires to put the 4,000-pound payload in orbit is:

$$W_f = (42.3)(4000) = 169,000 \text{ lb}$$

n. It must be remembered that the structure factors for each step were assumed values, and thus the respective step weights must be computed to obtain the correct values of s_s from the plot of structure factor versus step weight. The gross weight of a particular step of a vehicle is:

$$W_{s_n} = W_{f_n}\left[\frac{r_{v_n} - 1}{r_{v_n}(1 - s_{sn})}\right] = W_{fn} - W_{fn+1} \quad (135)$$

where:

$$W_{f_n} = W_{f_{n+1}} + W_{s_n}$$

For the example, the step weights and proper structure factors are:

Step	Assumed s_s	Step Weight (lb)	Actual s_s
1	0.07	108,500	0.055
2	0.10	45,400	0.100
3	0.15	11,200	0.163

After a comparison of structure factors, it is seen that the vehicle previously sized is now in error, and a new analysis must be performed. (One could compute the actual structure factor after computing each optimum stage ratio and iterate until the assumed value matches that desired).

o. Recalculate Steps a through n until the assumed structure factors approach the actual values with the desired accuracy. The actual structure factors obtained in Step n can be used as the assumed values for the next iteration. In the case of the example, the second iteration is seen to have considerably reduced the difference in structure factors which gives the following:

Step	Assumed s_s	Step Weight (lb)	Actual s_s
1	0.055	119,200	0.050
2	0.100	38,200	0.105
3	0.163	9,600	0.168

Using the above, a 171,000-pound vehicle (including payload) is required to perform the mission of interest.

After experience in the use of the nomograph, an engineer can optimally size a vehicle in a relatively short time.

10-3.6 Maneuvering Missiles (Air-to-Air, Surface-to-Air, and Air-to-Surface)

10-3.6.1 Velocity Staging

A considerable amount of attention has been given to the subject of velocity staging optimization for large ballistic missiles and space launch vehicles.[21] It is for these types of applications that the staging optimization technique described in previous sections (and other similar methods) has been developed. This technique is frequently based on certain assumptions which are generally valid:

a. Step mass fraction (or structure factor) does not vary with propellant weight (however, it may be handled by the methods of Paragraph 10-3.5).

b. Motor specific impulse does not vary with propellant weight.

c. The difference between impulsive velocity and delivered velocity is a predictable value which does not vary with propellant weight.

d. Axial acceleration does not vary significantly during motor burning of a given stage.

e. All stage velocity distributions, which produce the same total velocity, result in vehicles delivering the same mission performance.

Characteristically, the step mass fraction and specific impulse values for large ballistic missiles and space vehicles are relatively constant over wide ranges of propellant weights. The degradation of velocity due to drag is small such that impulsive velocity differs from actual delivered velocity primarily due to gravity and atmospheric thrust losses.

The velocity decrement due to gravity is nearly the motor burn time, times the gravitational constant for near vertical flight (10-2). The thrust atmospheric loss can be accounted for either by using delivered specific impulse at some average ambient pressure in the staging equations or by correcting vacuum I_{sp} to actual flight conditions. Therefore, a reasonably accurate optimization of velocity staging for a particular burnout velocity of a large ballistic missile or vehicle can be performed by using the vacuum staging equations, specifying the required impulsive velocity as the desired burnout velocity plus the loss due to gravity plus 3 percent to 5 percent, and using delivered specific impulse in the equations.

However, for smaller missiles, particularly high-performance interceptors, the assumptions listed above become inaccurate and/or invalid. This is illustrated by Figures 10-121 through 10-123 for a conical missile shape. Figure 10-121 is a plot of step mass fraction as a function of propellant weight for both stages of a typical two-stage interceptor. The impact of the structural weight, as a function of step size, is clearly shown by these curves. Configuration differences between first and second stage motors also affect the values. Figure 10-122 shows the variation of vacuum

MISSILE SHAPE:

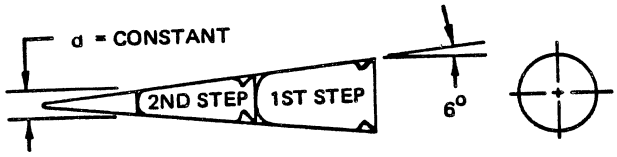

MOTOR CASE TAPER ~ 6° = CONSTANT
NOZZLE EXIT DIAMETER ≦ MOTOR CASE DIAMETER

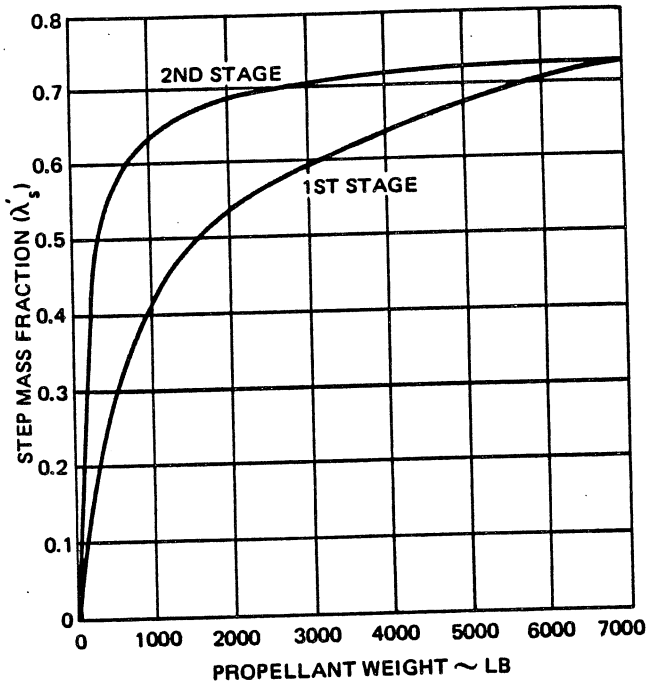

Figure 10-121. Typical Step Mass Fraction vs Propellant Weight

MISSILE SHAPE:

NOZZLE EXIT DIAMETER ≦ MOTOR CASE DIAMETER
MOTOR CASE TAPER ~ 6° = CONSTANT

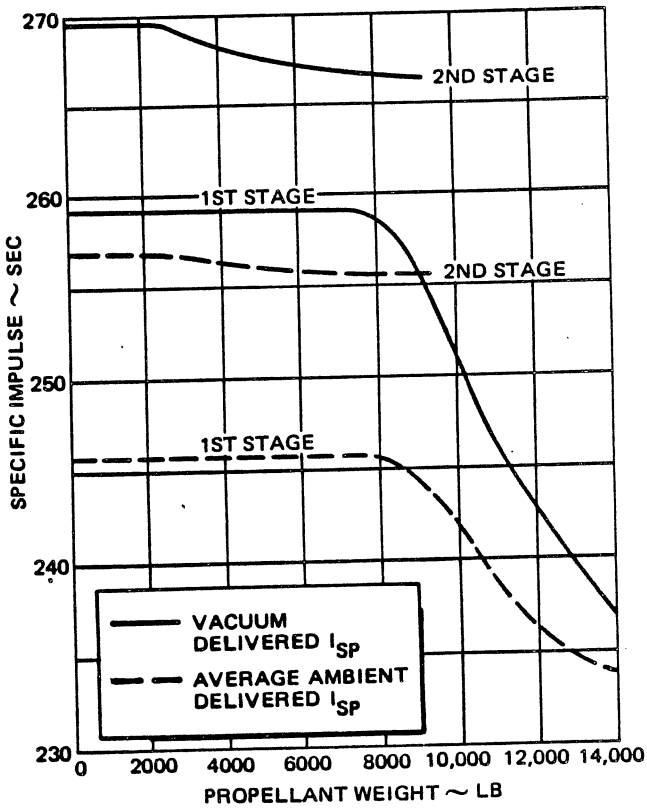

Figure 10-122. Typical Specific Impulse vs Propellant Weight Plot

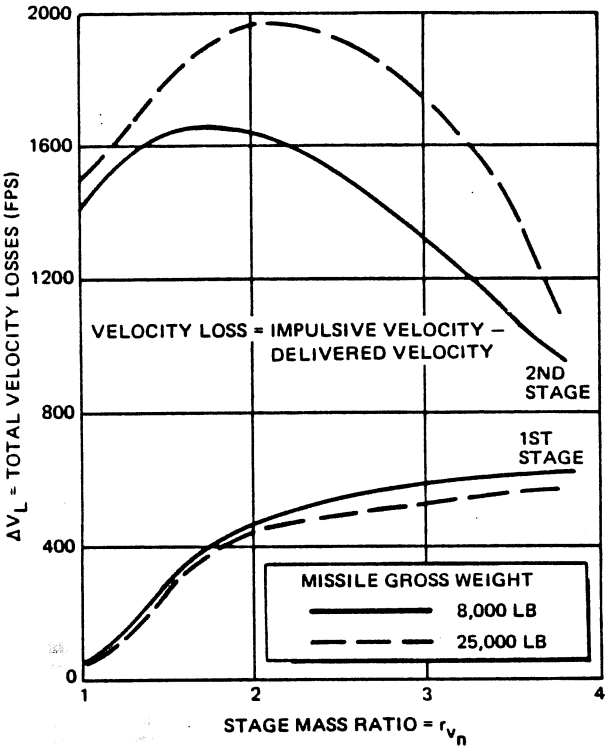

Figure 10-123. Typical Velocity Losses Versus Stage Mass Ratio

delivered, and average delivered, specific impulse for each stage of the same missile. The drop off in I_{sp} at large propellant weights is primarily due to the limitation in nozzle expansion ratio because of exit diameter limitations, and the larger mass flow rate through the nozzle for a given motor burning time of each step. The difference between first and second stage I_{sp} values are mainly due to the larger expansion ratio available for the second stage. However, since the missile system (both stages) illustrated is operated in the atmosphere the differential between vacuum and average altitude I_{sp} values is considerable.

Figure 10-123 shows the difference between the impulsive velocity increment and delivered increment of each stage as a function of stage mass ratio, illustrating the variation of the velocity losses with stage size and operating conditions (larger drag and gravity losses in second stage). As a result of the variation of the values of the staging parameters with propellant weight, both the prediction of the propellant weight required to deliver a particular impulsive velocity, and the calculation of the optimum stage velocity ratio (by staging equations using vacuum conditions) will be substantially in error unless the resultant stage propellant weights are close to those used in selecting the values of step mass fraction, specific impulse, and required impulsive velocity.

For multiple-stage missiles, principally in which the power-on phase of the missile's trajectory is a significant portion of the total trajectory, another factor arises which is not considered in the common staging techniques. For a given total burnout velocity and motor burn time, the slant range covered by a missile during power-on phase increases as the staging ratio (first stage burnout velocity/total burnout velocity) increases due to the increase in velocity-time integral. When it is desired to arrive at a designated space-point after motor burnout with a specified time of flight, the average velocity required in the coast phase decreases as the power-on range increases. Therefore, for a fixed time of flight to a space-point, the burnout velocity required to produce this performance decreases as the staging ratio increases or, alternately, the mission performance of a missile with fixed burnout velocity increases with staging ratio.

Typical velocity and range characteristics are illustrated in Figures 10-124 and 10-125 for two different vehicles having different velocity staging ratios and performance requirements. The same effects apply for a criterion of maximum velocity or maneuver capability at a space-point. These burnout velocity requirements may vary substantially as indicated in Figure 10-126. This figure also shows the burnout velocity required to deliver constant values of time of flight performance at short and long range intercepts as a function of staging ratio for a typical high-performance interceptor.

Figure 10-127 shows the resultant missile gross weight required for the two intercept points as a function of staging ratio and indicates the optimum staging ratio and resultant gross weight as indicated by the vacuum staging optimization technique. As shown by Figure 10-127, the vacuum staging technique results in a substantial increase in missile gross weight. The importance of considering power-on range to total range increases as the percentage of motor-burn time to total time of flight increases. It is notable that the effect of power-on range applies even to ballistic missiles since it is usually desired to maximize exit velocity occurring at some space point after burnout (with a given flight path angle). By increasing power-on range at a given burnout velocity and motor burn time, the duration of the coast phase is reduced and consequently the coast phase velocity loss due to gravity is reduced.

The reduction of missile gross weight with increasing velocity staging ratio, until a minimum is reached (Figure 10-127) is explained by the corresponding reduction in burnout velocity requirement as shown in Figure 10-126. However, if velocity staging ratios are increased beyond certain minimum values the two stages continue to grow in size (larger payload ratios) because of larger total velocity losses and vehicle mass becomes correspondingly larger. Note that the missile gross weight curve rises faster at longer total flight times for high staging ratios.

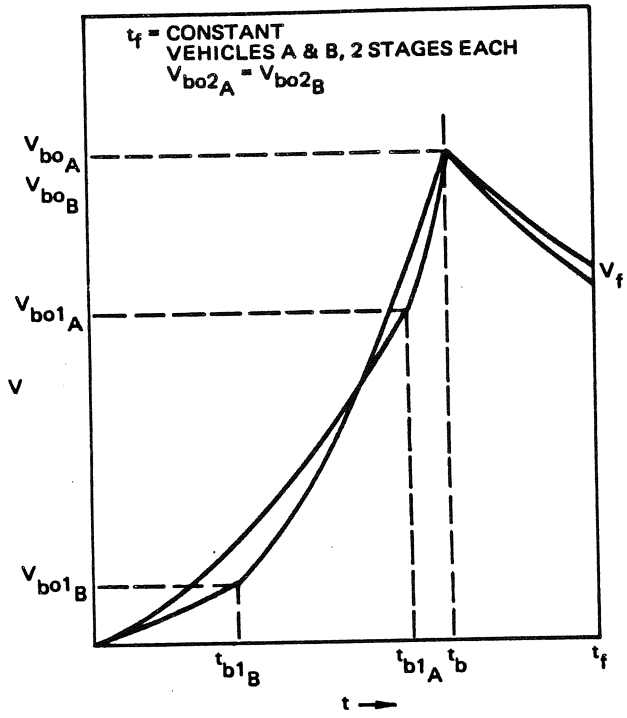

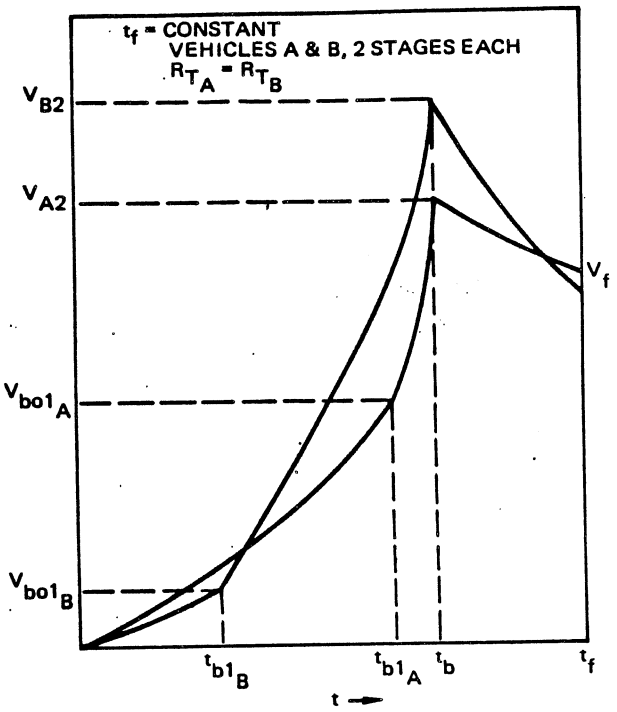

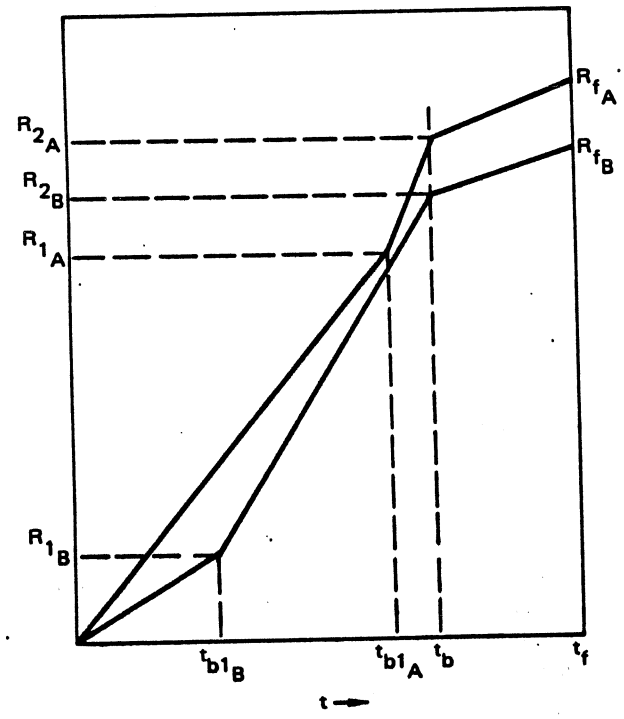

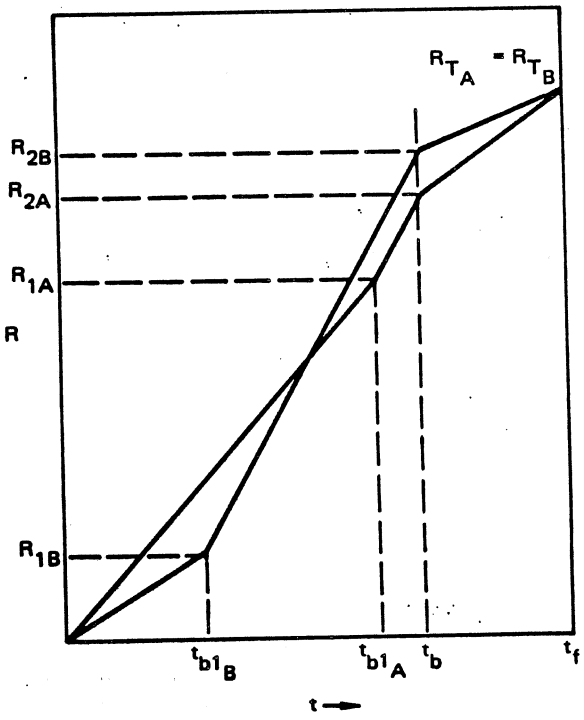

Figure 10-124. Interceptor Performance for Two Velocity Staging Ratios (V_{bo} = C)

Figure 10-125. Intercepter Performance for Two Velocity Staging Ratios (R_T = C)

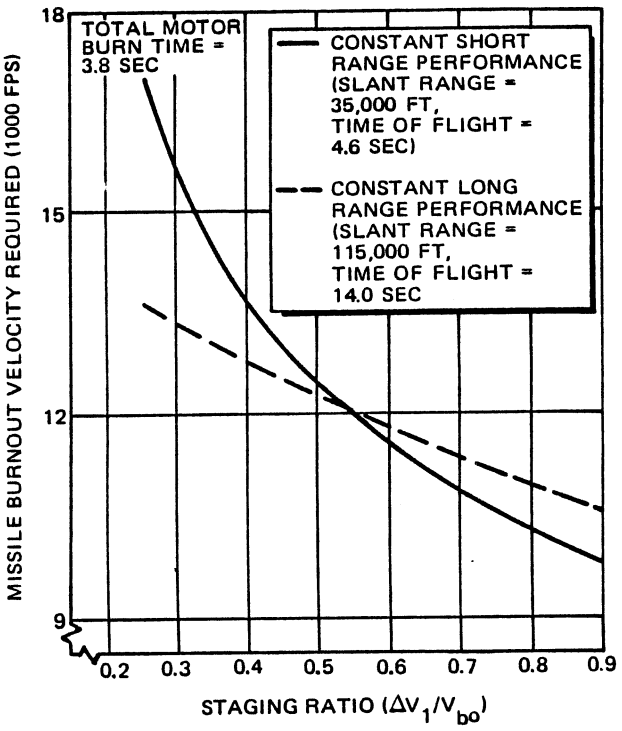

Figure 10-126. Typical Required Burnout Velocity vs Staging Ratio

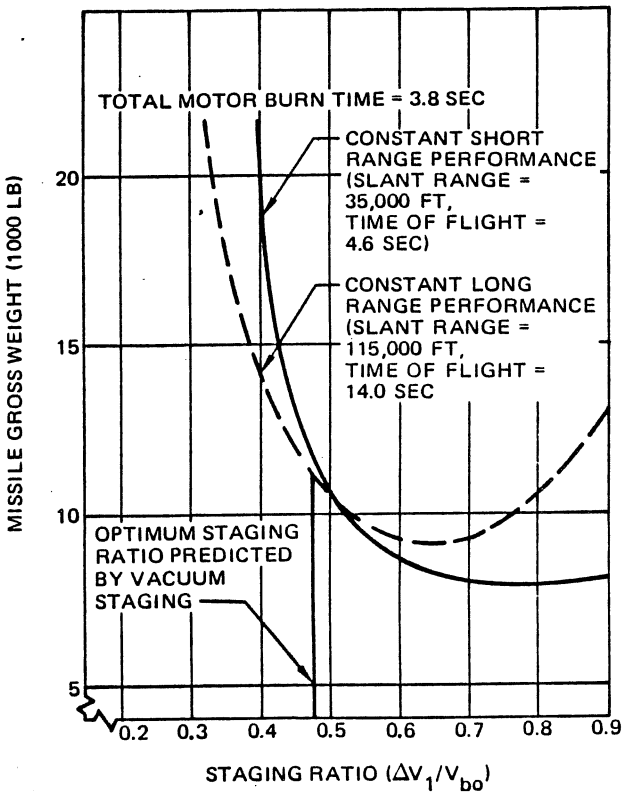

Figure 10-127. Typical Gross Weight vs Staging Ratio

The limitations of existing published staging optimization and stage scaling techniques have prompted the development of the "nonlinear staging" relationships used in computer programs for vehicle sizing analysis, e.g., GMSP. These relationships, for given inputs, permit accurate scaling of stage size over a wide range of propellant weights. They accurately predict the burnout velocity achieved as a function of stage gross and propellant weight, and result in stage velocity ratio optimization nearly equivalent in accuracy to that obtained by the individual design and mission trajectory performance analysis of a series of missiles at various staging ratios.

The necessity of an explicit staging optimization analysis can be readily seen by considering the number of individual missile designs required to perform a brute force staging optimization for a 3-stage missile. The nonlinear staging relationships can be considered to consist of two parts: (1) the stage scaling relationships required for both arbitrary and optimum staging, and (2) the velocity ratio optimization equations required for optimum staging.

The achieved burnout velocity increment of a stage can be expressed in terms of the impulsive velocity Equations 19 and 137.

$$\Delta V = I_{sp_{vac}}\, g_o \log_e (W_f/W_{bo}) - \Delta V_L \qquad (136)$$

However, this equation is not scalable using the common definitions of step mass fraction and specific impulse since, as has been shown, the step mass fraction, specific impulse, and drag and miscellaneous losses may vary as a function of step size.

Figure 10-128 shows a plot of step inert weight as a function of propellant weight for both stages of the two-stage interceptor for which step mass fraction is plotted in Figure 10-121. The near linear form of this plot is characteristic of all missile types (significant nonlinearity usually occurs only for very high performance interceptors). It can be seen that step gross weight, or empty weight, can be accurately predicted by the use of two terms, the constant weight occurring at the intercept (zero propellant weight due to interstage and other fixed step weight hardware). An effective mass fraction based on the slope of the inert weight vs. propellant weight plot, specifically, is equal to the slope of a plot of propellant weight as a function of gross weight which may be obtained from the inert-weight/propellant-weight plot. The step weight relationships are:

$$\lambda_{se} = \frac{W_{px}}{W_{s_n} - W_{sn}} \qquad (137)$$

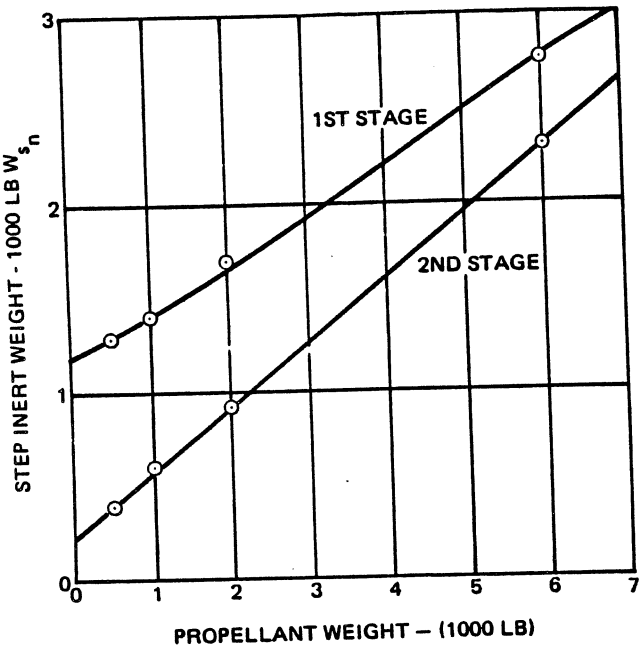

Figure 10-128. Typical Inert Weight vs Propellant Weight Weight

or

$$W_{s_n} = \frac{W_{px} + W_{sn}\lambda_{se}}{\lambda_{se}} \qquad (138)$$

λ_{se} = effective step mass fraction based on the local slope of gross weight vs. expendable weight,

W_{px} = total expendable weight,

W_{sn} = step constant weight based on inert weight vs. expendable weight,

W_{Sn} = step gross weight = $W_{f_n} - W_{f_{n+1}}$

The effective step mass fraction is equivalent to a term, sometimes referred to as the motor mass fraction because it relates only to the motor mass characteristics. Accurate values of effective step mass fraction and constant weight can be obtained by stage designs at two propellant weights from which stage size can be accurately scaled. It is notable that effective mass fraction falls within narrow bands which are primarily a function of missile type, state of the art, and performance. For example, the effective step mass fraction (motor mass fraction) varies between 0.75 to 0.8 for a high performance interceptor and 0.90 to 0.95 for a ballistic missile or launch vehicle booster. It is a term which gives the Propulsion engineer a basis for evaluating how effectively he is minimizing the weight of the propulsion system.

The method of defining velocity scaling parameters to relate stage burnout velocity ratio $\Delta V_1/\Delta V_2$ to stage gross-to-empty weight ratio r_{v1}/r_{v2} is similar to that used for weight scaling. Since a nonpropulsive terminal stage deaccelerates, and a nonpropulsive stage may be considered as a propulsive stage with zero propellant weight, the resultant velocity loss occuring over the duration of the motor burn time is an inherent fixed loss applying to the stage for all propellant weights. An additional drag loss, which is normally somewhat proportional to the resultant achieved velocity increment, occurs at stage size increases. The same logic applies to a booster, since a certain amount of propellant is required to produce a thrust-to-weight ratio of one resulting in no net velocity increment. It has been found that if the proper value of fixed velocity loss is selected (consisting primarily of the inherent loss), and if an effective specific impulse is used in place of specific impulse in the impulsive velocity equation, the resulting equation will accurately predict the burnout velocity increment of a stage through a wide range of gross-weight to empty-weight ratios. Thus, the nonlinear staging analysis is based on the equation for the burnout velocity increment of a stage, expressed as:

$$\Delta V_n = I_e\, g_o \log_e \left[\frac{PR_n}{PR_n(1-\lambda_{se}) + \lambda_{se}\left(\frac{1+W_{sn}}{W_{f_{n+1}}}\right)}\right] - \Delta V_L \qquad (139)$$

where

ΔV_n, g_o, λ_{se}, ΔV_L and W_{sn} are defined as before.

I_e = effective stage specific impulse, i.e., average value for stage trajectory.

The parameters λ_{se}, W_{sn}, I_e, and ΔV_L may be computed based on the results of a configuration design and power-on trajectory simulation, which is usually accomplished using a computer. The burnout velocity increment equation may be rearranged to express the stage payload ratio required to produce a desired burnout velocity increment:

$$PR_n = \frac{e^X \lambda_{se}\left(1 + \frac{W_{sn}}{W_{f_{n+1}}}\right)}{1 - (1-\lambda_{se})\, e^X} \qquad (140)$$

where:

$$X = (\Delta V_n + \Delta V_L)/(I_e g_o)$$

The gross weight of a step is computed from the payload ratio and the gross weight of the upper stage. The total expendable weight (consisting of motor and control system propellant weight) is computed based on Equation 137. The propellant weight is then computed from inputs defining the ratio of propellant weight to expendable weight which is assumed to be 1.0 in the first staging exercise and equal to the value occurring for the previous missile design in successive staging exercise.

Equations 137, 138, and 139 are the basic equations used in both arbitrary and optimum staging to relate stage burnout velocity increment to stage gross weight and propellant weight. Staging optimization, for the criterion of minimum gross weight for a burnout velocity requirement (or maximum burnout velocity for a gross weight requirement), is accomplished by an iterative process wherein Equations 137 through 139 are used to define the gross weight (or burnout velocity) of each stage and thus of the complete missile for each of a series of decreasing stage velocity ratios until a minimum gross weight (or maximum burnout velocity) is found.

10-3.6.2 Range Staging

For the optimization criteria (range staging) for a missile requiring staging optimization (minimum gross weight) with respect to a space-point e.g., minimum time of flight or maximum final velocity, a number of additional equations are required. The basic principle of range staging is that an increase of power-on range at constant burnout velocity produces a reduction of the coast phase average velocity required to satisfy a mission performance requirement by decreasing the coast range increment. The basic range staging equations which are used in combination with the scaling equations for short-range missiles are as follows.

For constant acceleration, the range increment is:

$$\Delta R_n = t_{b_n} (V_{bo_{n-1}} + \Delta V_n) \qquad (141)$$

and the velocity at the end of coast is:

$$V_f = \frac{4 V_{bo}}{(2 - K t_c \Delta V_{bo}^{1/2})^2} \qquad (142)$$

For variable acceleration, these parameters are:

$$\Delta R_n = t_{b_n} \left[V_{bo_{n-1}} + \Delta V_n \left(\frac{W_{f_n} + 2 W_{bo_n}}{W_{f_n} + W_{bo_n}} \right) \right] \qquad (143)$$

$$V_f = \left(\frac{K R_c + 2 V_{bo}^{1/2}}{2} \right)^2 \qquad (144)$$

where K is a slowdown coefficient

ΔR_n = increment in slant range traversed by the missile during the burn time (t_b) (power-on)

Equations 141 and 143 define the slant range increment achieved by a propulsive stage based on constant acceleration or progressive acceleration (inversely proportional to instantaneous missile weight), respectively. The designation of the type of thrust history applicable to each stage must be supplied or assumed. Equations 142 and 144 are equivalent equations expressing the missile velocity at an intercept point based on the burnout velocity, a constant slowdown coefficient, and either the duration, or the slant range increment, of the coast phase. These equations are based on an assumption that the instantaneous rate of change of velocity in the coast phase is proportional to the instantaneous velocity to the 1.5 power. Equations 145, 146, and 147 are rearrangements of Equations 142 and 144.

$$K = \frac{2R_c - 2V_{bo} t_c}{R_c t_c V_{bo}^{1/2}} \qquad (145)$$

$$K = \frac{2V_f^{1/2} - 2V_{bo}^{1/2}}{R_c} \qquad (146)$$

$$R_c = \frac{2V_{bo} t_c}{2 - K t_c V_{bo}^{1/2}} \qquad (147)$$

Range staging optimization when staging to a burnout velocity is accomplished by the following steps.

a. The gross and empty weights of each stage of a nominal missile with the desired burnout velocity are computed using the scaling equations. The velocity of each stage is based on input stage velocities, or, if not input, equal stage velocities are used.

b. Equation 141 or 143 is used to compute the slant range at burnout for the nominal missile.

c. Equation 145 or 146 is used to compute the slowdown coefficient (K) of the missile during the coast phase, based on the input total slant range and either the required time of flight or final velocity. This calculation is based on the assumption that the missile burnout velocity and burnout range will result in a missile performance at the total range equal to the performance requirement.

d. Minimum values of payload ratio are assigned to the upper stages, and the resultant weight and velocity increments are computed.

e. The velocity increment and resultant gross weight of the booster is then determined by an iterative solution such that the combination of the resultant total burnout velocity and power-on range satisfy the total range-performance requirement using Equation 147. The resultant missile gross weight is stored.

f. The growth factors of the upper stages are individually incremented, their weight and velocity increments are recomputed, and step e is repeated.

g. Step e and f are repeated until the missile gross weight minimizes. During this process, the total burnout velocity of the missile varies as a function of the staging ratios to maintain the total time of flight or final velocity constant.

h. The resultant stage velocities determined at the minimum gross weight in step g are to produce a total burnout velocity equal to the input burnout velocity requirement, maintaining the optimum ratios of stage velocity to total burnout velocity determined in step g. The resultant stage gross weight and propellant weights are computed from the scaling equations.

The procedure used for range staging optimization when sizing to a gross weight requirement is similar to the above. The nominal missile used in steps a, b, and c has a gross weight equal to the desired value rather than a designated burnout velocity. In the optimization process, steps d-g, the gross weight of the missile is held constant as the payload ratios of upper stages are incremented and the optimum staging is selected at the point at which terminal performance maximizes. The resultant missile then automatically satisfies the gross weight requirement and ratioing (Step h) is not required.

The effect of the staging optimization criterion on staging optimization of a two-stage interceptor is further illustrated by Figures 10-129, 10-130, and 10-131. This data has been assembled based on the design and trajectory optimization of a series of missile configurations. Figure 10-129 shows the missile gross weight as a function of staging ratio at constant burnout velocity. The predicted optimum values of staging ratio based on each of the three optimization criteria — minimum gross weight for the given ΔV, minimum gross weight for time of flight to a medium range intercept point, and minimum gross weight for final velocity at the space point — are indicated on the plot. As shown, the latter two criteria result in higher gross weight for the same burnout velocity. However, mission range performance continually increases with increasing staging ratio. Figure 10-130 shows the missile burnout velocity required for constant time of flight performance and constant final velocity at the medium range target point as a function of staging ratio (also see Figure 10-126). Figure 131 is a plot of the missile gross weight required to satisfy the time of flight performance requirement and the final velocity performance requirement as a function of staging ratio. The optimum staging as predicted by burnout velocity staging and by range staging is indicated on each curve.

10-3.6.3 Parametric Studies

10-3.6.3.1 Trajectory

The preliminary design engineer establishes and evaluates the various sensitivities necessary for completing missile designs, including tactical considerations which encompass the specified trajectory types. The basic parameter are then evaluated in a vehicle performance analysis. The results are combined with the propulsion system parametric design analysis for determining the reasonable solutions to the missile design problem, e.g., weight, performance level, etc. Sensitivities and flexibilities for the proposed designs, including variable launch altitudes, variable launch Mach numbers, subranging and field-of-fire, are then evaluated. Of specific interest and utility in conducting trajectory systems analysis is the MDAC GVPAT program which includes a complete Six-Degree-of Freedom Flight Path Generalized Analysis, Flight Path Error and Dispersion Analysis, Engine Analysis, and Guidance and Control for generalized classes of vehicles (GV2 Manual). Flight mechanics personnel are responsible for maintenance and use of these sophisticated analytical techniques and the GV2 Manual.

For overall design of multi-stage ground-to-air vehicle systems the GMSP is applicable and frequently used.[22] A special missile synthesis analysis program for air-to-ground, air-to-air, and short-range ground-to- ground missiles is available operationally at MDAC-E.[23] With the aid of the above programs the preliminary designer at MDAC can accomplish missile or space launch vehicle design synthesis and performance analysis for nearly all advanced chemically propelled vehicles currently being considered for use.

Trajectory parameterization studies usually proceed independently from similar propulsion system efforts. Graphical presentation of data obtained from the trajectory simulation models must therefore consistently contain variables common to the dependent propulsion system study. Proper selection of basic performance curves, mass consideration curves and motor performance curves results in a final presentation of design charts. Selected flight path and performance histories may be reconstructed for numerous inert weight considerations and delivered motor performance characteristics. Typical data presentations are illustrated in Figure 10-132 for the three typical air-launched models shown in Figure 10-133 and discussed later.

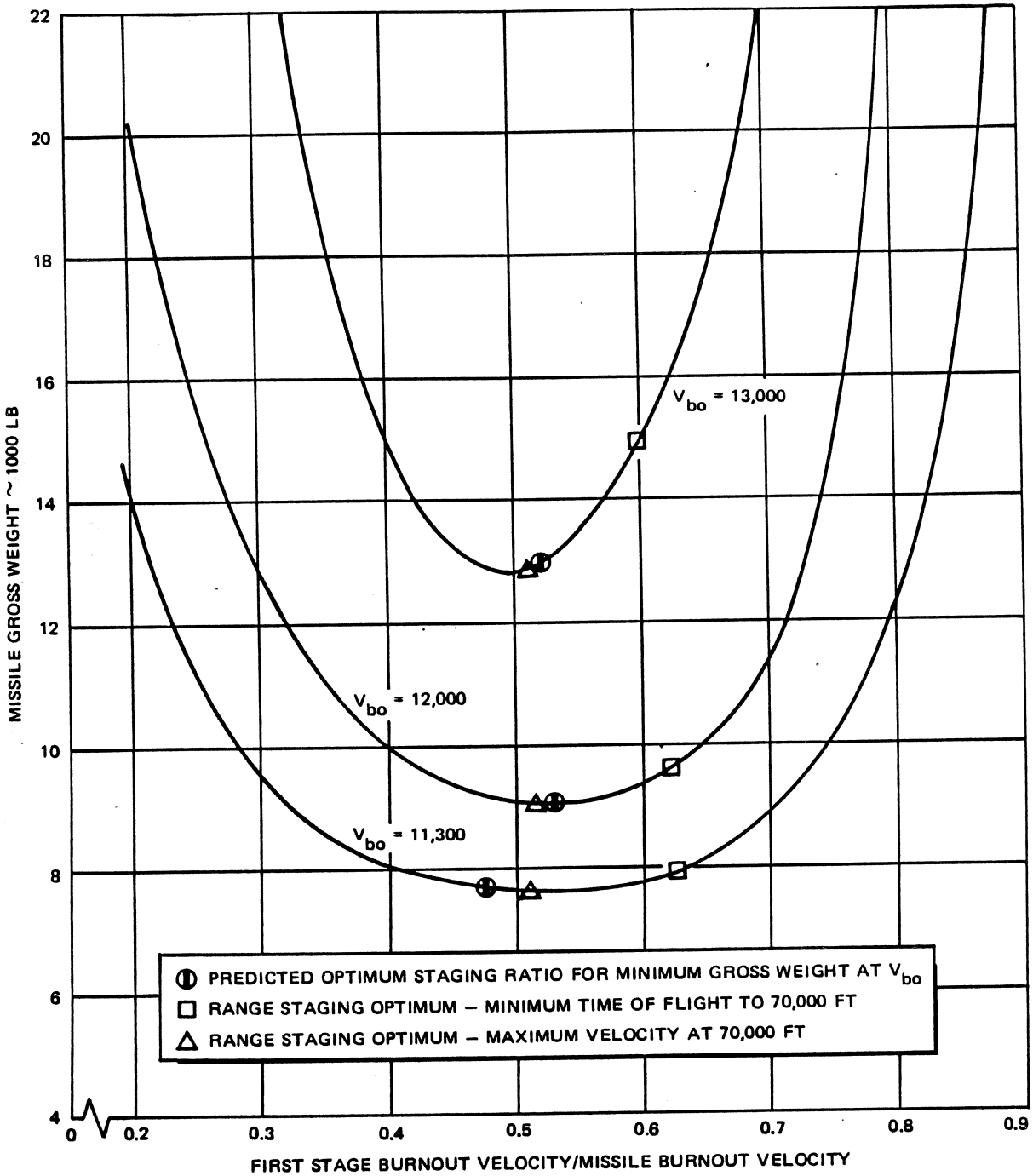

Figure 10-129. Typical Missile Gross Weight vs Staging Ratio

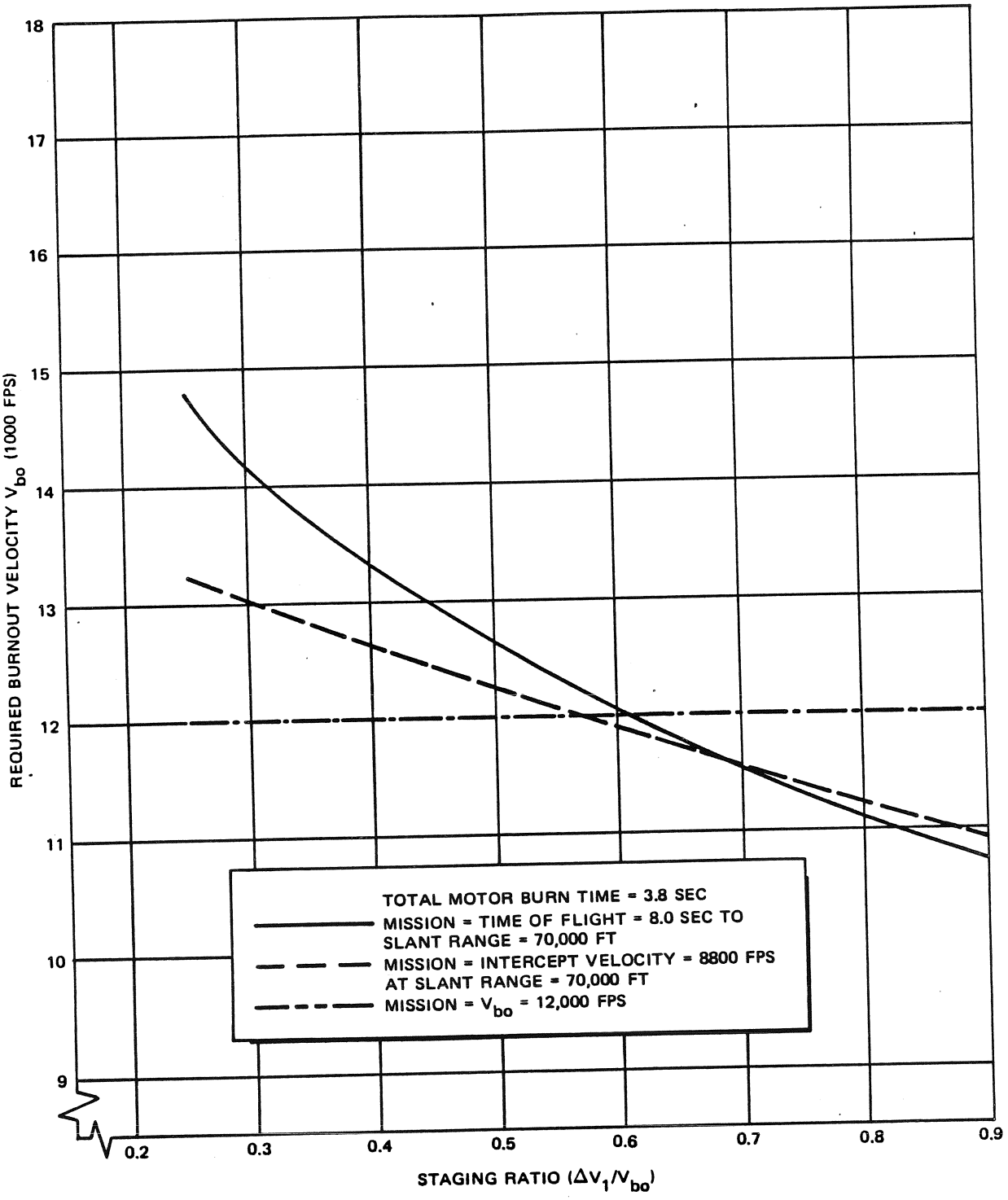

Figure 10-130. Typical Required Burnout Velocity vs Staging Ratio

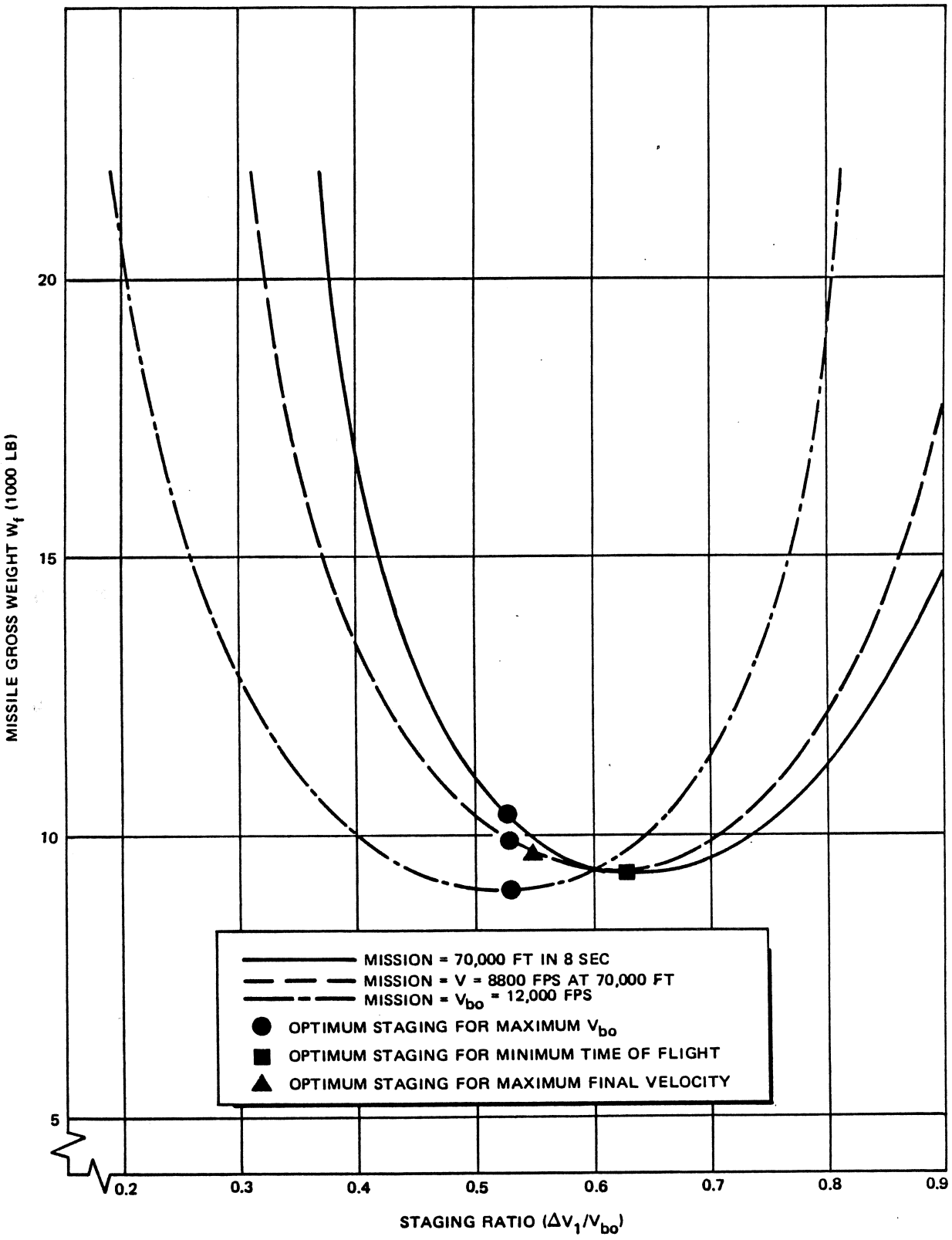

Figure 10-131. Effect of Staging Criteria

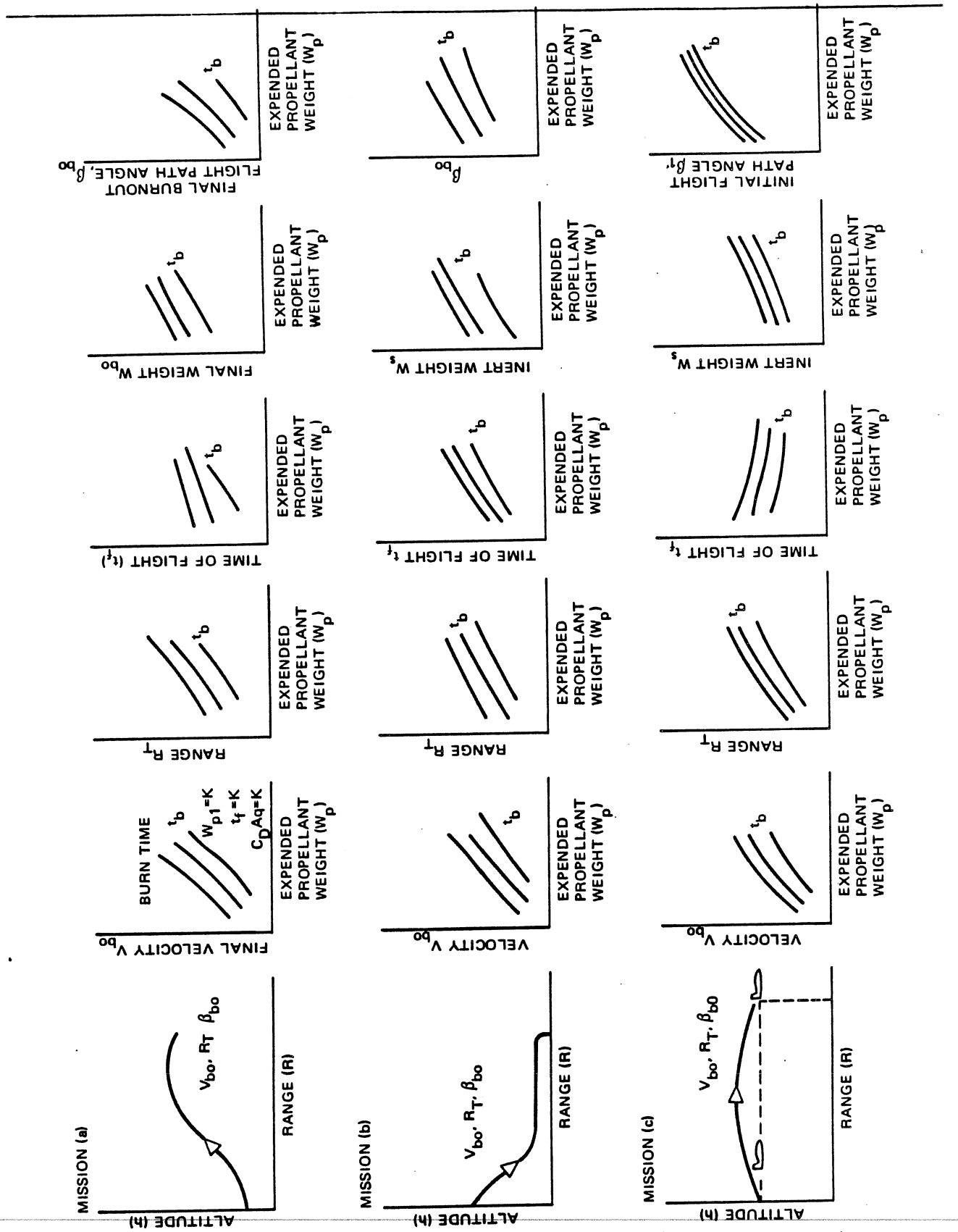

Figure 10-132. Typical Trajectory Parameterization Data Presentation

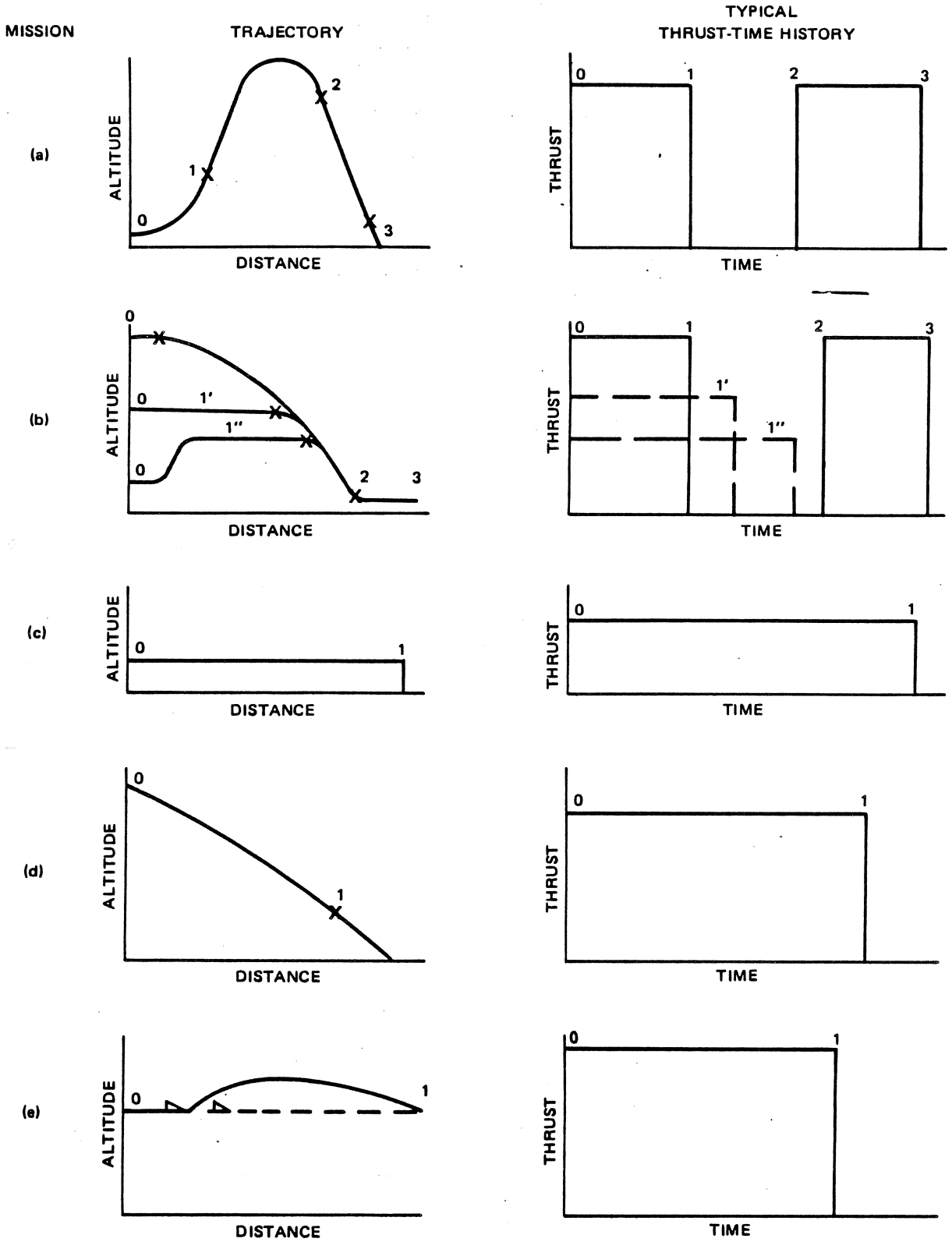

Figure 10-133. Typical Trajectory and Thrust Histories for Air-Launch Missile Systems

The common variables in Figure 10-132 are propellant weight and burn time. Each set of curves must be repeated for other combinations of gross weight, thrust level and drag (C_dAq) Equation 21. Selective crossplots will allow integration with the propulsion system parametric studies for the purpose of selecting parametric vehicles having specific performance capabilities.

Following the comprehensive analysis of various trajectory shaping and performance influencing factors, trajectory analysis models are established. These models can then be utilized to perform a trajectory parameterization study of trajectory profiles and performance variables to determine representative requirements for the mission of interest. These models are created by utilizing various existing computer programs to specifically study the variables which are considered pertinent to the intended propulsion system study, such as gross weight, propellant weight, total impulse, burn time, and drag impulse losses. These quantities are included in the matrix of variables constituting the gross parametric analysis.

10-3.6.3.2 Missile Design

To effectively initiate a realistic vehicle parametric design study, the relationships between subsystem weight, packaging, geometry, and vehicle weight, balance, and external geometry must be established. A characteristic vehicle packaging model is established for study in the form of a preliminary design layout. The model will:

a. Establish vehicle external envelope, center of gravity (CG), and center of pressure (CP).

b. Establish CG/CP relationships and CG/CP travel.

c. Establish Aircraft/Missile interface requirements or ensure compliance with specified requirements.

d. Ensure reasonable maintenance and accessibility requirements.

Completion of the parametric study design models will allow numerous geometric characteristics of the missile to be established for inclusion in ensuing weight and geometry parameterization. Carry-lug and aerodynamic-control-fin (if selected for consideration) connection designs are examined to determine where they best can be located. Assuming they must be located outside the area of motor cases or propellant tankage, geometric spacing requirements will be determined. These items are maintained at fixed lengths for geometric parameterization.

If control fins, flaps, elevons or canards are to be considered, actuator locations and spacing requirements are established and held proportionately constant. If a TVC system is to be used for the study, specific geometric characteristics of the missile peculiar to that system are established.

Parallel studies specify control system and warhead types for parametric study purposes. Layouts are therefore completed for vehicles utilizing selected control system and warhead types for both a solid and storable liquid propellant system, as well as for one or more payload weights (as required). Missile weight distributions can be established for the packaging arrangement selected. CG locations are established as a function of missile or subsystem length thereby allowing control system weight to be determined.

10-3.6.3.3 Propulsion System Sizing

The major output of propulsion system parameterization studies consists of weight, volume, and performance parameters for the principal components as functions of missile diameter, chamber pressure, burning time, and propellant weight. The effects of altitude, nozzle design, and expansion ratio on performance are assessed. The following sizing and selection techniques apply to prepackaged liquid and solid propellant missiles. Additional information on propulsion system sizing and selection are given in Paragraphs 10-4 and 10-5.

a. Prepackaged Liquid Propellant Engine Sizing Techniques – Figure 10-134 shows the general flow of the analytical procedures that are typically used in the sizing of a packaged liquid propulsion system.

   The major inputs to the sizing procedure are the thrust history requirements and, depending upon the mission, any thrust modulation requirements. Then the candidate propellants are compared and a system is chosen based primarily on I_{sp} and $\rho\ I_{sp}$. Ullage and outage requirements are determined for the selected propellants and serve as inputs for the propellant tank sizing. The design altitude and resulting nozzle expansion ratio are determined after propellant selection. The results can then be used to determine the thrust chamber design. An expulsion system is selected based on the flight environment and propellant combination, and is sized in conjunction with the propellant tanks.

   After the tankage size and weight have been determined, the pressurization system is selected and sized. In the final block the various components are integrated into the propulsion subsystem.

   The sizing of storable liquid propulsion systems can be performed with the aid of the general missile sizing program (GMSP/H215/H834). It is usually desirable, however, from a time and requirements viewpoint, to use the G806 Storable Liquid

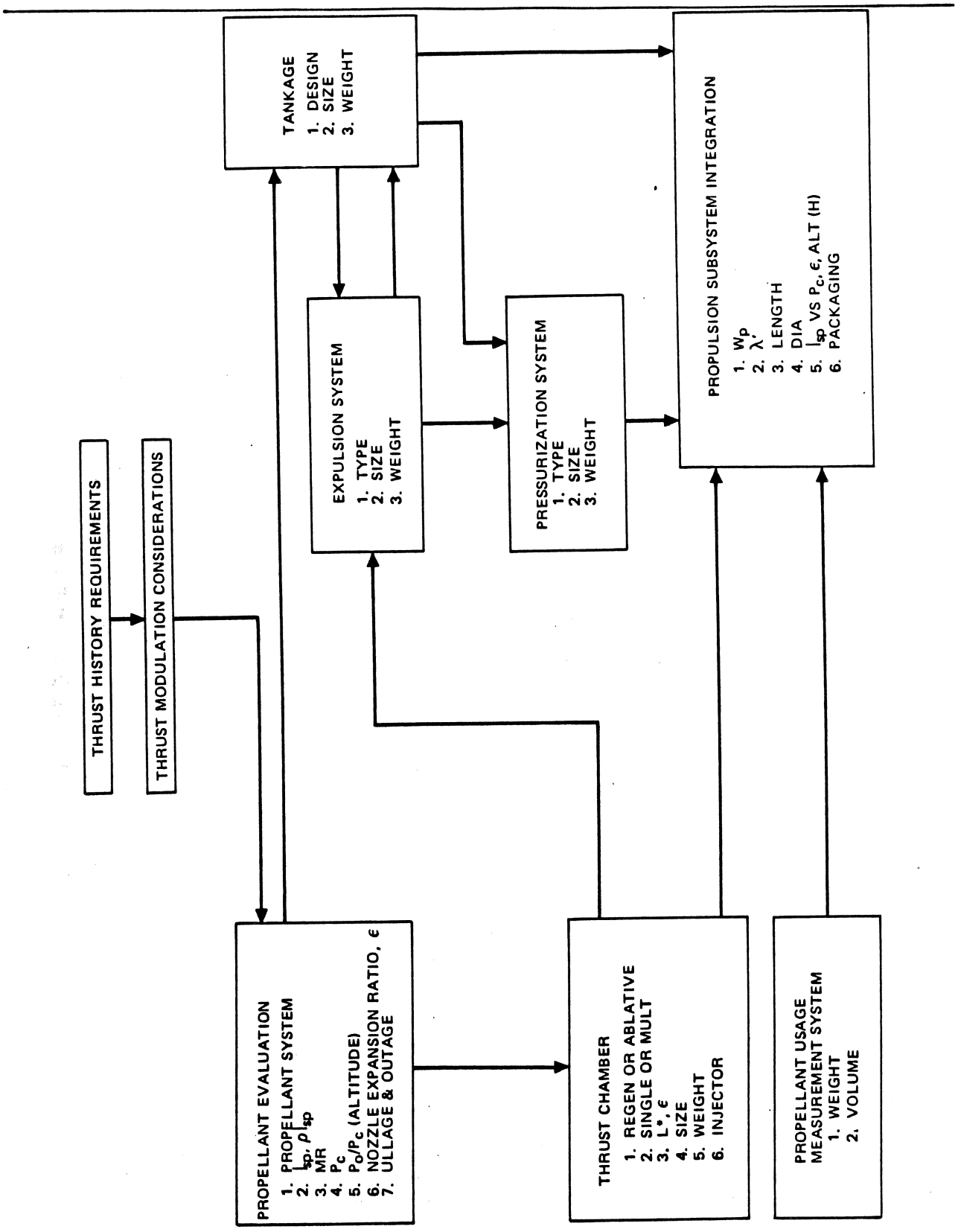

Figure 10-134. Sizing Sequence for Packaged Liquid Propulsion System

Propulsion System Sizing and Performance Computer Program for detailed propulsion subsystem design. This program is similar to the module used in GMSP (H834) and provides a means of sizing for up to ten groups of engines with any number of thrust chamber assemblies per group. It iterates on total system weight or computes the weight for a given total impulse. Various engine cooling types, propellant combinations, tank options, expulsion systems and pressurization concepts can be chosen for either pump or pressure fed systems (see paragraph 10-5).

b. Solid Propellant Motors Sizing Techniques — The sizing and performance of the solid motor includes the variational effects of physical dimensions (L/d;d) as well as predicted propellant ballistic properties, chamber pressures, and burning times. These analyses result in a matrix of information to be used in the total vehicle sizing and optimization studies.

The sizing study of the solid propellant motors can also be accommodated within the existing GMSP (H215) sizing program.[22] The propulsion subsystem sizing module (H218 or H-081) (see Figure 10-135)[24] computes the physical dimensions of the motor, designs the grain configuration, and computes the ballistic performance of the motors. The two motor structural modules (see Figure 10-136) use the physical dimensions and selected materials to design the motor case and nozzle, and calculate the weight, pitch moment of inertia, and the center of gravity of all the inert propulsion subsystem components. Program PA08 is also available for accurately predicting ballistic performance of a wide variety of grain designs. It also computes a complete time history of the burning surface area and the location and excursion of the center of gravity (see PS-1 Manual).

10-3.6.3.4 Nonpropulsion System

a. Parametric Subsystem Weight — Nonpropulsive subsystem weights are defined as payload and are limited to two distinct specified weights. The principal objective of the nonpropulsive subsystem weights study is to effectively distribute the specified weights throughout the missile envelope so as to represent realistic missile systems. Those missile subsystems which comprise the total payload include:

1. Guidance and electronic equipment.
2. Warhead
3. Control system
4. All associated structure.

The weight of each of these subsystems is held constant for each of the specified payload weights and for each of the trajectory profiles under consideration.

Past experience in parametric analysis of TASM systems and preliminary design investigations of packaging, environment and performance characteristics provides information for distributing this payload weight among the various missile subsystems. A nominal performance trajectory provides a basis for determining subsystem weights for all the missions shown in Figure 10-133. Performance dependent subsystem weights such as guidance, control and structure are determined first. The combined weight of these subsystems when subtracted from the total payload weight establishes warhead weight.

b. Parametric Subsystem Geometry — Nonpropulsion vehicle parametric geometry characteristics are determined as a function of a parameter common to and descriptive of each of the nonpropulsive subsystems.

Principal subsystems which most drastically effect vehicle geometry are the same as stated above. Weight, density, and volume of each of these selected systems is determined and fixed for parametric study purposes. Each of these subsystems is packaged in its most advantageous position within the missile envelope. Volume and total weight being fixed quantities, variations in missile diameter will cause commensurate variations in length of subystem packages. The variation of length with missile diameter can be plotted for each of the principal nonpropulsive subsystems, i.e., warhead, guidance, and electronics systems.

The control system, the remaining nonpropulsive subsystem, has little effect on length variations. The selected system is packaged within the electronics and controls section of the missile. This section length will normally be governed by electronics equipment package length requirements. However, control system effects on the section length are analyzed parametrically and documented in curve form to allow overall vehicle sizing.

10-3.6.3.5 Total Missile Parameterization

Culmination of the total vehicle weight parameterization is accomplished after all subsystem weights and lengths are known as a function of missile diameter and performance. The final ouputs of the vehicle weight and geometry parameterization are curves of gross and inert missile weight as functions of propellant weight, and total missile length as a function of propellant weight.

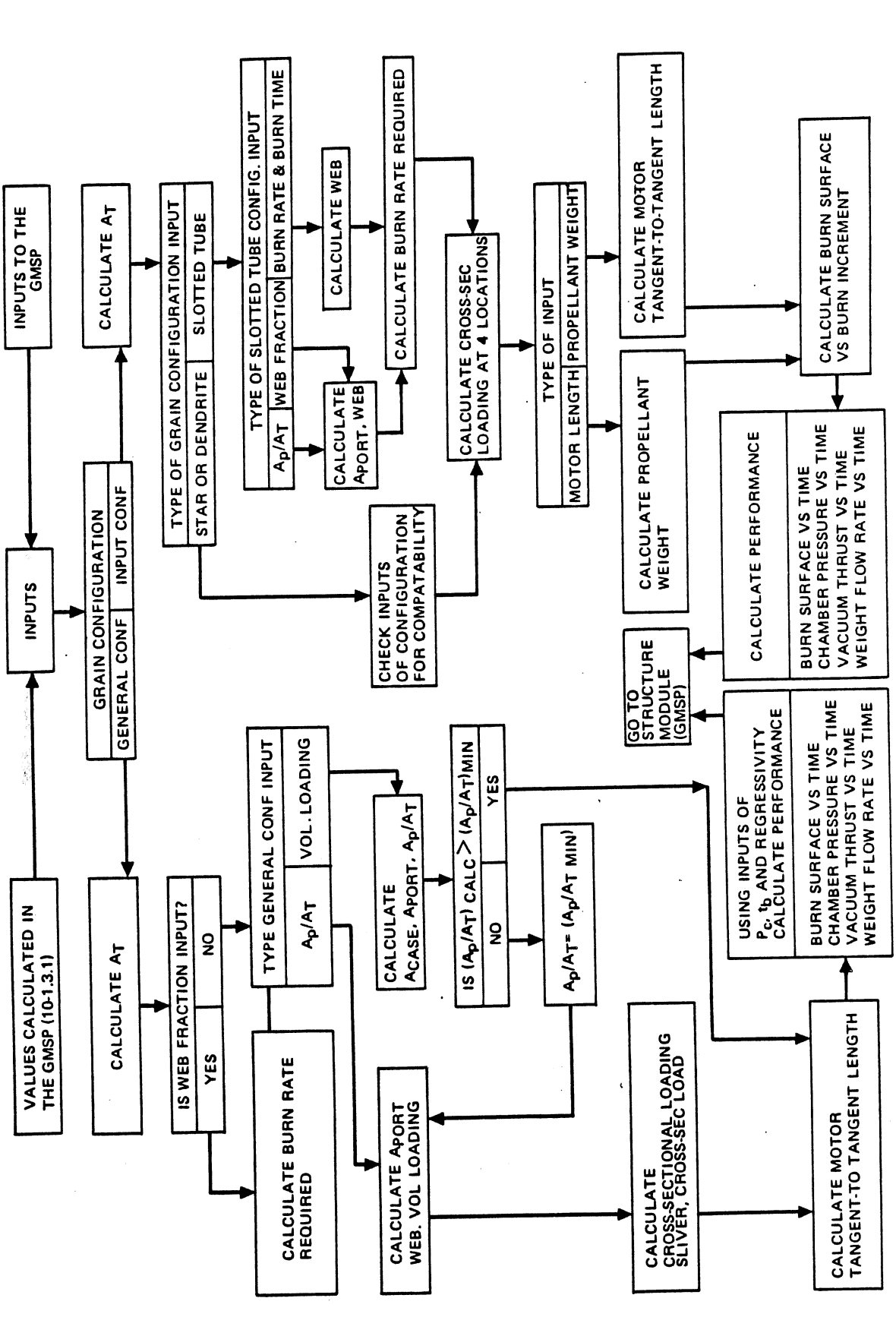

Figure 10-135. Sizing Sequence for Solid Propellant Motors

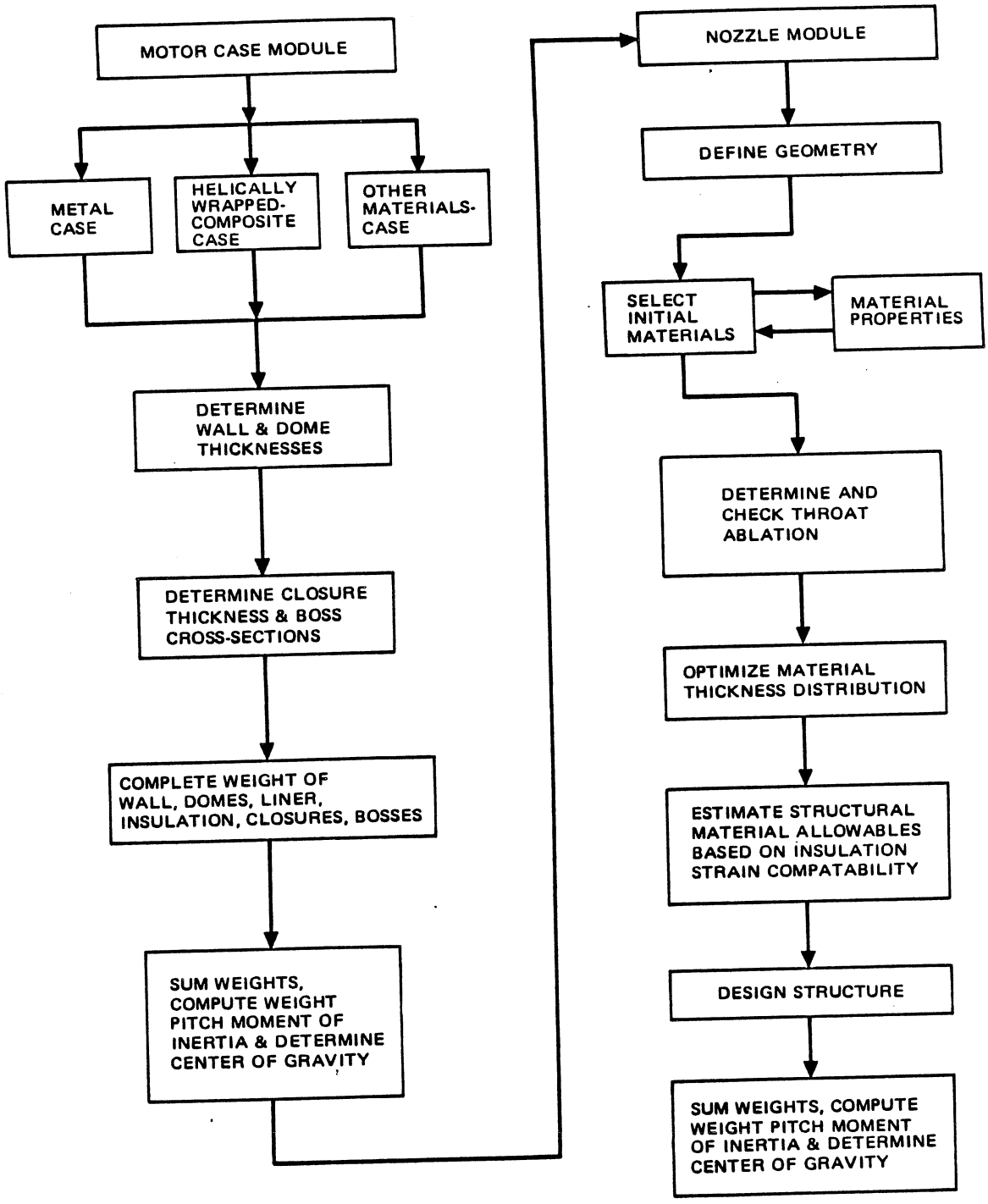

Figure 10-136. Motor – Structural Modules

A schematic showing the stepwise utilization of weight and geometry curves to arrive at total missile characteristics is shown in Figure 10-137. The procedure is described below for a typical prepackaged liquid propulsion system.

a. Summation of the first four curves in row I provides data to construct the total propulsion system weight curve. Combination of items 5 and 6 in row I allows plotting of curve number III, total missile inert and gross weights as a function of propellant weight.

b. Summation of all the subsystem length curves of row II allows the plotting of total missile length as shown as curve number IV.

   It should be noted that total missile weight, denoted by curve III, is for a particular propellant density. A propellant of different density simply causes a horizontal shifting of the missile weight curves by an amount equal to the ratio of the propellant densities. Similar effects can be found for propulsion system length. Determination of new propulsion system lengths by ratioing propellant density will allow the plotting of a new total missile length curves as denoted by curve IV.

10-3.6.4 Air-to-Surface Missile Design Selection

A multi-purpose air-launched missile (TASM) may satisfy many short range air-to-air and air-to-surface missions.

10-3.6.4.1 Major Technical Considerations

TASM studies have demonstrated that the maximum length allowable for the overall missile is a severe limitation when trying to choose between various propulsion system types. Since the volume requirements for the warhead, guidance and control, and electronics are essentially fixed by steering, penetration, and targeting considerations, it becomes of prime importantce to maintain the highest practical packaging efficiency for the propulsion system. This in turn usually makes it necessary to utilize propellants with maximum density-impulse, since the largest portion of the propulsion system weight is represented by the liquid propellant tankage or the solid propellant motor case.

Under these circumstances, the subsystem designer might immediately turn to the use of solid propellants (rather than storable liquid propellants) for TASM's because of their high density impulse. The choice of solid propellants, however, must be weighed against those constraints imposed by required thrust-time histories, operating altitudes, longtime carry heat-soaking environments, and radar signatures. In addition, the long motor burning times for a low altitude cruise mission usually result in solid propellant motor designs with high web fractions (greater than 80 percent) to be compatible with available propellant burning rates, r_b. Assuming an internal burning grain configuration, a trade must be made between reducing burning time below optimum or taking a loss in delivered propellant specific impulse at low burning rate conditions. Concommitant with high web fraction solid propellant motors is an increase in the severity of the bonding problem between grain and motor case, especially under conditions of extreme temperature cycling and high bonding-system/propellant interface temperatures.

To properly evaluate rocket propulsion system characteristics, all tactical air-launched vehicle parameters that influence the final propulsion system choice must be realistically defined. The variety of possible tactical missions requires that the parametric study of the various candidate propulsion modes be evaluated such that the study results are representative of flyable, buildable missile systems, and have not been prejudiced by the use of point-mass representations of items such as guidance modules and warheads.

Three major subsystems in tactical air launched missiles that directly influence the cost effectiveness of the weapon are propulsion, guidance (and associated electronics), and airframe controls (autopilot, etc.). The weapon system designer can take several approaches towards system design, some of which can lead to highly sophisticated trajectories requiring an elaborate (and costly) guidance system, or an expensive adaptive control scheme. Thus, the preliminary design studies should consider the cost and performance differences between the propulsion systems and other related system cost considerations; such as penetration tactics, aircraft compatibility, and production quantities.

Vehicles of this type must be easily maintainable, rugged, and reliable weapons that adequately adapt to candidate carrier aircraft without unnecessarily compromising the aircraft or missile capabilities. In addition, vehicle packaging arrangements should be confined to modular packaging concepts for easy field replacement of subsystems. The propulsion system and guidance/control system should be integral systems not requiring disassembly for removal and replacement in the missile.

a. Mission Constraints on Propulsion System — Two basic types of constraints are imposed upon the propulsion system by the mission and its associated flight trajectories — those related to the performance needed for the missile to attain the target and those related to the total weapon system requirements. The former type of constraints include such parameters as thrust-time history, operating altitudes, exhaust radar signature and missile accuracy requirements. The latter type includes such aircraft compatibility and logistic considerations as

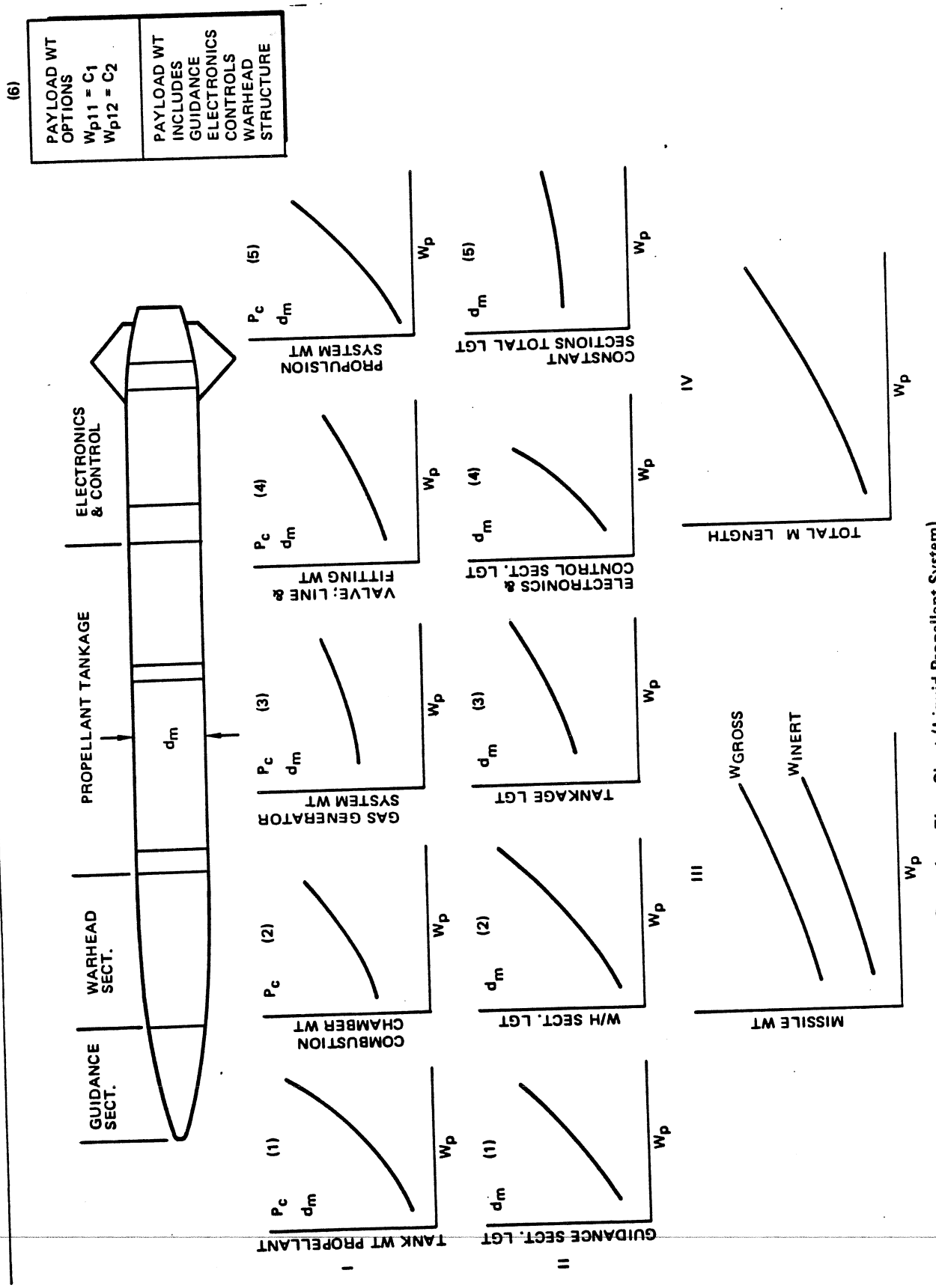

Figure 10-137. Typical Parametric Study Procedure Flow Chart (Liquid Propellant System)

volume and weight restraints, launch and carry conditions, flight and storage environments, carrier rack design, ejection loads during launch, and aircraft maneuver capabilities.

b. Performance Requirements – Examination of five typical trajectories (Figure 10-133) indicates that each will require a propulsion system which provides a distinctive thrust-time history while operating over widely varying altitudes and launch conditions. The extent of the thrust variations is also typified by the curves presented in Figure 10-133. Only in Missions (c), (d), and (e), where the criterion is principally minimum time to intercept rather than both minimum time and optimum trajectory for penetration, is it possible to utilize a single thrust level rather than variable thrust. In missions a and b on the other hand, not only is more than one thrust level required during flight, but also the manner in which the thrust is programmed differs according to the specific trajectory under consideration. Modulation of thrust, efficient operation over varying altitudes, and possible stop-restart capabilities are thus implied for any candidate propulsion system for TASM applications.

c. Comparison of Competitive Systems – Four basic propulsion design concepts require evaluation in light of mission and trajectory constraints before choosing candidate systems for more detailed study. These include:

1. Solid propellant motors
2. Packaged storable liquid propellant systems
3. Ramjet and air-augmented systems
4. Hybrid motors

All these concepts offer potential advantages for a tactical airborne weapon system, but at the same time involve questions of feasibility or development risks.

d. Solid Propellant Systems – This principal advantage of the solid propellant motor is its high density-impulse. Whereas a current high-performance storable liquid system yields an effective density-impulse in the order of 380-400 gm-sec/cc (based on density at 165°F plus allowances for ullage and outage), a competing solid propellant gives an effective density-impulse of 400-450 gm/cc (based on nominal density and volumetric loading efficiency of 85 to 90 percent). As a result, in past tactical missile studies, a solid propellant system has demonstrated a motor mass fraction advantage of 5 to 10 percent. On the other hand, the solid system will require external insulation for protection from the aerodynamic heating effects during carry, thus reducing the volume available for propellant and decreasing its competitive advantage. The overall effect of these trades on the delivered total impulse is shown for a typical TASM in Figure 10-138. Assuming a total impulse requirement of 280,000 lb-sec, the length of the solid motor would be 6.5 inches (10 percent) less than the liquid propulsion tankage length, Similar differences are demonstrated for other values of total impulse.

The major drawback of the solid propellant system is the difficulty of achieving all the thrust variations required by the trajectories for Mission (a) and (b) (Figure 10-133). Use of a two stage design also provides no satisfactory answer to the problems of thrust variation. While it gives more than on thrust level, it will not provide the flexibility demanded by Mission (b). In addition, motor mass fraction would be penalized, and the cost and complexity of the overall missile system would be greatly increased.

Two alternative approaches, therefore, remain for evaluation:

1. Step-thrust units
2. Throttleable systems (variable-area nozzle, dual-chamber, hybrid, etc.).

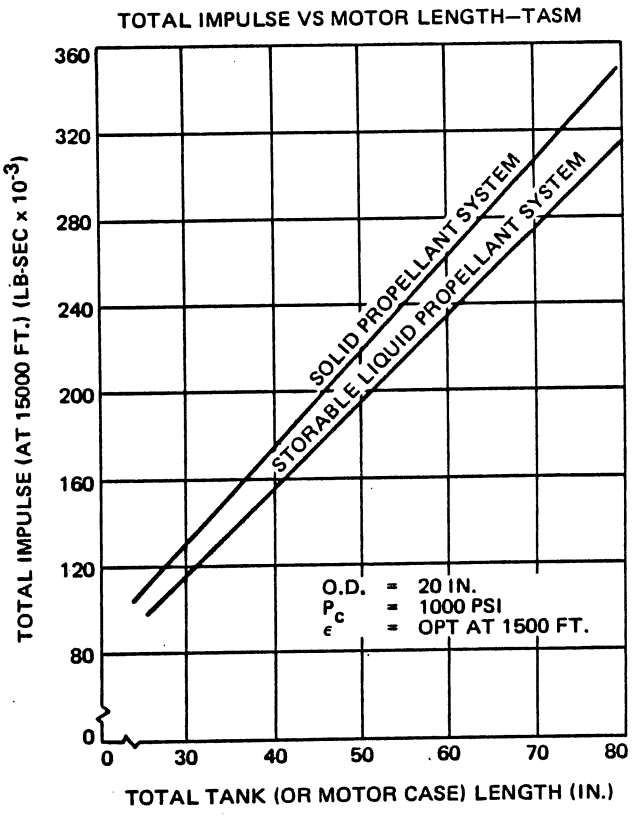

Figure 10-138. Total Impulse vs Motor Length – TASM

The first approach involves the programming of thrust by designing the propellant grain to provide discrete increments of thrust required by the trajectory. The second approach considers either the use of a controllable pintle nozzle or two tandem motor chambers, one (the forward chamber) containing a fuel-rich solid grain and the other (aft) an oxidizer-rich grain, separated by a pintle valve. In the dual-chamber design, thrust level is monitored by the pressure in the forward fuel-rich grain. Hybrid propulsion systems use a liquid oxidizer which can be controlled for injection into a chamber which contains an under-oxidized solid propellant.

Other potential problems in design of solid propellant systems arise from burning rate considerations and environmental temperature considerations. The first problem occurs because of the desire for long burning times when operating at relatively low altitudes. Assuming internal burning grains, a tradeoff must be made between reducing burning time to below optimum values or paying penalties in specific impulse. The latter problems relate to allowable stresses in the propellant charge and in the bond between the charge and the motor wall as a function of storage and inflight temperature conditions.

e. Packaged Storable Liquid Systems – No basic problems of feasibility exist in applying packaged storable liquid propellant systems to the type of mission and trajectories shown in Figure 10-133. The density-impulse values for the propellants employed in these systems, although lower than competitive solids, have been demonstrated in practice (Bullpup, Lance, etc.) to give sufficient total impulse within the volume and weight constraints. Table 5-1 in Section 5 of this manual outlines performance values for several candidate storable propellant combinations. Problems may occur, particularly in regard to customer acceptance of some of the propellant candidates shown in Table 5-1, because of the limited flight experience with their use, and safety and handling hazards. Development of an efficient positive expulsion system and design of components for much longer burning times may also be a problem. In general, however, utilization of these systems will involve an extension of current technology to higher performance and longer operating times rather than development of new technology.

f. Ramjet and Air-Augmented Systems – When considered in the light of the required flexibility in performance over varying flight Mach numbers, altitudes, and launch conditions, it is apparent that no conventional ramjet can be designed to operate efficiently. It would be required that a complex variable inlet design and fuel metering system be used which would respond on command to variations in air/fuel ratio needs.

Use of air-aumentation, offers some advantages in meeting the cruise trajectory represented by Mission (c). Past studies have shown that excessive gross weight penalties are encountered with a supersonic cruise rocket whereas a conventional supersonic cruise ramjet is competitive with a ballistic rocket (refer to Figure 10-139). It is possible that air-augmentation of a solid rocket motor, although not as efficient as a conventional ramjet, may offer a means of at least reducing weight and performance penalties associated with a supersonic cruise rocket. The secondary combustion chamber could be designed to be jettisonable for other flight modes. More detailed descriptions of the state-of-the-art for these options are presented in Reference 18.

g. Hybrid Systems – Hybrid systems offer many of the advantages and disadvantages of both solid and liquid systems. Quoted density-impulse values of the solid-liquid hybrid combinations are higher than solid propellants while motor mass fractions are about equal to the storable liquid systems. In addition, the hybrid system is as completely throttleable as the storable liquid system. Thus it shows considerable promise for use as a candidate system for some applications. Some flight demonstrations have been accomplished in the U.S. Navy target drones and a sizable technology ground test program has verified the performance capability and design feasibility of these systems. Development efforts are continuing.

10-3.6.4.2 Missile Sizing

Trajectory and vehicle parametric study results are integrated so as to provide a range of realistic parametric vehicles having specific performance capabilities. The resultant parametric vehicle can be graphically represented by the set of parametric curves shown in Figure 10-140.

These parametric curves represent a range of buildable missile which allow the evaluation of the propulsion systems under consideration. A comprehensive discussion of the propulsion system evaluation procedure is included in Paragraph 10-3.6.4.3.

In order to produce the set of parametric curves shown in Figure 10-141 the following procedures are followed. The particular trajectory discussed below is only one of those which could be considered, however, the procedure is similar regardless of trajectory profile. Assume the trajectory profile as shown in Figure 10-140 A. Divide it into two distinct trajectory profiles (Figure 10-140 B and C) which will be called trajectories B and C. The two trajectory curves of range as a function of propellant weight required for constant missile diameter, propellant weight, total impulse and burn time are obtained from trajectory parameterization studies.

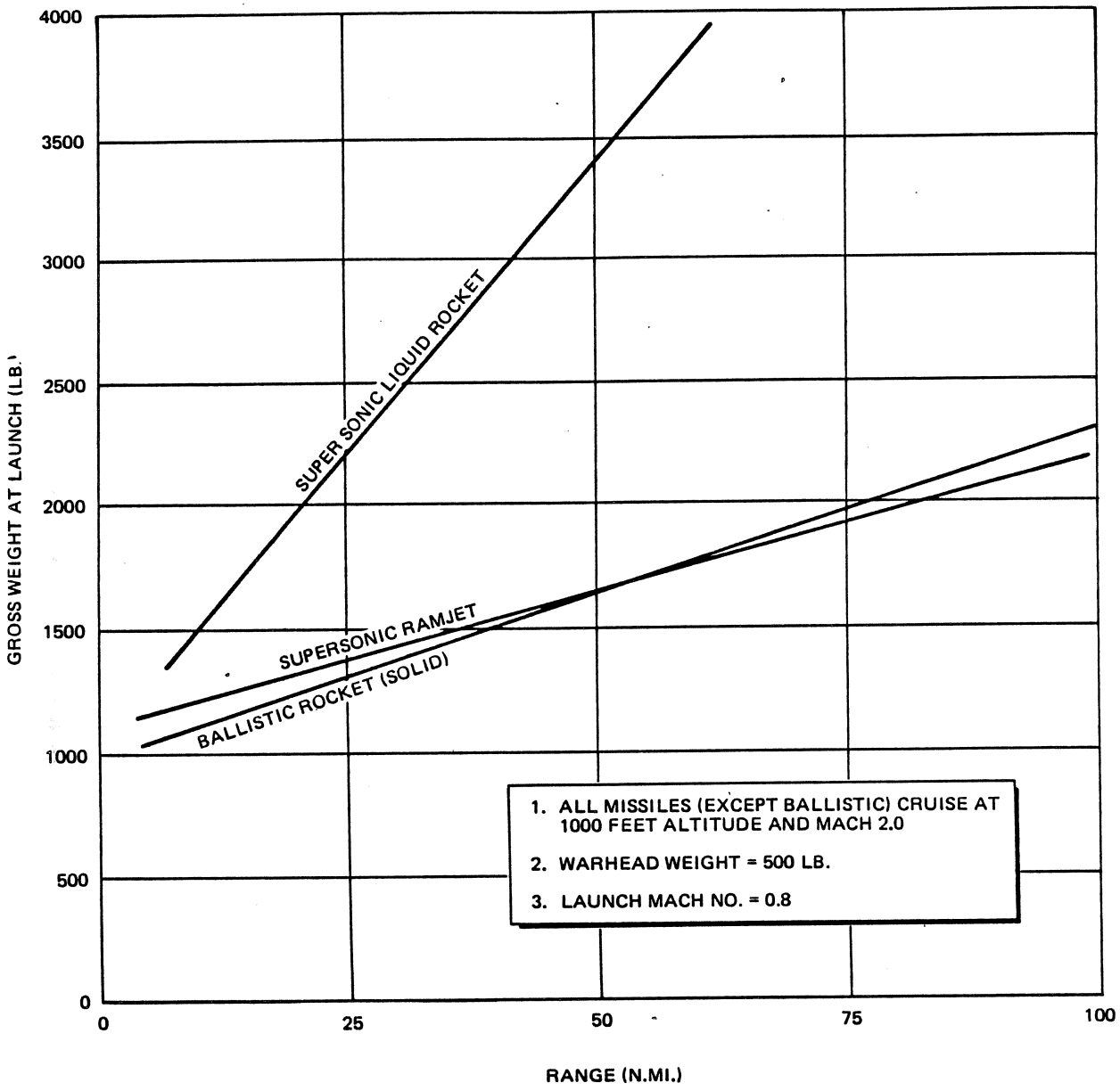

Figure 10-139. Gross Weight vs Range Low Altitude Launch (1000 ft)

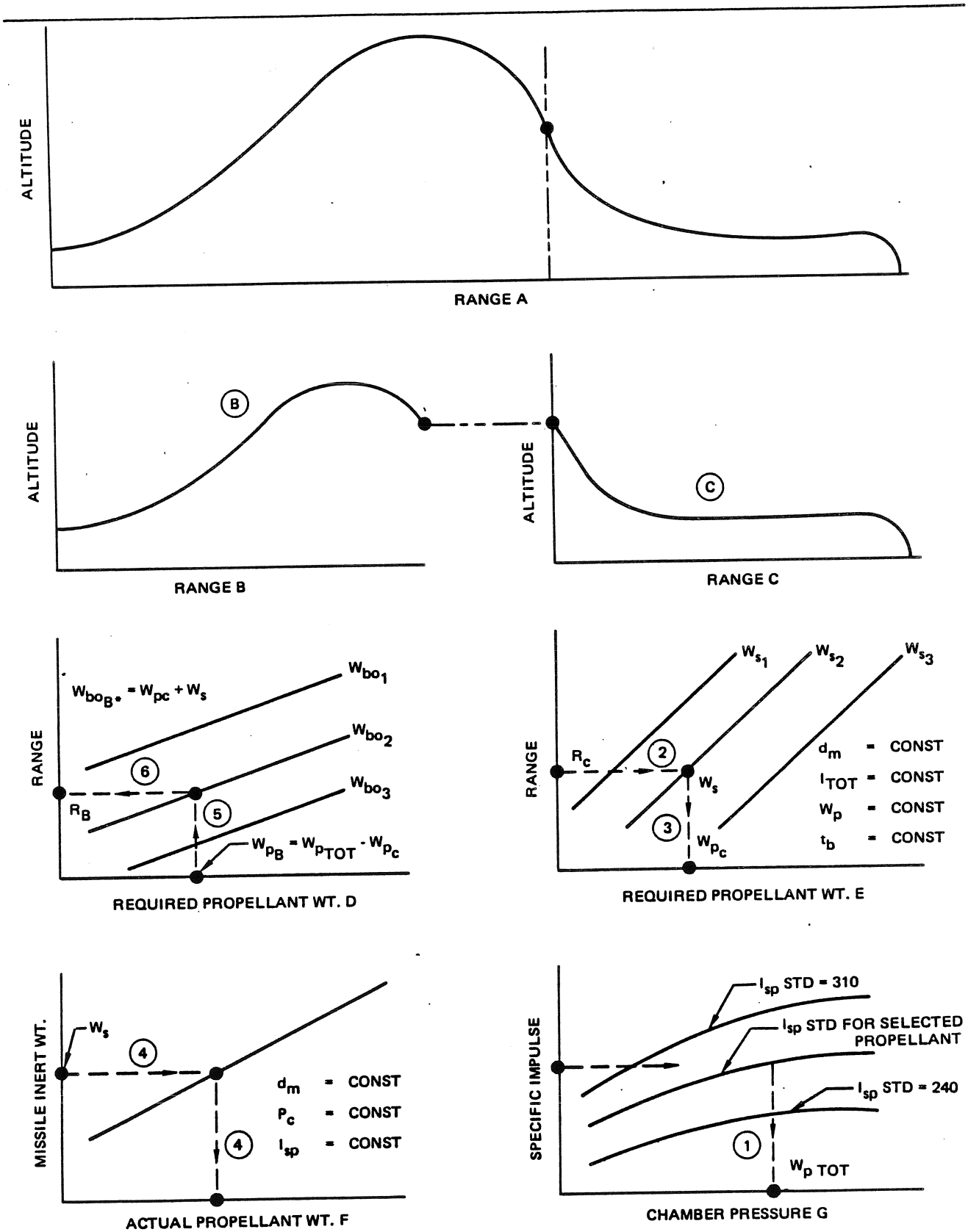

Figure 10-140. Missile Sizing Procedure

*Subscripts B & C refer to trajectory segments Ⓑ and Ⓒ

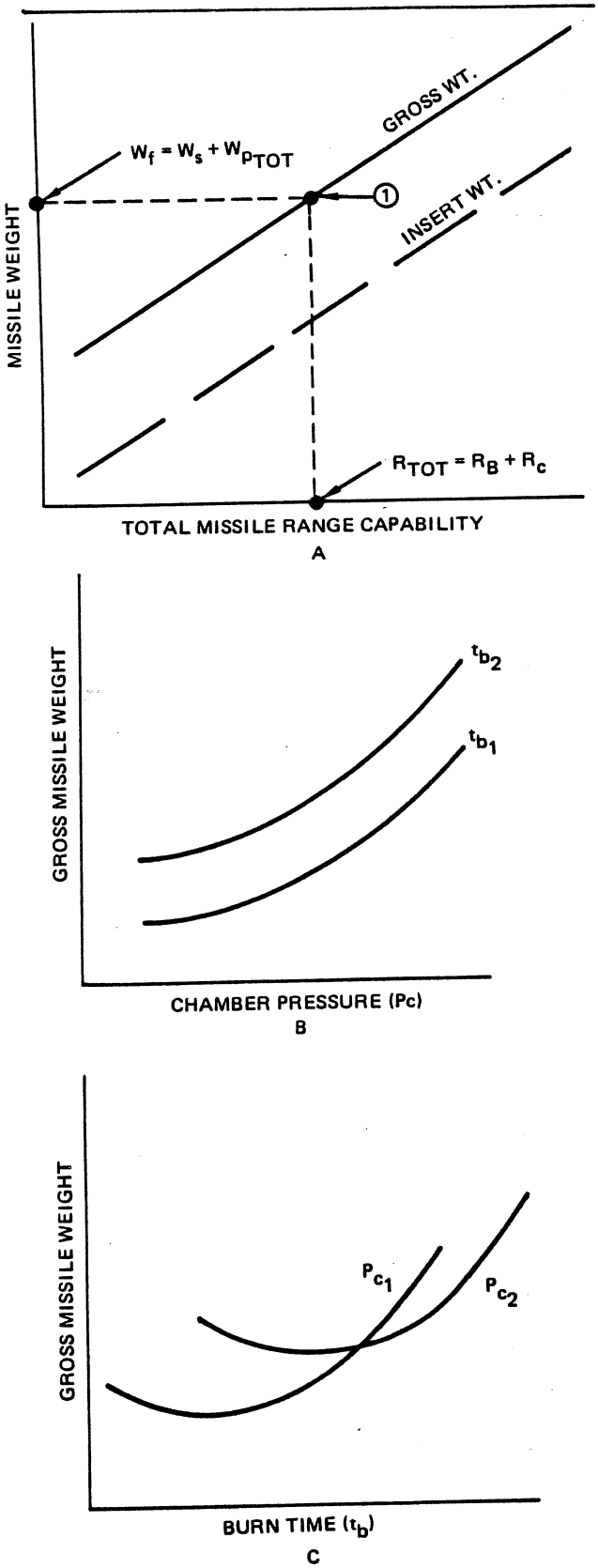

Figure 10-141. Missile Sizing Results

Typical trajectory parameterization curves for each trajectory, B and C, are shown as Figure 10-40 D and E. Two additional curves are required to completely define the range of parametric vehicles:

a. A curve of inert vehicle weight as a function of propellant weight for constant chamber pressure, missile diameter and specific impulse. This curve is the result of vehicle parameterization studies and is typified by Figure 10-140 F.

b. A curve of specific impulse as a function of chamber pressure for a specific propellant, is typified by Figure 10-140 G.

Having established the data required for the missile system parameterization, the following steps are:

a. Determine specific impulse for each of the range versus required propellant weight curves. Specific impulse is defined by the total impulse and propellant weight parameters. From Figure 10-140 G determine the chamber pressure corresponding to the established specific impulse. A missile weight curve (Figure 10-140 F) corresponding to a set of trajectory curves (Figure 10-140 D and E) as defined by the parameters d_m, P_c and I_{sp} is now established.

b. Select a range for trajectory C (R_C) and an inert missile weight to be considered (W_s).

c. From Figure 10-140 E find the propellant weight required (W_{p_C}) corresponding to the selected R_C, W_s. This is the propellant weight necessary for a vehicle having W_s to complete trajectory C.

d. Note the propellant weight corresponding to W_s in Figure 10-140 F. This propellant weight represents the amount of actual propellant which can be loaded into a realistic missile having an inert weight W_s. Call this propellant weight $W_{p_{tot}}$.

e. Subtract W_{p_C} from $W_{p_{tot}}$ to obtain W_{p_B}. This is the propellant weight which is available at the time of missile ignition to complete trajectory B. The total weight of W_{p_C} and W_s is the burnout weight for trajectory B. Denote this weight by W_{bo_B}.

f. Find in Figure 10-140 D, that range which can be attained in trajectory B which corresponds to W_{p_B} and W_{bo_B}. Call this range capability R_B.

By totaling R_B and R_C the total range capability (R_{tot}) of a missile, hanving the following characteristics, is established:

W_s = Inert missile weight

$W_{P_{tot}}$ = Total propellant weight

I_{sp} — per fixed value for Figure 10-140 F

P_c — per fixed value for Figure 10-140 F

d_m — per fixed value for Figure 10-140 F

This missile represents a point, (1) in the curve of Figure 10-141 A. Additional points may be obtained by the same procedure to complete necessary curves of Figure 10-141 A.

Data available from missile weight — range curves will allow plotting Figure 10-141 B and C which is the data needed for evaluation of the missile propulsion system.

10-3.6.4.3 System Trades

After the definition of vehicle performance and design characteristics has been accomplished (as described in previous paragraphs), the resulting data are then evaluated further in order to demonstrate the effects of propulsion system parameters upon total missile system performance, weight, and volume. The parameters investigated include specific impulse, density-impulse, diameter, length, burning time, and the effects of variations in system design (e.g., use of air-augmentation or altitude-compensating nozzles). The paragraphs which follow describe the methods by which this evaluation can be carried out.

a. Effects of Specific Impulse and Density Impulse — The objective of these analyses is to demonstrate the effects of specific impulse and density-impulse on the characteristics of vehicles designed to fly a given range and mission. In preliminary sizing studies (Paragraph 10-3.6.3.3) the influence of these performance parameters is related to their effect on total impulse and system weight and volume. It remains for this phase of the study, however, to show the actual effects on mission performance.

   The type of curves which result are illustrated in Figure 10-142.

b. Effects of Propulsion System Diameter and Length — This analysis evaluates the influence of propulsion system size on missile design and range. Trades are made for each of the propulsion system concepts carried through the study. For this analysis, as in the assessment of the effect of specific impulse and density-impulse variations, chamber pressure and burning time are assumed to be optimum values and the payload weights are specified as constant. Propulsion system weight is also assumed as constant where applicable. A range of propulsion system diameters are considered, and total missile lengths has a broad range.

   The method of presentation of results is illustrated in Figure 10-143 for several specified assumptions, W_{pl}, W_f, and d.

c. Effects of Propellant Burning Time — This analysis evaluates primarily the effects upon missile performance of propellant burning time during the boost phase of flight. In addition the effects of other periods of thrust are appraised.

   The type of curves which will result from this analysis are presented in Figure 10-144. A set of curves is generated for each trajectory flight mode and for each propulsion system carried through the parametric study. Comparison of the burning time giving minimum time-to-target with the burning time yielding the lightest weight vehicle will aid later evaluation of the proper design criteria for the selected propulsion systems for the missions of interest.

d. Evaluation of Air-Augmentation — This analysis will assess the potential advantages of using an air-augmented vehicle for the cruise flight mode, (Mission c)(Figure 10-133). In the air-augmented propulsion system the conventional solid rocket motor is built with a fuel-rich grain and atmospheric air is admitted through inlet scoops to supply the oxygen for complete solid grain combustion within the combustion chamber and then exhausted through a conventional exit nozzle to provide thrust. Representative diameters and payloads are used in this evaluation. Comparison can be made with nonaugmented systems employing the same basic propulsion concept (i.e., solid, liquid, hybrid, etc.). The region of design considered is that in which air-augmentation would offer most promise, (i.e., ranges of 50 miles or greater). Resulting curves are plotted as shown in Figure 10-145.

e. Evaluation of Altitude-Compensating Nozzles — This analysis appraises the potential improvements in missile system performance by using an altitude compensating nozzle, effectively a variable area ratio but physically resembling a plug or aero-spike design. All applicable flight modes are evaluated, and several missile diameters and the multiple payloads treated.

   Performance is compared to that achievable with conventional nozzle design with the same basic propulsion system concept. These comparisons are made for those design conditions for which altitude compensating nozzles appear most promising (i.e., motor operation over a large range of altitudes).

   The manner in which data can be presented is illustrated in Figure 10-146.

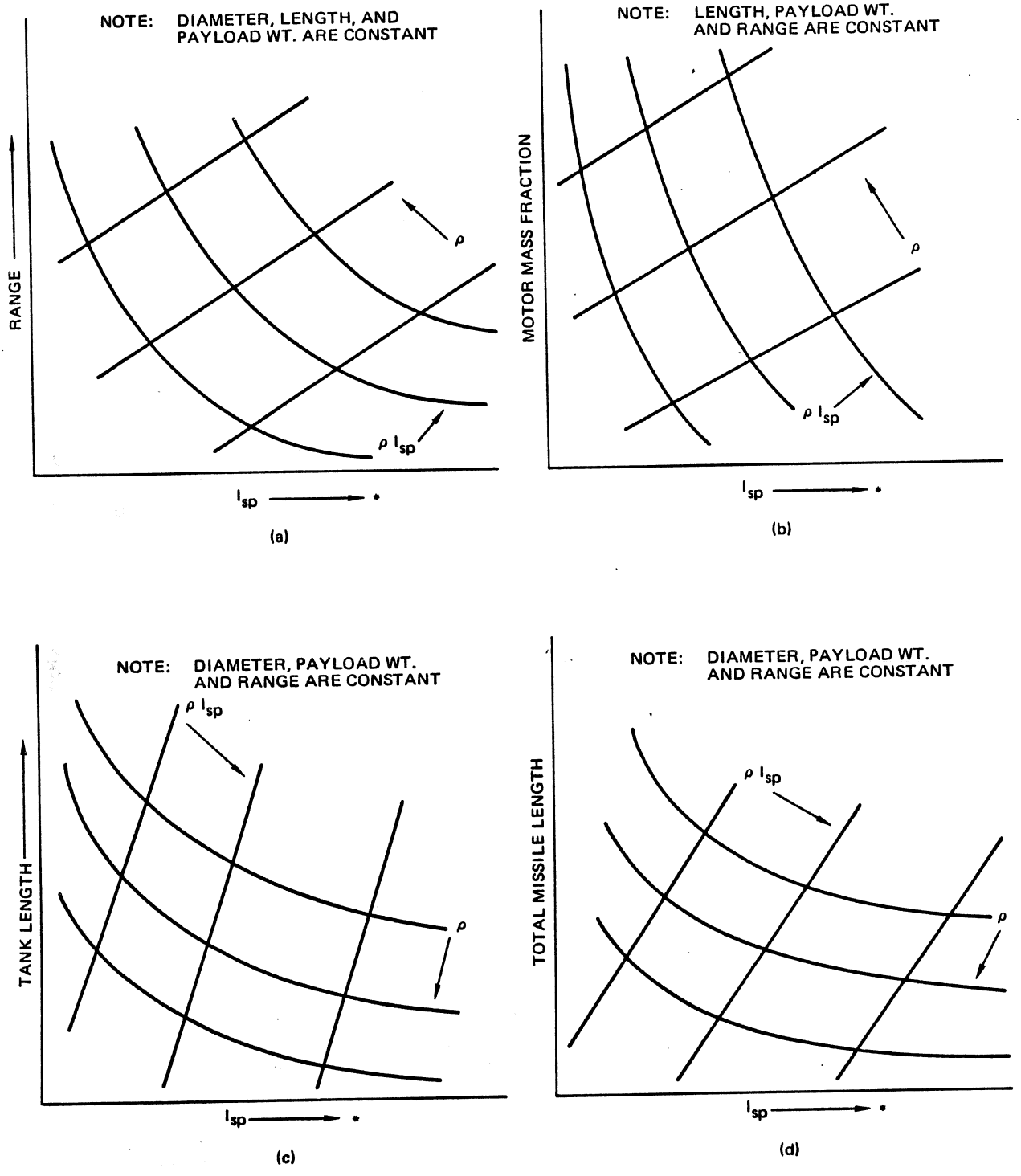

*Arrows indicate direction of increasing values

Figure 10-142. Effect of Specific Impulse and Density Impulse on Missile Performance

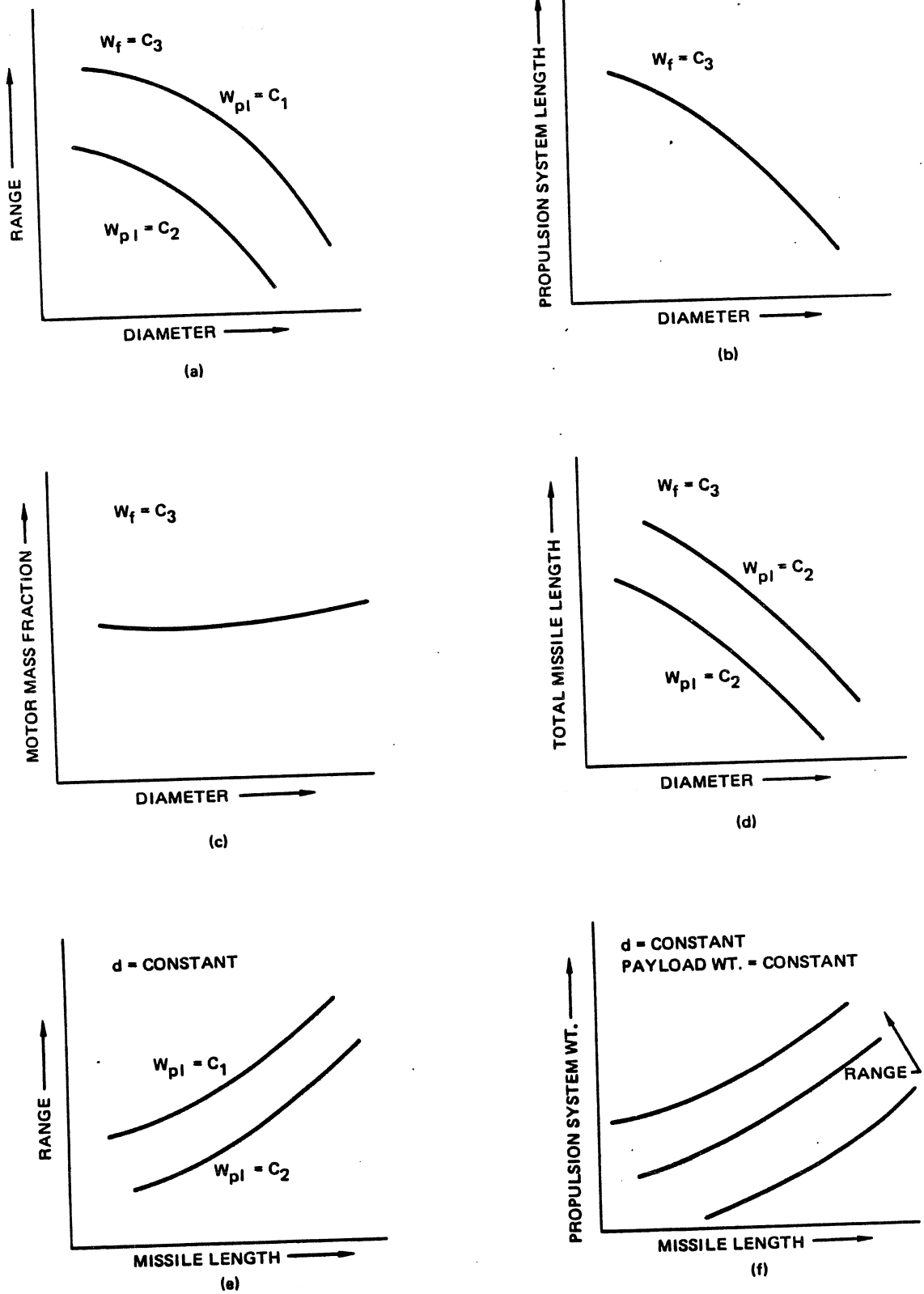

Figure 10-143. Effects of Diameter and Length on Missile Performance

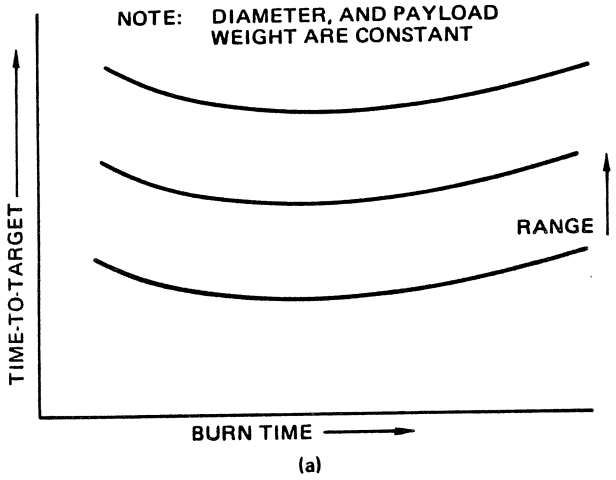

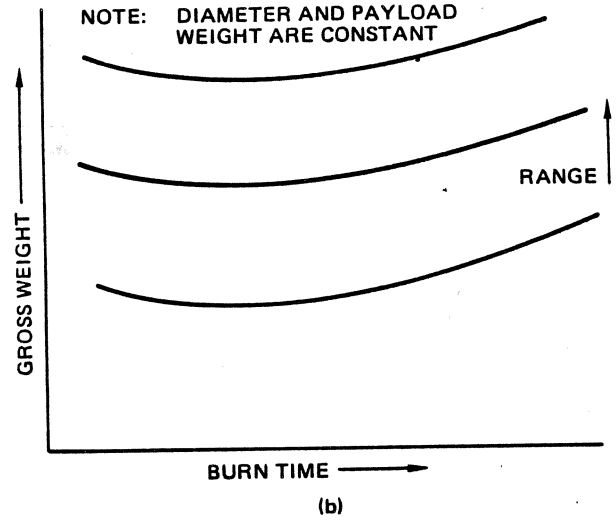

Figure 10-144. Effects of Propellant Burning Time on Missile Performance

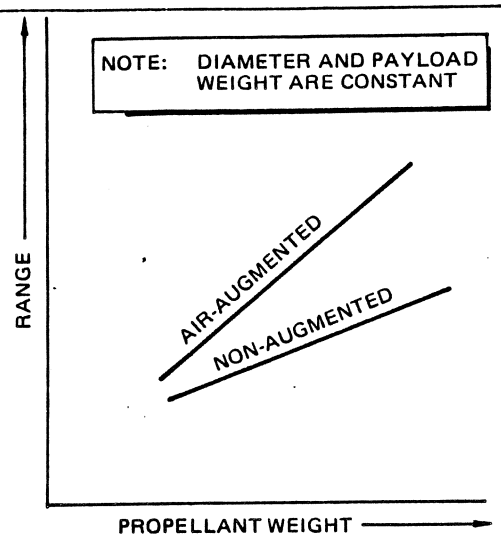

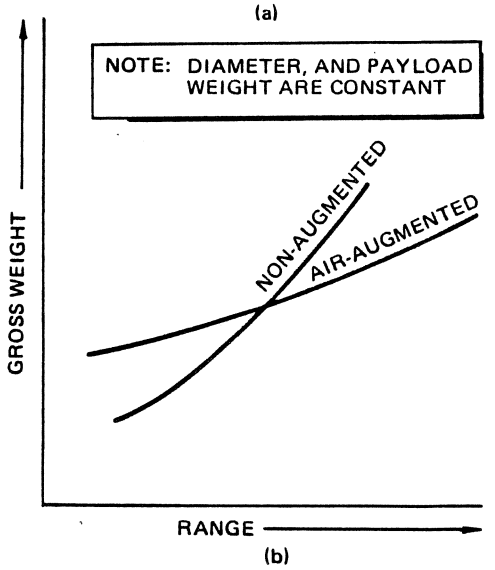

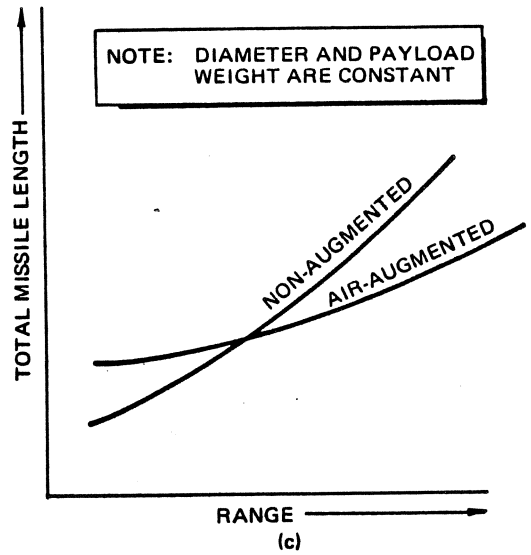

Figure 10-145. Benefits of Air-Augmentation

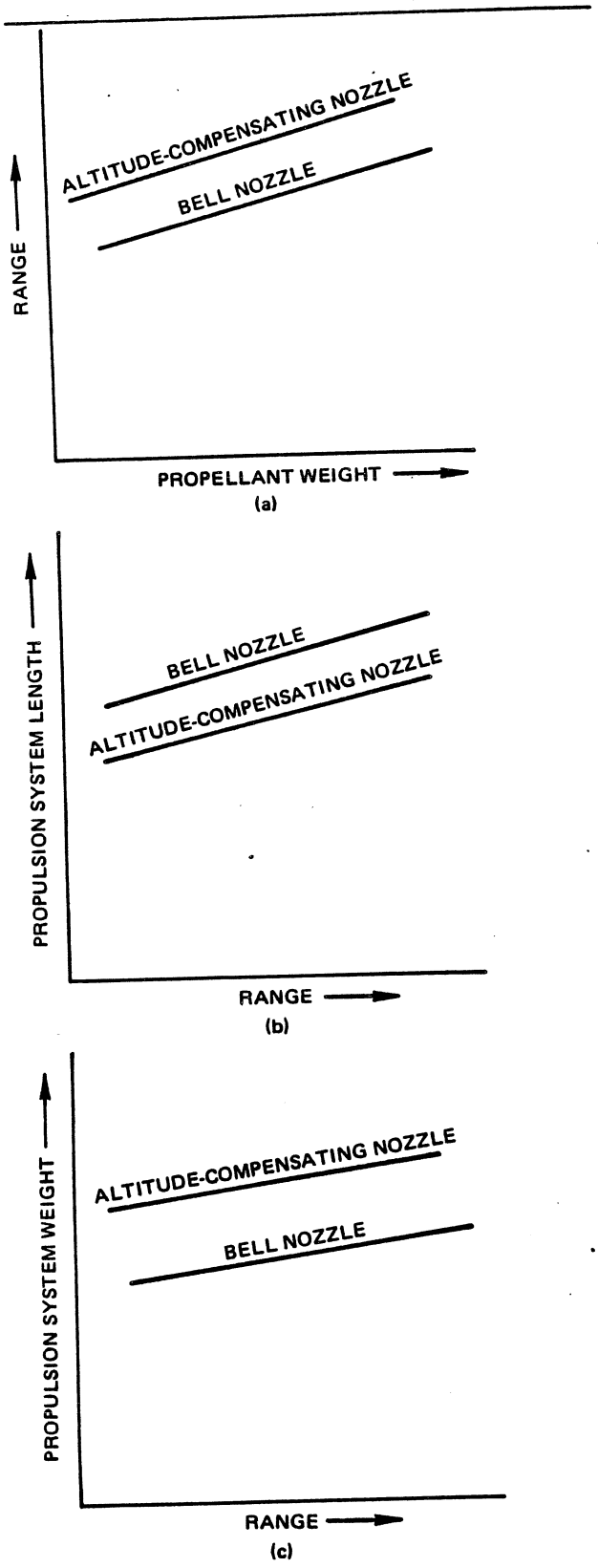

Figure 10-146. Benefits of Altitude – Compensating Nozzles – Cruise Flight Mode

f. Other System Evaluations – In addition to the foregoing analyses, assessments are made of the influence of other propulsion system variables on missile design and performance. Included in these variables are the following:

1. Thrust patterns (boost only, boost-sustain, restart capabilities, etc.).
2. Component design (e.g., the expulsion system design choice).
3. Packaging considerations.
4. Thrust transients, anomalies, and misalignments.

Many of these variables are fully assessed during initial selection of system and subsystem components. Others, such as thrust patterns, have their requirements defined by results of the trajectory and missile parameterization. However, if any of these variables demonstrate a strong potential influence on missile performance (i.e., range) and weight, separate graphical presentation can be made of the pertinent parameters in a manner similar to those illustrated above. In addition, all these variables are re-examined after completion of the initial study to demonstrate the validity of initial assumptions.

10-3.6.4.4 Presentation of Recommended Designs

Layouts of recommended designs are prepared in sufficient detail to describe the functionality of the system. Ballistic characteristics of the motors are calculated as well as the significant hardware designs (including an analysis of weight and balance, e.g., histories). From the trajectory and weight balance history an evaluation of control system duty cycle is defined.

Vehicle performance characteristics for missile(s) incorporating these designs are usually presented for the applicable mission or missions, for inclusion in the preliminary design specification. Potential problem areas of the suggested designs will be described and if alternate solutions exist in these problem areas they will also be described.

10-3.7 Generalized Exchange Ratio Analysis

During the initial design phases, the problem of estimating the effects of small design changes on vehicle payload performance is a continual one. In other instances, it may be desired to estimate the changes in vehicle characteristics required to maintain some minimum payload capability when a performance parameter is varied. In either case, exchange ratios provide the designer with an expedient and relatively accurate tool for predicting the effects of such changes without resorting to extensive hand calculations or digital computer solutions.

10-3.7.1 Analytical Relationships (Fixed Velocity)

The exchange ratios presented herein are derived from the theoretical expression for the total velocity gained at burnout by an N stage launch.[12]

$$V_{bo} = \sum_{n=1}^{N} \left(g_o I_{sp_n} \ln (r_{v_n}) - \Delta V_{L_{g_n}} - \Delta V_{L_{F_n}} \right) \tag{148}$$

In order to facilitate the computation of the exchange ratios, certain simplifing assumptions are made. In general, it is assumed that the perturbation of a single performance parameter will not affect the total velocity losses due to atmospheric effects and thrust vector not acting along the flight path. It is also assumed that the velocity losses due to gravitation effects can be approximated by the following expression:

$$\Delta V_{L_{g_n}} = g_o \, t_{b_n} \cos \bar{\beta}_n \tag{149}$$

Other assumptions which were made in the derivation of the exchange ratios are listed with the individual ratios presented below. The exact effects of these assumptions can only be determined from digital computer simulations of the vehicle and mission being considered. However, the accuracy obtained using the analytical expressions is believed to be adequate for most preliminary design studies.

10-3.7.1.1 Exchange Ratios for an N-Stage Vehicle

Equations for the exchange ratios of the nth stage of an N-stage vehicle are given below.

The payload to propellant specific impulse ratio of the nth stage is

$$\frac{dW_{pl}}{dI_{sp_n}} = \frac{\ln r_{v_n} - \bar{\theta}_n \left(1 - \frac{1}{r_{v_n}}\right)}{\sum_{n=1}^{N} \left[\left(\frac{I_{sp}}{W_f} \right)_n \left(r_{v_n} - 1 \right) \right]} \tag{150}$$

where

$$\bar{\theta} = \frac{x \cos \bar{\beta}}{r}$$

The payload to structural weight of the nth stage is:

$$\frac{dW_{pl}}{dW_{sn}} = -\frac{\sum_{n=1}^{n} \left[\left(\frac{I_{sp}}{W_{f_n}} \right) \left(r_{v_n} - 1 \right) \right]}{\sum_{n=1}^{N} \left[\left(\frac{I_{sp}}{W_f} \right)_n \left(r_{v_n} - 1 \right) \right]} \tag{151}$$

where the negative sign (—) refers to a negative slope, e.g., the payload decreases as the step structural weight increases.

The payload to initial gross weight of the nth stage (for a given total gross weight) is:

$$\frac{dW_{pl}}{dW_{f_n}} = -\frac{\sum_{n=1}^{n} \left[\left(\frac{I_{sp}}{W_f} \right)_n \left(1 - r_{v_n} \right) \right] + (1 - s_{sn}) \left(\frac{I_{sp}}{W_f} \right)_n \left(r_{v_n} - \bar{\theta}_n \right)}{\sum_{n=1}^{N} \left[\left(\frac{I_{sp}}{W_f} \right)_n \left(1 - r_{v_n} \right) \right] - (1 - s_n) \left(\frac{I_{sp}}{W_f} \right)_n \left(r_{v_n} - \bar{\theta}_n \right)} \tag{152}$$

The payload to propellant loading of the nth stage is:

$$\left(\frac{dW_{pl}}{dW_{pn}} \right)_{W_{sn}} = \frac{\left(\frac{I_{sp}}{W_f} \right)_n \left(1 - \bar{\theta}_n \right) - \sum_{n=1}^{n-1} \left[\left(\frac{I_{sp}}{W_f} \right)_n \left(r_{v_n} - 1 \right) \right]}{\sum_{n=1}^{N} \left[\left(\frac{I_{sp}}{W_f} \right)_n \left(r_{v_n} - 1 \right) \right]} \tag{153}$$

Payload to propellant weight, allowing for appropriate structural weight to accommodate the difference in propellant weight (rubber staging), is:

$$\frac{dW_{pl}}{dW_{p_n}} = \frac{\left(\frac{I_{sp}}{W_f} \right)_n \left(r_{v_n} - \bar{\theta}_n \right) - \left(\frac{1}{1 - s_{sn}} \right) \sum_{n=1}^{n} \left[\left(\frac{I_{sp}}{W_f} \right)_n \left(r_{v_n} - 1 \right) \right]}{\sum_{n=1}^{N} \left[\left(\frac{I_{sp}}{W_f} \right)_n \left(r_{v_n} - 1 \right) \right]} \tag{154}$$

Payload to initial thrust (percentage change of nominal thrust)

$$\frac{dW_{pl}}{dW_{p_n}} = \frac{x_n \, I_{sp_n} \cos \bar{\beta}_n \left(1 - 1/r_{v_n} \right)}{100 \; r_{v_n} \sum_{n=1}^{N} \left[\left(\frac{I_{sp}}{W_f} \right)_n \left(r_{v_n} - 1 \right) \right]} \tag{155}$$

Gross weight of the nth stage to the gross weight of the n+1 stage, assuming a constant thrust in the nth stage is:

$$\left(\frac{dW_{f_n}}{dW_{f_{n+1}}} \right)_{W_{pl}, F_n} = \frac{(1 - s_{sn}) \left(r_{v_n} - \bar{\theta}_n \right)}{1 - s_{sn} \, r_{v_n} - (1 - s_{sn}) \, \bar{\theta}_n} \tag{156}$$

Gross weight of any given stage (the kth stage) to the gross weight of any stage (the nth stage), assuming a constant thrust-to-wieght ratio for each stage below the nth stage, is:

$$\left(\frac{dW_{f_k}}{dW_{f_n}}\right)_{W_{pl},\, r_k} = \frac{W_{f_k}}{W_{f_n}} \qquad (157)$$

$(1 \leqslant k, \leqslant n-1), (k \leqslant n)$

Vehicle liftoff weight to gross weight of the nth stage, assuming a constant thrust-to-weight ratio in each stage, is:

$$\left(\frac{dW_{f_l}}{dW_{f_n}}\right)_{W_{pl},\, r_k} = \frac{1}{W_{f_n}} \sum_{n=1}^{N} W_{f_n} \qquad (158)$$

$(1 \leqslant k \leqslant n-1)\ (1 \leqslant n \leqslant n)$

The above equations also can be used when the payload weight is perturbed to estimate the changes in stage gross weights and vehicle liftoff weight required to achieve a fixed mission velocity requirement. Also, using the above equation in conjunction with those for the stage gross weight presented in Paragraph 10-3.7.1.2, one can evaluate the effect on the liftoff weight due to a perturbation of a vehicle parameter in the nth stage.

10-3.7.1.2 Exchange Ratios for One-Stage Vehicle

Exchange ratios for a one stage vehicle are given below.

Payload to specific impulse

$$\frac{dW_{pl}}{dI_{sp}} = \frac{\ln r_v - \bar{\theta}\,(1 - 1/r_v)}{\frac{I_{sp}}{W_f}\,(r_v - 1)} \qquad (159)$$

Payload to structural weight

$$\frac{dW_{pl}}{dW_s} = -1 \qquad (160)$$

Payload to initial gross weight

$$\frac{dW_{pl}}{dW_f} = \frac{1 - s_s r_v - (1 - s_s)\,\bar{\theta}}{(1 - s_s)\,(r_v - \bar{\theta})} \qquad (161)$$

$$= \frac{W_{pl}}{W_f} \text{ (neglecting gravitational and atmospheric effects)}$$

Payload to propellant loading

$$\left(\frac{dW_{pl}}{dW_p}\right)_{W_s} = \frac{1 - \bar{\theta}}{r_v - 1} \qquad (162)$$

structural

Payload to propellant weight, allowing the appropriate structural weight to accommodate the difference in propellant weight (rubber staging)

$$\frac{dW_{pl}}{dW_p} = \frac{1 - s_s r_v - (1 - s_s)\,\bar{\theta}}{(1 - s_s)\,(r_v - 1)} \qquad (163)$$

Payload to initial thrust (percentage change of nominal thrust)

$$\frac{dW_{pl}}{dF} = \frac{x\, W_{bo} \cos \bar{\beta}}{100\, r} \qquad (164)$$

Stage gross weight to specific impulse for a fixed payload capability

$$\left(\frac{dW_f}{dI_{sp}}\right)_{W_{pl}} = -\frac{\ln r_v - \bar{\theta}\,(1 - 1/r_v)}{\frac{I_{sp}}{W_f}\,[1 - s_s r_v - \bar{\theta}\,(1 - s_s)]} \qquad (165)$$

Stage gross weight to inert weight for a fixed payload capability

$$\left(\frac{dW_f}{dW_s}\right)_{W_{pl}} = \frac{(1 - s_s)\,(r_v - \bar{\theta})}{1 - s_s r_v - (1 - s_s)\,\bar{\theta}} \qquad (166)$$

Stage gross weight to initial thrust for a fixed payload capability and percentage change of thrust

$$\left(\frac{dW_f}{dF}\right)_{W_{pl}} = -\frac{W_f\,\bar{\theta}\,(1 - 1/r_v)}{100\,[1 - s_s r_v - (1 - s_s)\,\bar{\theta}]} \qquad (167)$$

In evaluating the parameter $\bar{\theta}$ which appears in the analytical exchange ratios, it is suggested that the time average of $\cos \bar{\beta}$ be used rather than the time average of $\bar{\beta}$, the arithmetic mean of the initial and burnout angles. Alternatively, use the data presented in Paragraph 10-2.2.1.3 to estimate "total" velocity losses, ΔV_L, and compute $\cos \bar{\beta}$ from the relation:

$$\cos \bar{\beta} = \frac{\Delta V_L}{g_o\, t_b} \qquad (168)$$

Use of this procedure is justified since gravity losses make up a major portion of the total losses for most booster vehicles. In computing the parameters, base F/W_f on sea level thrust and vehicle liftoff weight for first stage, and vacuum thrust and initial stage weight for

upper stages. The ratio of sea level to vacuum specific impulse, x, is usually assumed to be equal to one for upper stages.

10-3.7.2 Graphical Presentation (Fixed Velocity)

As an aid to the designer, the above exchange ratios for a single-stage vehicle are plotted in Figures 10-147 through 10-154 for representative values of the performance parameters.

In Figure 10-147, the ratio of payload to specific impulse is plotted as a function of r_v, θ, W_f, and I_{sp}. In Figure 10-148 the ratio of payload to initial gross weight is plotted as a function of r_v, s_s, and θ. The ratio of payload to propellant weight for a fixed stage structural weight is plotted in Figure 10-149 as a function of r_v and θ, and the ratio of payload to propellant weight for varying stage strctural weight is plotted in Figure 10-150 as a function of r_v, s_s, and θ.

The ratio of payload to initial thrust is plotted in Figure 10-151 as a function of r_v, x, β, and W_{bo}. The ratio of stage gross weight to specific impulse is plotted in Figure 10-152 as a function of r_v, s_s, W_f, and I_{sp} for θ. The ratio of stage gross weight to inert weight is plotted in Figure 10-153 as a function of r_v, s_s, and θ. This plot can also be used to determine the resulting perturbation in gross weight of the nth stage of a multistage vehicle due to a perturbation of gross weight of the n + 1 stage when a constant thrust is assumed in the nth stage. The ratio of stage gross weight to initial thrust is plotted in Figure 10-154 as a function of r_v, s_s, θ, and W_f.

10-3.7.3 Numerical Example (Fixed Velocity)

To illustrate the use of exchange ratio analysis, some sample calculations will be presented. It is suggested that the pertinent vehicle data be tabulated in some systematic fashion in order to facilitate the computations and minimize errors. A possible format, to be used in estimating the effect of simultaneously varying several parameters on vehicle payload capability, is shown in Table 10-16: In the first column the vehicle weights, propulsion parameters and trajectory parameters required in the computation are listed. In the second column the original or nominal value of each parameter is tabulated, and in the third column the parameter perturbations are given. In the fourth column the exchange ratios corresponding to each parameter are listed. The fifth column lists the change in payload weight caused by each parameter perturbation and the total payload net change.

The exchange ratios presented are computed based on the given configuration data as follows:

$$\left(\frac{dW_{pl}}{dW_{p_1}}\right)_{W_s} = \frac{\left(\frac{I_{sp}}{W_f}\right)_1 \left(1 - \bar{\theta}_1\right)}{\sum_{n=1}^{3} \left[\left(\frac{I_{sp}}{W_f}\right)_n \left(r_{v_n} - 1\right)\right]}$$

$$= \frac{\frac{275}{2500000}\left[1 - \frac{(4500000)(2500000)\cos 32^\circ}{(5000000)(4500000)}\right]}{\left(\frac{275}{2500000}\right)\left(\frac{2500000}{850000} - 1\right) + \left(\frac{400}{600000}\right)\left(\frac{600000}{245000} - 1\right) + \left(\frac{400}{215000}\right)\left(\frac{215000}{115000} - 1\right)}$$

$$= \frac{0.00011\,(1 - 0.424)}{0.000213 + 0.000966 + 0.001618}$$

$$= \frac{0.000634}{0.002797} = 0.023 \text{ lb/lb}$$

$$\frac{dW_{pl}}{dW_{s_2}} = -\frac{\sum_{n=1}^{2} \left[\left(\frac{I_{sp}}{W_f}\right)_n \left(r_{v_n} - 1\right)\right]}{\sum_{n=1}^{3} \left[\left(\frac{I_{sp}}{W_f}\right)_n \left(r_{v_n} - 1\right)\right]}$$

$$= -\frac{0.000213 + 0.000966}{0.002797}$$

$$= -0.422 \text{ lb/lb}$$

$$\frac{dW_{pl}}{dW_{s_3}} = -\frac{\sum_{n=1}^{3} \left[\left(\frac{I_{sp}}{W_f}\right)_n \left(r_{v_n} - 1\right)\right]}{\sum_{n=1}^{3} \left[\left(\frac{I_{sp}}{W_f}\right)_n \left(r_{v_n} - 1\right)\right]}$$

$$= -1.0 \text{ lb/lb}$$

$$\frac{dW_{pl}}{dI_{sp_3}} = \frac{\ln r_{v_3} - \bar{\theta}_3\left(1 - 1/r_{v_3}\right)}{\sum_{n=1}^{3} \left[\left(\frac{I_{sp}}{W_f}\right)_n \left(r_{v_n} - 1\right)\right]}$$

$$= \frac{\ln \frac{215000}{115000} - \frac{215000 \cos 85^\circ}{100000}\left(1 - \frac{115000}{215000}\right)}{0.002797}$$

$$= 192.5 \text{ lb/sec}$$

$$\frac{dW_{pl}}{dF_2} = \frac{x_2\, I_{sp_2} \cos \bar{\beta}_2 \left(1 - 1/r_{v_2}\right)}{100 \left(F/W_f\right)_2 \sum_{n=1}^{3} \left[\left(\frac{I_{sp}}{W_f}\right)\left(r_{v_n} - 1\right)\right]}$$

$$= \frac{(1.0)\,(400)\cos 65^\circ \left(1 - \frac{245000}{600000}\right)}{(100)\left(\frac{800000}{600000}\right)(0.002797)}$$

$$= 269.2 \text{ lb/percent}$$

Utilizing these ratios, payload perturbations are computed for the parameter perturbations. The individual payload perturbations combine algebraically to give the net change in payload capability, as shown at the bottom of Table 10-16.

10-3.7.4 Exchange Ratio Chart (Effects on Velocity)

In some instances the effect of weight changes, specific impulse variations and/or mass ratio on the burnout velocity are desired for a constant payload weight. These effects are graphically illustrated in Figure 10-155. It should be noted that these exchange ratios are based on the ideal velocity equation, e.g., no gravity drag or thrust atmospheric losses are included.

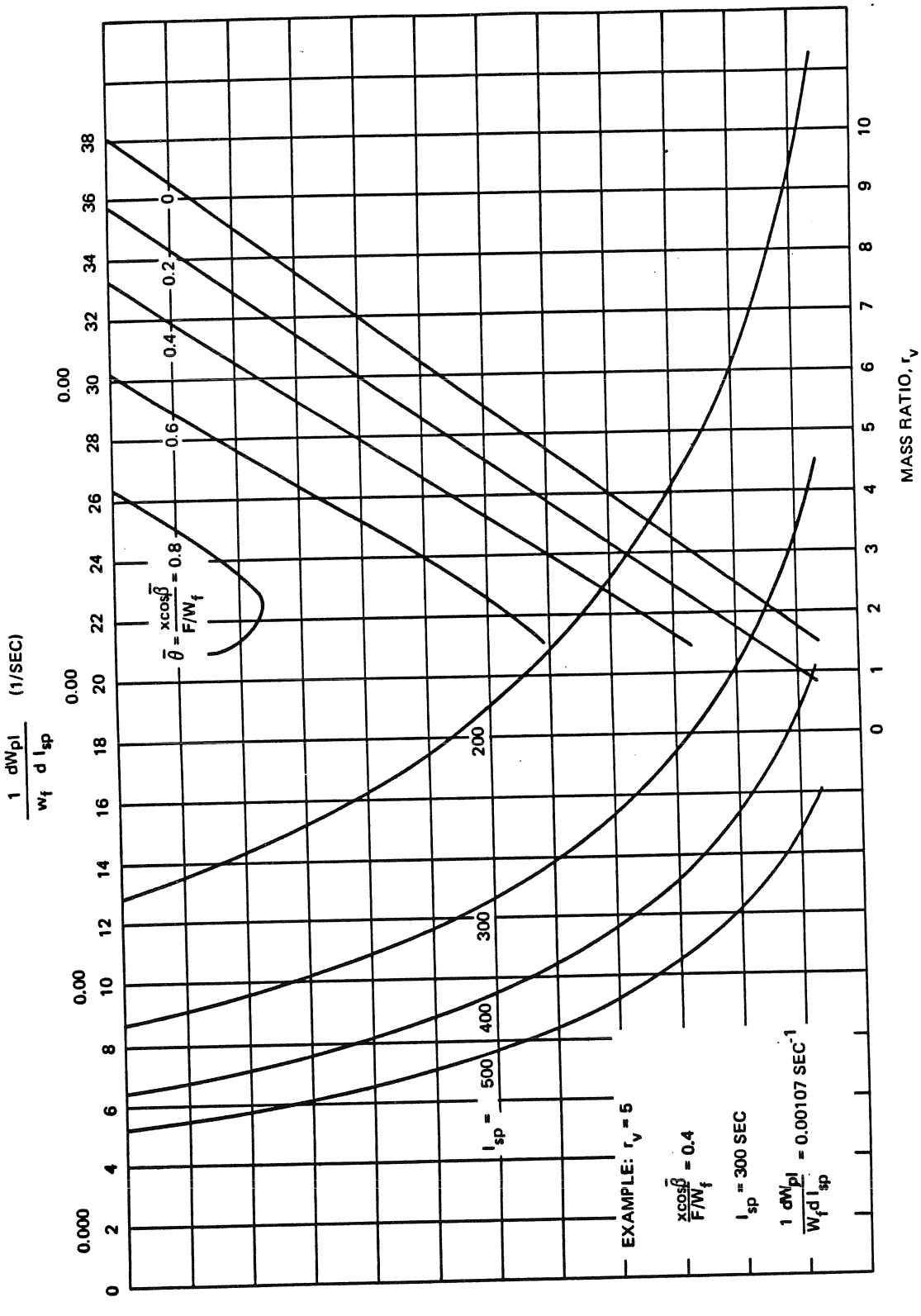

Figure 10-147. Stage Payload Weight – Specific Impulse Ratio

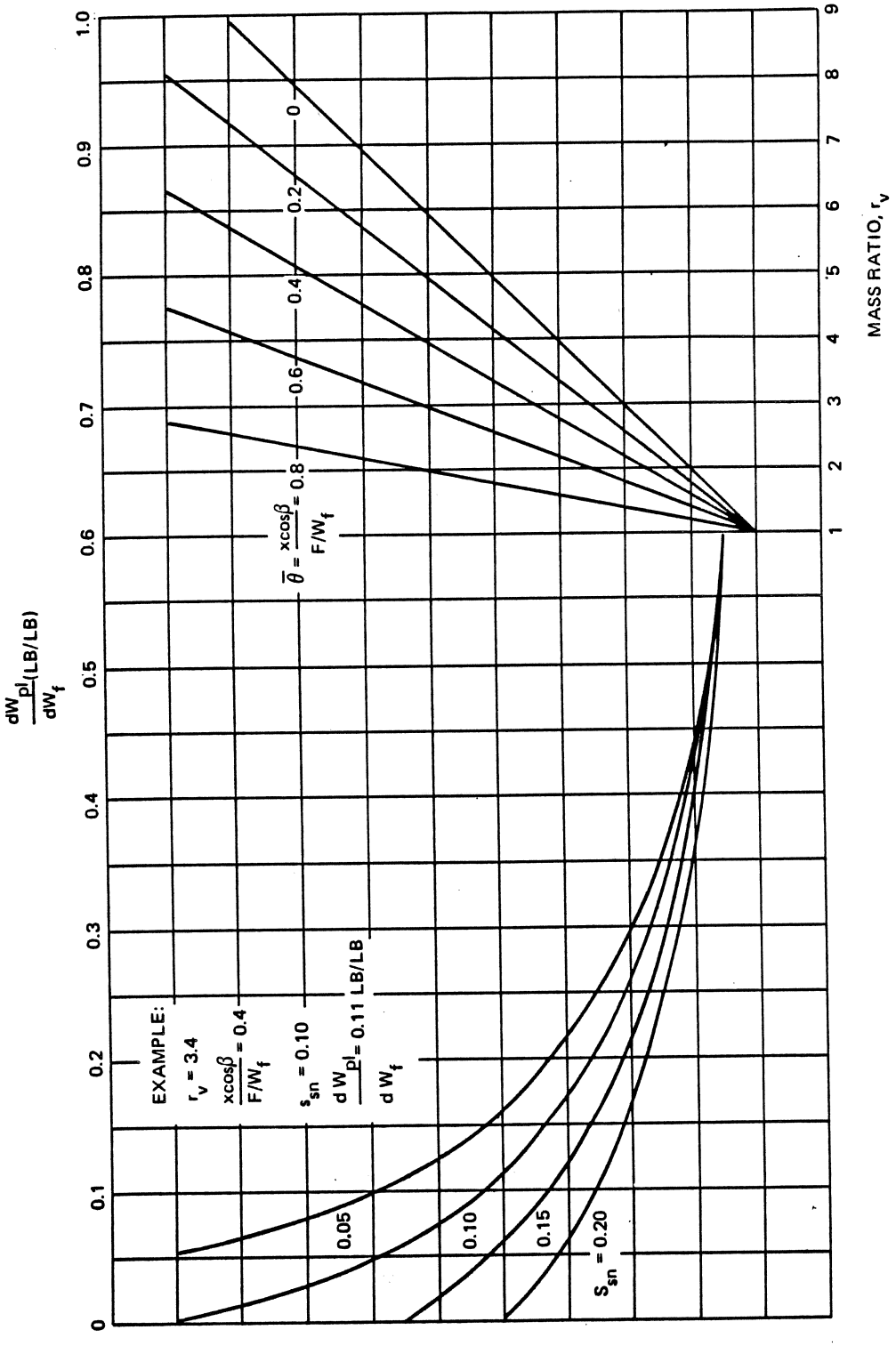

Figure 10-148. Stage Payload Weight — Stage Initial Gross Weight Exchange Ratio

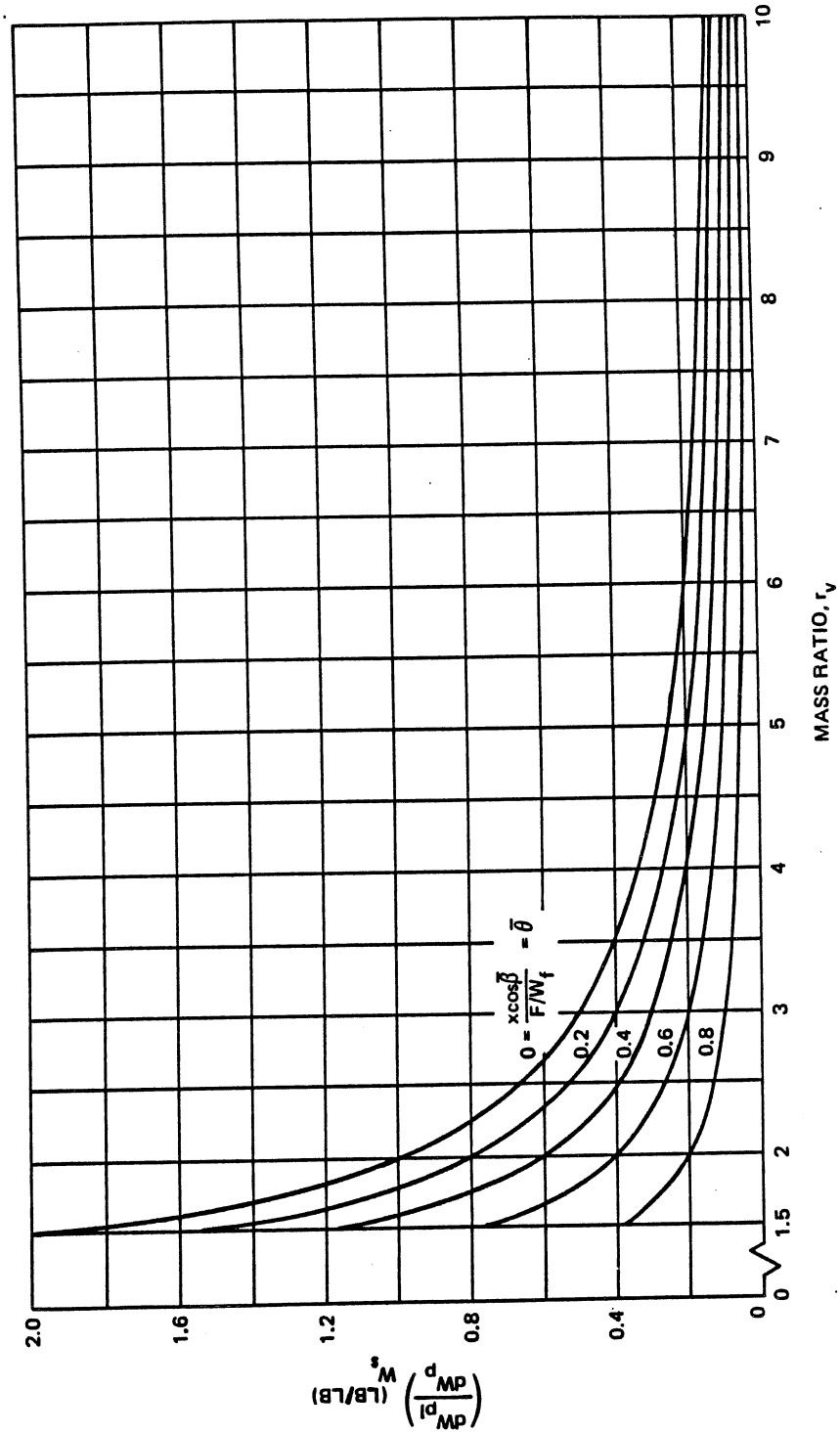

Figure 10-149. Stage Payload Weight – Propellant Weight Exchange Ratio (Fixed Structural Weight)

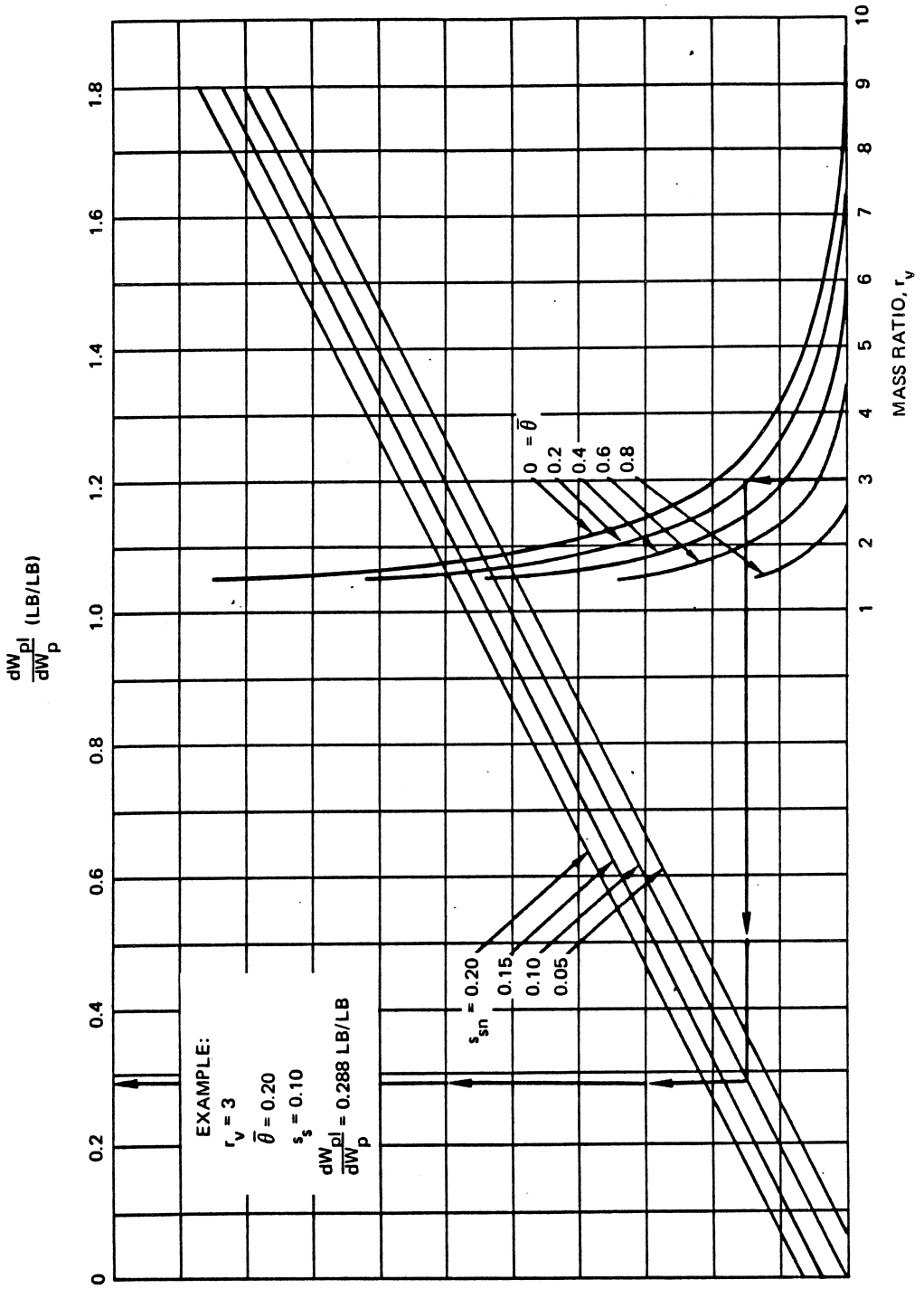

Figure 10-150. Stage Payload Weight — Propellant Weight Exchange Ratio (Variable Structural Weight)

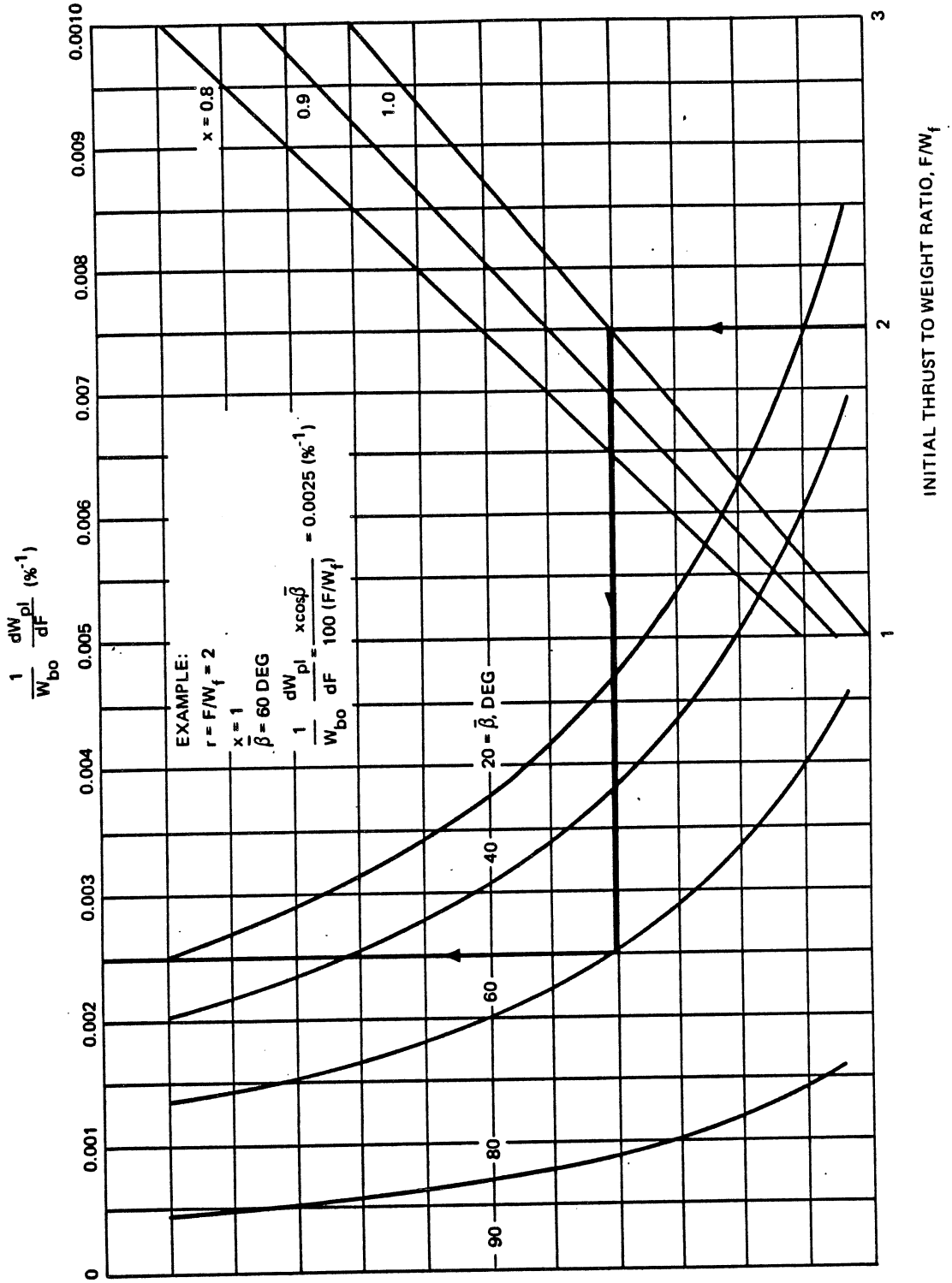

Figure 10-151. Stage Payload Weight – Thrust Exchange Ratio

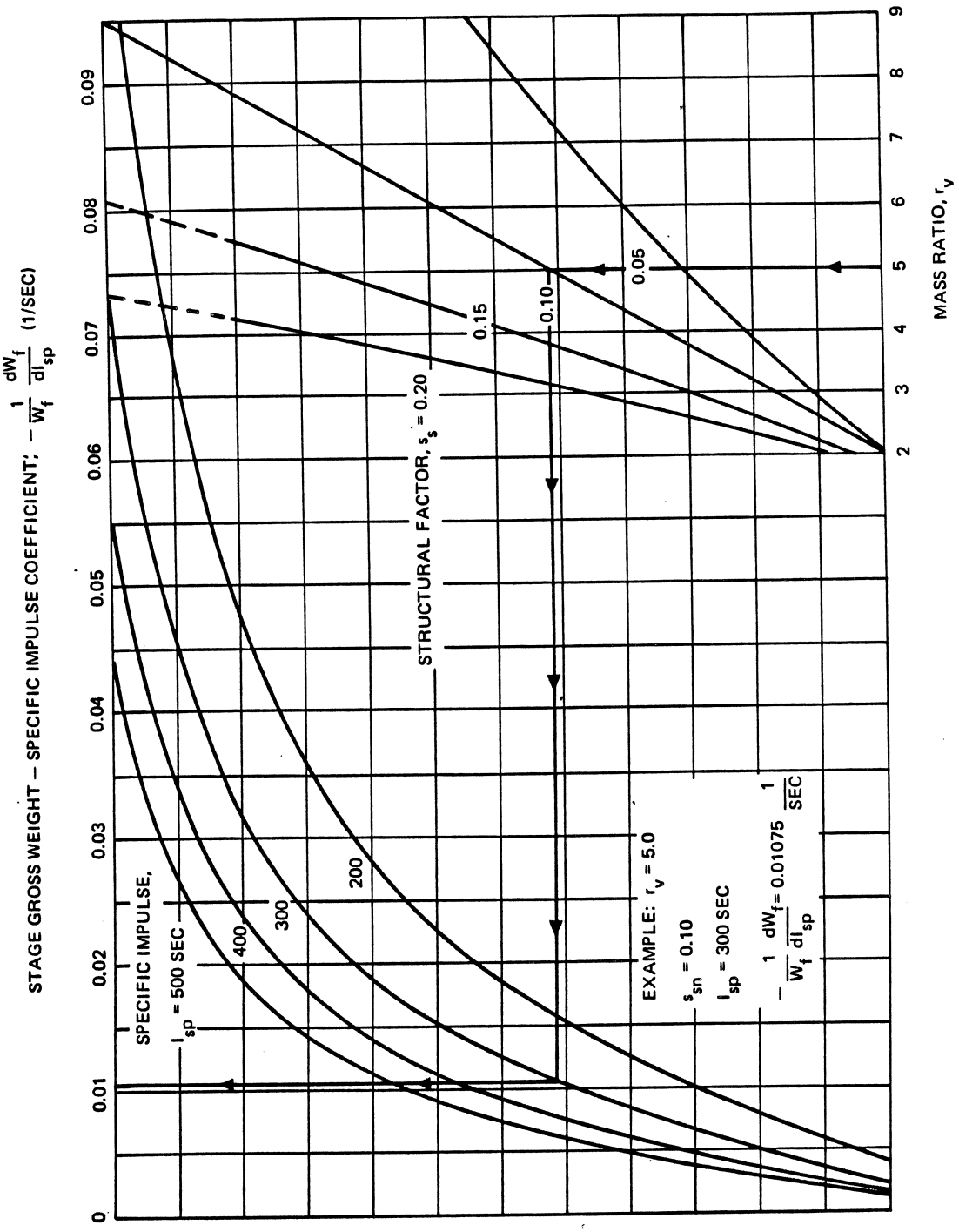

Figure 10-152. Stage Gross Weight – Specific Impulse Exchange Ratio

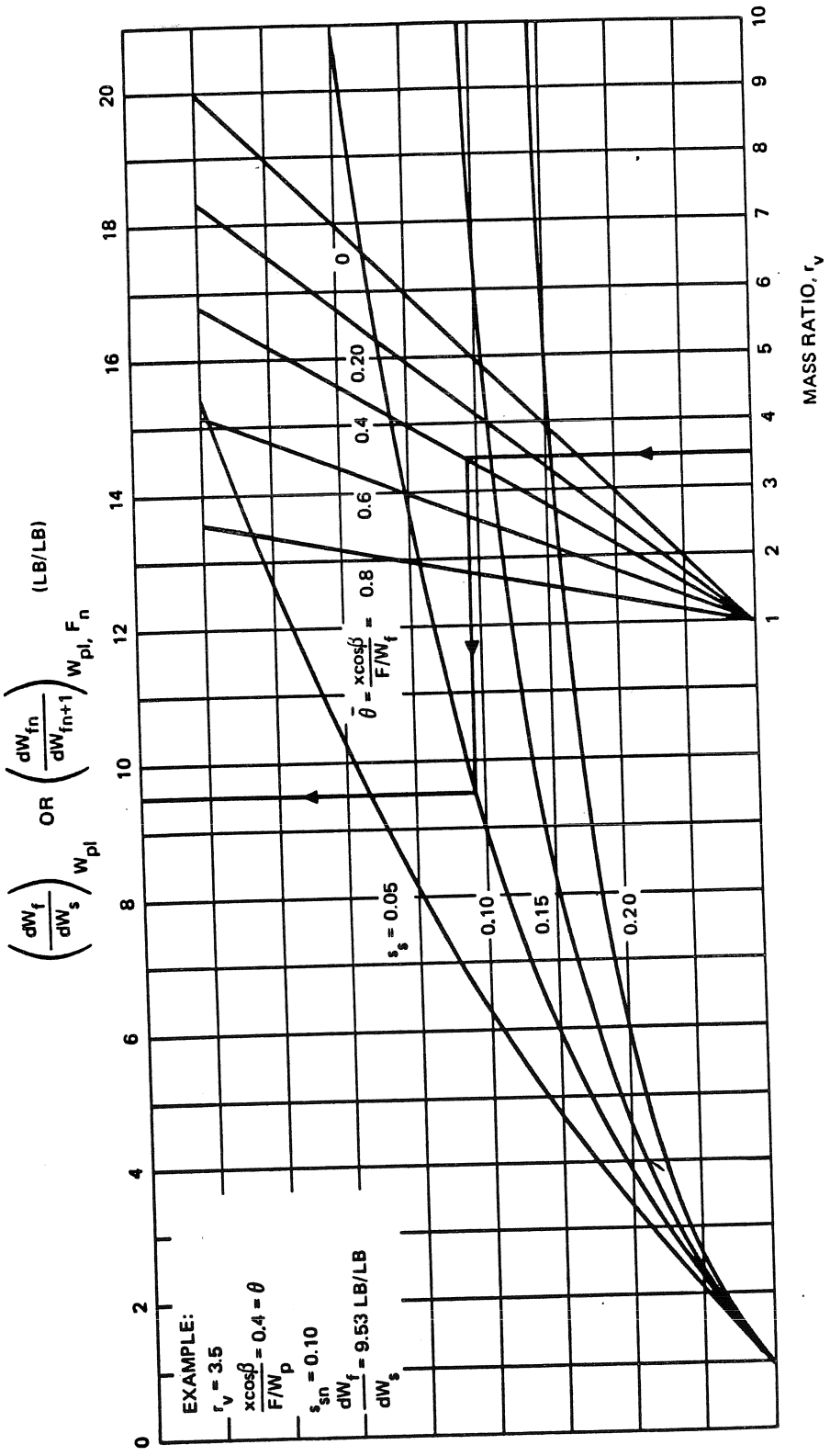

Figure 10-153. Stage Gross Weight – Inert Weight Exchange Ratio

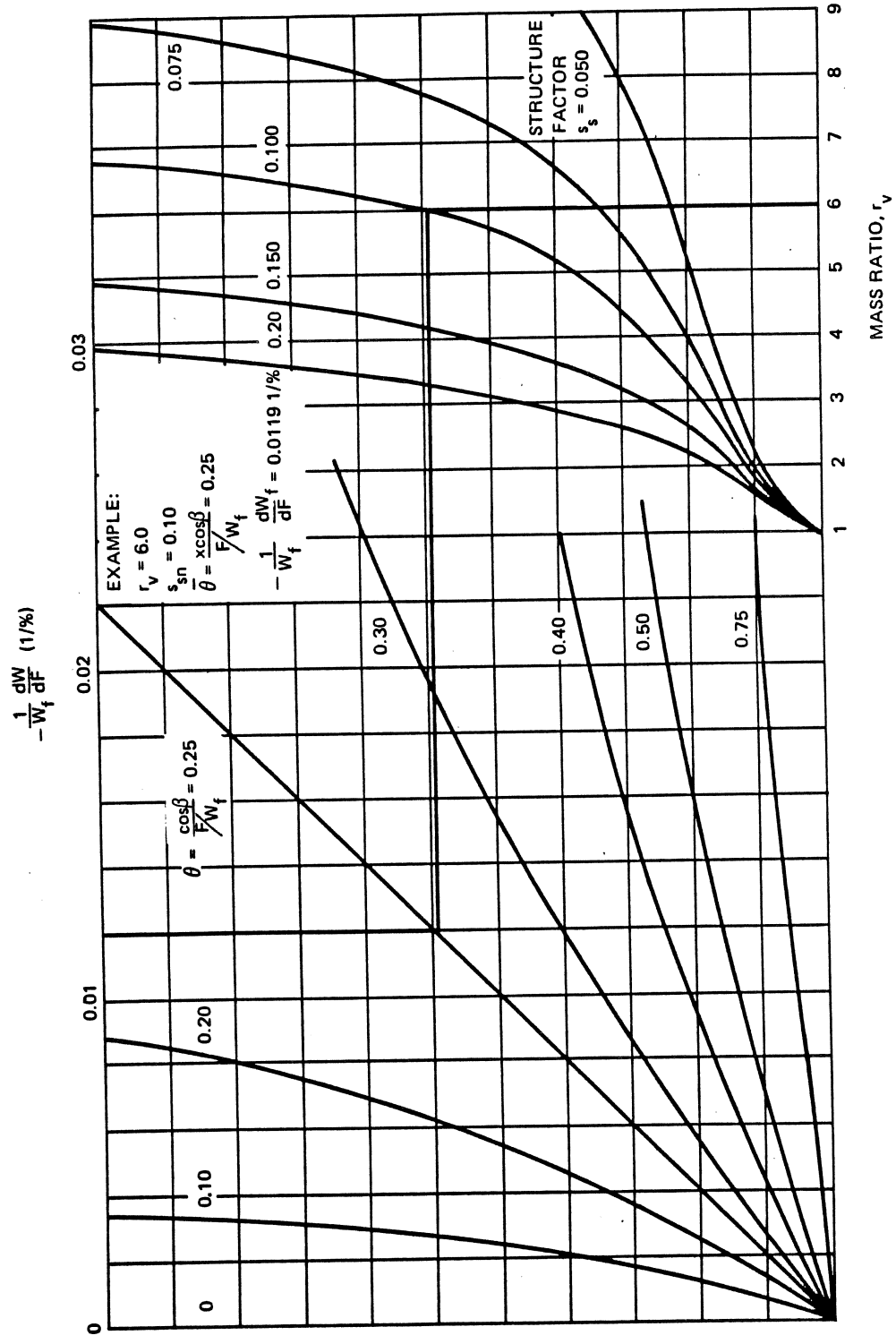

Figure 10-154. Stage Gross Weight – Thrust Exchange Ratio

Table 10-16. Exchange Ratio Analysis

Parameter	Value	Perturbation	Payload Exchange Ratio	Payload Perturbation
Trajectory				
$\overline{\beta_1}$	32 deg			
$\overline{\beta_2}$	65 deg			
$\overline{\beta_3}$	85 deg			
Propulsion				
F_1 (sea level)	4,500,000 lb			
F_1 (vacuum)	5,000,000 lb			
I_{sp_1} (vacuum)	275 sec			
F_2	800,000 lb	+50,000 lb (6.25%)	+269.2 lb/%	+1,683 lb
I_{sp_2}	400 sec			
F_3	100,000 lb			
I_{sp_3}	400 sec	+10 sec	+192.5 lb/sec	+1,925 lb
Weights				
W_{f_1}	2,500,000 lb			
W_{bo_1}	850,000 lb			
W_{p_1}	1,650,000 lb	+30,000 lb	+0.023 lb/lb	+690 lb
W_{s_1}	250,000 lb			
W_{f_2}	600,000 lb			
W_{bo_2}	245,000 lb			
W_{p_2}	355,000 lb			
W_{s_2}	30,000 lb	+5,000 lb	−0.422 lb/lb	−2,110 lb
W_{f_3}	215,000 lb			
W_{bo_3}	115,000 lb			
W_{p_3}	100,000 lb			
W_{s_3}	15,000 lb	−1,000 lb	−1.0 lb/lb	+1,000 lb
W_p1	100,000 lb			
			Net Change	+3,188 lb

EXCHANGE RATIOS, OR PARTIAL DERIVATIVES OF THE VELOCITY EQUATION, ARE USED TO DETERMINE THE EFFECT ON VELOCITY V_{bo} OF SMALL VARIATIONS IN SPECIFIC IMPULSE, I_{sp}, OR INCREMENTS OF INITIAL WEIGHT, W_f, OR MASS RATIO, r_v

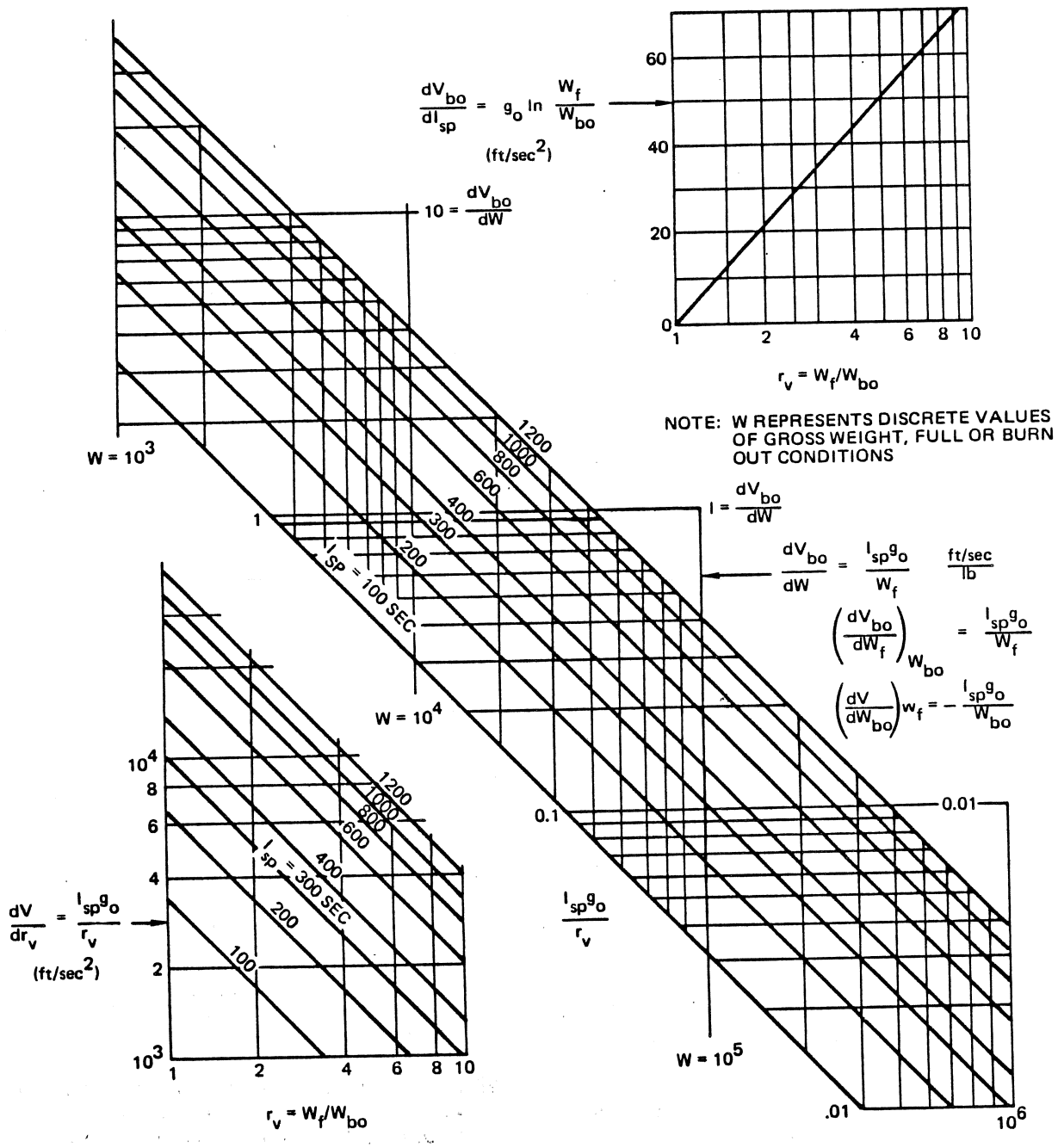

Figure 10-155. Exchange Ratios Derived From $V_{bo} = I_{sp}\, g_o \ln r_v$

10-4 through 10-6 (To be added)

10-7 NOMENCLATURE

The terminology used for missiles and space vehicle design and performance is extensive and in some cases no standardization of symbols exists. The terminology used in Section 10 is given in Table 10-17. Acronyms for certain commonly used terms are listed in Table 10-18.

10-8 REFERENCES AND BIBLIOGRAPHY

1. Seifert, H., et al, *Space Technology,* London: John Wiley & Sons (1959).

2. Whittaker, E. T., *Analytical Dynamics of Particles and Rigid Bodies,* New York Dover Publications, Fourth Edition, Chapter 1, 1944.

3. Perkins, C. D. and Hage, R. E., *Airplane Performance, Stability and Control,* New York, John Wiley & Sons, 1949.

4. Seifert, H. S., Mills, M. M. and Summerfield, M., *Physics of Rockets: Dynamics of Long Range Rockets,* Am. J. Physics, 15, 255–272 (1947).

5. Struble, R. A. and Black, H. D., *A Generalized Closed Form for Burnout Velocity,* Jet Propulsion, 26, 151, (1957).

6. Blatz, P. H., *Kinematics of a Veritical Booster,* Jet Propulsion, 24, 37, (1954).

7. West, D. D., *Boost Phase Trajectory Analysis Techniques,* Jet Propulsion, *Introduction to the Problem of Rocket Powered Aircraft Performance,* NACA TN 1401, 1947.

8. Malina, F. J. and Summerfield, N., *The Problem of Escape From the Earth by Rocket,* J. Aeronautical Science, 14, 471 (1947).

9. Sutton, G. P., *Rocket Propulsion Elements,* New York, John Wiley & Sons, 3rd Edition, Chapter 5, 1963.

10. Tsien, H. S., *A Method of Compairing Power Plants for Veritical Flight,* J. Am Rocket Society, 22, 200 (1952).

11. Feldman, A. L., *Evaluation of Competing Rocket Power Plant Components for Two Stage Long Range Vehicles,* Jet Propulsion, 23, 297, 1953.

12. Rubin, S., *General Equation for Rocket Velocity,* J. Am. Rocket Society, 29, 219, (1959).

13. White, Frederick, J., et al, *Flight Performance Handbook,* Space Technology Laboratories, Chapters 2 and 5, March 1962.

14. Edelbaum, T. N., *How Many Impluses,* Astronautics & Aeronautics, 64, November 1967.

15. Hohmann, W., *The Attainability of Heavenly Bodies,* NASA Technical Information F-44, November 1960.

16. *Design of Aerodynamically Stablized Free Rockets,* Engineering Design Handbook, U.S. Army Materiel Command, AMCP 706 – 280, July 1968.

17. *Study of Large Launch Vehicles Using Solid First Stages (U),* Technical Document Report No. SSD-TDR-62-144, December 1962, Prepared by the Boeing Company (Confidential).

18. *Proposal to Study Solid and Packaged – Storable – Liquid Propulsion Systems (U),* Douglas Report SM-45668, May 1964 (Confindential).

19. Bergquist, Bjorn, *The Optimization Problem for Rocket Vehicles Subjected to Medium and High Accelerations:* A Literature Survey, Astronautics (1959).

20. Builder, C. H., *General Solution for Optimization of Staging or Multistage Boost Vehicles,* American Rocket Society Journal, July 1959.

21. Coleman, J. J., *Optimum Stage-Weight Distribution of Multistage Rockets,* American Rocket Society Journal, February 1961.

22. Winton, W. R., *Theory, Coding, and Operation of the General Missile Sizing Program,* Douglas Report SM-48752, 1965.

23. *Air-to-Air and Air-to-Ground Missile Synthesis and Performance Program,* MDC Report, MDC-E 0160, Volume 1, May 7, 1970.

24. *The Solid Propellant Propulsion System Sizing Program,* (Computer Program H-081) Douglas Report, SM-45924, September 1964.

25. Kooy, J. M., Utenbogaart, J. W. H., *Ballistics of the Future,* Netherlands, Technical Publishing Co., Chapter 15, (1947).

26. Ivey, H. R., Bowen, E. N., Oborney, L. F., *Introduction to the Problem of Rocket-Powered Aircraft Performance,* NACA TN 1401 (1947).

27. *Table of Sine and Cosine Integrals for Arguments from 10-100,* U. S. National Bureau of Standards Applied Mathematics Series 32. U. S. Government Printing Office, Washington, 1954.

28. *Sine, Cosine and Exponential Intergrals, Vol. I – Argurments Between Zero and 2 at Intervals of 0.0001,* A. N. Lowman, Technical Director, Works Progress Adminstration (under sponsorship of the National Bureau of Standards) New York, 1940 (reprinted by Western Periodicals Co., North Hollywood, California, 1956).

29. *Sine, Cosine and Exponential Integrals, Vol. II – Arguments Between 2 and 10 at Intervals of 0.001,* A. N. Lowman, Technical Director, Works Progress New York, 1940 (reprinted by Western Periodicals Co., North Hollywood, California, 1956).

30. Saturn IB Improvement Study, SM 51896, Vol. I – Summary Report, March, 1966.

31. Thompson's, *Space Dynamics*

32. M. Vertret, *Principles of Astronatuics,* Elsevier Mongraphs.

33. R. Heitchue, *Space Age Fundamentals,* SM 47656, July 1964.

34. TRW Space Technology Laboratories, *Space Data,* 1965.

35. NASA-University Conference Report on the Science and Technology of Space Exploration, November 1–3, 1962.

36. NASA Conference on the Science and Technology of Space Exploration, November 1–3, 1962.

37. *Launch Vehicle Estimating Factors for Advanced Mission Planning,* NASA Headquarters, 1972.

38. *Aviation Week and Space Technology,* March 19, 1973.

Table 10-17. Nomenclature for Section 10

Symbol	Definitions	Defined By
A	Frontal or reference area of rocket for aerodynamic coefficients	Equation 21
A_p	Solid propellant grain exit port area	Figure 10-135
A_T	Nozzle throat area	Figure 10-135
A_Z	Launch azimuth angle, deg	Equation 103, Figure 10-17
ΔA_Z	Increment in launch azimuth angle, deg	Equation 103
a	Acceleration	Figure 10-70
a_{bo}	Maximum stage acceleration, g's	Equation 104
a_n	Structure factor curve fit coefficient	Equation 121, Figure 10-118
$a_{q_{max}}$	Acceleration at maximum dynamic pressure	Equation 105
a_x	Semi-major axis of an orbit	Equation 100
B_n	Structure factor curve fit constant	Figure 10-118
C	Ballistic coefficient	Equation 23
C'	Modified form of ballistic coefficient (W_{pl}/id^2)	Equation 24
C_1, C_2, C_3	Constants	Figures 10-137 and 10-143
C_D	Aerodynamic drag coefficient	Equation 21
$C_{D_{max}}$	Maximum drag coefficient on C_D vs. M curve (usually at M = 1)	Figure 10-8
$C_{D_{PD}}$	Drag coefficient at maximum drag force	Equation 54
c^*	Effective exhaust velocity = $g_o I_{sp}$	Equation 67
CG	Center of gravity of body	Paragraph 10-3.6.3.2
C_n	Structure factor curve fit coefficient	Equation 21
C_P	Center of pressure of body	Paragraph 10-3.6.3.2
D	Drag lbf	Equations 2 and 21
d or d_m	Missile diameter	Equation 23, Figure 10-137
e	Eccentricity of orbit or natural base for logarithms	Equations 97 and 98
E	Nozzle expansion ratio	Figure 10-134
F	Thrust, lbf	Equations 1 and 34 Figures 10-7 and 10-41

Table 10-17. Nomenclature for Section 10 (Continued)

Symbol	Definition	Defined By
F_B	Booster thrust, lbf	Paragraph 10-2.3.1.2
F_S	Sustainer thrust, lbf	Paragraph 10-2.3.1.2
F_a	Aerodynamic force, lbf	Equation 1
F_g	Gravitational force, lbf	Equation 1
g	Acceleration of gravity at rocket location, ft/sec^2; $g/g_o = \frac{(r_e)}{r_e + h}$	Equation 3, Figure 10-7
g^*	Effective gravitational constant at the average latitude of flight for a given period of flight	Equations 35 and 66
g_o	Reference gravitational constant $\cong$ 32.174 ft/sec^2 at earth's surface	Equation 3
h	Vehicle altitude at any time, feet or miles	Paragraph 10-2.1.6, Equation 28
h_a	Apogee altitude	Equation 97
h_{bo}	Burnout altitude in nonatmospheric vertical flight	Equations 35 and 56
h_m	Maximum altitude of vertical launched vehicle	Equations 36 and 37
h_o	Initial altitude at start of burning	Paragraph 10-2.1.6.1, Equation Equation 35
h_p	Perigee altitude	Equation 97
Δh_c	Vertical distance traversed during coast period	Equations 36 and 38
I_B	Total impulse of booster, lb-sec	Paragraph 10-2.3.1.2
I_S	Total impulse of sustainer, lbf-sec	Paragraph 10-2.3.1.2
I_e	Effective specific impulse, i.e., average for trajectory	Equation 139
I_{sp}	Specific impulse, lbf-sec/lbm	Equation 3
i	Drag form factor	Equation 24
i°	Inclination of the trajectory plane with respect to the equatorial phane	Figure 10-17
K	Slowdown coefficient for the coast phase	Equations 144 and 145
K_D	Empirical drag loss constant, lb/ft-sec	Equation 54, Figure 10-36
K_a	Empirical thrust-atmospheric loss constant, ft/sec	Equation 55, Figure 10-37
K_g	Empirical constant for gravity loss	Figures 10-32 through 10-34

Table 10-17. Nomenclature for Section 10 (Continued)

Symbol	Definition	Defined By
K'	Gravitational constant times the sum of the masses of two interacting bodies	Equation 100
K^*	Upper stage effective altitude constant	Equations 64 and 65
K_{gg}	Empirical constant for gravity loss correction, ft/sec	Equation 53 and Figure 10-31
K_h	Empirical constant for first stage burnout altitude, radians	Equation 56, Figure 10-38
L^*	Thrust chamber characteristic length (TCA volume divided by the nozzle throat area)	Figure 10-134
M	Mach number	Figure 10-8
M_{PD}	Mach number at maximum drag	Figure 10-35
MR	Mixture ratio, $\dot{W}_{ox}/\dot{W}_{fuel}$	Figure 10-134
m	Mass	Equation 1
$\dot{m}$	Mass flowrate	Equation 3
N	Number of propulsive stages in multistage vehicle	Equation 4
P_c	Chamber pressure	Figure 10-134
PR	Payload ratio, W_{fn}/W_{fn+1}	Equations 14 and 15
p	Instanteous pressure	Figure 10-72
p_{bo}	Atmospheric pressure at burnout	Equation 104
p_h	Atmospheric pressure at any missile altitude	Equation 29
p_o	Atmospheric pressure at start of burn	Equation 104, Figure 10-134
$p_{q_{max}}$	Atmospheric pressure at maximum q	Equation 105
p_{sl}	Atmospheric pressure at sea level	Equation 29
Q	Stage or step growth factor for a one stage vehicle	Table 10-9, Equation 18
QE	Quadrant elevation or launch angle, deg	Figures 10-91 and 10-92
q	Dynamic pressure	Equation 21, Figure 10-71
q_{bo}	Dynamic pressure at burnout	Equation 104, Figure 10-71
q_{max}	Maximum dynamic pressure	Figures 10-73 and 10-74 Equation 105
R	Range along surface of earth	Equation 41
R_c	Coast phase slant range increment	Equations 144, 146, 147

Table 10-17. Nomenclature for Section 10 (Continued)

Symbol	Definitions	Defined By
R_T	Range to target	Equation 106
ΔR_n	Increment in slant range traversed by nth stage during burning time	Equations 141 and 143
r	Thrust to weight ratio, F/W_f	Equations 39 and 40
r^*	Trajectory average radius from earth's center	Equation 64
r_c	Orbital distance from central body	Equation 100
r_e	Radius of the earth (3440 NM or 0.209029×10^8 ft)	Equations 28 and 66
r_i & r_f	Initial and final trajectory radius from earth's center	Figure 10-41
r_i	Radius of trajectory from center of earth at end of 1st stage burn	Equation 94
r_o	Earth parking orbit radius	Figure 10-56
r_v	Stage or step mass ratio for a one stage vehicle	Equation 7
S	Distance along rocket path from arbitrary reference point	Equation 2, Figure 10-7
s	Structure factor for a single stage vehicle	Equation 11
s_{sn}	Structure factor for one step (multiple stage)	Equation 12
s_s	Structure factor for a step (single stage)	Equation 11
t	Instantaneous time	
t_b	Stage burn time, (single stage)	Equation 34
t_c	Duration of coast phase	Equation 91
t_f	Flight time	Equation 106
$t_{q_{max}}$	Time of maximum dynamic pressure	Figure 10-75
t_v	Veritical rise time, sec	Figures 10-18 and 10-19
V	Instantaneous Velocity ft/sec	Equation 21
V_g or V_g'	Gravitational velocity component, or equivalent, f_{ps}	Figure 10-18
V_f	Final velocity at the end of coast	Equation 144, Figure 10-41
V_{I_N}	Ideal burnout velocity of N stage vehicle	Equation 133
V_{bo}	Burnout velocity ft/sec	Equation 42, Table 10-10
V_{bo_I}	Inertial or ideal burnout velocity, ft/sec	Equations 19, 49, and 57 Table 10-10

Table 10-17. Nomenclature for Section 10 (Continued)

Symbol	Definitions	Defined By
V_o	Initial velocity of vehicle, ft/sec	Equation 19, Table 10-10
V_{rot}	Velocity component due to earth's rotational effects (positive for an eastward launch)	Equation 57, Figure 10-69
ΔV	Velocity increment of single stage vehicle, ft/sec	Equations 42 and 136 Table 10-10
ΔV_I	Ideal or total velocity, ft/sec	Equation 19, Table 10-10
ΔV_L	Total velocity loss (gravity, drag and thrust-atmospheric)	Equations 32 and 52, Table 10-10
ΔV_{L_D}	Velocity loss due to drag of single stage vehicle Velocity loss due to drag o	Equations 25 and 54, Table 10-10
ΔV_{L_F}	Velocity loss due to thrust-atmospheric effects	Equation 29 and 55, Table 10-10
ΔV_{L_g}	Velocity loss due to gravity	Equations 28 and 53, Table 10-10
ΔV_T	$\Delta V_1 + \Delta V_2$	Figure 10-58
ΔV_1	Initial Hohmann transfer injection velocity requirement, ft/sec	Figures 10-56 and 10-58
ΔV_2	Velocity requirement to circularize orbit after Hohmann transfer, ft/sec	Figures 10-56 and 10-58
W	Discrete values of gross weight, lb	Figure 10-155
W_{s_n}	Gross weight of nth step, lbn	Equation 138
W_{bo}	burnout weight of a single stage vehicle	Table 10-9
W_f	Gross weight of a single or multistage vehicle (full weight)	Equation 4, Table 10-9
W_i	Vehicle weight at initation of calculation	Equation 68
W_p	Usable propellant for a single stage vehicle	Equation 9, Table 10-9
$W_{p\ell}$	Vehicle payload weight, total	Equation 13
W_{px}	Expendable weight of stage or step on a single stage vehicle	Equation 137
W_{sn}	Step weight of structure for the nth stage, lbm	Equation 137
W_{s_n}	Step weight of the nth stage, lbm	Equation 129
X	Velocity ratio, $\frac{\Delta V_n + \Delta V_L}{I_e g_o}$	Equation 140

Table 10-17. Nomenclature for Section 10 (Continued)

Symbol	Definitions	Defined By
x	Ratio of seal level I_{sp} to vacuum I_{sp}	Equation 29
x & y	Horizontal and vertical components of vehicle position	Figure 10-41
$\dot{x}_i$	Horizontal component of inertial velocity	Equations 61 and 83
$\dot{y}_i$	Vertical component of inertial velocity	Equations 62 and 83
α	Angle of attack	Equation 59, Figure 10-8
β	Angle of rocket velocity vector with respect to local vertical, deg or rad (compliment of angle γ)	Figure 10-7
β_{bo}	Burnout flight path angle (relative) deg or radians	Figure 10-18
β_{bo_i}	Inertial flight path angle at burnout, deg or radians	Equation 58, Figure 10-40
β_o	Initial kick angle, deg or radians	Figure 10-18
$\overline{\beta}$	Average flight path angle, deg. or radians	Equation 51
β_i	Initial inertial flight path angle	Figure 10-41
ϵ	Thrust orientation angle, deg.	Figure 10-41
ϵ_o	Thrust orientation angle, with respect to local vertical, deg	Figure 10-41
ϵ_{o_i}	Initial inertial thrust orientation angle, deg	Equation 60
$\dot{\epsilon}$	Rate of change of thrust attitude vs. time (pitch rate)	Equation 70, Figure 10-41
θ	Range angle	Figure 10-18
θ_{bo}	Range angle from launch to burnout	Figure 10-18
$\overline{\theta}$	$\frac{x \cos \overline{\beta}}{r}$	Equation 150
λ	Geocentric latitude of launch site	Equation 103, Figure 10-17
λ'	Stage mass fraction, W_p/W_f	Equation 9
λ'_{sn}	Propellant step mass fraction, $W_{p_n}/W_{f_n} - W_{f_{n+1}}$	Equation 10
λ_{se}	Effective step mass fraction (motor mass fraction)	Equation 137
μ_e	Gravitational parameter, 1.40766×10^{16} ft^3/sec^2, $\mu_e = g_o r_o^2$	Equation 99
ρ	Propellant or material density	Figure 10-134
ρ_a	Local air density	Equation 21

Table 10-17. Nomenclature for Section 10 (Continued))

Symbol	Definition	Defined By
γ	Angle of elevation between flight path direction and local horizontal, (flight path angle), degrees or radians (compliment of angle β)	Equation 108, Figure 10-7
σ	Sigma (variation of increment)	
η	Generalized initial thrust-to-weight ratio	Equation 68
ν	Defined in Equation 70	
ξ	Defined in Equation 70	
χ	Defined in Equation 72	
ζ	Defined in Equation 71	
∞	Infinity	
Σ	Summation	
d( )	Derivative	
Subscripts		
bo	Burnout conditions	
f	Final or total condition	
i	Initial conditions	
c	Coast condition	
k	kth stage	
max	Maximum	
N	Total for multistage vehicle	
n	nth stage	
sl	Sea level	
vac	Vacuum	
1	First stage or step	
2	Second stage or step	
3	Third stage or step	
I	Ideal or inertial conditions	

Table 10-17. Nomenclature for Section 10 (Continued) [1]

Symbol	Defintions	Defined By
Functions		
Im (Z)	Defined in Equations 73 through 81	
Im (ω)		
R (Z)		
R (ω)		
A,B,C,D,E,F,G,H		
Si (u), si		
Ci (u), ci		
σ		

Table 10-18. List of Acronyms

Acronym	Definition
AAMS	Air-to-Air Missile System
ACS	Attitude Control System
A.U.	Astronomical Unit (Distance from earth to the sun)
RCS	Reaction Control System
LITVC	Liquid Injection Thrust Vector Control
SITVC	Secondary Injection Thrust Vector Control
SAM	Surface to Air Missile
TASM	Tactical Air-to-Surface Missile
TCA	Thrust Chamber Assembly
TVC	Thrust Vector Control
P/L	Payload
FLEXSEAL NOZZLE	A movalbe nozzle using a rubber-compsite, flexible device for TVC
GMSP	General Missile Sizing Program
MSAP	Missile Synthesis and Analysis Program

Section 12
THERMODYNAMICS

Thermodynamics is the science which deals with energy and its transformations. This section considers the transformation of heat energy into work.

12-1 DEFINITIONS

The thermodynamics system is the region enclosing the material (working fluid) involved in the energy transformation being studied. The system is separated from the surroundings, the region outside of the system, by an imaginary or real line or envelope termed the boundary. The system is considered to be closed when no mass crosses the boundary, or to be open when there is mass exchange between the system and the surroundings. The boundary may be fixed or elastic. The solution of many thermodynamic problems dictates the limitation of the system to the working fluid or medium, while other problems are easily solved by including various pieces of equipment as well as the working fluid in the system.

A system is said to be in equilibrium when there is no tendency of the system to undergo a spontaneous change. A system may be in mechanical equilibrium, thermal equilibrium, and chemical equilibrium.

The working fluid is the system material which absorbs, rejects, or transports energy during a thermodynamic process or cycle.

A property is a function of the state (a point function) and depends only on the state, not on the method of change between two states.

Working fluids have extensive properties and intensive properties. The extensive properties, such as energy, volume, and area, depend on the extent of the system. The intensive properties, such as pressure, temperature, velocity and surface tension, are independent of the extent of the system. Changes in the intensive properties can cause a change in the fluid state.

A process occurs whenever a system changes from one state to another state. Changes in the values of the physical properties are independent of the manner in which the changes occur, and are evaluated by the end points only. The amounts of heat and work involved depend upon the process; therefore heat and work are termed path functions, indicating that their values are dependent upon the path or process.

A process is said to be reversible if, at the conclusion of the process, the system and surroundings can be restored to their initial states and no evidence remains that the process had taken place. The reversible process is an ideal process, wherein there is no decrease in available energy due to real system losses such as fluid turbulence.

When a system changes from its initial state to a final state by an irreversible process, evidence of the process remains if the system is restored to its initial state by any reversible process. All natural processes are irreversible but in many engineering problems the assumption of a reversible process yields useful approximations.

12-1.1 Stored Energy

Energy is defined as the capacity to do work and to transfer heat. Energy is a stored quantity that is available for use when needed. Forms of energy important in thermodynamic processes are potential energy, kinetic energy, flow work energy, internal energy, chemical energy, and nuclear energy.

A common basis for all energy units, based on the watt hour, was established by the International Steam Table Conference in 1929. By the use of this basis, the International British thermal unit (IT Btu) is established as equivalent to 778.16 ft-lb. This relationship is called Joule's equivalent, J, the mechanical equivalent of heat expressed by the equation

$$J = 778.16 \text{ ft-lb/IT Btu} \quad (1)$$

Potential energy is the energy possessed by a mass due to its relative elevation above an arbitrary datum. Potential energy is expressed by the relationship:

$$\text{Potential energy} = wz, \text{ ft-lb} \quad (2)$$

where:

w = Weight of body, lb

z = Elevation, ft

Kinetic energy is the energy possessed by matter due to its velocity. Kinetic energy is given as:

$$\text{Kinetic energy} = 1/2\,\frac{wv^2}{g}, \text{ ft-lb} \quad (3)$$

where:

g = Gravitational constant, 32.17 ft/sec^2

v = Velocity, ft/sec

Flow work is the energy possessed by a quantity of fluid in a flow stream because of the work done to displace the fluid. Flow work is expressed by the equation:

$$\text{Flow work} = 144\,PV, \text{ ft-lb} \quad (4)$$

where:

P = Fluid pressure, psia

V = Volume of fluid, ft^3

Internal energy, U, is the energy possessed by matter due to the activity and configuration of its molecules. The term internal energy includes all forms of energy contained within the mass of the working substance, whether or not a chemical change must occur to release the energy.

Chemical energy, the energy possessed by matter because of its atomic structure, is demonstrated by the energy that results from a chemical reaction. Chemical energy is considered part of the total internal energy of matter.

Nuclear energy is the energy that binds the particles within atomic nuclei, and is demonstrated by the energy that is released during the redistribution of the particles within the atomic nuclei. The relationship between the decrease in mass during a nuclear reaction and the energy released, as given by Einstein's equivalence relationship, is:

$$E = mc^2 \quad (5)$$

where:

E = Nuclear energy, ft-lb

m = Mass decrease, lb-sec^2/ft

c = Velocity of light 9.835 x 10^8 ft/sec

This relationship is important in thermodynamics only in the case of nuclear reactions.

12-1.2 Energy in Transition

Work is energy transferred, without a transfer of mass, across the boundary of a system because of an intensive property difference, other than temperature, that exists between the system and the surroundings. Work is performed when energy is transferred (without mass transfer) across a system boundary because of a gradient of an intensive property (other than temperature) between the system and its surroundings. This definition is expressed by the relationship:

$$W = Fs, \text{ ft-lb} \quad (6)$$

where:

F = Force, lb

s = Displacement, ft

Heat is energy transferred, without a transfer of mass, across the boundary of a system because of a temperature difference between the system and the surroundings. The quantity of heat transferred, Q, is expressed in terms of its change in temperature as:

$$Q = \int_{T_1}^{T_2} wc\,dT \quad (7)$$

where:

w = Weight of material, lb

c = Specific heat of material, Btu/lb-°R

dT = Change in temperature of body, °R

Equation 7 is the specific heat equation for transferred heat, and is based upon the assumption of a constant specific heat. In reality, specific heat is a variable that depends upon the process in which heat is transferred, and the temperature range of the process.

The three methods through which heat transfer occurs are conduction, radiation, and convection. These three modes of heat transfer are defined here; for further detail, see Section 14, Heat Transfer.

Heat transfer by conduction is energy transfer by tangible contact. Conduction occurs due to the transfer of internal molecular kinetic energy of the hotter body to the colder body. The rate of conduction heat transfer is given by Fourier's law.

$$\frac{dQ}{dt} = kA\left(\frac{dT}{dx}\right) \text{ Btu/hr} \quad (8)$$

where:

$\frac{dQ}{dt}$ = Heat transfer rate, Btu/hr

k = Thermal conductivity, Btu/hr-ft-°R

A = Surface area, ft^2

(dT/dx) = Temperature gradient, °R/ft

Radiation is energy transmission through space from a hot body to a cold body by means of electromagnetic waves. All bodies radiate heat; thus, a transfer of heat by radiation occurs because a hot body emits more electromagnetic waves than it receives. A perfect radiator, or black body, emits radiant energy from its surface at a rate given by the Stefan-Boltzmann equation:

$$\frac{dQ}{dt} = 0.1714 \times 10^{-8} A T^4, \text{ Btu/hr} \quad (9)$$

where:

A = Radiation area, ft^2

T = Absolute temperature, °R

Convection is a transfer of heat from a hot body to a cold body due to the mass movement of the working fluid from a locality where it receives heat, to a locality where it gives up heat. Since convection requires mass transport, it can occur only in fluids. The relationship for convective heat transfer is:

$$\frac{dQ}{dt} = h_c A \Delta T, \text{ Btu/hr} \quad (10)$$

where:

h_c = Average unit thermal convective conductance (often called the surface coefficient of heat transfer, or the convective heat transfer coefficient), Btu/hr-ft^2-°R

A = Heat transfer area, ft^2

ΔT = Temperature difference between surface and fluid, °R

12-1.3 Enthalpy

The enthalpy of a substance is defined as the sum of its internal energy and the product of its pressure and volume, or:

$$H = U + \frac{144 PV}{J}, \text{ Btu} \quad (11)$$

12-1.4 Entropy

Entropy is a thermodynamic property defined by the expression:

$$dS = \frac{dQ}{T}\Big]_{rev} \quad (12)$$

where:

dS = Change in entropy

rev = Reversible process

Entropy, which is a measure of the unavailability of energy, increases whenever heat is transferred from a hotter body to a colder body by a real (irreversible) process. The change in entropy for an irreversible process can be evaluated by following one or more reversible processes to the same end states.

12-1.5 Specific Heat

The heat capacity of a material is the quantity of heat absorbed by a unit quantity of the material during a unit temperature change. The ratio of the heat capacity of the material to the heat capacity of water at a standard state is termed the specific heat of the material. Since the heat transfer to the material per degree is numerically equal to its heat capacity, no distinction is made between heat capacity and specific heat in engineering usage. The quantity of heat required to cause a 1°R change in the temperature of a material depends upon the process; therefore the specific heat notation must specify the type of process such as constant-pressure or constant-volume specific heat.

12-2 THERMODYNAMIC LAWS

The science of thermodynamics is constrained to comply with several relationships that are so generally accepted that they are called laws.

A. Zeroth Law – Two bodies each in thermal equilibrium with a third body are in thermal equilibrium with each other, and it follows that all three bodies are at the same temperature. This fundamental concept is the foundation of temperature measurement.

B. First Law – When a system undergoes a cyclic process, the sum of the heat quantities and work quantities are equivalent for any given cycle. Stated mathematically the first law is:

$$\oint JdQ = \oint dW \quad (13)$$

Devices which violate this principle are called perpetual motion machines of the first kind.

C. Second Law – This second law may be stated in several ways, two of which are given here. It is impossible to construct a self-acting machine which, operating in a cycle, will produce no effect other than the absorption of heat from one reservoir and the performance of an equivalent amount of work. This is the Kelvin-Planck statement. Another statement is that it is impossible to construct a device which, operating in a cycle, will produce no effect other than the transfer of heat from a body at low temperature to a reservoir at a higher temperature. Devices which violate this law are called perpetual motion machines of the second kind.

D. Conservation of Mass – The principle of conservation of mass states that mass can be neither created nor destroyed; however, mass and energy are mutually convertible. For the thermodynamic system, mass is neither added to nor subtracted from the control volume, and so the weight flowrate of the working fluid into the control volume is equal to the weight flowrate out. This relationship is expressed by the continuity equation:

$$\dot{w} = \frac{Av\rho}{144}, \text{ lb/sec} \qquad (14)$$

where:

A = Flow area, in^2

v = Velocity of flow, ft/sec

ρ = Fluid density, lb/ft^3

12-2.1 General Energy Equation

The first law of thermodynamics is the Law of Conservation of Energy, which states that energy can be neither created nor destroyed. Based on this law, it is possible to express the energy balance for a thermodynamic device in the General Energy Equation.

The General Energy Equation for an ideal steady-flow process is:

$$wz_1 + \frac{1}{2}\frac{w}{g}v_1^2 + JU_1 + 144\,P_1V_1 + JQ =$$

$$wz_2 + \frac{1}{2}\frac{w}{g}v_2^2 + JU_2 + 144\,P_2V_2 + W \qquad (15)$$

where:

wz = Potential energy, ft-lb

$\frac{1}{2}\frac{w}{g}v^2$ = Kinetic energy, ft-lb

J = Joule's equivalent, 778.16 ft-lb/Btu

U = Internal energy, Btu

$144\,PV$ = Flow work energy, ft-lb

Q = Net heat input, Btu

W = Net work output, ft-lb

Other energy equations that are applicable to particular devices and processes can be derived from the General Energy Equation.

An ideal thermodynamic process is assumed to be quasi-static. In a quasi-static process, the thermodynamic system is at all times infinitesimally near a state of thermodynamic equilibrium, so that all the states through which the system passes can be described by means of thermodynamic coordinates referring to the system as a whole. Thermodynamic equilibrium requires that all parts of the control volume are at a constant temperature, so that heat transfer within the system occurs at a steady, unvarying rate.

It is conventional in expressing the general energy equation to consider transferred heat as an input quantity, and work as an output quantity. These conventions may be expressed by the auxiliary equations:

$$Q = Q_1 - Q_2, \qquad (16),$$

or

$$Q = Q_{added} - Q_{rejected}$$

and

$$W = W_2 - W_1, \qquad (17)$$

or

$$W = W_{out} - W_{in}$$

As a consequence of the sign conventions adopted, input values of transferred heat are positive, and output values are negative. Furthermore, output values of work are positive in sign, and input values are negative.

Another useful form of the general energy equation for steady flow is obtained by dividing equation 15 by the weight of the working fluid.

$$z_1 + \frac{v_1^2}{2g} + \frac{JU_1}{w} + \frac{144P_1}{\rho_1} + \frac{JQ}{w} =$$

$$z_2 + \frac{v_2^2}{2g} + \frac{JU_2}{w} + \frac{144P_2}{\rho_2} + \frac{W}{w} \qquad (18)$$

12-2.2 Simple Energy Equation

Many processes in thermodynamics occur without flow of the working fluid, such as the compression process in a reciprocating air compressor, or the expansion process in the cylinder of an internal combustion engine. If there is no flow, the kinetic energy and the flow work are zero, and the change in potential energy is negligible. Dropping these terms from equation 18 and rearranging terms, yields the simple energy equation for a non-flow process

$$Q = \Delta U + W/J \qquad (19)$$

where:

$\Delta U = U_2 - U_1$ = Change in internal energy, Btu

12-3 THERMODYNAMIC PROPERTIES

For a pure substance, there are six important thermodynamic properties:

Specific volume, v, ft^3/lb
Pressure, P, psia
Temperature, T, °R
Internal energy, U, ft-lb/lb
Enthalpy, h, Btu/lb
Entropy, S, Btu/lb-°R

It has been demonstrated experimentally that, except in the singular cases of phase equilibriums, any two of these properties uniquely determine the other four properties. When a phase equilibrium exists, the distribution of the total mass between phases must also be known.

The interrelation of these properties of pure substances is illustrated by the pressure-specific volume-temperature (P-v-T) surface for a substance that contracts on freezing, shown in Figure 12-1. In this diagram, all possible equilibrium states of the substance are represented by points on the surface. All points along a quasi-static process lie on the P-v-T surface (for example, constant temperature path abcdef), because a quasi-static process always passes through equilibrium states. The P-T and P-v planes of this surface are also shown in the illustration.

12-3.1 Pressure-Temperature Diagram

The P-T plane, commonly called the phase diagram, is subdivided into five distinct single-phase regions. The boundary lines between the phases are the loci of points at which two phases can coexist. Thus, OA is the sublimation line, and it represents the equilibrium between the solid and vapor phases. The melting or freezing line, OB, is the locus of equilibrium between the liquid and solid phases. Along the boiling-condensation line, OC, the liquid and vapor phases are in equilibrium. A vapor is defined as a fluid that can be liquified by compression alone. At temperatures above the critical isotherm, DCE, neither the liquid or vapor phase can exist. When vapor is superheated to temperatures above the critical isotherm, DCE, it enters the gas phase. At pressures above the critical isobar, CF, and above the critical isotherm, there exists a region in which the liquid and gas phases are indistinguishable. A substance in this region is called a supercritical fluid.

No upper limit has yet been found for the melting-freezing curve, OB. With a number of substances, pressures have been raised high enough so that the melting temperature exceeds the critical temperature, and the solid-liquid equilibrium line becomes a solid-gas equilibrium line. At the triple point, O, all three phases, solid, liquid, and gas, exist together.

12-3.2 Pressure-Specific Volume Diagram

On the P-v plane, the phase equilibrium loci are seen in Figure 12-1 as areas rather than lines.

The dome-shaped liquid-vapor region is of special interest in engineering problems. This region is bounded on the bottom by the triple line, on the left by the saturated-liquid line, O'C, (bubble-point locus) and on the right by the saturated-vapor line, CO (dew-point locus). Within this domed region, the material will consist of a mixture of liquid and vapor, or a wet vapor. To the left of the dome is the compressed liquid region, and to the right is the vapor region.

The quality, x, of a wet vapor is defined as the fraction, by weight, of the mixture which is vapor. The specific volume of a wet vapor mixture may be expressed by the relationship:

$$v_x = x \cdot v_g + (1-x)\, v_f$$
$$= v_f + x \cdot v_{fg} \qquad (20)$$

where:

v_x = Specific volume of wet vapor mixture of quality x, ft^3/lb

v_g = Specific volume of saturated vapor, ft^3/lb

v_f = Specific volume of saturated liquid, ft^3/lb

v_{fg} = Increase in specific volume from saturated liquid to saturated vapor, ft^3/lb

$v_{fg} = v_g - v_f$

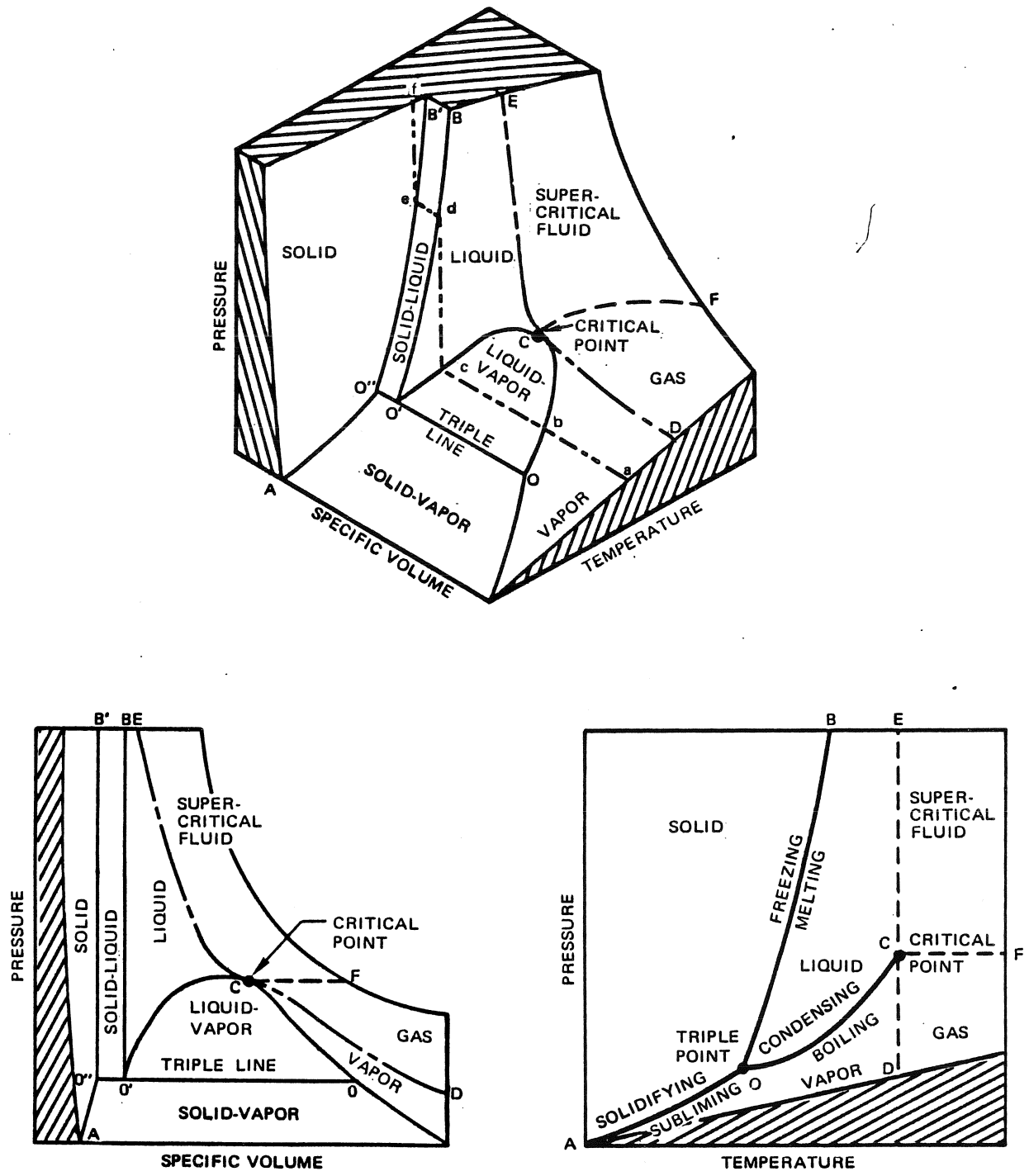

Figure 12-1. Pressure/Specific-Volume/Temperature Surface for a Material That Contracts on Freezing

The triple line has the same significance as the triple point in the P–T diagram. Along this locus the three phases, solid, liquid, and vapor, are in equilibrium. The solid-vapor equilibrium region is below the triple line.

The solid-liquid equilibrium region, bounded by O'O''B'B, is also shown in the P-v plane, to the left of the compressed liquid region. This region appears as the freezing-melting line, OB, on the phase diagram (P-T).

The critical isotherm DCE, and the critical isobar CF are shown on the P-v diagram, the P-T diagram and on the P-v-T surface. The critical isotherm is seen to have a point of inflection at the critical point.

In a material that contracts on freezing, the solidification temperature increases as the pressure increases. For such a material, the melting-freezing line, OB, has a positive slope on the P-T diagram. For a substance such as water, which expands on freezing, the pressure/specific volume/temperature is shown in Figure 12-2. For this substance, the freezing temperature decreases as pressure increases, and the melting-freezing line, OB, has a negative slope. Thus, as the vapor pressure is increased along the constant-temperature line abcdef, a fluid that expands on freezing first becomes solid and then liquid. For a fluid that contracts on freezing, Figure 12-1, the corresponding constant-temperature line indicates that as the pressure on the vapor is increased, it first becomes liquid and then solid.

12-3.3 Temperature-Entropy Diagram

Figure 12-3 shows a typical temperature-entropy (T-S) diagram. The particular advantage of the T-S diagram is that a reversible adiabatic process, which is a constant entropy process, can be traced as a straight line on this graph. Furthermore, the area under the curve for a reversible process represents the heat transferred, just as the area under the curve for a reversible process on a P-v diagram represents the work.

12-4 PERFECT GAS RELATIONSHIPS

According to the kinetic theory of gases, a perfect gas is one in which the molecules exhibit no mutual attraction and, therefore, do not affect the internal energy of the gas. Thus, the internal energy of a perfect gas is a function of temperature alone. At low pressures and high temperatures, most real gases closely approximate an ideal gas because their molecules are widely spaced and have very small mutual attraction.

The equation which relates the pressure, temperature, and volume of a substance is called the characteristic equation, or the equation of state. Each pure substance has its own equation of state, but the relationship may be so complex that it cannot be expressed in terms of simple mathematical functions. However, in many engineering situations, the working fluid is a gas with properties that may be closely approximated by the equation of state of an ideal, or perfect, gas:

$$144\,Pv = RT \tag{21}$$

where:

P = Pressure, psia

v = Specific volume, ft^3/lb

R = Particular gas constant, ft-lb/lb-°R

T = Temperature, °R

also

$$R = \mathcal{R}/M \tag{22}$$

where:

$\mathcal{R}$ = Universal gas constant, 1544 ft-lb/mole-°R

M = Molecular weight, lb/mole

An alternate form of the equation of state of an ideal gas that is encountered is:

$$144\,Pv = N\mathcal{R}T \tag{23}$$

where:

N = Number of moles of working substance, moles

N = w/M

w = Weight, lb

12-4.1 Process Equations for Perfect Gas

When a gas undergoes a process, it is changed from one equilibrium condition to another. For a fixed quantity (i.e., a nonflow process) of a perfect gas, the properties of the gas at the initial and final equilibriums can be related to an equation having the general form:

$$P_1 v_1^{\,n} = P_2 v_2^{\,n} \tag{24}$$

where:

n = Process exponent

For a reversible nonflow process, all points in the process will lie on the P-v-T equllibrium surface, and the general path equation for a perfect gas can be expressed as:

$$Pv^n = \text{Constant} \tag{25}$$

with the process exponent defined in Table 12-1.

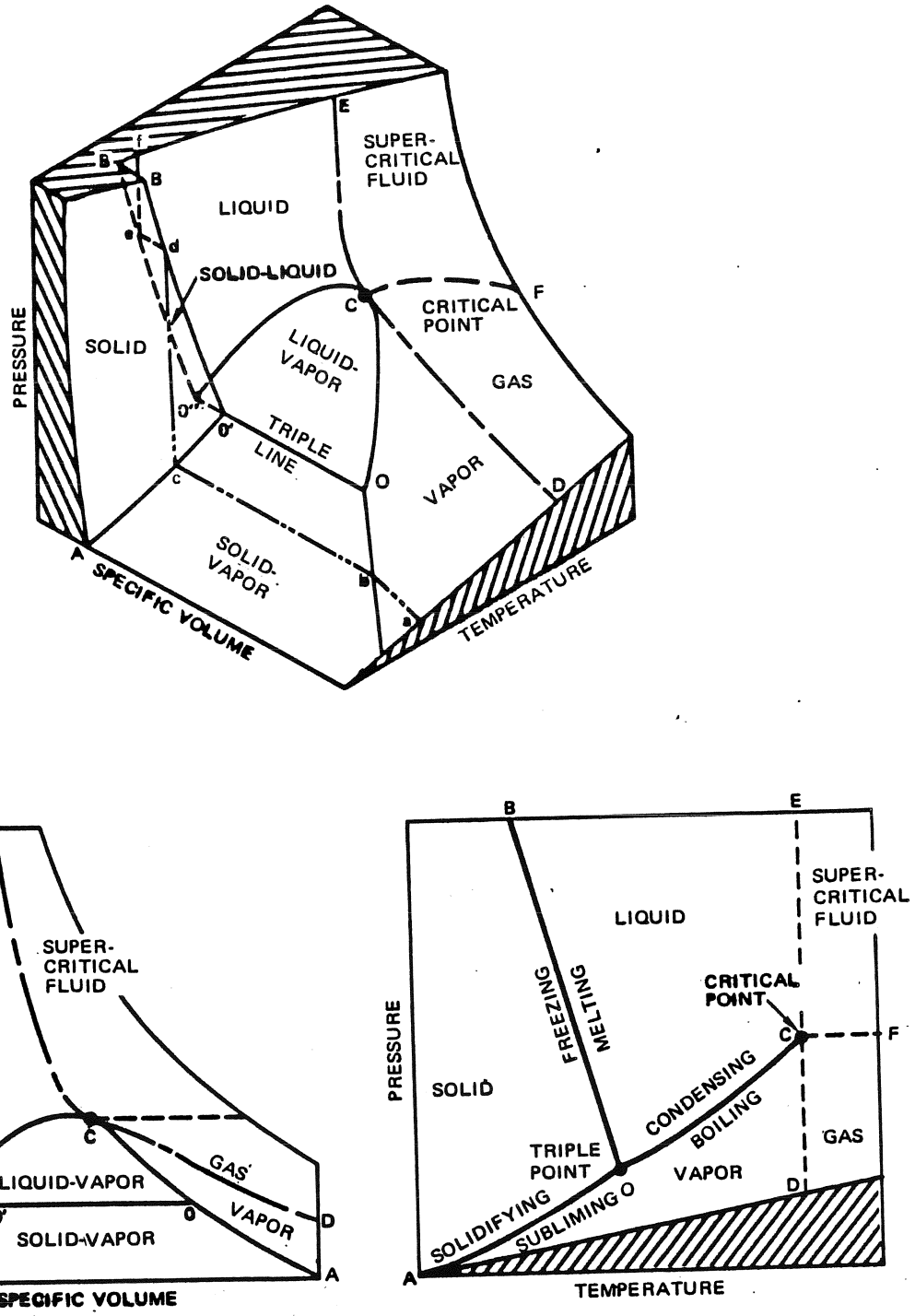

Figure 12-2. Pressure/Specific-Volume/Temperature for a Material That Expands on Freezing

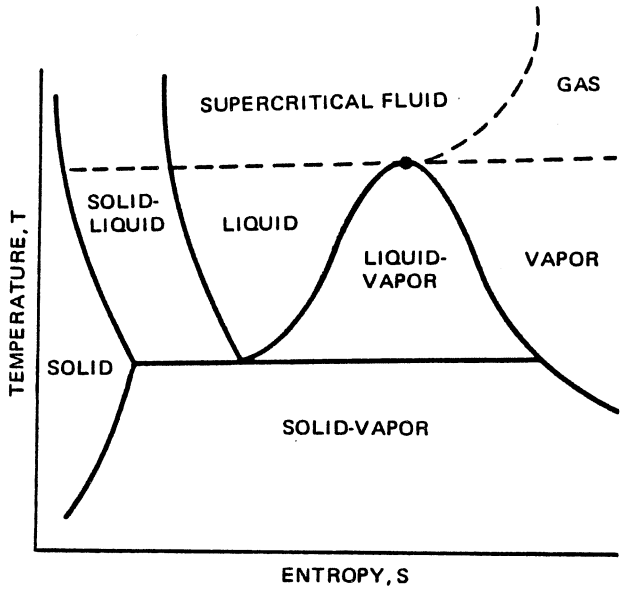

Figure 12-3. Temperature-Entropy Diagram

Table 12-1. Process Exponents for a Perfect Gas

Process Name	Process Exponent (n)
Polytropic	Any constant
Constant Pressure	0
Constant Temperature (Isothermal)	1
Constant Entropy (Isentropic)	γ
Constant Volume	∞

A process that follows equation 25 is called a polytropic process unless some property remains constant during the process, as indicated in the table. The relationship between these process paths on the pressure-volume plane is shown graphically in Figure 12-4. In this illustration, expansions or compressions of perfect gases by several processes are plotted as taking place through some common point.

Equation 25 does not trace every possible process between two states of a perfect gas, for this would require the exponent n to be a variable that changed in value during the process. However, it does provide a close approximation for many engineering processes.

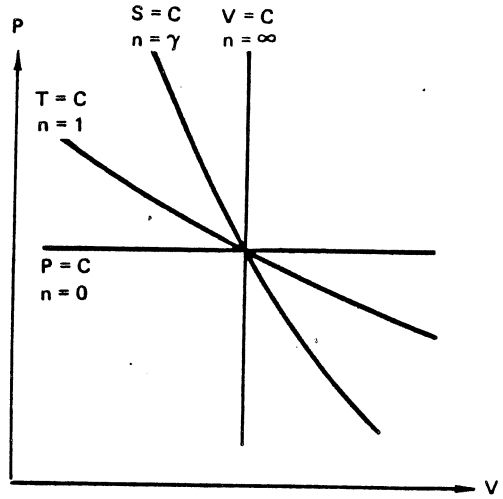

Figure 12-4. Perfect Gas Process Paths on the Pressure-Volume Diagram

Relationships between temperature and pressure, and temperature and volume for a polytropic process can be developed by substituting the equation of state for a perfect gas into equation 24, as:

$$\frac{T_2}{T_1} = \left(\frac{P_2}{P_1}\right)^{\frac{n-1}{n}} \tag{26}$$

$$\frac{T_2}{T_1} = \left(\frac{v_1}{v_2}\right)^{n-1} \tag{27}$$

with the exponent, n, defined by Table 12-1.

12-4.2 Work for Non-Flow Process

The total work done by the working fluid (gas or vapor) during a non-flow reversible process (no turbulence) is given by the equation:

$$W = 144 \int_1^2 PdV, \quad \text{ft-lb} \tag{28}$$

An example of a typical non-flow process with work output is illustrated in Figure 12-5. Figure 12-5a shows a piston in a cylinder containing a gaseous working fluid. If the gas in the cylinder is allowed to expand, moving the piston from (1) to (2), the volume of the gas increases, and the pressure decreases. This thermodynamic process is reversible if the piston moves without friction and the gas expands without turbulence. The total (and net) work delivered by a reversible thermodynamic process is equal to the area under the pressure-volume curve 1-2 in Figure 12-5b.

The equivalent irreversible thermodynamic process is represented by the broken-line path 1-2'. The net or useful work is equal to the total work minus the friction and turbulence losses. The area under the broken line does not represent the total work because, in this case, the path shape is indeterminate.

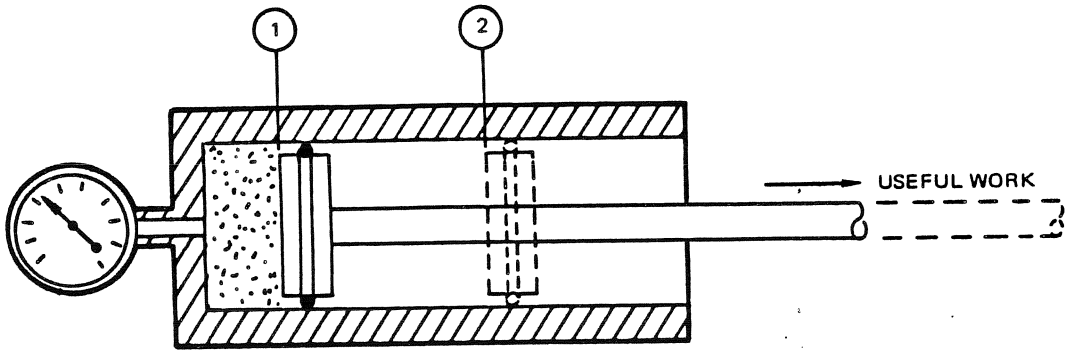

a. SCHEMATIC DIAGRAM OF EXPANSION PROCESS

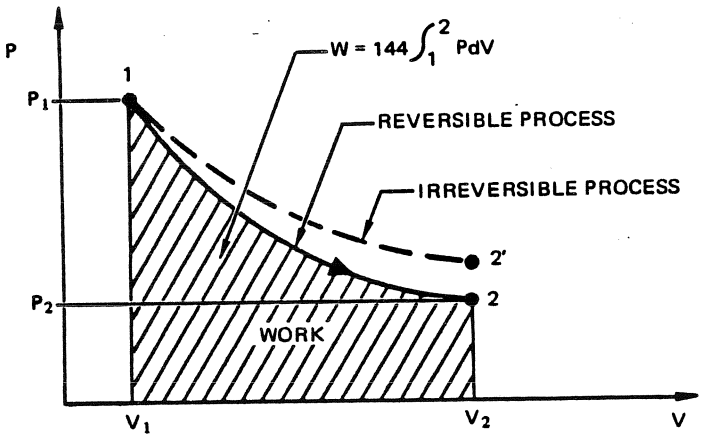

b. PRESSURE-VOLUME DIAGRAM OF AN EXPANSION PROCESS

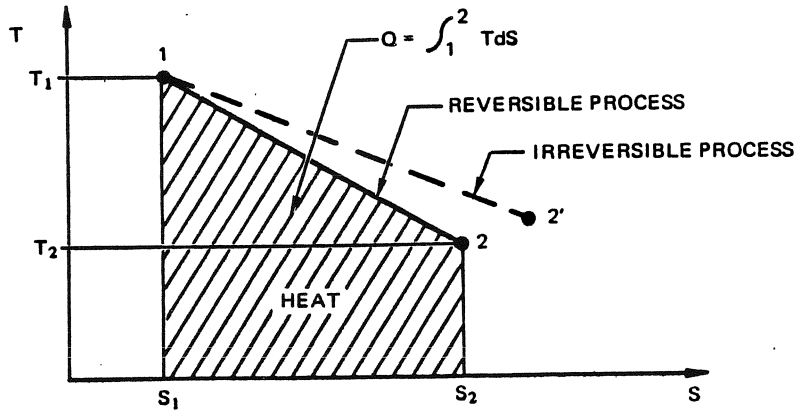

c. TEMPERATURE-ENTROPY DIAGRAM OF AN EXPANSION PROCESS

Figure 12-5. Non-Flow Process With Work Output

To perform the integration indicated in equation 28, it is necessary to establish a relationship between pressure and volume. This P-V relationship depends upon the process by which the work was generated, so that the quantity of work performed depends upon the process, and work is said to be a path function.

Similarly, Figure 12-5c shows the temperature-entropy diagram for any working fluid during an expansion process in which heat is transferred. Path 1-2 represents the reversible process and the area under the curve represents the heat rejected. Path 1-2' illustrates an irreversible expansion process. Its entropy is greater at the end state, and the area under the curve does not represent the heat transferred.

If the gas in the cylinder is assumed to be a perfect gas, the process equation 25 can be used to relate pressure and volume. Thus, in a polytropic process, pressure as a function of volume is given by:

$$P = cV^{-n}$$

and, the expression for work in a reversible polytropic process becomes:

$$W = 144\frac{P_2V_2 - P_1V_1}{1-n}, \text{ ft-lb} \quad (29)$$

12-4.3 Specific Heat, Internal Energy, and Enthalpy Relationships

The specific heat, or heat capacity, of a mass of working fluid, is the amount of heat that must be transferred to the fluid to increase its temperature one degree per unit weight. This may be expressed as:

$$C \equiv \frac{1}{w}\frac{\partial Q}{\partial T} = \frac{\partial q}{\partial T}, \text{ Btu/lb-°R} \quad (30)$$

The quantity of heat transferred to the working fluid depends upon the process by which the transfer is accomplished. That is, transferred heat is a path function. Since there are an infinite number of possible paths between two values of transferred heat, there are an infinite number of specific heats for a given working fluid. However, two particular values of specific heat are defined which are of great importance in thermodynamics. These are the specific heat at constant volume, c_v, and the specific heat at constant pressure, c_p, given by the relationships:

$$c_v \equiv \left.\frac{\partial q}{\partial T}\right)_v \quad (31)$$

and,

$$c_p \equiv \left.\frac{\partial q}{\partial T}\right)_p \quad (32)$$

An expression for the specific heat at constant volume is developed by taking the derivative of the simple energy equation 19, with respect to temperature, giving:

$$c_v = \left.\frac{\partial u}{\partial T}\right)_v \quad (33)$$

A relationship for the specific heat at constant pressure may also be developed from the definition of enthalpy:

$$c_p = \left.\frac{\partial h}{\partial T}\right)_p \quad (34)$$

The ratio of the specific heat at constant pressure to the specific heat at constant volume is used so often in thermodynamics that it is given a special symbol, γ. Thus, by definition:

$$\gamma \equiv c_p/c_v \quad (35)$$

If a perfect gas is assumed, the useful relationship between the specific heats at constant volume and pressure can be developed:

$$c_p = c_v + \frac{R}{J} \quad (36)$$

The absolute amount of internal energy in a quantity of working fluid cannot be determined, but if the fluid is a perfect gas, the change in internal energy can be determined. For a perfect gas, the change of internal energy depends only upon the temperature change of the fluid, and the increase in internal energy for any process is given as:

$$dU = w\,c_v\,dT, \text{ Btu} \quad (37)$$

where:

w = Weight of fluid, lb

c_v = Specific heat at constant volume, Btu/lb-°F

dT = Temperature change of working fluid, °F

Since the absolute quantity of internal energy cannot be measured, it is not possible to measure the absolute enthalpy of a substance. However, a relationship may be written for the change of enthalpy of a perfect gas as:

$$dH = w\,c_p\,dT \quad (38)$$

The specific heat for a polytropic process of a perfect gas may be developed by a procedure similar to those used for c_v and c_p. The polytropic specific heat may be defined as:

$$c_n \equiv \left.\frac{\partial q}{\partial T}\right)_n \quad (39)$$

Making use of the polytropic process equation and the specific heat equation for a perfect gas gives:

$$c_n = c_v\left(\frac{\gamma-n}{1-n}\right) \quad (40)$$

Figure 12-6 shows values of specific heats and specific heat ratio, as a function of temperature for several gases at one atmosphere. Additional fluid property data will be presented in Manual PD-1, Propellants.

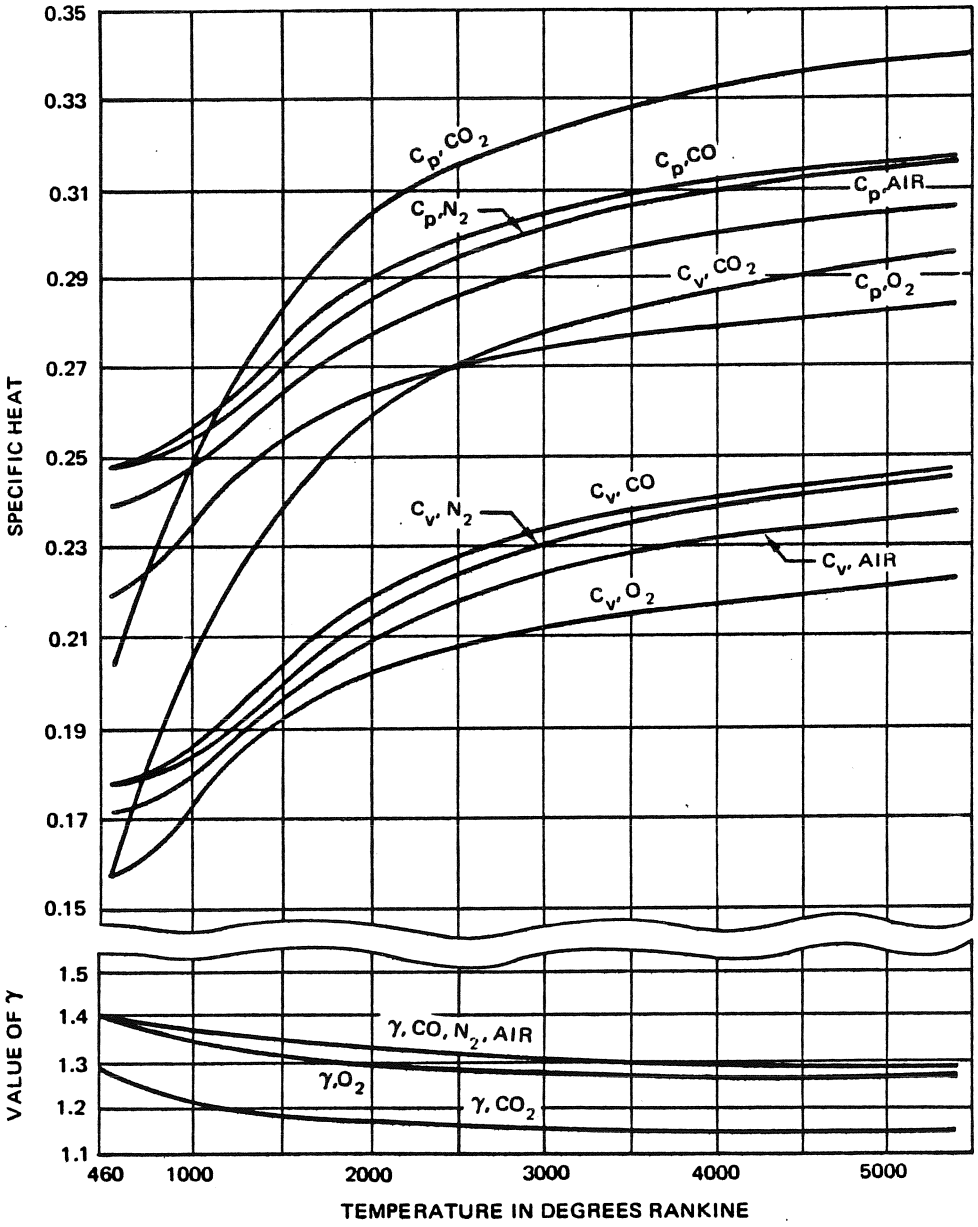

Figure 12-6. Values of Specific Heats and Gammas for Common Gases

In accordance with the kinetic theory, ideal gases in which vibration within the molecules is absent would have values of:

$c_v = (3/2)R/J$, $c_p = (5/2)R/J$, and
$\gamma = 5/3 = 1.667$ for monatomic gases;

$c_v = (5/2)R/J$, $c_p = (7/2)R/J$, and
$\gamma = 7/5 = 1.400$ for diatomic gases;

$c_v = 3R/J$, $c_p = 4R/J$, and
$\gamma = 4/3 = 1.333$ for polyatomic gases.

For the more nearly perfect gases, these values are in good agreement with those obtained from experimental data.

12-4.4 Entropy Relationships

Entropy is a thermodynamic property, and therefore it is a function of other thermodynamic properties. A functional relationship may be developed from the simple energy equation for a reversible process:

$$TdS = dU + \frac{144}{J} PdV \qquad (41)$$

Equation 41 is referred to as the first TdS equation.

The definition of enthalpy yields the second TdS equation:

$$TdS = dH - \frac{144}{J} \cdot VdP \qquad (42)$$

From the first TdS equation and the definition of c_v, the differential expression for entropy is given as:

$$dS\Big|_{v=c} = wc_v \cdot \frac{dT}{T} \qquad (43)$$

Also, combining the second TdS equation and the definition of c_p yields:

$$dS\Big|_{p=c} = wc_p \frac{dT}{T} \qquad (44)$$

Table 12-2 lists the expressions for entropy for several perfect gas processes, based on the foregoing equations. The relationship between these process paths on the temperature-entropy plane is shown graphically in Figure 12-7. In this illustration, expansions or compressions of ideal gases by several processes are plotted as taking place through some common point.

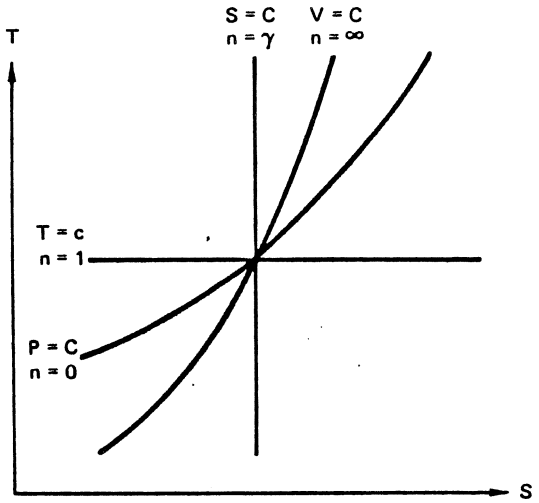

Figure 12-7. Ideal Gas Process Paths on the Temperature-Entropy Diagram

12-5 REAL GAS RELATIONSHIPS

Properties of real gases deviate appreciably from the values given by the perfect gas laws. For this reason, many different equations of state have been developed with varying degrees of specialization and complexity. One of the earliest attempts to provide a general model of real gas properties is the Van der Waals equation. In this equation terms have been added to the equation of state to account for the fact that molecules of real gases occupy space, and they exert an attractive force on each other, giving the relationship:

$$P = \frac{\mathcal{R}}{144} \cdot \frac{T}{\hat{v}-b} - \frac{a}{\hat{v}^2} \qquad (45)$$

where:

P = Pressure, psia

$\mathcal{R}$ = Universal gas constant, 1545.33 ft-lb/mol-°R

$\hat{v}$ = Specific volume, $ft^3/mol = v/M$

v = Specific volume, ft^3/lb

M = Molecular weight, lb/mol

a = Van der Waals constant, $psia-(ft^3/mol)^2$

b = Van der Waals constant, ft^3/mol

T = Temperature, °R

Values of the two constants, a and b, are given in Table 12-3 for several common gases. It is possible to derive theoretical expressions for these constants by differentiating the Van der Waals equation repeatedly at the critical point, giving:

$$a = 48.585 \frac{T_c^2}{P_c} \qquad (46)$$

and,

$$b = 1.3414 \frac{T_c}{P_c} \qquad (47)$$

Table 12-2. Equations for Reversible Nonflow Ideal Gas Processes, Assuming a Constant Specific Heat

Process	Isobaric p = constant	Isovolumic V = constant	Isothermal T = constant	Isentropic S = constant	Polytropic pV^n = constant
Process Exponent, n	0	∞	1	γ	Any constant
p V T	$\frac{V_1}{V_2} = \frac{T_1}{T_2}$ $p_1 = p_2$	$\frac{p_1}{p_2} = \frac{T_1}{T_2}$ $V_1 = V_2$	$p_1V_1 = p_2V_2$ $T_1 = T_2$	$p_1V_1^{\gamma} = p_2V_2^{\gamma}$ $\frac{T_2}{T_1} = \left(\frac{p_2}{p_1}\right)^{\frac{\gamma-1}{\gamma}}$ $\frac{T_2}{T_1} = \left(\frac{V_1}{V_2}\right)^{\gamma-1}$	$p_1V_1^n = p_2V_2^n$ $\frac{T_2}{T_1} = \left(\frac{p_2}{p_1}\right)^{\frac{n-1}{n}}$ $\frac{T_2}{T_1} = \left(\frac{V_1}{V_2}\right)^{n-1}$
Quantity of work W_2	$144\, p(V_2 - V_1)$	0	$144\, p_1V_1 \ln \frac{V_2}{V_1}$ $wRT \ln \frac{V_2}{V_1}$ $wRT \ln \frac{p_1}{p_2}$	$\left[\frac{p_2V_2 - p_1V_1}{1-\gamma}\right]144$ $Jwc_v(T_2 - T_1)$	$\left[\frac{p_2V_2 - p_1V_1}{1-n}\right]144$ $\frac{wR(T_2 - T_1)}{1-n}$
$U_2 - U_1$	$wc_p(T_2 - T_1)$ $144\left[\frac{p_2V_2 - p_1V_1}{(\gamma-1)J}\right]$	$wc_v(T_2 - T_1)$ $144\left[\frac{p_2V_2 - p_1V_1}{(\gamma-1)J}\right]$	0	$wc_v(T_2 - T_1)$ $144\left[\frac{p_2V_2 - p_1V_1}{(\gamma-1)J}\right]$	$wc_v(T_2 - T_1)$ $144\left[\frac{p_2V_2 - p_1V_1}{(\gamma-1)J}\right]$
$H_2 - H_1$	$wc_p(T_2 - T_1)$ $144\left[\frac{\gamma(p_2V_2 - p_1V_1)}{(\gamma-1)J}\right]$	$wc_p(T_2 - T_1)$ $144\left[\frac{\gamma(p_2V_2 - p_1V_1)}{(\gamma-1)J}\right]$	0	$wc_p(T_2 - T_1)$ $144\left[\frac{\gamma(p_2V_2 - p_1V_1)}{(\gamma-1)J}\right]$	$wc_p(T_2 - T_1)$ $144\left[\frac{\gamma(p_2V_2 - p_1V_1)}{(\gamma-1)J}\right]$
Specific heat c	$c_p = \frac{\gamma R}{(\gamma-1)J}$	$c_v = \frac{R}{(\gamma-1)J}$	∞	0	$c_n = c_v\frac{(\gamma-n)}{(1-n)}$
Quantity of heat Q_2	$wc_p(T_2 - T_1)$	$wc_v = (T_2 - T_1)$	$144\frac{p_1V_1}{J} \ln \frac{V_2}{V_1}$ $\frac{wRT}{J} \ln \frac{V_2}{V_1}$ $\frac{wRT}{J} \ln \frac{p_1}{p_2}$	0	$wc_n(T_2 - T_1)$
$S_2 - S_1$	$wc_p \ln \frac{T_2}{T_1}$ $wc_p \ln \frac{V_2}{V_1}$	$wc_v \ln \frac{T_2}{T_1}$ $wc_v \ln \frac{p_2}{p_1}$	$\frac{wR}{J} \ln \frac{V_2}{V_1}$ $\frac{wR}{J} \ln \frac{p_1}{p_2}$	0	$wc_n \ln \frac{T_2}{T_1}$

Table 12-3. Van der Waals Constants

Gas	Symbol	a $\frac{\text{psia ft}^6}{\text{mol}}$	b $\frac{\text{ft}^3}{\text{mol}}$
Air	--	5,053.0	0.585
Ammonia	NH_3	15,810.0	0.598
Butane	C_4H_{10}	54,010.0	1.944
Carbon Dioxide	CO_2	13,580.0	0.685
Carbon Monoxide	CO	5,507.0	0.630
Helium	He	132.1	0.384
Hydrogen	H_2	926.1	0.427
Methane	CH_4	8,508.0	0.684
Nitrogen	N_2	5,085.0	0.618
Oxygen	O_2	5,136.0	0.510
Propane	C_3H_8	34,890.0	1.446

where:

T_c = Critical temperature, °R

P_c = Critical pressure, psia

Critical temperatures and pressure for common fluids are given in Table 12-4.

One of the most widely used equations of state is that of Beattie and Bridgeman.

$$P = \frac{\mathcal{R}T}{144\hat{v}^2}\left[\hat{v} + B_o\left(1-\frac{b}{\hat{v}}\right)\right]\left[1-\frac{c}{\hat{v}T^3}\right] - \frac{A_o}{\hat{v}^2}\left[1-\frac{a}{\hat{v}}\right] \quad (48)$$

This equation contains five constants which must be determined for each particular gas. Values of these constants for several common gases are given in Table 12-5. Within the ranges of temperature, pressure, and volume indicated in the table, the Beattie-Bridgeman equation of state yields answers having an average deviation of 0.18 percent from accepted experimental values.

An empirical equation of state with eight empirical constants has been formulated by Benedict, Webb, and Rubin for the lighter hydrocarbons. This equation of state appears to provide accurate values for range of temperatures and pressures up to twice the critical density.

Another method commonly used to evaluate the deviation of a real gas from ideal behavior is the use of the compressibility factor, z, which is defined by the relationship:

$$z \equiv \frac{144\,Pv}{RT} \quad (49)$$

The compressibility factor is a complex function of any two of the variables P, v, and T; z-factors for several fluids have been calculated from experimental data, and detailed compressibility charts have been prepared. However, reasonable approximations to the P-v-T relations for all real fluids can be obtained from a generalized compressibility chart, as shown in Figures 12-8, 9 and 10 which cover the high, medium and low ranges of pressure respectively.

In each region, values of compressibility factor, z, are plotted as a function of reduced pressure, P_r, for a number of values of reduced temperature, T_r, and reduced specific volume, v_r. The generalized parameters of reduced pressure, temperature and specific volume are defined by the relationships:

$$P_r \equiv \frac{P}{P_c}; T_r \equiv \frac{T}{T_c}; v_r \equiv \frac{v}{v_c};$$

$$v'_r = \frac{P_c}{T_c}\frac{v}{R} = v_r z_c \quad (50)$$

where:

P_r = Reduced pressure

P_c = Critical pressure, psia

T_r = Reduced temperature

T_c = Critical temperature, °R

v'_r = Ideal reduced specific volume

v_r = Reduced specific volume

v_c = Critical specific volume, ft^3/lb

z_c = Compressibility factor at the critical point

Values of the critical constants for several fluids are listed in Table 12-4.

12-6 MIXTURES OF GASES

The individual gases or vapors in a mixture are called constituents or components. The description of the mixture is given by a volumetric analysis or by a gravimetric analysis. Sometimes one analysis is useful, sometimes the other; hence, it is desirable to convert from one to another.

The volumetric analysis expresses the amounts of the components in the mixture by the percentages of the total volume which each component would occupy if the various gases were placed in separate compartments at the pressure p_m and temperature T_m of the mixture. Thus each gas occupies a certain percentage or fraction of the entire volume, represented by B_x, B_y, and B_z (the symbol B suggesting bulk). Now if the partitions are removed and the gases mix, we say that the volumetric percentages of the gases X, Y, and Z are B_x, B_y, and B_z.

Table 12-4. Critical Constants

Substance	Formula	Molecular Weight	Temperature °K	Temperature °R	Pressure atm	Pressure lb/in.^{2}	Volume, ft^3/ mole
Ammonia	NH_3	17.03	405.5	729.8	111.3	1,636.0	1.16
Argon	A	39.944	151.0	272.0	48.0	705.0	1.20
Benzene	C_6H_6	78.11	562.0	1,012.0	48.6	714.0	4.17
Bromine	Br_2	159.832	584.0	1,052.0	102.0	1,500.0	2.17
Carbon dioxide	CO_2	44.01	304.2	547.5	72.9	1,071.0	1.51
Carbon monoxide	CO	28.01	133.0	240.0	34.5	507.0	1.49
Carbon tetrachloride	CCl_4	153.84	556.4	1,001.5	45.0	661.0	4.42
Chlorine	Cl_2	70.914	417.0	751.0	76.1	1,120.0	1.99
Chloroform	$CHCl_3$	119.39	536.4	965.8	54.0	794.0	3.85
Deuterium (Normal)	D_2	4.00	38.4	69.1	16.4	241.0	--
Ethane	C_2H_6	30.068	305.5	549.8	48.2	708.0	2.37
Ethyl alcohol	C_2H_5OH	46.07	516.0	929.0	63.0	926.0	2.68
Ethylene	C_2H_4	28.052	282.4	508.3	50.5	742.0	1.99
Freon-11	CCl_3F	137.38	471.2	848.1	43.2	635.0	3.97
Freon-12	CCl_2F_2	120.92	384.7	692.4	39.6	582.0	3.49
Freon-21	$CHCl_2F$	102.93	451.7	813.0	51.0	749.0	3.16
Helium	He	4.003	5.3	9.5	2.26	33.2	0.926
Helium[3]	He	3.00	3.34	6.01	1.15	16.9	--
Hydrogen (Normal)	H_2	2.016	33.3	59.9	12.8	188.1	1.04
Krypton	Kr	83.7	209.4	376.9	54.3	798.0	1.48
Methane	CH_4	16.042	191.1	343.9	45.8	673.0	1.59
Methyl alcohol	CH_3OH	32.04	513.2	923.7	78.5	1,154.0	1.89
Methyl chloride	CH_3Cl	50.49	416.3	749.3	65.9	968.0	2.29
n-Butane	C_4H_{10}	58.120	425.2	765.2	37.5	551.0	4.08
n-Hexane	C_6H_{14}	86.172	507.9	914.2	29.9	439.0	5.89
Neon	Ne	20.183	44.5	80.1	26.9	395.0	0.668
Nitrogen	N_2	28.016	126.2	227.1	33.5	492.0	1.44
Nitrous oxide	N_2O	44.02	309.7	557.4	71.7	1,054.0	1.54
Oxygen	O_2	32.00	154.8	278.6	50.1	736.0	1.25
Propane	C_3H_8	44.094	370.0	665.9	42.0	617.0	3.20
Propene	C_3H_6	42.078	365.0	656.9	45.6	670.0	2.90
Propyne	C_3H_4	40.062	401.0	722.0	52.8	776.0	--
Sulfur dioxide	SO_2	64.06	130.7	775.2	77.8	1,143.0	1.95
Water	H_2O	18.016	647.4	1,165.3	218.3	3,208.0	0.90
Xenon	Xe	131.3	289.75	521.55	58.0	852.0	1.90

Table 12-5. Beattie-Bridgeman Equation Constants

Gas	Chemical Symbol	A_o psia-$\left(\frac{ft^3}{mol}\right)^2$	a $\frac{ft^3}{mol}$	B_o $\frac{ft^3}{mol}$	b $\frac{ft^3}{mol}$	c $\frac{ft^3}{mol} \cdot °R^3$	Temperature Range, °R	Maximum Pressure, psia	Minimum Volume, ft^3/mol
Air	– –	4,905.7	0.30929	0.73854	–0.17635	4.054×10^6	230 to 850	2,600	2.0
Ammonia	NH_3	9,022.0	2.7279	0.54698	3.0612	445.4×10^6	425 to 1,100	1,910	5.5
Argon	Ar	4,866.1	0.37287	0.62963	0.0	5.595×10^6	220 to 1,200	1,675	2.7
Butane	C_4H_{10}	67,086.0	1.9478	3.9434	1.5093	326.9×10^6	760 to 1,030	1,735	4.5
Carbon Dioxide	CO_2	18,875.0	1.1423	1.6779	1.1588	61.65×10^6	490 to 670	1,630	2.9
Carbon Monoxide	CO	5,069.0	0.41916	0.80822	–0.11068	3.923×10^6	– –	– –	– –
Ethane	C_2H_6	22,168.0	0.93875	1.5056	0.30672	84.07×10^6	540 to 940	2,840	3.2
Ether	$(C_2H_5)_2O$	117,920.0	1.9903	7.2791	1.9147	31.13×10^6	760 to 1,100	1,320	5.9
Ethylene	C_2H_4	23,194.0	0.79508	1.9470	0.57613	21.19×10^6	490 to 850	4,200	2.0
Freon–12	CCl_2F_2	89,353.0	4.8852	9.4500	9.9625	0.0	545 to 720	272	22.9
Helium	He	81,440.0	0.95845	0.22424	0.0	0.00374×10^6	40 to 1,200	1,500	1.6
n-Heptane	$n\text{-}C_7H_{16}$	205,550.0	3.2140	11.343	3.0719	373.6×10^6	990 to 1,120	4,630	3.2
Hydrogen	H_2	744.60	–0.081046	0.33572	–0.69818	0.04708×10^6	50 to 850	1,515	1.6
Hydrogen*	H_2	467.60	0.89983	0.32386	–0.11564	1.868×10^6	365 to 1,030	14,696	1.0
Hydrogen**	H_2	467.60	0.89983	0.28030	–0.31521	1.868×10^6	365 to 1,030	14,696	0.6
Iso-Butene	$Iso\text{-}C_4H_8$	63,942.0	1.7394	3.8761	1.4015	233.5×10^6	760 to 940	3,680	1.8
Methane	CH_4	8,584.0	0.29711	0.89487	–0.25419	11.98×10^6	490 to 850	3,570	2.7
Methanol (Wood Alcohol)	CH_3OH	125,580.0	1.4809	9.6682	1.5903	29.92×10^6	– –	– –	– –
Neon	Ne	801.16	0.35173	0.32995	0.0	0.09434×10^6	100 to 1,200	1,560	1.9
Nitrogen	N_2	5,069.0	0.41916	0.80822	–0.11068	3.923×10^6	225 to 1,200	1,970	2.9
Nitrogen	N_2	4,719.1	0.29888	0.73726	–0.41436	5.754×10^6	365 to 1,200	1,235	1.3
Nitrous Oxide	N_2O	18,875.0	1.1423	1.6779	1.1588	61.65×10^6	– –	– –	– –
Oxygen	O_2	5,621.7	0.41035	0.74062	0.06740	4.484×10^6	280 to 670	1,515	1.8
Propane	C_3H_8	44,940.0	1.1726	2.8991	0.68761	112.0×10^6	670 to 990	4,480	1.6

*below critical density
**above critical density

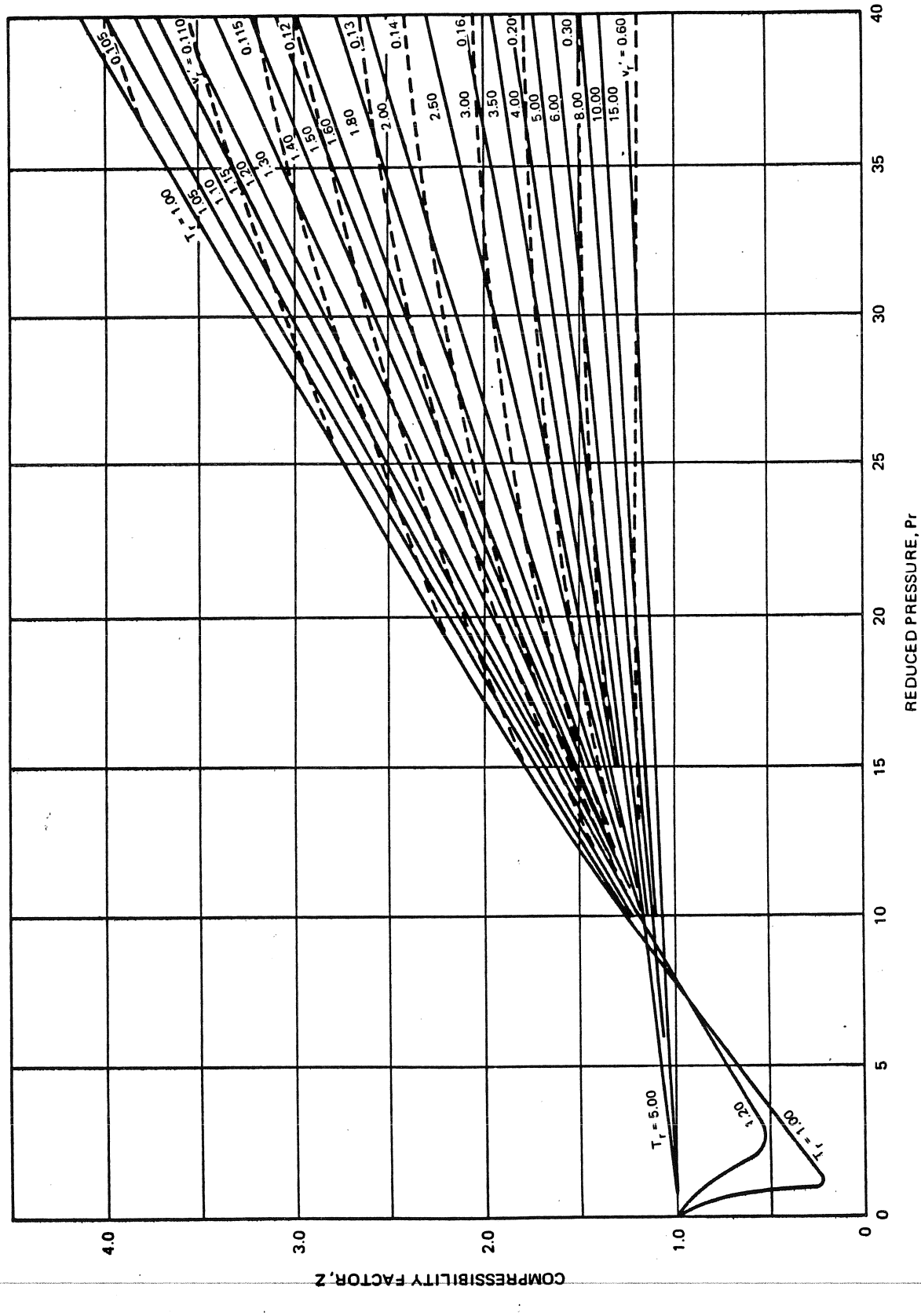

Figure 12-8. Nelson-Obert Generalized Compressibility Chart (High-Pressure Region)

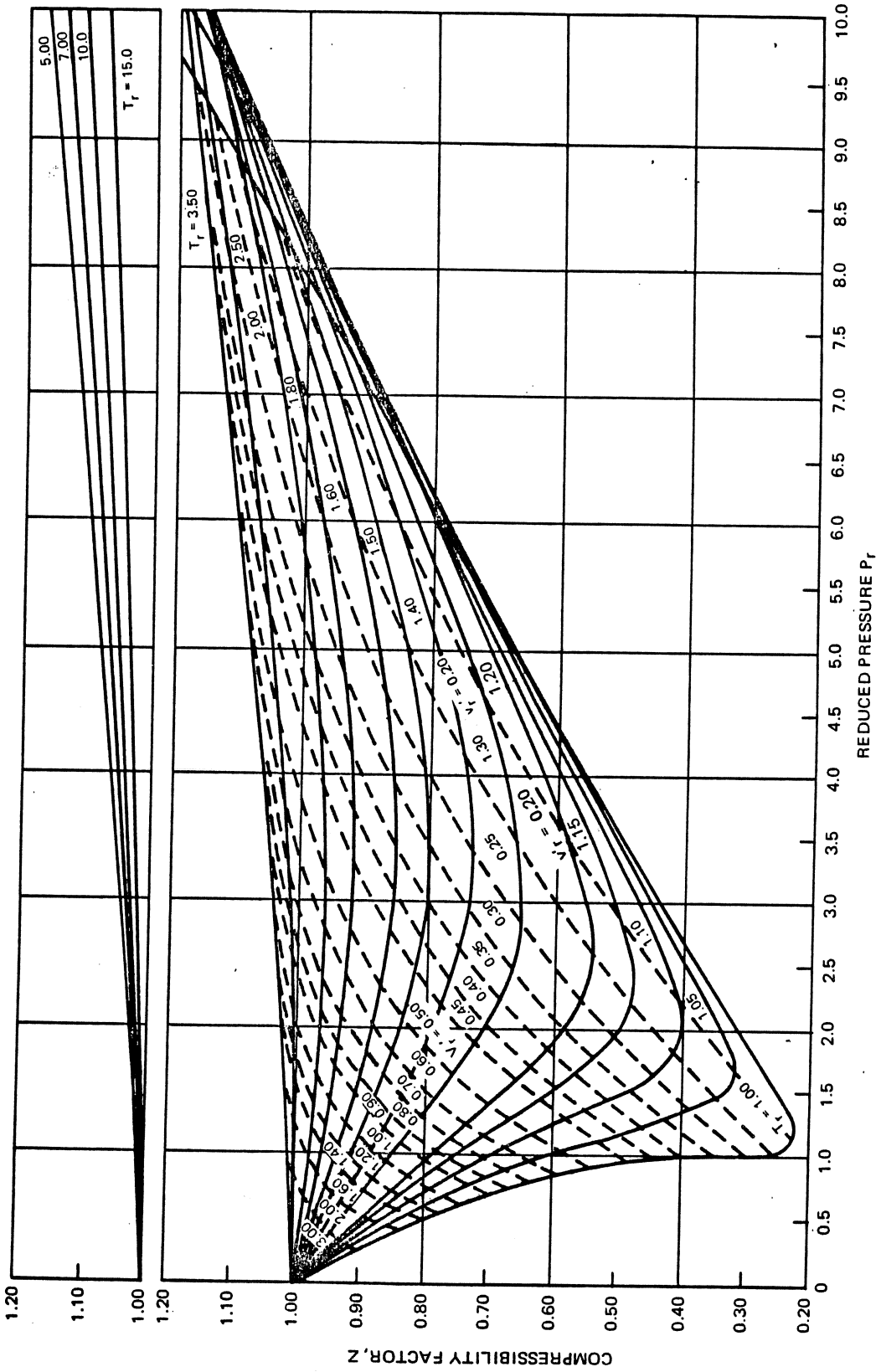

Figure 12-9. Nelson-Obert Generalized Compressibility Chart (Medium-Pressure Region)

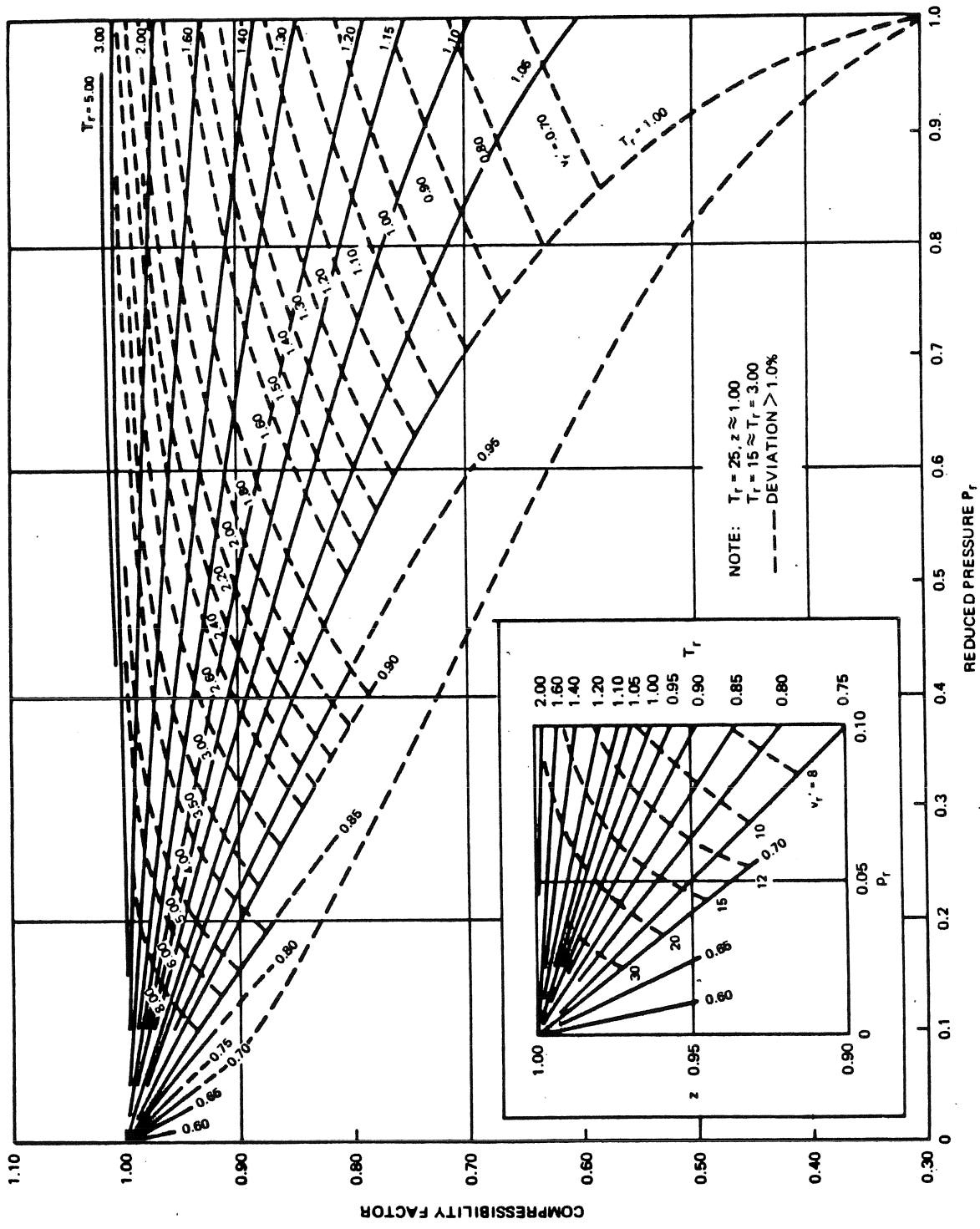

Figure 12-10. Nelson-Obert Generalized Compressibility Chart (Low-Pressure Region)

It is important to note that if the volume contains one mol of the total mixture, the mols of gases X, Y, and Z are B_X, B_Y, and B_Z. That is, the volumetric fraction B_X is the number of mols of gas X in a mixture which totals one mol; $B_X + B_Y + B_Z = 1$. The volumetric percentage B_X is the number of mols of X in a mixture which totals 100 mols;

$$B_X + B_Y + B_Z = 100,$$

when all gases are at the same temperature. In terms of the actual known mols of each gas, N_X N_Y, and N_Z, we write:

$$N_m = N_X + N_Y + N_Z,$$

where N_m is the total number of mols in the mixture. Notice that:

$$B_X = \frac{N_X}{N_m}, \quad B_Y = \frac{N_Y}{N_m}, \quad \text{and} \quad B_Z = \frac{N_Z}{N_m} \tag{51}$$

are the percentages by volume of the constituents X, Y, and Z, respectively. The volumetric percentage is also defined by:

$$B_X = \frac{\text{cu ft of gas X at } p_m \text{ and } T_m}{\text{cu ft of mixture at } p_m \text{ and } T_m},$$

and so on for gases Y and Z.

The gravimetric analysis describes the mixture by giving the percentages by weight (mass) of each constituent. For example, the gravimetric percentage or fraction of gas X is:

$$G_X = \frac{\text{mass of gas X}}{\text{total mass of the mixture}} \tag{52}$$

For a mixture of gases X, Y, and Z, the gravimetric analysis is G_X percent of X, G_Y percent of Y, and G_Z percent of Z, each expressed as a percentage of the mass; G also stands for the fractional part of the mass.

12-6.1 Volumetric Analysis to Gravimetric Analysis

Given three gases X, Y, and Z, mixed in the proportion B_X, B_Y, and B_Z fraction or percent by volume; which is the same thing as saying that there are B_X mols of X, B_Y mols of Y, and B_Z mols of Z in the mixture. Consider gas X as an example. There are M_X lb per mol; hence:

$$(B_X \text{ mols}) \left(M_X \frac{\text{lb}}{\text{mol}}\right) = B_X M_X \text{ lb}, \tag{53}$$

for one mol of mixture if B_X is a fraction. Equation 53 says that the product of the molecular weight and the volumetric percentage of gas X gives the mass (or a number proportional to the mass of gas X. If there are actually N_X mols of X, then the mass of X is $N_X M_X$ lb. Thus, the mass (or a number proportional to the mass) of the mixture is the sum of the masses of the components; $B_X M_X + B_Y M_Y + B_Z M_Z = \Sigma BM$ lb per mol, in general for any number of components, volume fraction B. When the number of mols N of each constituent is known, rather than the fraction B, the mass of the mixture is $N_X M_X + N_Y M_Y + N_Z M_Z = \Sigma NM$ lb. Thus, it is possible to convert from volumetric analysis to gravimetric analysis by multiplying the volumetric percentage or the number of mols of each gas by the corresponding molecular weight and apply as follows:

$$G_X = \frac{B_X M_X}{\Sigma BM}, \quad G_Y = \frac{B_Y M_Y}{\Sigma BM}, \quad G_Z = \frac{B_Z M_Z}{\Sigma BM},$$

$$G_X = \frac{N_X M_X}{\Sigma NM}, \quad G_Y = \frac{N_Y M_Y}{\Sigma NM}, \quad G_Z = \frac{N_Z M_Z}{\Sigma NM}. \tag{54}$$

The units of G are pounds per pound of mixture when decimals are used for B and pounds per 100 lb of mixture when percentage numbers are used for B. Equation 54 applies precisely to ideal gases only, but it is commonly employed for gaseous mixtures in general.

12-6.2 Gravimetric Analysis to Volumetric Analysis

If there are w_X lb of gas X whose molecular weight is $M_X$lb, then there are $w_X/M_X = N_X$ mols of X. Similarly, if there are G_X lb of gas X per lb of mixture or per 100 lb of mixture, depending upon whether it is a fraction or percentage number, we have:

$$G_X \left(\frac{\text{lb}}{\text{unit mixture}}\right)\left(\frac{1}{M_X \text{lb/mol}}\right) = \frac{G_X \text{ mol}}{M_X \text{ unit mixture}}; \tag{55}$$

that is, dividing the percentage or fractional weight by the molecular weight gives the corresponding number of mols of a particular gas in the mixture. Since all constituents are at the same pressure p_m and temperature T_m, the number of mols of each gas is proportional to the volume of the gas. Thus, the total volume of the mixture is the sum of the volumes of the constituents when each is at p_m and T_m, and the total volume is proportional to the sum of the G/M values. For three gases, the total volume is proportional to $G_X/M_X + G_Y/M_Y + G_Z/M_Z = \Sigma G/M$ in general for any number of components. Thus, the fraction or percentage volume B is given by:

$$B_X = \frac{G_X/M_X}{\Sigma G/M}, \quad B_Y = \frac{G_Y/M_Y}{\Sigma G/M}, \quad B_Z = \frac{G_Z/M_Z}{\Sigma G/M}. \tag{56}$$

If the actual masses of gases X, Y, and Z are w_X, w_Y, and w_Z, the actual total volume is $w_X/M_X + w_Y/M_Y + w_Z/M_Z = \Sigma w/M$ mols, and the actual volume of one component in mols is w_X/M_X, etc. Thus:

$$B_X = \frac{w_X/M_X}{\Sigma w/M}, \quad B_Y = \frac{w_Y/M_Y}{\Sigma w/M}, \quad B_Z = \frac{w_Z/M_Z}{\Sigma w/M}. \tag{57}$$

If more precise conversions than those given by equations 54, 56 and 57 are required for actual gases, use the density of each gas in place of M, all densities corresponding to the same temperature and pressure.

12-6.3 Dalton's Law of Partial Pressures

The total pressure p_m exerted by a mixture of gases (or vapors) is the sum of the pressures which each gas (or vapor) would exert were it to occupy the vessel alone. The pressure which one gas in a mixture exerts is called its partial pressure. Thus, if p_x, p_y, and p_z represent respectively the partial pressures of the mixed gases X, Y, and Z, Dalton's law states:

$$p_m = p_x + p_y + p_z + \cdots.$$

$$[T_m = T_x = T_y = T_z, \quad V_m = V_x = V_y = V_z] \qquad (58)$$

The characteristic equation of an ideal gas in terms of the number of mols is $pV = 1545NT$. Applying this equation to a component X and to the mixture gives:

$$p_x V_m = 1545 N_x T_m \text{ and } p_m V_m = 1545 N_m T_m.$$

By division:

$$\frac{p_x V_m}{p_m V_m} = \frac{1545 N_x T_m}{1545 N_m T_m} \text{ or } \frac{p_x}{p_m} = \frac{N_x}{N_m} = B_x.$$

In the foregoing, use the following principles: If the mixture is in internal thermal equilibrium, all gases are at the same temperature T_m; each gas occupies the same volume V_m; the number of mols N_x of X divided by the total number of mols N_m is the volumetric percentage; and the volumetric fraction B is equal to the ratio of the partial pressure divided by the total pressure; or:

$$p_x = B_x p_m, \quad p_y = B_y p_m, \quad p_z = B_z p_m, \qquad (59)$$

true for ideal gases and useful for actual gases.

12-6.4 Molecular Weight and Gas Constant for Mixture

Given N_x or B_x mols of X, N_y or B_y mols of Y, and N_z or B_z mols of Z, the corresponding masses are:

	(1)	(2)
	$N_x M_x$ lb	$B_x M_x$ lb/mol mixture
	$N_y M_y$ lb	$B_y M_y$ lb/mol mixture
	$N_z M_z$ lb	$B_z M_z$ lb/mol mixture
Total =	ΣNM lb	ΣBM lb/mol mixture (M_m).

If $B_x + B_y + B_z = 1$ in column (2), there is one mol of mixture and the mass in pounds per mol is the molecular weight; thus, $\Sigma BM = M_m$, the equivalent molecular weight of the mixture. By similar reasoning, there are $N_m = N_x + N_y + N_z$ mols in column (1), and $M_m = \Sigma NM/N_m$; or:

$$M_m = B_x M_x + B_y M_y + B_z M_z = \Sigma BM \text{ lb/mol},$$

$$M_m = \frac{N_x M_x + N_y M_y + N_z M_z}{N_m} = \frac{\Sigma NM}{N_m} \text{ lb/mol}, \qquad (60)$$

where, in ΣBM and ΣNM, B and N apply to the individual gases. Equations 54, 56, and 57 show that $\Sigma BM = 1/(\Sigma G/M)$; hence:

$$M_m = \frac{1}{\Sigma G/M}$$

also. Using the universal gas constant, the specific gas constant of the mixture is:

$$R_m = \frac{1545}{M_m} \text{ ft-lb/lb-°R}.$$

Also, using the gravimetric analysis,

$$R_m = G_x R_x + G_y R_y + G_z R_z = \Sigma GR. \qquad (61)$$

12-7 THERMODYNAMIC CYCLES

A substance undergoes a process if any of its properties change. A fluid undergoes a cycle if it passes through a series of processes and returns to its original state. Thus, a thermodynamic cycle consists of a combination of thermodynamic processes. These cycles describe methods of converting thermal energy into mechanical power. These heat engine cycles may be either open cycles or closed cycles as shown schematically in Figures 12-11 and 12-12.

In an open cycle the working fluid flows through the system and is exhausted. A continuous supply of new working fluid is required to maintain system operation.

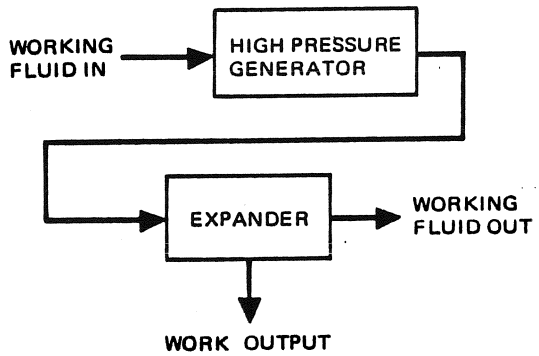

Figure 12-11. Open Loop Heat Engine Cycle

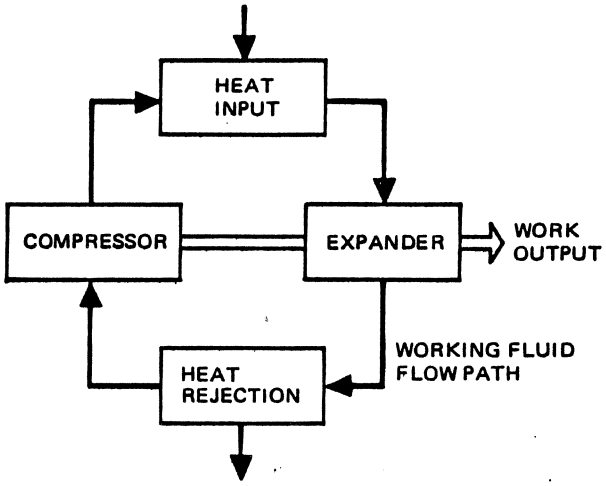

Figure 12-12. Closed Loop Heat Engine Cycle

Internal combustion engines which derive their thermal energy from fuel, which is also the working fluid, are typical open cycles.

In a closed cycle, the working fluid is retained in the system and returned to its original state for reuse. In this case thermal energy is added to the working fluid through a heat exchanger from an external source which is separated physically from the working fluid. Much of the heat added to the working fluid is converted to work during the expansion process. Additional heat is rejected external to the system through another heat exchanger to return the fluid to its initial condition. External combustion engines, such as the Sterling cycle engine, are typical closed cycles.

Table 12-6 presents a summary comparison of the most common thermodynamic cycles, shown in their basic configurations to facilitate comparison. The cycles are grouped by configuration (open or closed). The closed-cycle type is further subdivided by type (liquid or gaseous compression). Each named cycle is described by its temperature-entropy and pressure-specific volume cycle diagrams, and a typical application is identified.

The Carnot cycle is the most efficient cycle because all of the heat is added at the maximum temperature T_H, and all of the rejected heat is removed at the minimum temperature T_C. The ideal Carnot cycle can be either liquid or gaseous compression type.

In a liquid compression system, the Carnot cycle must operate under the vapor dome, as shown in Table 12-6, requiring adiabatic compression of a two-phase fluid. In a gas compression Carnot cycle, heat addition and removal must be accomplished during isothermal processes. These constraints made the Carnot cycle difficult to implement. Therefore, despite its high thermal efficiency, the Carnot cycle is not utilized for actual applications.

The thermal efficiencies of the other cycles are less than that of the Carnot cycle because heat is added, and rejected over a range of temperatures. The efficiency of each of these cycles approaches the Carnot efficiency as its average heat-input temperature approaches T_H, and its average heat-rejection temperature approaches T_C.

Superheating is a means of increasing the average heat-input temperature in liquid compression cycles that include condensation in the heat-rejection process. Regeneration is a means of increasing the average heat-input temperature and decreasing the average heat-rejection temperature in gaseous and liquid-compression cycles. Table 12-7 illustrates the required changes in the cycle diagrams and the system schematics when superheating, regeneration, or reheat and regeneration is added to the basic Rankine cycle.

12-7.1 Ideal Cycles

An ideal cycle has no friction or fluid losses and, therefore, is reversible. The efficiency of a reversible heat-engine cycle depends only upon the temperatures of the heat source and the heat sink, and the efficiency increases as the source temperature is increased, or the sink temperature is lowered. The simplest ideal (maximum efficiency) cycle is the Carnot cycle, which consists of four processes: an isentropic compression; an isothermal addition of heat; an isentropic expansion; and an isothermal rejection of heat. These reversible processes may be either flow or nonflow processes.

The thermal efficiency of the reversible Carnot cycle is:

$$\eta_t = \frac{Q_H - Q_c}{Q_H} = \frac{T_H - T_c}{T_H} \qquad (62)$$

where:

Q_H = Heat added

Q_c = Heat rejected

T_H = Temperature at which heat is added

T_c = Temperature at which heat is rejected

Table 12-6. Comparison of Common Thermodynamic Cycles

Cycle Description		Cycle Diagrams		Application
Type	Name	Temperature-Entropy	Pressure-Specific Volume	
Optimum Ideal (Vapor (shown) or Gaseous Compression)	Carnot	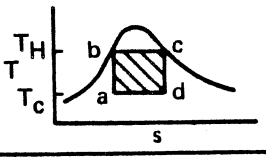	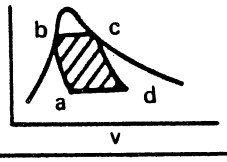	Reference: Simplest and most efficient cycle $\eta_t = \frac{T_H - T_c}{T_c}$ No practical applications
Ideal Liquid Compression-Closed Cycle	Rankine	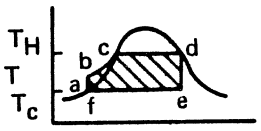	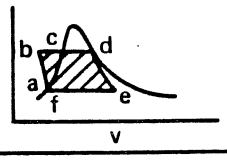	Steam Power
	Supercritical Rankine	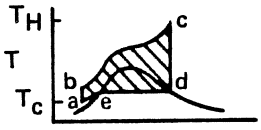	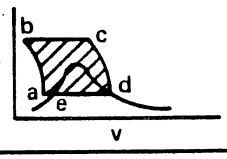	Space Power
	Feher	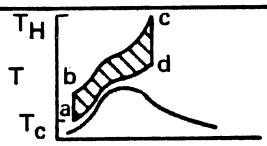	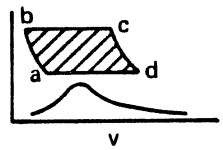	Space Power
Ideal Gaseous—Closed Cycle (External Combustion)	Stirling	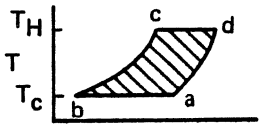	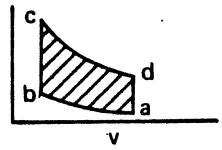	Space Power
	ERICSSON	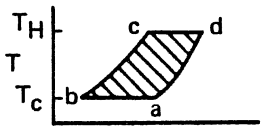	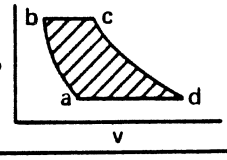	Limited Use Because of Low Mean Effective Pressure
	Brayton (Joule)	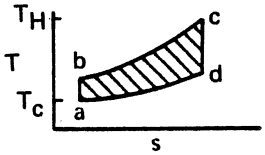	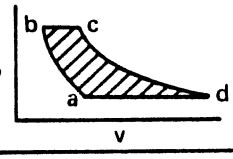	Space Power Gas Turbine
Ideal Gaseous—Open Cycle (Internal Combustion)	Otto	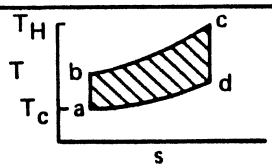	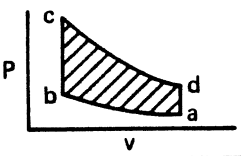	Gasoline Engine
	Diesel	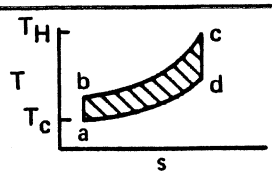	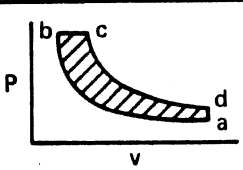	Diesel Engine

Note: Shade areas represent heat added in T-S diagrams and work output in P_v diagrams

Table 12-7. Variations of the Rankine Cycle

CYCLE DESCRIPTION	CYCLE DIAGRAMS		SYSTEM SCHEMATIC
	TEMPERATURE–ENTROPY	PRESSURE–SPECIFIC VOLUME	
IDEAL BASIC RANKINE CYCLE	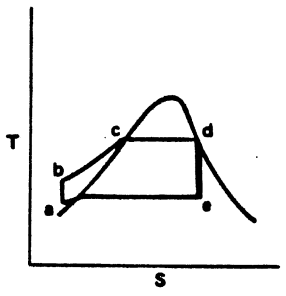	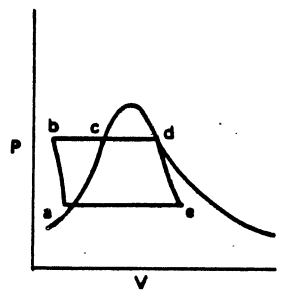	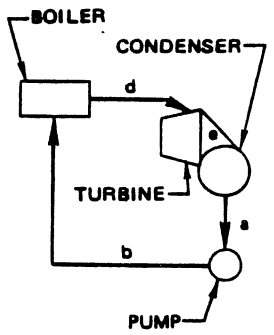
IDEAL RANKINE CYCLE WITH SUPER HEAT	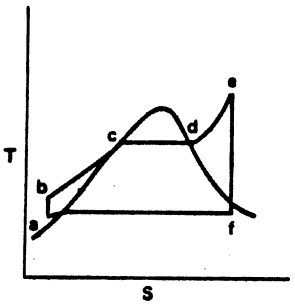	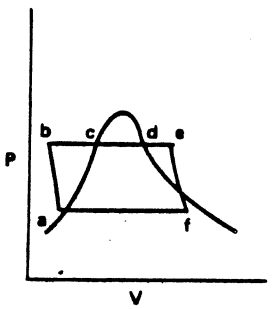	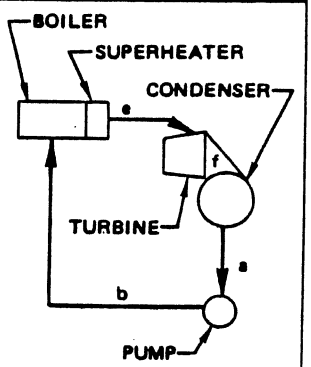
IDEAL RANKINE CYCLE WITH REGENERATION	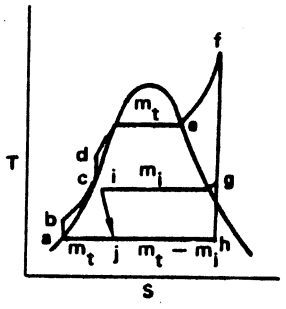	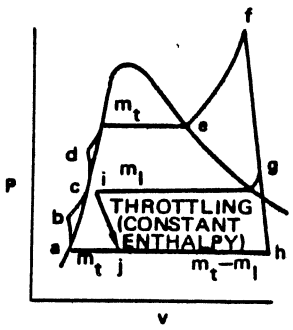	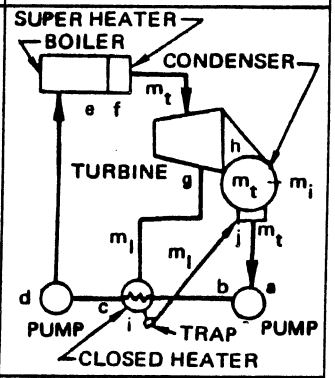
IDEAL RANKINE CYCLE WITH REHEAT AND REGENERATION	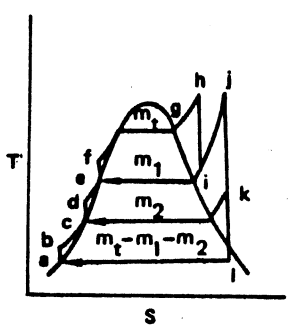	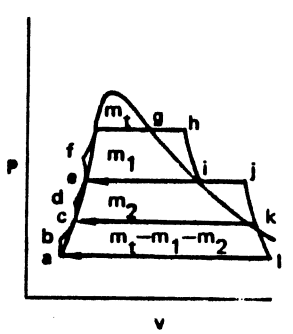	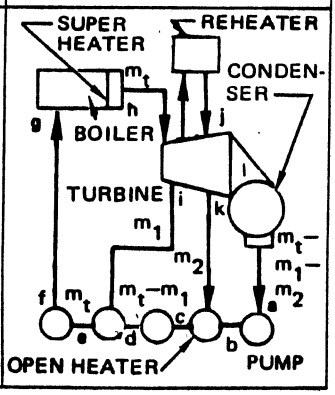

In any cycle, other than a Carnot cycle, the average temperature for heat addition T_H can be found from:

$$\bar{T}_H = \frac{b\int_a^c TdS}{S_c - S_a} \quad (63)$$

and the average temperature for heat rejection T_c can be found from:

$$\bar{T}_c = \frac{d\int_c^a TdS}{S_a - S_c} \quad (64)$$

Therefore the thermal efficiency of this new cycle is:

$$\eta_t = \frac{\bar{T}_H - \bar{T}_C}{\bar{T}_H} \quad (65)$$

12-7.1.1 Liquid Compression Cycles

The basic components of a closed loop liquid-compression cycle heat engine are shown in Figure 12-13. The heat engine consists of: a pump, a heat source, an expander, and a heat sink. These components are connected by tubing to permit continuous circulation of the working fluid.

Energy is added to the working fluid by the pump and the heat source. The pump increases the pressure of the working fluid while it is in the liquid state, and the heat source converts the fluid to the gaseous state.

Energy is extracted from the working fluid by the expander and the heat sink. The expander extracts energy by decreasing the fluid pressure while it is primarily in the gaseous state, and the heat sink extracts heat from the low pressure fluid to return it to the liquid state before it again enters the system pump.

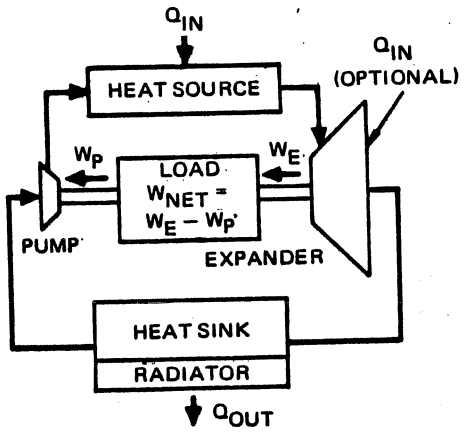

Figure 12-13. Liquid Compression Cycle

Power input is required to operate the pump, and power output is provided by the expander. The required pump power is usually obtained from the expander through a mechanical linkage. An advantage of a liquid compression cycle is that a relatively small portion of the expander output power is required to operate the pump.

Three types of liquid compression cycles are described in Table 12-6: the Rankine cycle, the Supercritical Rankine cycle, and the Feher cycle.

The Rankine cycle is the conventional boiling and condensing heat engine cycle which is used in virtually all major steam power plant installations. In terms of the components shown in Figure 12-13 the heat addition unit is a boiler, which may include a superheater section, and the heat rejection unit is a condenser. For those systems incorporating reheat, heat is added during the expansion process.

The Supercritical Rankine cycle is substantially the same as the Rankine cycle except that there is no phase change during the heat addition portion of the cycle. This is accomplished by compressing the fluid to a pressure greater than its critical pressure. The subsequent addition of heat changes the supercritical fluid into a gas without the appearance of a gas-liquid interface in the process. Reheat can also be used in this cycle.

The Feher cycle is similar to the Supercritical Rankine cycle except that all of the pressures in the cycle are above the critical pressure of the working fluid. Heat addition and heat rejection from the working fluid does not entail a change of phase. The low temperature in the Feher cycle is, in principle, below the critical temperature of the working fluid, and hence one may properly speak of liquid compression. The high temperature in the cycle is above the critical temperature of the working fluid. The material which expands through the prime mover may therefore be thought of as a gas or vapor.

12-7.1.2 Gaseous Compression Cycles

Table 12-6 also describes three types of closed loop gaseous compression cycles: the Brayton cycle, the Sterling cycle, and the Ericsson cycle. Each of these cycles operates entirely in the region above the vapor dome of the working fluid. The two open-loop cycles described (Otto and Diesel) are also of the gaseous compression category.

Figure 12-14, which illustrates schematically the essential features of gaseous compression cycles, is identical to the liquid compression cycle schematic except that the compressor is shown larger than the pump to emphasize that considerably more work is required to compress gas than to pump liquid to a given increased pressure.

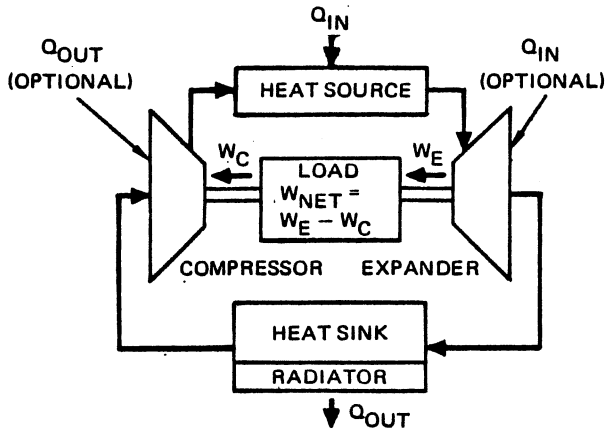

Figure 12-14. Gaseous Compression Cycle

Figure 12-14 describes the Brayton cycle. The Sterling cycle has basically the components shown in Figure 12-14, but the method of using these components is not readily shown. The Sterling cycle uses both constant temperature and constant specific-volume processes. Hence, heat is added and rejected during both the compression and expansion portions of the cycle. This is accomplished by regeneration which consists of using some of the heat rejected from the low pressure fluid to supply some of the heat added to the high pressure fluid. The Ericsson cycle is also regenerative but it consists of two isothermal, and two isobaric processes.

Figure 12-15 shows the basic configuration of a cycle that includes regeneration. Regenerative cycles increase the average temperature of heat addition, and decrease the average temperature of heat rejection; thus they increase the cycle thermal efficiency η_t.

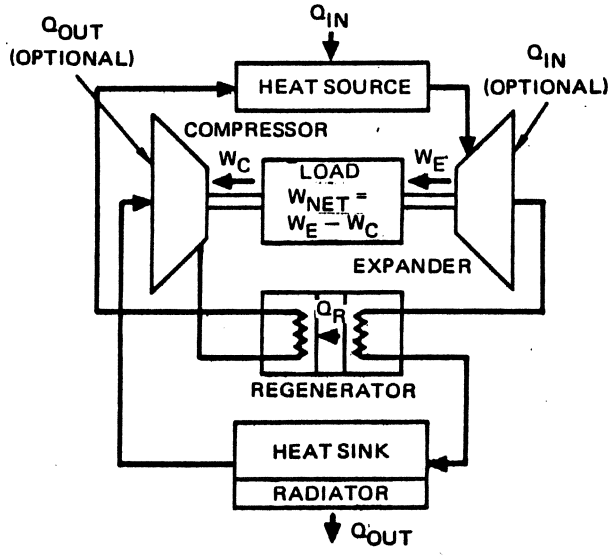

Figure 12-15. Regenerative Cycle

12-7.2 Real Cycles

All real cycles have losses associated with inefficient machinery, pressure drop during fluid flow, and inadvertent heat loss or unwanted internal heat transfer. Regenerative cycles have additional losses associated with the practical requirement for a driving temperature differential to accomplish regenerative heat transfer. In general, the liquid compression cycles are less sensitive to component performance than the gas compression cycles. In gaseous compression cycles, the compression efficiency is significant because the work of compression is relatively large. Pressure losses are a significant factor in these cycles. Liquid compression cycles use some of their work output for compression, but this normally is so small that the pump efficiency and cycle pressure losses are not a major factor in system design.

Only when the liquid is near its critical temperature does the work of compression become moderately significant. In a typical Rankine cycle, the compression work is one percent of the expansion work. In a typical Feher cycle with a minimum temperature near the critical value, the compression work is 10 percent of the expansion work. In a typical Brayton cycle the compression work is 65 percent of the expansion work.

12-7.2.1 Real Liquid Compression Cycles

Figure 12-16 shows the various temperature-entropy (T-S) diagrams which are of interest for the present discussion. Figures 12-16a and b are for fluids in which the vapor dome occupies a significant portion of the figure. Fluids whose vapor dome is similar to that shown in Figure 12-16a are referred to as type A fluids. This distinguishes them from the type B fluids, shown in the Figure 12-16b which have a retrograde vapor line, (i.e., a portion of the saturated vapor line has increasing entropy with increasing temperature). Figure 12-16c shows the T-S diagram for a liquid with a temperature range which greatly exceeds the critical temperature of the liquid. Diagrams of this type are of interest for supercritical Rankine cycles and Feher cycles. Figure 12-16d shows the typical T-S diagram for a gas in the region far above the critical temperature where essentially perfect gas behavior is observed.

12-7.2.1.1 Rankine Cycles

The Rankine cycle is the most widely known of all vapor power cycles. The majority of mechanical space power plant development activity in the United States has involved some version of the Rankine cycle.

A. Rankine Cycles Using Type A Working Fluids – Figure 12-17 shows a T-S diagram for a typical type A fluid (water) on which has been superimposed a Rankine cycle. The subcooled liquid is compressed from a to b in a pump with a

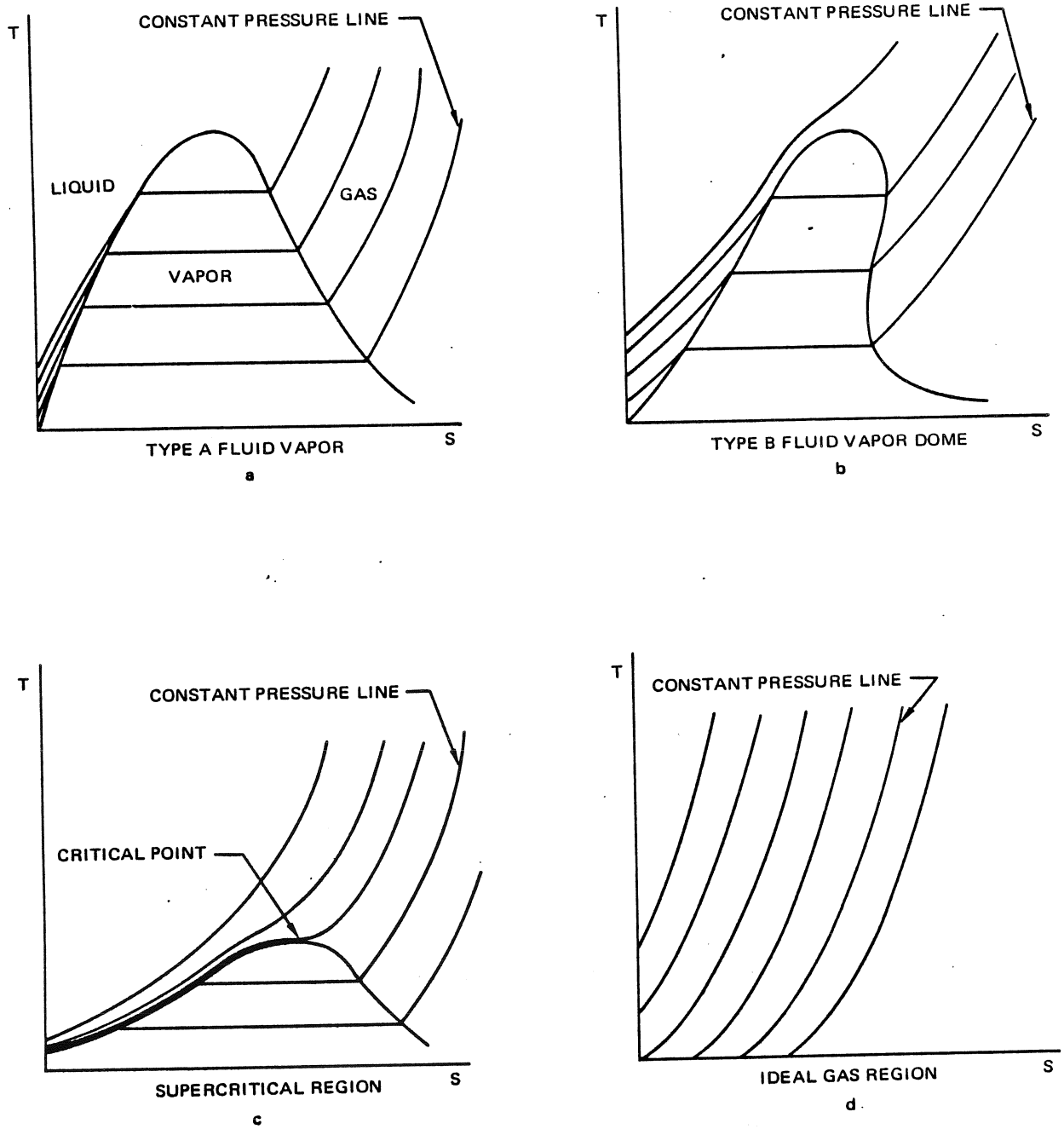

Figure 12-16. T-S Diagrams of Fluid Properties

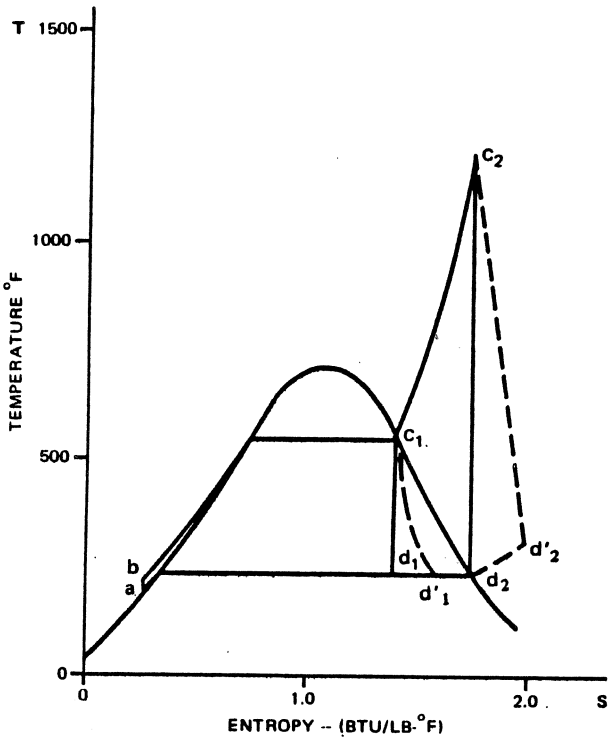

Figure 12-17. Rankine Cycle – Type A Fluid

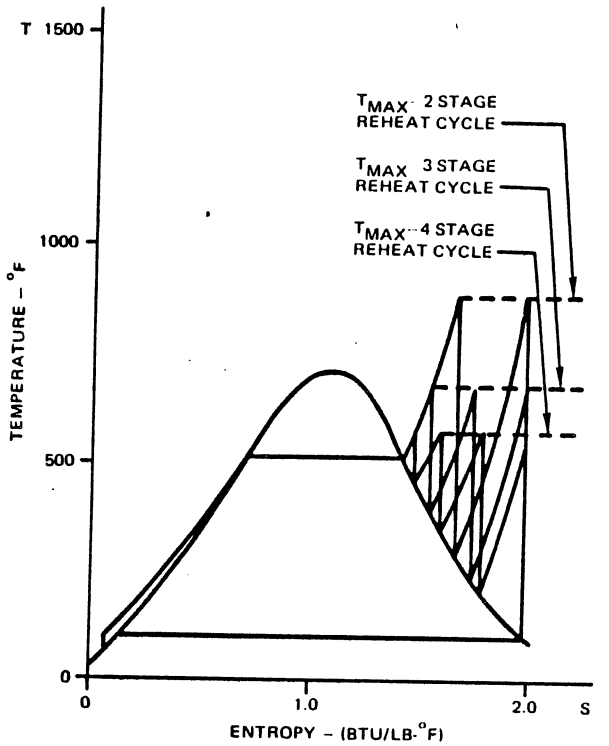

Figure 12-18. Rankine Cycle with Dry Expansion

negligible increase in temperature, and a very small amount of work involved. The fluid is then heated to the boiling temperature and evaporated. In addition, it may be superheated. Point c_1 is the maximum temperature point for a saturated Rankine cycle. Point c_2 is the maximum temperature point for a superheated cycle. Expansion takes place between points c and d, followed by condensation between d and a.

When the expansion of the working fluid causes the point d to lie within the vapor dome, as for example d_1 in Figure 12-17, liquid may form within the expansion machinery. Liquid droplet impingement on high speed turbine blades with resulting pitting and erosion is typical of the problems which can be encountered. The condensation problem does not always arise, because a finite time is required for liquid droplets to form and grow. Some fluids, notably mercury, can reach a high degree of supersaturation before condensation occurs.

When it is desired to completely avoid the possibility of condensation in the cycle, superheat can be used so that the point d_1 falls outside of the vapor dome as does point d_2. For a single stage expansion, this may require a high temperature at point c_2, or a low boiling temperature, which would yield a comparatively low thermal efficiency. The dashed lines $c_1d'_1$ and $c_2d'_2$ show the deviation of a real expansion from the ideal.

In a multi-stage expansion, wetness can be avoided by use of superheat and reheat as shown in Figure 12-18. The maximum temperature required to avoid wetness approaches the boiling temperature as the number of stages approaches infinity.

The thermal efficiency of a superheat or reheat cycle may increase or decrease compared to a saturated cycle with the same boiling temperature, depending on whether the extra heat addition takes place, on the average, above or below the boiling temperature of the cycle. In either case the effect is usually small since the amount of heat involved is normally quite small compared to the latent heat of vaporization of the fluid.

Studies have been made for the purpose of comparing different materials as Rankine cycle working fluids. Figure 12-19 shows typical data for the thermal efficiency achievable as a function of the boiling and condensing temperatures for various working fluids.

One approach to generalizing this data involves characterizing the fluid properties by a suitable dimensionless parameter such as the ratio of the latent heat of vaporization to the enthalpy of the saturated liquid. One can then plot values of the fluid parameter against temperature for various fluids together with other charts which allow the final cycle efficiency to be determined.

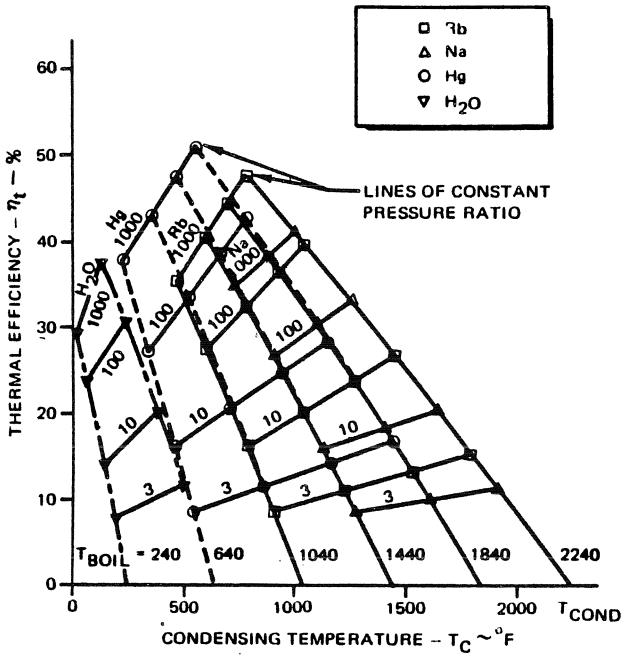

Figure 12-19. Rankine Cycle Thermal Efficiency

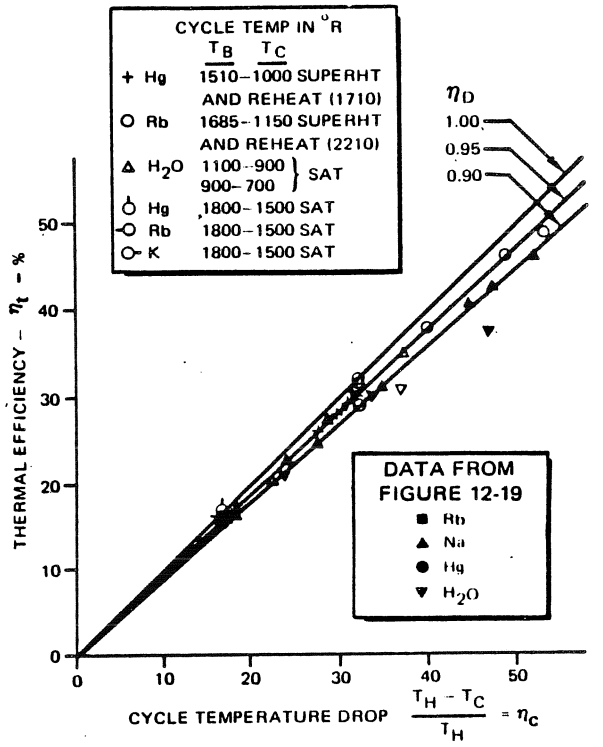

Figure 12-20. Rankine Cycle Diagram Efficiency

Cycles are frequently evaluated in terms of the diagram efficiency η_D.

$$\eta_D = \frac{\eta_t}{\eta_c} \qquad (66)$$

where:

η_c = Comparable Carnot cycle efficiency

The diagram efficiency is always less than 100 percent when the Carnot efficiency used is based on the maximum and minimum cycle temperatures. The real cycle efficiency is lower than the ideal thermal efficiency because processes in real systems are irreversible due to friction and turbulence, as illustrated by the dotted lines in Figure 12-17.

Figure 12-20 presents a plot of η_t versus η_c for specific η_D values forseveral type A fluids based on a Carnot cycle operating between the boiling and condensing temperatures in the Rankine cycle. The diagram efficiency is over 90 percent for a wide range of boiling and condensing temperatures for saturated cycles, superheated cycles and cycles employing superheat and reheat.

B. Rankine Cycles Using Type B Working Fluids – Many problems have arisen from the use of liquid metals in closed cycle power systems. These have been primarily associated with the corrosive nature of these working fluids. This has led to a search for other fluids, suitable for the generation of power in space, which do not exhibit the same corrosive character. Water, aluminum bromide, sulfur, and other inorganic compounds have been considered extensively. More recently, investigation and developmental work has been carried out using various organic working fluids. Aside from water, the inorganic nonmetallic fluids have been found to be excessively corrosive and thermally unstable. Some of the organic materials, however, have shown some promise.

Heat addition at a temperature that is high relative to the heat rejection temperature is necessary for high thermal efficiency. High heat rejection temperatures are also desirable to minimize the size and weight of the heat rejection devices. Maximum cycle temperatures on the order of 1,000°F or above are desirable for a practical system. Unfortunately there are very few organic materials which are thermally stable at temperatures above 700°F. Of the few relatively stable materials which have been investigated, perhaps the most important one is biphenyl and its derivatives, biphenyl oxide and monoisopropylbiphenyl. All of these fluids have type B T-S diagrams.

Figure 12-21 shows a T-S diagram for biphenyl on which has been superimposed a typical Rankine cycle. The maximum temperature in the cycle is a little over 600°F. This choice of temperature is based on the thermal decomposition characteristics of the material shown in Figure 12-22. Temperatures

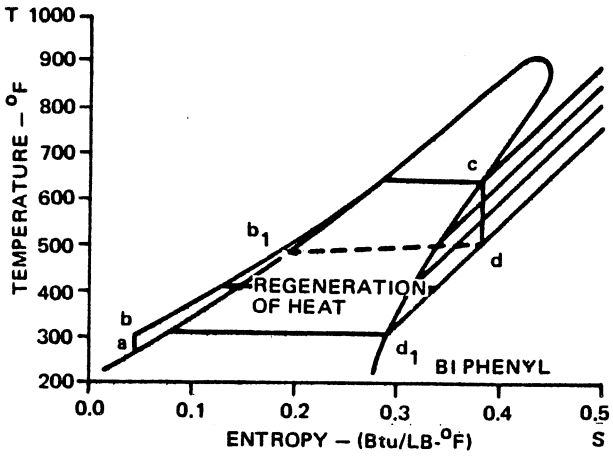

Figure 12-21. Rankine Cycle – Type B Fluid

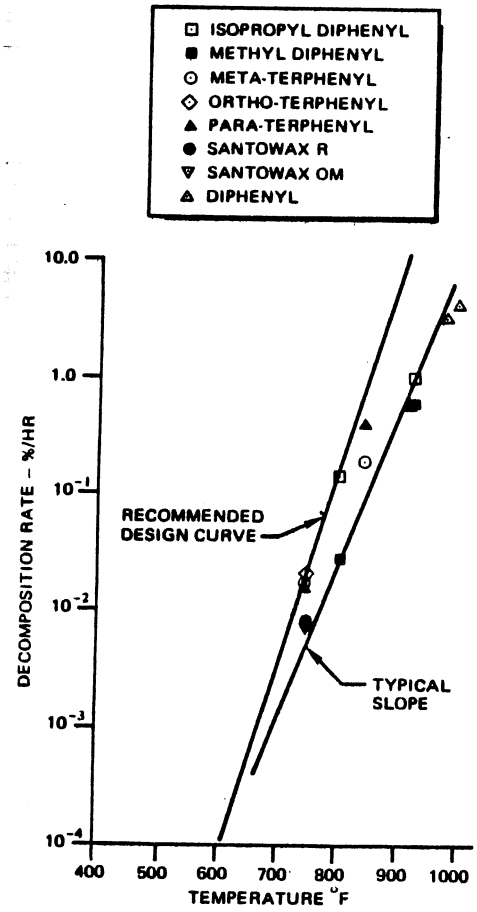

Figure 12-22. Thermal Decomposition Rates of Organic Fluids

of 700°F and above cause rapid pyrolysis of biphenyl and its derivatives. The products of thermal decomposition include high boiling polymers which will not vaporize in the boiler, and permanent gases that will not liquify in the condenser.

The undesirable characteristics of these decomposition products is obvious, and although some steps can be taken to remove them from the flow, it is not considered wise to operate an organic cycle at excessive temperatures. Examination of Figure 12-21 shows that the expansion from c to d causes the vapor to become increasingly superheated. The problem of liquid formation during expansion with subsequent impingement on the fast moving turbine blades does not arise in a Rankine cycle using a type B fluid. Superheat is therefore not required for a dry expansion.

Heat must be rejected from Type B working fluid at temperatures higher than the condensing temperature. A sizeable amount of heat must also be added to the fluid at less than the maximum cycle temperature. The high temperature heat rejection is a consequence of the superheat present in the prime mover exhaust. The low temperature heat addition is significant because the specific heat of these fluids is high while the latent heat of vaporization is quite low.

The thermal efficiency of a typical Type B Rankine cycle which does not employ regeneration is therefore much less than that of the Carnot cycle operating between the same temperature limits. Diagram efficiencies on the order of 60 percent are typical.

The thermal efficiency of a Type B Rankine cycle can be greatly improved by means of regeneration. The superheat in the prime mover exhaust can be used to preheat the fluid flowing from the pump to the boiler. The amount of heat which can be transferred in this way depends on the relative specific heats of the liquid and the vapor. The temperature differential necessary to drive heat through the regenerative heat exchanger is established at the low temperature end of the system as indicated in Figure 12-23. This will normally be accomplished by subcooling the liquid as it leaves the condensor, a practice which is desirable for efficient pump operation.

Figure 12-24 shows the thermal efficiency of some ideal Type B Rankine cycles, with and without regeneration using biphenyl as the working fluid.

C. Regenerative Rankine Cycles Using Type A Fluids – It has frequently been assumed that liquid metals were necessary ingredients in high

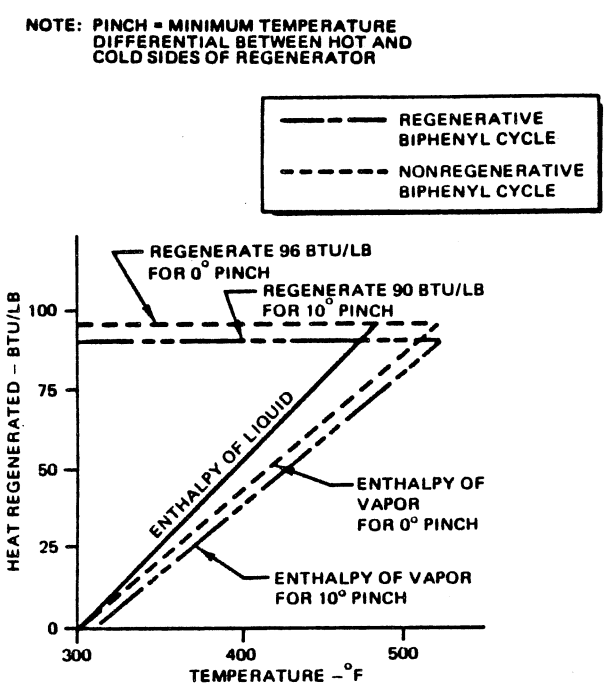

Figure 12-23. Regenerator Analysis for Biphenyl Rankine Cycle

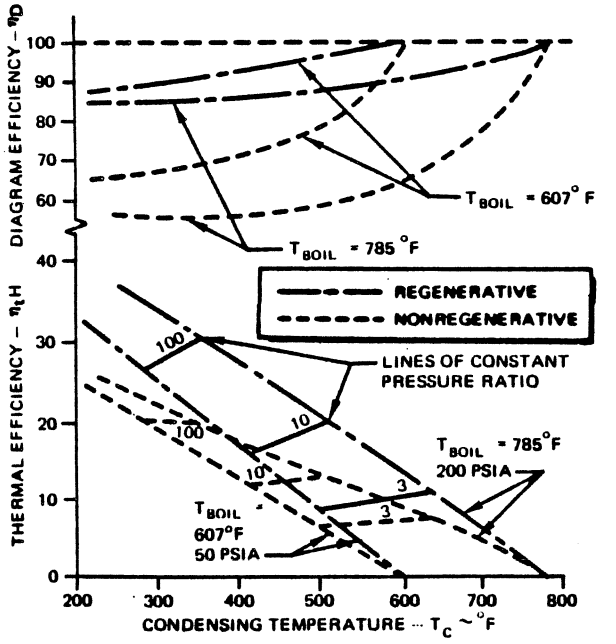

Figure 12-24. Thermal and Diagram Efficiencies for Type B Rankine Cycle (Biphenyl)

temperature Rankine cycle space power plants. The organic working fluids do not exhibit the thermal stability necessary to operate at temperatures above 700°F. Most of the nonmetallic inorganic working fluids, such as water, have critical temperatures which are well below the temperature range of interest. Water can, however, be used in a Rankine cycle with very high peak temperatures by the simple expedient of superheating the water vapor after it has been boiled at a lower temperature. For low-cycle pressure ratios, the expander exhaust is highly superheated, permitting regeneration to the liquid flowing from the pump.

Figure 12-25 shows a T-S diagram for a regenerative steam Rankine cycle boiling at 200 psia (382°F), superheated to 1,600°F, and condensing at 20 psia (228°F). Regeneration is from d-d_1 to b-b_1. Regeneration increases the thermal efficiency from 25.4 percent to 30.2 percent.

Figures 12-26 and 12-27 show that large efficiency gains can be made at low pressure ratios, but the peak thermal efficiency is not improved because no regeneration is possible at high pressure ratios.

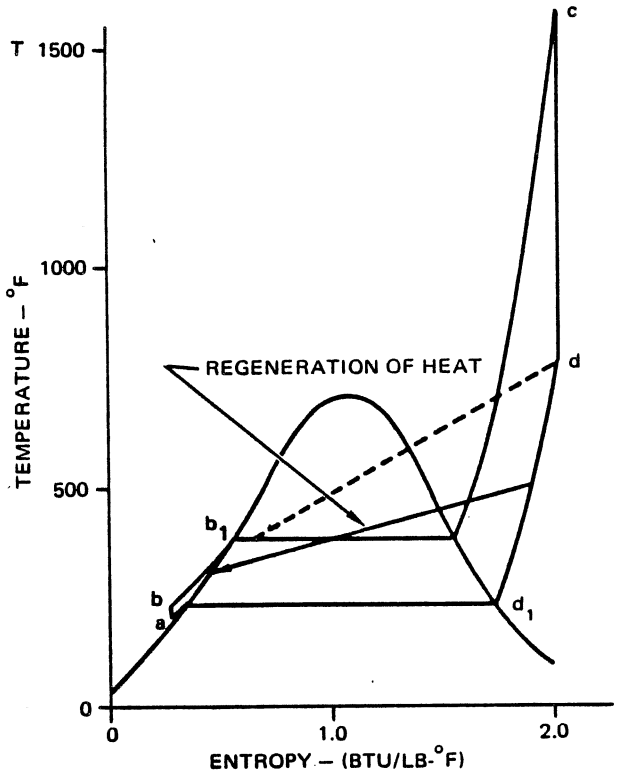

Figure 12-25. Regenerative Rankine Cycle

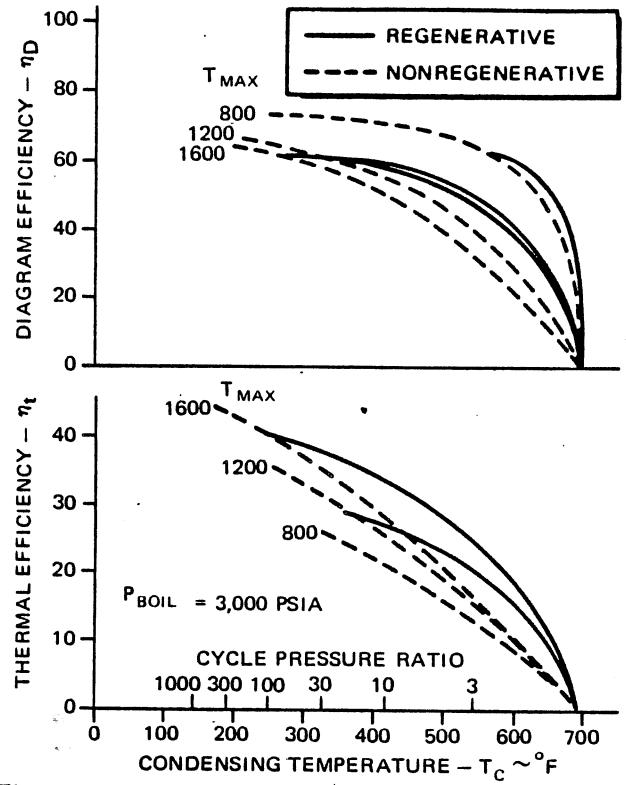

Figure 12-26. High Pressure Regenerative Rankine Cycle Efficiency

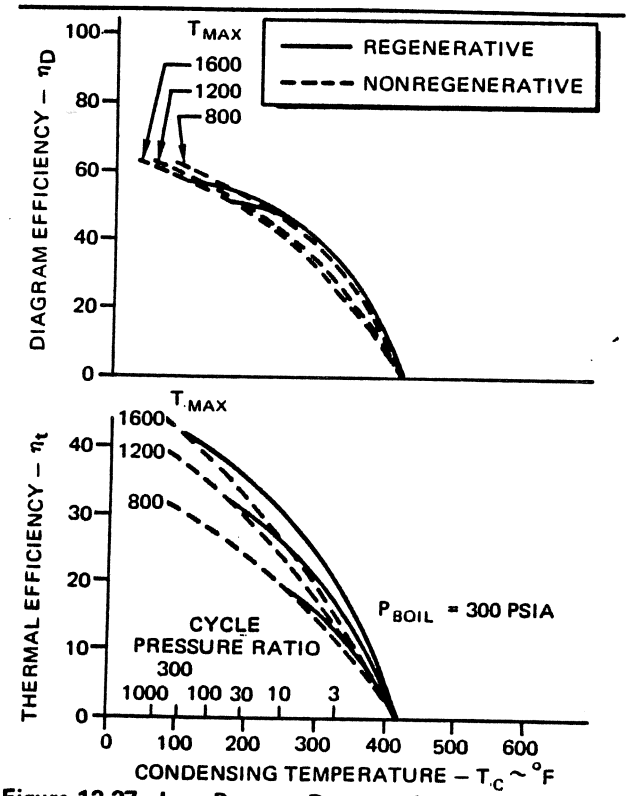

Figure 12-27. Low Pressure Regenerative Rankine Cycle Efficiency

12-7.2.1.2 Supercritical Cycles

A logical extension of the regenerative Rankine cycle with superheat is a thermodynamic cycle which uses a maximum cycle pressure in excess of the critical pressure of the fluid. The two such cycles to be discussed here are designated the supercritical Rankine cycle and the Feher cycle. T-S diagrams for these two cycles are shown in Figures 12-28 and 12-29.

A. Supercritical Rankine Cycle – A conventional Rankine cycle is characterized by boiling of the working fluid during heat addition and condensation of the working fluid during heat rejection from the cycle. If the maximum pressure in a Rankine cycle is higher than the critical pressure of the working fluid, the heat addition will be characterized by expansion of the fluid, without phase change, and the cycle is termed a supercritical Rankine cycle.

The statement that there is no phase change during heat addition, means that there is no liquid-vapor interface within the fluid passages. The fluid leaving the pump is a liquid, since it is a single-phase fluid which exists at a temperature less than the critical temperature and the pressure is greater than the vapor pressure of the fluid. The fluid which expands in the prime mover is a gas, since it is a single-phase

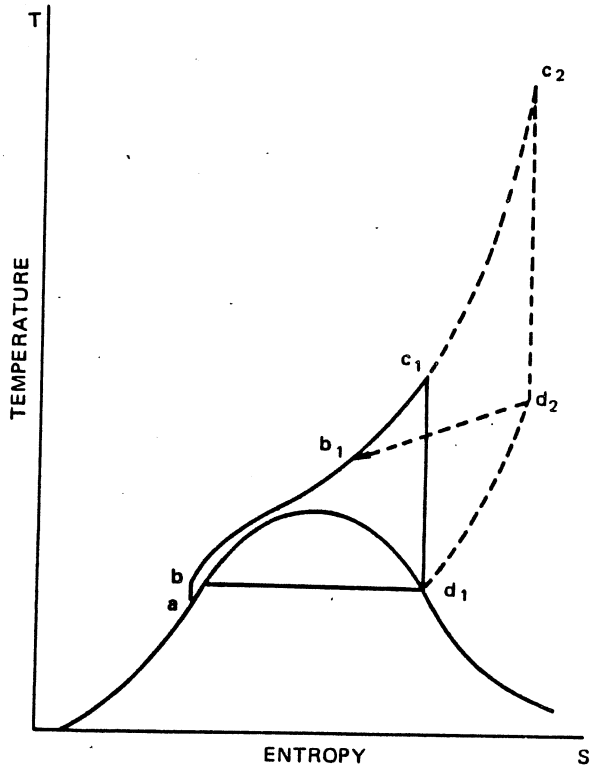

Figure 12-28. Supercritical Rankine Cycle

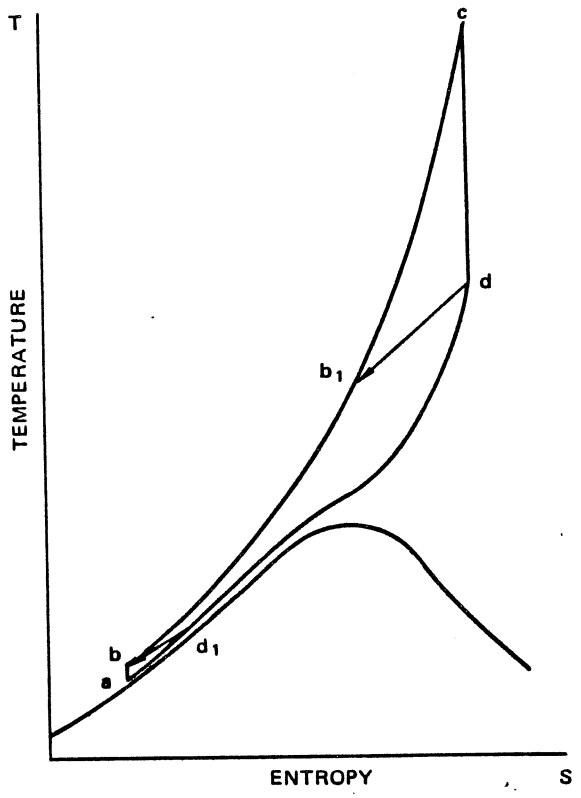

Figure 12-29. Feher Cycle

fluid which exists at a temperature in excess of its critical temperature. The heat rejection and condensation processes in a supercritical Rankine cycle are the same as those encountered in a conventional Rankine cycle.

The solid lines in Figure 12-28 show a nonregenerative supercritical Rankine cycle while the dotted lines indicate a regenerative cycle. In general the thermal efficiency for the nonregenerative cycle will be low compared to that of a Carnot cycle operating between the extremes of temperature indicated, due to the wide range of temperatures over which heat is added. The thermal efficiency of the regenerative supercritical Rankine cycle can be quite high, since low temperature heat addition in the cycle is provided by heat rejection from the prime mover exhaust.

Figure 12-30 presents supercritical cycle temperature-entropy diagrams for a Type A and Type B fluid. Figure 12-31 shows thermal and diagram efficiencies for several fluids as a function of pressure ratio.

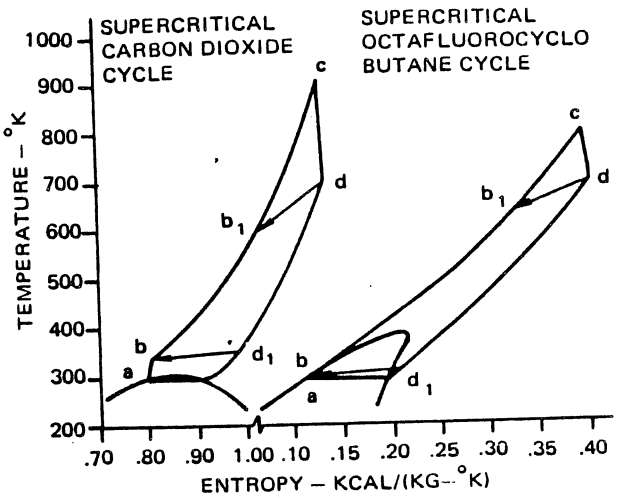

Figure 12-30. Supercritical Rankine Cycles for Type A and B Fluids

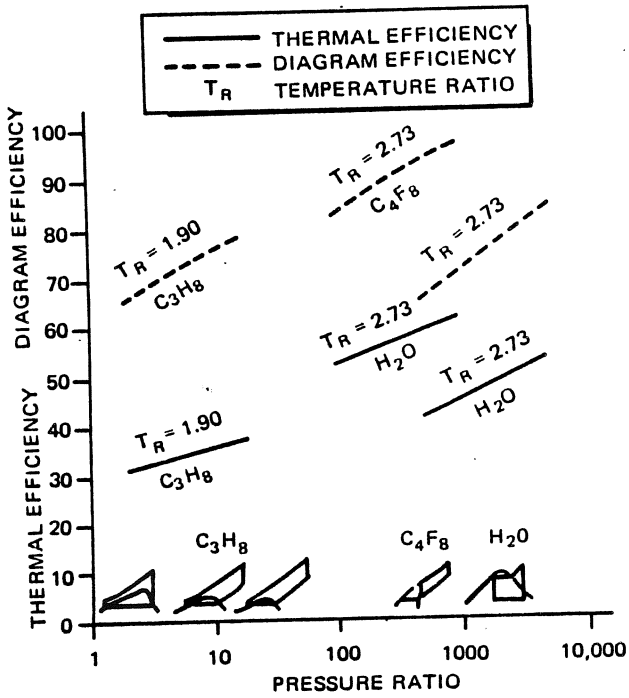

Figure 12-31. Supercritical Rankine Cycle Efficiency

B. Feher Cycle – The Feher cycle shown in Figure 12-29 is a further extension into the supercritical region of the concepts illustrated by the supercritical Rankine cycle discussed in A. In the Feher cycle, the minimum cycle pressure is above the critical pressure of the working fluid. There is no phase change during either heat addition or heat rejection from the cycle. In this respect, the Feher cycle resembles the Brayton cycle and other gaseous compression cycles since no liquid-vapor interfaces are formed.

In both the supercritical Rankine cycle and the Feher cycle, however, the fluid is in a liquid state when it is compressed, and a vapor or gaseous state during expansion. It is the use of liquid compression which gives these two cycles their interesting characteristics.

The Feher cycle without regeneration has a very low diagram efficiency relative to the extreme cycle temperature. This is readily corrected by the use of a regenerative heat exchanger. The Feher cycle illustrated in Figure 12-29 is a regenerative cycle. Figure 12-32 shows some ideal efficiency data for the Feher cycle.

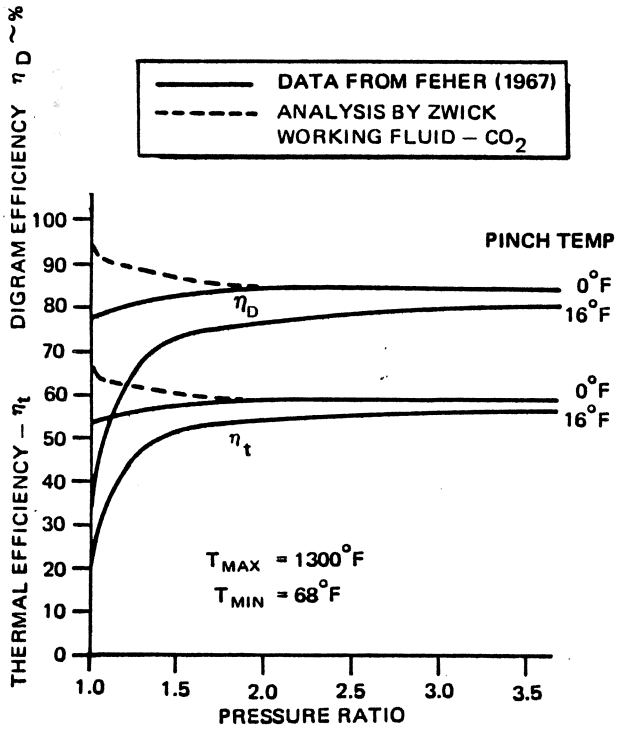

Figure 12-32. Feher Cycle Efficiency

12-7.2.2 Real Gaseous Compression Cycles

Figure 12-16d is a typical temperature-entropy diagram for a gas in the region far above the critical temperature where essentially perfect gas behavior occurs. This type of diagram is of interest for gas-compression heat engine cycles, such as the Brayton, Stirling and Ericsson cycles.

12-7.2.2.1 Brayton Cycles

The Brayton cycle, or as it is sometimes designated the Joule cycle, is a gaseous compression cycle using working fluids whose critical temperatures are far below the lowest temperatures found in the system.

A. The Basic Brayton Cycle – Figure 12-33 shows a Brayton cycle which has no regeneration. From a to b, the working fluid is compressed isentropically. From b to c, heat is added at constant pressure. From c to d, there is an isentropic expansion through a prime mover. From d to a, constant pressure heat rejection occurs.

In computing the thermal efficiency of the cycle, the compression work must be subtracted from the output of the expansion engine. The work of compression is quite large in the typical Brayton cycle. The thermal efficiency of a Brayton cycle is less than that of an ideal Carnot engine, because heat is added to and rejected from the cycle as sensible heat of the working fluid, and this takes place over a range of temperatures.

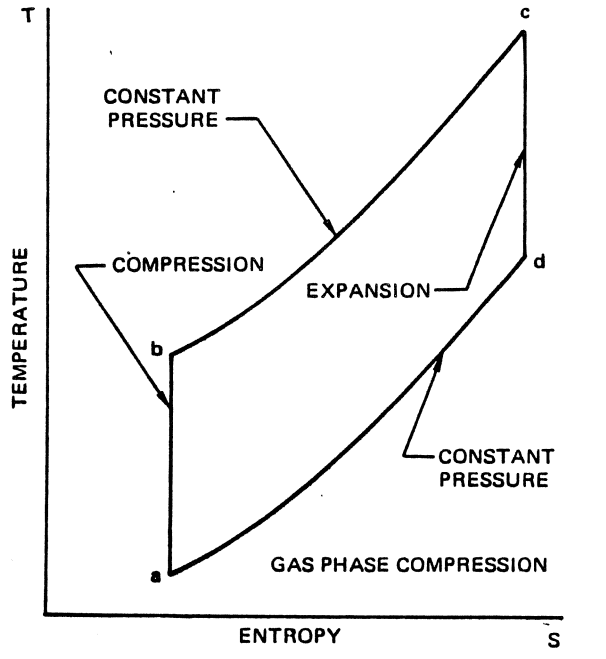

Figure 12-33. Brayton Cycle

The limiting case, for which b approaches c, has constant temperature heat addition and heat rejection, but the work output is zero because the compression work is equal to the expansion work. Another limiting case is the one which occurs when the Brayton cycle pressure ratio becomes infinitely large. For this case the thermal efficiency of the cycle will approach that of a Carnot cycle.

The thermal efficiency of an ideal Brayton cycle is shown in Figure 12-34 as a function of pressure ratio and γ, the specific heat ratio of the gas. It is clear that monatomic gases with $\gamma = 1.67$ have a decided advantage over other Brayton cycle working fluids. The thermal efficiency of the ideal Brayton cycle is a function of pressure ratio and γ only. It does not depend on the cycle temperature ratio, although the minimum temperature ratio is a function of the pressure ratio. In a real Brayton cycle, the temperature ratio has an important bearing on the thermal efficiency, and the cycle efficiency is greatly influenced by the performance of the components.

The Brayton cycle and related cycles are widely used in the fields of power and propulsion. Brayton cycles are used in turboprops and turbojets for aircraft and in many ground power installations.

B. Regenerative Brayton Cycle – A heat exchanger which transfers heat from the prime mover exhaust into the compressor discharge converts a conventional Brayton cycle into a regenerative cycle. The T-S diagram of this cycle is shown in Figure 12-35. After isentropic compression from a to b, heat is added in the regenerator between b and b_1. Additional heat is added from an external heat source between b_1 and c. Isentropic expansion between c and d is followed by heat rejection from the gas between d and d_1 in the regenerator. Heat rejection out of the cycle occurs between d_1 and a, the inlet to the compressor. A Brayton cycle can only be regenerated if the temperature at d is greater than the temperature at b. For each value of cycle temperature ratio, T_a/T_c, there is a limiting pressure ratio, P_b/P_a above which regeneration cannot take place.

Thermal efficiency of the regenerative Brayton cycle is less than that of the corresponding Carnot engine because heat addition occurs over a range of temperatures. The range is greatly reduced by the regenerator, but it can only be eliminated as a limiting case. The ideal regenerative Brayton cycle approaches Carnot efficiency only when the pressure ratio approaches 1.0. This is in contrast to the simple Brayton cycle which has zero efficiency at a pressure ratio of 1.0 but approaches Carnot efficiency as the pressure ratio increases. Figure 12-36 shows the thermal and diagram efficiencies of some regenerative Brayton cycles. Note that the efficiency becomes the same as that of the nonregenerative cycle at the regenerative limit.

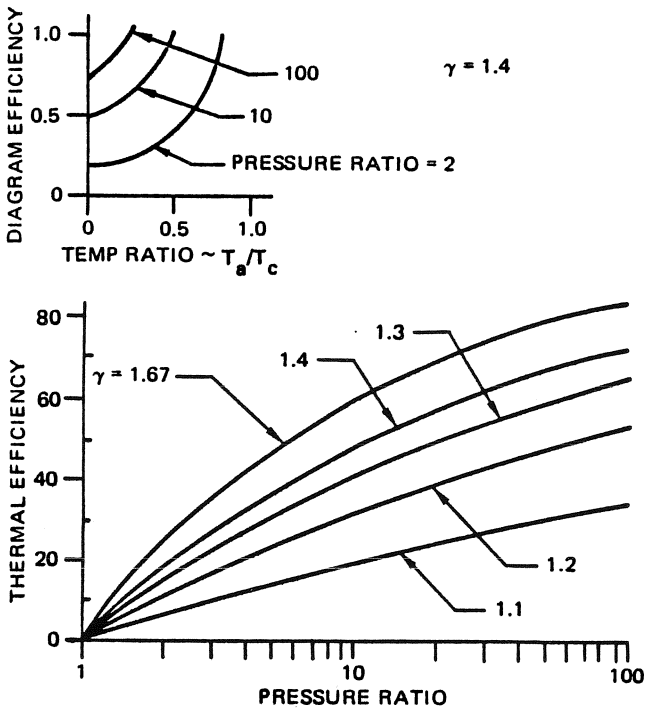

Figure 12-34. Brayton Cycle Efficiency

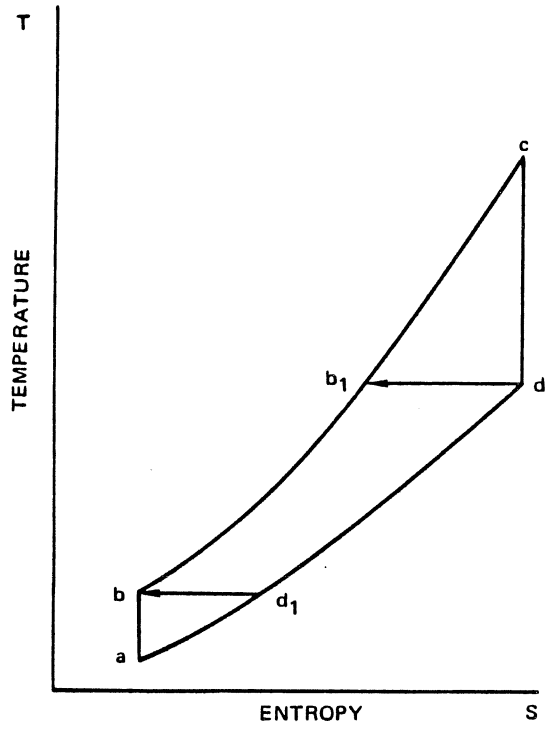

Figure 12-35. Regenerative Brayton Cycle

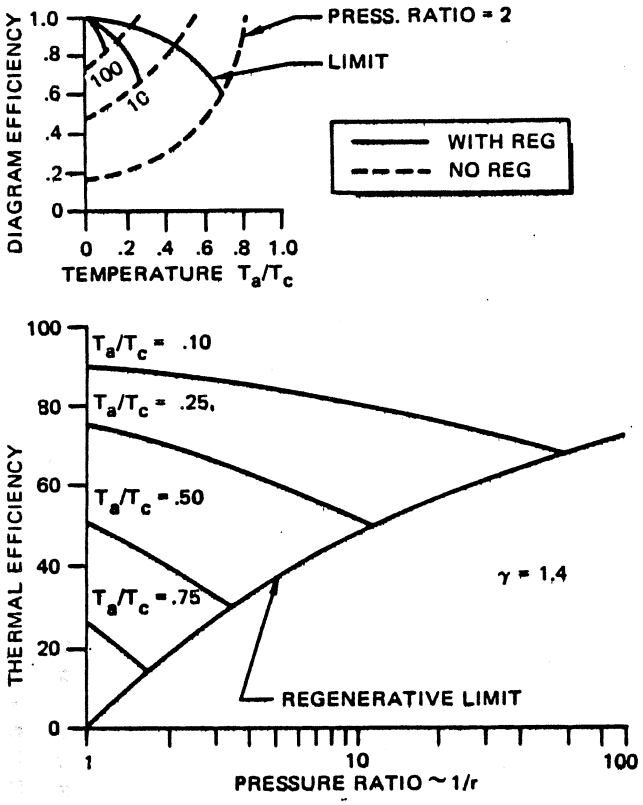

Figure 12-36. Brayton Cycle – With Regeneration

The regenerative Brayton cycle, like the conventional Brayton cycle, is quite sensitive to the performance of its components. The sensitivity is less marked, however, when regeneration is used, since some of the inefficiency of expansion is recovered in the form of heat input to the fluid flowing from the compressor. Regeneration is becoming increasingly important in Brayton cycle applications. The improved performance frequently offsets the cost and weight of the regenerator. Many modern industrial and automotive gas turbines incorporate regeneration.

12-7.2.2.2 Stirling Cycle

The Stirling cycle T-S diagram, Figure 12-37, involves constant volume and constant temperature processes. Between a and b, constant volume heating occurs, accompanied by an increase in the pressure level of the working fluid. Between b and c, constant temperature heating takes place as the volume increases and the pressure falls. Between c and d, constant volume cooling occurs with a corresponding reduction in pressure. Finally, from d to a an isothermal compression occurs during which the volume is reduced, heat is rejected and

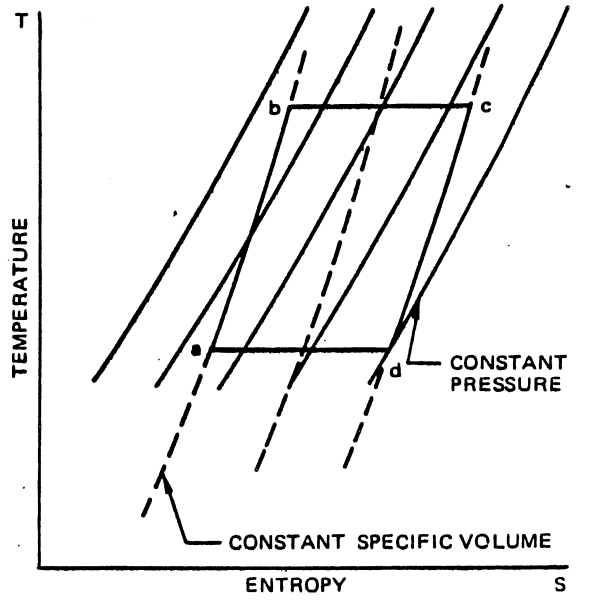

Figure 12-37. Stirling Cycle

the pressure rises. The expressions that describe the Stirling cycle, are apparently self-contradictory. Process a-b is a constant volume compression; b-c is constant temperature heating; c-d is constant volume expansion; while d-a is constant temperature heat rejection.

The Stirling cycle is basically a regenerative cycle, and it is clear that for a fluid with constant specific heat, the ideal cycle will have Carnot efficiency. Under these circumstances all of the heat addition to the cycle takes place at the maximum cycle temperature while all of the heat rejection occurs at the minimum cycle temperature.

The performance of a real Stirling cycle engine depends on the efficiency of the components used during the gaseous compression and expansion processes. The departure from ideal performance involves the losses in the expansion and compression processes and the finite temperature differences required to transfer heat throughout the cycle.

12-7.2.2.3 Ericsson Cycle

The Ericsson cycle, which also includes regeneration, consists of two isothermal and two isobaric processes, as shown in Figure 12-38. Heat, from an external source, is added to the working fluid (gas) at constant temperature T_H, during expansion in a cylinder along path a-b. The gas then leaves the cylinder and passes through a regenerator where it rejects heat at constant pressure along path b-c. The gas then reenters the cylinder where it is compressed at constant temperature along path c-d by rejecting heat to an external sink. The gas then flows through the regenerator in the opposite direction, absorbing heat at constant pressure along path d-a.

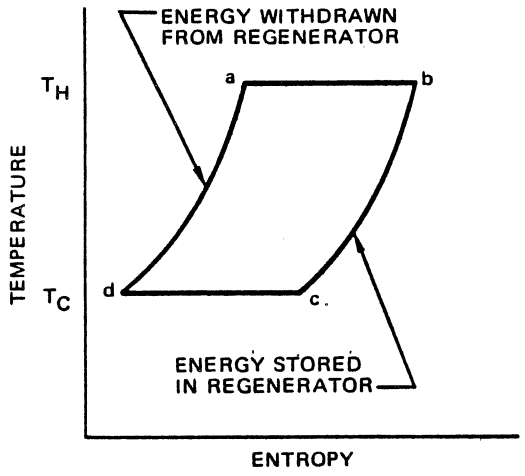

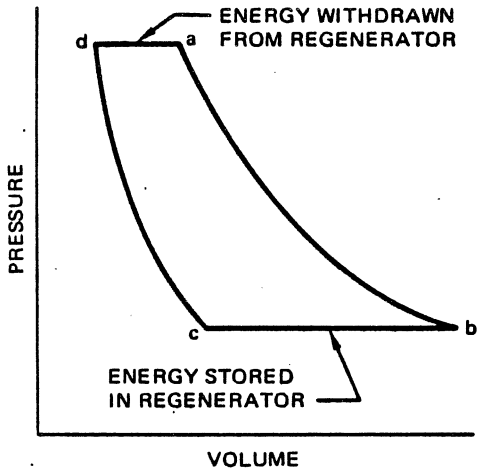

Figure 12-38. Regenerative Ericsson Cycle

In reciprocating engine cycles such as the Ericsson cycle and the Stirling cycle, the regenerator usually is a chamber that contains a high-heat-content material with a high surface-to-weight ratio, such as stainless steel wool. Hot gas passes through the chamber in one direction and the cooled gas passes through in the opposite direction, creating a temperature gradient across the regenerator.

Ericsson engines have been used to a limited extent, but their mean-effective-pressure is too low for them to be a competitor of modern reciprocating engines.

12-7.3 Refrigeration Cycles

Paragraphs 12-7.1 and 12-7.2 discussed power cycles wherein heat energy is converted to work and rejected heat. If the cycle direction is reversed, work is converted to refrigeration. The differences between a power cycle and a refrigeration (reverse) cycle are illustrated schematically in Figure 12-39, and diagramatically in Figure 12-40 for the Carnot cycle.

In the Carnot refrigeration cycle, as shown in Figure 12-40, the system fluid (refrigerant) is isentropically compressed along cd from a cold temperature T_A to a temperature T_R that is higher than T_O, the temperature of some available heat sink. The system then rejects heat at constant temperature T_R along da. The refrigerant temperature is then decreased to T_A by isentropic expansion ab, and the refrigerant absorbs heat from bodies at temperatures above T_A, typically a refrigerator at T_C.

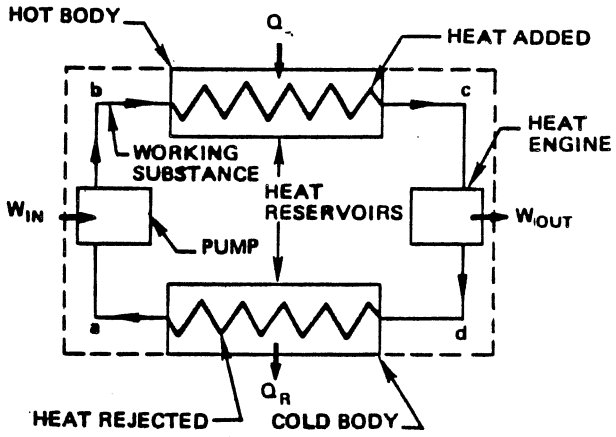

(a) POWER SYSTEM

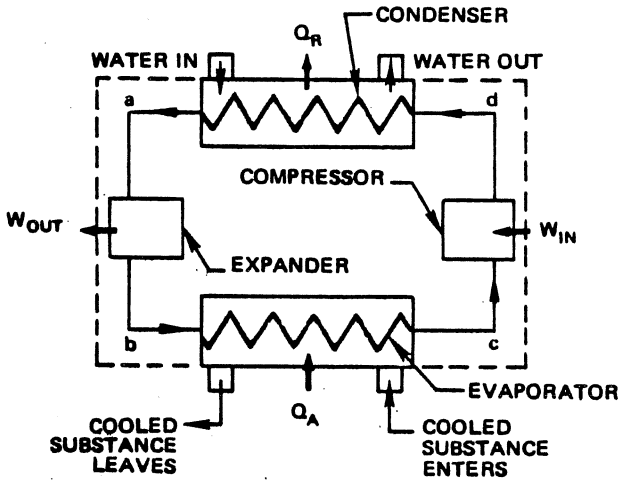

(b) REFRIGERATION SYSTEM

Figure 12-39. Comparison of Power and Refrigeration Systems

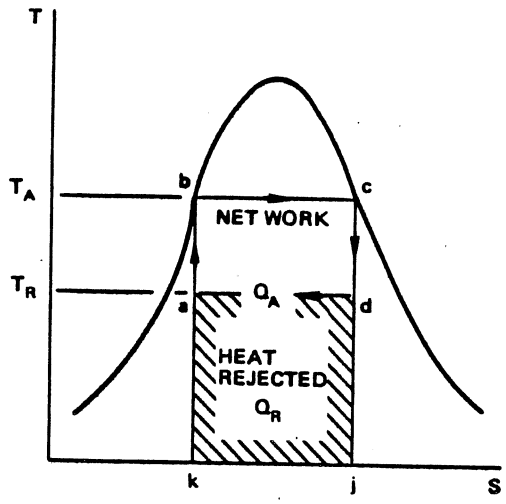

(a) POWER CYCLE

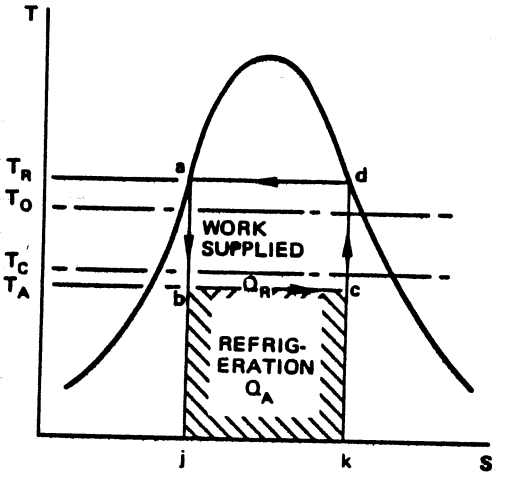

(b) REFRIGERATION CYCLE

Figure 12-40. Comparison of Power and Refrigeration Cycles

From a performance viewpoint, refrigerants should have a high latent heat at the evaporator temperature, a low specific volume, and low saturation pressure at normal operating temperatures. Other desirable performance features include: good thermal conductivity, wetting ability, low toxicity, chemical inertness and stability, low viscosity, high critical temperature, high dielectric strength, and a freezing temperature that is lower than the lowest temperature in its cycle. Table 12-8 lists some physical properties of frequently used refrigerants.

Figure 14-40b shows that the refrigeration capability Q_A of the reverse cycle is proportional to the area jbck, work supplied W is proportional to the area abcd, and the heat rejected Q_R is proportional to the area jadk. Therefore, the work supplied ($W = Q_A - Q_R$) is a negative number because $Q_R > Q_A$. In a reverse cycle,

Table 12-8. Refrigerant Data

	Formula	Pres at 5°F	Pres at 86°F	Q_A Btu/lb
Ammonia	NH_3	34.3	169.2	474.4
Butane	C_4H_{10}	8.2	41.6	123.5
Carbon dioxide	CO_2	332.2	1045.7	56.7
Carrene 1	CH_2Cl_2	1.16	10.6	134.1
Carrene 7	(a)	31.1	128.1	59.8
Freon 11	CCl_3F	2.93	18.3	67.5
Freon 12	CCl_2F_2	26.5	107.9	51.1
Freon 22	$CHClF_2$	43.0	174.5	69.3
Freon 113	$C_2Cl_3F_3$	0.98	7.9	53.67
Freon 114	$C_2Cl_2F_4$	6.8	36.7	43.1
Methyl chloride	CH_3Cl	21.2	94.7	150.3
Sulfur dioxide	SO_2	11.8	66.4	141.4
Propane	C_2H_8	41.9	156.2	123.0

(a) An azeotropic mixture of Freon 12 and $C_2H_4F_2$

efficiency is measured by a ratio, generally greater than one, called the coefficient of performance (COP).

$$COP = \frac{\text{output}}{\text{input}} = \frac{Q_A}{-W} = \frac{Q_A}{Q_R - Q_A} = \frac{T_A}{T_R - T_A} \quad (67)$$

Equation 67 defines the highest possible COP for all reversible cycles operating between the temperature limits T_R and T_A. As a real cycle approaches the ideal Carnot cycle, T_O approaches T_R and T_C approaches T_A. For maximum coefficient of performance, T_R should be the lowest possible temperature and T_A should be the highest possible temperature.

The most common method of producing refrigeration is by a vapor-compression system, shown schematically in Figure 12-39b and diagramatically in Figure 12-40b. Figure 12-41 is a modification of Figure 12-40b that more accurately describes the cycle. The vapor is

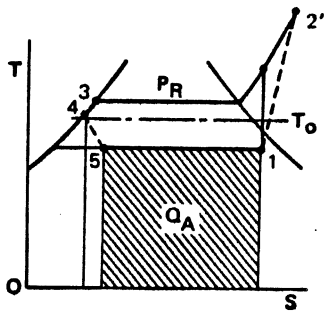

Figure 12-41. Ideal Vapor/Compression Refrigeration Cycle

compressed to raise its temperature (1 to 2'); and the condenser removes any superheat, the latent heat of vaporization, and generally subcools the liquid a small amount, say from 3 to 4 (Figure 12-41). The liquid leaves the condenser, passes through an expansion valve, reducing the pressure and vaporizing some of the refrigerant (4 to 5). The wet mixture enters the evaporator, absorbing heat Q_A from the surroundings (doing refrigeration) and increasing the percentage of vapor in the refrigerant mixture (5 to 1).

Other refrigeration systems include air-refrigeration, shown schematically and diagramatically in Figure 12-42; ammonia-water absorption shown schematically in Figure 12-43; and a cascade refrigeration system, shown schematically and diagramatically in Figure 12-44.

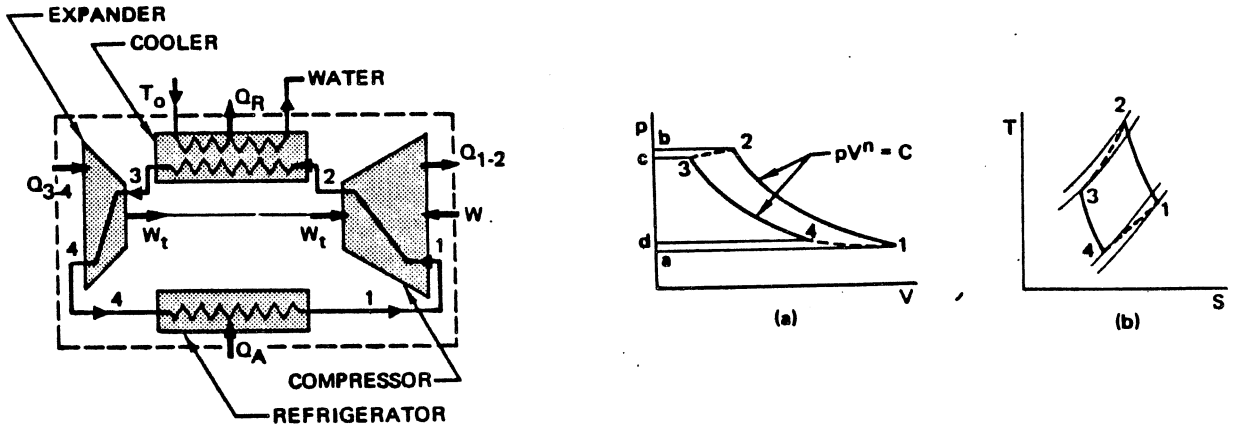

Figure 12-42. Air Refrigeration System

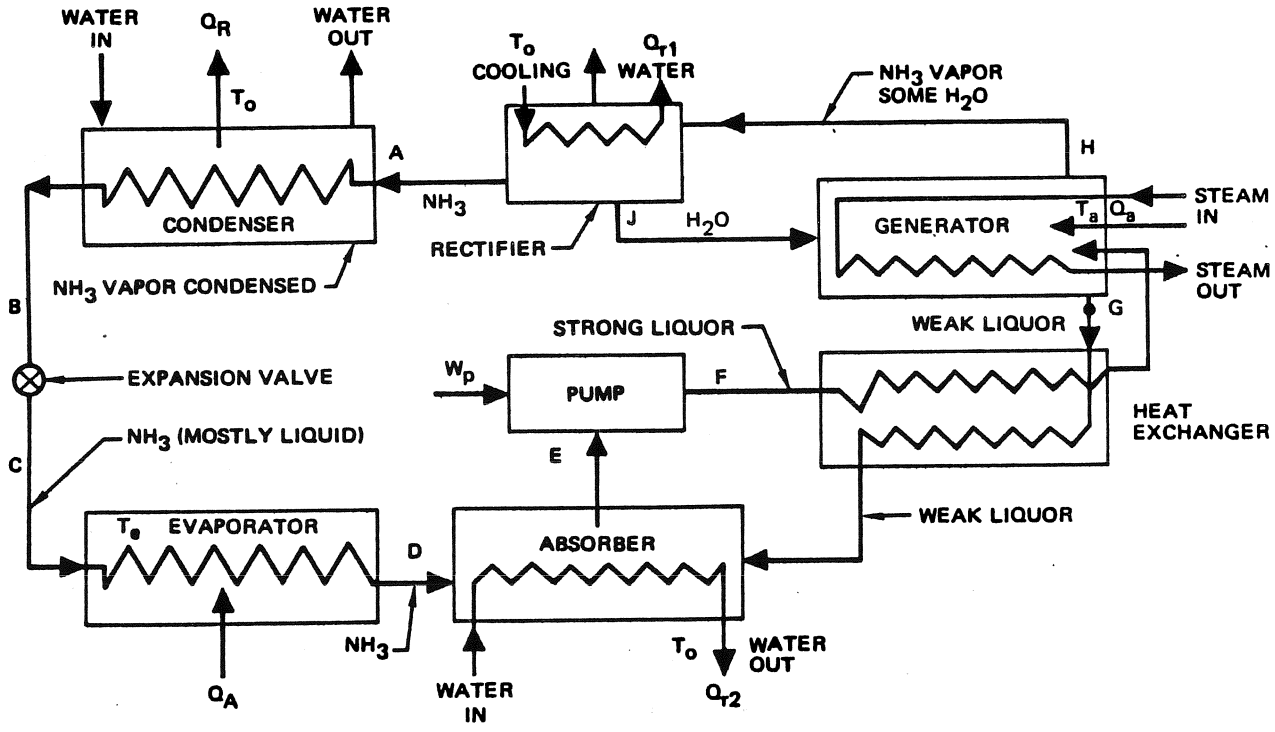

Figure 12-43. Ammonia-Water Absorption Refrigeration System

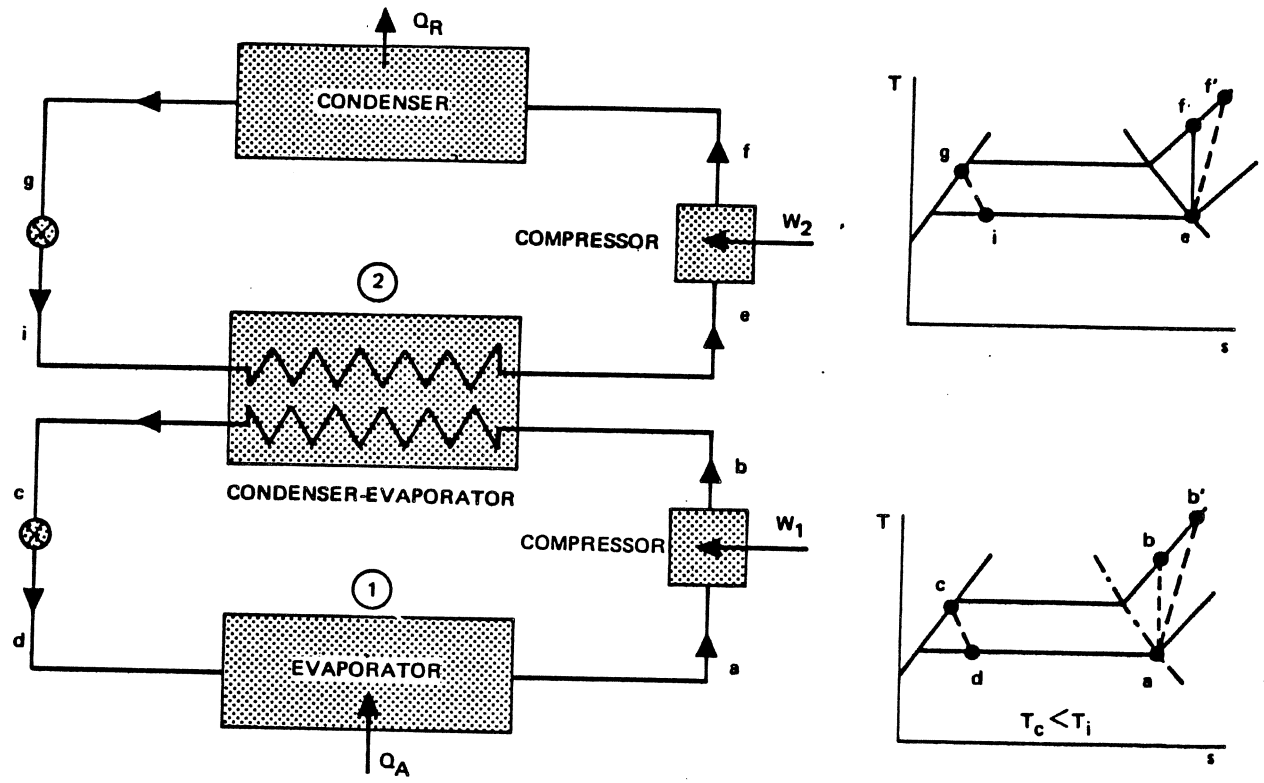

Figure 12-44. Cascade Refrigerating System

12-8 BIBLIOGRAPHY

1. Faires, V. M., *Thermodynamics,* Macmillan Co., New York, 1957

2. Obert, E. F., *Thermodynamics,* McGraw-Hill Book Co., New York, 1948

3. Marks, L. S., *Marks Handbook,* McGraw-Hill Book Co., New York, 1951

4. Lee, J. F., and Sears, F. W., *Thermodynamics,* Addison Wesley Publishing Co., Cambridge, 1952

5. Wylen, G. J., and Sonntag, R. E., *Fundamentals of Classical Thermodynamics,* John Wiley and Sons, Inc., New York, 1967

6. Angelino, G. *Perspectives for the Liquid-Phase Compression Gas Turbine,* ASME Paper No. 65-GT-111

7. Angelino, G., *Liquid-Phase Compression Gas Turbine for Space Power Applications,* Journal of Spacecraft and Rockets, Vol. 4 No. 2, February 1967

8. Douglas Aircraft Co., Inc., Pu-238 *Feher Cycle System for the Manned Orbiting Laboratory,* DAC-57957, December 1966

9. Feher, Ernest G., *The Supercritical Thermodynamic Power Cycle,* I.E.C.E.C. Conference, 1967

10. Zwick, E. B., and Zimmerman, R. L., *Space Vehicle Power Systems,* ARS, Vol. 29, No. 8, 1959

Section 14
HEAT TRANSFER

This section presents information on basic heat transfer processes for use in design analyses of rocket propulsion systems. Examples of applications of the data are included in appropriate sections of manuals PB-1 Liquid Propulsion Systems, and PC-1 Solid Propulsion Systems.

Whenever a temperature gradient exists within a system, or when two systems at different temperatures are brought into contact or are exposed to one another, energy is transferred. The process by which the energy transport takes place is known as heat transfer, and is a process by which the internal energy of a system is changed. The direction of net heat transfer is always from a point at a higher temperature to one at a lower temperature.

The fundamental modes of heat transfer are conduction, radiation, and convection. Conduction is the net transfer of energy within a fluid or solid due to the collision of molecules or to the motion of free electrons. Thermal radiation is energy transferred by electromagnetic waves that originate from a system due solely to the temperature of the system, and is the process for the transfer of energy from one point to another in the absence of a transporting medium. Convection is the transfer of energy resulting from fluid motion and involves the processes of conduction and fluid motion. Convection is most important as the mechanism of energy transfer between a solid surface and a liquid or gas.

Heat transfer processes can be either steady or unsteady. When the rate of heat flow in a system does not vary with time (when it is constant), the temperature of each and every point within the system remains the same and the heat transfer is steady or steady-state. The heat flow in a system is transient or unsteady when the temperatures within the system vary with time.

In practical applications, several modes of heat transfer occur simultaneously. For example, heating of a rocket nozzle includes convection and radiation to the surface, convection and radiation away from the surface, conduction through the surface structure, and, in the case of ablative materials, phase change and mass transfer.

14-1 BASIC LAWS OF HEAT TRANSFER

The steady-state one dimensional laws of heat transfer are presented here to illustrate the relative magnitudes and interactions of the basic methods of heat transfer. Later portions of Section 14 provide detailed information which can be used for the solution of more complex heat transfer problems.

14-1.1 Fundamentals of Conduction

When the direction of positive heat flow is in the direction of increasing distance, x, the elementary equation for one dimensional conduction in steady-state is:

$$q_k = -k A \frac{dT}{dx} \qquad (1)$$

which after integration reduces to:

$$q_k = A \frac{k}{L} (T_{hot} - T_{cold}) \qquad (2)$$

if k is independent of the temperature T

where:

q_k = Rate of heat flow, Btu/hr

A = Cross-section area, ft^2

$\frac{dT}{dx}$ = Temperature gradient, °F/ft

L = Length of the conductive path, ft

k = Thermal conductivity, Btu/hr-ft-°F

A k/L = Thermal conductance, Btu/hr-°F

The reciprocal of thermal conductance, called the thermal resistance, is:

$$R_k = \frac{L}{A k}, \text{ hr-°F/Btu} \qquad (3)$$

Since heat flows from points at higher temperatures to those at lower temperatures, equation 1 states that heat flow will be positive when the temperature gradient is negative as shown in Figure 14-1.

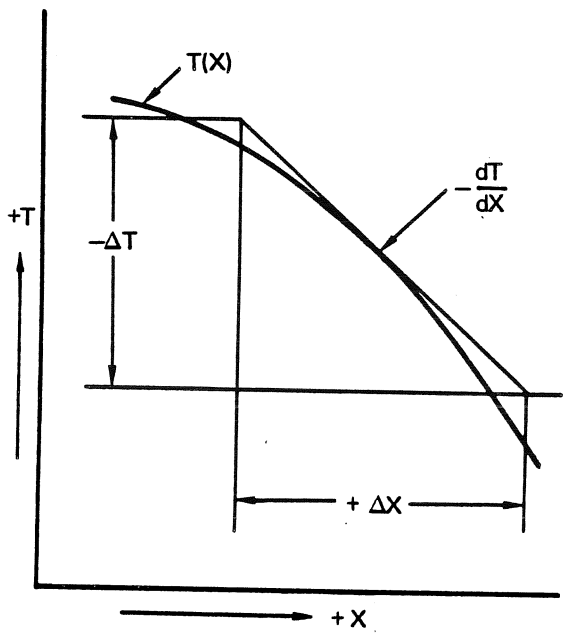

Figure 14-1. Conduction Heat Flow

Thermal conductivity, k, is a property of the material which, in general, varies with temperature. Figure 14-2 presents order of magnitude of thermal conductivity for various classes of material.

14-1.2 Fundamentals of Radiation

The elementary equation for heat flow from the surface of a perfect radiator (black body) is:

$$q_r = \sigma A_1 T_1^4 \quad (4)$$

where:

q_r = Rate of heat flow, Btu/hr

A_1 = Surface area, ft^2

T_1 = Surface temperature, °R

σ = Stefan-Boltzmann constant, 0.1714×10^{-8}, Btu/hr-ft^2-°R^4.

If a black body radiates to a black surfaced enclosure which completely surrounds it, the net rate of radiant heat transfer is:

$$q_r = \sigma A_1 (T_1^4 - T_2^4) \quad (5)$$

where:

T_2 = Surrounding body temperature in °R.

Real bodies emit radiation at a lower rate than black bodies. If, at a temperature equal to a black body, they emit a constant fraction of black-body emission at each wave length, they are called gray bodies. The net rate of heat transfer from a gray body at temperature T_1 to a black surrounding body at temperature T_2 is:

$$q_r = \sigma A_1 \epsilon_1 (T_1^4 - T_2^4) \quad (6)$$

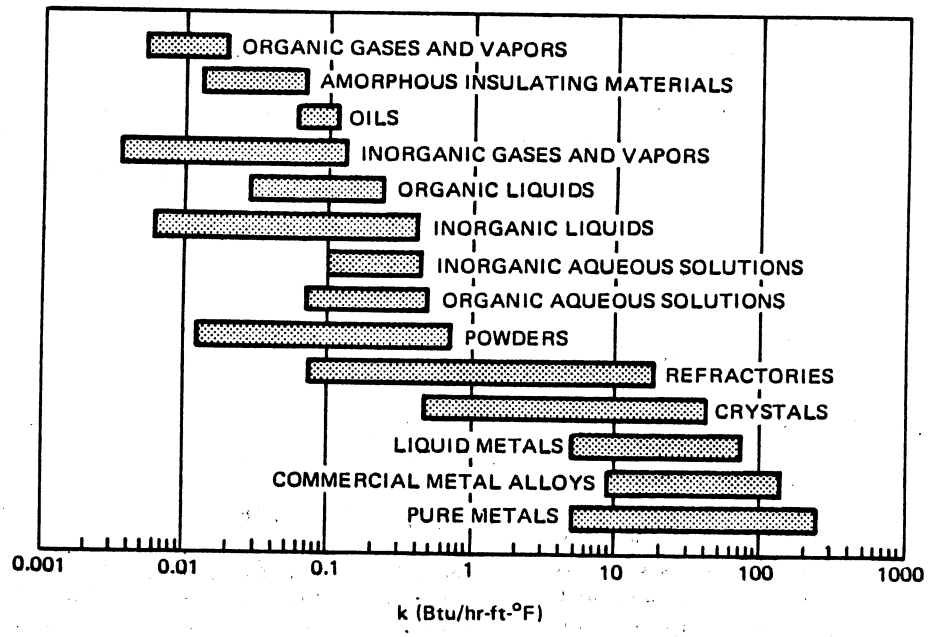

Figure 14-2. Order-of-Magnitude of Thermal Conductivity

where ϵ_1, the emittance of the gray surface, is equal to the ratio of radiant emission from the gray surface to that from a black surface at the same temperature. If neither of the two bodies is a perfect radiator and if the two bodies possess a given geometrical relationship to each other, the net radiation heat transfer between them is given by:

$$q_r = \sigma A_1 \mathcal{F}_{1-2} (T_1^4 - T_2^4) \quad (7)$$

where $\mathcal{F}_{1-2}$ is a modulus which modifies the equation for perfect radiators to account for the emittances, and for relative geometries of the actual bodies.

An equivalent radiation thermal conductance can be defined so that:

$$q_r = K_r (T_1 - T_2) \quad (8)$$

where:

$$K_r = \sigma A_1 \mathcal{F}_{1-2} (T_1^2 + T_2^2) (T_1 + T_2) \text{ Btu/hr-}^\circ\text{R} \quad (9)$$

The unit thermal conductance for radiation, h_r, is:

$$h_r = \frac{K_r}{A_1}$$

$$= \sigma \mathcal{F}_{1-2} (T_1^2 + T_2^2) (T_1 + T_2) \text{ Btu/hr-ft}^2\text{-}^\circ\text{R} \quad (10)$$

and the thermal resistance for radiation, R_r, is:

$$R_r = \frac{1}{K_r} = \frac{1}{\sigma A_1 \mathcal{F}_{12} (T_1^2 + T_2^2) (T_1 + T_2)} \quad (11)$$

14-1.3 Fundamentals of Convection

The rate of heat transfer by convection between a surface and a fluid may be computed by the relationship:

$$q_c = \bar{h}_c A \Delta T \quad (12)$$

where:

q_c = Rate of heat transfer by convection, Btu/hr

A = Heat transfer area, ft^2

ΔT = Difference between the surface temperature and the fluid temperature T_∞ at a distance remote from the surface, °F

$\bar{h}_c$ = Average convective heat transfer coefficient, Btu/hr-ft^2-°F

The thermal conductance for convective heat transfer is defined as:

$$K_c = \bar{h}_c A \quad (13)$$

and the thermal resistance for convective heat transfer is defined as:

$$R_c = \frac{1}{\bar{h}_c A} \quad (14)$$

Convective heat transfer results from relative motion between a fluid and a solid immersed in the fluid when the two are at different temperatures. The relative motion of the fluid with respect to the solid can be induced by either one of two processes, and can be either one of two types. When the fluid is set in motion solely as a result of density differences, due to temperature variations in the fluid, it is called free or natural convection. It is called forced convection when the motion is caused solely by some external force, such as a pressure difference created by a fan or blower or the combustion of propellants within a rocket engine.

When the fluid moves in smooth layers or streamlines and each particle follows a smooth, orderly, and continuous path, the type of flow is called laminar, and heat is transferred between the fluid layers by molecular motion. In turbulent flow, the conduction mechanism is modified and aided by eddies which transport particles of fluid across streamlines and transfer energy by mixing with other particles of the fluid.

In general, heat transfer rates for free convection are lower than for forced convection because of the slower fluid motion associated with free convection. Heat transfer rates are also generally lower for laminar than turbulent flow because the increased mixing of the fluid associated with turbulent flow enhances and increases its heat transfer over that for laminar flow.

Table 14-1 presents orders of magnitude of average heat transfer coefficients for typical fluids.

Table 14-1. Order-of-Magnitude of Convective Heat-Transfer Coefficients

Condition	h_c in Btu/hr-ft^2-F
Air, free convection	1–5
Superheated stream or air, forced convection	5–50
Oil, forced convection	10–300
Water, forced convection	50–2000
Water, boiling	500–10,000
Stream condensing	1000–20,000

14-1.4 Combined Heat Transfer

In practice, heat is usually transferred in steps through a number of different series-connected sections, the transfer frequently occurring by two mechanisms in parallel for a given section in the system. For example, in a rocket nozzle, heat is transferred from the combustion products to the nozzle walls by convection and radiation acting in parallel. In the steady state, heat is conducted through the nozzle wall at the same rate. After passing through the wall, the heat flows through the third section of the system by convection and radiation to the coolant or heat sink. Figure 14-3 illustrates the physical system and the thermal circuit for this type of heat transfer system. The energy equation for this system is:

$$q = q_{cg} + q_{rg} = q_k = q_{cc} + q_{rc} \qquad (15)$$

which can also be expressed as:

$$q = (K_c + K_r)(T_g - T_{sg}) = K_k (T_{sg} - T_{sc})$$
$$= (K_c + K_r)(T_{sc} - T_c) \qquad (16)$$

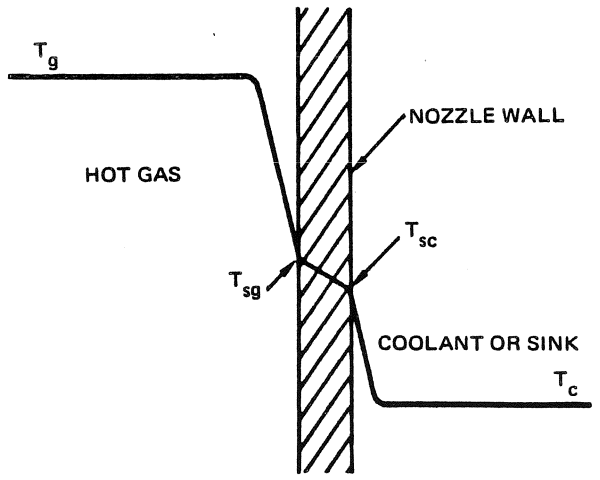

PHYSICAL SYSTEM

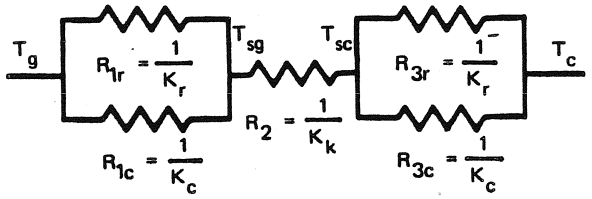

THERMAL CIRCUIT

Figure 14-3. Heat Transfer System

or:

$$q = \frac{T_g - T_{sg}}{R_1} = \frac{T_{sg} - T_{sc}}{R_2} = \frac{T_{sc} - T_c}{R_3} \qquad (17)$$

If the temperatures of the hot gas and the coolant or sink are known, the intermediate temperatures can be eliminated by algebraic addition of the equalities of equation 17 resulting in:

$$q = \frac{T_g - T_c}{R_1 + R_2 + R_3} = \frac{\Delta T_{total}}{R_1 + R_2 + R_3} \qquad (18)$$

Equation 18 expresses the heat flow rate in terms of an overall temperature potential and the heat-transfer characteristics of individual sections in the flow path. From these relations, it is possible to evaluate quantitatively the importance of each individual thermal resistance in the path.

There are certain types of problems, notably in the design of heat exchangers, where it is convenient to combine the individual resistances or conductances of the thermal system into one quantity called the overall unit conductance, the overall transmittance, or the overall coefficient of heat transfer, U. Writing equation 18 in terms of U gives:

$$q = UA\,\Delta T_{total} \qquad (19)$$

where, for the general case of n thermal sections:

$$UA = \frac{1}{R_1 + R_2 + \ldots + R_n} = \frac{1}{\frac{1}{K_1} + \frac{1}{K_2} + \ldots + \frac{1}{Kn}} \qquad (20)$$

14-1.5 Dimensional Analysis

The majority of fluid mechanics and heat transfer problems do not lend themselves to direct analysis and, consequently, their solutions are based on empirical equations obtained by correlating experimental data. Dimensional analysis greatly simplifies the categorization and application of experimental data by minimizing the number of problem variables.

Consider a case where it is desirable to solve for a parameter H which is a function of geometry and six other variables: J, K, L, M, N, and P.

$$H = f[\text{Geometry, J, K, L, M, N, P}] \qquad (21)$$

If the geometry is fixed, equation 21 becomes:

$$H = f[J, K, L, M, N, P] \qquad (22)$$

Since for this condition one variable H is a function of six others, a large number of experiments would be required to determine H for any situation with the specified geometry. Thus to simplify testing, the number of parameters is minimized by grouping the seven

independent variables into significant dimensionless ratios.

Dimensional analysis is based on the fact that all equations must be dimensionally homogeneous. Thus, it is assumed that H may be expressed as:

$$H = C[(J)^a (K)^b (L)^c (M)^d (N)^e (P)^f] \quad (23)$$

where the exponents, a through f, must be such that the units are consistent. Substitution of the four primary dimensions – mass M, length L, time t, and temperature T – into the assumed equation will produce four equations relating the six exponents a, b, c, d, e, and f. These equations, solved simultaneously in terms of two selected exponents such as b and e, will reduce the above equations to:

$$\eta_1 = C\left[\eta_2\right]^{\phi_1 (b)} \left[\eta_3\right]^{\phi_2 (e)} \quad (24)$$

where η_1, η_2 and η_3 are dimensionless groups formed from the seven variables H, J, K, L, M, N, and P.

For example, consider forced convection between a surface at temperature T_w and a fluid at T_∞. The convective-heat-transfer coefficient h_c is a function of geometry and six other variables:

$$h_c = \frac{q_c}{A (T_w - T_\infty)}$$

$$= f \text{ [Geometry; plate, pipe, etc., Location x and/or size L, D, u, } \rho, \mu, C_p, k] \quad (25)$$

where:

- x = Distance from leading edge
- L = Characteristic length
- D = Diameter
- u = Velocity of fluid
- ρ = Fluid density
- μ = Fluid viscosity
- C_p = Constant pressure specific heat
- k = Thermal conductivity

If the geometry is fixed, equation 25 becomes:

$$h_c = f[(x, L \text{ or } D), u, \rho, \mu, C_p, k] \quad (26)$$

Assume h_c may be expressed as:

$$h_c = K_1 [(L)^a (u)^b (\rho)^c (\mu)^d (C_p)^e (K)^f] \quad (27)$$

where the exponents, a through f, must be such that the units are consistent. Substitution of the four primary dimensions into equation 27 produces four equations relating the six exponents a, b, c, d, e and f.

Simultaneous solution of these equations in terms of two selected exponents, such as b and e, reduces equation 27 to:

$$\frac{h_c L}{k} = K_1 \left[\frac{\rho u L}{\mu}\right]^{\phi_1 (b)} \left[\frac{C_p \mu}{k}\right]^{\phi_2 (e)} \quad (28)$$

Although there is insufficient information to determine the form of the equations, the technique has served to reduce the original system of seven variables to one of three dimensionless variables. Since only these three variables need be considered in categorizing experimental data for a given geometry, the task of correlating experimental data is greatly reduced.

Table 14-2 presents dimensionless groups that are encountered in fluid mechanics and heat transfer and identifies their physical significance and application. The definitions and dimensions of the symbols listed in the Group column are presented in paragraph 14-10, Nomenclature.

14-2 CONDUCTION

Conduction is a process by which heat flows from a region of higher temperature to a region of lower temperature within a medium (solid, liquid, or gas) or between different media in direct physical contact. In conduction heat flow, the energy is transmitted by direct molecular communication without appreciable displacement of the molecules.

Conduction is the primary mechanism by which heat can flow in solids. Heat can also be transferred in solids by radiation; however, measurements of thermal conductivity of solids generally include the effects of the radiation contribution to the heat transfer so that heat transfer in solids can almost always be analyzed as conduction. Conduction is also important in fluids, but in fluid media, it is usually combined with convection and, in some cases, also with radiation. Heat conduction analysis can be conveniently divided into steady-state and unsteady or transient conditions.

14-2.1 Steady-State One-Dimensional Conduction

Steady-state heat conduction occurs when the heat flow into a region plus the heat generated in the region is matched by the heat flow out. For this condition, the temperature at any specific location in the region remains constant. Heat flows by conduction in one dimension in simple geometric configurations such as those bounded by parallel surfaces at uniform but different temperatures. However, in most engineering applications, heat is conducted in two or three dimensions.

Table 14-2. Dimensionless Groups

Name of Group	Symbol	Group (1)	Physical Significance	Application
Biot Number	Bi	$\frac{\bar{h}L}{k_s}$	Internal Thermal Resistance / External Thermal Resistance	Transient Heat Transfer
Bond Number	Bo	$\frac{\rho g L^2}{\sigma}$	Gravitational Force / Surface Tension Force	Atomization and Motion of Bubbles and Drops
Brinkman Number	Br	$\frac{\mu v^2}{k\Delta T}$	Viscous Heating / Conductive Heat Transfer	Viscous Flow
Cauchy Number	Ca	$\frac{\rho v^2}{E_b}$	Inertia Force / Compressibility Force	Compressible Flow
Condensation Number	Co	$\frac{\bar{h}}{k}\left(\frac{\mu^2}{\rho^2 g}\right)^{1/3}$	Dimensionless Heat – Transfer Coefficient for Condensation	Condensation
Darcy Friction Factor	f_D	$\frac{\tau_s}{(\rho v^2/8g_c)} = \frac{\Delta P}{(L/D)(\rho v^2/2g_c)} = 4f$	Pressure Drop / L/D x Velocity Head	Fluid Friction in Conduits
Eckert Number	Ec	$\frac{V_\infty^2}{C_p (T_w - T_\infty)}$	Dynamic Temperature / Reference Temperature Difference	Compressible Flow
Euler Number	Eu	$\frac{\Delta P}{(\rho v^2/g_c)}$	Friction Head / 2 x Velocity Head	Fluid Friction in Conduits
Fanning Friction Factor	f	$\frac{\tau_s}{(\rho v^2/2g_c)} = \frac{\Delta P}{(L/D)(2\rho v^2/g_c)} = \frac{f_D}{4}$	Shear Stress at Pipe Wall / Velocity Head	Fluid Friction in Conduits
Fourier Modulus	Fo	$\frac{k_s \theta}{\rho C_p L^2} = \frac{a\theta}{L^2}$	Exposure Time / Thermal Capacity	Transient Heat Transfer

Table 14-2. Dimensionless Groups (Continued)

Name of Group	Symbol	Group (1)	Physical Significance	Application
Local Friction (Drag) Coefficient	C_f	$\frac{\tau_s}{(\rho v_\infty^2/2g_c)}$	Shear Stress at Plate Wall / Velocity Head	Flow About Immersed Objects
Froude Number	Fr	$\frac{v^2}{g\,L}$	Inertia Force / Gravitational Force	Wave and Surface Behavior
Graetz Number	Gz	$Re_D\,Pr\,\frac{D}{L}$	Thermal Capacity of Fluid / Conductive Heat Transfer Near Inlet	Convection in Pipe inlet Region
Grashof Number	Gr	$\frac{\rho^2 g\,\beta\,(T-T_\infty)L^3}{\mu^2}$	Bouyant Force / Viscous Force	Free Convection
J-Factor	j	$\frac{Nu_D}{Re_D\,Pr^{1/3}} = St\,Pr^{2/3} = \frac{f}{8}$	Shear Stress at Pipe Wall / 8 x Velocity Head	Heat and Momentum Transfer
Knudsen Number	Kn	$\frac{\lambda}{L}$	Molecular Mean Free Path / Characteristic Dimension	Rarified Gas Flow
Lewis Number	Le	$\frac{\alpha}{D_v}$	Thermal Diffusivity / Chemical Molecular Diffusivity	Heat and Mass Transfer
Mach Number	M	$\frac{V}{a}$	Velocity / Sonic Velocity	Compressible Flow
Nusselt Number	Nu	$\frac{h_c\,L}{k}$	Characteristic Dimension / Thickness of Laminar Layer	Convection

Table 14-2. Dimensionless Groups (Continued)

Name of Group	Symbol	Group (1)	Physical Significance	Application
Peclet Number	Pe	Re Pr	Thermal Capacity of Fluid / Conductive Heat Transfer	Forced Convection
Prandtl Number	Pr	$\frac{\mu C_p}{k} = \frac{\nu}{\alpha}$	Momentum Diffusivity / Thermal Diffusivity	Convection
Rayleigh Number	Ra	Gr Pr	Thermal Capacity of Fluid / Conductive Heat Transfer	Free Convection
Recovery Factor	R_T	$\frac{T_{aw} - T_\infty}{(V_\infty^2/2C_p g_c)} = \frac{T_{aw} - T_\infty}{To_\infty - T_\infty}$	Fraction of Free-Stream Dynamic-Temperature Rise Recovered at Wall	Convection in High-Speed Flow
Reynolds Number	Re	$\frac{\rho V L}{\mu}$	Inertia Force / Viscous Force	Fluid Flow
Schmidt Number	Sc	$\frac{\mu}{\rho D_v}$	Kinetic Viscosity / Molecular Diffusivity	Diffusion in Flowing
Sherwood Number	Sh	$\frac{k_c L}{D_v}$	Mass Diffusivity / Molecular Diffusivity	Mass Transfer
Stanton Number	St	$\frac{h_c}{\rho V C_p} = \frac{Nu}{Re_D\ Pr}$	Heat Transfer / Thermal Capacity of Fluid	Forced Convection
Weber Number	We	$\frac{\rho v^2 L}{\sigma}$	Inertia Force / Surface Tension Force	Bubble Formation

(1) Symbols are defined in 14-10 Nomenclature

Steady-state heat conduction problems can be solved by analytical, graphical, analogical and numerical methods without resorting to experimental techniques. Although analytical solution techniques are available for some idealized conditions, most complex problems are more conveniently handled by the latter three techniques. The graphical and analogical methods permit rapid evaluation where approximate solutions are acceptable. The numerical method is adaptable to use on digital computers and, as such, is capable of rapidly providing solutions that closely approach actual conditions.

As an aid in calculating steady one-dimensional temperature distributions and heat flow rates, a summary of equations for the three basic geometries, i.e., slab, cylinder, and sphere is presented in Table 14-3. The basis for these equations is discussed in the following paragraphs.

14-2.1.1 Walls of Simple Geometrical Configuration

Thermal conductivity of materials varies with temperature. For numerous materials, especially within a limited temperature range, the temperature dependency of conductivity can be represented by the linear function:

$$k(T) = k_o (1 + \beta_k T) \tag{29}$$

where k_o is the thermal conductivity at T = 0 and β_k is a constant called the temperature coefficient of thermal conductivity. Using a linear approximation of the temperature variation of thermal conductivity in the basic conductivity equation 1, the rate of heat flow by conduction through a plane homogeneous slab is:

$$\frac{q_k}{A}\int_o^L dx = \int_{T_{hot}}^{T_{cold}} k_o (1 + \beta_k T)\, dT \tag{30}$$

which upon integration reduces to:

$$q_k = \frac{T}{L/(A\, k_m)} \tag{31}$$

where:

$$k_m = k_o[1 + \beta_k (T_{hot} + T_{cold})/2]$$

represents a mean value of thermal conductivity.

Where the sense of positive heat flow is in the direction of increasing radial distance, r, radial heat flow by conduction through a long hollow circular cylinder of homogeneous material, as shown in Figure 14-4, is

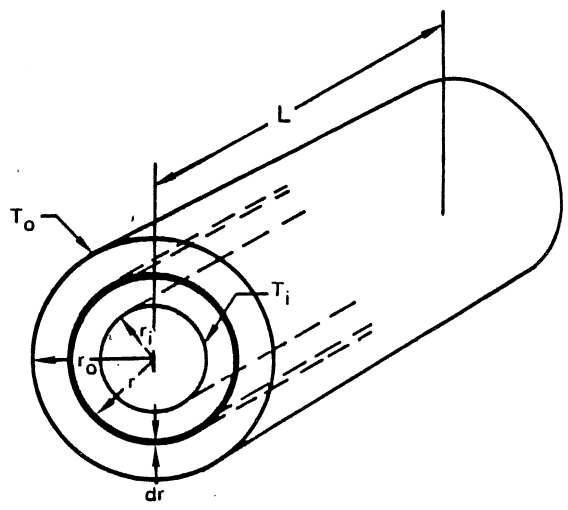

Figure 14-4. Nomenclature for Conduction Through a Hollow Cylinder

dependent on the cylinder length as well as the inside and outside radii and temperatures in the equation:

$$q_k = \frac{T_i - T_o}{\frac{\ln (r_o/r_i)}{2\pi L k}} = \frac{T_i - T_o}{\frac{r_o - r_i}{k\bar{A}}} \tag{32}$$

where:

$$\bar{A} = \frac{A_o - A_i}{\ln(A_o/A_i)},$$

A_o is the outside surface area, and A_i is the inside surface area of the cylinder.

The temperature distribution in the curved wall of a hollow cylinder is a logarithmic function of the radius and is given by:

$$T(r) = T_i - \frac{T_i - T_o}{\ln (r_o/r_i)} \ln (r/r_i) \tag{33}$$

If the thermal conductivity of the material varies linearly with temperature, the conductive heat flow rate is:

$$q_k = \frac{T_i - T_o}{(r_o - r_i)/(k_m \bar{A})} \tag{34}$$

where the mean thermal conductivity, k_m, is given by:

$$k_m = K_o[1 + \beta_k(T_i + T_o)/2]$$

Conduction through a spherical shell, shown in Figure 14-5, is also one dimensional if the interior and exterior surface temperatures are uniform and constant. Where

Table 14-3. One-Dimensional Steady-State Heat Conduction Equations

Item No.	Description	Equation
1.	Homogeneous Slab 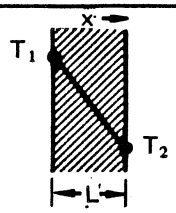	$T_x = T_1 - (T_1 - T_2)\frac{x}{L}$ $q = \frac{kA}{L}(T_1 - T_2)$
2.	Homogeneous Cylinder 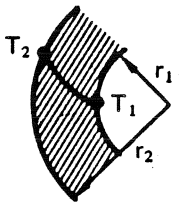	$T_r = T_1 - (T_1 - T_2)\frac{\ln(r/r_1)}{\ln(r_2/r_1)}$ $\frac{q}{\text{unit length}} = \frac{2\pi k(T_1 - T_2)}{\ln\left(\frac{r_2}{r_1}\right)}$
3.	Homogeneous Sphere 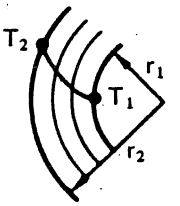	$T_r = T_1 - \frac{T_1 - T_2}{\left(1 - \frac{r_1}{r_2}\right)} + \frac{T_1 - T_2}{\left(\frac{1}{r_1} - \frac{1}{r_2}\right)r}$ $q = \frac{4\pi k(T_1 - T_2)}{\left(\frac{1}{r_1} - \frac{1}{r_2}\right)}$
4.	Composite Slab 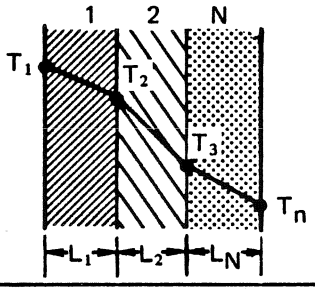	$T_x = T_1 - (T_1 - T_n)\frac{\left[\frac{L_1}{k_1} + \frac{L_2}{k_2} + \ldots + \frac{\Delta x}{kx}\right]}{\sum_1^N \frac{L_n}{k_n}}$ $q = \frac{A(T_1 - T_n)}{\frac{L_1}{k_1} + \frac{L_2}{k_2} + \ldots + \frac{L_n}{k_n}} = UA(T_1 - T_n)$
5.	Composite Cylinder 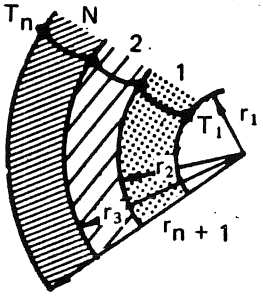	$T_r = T_1 - (T_1 - T_n)\frac{\left[\frac{1}{k_1}\ln\frac{r_2}{r_1} + \ldots + \frac{1}{k_i}\ln\frac{r}{r_i}\right]}{\sum_1^N \frac{1}{k_n}\ln\left(\frac{r_n + 1}{r_n}\right)}$ $\frac{q}{\text{unit length}} = \frac{2\pi(T_1 - T_n)}{\sum_1^N \frac{1}{k_n}\ln\left(\frac{r_n + 1}{r_n}\right)}$
6.	Composite Sphere 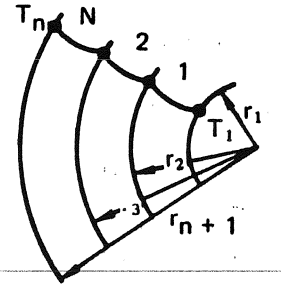	$T_r = T_1 - (T_1 - T_n)\frac{\left[\frac{1}{k_1}\left(\frac{1}{r_1} - \frac{1}{r_2}\right) + \ldots + \frac{1}{k_i}\left(\frac{1}{r_i} - \frac{1}{r}\right)\right]}{\sum_1^N \frac{1}{k_n}\left(\frac{1}{r_n} + \frac{1}{r_n + 1}\right)}$ $q = \frac{4\pi(T_1 - T_n)}{\sum_1^N \frac{1}{k_n}\left(\frac{1}{r_n} - \frac{1}{r_n + 1}\right)}$

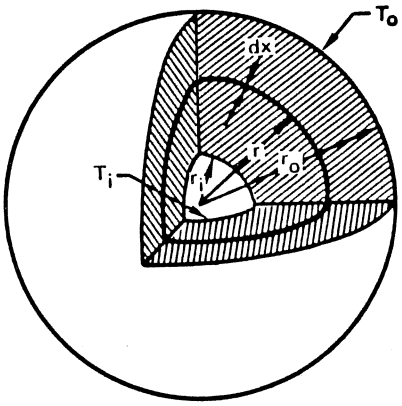

Figure 14-5. Nomenclature for Conduction Through a Hollow Sphere

the sense of positive heat flow is in the direction of increasing radial distance, r, the rate of heat conduction through homogeneous material for this case is given by:

$$q_k = k\sqrt{A_o A_i}\,\frac{T_i - T_o}{r_o - r_i} \qquad (35)$$

where A_o is the outside surface area, and A_i is the inside surface area of the sphere.

If the thermal conductivity of the sphere is a linear function of temperature, then it should be calculated at the arithmetic mean value between the inner and outer surface temperatures as was done for the homogeneous slab and hollow circular cylinder.

14-2.1.2 Composite Structures

If heat is conducted through a composite structure with series and/or parallel conductive paths, the overall unit conductance can be determined by identifying the equivalent electrical network and writing its equation in a form similar to equation 20.

Heat flow through a composite slab, such as that shown in Figure 14-6 is given by:

$$q_k = \frac{T_1 - T_4}{\sum_{n=1}^{3} R_n} \qquad (36)$$

Radial heat flow through concentric cylinders of different thermal conductivity, such as the insulated pipe shown in Figure 14-7, is described by:

$$q = \frac{T_1 - T_3}{\sum_{n=1}^{2} R_n} \qquad (37)$$

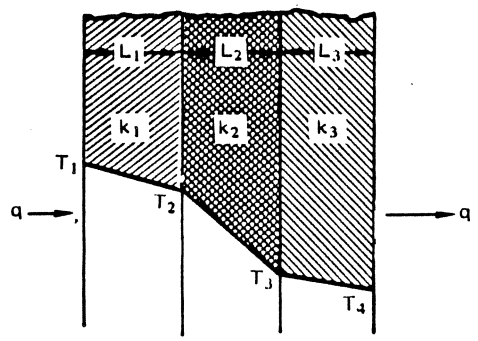

Figure 14-6. Nomenclature for Conduction Through a Composite Slab

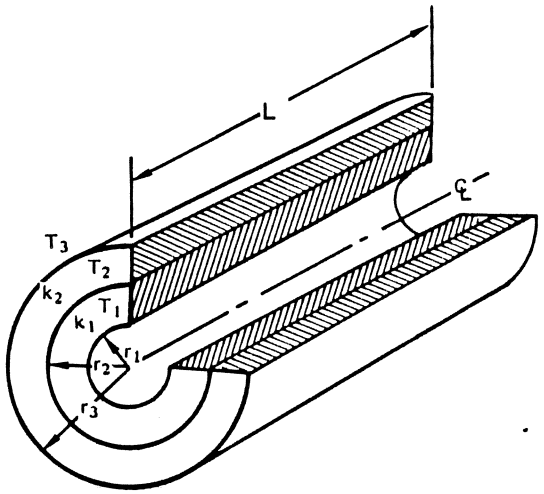

Figure 14-7. Nomenclature for Conduction Through a Composite Cylinder

The addition of insulation to the outside of small pipes or wires does not always reduce heat transfer. For a single-wall tube of fixed inner radius r_i, an increase in outer radius r_o (e.g., insulation thickness) increases the thermal resistance due to conduction logarithmically and, at the same time, reduces the thermal resistance at the outer surface linearly with increasing r_o. Since the total thermal resistance is proportional to the sum of these resistances, the rate of heat flow may increase as insulation is added to a bare pipe or wire until a critical value of the radius is reached. If the insulation is then further increased, the heat loss gradually drops below the loss for a bare wire. The radius for maximum heat transfer, called the critical radius, is:

$$r_{oc} = \frac{k}{\bar{h}_o} \qquad (38)$$

where $\bar{h}_o$ is the convective heat transfer coefficient at r_o.

For cases where r_i is larger than $k/\bar{h}_o$, the addition of insulation will always reduce the rate of heat transfer.

14-2.1.3 Systems with Heat Sources

In a uniformly internally-heated plate of homogeneous material which is long enough that end effects may be neglected, as shown in Figure 14-8, the temperature distribution across the plate is described by:

$$T - T_o = \frac{qL^2}{2k}\left[2\left(\frac{x}{L}\right) - \left(\frac{x}{L}\right)^2\right] \qquad (39)$$

where q is the rate of heat generation per unit volume in Btu/hr-ft^3.

Equation 39 describes a parabolic temperature distribution across the plate with the apex at the median plane, x = L.

Similarly for a long solid circular cylinder, with uniform internal heat generation, as shown in Figure 14-9, the temperature distribution is given by:

$$T = T_o + \frac{\dot{q}r_o^2}{4k}\left[1 - \left(\frac{r}{r_o}\right)^2\right] \qquad (40)$$

The maximum temperature, T_{max} is at the center and is equal to:

$$(qr_o^2/4k) + T_o$$

14-2.1.4 Heat Transfer from Extended Surfaces

Steady heat transfer and temperature distributions in solids of relatively small cross-sectional area which extend from a large body into a fluid at a different temperature for the pupose of enhancing heat transfer, such as heat exchanger fins, can be treated by one dimensional conduction heat transfer analysis techniques. The applicable equations for several configurations are summarized in Table 14-4.

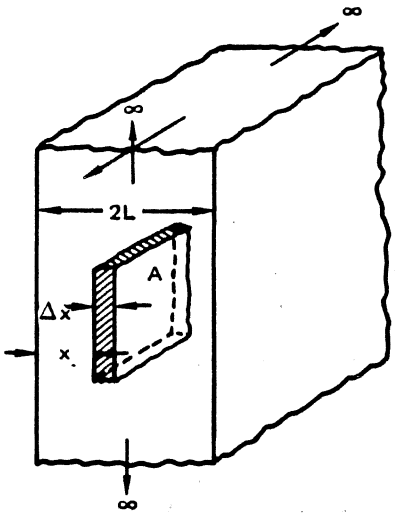

Figure 14-8. Nomenclature for Heat Conduction in Plane Wall with Internal Heat Generation

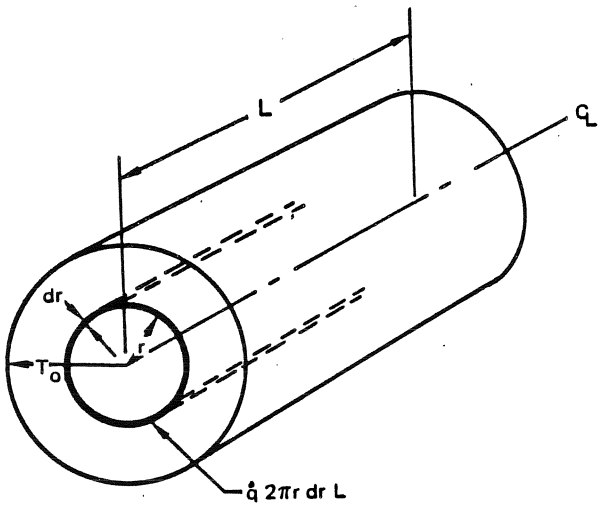

Figure 14-9. Nomenclature for Heat Conduction in a Long Circular Cylinder with Internal Heat Generation

Consider a pin fin of uniform cross-sectional area A (Table 14-4, Case 1) made of a material having a uniform thermal conductivity k, with a heat transfer coefficient h between its surface and the fluid. If radiation from the fin surface is negligible with respect to convection and if the fin is of infinite length, its temperature distribution can be described by:

$$T - T_\infty = (T_s - T_\infty)\ e^{-mx} \qquad (41)$$

and the heat flow through the fin is given by:

$$q_{fin} = \sqrt{h\,Pk\,A}\ (T_s - T_\infty) \qquad (42)$$

where:

T = Fin temperature at a distance x from the wall

T_s = Rod surface temperature at the wall

T_∞ = Fluid temperature

$m = \sqrt{hP/kA}$

P = Perimeter of the rod.

If the rod is of finite length, L, but the heat loss from the end of the rod is neglected, the temperature distribution can be described by:

$$T - T_\infty = (T_s - T_\infty)\ \frac{\cosh\,[m\,(L - x)]}{\cosh\,(mL)} \qquad (43)$$

Table 14-4. Equations for Steady-State Heat Transfer From Extended Surfaces

Case No.	Description	Equation
1.	Rod 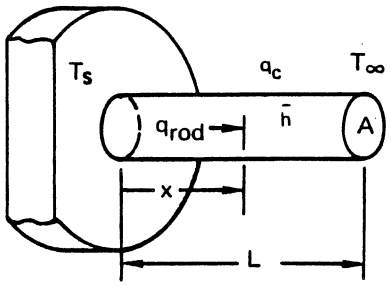 P is the perimeter of the rod $m = \sqrt{\bar{h}P/kA}$	For an infinite length rod (L = ∞) $T - T_\infty = (T_s - T_\infty)\ e^{-mx}$ $q_{rod} = \sqrt{\bar{h}\,P\,k\,A}\ \ (T_s - T_\infty)$ For a finite length rod and negligible end heat loss $T - T_\infty = (T_s - T_\infty)\ \dfrac{\cosh m(L - x)}{\cosh (mL)}$ $q_{rod} = \sqrt{P\,\bar{h}\,kA}\ \ (T_s - T_\infty) \tanh (mL)$ For a finite length rod and connective end heat loss $\dfrac{T - T_\infty}{T_s - T_\infty} = \dfrac{\cosh m(L - x) + (\bar{h}_L/mk) \cosh (mL)}{\cosh mL + (\bar{h}_L/mk) \sinh (mL)}$ $q_{rod} = \sqrt{P\,\bar{h}\,k\,A}\ \ (T_s - T_\infty)\ \dfrac{\sinh mL + (\bar{h}_L/mk) \cosh mL}{\cosh mL + (\bar{h}_L/mk) \sinh mL}$
2.	Rectangular Fin 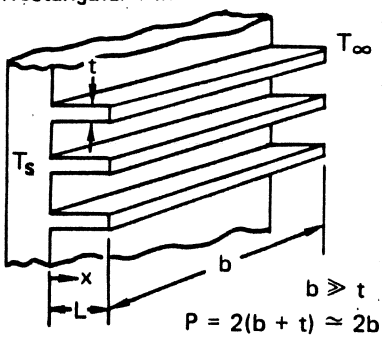 $b \gg t$ $P = 2(b + t) \simeq 2b$ $m = \sqrt{\dfrac{\bar{h}P}{kA}} \simeq \sqrt{\dfrac{2\bar{h}}{kt}}$	Use equations 41 through 46 (case 1 above) for the indicated fin lengths and heat loss conditions but use the values of P and m calculated for the rectangular fin configuration.
3.	Tapered Fin 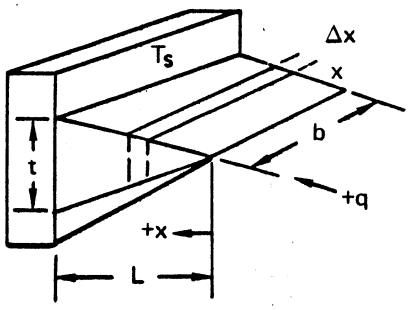 $B = \sqrt{\dfrac{2L\bar{h}}{kt}}$	$\dfrac{T - T_\infty}{T_s - T_\infty} = \dfrac{I_0\,(2B\sqrt{x})}{I_0\,(2B\sqrt{L})}$ $q_{fin} = b\sqrt{2\bar{h}kt\,(T_s - T_\infty)}\ \dfrac{I_1\,(2B\sqrt{L})}{I_0\,(2B\sqrt{L})}$ See Table 14-5 for values of the Bessel functions I_0 and I_1

and the heat flow through the fin is given by:

$$q_{rod} = \sqrt{P\bar{h}\,kA}\;(T_s - T_\infty)\tanh(mL) \qquad (44)$$

If the end of the rod loses heat by convection, the temperature distribution can be described by:

$$\frac{T - T_\infty}{T_s - T_\infty} = \frac{\cosh[m(L-x)] + (\bar{h}_L/mk)\sinh m(L-x)}{\cosh(mL) + (\bar{h}_L/mk)\sinh(mL)} \qquad (45)$$

and the heat-flow rate is:

$$q = \sqrt{P\bar{h}\,Ak}\,(T_s - T_\infty)\left[\frac{\sinh(mL) + (\bar{h}_L/mk)\cosh(mL)}{\cosh(mL) + (\bar{h}_L/mk)\sinh(mL)}\right] \qquad (46)$$

A straight rectangular fin (Table 14-4 Case 2) can be treated by the same methods used for rods. If the fin width b is large compared to its thickness t, the fin perimeter is $P = 2(b + t) \simeq 2b$, the cross-sectional area $A = bt$, and

$$m = \sqrt{\frac{\bar{h}P}{kA}} \simeq \sqrt{\frac{2\bar{h}}{kt}} \qquad (47)$$

The tapered fin (Table 14-4 Case 3) closely approximates the shape which yields the maximum heat flow per unit weight. The temperature distribution in this fin can be described by:

$$\frac{T - T_\infty}{T_s - T_\infty} = \frac{I_0(2B\sqrt{x})}{I_0(2B\sqrt{L})} \qquad (48)$$

and the heat flow from the fin is:

$$q_{fin} = b\sqrt{2\bar{h}\,kt}\,(T_s - T_\infty)\frac{I_1(2B\sqrt{L})}{I_0(2B\sqrt{L})} \qquad (49)$$

where $B = \sqrt{2L\bar{h}/kt}$, and I_0 and I_1 are modified Bessel functions of the first kind and of zero and first order respectively which can be found in Table 14-5.

14-2.2 Two-Dimensional and Three-Dimensional Steady-State Conduction

When the boundaries of a system are irregular or when the temperature along a boundary is nonuniform, it is necessary to evaluate conduction in two or three dimensions. Figure 14-10 shows the elemental heat flow through a control volume in Cartesian coordinates. The general differential equation which governs the temperature distribution in a body is:

$$\frac{\partial}{\partial x}\left(k\frac{\partial T}{\partial x}\right) + \frac{\partial}{\partial y}\left(k\frac{\partial T}{\partial y}\right) + \frac{\partial}{\partial z}\left(k\frac{\partial T}{\partial z}\right) + \dot{q} = c\rho\frac{\partial T}{\partial \theta} \qquad (50)$$

where k is the conductivity, c is the specific heat, ρ is the density, $\dot{q}$ is the rate of heat generation per unit volume, and θ is time. Equation 50 is called the general heat conduction equation.

Table 14-5. Selected Magnitudes of Modified Bessel Functions

z	Io(z)	I1(z)
0.0	1.0000	0.0000
0.2	1.0100	0.1005
0.4	1.0404	0.2040
0.6	1.0920	0.3137
0.8	1.1665	0.4329
1.0	1.2661	0.5652
1.2	1.3937	0.7147
1.4	1.5534	0.8861
1.6	1.7500	1.0848
1.8	1.9896	1.3172
2.0	2.2796	1.5906
2.2	2.6291	1.9141
2.4	3.0493	2.2981
2.6	3.5533	2.7554
2.8	4.1573	3.3011
3.0	4.8808	3.9534
3.2	5.7472	4.7343
3.4	6.7848	5.6701
3.6	8.0277	6.7927
3.8	9.5169	8.1404
4.0	11.3019	9.7595
4.2	13.4425	11.7056
4.4	16.0104	14.0462
4.6	19.0926	16.8626
4.8	22.7937	20.2528
5.0	27.2399	24.3356
5.2	32.5836	29.2543
5.4	39.0088	35.1821
5.6	46.7376	42.3283
5.8	56.0381	50.9462
6.0	67.2344	61.3419
6.2	80.72	73.89
6.4	96.98	89.03
6.6	116.54	107.30
6.8	140.14	129.38
7.0	168.6	156.04
7.2	202.9	188.3
7.4	244.3	227.2
7.6	294.3	274.2
7.8	354.7	331.1
8.0	427.6	399.9
8.2	515.6	483.0
8.4	621.9	583.7
8.6	750.5	705.4
8.8	905.8	852.7
9.0	1093.6	1030.9
9.2	1320.7	1246.7
9.4	1595.3	1507.9
9.6	1927.	1824.
9.8	2329.	2207.
10.0	- - - -	- - - -

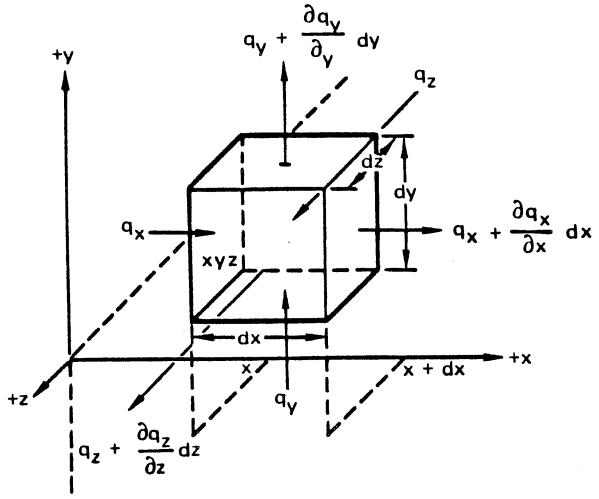

Figure 14-10. Nomenclature for 3-Dimensional Heat Conduction in Cartesian Coordinates

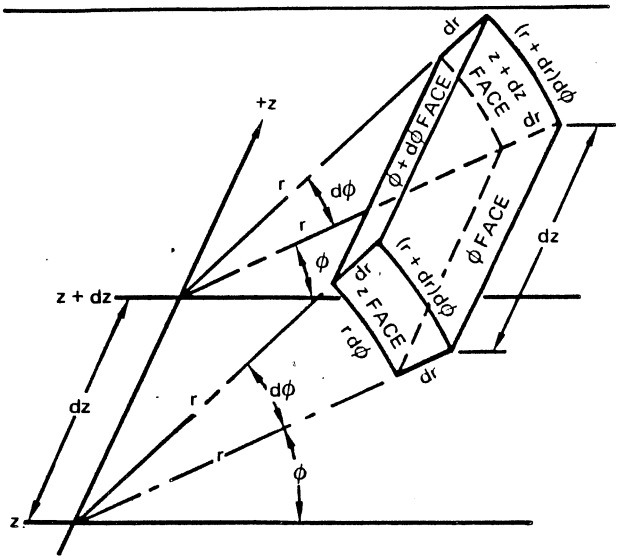

Figure 14-11. Nomenclature for Heat Conduction in Cylindrical Coordinates

If k is assumed to be uniform in all directions (true for isotropic materials) and independent of temperature, equation 49 reduces to:

$$\frac{\partial^2 T}{\partial x^2} + \frac{\partial^2 T}{\partial y^2} + \frac{\partial^2 T}{\partial z^2} + \frac{\dot{q}}{k} = \frac{1}{a}\frac{\partial T}{\partial \theta} \qquad (51)$$

where the constant $a = k/c\rho$ is called the thermal diffusivity.

If the system contains no heat sources, equation 51 reduces to the Fourier equation:

$$\frac{\partial^2 T}{\partial x^2} + \frac{\partial^2 T}{\partial y^2} + \frac{\partial^2 T}{\partial z^2} = \frac{1}{a}\frac{\partial T}{\partial \theta} \qquad (52)$$

If the system is steady, but heat sources are present, equation 51 reduces to the Poisson equation:

$$\frac{\partial^2 T}{\partial x^2} + \frac{\partial^2 T}{\partial y^2} + \frac{\partial^2 T}{\partial z^2} + \frac{\dot{q}}{k} = 0 \qquad (53)$$

In steady-state, the temperature distribution in a body free of heat sources must satisfy the Laplace equation:

$$\frac{\partial^2 T}{\partial x^2} + \frac{\partial^2 T}{\partial y^2} + \frac{\partial^2 T}{\partial z^2} = 0 \qquad (54)$$

Many heat conduction problems can be handled more conveniently in a cylindrical or spherical coordinate system. The general heat conduction equation in the cylindrical coordinate system shown in Figure 14-11 is:

$$\frac{\partial^2 T}{\partial r^2} + \frac{1}{r}\frac{\partial T}{\partial r} + \frac{1}{r^2}\frac{\partial^2 T}{\partial \phi^2} + \frac{\partial^2 T}{\partial z^2} + \frac{\dot{q}}{k} = \frac{1}{a}\frac{\partial T}{\partial \theta} \qquad (55)$$

In the spherical coordinate system shown in Figure 14-12, the general heat conduction equation becomes:

$$\frac{1}{r^2}\frac{\partial}{\partial r}\left(r^2\frac{\partial T}{\partial r}\right) + \frac{1}{r^2 \sin\phi}\frac{\partial}{\partial \phi}\left(\sin\phi\frac{\partial T}{\partial \phi}\right) + \frac{1}{r^2 \sin^2\phi}\frac{\partial^2 T}{\partial \psi^2} + \frac{\dot{q}}{k} = \frac{1}{a}\frac{\partial T}{\partial \theta} \qquad (56)$$

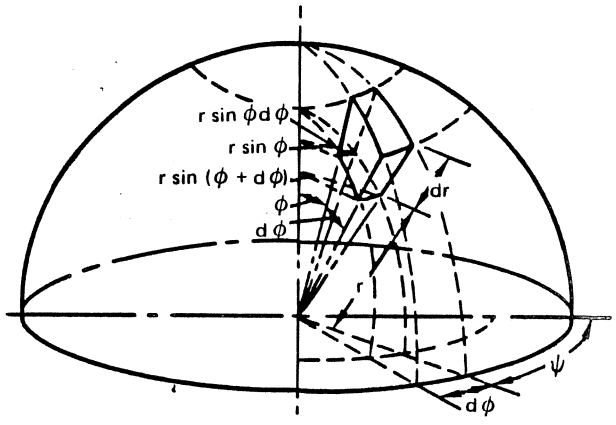

Figure 14-12. Nomenclature for Heat Conduction in Spherical Coordinates

14-2.2.1 Potential-Field Plotting

An approximate solution of the Laplace equation for a two-dimensional system can be obtained graphically by plotting the temperature field freehand. The graphical method is particularly simple in systems with isothermal boundaries.

The graphical method can also be applied to cases in which heat flows across a boundary of unknown temperature by convection or radiation from a source, or to a sink, of known temperature; however, analogical or numerical methods will give an answer more quickly.

The object of a graphical solution is to construct a network consisting of isotherms and lines of constant heat flow. The heat-flow lines are analogous to streamlines in a fluid-flow field, since they are tangent to the direction of heat flow at any point. Consequently, no heat can flow across heat-flow lines, and a constant amount of heat flows between any two of them. As shown in Figure 14-13, isotherms and heat flow lines cross at right angles everywhere. Once such a potential-field net has been drawn, the temperature distribution and the rate of heat flow can be determined.

In making a flux plot, the body is divided into curvilinear squares by trial and error while satisfying boundary conditions. The problem is solved when the network satisfies the following requirements:

a. Boundary conditions

   1. Flow lines are perpendicular to isothermal boundaries.

   2. Isotherms are perpendicular to insulated boundaries.

   3. Flow lines leading to a corner of an isothermal boundary bisect the angle between the surfaces of the boundary at the corner.

b. Isotherms and flow lines intersect each other at right angles.

c. Isotherms and flow lines form a network of curvilinear squares.

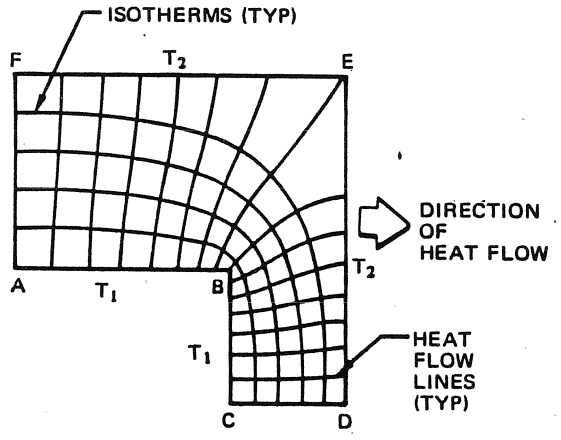

Figure 14-13. Isotherms and Heat Flow Lines in a Potential Field

d. Diagonals of curvilinear squares bisect each other at 90 degrees and bisect the corners.

Any network which satisfies all of these conditions represents the correct solution to a problem.

The rate of heat flow between isothermal boundaries can be found from:

$$\Delta\tilde{q} = \frac{k}{M}(T_1 - T_2) \qquad (57)$$

where:

$\tilde{q}$ = Rate of heat flow per unit area (heat flux), Btu/hr-ft^2

M = Number of curvilinear squares in the channel

For N tubes in a system of unit thickness:

$$q = \frac{N}{M} k (T_1 - T_2) = Sk (T_1 - T_2) \qquad (58)$$

where S = N/M is called the shape factor of the system.

Since the number of flow tubes and the number of temperature increments are considered only as a ratio, the size of the unit curvilinear square does not influence the results. If the number of flow tubes or temperature increments is not integral, a fraction of a tube or curvilinear square must be interpolated. Table 14-6 lists conduction shape factors for several systems.

The following suggestions will facilitate construction of a potential field:

- Note conditions of symmetry. Lines of symmetry are flow lines and divide the temperature field into compartments.
- Select a known isotherm as a datum, and mark all known isotherms.
- At each corner of an isothermal boundary, draw a short line bisecting the angle. All such lines are the beginnings of flow lines. Tentatively, extrapolate the lines to other isotherms.
- Start isotherms in any region where flow lines are uniformly spaced.
- Begin with a crude network and first find the approximate orientation of the isothermal and heat flow lines.
- At first attempt, it will usually be found that the flow lines cannot be made orthogonal to the isotherms and, at the same time, form a network of curvilinear squares. Individual or simultaneous adjustments may have to be made in the location of isotherms and flow lines.

Table 14-6. Conduction Shape Factor S for Various Systems $[q_k = Sk\ (T_1 - T_2)]$ *

DESCRIPTION OF SYSTEM	SYMBOLIC SKETCH	SHAPE FACTOR S
Conduction through a homogenous medium of thermal conductivity k between an isothermal surface and a sphere buried a distance z below.	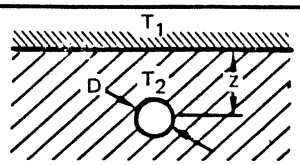	$\frac{2\pi D}{1-(D/4z)}$
Conduction through a homogenous medium of thermal conductivity k between an isothermal surface and a horizontal cylinder of length L buried with its axis a distance z below the surface.	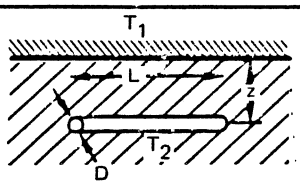	$\frac{2\pi L}{\cosh^{-1}(2z/D)}$ if $z/L \ll 1$.
Conduction through a homogenous medium of thermal conductivity k between an isothermal surface and an infinitely long cylinder buried a distance z below (per unit length of cylinder).	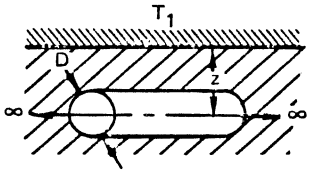	$\frac{2\pi}{\cosh^{-1}(2z/D}$
Conduction through a homogenous medium of thermal conductivity k between an isothermal surface and a vertical circular cylinder of length L.	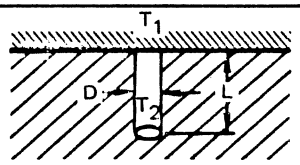	$\frac{2\pi L}{\ln(4L/D)}$ IF $D/L \ll 1$.
Horizontal thin circular disc buried far below an isothermal surface in a homogenous material of thermal conductivity k.	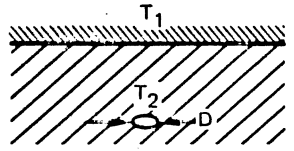	$\frac{4.45D}{1-\frac{D}{5.67\,z}}$
Conduction through a homogenous material of thermal conductivity k between two long parallel cylinders a distance L apart (per unit length of cylinders).	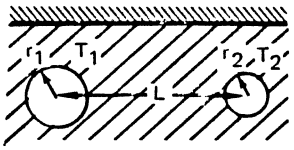	$2\pi/\cosh^{-1}\left(\frac{L^{*2}-1+r^{*2}}{2L^*r^*}\right) + \cosh^{-1}\left(\frac{L^*+1-r^*}{2L^*}\right)$ WHERE $r^* = r_1/r_2$ AND $L^* = L/r_2$.
Conduction through two plane sections and the edge section of two walls of thermal conductivity k—inner and outer surface temperatures uniform†	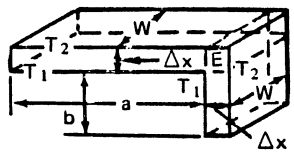	$\frac{aW}{\Delta x} + \frac{bW}{\Delta x} + 0.54W$
Conduction through the corner section c of three homogenous walls of thermal conductivity k—inner and outer surface temperature uniform†	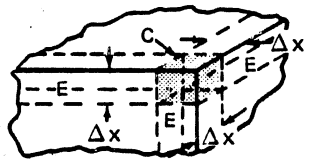	$0.15\,\Delta x$ if Δx is small compared to the lengths of walls.

*All dimensions should be in feet.
†These shape factors apply only to enclosures whose inside dimensions are greater than one-fifth the wall thickness Δx.

After a plausible-appearing network has been drawn, it is advisable to sketch in diagonals to expose any errors. The diagonals should also form an orthogonal grid and bisect each other at right angles in each square.

14-2.2.2 Analogical Methods

When two or more phenomena can be described mathematically by the same equation, the phenomena are said to be analogous and the variables in one system are called the analogues of the corresponding variables in any other system. Table 14-7 illustrates such an analogy.

There are many experimental-analogic methods by which heat flow problems can be solved including Moore's fluid mapper,[1] the membrane analogy, and several electric analogies. The Analog Field Plotter is an electrical-geometrical analogue which is simple and has been used more widely on two-dimensional steady-state problems than any of the other methods.

The Analog Field Plotter makes use of a thin sheet (0.004 in.) of electrically conducting "Teledeltos" paper of relatively high resistivity which can be cut to a shape geometrically similar to that of the heat conductor. An electrical-current-flow pattern can be set up in the paper by means of suitably attached and energized electrodes. The resultant pattern of constant-voltage lines is detected and marked (plotted) directly on the paper by means of a searching stylus which is attached to a high-sensitivity detecting instrument. Figure 14-14 shows schematically how a plotter would be used to determine isotherms and heat flow lines for the configuration shown in Figure 14-13.

Boundary conditions corresponding to a constant-temperature potential in the heat flow are obtained in the electrical field by applying copper wires, or highly conductive areas of silver paint to the surface of the paper and attaching them to a direct-voltage source.

Table 14-7. Analogical Systems Comparisons

Type of Flow Field	Potential Lines	Flow Lines
Heat	Constant Temperature or Isotherms	Heat-Flow Lines
Incompressible inviscid fluid	Constant Velocity Potential	Streamlines
Electricity	Constant Voltage Potential	Lines of Force or Electric Current

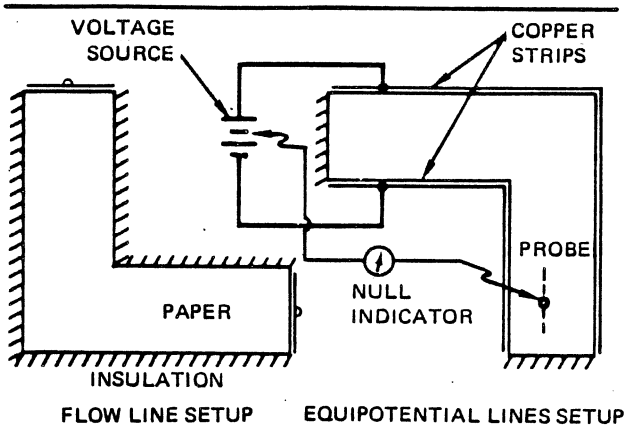

Figure 14-14. Arrangement of the Analog Field Plotter

Insulated surfaces in the heat-flow field correspond to plain edges of the conducting paper. Lines of constant voltage are obtained directly by selecting a voltage level on the *null detector*, moving the stylus to maintain a zero reading on the instrument, and making small perforations in the paper while tracing the equipotential lines. The voltage level of the particular equipotential being traced is determined by the slider position chosen on the voltage-dividing potentiometer of the null detector. By selecting equal increments of voltage, adjacent lines become analogous to isotherms separated by the same temperature difference.

Since the heat-flow, or current-flow, lines are everywhere perpendicular to the potential lines, they can usually be sketched in freehand, so that the resulting network forms curvilinear squares. The flow lines can also be traced by simply reversing the insulating and conducting portions of the boundary. By selecting appropriate voltage increments, a curvilinear network is then obtained.

Teledeltos paper has a resistance of 10^{-4} ohms/square. It is obtainable from Western Union, 60 Hudson Street, New York, N. Y. at a cost of about one cent/ft in minimum lengths of 1,000 ft.

14-2.2.3 Numerical Methods

Numerical methods can be used to solve a set of algebraic equations or a differential equation such as the heat conduction equation. Numerical methods provide approximate solutions of equations by substituting selected numerical values for the variables in the equations. The resulting solution is then compared with the exact solution. If the residual difference or error is beyond acceptable limits, the numerical substitution process is iterated until the error is reduced to an acceptable value. In order to minimize the number of iterations required, techniques have been developed to select initial numerical values which approximate the

real values, and to assure that iterative solutions converge toward the exact answer.

To apply a numerical analysis method to the solution of a heat transfer problem, the heat flow differential equation and the boundary conditions must be approximated by a set of algebraic equations. These equations can be obtained mathematically or physically. In the mathematical approach, the derivatives in the differential equation are replaced with finite-difference approximations.

In the physical approach, the system is divided into a number of small but finite subvolumes with a reference number assigned to each. Each subvolume is assumed to be at the temperature corresponding to its center, and the physical system is replaced by a network of fictitious heat-conducting rods between the centers, or nodal points, or the subvolumes. A thermal conductance corresponding to the conductance of the material between nodal points is assigned to each rod so that the heat flow in the rod network approximates the heat flow in the continuous system. This sort of approach is called the lumped parameter approach.

In the absence of heat sources or sinks within the system, the rate of heat flow toward each nodal point must equal the rate of heat flow away from it in steady state. To satisfy this condition, heat balances are set up for each nodal point, the nodal point temperatures are estimated, and then are corrected in successive steps until the rate of heat inflow equals, within an acceptable residual error, the rate of heat outflow at every point in the system. Since a large number of nodal points is required to realistically model most thermal conduction problems, manual numerical analysis methods are impractical and digital computers are almost always used to obtain accurate solutions.

Typical nodal networks are shown in Figures 14-15, 14-16, and 14-17 for one-, two- and three-dimensional rectilinear heat conduction systems respectively. Internal nodes are handled with conventional network techniques. Nodes which occur at boundaries require special analytical procedures because they are influenced by the geometry and the boundary conditions.

The residual equation for an interior point in a two-dimensional system (Figure 14-16) is:

$$Q_o' = \frac{Q_o}{kb} = T_1 + T_2 + T_3 + T_4 - 4T_o \qquad (59)$$

In the process of subdividing a two-dimensional system, it is usually convenient to start by selecting a square network of nodes. Interior points are then surrounded by full squares of material, but the nodal points at the edges have less material associated with them. The residual equations for nodal points at a boundary depend on the geometry as well as the particular boundary conditions.

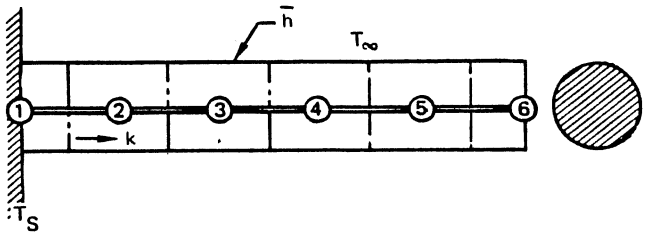

Figure 14-15. One-Dimensional Nodal Network

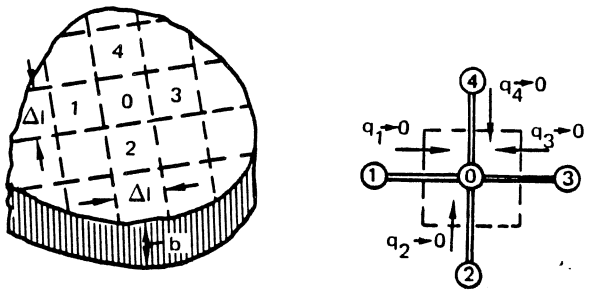

Figure 14-16. Two-Dimensional Nodal Network

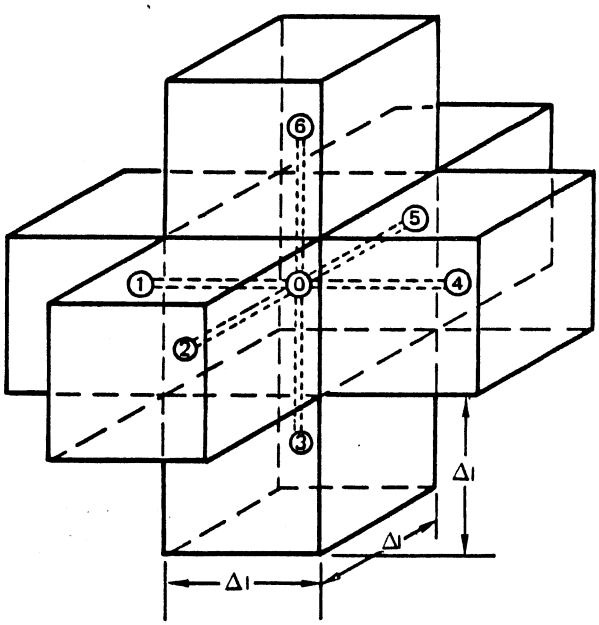

Figure 14-17. Three-Dimensional Nodal Network

Figure 14-18 illustrates the treatment of nodal points at various boundaries of a two-dimensional rectilinear system. Each of these cases is discussed as follows:

a. Nodal point at an isothermal boundary (Figure 14-18a). Since $T_2 = T_4 = T_o$, heat can only flow along the fictitious rod between 3 and 0 and from the outside to 0. Thus:

$$Q_o' = \frac{Q_o}{kb} = \bar{q}\frac{\Delta\ell}{k} + T_3 - T_o$$

where Q_o' is the unit residual or error which approaches zero, and $\bar{q}$ is the rate of heat flow per unit area from the outside to the subvolume having its nodal point at 0.

b. Nodal point at an insulated surface (Figure 14-18b). In this case, heat can flow between the points 1 and 0, 3 and 0, and 4 and 0. However, the area between points 1 and 0, and points 3 and 0 is only $\Delta\ell b/2$,i.e., one half of the heat-flow area between points 4 and 0.

Thus:

$$Q_o' = \frac{Q_o}{kb} = 1/2\,(T_1 + T_3) + T_4 - 2T_o$$

c. Nodal point at a surface in contact with a fluid at T_∞, unit-surface conductance $\bar{h}$ (Figure 14-18c). The rate of heat flow from the fluid to a subvolume around the nodal point is given by equation 12, and the residual equation is:

$$Q_o' = 1/2\,(T_2 + T_4) + T_1 + T_\infty\frac{\bar{h}\Delta\ell}{k} - T_o\left(2 + \frac{\bar{h}\Delta\ell}{k}\right)$$

d. A nodal point in an exterior corner between isothermal surfaces (Figure 14-18d) has no residual equation because no heat can flow to or from it.

e. Nodal point at an exterior corner between insulated surfaces (Figure 14-18e). Heat can flow from 1 to 0 and from 2 to 0. The conductance in each case is equal to kb/2. The residual equation is:

$$Q_o' = 1/2\,(T_1 + T_2) - T_o$$

f. Nodal point at an exterior corner whose surfaces are in contact with a fluid at T_∞, unit-surface conductance $\bar{h}$ (Figure 14-18f). For this case, the residual equation is:

$$Q_o' = 1/2\,(T_3 + T_4) + T_\infty\frac{h\Delta\ell}{k} - T_o\left(\frac{h\Delta\ell}{k} + 1\right)$$

g. For a nodal point at an interior corner between insulated surfaces (Figure 14-18g) the residual equation is:

$$Q_o' = 1/2\,(T_1 + T_2) + (T_3 + T_4) - 3T_o$$

h. For a nodal point at an interior corner whose surfaces are in contact with a fluid at T_∞ (Figure 14-18h) the residual equation is:

$$Q_o' = 1/2\,(T_1 + T_2) + (T_3 + T_4) - 3T_o$$

When a body has an irregular shape, a square net will not fit the contour exactly. In such a case. The residual or error equations for the nodal points adjacent to the boundary must be modified, but in the interior a uniform square network and the corresponding regional equations can be used without change.

Figure 14-19 shows a nodal point in the vicinity of a curved boundary. The boundary cuts across two of the fictitious rods of the square network and thereby affects the conductances between the nodal point 1 and its neighbors. The conductance can be evaluated by suvdividing the region near the boundary as shown in Figure 14-19. The temperatures at the boundary are designated by primed numbers corresponding to the numbers of the nodal points along the rod outside the boundary. The distance along a fictitious rod from nodal point 1 to the boundary are given in percent $\Delta\ell$, the distance between interior points. The symbols with appropriate subscripts indicate the fraction of $\Delta\ell$. The residual equation for this case becomes:

$$Q_1' = \frac{2}{S_{12}\,(1 + S_{12})}T_2' + \frac{2}{1 + S_{15}}T_3 + \frac{2}{1 + S_{12}}T_4 + \frac{2}{S_{15}\,(1 + S_{15})}T_5' - 2\left(\frac{1}{S_{12}} + \frac{1}{S_{15}}\right) \qquad (60)$$

when $S_{12} = S_{15} = 1$ equation 60 reduces to equation 59.

MDAC JA26 is a computer program that calculates three-dimensional heat transfer using a lumped parameter system which can be defined in rectilinear and curvilinear coordinates. The system can be divided into an arbitrary number of nodes that are classified as right rectangular, cylindrical, and spherical in shape. JA26 uses standard equations for the calculation of conduction, convection, and radiation. Incremental temperature change of a node is defined as the net heat exchange at the node divided by the heat capacitance. An approximation to the temperature history of the system and/or the steady-state temperature solution may be obtained. The JA26 computer program can also be used to solve heat conduction equations which include convection and radiation boundary conditions. The program is documented in MDAC Manual XF 1.

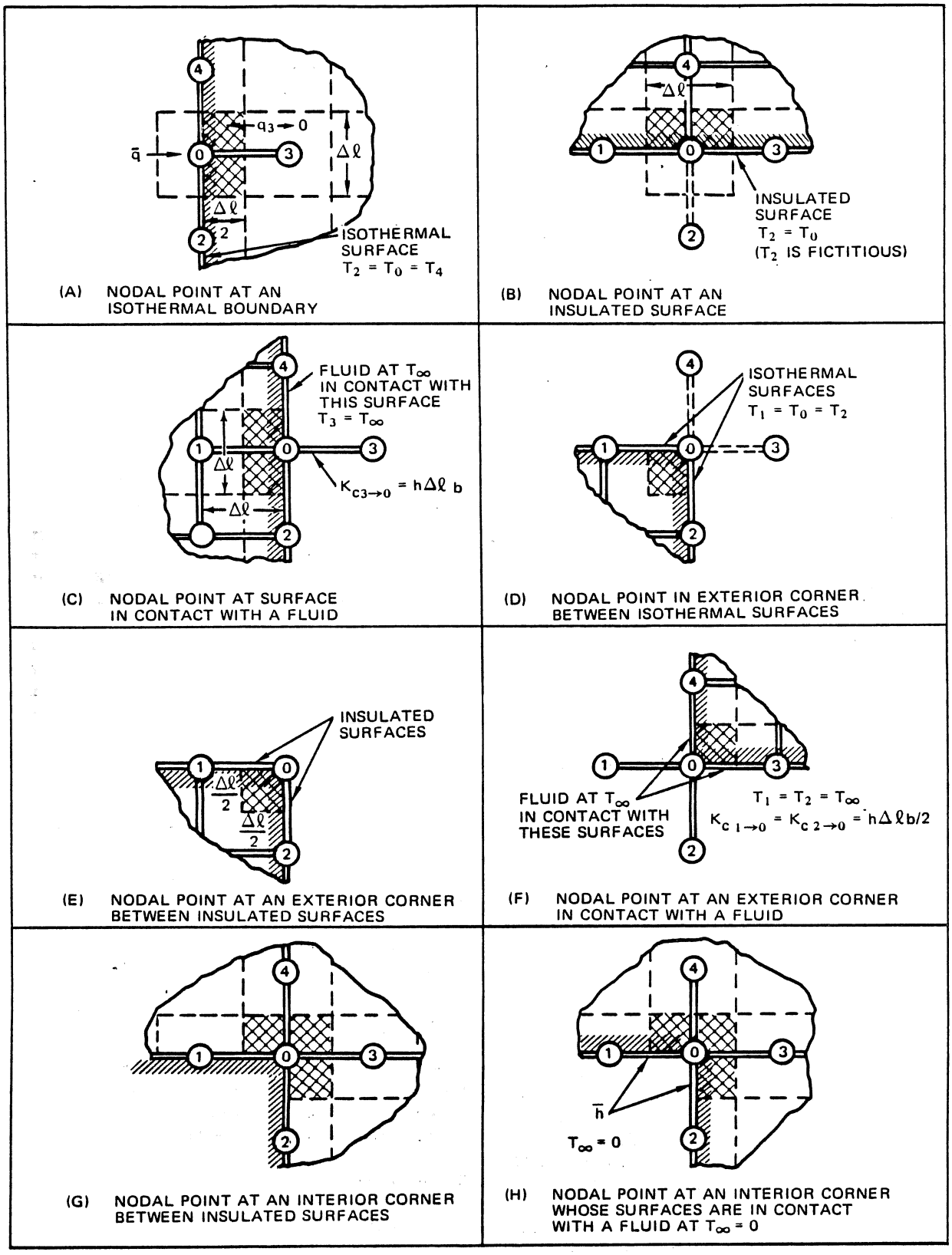

Figure 14-18. Two-Dimensional Nodal Point Boundary Conditions

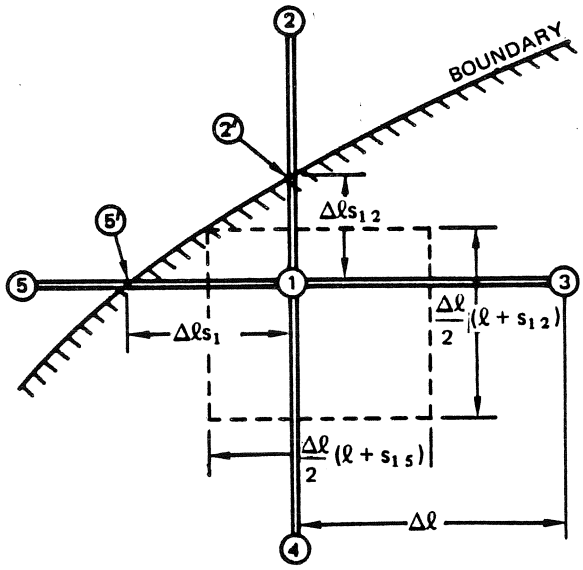

Figure 14-19. Nodal Nomenclature at an Irregular Boundary

Computer programs JA03, MH02, and CINDA are three other computer programs which can also be used to solve one-, two-, and three-dimensional heat conduction problems with convection and/or radiation boundary conditions.

14-2.3 Transient Heat Conduction

The unsteady or transient condition implies that the heat transfer is time variant and, therefore, that energy stored must be considered in addition to heat conduction. This may be expressed in differential form as:

$$q = c\rho V \frac{dT}{d\theta} \tag{61}$$

where q is the net heat flow into or out of storage, ρV is an elemental mass, c is the specific heat per unit mass, and $dT/d\theta$ is the rate of temperature change.

In transient heat conduction, the temperature distribution through the system is a function of time as well as distance. Solutions for one-dimensional transient heat conduction presented here are for a system which has an initial uniform temperature with a step change in boundary conditions at time zero. Solutions for other initial and boundary conditions and the conversion of the step change to an arbitrary time-dependent input are contained in Carslaw, H. S. and J. C. Jaeger, *Conduction of Heat in Solids*, 2nd edition, Oxford Press, 1959. Table 14-8 summarizes the solutions for one-dimensional unsteady heat conduction which are discussed in the paragraphs that follow.

14-2.3.1 Negligible Internal Resistance

Even though no materials possess an infinite thermal conductivity, many transient heat flow problems can be solved with acceptable accuracy by assuming that the internal conductive resistance of the system is so small that the temperature, within the system is substantially uniform at any instant.

The equation which describes this system is:

$$\bar{h}A_s (T - T_\infty) = c\rho V \frac{dT}{d\theta} \tag{62}$$

for which the solution is:

$$\frac{T - T_\infty}{T_o - T_\infty} = e^{-(\bar{h}A_s/c\rho V)\,\theta} \tag{63}$$

where the quantity $(c\rho V/\bar{h}\,A_s)$ has the dimension of time and is called the time constant. Its value is indicative of the rate of response of a single capacity system to a sudden change in its environment. When $\theta = (c\rho V/\bar{h}\,A_s)$ the temperature difference $(T - T_\infty)$ drops to 36.8 percent of the initial temperature difference $(T_o - T_\infty)$.

Equation 63 can also be expressed as:

$$\frac{T - T_\infty}{T_o - T_\infty} = e^{-(Bi)(Fo)} \tag{64}$$

where Bi is the Biot modulus and F_o is the Fourier modulus, two dimensionless ratios which have been found to facilitate evaluation of transient heat flow. Figure 14-20 is a plot of equation 64.

The Biot number is the ratio of the internal to the external resistance of a body. It provides a measure of the relative importance of the internal thermal resistanc ɔ.

$$Bi = \frac{\bar{h}L}{k_s} \tag{65}$$

where $\bar{h}$ is the average unit surface conductance, L is a significant length dimension obtained by dividing the volume of the body by its surface area, and k_s is the thermal conductivity of the solid body.

The Fourier number is:

$$F_o = \frac{a\theta}{L^2} \tag{66}$$

where a, the thermal diffusivity, is the ratio of the body's thermal conductivity to its heat capacity, $(k_s/c\rho)$.

Table 14-8. Transient One-Dimensional Heat Conduction Equations

Case No.	Description	Configuration	Corresponding Figure No.	Temperature Distribution Equation
1.	Solid of Infinite Thermal Conductivity	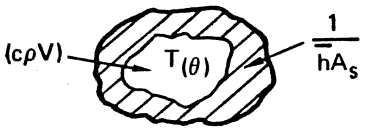	14-20	$\frac{T - T_\infty}{T_o - T_\infty} = e^{-(\bar{h}A_s/c\rho V)\theta} = e^{-(Bi)(Fo)}$
2.	Slab Suddenly Immersed in a Constant Temperature Fluid	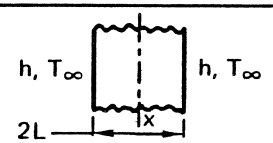	14-22 14-28 14-29	$\frac{T - T_\infty}{T_o - T_\infty} = 4\sum_{n=1}^{\infty}\left(\frac{\sin M_n}{2M_n + \sin 2M_n}\right) e^{-M_n^2\theta} \cos M_n \frac{x}{L}$ where the M_n are solutions to $M_n \tan M_n = B_i$
3.	Long Cylinder Suddenly Immersed In a Constant Temperature Fluid	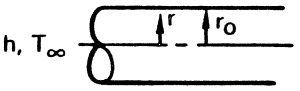	14-24 14-30 14-31	$\frac{T - T_\infty}{T_o - T_\infty} = 2\sum_{n=1}^{\infty}\frac{1}{M_n}\frac{J_1(M_n)}{J_o^2(M_n) + J_1^2(M_n)} e^{-M_n^2\theta} \cos M_n \frac{x}{L}$ where the M_n are solutions to $M_n J_1(M_n)/J_o(M_n) = Bi$
4.	Sphere Suddenly Immersed in a Constant Temperature Fluid	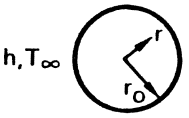	14-26 14-32 14-33	$\frac{T-T_\infty}{T_o-T_\infty} = 4\left(\frac{r_o}{r}\right)\sum_{n=1}^{\infty}\frac{\sin M_n - M_n \cos M_n}{2M_n - \sin 2M_n} e^{-M_n^2\theta} \sin\left(M_n \frac{r}{r_o}\right)$ where the M_n are solutions to $1 - M_n \cot M_n = Bi$
5.	Semi-Infinite Solid with known Surface Temperature	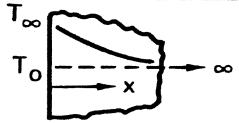	14-35 14-36 $\left(\frac{hx}{k}\right) = \infty$	$\frac{T-T_o}{T_\infty-T_o} = 1 - \text{erf}\left(\frac{x}{2\sqrt{a\theta}}\right) = \text{erfc}\left(\frac{x}{2\sqrt{a\theta}}\right)$
6.	Semi-Infinite Solid with Convection at the Surface	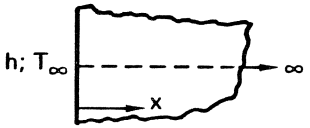	14-35 14-36	$\frac{T-T_o}{T_\infty-T_o} = \text{erfc}\left(\frac{x}{2\sqrt{a\theta}}\right) - e^{\left(\frac{hx}{h^2} + \frac{h^2}{k^2}a\theta\right)} \text{erfc}\left(\frac{x}{2\sqrt{a\theta}} + \frac{h}{k}\sqrt{a\theta}\right)$
7.	Semi-Infinite Solid with Constant Heat Flux at the Surface	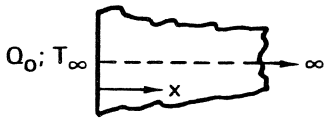	14-37	$\frac{T-T_o}{Q_o x/k} = \frac{2}{x}\sqrt{\frac{a\theta}{\pi}} e^{x^2/4a\theta} - \text{erfc}\frac{x}{2\sqrt{a\theta}} = \frac{2\sqrt{a\theta}}{x}\,\text{ierfc}\frac{x}{2\sqrt{a\theta}}$
8.	Infinitely Long Fin	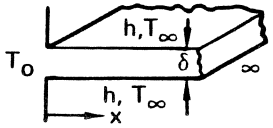	14-38	$\frac{T-T_o}{T_\infty-T_o} = \frac{1}{2} e^{-x\sqrt{2h/k\delta}} \text{erfc}\left[\frac{x}{2\sqrt{a\theta}} - \sqrt{\frac{2h}{k\delta}}\sqrt{a\theta}\right] + \frac{1}{2} e^{x\sqrt{2h/k\delta}} \text{erfc}\left[\frac{x}{2\sqrt{a\theta}} + x\frac{2h}{k\delta}\sqrt{\frac{a\theta}{x}}\right]$

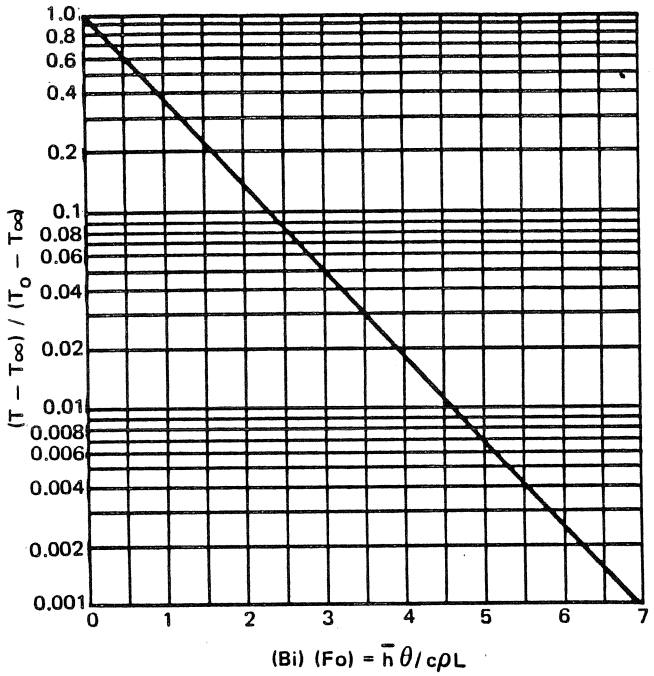

Figure 14-20. Dimensionless Temperature Ratio versus Product of Biot and Fourier Moduli (Bi)(Fo)

14-2.3.2 Measurable Internal Resistance

In materials with measurable internal resistance, the temperature is not distributed uniformly during transient heat flow. Solutions for temperature distribution and heat flow have been calculated for transient heat conduction in several simple shapes, subject to boundary conditions of practical importance, and the results are available in the form of analytical expressions and charts. For the most part, the analytical expressions consist of infinite series and are time consuming to evaluate, whereas the charts are much easier to use. Consequently, emphasis is placed on the charts although the analytical expressions are presented in Table 14-8. Figure 14-21 presents central temperature histories in several solid shapes, as a function of the Fourier modulus, where each solid was initially at temperature $T_0 = 0$, and its surfaces were then suddenly changed to temperature T_∞.

The first series of dimensionless temperature-time charts (Figures 14-22 and 14-23) apply to a large flat plate of thickness 2L. Initially, the plate temperature is uniform at T_0. At some instant in time $\theta = 0$, the plate is immersed in a fluid at T_∞. If T_∞ is larger than T_0 heat begins to flow from the fluid to the plate. The rate of heat flow depends on the temperature difference $(T_\infty - T_0)$, the unit-surface conductance $\bar{h}$ between the plate and the fluid, the physical properties of the plate, and the plate thickness. The temperature distribution and the internal energy in the plate at any instant are functions of the same variables.

In Figure 14-22, there are six separate graphs for depth ratios x/L of 0, 0.2, 0.4, 0.6, 0.8 and 1.0 where x is the distance from the central plane. The upper left-hand graph (x/L = 0) shows the temperature at the center plane. The graph in the lower right-hand corner (x/L = 1.0) applies to the surface of the slab in contact with the fluid. The constant parameter for each of these dimensionless temperature-time curves is the reciprocal of the Biot modulus; i.e., $k_s/\bar{h}L$. The curves labeled $k_s/\bar{h}L = 0$ are for an infinite surface conductance, that is, a sudden change in the temperature of the face x = L. An inspection of the graph for x/L = 1 shows that the temperature at the face x = L is equal to T_∞ at $\theta \geqslant 0$. For small values of the Biot modulus, say $\bar{h}L/k_s < 0.1$, there is little difference between the temperatures at x = L and x = 0 for any time, which implies that equations 63 and 64 and Figure 14-20 can be used for these conditions.

Figure 14-23 is a plot of Q/Q_0 versus the Biot modulus for various values of the Fourier modulus F_0. Q represents the total change in internal energy per unit area, i.e., the amount of heat transferred per unit area in the time interval between $\theta = 0$ and $\theta = \theta$ in Btu per square foot. Q_0 represents the initial internal energy per unit area relative to the fluid temperature T_∞. i.e., $c\rho L\,(T_0 - T_\infty)$. A positive value of Q indicates, therefore, that heat is transferred from the wall to the fluid, while a negative value of Q shows that the direction of heat flow is into the slab.

Similarly, for a long cylinder, transient temperature distribution and heat flow can be calculated from Figures 14-24 and 14-25; and, for a sphere, transient temperature distribution and heat flow can be found from Figures 14-26 and 14-27.

If the temperature in the interior of a slab does not change during a process, the temperature distribution near the surface is identical to that in an infinitely thick slab, and the body is called a semi-infinite solid. The following initial and boundary conditions apply:

a. The original temperature T_0 is uniformly distributed.

b. At time $\theta = 0$, the face of the semi-infinite solid is brought in contact with a fluid at T_∞.

c. The unit surface conductance $\bar{h}$ over the face x = 0 is constant and uniform.

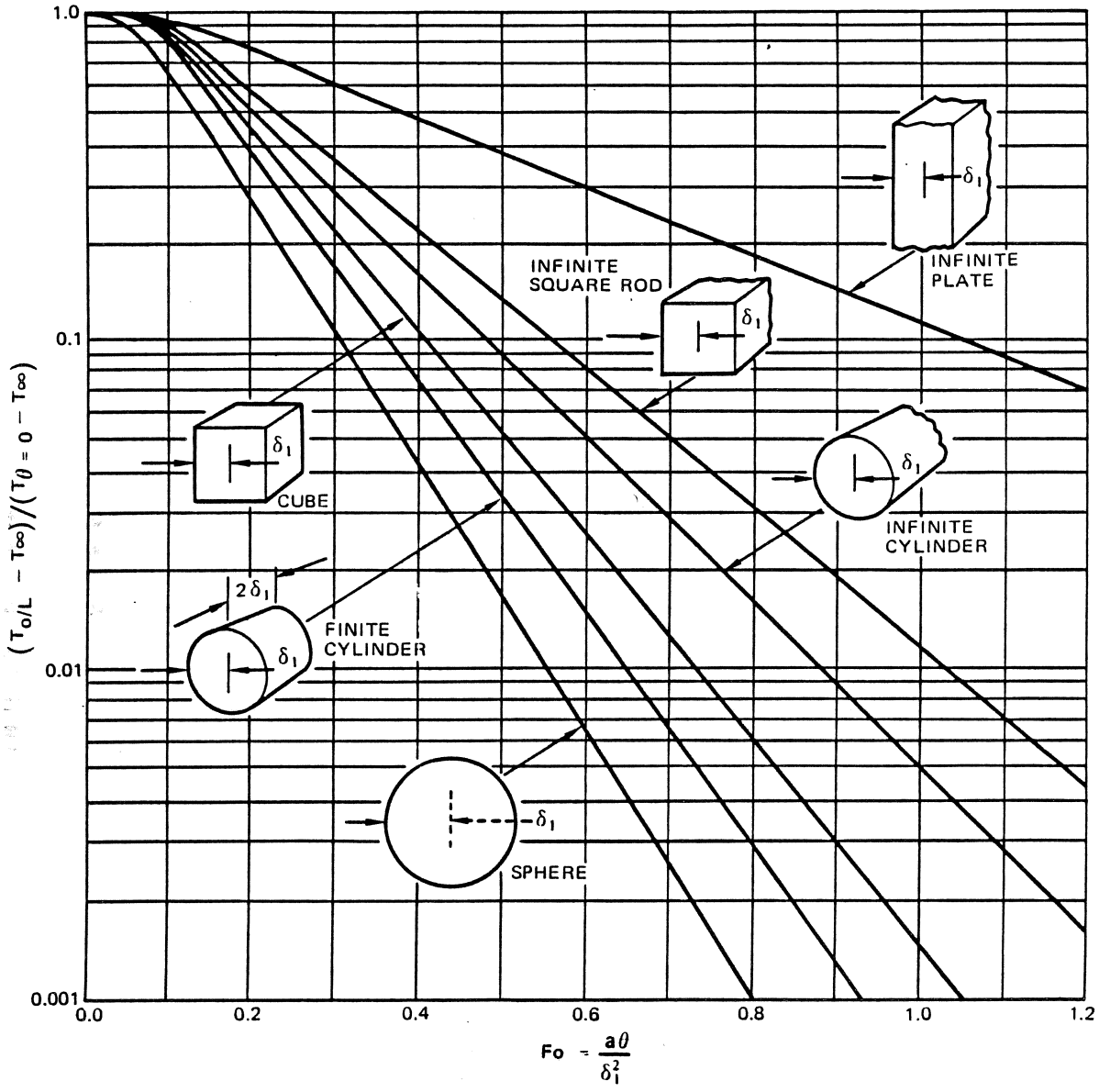

Figure 14-21. Central Temperature Histories in Various Solids

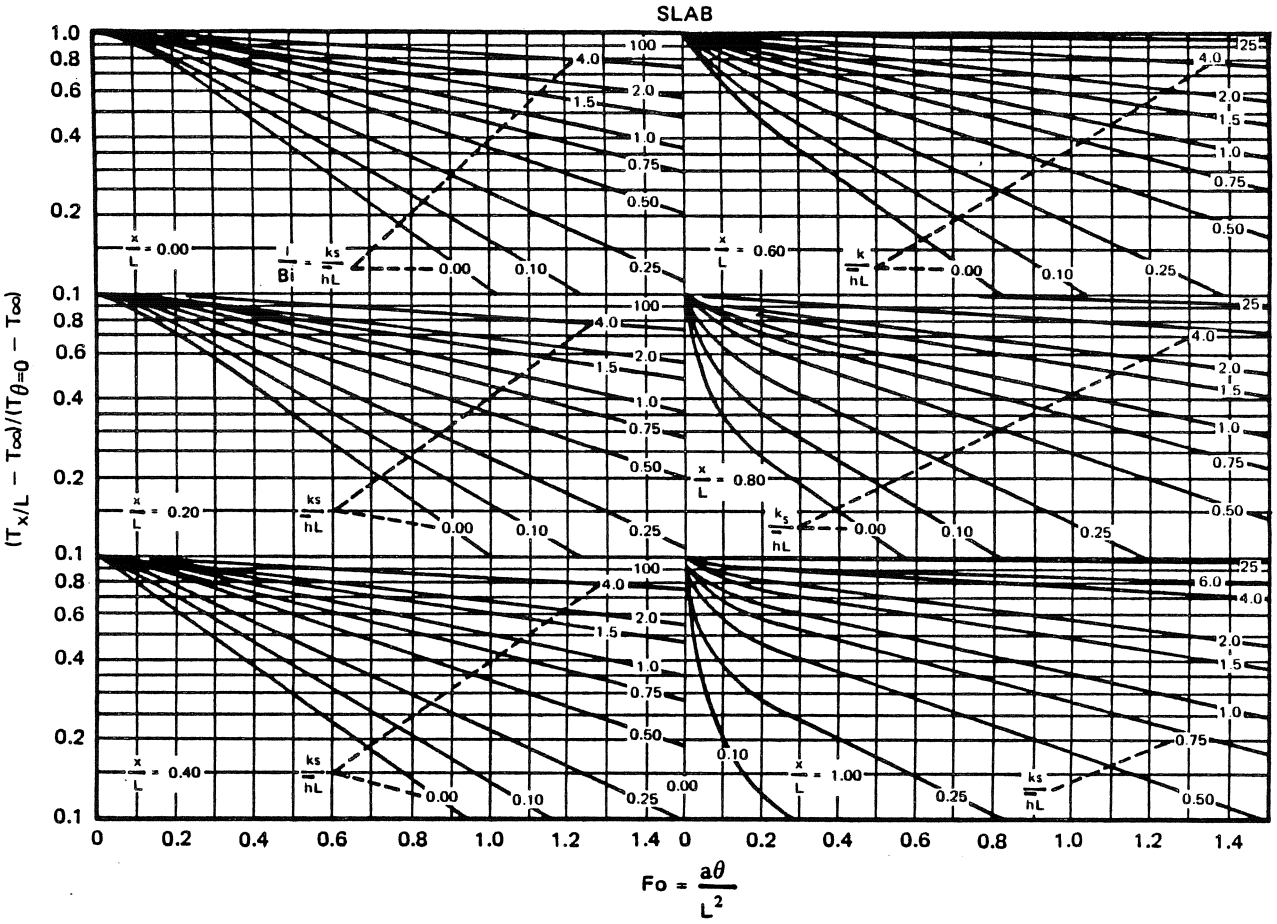

Figure 14-22. Dimensionless Temperature Distribution in a Wall Subjected to a Sudden Change in Environmental Temperature

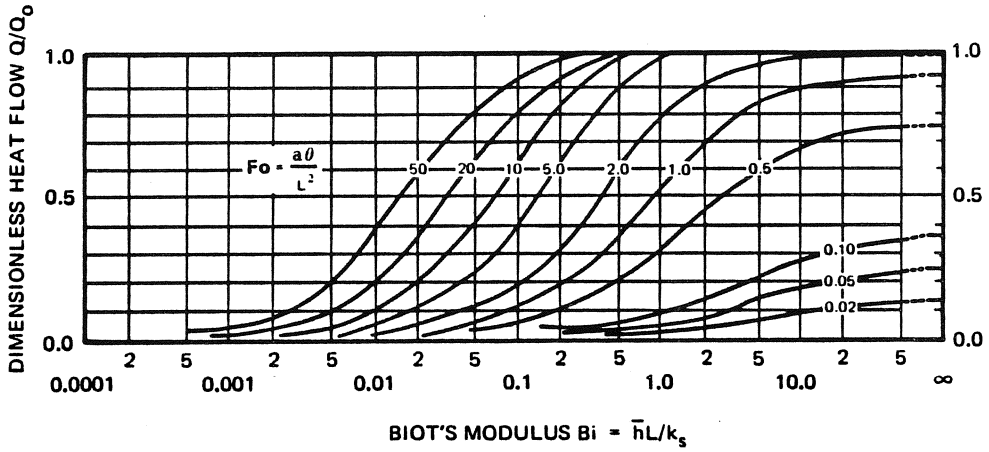

Figure 14-23. Dimensionless Heat Flow to or from a Wall Subjected to a Sudden Change in Environmental Temperature

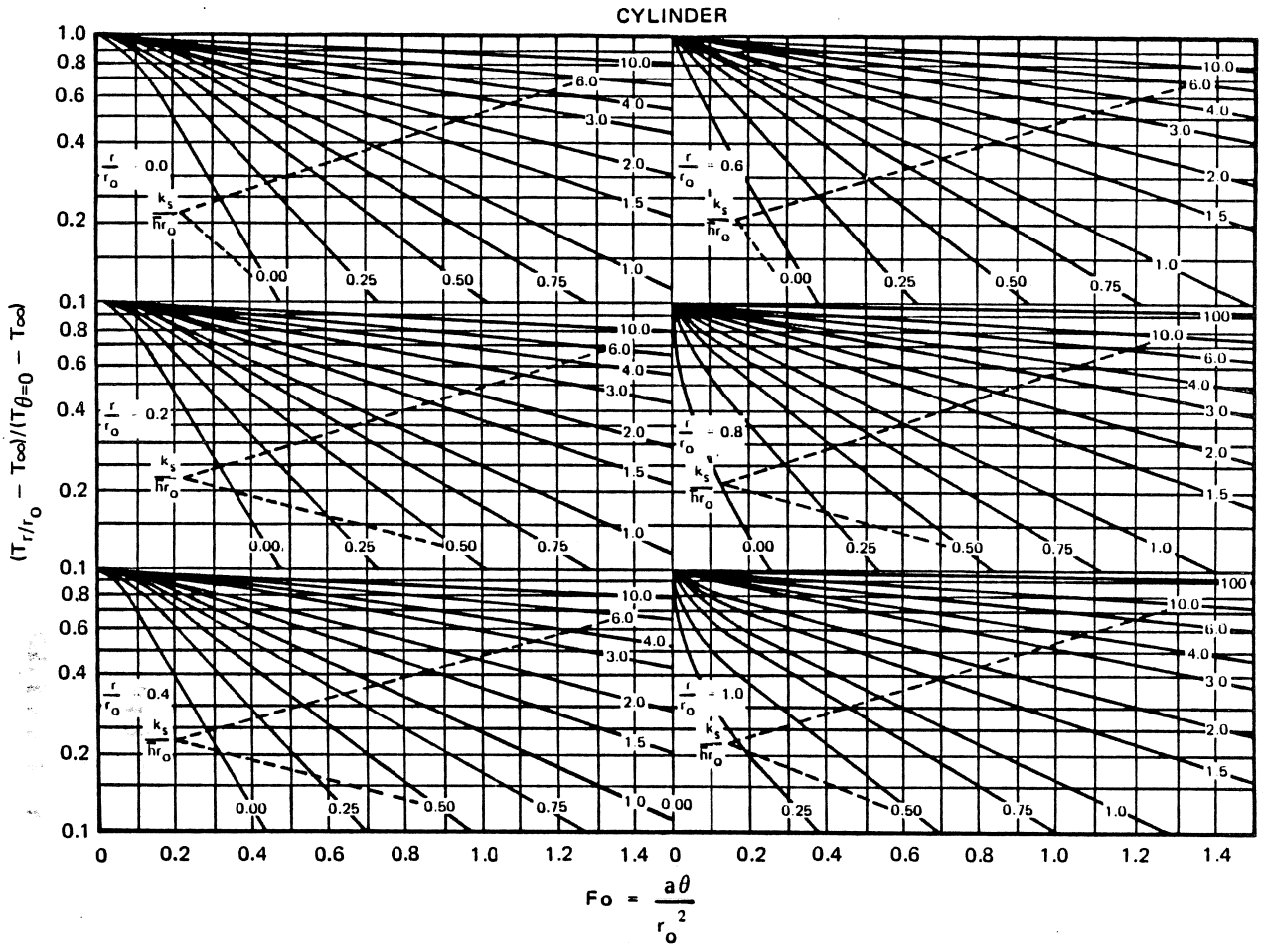

Figure 14-24. Dimensionless Temperature Distribution in a Long Circular Cylinder Subjected to a Sudden Change in Environmental Temperature

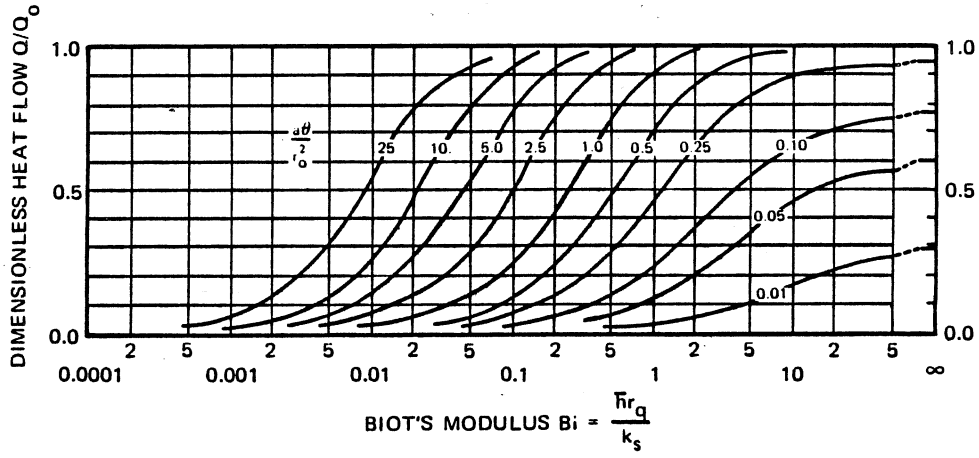

Figure 14-25. Dimensionless Heat Flow to or From a Long Circular Cylinder Subjected to a Sudden Change in Environmental Temperature

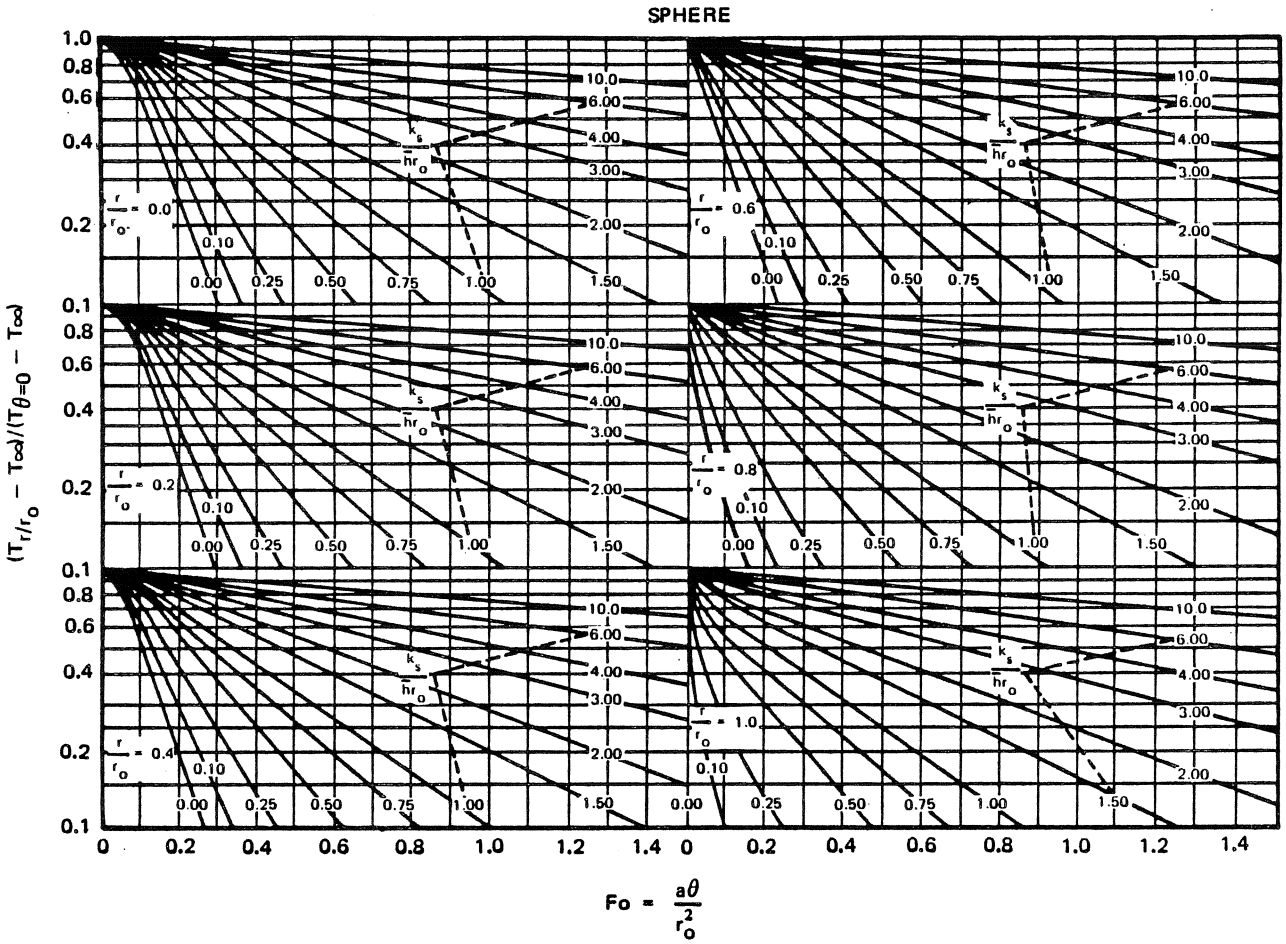

Figure 14-26. Dimensionless Temperature Distribution in a Sphere Subjected to a Sudden Change in Environmental Temperature

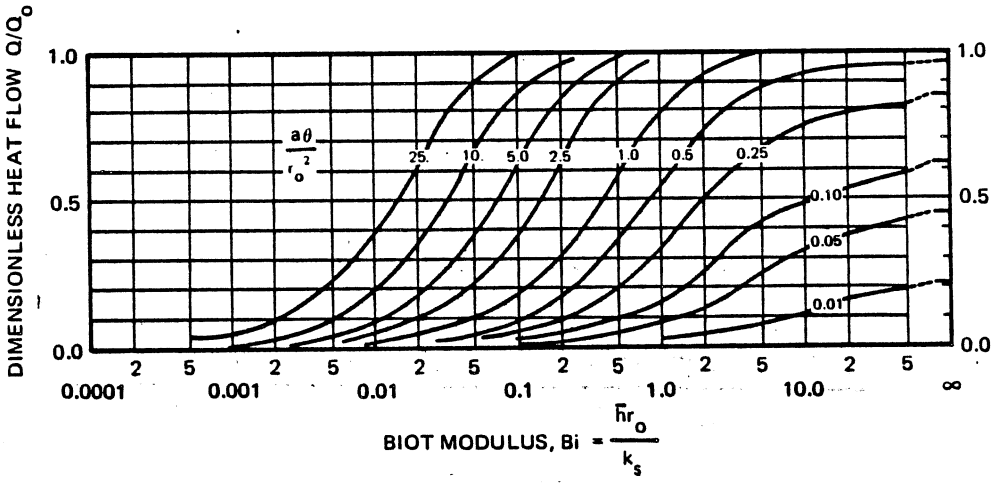

Figure 14-27. Dimensionless Heat Flow to or from a Sphere Subjected to a Sudden Change in Environmental Temperature

These boundary conditions are also valid for a wall of finite thickness, or for a long rod which is insulated around its circumference when $L/2\sqrt{a\theta}$ is larger than 0.5. These conditions are approximately correct for cylinders and spheres as long as the depth to which the heat conduction has penetrated is small compared with the radius of curvature.

Figures 14-21 through 14-27 are useful for values of the Fourier modulus F_o up to 1.5. For larger values of F_o, the Heisler charts presented in Figures 14-28 through 14-33 should be used to determine the transient temperature distribution in the infinite plates, infinite cylinders, and spheres respectively. Figures 14-28, 14-30, and 14-32 permit determination of the body central temperature $T_{o/L}$ as a function of F_o and $K_s/hL = (1/Bi)$, if the initial body temperature $T_\theta = 0$ and the fluid temperature T_∞ are known. The temperatute at any position x between the center and the surface $T_{x/L}$ can be found from Figures 14-29, 14-31, and 14-33 as a function of 1/Bi and x/L if $T_{o/L}$ and T_∞ are known.

For the special case of one-dimensional transient heat conduction in a semi-infinite solid with no thermal resistance at the surface, the temperature distribution can be found from:

$$\frac{T - T_\infty}{T_o - T_\infty} = G\left(\frac{x}{2\sqrt{a\theta}}\right) \qquad (67)$$

where $G\,(x/2\sqrt{a\theta})$ is the Gaussian error integral which can be computed from Figure 14-34.

For a finite value of the surface conductance at the face of a semi-infinite slab, the temperature distribution can be found as a function of the local Biot modulus and the boundary Fourier modulus in Figure 14-35. Figure 14-36 presents similar information as a function of $x/2\sqrt{a\theta}$ and the Biot modulus. Figures 14-37 and 14-38 plot similar data for a semi-infinite solid with constant heat flux at the surface, and for an infinitely long fin respectively.

The dimensionless temperature distribution solutions for one-dimensional problems can be combined (by multiplication) to yield solutions for certain two- and three-dimensional transient heat conduction systems. Table 14-9 lists dimensionless temperature distribution equations for several common two- and three-dimensional configurations.

Many other graphical solutions to transient heat conduction problems in slabs, cylinders, spheres, and ellipsoids with boundary conditions of constant and variable surface temperature, constant ambient temperature, constant and variable heat input, and surface radiation are contained in P. J. Schneider, *Temperature Response Charts*, John Wiley and Sons, Inc., New York, N. Y., 1963.

Table 14-9A summarizes the application of the Schneider charts for cylindrical and spherical shells (insulated at the inner or outer surface) that are presented in Figures 14-38A, B, C, and D. Each of these four charts consists of six graphs, one each for a specific radius ratio $R_i = r_i/r_e$ (R_i = 0.2, 0.4, 0.6, 0.8, 0.9 and 0.99), where r_i is the radius of the internal surface and r_e is the radius of the external surface. Each graph contains temperature-response curves, presented in terms of $(T - T_o)/(T_\infty - T_o)$ versus F_o and plotted at several values of Bi.

Transient temperature solutions can be obtained on each graph for both the internal and the external shell surfaces. The temperature response for all internal surfaces is read on the left-hand ordinate, and from Bi curves representing $r = r_i$.

The temperature response for all external surfaces is read on the right-hand ordinate. The Biot number is calculated from $Bi = h\,r_e/k$. An example of the use of these graphs is presented in subsection 14-9.3.

14-2.3.3 Graphical Method

A graphical method, known as the Schmidt plot, can be used to obtain approximate solutions to transient one-dimensional heat conduction problems. It is particularly useful for problems which have such complicated boundary conditions that they cannot be handled conveniently by analytical methods. The Schmidt plot is a step-by-step solution, by the finite difference method, of the unsteady conduction equation in one dimension, without heat sources or sinks, which, in rectilinear coordinates is:

$$\frac{1}{a}\frac{\partial T}{\partial \theta} = \frac{\partial^2 T}{\partial x^2} \qquad (68)$$

Equation 68 can be rewritten as a finite difference equation:

$$\frac{1}{a}\frac{\Delta_\theta T}{\Delta \theta} = \frac{\Delta_x{}^2 T}{\Delta x^2} \qquad (69)$$

where the subscripts θ and x indicate whether the time θ or the location x is the variable effecting the change in T.

Figure 14-39 is an illustration of the Schmidt plot for an infinitely thick wall having a plane face whose temperature is constant at T_s. The temperature at a certain time $\theta = 0$ is represented by the heavy dashed line. The wall is divided into layers Δx thick, and the

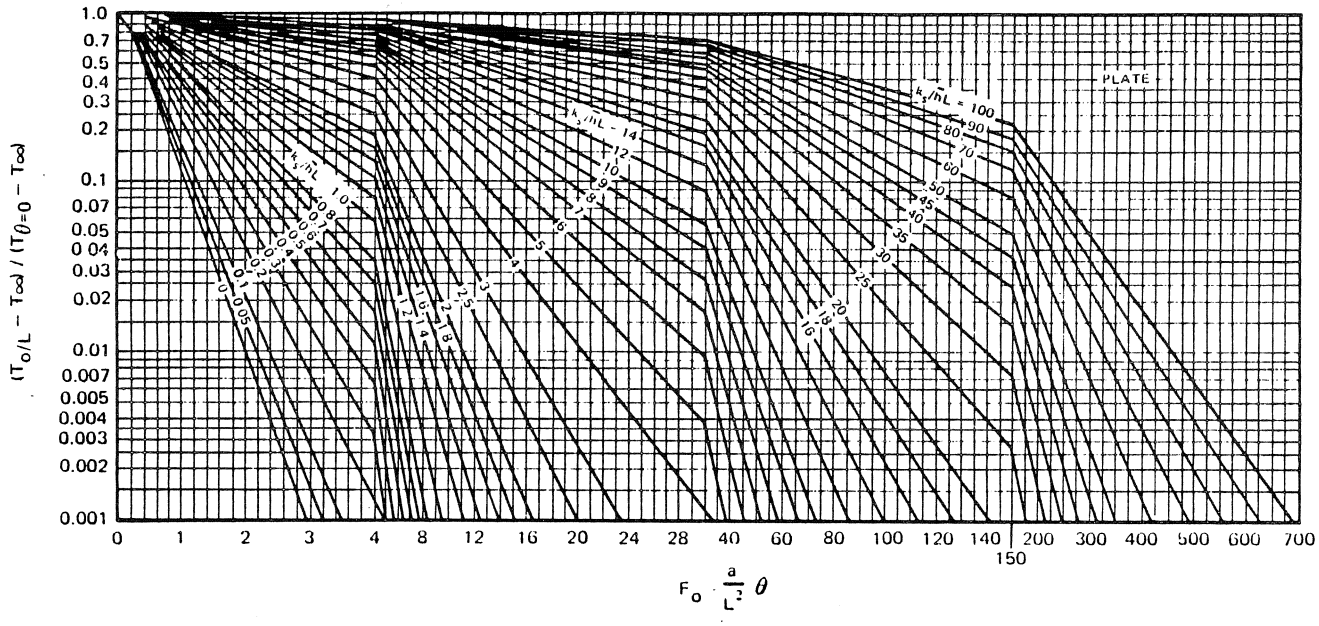

Figure 14-28. Central Temperature History in an Infinite Plate

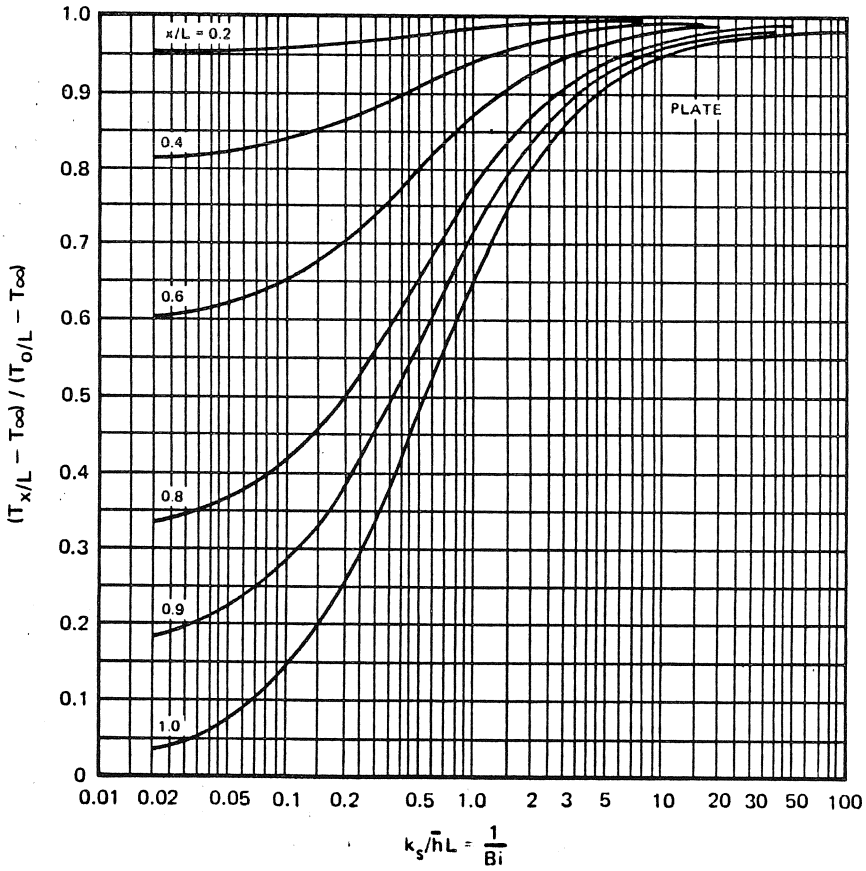

Figure 14-29. Position Correction Chart for an Infinite Plate

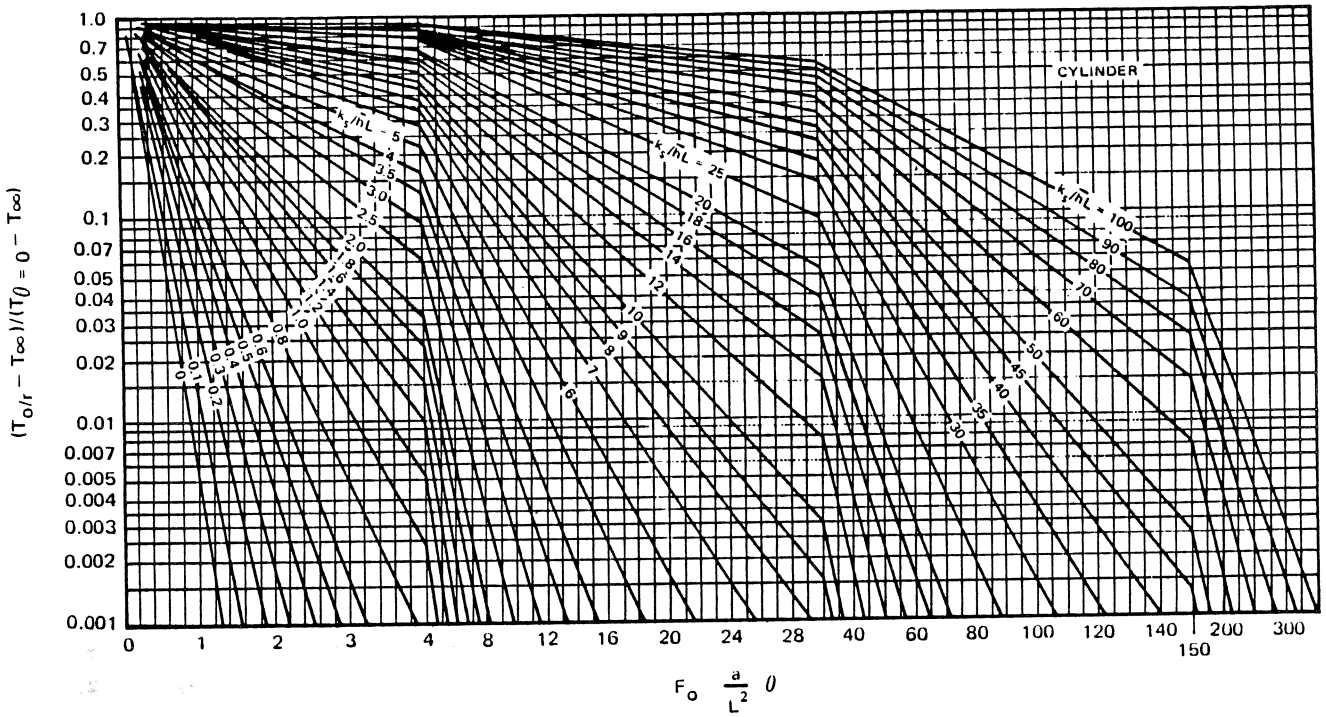

Figure 14-30. Central Temperature History in an Infinite Cylinder

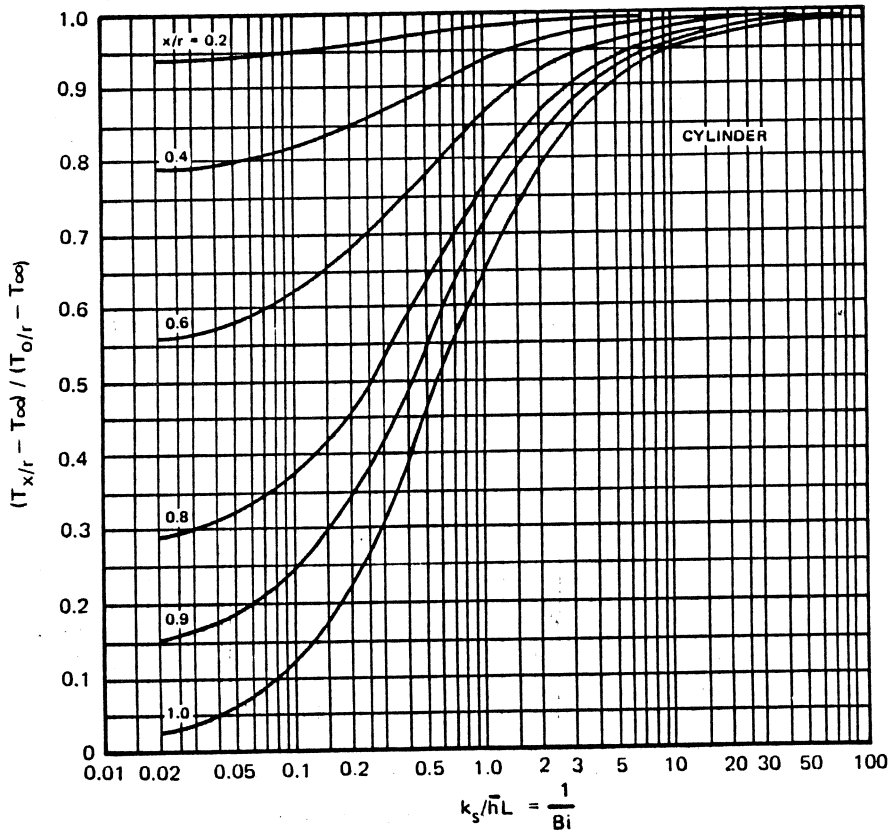

Figure 14-31. Position Correction Chart for an Infinite Cylinder

continuous heavy dashed curve is approximated by short straight lines between sectional planes. Each line has a slope which closely approximates the temperature gradient at the center of the layer. The accuracy of this linearization increases as the selected layer thickness Δx is decreased.

Since a temperature difference exists, heat will flow from the higher to the lower temperature at a rate proportional to the temperature gradient. In the first layer, the average initial temperature gradient is $(T_s - T_1^0)/\Delta x$ and in the second layer it is $(T_1^0 - T_2^0)/\Delta x$. During a time interval $\Delta\theta$, heat is therefore conducted from the surface to cross-sectional plane 1 and also from plane 1 to plane 2. The amount of heat flowing toward plane 1 is greater than the amount of heat flowing from the same plane, as seen by inspection of the respective temperature gradients.

This difference in heat flow rates changes the internal energy, and temperature, in a layer ab extending $\Delta x/2$ to the left and to the right of plane 1. After time interval

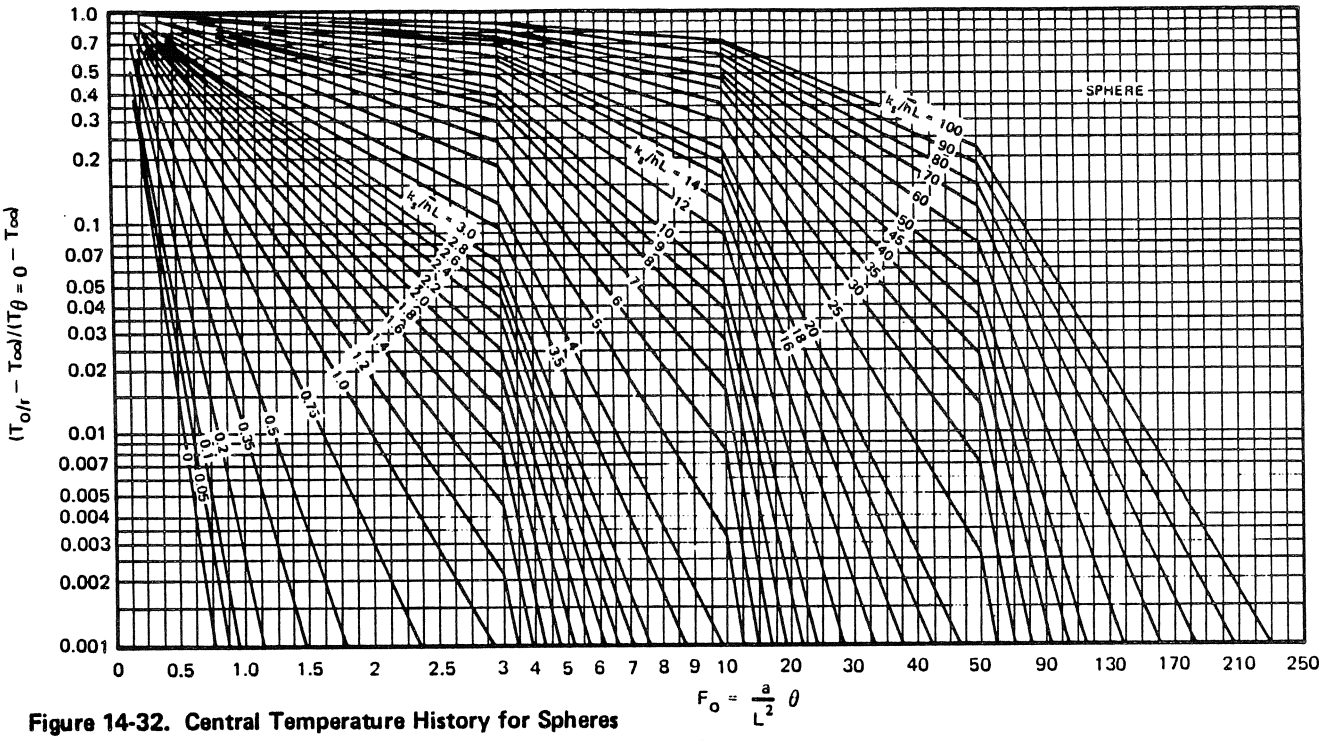

Figure 14-32. Central Temperature History for Spheres

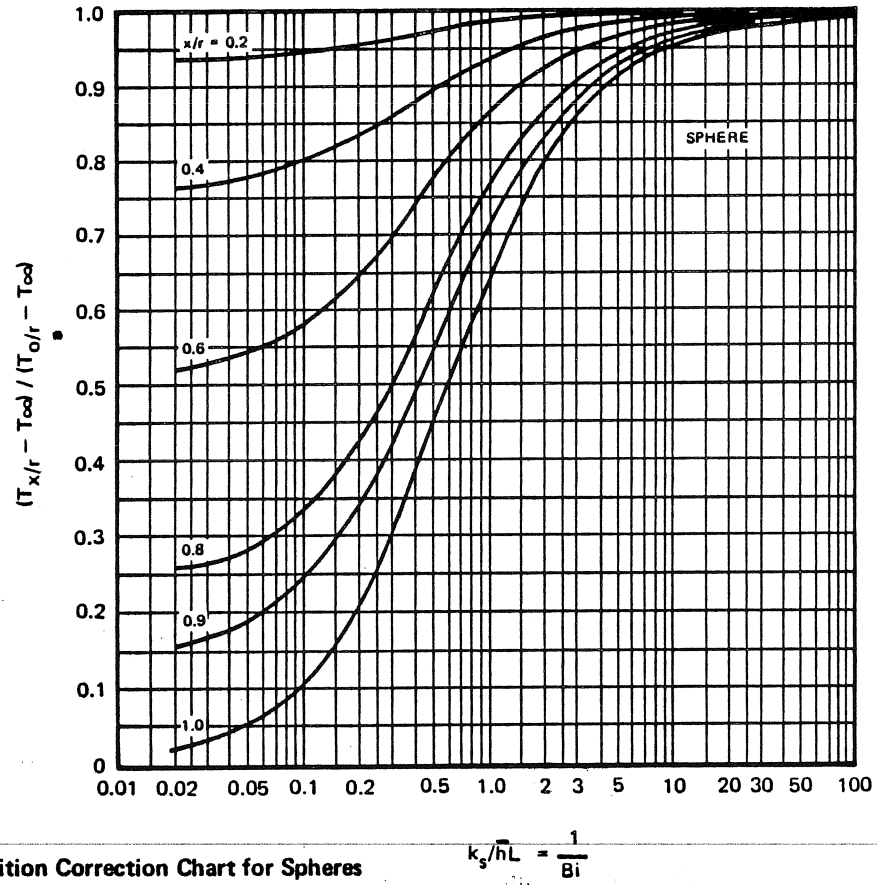

Figure 14-33. Position Correction Chart for Spheres

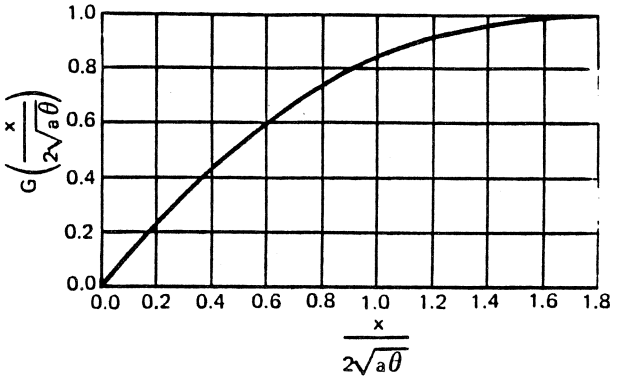

Figure 14-34. Gaussian Error Integral

$\Delta\theta$, the temperature at plane 1 is approximated by T_1^1, which is obtained by drawing a straight line between T_s and T_2^0. Figure 14-39 shows the change in temperature distribution through several layers for two $\Delta\theta$ time intervals.

The Schmidt method is also applicable to the boundary condition where the surface is in contact with a fluid whose temperature is either constant or is a known function of time. Figure 14-40 is an illustration of a Schmidt plot where the boundary condition varies with time. In this example, a large plate is exposed initially to a hot environment on one side and a cold environment on the other side, with an initial temperature distribution shown by the dashed line. The temperature on the hot side is then suddenly reduced to the temperature represented by the horizontal dashed line. The extension of the wall on the hot side represents the thermal resistance between the surface and the fluid. This resistance is not combined with a thermal capacitance.

14-2.3.4 Numerical Methods

In transient systems, the initial temperature distribution is assumed known, but its variation with time must be determined. This kind of problem can be readily solved by numerical methods on a digital computer using a computer program such as MDAC Computer Program JA 26, which was described in 14-2.2.3.

For transient systems, the general conduction equation for isotropic materials:

$$\frac{\partial^2 T}{\partial x_2} + \frac{\partial^2 T}{\partial y^2} + \frac{\partial^2 T}{\partial z^2} + \frac{\dot{q}}{k} = \frac{1}{a}\frac{\partial T}{\partial \theta} \qquad (70)$$

is transformed into a finite difference equation for the interior three-dimensional conduction region shown in Figure 14-41, where $\Delta x = \Delta y = \Delta z$,

$$T_{ot+1} = \frac{1}{M}(T_1 + T_2 + T_3 + T_4 + T_5 + T_6)^t + \left(1 - \frac{6}{M}\right)T_{ot} + \frac{\dot{q}_{ot}\Delta x^2}{k\,M} \qquad (71)$$

where the subscripts 0, 1, 2, 3, etc., refer to nodal points, the superscripts t and t + 1 refer to time intervals $\Delta\theta$ apart, and $M = \Delta x^2/a\Delta\theta$. The corresponding relations for two- and one-dimensional systems, respectively, are:

$$T_{ot+1} = \frac{1}{M}(T_1 + T_2 + T_3 + T_4)^t + \left(1 - \frac{4}{M}\right)T_{ot} + \frac{\dot{q}_{ot}\Delta x^2}{k\,M} \qquad (72)$$

$$T_{ot+1} = \frac{1}{M}(T_1 + T_3)^t + \left(1 - \frac{2}{M}\right)T_{ot} + \frac{\dot{q}_{ot}\Delta x^2}{k\,M} \qquad (73)$$

If the temperature distribution at time θ is known, equations 71, 72 and 73 can be used to predict the temperature at nodal point 0 after a time interval $\Delta\theta$ has elapsed. By applying the same procedure to every point in a network, the temperature distribution in a body at time $\theta + \Delta\theta$ can be computed from a given distribution at time θ.

For a one-dimensional transient system, as shown in Figure 14-42, equation 73 can be written for any arbitrary interior nodal point n in the form:

$$T_{nt+1} = \frac{1}{M}(T_{n+1} + T_{n-1})^t + \left(1 - \frac{2}{M}\right)T_{nt} \qquad (74)$$

Equation 74 can be used to calculate the temperature at section n at time $\theta = (t+1)\,\Delta\theta$ from the temperatures at sections n+1, n, and n−1 at time $\theta = t\Delta\theta$. The coefficients for $T_{n+1}t$ and $T_{n-1}t$ are positive for any value of M, but the coefficient of T_nt will be negative if the time interval $\Delta\theta$, is chosen so large that M becomes less than two.

If the coefficient of T_nt, the present temperature at nodal point n, were negative, equation 74 would imply that the higher the temperature T_n is at time t, the lower it will be at a time $\Delta\theta$ later. This would be in violation of thermodynamic principles, and would also lead to instabilities in the numerical solution. Therefore, in order to obtain valid solutions for temperature distribution of interior points in an unsteady conduction network, negative coefficients must be avoided by appropriate choice of $\Delta\theta$ and Δx. Negative coefficients will be avoided, and numerical solutions will converge if:

$M \geq 2$ for one-dimensional cases
$M \geq 4$ for two-dimensional cases
$M \geq 6$ for three-dimensional cases

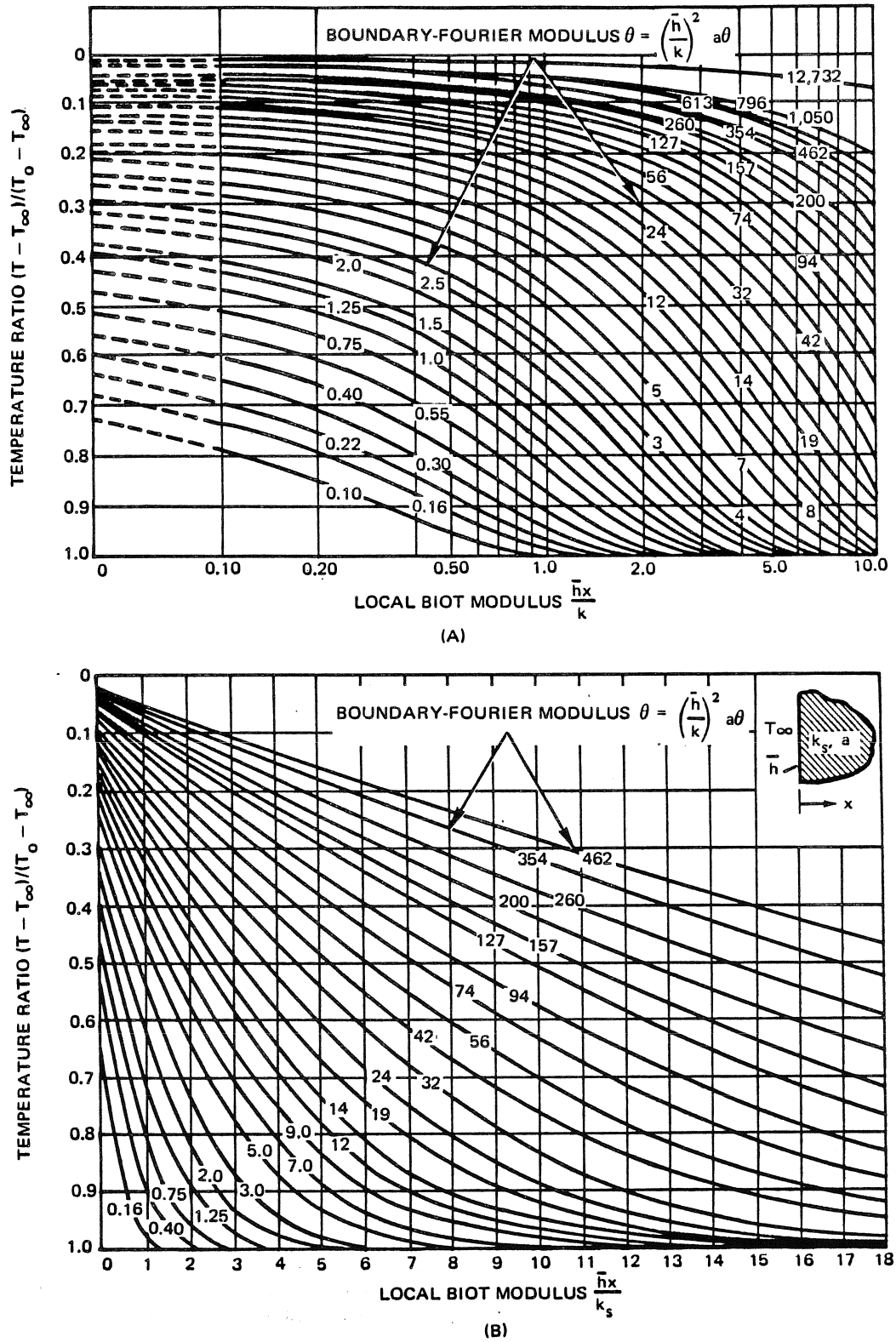

Figure 14-35. Dimensionless Temperature Distribution in a Semi-Infinite Slab Subjected to a Sudden Change in Environmental Temperature

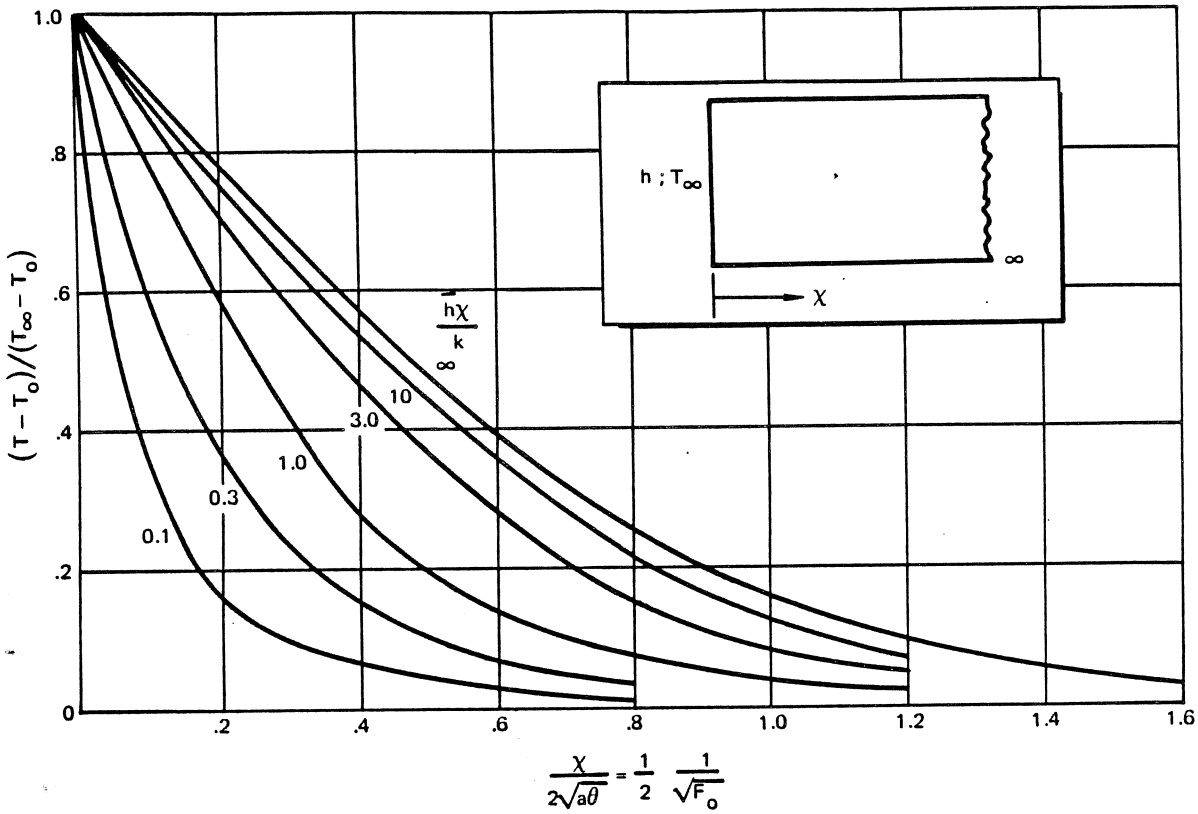

Figure 14-36. Dimensionless Temperature Ratio in a Semi-Infinite Solid with Convection at the Surface

The accuracy of a numerical solution increases as the distance Δx between nodes is decreased. The establishment of a value of Δx places an upper limit on the permissible value of the time interval $\Delta\theta$. Therefore, an accurate and stable numerical solution requires that $\Delta\theta$ be quite small. If Δx is not made very small, reasonable accuracy usually can be obtained by increasing M significantly above the foregoing minimum values.

Heat transfer across a boundary must be expressed in finite-difference equations which are different than the equations for the interior of the system. In a one-dimensional system of surface area A with a unit surface conductance h_c and a heat flux q_o per unit area, the future surface node temperature T_o^{t+1} is obtained from:

$$T_{ot+1} = \left(1 - \frac{2N+2}{M}\right)T_{ot} + \frac{2N}{M}T_\infty + \frac{2}{M}T_1 t + \frac{2\Delta x}{k\,M}q_o \qquad (75)$$

where:

$$M = \Delta x^2/a\Delta\theta$$

$$N = h_c\Delta x/k.$$

Similarly, the finite different equation for the future temperature at a surface nodal point in a two-dimensional system, as shown in Figure 14-43 is:

$$T_{ot+1} = \left(1 - \frac{2N+4}{M}\right)T_{ot} + \frac{1}{M}(T_2 t + T_3 t + 2T_1 t) + \frac{2N}{M}T_\infty t + \frac{2\Delta x}{kM}q_{ot} \qquad (76)$$

If the nodal point 0 is in a corner and the heat flux q_o and the convective flux are the same on both surfaces:

$$T_{ot+1} = \left(1 - \frac{4N+4}{M}\right)T_{ot} + \frac{2}{M}(T_2 t + 2T_1 t) + \frac{4N}{M}T_\infty t + \frac{4\Delta x}{kM}q_{ot} \qquad (77)$$

The presence of surface-nodal-point equations requires a reconsideration of the lower limit of M for which the numerical solution converges. To avoid negative coefficients, it is necessary to select Δx and $\Delta\theta$ so that:

$M \geq 2N + 2$ for one-dimensional cases

$M \geq 2N + 4$ for two-dimensional systems without corners

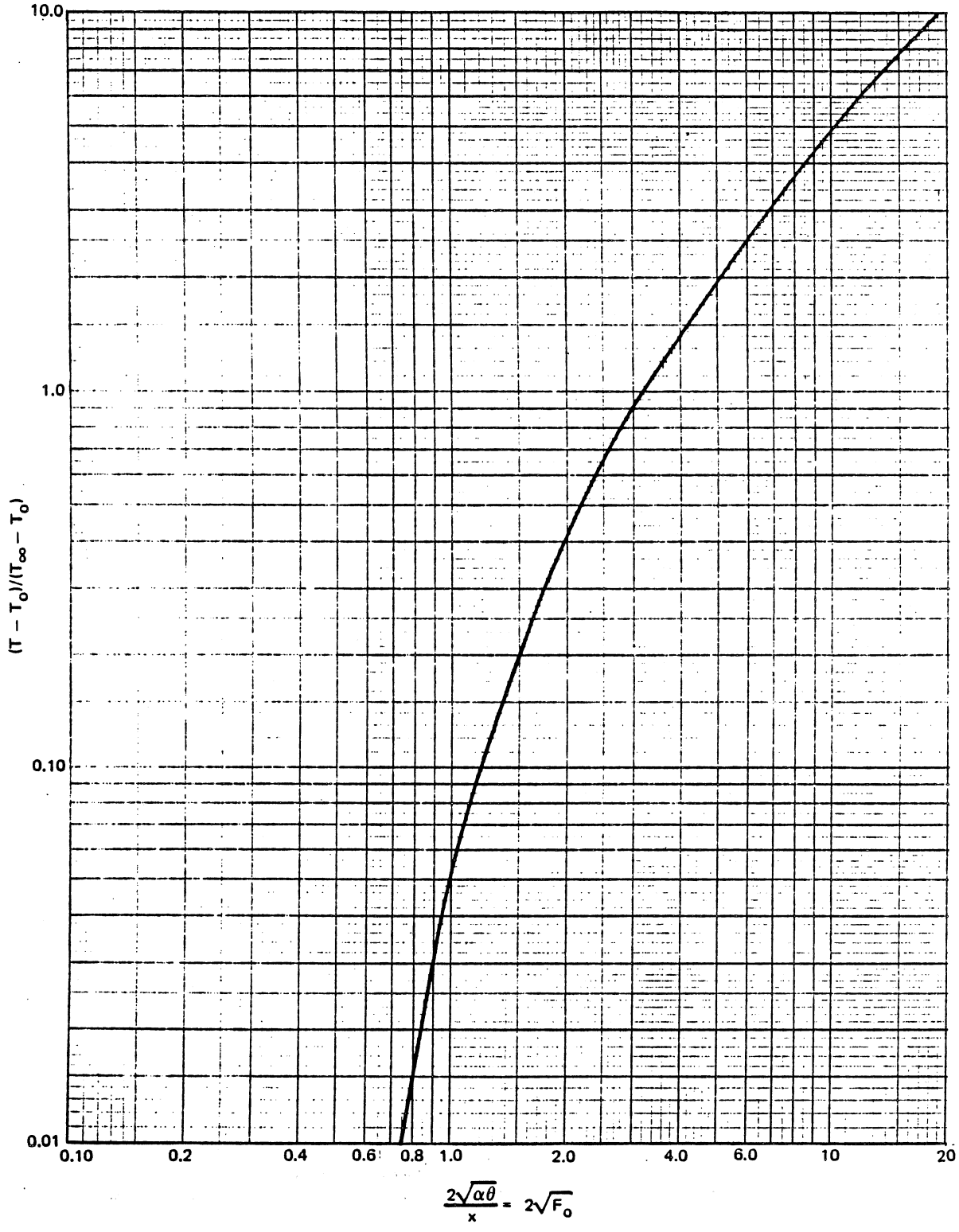

Figure 14-37. Semi-Infinite Solid with Constant Heat Flux at the Surface

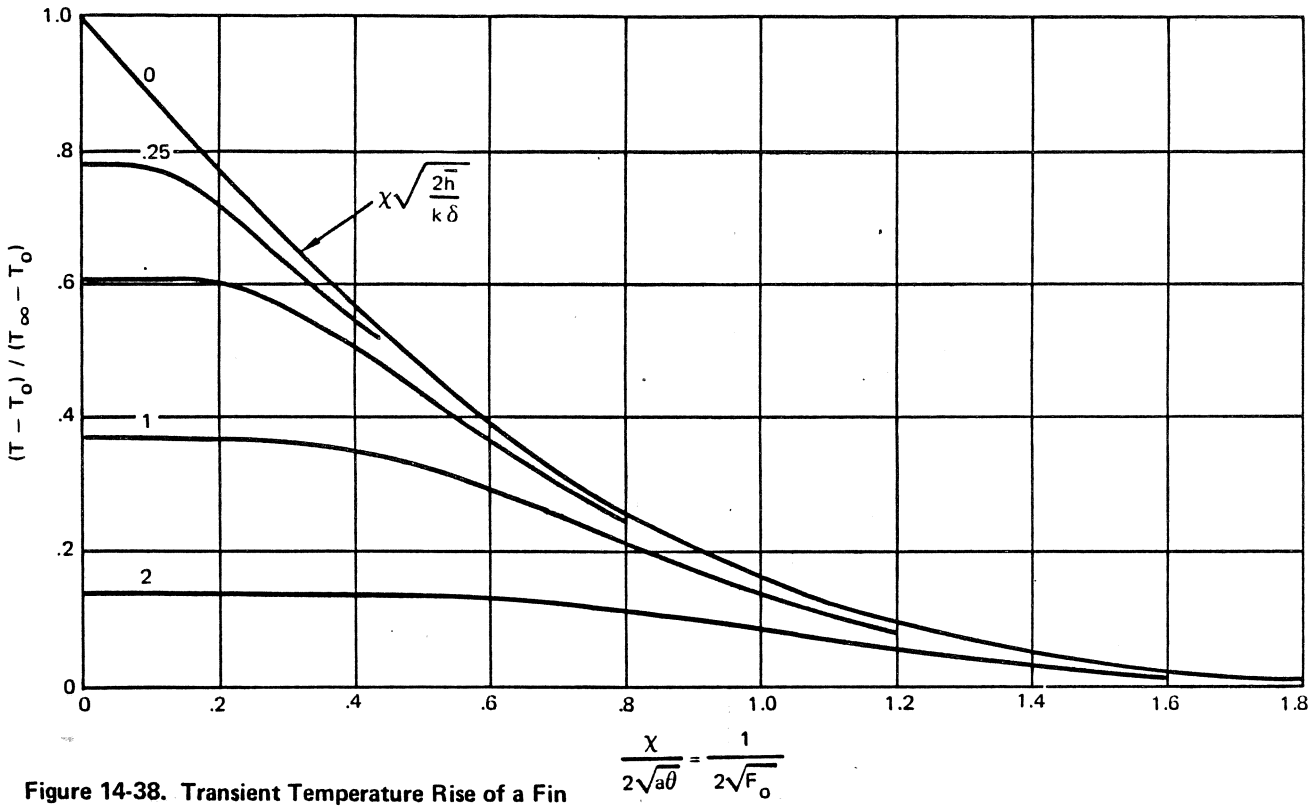

Figure 14-38. Transient Temperature Rise of a Fin

$M \geq 4N + 4$ for two-dimensional systems with corners

An inspection of the stability limits for equations 75, 76 and 77 shows that for large values of N, i.e., for systems with a large ratio of surface conductance to thermal conductivity, the value of M required for stability can become very large. This means that either very many subdivisions or a very small time increment must be used. Other techniques of avoiding computational instability, and the application of numerical methods to flow systems and complex boundary conditions involving radiation and phase change are discussed in G. M. Dusinberre, *Heat Transfer Calculations by Finite Differences*, Scranton, Pa., International Textbook Co., 1961.

14-3 RADIATION

Thermal radiation heat transfer consists of a continuous spectrum of electromagnetic waves which are produced by an emitting body, solely due to its temperature, and are absorbed by a receiving body. All bodies continuously emit thermal radiation over a wide range of wave lengths. For practical purposes, the radiation of importance in heat transfer calculations is limited to wave lengths ranging from 0.1 to 100 microns (μ). The total amount of radiation emitted by a body per unit area and time, called the total emissive power E, depends on the temperature and the characteristics of the surface of the body. At any particular temperature, the quantity of radiation emitted per unit wave length is different at the various wavelengths.

14-3.1 Radiation Laws

Observations of thermal radiation effects have resulted in the establishment of equations which describe these effects. The principles upon which these equations are based are so generally accepted that they are called laws. Each law, identified with the names of the investigators who developed the specific equations, is summarized in Table 14-10 and discussed in the following paragraphs.

14-3.1.1 Stephan-Boltzman Law

The total energy or emissive power E_b radiated by a black body is a function of the fourth power of the absolute temperature. It is described mathematically as:

$$E_b = \sigma T^4 \tag{78}$$

where σ is the Stephan-Boltzman constant = 0.1714×10^{-8} Btu/hr-ft^2-°R^4 and E_b is in Btu/hr-ft^2.

Reference to equation 4 shows that E_b is also equal to the radiation heat flow rate q_r divided by the radiating surface area, or $q_r/A = \sigma T^4$.

14-3.1.2 Planck's Law

A relationship known as Planck's law, which shows how emissive power is distributed among the different wavelengths, was derived mathematically as:

$$E_{b\lambda} = \frac{C_1 \lambda^{-5}}{e^{(C_2/\lambda T)} - 1} \tag{79}$$

Table 14-9. Transient Temperature Distribution in Two- and Three-Dimensional Systems

CASE NO.	DESCRIPTION	EQUATION
1.	Long Rectangular Bar 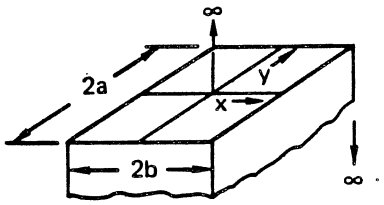	$\left(\frac{T-T_\infty}{T_o-T_\infty}\right)_{bar} = \left(\frac{T-T_\infty}{T_o-T_\infty}\right)_{2a\ plate} \left(\frac{T-T_\infty}{T_o-T_\infty}\right)_{2b\ plate}$
2.	Brick Shaped Body 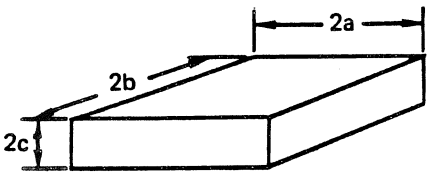	$\left(\frac{T-T_\infty}{T_o-T_\infty}\right)_{brick} = \left(\frac{T-T_\infty}{T_o-T_\infty}\right)_{2a\ plate} \left(\frac{T-T_\infty}{T_o-T_\infty}\right)_{2b\ plate} \left(\frac{T-T_\infty}{T_o-T_\infty}\right)_{2c\ plate}$
3.	Finite Cylinder 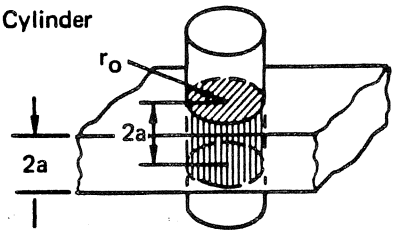	$\left(\frac{T-T_\infty}{T_o-T_\infty}\right)_{cyl\ 2a\ long} = \left(\frac{T-T_\infty}{T_o-T_\infty}\right)_{inf.\ cyl} \left(\frac{T-T_\infty}{T_o-T_\infty}\right)_{2a\ plate}$
4.	Quarter-Infinite Body (Edge bounded by two planes) 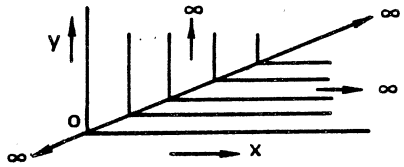	$\left(\frac{T-T_\infty}{T_o-T_\infty}\right)_{x,y} = \left(\frac{T-T_\infty}{T_o-T_\infty}\right)_x \left(\frac{T-T_\infty}{T_o-T_\infty}\right)_y$
5.	Eighth-Infinite Body (Corner bounded by three planes) 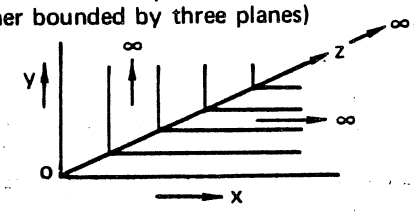	$\left(\frac{T-T_\infty}{T_o-T_\infty}\right)_{x,y,z} = \left(\frac{T-T_\infty}{T_o-T_\infty}\right)_x \left(\frac{T-T_\infty}{T_o-T_\infty}\right)_y \left(\frac{T-T_\infty}{T_o-T_\infty}\right)_z$
6.	Semi-Infinite Cylinder 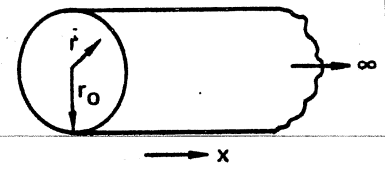	$\left(\frac{T-T_\infty}{T_o-T_\infty}\right)_{r,x} = \left(\frac{T-T_\infty}{T_o-T_\infty}\right)_r \left(\frac{T-T_\infty}{T_o-T_\infty}\right)_x$

Table 14-9A. Schneider Chart Application Summary

FIGURE NUMBER		CONFIGURATION		HEAT TRANSFER CONDITION		
BASIC	SHEET	r_i/r_e	SHELL TYPE	INSULATED SURFACE	HEAT SOURCE OR SINK*	SCHEMATIC
14-38A	1 2 3 4 5 6	0.2 0.4 0.6 0.8 0.9 0.99	CYLINDER	INNER	OUTER SURFACE	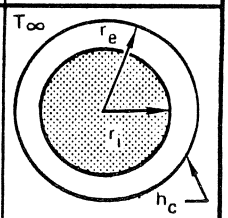
14-38B	1 2 3 4 5 6	0.2 0.4 0.6 0.8 0.9 0.99	CYLINDER	OUTER	INNER SURFACE	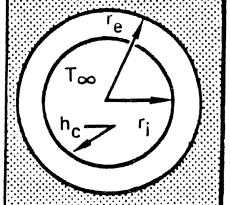
14-38C	1 2 3 4 5 6	0.2 0.4 0.6 0.8 0.9 0.99	SPHERE	INNER	OUTER SURFACE	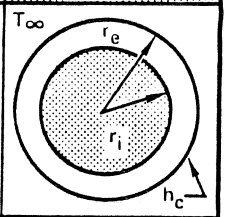
14-38D	1 2 3 4 5 6	0.2 0.4 0.6 0.8 0.9 0.99	SPHERE	OUTER	INNER SURFACE	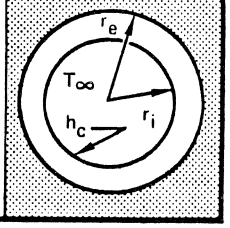

*SUDDEN APPLICATION OF A UNIFORM-TEMPERATURE CONVECTIVE ENVIRONMENT T_∞ AT $r = r_e$

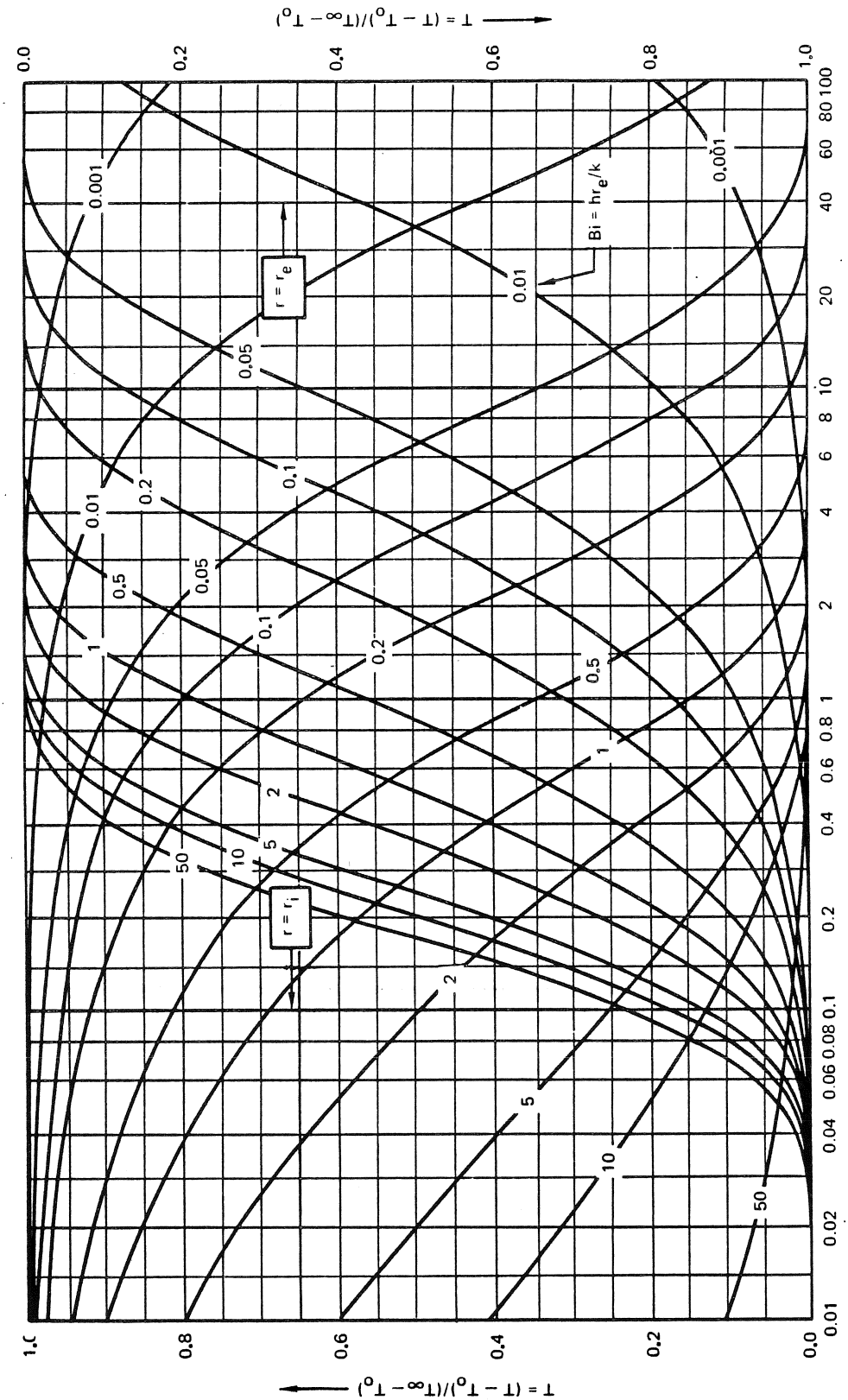

$R_i = r_i/r_e = 0.2$

TEMPERATURE RESPONSE OF A CYLINDRICAL SHELL INSULATED AT ITS INTERNAL SURFACE $r = r_i$ AFTER SUDDEN EXPOSURE TO A UNIFORM-TEMPERATURE CONVECTIVE ENVIRONMENT t_a AT $r = r_e$.

Figure 14-38A. Cylindrical Shell — Internal Surface Insulated (Sheet 1 of 6)

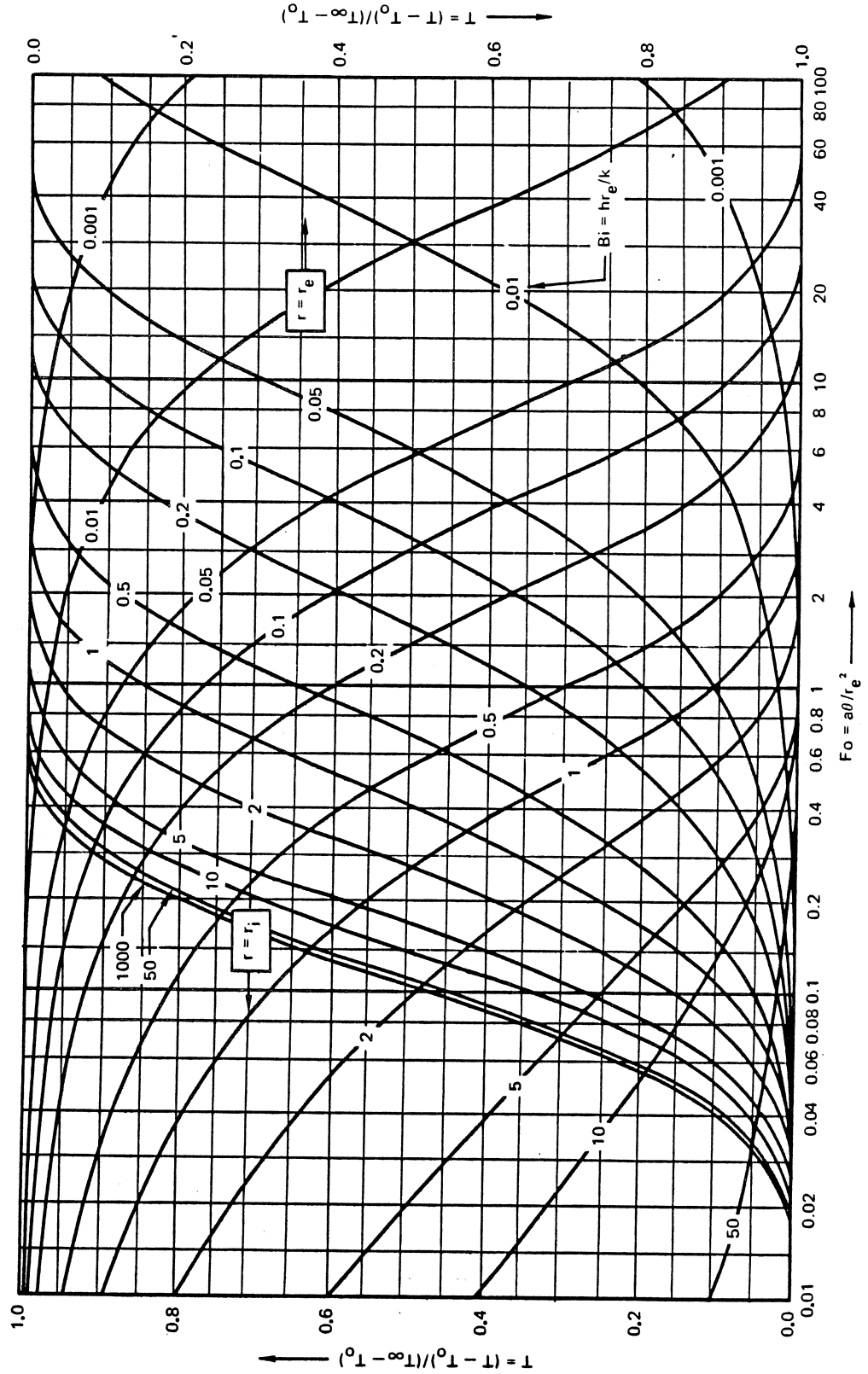

Figure 14-38A. Cylindrical Shell – Internal Surface Insulated (Sheet 2 of 6)

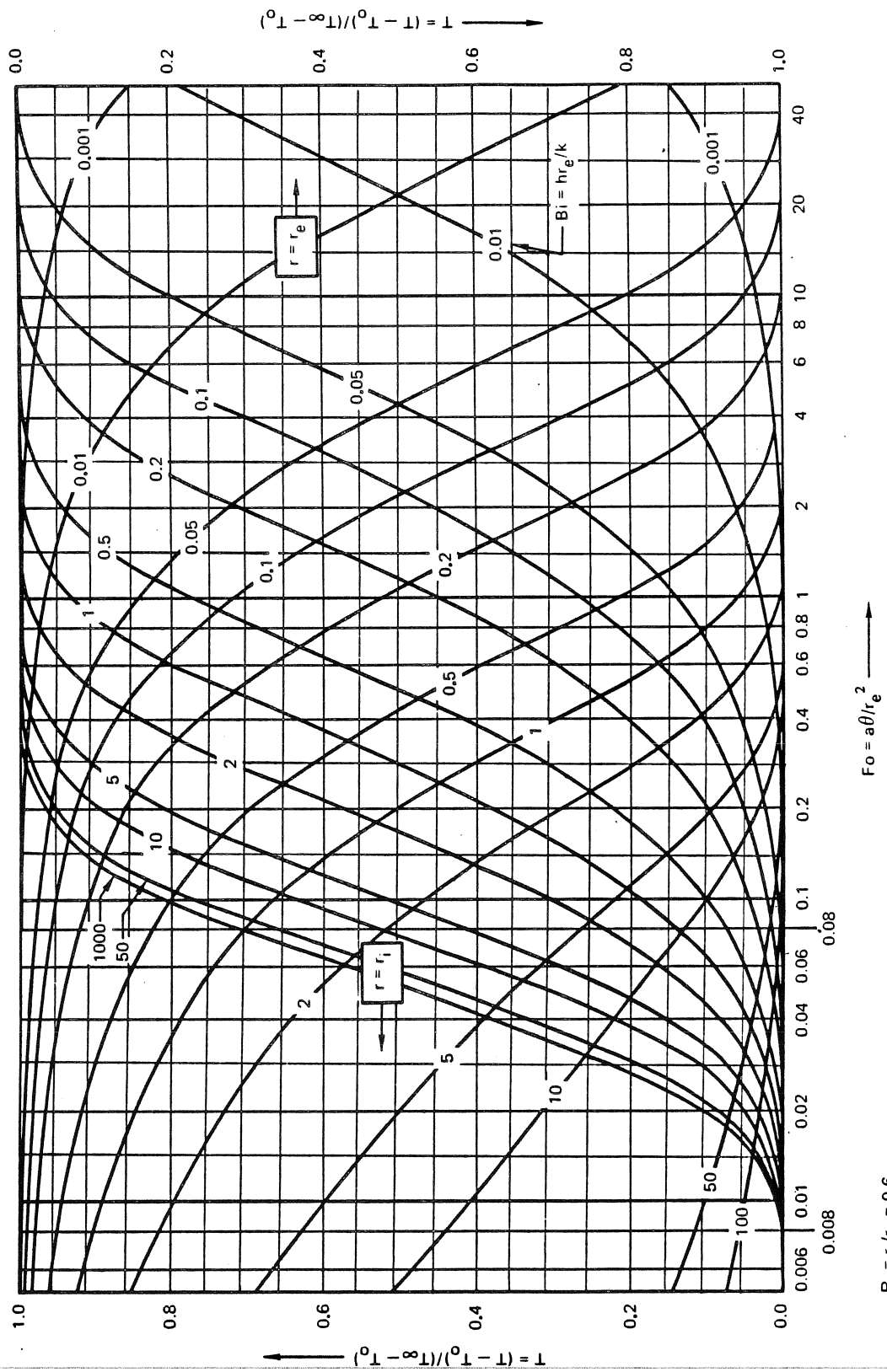

Figure 14-38A. Cylindrical Shell — Internal Surface Insulated (Sheet 3 of 6)

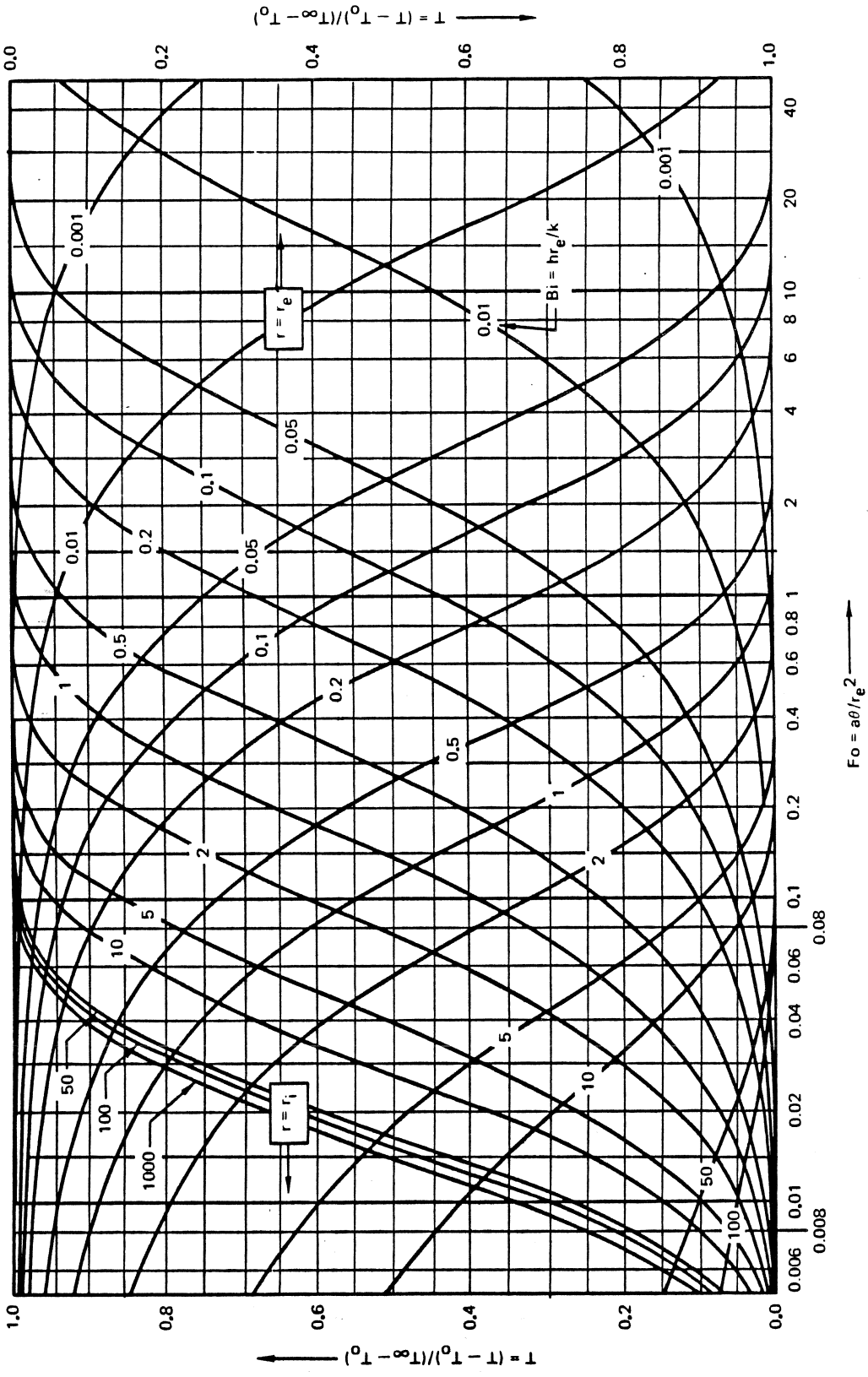

Figure 14-38A. Cylindrical Shell – Internal Surface Insulated (Sheet 4 of 6)

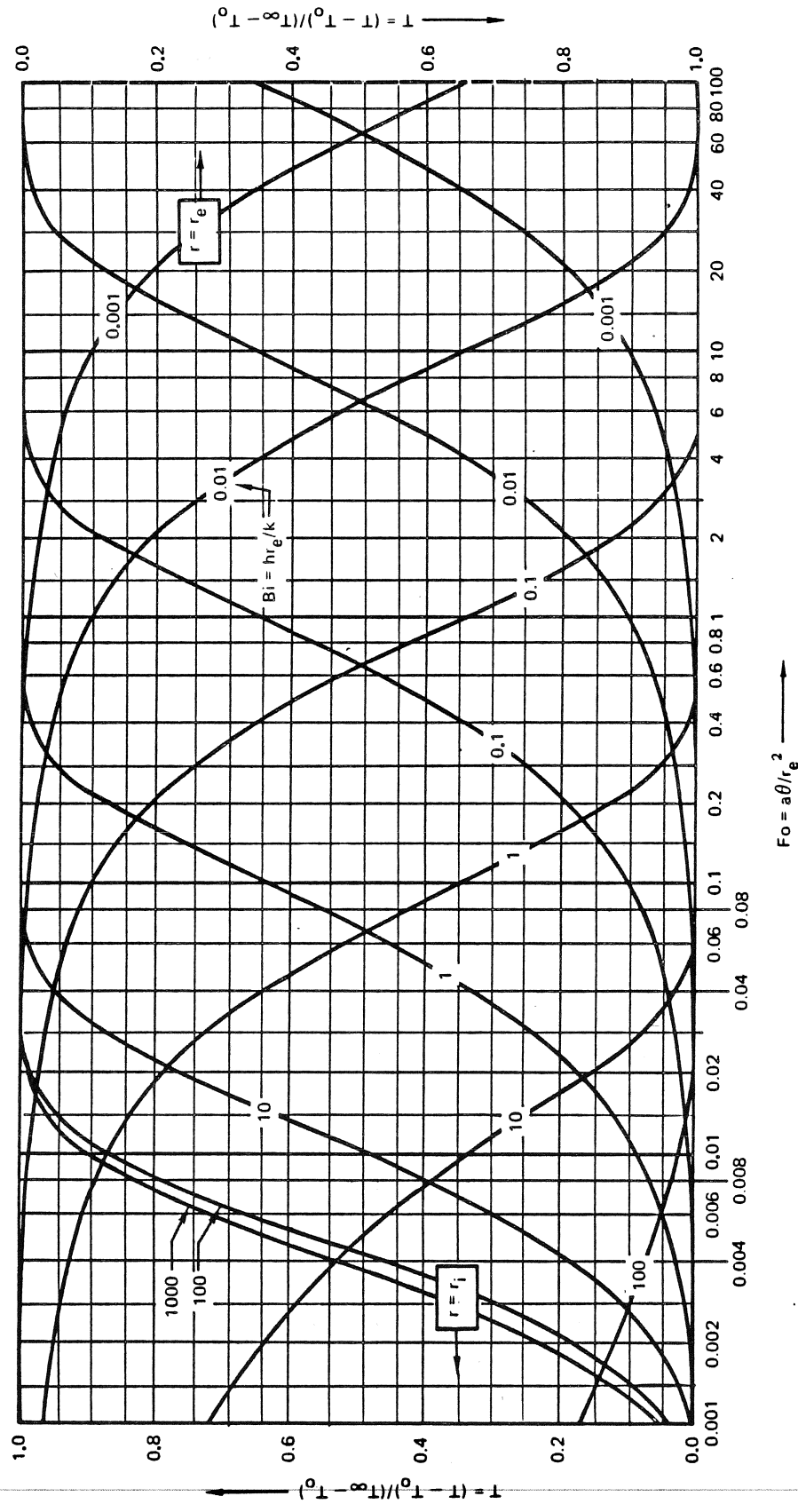

Figure 14-38A. Cylindrical Shell – Internal Surface Insulated (Sheet 5 of 6)

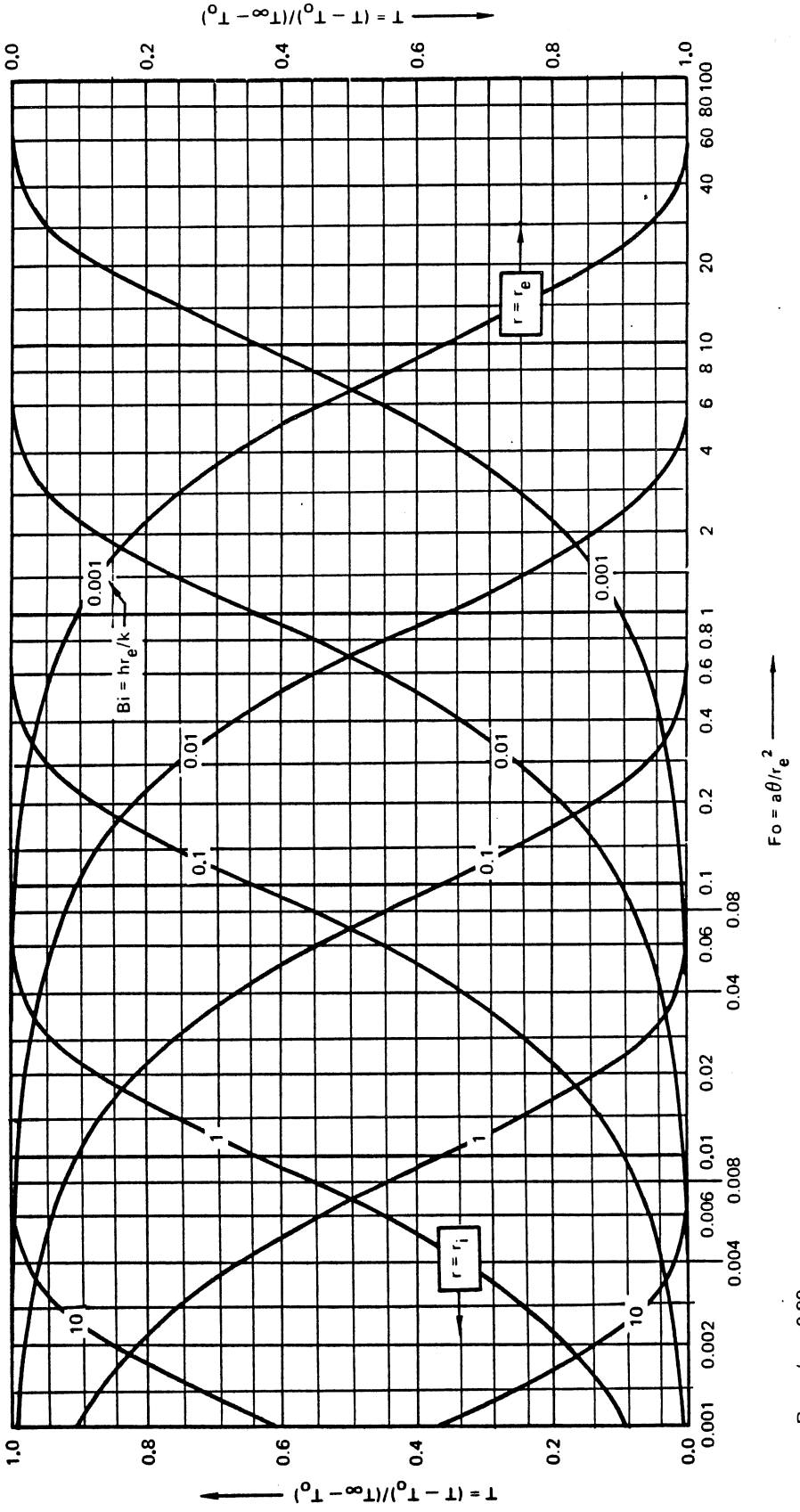

Figure 14-38A. Cylindrical Shell – Internal Surface Insulated (Sheet 6 of 6)

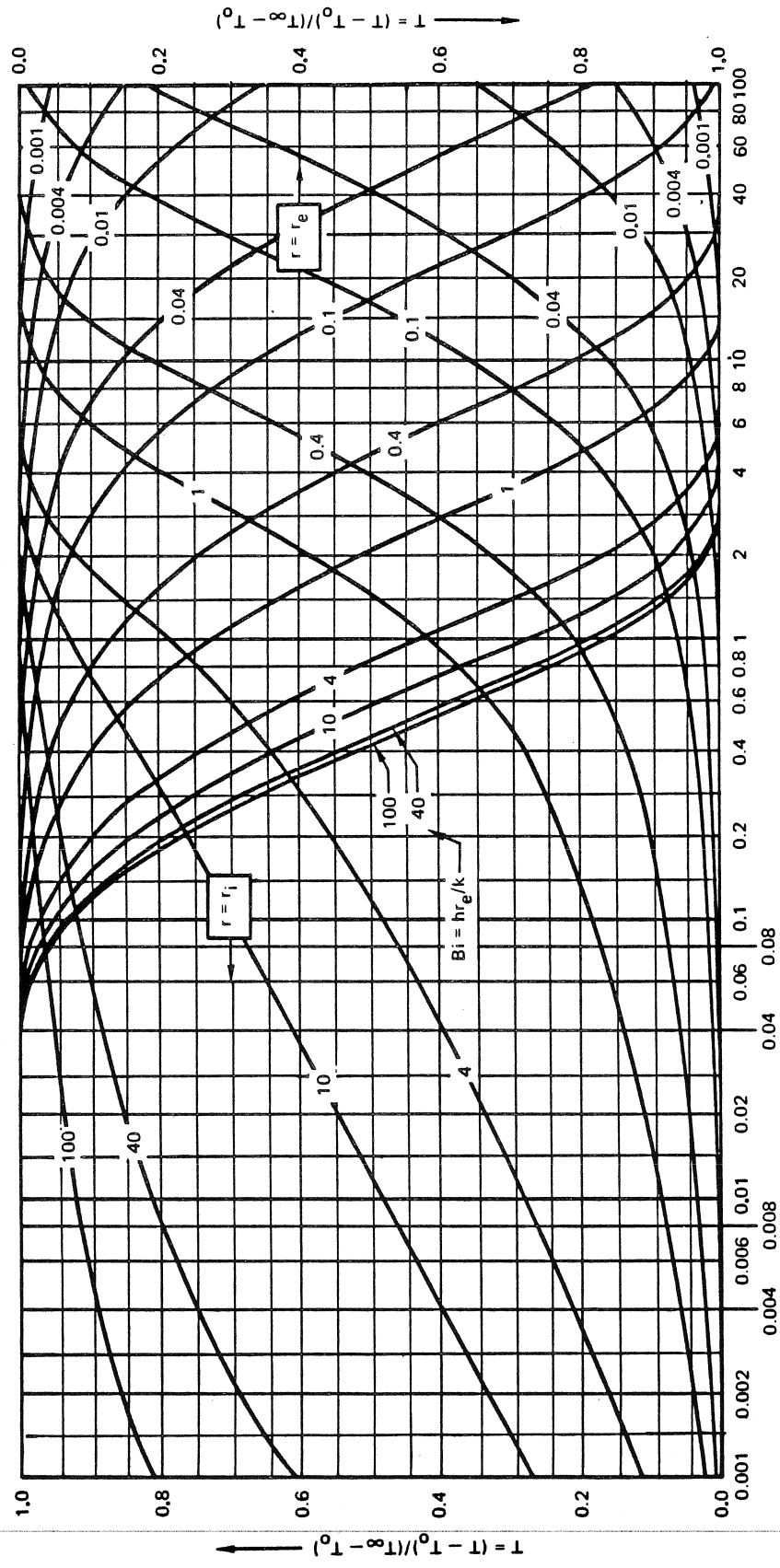

$R_i = r_i/r_e = 0.2$

TEMPERATURE RESPONSE OF A CYLINDRICAL SHELL INSULATED AT ITS EXTERNAL SURFACE $r = r_e$
AFTER SUDDEN EXPOSURE TO A UNIFORM-TEMPERATURE CONVECTIVE ENVIRONMENT t_a AT $r = r_i$.

Figure 14-38B. Cylindrical Shell – External Surface Insulated (Sheet 1 of 6)

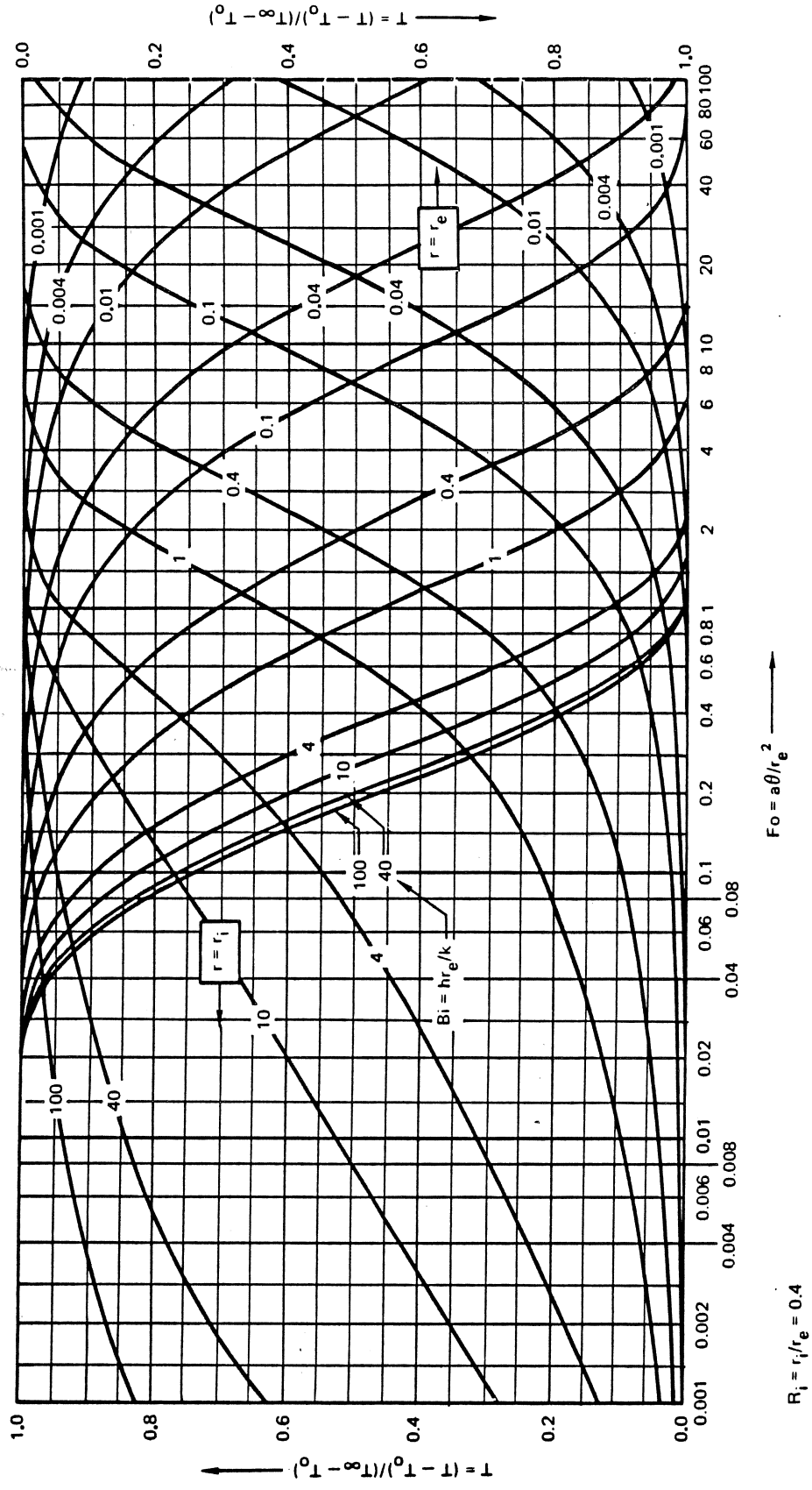

Figure 14-38B. Cylindrical Shell — External Surface Insulated (Sheet 2 of 6)

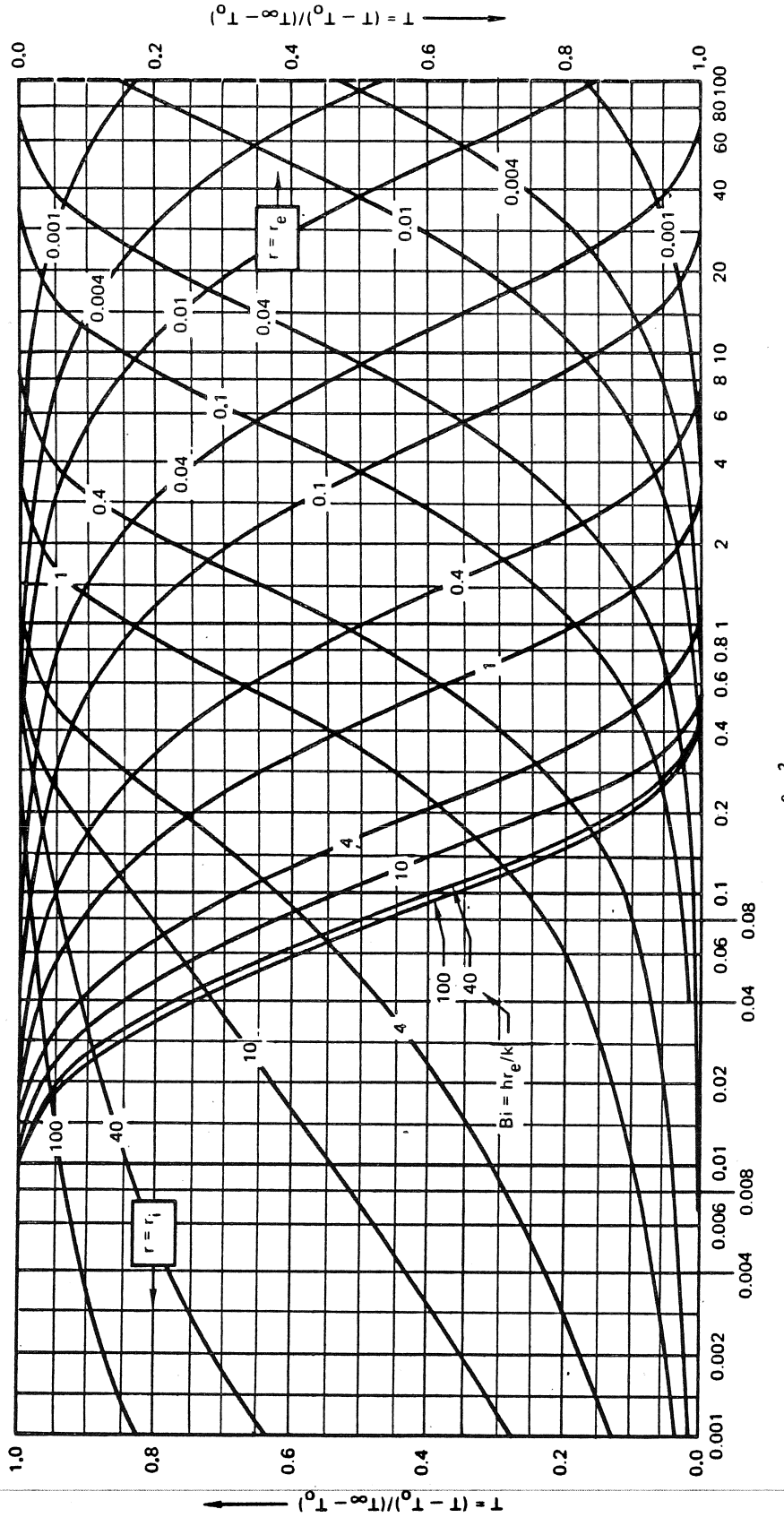

$R_i = r_i/r_e = 0.6$

Figure 14-38B. Cylindrical Shell – External Surface Insulated (Sheet 3 of 6)

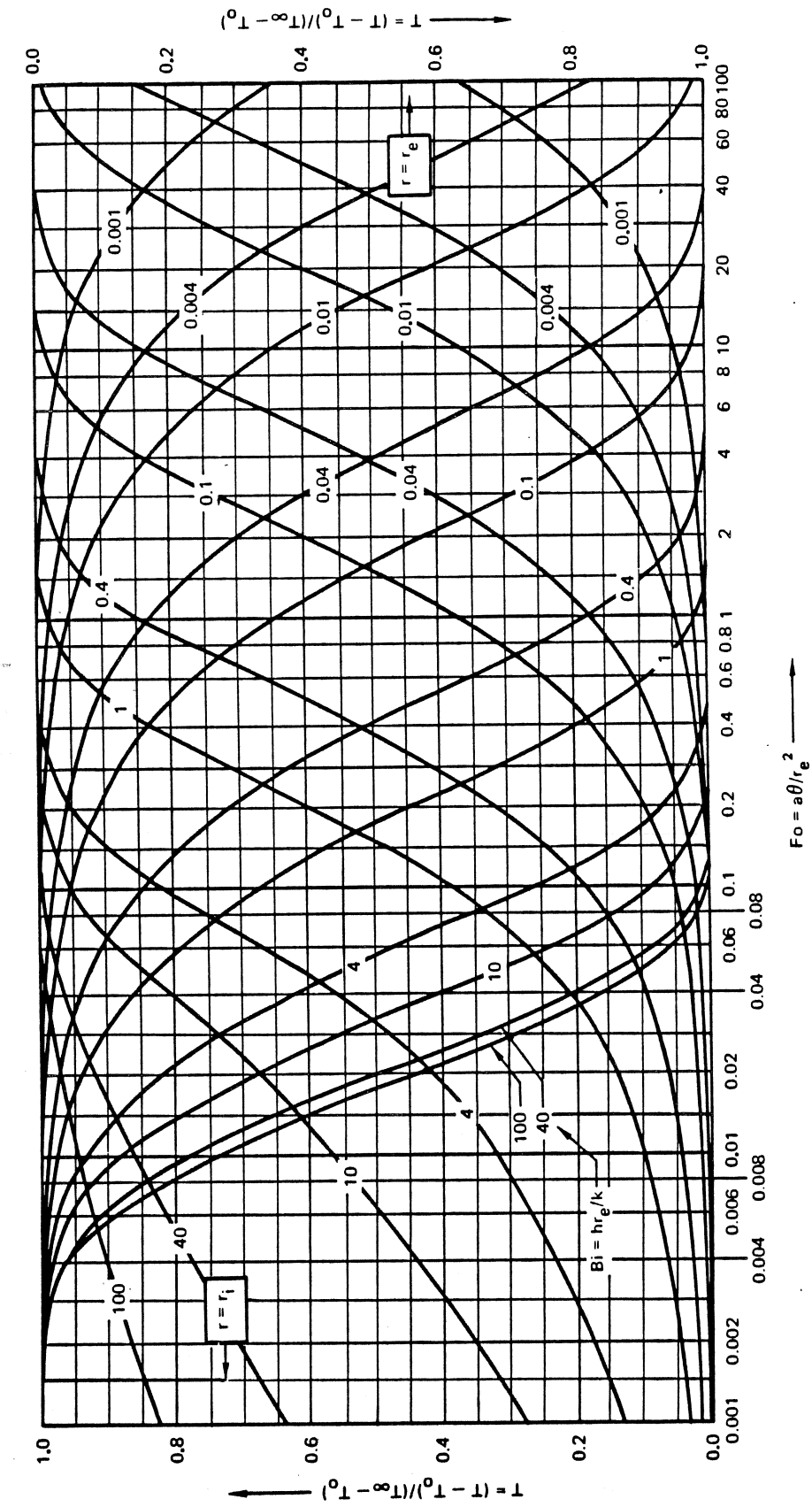

Figure 14-38B. Cylindrical Shell – External Surface Insulated (Sheet 4 of 6)

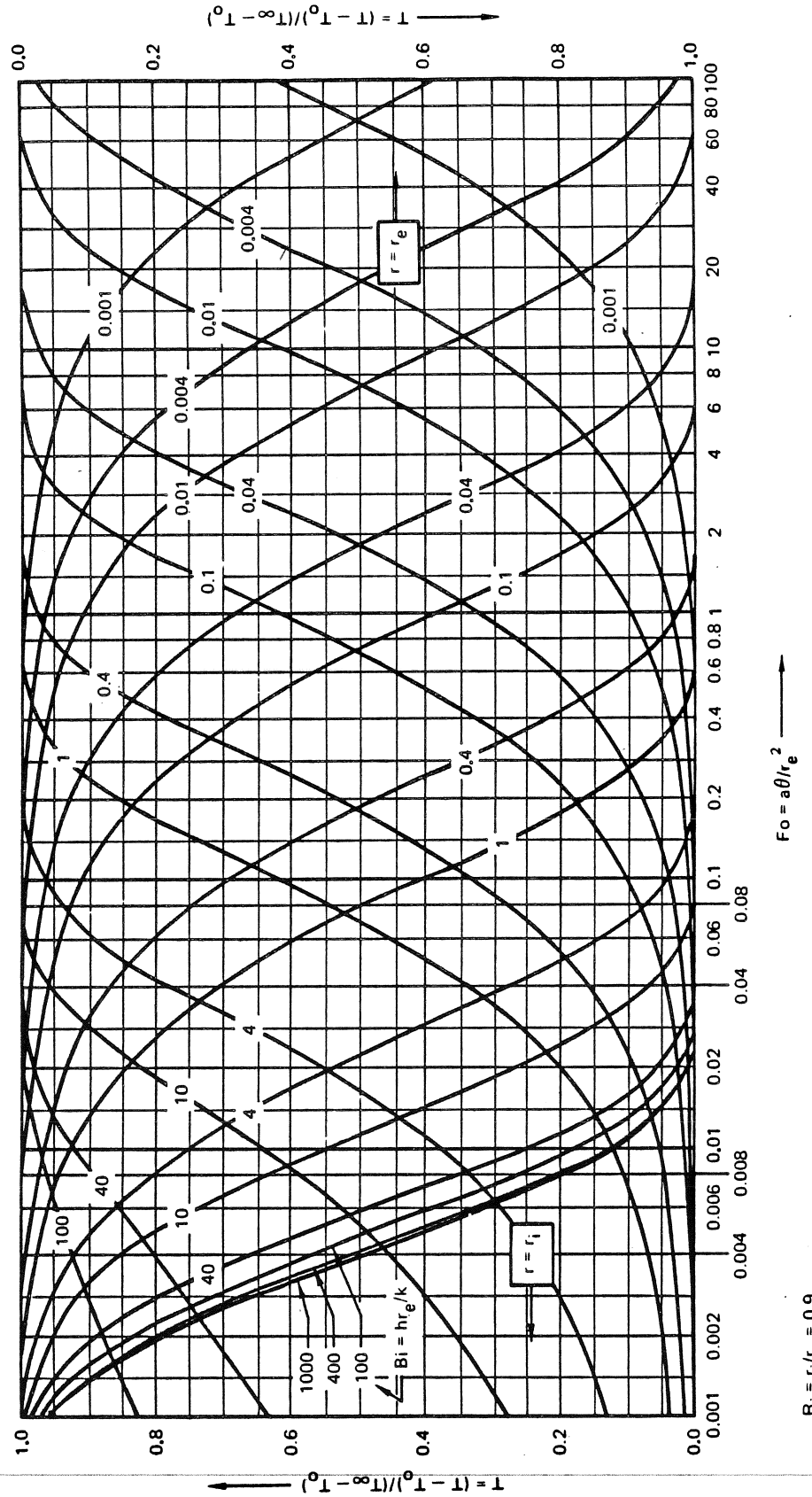

Figure 14-38B. Cylindrical Shell – External Surface Insulated (Sheet 5 of 6)

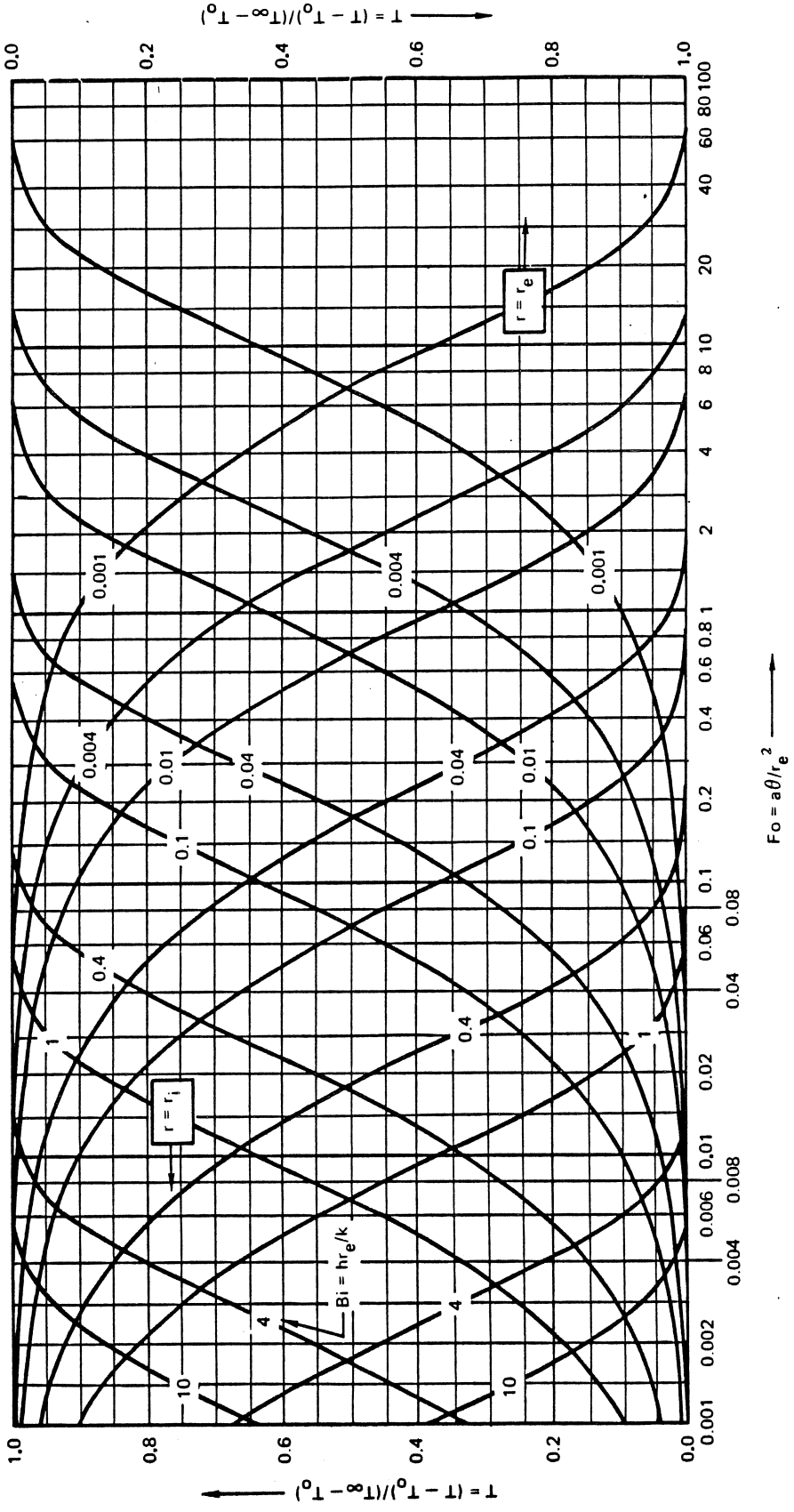

Figure 14-38B. Cylindrical Shell – External Surface Insulated (Sheet 6 of 6)

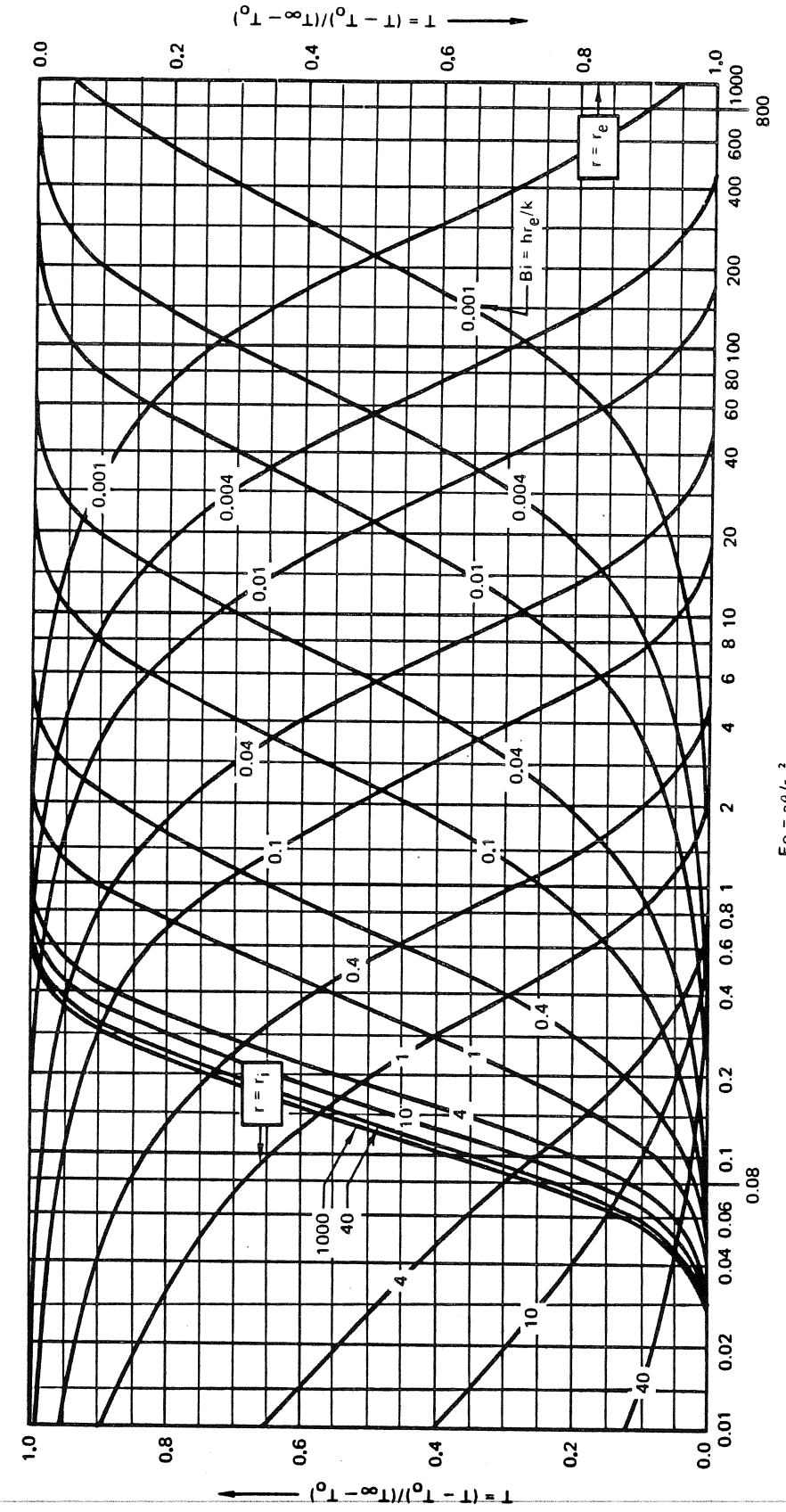

$R_i = r_i/r_e = 0.2$

TEMPERATURE RESPONSE OF A SPHERICAL SHELL INSULATED AT ITS INTERNAL SURFACE $r = r_i$
AFTER SUDDEN EXPOSURE TO A UNIFORM-TEMPERATURE CONVECTIVE ENVIRONMENT t_a AT $r = r_e$.

Figure 14-38C. Spherical Shell — Internal Surface Insulated (Sheet 1 of 6)

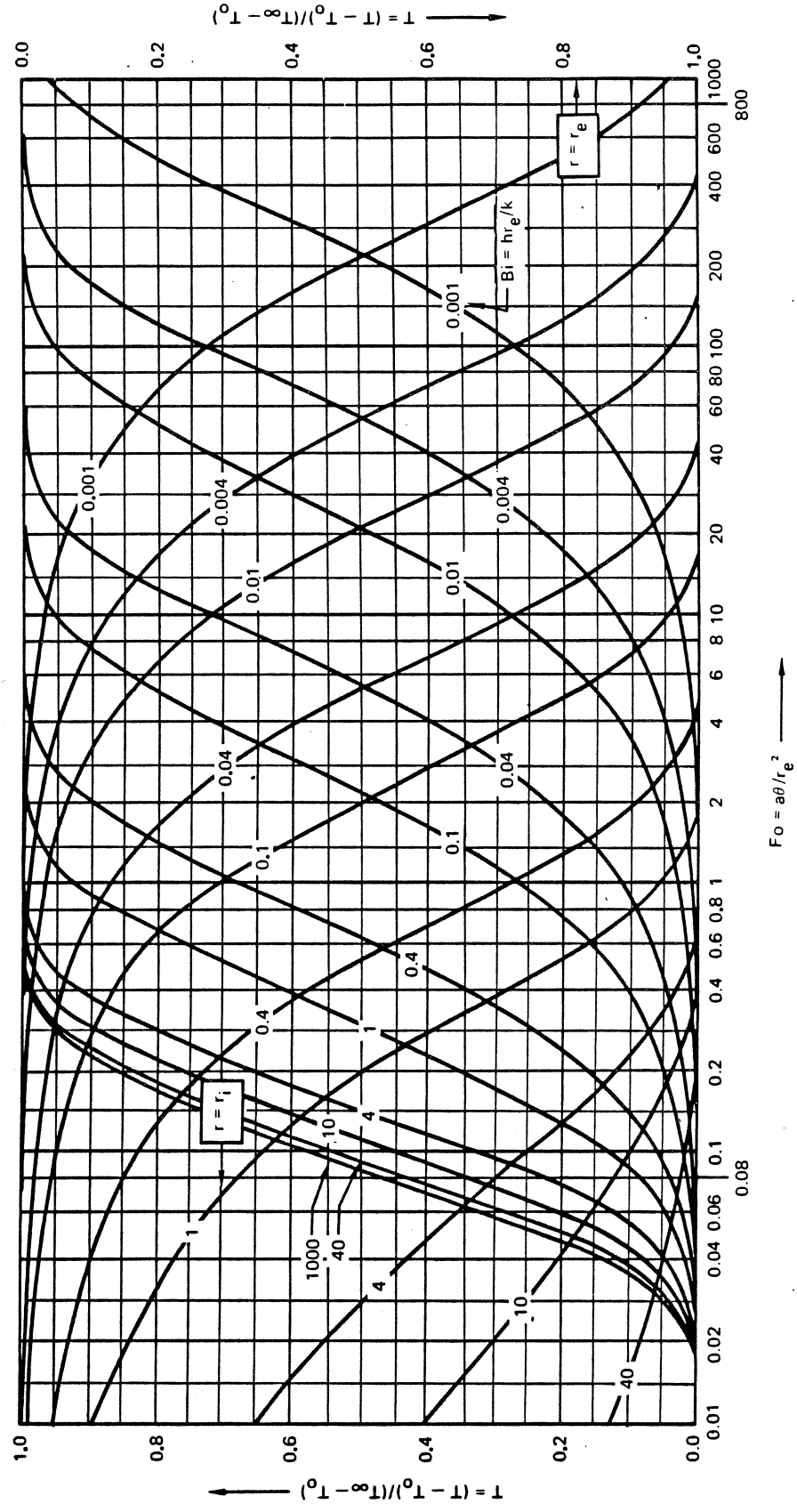

Figure 14-38C. Spherical Shell — Internal Surface Insulated (Sheet 2 of 6)

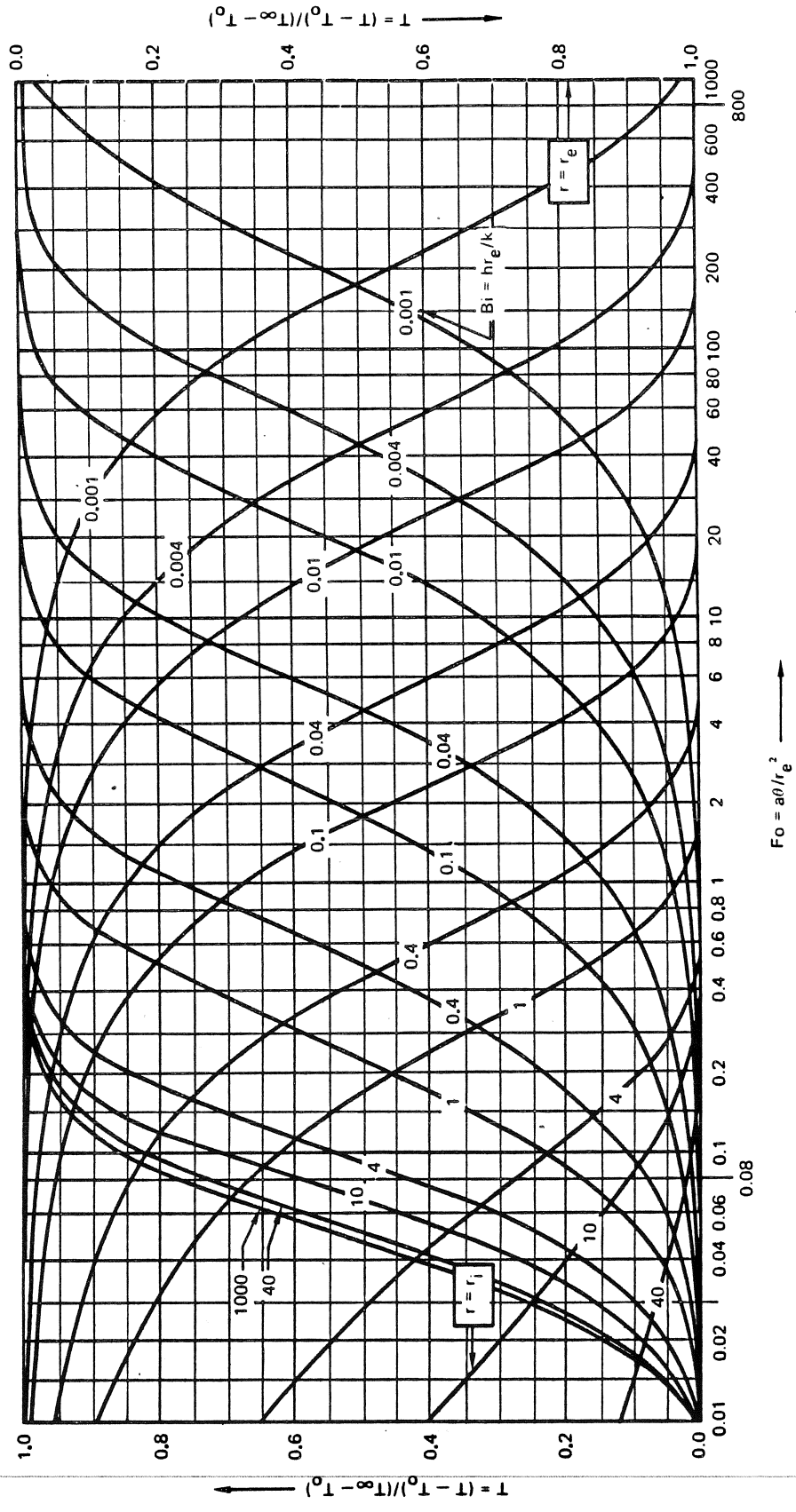

Figure 14-38C. Spherical Shell – Internal Surface Insulated (Sheet 3 of 6)

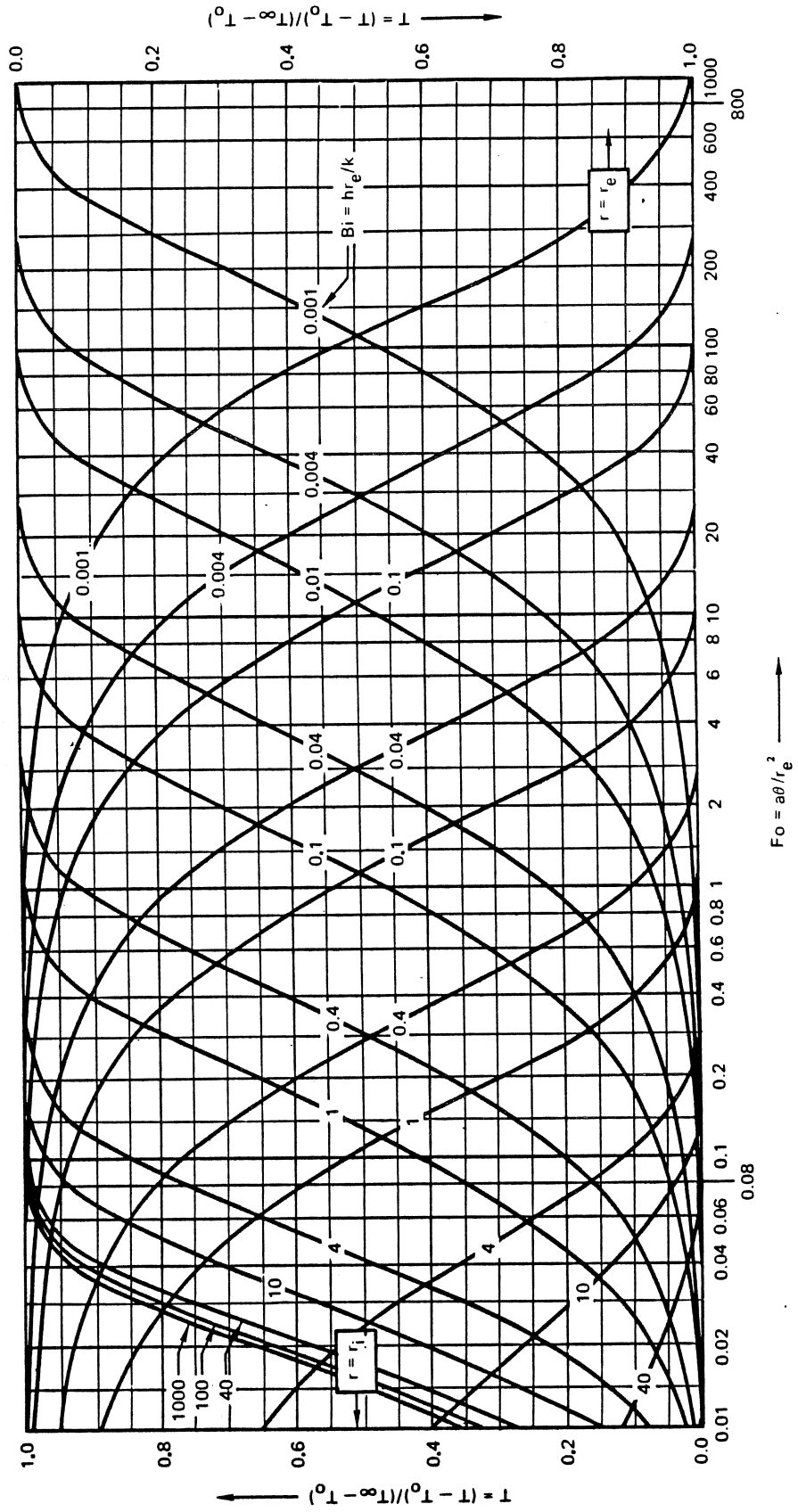

Figure 14-38C. Spherical Shell — Internal Surface Insulated (Sheet 4 of 6)

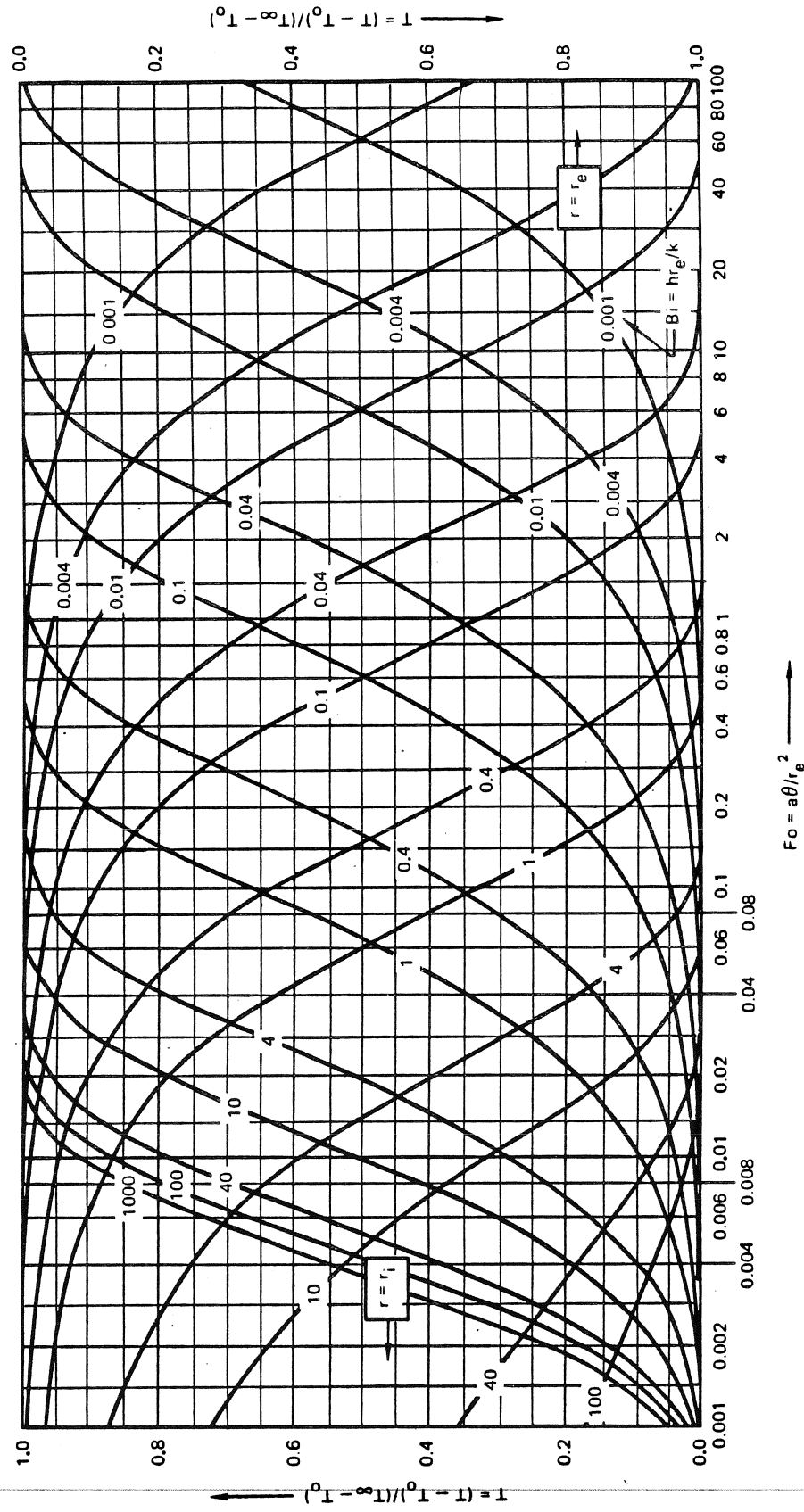

Figure 14-38C. Spherical Shell — Internal Surface Insulated (Sheet 5 of 6)

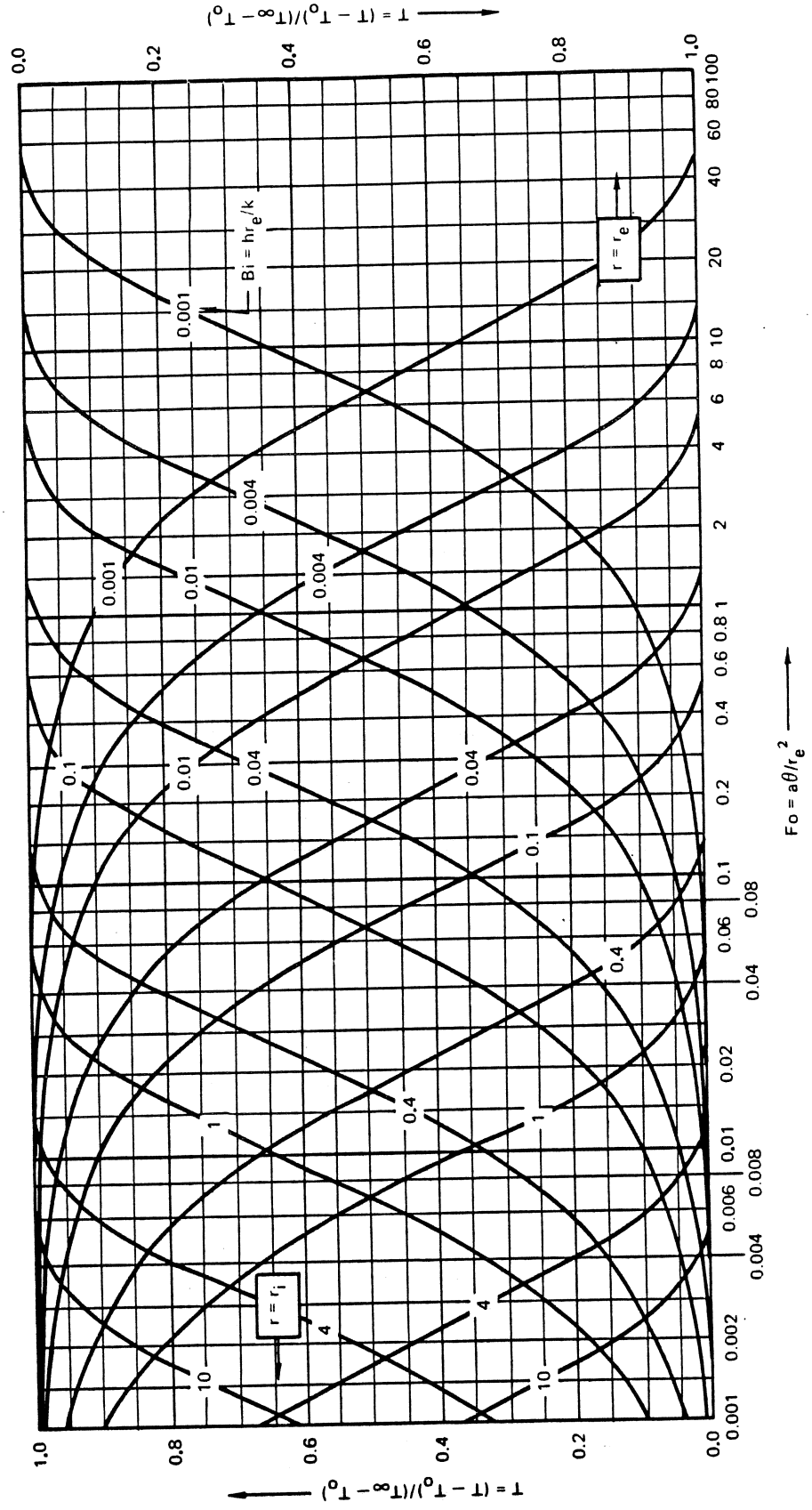

Figure 14-38C. Spherical Shell — Internal Surface Insulated (Sheet 6 of 6)

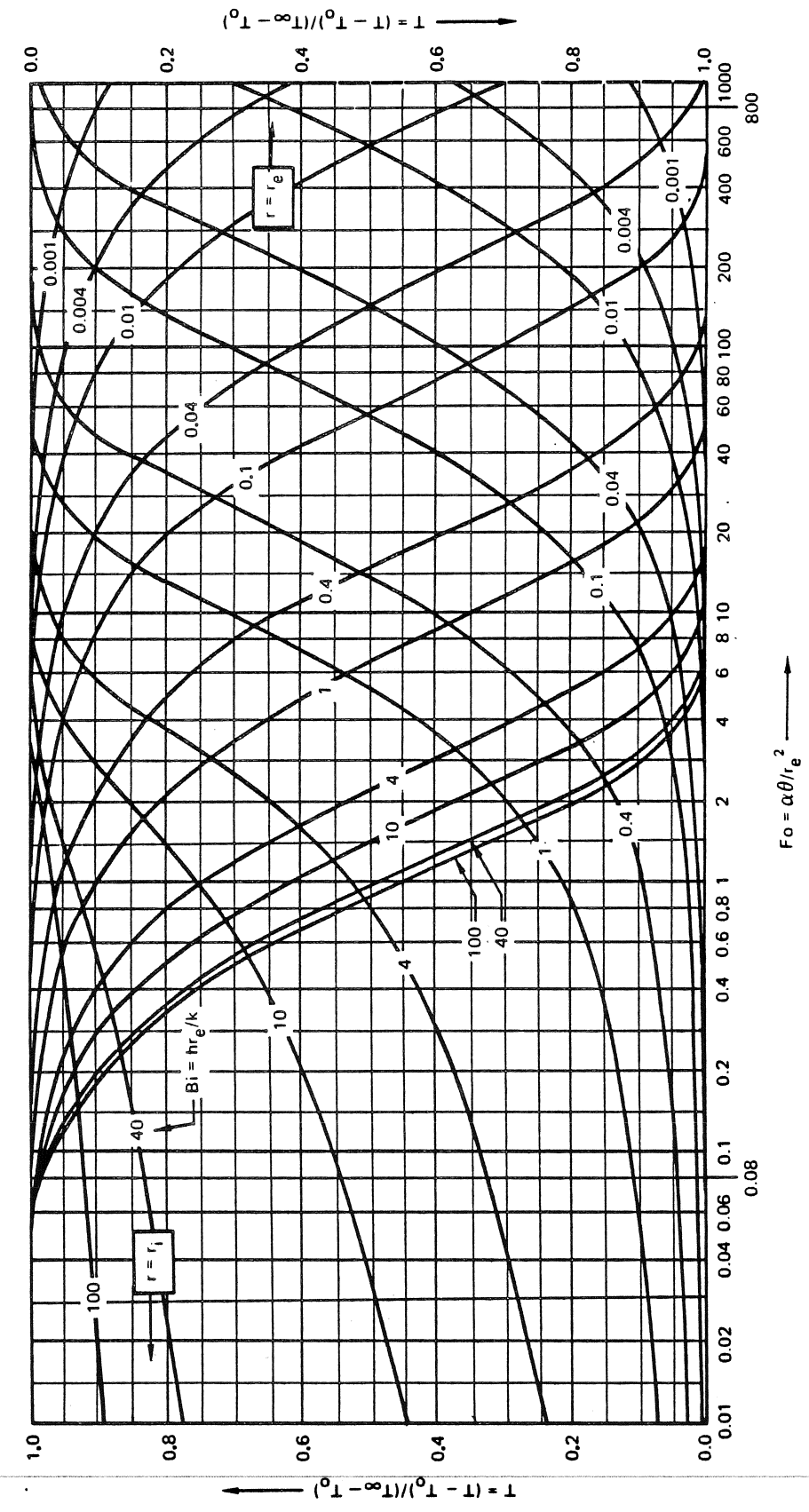

$R_i = r_i/r_e = 0.2$

TEMPERATURE RESPONSE OF A SPHERICAL SHELL INSULATED AT ITS EXTERNAL SURFACE $r = r_e$ AFTER SUDDEN EXPOSURE TO A UNIFORM-TEMPERATURE CONVECTIVE ENVIRONMENT t_a AT $r = r_i$.

Figure 14-38D. Spherical Shell — External Surface Insulated (Sheet 1 of 6)

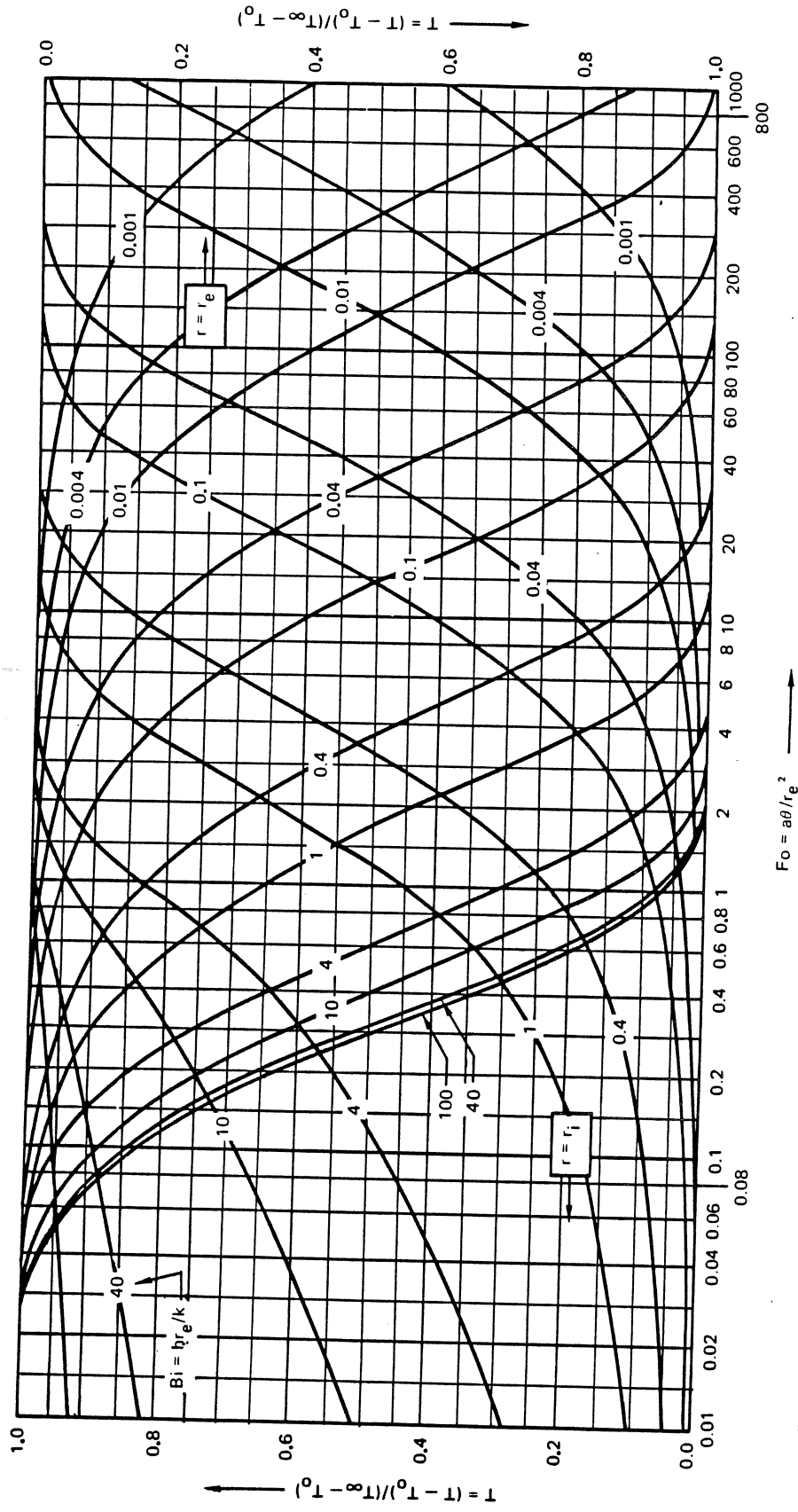

Figure 14-38D. Spherical Shell – External Surface Insulated (Sheet 2 of 6)

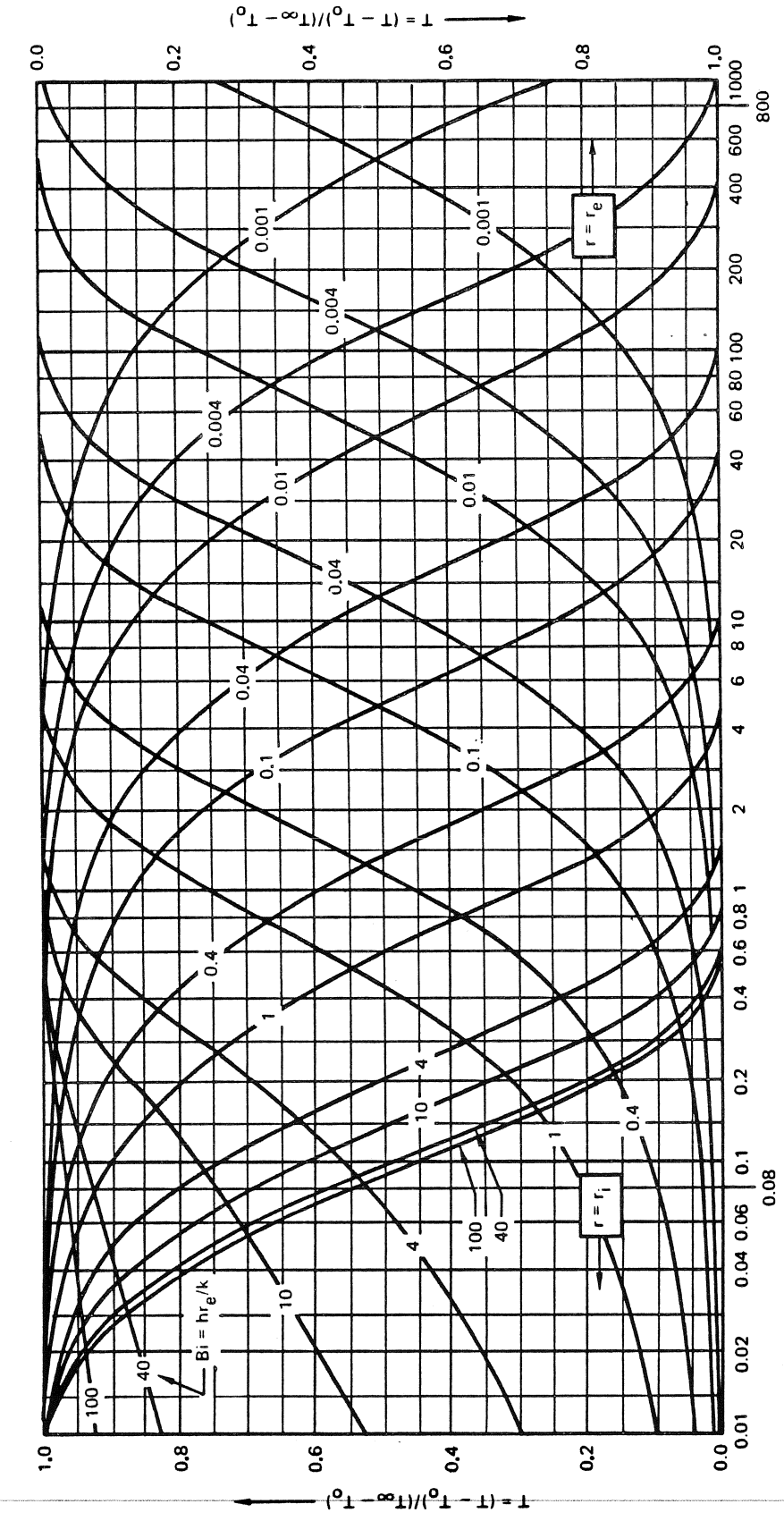

Figure 14-38D. Spherical Shell – External Surface Insulated (Sheet 3 of 6)

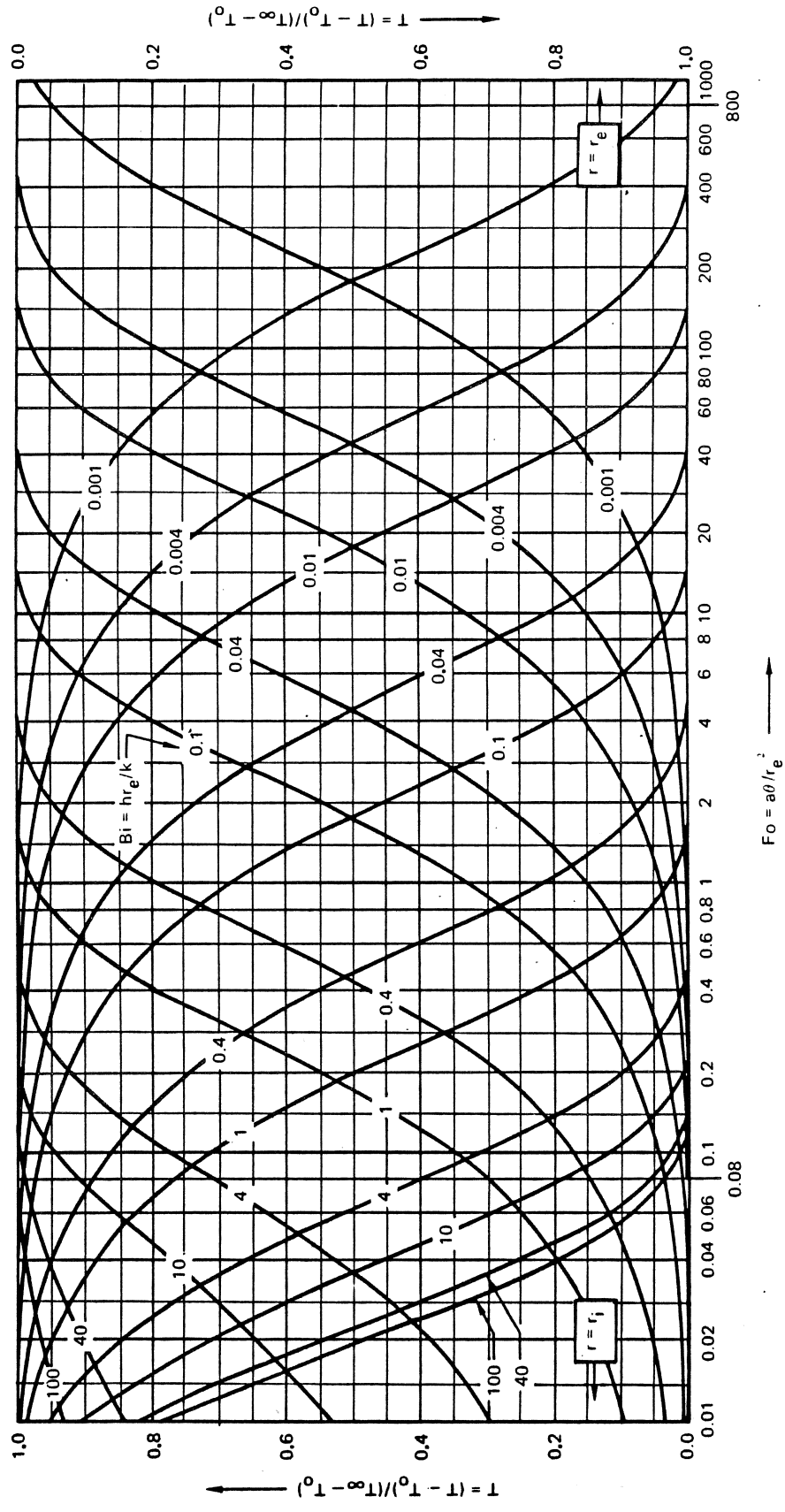

Figure 14-38D. Spherical Shell — External Surface Insulated (Sheet 4 of 6)

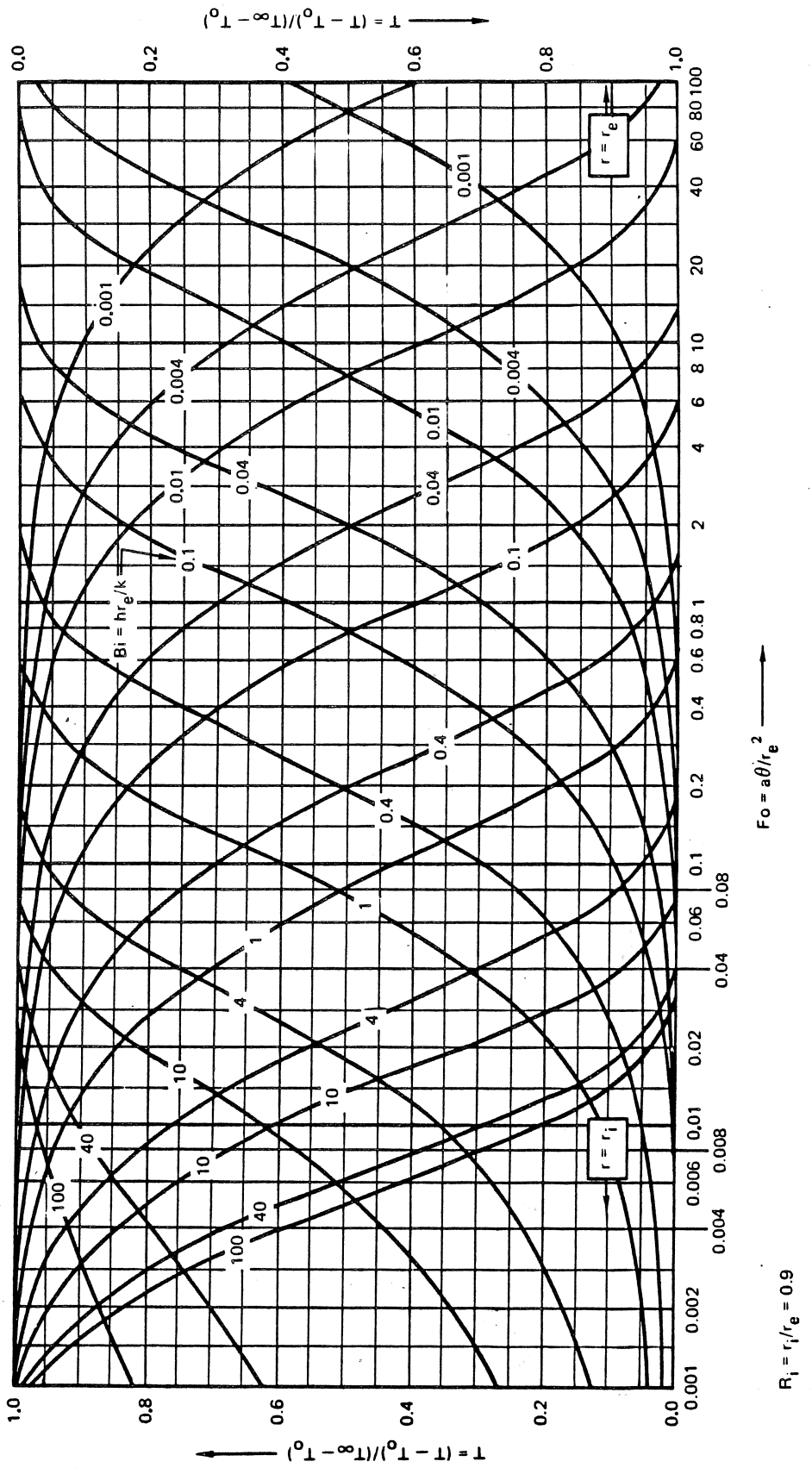

Figure 14-38D. Spherical Shell – External Surface Insulated (Sheet 5 of 6)

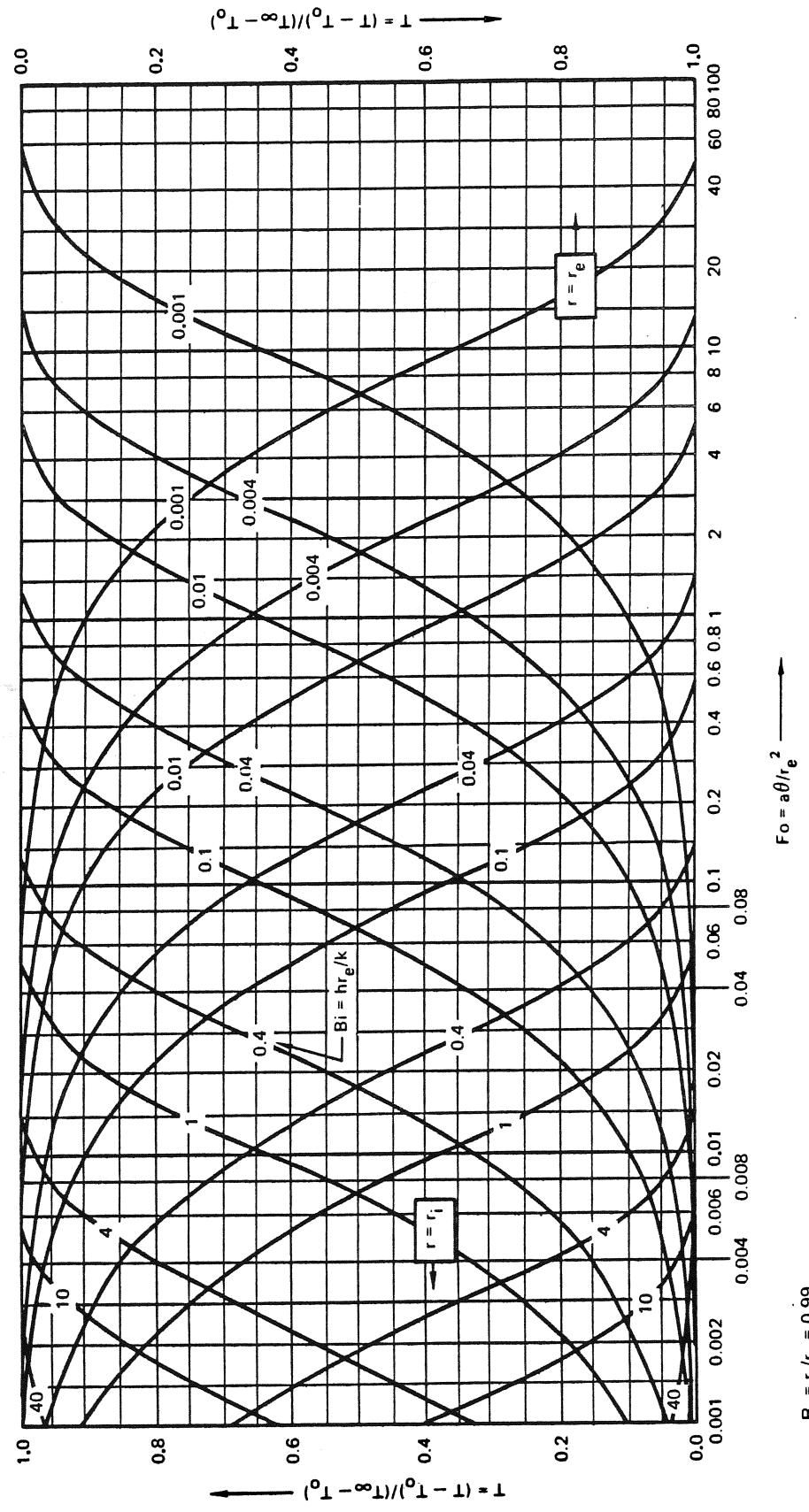

Figure 14-38D. Spherical Shell – External Surface Insulated (Sheet 6 of 6)

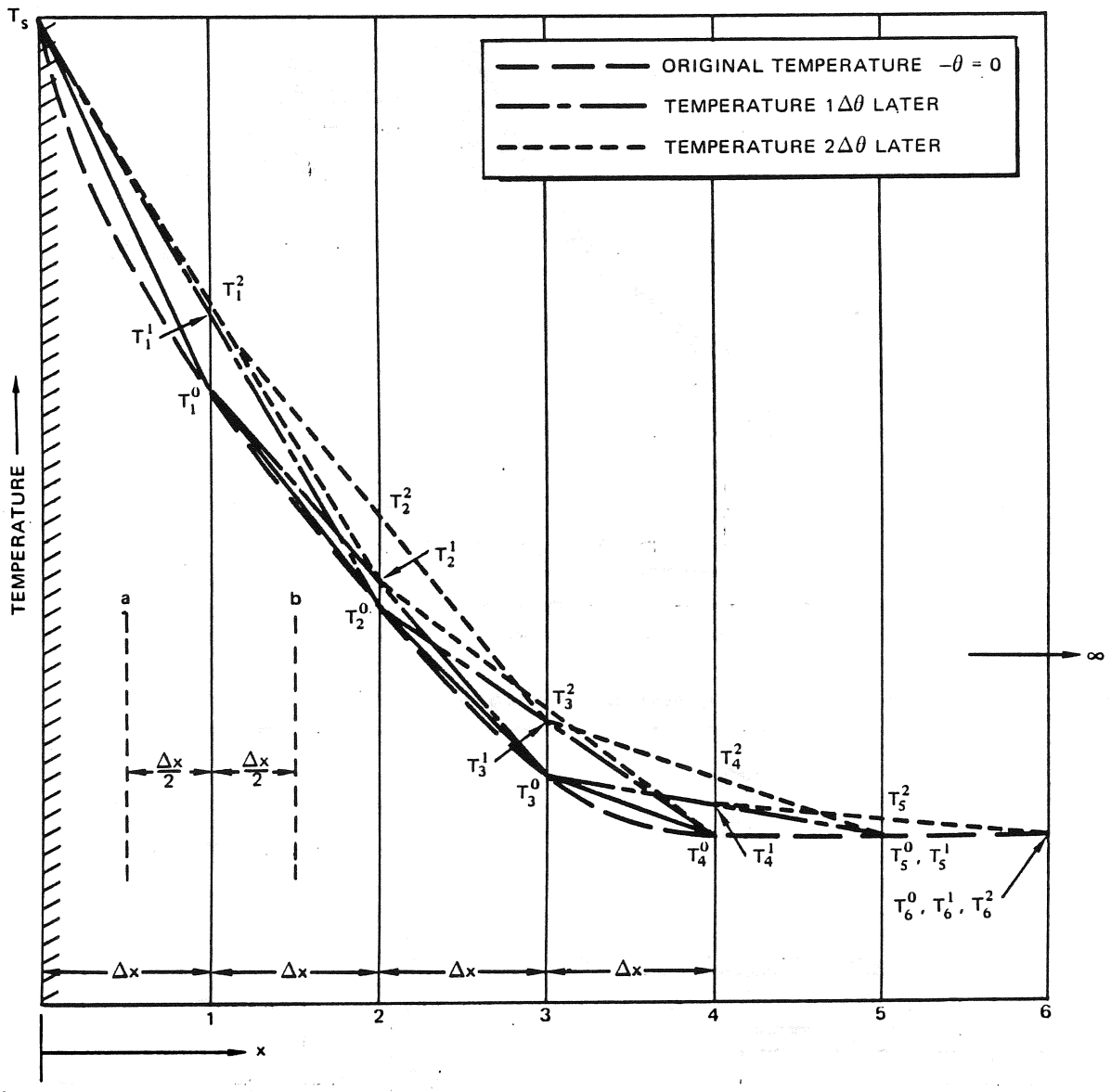

Figure 14-39. Schmidt Plot in an Infinitely Thick Wall

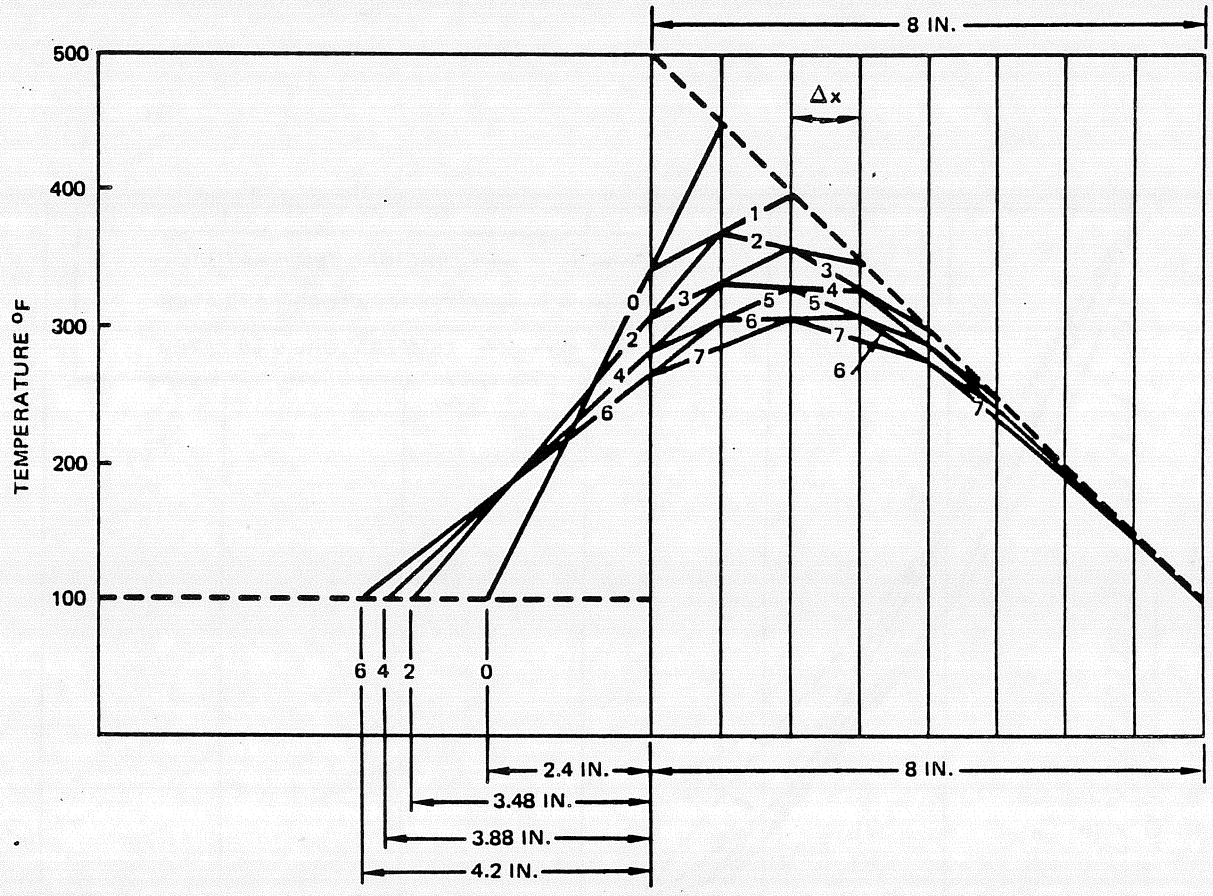

Figure 14-40. Schmidt Plot for a Time-Dependent Boundary Condition

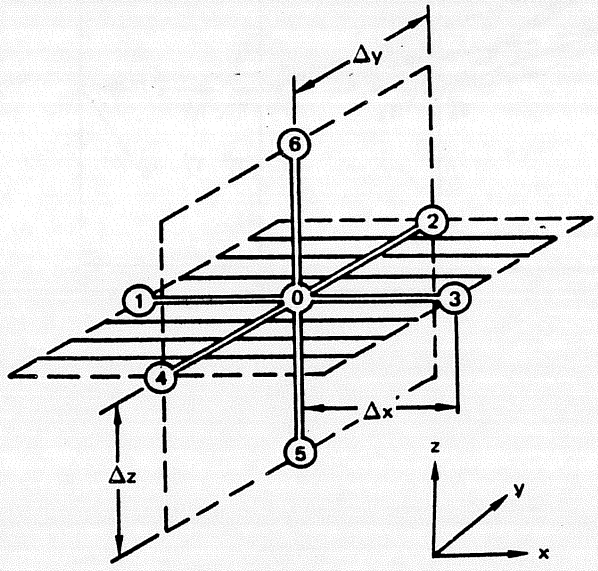

Figure 14-41. Three-Dimensional Network for the Numerical Method

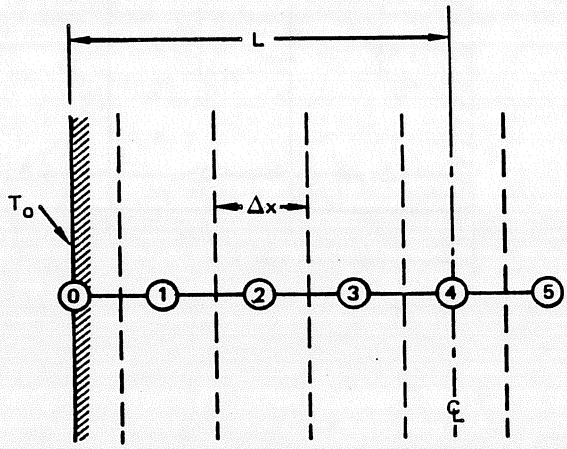

Figure 14-42. Subdivison of a Plate for a Transient-Numerical Solution

Table 14-10. Thermal Radiation Laws

RADIATION LAW	EQUATION	NOMENCLATURE
STEPHAN-BOLTZMAN LAW	$E_b = \sigma T^4$	E_b = BLACK BODY TOTAL EMISSIVE POWER, Btu/hr-ft^2 σ = STEPHAN-BOLTZMAN CONSTANT 0.1714 X 10^{-8}, Btu/hr-ft^2-R^4 T = ABSOLUTE TEMPERATURE, °R λ = WAVELENGTH, μ (microns) $E_{b\lambda}$ = BLACK BODY MONOCHROMATIC EMISSIVE POWER, Btu/hr-ft^2-μ C_1 = CONSTANT 1.1870 X 10^8 Btu μ^4/ft^2-hr C_2 = CONSTANT 2.5896 X 10^4, μ °R e = NAPERIAN BASE OF LOGARITHMS I_ϕ = DIRECTIONAL RADIATION INTENSITY Btu/hr-unit SOLID ANGLE I_n = NORMAL RADIATION INTENSITY Btu/hr-unit SOLID ANGLE ϕ = ANGLE FROM NORMAL TO RADIATING SURFACE α = ABSORPTIVITY FOR RADIATION ($\alpha \leq 1.0$)
PLANCK'S LAW	$E_{b_\lambda} = \dfrac{C_1 \lambda^{-5}}{e^{(C_2/\lambda T)} - 1}$	
WEIN'S DISPLACEMENT LAW	$\lambda_{max} T = 5215.6\ \mu R$	
LAMBERT'S COSINE LAW	$I_\phi = I_n \cos\phi$	
KIRCHOFF'S LAW	$\dfrac{E_1}{\alpha_1} = \dfrac{E_2}{\alpha_2} = \dfrac{E}{\alpha} = \dfrac{E_b}{1}$	

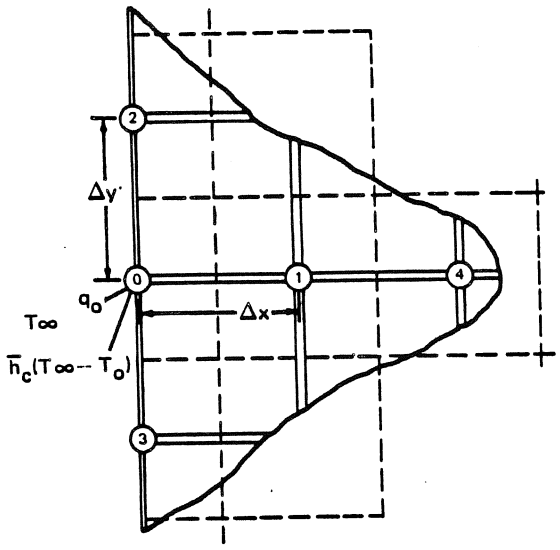

Figure 14-43. Heat Balance on an Exterior Nodal Point with Convection and Radiation

where:

$E_{b\lambda}$ = Monochromatic emissive power of a black body in Btu/hr-ft^2 = μ

λ = Wave length, μ

T = Temperature of the body, °R

e = Naperian base of logarithms

C_1 = Constant = 1.1870 x 10^8 Btu-μ^4/ft^2-hr

C_2 = Constant = 2.5896 x 10^4 °R-μ

Equation 78 can be obtained from equation 79 by the following integration.

$$\int_0^\infty E_{b\lambda}\, d\lambda = \sigma T^4 \qquad (80)$$

The monochromatic emissive power of black bodies $E_{b\lambda}$ for various temperatures is plotted in Figure 14-44 as a function of wave length. The height of each curve describes the amount of radiation emitted per unit time and area at a particular wavelength. The area under each curve described the total amount of radiation emitted over all wavelengths. At temperatures of engineering interest, the emissive power is appreciable over wavelengths from 0.3 to 50 μ.

14-3.1.3 Wein's Displacement Law

The wavelength, at which the monochromatic emissive power is a maximum, shifts with increasing temperature to shorter wavelengths. The relationship between the absolute temperature T and the wavelength λ_{max} at

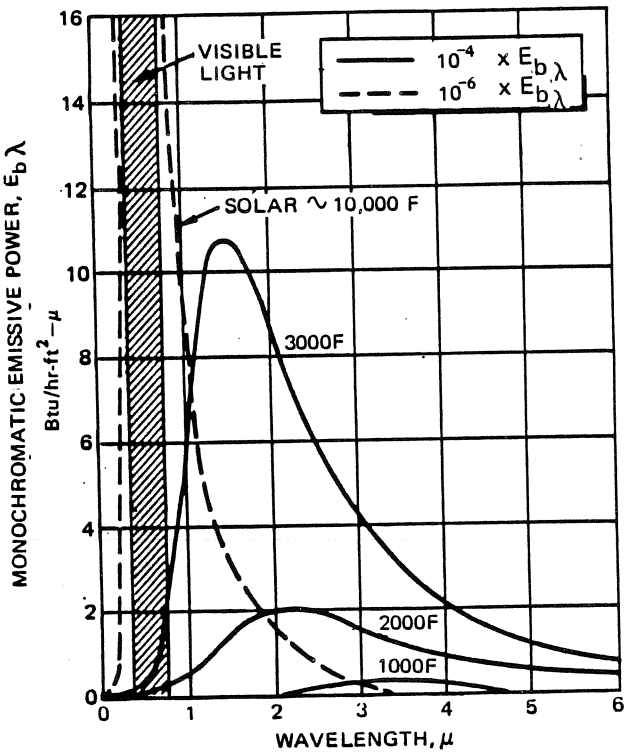

Figure 14-44. Spectral Distribution of Emissive Power

which $E_{b\lambda}$ is a maximum is given by Wein's displacement law which is expressed mathematically as:

$$T\lambda_{max} = 5215.6\ °R\text{-}\mu \qquad (81)$$

The maximum $E_{b\lambda}$ at a given temperature is obtained by combining equations 79 and 81 which yields:

$$E_{b\lambda_{max}} = 2.161 \times 10^{-13} T^5\ \text{Btu/hr-ft}^2\text{-}\mu \qquad (82)$$

Values of $E_{b\lambda_{max}}$ are plotted as a function of absolute temperature in Figure 14-45.

The ratio of monochromatic emissive power of a black body $E_{b\lambda}$, to its maximum monochromatic emissive power $E_{b\lambda_{max}}$ can be determined from:

$$\frac{E_{b\lambda}}{E_{b\lambda_{max}}} = \left(\frac{5215.6}{\lambda T}\right)^5 \left(\frac{e^{4.965}-1}{e^{25896/\lambda T}-1}\right) \qquad (83)$$

Values of the ratio $E_{b\lambda}/E_{b\lambda_{max}}$ are plotted as a function of the wavelength ratio λ/λ_{max}, and the product λT in Figure 14-46. The black body emissive power over a specified wavelength range can be obtained from Figure 14-47 or from Table 14-11.

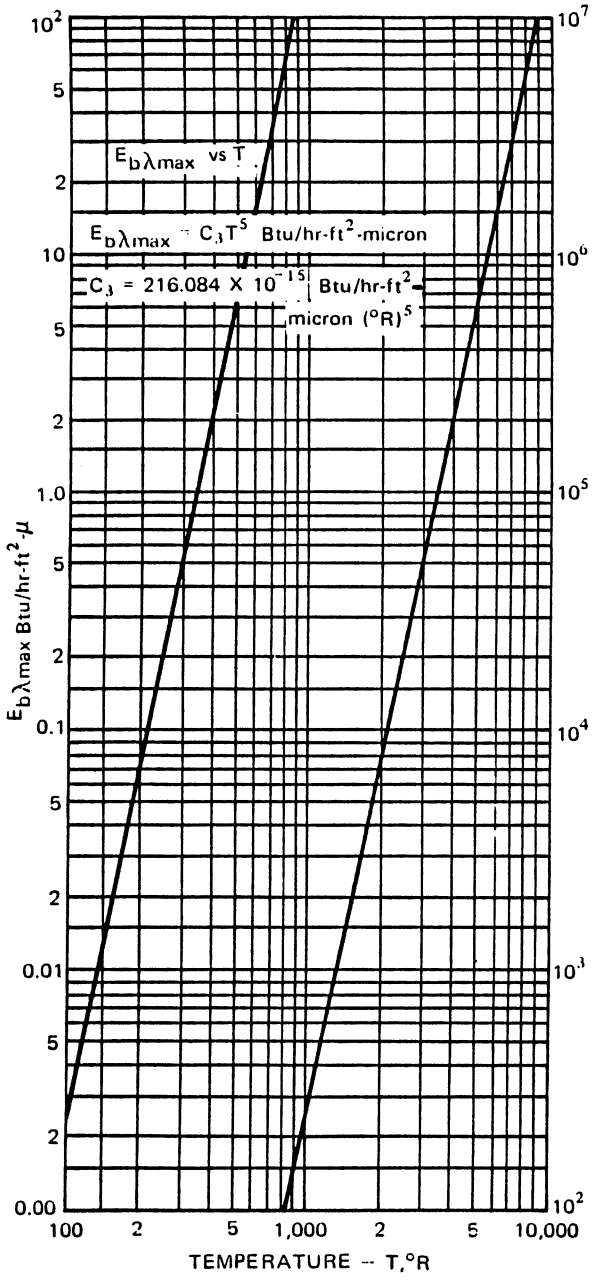

Figure 14-45. Maximum Monochromatic Emissive Power versus Temperature

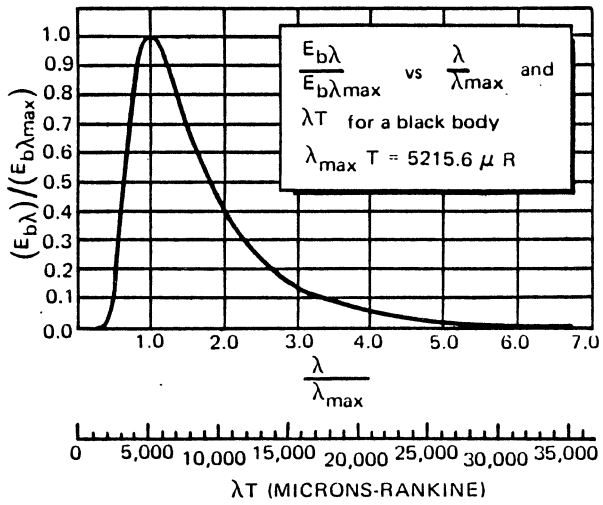

Figure 14-46. Emissive Power Ratio versus Wavelength Ratio

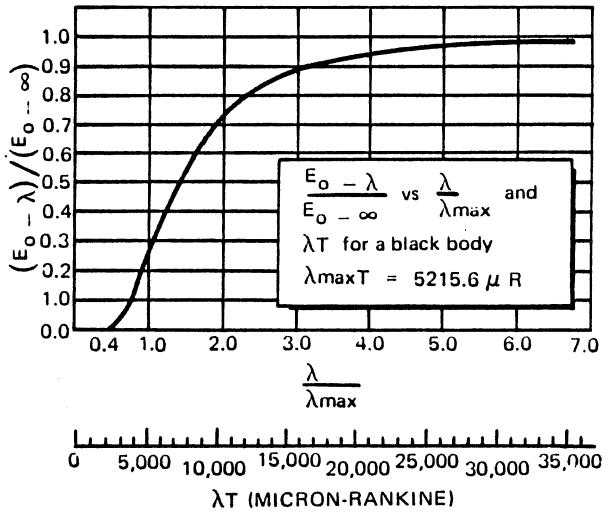

Figure 14-47. Fraction of Total Emissive Power versus Wavelength Ratio

Table 14-11. Radiation Functions

λT	$\frac{E_{\lambda b} \times 10^5}{\sigma T^5}$	$\frac{E_b(0-\lambda T)}{\sigma T^4}$	λT	$\frac{E_{\lambda b} \times 10^5}{\sigma T^5}$	$\frac{E_b(0-\lambda T)}{\sigma T^4}$	λT	$\frac{E_{\lambda b} \times 10^5}{\sigma T^5}$	$\frac{E_b(0-\lambda T)}{\sigma T^4}$
1000	.0000394	0	7200	10.089	.4809	13400	2.714	.8317
1200	.001184	0	7400	9.723	.5007	13600	2.605	.8370
1400	.01194	0	7600	9.357	.5199	13800	2.502	.8421
1600	.0618	.0001	7800	8.997	.5381	14000	2.416	.8470
1800	.2070	.0003	8000	8.642	.5558	14200	2.309	.8517
2000	.5151	.0009	8200	8.293	.5727	14400	2.219	.8563
2200	1.0384	.0025	8400	7.954	.5890	14600	2.134	.8606
2400	1.791	.0053	8600	7.624	.6045	14800	2.052	.8648
2600	2.753	.0098	8800	7.304	.6195	15000	1.972	.8688
2800	3.872	.0164	9000	6.995	.6337	16000	1.633	.8868
3000	5.081	.0254	9200	6.697	.6474	17000	1.360	.9017
3200	6.312	.0368	9400	6.411	.6606	18000	1.140	.9142
3400	7.506	.0506	9600	6.136	.6731	19000	.962	.9247
3600	8.613	.0667	9800	5.872	.6851	20000	.817	.9335
3800	9.601	.0850	10000	5.619	.6966	21000	.702	.9411
4000	10.450	.1051	10200	5.378	.7076	22000	.599	.9475
4200	11.151	.1267	10400	5.146	.7181	23000	.516	.9531
4400	11.704	.1496	10600	4.925	.7282	24000	.448	.9589
4600	12.114	.1734	10800	4.714	.7378	25000	.390	.9621
4800	12.392	.1979	11000	4.512	.7474	26000	.341	.9657
5000	12.556	.2229	11200	4.320	.7559	27000	.300	.9689
5200	12.607	.2481	11400	4.137	.7643	28000	.265	.9718
5400	12.571	.2733	11600	3.962	.7724	29000	.234	.9742
5600	12.458	.2983	11800	3.795	.7802	30000	.208	.9765
5800	12.282	.3230	12000	3.637	.7876	40000	.0741	.9881
6000	12.053	.3474	12200	3.485	.7947	50000	.0326	.9941
6200	11.783	.3712	12400	3.341	.8015	60000	.0165	.9963
6400	11.480	.3945	12600	3.203	.8081	70000	.0092	.9981
6600	11.152	.4171	12800	3.071	.8144	80000	.0055	.9987
6800	10.808	.4391	13000	2.947	.8204	90000	.0035	.9990
7000	10.451	.4604	13200	2.827	.8262	100000	.0023	.9992
						∞	0	1.000

14-3.1.4 Lambert's Cosine Law

Referring to Figure 14-48, the radiation emitted in any direction from an elemental area dA can be defined in terms of the intensity, I. For a diffuse surface, the intensity does not vary with emission angle, ϕ. However, the emissive power E is dependent on ϕ in the following manner, which is known as Lambert's cosine law

$$E_\phi = I \cos \phi \qquad (84)$$

where:

E_ϕ = Radiant emission at an angle ϕ from the normal to dA

I = Radiant intensity, Btu/hr-unit solid angle

The total radiation emitted from dA can be determined by integrating equation 84 over the half-space above dA, thus:

$$E = \pi I \qquad (85)$$

14-3.1.5 Kirchoff's Law

Kirchoff's Law states that no surface can absorb or emit more radiation than a black surface. This is expressed mathematically as:

$$(E_1/\alpha_1) = (E_2/\alpha_2) = (E/\alpha) = (E_b/1) \qquad (86)$$

where α is the absorptance and E is the emissive power. Absorptance is limited to values between 0 and 1. The maximum emissive power occurs when α has its

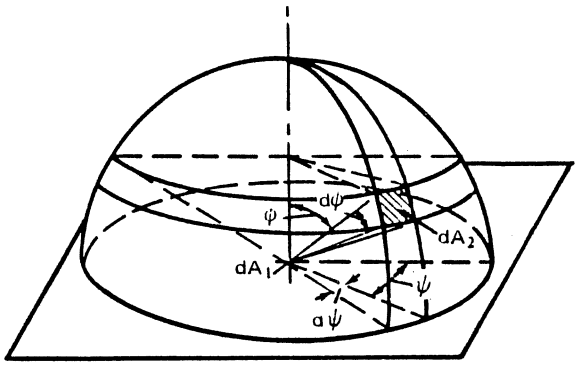

Figure 14-48. Nomenclature for Intensity of Radiation

maximum value of unity, a condition which applies only to a black body. The emissive power of other bodies is less than that of a black body, and the ratio E/E_b is called the emittance, ϵ of the body. At thermal equilibrium, the absorptance, α, and the emittance, ϵ, of a body are equal. For the black body, α and ϵ are equal to unity.

14-3.2 Radiation from Real Bodies

Radiation from real surfaces differs in several aspects from black-body radiation. According to Kirchoff's law, a real surface always radiates less than a black body at the same temperature. If, at a given temperature, the ratio of the monochromatic emissive power of a body to the monochromatic emissive power of a black body at the same wavelength is constant over the entire wavelength spectrum, the body is said to be gray and its emissive power E_g is given by:

$$E_g = \epsilon_g \sigma T^4 \text{ Btu/hr-ft}^2 \qquad (87)$$

where:

ϵ_g = Radiation emittance for a gray surface.

The shape of a spectroradiometric curve for a gray surface is similar to that of a black surface at the same temperature, but the height is reduced proportional to the numerical value of the emittance. For the purpose of heat-transfer calculations, surfaces are usually regarded as gray even though the characteristics of most surfaces deviate from gray-body specifications.

Figures 14-49 and 14-50 show the variation of monochromatic absorptance and emittance for typical electrical conductors and nonconductors. Absorptance and emittance decrease with increasing wavelength for good conductors, as typified by the curve for polished aluminum in Figure 14-49, but they increase somewhat irregularly with increasing wave length for nonconductors, as shown in Figure 14-50.

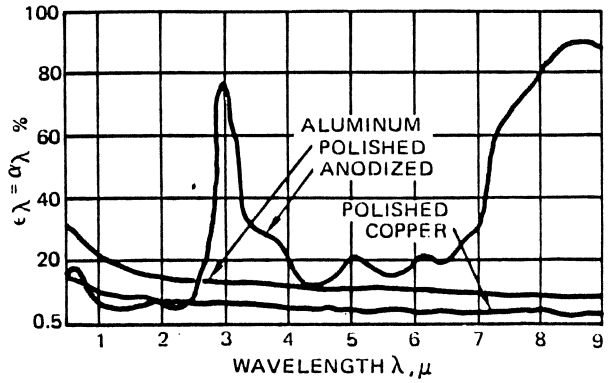

Figure 14-49. Variation of Monochromatic Absorptance or Emittance with Wavelength for an Electrical Conductor

In addition to its variation with wavelength, the emittance of many bodies also has directional properties which do not conform to Lambert's cosine law. This is illustrated in Figures 14-51 and 14-52 where the directional properties of several electrical conductors and nonconductors are plotted in polar diagrams. For surfaces whose radiation intensity follows Lambert's cosine law and depends only on projected area, the emittance curves would be semicircles.

Figure 14-51 shows that for nonconductors the emittance decreases at large values of the emission angle ϕ, but Figure 14-52 shows the reverse trend for conductors. A satisfactory approximation for many calculations is to assume a mean value of ϵ_H/ϵ_N of 1.2 for polished metallic surfaces, and of 0.96 for nonmetallic surfaces, where ϵ_H is the average emittance through a hemispherical solid angle of 2π steradians and ϵ_N is the emittance in the direction normal to the surface.

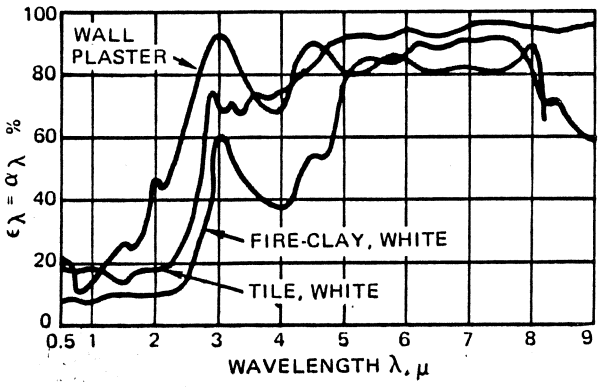

Figure 14-50. Variation of Monochromatic Absorptance or Emittance with Wavelength for an Electrical Nonconductor

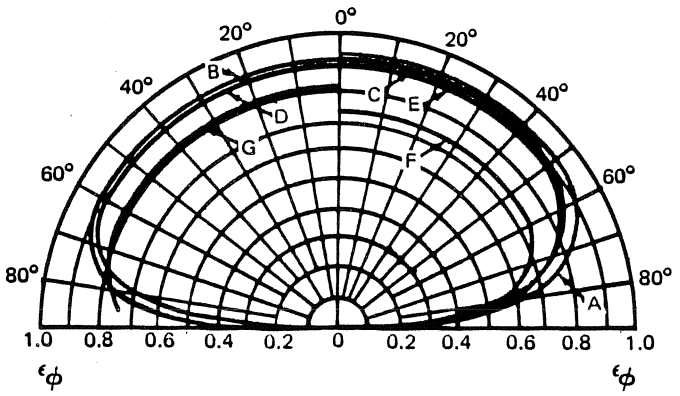

A WET ICE
B WOOD
C GLASS
D PAPER
E CLAY
F COPPER OXIDE
G ALUMINUM OXIDE

Figure 14-51. Directional Variation of Emittance for Electrical Nonconductors

When a more accurate knowledge of the ratio of hemispherical to normal emittance is needed, theoretical predictions can be made based on electromagnetic theory for smooth surfaces which are physically and chemically uncontaminated. Figures 14-53a and b show the theoretical variation of ϵ_H/ϵ_N as a function of the indices of absorption (k) and refraction (n) for smooth uncontaminated surfaces.

14-3.3 Irradiation of Real Bodies

Irradiation, G, is the radiation per unit time which impinges on a unit surface area. Radiation falling on a real body is either reflected, absorbed or transmitted. The sum of the reflected fraction ρ (reflectance), the absorbed fraction, α (absorptance), and the transmitted fraction, τ (transmittance) is equal to one.

$$\alpha + \rho + \tau = 1 \qquad (88)$$

A body is:

White – When it reflects all energy falling on it (ρ=1, α=τ=0),

Black – When it absorbs all energy falling on it (α=1, ρ=τ=0),

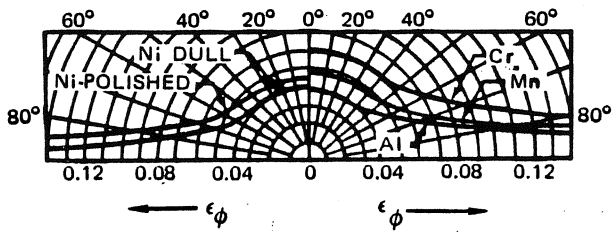

Figure 14-52. Directional Variation of Emittance for Electrical Conductors

Gray – When it reflects the same fraction of energy over all wave lengths,

Colored – When it reflects different fractions of energy in some wavelengths.

All gases and most liquids are transparent to radiation of some wavelengths. Most solids, with the exception of glass-like materials, do not transmit radiation. Figure 14-54 shows the variation of transmittance with thickness of typical transparent solid materials.

For opaque materials, equation 88 reduces to:

$$\alpha + \rho = 1 \qquad (89)$$

For highly polished surfaces (called spectral reflectors), the angle of incidence is equal to the angle of reflection. In practice; however, the surfaces of most materials are relatively rough and reflection will occur in an indiscriminant (diffuse) manner. A diffuse reflecting surface reflects with the same spatial energy distribution as a black body. The relative magnitudes of α, ρ, and τ depend not only on the material, its thickness and surface finish, but vary also with the wavelength of the radiation.

An average emittance or absorptance for the wavelength band in which the bulk of the radiation is emitted or absorbed, is highly desirable for heat transfer calculations. The wavelength band of interest depends on the temperature of the body from which the radiation originates. If the distribution of the monochromatic emittance is known, the emissive power of the body can be obtained by plotting the product $\epsilon_\lambda E_{b\lambda}$ versus λ over the wavelength range in which appreciable emission occurs at a given temperature, measuring the area under the curve. An average

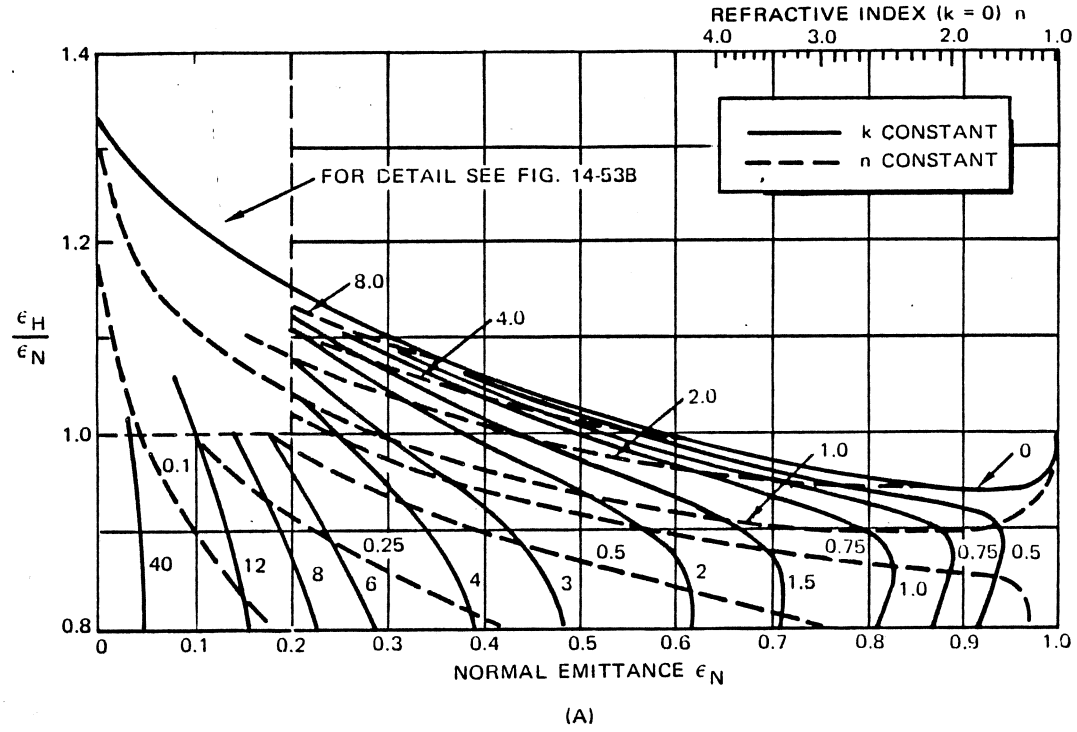

(A)

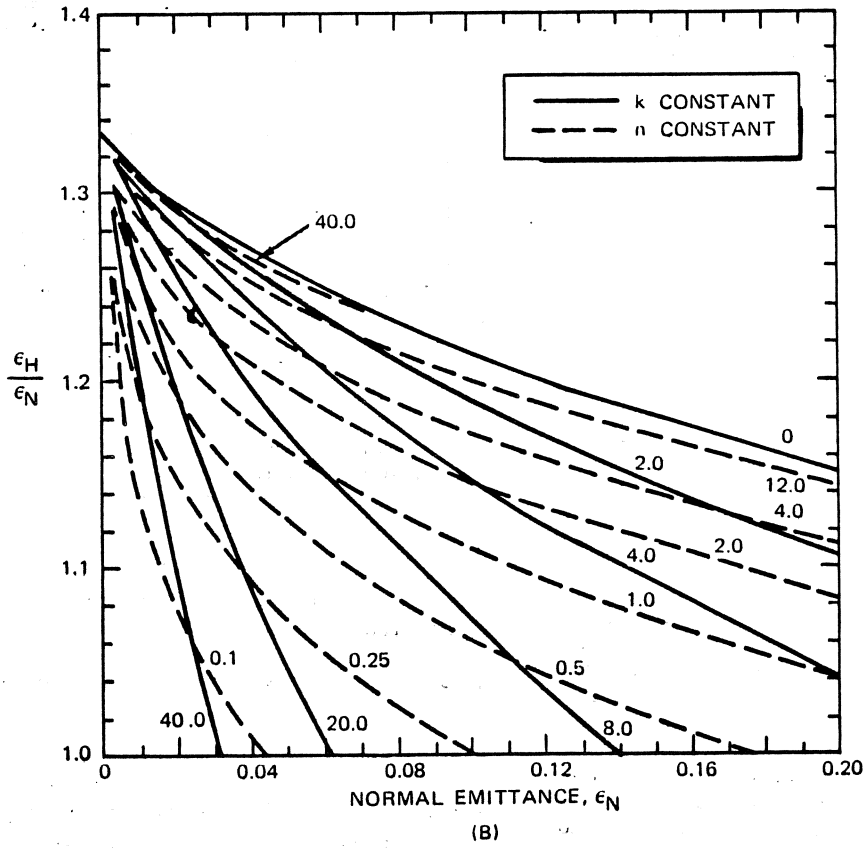

(B)

Figure 14-53. Ratio of Hemispherical Emittance to Normal Emittance

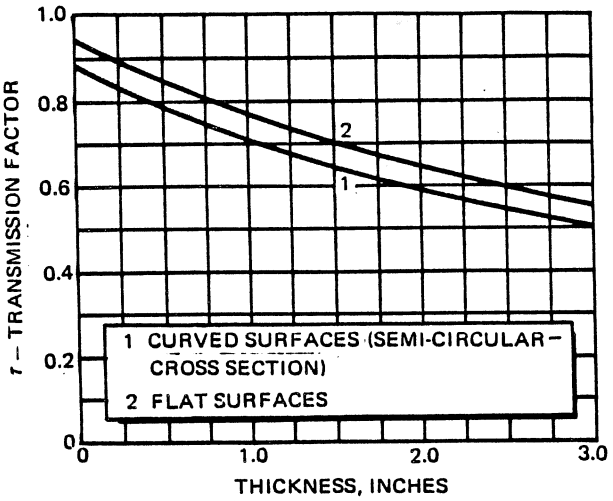

NOTE: THE CURVES ARE VALID FOR GLASS THICKNESSES UP TO 1.5 INCHES AND PLEXIGLASS UP TO 3 INCHES FOR TRANSPARENT MATERIAL, DIMENSIONLESS.

Figure 14-54. Transmission Factor for Various Transparent Areas

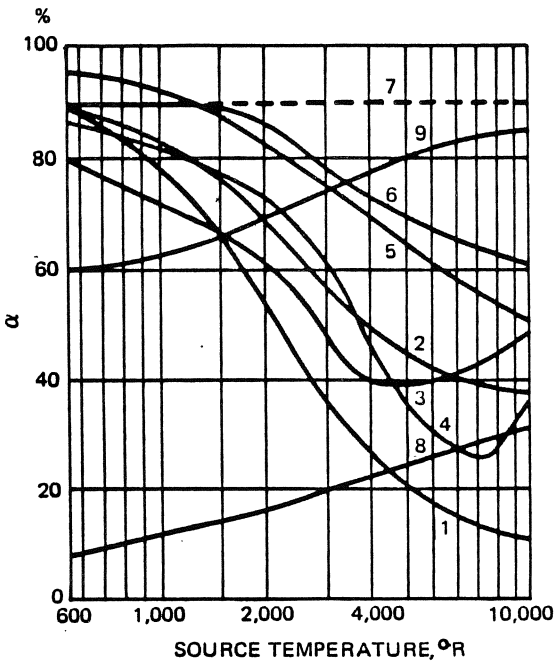

1. WHITE FIRE CLAY
2. ASBESTOS
3. CORK
4. WOOD
5. PORCELAIN
6. CONCRETE
7. ROOF SHINGLES
8. ALUMINUM
9. GRAPHITE

Figure 14-55. Variation of Average Absorptance with Emitter Temperature

emittance for each temperature can be obtained by dividing this area by the area under the spectroradiometric curve of a black body at the same temperature.

The total average absorptance α for a surface receiving radiation from a gray or black body can be obtained by evaluating:

$$\alpha = \int_0^\infty \alpha_\lambda \frac{E_{b\lambda}}{\sigma T^5} d(\lambda T) \qquad (90)$$

The quantity $E_{b\lambda}/\sigma T^5$ is tabulated as a function of λT in Table 14-11. If a curve of α_λ versus λ is available, α can be evaluated numerically by taking suitable increments of λT, tabulating the individual products of $\alpha_\lambda (E_{b\lambda}/\lambda T^5)\, \Delta(\lambda T))$, and finally summing then. Figure 14-55 presents variation of α for several materials as a function of the emitter temperature.

According to Kirchoff's law, the absorptance of a surface equals its emittance at thermal equilibrium. For gray bodies, α_λ and ϵ_λ are constant over the entire wave spectrum; consequently $\alpha = \epsilon$ irrespective of the temperatures of the emitter and receiver. Note that when ϵ varies with wavelength, this relation only holds at a given temperature or at a given wavelength. In practice a body usually emits the bulk of its radiation at wavelengths which are different from those at which it receives radiation. Therefore the average values of ϵ and α are not necessarily the same. To evaluate ϵ and α for a real body correctly, choose α corresponding to the wavelength or the temperature at which the radiation striking the body was emitted and ϵ corresponding to the actual temperature of the body.

Table 14-12 lists average values for the total or hemispherical emittance of several materials at specified temperatures. Note that clean and polished metal surfaces usually have low values, whereas many other surfaces which find application in engineering have an emittance in excess of 0.85 and are therefore excellent absorbers as well as emitters of radiation. It is also apparent that the visual color bears no resemblance to the definition of a black body. For example ice, which appears white to our eyes, absorbs nearly all radiation in the long-wavelength range.

A very comprehensive book-length listing of emittances for several materials is contained in G. G. Gubareff, J. E. Janssen, and R. H. Torborg, *Thermal Radiation Properties Survey*, 2nd edition, Honeywell Research Center, 1960, Minneapolis, Minnesota.

14-3.4 Radiant Heat Exchange Between Black Bodies

To evaluate the net exchange of thermal radiation between two or more bodies, it is necessary to determine the fraction of the total emission from each of the radiating surfaces which reaches, and is absorbed by, the others. If only black surfaces are involved, all of the incident radiation is absorbed and only the geometric relation between the surfaces need be considered.

Table 14-12. Total Emittance Data

Surface	Temperature, °F	ϵ
I. METALS		
Aluminum		
polished, 98 percent pure	400-1100	0.04-0.06
commercial sheet	200	0.09
rough plate	100	0.07
heavily oxidized	200-1000	0.20-0.33
Antimony		
polished	100-500	0.28-031
Bismuth		
bright	200	0.34
Brass		
highly polished	500	0.03
polished	100	0.07
dull plate	100-500	0.22
oxidized	100-500	0.46-0.56
Chromium		
polished sheet	100-1000	0.08-0.27
Cobalt		
unoxidized	500-1000	0.13-0.23
Copper		
Highly polished electrolytic	200	0.02
polished	100	0.04
slightly polished	100	0.12
polished, lightly tarnished	100	0.05
dull	100	0.15
black oxidized	100	0.76
Gold		
pure, highly polished	200-1100	0.02-0.035
Inconel		
X, stably oxidized	450-1600	0.55-0.78
B, stably oxidized	450-1750	0.32-0.55
X and B, polished	300-600	0.20
Iron and Steel		
mild steel, polished	300-900	0.14-0.32
steel, polished	100-500	0.07-0.10
sheet steel, ground	1700	0.55
sheet steel, rolled	100	0.66
sheet steel, strong rough oxide	100	0.80
steel, oxidized at 1100°F	500	0.79
cast iron, with skin	100	0.70-0.80
cast iron, newly turned	100	0.44
cast iron, polished	400	0.21
cast iron, oxidized	100-500	0.57-0.66
iron, red rusted	100	0.61
iron, heavily rusted	100	0.85
wrought iron, smooth	100	0.35
wrought iron, dull oxidized	70-680	0.94
stainless, polished	100	0.07-0.17
stainless, after repeated heating and cooling	450-1650	0.50-0.70
Lead		
polished	100-500	0.05-0.08
gray, oxidized	100	0.28
oxidized at 390°F	400	0.63
oxidized at 1100°F	100	0.63
Magnesium		
polished	100-500	0.07-0.13
Manganin		
bright rolled	200	0.05
Mercury		
pure, clean	100-200	0.10-0.12
Molybdenum		
polished	100-500	0.06-0.08
polished	1000-2000	0.11-0.18
filament	1000-5000	0.08-0.29
Monel		
after repeated heating and cooling	450-1650	0.45-0.70
oxidized at 1100°F	400-1100	0.41-0.46
polished	100	0.17
Nickel		
polished	100-500	0.05-0.07
oxidized	100-500	0.35-0.49
wire	500-2000	0.10-0.19
Platinum		
pure, polished plate	400-1100	0.05-0.10
oxidized at 1100°F	500-1000	0.07-0.11
electrolytic	500-1000	0.06-0.10
strip	1000-2000	0.12-0.14
filament	100-2000	0.04-0.19
wire	400-2500	0.07-0.18
Silver		
polished or deposited	100-1000	0.01-0.03
oxidized	100-1000	0.02-0.04
German silver,* polished	500-1000	0.07-0.09

*German silver is actually an alloy of copper, nickel and zink.

Table 14-12. Total Emittance Data (Continued)

Surface	Temperature, °F	ϵ
Tin		
bright tinned iron	100	0.04-0.06
bright	100	0.06
polished sheet	200	0.05
Tungsten		
filament	1000-2000	0.11-0.16
filament	5000	0.39
filament, aged	100-6000	0.03-0.35
polished	100-1000	0.04-0.08
Zinc		
pure polished	100-500	0.02-0.03
oxidized at 750°F	750	0.11
galvanized, gray	100	0.28
galvanized, fairly bright	100	0.23
dull	100-500	0.21
II. NONMETALS		
Asbestos		
board	100	0.96
cement	100	0.96
paper	100	0.93-0.95
slate	100	0.97
Brick		
red, rough	100	0.93
silica	1800	0.80-0.85
fireclay	1800	0.75
ordinary refractory	2000	0.59
magnesite refractory	1800	0.38
white refractory	2000	0.29
gray, glazed	2000	0.75
Carbon		
filament	1900-2600	0.53
lampsoot	100	0.95
Clay		
fired	200	0.91
Concrete		
rough	100	0.94
Corundum		
emery rough	200	0.86
Glass		
smooth	100	0.94
quartz glass (2 mm)	500-1000	0.96-0.66
pyrex	500-1000	0.94-0.75
Gypsum	100	0.80-0.90
Ice		
smooth	32	0.97
rough crystals	32	0.99
hoarfrost	0	0.99
Limestone	100-500	0.95-0.83
Marble		
light gray, polished	100	0.93
white	100	0.95
Mica	100	0.75
Paints		
aluminum, various ages and compositions	200	0.27-0.62
black gloss	100	0.90
black lacquer	100	0.80-0.93
white paint	100	0.89-0.97
white lacquer	100	0.80-0.95
various oil paints	100	0.92-0.96
red lead	200	0.93
Paper		
white	100	0.95
writing paper	100	0.98
any color	100	0.92-0.94
roofing	100	0.91
Plaster		
lime, rough	100-500	0.92
Porcelain		
glazed	100	0.93
Quartz	100-1000	0.89-0.58
Rubber		
hard	100	0.94
soft, gray rough	100	0.86
Sandstone	100-500	0.83-0.90
Snow	10-20	0.82
Water		
0.1 mm or more thick	100	0.96
Wood		
oak, planed	100	0.90
walnut, sanded	100	0.83
spruce, sanded	100	0.82
beech	100	0.94
planed	100	0.78
various	100	0.80-0.90
sawdust	100	0.75

Figure 14-56 shows the surfaces of two black bodies separated by a medium which does not absorb radiation appreciably (e.g., air). To determine the fraction of the energy leaving surface, A_1, that strikes surface A_2, consider first the two differential surfaces dA_1 and dA_2. If the distance between them is r, then $dq_{1\to 2}$, the rate at which radiation from dA_1 is received by dA_2, is given by:

$$dq_{1\to 2} = I_1 \cos\phi_1 \, dA_1 \, d\omega_{1-2} \qquad (91)$$

where:

I_1 = Intensity of radiation from dA_1;

$dA_1 \cos\phi_1$ = Projection of area element dA_1 as seen from dA_2;

$d\omega_{1-2}$ = Solid angle subtended by receiving area dA_2 with respect to center point of dA_1;

From equations 85 and 91, it can be shown that:

$$q_{1\rightleftarrows 2} = (E_{b1} - E_{b2}) \int_{A_1}\int_{A_2} \frac{\cos\phi_1 \cos\phi_2 \, dA_1 dA_2}{\pi r^2} \qquad (92)$$

The term $(E_{b1} - E_{b2})$ can be written in the form $\sigma(T_1^4 - T_2^4)$. The double integral can be written in the form $A_1 F_{1-2}$ or $A_2 F_{2-1}$, where F_{1-2} is called the shape factor (or configuration factor) evaluated on the basis of area A_1, and F_{2-1} is called the configuration factor evaluated on the basis of A_2. Physically, F_{1-2} represents the fraction of the total radiant energy leaving A_1 which is intercepted by A_2, and F_{2-1} is the fraction of energy reaching A_1 from A_2. The equality;

$$A_1 F_{1-2} = A_2 F_{2-1} \qquad (93)$$

is known as the reciprocity theorem. Substituting equation 93 for the double integral in equation 92 yields:

$$q_{1\rightleftarrows 2} = (E_{b1} - E_{b2}) F_{1-2} A_1 = (E_{b1} - E_{b2}) F_{2-1} A_2 \qquad (94)$$

Thus the net rate of heat flow between two black bodies can be determined by evaluating the radiation from either one of the surfaces to the other surface and replacing its emissive power by the difference of the emissive powers of both surfaces. Since the end result is independent of the choice of the emitting surface, it is convenient to select the surface whose shape factor can be determined more easily. A summary of the more commonly used configuration factors and a catalog of factors for over 150 geometric combinations is contained in 14-3.8.

The net radiation from a surface A_i in a black body enclosure consisting of several surfaces can be evaluated by a simple extension of equation 94 namely:

$$q_{i_{net}} = \sum_{k=1}^{k=n} A_i F_{ik} (E_{bi} - E_{bk}) \qquad (95)$$

Inspection of equation 95 shows that there is an analogy between heat flow by radiation and the flow of electric current. If the black body emissive power E_b is considered to act as a potential, and the shape factor $A_i F_{i-k}$ as the conductance between two nodes at potentials E_{bi} and E_{bk}, then the resulting net heat flow $q_{i_{net}}$ is analogous to the flow of electric current in an analogous network. Figure 14-57 shows equivalent networks for three black body radiation conditions of interest.

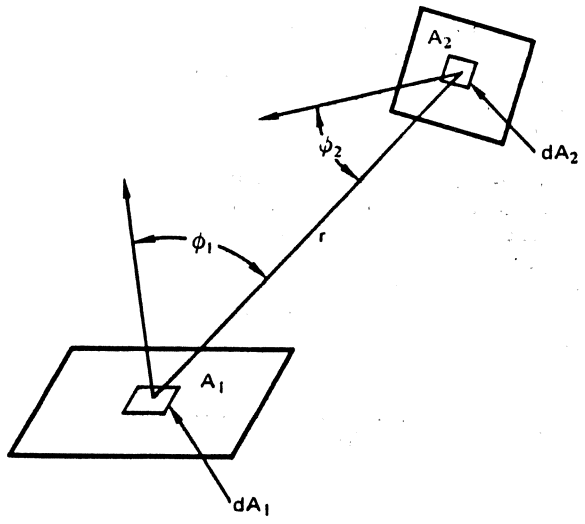

Figure 14-56. Geometrical Shape-Factor Notation

14-3.5 Radiant Heat Exchange between Gray Bodies

The assumption that a surface is black simplifies heat-transfer calculations because all of the incident radiation is absorbed. If the radiating surfaces are not black, the analysis becomes very difficult unless the surfaces are considered to be gray surfaces which reflect and emit diffusely according to Lambert's cosine law. Radiation from such surfaces can be treated conveniently in terms of the radiosity J which is the rate at which radiation leaves a given surface per unit area. The radiosity is the sum of radiation emitted by, reflected from, and transmitted through a body. For opaque bodies, the radiosity can be defined as:

$$J = \rho G + \epsilon E_b \qquad (96)$$

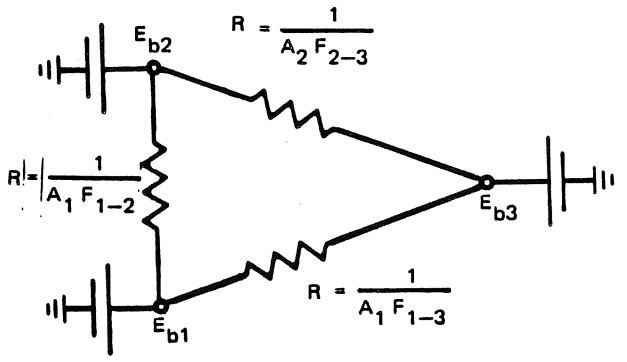

(A) THREE BLACK BODY SURFACES IN A BLACK BODY ENCLOSURE

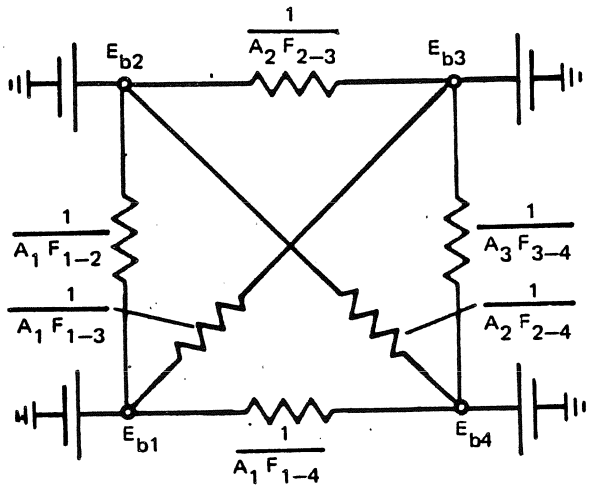

(B) FOUR BLACK BODY SURFACES IN A BLACK BODY ENCLOSURE

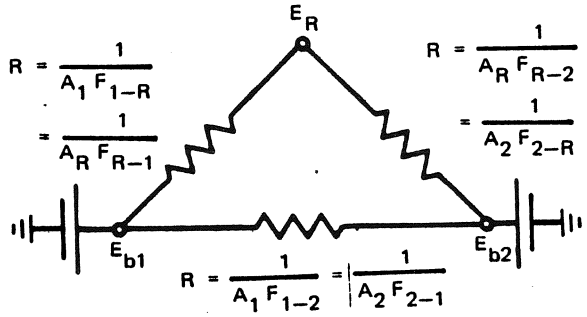

(C) TWO BLACK BODIES IN A RERADIATING ENCLOSURE

Figure 14-57. Equivalent Black Body Thermal Radiation Networks

where:

- J = Radiosity, in Btu/hr-ft^2
- G = Irradiation or radiation per unit time incident on unit surface area, Btu/hr-ft^2
- E_b = Black-body emissive power, Btu/hr-ft^2
- ρ = Reflectance
- ϵ = Emittance

The net rate at which radiation leaves a gray surface per unit area and time is equal to the difference between the radiosity and the irradiation, that is:

$$dq_{net}/dA = J - G = (\epsilon/\rho)(E_b - J) \qquad (97)$$

since ρ is a constant for gray bodies and $\rho + \epsilon = 1$.

If irradiation and radiosity are uniformly distributed over the surface, the net radiation rate leaving a surface A is obtained by integrating equation 97 resulting in:

$$q_{net} = (\epsilon/\rho)A\,(E_b - J) \qquad (98)$$

The effect of the system geometry on the net radiation between two gray surfaces A_i and A_k emitting radiation at the rate J_i and J_k respectively, is the same as for similar black surfaces. Therefore, the direct radiation exchange between any two opaque and diffuse surfaces A_i and A_k is:

$$q_{i \rightleftarrows k} = (J_i - J_k)\,A_i \mathscr{F}_{i\text{-}k} = (J_i - J_k)A_k \mathscr{F}_{k\text{-}i} \qquad (99)$$

Equations 98 and 99 provide the basis for determining the net radiant heat transfer rate between gray bodies in a gray enclosure by means of an equivalent network. With the stipulation that a heat transfer surface is that portion of an area which is at a constant temperature and is uniformly irradiated, the effect of reflectance and emittance can be taken into account by connecting a black-body potential node E_b to each of the nodal points in the network by means of a finite conductance $A\epsilon/\rho$. In the case of a black body, $A\epsilon/\rho$ is infinite since $\rho_b = 0$.

Figure 14-58 shows equivalent networks for three gray body conditions which are similar to the black body conditions shown in Figure 14-57. Figure 14-58a is typical of two-component gray enclosures such as two parallel and infinite plates where end effects can be neglected. In this case, for example, the equivalent conductance is:

$$A_1 \mathscr{F}_{1\text{-}2} = \frac{1}{\rho_1/A_1\epsilon_1 + 1/A_1 + \rho_2/A_2\epsilon_2}$$

and:

$$\mathscr{F}_{1\text{-}2} = \frac{1}{1/\epsilon_1 + 1/\epsilon_2 - 1}$$

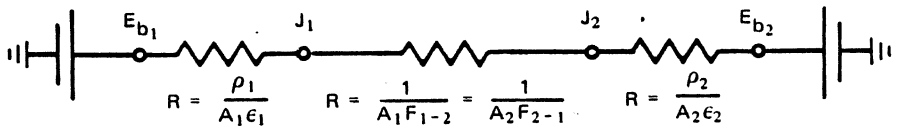

(A) TWO GRAY BODY SURFACES IN A GRAY BODY ENCLOSURE

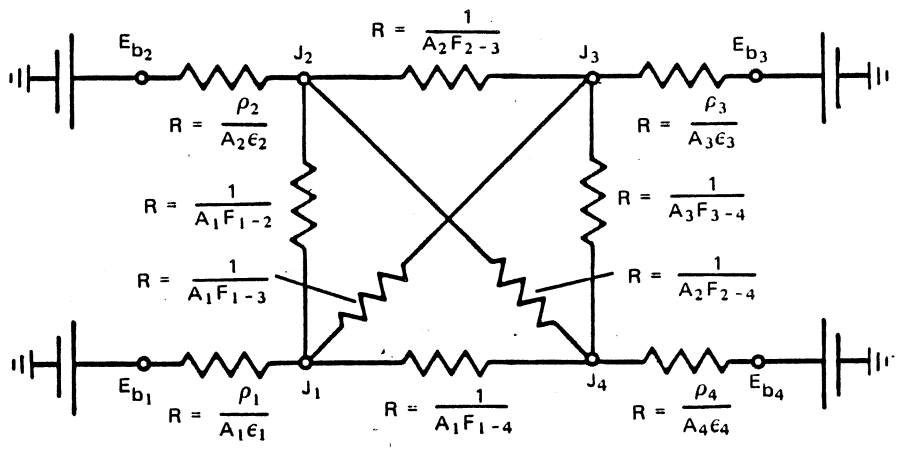

(B) FOUR GRAY BODY SURFACES IN A GRAY BODY ENCLOSURE

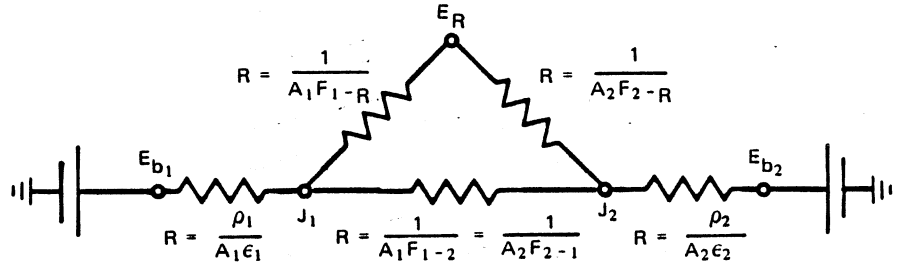

(C) TWO GRAY BODY SURFACES IN A RERADIATING ENCLOSURE

Figure 14-58. Equivalent Gray Body Thermal Radiation Networks

The gray-body shape factor is identified as F_{ik} which consists of the product of a geometric shape factor and a factor that allows for the departure of the surface from black-body conditions.

14-3.6 Radiation from Gases

Some gases, such as CO_2, H_2O, SO_2, CO, and NH_3 emit or absorb appreciable amounts of radiant energy at temperatures of practical interest. CO_2 and H_2O are the principal constituents of propellant combustion and, as such, should be considered in radiant heat-transfer calculations.

Whereas solids radiate at all wavelengths over the entire spectrum, gases emit and absorb radiation only in narrow regions of wavelengths called bands. Gas radiation also differs from solid-body radiation in another respect. The emission and absorption of radiant energy are essentially surface phenomena for a solid body, but in calculating the radiation emitted or absorbed by a gas layer, its thickness, pressure, and shape as well as its surface area must be taken into account.

The absorptance and emittance of a gas at wavelength λ can be expressed by:

$$\alpha_{G\lambda} = \epsilon_{G\lambda} = 1 - e^{-k'_{\lambda} L} \qquad (100)$$

where k' is the monochromatic absorption coefficient, a proportionality constant whose value depends on the pressure and temperature of the gas, and L is the gas layer thickness.

For large values of L, gas radiation approaches black-body conditions within the wavelengths of its bands. For gas bodies of finite dimensions, the effective absorptance or emittance depends on the shape and size of the gas body, since radiation is not confined to one dimension.

Figures 14-59 through 14-62 present values of emittance for water vapor and carbon dioxide respectively, as a function of pressure and temperature for a hemispherical gas mass of radius L which radiates to an element of surface located at the center of the hemisphere's base. For shapes other than hemispheres, an effective beam length can be calculated. For rough approximations, L can be taken as 3.4 x volume/surface area. Table 14-13 lists the constants by which the characteristic dimensions of several simple shapes are to be multiplied to obtain an equivalent mean hemispherical beam length L for Figures 14-59 and 14-61.

The curves in Figures 14-59 and 14-61 give the emittance of pure water vapor and pure carbon dioxide, respectively, at a total pressure p_t of one atmosphere as functions of the temperature in degrees F, and the

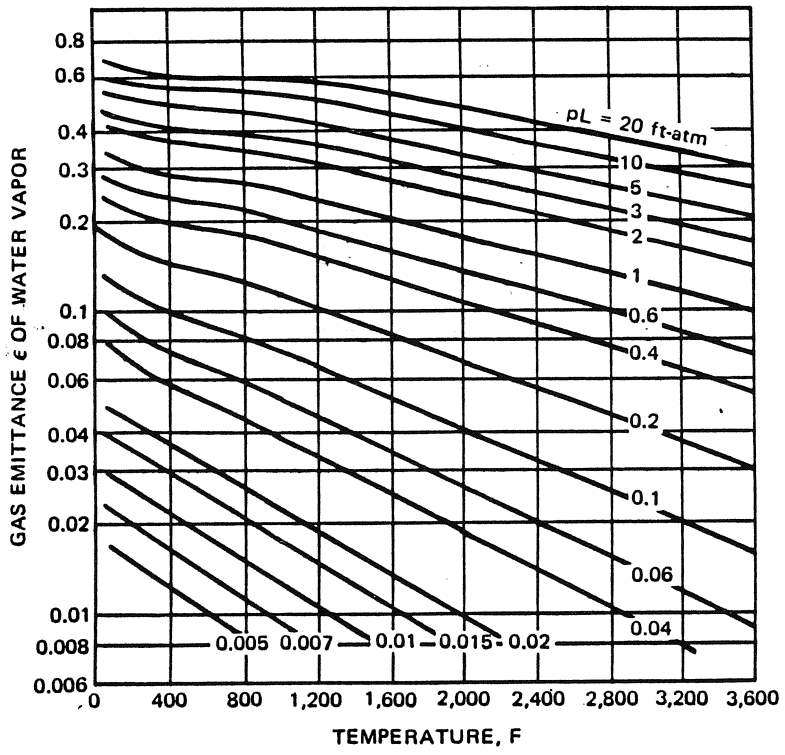

Figure 14-59. Water Vapor Emittance at One Atmosphere Total Pressure and Zero Partial Pressure

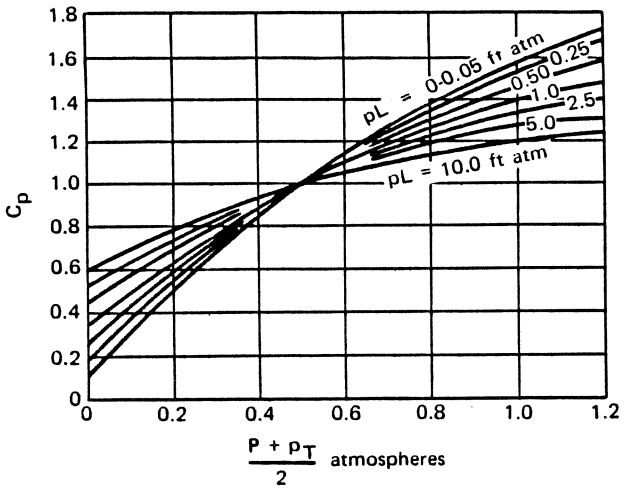

Figure 14-60. Emittance Correction Factor for Water Vapor to Values Other than One Atmosphere and Zero Partial Pressure

Table 14-13. Average Lengths of Radiant Beams in Various Gas Shapes

Shape	L
1. Sphere	2/3 X diameter
2. Infinite cylinder	1 X diameter
3. Space between infinite parallel planes	1.8 X distance between planes
4. Cube	2/3 X side
5. Space outside infinite bank of tubes with centers on equilateral triangles; tube diameter equals clearance	2.8 X clearance
6. Same as (5) except tube diameter equals one-half clearance	3.8 X clearance

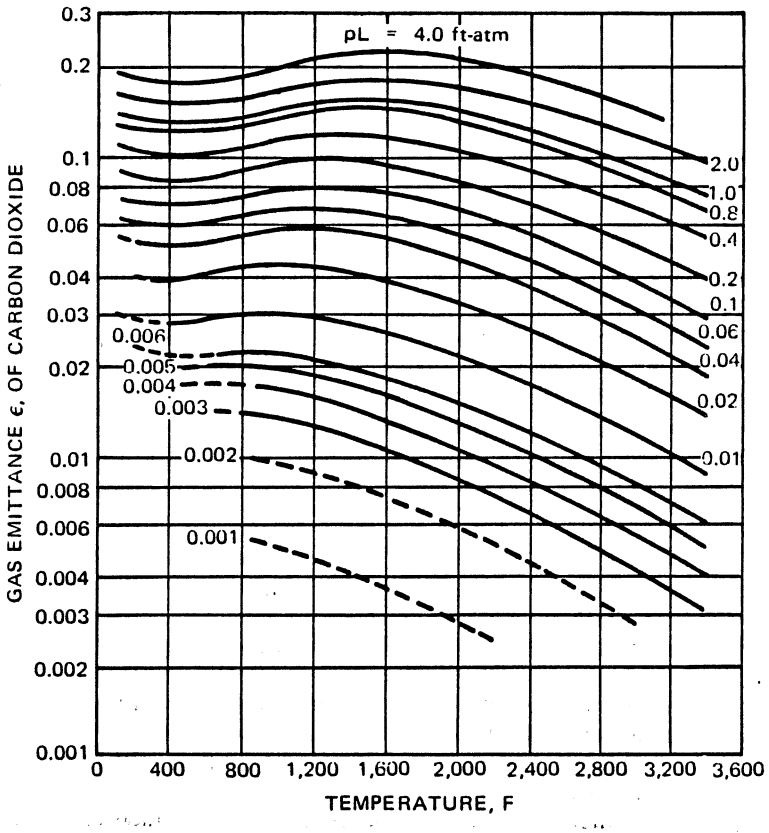

Figure 14-61. Carbon Dioxide Emittance at One Atmosphere Total Pressure

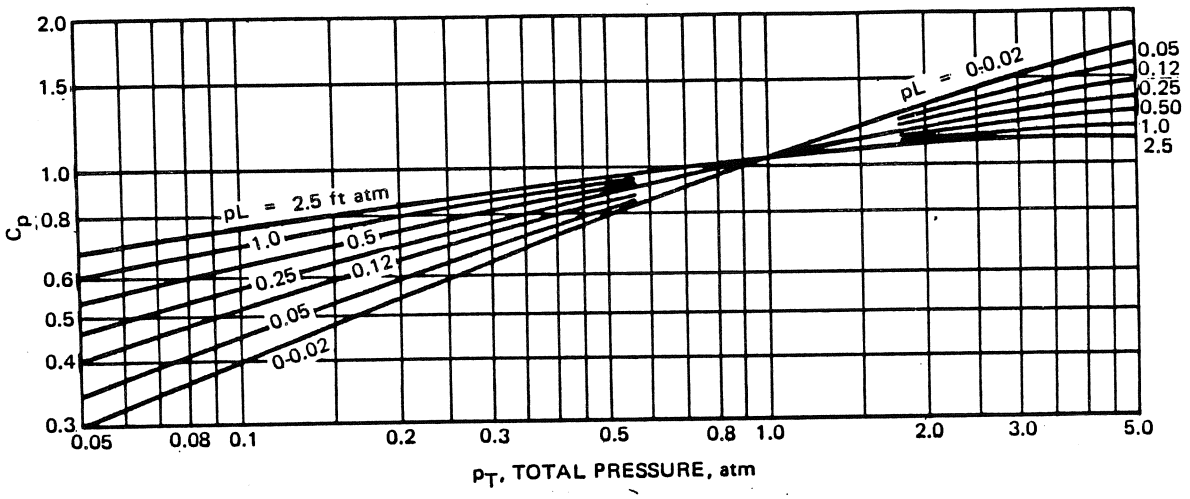

Figure 14-62. Emittance Correction Factor for Carbon Dioxide to Values Other Than One Atmosphere Total Pressure

product of the gas partial pressure p, in atmospheres, and the hemispherical beam length of the gas body L, in feet. The effects of the actual values of both total and partial pressures on the emittance of water vapor, and of total pressure on the emittance of CO_2, are accounted for by means of the auxiliary charts in Figures 14-60 and 14-62 which give correction factors to the curves in Figures 14-59 and 14-61. For example, the carbon dioxide emittance obtained from Figure 14-61 at one atmosphere must be multiplied by the correction factor C_p from Figure 14-62 to compensate for the changing of the absorption bands with change of total pressure.

Figure 14-63 presents curves of correction for the superimposed radiation from mixtures of carbon dioxide and water vapor. These curves take into account the overlapping of the absorption spectra of the two gases. The values of $\Delta\epsilon$ of the figure are to be subtracted from the sum of the separately calculated values of ϵ for water vapor and carbon dioxide.

14-3.7 Solar, Terrestial, and Atmospheric Radiation

The rate at which solar energy impinges on a surface of unit area normal to the sun's rays at the outer edge of the earth's atmosphere is called the solar constant G_o. The value of G_o is 442 Btu/hr-ft^2. The rate at which solar energy reaches the earth's surface is somewhat lower because water vapor, carbon dioxide and dust in the atmosphere absorb and scatter radiant energy. The amount of solar radiation received by a surface on the earth depends on the altitude of the sun, location, time of day, time of year, the weather, and the tilt of the surface. Figure 14-64 presents information on the variation of the intensity of solar energy within the atmosphere at a specific location, at a specific time, and under specific conditions.

Figure 14-65 is a nomogram for determining solar altitude and azimuth which in turn can be used to determine the amount of solar radiation that the earth receives, using a method described in *Handbook of Geophysics,* Shea L. Valley, McGraw Hill, 1965.

Use of the solar altitude and azimuth nomogram is as follows:

True Solar Time (also referred to as Local Apparent Time or Sun-Dial Time) determines a point P_5 on the cos h scale, which is graduated directly in terms of time. The solar declination and geographic latitude determine a point P_3 on the $\phi - \delta$ grid. If P_3 and P_5 are joined by a straight line, which is extended to intersect the sin α scale at P_1, the solar altitude (actually sin α) may be read off directly at P_1.

The solar azimuth angle, α (measured from north), is given by:

$$\sin a = \sin h \, (\cos \delta / \cos \alpha) \qquad (101)$$

where:

α = Solar altitude (angular elevation above the horizon)

ϕ = Geographic latitude

δ = Declination of the sun

h = Hour angle of the sun

The existing solar altitude scale may be used for cos α noting that:

$$1 - \cos \alpha = 1 - \sin (\pi/2 - \alpha) \qquad (102)$$

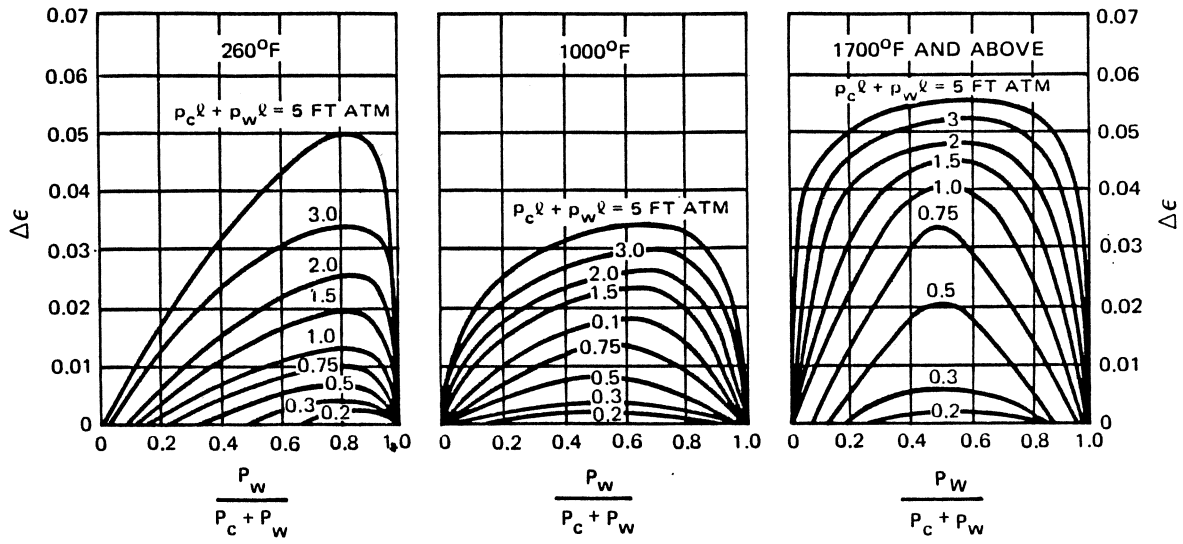

Figure 14-63. Correction to Gas Emittance Due to Spectral Overlapping of Carbon Dioxide and Water Vapor

An auxiliary scale, calibrated in $1 - \sin(\pi/2 - \alpha)$ is located immediately adjacent and parallel to the sin α scale. Once sin α is determined, the corresponding value of $1 - \sin(\pi/2 - \alpha)$ is read off on the adjacent scale and the sin α scale reentered at this value. Let this point be P_2.

The existing time scale may also be used, since:

$$\sin h = \cos(\pi/2 - h) = -\cos(3\pi/2 - h). \qquad (103)$$

Only the lower half of the true solar time scale is used for the azimuth calculation. To determine the point P_4 at which to enter this scale, use either $\pm(h - 6\ hr)$ or $\pm(h - 18\ hr)$, whichever will give a point on the lower half of the time scale.

Points P_2 and P_4 are joined by a straight line which intersects the uncalibrated diagonal at P_6. Then P_6 is joined with P_7 on the solar declination scale at the bottom of the nomogram and the azimuth is read off at P_8 on the azimuth scale.

In the Northern Hemisphere, the solar azimuth is measured from north. During the time of year when $\delta > 0$, confusion may exist as to whether, for example, 70° or 110° should be read off the azimuth scale. When such confusion exists, the azimuth should be determined for a time a little closer to noon. If the new azimuth is closer to the 90° point, then the correct azimuth was 70°. If the new azimuth is slightly farther from the 90° point, then 110° is the correct azimuth.

Figure 14-66 presents typical equilibrium temperature data for several surfaces exposed to solar radiation. It shows that surfaces that have large absorptances in the solar-wavelength range reach substantially higher equilibrium temperatures than surfaces with low absorptances. The lowest equilibrium temperatures are reached by white paints which are selective emitters. They are poor absorbers (i.e., good reflectors) for the solar spectral radiation range, but are good absorbers (hence good emitters) in the spectral range associated with relatively low temperatures.

On cold clear nights, the effective sky temperature for an object on earth is approximately 410 °Rankine (−50°F). This accounts for the freezing of water during the night even when the atmospheric temperature is above 32°F.

The radiant energy incident upon a surface on the earth placed normal to the sun's rays G_n can be estimated from:

$$G_n = G_o \tau_a^m \qquad (104)$$

where:

G_o = Solar constant, 442 Btu/hr-ft^2

τ_a = Transmission coefficient for unit air mass which varies from 0.62 to 0.81 and has a mean of about 0.7

m = Relative air mass, defined as the ratio of the actual path to the shortest possible path.

In some situations, the spectral distribution of solar irradiation must be known in order to solve a problem. For example, when the amount of solar irradiation that a spectrally selective absorber will absorb must be determined, it can be evaluated by integrating the

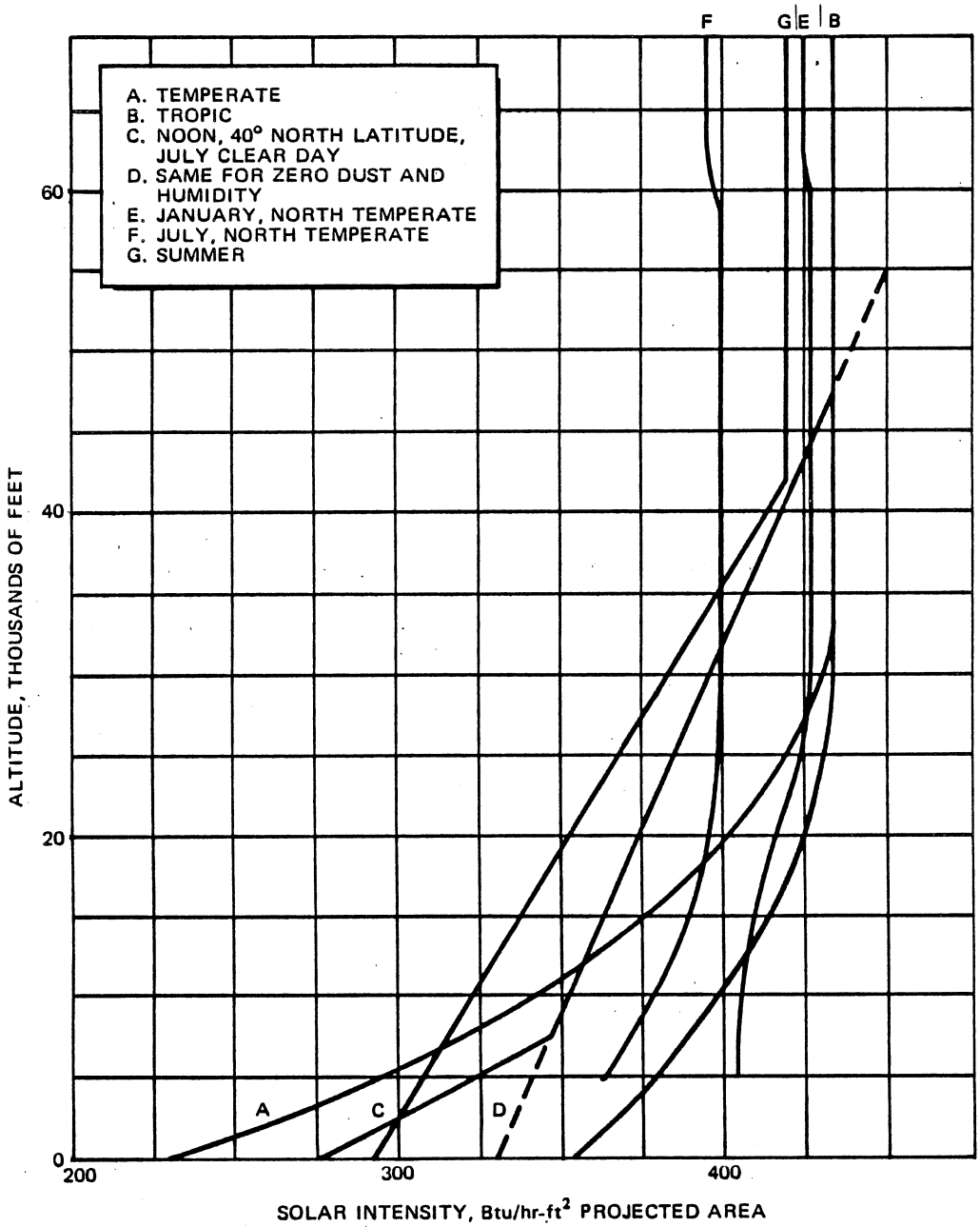

NOTE:
Use curve B unless application is limited to a particular climatic zone.

Figure 14-64. Variation of Solar Energy with Altitude

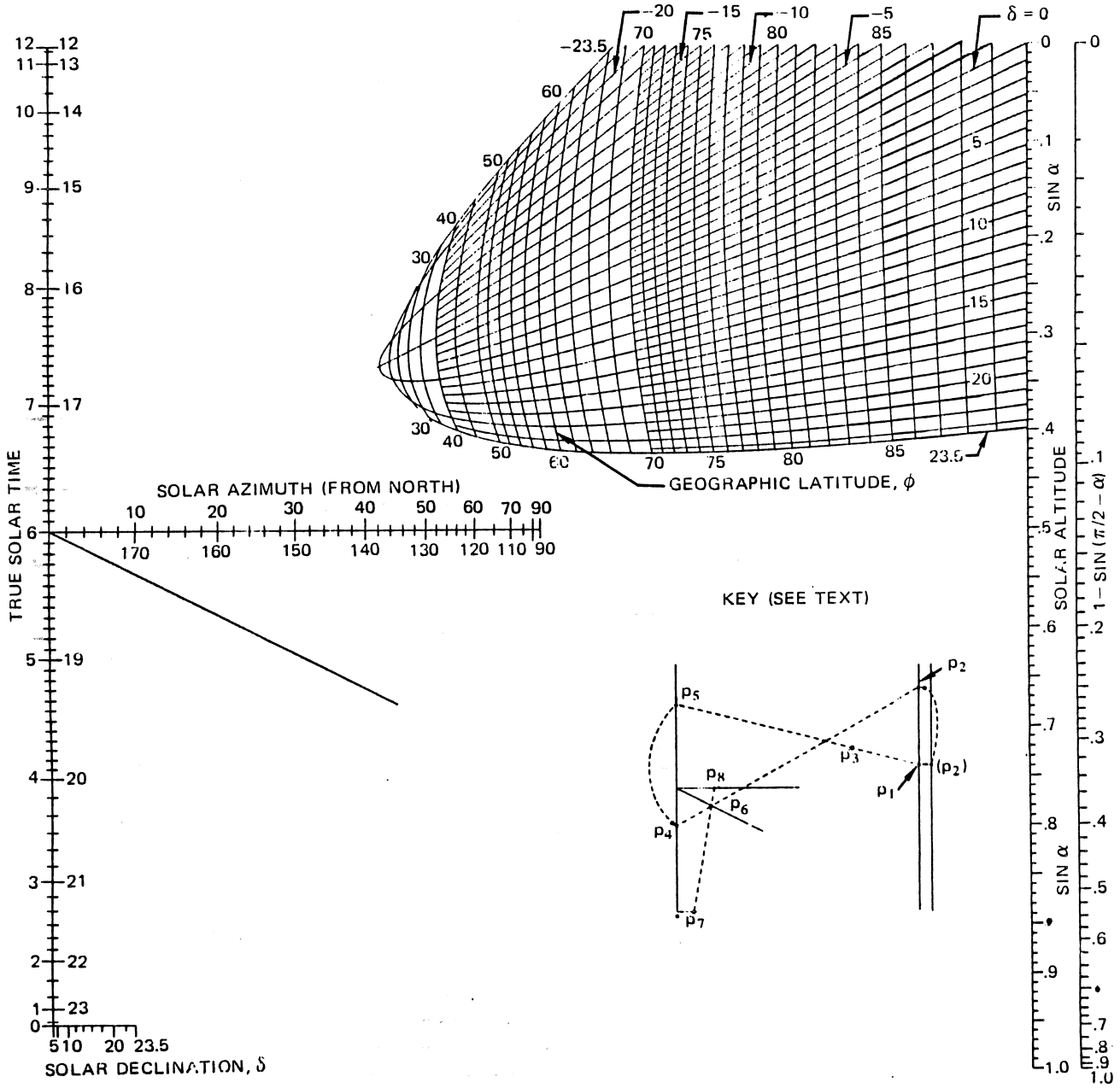

Figure 14-65. Combination Nomogram for Solar Altitude and Azimuth

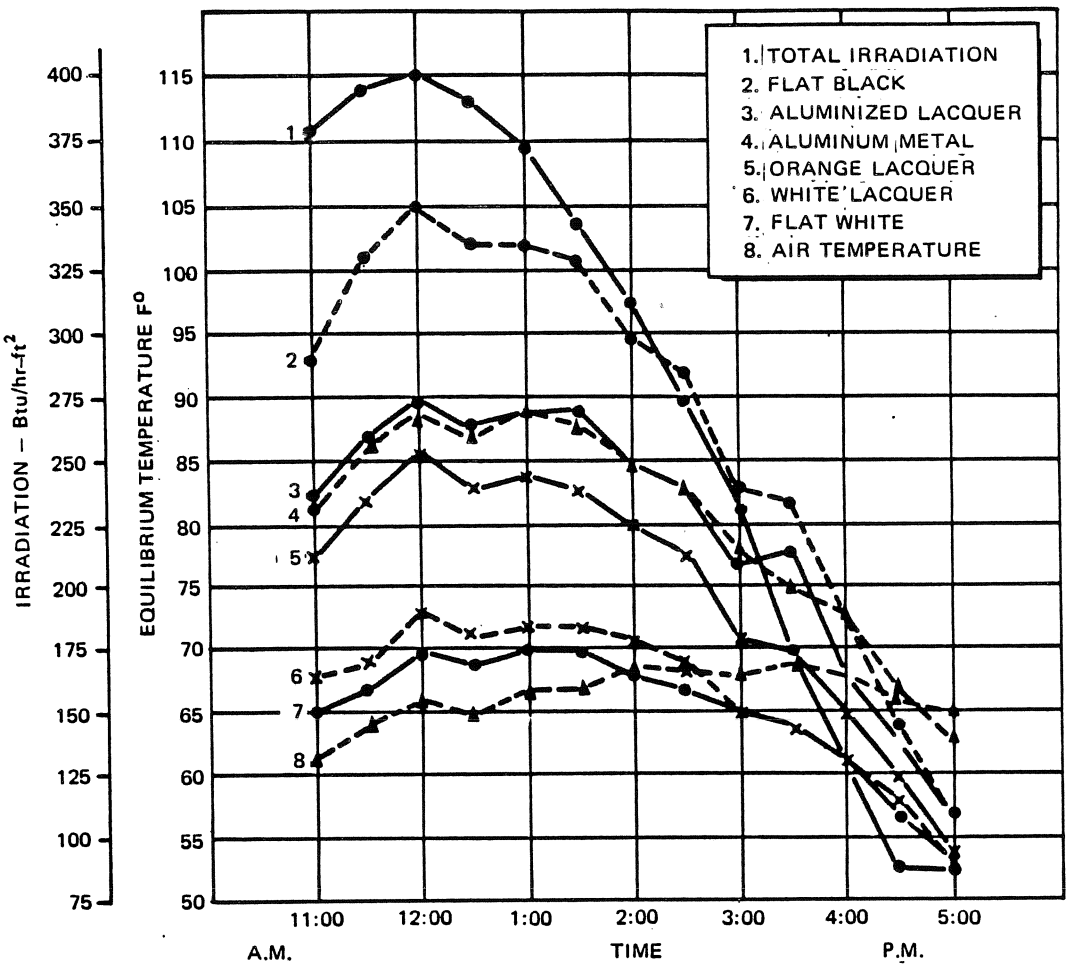

Figure 14-66. Equilibrium Temperature of Various Surfaces

product of spectral absorptance and solar spectral irradiation over all wavelengths, i.e.,

$$\int_0^\infty \alpha_\lambda G_{o\lambda} \, d\lambda \qquad (105)$$

where:

$G_{o\lambda}$ = Solar irradiation at wavelength λ

The spectral distribution of solar irradiation outside the earth's atmosphere is presented in Table 14-14 where it can be seen that although the bandwidth of solar irradiation extends from below 0.22μ to beyond 7μ, 99 percent of solar irradiation is contained between 0.25 and 4.1μ. Consequently, the total absorbed irradiation for this situation can be calculated from:

$$\int_{0.25\mu}^{4.1\mu} \alpha_\lambda G_{o\lambda} \, d\lambda$$

At the surface of the earth, solar irradiation is significantly diminished due to absorption by the constituents of the earth's atmosphere, so that the total incident irradiation is reduced from approximately 442 Btu/hr-ft^2 outside the earth's atmosphere to approximately 360 Btu/hr-ft^2 when the sun is at zenith. Figure 14-67 shows a comparison of the spectral distribution of solar irradiation outside the earth's atmosphere with that at sea level for the sun at zenith, with the absorption due to each absorbing band in the atmosphere. Also shown, for comparison is the Planckian curve for a black body at a temperature of 5900°K (10620°R).

Table 14-14. Solar-Spectral-Irradiance Data

λ (μ)	$G_{o\lambda}$* (w/cm^2 μ)	P_λ (%)	λ (μ)	$G_{o\lambda}$* (w/cm^2 μ)	P_λ (%)	λ (μ)	$G_{o\lambda}$* (w/cm^2 μ)	P_λ (%)	λ (μ)	$G_{o\lambda}$* (w/cm^2 μ)	P_λ (%)
0.22	0.0030	0.02	0.395	0.120	3.54	0.57	0.187	33.2	1.9	0.01274	93.02
0.225	0.0042	0.03	0.40	0.154	9.03	0.575	0.187	33.9	2.0	0.01079	93.87
0.23	0.0052	0.05	0.405	0.188	9.65	0.58	0.187	34.5	2.1	0.00917	94.58
0.235	0.0054	0.07	0.41	0.194	10.3	0.585	0.185	35.2	2.2	0.00785	95.20
0.24	0.0058	0.09	0.415	0.192	11.0	0.59	0.184	35.9	2.3	0.00676	95.71
0.245	0.0064	0.11	0.42	0.192	11.7	0.595	0.183	36.5	2.4	0.00585	96.18
0.25	0.0064	0.13	0.425	0.189	12.4	0.60	0.181	37.2	2.5	0.00509	96.57
0.255	0.010	0.16	0.43	0.178	13.0	0.61	0.177	38.4	2.6	0.00445	96.90
0.26	0.013	0.20	0.435	0.182	13.7	0.62	0.174	39.7	2.7	0.00390	97.21
0.265	0.020	0.27	0.44	0.203	14.4	0.63	0.170	40.9	2.8	0.00343	97.47
0.27	0.025	0.34	0.445	0.215	15.1	0.64	0.166	42.1	2.9	0.00303	97.72
0.275	0.022	0.43	0.45	0.220	15.9	0.65	0.162	43.3	3.0	0.00268	97.90
0.28	0.024	0.51	0.455	0.219	16.7	0.66	0.159	44.5	3.1	0.00230	98.08
0.285	0.034	0.62	0.46	0.216	17.5	0.67	0.155	45.6	3.2	0.00214	98.24
0.29	0.052	0.77	0.465	0.215	18.2	0.68	0.151	46.7	3.3	0.00191	98.39
0.295	0.063	0.98	0.47	0.217	19.0	0.69	0.148	47.8	3.4	0.00171	98.52
0.30	0.061	1.23	0.475	0.220	19.8	0.70	0.144	48.8	3.5	0.00153	98.63
0.305	0.067	1.43	0.48	0.216	20.6	0.71	0.141	49.8	3.6	0.00139	98.74
0.31	0.076	1.69	0.485	0.203	21.3	0.72	0.137	50.8	3.7	0.00125	98.83
0.315	0.082	1.97	0.49	0.199	22.0	0.73	0.134	51.8	3.8	0.00114	98.91
0.32	0.085	2.26	0.495	0.204	22.8	0.74	0.130	52.7	3.9	0.00103	98.99
0.325	0.102	2.60	0.50	0.198	23.5	0.75	0.127	53.7	4.0	0.00095	99.05
0.33	0.115	3.02	0.505	0.197	24.2	0.80	0.1127	57.9	4.1	0.00087	99.13
0.335	0.111	3.40	0.51	0.196	24.9	0.85	0.1003	61.7	4.2	0.00080	99.18
0.34	0.111	3.80	0.515	0.189	25.6	0.90	0.895	65.1	4.3	0.00073	99.23
0.345	0.117	4.21	0.52	0.187	26.3	0.95	0.0803	68.1	4.4	0.00067	99.29
0.35	0.118	4.63	0.525	0.192	26.9	1.0	0.0725	70.9	4.5	0.00061	99.33
0.355	0.116	5.04	0.53	0.195	27.6	1.1	0.0606	75.7	4.6	0.00056	99.38
0.36	0.116	5.47	0.535	0.197	28.3	1.2	0.0501	79.6	4.7	0.00051	99.41
0.365	0.129	5.89	0.54	0.198	29.0	1.3	0.0406	82.9	4.8	0.00048	99.45
0.37	0.133	6.36	0.545	0.198	29.8	1.4	0.0328	85.5	4.9	0.00044	99.48
0.375	0.132	6.84	0.55	0.195	30.5	1.5	0.0267	87.6	5.0	0.00042	99.51
0.38	0.123	7.29	0.555	0.192	31.2	1.6	0.0220	89.4	6.0	0.00021	99.74
0.385	0.115	7.72	0.56	0.190	31.8	1.7	0.0182	90.83	7.0	0.00012	99.86
0.39	0.112	8.13	0.565	0.189	32.5	1.8	0.0152	92.03			

λ is wavelength; $G_{o\lambda}$ is spectral irradiance; and P_λ is the percentage of the solar constant associated with wavelengths shorter than λ.

**These values can be converted to Btu /ft^2-hr-μ by multiplying the tabulated values of $G_{o\lambda}$ by 3160.*

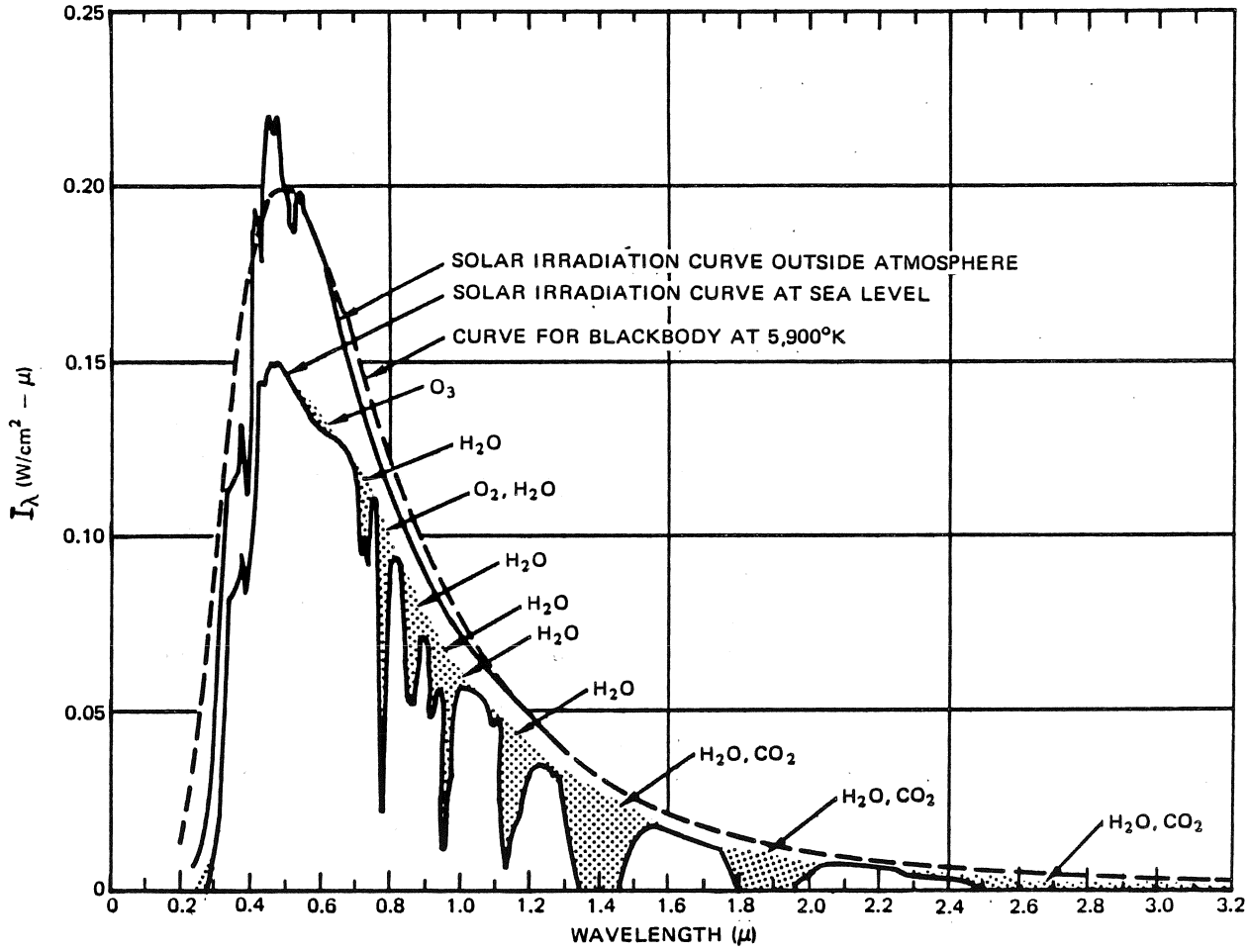

SHADED AREAS INDICATE ABSORPTION, AT SEA LEVEL, DUE TO THE ATMOSPHERIC CONSTITUENTS SHOWN.

Figure 14-67. Spectral Distribution Curves Related to the Sun

14-3.8 Configuration Factors

14-3.8.1 Numerical Values

Algebraic expressions and graphical displays of configuration factors for the geometries shown in Figure 14-68 are discussed in this paragraph. The first seven geometries relate to radiant interchange between two finite surfaces, i.e.,

$$F_{A_1\text{-}A_2} = \frac{1}{A_1} \int_{A_1} \int_{A_2} \frac{\cos\phi_1 \cos\phi_2}{\pi r^2} \, dA_2 \, dA_1 \qquad (106)$$

The last eight geometries relate to radiant interchange between an infinitesimal element and a finite area:

$$F_{dA_1\text{-}A_2} = \int_{A_2} \frac{\cos\phi_1 \cos\phi_2}{\pi r^2} \, dA_2 \qquad (107)$$

It can be seen that equation 106 is related to equation 107 as follows:

$$F_{A_1\text{-}A_2} = \frac{1}{A_1} \int_{A_1} F_{dA_1\text{-}A_2} \, dA_1 \qquad (108)$$

Algebraic expressions are given for all fifteen of the geometries shown; however, graphic solutions are presented for geometries 1, 2, 3, 4, 8, 9, 10, and 11 only, the only ones for which solutions are available. These graphical solutions are presented in Figures 14-69 through 14-77.

14-3.8.1.1 Algebraic Expressions

Geometry 1: X = a/c, Y = b/c

$$F_{A_1-A_2}\left(\frac{\pi XY}{2}\right) = \ln\left[\frac{(1+X^2)(1+Y^2)}{1+X^2+Y^2}\right]^{1/2}$$

$$+ Y\sqrt{1+X^2}\tan^{-1}\left(\frac{Y}{\sqrt{1+X^2}}\right)$$

$$+ X\sqrt{1+Y^2}\tan^{-1}\left(\frac{X}{\sqrt{1+Y^2}}\right) \qquad (109)$$

$$- Y\tan^{-1} Y - X\tan^{-1} X$$

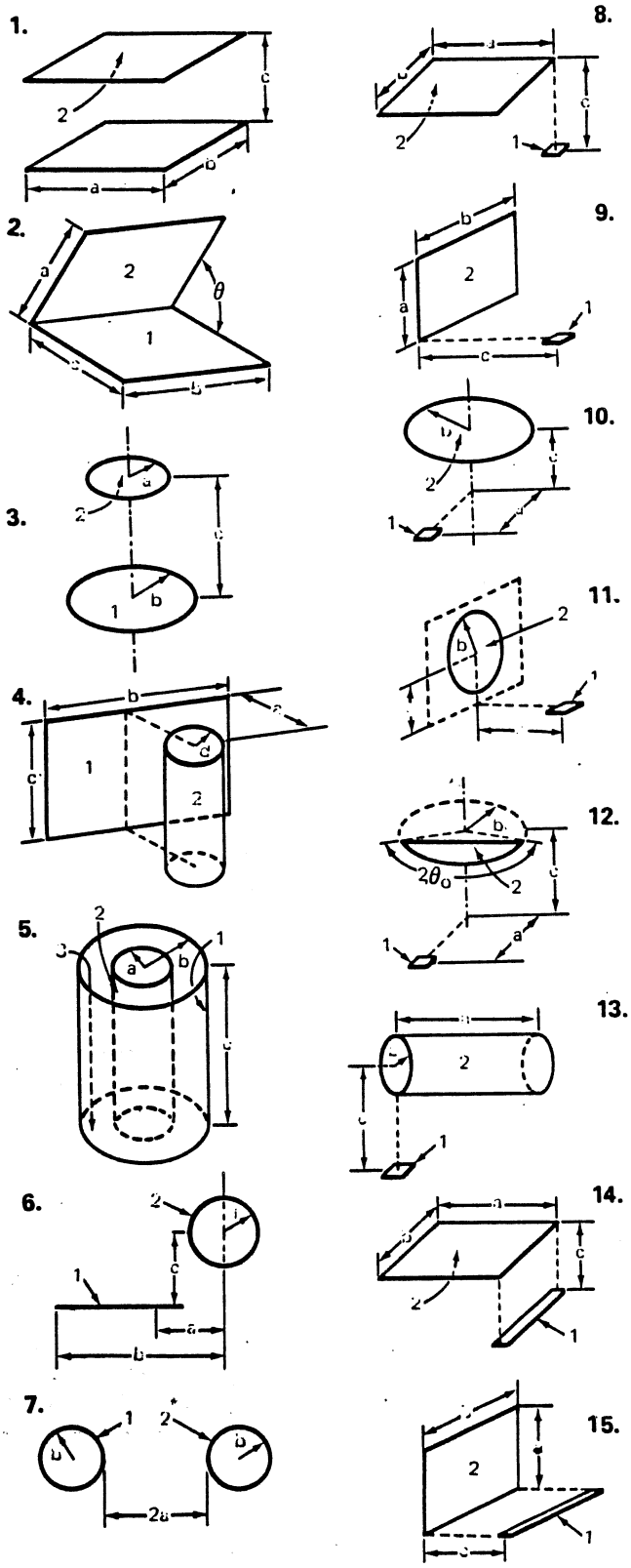

Figure 14-68. Configuration Factor – Basic Geometries

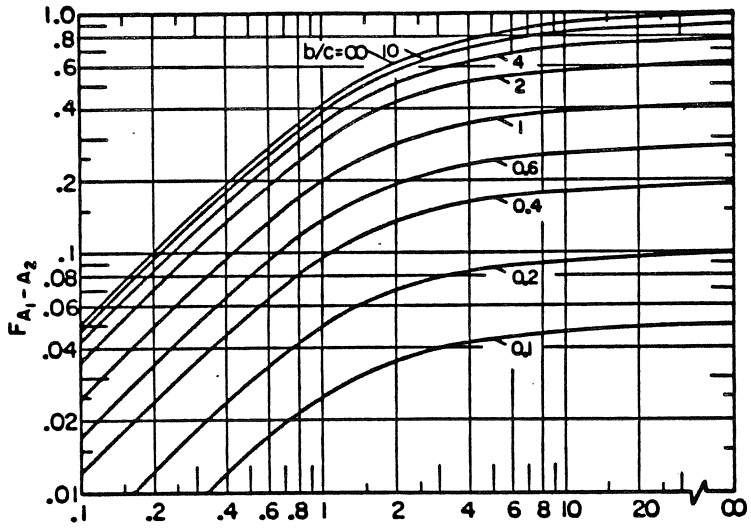

Figure 14-69. Configuration Factors for Geometry 1

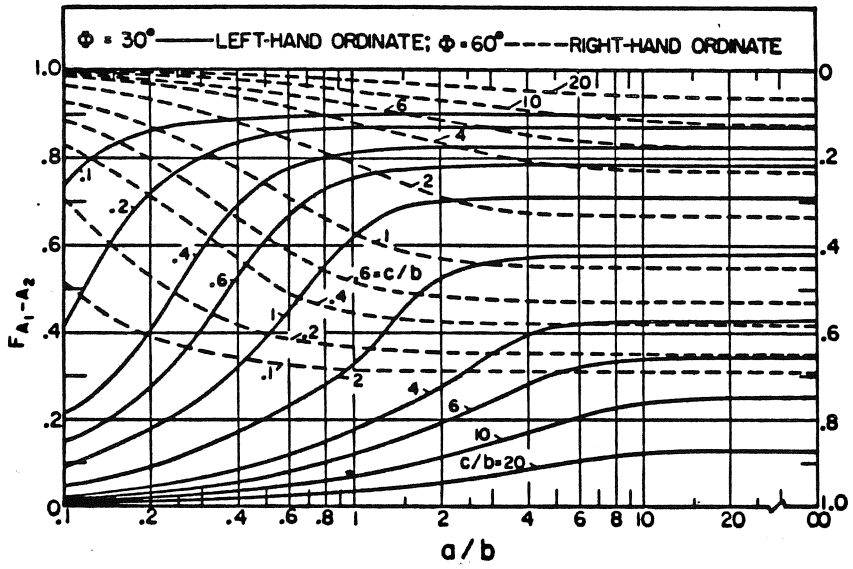

Figure 14-70. Configuration Factors for Geometry 2, Φ = 30 and 60°

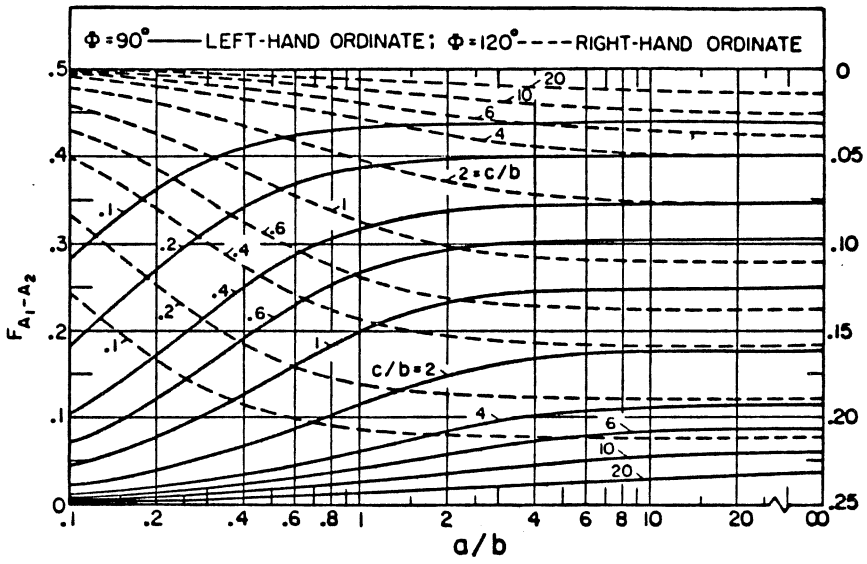

Figure 14-71. Configuration Factors for Geometry 2, Φ = 90 and 120°

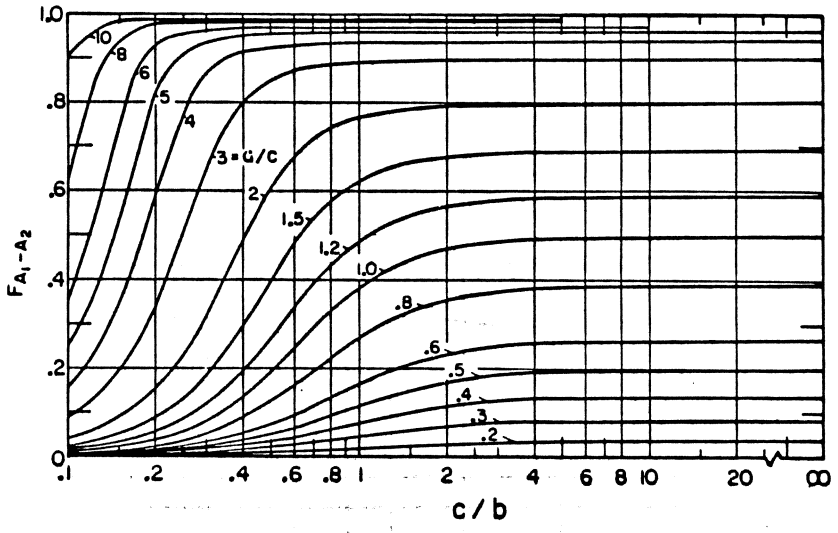

Figure 14-72. Configuration Factors for Geometry 3

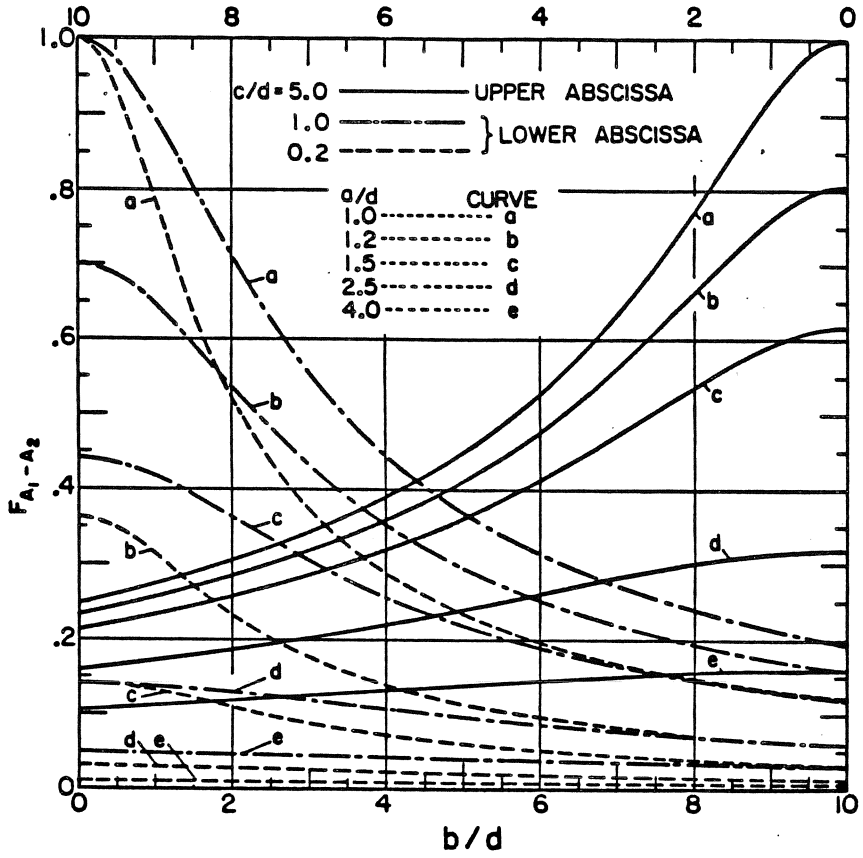

Figure 14-73. Configuration Factors for Geometry 4

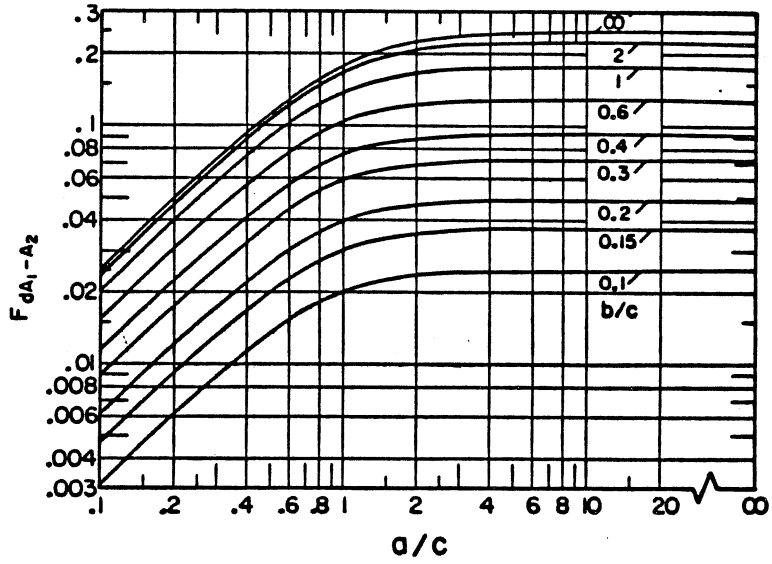

Figure 14-74. Configuration Factors for Geometry 8

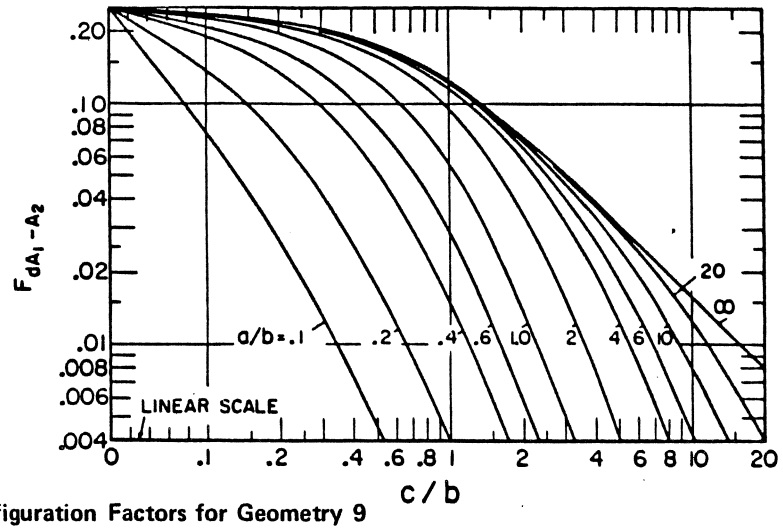

Figure 14-75. Configuration Factors for Geometry 9

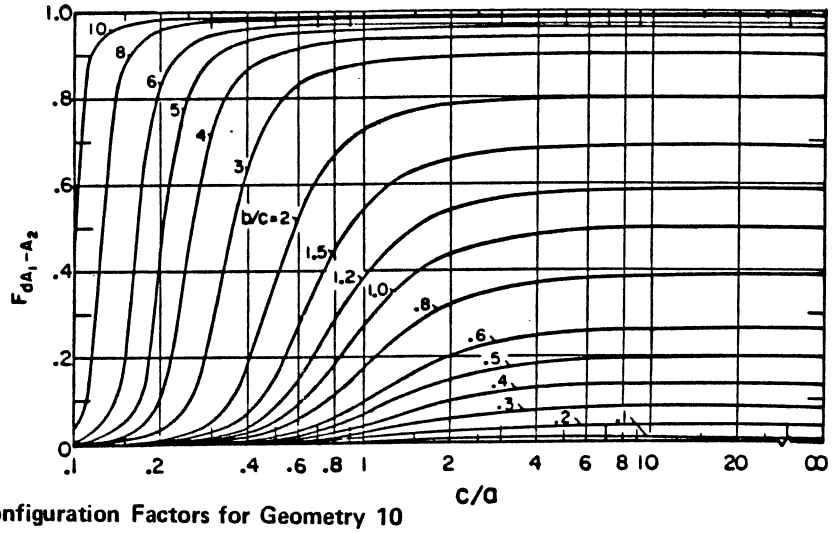

Figure 14-76. Configuration Factors for Geometry 10

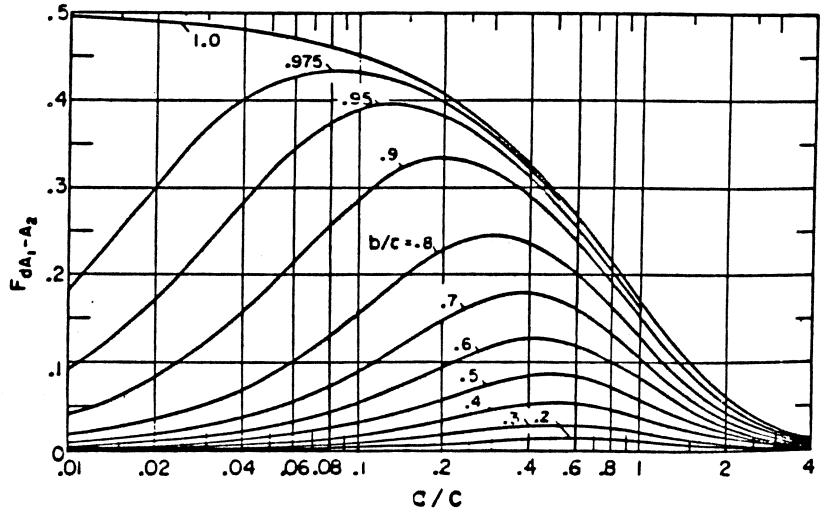

Figure 14-77. Configuration Factors for Geometry 11

Geometry 2:

$X = a/b,\ Y = c/b,$

$Z = X^2 + Y^2 - 2XY\cos\Phi$

$$F_{A_1-A_2}(\pi Y) = -\frac{\sin 2\Phi}{4}\left[XY\sin\Phi\right. \tag{110}$$

$$+\left(\frac{\pi}{2}-\Phi\right)(X^2+Y^2)$$

$$+Y^2\tan^{-1}\left(\frac{X-Y\cos\Phi}{Y\sin\Phi}\right)$$

$$\left.+X^2\tan^{-1}\left(\frac{Y-X\cos\Phi}{X\sin\Phi}\right)\right]$$

$$+\frac{\sin^2\Phi}{4}\left\{\left(\frac{2}{\sin^2\Phi}-1\right)\ln\left[\frac{(1+X^2)(1+Y^2)}{1+Z}\right]\right.$$

$$\left.+Y^2\ln\left[\frac{Y^2(1+Z)}{(1+Y^2)Z}\right]+X^2\ln\left[\frac{X^2(1+X^2)^{\cos 2\Phi}}{Z(1+Z)^{\cos 2\Phi}}\right]\right\}$$

$$+Y\tan^{-1}\left(\frac{1}{Y}\right)+X\tan^{-1}\left(\frac{1}{X}\right)-\sqrt{Z}\tan^{-1}\left(\frac{1}{\sqrt{Z}}\right)$$

$$+\frac{\sin\Phi\sin 2\Phi}{2}\times\sqrt{1+X^2\sin^2\Phi}$$

$$\times\left[\tan^{-1}\left(\frac{X\cos\Phi}{\sqrt{1+X^2\sin^2\Phi}}\right)\right.$$

$$\left.+\tan^{-1}\left(\frac{Y-X\cos\Phi}{\sqrt{1+X^2\sin^2\Phi}}\right)\right]$$

$$+\cos\Phi\int_0^Y\sqrt{1+\xi^2\sin^2\Phi}\left[\tan^{-1}\left(\frac{X-\xi\cos\Phi}{\sqrt{1+\xi^2\sin^2\Phi}}\right)\right.$$

$$\left.+\tan^{-1}\left(\frac{\xi\cos\Phi}{\sqrt{1+\xi^2\sin^2\Phi}}\right)\right]d\xi$$

Geometry 3:

$X = a/c,\ Y = c/b,\ Z = 1 + (1+X^2)Y^2$

$$F_{A_1-A_2} = \frac{1}{2}\left(Z-\sqrt{Z^2-4X^2Y^2}\right) \tag{111}$$

Geometry 4:

$X = a/d,\ Y = b/d,\ Z = c/d$

$A = Z^2 + X^2 + \xi^2 - 1, \quad B = Z^2 - X^2 - \xi^2 + 1$

$$F_{A_1-A_2} = \frac{2}{Y}\int_0^{Y/2} f(\xi)\,d\xi \tag{112}$$

$$f(\xi) = \frac{X}{X^2+\xi^2} - \frac{X}{\pi(X^2+\xi^2)}\cdot$$

$$\times\left\{\cos^{-1}\frac{B}{A}-\frac{1}{2Z}\right.$$

$$\left[\sqrt{A^2+4Z^2}\cos^{-1}\left(\frac{B}{A\sqrt{X^2+\xi^2}}\right)\right.$$

$$\left.\left.+B\sin^{-1}\left(\frac{1}{\sqrt{X^2+\xi^2}}\right)-\frac{\pi A}{2}\right]\right\}$$

Geometry 5:

$X = b/a,\ Y = c/a$

$$A = Y^2 + X^2 - 1, \quad B = Y^2 - X^2 + 1$$

$$F_{A_1-A_2} = \frac{1}{X} - \frac{1}{\pi X}\left\{\cos^{-1}\frac{B}{A} - \frac{1}{2Y}\right. \tag{113}$$

$$\left[\sqrt{(A+2)^2 - (2X)^2}\cos^{-1}\frac{B}{XA}\right.$$

$$\left.\left. + B\sin^{-1}\frac{1}{X} - \frac{\pi A}{2}\right]\right\}$$

$$F_{A_1-A_1} = 1 - \frac{1}{X} + \frac{2}{\pi X}\tan^{-1}\left(\frac{2\sqrt{X^2-1}}{Y}\right) \tag{114}$$

$$\frac{Y}{2\pi X}\left\{\frac{\sqrt{4X^2+Y^2}}{Y}\right.$$

$$\sin^{-1} x\left[\frac{4(X^2-1) + \frac{Y^2}{X^2}(X^2-2)}{Y^2 + 4(X^2-1)}\right]$$

$$\left. - \sin^{-1}\left(\frac{X^2-2}{X^2}\right) + \frac{\pi}{2}\left(\frac{\sqrt{4X^2+Y^2}}{Y} - 1\right)\right\}$$

$$F_{A_1-A_3} = \frac{1}{2}(1 - F_{A_1-A_2} - F_{A_1-A_1}) \tag{115}$$

Geometry 6:

$X = c/d,\ Y = a/d,\ Z = b/d$

$$F_{A_1-A_2} = \frac{1}{Z-Y}\left(\tan^{-1}\frac{Z}{X} - \tan^{-1}\frac{Y}{X}\right) \tag{116}$$

Geometry 7:

$X = 1 + (a/b)$

$$F_{A_1-A_2} = \frac{2}{\pi}\left(\sqrt{X^2-1} - X + \frac{\pi}{2} - \cos^{-1}\frac{1}{X}\right) \tag{117}$$

Geometry 8:

$X = a/c,\ Y = b/c$

$$F_{da_1-A_2} = \frac{1}{2\pi}\left[\frac{X}{\sqrt{1+X^2}}\tan^{-1}\left(\frac{Y}{\sqrt{1+X^2}}\right)\right. \tag{118}$$

$$\left. + \frac{Y}{\sqrt{1+Y^2}}\tan^{-1}\left(\frac{X}{\sqrt{1+Y^2}}\right)\right]$$

Geometry 9:

$X = a/b,\ Y = c/b$

$$A = 1/\sqrt{X^2+Y^2}$$

$$F_{dA_1-A_2} = \frac{1}{2\pi}\left(\tan^{-1}\frac{1}{Y} - AY\tan^{-1}A\right) \tag{119}$$

Geometry 10:

$X = c/a,\ Y = b/c,\ Z = 1 + (1+Y^2)X^2$

$$F_{dA_1-A_2} = \frac{1}{2}\left(1 - \frac{Z - 2Y^2X^2}{\sqrt{Z^2 - 4Y^2X^2}}\right) \tag{120}$$

Geometry 11:

$X = a/c,\ Y = b/c$

$$F_{dA_1 - A_2} = \frac{X}{2}\left[\frac{1 + Y^2 + X^2}{\sqrt{(1 + Y^2 + X^2)^2 - 4Y^2}} - 1\right] \quad (121)$$

Geometry 12:

$X = a/b,\ Y = c/b,$

$Z = [(1 + X^2 + Y^2)^2 - 4X^2]^{1/2}$

$$F_{dA_1 - A_2} = \frac{\theta_o}{2\pi} + \frac{(1 - X^2 + Y^2)}{\pi Z} \quad (122)$$

$$\times \tan^{-1}\left[\frac{Z \tan(\theta_o/2)}{1 + X^2 + Y^2 - 2X}\right]$$

$$+ \frac{X - \cos\theta_o}{\pi\sqrt{(X - \cos\theta_o)^2 + Y^2}}$$

$$\times \tan^{-1}\left[\frac{\sin\theta_o}{\sqrt{X - \cos\theta_o)^2 + Y^2}}\right]$$

Geometry 13:

$X = a/b,\ Y = c/b$

$A = (1 + Y)^2 + X^2, \quad B = (1 - Y)^2 + X^2$

$$F_{dA_1 - A_2} = \frac{1}{\pi Y}\tan^{-1}\left(\frac{X}{\sqrt{Y^2 - 1}}\right) \quad (123)$$

$$+ \frac{X}{\pi}\left\{\frac{(A - 2Y)}{Y\sqrt{AB}}\tan^{-1}\left[\sqrt{\frac{A(Y - 1)}{B(Y - 1)}}\right]\right.$$

$$\left. - \frac{1}{Y}\tan^{-1}\left[\sqrt{\frac{(Y - 1)}{(Y + 1)}}\right]\right\}$$

Geometry 14:

$X = b/c,\ Y = a/c$

$$F_{dA_1 - A_2} = \frac{1}{\pi X}\left[\sqrt{1 + X^2}\tan^{-1}\left(\frac{Y}{\sqrt{1 + X^2}}\right)\right. \quad (124)$$

$$\left. - \tan^{-1} Y + \frac{XY}{\sqrt{1 + Y^2}}\tan^{-1}\left(\frac{X}{\sqrt{1 + Y^2}}\right)\right]$$

Geometry 15:

$X = a/b,\ Y = c/b,\ Z = X^2 + Y^2$

$$F_{dA_1 - A_2} = \frac{1}{\pi}\left\{\tan^{-1}\left(\frac{1}{Y}\right) + \frac{Y}{2}\ln\left[\frac{Y^2(Z + 1)}{(Y^2 + 1)Z}\right]\right. \quad (125)$$

$$\left. - \frac{Y}{\sqrt{Z}}\tan^{-1}\left(\frac{1}{\sqrt{Z}}\right)\right\}$$

14-3.8.2 Configuration Factor Catalogue

Table 14-15 contains references to over 150 configuration factors that are available in the literature. The table is composed of three parts. Part A is for configuration factors betwen two elemental surfaces, part B gives references for factors between an elemental and a finite surface, and part C is for factors between two finite areas. More than one reference is given for some factors, and in certain cases the reference in which a factor was originally derived is not given because of the difficulty in obtaining such earlier works.

The factors are arranged in the following manner: Factors involving only plane surfaces are given first, followed by those involving cylindrical bodies, conical bodies, spherical bodies, and more complex bodies. Within each such category, progression is made from simpler to more complex geometries.

Table 14-15. Table of References for Configuration Factors

Configuration Number	Geometry	Configuration	Reference at end of table
	A. Factors for Two Differential Elements		
A-1	Two elemental areas in arbitrary configuration	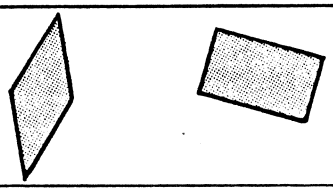	1
A-2	Two elemental areas lying on parallel generating lines		1
A-3	Elemental area to infinitely long strip of differential width lying on parallel generating line	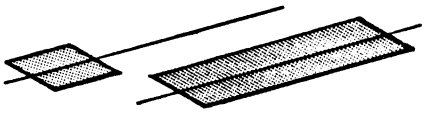	1, 2
A-4	Infinitely long strip of differential width to similar strip on parallel generating line	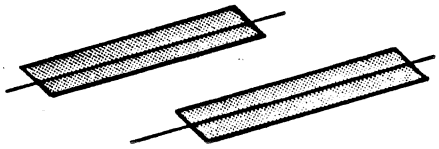	1, 2
A-5	Strip of finite length and differential width to strip of same length on parallel generating line	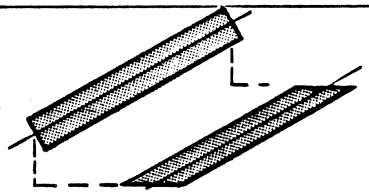	3
A-6	Corner element of end of square channel to sectional wall element on channel	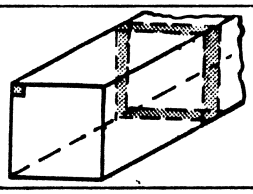	1
A-7	Exterior element on tube surface to exterior element on adjacent parallel tube of same diameter	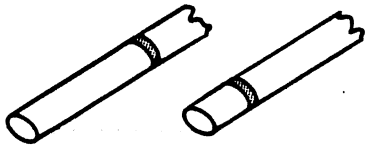	4
A-8	Exterior element on partitioned tube to similar element on adjacent parallel tube of same diameter	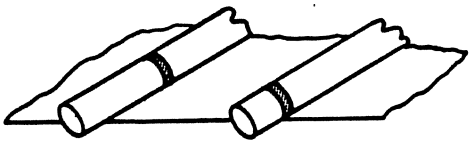	4

Table 14-15. Table of References for Configuration Factors (Continued)

Configuration Number	Geometry	Configuration	Reference at end of table
B. Factors for Exchange Between Differential Element and Finite Area			
B-1	Plane element to plane extending to infinity and intersecting plane of element at angle Φ	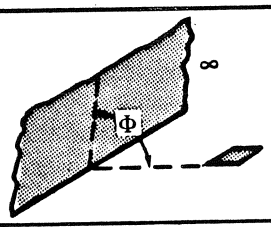	16 to 18
B-2	Plane strip element of any length to plane of finite width and infinite length	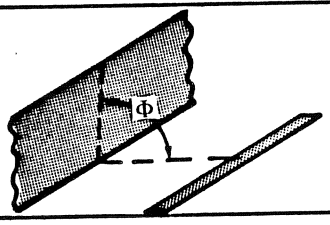	1
B-3	Plane element to infinitely long surface of arbitrary shape generated by line moving parallel to itself and plane of element	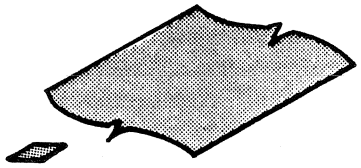	16 to 20
B-4	Strip element of finite length to rectangle in plane parallel to strip; strip is opposite to one edge of rectangle	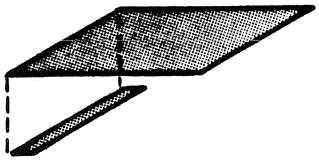	6, 16 to 18
B-5	Strip element of finite length to plane rectangle that intercepts plane of strip at angle Φ and with one edge parallel to strip	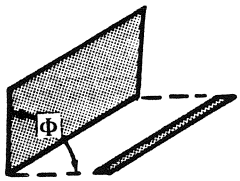	6 (for $\Phi = 90°$ only), 16 to 18
B-6	Plane element to plane rectangle; normal to element passes through corner of rectangle; surfaces are on parallel planes	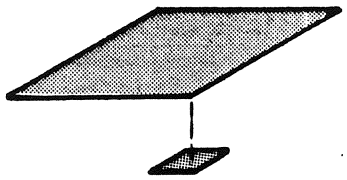	2, 6, 16 to 19, 21, 22
B-7	Area element to any parallel rectangle	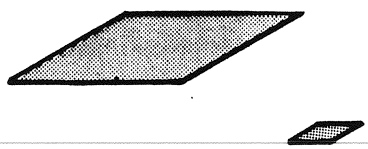	2

Table 14-15. Table of References for Configuration Factors (Continued)

Configuration Number	Geometry	Configuration	Reference at end of table
A. Factors for Two Differential Elements (Continued)			
A-9	Two ring elements on interior of right circular cylinder	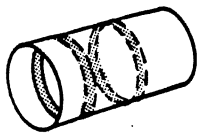	5, 6
A-10	Band of differential length on inside of cylinder to differential ring on cylinder base	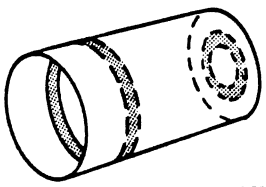	7
A-11	Ring element on fin to ring element on adjacent fin	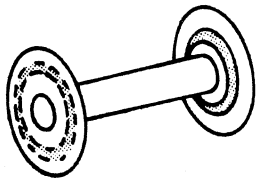	8
A-12	Two elements on interior of right circular cone	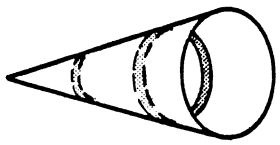	9, 10
A-13	Two differential elements on interior of spherical cavity	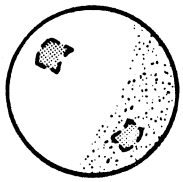	2, 6, 10 to 13
A-14	Band on outside of sphere to band on another sphere		13, 14 (equal radius)
A-15	Element on exterior of toroid to ring element on exterior of toroid	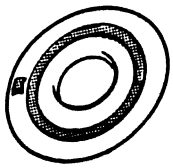	15
A-16	Element on exterior of toroid to hoop element on exterior of toroid	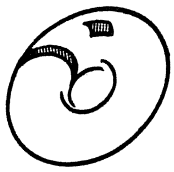	15

Table 14-15. Table of References for Configuration Factors (Continued)

Configuration Number	Geometry	Configuration	Reference at end of table
B. Factors for Exchange Between Differential Element and Finite Area (Continued)			
B-8	Plane element to plane rectangle; planes containing two surfaces intersect at angle Φ	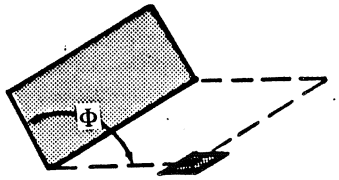	2, 6 (for $\Phi = 90°$ only) 16 to 18
B-9	Plane element to right triangle in plane parallel to plane of element; normal to element passes through vertex of triangle	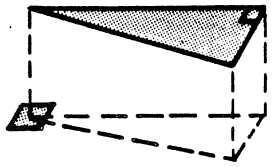	1
B-10	Plane element to plane area with added triangular area; element is on corner of rectangle with one side in common with plane area at angle Φ	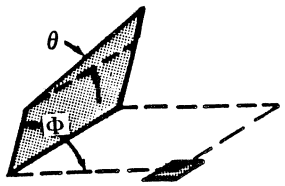	16 to 18
B-11	Same geometry as preceding with triangle reversed relative to plane element	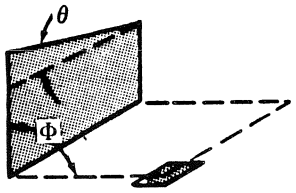	16 to 18
B-12	Plane element to circular disk on plane parallel to that of element	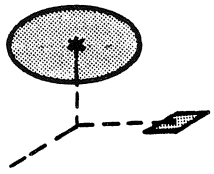	2, 6, 16 to 18
B-13	Plane element to segment of disk in plane parallel to element	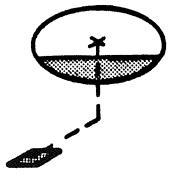	6
B-14	Plane element to circular disk; planes containing element and disk intersect at 90°, and centers of element and disk lie in plane perpendicular to those containing areas	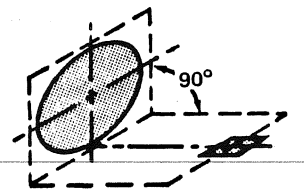	1, 6, 16 to 18, 20, 23

Table 14-15. Table of References for Configuration Factors (Continued)

Configuration Number	Geometry	Configuration	Reference at end of table
B. Factors for Exchange Between Differential Element and Finite Area (Continued)			
B-15	Strip element of finite length to perpendicular circular disk located at one end of strip	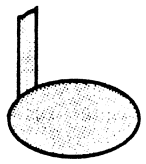	20, 23
B-16	Plane element to ring area in plane perpendicular to element	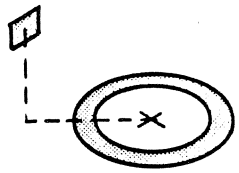	1
B-17	Radial and wedge elements on circle to disk in parallel plane	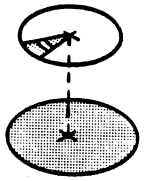	21, 23
B-18	Area element to parallel elliptical plate	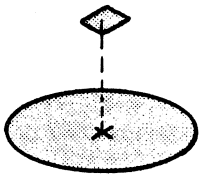	19
B-19	Infinite cylinder to parallel infinitely long strip	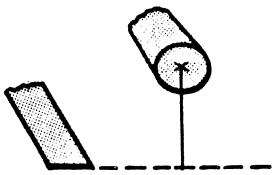	16 to 18
B-20	Plane of finite width and infinite length to infinitely long strip on the surface of a parallel cylinder	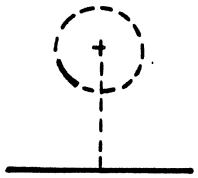	16 to 18
B-21	Plane element to right circular cylinder of finite length; normal to element passes through center of one end of cylinder and is perpendicular to cylinder axis	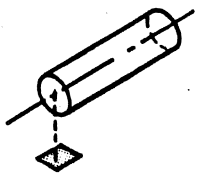	6, 16 to 18

Table 14-15. Table of References for Configuration Factors (Continued)

Configuration Number	Geometry	Configuration	Reference at end of table
B. Factors for Exchange Between Differential Element and Finite Area (Continued)			
B-22	Element is at end of wall on inside of finite length cylinder enclosing concentric cylinder of same length; factor is from element to inside surface of outer cylinder	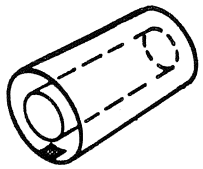	16 to 18 20, 22
B-23	Elemental strip of finite length to parallel cylinder of same length; normals at ends of strip pass through cylinder axis	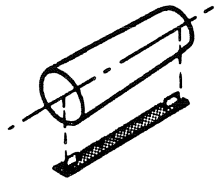	16 to 18, 20, 21
B-24	Strip or element on plane parallel to cylinder axis to cylinder of finite length	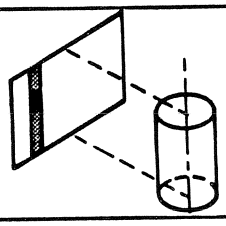	20, 23
B-25	Infinitely long strip of differential width to parallel semicylinder	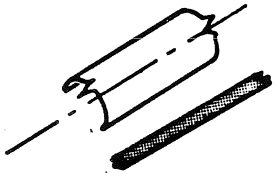	24
B-26	Infinite strip on any side of any of three fins to tube or environment, and infinite strip on tube to fin or environment	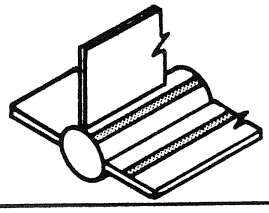	25
B-27	Element and strip element on interior of finite cylinder to interior of cylindrical surface	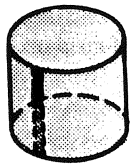	20, 23
B-28	Elemental strip on inner surface of outer concentric cylinder to surface of outer concentric cylinder	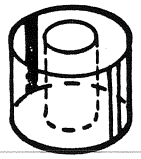	16 to 18, 20, 23

Table 14-15. Table of References for Configuration Factors (Continued)

Configuration Number	Geometry	Configuration	Reference at end of table
B. Factors for Exchange Between Differential Element and Finite Area (Continued)			
B-29	Elemental strip on inner surface of outer concentric cylinder to either annular end		16 to 18, 20, 23
B-30	Element on inside of outer finite concentric cylinder to inside cylinder or annular end	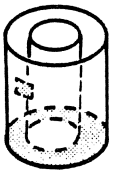	20, 23
B-31	Strip element on exterior of inner finite length concentric cylinder to inside of outer cylinder or to annular end	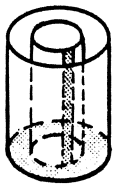	20, 23
B-32	Strip on plane inside cylinder of finite length to inside of cylinder	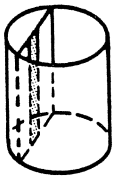	20, 23
B-33	Area element on interior of cylinder to base of second concentric cylinder; cylinders are one atop other	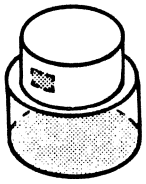	20, 23
B-34	Ring element on fin to tube	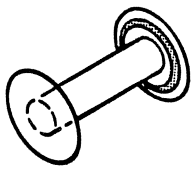	8
B-35	Ring element on interior of right circular cylinder to end or cylinder	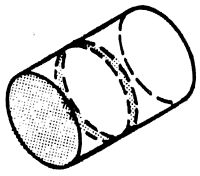	5

Table 14-15. Table of References for Configuration Factors (Continued)

Configuration Number	Geometry	Configuration	Reference at end of table
B. Factors for Exchange Between Differential Element and Finite Area (Continued)			
B-36	Exterior element of tube surface to finite area on adjacent parallel tube of same diameter	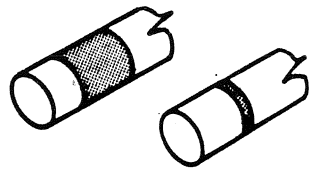	4
B-37	Exterior element on tube surface of partitioned tube to finite area on adjacent parallel tube of same diameter	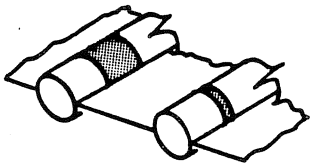	4
B-38	Element on wall of right circular cone to base of cone	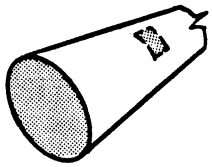	26
B-39	Any infinitesimal element on interior of sphere to any finite element on interior of same sphere	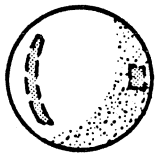	1, 2
B-40	Spherical point source to rectangle. Point source is on one corner of rectangle that intersects with receiving rectangle at angle Φ	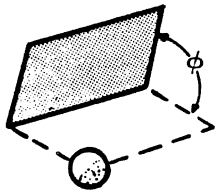	2, 16 to 18
B-41	Area element to sphere	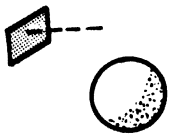	17, 27 to 29
B-42	Sphere to ring element oriented normal to sphere axis	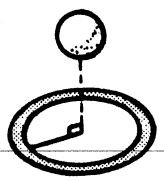	30

Table 14-15. Table of References for Configuration Factors (Continued)

Configuration Number	Geometry	Configuration	Reference at end of table
B. Factors for Exchange Between Differential Element and Finite Area (Continued)			
B-43	Elemental area on sphere to patch on second sphere	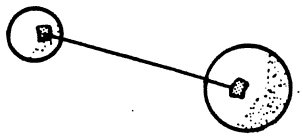	13
B-44	Area element to axisymmetric surface – parabolic, cone cylinder (formulation given – factors are not evaluated)	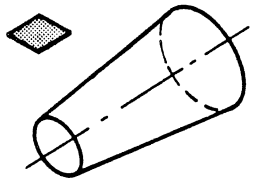	31
B-45	Element on interior (or exterior) of any axisymmetric body of revolution to band of finite length on interior (or exterior)	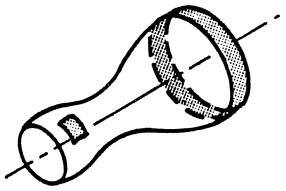	[a]32, [a]33
B-46	Ring element on exterior of toroid to entire exterior of toroid	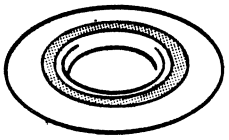	15
B-47	Slender torus to point on perpendicular axis	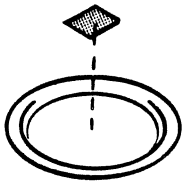	19

[a]*Kernel of intergrals and limits are formulated in terms of appropriate variables, but integrations are not carried out explicitly.*

Table 14-15. Table of References for Configuration Factors (Continued)

Configuration Number	Geometry	Configuration	Reference at end of table
	C. Factors for Two Finite Areas		
C-1	Two infinitely long plates of equal finite width W and one common edge of included angle Φ	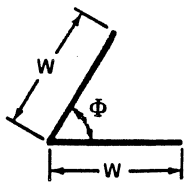	1
C-2	Two infinitely long plates of unequal width with one common edge and included angle $\Phi = 90^\circ$	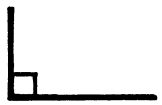	17
C-3	Finite rectangle to infinitely long rectangle of same width and with one common edge	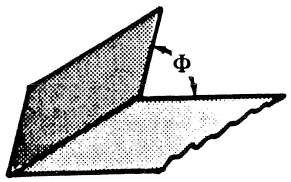	34
C-4	Two finite rectangles of same width and common edge and included angle Φ	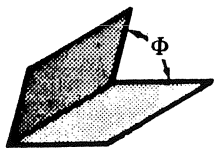	2, 21, 22 (for $\Phi = 90^\circ$ only), 7, 16 to 18, 20,[b]34
C-5	Two rectangles with common edge and included angle Φ	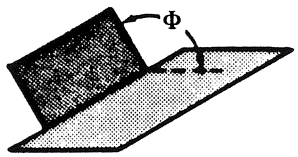	17
C-6	Two rectangles with one side of each parallel, and with one corner touching; planes containing rectangles intersect at angle Φ	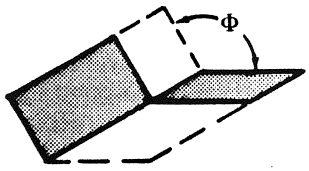	17
C-7	Two rectangles of same width with one parallel edge; planes containing rectangles intersect at angle Φ	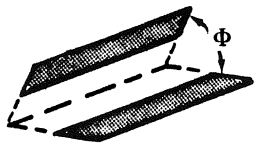	6 (for $\Phi = 90^\circ$ only), 7

[b] *Reference 34 indicates that tabulated values for this case are incorrect in all other references. Corrected values are listed in reference 34.*

Table 14-15. Table of References for Configuration Factors (Continued)

Configuration Number	Geometry	Configuration	Reference at end of table
C. Factors for Two Finite Areas (Continued)			
C-8	Two rectangles with one parallel edge; planes containing rectangles intersect at angle Φ	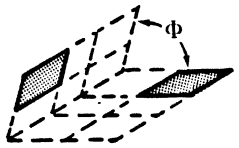	16, 17, 20
C-9	Two infinitely long directly opposed parallel strips of same finite width	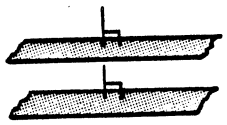	17, 21
C-10	Parallel, directly opposed rectangles of same width and length	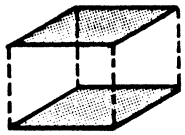	2, 6, 16 to 18, 21, 22, 35
C-11	Two rectangles in parallel planes with one rectangle directly opposite portion of other	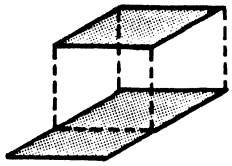	17, 19, 35
C-12	Two rectangles of arbitrary size in parallel planes; all sides lie parallel to x and y axes	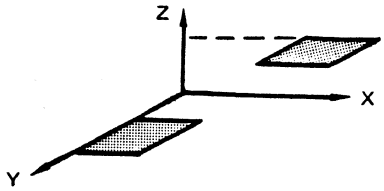	16, 17, 20, 35
C-13	Rectangle to arbitrarily oriented rectangle of arbitrary size	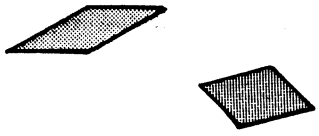	[c]36
C-14	Two flat plates of arbitrary shape and arbitrary orientation	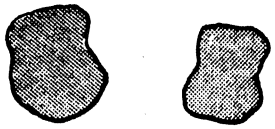	[a]37

[a] *Kernel of integrals and limits are formulated in terms of appropriate variables, but integrations are not carried out explicitly.*

[c] *Available as general computer program only.*

Table 14-15. Table of References for Configuration Factors (Continued)

Configuration Number	Geometry	Configuration	Reference at end of table
C. Factors for Two Finite Areas (Continued)			
C-15	Finite areas on interior of square channel	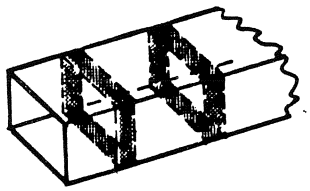	20
C-16	Factor between bases of right convex prism of regular triangular, square, pentagonal, hexagonal, or octagonal cross section	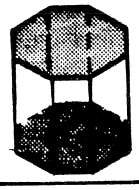	34
C-17	Factors between various sides, and sides and bases of regular hexagonal prism	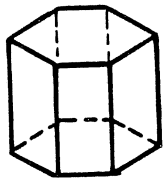	34
C-18	Circular disk to arbitrarily placed rectangle in parallel plane (using configuration factor algebra with configuration number C-21)	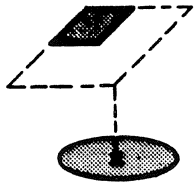	38
C-19	Circle to arbitrarily placed rectangle in plane parallel to normal to circle (using configuration factor algebra with configuration number C-21)	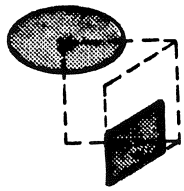	38
C-20	Disk to arbitrarily oriented rectangle or disk of arbitrary size	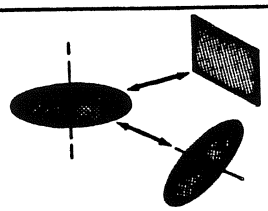	[c]36
C-21	Circular disk to parallel right triangle; normal from center of circle passes through one acute vertex	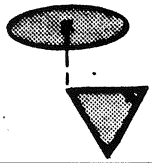	38

[c] *Available as general computer program only.*

Table 14-15. Table of References for Configuration Factors (Continued)

Configuration Number	Geometry	Configuration	Reference at end of table
C. Factors for Two Finite Areas (Continued)			
C-22	Parallel, directly opposed plane circular disks	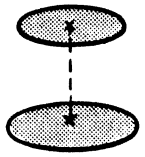	2, 6, 10, 16 to 18, 20, 21, 23
C-23	Directly opposed ring and disk of arbitrary radii	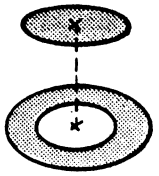	17, 23
C-24	Parallel, directly opposed plane ring areas	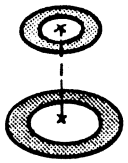	1, 16, 23
C-25	Entire inner wall of finite cylinder to ends	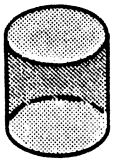	39, 40
C-26	Internal surface of cylindrical cavity to cavity opening	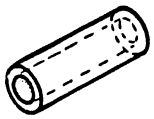	17 (Figures 6 to 14), 41
C-27	Inner surface of cylinder to annulus on one end	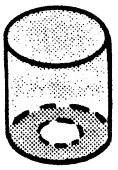	23, 40
C-28	Inner surface of cylinder to disk at one end of cylinder		23, 40

Table 14-15. Table of References for Configuration Factors (Continued)

Configuration Number	Geometry	Configuration	Reference at end of table
C. Factors for Two Finite Areas (Continued)			
C-29	Portion of inner surface of cylinder to remainder of inner surface	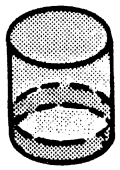	21, 23, 40
C-30	Finite ring areas on interior of right circular cylinders to separate similar areas and to ends	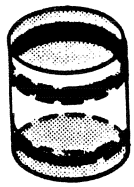	20, 21, 40
C-31	Finite areas on interior of right circular cylinder		20
C-32	Infinite cylinder to parallel infinitely long plane of finite width	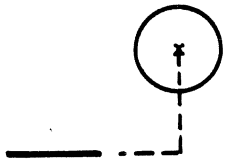	[d]6, [d]16, [d]17, 30
C-33	Infinitely long plane of finite width to infinitely long cylinder	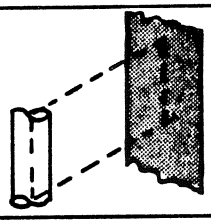	23
C-34	Infinite plane to first, second, and first plus second rows of infinitely long parallel tubes of equal diameter	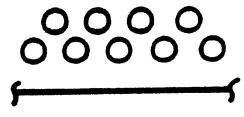	2, 21, 22
C-35	Finite length cylinder to rectangle with one edge parallel to cylinder axis and of length equal to cylinder	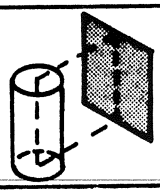	6

[d] *This factor is given incorrectly in all references except reference 30.*

Table 14-15. Table of References for Configuration Factors (Continued)

Configuration Number	Geometry	Configuration	Reference at end of table
C. Factors for Two Finite Areas (Continued)			
C-36	Finite cylinder to finite rectangle of same length	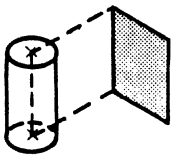	42
C-37	Cylinder to any rectangle in plane perpendicular to cylinder axis (using configuration factor algebra with configuration number C-42)	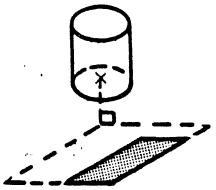	38
C-38	Cylinder to any rectangle in plane parallel to cylinder axis (using configuration factor algebra with configuration number C-42)	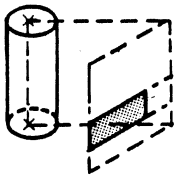	38
C-39	Finite area on exterior of cylinder to finite area on plane parallel to cylinder axis	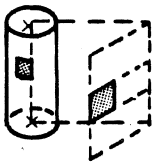	20
C-40	Finite area on exterior of cylinder to finite area on skewed plane	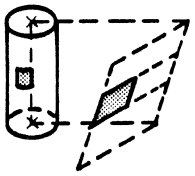	20
C-41	Outside surface of cylinder to perpendicular right triangle; triangle is in plane of cylinder base with one vertex of triangle at center of base	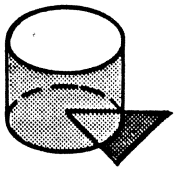	38
C-42	Cylinder and plane of equal length parallel to cylinder axis; plane inside cylinder; all factors between plane and inner surface of cylinder	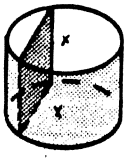	20, 23

Table 14-15. Table of References for Configuration Factors (Continued)

Configuration Number	Geometry	Configuration	Reference at end of table
C. Factors for Two Finite Areas (Continued)			
C-43	Inner surface of cylinder to disk of same radius	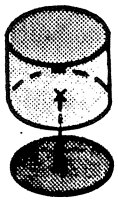	20, 23
C-44	Interior surface of circular cylinder of radius R to disk of radius r where r<R; disk is perpendicular to axis of cylinder, and axis passes through center of disk (using configuration factor algebra with configuration number C-22)	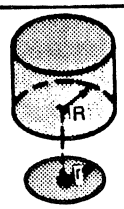	1
C-45	Annular ring to similar annular ring each at end of cylinder	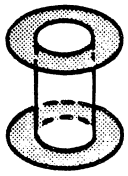	8, 20, 23
C-46	Factors for interchange between fins and tube (given in algebraic form, untabulated)	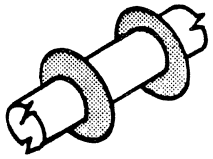	8
C-47	Finite area on exterior of cylinder to finite area on exterior of parallel cylinder		20
C-48	Cylinder or arbitrary length and radius to rectangle, disk, or cylinder of arbitrary size and orientation	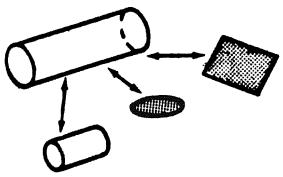	[c]36
C-49	Cylinder and plate with arbitrary orientation	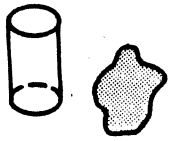	[a]37

[a] *Kernel of integrals and limits are formulated in terms of appropriate variables, but integrations are not carried out explicitly.*

[c] *Available as general computer program only.*

Table 14-15. Table of References for Configuration Factors (Continued)

Configuration Number	Geometry	Configuration	Reference at end of table
C. Factors for Two Finite Areas (Continued)			
C-50	Concentric cylinders of infinite length; inner to outer cylinder; outer to inner cylinder; outer cylinder to itself	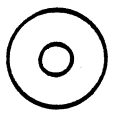	16
C-51	Inside surface of outer concentric cylinder of finite length to inner cylinder of the same length	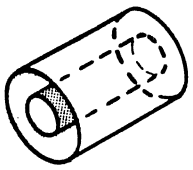	6, 16, 21, 23, 43
C-52	Inside surface of outer concentric cylinder to itself	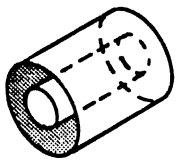	6, 8, 16, 23, 43
C-53	Inside surface of outer concentric cylinder to either end of annulus	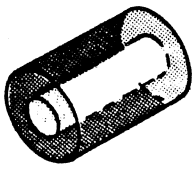	6, 16, 23 43
C-54	Concentric cylinders of different finite lengths – portion of inner cylinder to entire outer cylinder	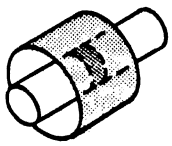	23
C-55	Concentric cylinders of different finite lengths – portion of inside of outer to outside of entire inner cylinder	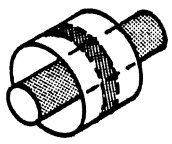	20, 23, [a]37
C-56	Parallel cylinders of different radii and length – any portions of outer curved surfaces	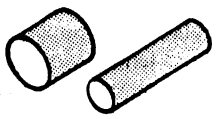	[a]37

[a]*Kernel of integrals and limits are formulated in terms of appropriate variables, but integrations are not carried out explicitly.*

Table 14-15. Table of References for Configuration Factors (Continued)

Configuration Number	Geometry	Configuration	Reference at end of table
C. Factors for Two Finite Areas (Continued)			
C-57	Concentric cylinders of different radii, one atop other; factors between inside of upper cylinder and inside or base of lower cylinder	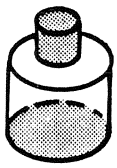	20, 23
C-58	Infinitely long parallel semicylinders of same diameter	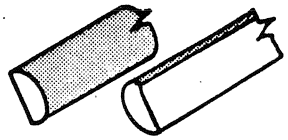	1, 6
C-59	Finite area on exterior of inner cylinder to finite area on interior of concentric outer cylinder		20
C-60	Two tubes connected with fin of finite thickness; length can be finite or infinite; all factors between finite surfaces formulated in terms of integrations between differential strips	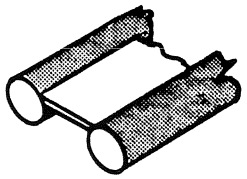	3
C-61	Two tubes connected with tapered fins of finite thickness; length can be finite or infinite; all factors between finite surfaces formulated in terms of integrations between differential strips	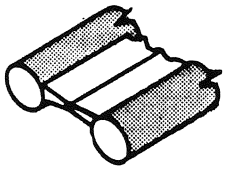	3
C-62	Sandwich tube and fin structure of infinite or finite length; all factors between finite surfaces formulated in terms of integrations between differential strips	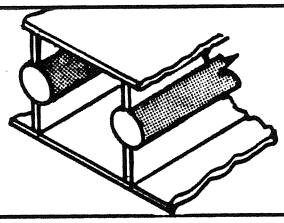	3
C-63	Concentric cylinders connected by fin of finite thickness; length finite or infinite; all factors between finite surfaces formulated in terms of integrations between differential strips	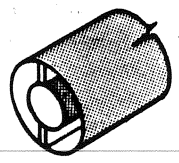	3

Table 14-15. Table of References for Configuration Factors (Continued)

Configuration Number	Geometry	Configuration	Reference at end of table
C. Factors for Two Finite Areas (Continued)			
C-64	Exterior of infinitely long cylinder to interior of concentric semicylinder		1
C-65	Interior of infinitely long semicylinder 1 to interior of semicylinder 2 when concentric parallel cylinder 3 is present	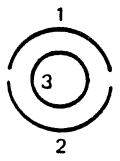	1
C-66	Between axisymmetrical sections of right circular cone		20, 40
C-67	Between axisymmetrical sections of right circular cone and base or ring or disk on base	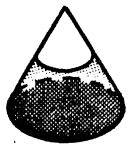	21, 40
C-68	Internal surface of conical cavity to cavity opening	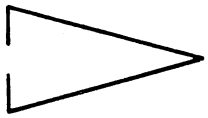	17 (Figures 6 to 14), 40, 41
C-69	Entire inner surface of frustum on cone to ends	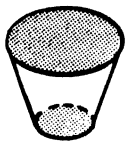	39, 40
C-70	Right circular cone of arbitrary size to rectangle, disk, cylinder, or cone of arbitrary size and orientation	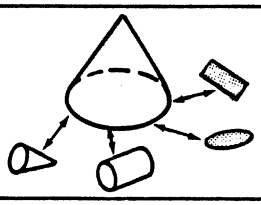	[c]36

[c] *Available as general computer program only.*

Table 14-15. Table of References for Configuration Factors (Continued)

Configuration Number	Geometry	Configuration	Reference at end of table
C. Factors for Two Finite Areas (Continued)			
C-71	Cone to arbitrarily skewed plate	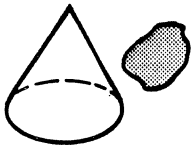	[a]37
C-72	Internal surface of spherical cavity to cavity opening		17 (Figures 6 to 14), 41
C-73	Any finite area on interior of sphere to any other finite area on interior		1, 2
C-74	Sphere to coaxial disk	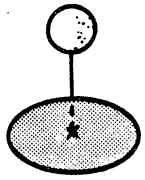	30
C-75	Sphere to segment of coaxial disk	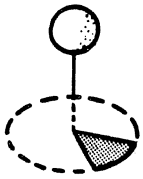	30
C-76	Sphere to sector of coaxial disk	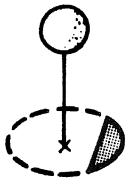	30
C-77	Finite sphere to rectangle		38

[a]*Kernel of integrals and limits are formulated in terms of appropriate variables, but integrations are not carried out explicitly.*

Table 14-15. Table of References for Configuration Factors (Continued)

Configuration Number	Geometry	Configuration	Reference at end of table
C. Factors for Two Finite Areas (Continued)			
C-78	Sphere to rectangle normal to sphere axis	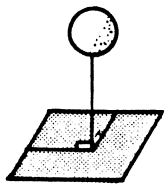	30
C-79	Sphere to arbitrary rectangle (using configuration factor algebra and configuration number C-75)	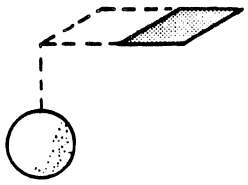	[c]36, 38
C-80	Sphere to regular polygon normal to sphere axis	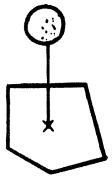	30
C-81	Sphere to disk not on axis	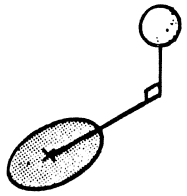	30
C-82	Sphere of arbitrary diameter to disk or cone of arbitrary size and orientation	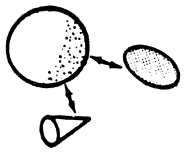	[c]36
C-83	Sphere to arbitrarily skewed plate	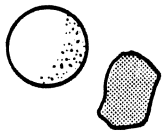	[a]37
C-84	Sphere to cylinder	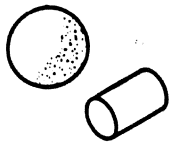	[c]36, 44

[a] *Kernel of integrals and limits are formulated in terms of appropriate variables, but integrations are not carried out explicitly.*
[c] *Available as general computer program only.*

Table 14-15. Table of References for Configuration Factors (Continued)

Configuration Number	Geometry	Configuration	Reference at end of table
C. Factors for Two Finite Areas (Continued)			
C-85	Cone to sphere having same diameter as base of cone; axis of cone passes through center of sphere	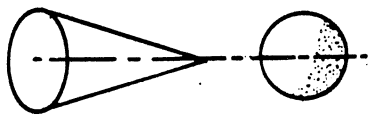	14, [c]36
C-86	Concentric spheres; inner to outer sphere; outer to inner sphere; outer sphere to itself		1, 16, 17
C-87	Area on surface of sphere to rectangle in plane perpendicular to axis of sphere	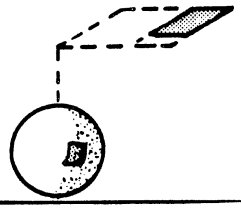	20
C-88	Sphere to sphere		14 (equal spheres), [c]36, 44, 45
C-89	Patch on sphere to cap on another sphere	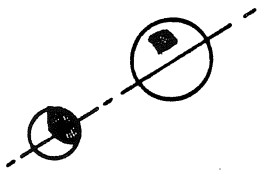	13
C-90	Cap on sphere to cap on another sphere	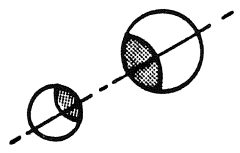	13
C-91	Patch on sphere to patch on another sphere	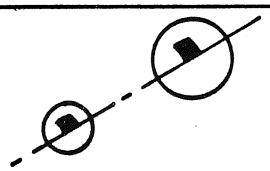	13

[c]*Available as general computer program only.*

Table 14-15. Table of References for Configuration Factors (Continued)

Configuration Number	Geometry	Configuration	Reference at end of table
C. Factors for Two Finite Areas (Continued)			
C-92	Cap on sphere to band on another sphere	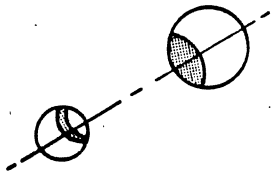	13
C-93	Band on one sphere to band on another sphere	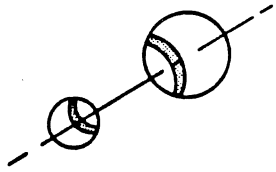	13
C-94	Internal surface of hemispherical cavity to cavity opening	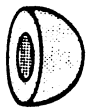	17 (Figures 6 to 14), 40, 41
C-95	Between axisymmetrical section of hemisphere and base or ring or disk on base	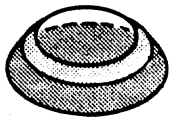	40
C-96	Between axisymmetrical sections of hemisphere	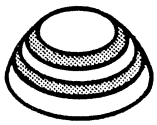	20, 40
C-97	Hemisphere to coaxial hemisphere in contact	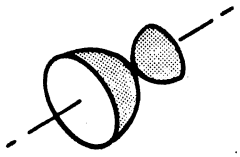	46
C-98	Sphere to hemisphere	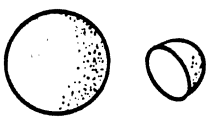	44

Table 14-15. Table of References for Configuration Factors (Continued)

Configuration Number	Geometry	Configuration	Reference at end of table
C. Factors for Two Finite Areas (Continued)			
C-99	Sphere to ellipsoid		[c]36, 44
C-100	Ellipsoid of arbitrary major and minor axes to rectangle, disk, cylinder, cone, or ellipsoid of arbitrary size and orientation	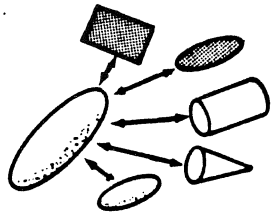	[c]36
C-101	From Moebius strip to itself	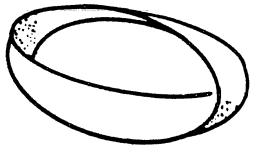	47
C-102	Exterior of toroid to itself	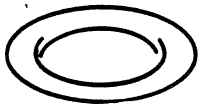	15, 48
C-103	Toroid of arbitrary size to rectangle, disk, cylinder, sphere, cone, ellipsoid, or toroid of arbitrary size and orientation	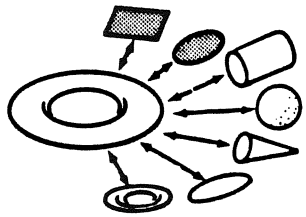	[c]36
C-104	Arbitrary polynomial of revolution to rectangle, disk, cylinder, sphere, cone, ellipsoid, toroid, or other arbitrary polynomial of revolution of arbitrary size and orientation (polynomials of fifth order or less)	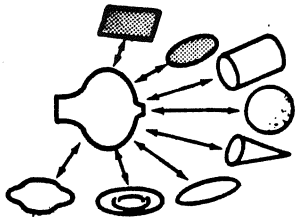	[c]36

[c]*Available as general computer program only.*

Table 14-15. Table of References for Configuration Factors (Continued)

References

1. Howell, John R. and Siegel, R.: *Thermal Radiation Heat Transfer, Vol. II: Enclosure Theory.* NASA SP-164, 1969.
2. Jakob, Max: *Heat Transfer.* Vol. 2. John Wiley & Sons, Inc., 1957.
3. Sotos, Carol J.; and Stockman, Norbert O.: *Radiant-Interchange View Factors and Limits of Visibility for Differential Cylindrical Surfaces with Parallel Generating Lines.* NASA TN D-2556, 1964.
4. Sparrow, E. M.; and Jonsson, V. K.: "Angle Factors for Radiant Interchange between Parallel-Oriented Tubes." *J. Heat Transfer,* Vol. 85, No. 4, Nov. 1963, pp. 382-384.
5. Usiskin, C. M.; and Siegel, R.: "Thermal Radiation from a Cylindrical Enclosure with Specified Wall Heat Flux." *J. Heat Transfer,* Vol. 82, No. 4, Nov. 1960, pp. 369-374.
6. Sparrow, E. M.; and Cess, R. C.: *Radiation Heat Transfer,* Brooks/Cole Publ. Co., 1966.
7. Sparrow, E. M.; Albers, L. U.; and Eckert, E. R. G.: "Thermal Radiation Characteristics of Cylindrical Enclosures." *Heat Transfer,* Vol. 84, No. 1, Feb. 1962, pp. 73-81.
8. Sparrow, E. M.; Miller, G. B.; and Jonsson, V. D.: "Radiative Effectiveness of Annular-Finned Space Radiators, Including Mutual Irradiation Between Radiator Elements," *J. Aerospace Sci.,* Vol. 29, No. 11, Nov. 1962, pp. 1291-1299.
9. Sparrow, E. M.; and Jonsson, V. K.: "Radiant Emission Characteristics of Diffuse Conical Cavities." *J. Opt. Soc. Am.,* Vol. 53, No. 7, July 1963, pp. 816-821.
10. Kezios, Stotle P.; and Wulff, Wofgang: "Radiative Heat Transfer Through Openings of Variable Cross Sections." *Proceedings of the Third International Heat Transfer Conference.* Vol. 5. AIChE, 1966, pp. 207-218.
11. Sparrow, E. M.; and Jonsson, V. K.: *Absorption and Emission Characteristics of Diffuse Spherical Enclosures.* NASA TN D-1289, 1962.
12. Nichols, Lester D.: *Surface-Temperature Distribution on Thin-Walled Bodies Subjected to Solar Radiation in Interplanetary Space.* NASA TN D-584, 1961.
13. Grier, Norman T.: *Tabulations of Configuration Factors Between any Two Spheres and Their Parts.* NASA SP-3050, 1969.
14. Campbell, James P.; and McConnell, Dudley G.: *Radiant-Interchange Configuration Factors for Spherical and Conical Surfaces to Spheres.* NASA TN D-4457. 1968.
15. Grier, Norman T.; and Sommers, Robert: *View Factors for Toroids and Their Parts.* NASA TN D-5006, 1969.
16. Hamilton, D. C.; and Morgan, W. R.: *Radiant-Interchange Configuration Factors.* NASA TN 2836, 1952.
17. Kreith, Frank: *Radiation Heat Transfer.* International Textbook Co., 1952.
18. Wiebelt, John A.: *Engineering Radiation Heat Transfer.* Holt, Rinehart and Winston, 1966.
19. Moon, Parry: *The Scientific Basis of Illuminating Engineering.* Dover Publications, Inc., 1961.
20. Stevenson, J. A.; and Grafton, J. C.: *Radiation Heat Transfer Analysis for Space Vehicles.* Rep. SID-61-91, North American Aviation (AFASD TR 61-119, pt. 1), Sept. 9, 1961.
21. Hottel, H. C.; and Sarofim, A. F.: *Radiation Transfer.* McGraw Hill Book Co., Inc., 1967.
22. Hottel, H. C.: *Radiant-Heat Transmission, Heat Transmission.* Third ed., William H. McAdams, ed., McGraw-Hill Book Co., Inc., 1954, pp. 55-125.
23. Leuenberger, H.; and Person, R. A.: *Compilation of Radiation Shape Factors for Cylindrical Assemblies.* Paper No. 56-A-144, ASME, Nov. 1956.
24. Sparrow, E. M.; and Eckert, E. R. G.: "Radiant Interaction between Fin and Base Surfaces." *J. Heat Transfer,* Vol. 84, No. 1, Feb. 1962, pp. 12-18.
25. Holcomb, R. S.; and Lynch, F. E.: *Thermal Radiation Performance of a Finned Tube with a Reflector.* Rep. No. ORNL-TM-1613, Oak Ridge National Lab., Apr. 1967.
26. Joerg, Pierre; and McFarland, B. L.: *Radiation Effects in Rocket Nozzles.* Rep. No. S62-245, Aerojet-General Corp. 1962.

Table 14-15. Table of References for Configuration Factors (Continued)

References

27. Cunningham, F. G.: *Power Input to a Small Flat Plate from a Diffusely Radiating Sphere, with Application to Earth Satellites.* NASA TN D-710, 1961.

28. Liebert, Curt H.; and Hibbard, Robert R.: *Theoretical Temperatures of Thin-Film Solar Cells in Earth Orbit.* NASA TN D-4331, 1968.

29. Goetze, Dieter; and Grosch, Charles B.: "Earth-Emitted Infrared Radiation Incident Upon a Satellite." *J. Aerospace Sci.,* Vol. 29, No. 5, May 1962, pp. 521-524.

30. Feingold, A.; and Gupta, K. G.: *New Analytical Approach to the Evaluation of Configuration Factors in Radiation from Spheres in Infinitely Long Cylinders.* Paper No. 69-HT-J, ASME, Nov. 1968.

31. Morizumi, S. J.: "Analytical Determination of Shape Factors from a Surface Element to an Axisymmetric Surface." *AIAA J.,* Vol. 2, No. 11, Nov. 1964, pp 2028-2030.

32. Robbins, William H.; and Todd, Carroll A.: *Analysis, Feasibility, and Wall-Temperature Distribution of A Radiation-Cooled Nuclear-Rocket Nozzle.* NASA TN D-878, 1962.

33. Robbins, William H.: *An Analysis of Thermal Radiation Heat Transfer in a Nuclear-Rocket Nozzle.* NASA TN D-586, 1961.

34. Feingold, A.: "Radiant-Interchange Configuration Factors Between Various Selected Plane Surfaces." *Pro. Roy. Soc.* Series A, Vol 292 No. 1428, May 3, 1966, pp 51-60.

35. Hsu, Chia-Jung: "Shape Factor Equations for Radiant Heat Transfer Between Two Arbitrary Sizes of Rectangular Planes. *Can. J. Chem. Eng.,* Vol. 45, No. 1, Feb 1967, pp. 58-60.

36. Dummer, R. S.; and Breckenridge, W. T., Jr.: *Radiation Configuration Factors Program.* Rpt. ERR-AN-224, (Available at MDAC-West as computer program MVO3.) General Dynamics/ Astronautics, Feb. 1963.

37. Plamondon, Joseph A.: *Numerical Determination of Radiation Configuration Factors for Some Common Geometrical Situations.* Tech. Rpt. 32-127, Jet Propulsion Lab., California Inst. Tech., July 7, 1961.

38. Tripp, W.; Hwang, C.; and Crank, R. E.: *Radiation Shape Factors for Plane Surfaces and Spheres, Circles or Cylinders.* Special Rpt. No. 16, Kansas State Univ. Bull., Vol. 46, No. 4, Apr. 1962.

39. Bien, Darl D.: "Configuration Factors for Thermal Radiation from Isothermal Inner Walls of Cones and Cylinders." *J. Spacecraft Rockets,* Vol. 3, No. 1, Jan. 1966, pp. 155-156.

40. Buschman, Albert J., Jr.; and Pittman, Claud M.: *Configuration Factors for Exchange of Radiant Energy Between Axisymmetrical Sections of Cylinders, Cones, and Hemispheres and Their Bases.* NASA TN D-944, 1961.

41. Stephens, Charles W.; and Haire, Alan M.: "Internal Design Considerations for Cavity-Type Solar Absorbers." *ARS J.,* Vol. 31, No. 7, July 1961, pp. 896-901.

42. Wiebelt, J. A.; and Ruo, S. Y.: "Radiant-Interchange Configuration Factors for Finite Right Circular Cylinder to Rectangular Planes." *Int. J. Heat Mass Transfer,* Vol. 6, No. 2, Feb. 1963, pp. 143-146.

43. Aleksandrov, V. T.: "Determination of the Angular Radiation Coefficients for a System of Two Coaxial Cylindrical Bodies." *Ina.-Fiz. Zh.,* Vol. 8, No. 4, May 1965, pp. 609-612.

44. Watts, R. G.: "Radiant Heat Transfer to Earth Satellites," *J. Heat Transfer,* Vol. 87, No. 3, Aug. 1965, pp. 369-373.

45. Jones, L. R.: "Diffuse Radiation View Factors between Two Spheres." *J. Heat Transfer,* Vol. 87, No. 3, Aug. 1965, pp. 421-422.

46. Wakao, Noriaki; Kato, Koichi; Furuya Nobus: "View Factor Between Two Hemispheres in Contact and Radiation Heat-Transfer Coefficient in Packed Beds." *Int. Jour. Ht. and Mass Trans.,* Vol. 12, No. 1, Jan. 1969, pp. 118-120.

47. Stasenko, A. L.: "Self-Irradiation Coefficient of a Moebius Strip of Given Shape." *Akad. Nauk SSSR, Izv. Energetika i Transport,* July-Aug. 1967, pp. 104-107.

48. Sommers, Ralph D.; and Grier, Norman T.: "Radiation View Factors for a Toroid: Comparison of Echert's Technique and Direct Computation." *ASME Jour. of Heat Trans.,* Aug., 1969.

14-4 CONVECTION

Convective heat transfer between a solid boundary and a fluid is a combination of conduction and mass transport. When the wall is hotter than the fluid, heat is conducted to the fluid near the wall, and the heated fluid particles are carried away by the fluid motion. When removed from the wall, the particles reject heat to the bulk of the fluid. The heat flow may be directed toward the wall, i.e., the particles carry heat from the fluid bulk to the cooler wall. Regardless of the direction of the heat flow, the mechanism is the same and thus, the equations presented in this subsection apply to both cases.

The convective-heat-transfer coefficient h_c relates the heat transfer rate per unit surface area to a convenient reference temperature difference.

$$(q_c/A)_{\text{surface to fluid}} = h_c (T_W - T_\infty) \qquad (126)$$

where:

q_c = Convective heat transfer rate, Btu/hr

A = Surface area, ft^2

h_c = Convective-heat-transfer coefficient, $Btu/ft^2\text{-}hr\text{-}^\circ R$

T_W = Wall temperature, $^\circ R$

T_∞ = Temperature of surrounding fluid far removed from the wall, $^\circ R$

The magnitude of h_c is a function of the fluid flow, thermal properties of the fluid, and the geometry of the system. Once h_c is known, the heat transfer rate may be easily obtained from equation 126.

14-4.1 Fluid Flow

Fluid motion can be induced by two processes. When density differences due to temperature variation set the fluid in motion, the mechanism is called free, or natural convection. Forced convection refers to fluid motion caused by an external agency, such as a pump or a blower.

Fluid flow may be either laminar or turbulent in free or forced convection. In laminar flow, fluid particles follow a smooth continuous path, and heat is transferred only by molecular conduction from the wall through the layers of fluid. Fluid particles in turbulent flow follow an irregular, unpredictable path and, in addition to conduction, energy is transferred due to eddies and mixing currents, which transport fluid particles (energy carriers) across the streamlines. Thus, turbulent flow provides a more effective heat transfer mechanism than does laminar flow.

14-4.2 Dimensionless Parameters for Convective Heat Transfer

Convective heat transfer is closely tied to fluid motion. The characteristics of the flow field must be known before the heat transfer rate can be obtained from an energy balance. Exact analytical solutions are available for most laminar convection problems because the flow field is simple and easily determined. However, the majority of practical applications involve turbulent flow, for which exact solutions are not available because turbulent fluid motion is complex and erratic and cannot be described by a simple mathematical expression. Consequently, solutions for turbulent convection problems are based on analogy and experimental data. Most of the practical heat transfer information is in the form of empirical equations.

Since experimental data is heavily relied upon in solving convection problems, dimensionless groups of key parameters, which greatly simplify the management of experimental data, are widely used. Convective heat transfer information is generally expressed in terms of four dimensionless parameters — the Nusselt, Reynolds, Grashof, and Prandtl numbers.

The Nusselt number Nu is essentially the dimensionless form of h_c, the convective-heat-transfer coefficient:

$$Nu = h_c L^*/k \qquad (127)$$

where:

L^* = Characteristic dimension of the geometry, i.e., length of plate, diameter of tube, etc., ft.

k = Thermal conductivity of the fluid, $Btu/hr\text{-}ft\text{-}^\circ R$

The Reynolds number Re characterizes the dynamics of the fluid flow, and is defined by:

$$Re = \rho v L^*/\mu \quad (128)$$

where:

ρ = Fluid density, lb/ft^3

v = Fluid velocity, ft/sec

L^* = Characteristic dimension, ft

μ = Fluid viscosity, lb/ft-sec

The Reynolds number is the ratio of inertia forces to viscous forces in the fluid and it describes the flow field in forced convection.

The Grashof number Gr is analogous to the Reynolds number in that it characterizes the flow field in free convection. The definition of Gr is:

$$Gr = \rho^2 \beta g \Delta T L^{*3}/\mu^2 \quad (129)$$

where:

ρ = Fluid density, lb/ft^3

β = Coefficient of thermal expansion (= $1/T_\infty$ for ideal gases), $1/^\circ R$

g = Acceleration of gravity, ft/sec^2

ΔT = Absolute value of difference between the wall and fluid (far removed from wall) temperatures = $|T_w - T_\infty|, ^\circ R$

L^* = Characteristic dimension, ft.

μ = Fluid viscosity, lb/ft-sec

Physically, Gr is the ratio of bouyant forces to viscous forces and it indicates the strength of the velocity field generated by the density differences in free convection.

The Prandtl number Pr is the connecting link between the velocity field and the temperature field in the fluid. The Prandtl number is a function of fluid properties alone:

$$Pr = \mu C_p/k = \upsilon/a \quad (130)$$

where:

μ = Viscosity, lb/ft-hr

C_p = Constant pressure specific heat, Btu/lb-$^\circ R$

k = Thermal conductivity of the fluid Btu/hr-ft-$^\circ R$

ρ = Fluid density, lb/ft^3

$\upsilon = \mu/\rho$ = Kinematic viscosity, ft^2/hr

$a = k/\rho C_p$ = Thermal diffusivity, ft^2/hr

The kinematic viscosity is a measure of the rate at which momentum may diffuse through the fluid because of molecular motion. The thermal diffusivity, the ratio of heat transmission and energy storage capacity, measures the diffusion rate of heat in the fluid. The ratio of these quantities ($Pr = \upsilon/a$) relates the diffusion of momentum and heat in the fluid and thus, links the temperature gradient to the velocity profile. Consequently, for a given flow field the heat transfer rate, which is proportional to the temperature gradient in the fluid, is dependent on the Prandtl number. The heat-transfer coefficient h_c increases with Pr.

The heat transfer rate, characterized by the dimensionless heat transfer coefficient (Nu), is a function of the fluid flow dynamics (Re or Gr) and the relation between the flow dynamics and the temperature gradient in the fluid (Pr):

$$Nu = f(Re, Pr) \text{ Forced convection} \quad (131)$$

or

$$Nu = f(Gr, Pr) \text{ Free convection} \quad (132)$$

This is the form most often used to present convective heat transfer relationships. Once the Nusselt number is known, the heat transfer rate q_c may be quickly determined from equations 126 and 127.

14-4.3 Basic Equations

Many solutions exist for laminar convection problems. Three basic equations must be solved in order to obtain the convective-heat-transfer coefficient. The following equations apply to incompressible, steady, two-dimensional flow:

Continuity:

$$\partial u/\partial x + \partial v/\partial y = 0 \quad (133)$$

Momentum:

$$u\frac{\partial u}{\partial x} + v\frac{\partial u}{\partial y} = \beta g (T - T_\infty) + \upsilon\frac{\partial^2 u}{\partial y^2} \quad (134)$$

Energy:

$$u\frac{\partial T}{\partial x} + v\frac{\partial T}{\partial y} = a\frac{\partial^2 T}{\partial y^2} \quad (135)$$

where:

x = Distance along surface

y = Distance from surface (normal direction)

u = Velocity component in x-direction

v = Velocity component in y-direction

β = Coefficient of thermal expansion

g = Acceleration of gravity

T = Fluid temperature

υ = Kinematic viscosity

a = Thermal diffusivity

In solving pipe flow problems, the energy equation in cylindrical coordinates is required:

$$u\frac{\partial T}{\partial x} = \left(\frac{\partial^2 T}{\partial r^2} + \frac{1}{r}\frac{\partial T}{\partial r}\right) \qquad (136)$$

where:

r = Pipe radius

14-4.4 Convective-Heat-Transfer Coefficients

Convective heat transfer equations for a variety of situations are presented in Table 14-16 in terms of the convective-heat-transfer coefficients. Table 14-16 is a compact compilation of heat-transfer coefficients for quick reference, which emphasizes the similarities and the differences in the form of h_c for specific applications. Most of the equations are discussed in greater detail in the text. All parameters used in Table 14-16 are defined in the nomenclature list in paragraph 14-9. The dimensionless groups are defined in Table 2.

Convective heat transfer equations are presented for a number of geometric shapes of practical interest. Each shape is identified by a characteristic dimension, such as its length L, diameter D, etc. The characteristic dimension is attached as a subscript to the dimensionless numbers Nu, Re and Gr.

The local value of the convective-heat-transfer coefficient h_{c_x} indicates the heat transfer characteristics at a given location x on a solid body exposed to a fluid. The heat transfer for the entire body is represented by the average convective-heat-transfer coefficient $\overline{h}_c$, which is obtained by integrating the local value:

$$\overline{h}_c = \frac{1}{L}\int_0^L h_{c_x}\,dx \qquad (137)$$

Similarly, Nu_x and Nu_L represent the local and average values of the Nusselt number, respectively.

The right hand column in Table 14-16 indicates the reference temperature at which the fluid properties are evaluated. In submerged flow, the free stream fluid temperature is constant with respect to the heat transfer surface, and the properties are usually evaluated at the film temperature T_f.

$$T_f = (T_w + T_\infty)/2 \qquad (138)$$

where:

T_w = Temperature of the solid boundary (wall)

T_∞ = Temperature of fluid far removed from the surface (free stream)

In channel (pipe) flow, the fluid temperature changes along the heat transfer surface. The bulk temperature T_b at any station along a pipe is often called the cup mixing temperature because it is the temperature which the fluid passing a cross-sectional area of the pipe during a given time interval would assume if the fluid were collected and mixed in a cup. In channel flow, the reference temperature is usually the mean bulk temperature $\overline{T}_b$.

$$\overline{T}_b = (T_1 + T_2)/2 \qquad (139)$$

where:

T_1 = Fluid bulk temperature at the channel inlet

T_2 = Fluid bulk temperature at the channel exit

Since most of the equations appearing in Table 14-16 are empirical, precise results should not be expected. The accuracy with which the convective-heat-transfer coefficients can be predicted is generally no better than 20 percent.

14-4.5 Forced Convection Over Flat Plates

14-4.5.1 Laminar Flow

In a laminar flow field, the fluid particles move in parallel layers, or laminae, sliding past adjacent laminae but not mixing with them. Prandtl's boundary layer concept divides the flow field around a body into two domains: a thin layer covering the surface of the body where the velocity gradient is great and the viscous forces are large, and a region outside this layer where the velocity is nearly equal to the free-stream value and the effects of viscosity are negligible (potential flow).

Table 14-16. Convective Heat Transfer Coefficients

	Geometry and Convection Mode	Flow Type	Valid Range	Equations	Reference Temperature
Flat Plates	Forced 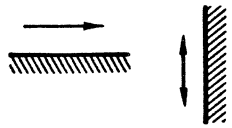	Laminar	$R_e < 500{,}000$	$h_{c_x} = 0.332 \frac{k}{x} Re_x^{1/2} Pr^{1/3}$ $\bar{h}_c = 0.664 \frac{k}{L} Re_L^{1/2} Pr^{1/3}$	T_f
		Turbulent	$R_e > 500{,}000$	$h_{c_x} = 0.0288 \frac{k}{x} Re_x^{0.8} Pr^{1/3}$ $\bar{h}_c = 0.036 \frac{k}{L} Re_L^{0.8} Pr^{1/3}$	T_f
	Free 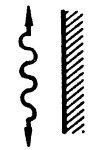	Laminar	$Gr < 10^9$	$h_{c_x} = 0.508 \frac{k}{x} Gr_x^{1/4} \left(\frac{Pr^2}{0.952 + Pr}\right)^{1/4}$ $\bar{h}_c = 0.678 \frac{k}{L} Gr_L^{1/4} \left(\frac{Pr^2}{0.952 + Pr}\right)^{1/4}$	T_f
		Turbulent	$Gr > 10^9$	$h_{c_x} = 0.029 \frac{k}{x} Gr_x^{2/5} \left(\frac{Pr^{1.17}}{1+0.494\, Pr^{2/3}}\right)^{2/5}$ $\bar{h}_c = 0.024 \frac{k}{L} Gr_L^{2/5} \left(\frac{Pr^{1.17}}{1+0.494\, Pr^{2/3}}\right)^{2/5}$	T_f
			(For Gases Only)	$\bar{h}_c = 0.13 \frac{k}{L} Gr_L^{1/3} Pr^{1/3}$	T_f
	Free 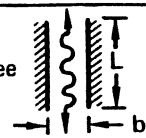	Both	$0.1 < Gr_b Pr \frac{b}{L} < 10^5$	$\bar{h}_c = \frac{k}{b} \overline{Nu}_b$ $\overline{Nu}_b$ From Figure 14-72	T_w (β at T_∞)
	Free 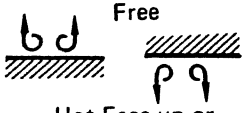 Hot Face up or Cold Face Down	Laminar	$10^5 < Gr_L < 2 \times 10^7$	$\bar{h}_c = 0.54 \frac{k}{L} Gr_L^{1/4} Pr^{1/4}$	T_f
		Turbulent	$2 \times 10^7 < Gr_L < 3 \times 10^{10}$	$\bar{h}_c = 0.14 \frac{k}{L} Gr_L^{1/3} Pr^{1/3}$	T_f
	Free  Cold Face Up or Hot Face Down	Laminar	$3 \times 10^5 < Gr_L < 3 \times 10^{10}$	$\bar{h}_c = 0.27 \frac{k}{L} Gr_L^{1/4} Pr^{1/4}$	T_f
		Turbulent	$Gr_L > 3 \times 10^{10}$	$\bar{h}_c = 0.08 \frac{k}{L} Gr_L^{1/3} Pr^{1/3}$	T_f

Table 14-16. Convective Heat Transfer Coefficients (Continued)

	Geometry and Convective Mode	Flow Type	Valid Range	Equations	Reference Temperature
Pipes and Ducts	Forced # 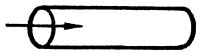	Laminar*	Fully-Developed Flow $Re_D < 2100$ $Gz < 100$	$\bar{h}_c = 3.65\frac{k}{D}$ (Const Wall Temp) $\bar{h}_c = 4.36\frac{k}{D}$ (Uniform Heat Flux)	$\bar{T}_b$
			Inlet Region $Re_D < 2100$ $Gz > 100$	$\bar{h}_c = 3.65 + \frac{0.0688\ Gz}{1+0.04\ Gz^{2/3}}$	$\bar{T}_b$
		Turbulent	Fully-Developed Flow $Re_D > 10{,}000$ $\frac{L}{D} > 60$	$\bar{h}_c = 0.023\frac{k}{D} Re_D^{0.8} Pr^{1/3}\left(\frac{\mu_b}{\mu_w}\right)^{0.14}$	$\bar{T}_b$
			Inlet Region $Re_D > 10{,}000$ $\frac{L}{D} < 60$	$\bar{h}_c = 0.116\frac{k}{D}\left(Re_D^{2/3}-125\right)Pr^{1/3}\left[1+\left(\frac{D}{L}\right)^{2/3}\right]\left(\frac{\mu_b}{\mu_w}\right)^{0.14}$	$\bar{T}_b$
		Transition	$2100 < Re_D < 10{,}000$		
		Liquid Metals	$Pr < 0.1$ $\frac{L}{D} > 60$ $10^2 < Pe < 10^4$	$\bar{h}_c = \frac{k}{D}\left[5.0 + 0.025\ Pe^{0.8}\right]$ (Const Wall Temp) $\bar{h}_c = 0.625\frac{k}{D} Pe^{0.4}$ (Uniform Heat Flux)	$\bar{T}_b$
	Free 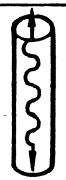	Various** Cross-Sectional Geometries ○ ▭ □ △	$0.1 < Gr_r\ Pr\frac{r}{L} < 10^4$	$\bar{h}_c = \frac{k}{r}\overline{Nu}_r$ Nu_r From Figure 14-74	T_w
Nozzles	Forced 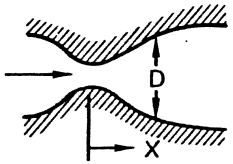	Turbulent	Upstream of Throat	$h_{c_x} = 0.023\frac{k}{D} Re_D^{0.8} Pr^{1/3}$	T_{f_p}
			Downstream of Throat	$h_{c_x} = 0.0265\frac{k}{x} Re_x^{0.8} Pr^{1/3}$	T_f' (Defined by Eq. 14-197)
			Throughout † Nozzle	$h_{c_x} = \left[\frac{0.026}{(D^*)^{0.2}}\left(\frac{\mu^{0.2} C_p}{Pr^{0.6}}\right)_o\left(\frac{P_o}{c^*}\right)^{0.8}\left(\frac{D^*}{r_c}\right)^{0.1}\right]\left(\frac{A^*}{A}\right)^{0.9}\sigma$	T_o

Table 14-16. Convective Heat Transfer Coefficients (Continued)

	Geometry and Convection Mode	Flow Type	Valid Range	Equations	Reference Temperature
Cylinders	Forced 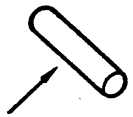	Cross Flow	$0.4 < Re_D < 400{,}000$	$\bar{h}_c = C\frac{k}{D} Re_D^{\,n} Pr^{0.31}$ C and n From Table 14-18	T_f
		Noncircular Cylinders in Cross Flow	Variable	$\bar{h}_c = C\frac{k}{D} Re_D^{\,n} Pr^{0.31}$ C and n From Table 14-19	T_f
	Free 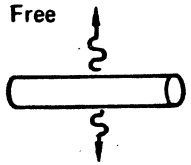	Both	$10^{-4} < Gr_D\, Pr < 10^9$	$\bar{h}_c = \frac{k}{D}\overline{Nu}_D$ $\overline{Nu}_D$ From Figure 14-73	T_f
			$10^3 < Gr_D\, Pr < 10^9$	$\bar{h}_c = 0.53\frac{k}{D} Gr_D^{1/4} Pr^{1/4}$	T_f
	Free 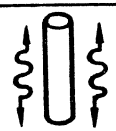	Both		Use Results for Vertical, Flat Plates	T_f
Spheres	Forced 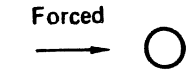	Both	For Gases Only $17 < Re_D < 150{,}000$	$\bar{h}_c = 0.37\frac{k}{D} Re_D^{0.6}$	T_f
			For Liquids Only $1 < Re_D < 200{,}000$	$\bar{h}_c = \frac{k}{D}\left[1.2 + 0.53 Re_D\right]^{0.54} Pr^{0.3}\left(\frac{\mu_\infty}{\mu_w}\right)^{0.25}$	T_∞
	Free 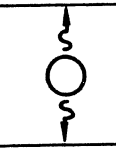	Both	$10^{-4} < Gr_r\, Pr < 10^9$	Use Results for Horizontal Cylinder, taking Radius r as the Characteristic Dimension	T_f

#Equations for Forced Convection in Pipes May be Used for Various Cross-Sectional Geometries when D is taken as the Hydraulic Diameter,

$$D_H = 4\frac{\text{cross-sectional area}}{\text{wetted perimeter}}$$

*For Large ΔT use Viscosity Corrections
Gases: Evaluate fluid properties at T_f
Liquids: Multiply by $\left(\frac{\mu_b}{\mu_w}\right)^{0.14}$

**$_r$ = Hydraulic radius = $\frac{D_H}{2}$

†Bartz's Equation: * Indicates throat conditions; subscript o denotes stagnation conditions; and σ is a function of mach number, defined by Eq. 14-199.

Figure 14-78 depicts Prandtl's concept. Fluid particles next to the surface stick to it and have zero velocity ($u = v = 0$). As the fluid proceeds along the plate, more and more fluid particles are retarded by viscous forces and the boundary layer thickness increases. Laminar flow occurs when Re_x is less than 5×10^5 (Re_x is defined by equation 128 with the characteristic dimension x, the distance from the leading edge).

In order to analytically determine the heat transfer rate in the laminar boundary layer, it is necessary to obtain the temperature distribution by solving the continuity, momentum and energy equations for two-dimensional, steady, incompressible flow. First, the fluid dynamics problem is solved. Then, the velocity profile is used in determining the temperature distribution.

Blasius solved the continuity and momentum equations (equations 133 and 134) to obtain the velocity distribution (u as a function of x and y) in the laminar boundary layer.

$$u = f(x, y, u_\infty \upsilon) \qquad (140)$$

where:

x = Distance from leading edge, ft

y = Distance from plate (normal to surface), ft

u_∞ = Free stream velocity, ft/sec

υ = Kinematic viscosity, ft^2/sec

The solution is, however, a series form which requires laborious detail calculations. But, in dimensionless form, the results may be presented on a single graph, Figure 14-79. This curve permits ready calculation of u versus y for any fluid (υ) and any location (x) along the plate.

The hydrodynamic boundary layer thickness δ is defined as the value of y where $u/u_\infty = 0.99$. An expression for δ is obtained from the curve in Figure 14-79 by choosing the value of y at which $u/u_\infty = 0.99$:

$$\delta = 5x/\sqrt{Re_x} \qquad (141)$$

Substitution of the expression for Re_x (equation 128) in equation 141 discloses that δ is proportional to $\sqrt{x}$.

The velocity profile solution shown in Figure 14-79 can be used to determine the fluid friction characteristics of laminar flow. The local skin friction coefficient C_{f_x} is defined as:

$$C_{f_x} = \frac{\tau}{\rho u_\infty^2 / 2g_c} \qquad (142)$$

where:

τ = Shearing stress = $(\mu/g_c)(\partial u/\partial y)$, lb/ft^2

μ = Viscosity, lb/sec-ft

ρ = Density, lb/ft^3

u_∞ = Free stream velocity, ft/sec

g_c = Gravitational constant = 32.2, lb-ft/lb-sec^2

The shearing stress τ is proportional to the velocity gradient $\partial u/\partial y$. An expression for the shearing stress at the wall (y = o) is determined from Figure 14-79 which provides the value of

$$\left.\frac{\partial u}{\partial y}\right|_{y=0}$$

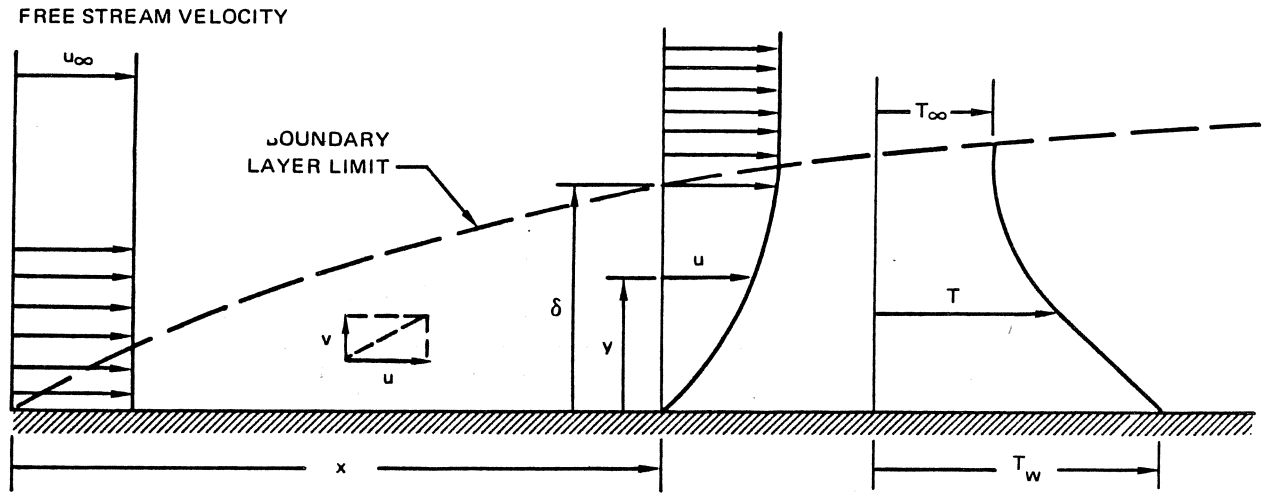

Figure 14-78. Velocity and Temperature Profiles for Laminar Boundary Layer In Flow Over a Flat Plate

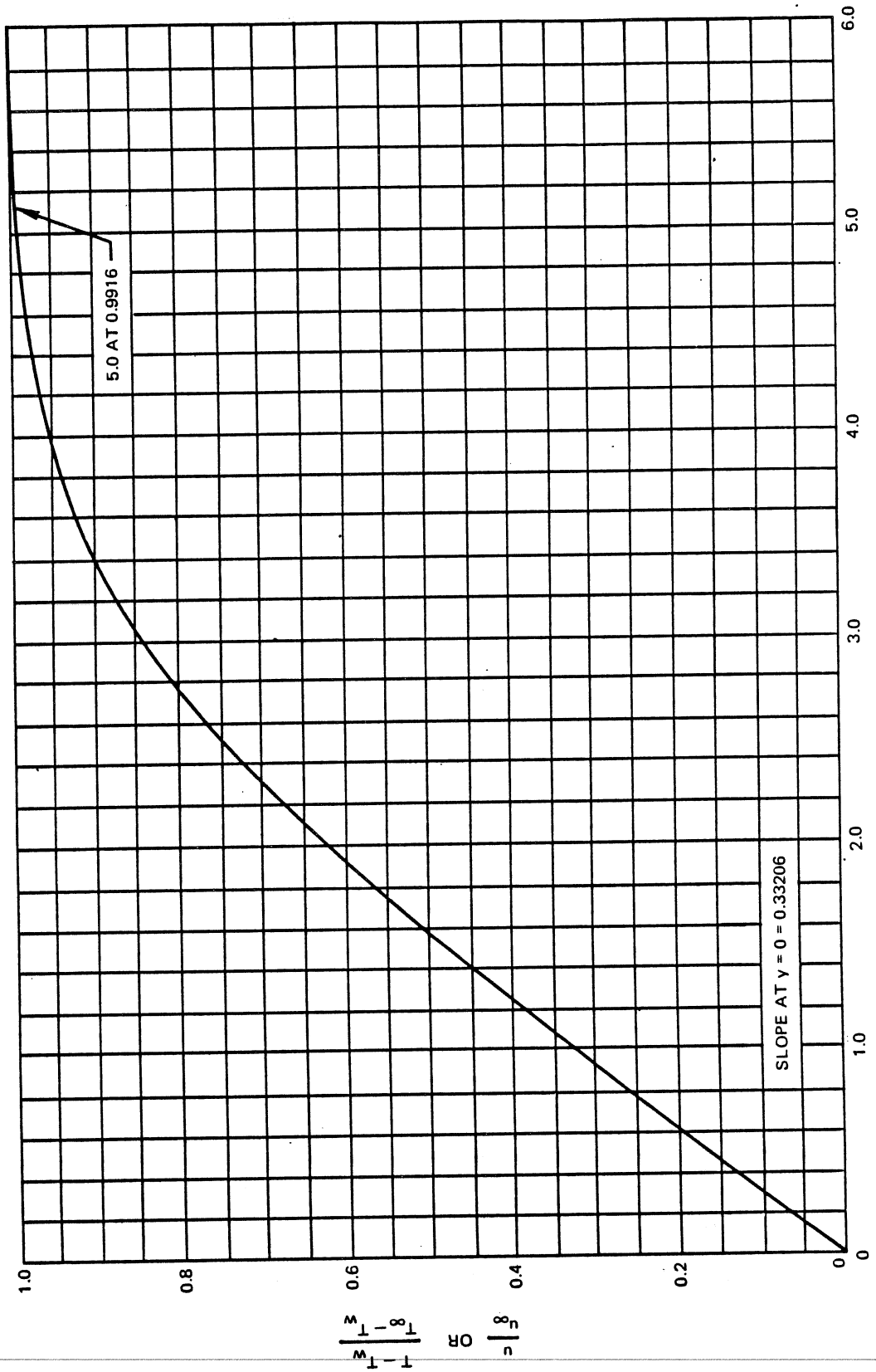

Figure 14-79. Dimensionless Velocity and Temperature Profiles in Laminar Boundary Layer for Flow Over a Flat Plate at Constant Temperature

$$\tau_w = 0.332 \frac{\mu}{g_c} \frac{u_\infty}{x} \sqrt{Re_x} \qquad (143)$$

Equations 142 and 143 are then combined to determine C_{f_x}

$$C_{f_x} = \frac{0.664}{\sqrt{Re_x}} \qquad (144)$$

The average skin friction coefficient C_f for a plate of length L is obtained by integrating equation 144:

$$\overline{C_f} = \frac{1}{L} \int_0^L C_{f_x}\, dx = \frac{1.33}{\sqrt{Re_L}} \qquad (145)$$

Finally, the temperature distribution in the boundary layer is obtained by solving the energy equation (equation 135), where the velocities u and v are determined by Blasius' results for the hydrodynamic problem. Again the solution is a series form requiring extensive numerical calculation. The results in dimensionless form are presented in Figure 14-79. With this curve, T versus y can readily be calculated for any fluid (Pr, υ) and any location (x) along the plate.

The thermal boundary layer thickness δ_{th} is obtained from the curve in Figure 14-79 by choosing the value of y at which $(T-T_w)/(T_\infty - T_w) = 0.99$

$$\delta_{th} = \frac{5x}{Re_x^{1/2} Pr^{1/3}} = \frac{\delta}{Pr^{1/3}} \qquad (146)$$

where Pr, defined by equation 130, is the ratio of the diffusion rates of momentum (υ) and heat (a) in the fluid. The relationship of the hydrodynamic and the thermal boundary layer thicknesses, δ and δ_{th} respectively, is shown in equation 146 in terms of the Prandtl number which is the connecting link between the velocity and temperature profiles (reference paragraph 14-4.2).

For a fluid having Pr greater than 1, the diffusion rate of momentum is greater than that of heat and thus, the momentum effects penetrate the fluid further than the heat transfer effects, i.e., δ greater than δ_{th}. Similarly, for Pr less than 1, δ_{th} is greater than δ. The boundary layer thicknesses δ and δ_{th} are equal in a fluid that has a Prandtl number of unity.

The heat transfer characteristics are obtained from the temperature gradient at the wall (y = 0) given by Figure 14-79. It can be shown that the local Nusselt number is:

$$Nu_x = \left. \frac{\partial \left(\frac{T - T_w}{T_\infty - T_w} \right)}{\partial \left(\frac{y}{x} \right)} \right|_{y=0} = 0.332\, Re_x^{1/2}\, Pr^{1/3} \qquad (147)$$

Also, integration of equation 147 with respect to x indicates that the average Nusselt number for a plate of length L is twice the local value at x = L:

$$\overline{Nu}_L = 0.664\, Re_L^{1/2}\, Pr^{1/3} \qquad (148)$$

These results agree with experimental data (less than 10 percent error in $\overline{Nu}_L$ for $0.5 < Pr < 1000$) if the properties are evaluated at the film temperature T_f, defined by equation 138.

14-4.5.2 Turbulent Flow

In flow along a flat plate, a critical distance x_c from the leading edge is reached where the ratio of viscous to inertia forces is not large enough to damp small disturbances in the flow. At this transition point, usually near $Re_x = 5 \times 10^5$, turbulent flow begins to develop, as shown in Figure 14-80. Fluid particles are no longer retained in layers but move in heterogeneous fashion, sliding past and colliding with other fluid particles in an entirely haphazard, unpredictable manner, causing mixing of the fluid. No one has succeeded in predicting skin friction and heat transfer coefficients for turbulent flow by direct analysis because the fluctuating velocity components cannot be described by simple equations.

The turbulent flow problem may be solved by employing the Reynolds analogy and experimental data. The Reynolds analogy states that for fluids with a Prandtl number of unity, the heat and momentum transfer processes are analogous and that an expression may be derived which relates the heat transfer characteristics to the frctional drag on the plate. For Prandtl numbers over a wide range, a modification of Reynolds analogy, verified by experiment, is expressed by:

$$St_x\, Pr^{2/3} = C_{f_x}/2 \qquad (149)$$

where:

S_{t_x} = $[Nu_x/(Re_x Pr)]$ = Stanton Number

C_{f_x} = Local skin friction coefficient

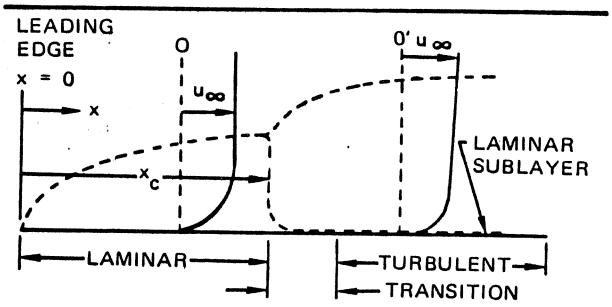

Figure 14-80. Velocity Profiles for Laminar and Turbulent Boundary Layers in Flow Over a Flat Plate

By combining equation 149 with experimental measurements of fluid friction, the heat transfer characteristics may be determined.

An empirical expression for the local skin friction coefficient C_{f_x} has been developed from test data for turbulent flow in the range $5 \times 10^5 < Re_x < 10^7$

$$C_{f_x} = 0.0576\, Re_x^{-0.2} \qquad (150)$$

The average skin friction coefficient $\overline{C}_f$ for a plate of length L is obtained by integrating equation 150:

$$\overline{C}_{f_x} = (1/L) \int_0^L C_{f_x}\, dx = 0.072\, Re_L^{-0.2} \qquad (151)$$

Finally, the heat transfer solution is obtained by combining the Reynolds analogy (equation 149) with the empirical equation relating fluid friction data (equation 150):

$$Nu_x = 0.0288\, Re_x^{0.8}\, Pr^{1/3} \qquad (152)$$

The average Nusselt number $\overline{Nu}_L$ is derived by integrating equation 152 over the length L of the plate:

$$\overline{Nu}_L = 0.036\, Re_L^{0.8}\, Pr^{1/3} \qquad (153)$$

The fluid properties are evaluated at the film temperature T_f, defined by equation 138.

An expression for the hydrodynamic boundary layer thickness δ has been experimentally determined to be:

$$\delta = 0.376x/Re_x^{0.2} \qquad (154)$$

Comparison of equations 141 and 154 (Re_x is defined by equation 14-126), shows that δ_{turb} is proportinal to $x^{0.8}$ and grows faster than δ_{lam}, which is proportional to $x^{0.5}$.

Equation 153 assumes a completely turbulent boundary layer and is valid only when the laminar region ($0 < x < x_c$) is small compared to the turbulent region ($x_c < x < L$), where x_c is the laminar-turbulent transition point shown in Figure 14-80. If the laminar zone is significant, the Nusselt number for laminar flow on the leading edge and turbulent flow beyond x_c is obtained from equation 153 by subtracting the turbulent effect and adding the laminar contribution for the laminar region ($0 < x < x_c$). This procedure gives:

$$Nu_L = 0.036 \left[Re_L^{0.8} - Re_{x_c}^{0.8} + \frac{0.664}{0.036} Re_{x_c}^{1/2} \right] Pr^{1/3} \qquad (155)$$

with the transition point at $Re_{x_c} = 500{,}000$, equation 155 reduces to:

$$\overline{Nu}_L = 0.036 \left[Re_L^{0.8} - 23{,}200 \right] Pr^{1/3} \qquad (156)$$

14-4.6 Free Convection

Free convection occurs whenever a body is placed, in the presence of a force field, in a fluid at a higher or a lower temperature than that of the body. Heat flows between the body and the fluid, changing the fluid density near the surface. The fluid motion is driven by the density differences.

Although free convection currents transfer energy in essentially the same manner as the forced-convection currents, the intensity of the mixing motion is generally less and the heat-transfer coefficient is lower than in forced convection. The bouyant effects may result from acceleration, as well as gravitational, forces. When there is no force field present, e.g., zero-g, convection does not occur, and heat transfer is by conduction through layers of stagnant fluid.

14-4.6.1 Flat Plates

Velocity in the free convection boundary layer on a flat plate is zero at the wall, reaches a maximum at a certain distance from the wall, and approaches zero again at the edge of the boundary layer, as shown in Figure 14-81.

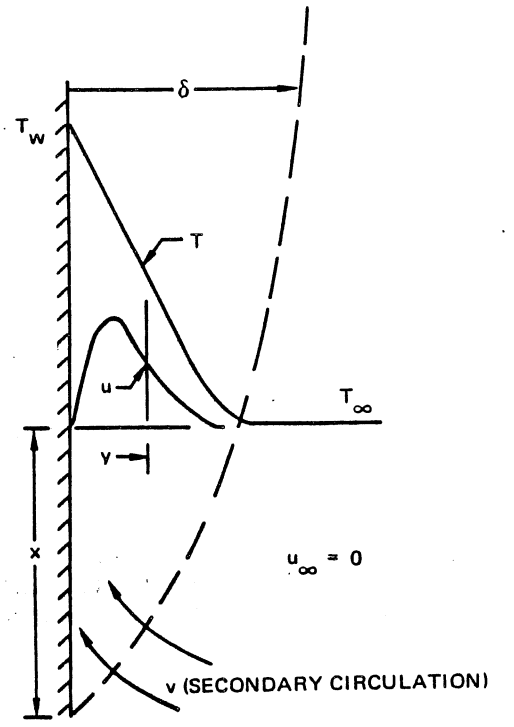

Figure 14-81. Velocity and Temperature Profiles Near a Vertical Heated Plate

This velocity profile differs from that for forced convection, where the maximum velocity is reached at the edge of the boundary layer, as shown in Figure 14-78. As in forced convection, the temperature varies across the boundary layer from the wall temperature to the free stream temperature.

Dimensional analysis (paragraph 14-1.5) indicates that free convective heat transfer is a function of the Grashof number Gr, defined by equation 129. The Grashof number represents the ratio of bouyant to viscous forces. When bouyancy is the only driving force, the fluid velocity is determined entirely by the quantities contained in the Grashof number and, therefore, the Reynolds number is not useful in free convection. Equality of the Grashof numbers in the evaluation of different conditions, establishes dynamic similarity. On vertical surfaces the fluid flow is laminar up to a Grashof number of about 10^8, passes through a transition regime between 10^8 and 10^{10}, and becomes fully turbulent at Grashof numbers above 10^{10}. Under normal conditions the critical value is usually taken as 10^9.

Heat transfer characteristics for free convection over a vertical plate are obtained by simultaneous solution of the continuity, momentum and energy equations 133, 134 and 135 respectively. An approximate method of solution is used which assumes velocity profiles for laminar and turbulent flow based on experimental observation. For laminar flow ($Gr < 10^9$) the local Nusselt number is:

$$Nu_x = 0.508 \left(Gr_x \frac{Pr^2}{0.952 + Pr} \right)^{1/4} \qquad (157)$$

The average Nusselt number is obtained by integrating equation 157:

$$\overline{Nu}_L = 0.678 \left(Gr_L \frac{Pr^2}{0.952 + Pr} \right)^{1/4} \qquad (158)$$

The local and average Nusselt numbers for turbulent flow are:

$$Nu_x = 0.029 \left(Gr_x \frac{Pr^{1.17}}{1 + 0.494\, Pr^{2/3}} \right)^{2/5} \qquad (159)$$

and

$$\overline{Nu}_L = 0.024 \left(Gr_L \frac{Pr^{1.17}}{1 + 0.494\, Pr^{2/3}} \right)^{2/5} \qquad (160)$$

These equations assume a completely turbulent boundary layer and yield good results only at Grashof numbers so high ($Gr > 10^{10}$) that the extent of the laminar region is small compared to the turbulent region. In the turbulent region, the local heat-transfer coefficient is nearly constant along the surface and, for gases in the range of $Gr > 10^9$, the following equation may be used:

$$\overline{Nu}_L = 0.13(Gr_L Pr)^{1/3} \qquad (161)$$

where the length L actually cancels ($\overline{Nu}_L$ contains L and Gr_L contains L^3).

The equations for a vertical plate apply to moderately inclined surfaces if the component of the acceleration of gravity parallel to the surface $g \cos\theta$ is used instead of g, where θ is the angle between the surface and the vertical.

Empirical equations have been established for free convection from horizontal square plates. For a warm surface facing up (or cool surface facing down):

Laminar:

$$10^5 < Gr_L < 2 \times 10^7$$

$$\overline{Nu}_L = 0.54\,(Gr_L Pr)^{1/4} \qquad (162)$$

Turbulent:

$$2 \times 10^7 < Gr_L < 3 \times 10^{10}$$

$$\overline{Nu}_L = 0.14\,(Gr_L Pr)^{1/3} \qquad (163)$$

Where L is the side of the square. For warm plates facing down (or cool plates facing up) in the laminar range $3 \times 10^5 < Gr_L < 3 \times 10^{10}$

$$\overline{Nu}_L = 0.27\,(Gr_L Pr)^{1/4} \qquad (164)$$

Data in the turbulent range are lacking. The foregoing three equations can be applied to horizontal circular disks if L is replaced by 0.9D, where D is the diameter of the disk.

Empirical results for free convection between two parallel vertical flat plates are shown in Figure 14-82. The characteristic dimension is the distance between the plates b. In this correlation all of the properties except β are evaluated at the wall temperature T_w. The coefficient of thermal expansion β is evaluated at T_∞, the temperature of the fluid far removed from the wall.

14-4.6.2 Cylinders, Spheres and Ducts

For free convection flow over a horizontal cylinder, the local convective-heat-transfer coefficient is larger over the lower portion of the cylinder than over the top

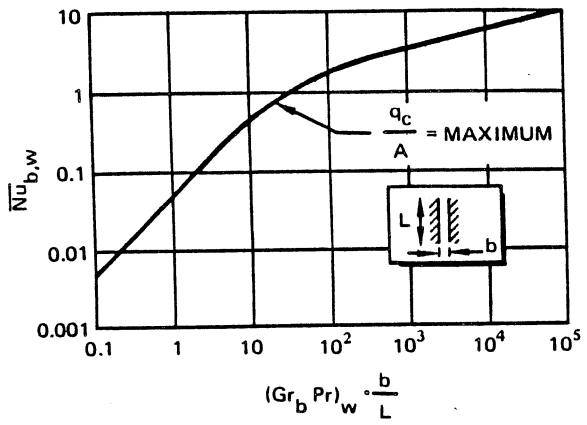

Figure 14-82. Free-Convection Heat Transfer From Two Parallel Vertical Plates Spaced a Distance b Apart

portion. The average Nusselt number for a horizontal cylinder may be obtained from the data correlation presented in Figure 14-83. The characteristic dimension is the cylinder diameter D, and fluid properties are evaluated at the film temperature T_f, defined by equation 138. The equation:

$$\overline{Nu}_D = 0.53 (Gr_D Pr)^{1/4} \qquad (165)$$

may be used for $Pr > 0.5$ and $10^3 < Gr_D < 10^9$.

The equations developed for veritical plates (equations 157 through 161) can also be used to calculate free-convection heat-transfer coefficients for vertical cylinders with satisfactory accuracy.

The average Nusselt number for free convection over a sphere may also be obtained from Figure 14-83 and equation 165 if the sphere radius r is used as the characteristic dimension. For very small spheres when

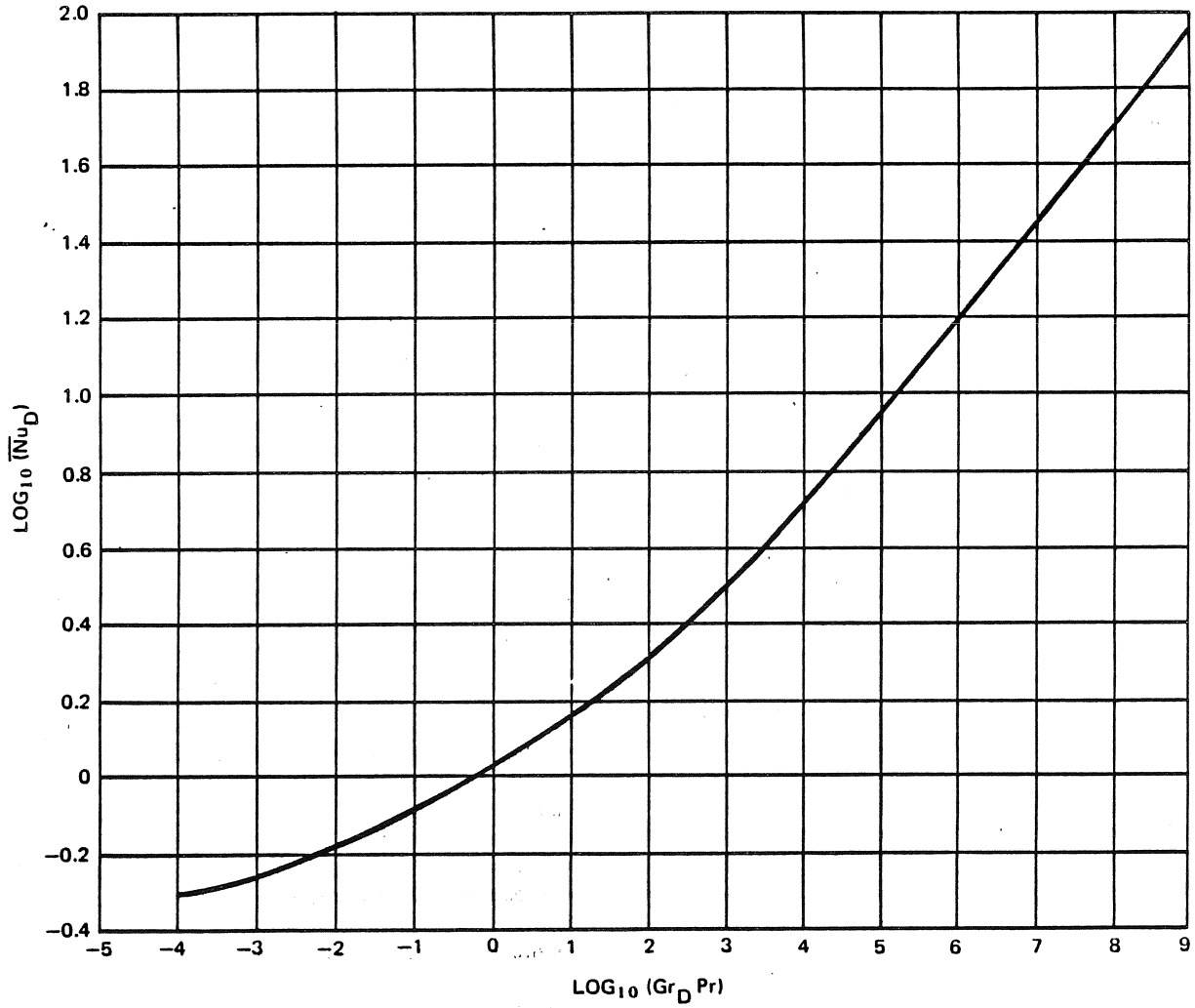

Figure 14-83. Correlation of Data for Free-Convection Heat Transfer From Horizontal Cylinders in Gases and Liquids

the Grashof number approaches zero, the average Nusselt number approaches one, i.e., $(h_c r/k) \rightarrow 1$. This condition corresponds to pure conduction through a stagnant layer adjacent to the surface.

Approximate results for free convection over miscellaneous three-dimensional shapes such as blocks and short cylinders may be obtained from Figure 14-83 if the characteristic dimension L is taken as:

$$1/L = 1/L_{hor} + 1/L_{vert} \qquad (166)$$

where:

L_{vert} = Height of object

L_{hor} = Average horizontal dimension

Average Nusselt numbers for laminar free convection at the inside surfaces of vertical ducts having various cross-sectional geometries may be obtained from Figure 14-84. The characteristic dimension for Nu and Gr is the hydraulic radius r, which is one-half the hydraulic diameter D_H where:

$$D_H = 4 \frac{\text{flow cross-sectional area}}{\text{wetted perimeter}} \qquad (167)$$

All properties except β are evaluated at the wall temperature T_w. The coefficient of thermal expansion β is evaluated at T_∞. The small symbols in Figure 14-84 indicate the cross-sectional geometry. L is the length of the duct. When the duct is inclined by an angle θ from the vertical, the component of the acceleration of gravity parallel to the duct axis $g \cos\theta$ is used in Gr_r instead of g.

14-4.6.3 Free Convection Caused By Centrifugal Forces

Free convection processes occur in the presence of a centrifugal force, as well as a gravitational force. The centrifugal-force field in rotating components of turbines and compressors may be many times larger than the gravitational force, and substantial free-convection velocities and effective heat transfer can be achieved without external pumps or fans.

Gas turbine blades, may be cooled by free convective flow through holes drilled into the blade from the root as shown in Figure 14-85. Coolant, supplied to the passage, is subjected to a centrifugal acceleration equal to $r\omega^2$, where ω is the angular velocity and r is the radius. The fluid heated at the surface of the holes is less dense and moves toward the axis of rotation. This motion is similar to that of hot air rising from a vertical heated plate. Continuous circulation occurs because cool fluid flows outward from the core to replace the hot fluid that is leaving the passages.

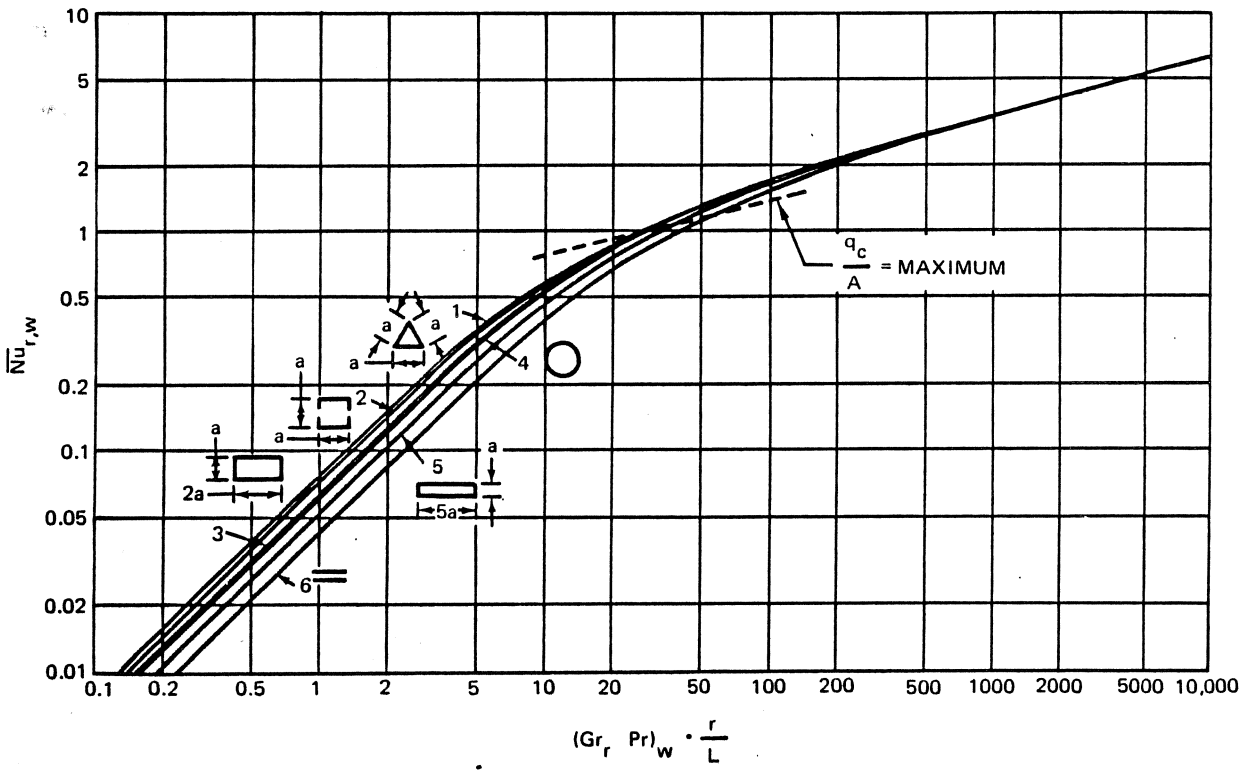

Figure 14-84. Free-Convection Heat Transfer From the Interior Surfaces of Vertical Ducts Having Various Cross-Sectional Geometries

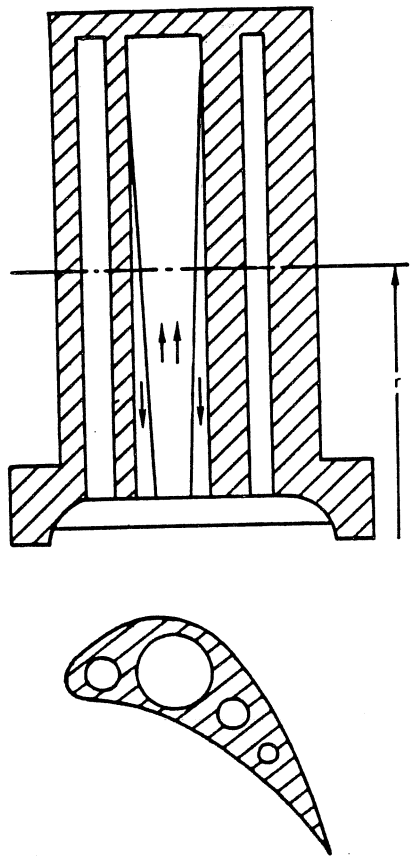

Figure 14-85. Free-Convection-Cooled Gas-Turbine Blade

The average Nusselt number can be computed from equation 160 or 161 if the Grashof number, defined by equation 129, is based on the centrifugal acceleration $r\omega^2$ instead of the acceleration of gravity g. The angular velocity ω is in radians/sec, and the distance r in feet is from the axis of rotation to the midpoint of the cooling passage.

When the diameter of the cooling passage is small compared with its length, the boundary layer may become large enough to fill most of the passage and the cooler core becomes too small to provide effective circulation. If the flow is restricted by the passage size, the heat transfer will be reduced.

14-4.6.4 Rotating Bodies

Heat transfer by convection between a rotating body and a surrounding fluid is important in the thermal analysis of shafting, flywheels, turbine rotors, and other rotating components. For a heated horizontal cylinder rotating at low speeds, the flow clings to the surface and the heated air rises vertically in a narrow chimney. When the speed is increased to a critical value, where the surface speed equals the free-convection velocity at the side of a stationary cylinder, the flow becomes turbulent. In air at 1 g, the transition occurs at:

$$Re_\omega = \rho\omega\pi D^2/\mu = 8000 \qquad (168)$$

where:

Re_ω = Peripheral speed Reynolds number

ω = Angular velocity, radians/sec

D = Diameter of cylinder, ft

ρ = Density, lb/ft^3

μ = Viscosity, lb/sec-ft

Below the critical velocity, heat transfer may be estimated by using the results for stationary horizontal cylinders (reference paragraph 14-4.6.2). The following empirical equation may be used for speeds above the critical velocity:

$$\overline{Nu}_D = 0.11\left[(0.5\,Re_\omega^2 + Gr_D)\,Pr\right]^{0.35} \qquad (169)$$

The velocity and boundary layer profiles for a rotating horizontal disk are illustrated schematically in Figure 14-86. Rotating fluid particles tend to be thrown outward. When the rotational Reynolds number $\rho\omega r^2/\mu$ exceeds 250,000, the flow changes from laminar to turbulent and the boundary layer begins to thicken. For disks rotating below the critical velocity:

$$\overline{Nu}_{r_o} = C\left(\frac{\rho\omega r_o^{\,2}}{\mu}\right)^{1/2} \qquad (170)$$

where:

r_o = Radius of disc, ft

C = Coefficient, as a function of Pr; e.g.,:

Pr	0.7	1.0	2.0	5.0	10.0
C	0.35	0.38	0.5	0.8	1.1

For disks rotating above the critical speed, the laminar-turbulent transition occurs at the radius r_c where $(\rho\omega r_c^2/\mu) = 250{,}000$, as shown in Figure 14-86. The average Nusselt number for laminar flow between r=0 and $r=r_c$ and turbulent flow between $r=r_c$ and $r=r_o$ is approximately:

$$\overline{Nu}_{r_o} = 0.015\left(\frac{\rho\omega r_o^2}{\mu}\right)^{0.8} - 100\left(\frac{r_c}{r_o}\right)^2 \qquad (171)$$

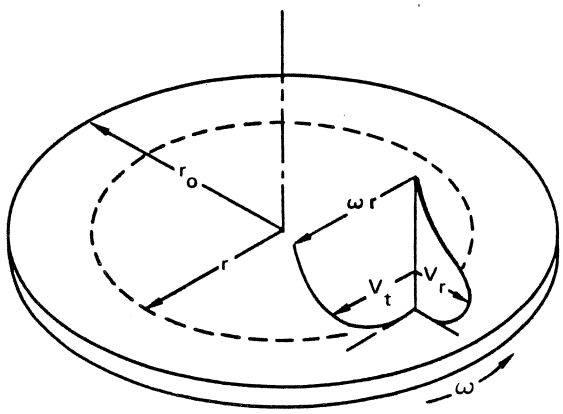

(a)

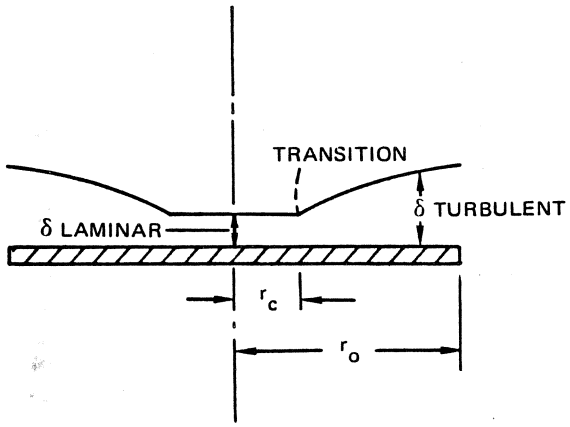

(b)

Figure 14-86. Velocity and Boundary Layer Profiles for a Disk Rotating in an Infinite Environment

14-4.6.5 Combined Forced and Free Convection

In any convective heat transfer process, density gradients occur and in the presence of a force field, natural-convection currents arise. If the forced-convection effects are very large, the free-convection currents may be ignored and, similarly, when the free-convection forces are very strong, the forced-convection effects may be negligible.

The ratio of Gr/Re^2 gives a qualitive indication of the relative importance of free-convection and forced-convection effects.

When:

$$Gr/Re^2 \simeq 1 \qquad (172)$$

both the free- and forced-convection effects are significant and neither may be neglected. When $Gr/Re^2 > 10$, bouyant forces are dominant and forced-convection is insignificant. If $Gr/Re^2 < 1/10$, forced-convection is important and free-convection may be neglected.

In the region where neither process can be ignored, heat transfer is increased by bouyancy effects acting in the direction of flow, and decreased when acting against the flow. The usual practice is to calculate the heat-transfer coefficient using both the free- and the forced-convection relations, and to use the larger value.

14-4.7 Forced Convection Inside Pipes, Ducts, and Nozzles

14-4.7.1 Effect of Reynolds Number

Heat transfer characteristics for a given fluid flowing through a long pipe or duct depend primarily on the flow conditions, which are represented by the Reynolds number Re_D, defined by equation 128, or a form that is more convenient for pipe flow:

$$Re_D = \frac{\dot{w}\, D_H\, g_c}{\mu\, A\, g} \qquad (173)$$

where:

$\dot{w}$ = Weight flowrate, lb/sec

μ = Viscosity, lb/sec-ft

A = Cross-sectional area of pipe or duct, ft^2

D_H is the characteristic dimension, the hydraulic diameter, defined in equation 167 which may be used for any arbitrary cross-section. For a circular cross-section pipe $D_H = D$, the inside diameter. For an annulus formed by two concentric tubes $D_H = D_2 - D_1$, the difference between the diameters of the annular surfaces.

In long ducts where entrance effects are not important, the flow is laminar up to $Re_D = 2100$, undergoes a laminar-to-turbulent transition between $Re_D = 2100$ and 10,000, and is fully turbulent for $Re_D > 10{,}000$. As with flow over a flat plate, heat transfer in laminar flow is due solely to conduction.

In transitional flow, even though the mixing motion only exists on a small scale, the heat transfer is greatly increased. Further improvement occurs in the fully developed turbulent regime, where the eddies and mixing currents become large. In heat exchanger design, the high heat transfer rates in the turbulent regime are weighed against the accompanying high pressure losses and pumping expense. In practice, laminar flow is avoided but Reynolds numbers seldom exceed 50,000.

14-4.7.2 Entrance Effects

As a fluid enters a circular pipe with uniform velocity, the fluid immediately adjacent to the wall is brought to rest. For a short distance from the entrance a laminar boundary layer is formed along the pipe wall. If the turbulence level of the incoming stream is high, the boundary layer will quickly become turbulent. Irrespective of whether the boundary layer remains laminar or becomes turbulent, it will increase until its thickness δ fills the duct ($2\delta = D$). The entry length L_e is the distance required for the flow to become fully developed. Beyond this point the velocity profile remains essentially unchanged.

Velocity and temperature profiles and the local heat-transfer coefficient for laminar flow near the inlet of a pipe are shown in Figure 14-87. The heat-transfer coefficient is largest near the inlet and decreases along the pipe until both the velocity and the temperature profiles for fully developed flow have been established. The entry length for laminar flow may be estimated by combining:

a. Boundary layer solution for a flat plate, equation 141.

b. Parabolic velocity distribution, where the pipe centerline velocity $u = u_\infty = 2u_{mean}$.

c. The condition that the boundary layer thickness equals one-half the pipe diameter, $\delta = D/2$

$$\frac{L_e}{D} = 0.02 \frac{\rho u_m D}{\mu} = 0.02\ Re_D \qquad (174)$$

where:

u_m = Mean velocity, ft/sec

For example, at $Re_D = 2000$, $L_e/D = 40$.

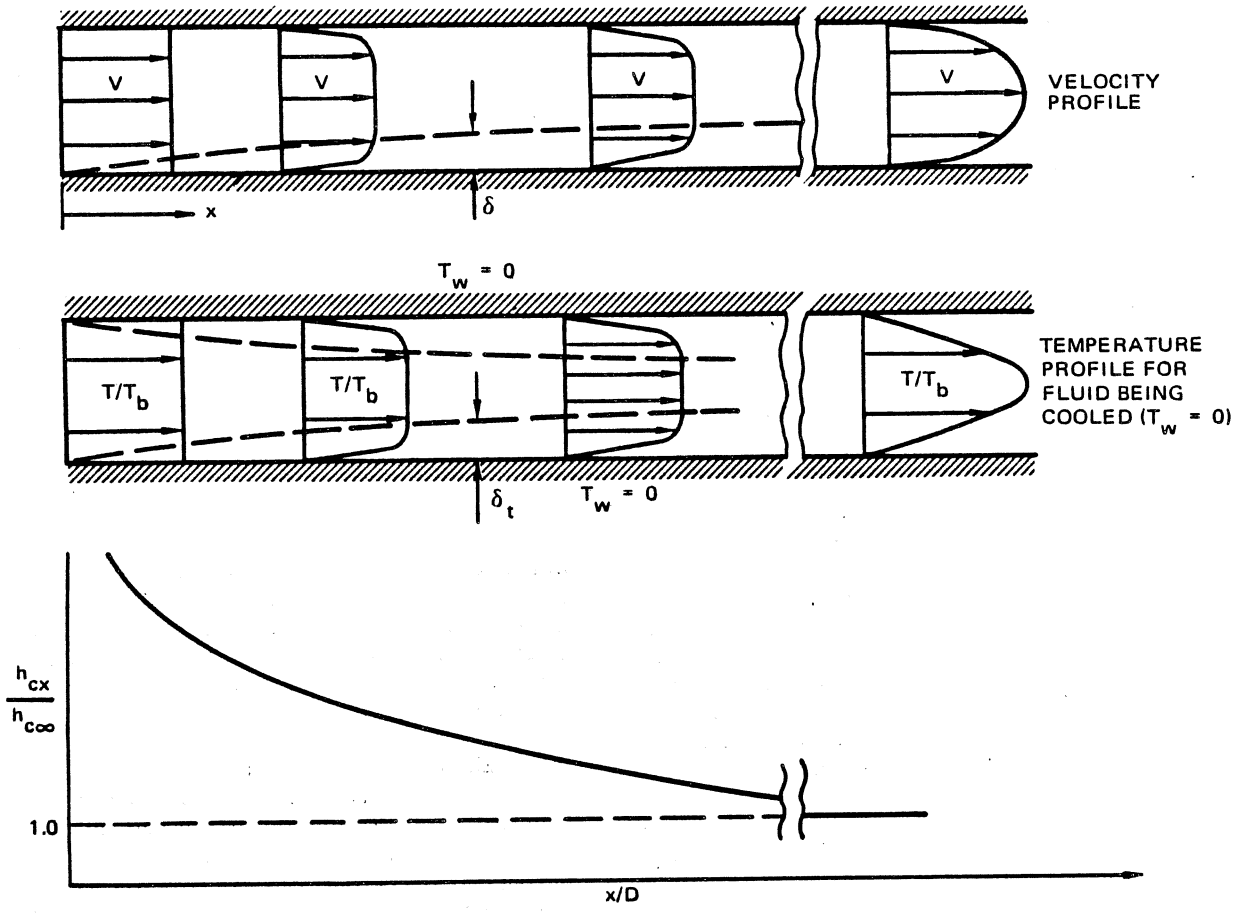

Figure 14-87. Velocity Distributions, Temperature Profiles and Variation of the Unit-Convective Conductance Near the Inlet of a Tube for Air Being Cooled in Laminar Flow

The velocity profile and variation in local heat-transfer coefficient h_{c_x} for turbulent flow near a pipe inlet are shown in Figure 14-88. A significant increase occurs in h_{c_x} when the laminar boundary layer becomes turbulent. Again the entry length is estimated from the flat plate boundary layer solution (equation 154) and the approximate velocity profile (center line velocity $u = u_\infty = u_m/0.8$)

$$\frac{Le}{D} = 1.51\left(\frac{\rho u_m D}{\mu}\right)^{1/4} = 1.51\ Re_D^{1/4} \qquad (175)$$

For example, at $Re_D = 10{,}000$, $L_e/D = 15$.

For pipes with L/D much greater than L_e/D, the entrance effects may be neglected and the heat transfer results for fully-developed flow should be used.

14-4.7.3 Log Mean Temperature Difference

Pipe flow differs from submerged flow in that the fluid temperature changes along the heat transfer surface, rather than remaining constant. The usual method of accounting for this changing fluid temperature is to define a mean heat-transfer coefficient $\bar{h}_c$ which is to be constant along the pipe. This definition then requires that a corresponding log mean temperature difference ΔT_L be determined by integrating the heat transfer over the total area. The heat transfer rate q_c is:

$$q_c = \bar{h}_c A \Delta T_L \qquad (176)$$

Consider a fluid at a mean bulk temperature $\bar{T}_b$, defined by equation 139 flowing through a pipe at constant wall temperature T_w (Figure 14-89). The fluid enters at T_1, is heated, and leaves at T_2. An energy balance on the element of heat transfer area da requires:

$$dq_c = \bar{h}_c(T_w - T_b)da = \frac{\dot{w}g_c\, C_p\, dT_b}{g} \qquad (177)$$

where:

$$\frac{\dot{w}g_c\ C_p\, dT_b}{g}$$

is the differential rate of change of enthalpy of the fluid (changes in kinetic and potential energies are neglected). Separating variables and integrating (with h_c = constant).

$$\int_{T_1}^{T_2} \frac{dT_b}{T_w - T_b} = \int_0^A \frac{\bar{h}_c}{\frac{\dot{w}g_c\, C_p}{g}} da \qquad (178)$$

or

$$\bar{h}_c A = \frac{\dot{w}g_c\, C_p}{g}\ Ln\left(\frac{T_w - T_1}{T_w - T_2}\right) \qquad (179)$$

Combining with equation 176 and

$$q_c = \frac{\dot{w}g_c}{g}\, C_p(T_2 - T_1)$$

$$\Delta T_L = \frac{T_2 - T_1}{Ln\left(\frac{T_w' - T_1}{T_W - T_2}\right)} = LMTD \quad \text{(Heating)} \qquad (180)$$

For cooling the fluid, the result is:

$$\Delta T_L = \frac{T_1 - T_2}{Ln\left(\frac{T_1 - T_w}{T_2 - T_w}\right)} = LMTD \quad \text{(Cooling)} \qquad (181)$$

where:

T_1 = Inlet bulk temperature, °R

T_2 = Outlet bulk temperature, °R

T_w = Wall temperature, °R

LMTD = Log mean temperature difference

If $T_1 - T_w$ is not more than 50 percent greater than $T_2 - T_w$, the arithmetic mean temperature difference will be within 1 percent of the LMTD and may be used to simplify calculations.

14-4.7.4 Laminar Flow in Pipes

The heat-flow mechanism in purely laminar flow is conduction. The heat transfer rate between the fluid and the pipe wall can be obtained analytically by simultaneous solution of the equations of motion and conduction. For fully developed laminar pipe flow, Graetz used a parabolic velocity profile and solved the energy equation in cylindrical coordinates, equation 136.

The local Nusselt number Nu_D (based on the local difference between wall and bulk temperatures) is 3.65 for a pipe with constant wall temperature and 4.36 for a pipe with uniform heat flux along its axis. Nu_D, defined by equation 127 with the pipe diameter D as the characteristic dimension, is evaluated at the bulk temperature. The local values may be taken as the average Nusselt numbers $\overline{Nu}_D$ for a long pipe if the entrance effects are negligible and the properties are evaluated at the mean bulk temperature $\bar{T}_b$, defined by equation 139.

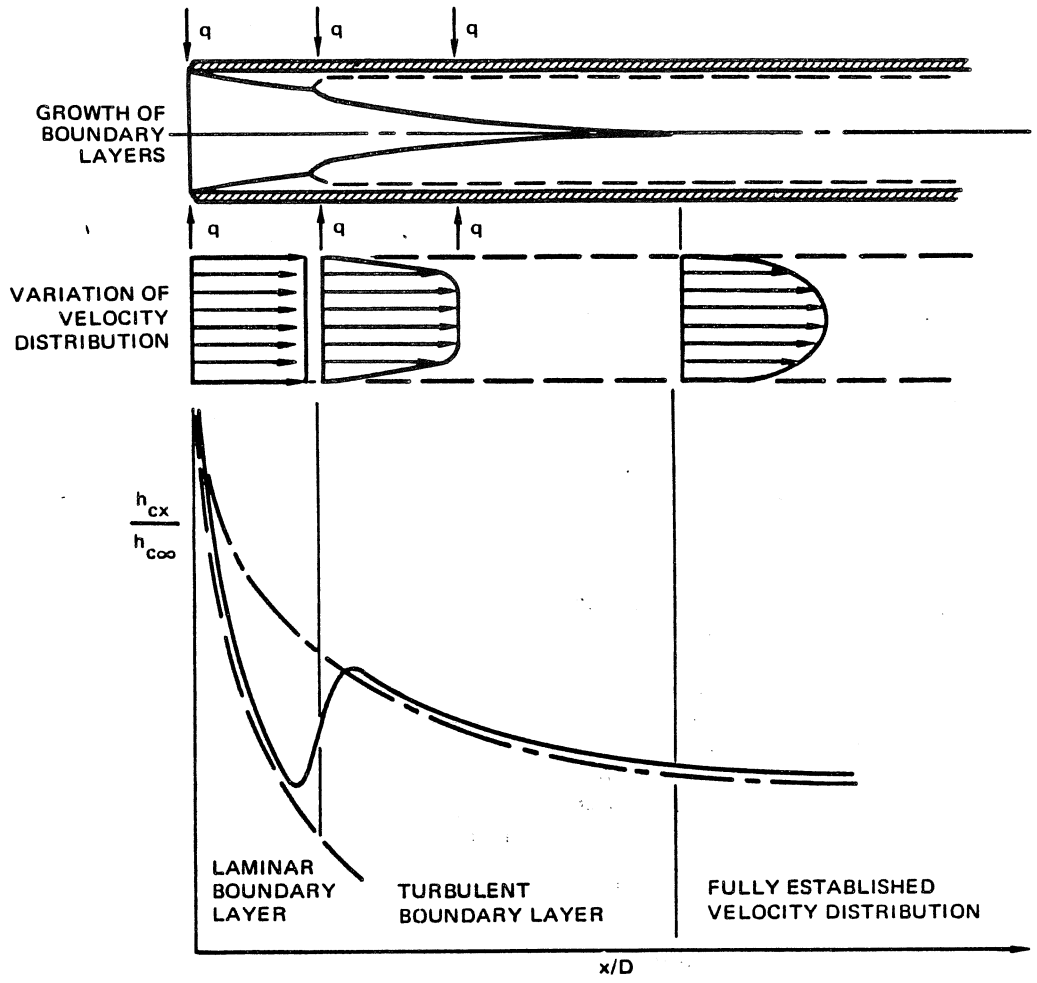

Figure 14-88. Velocity Distribution and Variation of Unit-Convective Conductance Near the Entrance of a Tube for a Fluid in Turbulent Flow

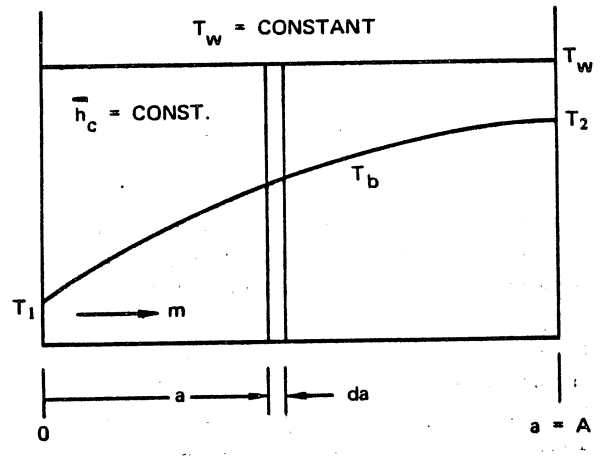

Figure 14-89. Temperature Distribution for a Fluid Heated by a Pipe at Constant Temperature

For heat transfer in the inlet region of a pipe, the average Nusselt number is expressed as a function of a dimensionless group known as the Graetz number Gz.

$$Gz = Re_D \, Pr \, D/L \qquad (182)$$

where:

D = Hydraulic diameter

L = Length of pipe

The following empirical equation for $\overline{Nu}_D$ in the inlet region agrees very well with experimental data:

$$\overline{Nu}_D = 3.65 + \frac{0.0668\,Gz}{1 + 0.04\,Gz^{2/3}} \qquad (183)$$

where $\overline{Nu}_D$ and Gz are evaluated at the mean bulk temperature $\overline{T}_b$.

The foregoing expression for $\overline{Nu}_D$ is based on the assumption of constant fluid properties. In cases where the viscosity variation with temperature may not be neglected — for large temperature differences or highly viscous fluids (oils) — a correction factor is required. The Nusselt number must be adjusted because the viscosity variation distorts the velocity profile, which influences both the temperature profile and the heat transfer.

For liquids, the Nusselt number is multiplied by $(\mu_b/\mu_w)^{0.14}$, where μ_b and μ_w are the viscosities at the bulk temperature and at the wall temperature respectively. For gases it is recommended that the expressions for Nu_D be used without the addition of the viscosity ratio and that the properties be evaluated at the film temperature for pipe flow T_{f_p}, defined by:

$$T_{f_p} = (\overline{T}_b + T_w)/2 \qquad (184)$$

where T_b is the mean bulk temperature, defined by equation 139 and T_w is the wall temperature.

14-4.7.5 Turbulent Flow in Pipes

Turbulent pipe flow, like turbulent plate flow, does not lend itself to direct analysis because the irregular velocity distribution cannot be modeled with a simple mathematical expression. Consequently, the Reynolds analogy and empirical correlations must again be used to obtain heat transfer results for fully developed turbulent flow in a pipe.

The Reynolds analogy states that for fluids with a Prandtl number of unity, the heat and momentum transfer processes are analogous and that, in pipe flow, the heat transfer characteristics may be related to the frictional drag by:

$$St = \frac{Nu_D}{Re_D\, Pr} = \frac{f}{8} \qquad (185)$$

where the Fanning friction coefficient f is defined as:

$$f = \frac{\Delta p}{(L/D)(\rho V^2/2g_c)} \qquad (186)$$

where:

Δp = Pressure drop, lb/ft^2

$\frac{\rho v^2}{2g_c}$ = Dynamic head, lb/ft^2

L = Pipe length, ft

D = Hydraulic diameter, ft.

Equation 185 agrees fairly well with experimental data for gases whose Prandtl number is near unity.

For Prandtl numbers other than unity ($1/2 < Pr < 100$), Colburn recommends, based on experimental observation, the following expression:

$$St\, Pr^{2/3} = j = f/8 \qquad (187)$$

where the term $St\, Pr^{2/3}$ is known as the Colburn j-factor. Equation 187 has the advantage of permitting estimates of the heat-transfer coefficient h_c based on simple pressure drop tests. For odd shapes or an excessively rough surface, it is only necessary to determine the friction factor f and by substitution into equation 187 obtain h_c.

Combined with the empirical equation:

$$f = 0.184\, Re_D^{-0.2}$$

(valid for $10{,}000 < Re_D < 120{,}000$), the Colburn equation becomes:

$$\frac{\bar{h}_c}{C_{p_b} G} Pr^{2/3} = j = \frac{f}{8} = 0.023\,(Re_D)^{-0.2}_{f_p} \qquad (188)$$

where:

C_p = Constant pressure specific heat, Btu/lb-°R

G = ρv = Mass velocity per square foot of cross-section, lb/hr-ft^2

h_c = Average heat-transfer coefficient, Btu/hr-ft^2-°R

The subscripts b and f_p denote the reference bulk and pipe film temperatures respectively. All properties, except C_p are evaluated at the pipe film temperature T_{fp}, defined by equation 184; C_p is evaluated at the bulk temperature. Equation 188 is valid only for moderate temperature differences.

For fully developed turbulent flow involving large temperature differences, the following equation may be used for $10{,}000 < Re_D < 500{,}000$

$$\overline{Nu}_D = 0.023\, Re_D^{0.8}\, Pr^{1/3} \left(\frac{\mu_b}{\mu_w}\right)^{0.14} \qquad (189)$$

where:

μ = Viscosity

and the subscripts b and w indicate the reference temperatures, the bulk and wall temperatures respectively.

Equation 189 is more convenient than the Colburn equation because the physical properties are evaluated at the mean bulk temperature T_b, rather than the pipe film temperature. Variation in properties due to temperature gradients are accounted for by the viscosity correction factor $(\mu_b/\mu_w)^{0.14}$.

Equations 188 and 189 are applicable for fully developed turbulent flow. In the pipe inlet region, greater heat-transfer coefficients may be expected. The following empirical equation provides the average Nusselt number $\overline{Nu}_D$ for the inlet region

$$\overline{Nu}_D = 0.116\,(Re_D^{2/3} - 125)\,Pr^{1/3} \left[1 + \left(\frac{D}{L}\right)^{2/3}\right]\left(\frac{\mu_b}{\mu_w}\right)^{0.14} \qquad (190)$$

where:

D = Hydraulic Diameter, ft.

L = Distance from inlet; i.e., length of intake section, ft.

μ = Viscosity, lb/ft-sec

All properties are evaluated at the mean bulk temperature except μ_w, the viscosity at the wall temperature. This equation accounts for entrance effects and is valid for large temperature differences. It also satisfactorily reproduces values in the transition zone, $2100 < Re_D < 10{,}000$.

The turbulent pipe flow Nusselt numbers presented herein are mean values and require the use of the log mean temperature difference LMTD (reference paragraph 14-4.7.3).

In calculating the hydraulic diameter, the whole perimeter is used in the case where only part of the tube is heated. Only in calculating the heat flow (equation 126) is the heated area alone to be used.

14-4.7.6 Forced Convection Inside Nozzles

A major problem in the construction of a rocket thrust chamber is cooling the surfaces exposed to the hot gases. The thrust chamber wall must be kept below the temperature at which it melts or loses its strength. An estimate of the convective heat-transfer coefficient inside the nozzle is required for the solution of the cooling problem.

Although nozzles are not of constant diameter and the propellant flow is not fully developed, the following form of Colburn's equation for pipe flow (reference paragraph 14-4.7.5) provides a reasonably good approximation of the actual nozzle heat-transfer rate, if D is the local nozzle diameter:

$$\frac{h_c}{GC_p} = 0.023\left(\frac{GD}{\mu}\right)^{-0.2} Pr^{-2/3} \qquad (191)$$

where:

h_c = Local heat-transfer coefficient, Btu/sec-ft^2-$^\circ$R

G = Mass velocity

$= \dfrac{4\,\dot{w}g_c}{\pi D^2\,g}$ lb/sec-ft^2

D = Local nozzle diameter, ft

μ = Viscosity, lb/ft-sec

Gas properties are evaluated at the film temperature T_{f_p}, defined by equation 184.

Although this equation may not always provide suitable accuracy of the magnitude, it does correctly predict the trends of variation of h_c with nozzle diameter and pressure. Since:

$$G = \frac{4\,\dot{w}g_c}{\pi D^2\,g}$$

and $\dot{w}$ is constant, equation 191 indicates that h_c is proportional to $1/D^{1.8}$.

Neglecting the variation of Pr and the thermal conductivity k with temperature, the maximum h_c occurs at the nozzle throat, where D is a minimum. Experimentally, the maximum heat transfer rate is observed slightly upstream of the throat. Also, since the gas temperature is relatively insensitive to pressure for most propellants, and μ, C_p, and k vary primarily with temperature, not pressure, equation 191 indicates (with $G = \rho v$) that h_c is proportional to $\rho^{0.8}$ and to $P^{0.8}$.

Thus heat-transfer rates increase nearly linearly with increasing chamber pressure.

Equation 191 is adequate to determine the heat transfer rate in the combustion chamber and at the throat. In the supersonic portion of the nozzle an alternate form has been suggested:

$$Nu_x = \frac{h_c\,x}{k} = a\left(\frac{Gx}{\mu}\right)^{0.8} Pr^{1/3} \qquad (192)$$

where x is the distance downstream of the throat and a varies from 0.025 to 0.028. The fluid properties are evaluated at an empirical film temperature T_f:

$$T_f' = T_w + 0.23\,(T_b - T_w) + 0.19\,(T_{aw} - T_w) \qquad (193)$$

where:

T_{aw} = Adiabatic wall temperature.

Bartz has developed an equation for h_c which can be shown to be almost equivalent in form to equation 192

$$h_c = \left[\frac{0.026}{(D_*)^{0.2}}\left(\frac{\mu^{0.2} C_p}{Pr^{0.6}}\right)_o\left(\frac{P_o}{c^*}\right)^{0.8}\left(\frac{D_*}{r_c}\right)^{0.1}\right]\left(\frac{A_*}{A}\right)^{0.9}\sigma \qquad (194)$$

where the subscript o signifies stagnation conditions, the subscript $_*$ denotes value at the nozzle throat, and

c^* = Characteristic velocity

$$= \frac{P_o A_* g}{\dot{w} g_c}, \text{ ft/sec}$$

D_* = Throat diameter, ft

r_c = Throat radius of curvature, ft

P = Pressure, lb/ft^2

A = Cross-sectional area, ft^2

and

$$\sigma = \frac{1}{\left[\frac{1}{2}\frac{T_w}{T_o}\left(1+\frac{\gamma-1}{2}M^2\right)+\frac{1}{2}\right]^{0.8-0.2\omega}\left(1+\frac{\gamma-1}{2}M^2\right)^{0.2\omega}} \qquad (195)$$

where:

T_o = Gas temperature at stagnation, °R

γ = Specific heat ratio

M = Local Mach number

ω = Exponent of the viscosity-temperature relation ($\omega = 0.6$ for diatomic gases.)

An advantage of this unusual grouping of terms is the fact that the bracketed term in equation 194 is a constant, since all properties are evaluated at the stagnation temperature. Douglas Report SM-52339 presents a graphical aid which simplifies the evaluation of Bartz' equation.

The nozzle heat transfer problem has been solved by boundary-layer analysis. The results are more accurate than those based on pipe flow (equations 191, 192, and 194) but a numerical solution involving extensive calculation is required. Figure 14-90 compares the Colburn method with three boundary layer methods of calculating the combustion gas convective heat transfer coefficient throughout the nozzle boundary layer. MDAC computer programs which employ these three methods are available:

a. H660, the ICRPG (Interagency Chemical Rocket Propulsion Group) standard program, employs a solution developed by Elliott, Bartz, and Silver and yields the most accurate results. The use of H660, which is also known as the TBL (Turbulent Boundary Layer) program, is described in MDAC Report G0443.

b. F586 is more convenient to use than H660 because it is easier to load and requires much less computer time. F586, described in Douglas Report SM-45735, employs Mayer's extended solution and provides accurate results.

c. JA28, which uses the Persh-Lee method, overestimates the heat transfer coefficient, particularly at the nozzle throat, and is seldom used.

14-4.7.7 Liquid Metals

Since liquid metals ($Pr < 0.1$) have high thermal conductivities, they can achieve high heat transfer rates and are particularly applicable to situations where large amounts of energy must be removed from a relatively small space, such as in a nuclear reactor. However, liquid metals are difficult to handle because of their corrosive nature and the violent reaction which may result when they come into contact with water or air.

The Peclet number Pe is useful in correlating liquid metal heat transfer data:

$$Pe = Re_D Pr \qquad (196)$$

For fully developed turbulent flow in smooth tubes with uniform heat flux at the wall:

$$\overline{Nu}_D = 0.625\, Pe^{0.4} \qquad (197)$$

This equation is valid for $10^2 < Pe < 10^4$ and $L/D > 60$. All properties are evaluated at the bulk temperature. For heat transfer to liquid metals in tubes with constant wall temperature:

$$\overline{Nu}_D = 5.0 + 0.025\, Pe^{0.8} \qquad (198)$$

This equation is valid for $Pe > 100$ and $L/D > 60$.

All properties are evaluated at the bulk temperature.

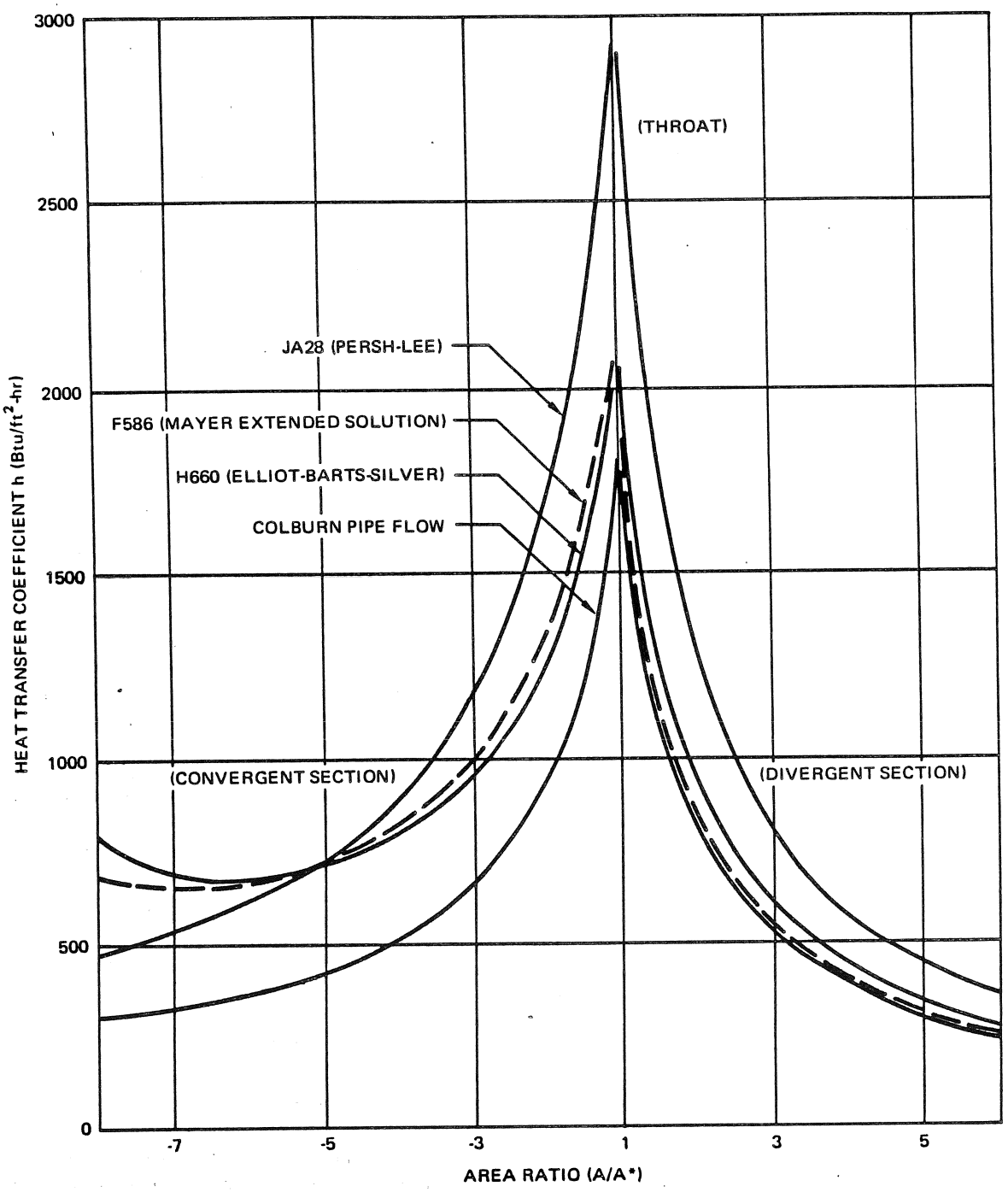

Figure 14-90. Comparison of Convective Heat Transfer Coefficients

14-4.8 Forced Convection Over Exterior Surfaces

14-4.8.1 Cylinders

Heat transfer characteristics for a cylinder in cross flow (flow that is perpendicular to the axis) are determined by the boundary layer development. As long as the boundary layer remains laminar, the local Nusselt number may be computed by analytic methods. The average Nusselt number, which includes the separated-flow region on the back side of the cylinder, must be obtained from empirical equations.

The phenomenon of boundary-layer separation is illustrated in Figure 14-91. The pressure through the boundary layer is essentially constant at any distance x from the front stagnation point of the cylinder. Thus, the pressure in the boundary layer follows that of the free stream for potential flow around a cylinder. The pressure decreases and the free stream velocity increases along the front side. As flow proceeds to the back side, the pressure increases, causing a reduction in velocity in the free stream and throughout the boundary layer. Reverse flow begins when the momentum of the fluid layers near the surface is not sufficiently high to overcome the increase in pressure.

When the velocity gradient at the surface becomes zero, the flow is said to have reached a separation point. Eventually, the separated-flow region on the back side of the cylinder becomes turbulent and random in motion.

The local Nusselt number for heat-transfer from a cylinder in cross flow is shown in Figure 14-92. At the lower Reynolds numbers a minimum point in the heat-transfer coefficient occurs at approximately the point of separation. The increase in heat transfer on the rear side of the cylinder is due to the turbulent eddy motion in separated flow. At the higher Reynolds numbers two minimum points occur. The first occurs at the point of transition from laminar to turbulent boundary layer, while the second minimum occurs when the turbulent boundary layer separates. There is rapid increase in heat transfer when the boundary layer becomes turbulent, and another when the increased eddy motion at separation is encountered.

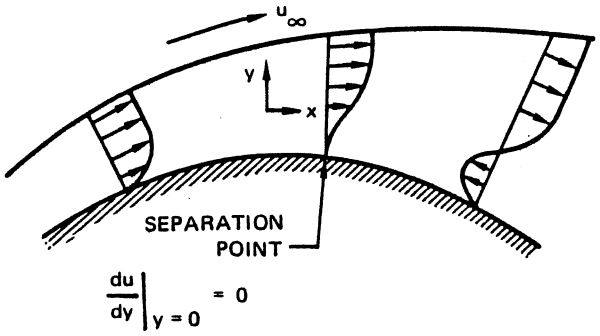

Figure 14-91. Velocity Distributions Indicating Flow Separation on a Cylinder in Cross Flow

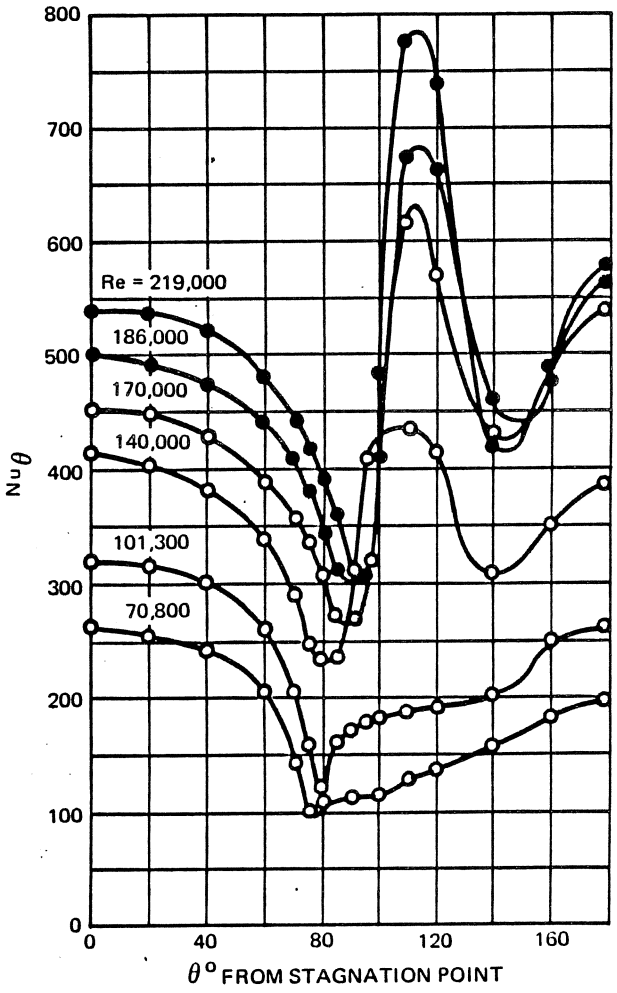

Figure 14-92. Local Nusselt Number for Heat Transfer From a Cylinder in Cross Flow

The average Nusselt number $\overline{Nu}_D$ for a circular cylinder in cross flow is obtained from empirical data:

$$\overline{Nu}_D = C\, Re_D\, Pr^{0.31} \qquad (199)$$

where C and n are given in Table 14-17 and Re_D is defined by equation 128 with the cylinder diameter D as the characteristic dimension. Re_D is based on the free stream velocity u_∞ approaching the cylinder. All properties are evaluated at the film temperature T_f, defined in equation 138.

Table 14-17. Coefficients for Calculating $\overline{Nu}_D$ for a Circular Cylinder in Cross Flow

Re_D	C	n
0.4–4	0.999	0.330
4–40	0.920	0.385
40–4,000	0.639	0.466
4,000–10,000	0.195	0.618
40,000–400,000	0.0258	0.805

For noncircular cylinders in cross flow, equation 199 may be used with the empirical constants C and n given in Table 14-18. $\overline{Nu}_D$ and Re_D are based on the diameter of a circular cylinder with surface area equal to that of the noncircular cylinder. The fluid properties are evaluated at the film temperature T_f, defined by equation 138.

14-4.8.2 Spheres

The heat-transfer characteristics for spherical bodies are important in problems involving the heating or cooling of spherical tanks in a stream of fluid. When the body has an irregular shape, the data for spheres will yield satisfactory results if the sphere diameter is replaced by an equivalent diameter; i.e., if D is taken as the diameter of a spherical body having the same surface area as the irregular body.

The average Nusselt number for heat transfer from a sphere to a flowing gas in the range $17 < Re_D < 150{,}000$ is:

$$\overline{Nu}_D = 0.37\, Re_D^{0.6} \qquad (200)$$

where the Reynolds number Re_D, defined by equation 128 is based on the free stream velocity u_∞ approaching the sphere. All properties are evaluated at the film temperature T_f, defined by equation 138. As the Reynolds number approaches zero, the Nusselt number approaches a constant value of two, which represents heat transfer by conduction through a stagnant layer adjacent to a sphere.

Table 14-18. Coefficients for Calculating $\overline{Nu}_D$ for Noncircular Cylinders in Cross Flow

CONFIGURATION	RANGE OF Re_D	n	C
→ ◇	5,000–100,000	0.588	0.249
→ □	5,000–100,000	0.675	0.103
→ ⬡	5,000–100,000	0.638	0.155
→ ◇	5,000–19,500	0.638	0.161
	19,500–100,000	0.782	0.389
→ |	4,000–15,000	0.731	0.230

For heat transfer from spheres to liquids in the range $1 < Re_D < 200{,}000$:

$$\overline{Nu}_D = \left[1.2 + 0.53\, Re_D^{0.54}\right] Pr^{0.3} \left(\frac{\mu}{\mu_w}\right)^{0.25} \qquad (201)$$

where all fluid properties are evaluated at free stream conditions, except μ_w, the viscosity at the wall temperature of the sphere.

14-5 HEAT TRANSFER WITH PHASE CHANGE

Heat transfer with boiling liquids or condensing vapors is a convection process involving a change in phase. Boiling heat transfer depends on many variables, including: surface roughness, surface wettability, latent heat of vaporization, pressure, vapor density, surface tension of the fluid, and the variables associated with single-phase convection. The boiling process is so complex that there are no general analytic equations which describe it. In contrast, the condensation process may be analyzed directly because it involves fewer variables and usually a laminar flow field.

This subsection describes the various physical mechanisms and regimes of boiling and condensation. Empirical correlations and analytic equations for the heat-transfer coefficients in the various regimes are presented in Table 14-19. Many of the empirical correlations cannot be regarded as general because they have not been verified for a variety of experiments, and they should be used with caution. These correlations are included because they provide insight in areas where general information is not available.

14-5.1 Fundamentals of Boiling Heat Transfer

14-5.1.1 Regimes of Boiling

a. Pool Boiling – The various regimes of pool boiling may be demonstrated by a simple system consisting of a heating surface submerged in a pool of water at the saturation temperature. A familiar example of pool boiling is heating a kettle of water on a stove. Figure 14-93 shows the relationship of the heating rate q/A to the degree of superheating ΔT_s.

$$\Delta T_s = T_w - T_{sat} \qquad (202)$$

where:

T_w = Temperature of heating surface, °R

T_{sat} = Liquid saturation temperature, °R

Table 14-19. Heat Transfer Coefficients for Boiling and Condensation

	Flow Type	Geometry	Valid Range	Equation
Boiling	Nucleate Pool Boiling	Arbitrary	$q/A \leq (q/A)_{max}$	$\bar{h}_b = 1.904 \times 10^{-9} \left[\frac{k_L \rho_L^{1.282} P^{1.75} g_c^{0.846}}{\sigma^{0.906} \mu_L^{0.626} g^{0.533}}\right]\left(\frac{C_L}{\rho_v h_{fg}}\right)^{1.5} \Delta T_s^{1.5}$
	Film Pool Boiling	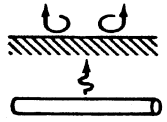	$q/A \geq (q/A)_{min}$ $P = 1$ ATM	$\bar{h}_{fb} = \left[0.37 + 0.28\left(\frac{g_c \sigma}{g D^2 \Delta\rho_f}\right)^{1/2}\right]\left(\frac{g \Delta\rho_f}{g_c \sigma}\right)^{1/8}\left(\frac{k_f^3 \rho_f \Delta\rho_f g\lambda'}{\mu_f}\right)^{1/4}\left(\frac{1}{\Delta T_s}\right)^{1/4}$ **
			Laminar $L < L_{cr}$*	$\bar{h}_{fb} = 0.943\left[\frac{k_f^3 \rho_f (\rho_L - \rho_f) g \lambda'}{L \mu_f \Delta T_s}\right]^{1/4}$ **
			Turbulent $L > L_{cr}$*	$\bar{h}_{fb} = 0.20 \rho_f C_{p_f}\left(\frac{g^2 L \mu}{\rho_f}\right)^{1/5}\left(\frac{\rho_L - \rho_f}{\rho_f}\right)^{2/5}\left(\frac{C_{p_f}}{h_{fg}}\right)^{1/5} \Delta T_s^{1/5}$
Condensation	Filmwise Condensation		Laminar $Re_f < 2000$	$\bar{h}_c = 0.943\left[\frac{\rho_L (\rho_L - \rho_v) g h_{fg}' k_L^3 \sin\theta}{\mu_L L (T_{sat} - T_w)}\right]^{1/4}$ #
		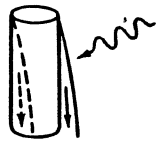	Turbulent $Re_f > 2000$	$h_x = 0.056\left(\frac{4\Gamma_c}{\mu_L}\right)^{0.2}\left(\frac{k_L^3 \rho_L^2 g}{\mu_L^2}\right)^{1/3} Pr_L^{1/3}$ ***
		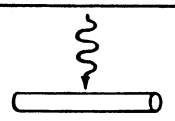	Laminar	$\bar{h}_c = 0.725\left[\frac{\rho_L (\rho_L - \rho_v) g h_{fg}' k_L^3}{D \mu_L (T_{sat} - T_w)}\right]^{1/4}$ #

*L_{cr} is obtained from EQ. 221.

**$\lambda' = \dfrac{(h_{fg} + 0.34\, C_{p_f} \Delta T_s)^2}{h_{fg}}$

***$\Gamma_c = \dfrac{\dot{w}}{W}\dfrac{g_c}{g}$, W = width

#$h_{fg}' = h_{fg} + \dfrac{3}{8} C_{p_L} (T_{sat} - T_w)$

Subscripts:
L = Liquid
v = Vapor
f = Film (Evaluate Properties at $T_f = \dfrac{(T_w + T_{sat})}{2}$)

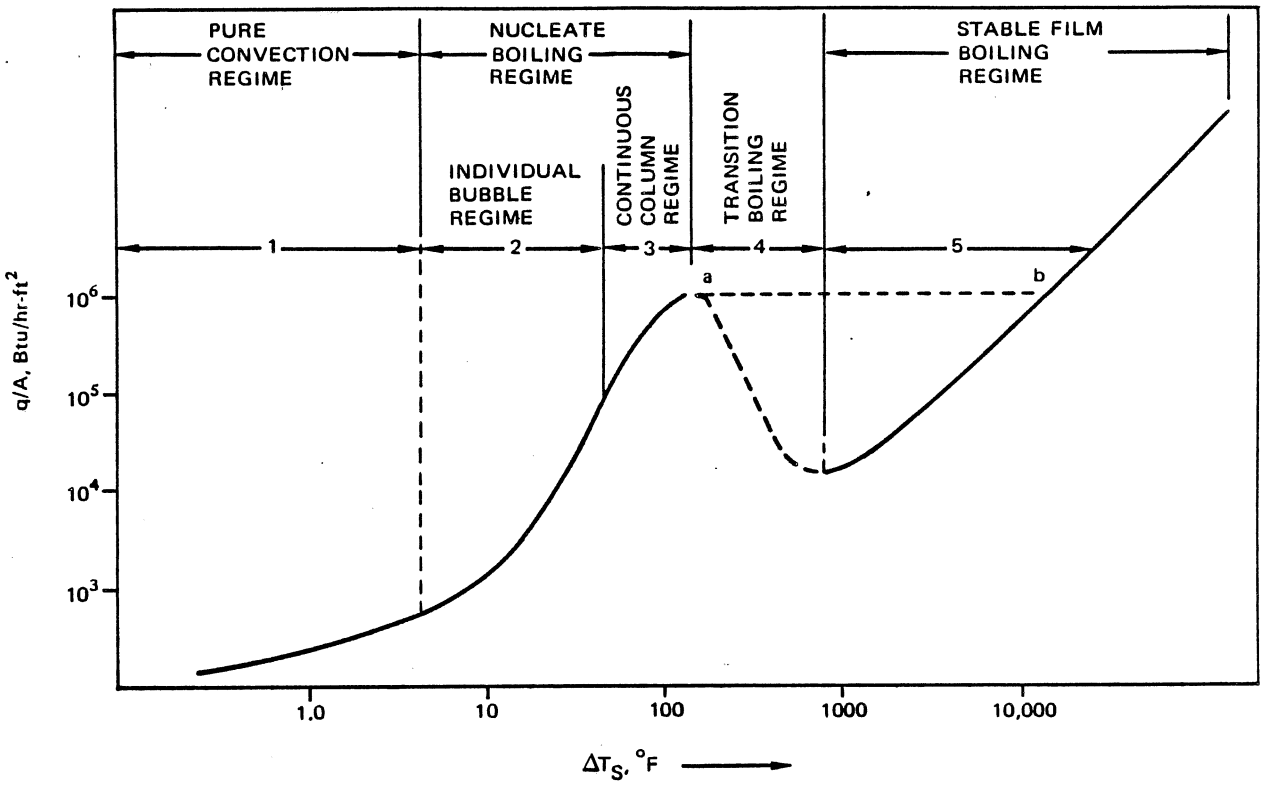

Figure 14-93. Typical Boiling Curves for a Pool of Water at Atmospheric Pressure

Free convection, rather than boiling, occurs as long as ΔT_s is only a few degrees. Currents circulate the superheated liquid and evaporation takes place at the free surface (Regime 1). As the surface temperature increases, the energy level of the liquid adjacent to the heating surface becomes so high that some molecules are transformed into vapor and form a low density bubble. This process occurs at surface irregularities (nucleation sites) such as pits and scratches. As the bubbles rise from the surface (Regime 2), hot liquid is pushed into the vacated volume and colder liquid rushes in to replace the hot liquid. This agitation of the fluid, rather than latent heat effects, accounts for the high heat transfer rates possible in the nucleate boiling regime.

As the surface temperature (or heat flux) increases further, the number of nucleation sites, the bubble formation rate at each site, and the rate of growth of the bubbles also increase. Eventually successive bubbles merge into more or less continuous columns of vapor (Regime 3). As the number of columns increases, a limiting condition (point a in Figure 14-93) is reached where the space between the columns can no longer accommodate the streams of liquid required to fill the void at the heating surface. This is the point of maximum heat flux.

If the heater temperature is the independent variable and the heat flux is dependent, for example, a surface heated by a condensing vapor, a further increase in ΔT_s will generate an unstable film which rapidly collapses and reforms on the heater surface (Regime 4). This film increases the thermal resistance and decreases the heat flux in the transition regime.

If the heat flux is the independent variable, for example, an electrically-heated wire, an increase in ΔT_s beyond the maximum heat flux value will result in a transition from nucleate to stable-film boiling. The film does not collapse and large bubbles originate at its outer surface (Regime 5). The heater will operate at a much higher temperature (corresponds to a jump from point a to b in Figure 14-93) and radiant heat transfer may become significant. If the heater material has a low melting point, the heater may fail before the high temperature (point b) in the stable-film boiling regime is reached. Thus, a, the point of maximum heat flux, is sometimes referred to as the burnout point.

b. Boiling With Forced Convection – Boiling with forced convection is similar to pool boiling, except that the bubbles are removed from the surface by

entrainment in the liquid flow, rather than by bouyant effects. In two-phase flow in a tube, the heat addition causes the quality, defined as the percentage of the total mass which is vapor, to increase along the tube.

Figure 14-94 illustrates the flow regimes encountered in two-phase flow through a duct. When the liquid at the duct wall is heated to the saturation temperature, bubbles form at nucleation sites and are carried into the mainstream (Regime A). The bubbly-flow regime occurs at very low quality. As the vapor volume fraction increases, individual bubbles begin to agglomerate and form slugs (Regime B).

In the annular-flow regime (Regime C), heat is transferred through the liquid film that covers the tube wall. Vaporization occurs at the liquid-vapor interface. The vapor core flows faster than the liquid film and contains liquid droplets.

At the transition to the mist-flow regime, the heat-transfer coefficient decreases sharply (Figure 14-94) because portions of the high conductivity liquid film are replaced by low conductivity vapor and thus, burnout may occur. The point of maximum heat flux is similar to that in pool boiling (Figure 14-93) in that it represents the beginning of the transition to film boiling.

The film boiling regime with convection is known as mist flow (Regime D). Most of the heat transfer in mist flow is from the dry wall to the vapor core. Vaporization of droplets takes place in the core, rather than at the wall.

14-5.1.2 Nucleation

Nucleate boiling involves two separate processes – the formation of bubbles (nucleation) and the subsequent growth and motion of these bubbles. The commonly accepted theory of nucleation suggests that bubbles originate at small conelike cavities in the heating surface. At equilibrium the pressure differential across a spherical bubble is:

$$\Delta P = P_V - P_L = \frac{2\sigma}{r} \qquad (203)$$

where:

P_V = Pressure of the vapor, lb/ft^2

P_L = Pressure of the liquid, lb/ft^2

σ = Liquid surface tension, lb/ft

r = Radius of bubble (cavity), ft

For a bubble in thermal equilibrium, the liquid and vapor temperatures are equal, and the vapor is saturated. The liquid, which is at a pressure less than that of the vapor, must be superheated. The amount of superheating that exists for a bubble of radius r in equilibrium is:

$$(T_L - T_{sat})_{equil} = \frac{2\,R_V T_{sat}^{\,2}\,\sigma}{h_{fg}\,J\,P_L\,r} \qquad (204)$$

where:

T_L = Liquid temperature, °R

T_{sat} = Saturation temperature at liquid pressure, °R

R_V = Gas constant of the vapor, lb-ft/lb°R

h_{fg} = Latent heat of vaporization, Btu/lb

J = Mechanical equivalent of heat
= 778 ft-lb/Btu

If $T_L - T_{sat}$ is greater than $(T_L - T_{sat})_{equil}$, a bubble of radius r will grow; if smaller, the bubble will collapse. Thus, the onset of nucleation (minimum superheat required) can be predicted from equation 204 for a conelike cavity if the radius r is known.

Inert, noncondensable gas molecules are usually present in the liquid. If, in addition to the vapor at P_V, an inert gas at partial pressure P_g is present in a bubble at equilibrium, equations 203 and 204 are modified as follows:

$$P_V - P_L = \frac{2\sigma}{r} - P_g \qquad (205)$$

$$(T_L - T_{sat})_{equil} = \frac{R_V\,T^2_{sat}}{h_{fg}\,J\,P_L}\left(\frac{2\sigma}{r} - P_g\right) \qquad (206)$$

Equation 206 indicates that less liquid superheat is required when noncondensable gas is present in the bubble.

14.5.1.3 Bubble Growth and Motion

In a superheated liquid, a bubble grows by heat conduction to the liquid-vapor interface, with resulting evaporation into the bubble. The radius of the growing bubble is:

$$r = \sqrt{\pi (k\rho\, C_p)_L\, t}\left(\frac{T_L - T_v}{h_{fg}\,\rho_V}\right) \qquad (207)$$

where:

r = Bubble radius, ft

t = Growth time, sec

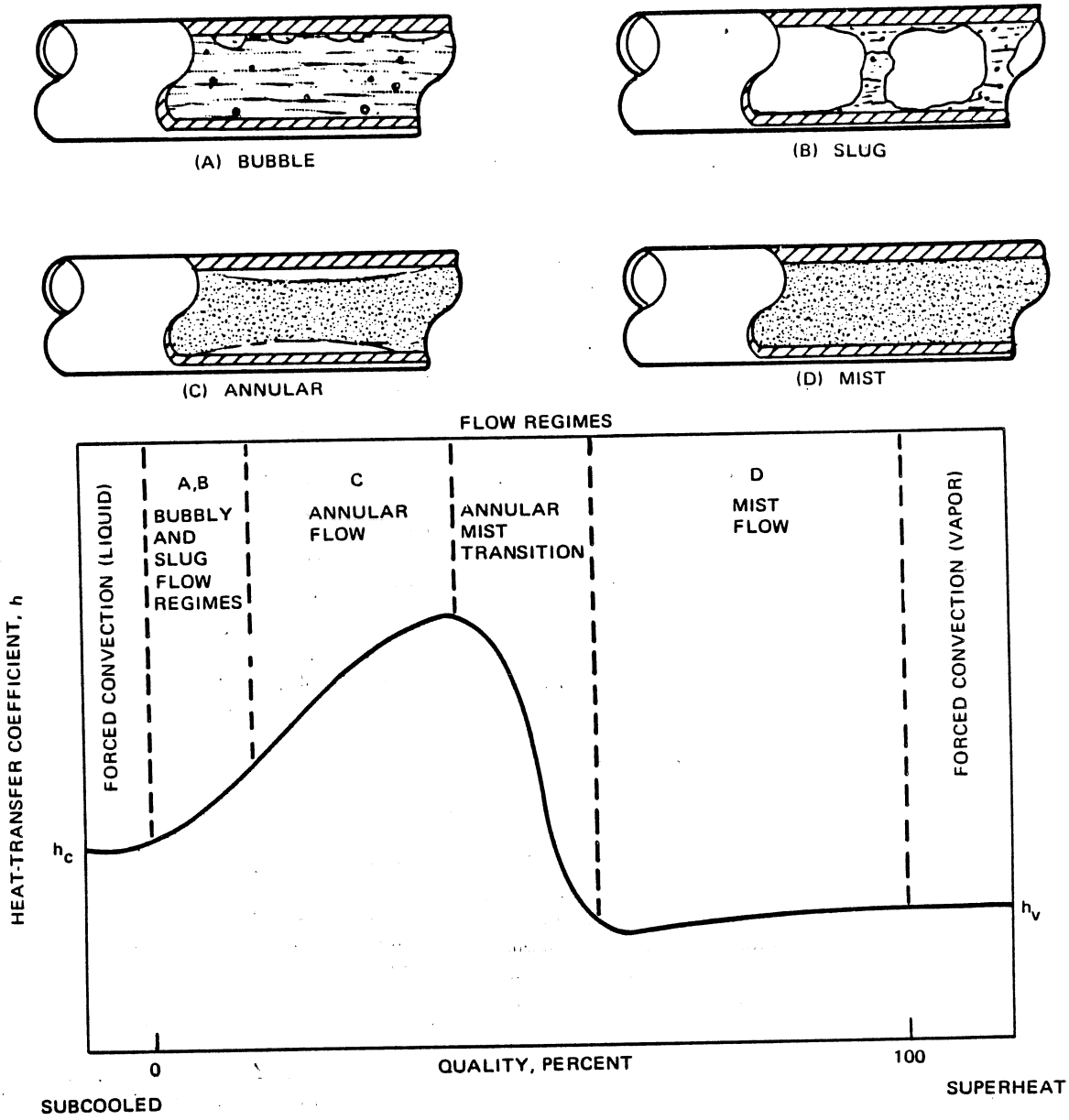

Figure 14-94. Characteristics of Forced-Convection Vaporization – Heat-Transter Coefficients Versus Quality and Types of Flow Regimes

k = Thermal conductivity, Btu/sec-ft-°R

ρ = Density, lb/ft^3

C_p = Constant pressure specific heat, Btu/lb-°R

and subscripts v and L denote vapor and liquid. The rate of bubble growth $\dot{r}$ in ft/sec is:

$$\dot{r} = \frac{\pi}{2r}\left(\frac{\sqrt{(k\rho\, C_p)_L}\,(T_L - T_v)}{\rho_v\, h_{fg}}\right)^2 \qquad (208)$$

where r is obtained from equation 207.

The bubble diameter D_b at detachment from the heating surface is:

$$D_b = C_d\,\beta\sqrt{\frac{2\,g_c\,\sigma}{g\,(\rho_L - \rho_v)}} \qquad (209)$$

where:

C_d = Constant = 0.0148 for H_2O and H_2 bubbles

β = Bubble contact angle, measure through the liquid (as shown in Figure 14-95), degrees

g_c = Conversion factor = 32.2 ft/sec^2

Bubbles issue at active nucleation sites in a steady stream. A bubble grows while attached to the surface for time t_c; then a delay time t_d elapses before the next bubble forms. The frequency f in 1/sec times D_b in ft is:

$$fD_b = 1.18\left(\frac{t_c}{t_c + t_d}\right)\left[\frac{g\,g_c\sigma\,(\rho_L - \rho_v)}{\rho_L^{\,2}}\right]^{1/4} \qquad (210)$$

Usually $t_c \cong t_d$. In this case, the bubble center travels a distance D_b in time $(t_c + t_d)$ or (1/f); hence, bubble velocity is:

$D_b/(1/f)$

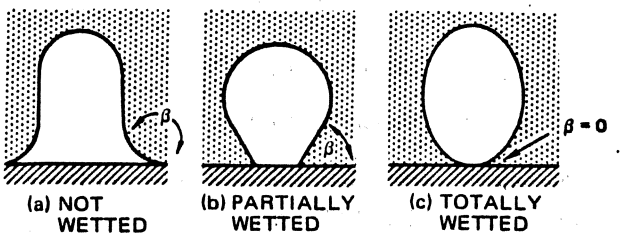

Figure 14-95. The Effect of Surface Wettability on the Bubble Contact Angle

or

$$V_b \cong fD_b \qquad (211)$$

where:

V_b = Bubble velocity, ft/sec

In nucleate boiling, fD_b is a function of pressure, but not heat flux q/A. The relation between q/A and the number of active nucleation sites n on a surface is given by:

$$q/A \sim n^m \qquad (212)$$

where m = 1 at low q/A, but decreases to around 1/2 at high q/A.

14-5.1.4 Pool Boiling Heat Transfer

The influence of certain variables on the heat transfer rate in nucleate pool boiling may be determined by examining equation 206. This expression, representing equilibrium conditions, provides the minimum superheat ($\Delta T_s = T_L - T_{sat}$) required to activate a cavity of radius r.

Increasing the superheat permits smaller and smaller surface cavities (r) to become active nucleation sites, thus increasing liquid agitation and heat transfer q/A. Similarly, increasing surface roughness (r) reduces the superheat required and shifts the q/A versus ΔT_s curve (Figure 14-93) to the left. The heat transfer performance of surfaces that have been in service for long periods is often lowered by mild oxidation which reduces cavity sizes and adds a layer of low conductivity scale.

Equation 206 indicates that increased system pressure P or the existence of inert, noncondensable gas P_g lowers the superheat required to activate a cavity of given size. Thus the q/A versus ΔT_s curve is shifted to the left.

Surface geometry may be significant at low ΔT_s where convection effects are dominant. However, in the nucleate boiling regime, surface geometry (flat or curved, vertical or horizontal, etc.) has very little influence on heat transfer.

In a subcooled liquid, local boiling may occur at the heater surface. The bubbles increase in number while their size and average lifetime decrease with decreasing bulk temperature. The liquid agitation is more intense than in a saturated pool and much larger heat fluxes can be attained before burnout occurs.

The gravity level determines the strength of the bouyant forces that remove bubbles from the heating surface. At zero g, nucleate boiling stops, and a large bubble of vapor surrounds the surface. At high g levels, the fluid

agitation increases significantly in Regimes 1 and 2 (Figure 14-93) and the q/A versus ΔT_s curve is shifted to the left.

14-5.2 Correlation of Boiling Heat Transfer Data

Due to the complexity of the boiling process, no analytical heat transfer solutions have been developed. Most heat transfer information is expressed in terms of correlations (empirical equations) that are not general. These equations may be inaccurate for some applications because the correlations have not been verified for a range of cases. Experimental data for a particular system should be used when available.

14-5.2.1 Nucleate Pool Boiling

Surface effects, such as wettability and roughness, limit the repeatability of pool boiling experiments. Variations due to surface effects may be as large as 25 percent. When experimental data is lacking, correlations that attempt to account for surface effects can be used, if information about the particular fluid-surface combination is available. General correlations may be used if their limitations are recognized.

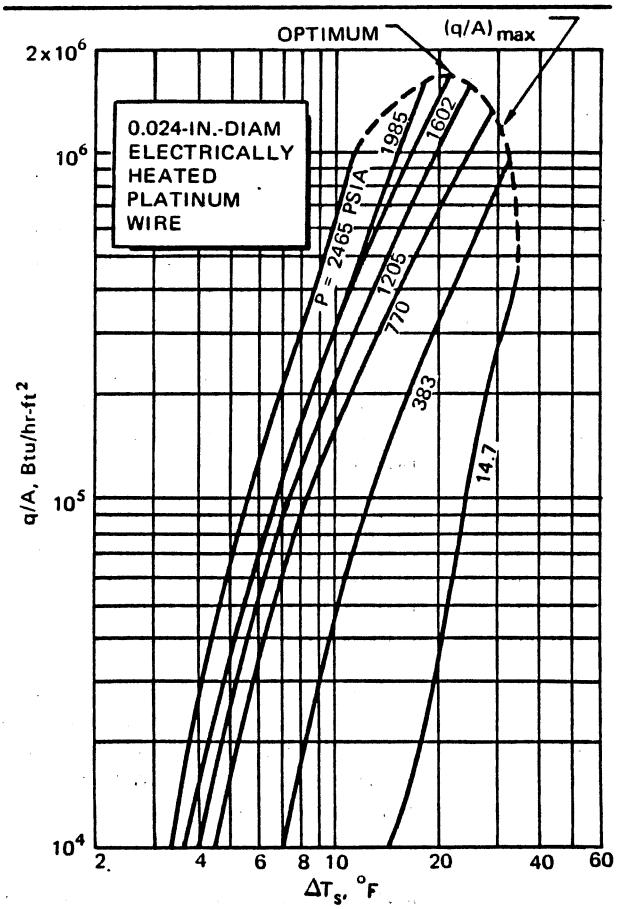

Figure 14-96. Heat Flux Versus Degree of Superheating for Nucleate Boiling of Water

Experimental data for nucleate boiling of water heated by a platinum wire is shown in Figure 14-96. The heating rate q/A is a function of ΔT_s and the pressure, and is relatively insensitive to heating surface geometry. The dotted line represents the peak (maximum) heat fluxes at various pressures. The optimum heat flux is the largest of the various peak heat fluxes.

Nucleate pool boiling (and film pool boiling) correlations for the cryogenic liquids, O_2, N_2, H_2 and He, are presented in Figures 14-97 through 14-100. The family of curves shown for the nucleate boiling regime represents the q/A versus ΔT_s relation for various pressures. The surface geometry has little effect on the heat transfer rate. In contrast, the film boiling correlation is presented as a function of geometry at atmosphere pressure. The critical heat fluxes, maximum in nucleate boiling and minimum in film boiling, are designated by small circles.

One correlation which attempts to account for surface effects requires an experimentally determined coefficient C_{sf} for each fluid-surface combination:

$$\frac{C_L \Delta T_s}{h_{fg} Pr^{1.7}} = C_{sf} \left[\frac{q/A}{\mu_L h_{fg}} \sqrt{\frac{g_c \sigma}{g(\rho_L - \rho_v)}} \right]^{0.33} \quad (213)$$

where:

C_L = Specific heat of saturated liquid, Btu/lb-°R

ΔT_s = Degree of superheating, °R

h_{fg} = Latent heat of vaporization, Btu/lb

q/A = Heat flux, Btu/hr-ft²

μ_L = Viscosity of liquid, lb/hr-ft

σ = Surface tension, lb/ft

g = Acceleration of gravity, ft/hr²

g_c = Conversion constant = 4.17×10^8 ft/hr²

ρ_L = Liquid density, lb/ft²

ρ_v = Vapor density, lb/ft³

The coefficient C_{sf} depends on surface roughness and wettability. Table 14-20 provides values of C_{sf} for various fluid-surface combinations. In the absence of experimental data C_{sf} is taken as 0.015 for cryogenics and 0.013 for noncryogenics.

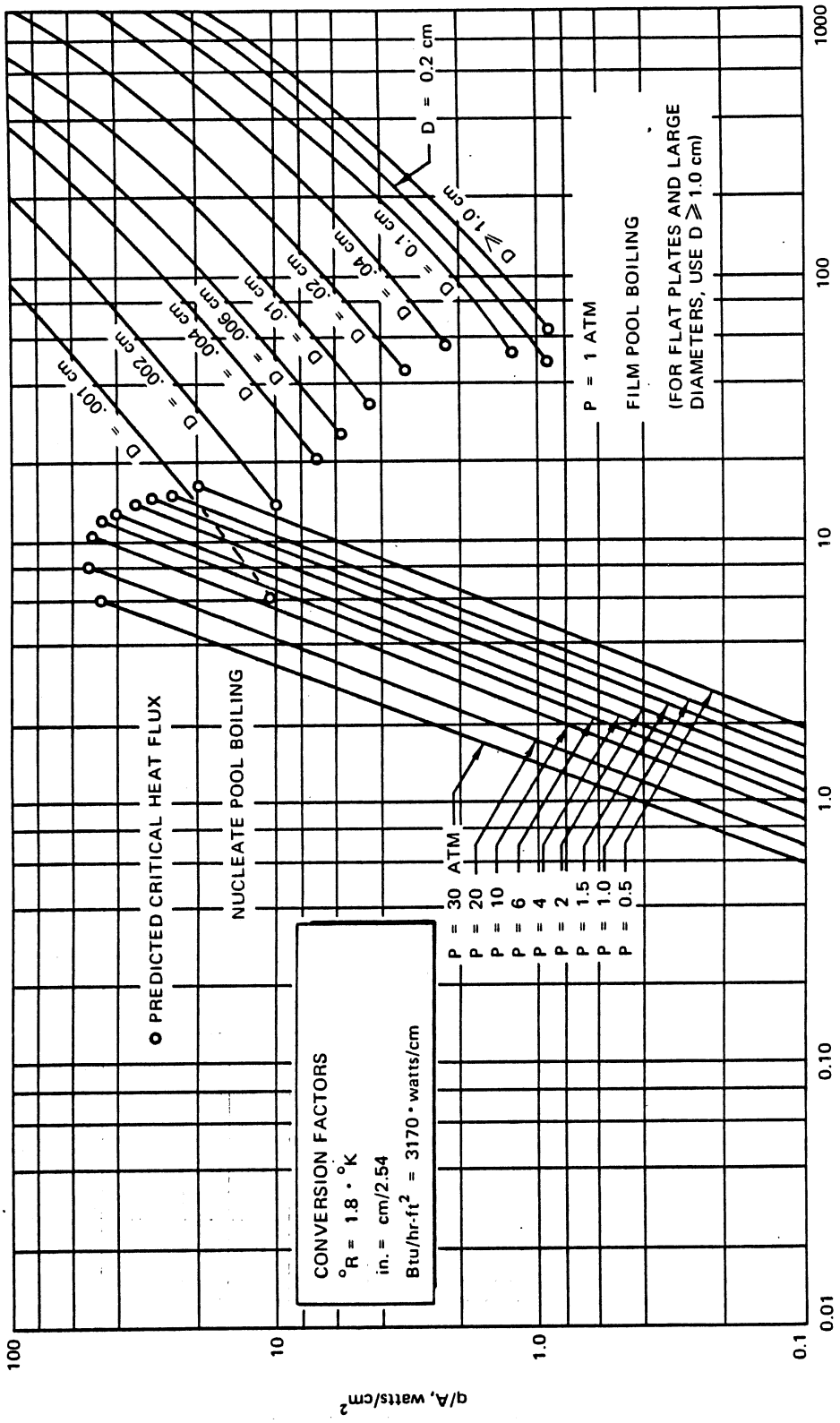

Figure 14-97. Predicted Nucleate and Film Pool Boiling Correlations for Oxygen

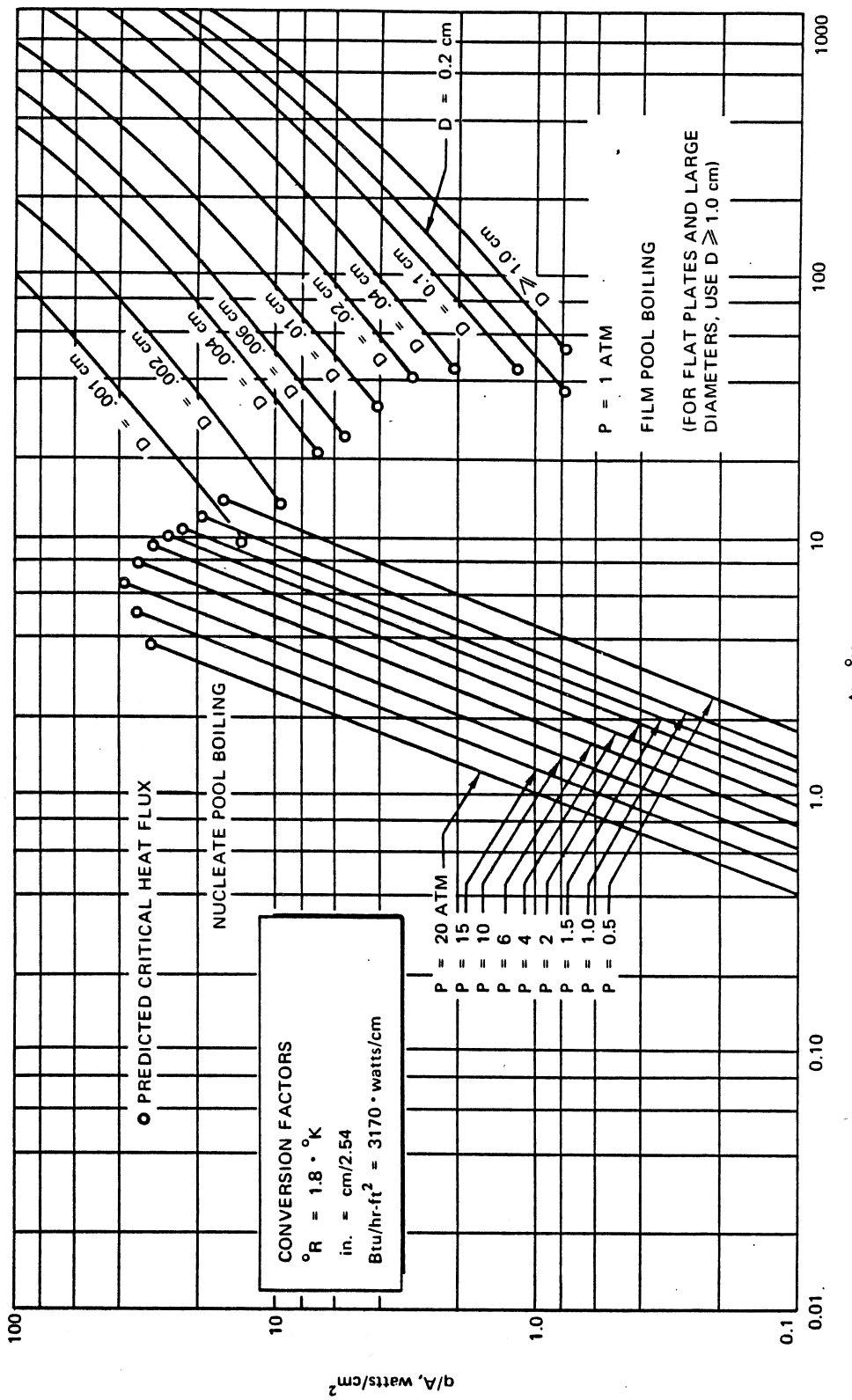

Figure 14-98. Predicted Nucleate and Film Pool Boiling Correlations for Nitrogen

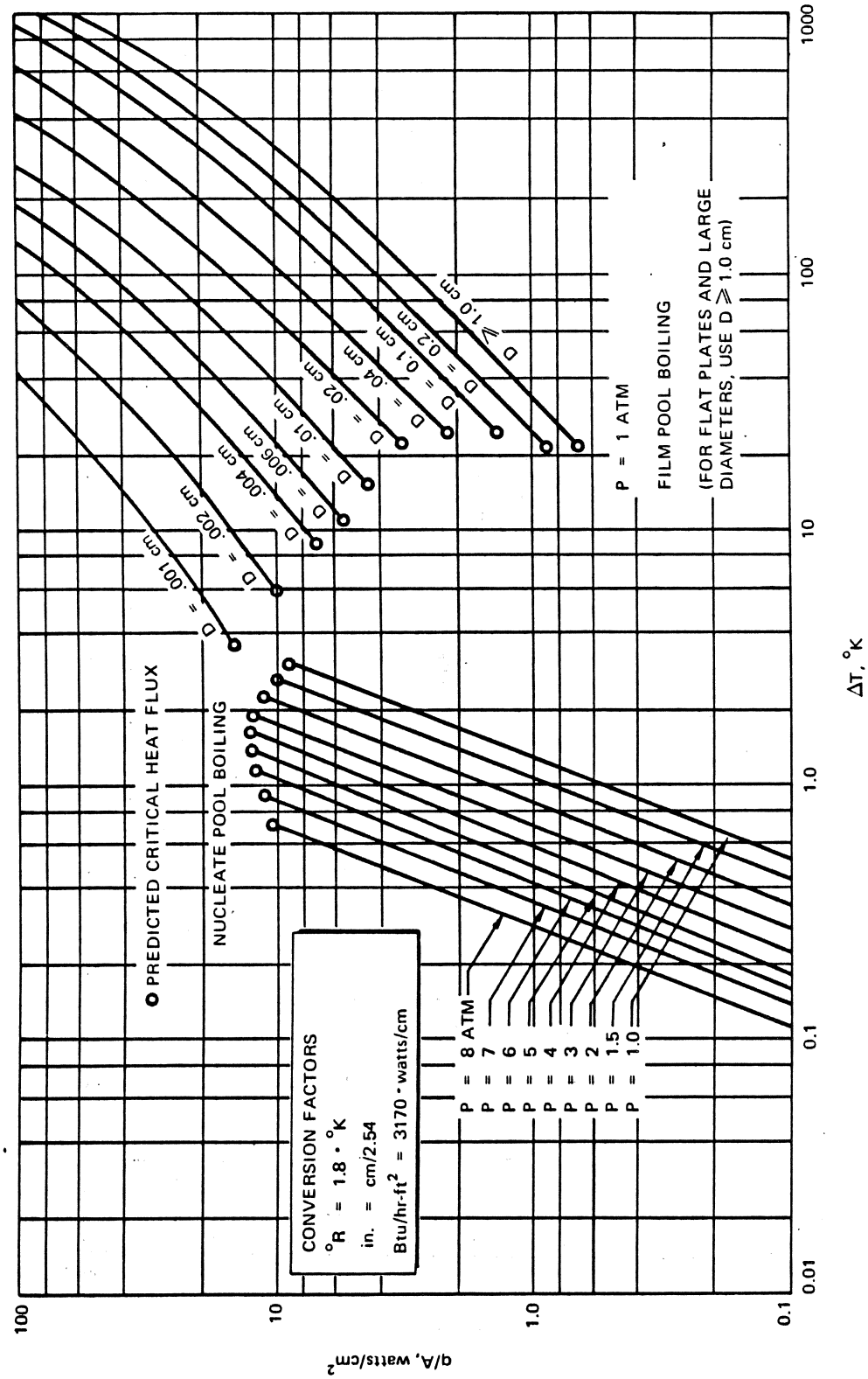

Figure 14-99. Predicted Nucleate and Film Pool Boiling Correlations for Hydrogen

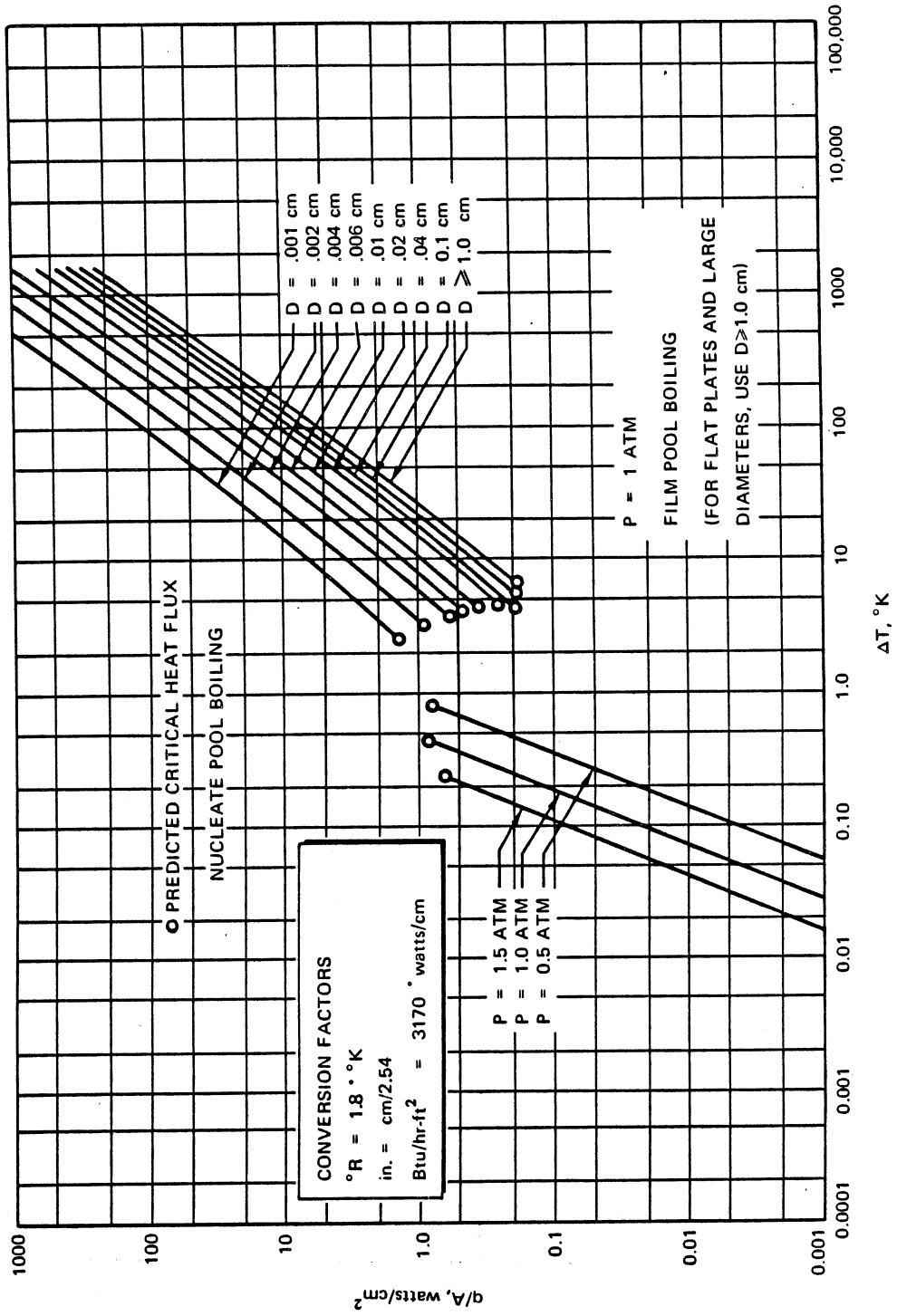

Figure 14-100. Predicted Nucleate and Film Pool Boiling Corrections for Helium

Table 14-20. Values of the Coefficient Csf in Equation 213 for Various Liquid-Surface Combinations

Fluid-Heating Surface Combination	C_{sf}
Water-Copper	0.013
Carbon Tetrachloride-Copper	0.013
35% K_2CO_3–Copper	0.0054
n-Butyl Alcohol-Copper	0.00305
50% K_2CO_3–Copper	0.00275
Isopropyl Alcohol-Copper	0.00225
n-Pentane-Chromium	0.015
Water-Platinum	0.013
Benzene-Chromium	0.010
Water-Brass	0.0060
Ethyl Alcohol-Chromium	0.0027
Hydrogen-Karma Alloy	0.0147

The boiling heat-transfer coefficient $\bar{h}_b$ is obtained from equation 213 by substituting $\bar{h}_b \Delta T_s$ for q/A and rearranging

$$\bar{h}_b = \frac{k_L^{5.1}}{C_{sf}^{3}\, C_L^{2.1}\, \mu_L^{4.11}\, h_{fg}^{2}} \sqrt{\frac{g\,(\rho_L - \rho_v)}{g_c\,\sigma}}\; \Delta T_s^{2} \qquad (214)$$

where:

$\bar{h}_b$ = Boiling heat-transfer coefficient

= $\frac{q/A}{\Delta T_s}$, Btu/hr-ft^2-°R

k_L = Thermal conductivity of liquid, Btu/hr-ft-°R

The following dimensionless equation provides a good general correlation for most of the available boiling heat transfer data.

$$\frac{\bar{h}_b}{k_L}\sqrt{\frac{g_c\,\sigma}{g\rho_L}} = 3.25 \times 10^{-4} \left[\frac{q/A}{\mu_L\, h_{fg}}\,\frac{\rho_L}{\rho_v}\sqrt{\frac{g_c\,\sigma}{g\rho_L}}\right]^{0.6} Pr^{0.6} \left\{\frac{g\rho_L^{2}}{\mu_L^{2}}\left(\frac{g_c\,\sigma}{g\rho_L}\right)^{3/2}\right\}^{0.125} \left(\sqrt{\frac{P}{\sigma g \rho_L / g_c}}\right)^{0.7} \qquad (215)$$

where:

P = System pressure, lb/ft^2

Analogous to convection, the term on the left of equation 215 may be considered a Nusselt number and the first bracketed term, a Reynolds number. By substituting $\bar{h}_b \Delta T_s$ for q/A and rearranging:

$$\bar{h}_b = 1.904 \times 10^{-9} \left[\frac{k_L \rho_L^{1.282}\, P^{1.75}\, g_c^{0.846}}{\sigma^{0.906}\, \mu_L^{0.626}\, g^{0.533}}\right] \left(\frac{C_L}{\rho_v\, h_{fg}}\right)^{1.5} \Delta T_s^{1.5} \qquad (216)$$

Results obtained from these correlations must be checked to verify that they are included in the nucleate boiling regime. Equations for the maximum heat flux are presented in paragraph 14-5.2.2. If the calculated heat flux is greater than the maximum heat flux, operation in the transition or film boiling regime is indicated and the correlations in this paragraph are not applicable.

14-5.2.2 Maximum Heat Flux

The maximum heat flux (burnout point) is more predictable than the nucleate boiling mechanism because it is insensitve to surface conditions. The limiting factor, the stability of the vapor columns, is basically a hydrodynamic consideration. The maximum heat flux for a saturated liquid, in Btu/ft^2-hr, is:

$$(q/A)_{max} = 0.13\, \rho_v\, h_{fg} \left[\frac{\sigma(\rho_L - \rho_v) g\, g_c}{\rho_v^{2}}\right]^{1/4} \left(\frac{\rho_L}{\rho_L + \rho_v}\right)^{1/2} \qquad (217)$$

Pressure affects the maximum heat flux because it changes the vapor density and the boiling point, which determines the heat of vaporization and the surface tension. Consequently, for each liquid, there exists a certain pressure which yields the highest maximum heat flux. This optimum heat flux occurs at a reduced pressure ($P/P_{critical}$) of 0.3.

The points of maximum (or critical) heat flux at various pressures for water (experimental), and for O_2, N_2, H_2 and He (based on equation 217) are shown in Figures 14-96 through 14-100. The maximum heat flux correlation (equation 217) is not valid for reduced pressures greater than 0.6 and this range is not included in Figures 14-97 through 14-100.

Equation 217 applies to pool boiling in a saturated liquid. The maximum heat flux for a subcooled liquid may be significantly greater than for the saturated liquid and may be obtained from:

$$(q/A)_{max} = (q/A)_{max\ sat} \left\{1 + \left[\frac{2k_L\,(T_{sat} - T_L)}{\sqrt{\pi\, a_L\, \tau}}\right]\frac{24}{\pi\, h_{fg}\, \rho_v} \left[\frac{\rho_v^{2}}{\sigma g g_c (\rho_L - \rho_v)}\right]^{1/4}\right\} \qquad (218)$$

where:

$$\tau = \frac{\pi}{3}\sqrt{2\pi}\left[\frac{g_c\,\sigma}{g\,(\rho_L-\rho_v)}\right]^{1/2}\left[\frac{\rho_v^{\,2}}{\sigma\,g\,g_c\,(\rho_L-\rho_v)}\right]^{1/4}, \text{ hr}$$

a_L = Thermal diffusivity of the liquid, ft^2/hr

$(q/A)_{max\ sat}$ is obtained from equation 217.

14-5.2.3 Film Pool Boiling

Since film boiling is inefficient and requires large temperature differences, it is used only when circumstances make it unavoidable. An example is the use of cryogenic propellants to cool rocket engines.

The heat-transfer coefficient $\bar{h}_{fb}$ for film boiling with a laminar film (horizontal wires, tubes or horizontal flat surfaces) is obtained from the following dimensionless correlation

$$\bar{h}_{fb}\left(\frac{g_c\sigma}{g\Delta\rho_f}\right)^{1/8}\left(\frac{\mu_f\,\Delta T_s}{k_f^{\,3}\,\rho_f\,\Delta\rho_f\,g\,\lambda'}\right)^{1/4} = 0.37 + 0.28\left(\frac{g_c\sigma}{g\,D^2\,\Delta\rho_f}\right)^{1/2} \qquad (219)$$

where:

$\bar{h}_{fb}$ = Film boiling heat-transfer coefficient, $Btu/hr\text{-}ft^2\text{-}^\circ R$

$\Delta\rho_f$ = $\rho_L - \rho_f$, lb/ft^3

ρ_f = Density of vapor film, lb/ft^3

k_f = Thermal conductivity of vapor film, $Btu/hr\text{-}ft\text{-}^\circ R$

μ_f = Viscosity of vapor film, lb/hr-ft

D = Wire diameter (for flat plates or $D > 0.03$ ft, use D = 0.03 ft), ft

λ' = $\dfrac{(h_{fg} + 0.34\,C_{p_f}\,\Delta T_s)^2}{h_{fg}}$, Btu/lb

C_{p_f} = Specific heat of vapor film, $Btu/lb\text{-}^\circ R$

The subscript f indicates vapor properties evaluated at the film temperature,

$$T_f = \frac{T_w + T_{sat}}{2}$$

If q/A ($= \bar{h}_{fb}\,\Delta T_s$) or ΔT_s is less than the minimum (critical) value, presented in the next paragraph, heat transfer does not take place in the film boiling regime and equation 219 is not applicable.

The heat transfer rate q/A for film boiling depends on the surface geometry and ΔT_s. Figures 14-97 through 14-100 present the film boiling characteristics, based on equation 219, for wires of various sizes in O_2, N_2, H_2 and He at atmospheric pressure. The variation of q/A with pressure is uncertain. For flat plates or $D > 1.0$ cm (0.03 ft), the $D \geq 1.0$ cm curve is used. The minimum (or critical) heat fluxes are designated by small circles.

For vertical surfaces with a laminar film,

$$\bar{h}_{fb} = 0.943\left[\frac{k_f^{\,3}\,\rho_f\,(\rho_L-\rho_f)\,g\,\lambda'}{L\,\mu_f\,\Delta T_s}\right]^{1/4} \qquad (220)$$

where:

L = Height of surface, ft

The vapor film becomes turbulent at the critical height L_{cr} given by:

$$L_{cr} = \frac{50\,\mu_f\,\lambda'}{k_f\,\Delta T_s}\left[\frac{200\,\mu_f^{\,2}}{g\,\rho_f\,(\rho_L-\rho_f)}\right]^{1/3} \qquad (221)$$

For surfaces of height larger than L_{cr} the average heat-transfer efficient is:

$$\bar{h}_{fb} = 0.20\,\rho_f\,C_{p_f}\left(\frac{g^2\,L\mu}{\rho_f}\right)^{1/5}\left(\frac{\rho_L-\rho_f}{\rho_f}\right)^{2/5}\left(\frac{C_{p_f}\,\Delta T_s}{h_{fg}}\right)^{1/5} \qquad (222)$$

The heat-transfer coefficient given in equation 219 does not include the the effects of radiation, which may be significant at the high temperature differences experienced in film boiling. Radiation increases the vapor film thickness and decreases the boiling heat transfer. The coefficient $\bar{h}_{fb}$ is influenced by the radiant-heat-transfer coefficient $\bar{h}_r$. When radiation is appreciable, the overall conductance $\bar{h}$ can be obtained from:

$$\bar{h} = \bar{h}_{fb}\,(\bar{h}_{fb}/\bar{h})^{1/3} + \bar{h}_r \qquad (223)$$

where:

$$\bar{h}_r = F_{1-2}\left[\frac{\sigma\,(T_1^{\,4} - T_2^{\,4})}{T_1 - T_2}\right] \qquad (224)$$

where:

F_{1-2} = Gray-body shape factor

σ = Stefan-Boltzmann constant = 0.1714×10^{-8} $Btu/hr\text{-}ft^2\text{-}^\circ R^4$

T_1 = Wall temperature, °R

T_2 = Liquid saturation temperature, °R

$\Delta T_s = T_1 - T_2$, °R

A trial and error solution is required for equation 223.

14-5.2.4 Minimum Heat Flux

The minimum heat flux required to maintain stable film boiling is:

$$(q/A)_{min} = 0.09\,\rho_f\,h_{fg}\left[\frac{g\,\rho_L\,\rho_v}{\rho_L+\rho_v}\right]^{1/2}\left[\frac{g_c\sigma}{g\,(\rho_L-\rho_v)}\right]^{1/4} \quad (225)$$

The temperature difference at the minimum heat flux point is:

$$\Delta T_{s_{min}} = 0.127\,\frac{\rho_f\,h_{fg}}{k_f}\left[\frac{g\,(\rho_L-\rho_v)}{\rho_L+\rho_v}\right]^{2/3}\left[\frac{g_c\sigma}{g\,\rho_L\,\rho_v}\right]^{1/2}\left[\frac{\mu_f}{g_c\,(\rho_L-\rho_v)}\right]^{1/3} \quad (226)$$

where the subscripts v and f indicate vapor properties evaluated at

$$T_{sat} \text{ and } T_f = \frac{T_w + T_{sat}}{2}, \text{ respectively.}$$

For ΔT_s or q/A less than minimum values, the boiling will occur in the transition or nucleate regimes. Heat fluxes based on the equations in paragraph 14-5.2.3 should be compared with q/A_{min} (equation 225) to verify that they are included in the film boiling regime.

14-5.2.5 Boiling With Forced Convection

The heat transfer characteristics of forced convection boiling play an important part in the design of rocket engine cooling and preconditioning systems, environmental control systems for spacecraft, and nuclear reactors. Due to the great number of variables and the complexity of the various two-phase flow patterns which occur as the quality increases due to vaporization, it is not possible to predict all of the characteristics of this process quantitatively.

The following sections present correlations for boiling with forced convection for the various flow regimes in paragraph 14-5.1.1 (b). The results should be recognized as approximate.

a. Bubbly-Flow Regime – The fluid quality (percentage of total mass which is vapor) is less than one percent in the bubbly-flow regime. No net vaporization occurs because the bulk is subcooled and condenses bubbles formed at the wall. The total heat flux, obtained by "superimposing" the contributions of nucleate boiling and forced convection, is:

$$q/A = (q/A)_{fc}\left\{1+\left[\frac{(q/A)_b}{(q/A)_{fc}}\right]^2\right\}^{1/2} \quad (227)$$

where:

$(q/A)_b$ = Nucleate boiling heat flux
= $\bar{h}_b \Delta T_s$ ($\bar{h}_b$ is obtained from equation 214), Btu/hr-ft²

$(q/A)_{fc}$ = Forced convection heat flux
= $\bar{h}_c\,(T_w - T_L)$, Btu/hr-ft²

Note that the liquid bulk temperature T_L, not T_{sat}, is used in the temperature difference for the $(q/A)_{fc}$ term. The forced convection heat transfer coefficient $\bar{h}_c$ is obtained from:

$$\bar{h}_c = 0.023\,\frac{k_L}{D}\,Re_D^{0.8}\,Pr^{0.4} \quad (228)$$

where:

D = Tube diameter, ft

k_L = Thermal conductivity of the liquid, Btu/hr-ft-°R

Re_D = DG/μ_L = Diameter Reynolds No.

G = Mass flow rate, lb/sec-ft²

μ_L = Liquid viscosity, lb/sec-ft

The properties in equation 228 are evaluated at the bulk temperature.

No correlations are available for the slug flow regime.

b. Annular-Flow Regime – In the annular-flow regime the bulk is no longer subcooled and significant vaporization occurs, with the quality increasing along the duct. A liquid film totally wets the wall, and the two-phase core contains many liquid droplets. The heat-transfer coefficient $\bar{h}_{af}$ for the

annular-flow regime is obtained with a superposition of boiling and forced convection effects. The following correlation has shown good agreement with experimental data over a quality range of 1 to 70 percent.

$$\bar{h}_{af} = \bar{h}_c F + \bar{h}_b S \quad (229)$$

where:

F,S = Correction factors (described below)

$\bar{h}_c$ = Forced convection coefficient given by equation 228, Btu/hr-ft^2-°R

$\bar{h}_b$ = Boiling heat transfer coefficient given by:

$$\bar{h}_b = 0.00122 \left[\frac{k_L^{0.79} C_{p_L}^{0.45} \rho_L^{0.49} g_c^{0.25} \Delta P^{0.75} \Delta T_s^{0.24}}{\sigma^{0.5} \mu_L^{0.29} h_{fg}^{0.24} \rho_v^{0.24}}\right] \quad (230)$$

where:

ΔP = Saturation pressure difference corresponding to ΔT_s, lb/ft^2

F is a two-phase correction given as a function of the Martinelli parameter X_{tt} in Figure 14-101. It accounts for an increase in forced convection turbulence due to the presence of vapor. The Martinelli parameter is defined as:

$$X_{tt} = \left(\frac{1-x}{x}\right)^{0.9} (\rho_L/\rho_v)^{0.5} (\mu_L/\mu_v)^{0.1} \quad (231)$$

where:

x = Mass fraction of vapor (quality)

S is a suppression factor given as a function of $Re_L F^{1.25}$ in Figure 14-102. It accounts for the suppression of bubble growth due to flow. The single-phase Reynolds Number is defined as

$$Re_L = \frac{DG(1-x)}{\mu_L} \quad (232)$$

where:

D = Tube diameter, ft

G = Mass flow rate of mix, lb/sec-ft^2

μ_L = Liquid viscosity evaluated at bulk temperature, lb/sec-ft

c. Maximum Heat Flux With Forced Convection – The heat-transfer coefficient decreases sharply in the annular-mist transition regime (Figure 14-94) as the fluid layer at the wall changes from high conducting liquid to low conducting vapor. Correlations for the maximum heat flux (burnout point) must be treated with caution because they were obtained under specific flow conditions and may not be applicable to other configurations and fluids. The correlations are based on empirical data for noncryogenics.

Figure 14-103 presents a complex relation that correlates burnout heat flux data as a function of reduced pressure with ±33 percent accuracy. The correlation is based on data for water and organic liquids at velocities from 0 to 100 ft/sec, at subcooling from 0 to 280°R, and at qualities from 0 to 70 percent.

The factor F in Figure 14-103 is:

$$F = 1 + 0.0144\left[\frac{\rho_L C_L (T_{sat} - T_b)}{\rho_v h_{fg}}\right] + 10^{-6}\left(\frac{VD\rho_L}{\mu_L}\right) + 0.5 \times 10^{-3}\left[\left(\frac{VD\rho_L}{\mu_L}\right)\left(\frac{\rho_L C_L (T_{sat} - T_b)}{h_{fg}\rho_v}\right)\right]^{0.5} \quad (233)$$

where:

C_L = Specific heat of saturated liquid, Btu/lb-°R

$VD\rho_L/\mu_L = DG/\mu_L$ = Reynolds number

T_{sat} = Temperature of duct surface, °R

T_b = Bulk temperature, °R

h_g = Saturated vapor enthalpy, Btu/lb

h_b = Bulk enthalphy of the fluid (which may saturated, subcooled, or two-phase with X < 70 percent), Btu/lb

Another correlation is based on empirical data for water, at pressures from 1 to 7 atmospheres in tubes with L/D from 25 to 250, velocities between 0.1 and 98 ft/sec, and subcooling from 140 to 0°R (saturation). The equations are more convenient and provide reasonable results. For conditions combining a low velocity with high quality, and

$$1 < \frac{G}{(L/D)^2} < 150,$$

$$(q/A)_{max} = \frac{270\, G^{0.85}}{D^{0.2} (L/D)^{0.85}} \quad (234)$$

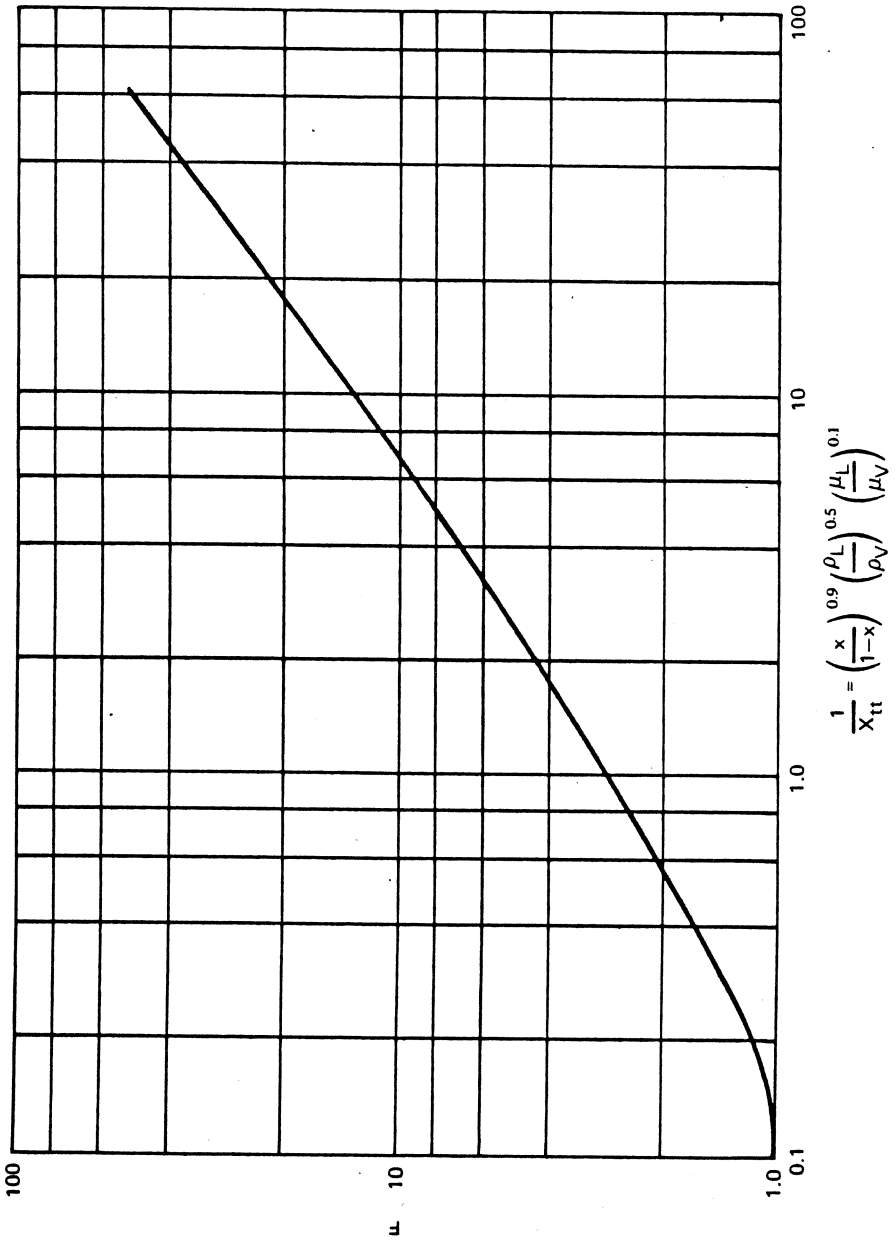

Figure 14-101. Reynolds Number Factor, F

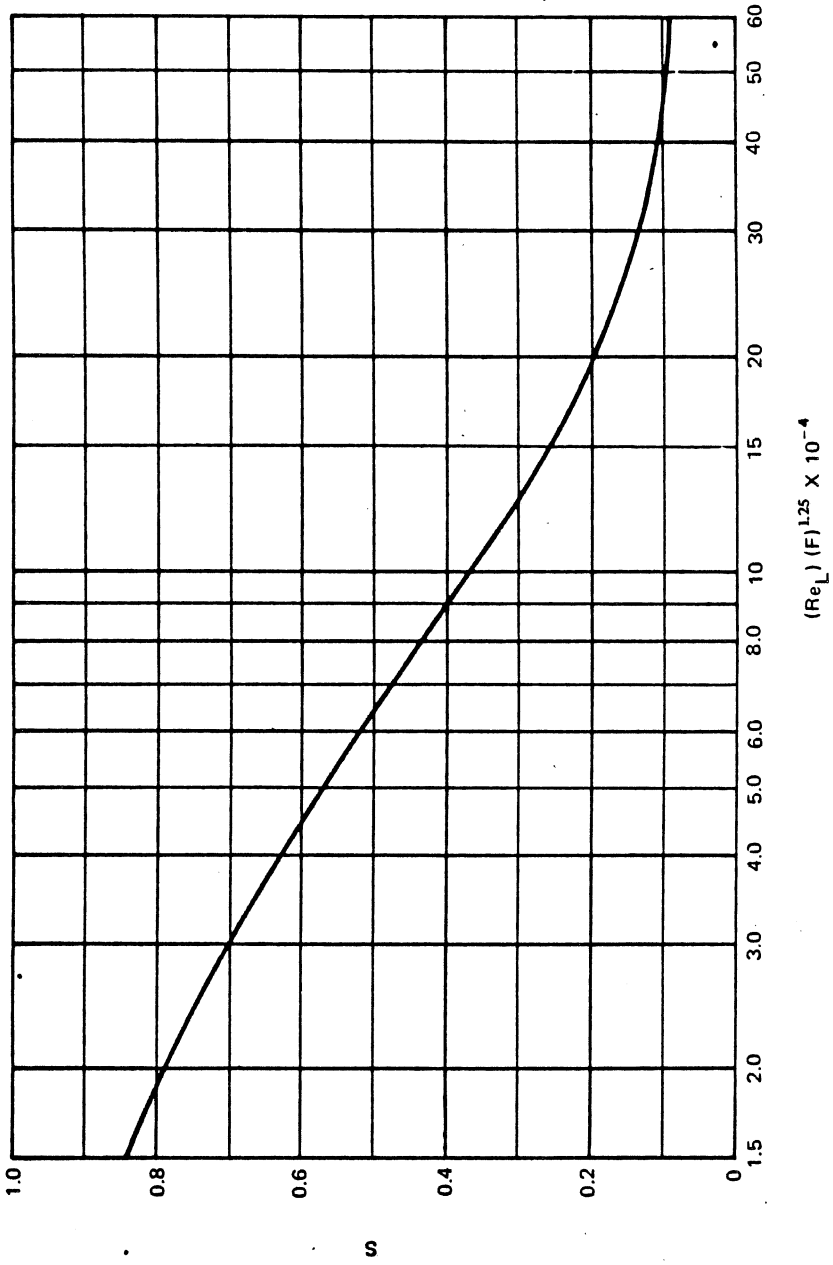

Figure 14-102. Suppression Factor, S

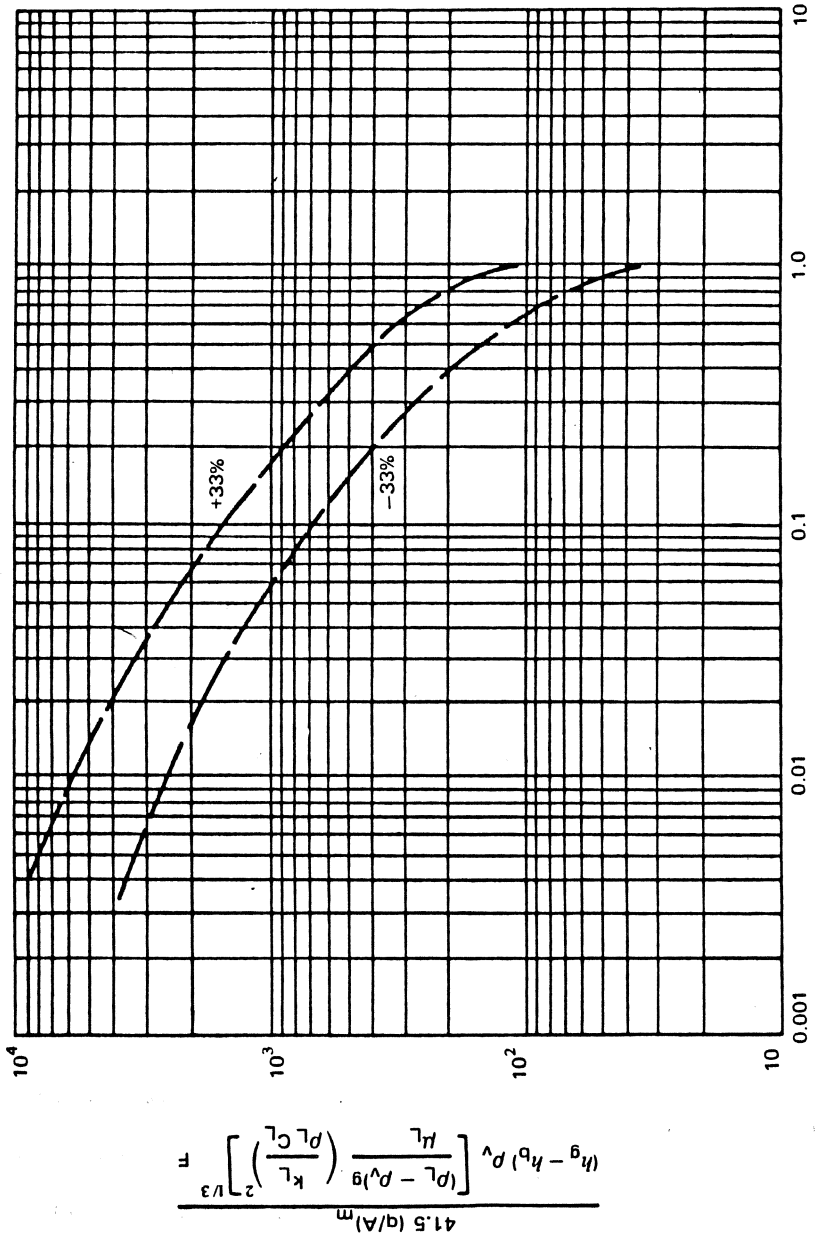

$$\frac{41.5\,(q/A)^m}{(h_g - h_b)\,\rho_v \left[\dfrac{(\rho_L - \rho_v)g}{\mu_L}\left(\dfrac{k_L}{\rho_L C_L}\right)^2\right]^{1/3}} F$$

Figure 14-103. Peak-Heat-Flux Correlation for Forced-Convection Boiling and Vaporation

For condition of high velocity and low quality, and

$$150 < \frac{G}{(L/D)^2} < 10{,}000,$$

$$(q/A)_{max} = \frac{1400\, G^{0.50}}{D^{0.2}\,(L/D)^{0.15}} \qquad (235)$$

where:

G = Mass Flux, lb/hr

L = Tube length, ft

D = Inside tube diameter, ft

$(q/A)_{max}$ = Burnout heat flux, Btu/hr-ft^2

d. Mist-Flow Regime — In the mist-flow regime the duct wall is dry and the two-phase core consists of numerous droplets entrained in the vapor flow. A reasonable estimate of the heat-transfer coefficient $\bar{h}_{mf}$ is obtained by combining the film pool boiling and vapor forced convection effects

$$\bar{h}_{mf} = \bar{h}_{c_{vapor}} + \bar{h}_{fb} \qquad (236)$$

where:

$\bar{h}_{fb}$ = Heat-transfer coefficient for film pool boiling, obtained from equation 219, Btu/hr-ft^2-$^\circ$ R

$\bar{h}_{c_{vapor}}$ = Forced convection heat-transfer coefficient for vapor phase (given below), Btu/hr-ft^2-$^\circ$R

$$\bar{h}_{c_{vapor}} = 0.026 \frac{k_v}{D} Re_D^{0.8}\, Pr_v^{1/3} (\mu_v/\mu_w)^{0.14} \qquad (237)$$

where:

D = Tube diameter, ft

k = Thermal conductivity, Btu/hr-ft-$^\circ$R

μ = Viscosity, lb/sec-ft

Pr_v = Prandtl number $= \frac{Cp_v \mu_v}{k_v}$

Re_D = Reynolds number $= \frac{\rho_v U_{ave} D}{\mu_v}$

U_{ave} = Average fluid velocity, ft/sec

and the subscripts v and w indicate vapor properties evaluated at the saturation and wall temperatures, respectively.

14-5.3 Fundamentals of Condensation

When a cold surface at temperature T_w, below saturation temperature T_{sat}, is exposed to saturated or superheated vapor, liquid condensate forms on the surface. If the liquid wets the surface, it spreads out and flows downward under the influence of gravity. In this process, known as film condensation, vapor condenses on the liquid at the interface because of the heat transferred through the liquid film by conduction. The heat flux depends primarily on the film thickness, which in turn depends on the rate of condensation and the rate at which the condensate is removed. On a vertical surface the film thickness increases continuously from top to bottom. As the plate is inclined from the vertical, the drainage rate decreases, resulting in a thicker film and lower heat transfer rates.

If the condensate does not wet the surface, droplets form and run down the surface, coalescing as they travel downward. This is known as dropwise condensation. A large part of the surface is not covered by an insulating film and the heat-transfer coefficients are four to eight times as high as in filmwise condensation. Since dropwise condensation is difficult to maintain, condensing equipment is designed on the assumption that film condensation will exist.

14-5.4 Heat-Transfer Coefficients for Filmwise Condensation

The condensation heat transfer rate q/A is obtained from:

$$q/A = \bar{h}_c\,(T_{sat} - T_w) \qquad (238)$$

where:

$\bar{h}_c$ = Condensation-heat-transfer coefficient, Btu/hr-ft^2-$^\circ$R

T_{sat} = Temperature of saturated vapor, $^\circ$R

T_w = Wall Temperature, $^\circ$R

14-5.4.1 Equation for Laminar Flow

The heat-transfer coefficient for filmwise condensation may be obtained from direct analysis, provided the flow is laminar. The equations presented in this paragraph yield good results as long as the assumptions of laminar flow, low vapor velocity (negligible vapor shear stress), and surface wettability are not violated.

The expression for the local heat-transfer coefficient h_x for condensation on a vertical plate is:

$$h_x = \left[\frac{\rho_L (\rho_L - \rho_v) g\, h'_{fg}\, k_L^3}{4\mu_L \times (T_{sat} - T_w)}\right]^{1/4} \quad (239)$$

where:

h_x = Local heat-transfer coefficient, Btu/hr-ft^2-°R

g = Acceleration of gravity, ft/hr^2

$h'_{fg} = h_{fg} + \frac{3}{8} C_{p_L} (T_{sat} - T_w)$

k_L = Thermal conductivity of liquid, Btu/hr-ft-°R

μ_L = Viscosity of liquid, lb/hr-ft

x = Distance from top of plate, ft

T_{sat} = Saturation temperature, °R

T_w = Temperature of wall surface, °R

Liquid film properties are evaluated at the average film temperature $T_f = (T_w + T_{sat})/2$. The magnitude of h_x decreases with increasing distance x from the top because the film thickens. Also, increasing $(T_{sat} - T_w)$ has the same effect because the greater condensation rate increases the film thickness.

The average heat-transfer coefficient $\bar{h}_c$ for a vertical plate of length L is obtained by integrating equation 239.

$$\bar{h}_c = 0.943 \left[\frac{\rho_L (\rho_L - \rho_v) g\, h'_{fg}\, k_L^3 \sin\theta}{\mu_L L (T_{sat} - T_w)}\right]^{1/4} \quad (240)$$

The $\sin\theta$ term is inserted to account for inclined surfaces, θ is the angle of inclination from the horizontal. For $Pr > 0.5$ and $C_{p_L} (T_{sat} - T_w)/h'_{fg} < 1.0$, more accurate results will be obtained from equations 239 and 240 if h'_{fg} is replaced by

$$[h_{fg} + 0.68\, C_{p_L} (T_{sat} - T_w)].$$

Equations 239 and 240 are valid for the inside and outside surfaces of vertical (but not inclined) tubes, as long as the film thickness ($\delta = k_L/h_x$) is small compared to the diameter. The equations are also valid for condensation on the lower side of an inclined plate if the inclination is small or the film is sufficiently thin.

The laminar-film analysis may be extended to condensation on a horizontal cylinder. The average heat-transfer coefficient for a cylinder with diameter D in feet is:

$$\bar{h}_c = 0.725 \left[\frac{\rho_L (\rho_L - \rho_v) g\, h'_{fg}\, k_L^3}{D\mu_L (T_{sat} - T_w)}\right]^{1/4} \quad (241)$$

The equations presented in this section yield good results provided the assumptions of laminar flow, low vapor velocity (negligible vapor shear stress), and surface wettability are not violated.

The laminar condensation equations may be transformed into dimensionless form which is analogous to the convection equations. Two dimensionless numbers must be introduced. The condensation number Co is:

$$Co = \bar{h}_c \left(\frac{\mu_L^2}{k_L^3 \rho_L^2 g}\right)^{1/3} \quad (242)$$

and the film Reynolds number Re_f is:

$$Re_f = \frac{4\Gamma_c}{\mu_L} \quad (243)$$

where:

Γ_c = Mass flow rate of condensate per unit width

= $\hat{w} g_c/\pi D g$ for vertical tube, lb/hr-ft

Using these parameters, equation 240 becomes:

$$Co = 1.47 (\sin\theta)^{1/3} Re_f^{-1/3} \quad (244)$$

and equation 241 becomes:

$$Co = 1.51 Re_f^{-1/3} \quad (245)$$

These forms are often convenient because of the importance of the film Reynolds number in determining the heat transfer rate.

14-5.4.2 Effect of Turbulence

The flow of a condensate film may become turbulent over the lower portion of a vertical surface. The thermal resistance in the turbulent region is lower and the average heat-transfer coefficient for the surface increases with the length of the plate. The flow becomes turbulent at a film Reynolds number (defined by equation 243) of about 2000.

The local heat-transfer coefficient for turbulent flow is:

$$h_x = 0.056\, Re_f^{0.2} \left(\frac{k_L^3 \rho_L^2 g}{\mu_L^2} \right)^{1/3} Pr_L^{1/2} \qquad (246)$$

The average heat-transfer coefficient $\bar{h}$ for a vertical surface, obtained by integrating equation 239 over the laminar region and equation 246 over the turbulent region, may be determined from the plot of Co versus Re_f shown in Figure 14-104.

If the mass flow rate per unit breadth Γ_c is unknown, an iterative solution is required, employing the Co versus Re_f relation from Figure 14-104 and the following expression for Γ_c obtained from an energy balance on the condensate film

$$\Gamma_c = \frac{w}{W(g/g_c)} = \frac{\bar{h}_c (T_{sat} - T_w)}{h'_{fg}} \cdot \frac{A}{W} \qquad (247)$$

where:

$\dot{w}$ = Weight flow rate of condensate, lb/hr

W = Width of vertical surface, ft

A = Vertical Surface area, ft^2

$\frac{A}{W}$ = L (height) for plates and vertical tubes, ft

14-5.4.3 Effect of High Velocity Vapor

For condensation in a confined space such as a tube or between parallel plates, the velocity of the incoming vapor may be high, particularly for large length-to-diameter ratios. When the vapor velocity is substantial compared to the liquid velocity at the vapor-condensate interface, the viscous shear force at the interface must be considered. The analysis for condensation on flat plates and on the outside of tubes did not include the shear force.

For upward vapor flow, the retarding viscous shear force causes the film thickness to increase. With downward flow, the thickness decreases, and surface conductances substantially larger than those predicted from equation 240 can be obtained. Also, the laminar-turbulent transition occurs near $Re_f = 300$ for downward flow.

The average heat-transfer coefficient for condensation in a 1/2 in. x 8 ft vertical tube, with inlet vapor velocities at the top up to 500 ft/sec, is given by:

$$\frac{\bar{h}_c}{C_{p_L} G_m} Pr_L^{1/2} = 0.046 \, (\rho_L f / \rho_v)^{1/2} \qquad (248)$$

where:

f = Fanning pipe-friction coefficient evaluated at the average vapor velocity (Table 14-2).

G_m = Mean value of mass velocity of vapor, lb/hr-ft^2

The value of G_m can be taken as:

$$G_m = \sqrt{\frac{G_1^2 + G_1 G_2 + G_2^2}{3}} \qquad (249)$$

where:

G_1 = Mass velocity at top of tube, lb/hr-ft^2

G_2 = Mass velocity at bottom of tube, lb/hr-ft^2

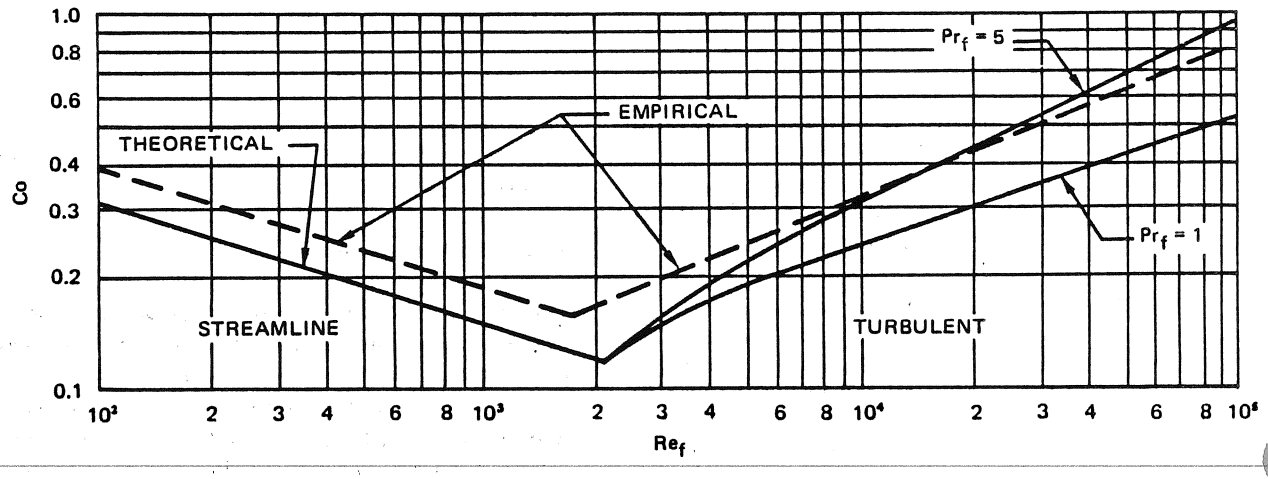

Figure 14-104. Effect of Turbulence in Film on Heat Transfer With Condensation

All properties of the liquid are evaluated at $T_f' = T_w + \Delta T/4$. The applicability of these equations to other configurations has not been verified.

14-5.4.4 Effect of Superheated Vapor

Superheated vapor will condense on a cold wall as long as the wall temperature is below the saturation temperature. The condensation rate is only slightly increased by greater superheat. Assuming the liquid vapor interface remains very near the saturation temperature, the analyses for laminar and turbulent flow need be modified only by accounting for the greater enthalpy change from superheated vapor to slightly subcooled liquid. The enthalpy change h'_{fg} of equations 239, 240, and 241 should be replaced by:

$$h''_{fg} = C_v (T_v - T_{sat}) + h_{fg} + \frac{3}{8} C_{p_L} (T_{sat} - T_w) \quad (250)$$

where:

C_v = Constant volume specific heat of vapor, Btu/lb-°R

T_v = Temperature of superheated vapor, °R

The heat transfer rate is calculated by:

$$q/A = h_c (T_{sat} - T_w) \quad (251)$$

$(T_{sat} - T_w)$ is still the driving force for heat transfer across the liquid condensate film. The condensate rate is obtained from equation 247 by replacing h'_{fg} with h''_{fg}.

14-6 MASS TRANSFER

The transport of one constituent of a fluid solution from a region of higher concentration to a region of lower concentration is called mass transfer. Mass transfer is analogous to heat transfer. Heat is transferred in a direction which reduces an existing temperature gradient; mass is transferred in a direction which reduces an existing concentration gradient. Heat and mass transfer both cease when the driving potentials, the temperature and the concentration gradients, are reduced to zero.

14-6.1 Definitions

The diffusion rate, mass flux, is proportional to the concentration gradient:

$$\frac{N_A}{A} = -D_v \frac{dC_A}{dx} \quad (252)$$

where:

$\frac{N_A}{A}$ = mass flux, lb-mole/hr-ft^2

D_v = mass diffusivity, ft^2/hr

C_A = concentration of component A in a mixture, lb-moles/ft^3

x = distance in the direction of diffusion, ft.

The negative sign appears because the concentration gradient is negative in the direction of mass transfer. Equation 252 states that mass will be transferred between two points in a fluid if a difference in concentration exists between the points.

Consider a mixture of n components which is itself in bulk motion in the x-direction by free or forced convection. The bulk velocity v_x of the mixture is defined as the velocity of the center of mass of a volume element:

$$v_x \equiv \frac{1}{\rho} \sum_{i=1}^{n} C_i v_{ix} \quad (253)$$

where:

v_{ix} = statistical mean velocity of component i with respect to stationary coordinate axes, ft/hr

ρ = density of the mixture, lb-mole/ft^3

The mass flux of component A can be expressed relative to either a fixed observer or an observer moving with the bulk velocity v_x. The diffusion flux given by equation 252 is that seen by an observer moving at v_x. The absolute flux of A seen by the stationary observer is $C_A v_{Ax}$, the sum of the diffusion flux $(N_A/A)_x$ and a mass flux $C_A v_x$ due to the bulk motion:

$$C_A v_{Ax} = (N_A/A)_x + C_A v_x \quad (254)$$

14-6.2 Mass Transfer Coefficients

The processes of heat and mass transfer in the boundary layer are similar. In flow over a flat plate, a concentration boundary layer grows from the leading edge in the same way that a thermal boundary layer grows (Figure 14-105). The thickness of the concentration boundary layer is defined as the distance from the plate where:

$$(C_{A_o} - C_A) = 0.99 (C_{A_o} - C_{A_\infty}) \quad (255)$$

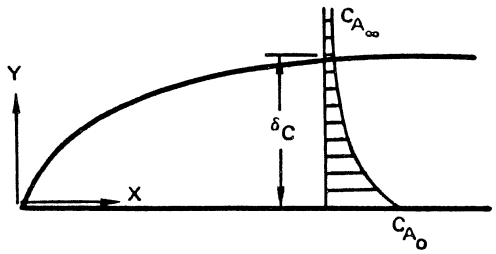

Figure 14-105. Concentration Boundary Layer on a Flat Plate

where:

C_{A_∞} = free-stream concentration of component A, lb-mole/ft^3

C_{A_o} = concentration of A at the plate wall ($C_{A_o} > C_{A_\infty}$), lb-mole/ft^3

The equations and solutions for mass transfer are analogous to those for convective heat transfer. A mass transfer coefficient h_D is defined, with reference to Figure 14-105, as:

$$h_D = \frac{(N_A/A)_{y=0}}{C_{A_o} - C_{A_\infty}} \qquad (256)$$

When the mass transfer coefficient is determined for a particular system, the diffusion flux at the wall $(N_A/A)_{y=o}$ may be calculated from equation 256. Generally there is a contribution to mass transfer by bulk flow normal to the surface and the diffusion flux is substituted in equation 254 to obtain the absolute flux. For a dilute mixture of A, the diffusion flux and the absolute mass flux are essentially equal and the absolute flux is obtained directly from equation 256.

At low mass transfer rates at a surface, a heat transfer analog with comparable boundary conditions exists for most mass diffusion problems. The equations in paragraph 14-4 for convective heat transfer may be applied to mass transfer by simply substituting the diffusion parameters for their heat-transfer analogs.

$q/A \rightarrow N_A/A$

$h_c \rightarrow h_D$

$T \rightarrow C_A$

$a \rightarrow D_v$

$Nu \rightarrow Sh$

$Pr \rightarrow Sc$

The flow parameters, Re and Gr, will be the same.

The dimensionless mass transfer numbers corresponding to the Nusselt and the Stanton numbers in heat transfer are respectively:

Sherwood number

$$Sh = \frac{h_D L}{D_v} \qquad (257)$$

and

$$\frac{h_D}{V} = \frac{Sh}{Re\,Sc} \qquad (258)$$

where:

h_D = mass transfer coefficient, ft/hr

L = characteristic length of system, ft

V = characteristic velocity of system, ft/hr

Re = Reynolds number

Sc = Schmidt number = ν/D_v

The Schmidt number, the ratio of kinematic viscosity (momentum diffusivity) and mass diffusivity, determines the relative rates of growth of the hydrodynamic and concentration boundary layers.

The mass transfer rate, characterized by the dimensionless mass transfer coefficient (Sh), is a function of the fluid flow dynamics (Re or Gr) and the relation between the flow dynamics and the concentration gradient in the fluid (Sc):

Sh = f(Re, Sc) forced convection (259)

or

Sh = f(Gr, Sc) free convection (260)

where:

Re = Reynolds number, defined by equation 14-126.

Gr = Grashof number

The most convenient form of the Grashof number for mass transfer problems is:

$$Gr = \frac{g\,L^{*3}}{\nu^2}\left(\frac{\rho_\infty}{\rho_w} - 1\right) \qquad (261)$$

where:

g = acceleration of gravity, ft/hr^2

L^* = characteristic dimension, ft

ν = kinematic viscosity, ft^2/hr

ρ = fluid density, lb/ft^3

The subscripts w and ∞ indicate conditions at the wall and outside the boundary layer, respectively.

Where direct mass-transfer data for a new system are not available, the mass-transfer coefficients may be predicted from heat transfer data taken in a system of identical geometry and flow characteristics. Many of the mass transfer solutions for forced convection obtained by analogy to heat transfer equations have been verified by experiment. There is very little data available for experiments in free convection mass transfer. The analog solutions are not applicable to free convection with simultaneous heat and mass transfer.

14-6.3 Molecular Diffusion

Mass transfer by molecular diffusion is directly analogous to conduction heat transfer or to momentum transfer in laminar flow. Molecular diffusion may occur in a stagnant fluid or in a fluid in laminar flow. The transient one-dimensional mass-transfer equation can be written in a form identical to the Fourier heat-transfer equation:

$$\frac{\partial C_A}{\partial t} = D_V \frac{\partial^2 C_A}{\partial x^2} \qquad (262)$$

where:

C_A = concentration of component A in a mixture, lb-mole/ft^3

t = time, hr

D_V = mass diffusivity, ft^2/hr

x = distance in the direction of diffusion, ft

Mass transfer occurs at an appreciable rate only in gases and liquids. In solids, mass transfer is suppressed by the relative immobility of the molecules. Mass diffusivities for several gases and liquids are presented in Table 14-21.

When experimental data is not available, the mass diffusivity for gases may be estimated with the empirical equation:

$$D_V = 0.0069 \frac{T^{3/2}}{P(V_A^{1/3} + V_B^{1/3})^2} \sqrt{\frac{1}{M_A} + \frac{1}{M_B}} \qquad (263)$$

where:

T = temperature, °R

P = pressure, atm

Table 14-21. Mass Diffusivities for Gases and Liquids

Gases at 77°F, 1 ATM

System	Diffusivity (sq ft/Hr)
Ammonia-air	.1.08
Water vapor-air	.0.99
Ethanol-air	.0.46
CO_2-air	.0.64
O_2-air	.0.80
H_2-air	.1.60
Benzene-air	.0.34

Liquid Phase at 68°F, Dilute Solutions

Oxygen in water	7.0×10^{-5}
Ammonia in water	6.8×10^{-5}
Ethanol in water	3.8×10^{-5}
CO_2 in water	6.9×10^{-5}
H_2 in water	20.0×10^{-5}
HCl in water	10.0×10^{-5}
Sucrose in water	1.8×10^{-5}
NaCl in water	5.3×10^{-5}
CO_2 in ethanol	13.2×10^{-5}

M = molecular weight

V = atomic volume

and the subscripts A and B refer to the two component gases. The atomic volumes are given in Table 14-22. For compounds, the law of additive volumes applies. For example, for CO_2, V = 14.8 + 2(7.4) = 29.6.

14-6.3.1 Diffusion Through Solids

Steady-state diffusion through a plane membrane is analogous to heat conduction through a slab. With the boundary conditions, $C_A = C_{A_1}$ at X = 0 and $C_A = C_{A_2}$ at x = L, the solution of equation 262 is:

$$C_A = (C_{A_2} - C_{A_1})\, x/L + C_{A_1} \qquad (264)$$

The mass transfer rate is:

$$\frac{N_A}{A} = D_V/L\,(C_{A_1} - C_{A_2}) \qquad (264)$$

where:

L = thickness of the membrane, ft.

The mass tranfer rate may be expressed in terms of vapor pressures on the two sides of the membrane rather

Table 14-22. Atomic Volumes

Air	29.9
Antimony	24.2
Arsenic	30.5
Bismuth	48.0
Bromine	27.0
Carbon	14.8
Chlorine, terminal as in R—Cl	21.6
Medial as in R—CHCl—R'	24.6
Chromium	27.4
Fluorine	8.7
Germanium	34.5
Hydrogen, molecule (H_2)	14.3
In compounds	3.7
Iodine	37.0
Nitrogen, molecule (N_2)	15.6
N_2 in primary amines	10.5
N_2 in secondary amines	12.0
Oxygen, molecule (O_2)	7.4
Oxygen coupled to two other elements:	
In aldehydes and ketones	7.4
In methyl esters	9.1
In ethyl esters	9.9
In higher esters and ethers	11.0
In acids	12.0
In union with S, P, N	8.3
Phosphorus	27.0
Silicon	32.0
Sulfur	25.6
Tin	42.3
Titanium	35.7
Vanadium	32.0
Zinc	20.4

For 3-membered ring, deduct 6.0.
For 4-membered ring, deduce 8.5.
For 5-membered ring, deduct 11.5.
For 6-membered ring, deduct 15.0.
For naphthalene ring, deduct 30.0.
For anthracene ring, deduct 47.5.

than in terms of surface concentrations. The permeability of the membrane is defined as:

$$\mathscr{P} = \frac{N_A/A}{(P_{A_1} - P_{A_2})/L} \qquad (266)$$

where:

$\mathscr{P}$ = permeability, lb-mole/hr-ft-atm

P_A = vapor pressure of component A, atm

The permeability $\mathscr{P}$ may be expressed directly as a function of the mass diffusivity D_v:

$$\mathscr{P} = D_v/RT$$

where:

$\mathscr{R}$ = universal gas constant
= 0.730 ft^3-atm/lb-mole-°R

T = gas temperature, °R

Composite membranes in series and in parallel can be treated in a manner similar to thermal or electrical resistances in series and in parallel. The diffusional resistance for each membrane is defined as:

$$R_D = \frac{C_{A_1} - C_{A_2}}{N_A} = \frac{L}{A\,D_v} \qquad (267)$$

where:

R_D = diffusional resistance, hr/ft^3

N_A = mass transfer rate, lb-moles/hr

A = membrane area, ft^2

The process of drying a wet solid occurs in two phases. When the surface is wet, the primary resistance to mass transfer is at the gas-liquid interface. When the surface becomes dry, the rate of drying decreases and the internal resistance to diffusion becomes significant. The former case is covered by the appropriate convective heat transfer analog (paragraph 14-6.2), the latter is approximated by the solution to equation 262 with the boundary conditions

$t = 0$ $\quad C_A = C_{A_i}$ everywhere

$t > 0$ $\quad C_A = 0$ at $x = 0$

For these conditions, the concentration profile is

$$\frac{C_A}{C_{A_i}} = \text{erf}\,\frac{x}{2\sqrt{D_v t}} \qquad (268)$$

where:

C_{A_i} = initial concentration of component A in the solid, lb-moles/ft^3

The diffusion rate at the surface is:

$$\frac{N_A}{A} = -\frac{D_v}{\sqrt{\pi t}}\,C_{A_i} \qquad (269)$$

14-6.3.2 Diffusion in Binary Gas Mixtures

In a binary mixture of perfect gases the concentrations may be expressed as partial pressures:

$$P_A = \frac{n_A \mathcal{R} T}{V} = C_A \mathcal{R} T \qquad (270)$$

where:

P_A = partial pressure of gas A, atm

n_A = number of moles of gas, lb-moles

V = gas volume, ft^3

The mass flux is obtained by combining equations 252 and 270:

$$\frac{N_A}{A} = \frac{-D_v}{\mathcal{R} T} \frac{dP_A}{dx} \qquad (271)$$

a. Equimolar counterdiffusion – In equimolar counterdiffusion gases A and B diffuse simultaneously in opposite directions through each other. The diffusion flux is obtained from integration of equation 271:

$$\frac{N_A}{A} = \frac{-D_v}{\mathcal{R} T} \left(\frac{P_{A_2} - P_{A_1}}{x_2 - x_1} \right) \qquad (272)$$

The total pressure P is constant throughout the gas and

$$P = P_A + P_B \qquad (273)$$

The partial pressure gradients must be equal but of opposite sign, as shown in Figure 14-106. The rates of diffusion are equal but in opposite directions, i.e., $N_A = -N_B$. Since there is no bulk flow, the diffusion flux equals the absolute mass flux.

b. Diffusion of gas A through a stationary gas B – Consider the case of gas A diffusing through a stationary gas B to a gas-liquid interface where gas A is absorbed but gas B is not (see Figure 14-107). As with equimolar counterdiffusion, the partial pressure gradients and diffusion rates are equal but in opposite direction at any point x in the gas phase.

Since gas B is not being produced at the interface, even though it is diffusing away from the interface, some other mechanism must supply gas B to maintain a constant concentration of gas B at the interface. A bulk flow of gas (A and B) toward the interface replenishes the gas B which is diffusing away and increases the effective rate of transfer of gas A toward the interface.

The "stationary" characteristic of B does not imply that B is not moving, but refers to the *net* behavior of B. Since B is supplied by bulk flow at the same rate it diffuses away, there is no *net* movement of B. When the bulk flow mechanism is included, the equation for the mass flux of gas A diffusing through a stationary gas B is:

$$\frac{N_A}{A} = \frac{-D_v}{\mathcal{R} T} \frac{P}{P_{B_m}} \left(\frac{P_{A_2} - P_{A_1}}{x_2 - x_1} \right) \qquad (274)$$

where the logarithmic mean pressure of B is:

$$P_{B_m} = \frac{P_{B_2} - P_{B_1}}{\ln (P_{B_2}/P_{B_1})}$$

Equation 274 accounts for bulk motion and represents the absolute mass flow of component A. For a dilute mixture of A in B, P_{B_m} is approximately equal to P and equation 274 reduces to equation 272.

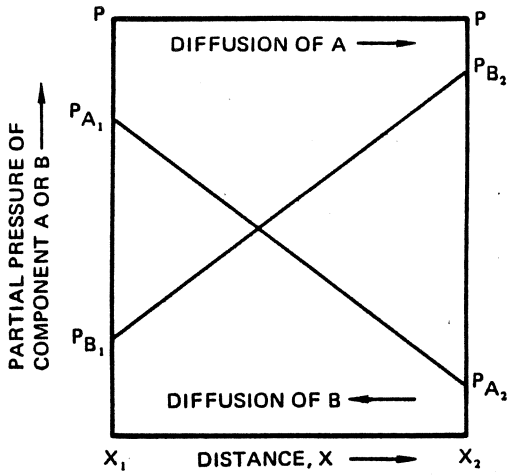

Figure 14-106. Partial Pressure Gradients in Equimolar Counterdiffusion of Two Gases

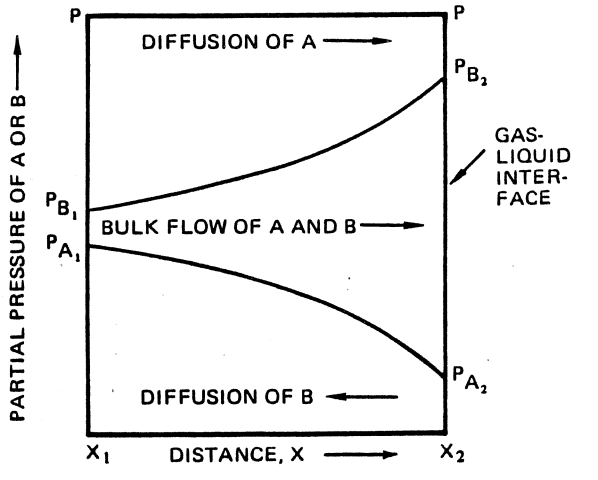

Figure 14-107. Partial Pressure Gradients in the Diffusion of Gas A Through a Stationary Gas B

The mass flux through a stationary liquid is analogous to equation 274:

$$\frac{N_A}{A} = \frac{-D_V C_t}{C_{B_m}} \left(\frac{C_{A_2} - C_{A_1}}{x_2 - x_1} \right) \qquad (276)$$

where:

C_t = total concentration ($C_A + C_B$), lb-mole/ft^3

C_{B_m} = log-mean concentration of B (similar to P_{B_m} defined by equation 275), lb-mole/ft^3

14-6.4 Interphase Mass Transfer

The total resistance to mass transfer in two phases may be expressed in terms of an over-all mass-transfer coefficient similar to an over-all heat-transfer coefficient. For heat transfer, the driving potential (temperature) at the interface is identical for each phase. However, for mass transfer there is a discontinuity in the driving potential (concentration) at the interface. For example, consider air (saturated) in equilibrium with water at 77°F and 1 atm. The mole fraction of water vapor is 0.031 in the gas phase and 1.0 in the liquid phase.

The concentrations that exist when two phases reach equilibrium must be determined experimentally for each system. However, equilibrium concentrations may be predicted for systems which follow Henry's law, which is expressed as:

$$P_A = m C_A \qquad (277)$$

where:

P_A = partial pressure of component A in the gas phase, atm.

C_A = concentration of component A in the liquid phase in equilibrium with the gas, lb-mole/ft^3

m = Henry's law constant, experimentally determined, atm-ft^3/lb-mole

Values for the Henry's law constant for many gases, such as oxygen, nitrogen, and carbon dioxide dissolved in water, are given in Table 14-23.

Using partial pressures calculated by equation 277 the overall mass-transfer coefficient may be derived for systems that follow Henry's law. Consider mass transfer between a liquid phase with the concentration C_{A_L} and a gas phase with the partial pressure P_{A_G}. The mass transfer equations for the gas and liquid phases are usually written:

$$\frac{N_A}{A} = k_G (P_{A_G} - P_{A_i}) \qquad (278)$$

Table 14-23. Henry's Law Constants for Various Gases in Water at Moderate Pressures ($m \times 10^{-4}$, atm/(lb mole/cu ft)

Temperature					
°C	°R	Air	O_2	N_2	CO_2
0	492	1.25	0.736	1.53	0.021
10	510	1.58	0.944	1.93	0.030
20	528	1.92	1.16	2.32	0.041
30	546	2.24	1.38	2.68	0.054
40	564	2.52	1.56	3.02	0.067
50	582	2.76	1.72	3.30	0.083
60	600	2.96	1.85	3.52	0.100
70	618	3.10	1.96	3.69	.....
80	636	3.18	2.04	3.74	.....
90	654	3.23	2.09	3.77	.....
100	672	3.22	2.11	3.79	.....

and

$$\frac{N_A}{A} = k_L (C_{A_i} - C_{A_L}) \qquad (279)$$

where:

k_G = gas-phase mass-transfer coefficient = $h_D \mathscr{R}T$, lb-mole/hr-ft^2-atm

k_L = liquid-phase mass-transfer coefficient = h_D, ft/hr

The coefficients k_G and k_L may be determined from the mass-transfer coefficient h_D, described in paragraph 14-6-2. The expressions for k_G and k_L for diffusion through stationary media may obtained from equations 274 and 276.

Since it is not practical to measure concentrations at the gas-liquid interface, P_{A_i} and C_{A_i} are unknown. However, Henry's law may be used to determine two fictitious concentrations, P_A^* and C_A^*, which represent the equilibrium states that correspond to the actual liquid and gas concentrations, C_{A_L} and P_{A_G}, respectively:

$$P_A^* = m C_{A_L} \qquad (280)$$

and

$$C_A^* = P_{A_G}/m \qquad (281)$$

It is convenient to define overall mass-transfer coefficients in terms of the actual and fictitious concentrations:

$$\frac{N_A}{A} = K_G (P_{A_G} - P_A^*) \qquad (282)$$

and

$$\frac{N_A}{A} = K_L (C_A^* - C_{A_L}) \qquad (283)$$

where:

K_G = overall mass-transfer coefficient for gas-phase, lb-mole/hr-ft^2-atm

K_L = overall mass-transfer coefficient for liquid phase, ft/hr

The overall mass-transfer coefficients K_G and K_L may be expressed as a function of k_G, k_L, and m:

$$\frac{1}{K_G} = \frac{1}{k_G} + \frac{m}{k_L} \qquad (284)$$

and

$$\frac{1}{K_L} = \frac{1}{mk_G} + \frac{1}{k_L} \qquad (285)$$

The overall coefficient based on either phase may be determined and used (in equations 282 or 283) to calculate the mass flux. It is conventional to use the overall mass-transfer coefficient based on the phase where the major resistance to mass transfer lies.

In many cases the major resistance lies in one phase. For example, slightly soluble gases like oxygen and nitrogen have very large values of m and (from equation 285) $K_L \cong k_L$. Absorption of a slightly soluble gas is therefore said to be "liquid-phase controlling." Similarly, for a very soluble gas, m is small, $K_G \cong k_G$ (from equation 284), and the absorption is "gas-phase controlling." Whenever possible the gas- or liquid-phase controlled approximation is made because calculations then require knowledge of only one individual phase coefficient. In cases where a pure phase is involved, no resistance to mass transfer exists in the pure phase.

14-6.5 Simultaneous Heat and Mass Transfer

Simultaneous heat and mass transfer must be considered in vaporization and condensation operations. The humidification of air will be discussed, but the theory also applies to any system of a condensing and noncondensing gas.

The absolute humidity Y of air, the ratio of the mass of water vapor to the mass of dry air, may be expressed in terms of partial pressure:

$$Y = \frac{M_W}{M_G}\left(\frac{P_W}{P - P_W}\right) \qquad (286)$$

where:

M_W = Molecular weight of water

M_G = Molecular weight of air

P_W = Partial pressure of water vapor, atm

P = Total pressure = $P_{air} + P_W$, atm

When an air stream is in contact with a stream of water, vaporization occurs and the absolute humidity of the air increases. The heat required for vaporization is supplied by the gas, the liquid, or an outside source.

In adiabatic systems (no external heat sources), if the quantity of air is sufficiently large, the air temperature does not change appreciably and the vaporization tends to lower the temperature of the remaining water. The water temperature will decrease until an equilibrium condition is reached where the heat transferred to the water just balances the heat removed in vaporization. The humidity can be expressed in terms of wet- and dry-bulb temperatures as:

$$Y_{wb} - Y_G = \frac{1}{h_{fg}} \frac{h_G}{k_G M_G P} (T_G - T_{wb}) \qquad (287)$$

where:

Y_{wb} = absolute humidity at the gas-liquid interface at the water temperature T_{wb}, lb of water vapor/lb of dry air.

Y_G = absolute humidity of the bulk of the gas, lb of water vapor/lb of dry air.

h_{fg} = heat of vaporization of water, Btu/lb

h_G = gas-phase heat-transfer coefficient, Btu/hr-ft^2-°R

k_G = gas-phase mass-transfer coefficient defined by equation 278, lb-mole/hr-ft^2-atm

M_G = Molecular weight of the gas-phase (air), lb/lb-mole

P = Total pressure, atm

T_G = Dry-bulb temperature of the bulk of the gas, °R.

T_{wb} = Wet-bulb temperature of the gas (equals temperature of the water in the equilibrium condition), °R.

Since mass and heat are transferred by similar mechanisms, the ratio h_G/k_G is essentially constant. An

approximation of the group $h_G/k_G M_G P$ for any gas may be obtained from:

$$\frac{h_G}{k_G M_G P} = C_p\,(Sc/Pr)^{0.67} \qquad (288)$$

If the supply of air in the humidification process is limited, the water will remain at a constant temperature T_{as} and the heat required for vaporization must be supplied by the gas-phase. The change in humidity at equilibrium is:

$$Y_{as} - Y_G = 1/h_{fg}(c_a + Y_G c_w)\,(T_G - T_{as}) \qquad (289)$$

where:

Y_{as} = Absolute humidity of the air at T_{as}, lb water vapor/lb dry air

Y_G = Absolute humidity of the initial air, lb water vapor/lb dry air

c_a = Specific heat of air, Btu/lb-°R

c_w = Specific heat of water, Btu/lb-°R

T_G = Initial air temperature, °R

T_{as} = Final equilibrium (adiabatic saturation) temperature of the air, °R.

For air-water systems, the quantities $h_G/k_G M_G P$ and $(c_a + Y_G c_w)$, in equations 287 and 289 respectively, are essentially equal and, therefore, $T_{as} = T_{wb}$. However, the adiabatic saturation temperature and the wet-bulb temperature are generally not equal for other gas-liquid combinations.

The changes in humidity given by equations 287 and 289 represent conditions existing at the equilibrium of an air stream flowing past a water stream. In actual practice equilibrium is only approached and these results are limiting values for mass transfer equipment. The mass transfer rate at an equilibrium condition is:

$$\dot{w}_{H_2O} = \dot{w}_{air}\,\Delta Y \qquad (290)$$

where:

$\dot{w}_{H_2O}$ = Water vaporization rate, lb/hr

$\dot{w}_{air}$ = Flowrate of dry air, lb/hr

ΔY = Change in absolute humidity, lb water vapor/lb dry air

14-7 HEAT TRANSFER IN HIGH-SPEED FLOW

In fluid flow at high velocities over solid surfaces, the fluid temperature increases significantly due to frictional effects, commonly known as aerodynamic heating. The viscous stresses within the boundary layer do shearing work on the fluid and raise its temperature, and that of the contiguous solid surface. The calculation of heating rates may be complicated by shock waves, dissociation and ionization of gas molecules, and gas rarefaction. Assumption of constant fluid properties may no longer be valid because of steep temperature gradients within the boundary layer.

14-7.1 Flow Regimes

The analysis of low-speed forced convection discussed in subsection 14-4 used the Reynolds number (equation 128) to describe the nature of the flow. In high-speed flow the Mach number must be introduced to describe the influence of compressibility on heat transfer and flow phenomena. The Mach number M is defined as

$$M = \frac{v_\infty}{a} \qquad (291)$$

where:

v_∞ = Gas or flight velocity, ft/sec

a = Speed of sound in the gas, ft/sec

Compressibility effects may be neglected at Mach numbers below 0.5.

At very low pressures (high altitudes), the rarefaction (coarseness of the molecular structure of the flow) results in velocity and temperature discontinuities, and thus, the continuum relations are not applicable. The molecular mean free path λ (the average distance travelled by a molecule between collisions) is of the same order of magnitude as the characteristic dimension L^* of the solid surface. The transfer mechanisms are no longer governed solely by intermolecular collision in the boundary layer, but depend also upon the interaction of the gas molecules and the wall.

The Knudsen number Kn, a measure of the degree of rarefaction, is defined as:

$$Kn = \frac{\lambda}{L^*} \qquad (292)$$

where:

λ = Molecular mean free path, ft

L^* = Characteristic length, ft

Kn is related to the Reynolds and Mach numbers by the equation:

$$Kn = \frac{M}{Re}\sqrt{\frac{\pi\gamma}{2}} \qquad (293)$$

where:

γ = Specific heat ratio = c_p/c_v

Figure 14-108 shows the subdivision of gas dynamics into various flow regimes. Two forms of the Knudsen number, M/Re and $M/\sqrt{Re}$, are used to define the boundaries between the regimes. The free molecule flow regime exists at values at M/Re greater than three. At large Reynolds numbers the characteristic dimension is the boundary layer thickness δ. The ratio $M/\sqrt{Re}$ is used in subdivision of this region because it more closely approximates the ratio λ/δ. The shaded area represents the low-speed, continuum regime considered in subsection 14-4.

14-7.2 Continuum Regime

In high speed flow, the viscous forces developed in the boundary layer slow down the gas and dissipate the kinetic energy of the free stream, causing the gas temperature to increase in a direction toward the solid surface. According to thermodynamic principles, when a flowing gas is slowed down adiabatically to zero velocity, its temperature rises to the stagnation temperature T_{o_∞}. The stagnation temperature is related to the free-stream temperature T_∞ and velocity v_∞ by the equation:

$$T_{o_\infty} = T_\infty + \frac{v_\infty}{2Jg_c c_p} \qquad (294)$$

where:

T_∞ = Free-stream temperature, °R

J = Mechanical equivalent of heat = 778 ft-lb/Btu

c_p = Constant pressure specific heat, Btu/lb-°R

The last term is the free-stream dynamic-temperature rise. The free stream and stagnation temperatures are related by the free-stream Mach number M_∞.

$$T_{o_\infty} = T_\infty \left(1 + \frac{\gamma-1}{2} M_\infty^2\right) \qquad (295)$$

When a gas flows past an insulated (adiabatic) surface, the temperature at the surface rises above the free-stream temperature T_∞, but will not quite reach the stagnation temperature T_{o_∞}. The actual temperature at an adiabatic surface is called the adiabatic wall temperature T_{aw}.

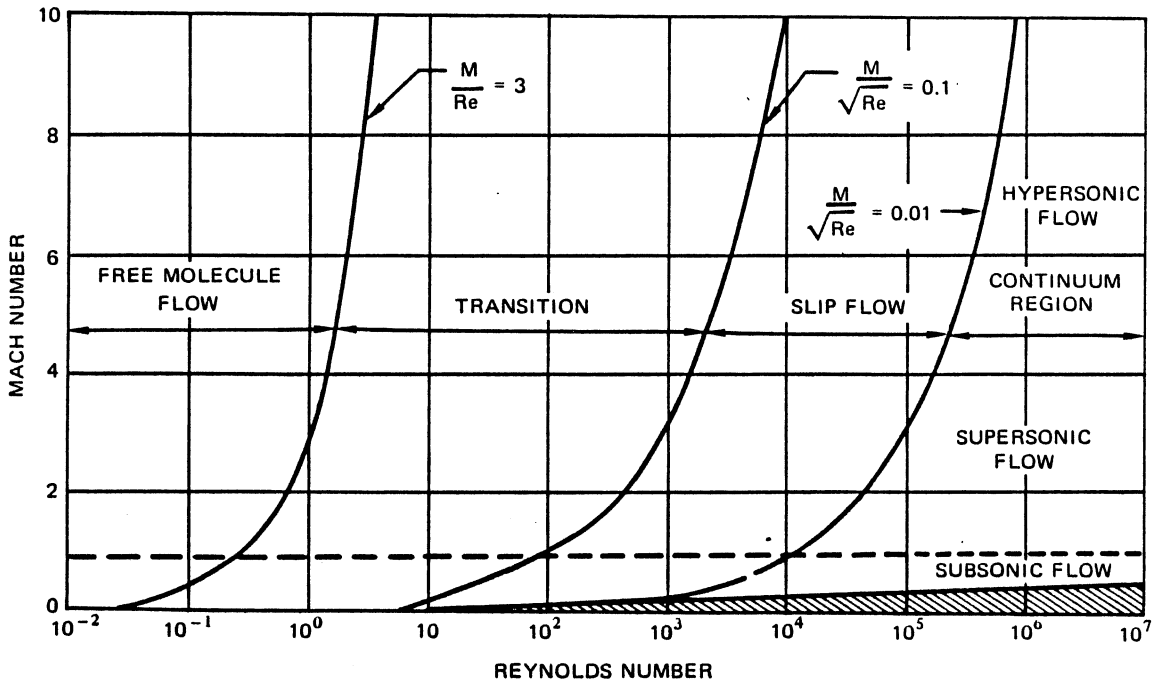

Figure 14-108. Flow Regimes of Gas Dynamics

The recovery factor R_T, the fraction of the free-stream dynamic-temperature rise recovered at the wall, is defined as:

$$R_T = \frac{T_{aw} - T_\infty}{V_\infty^2/2c_pJg_c} = \frac{T_{aw} - T_\infty}{T_{o_\infty} - T_\infty} \quad (296)$$

In terms of the Mach number, R_T is:

$$R_T = \frac{2}{(\gamma-1)M_\infty^2}\left(\frac{T_{aw}}{T_\infty} - 1\right) \quad (297)$$

The three basic boundary layer temperature profiles that may develop in high-speed flow are shown in Figure 14-109. With each profile, the wall temperature T_W is greater than the free-stream temperature T_∞. In the adiabatic case (curve a), the wall temperature is equal to the adiabatic wall temperature T_{aw}. No temperature gradient exists in the fluid at the wall and the heat transfer rate, which is proportional to the gradient, is zero.

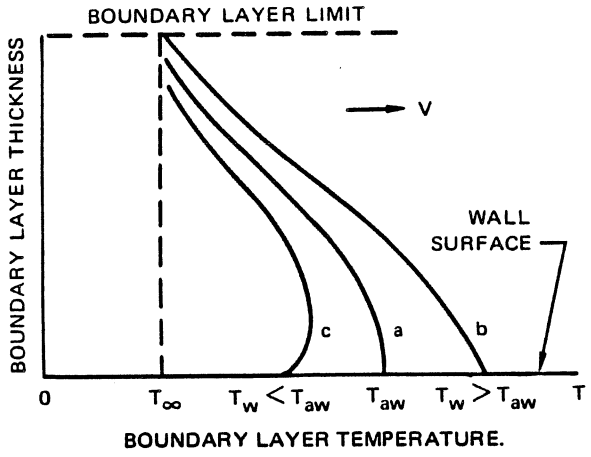

Figure 14-109. Boundary Layer Temperature Profiles During High-Velocity Flow

When T_W is greater than T_{aw} (curve b), the direction of heat transfer is from the wall to the fluid. However, when T_W is less than T_{aw} (curve c), the sign of the temperature gradient and the direction of heat transfer are reversed. Heat is transferred from the fluid to the wall, even though the free stream temperature is less than the wall temperature ($T_\infty < T_W$). The direction of heat flow depends on the difference between the wall temperature T_W and the adiabatic wall temperature T_{aw}, rather than the free-stream temperature T_∞. Consequently, $(T_W - T_{aw})$ is used in heat transfer calculations for high-speed flow, and the convective heat-transfer coefficient h_c is defined as:

$$h_c = \frac{q_c}{A(T_W - T_{aw})} \quad (298)$$

14-7.2.1 Laminar Flow

Heat transfer rates for laminar high-speed flow may be obtained from the equations for low-speed flow. To account for the steep temperature gradients, the fluid properties must be evaluated at a reference temperature T^* defined by:

$$T^* = T_\infty + 0.58(T_W - T_\infty) + 0.19(T_{aw} - T_\infty) \quad (299)$$

where:

T_W = Temperature of the wall (solid surface), °R

T_{aw} = Adiabatic wall temperature, °R

Experiments in the laminar flow regime have shown that, for $0.5 < Pr < 8$,

$$R_T \simeq \sqrt{Pr} \quad (300)$$

The adiabatic wall temperature is determined from equations 297 and 300 and is used in equation 298 to calculate the heating rate.

The heat-transfer coefficients for a flat plate are obtained from the Nusselt numbers for low-speed flow, equations 147 and 148. For laminar flow over a cone, with a shock attached to the nose, equations 147 and 148 are modified to:

$$Nu_x = 0.575\, Re_x^{1/2} Pr^{1/3} \quad (301)$$

and

$$\overline{Nu}_L = 0.767\, Re_L^{1/2}\, Pr^{1/3} \quad (302)$$

where x and L are measured along the surface from the tip. Physical properties and the velocity are based on conditions behind the shock.

14-7.2.2 Turbulent Flow

Similar to laminar flow, the heat transfer rates for turbulent high-speed flow may be obtained from equations developed for low-speed applications. The properties must be evaluated at T^*, defined by equation 299.

For turbulent flow and $0.5 < Pr < 2.0$, the recovery factor is approximated by:

$$R_T \simeq Pr^{1/3} \quad (303)$$

The adiabatic wall temperature is determined from equations 297 and 303 and is used in equation 298 to calculate the heating rate.

The Nusselt numbers for turbulent flow over a plate or a cone with an attached shock may be approximated by equations 152 and 153, the expressions for low-speed flow. For turbulent high-speed subsonic flow through tubes ($2{,}100 < Re_D < 10^5$), the Nusselt number is:

$$\overline{Nu_D} = 0.0395\, Re_D^{0.75}\, Pr \qquad (304)$$

14-7.3 Free Molecule Flow

In the free molecule flow regime, the molecular mean free path λ is much larger than the characteristic length. Molecules which impinge on the body and are then re-emitted will, on the average, travel a long distance before colliding with other molecules. The incident stream of molecules is unaffected by re-emitted molecules and no boundary layer exists in this regime. Free molecule flow exists when the ratio M/Re (a form of the Knudsen number) is greater than three.

The heat transfer rate equals the rate at which the gas molecules strike the surface multiplied by the difference between their impinging and re-emitted energies. Due to the nature of the gas and the condition of the surface, some of the impinging molecules do not reach equilibrium with the body surface and leave the surface at their original temperature T_∞, without transferring energy. The thermal accommodation coefficient α, an experimentally determined value for each gas-surface combination (see Table 14-24), is the fraction of the impinging molecules that are re-emitted at the wall temperature T_w.

Table 14-24. Thermal Accommodation Coefficient, α

Gas	Surface	α
H_2	Bright paint	0.32
H_2	Black paint	0.74
O_2	Bright paint	0.81
O_2	Black paint	0.93
CO_2	Bright paint	0.84
CO_2	Black paint	0.96
Air	Flat lacquer on bronze	0.88–0.89
Air	Polished bronze	0.91–0.94
Air	Machined bronze	0.89–0.93
Air	Polished cast iron	0.87–0.93
Air	Machined cast iron	0.87–0.88
Air	Polished aluminum	0.87–0.95
Air	Machined aluminum	0.95–0.97
Air	Etched aluminum	0.89–0.97

The Stanton number St is used to calculate heat transfer rates, in the free molecule flow regime. The Stanton number, a dimensionless form of the heat-transfer coefficient, is:

$$St = \frac{h_c}{v_\infty c_p \rho_\infty} \qquad (305)$$

where:

v_∞ = Free-stream velocity, ft/sec

ρ_∞ = Free-stream density, lb/ft^3

The Stanton number for free molecule flow multiplied by $\gamma/\alpha(\gamma + 1)$ is shown in Figure 14-110 as a function of the molecular speed ratio s, which is the ratio of the free-stream velocity v_∞ to the most probable molecular speed v_m.

Since,

$$v_m = \sqrt{2 g_c R T_\infty}$$

and,

$$v_\infty = M_\infty \sqrt{\gamma g_c R T_\infty}$$

the speed ratio may be expressed as:

$$s = M_\infty \sqrt{\frac{\gamma}{2}} \qquad (306)$$

where:

M_∞ = Free stream Mach number

Using the appropriate accommodation coefficient and speed ratio, the Stanton number is obtained from Figure 14-110. The heat-transfer coefficient is then calculated from equation 305. The recovery factor R_T in the free molecule flow regime is obtained from Figure 14-111 and used in equation 297 to determine the adiabatic wall temperature. The heat transfer rate is then calculated from equation 298.

14-7.4 Transition and Slip Flow Regimes

In the transition regime (between: $M/\sqrt{Re} > 0.1$ and $M/Re < 3$) the collisions between gas molecules, and the collisions of gas molecules with the body are of equal importance. The regime of small, but not negligible Knudsen numbers: $0.01 < M/\sqrt{Re} < 0.1$ is called the slip flow regime. As the name implies, in this regime the molecules immediately adjacent to a surface do not stick to it, but slide over it with a definite tangential velocity.

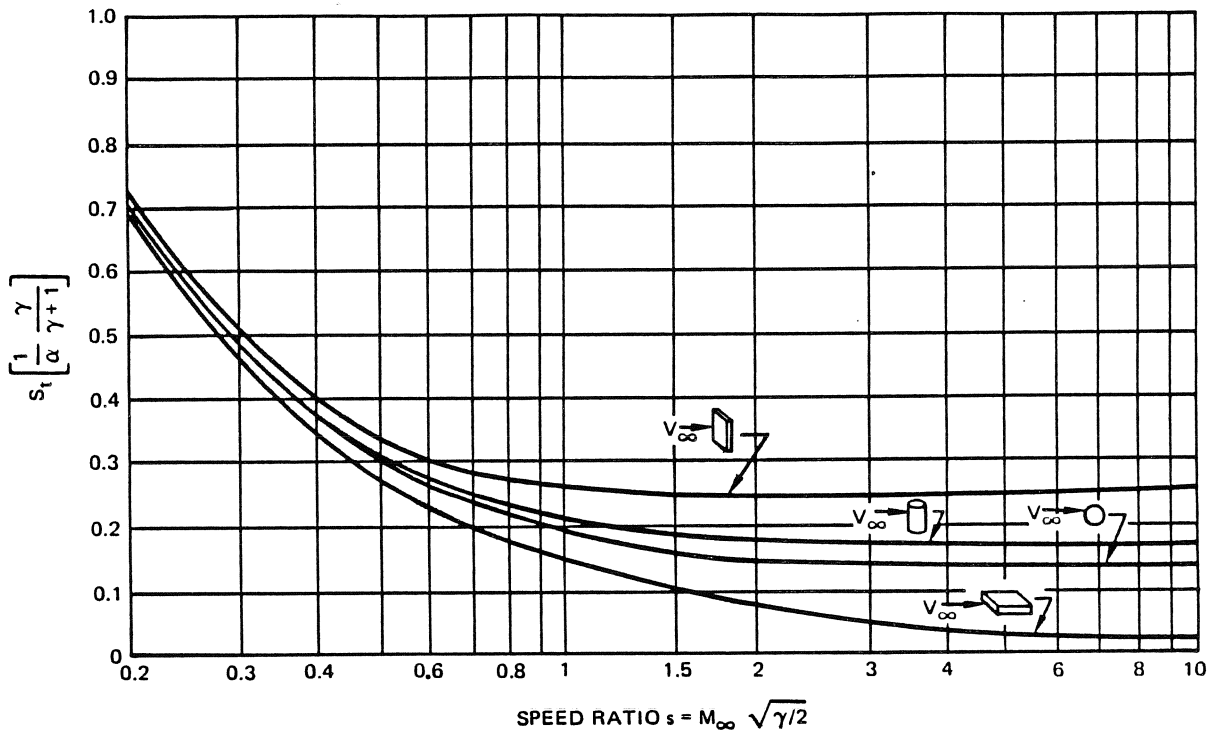

Figure 14-110. High-Speed Stanton Number for Free Molecule Flow

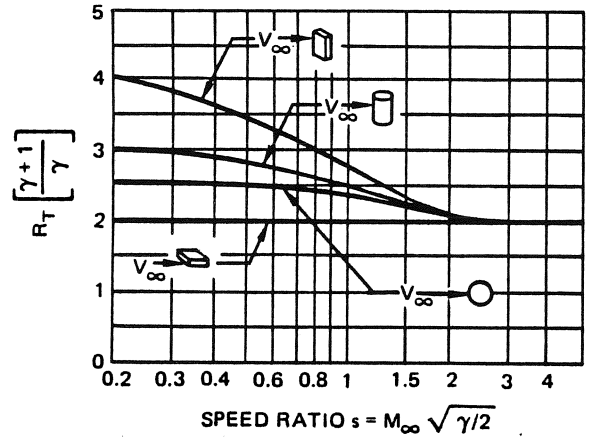

Figure 14-111. Recovery Factor for Free Molecule Flow

The flow and heat transfer phenomena in the transition and slip flow regimes are complex, and exact solutions are not available. The results of an approximate analysis, which are fairly well corroborated by experimental data, provide an expression for the average Stanton number over a flat plate,

$$St = \frac{0.38}{Z^2 M_\infty}\left[\exp(Z^2)\,\mathrm{erfc}\,Z - 1 + \frac{2}{\sqrt{\pi}}Z\right] \quad (307)$$

where:

$$Z = \frac{\sqrt{RePr}}{2.63\,M_\infty}$$

The Stanton number is obtained from equation 307 or Figure 14-112 and used in equation 305 to evaluate the heat transfer coefficient. Figure 14-112, which presents the product StM_∞ as a function of Z, shows how the results from equation 307 compare with the free molecule flow and continuum solutions.

14-7.5 Ablation

The ablation process involves a physical evaporation or a pyrolysis at the surface of a material exposed to a high-temperature gas, but it does not rely solely on the heat absorbed by the evaporation process for thermal protection. The change of phase of the ablating material

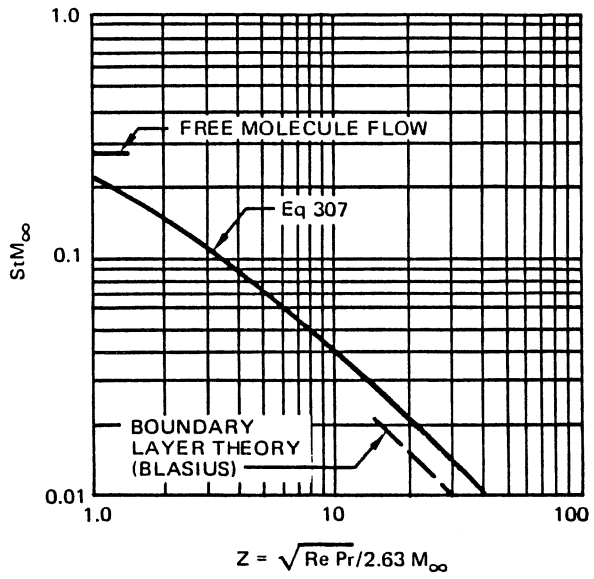

Figure 14-112. Stanton Number for Slip Flow Over a Flat Plate

produces a gaseous efflux from the surface into the aerodynamic boundary layer, causing the thickness of the boundary layer to increase, thus decreasing the rate of heat transfer.

Ablative cooling of rocket nozzles is discussed in Section 5, subsection 5-3.1.2.4. A complete treatment of the heat-transfer phenomena associated with ablation is very complex. However, the following simple theory provides a physical understanding of the ablation mechanism and of the parameters of importance in the process.

If the ablation velocity v (surface recession rate) for a subliming or melting material is assumed constant, the temperature distribution is given by equation 16 in Section 5. (Repeated here for convenience).

$$\frac{T - T_i}{T_s - T_i} = \exp\left[\frac{-q_m Z}{\alpha \rho Q^*}\right]$$

The ablation velocity is expressed as:

$$v = \frac{(q/A)_o}{\rho_s [H_{eff} + c_s(T_s - T_i)}} \qquad (308)$$

where:

$(q/A)_o$ = Heating rate at surface, Btu/ft^2–hr

ρ_s = Density of ablation material, lb/ft^3

H_{eff} = Effective heat of ablation, i.e., total energy absorbed per unit mass of ablated material, Btu/lb

c_s = Heat capacity of ablation material, Btu/lb–°R

T_s = Surface (melting or subliming) temperature, °R

T_i = Interior temperature of ablation material, °R

The fraction of the total heat transferred to the surface which is conducted into the solid is:

$$\frac{(Q/A)_{conducted}}{(Q/A)_{total}} = \frac{\rho_s k_s (T_s - T_i)\,[H_{eff} + c_s(T_s - T_i)]}{(q/A)_o^2} \qquad (309)$$

where:

k_s = Thermal conductivity of ablation material, Btu/hr–ft °R

It is desirable to minimize the fraction of heat conducted into the solid, and to minimize the ablation velocity, which determines the amount of material required. But comparing equations 308 and 309 indicates an apparent conflict: a small ablation velocity requires a large value of the term $[H_{eff} + c_s(T_a - T_\infty)]$, while minimizing the fraction of heat conducted into the solid requires a small value of this term. The most desirable material should have a large H_{eff}, but the smallest possible product of ρ_s, k_s, T_a and H_{eff}.

The design of any ablation system must simultaneously consider the combined insulation and ablation requirements. If a large amount of heat is conducted into the body, a weight penalty in the form of insulation may be necessary to prevent overheating of the interior, no matter how effectively the incoming energy is absorbed by the ablation material.

14-8 HEAT EXCHANGERS

A heat exchanger is a device which effects the transfer of heat from one fluid to another. Some exchangers simply mix the hot and cold fluids. This section considers the common types of heat exchangers in which one fluid is separated from the other by a wall or a partition through which the heat flows. Mechanical pumping power is expended to overcome fluid friction and move the fluids through the heat exchanger.

For heat exchangers, the heat transfer rate varies approximately as $v^{0.8}$ (equation 189), and the friction (pressure drop) varies by at least v^2 (equation 186). The design of an efficient system requires a compromise on velocity which optimizes the tradeoff between heat transfer rate and pumping-power expenditure. The power expenditure is usually not significant for high density fluids, but it may become the controlling factor for low density fluids.

14-8.1 Types of Heat Exchangers

Representative types of heat exchangers are shown in Figure 14-113. The simplest exchanger (a) is comprised of two concentric tubes. A similar design, the shell and tube heat exchanger (b and c), is widely used, highly standardized, versatile and reliable. Baffles are employed in the shell (c, d and e) to assure uniform distribution of the fluid and to interrupt the boundary-layer development, and thus, increase the heat transfer coefficient without increasing flow velocity.

For applications where the rate of heat transfer per unit weight and unit volume is the prime consideration, compact heat exchangers, such as the crossflow tubular and plate-fin exchangers (f and g), are used. When the two fluids are a gas and a liquid, a finned-tube heat exchanger (h) may be employed to increase the surface area on the gas side.

14-8.2 Heat Transfer Rate

The heat transfer rate q for a heat exchanger is given by:

$$q = UA_rF\Delta T_L \qquad (310)$$

where:

- U = Overall heat-transfer coefficient, Btu/hr–ft^2–°R
- A_r = Reference surface area, ft^2
- F = Temperature correction factor
- ΔT_L = Log mean temperature difference (LMTD), °R

The significance of each of these parameters is discussed in the following subsections.

14-8.2.1 Overall Heat Transfer Coefficient

The overall heat transfer coefficient is the reciprocal of the sum of the thermal resistances between the hot and cold fluids:

$$\frac{1}{U} = \frac{1}{h_c}\frac{A_r}{A_c} + \frac{L_w}{K_w}\frac{A_r}{A_w} + \frac{1}{h_h}\frac{A_r}{A_h} \qquad (311)$$

where:

- h_h, h_c = Convective heat transfer coefficients for hot and cold sides, Btu/hr-ft^2-°R
- A_h, A_c = Surface area on hot and cold sides, ft^2
- A_w = Log mean wall area, ft^2
- L_w = Thickness of wall, ft
- k_w = Thermal conductivity of wall, Btu/hr-ft-°R

Since the convective heat-transfer coefficients (h_h and h_c) depend on the flow velocity and fluid properties, the overall heat-transfer coefficient is not constant for a given heat exchanger, but varies with operating conditions. The values of h for flow through tubes are obtained from 14-4.7. The heat-transfer coefficients, in terms of the Colburn j-factor (equation 188), and the friction factors for some complex heat exchanger geometries are presented in Figures 14-114 through 14-117. The friction factor f is defined as:

$$f = \frac{\rho \tau_o}{G^2/2g_c} \qquad (312)$$

where:

- τ_o = Shear stress, lb/ft^2
- ρ = Fluid density, lb/ft^3
- G = Mass flowrate per unit of minimum free-flow area, lb/ft^2-sec

The information presented in Figures 14-114 through 14-117 is for the specific geometries indicated. These typical values are included for comparison purposes. Additional information may be obtained from "Compact Heat Exchangers" by Kays and London, which catalogues 92 different heat transfer surfaces.

An effective heat transfer surface should have a low f/j ratio (friction/heat-transfer coefficient). Figure 14-118 compares the f/j ratios for the surfaces presented in Figures 14-114 through 14-117. The plain plate-fin surface (Figure 14-116) is shown to be very effective in the region of high Reynolds numbers.

14-8.2.2 Reference Area

The reference area A_r used in equation 311 is usually the surface area of either the hot or the cold side (A_h or A_c). For a flat plate $A_h = A_c = A_w$, where A_w is the wall area. For a tube the wall area is:

$$A_w = \frac{A_o - A_i}{\ln(A_o/A_i)} \qquad (313)$$

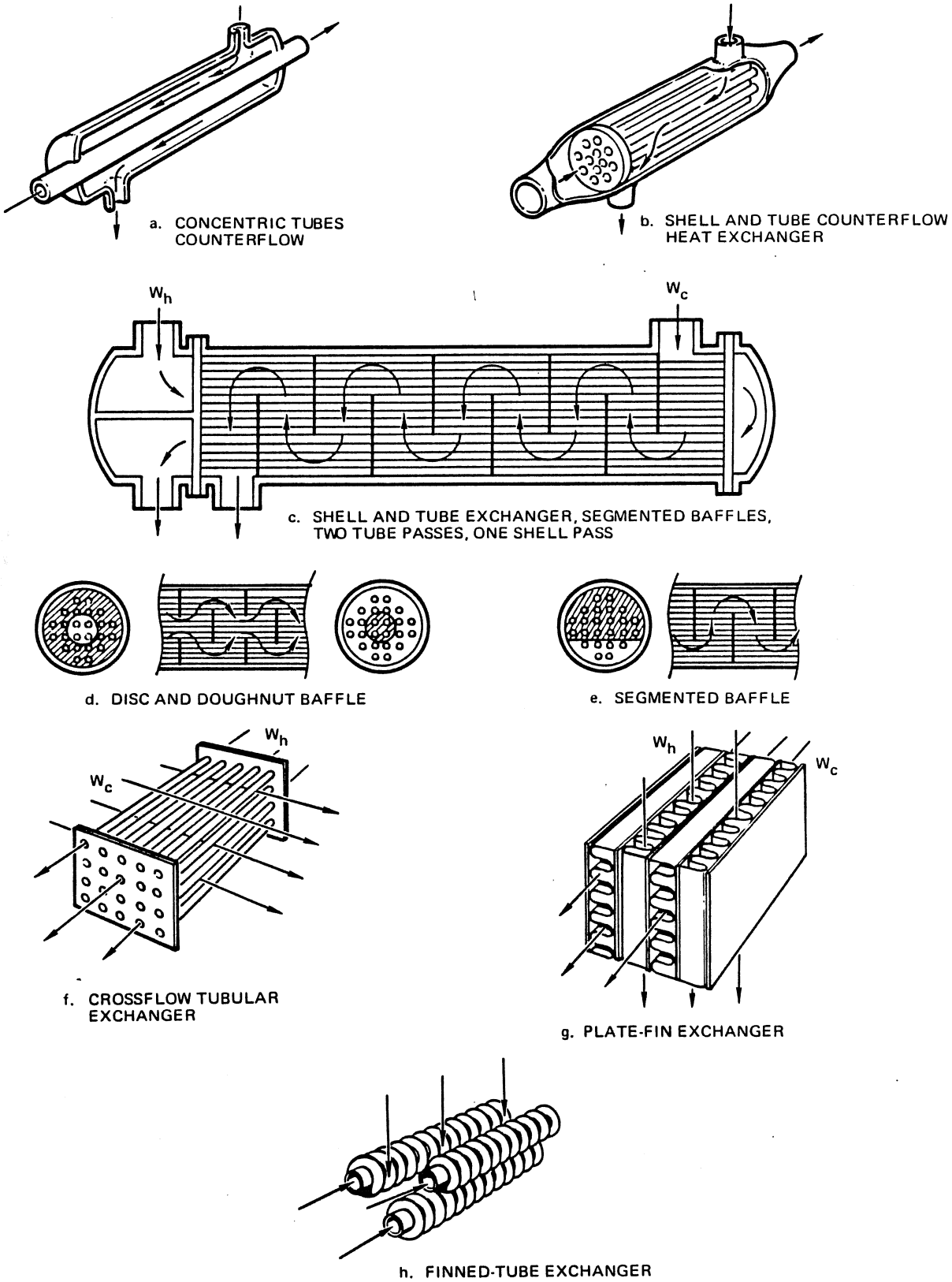

a. CONCENTRIC TUBES COUNTERFLOW

b. SHELL AND TUBE COUNTERFLOW HEAT EXCHANGER

c. SHELL AND TUBE EXCHANGER, SEGMENTED BAFFLES, TWO TUBE PASSES, ONE SHELL PASS

d. DISC AND DOUGHNUT BAFFLE

e. SEGMENTED BAFFLE

f. CROSSFLOW TUBULAR EXCHANGER

g. PLATE-FIN EXCHANGER

h. FINNED-TUBE EXCHANGER

Figure 14-113. Representative Types of Heat Exchangers

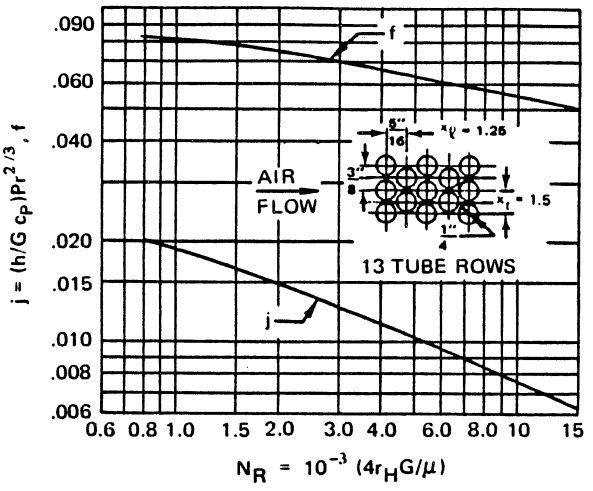

Tube outside diameter = 0.250 in.
Hydraulic diameter, $4r_H$ = 0.0166 ft
Free-flow area/frontal area, σ = 0.333
Heat transfer area/total volume,
α = 80.3 ft^2/ft^3

NOTE: Minimum free-flow area is in spaces transverse to flow.

Figure 14-114. Heat Transfer in Flow Normal to a Staggered Tube Bank

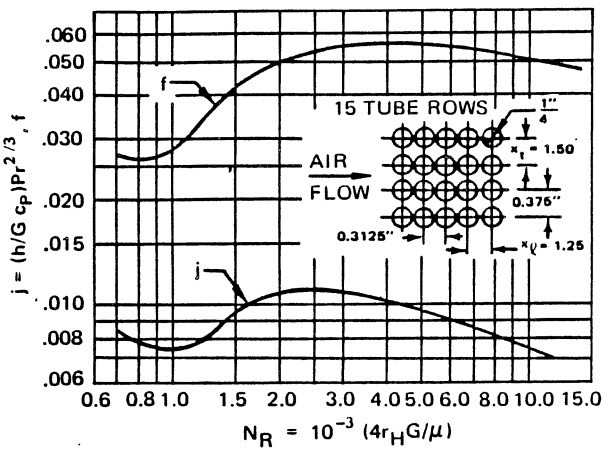

Tube outside diameter = 0.250 in.
Hydraulic diameter, $4r_H$ = 0.166 ft
Free-flow area/frontal area, σ = 0.338
Heat transfer area/total volume,
α = 80.4 ft^2/ft^3

Figure 14-115. Heat Transfer in Flow Normal to an In-Line Tube Bank

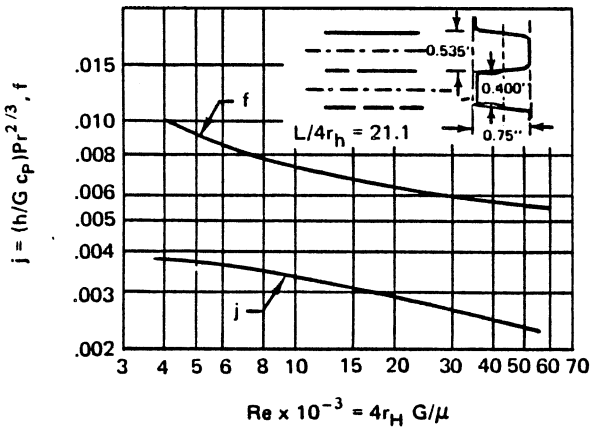

Fin pitch = 2.0 per in.
Plate spacing, b = 0.750 in.
Fin length = 12.0 in.
Flow passage hydraulic diameter,
$4r_H$ = 0.0474 ft
Fin metal thickness = 0.032 in.
Aluminum
Total heat transfer area/volume between plates, β = 76.1 ft^2/ft^3
Fin area/total area = 0.606

Figure 14-116. Heat Transfer in Flow Through Plain Plate-Fins

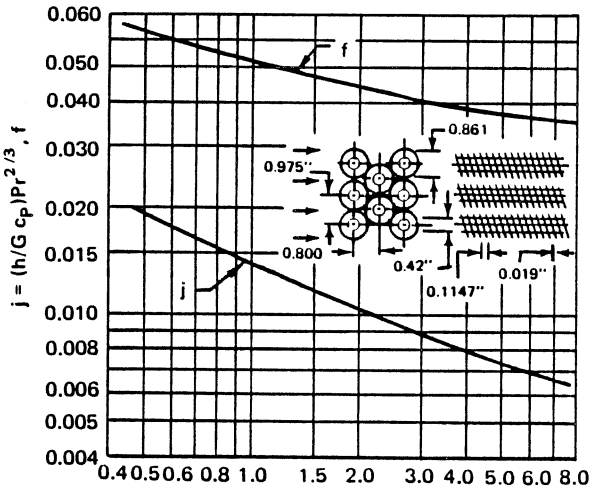

Tube outside diameter = 0.42 in.
Fin pitch = 8.72 per in.
Flow passage hydraulic diameter,
$4r_H$ = 0.01452 ft
Fin thickness (average) = 0.019 in., copper*
Free-flow area/frontal area, σ = 0.494
Heat transfer area/total volume,
α = 136 ft^2/ft^3
Fin area/total area = 0.876

**Fins slightly tapered*

Figure 14-117. Heat Transfer in Flow Transverse to Finned Circular Tubes

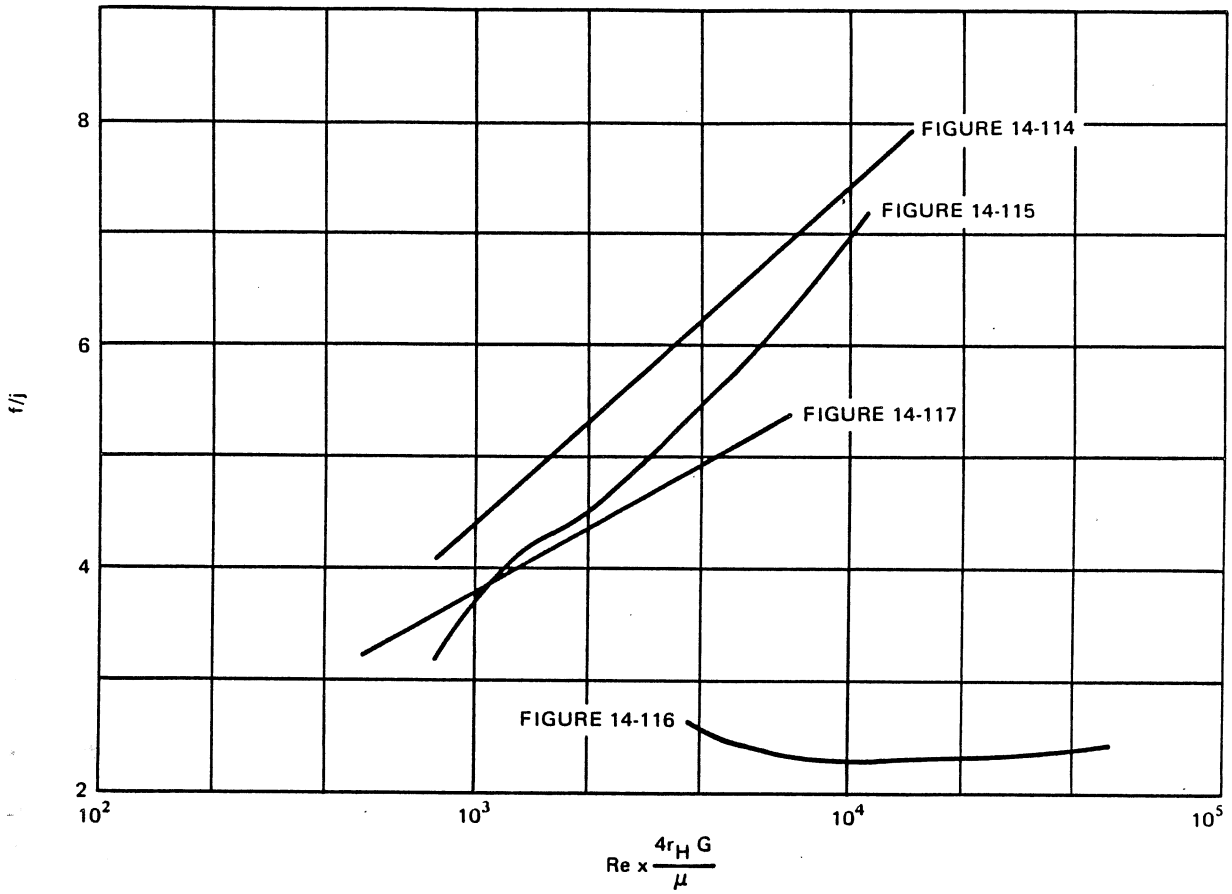

Figure 14-118. Comparison of f/j Ratios for Various Heat Exchanger Geometries

where:

A_o = Outer surface area, in.^{2}

A_i = Inner surface area, in.^{2}

For values of $A_o/A_i < 2$ the arithmetic mean area $(A_o + A_i)/2$ provides satisfactory accuracy.

14-8.2.3 Log Mean Temperature Difference

The log mean temperature difference LMTD provides the best average temperature difference for use in equation 310. Derivation of the LMTD is shown in 14-4.7.3. For counter flow in a heat exchanger (Figure 14-113 a), the LMTD is:

$$\Delta T_L = \frac{(T_{h_{out}} - T_{c_{in}}) - (T_{h_{in}} - T_{c_{out}})}{\ln\left[\frac{(T_{h_{out}} - T_{c_{in}})}{(T_{h_{in}} - T_{c_{out}})}\right]} \quad (314)$$

where:

T_h, T_c = Temperature of hot and cold fluids, °R

The subscripts "in" and "out" indicate conditions taken at the heat exchanger inlets and outlets. The LMTD for parallel flow is obtained from equation 314 by reversing the "in" and "out" subscripts on T_h.

14-8.2.4 Temperature Correction Factor

The temperature correction factor F in equation 310 corrects the LMTD for *counterflow* (equation 314) to provide the true mean temperature for shell-and-tube or crossflow heat exchangers. Figures 14-119 and 14-120 present F for two shell-and-tube configurations plotted as a function of the temperature ratio P and a parameter Z.

$$P = \frac{T_{t_{out}} - T_{t_{in}}}{T_{s_{in}} - T_{t_{in}}} \quad (315)$$

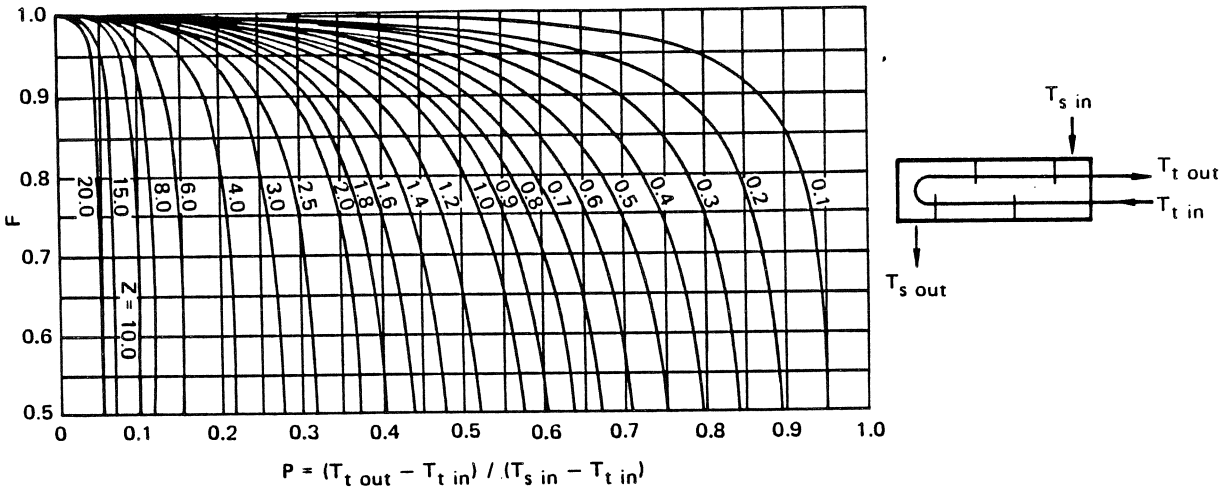

Figure 14-119. Correction Factor to Counterflow LMTD for Heat Exchanger with One Shell Pass and Two, or a Multiple of Two, Tube Passes

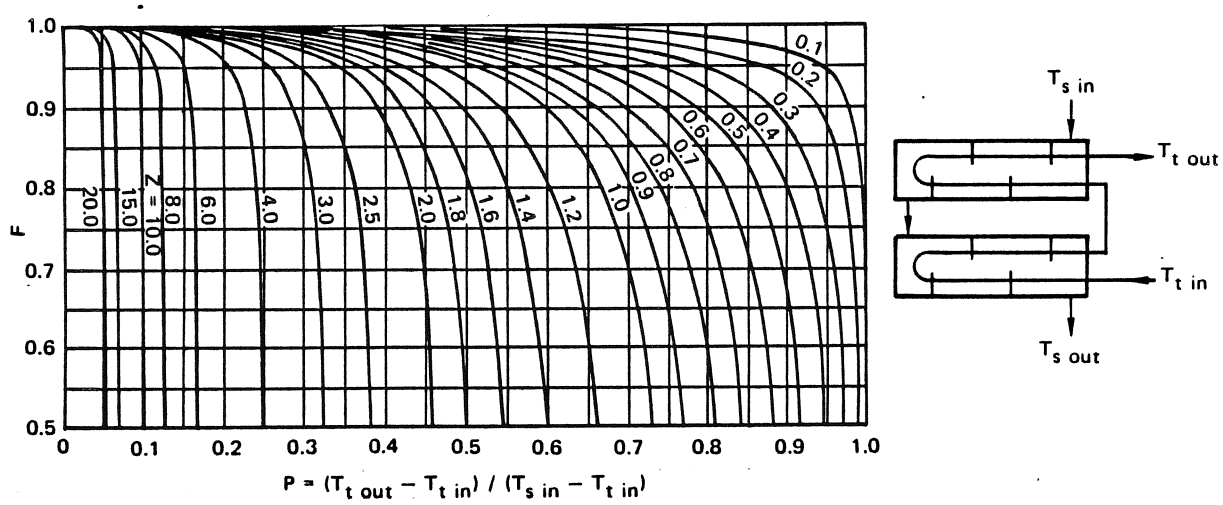

Figure 14-120. Correction Factor to Counterflow LMTD for Heat Exchanger with Two Shell Passes and a Multiple of Two Tube Passes

The subscripts t and s indicate tube and shell.

The parameter Z is defined as:

$$Z = \frac{\dot{w}_t c_{P_t}}{\dot{w}_s c_{P_s}} = \frac{T_{s_{in}} - T_{s_{out}}}{T_{t_{out}} - T_{t_{in}}} \qquad (316)$$

where:

$\dot{w}$ = Weight flow rate, lb/hr

c_p = Constant pressure specific heat, Btu/lb-°R

In the application of the correction factors it is immaterial whether the warmer fluid flows through shells or tubes. If the temperature of either of the fluids remains constant, the direction of flow is also immaterial, since F equals 1 and the LMTD applies directly.

Figure 14-121 presents F for crossflow with the fluid on the shell side mixed, and the other fluid unmixed (for example, the configuration in Figure 14-113, f with the cold fluid on the shell side). Figure 14-122 shows F for crossflow with both fluids unmixed (for example, the configuration in Figure 14-113 g).

14-8.2.5 Core Pressure Drop

The core pressure drop in compact heat exchangers is obtained from:

$$\frac{\Delta P}{P_{in}} = \frac{v_{in}^2 \rho_{in}}{2 P_{in} g_c} \left[(K_c + 1 - \sigma^2) + 2\left(\frac{\rho_{in}}{\rho_{out}} - 1\right) + f \frac{L}{r_H} \frac{\rho_{in}}{\rho_{in}} - (1 - \sigma^2 - K_e) \frac{\rho_{in}}{\rho_{out}} \right] \qquad (317)$$

where:

ΔP = Core pressure drop, lb/ft^2

P_{in} = Fluid inlet pressure, lb/ft^2, absolute

v_{in} = Fluid velocity at the inlet, ft/sec

ρ = Fluid density, lb/ft^3

K_c, K_e = Entrance and exit loss coefficients (approximately 0.3)

σ = Ratio of free-flow area to frontal area

f = Fluid friction factor

L = Length of flow passage, ft

r_H = Hydraulic radius (equation 167), ft

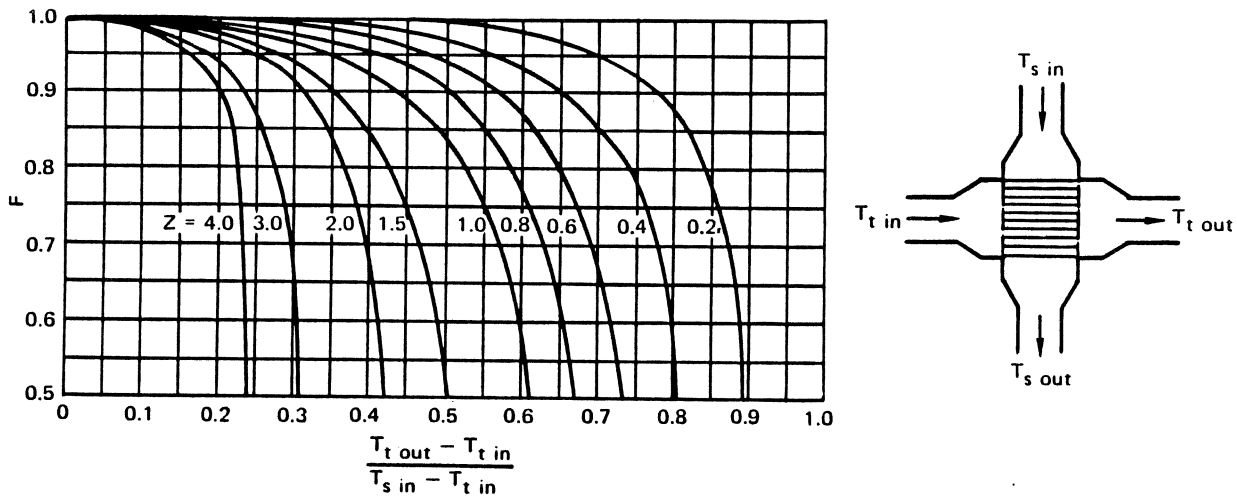

Figure 14-121. Correction Factor to Counterflow LMTD for Crossflow Heat Exchangers, Fluid on Shell Side Mixed, Other Fluid Unmixed, One Tube Pass

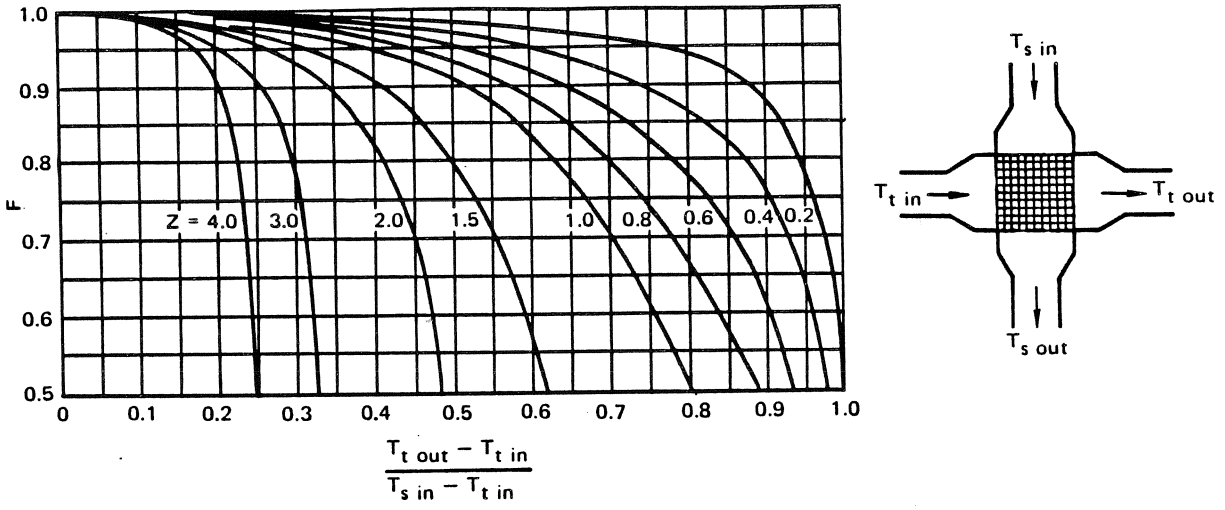

Figure 14-122. Correction Factor to Counterflow LMTD for Crossflow Heat Exchanger, Both Fluids Unmixed, One Tube Pass

The subscripts "in" and "out" denote inlet and outlet conditions. The subscript m indicates the mean value, $\rho_m = (\rho_{in} + \rho_{out})/2$. Friction factors for some complex geometries are presented in Figures 14-114 through 14-117.

14-8.3 Heat-Exchanger Effectiveness

Equation 310 is convenient for calculating heating rates when the terminal temperatures necessary for the evaluation of the LMTD are known. However, there are occasions when the heat exchanger coefficient U is known, or can be estimated, but the temperatures of the fluids leaving the exchanger are not known. If equation 310 is used to calculate outlet temperatures and heating rates, a tedius trial-and-error procedure is required.

The heat-exhange effectiveness ϵ is used to obtain an equation for the heat transfer rate which does not involve the outlet temperatures. The effectiveness is the ratio of the actual and the maximum possible heat transfer rates. The expression for ϵ depends on the magnitudes of the hourly heat capacities, C_h and C_c. When C_h is less than C_c, ϵ is defined as:

$$\epsilon = \frac{C_h(T_{h_{in}} - T_{h_{out}})}{C_{min}(T_{h_{in}} - T_{c_{in}})} \qquad (318)$$

when C_h is greater than C_c, ϵ is:

$$\epsilon = \frac{C_c(T_{c_{out}} - T_{c_{in}})}{C_{min}(T_{h_{in}} - T_{c_{in}})} \qquad (319)$$

where:

C_h = Hourly heat capacity of the hotter fluid = $\dot{w}_h c_{ph}$, Btu/hr-°R

C_c = Hourly heat capacity of the colder fluid = $\dot{w}_c c_{pc}$, Btu/hr-°R

C_{min} = The smaller of the two capacities, C_h and C_c.

Once the effectiveness is known, the heat transfer rate is determined directly from:

$$q = \epsilon\, C_{min}(T_{h_{in}} - T_{c_{in}}) \qquad (320)$$

The effectiveness for various types of heat exchangers is presented in Figures 14-123 through 14-127 as a function of C_{min}/C_{max} and AU/C_{min}. The latter parameter is called the number of heat-transfer units (NTU). The larger the value of NTU, the closer the heat exchanger approaches its thermodynamic limit. For an evaporator or condenser, $C_{min}/C_{max} = 0$, because by definition if one fluid remains at constant temperature throughout the exchanger, its effective specific heat, and thus its capacity rate, is by definition equal to infinity.

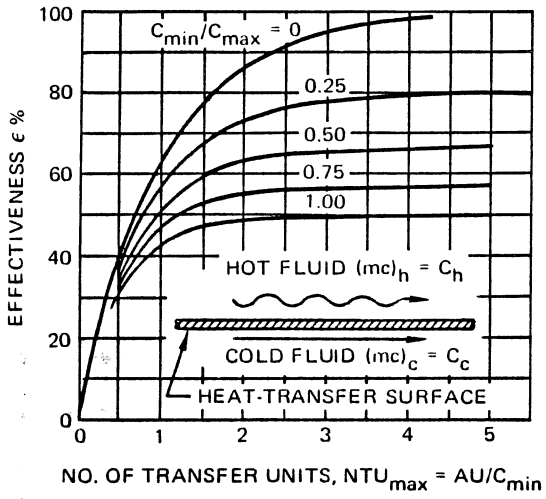

Figure 14-123. Heat-Exchanger Effectiveness for Parallel Flow

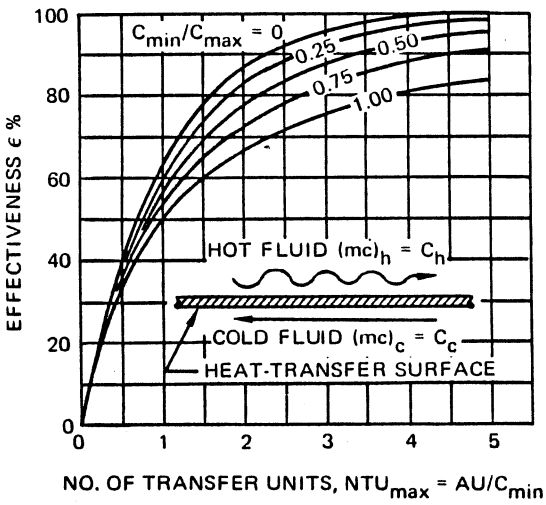

Figure 14-124. Heat-Exchanger Effectiveness for Counterflow

14-8.4 Fouling Factors

The performance of heat exchangers under service conditions is difficult to predict because a dirt film usually builds up and increases the thermal resistance to heat transfer. The deposit typically may be rust, scale, silt or coke. Manufacturers usually cannot predict the nature of the dirt deposit and its fouling effect. Thus, only the performance of clean exchangers can be guaranteed.

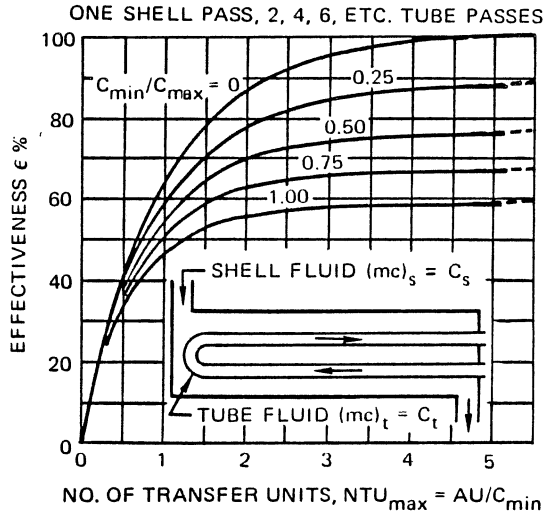

HEAT-EXCHANGER EFFECTIVENESS FOR SHELL-AND-TUBE HEAT EXCHANGER WITH ONE WELL-BAFFLED SHELL PASS AND TWO, OR A MULTIPLE OF TWO, TUBE PASSES

Figure 14-125. 1-2 Parallel-Counterflow Exchanger Performance

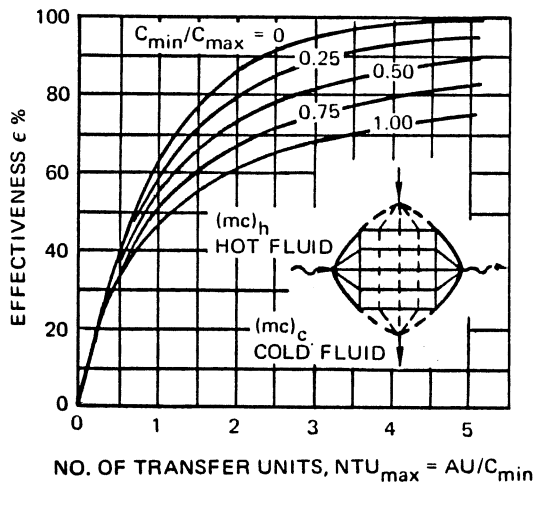

Figure 14-126. Heat-Exchanger Effectiveness for Crossflow with Both Fluids Unmixed

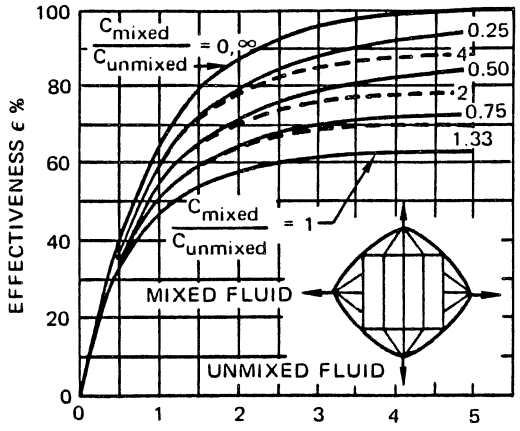

Figure 14-127. Heat-Exchanger Effectiveness for Crossflow with One Fluid Mixed, the Other Unmixed

An estimate of the fouling effect can be obtained from:

$$R_d = \frac{1}{U_a} + \frac{1}{U} \qquad (321)$$

where:

U = Overall heat-transfer coefficient of the clean exchanger, Btu/hr-ft^2-°R

U_a = Overall coefficient after fouling has occurred, Btu/hr-ft^2-°R

R_d = Unit thermal resistance of the scale, hr-ft^2-°R/Btu

Fouling factors for various applications have been compiled in "Standards of Tubular Exchanger Manufacturers Association." A few samples are listed in Table 14-25.

14-9 APPLICATIONS

The equations presented in Section 14 can be used in manual computations to obtain approximate solutions of heat transfer problems. When more accurate solutions are required, applicable equations are utilized in digital computer programs that perform many iterative solutions over small increments of significant parameters such as time, distance, and temperature. This subsection presents examples of heat transfer problems, drawn from MDAC programs, that are solved by manual methods and by computer methods. The nomenclature used in these examples is defined in subsection 14-10.

Table 14-25. Normal Fouling Factors

Types of Fluid	Fouling Resistance (hr-°F-ft^2/Btu)
Sea water below 125 F	0.0005
Sea water above 125 F	0.001
Treated boiler feed water above 125F	0.001
East River water below 125F	0.002-0.003
Fuel oil	0.005
Quenching oil	0.004
Alcohol vapors	0.0005
Steam, non-oil bearing	0.0005
Industrial air	0.002
Refrigerating liquid	0.001

14-9.1 Application No. 1 – Liquid/Gas Heat Exchanger Design

Design a GSE heat exchanger for the Saturn S-IVB stage to cool helium during acceptance tests and launch countdown. The helium is used to prechill the J-2 engine prior to ignition, to pressurize the stage cold helium storage bottles, and to pressurize the stage propellant tanks prior to launch. The heat exchanger configuration to be used, (Figure 14-128) is similar to a design that was used successfully in the S-IVB program.

14-9.1.1 Design Requirements

The heat exchanger must be able to chill ambient temperature helium to 50°R when it is flowing at a rate of 40 lb/min, using liquid hydrogen as the coolant.

14-9.1.2 Nomenclature

The following notation will be used in the analysis.

A = Area, ft^2

c_p = Heat capacity, Btu/lb – °R

D = Diameter, ft

h = Heat transfer coefficient, Btu/hr-ft^2-°R

k = Thermal conductivity, Btu/hr-ft-°R

Pr = Prandtl number

q = Heat flow, Btu/hr

R = Thermal resistance, hr-°R/Btu

Re = Reynolds number

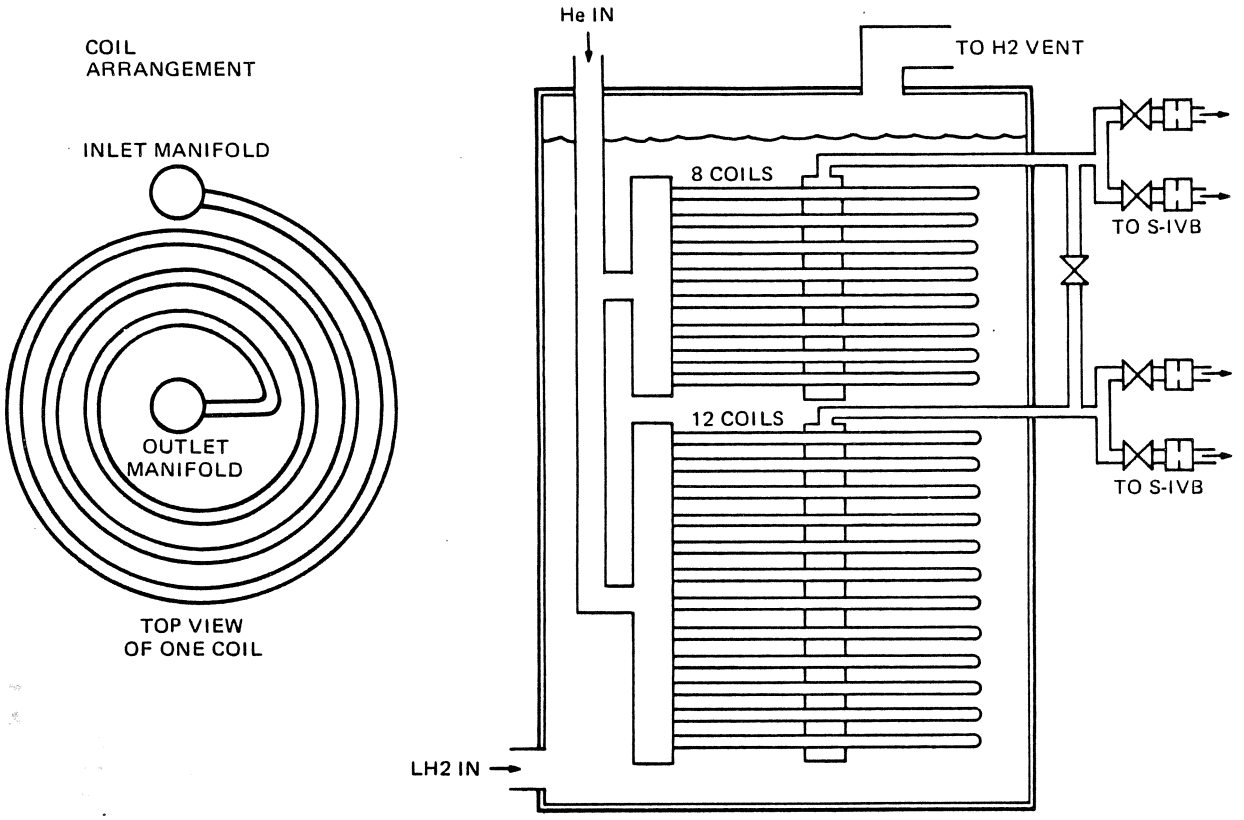

Figure 14-128. Heat Exchanger Configuration

T	=	Temperature, °R
$\overline{T}$	=	Average temperature, °R
U	=	Overall heat transfer coefficient, Btu/hr-ft^2-°R
$\dot{w}$	=	Weight flowrate, lb/min
μ	=	Absolute viscosity, lb/ft-hr

Subscripts

b	=	Bulk gas
F	=	At end of incremental length
G	=	Gas
in	=	At the inner surface of pipe wall
L	=	Liquid
LH_2	=	Liquid hydrogen
out	=	At the outer surface of pipe wall
P	=	Pipe
W	=	Pipe wall

14-9.1.3 Given Data

The heat exchanger coils are arranged in two interconnected branches with orifices and valves to control the helium flow for the various functions. The coils in each branch are manifolded together with equal flow in each coil.

The hydrogen boiling heat transfer coefficient is shown in Figure 14-129.

Initial helium temperature is 520° R.

Liquid hydrogen temperature is 36.5° R.

Coils are made of stainless steel with an internal diameter = 0.0296 ft, and an external diameter = 0.0416 ft.

14-9.1.4 Assumptions

The following assumptions were made to simplify the analysis.

Steady-state conditions exist.

Fluid viscosity is uniform at any station.

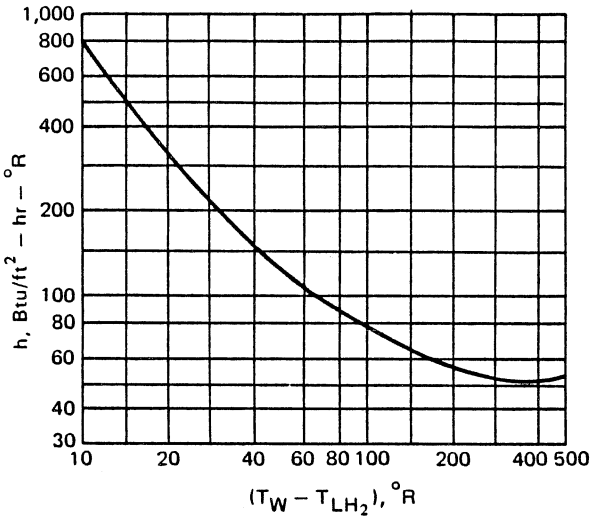

Figure 14-129. Pool Boiling Hydrogen Heat Transfer Coefficient

Average wall temperature is equal to the gas temperature.

Bubbles from coils do not affect the heat transfer of adjacent coils.

14-9.1.5 Procedure

The heat transfer properties of the helium and the liquid hydrogen film coefficient vary with distance along the coil, due to changing temperature. Since these variations are not linear functions, it is desirable to make the calculations along incremental lengths of the coil to avoid errors introduced by using a mean temperature over the entire length of the coil. Figure 14-130 is a cross-section sketch that illustrates the temperature gradient across the coil wall and identifies significant parameters used in the solution of the problem.

The basic equation for heat transfer, $Q = UA\Delta T$, for this case becomes:

$$Q = \pi U_{in} D_{in} \Delta X (T_G - T_{LH_2}) \quad (322)$$

where:

$$U_{in}D_{in} = (R_G + R_W + R_L)^{-1} \quad (323)$$

$$R_G = (D_{in} h_{in})^{-1} \quad (324)$$

$$R_W = \ell n(D_{out}/D_{in})(2k_p)^{-1} \quad (325)$$

$$R_L = (D_{out} h_{out})^{-1} \quad (326)$$

$$h_{in} = 0.026\left[\frac{k_G}{D_{in}}\right] Re^{.8} Pr^{1/3} \left[\frac{\mu_b}{\mu_w}\right]^{.14}$$

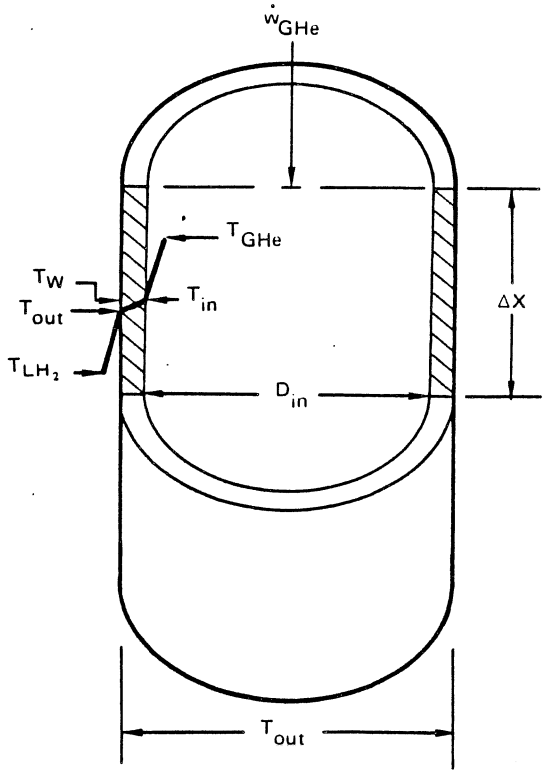

Figure 14-130. Heat Transfer Nomenclature

It was assumed that $\mu_b \approx \mu_w$, therefore

$$h_{in} = 0.026\left(\frac{k_G}{D_{in}}\right) Re^{.8} Pr^{1/3} \quad (327)$$

Steady-state heat transfer is assumed in each increment, therefore:

$$Q = \Delta T/R = \Delta T_L/R_L = \Delta T_W/R_W = \Delta T_G/R_G \quad (328)$$

also,

$$\Delta T = \Delta T_L + \Delta T_W + \Delta T_G \quad (329)$$

Since thermal conductivity of the coil depends on the wall temperature, and the LH_2 film coefficient depends on the wall-to-liquid ΔT, an iterative process must be used to determine the average wall temperature in each incremental length of coil. The average wall temperature is:

$$\overline{T}_W = T_{LH_2} + \Delta T_L + 0.5\Delta T_W$$

Using Equations 328 and 329,

$$\overline{T}_W = T_{LH_2} + \Delta T_L + 0.5(R_W)(R_W + R_L + R_G)^{-1}(T_G - T_{LH_2}) \quad (330)$$

Step-by-step procedure for the calculations is as follows.

a. Make a first approximation of the average wall temperature by assuming it is equal to the gas temperature. This assumption means, in effect, that film boiling is occurring around the coil, and the drop from gas to liquid temperature occurs in the film boiling.

b. Calculate the thermal resistances at the inside wall of the pipe (coil), through the pipe wall, and at the outside wall of the pipe using equations 324, 325 and 326.

c. Check to see if $R_L >> R_G + R_W$. If it is, the first approximation is good, and the heat transfer may be calculated in Step d using equation 322. The gas temperature at the end of the increment may then be calculated, using $T_F = T_G - Q/(\dot{w}_{HE} c_p)$, and used as the initial temperature of the next increment (Step e).

d. If R_L is not $>> R_G + R_W$, make a second approximation:

$$\Delta T_L = R_L(R_L + R_G + R_W)^{-1}(T_G - T_{LH_2})$$

e. Calculate a new R_L from equation 326.

f. Calculate $\overline{T}_W$ from equation 330.

g. Find k_P based on $\overline{T}_W$. If this k_P is approximately equal to the one used in step b, the second approximation is good, and the heat transfer and final gas temperature may be calculated as in step c. If the two k_P's are not equal, make a third approximation.

h. Calculate a new R_W from equation 325 using k_P based on the new $\overline{T}_W$.

i. Calculate ΔT_L as in step d, using the new R_W and R_L.

j. Calculate a new R_L based on the ΔT_L and equation 326.

k. Calculate a new $\overline{T}_W$, using the new R_L and equation 330.

l. If the new $\overline{T}_W$ is approximately equal to the old $\overline{T}_W$, the approximation is good enough, and the heat transfer and final temperature may be calculated as in step c.

m. If the new $\overline{T}_W$ and old $\overline{T}_W$ are not close, go to step h.

A FORTRAN computer program (F633) was run on the IBM 7090 computer to make the calculations. The results are presented in Figure 14-131. A flow chart of the program is shown in Figure 14-132 and a sample hand calculation follows.

14-9.1.6 Calculations

a. Assume average wall temperature is equal to the gas temperature.

$$\overline{T}_W = T_G = 520^\circ R$$

b. Calculate thermal resistances at the inside wall of the pipe (coil), through the pipe wall, and at the outside wall of the pipe.

1. Resistance at inside wall

$\dot{w}_{HE} = 2$ lb/min

$k_G = 0.083$ Btu/ft-hr-°R

$c_p = 1.254$ Btu/lb-°R

$\mu = 0.051$ lb/ft-hr

$$Re = 4\,w_{HE}/(\pi D_{in}\mu)$$
$$= 4(2(60))6(\pi(0.0296)(0.051))$$
$$= 1.012 \times 10^5$$

$$Pr = c_p\mu/k_G$$
$$= 1.254(0.051)/0.083 = 0.771$$

$$h_{in} = 0.026(k_G/D_{in})(Re)^{0.8}Pr^{1/3}$$
$$= 0.026\left(\frac{0.083}{0.0296}\right)\left(1.012\times10^5\right)^{0.8}(Pr)^{1/3}$$
$$= 675 \text{ Btu/ft}^2\text{-hr-}^\circ R$$

$$R_G = 1/(D_{in}h_{in}) = 1/(0.0296(675))$$
$$= 0.05 \text{ hr-ft-}^\circ R/\text{Btu}$$

2. Resistance through wall

$k_P = 8.5$ Btu/ft-hr-°R (from material properties)

$$R_W = \ell n(D_{out}/D_{in})/(2k_P)$$
$$= \ell n(0.0416/0.0296)/(2(8.5))$$
$$= 0.020 \text{ ft-hr-}^\circ R/\text{Btu}$$

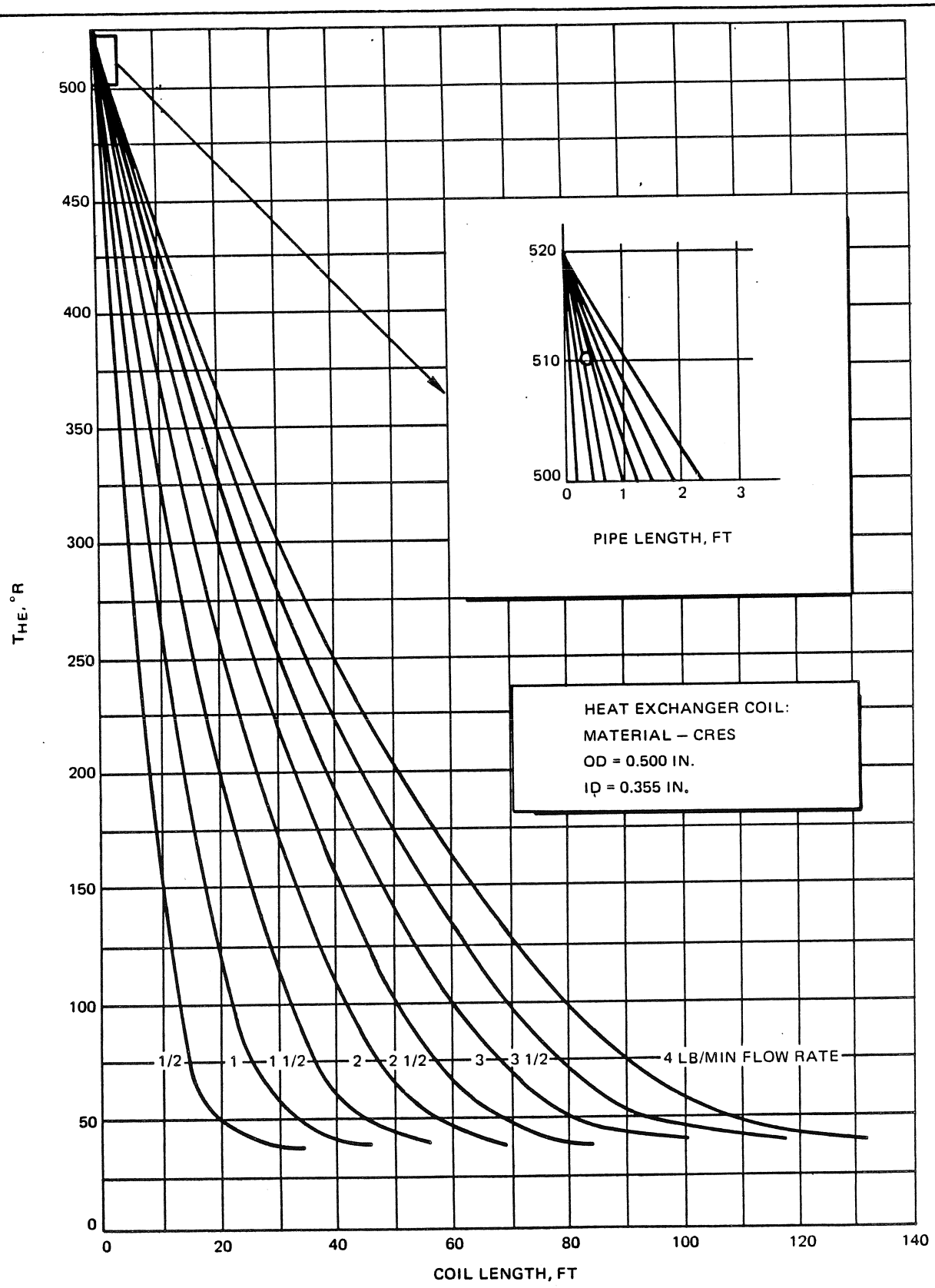

Figure 14-131. Helium Cooling Data

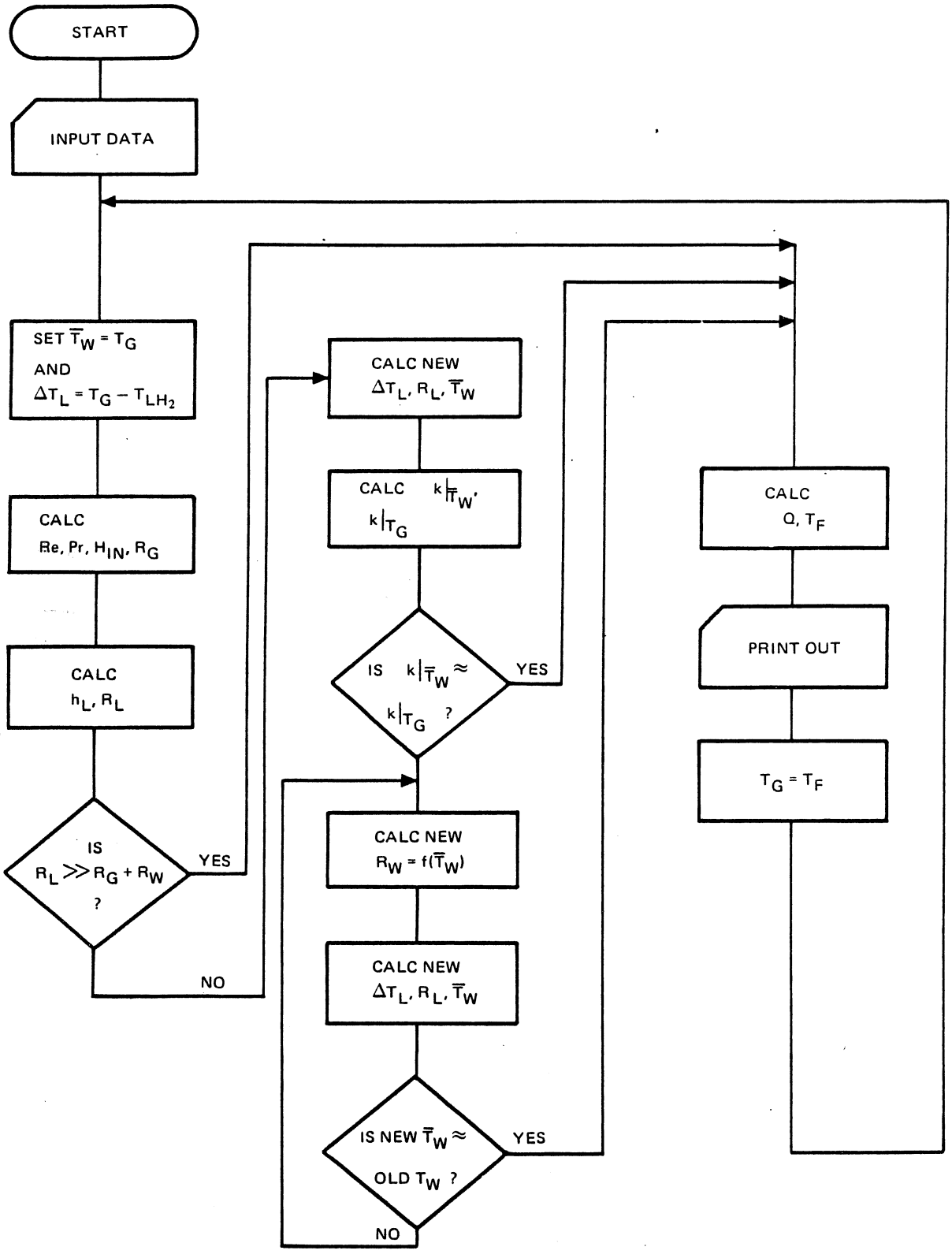

Figure 14-132. Computer Program Flow Chart

3. Resistance at outside wall from Figure 14-129, with $\Delta T_L = 483.5^\circ R$,

$$h_L = 51.5 \text{ Btu/ft}^2\text{-hr-}^\circ R$$

$$R_L = 1/(D_{out}h_{out})$$

$$= 1/(0.0416(51.5))$$

$$= 0.0467 \text{ ft-hr-}^\circ R/\text{Btu}$$

c. Check to see if $R_L >> R_G + R_W$

$$0.0467 >> 0.050 + 0.020$$

Since R_L is much greater than the other resistances, the first approximation is good enough, i.e., a high proportion of the temperature drop does occur in the film boiling region (as assumed in Step a). The heat transfer may now be calculated.

d. Calculate the heat transfer rate through the incremental length of pipe.

$$\Delta X = 0.5 \text{ ft}$$

$$q = \pi\Delta X(R_G + R_W + R_L)^{-1} (T_G - T_L)$$

$$= \pi(0.5(0.050 + 0.020 + 0.467)^{-1} (520 - 36.5)$$

$$q = 1415 \text{ Btu/hr}$$

e. Calculate the temperature of the gas at the end of the 0.5-foot increment for use as the initial temperature for the next increment.

$$T_F = T_G - q/\dot{w}_{HE}c_p)$$

$$= 520 - 1415/(2(60)(1.254))$$

$$= 520 - 9.4$$

$$T_F = 510.6^\circ R$$

This point is shown on the inset on Figure 14-131.

14-9.2 Application No. 2 – Tank Vent Duct Heater Requirements

Liquid waste from the Orbital Workshop will be dumped into the waste tank which is vented to the orbital environment to maintain a pressure below the triple point pressure for water (0.089 psia). Approximately 15 percent of the liquid entering this low pressure volume will flash to a gas, absorbing sufficient heat from the remaining liquid to freeze it.

Screens in the waste tank will prevent large ice particles from escaping through the two opposed nonpropulsive vent (NPV) ducts. However, the cold exterior environment can cause condensation of water vapor on the inside duct wall. This condensation, plus empingement of small ice particles, could cause undesired unbalanced thrust through the NPV ducts. Therefore, the NPV duct walls will be heated to prevent the buildup of ice during venting.

The duct temperature during flow must be determined as a function of the distance from the duct entrance for several candidate wall thicknesses and heater power loads.

14-9.2.1 Design Requirements

The NPV duct temperature must be kept above $492^\circ R$, and the electrical requirements for the duct heaters be kept to a minimum to conserve electrical power. The duct size shall be large enough that the waste tank pressure will not rise to 0.089 psia during any anticipated liquid dump. A previous analysis determined that the duct inside diameter should be 1.5 inches for a duct length of one foot in order to maintain the waste tank pressure below 0.089 psia during the maximum liquid dump rate (2.0 lb/min).

14-9.2.2 Nomenclature

L = Duct length, ft

X = Distance along the duct, ft

D_i = Duct inside diameter, ft

D_o = Duct outside diameter, ft

T = Duct Temperature, $^\circ R$

T_G = Gas Temperature, $^\circ R$

T_R = Radiant Sink Temperature, $^\circ R$

A_C = Area of section thru which heat flows by conduction, ft^2

q_H = Heater power, btu/hr

k = Thermal Conductivity of duct material, $Btu/hr\text{-}ft^2\text{-}^\circ R$

h_G = Convective heat transfer coefficient, $Btu/hr\text{-}ft^2\text{-}^\circ R$

h_R = Unit thermal conductance for radiation, $Btu/hr\text{-}ft^2\text{-}^\circ R$

σ = Stefan-Boltzman radiation constant = 0.17×10^{-8} Btu/hr-ft^2-°R^4

ϵ = Emissivity for radiation

F = Geometric shape factor for radiation from one black body to another

14-9.2.3 Given Data

The waste tank configuration is shown in Figure 14-133.

Vent duct inside diameter is 1.5 inches (0.125 feet).

Temperature of the gas entering the NPV ducts is a function of the waste tank pressure, as defined in Figure 14-134.

Each of the two NPV ducts is 12 inches (1 foot) long and is made of an aluminum alloy.

14-9.2.4 Assumptions

Steady-state pressure and temperature conditions exist during each venting period.

Duct material is homogeneous.

Heat loss from the end of the duct is negligible.

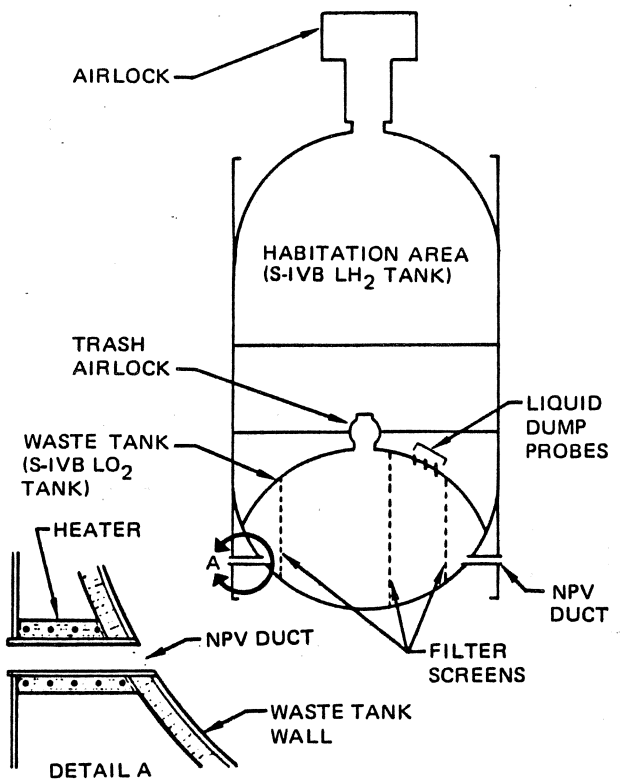

Figure 14-133. Orbital Workshop Waste Tank Configuration

An electric heater distributes energy uniformly on the exterior surface of the vent ducts to prevent icing of the duct interior walls.

Temperature at the vent duct inlet is 492°R (triple point temperature).

Waste tank pressure never exceeds 0.089 psia (triple point pressure) during venting.

The gas is homogeneous and its temperature is 448°R.

The radiant sink temperature is 310°R

Emissivity is 0.1.

Radiation shape factor is 1.0.

14-9.2.5 Procedure

In order to derive an equation for the temperature distribution of the duct, a heat balance is made for a small elemental section of the duct as shown in Figure 14-135, the thermal model for the waste tank vent duct.

Under steady-state conditions the rate of heat flow into the element is equal to the rate of the heat flow out of the element, as described in equation 331.

$$q_H - kA_C \frac{dT}{dx} = h_G(\pi D_i\, dx)(T - T_G) + h_R(\pi D_o\, dx)(T - T_R) - kA_C \left.\frac{dT}{dx}\right|_{x+dx} \qquad (331)$$

where:

Heat in, consists of:

The rate of heat flow by conduction into the element at X or $-kA_C\,(dT/dx)$

The heater power q_H and

Heat out, consists of:

The rate of heat flow by convection from the surface between x and (x + dx) or $h_G(\pi\, D\, dx)(T - T_G)$

The rate of heat flow by radiation from the surface between x and (x + dx) or $h_R(\pi\, D\, dx)(T - T_R)$

The rate of heat flow by conduction out of the element at (x + dx) or $-kA_C\,(dT/dx)\big|_{x+dx}$.

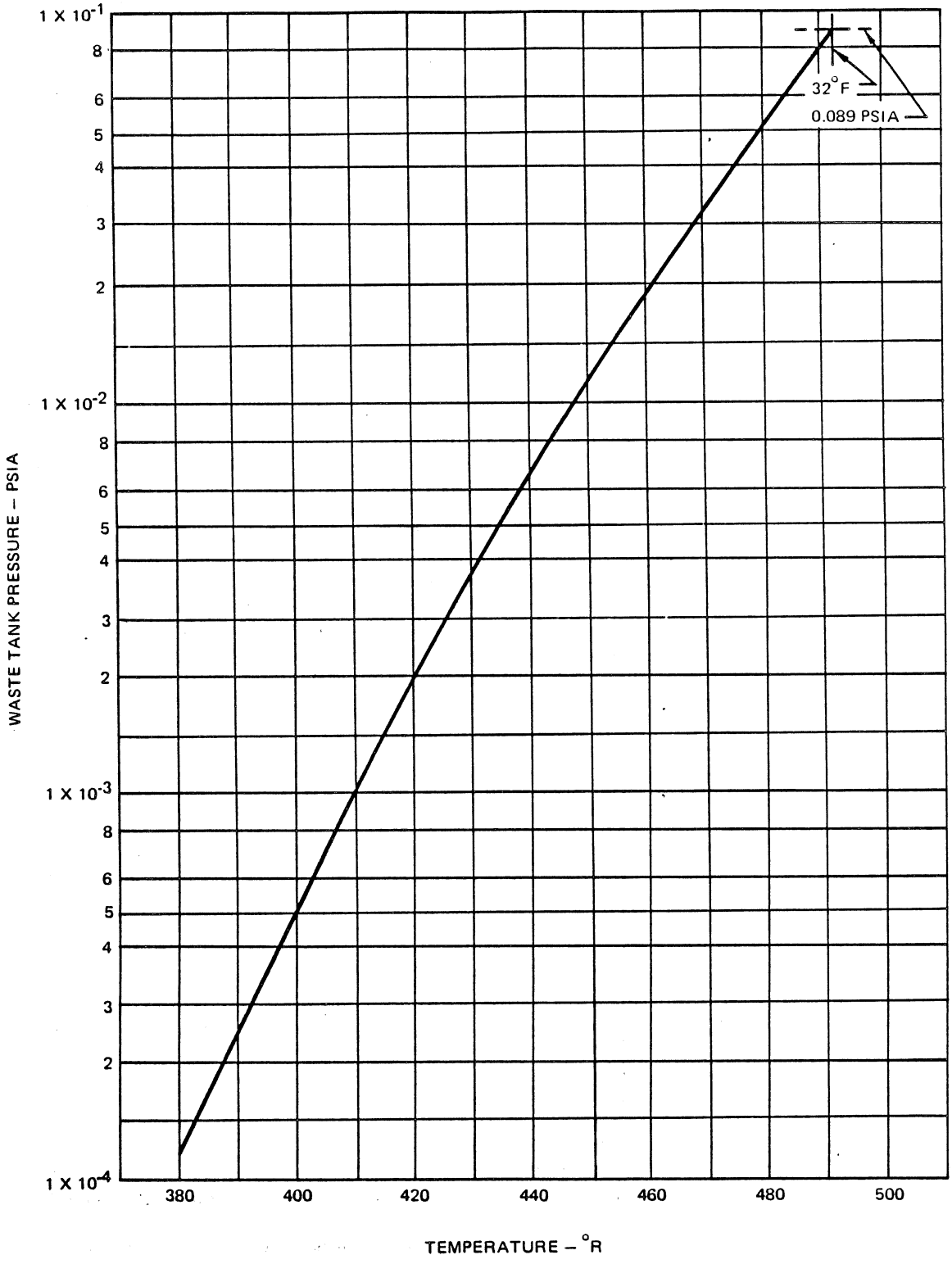

Figure 14-134. Water Ice Separation Temperature

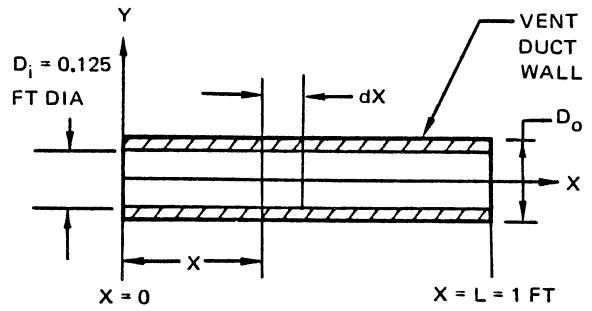

Figure 14-135. Thermal Model, Waste Tank Vent Duct

The rate of heat transfer by radiation h_R is derived as follows:

The net rate of heat transfer from a body at temperature T_1 to a black surrounding body at T_2 is given by:

$$q_R = \sigma A \epsilon F (T_1^4 - T_2^4). \quad (332)$$

If the heat transfer by radiation is written as

$$q_R = k_R (T_1 - T_2)$$

(where the definition of k_R is similar to k_C, the thermal conductance for conduction), the unit thermal conductance for radiation,

$$h_R = \frac{k_R}{A} = \frac{\sigma \epsilon F (T_1^4 - T_2^4)}{T_1 - T_2} \quad (333)$$

The rate of heat flow by conduction out of the element at (x + dx) is:

$$-kA_c \frac{dT}{dx}\bigg|_{x+dx}.$$

Evaluation of this expression will give:

$$-kA_c \frac{dT}{dx}\bigg|_{x+dx} = -kA_c\left(\frac{dT}{dx}\right) + \frac{d}{dx}\left(-kA_c \frac{dT}{dx}\right)dx$$

$$= -kA_c\left(\frac{dT}{dx} + \frac{d^2T}{dx^2}\,dx\right) \quad (334)$$

Substituting this expression in the equation of the heat balance, and after cancelling equal terms, the equation becomes:

$$kA_c \frac{d^2T}{dx^2} + q_H/L - h_G \pi D_i (T - T_G)$$

$$- h_R \pi D_o (T - T_R) = 0 \quad (335)$$

This form can be simplified to:

$$\frac{d^2T}{dx^2} - aT + b = 0 \quad (336)$$

where

$$a = \frac{(h_G D_L + h_R D_o)\pi}{kA_c} \quad (337)$$

$$b = \frac{q_{H/L} + h_G \pi D_i T_G + h_R \pi D_o T_R}{kA_c} \quad (338)$$

The solution for this differential equation is:

$$T = \alpha \sinh a^{1/2} x + \beta \cosh a^{1/2} x + b/a \quad (339)$$

α and β can be evaluated in terms of initial duct temperature (T_o) and a and b. The constraints of integration are determined by the boundary conditions. One of the boundary conditions is $T = T_o$ at $x = 0$.

Since it was assumed that the heat loss from the end of the vent duct is to be neglected, the second boundary condition requires that the temperature gradient at $x = L$ be zero or $dT/dX = 0$ at $x = L$.

Solution of equation 339 at these boundary conditions results in equation 340 for the dimensionless temperature profile,

$$\frac{T - b/a}{T_o - b/a} = \cosh a^{1/2} x - \tanh a^{1/2} \sinh a^{1/2} x \quad (340)$$

The steady-state dimensionless temperature ratio $(T - b/a)/(T_o - b/a)$ can be determined at any duct wall station x by solving equation 340.

When an initial duct temperature T_o is assumed, the steady-state duct temperature can be expressed in terms of T_o, x, a, and b as shown in equation 341.

$$T = (T_o - b/a)[\cosh a^{1/2} x$$

$$-(\tanh a^{1/2} \cosh a^{1/2}) x] - b/a \quad (341)$$

For this problem, the initial temperature T_o was assumed to be 492°R.

Solution of equation 340 or 341 requires calculation of a and b using equations 337 and 338. Both of these latter equations contain D_o and D_i terms, and equation 338 contains a q_H term. Therefore, since D_i is held constant, equation 341 can be used to calculate the duct wall temperature profile for a range of duct wall thicknesses (D_o) and heater powers.

14-9.2.6 Calculations

The following computations must be performed to solve equations 340 and 341 for the desired duct temperature profiles:

A. For a circular cross-section duct,

$$A_c = \pi/4\,(D_o^2 - D_i^2)$$

B. Equation 333 is used to calculate,

$$h_R = \frac{0.017 \times 10^{-8}(1)(0.1)(310^4 - 500^4)}{310 - 500}$$

$$= 0.05 \text{ Btu/hr-ft}^2\text{-}^\circ\text{R}$$

C. Selection of the appropriate heat transfer coefficient equation for forced flow in a duct, listed in Table 14-16, is dependent on the magnitude of the Reynolds number.

$$Re_D = \frac{\rho v D_H}{\mu} = \frac{1.2 \times 10^{-4} \text{ lb/ft}^3 \text{ (v ft/hr)} 0.125 \text{ ft}}{0.02 \text{ lb/ft-hr}}$$

$$= 7.5 \times 10^{-4} \text{ v ft/hr}$$

During liquid dumps, the waste tank pressure rises sufficiently to produce choked flow in the duct. Therefore:

$$v = \sqrt{\gamma g R T}$$

and for saturated water vapor,

$$v = \sqrt{1.32 \times 32.2 \times 86 \times 448} = \sqrt{1.64 \times 10^6}$$

$$= 1{,}280 \text{ ft/sec}$$

$$v = 1{,}280 \text{ ft/sec} \times 3{,}600 \text{ sec/hr}$$

$$= 4.61 \times 10^6 \text{ ft/hr}$$

$$Re = 7.5 \times 10^{-4} \times 4.61 \times 10^6 = 3{,}460$$

Since $2{,}100 < Re_D < 10{,}000$, flow is in the transition region and the applicable heat transfer coefficient equation in Table 14-16 is

$$h_c = 0.116 \frac{k}{D}\left(Re_D^{2/3} - 125\right) Pr^{1/3} \left[1 + \left(\frac{D}{L}\right)^{2/3}\right] \left(\frac{\mu_b}{\mu_w}\right)^{0.14}$$

The Prandtl number for saturated steam at 448° R is

$$Pr = \frac{\mu c_p}{k} = \frac{0.02 \text{ lb/ft-hr} \times 0.5 \text{ Btu/lb-}^\circ\text{R}}{0.008 \text{ Btu/hr-ft-}^\circ\text{R}} = 1.25$$

Since fluid properties were assumed to be uniform in the duct, bulk viscosity $\mu_b = \mu_w$, the viscosity at the duct wall, and $(\mu_b/\mu_w)^{0.14} = 1$.

Therefore:

$$h_c = 0.116\left(\frac{0.008}{0.125}\right)\left(3460^{2/3} - 125\right) 1.25\left[1 + \left(\frac{0.125}{1}\right)^{2/3}\right](1)^{0.4}$$

$$h_c = 0.14 \text{ Btu/hr-ft}^2\text{-}^\circ\text{R}$$

Since condensation of any steam on the duct walls will significantly increase the effective heat transfer coefficient, the value selected for solutions of equations 340 and 341, to be conservative, was

$$h_c = 0.5 \text{ Btu/hr-ft}^2\text{-}^\circ\text{R}.$$

Table 14-26 lists calculated values of A_c and a for the three duct outside diameters considered. Table 14-27 lists calculated values of b and b/a at D_o = 1.75 inch at each of four heater powers. Table 14-28 lists calculated values of $(T - b/a)/(T_o - b/a)$ at six positions along the duct for each of the considered duct sizes at one of the intermediate heater powers. Table 14-29 lists calculated values of the duct temperature T for the middle duct size at six positions along the duct for each of the four heater powers considered.

Figure 14-136 is a plot of the data presented in Table 14-28, and Figure 14-137 is a plot of the data presented in Table 14-29. Figure 14-137 shows that a heater power of 17 btu/hr-ft will maintain the duct temperature profile above the triple point temperature (492° R) and that the thinner wall provides a higher temperature profile.

Table 14-26. Values of A_c and a

Parameter	O. D.		
	1.75 in. (0.146 ft)	1.875 in. (0.156 ft)	2.00 in. (0.167 ft)
A_c	0.00443	0.00690	0.0095
a	0.56	0.36	0.26

Table 14-27. Values of b and b/a at O.D. = 1.75 in.

q_H	0	8	17	34
b	249.48	269.77	292.60	335.71
b/a	446	482	523	599

Table 14-28. Values of $(T-b/a)/(T_o-b/a)$ at q_H = 17 Btu/hr

X	D_o, in. (ft)		
	1.75 (0.146)	1.875 (0.156)	2.00 (0.167)
0	1.	1.	1.
0.2	0.91564	0.94261	0.95719
0.4	0.85192	0.89881	0.92435
0.6	0.80741	0.86796	0.90114
0.8	0.78110	0.84963	0.88720
1.0	0.77238	0.84356	0.88269

Table 14-29. Duct Temperature T, °R at O.D. = 1.75 in.

X	q_H, Btu/hr			
	0	8	17	34
0	492.	492.	492.	492.
0.2	488.119	491.156	494.615	501.027
0.4	485.188	490.519	496.591	507.845
0.6	483.141	490.074	497.970	512.607
0.8	481.931	489.811	498.786	515.422
1.0	481.529	489.724	499.056	516.355

14-9.3 Application No. 3 – Rocket Motor Throat Transient Temperature Calculation

The S-IVB ullage solid rocket motor nozzle assembly, shown in Figure 14-138, has a solid graphite throat insert that is a press fit in a steel nozzle shell. To prevent overheating the shell, the graphite-steel interface must not exceed 1,000°F during the web burning time.

A comprehensive multidimensional heat transfer model must be developed for use in the JA 26 computer program to determine the interface temperature accurately. A preliminary heat transfer analysis,

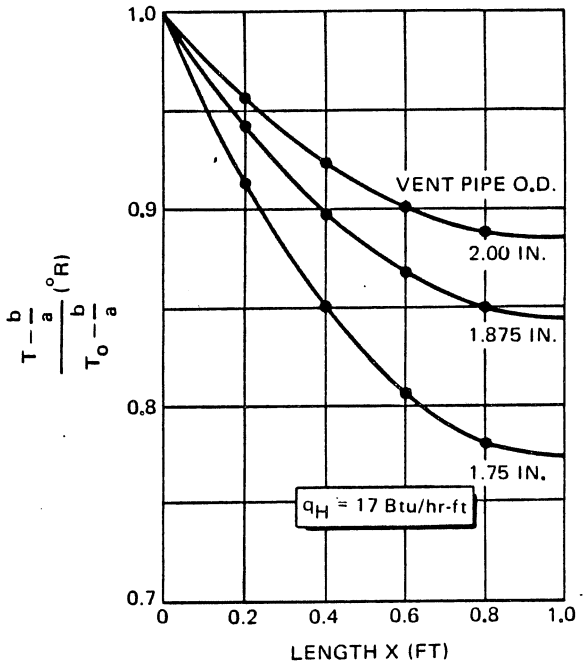

Figure 14-136. Duct Dimensionless Temperature Profile

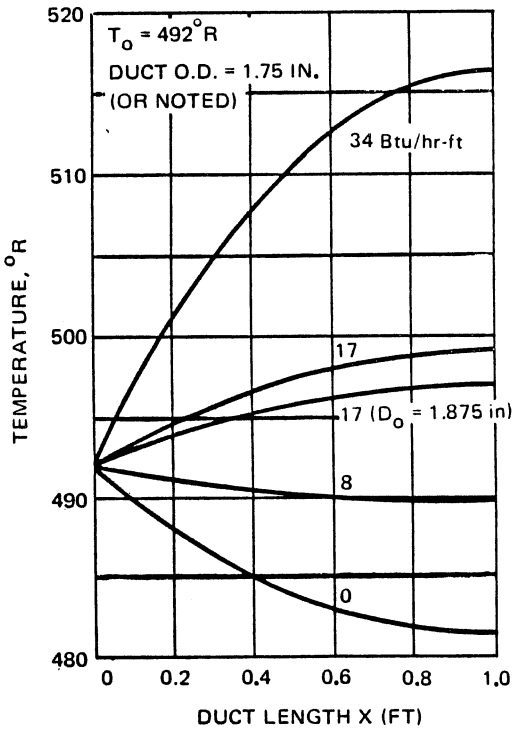

Figure 14-137. Duct Temperature Profile

documented in this application, was performed to establish the feasibility of the proposed design configuration, before initiating development of the multidimensional model.

14-9.3.1 Design Requirements

The graphite-steel interface temperature must not exceed 1,000°F during the solid propellant grain web burning time (3.82 seconds) for the given conditions and assumptions listed.

14-9.3.2 Nomenclature

- a = Thermal diffusivity, ft^2/hr
- Bi = Biot number
- c = Specific heat of graphite insert, Btu/lb-°R
- D_t = Diameter of nozzle throat, ft
- Fo = Fourier modulus
- h_c = Convective heat transfer coefficient, btu/hr-ft^2-°R
- k = Conductivity of graphite insert, btu/hr-ft-°R
- $\bar{m}$ = Average molecular weight of combustion gas, lb/lb-mole
- M = Mach number
- P_c = Average combustion pressure, lb/in^2 abs
- r = Radius of graphite insert, in
- T = Temperature of graphite insert, °R
- T_c = Combustion gas temperature, °R
- T_o = Initial propellant grain temperature, °R
- T_∞ = Free stream or sink temperature, °R
- γ = Specific heat ratio of combustion gas
- ρ = Density of graphite insert, lb/ft^3
- θ = Web burning time, sec

14-9.3.3 Given Data

The nozzle configuration is shown in Figure 14-139:

- $\bar{m}$ = 26.25 lb/lb-mole
- $\bar{P}_c$ = 1,000 $lb/in.^2$ abs
- T_c = 5060°R (4600°F)
- γ = 1.17
- c = 0.344 Btu/lb-°F
- k = 38.2 Btu/hr-ft°F
- T_o = 530°R (70°F)
- ρ = 105 lb/ft^3
- θ = 3.82 sec

14-9.3.4 Assumptions

No heat is transferred across the graphite-steel interface.

No erosion of the graphite throat occurs.

Maximum web burning time is 4 seconds.

Graphite material properties are determined at the average graphite temperature during the web burning time.

Heat transfer coefficient is computed at the average throat pressure.

The graphite throat model is a long concentric ring that is heated internally.

14-9.3.5 Procedure

The transient temperature of the outer surface of the cylindrical graphite throat can be determined by the use of the Schneider charts in Figure 14-38B. In order to use these charts, the following calculations must be made:

A. Calculate the Fourier modulus,

$$F_o = a\theta/r^2$$

B. Calculate the Biot number,

$$Bi = \bar{h}L/k_s = \bar{h}_c r/k$$

C. Calculate the radius Ratio,

$$R_i = r_i/r_e \qquad (342)$$

D. Using the graph for R_i closest to the value of R_i so calculated, determine the value of $T = (T - T_o)/T_\infty - T_o)$ that occurs at the intersection of the values of F_o and Bi determined previously. If the calculated value of R_i is not close to the value of one of the available graphs, a more accurate value of T can be obtained by cross-plotting T versus R_i at the previously calculated values of F_o and Bi, using each of the available constant-R_i graphs.

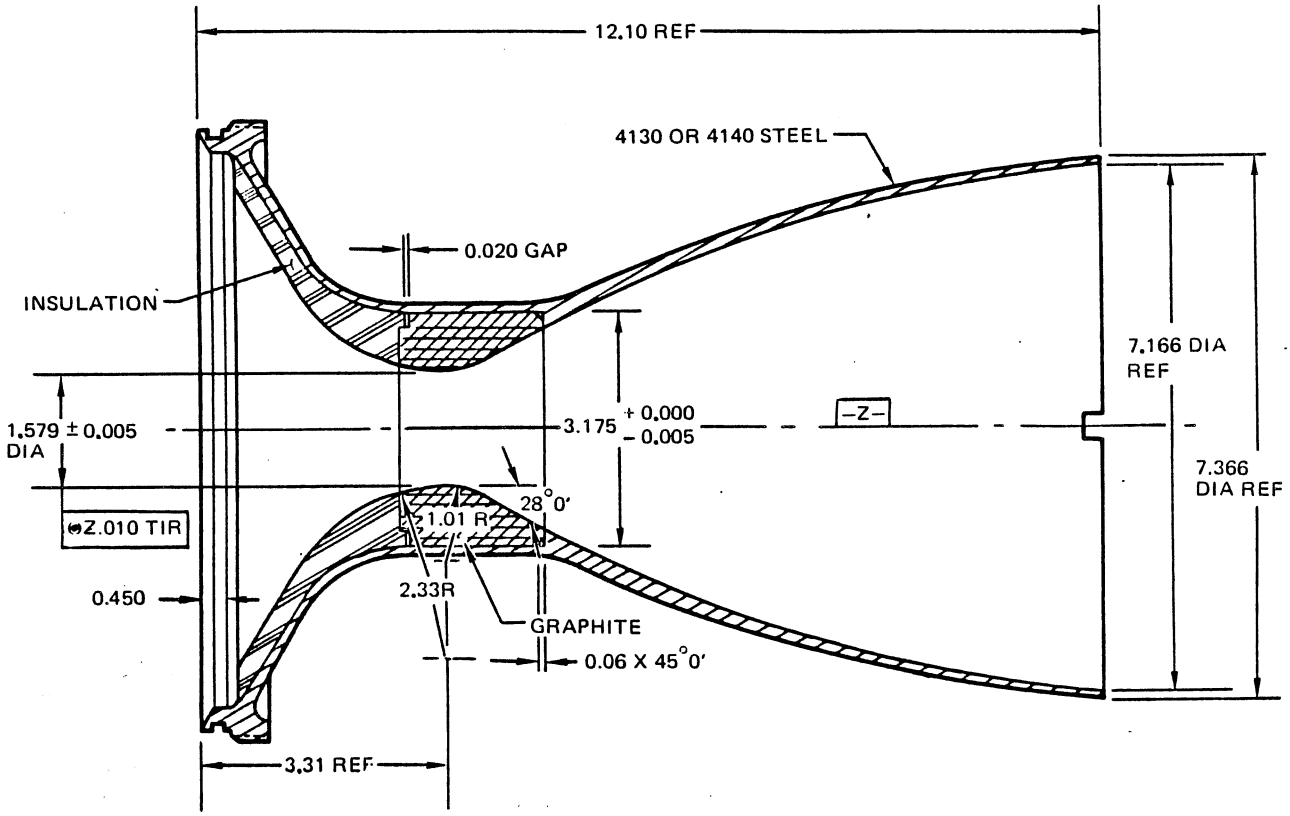

Figure 14-138. Ullage Rocket Motor Nozzle Assembly

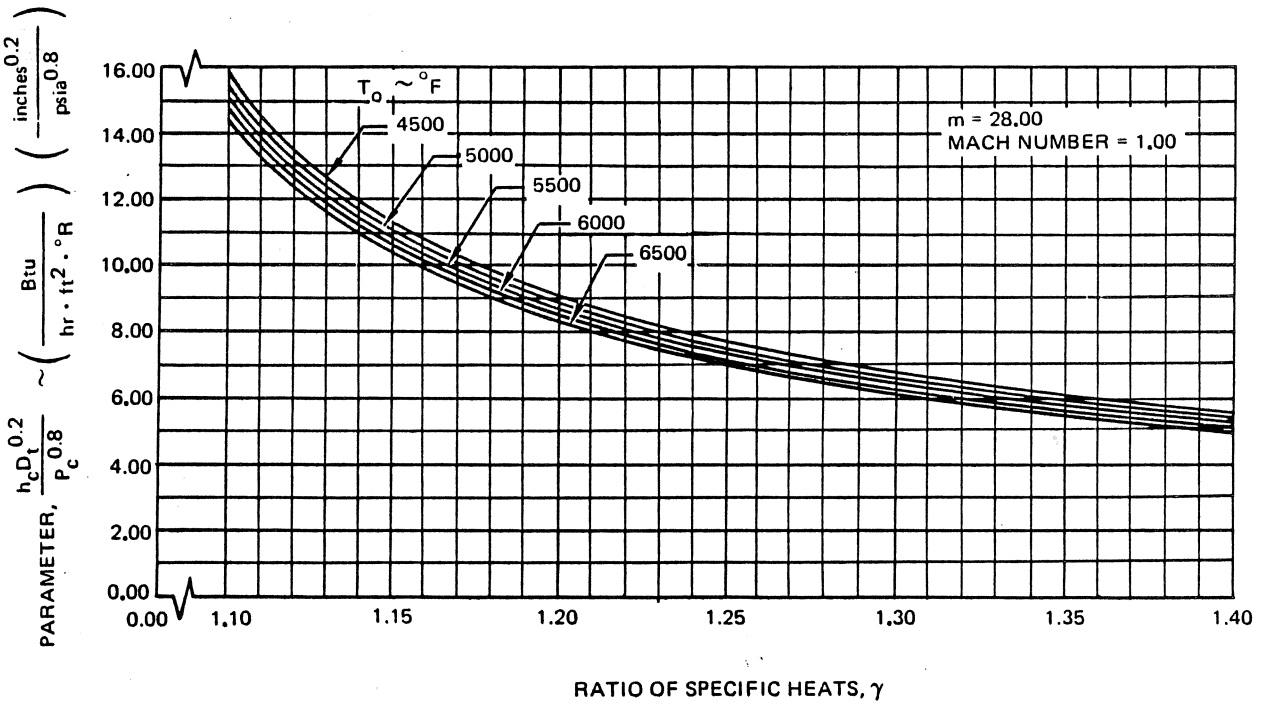

Figure 14-139. Film Coefficient Parameter vs Ratio of Specific Heats

E. Determine the graphite exterior surface temperature

$$T_e = T(T_\infty - T_o) + T_o \qquad (343)$$

where T was obtained in step D, and

$$T_\infty = T_c$$

14-9.3.6 Calculations

A. Fourier Modulus, $F_o = a\theta/r^2$

The thermal diffusivity of the graphite insert

$$a = k/\rho c = \frac{38.2 \text{ Btu/hr-ft-}^\circ\text{F}}{(0.344 \text{ Btu/lb-}^\circ\text{F})(105.0 \text{ lb/ft}^3)}$$

$$= 1.058 \text{ ft}^2/\text{hr}$$

$$r = r_e = 1.588 \text{ in.}$$

$$\theta = 4 \text{ sec}$$

$$F_o = \frac{(1.058 \text{ ft}^2/\text{hr})[(144 \text{ in.}^2/\text{ft}^2)/(3600 \text{ sec/hr})](4.0 \text{ sec})}{(1.588 \text{ in.})^2}$$

$$= 0.067$$

B. Biot Number, $Bi = h_c r/k$

$$r = r_e = 1.588 \text{ in.}$$

$$k = 38.2 \text{ Btu/hr-ft-}^\circ\text{F}$$

The convective heat transfer coefficient h_c in a rocket nozzle, discussed in Subsection 14-4.7.6, can be calculated using equation 194, which involves considerable computation, or it can be determined graphically using curves in Douglas Report SM-52339. That report contains parameterized heat transfer data based on a computer solution of a modification of equation 194. That graphical method is used in this example to obtain h_c.

SM-52339 contains four sets of heat transfer curves that plot the heat transfer parameter

$$(h_c D_t^{0.2})/P_c^{0.8}$$

versus γ for several combustion gas stagnation temperatures T_o at throat conditions (M = 1.0). One each of the curve-sets is plotted for a combustion gas average molecular weight m of 20.00, 24.00, 28.00 and 32.00. One of these curve-sets (m = 28.00) (Figure 14-139) shows that the heat transfer parameter is 10.30 at $\gamma = 1.17$ and $T_o = 4{,}600^\circ$F.

Since m is 26.25 in this problem, the cross-plot of the m curves at $\gamma = 1.17$ and $T_o = 4{,}600^\circ$F, shown in Figure 14-139, is required to determine the value of $h_c D_t^{0.2}/P_c^{0.8}$. For the given throat conditions, Figure 14-140 shows that $h_c D_t^{0.2}/P_c^{0.8} = 10.60$.

Therefore,

$$h_c = 10.60\left[\frac{P_c'^{0.8}}{D_t^{0.2}}\right] = 10.60\left[\frac{1.000^{0.8}}{1.579^{0.2}}\right]$$

$$= 2420 \text{ Btu/hr-ft-}^\circ\text{F}$$

Using these values of h_c, r_e and K,

$$Bi = \frac{(2420 \text{ Btu/hr-ft}^2\text{-}^\circ\text{R})(1.588 \text{ in.})}{(38.2 \text{ Btu/hr-ft-}^\circ\text{R})(12.\text{in./ft})} = 8.38$$

C. The radius ratio:

$$R_i = r_i/r_e = 1.579/3.175 = 0.497$$

which is reasonably approximated by 0.5.

D. For cylindrical shells that are heated on the interior surface and insulated on the exterior surface, the value of the temperature parameter T can be determined from the graphs in Figure 14-38B. Since the caluclated value $R_i = 0.5$ is not close to either of the appropriate available constant-R_i charts (Figure 14-38B-2 and -3), the cross-plot shown in Figure 14-141 was generated. This plot used the graphs in Figures 14-38B-1, -2, -3 and -4 (R_i - 0.2, 0.4, 0.6 and 0.8 respectively), holding Bi = 8.4 and Fo = 0.067. From Figure I4-141, at $R_i = 0.5$:

$$T = \frac{T - T_o}{T_\infty - T_o} = 0.153$$

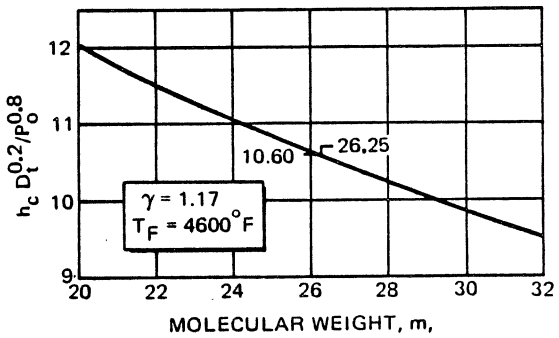

Figure 14-140. h_c Crossplot

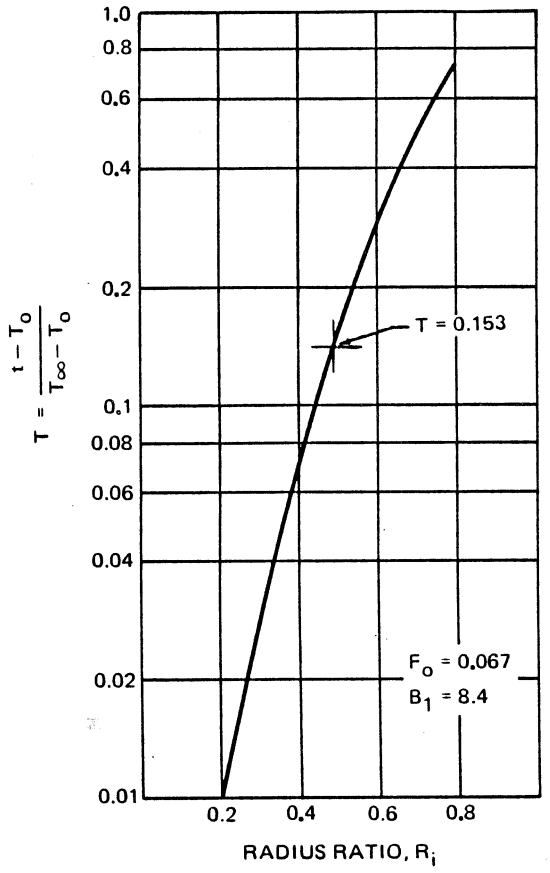

Figure 14-141. Temperature Ratio Crossplot

E. The temperature of the exterior surface of the graphite cylinder $T = T_e$ after 4 seconds of combustion thus is:

$$T_e = 0.153(T_\infty - T_o) + T_\infty$$

$$= 0.153(5060 - 530) + 530 = 1223^\circ R = 763^\circ F$$

Therefore, since the temperature of the graphite exterior surface will be less than 1,000°F, the design is feasible, and is an acceptable candidate for the computerized multidimensional analysis.

14-9.4 Application No. 4 — Rocket Nozzle Heat Transfer Computer Solution

The Delta third stage solid propellant motor (TE-364-4) has a composite nozzle construction (Figure 14-142) that consists of:

A glass-cloth phenolic primary structure.

An asbestos phenolic insulation in the submerged section.

A carbon or graphite phenolic-tape wrapped exit cone liner.

A G-90 graphite throat insert.

A 6Al-4V titanium nozzle closure for attachment to the motor case.

The temperature of the glass-cloth phenolic must be kept below a critical value during motor operation in order to prevent an unacceptable structural degradation.

This application is similar to the problem presented in Subsection 14-9.3 but the solution was obtained by a more precise method.

14-9.4.1 Design Requirements

The glass-cloth phenolic primary structure temperature must not exceed 600°F during the motor operating time (45 seconds).

14-9.4.2 Nomenclature

c	=	Specific heat of individual nozzle materials, Btu/lb-°R
$\bar{c}_p$	=	Average specific heat of combustion gases, Btu/lb-°R
h_c	=	Convective heat transfer coefficient, Btu/hr-ft^2-°R
k	=	Thermal conductivity of individual nozzle materials, Btu/hr-ft-°R
$\bar{m}$	=	Average molecular weight of combustion gases, lb/lb-mole
P_c	=	Combustion gas pressure, lb/in.^{2} abs
P_n	=	Nozzle gas pressure, lb/in.^{2} abs
Pr	=	Prandtl number
S	=	Boundary surfaces
$T_{\bar{AW}}$	=	Adiabatic wall temperature, °R
T_c	=	Combustion gas temperature, °R
T_n	=	Nozzle gas temperature, °R
T_w	=	Wall temperature, °R
γ	=	Specific heat ratio of combustion gases
ρ_G	=	Density of combustion gases, lb/ft^3

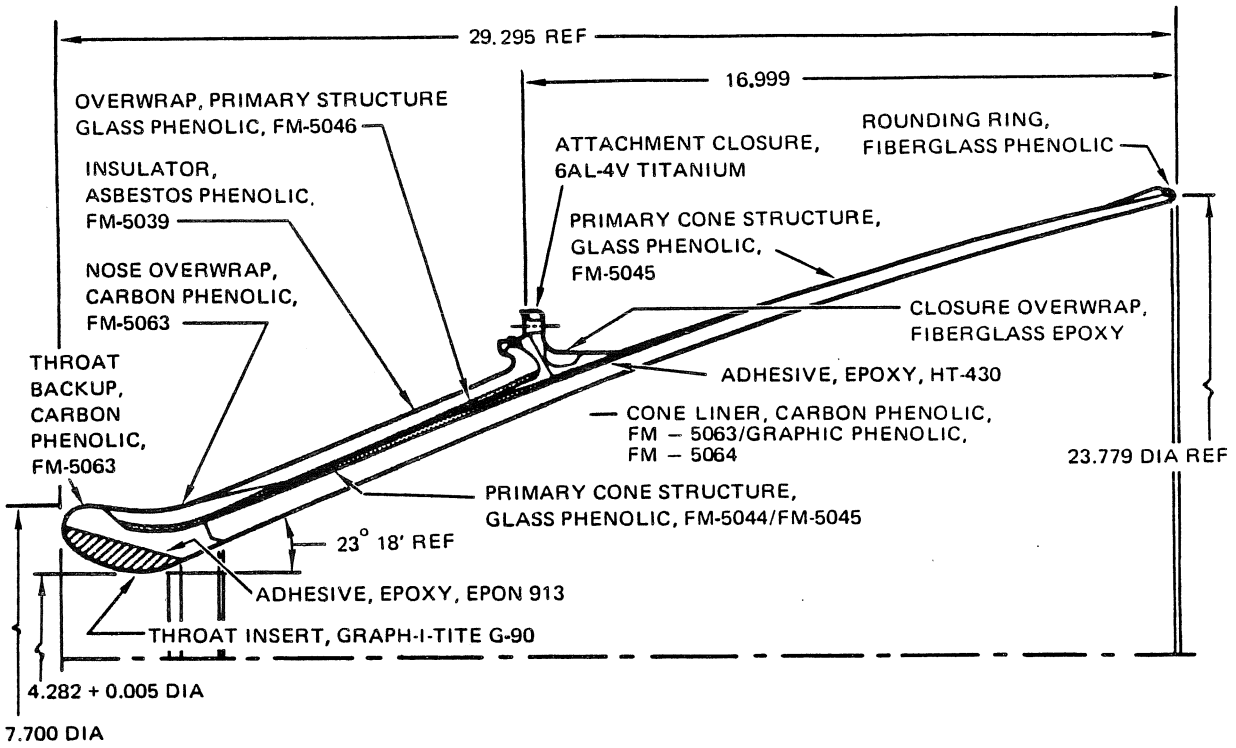

Figure 14-142. Nozzle Assembly (TE-364-4)

ρ = Density of individual nozzle materials, lb/ft^3

μ = Absolute viscosity of combustion gases, lb/ft-hr

14-9.4.3 Given Data

The nozzle configuration is shown in Figure 14-142.

Nozzle material properties (k, ρ, and c) as a function of temperature are listed in Tables 14-30 through 14-34.

T_c = 6,134°R = 5,674°F

m = 28.4 lb/lb-mole

c_p = 0.43 Btu/lb-°F

γ = 1.18

P_n along the nozzle length is defined in Figure 14-143.

T_n and T_{AW} along the nozzle length are defined in Figure 14-144.

14.9.4.4 Assumptions

Radiant energy interchange between the nozzle surfaces and the exhaust gases is not considered, but this is partly offset by the selection of conservatively high values of heat transfer coefficients.

14-9.4.5 Procedure

The method used to generate the temperature distribution within the nozzle was the MDAC modified axisymmetric finite element heat conduction computer program (AMG065) originated by Rohm and Haas. The modification was made to provide the program with the capability to accept and to use temperature dependent material properties. The input information for this program consisted of the nozzle geometry, temperature dependent material properties, and the convective boundary conditions at the nozzle walls.

The basic functional relationship chosen for this finite element heat conduction program in vector notation is $\pi(u,u)$:

$$\pi(u,\dot{u}) = \int_V \left[(1/2)\underset{\sim}{\nabla}u \cdot \underset{\approx}{k}\underset{\sim}{\nabla}u + \rho c u\dot{u} - Qu\right] dv - \int_S \underset{\sim}{n} \cdot \underset{\sim}{q} u ds \qquad (344)$$

Table 14-30. FM-5063 Carbon Phenolic Thermal Properties

Temperature °F	Density lbs/in.3	Specific Heat Btu/lb-°F	Thermal Conductivity Btu/in.-sec-°F (x 10^4)	
			*	**
0	0.0534	0.210	0.11	0.19
300	0.0522	0.266	0.13	0.22
600	0.0493	0.331	0.15	0.24
900	0.0439	0.421	0.17	0.26
1,200	0.0432	1.820	0.18	0.30
1,500	0.0428	1.850	0.20	0.38
1,800	0.0426	1.870	0.24	0.47
2,500	0.0426	1.910	0.44	0.73
3,000	0.0426	0.520	0.66	0.97
4,000	0.0426	0.498	1.24	1.48
5,000	0.0426	0.500	1.86	2.04
6,500	0.0426	0.500	2.85	2.94

*Across laminate
**Along cloth fibers (warp)

Table 14-31. FM-5064 Graphite Phenolic Thermal Properties

Tempterature °F	Density lbs/in.3	Specific Heat Btu/lb-°F	Thermal Conductivity Btu/in.-sec-°F (x 10^4)	
			*	**
0	0.0516	0.20	0.16	0.50
300	0.0509	0.325	0.17	0.54
600	0.0485	0.375	0.19	0.58
900	0.0457	0.435	0.27	0.69
1,200	0.0449	1.820	0.35	0.76
1,500	0.0466	1.850	0.49	0.81
1,800	0.0466	1.870	0.49	0.88
2,500	0.0466	1.910	0.71	1.07
3,000	0.0466	0.510	0.90	1.24
4,000	0.0466	0.5	1.36	1.64
5,000	0.0466	0.5	1.92	2.15
6,500	0.0466	0.5	2.55	2.75

*Across laminate
**Along cloth fibers (warp)

Table 14-32. FM-5044 and FM-5045 Glass Phenolic Thermal Properties

Temperature °F	Density lbs/in.3	Specific Heat Btu/lb-°F	Thermal Conductivity Btu/in.-sec-°F (x 10^{-4})	
			*	**
0	0.0700	0.190	0.039	0.055
300	0.0693	0.248	0.040	0.060
600	0.0638	0.344	0.049	0.072
900	0.0596	0.438	0.050	0.086
1,200	0.0588	0.475	0.050	0.090
1,500	0.0584	0.482	0.052	0.100
1,800	0.0584	0.584	0.053	0.101
2,500	0.0584	0.490	0.054	0.132
3,000	0.0584	0.495	0.073	0.170
4,000	0.0584	0.498	0.200	0.335
5,000	0.0584	0.500	0.505	0.518
6,500	0.0584	0.500	1.340	1.390

*Across laminate
**Along cloth fibers (warp)

Table 14-33. FM-5046 Glass Phenolic Thermal Properties

Temperature °F	Density lbs/in.3	Specific Heat Btu/lb-°F	Thermal Conductivity Btu/in.-sec.-°F (x 10^{-4})	
			*	**
0	0.0758	0.190	0.039	0.055
300	0.0749	0.248	0.040	0.060
600	0.0710	0.344	0.049	0.072
900	0.0668	0.438	0.050	0.086
1,200	0.0658	0.475	0.050	0.090
1,500	0.0654	0.482	0.052	0.100
1,800	0.0652	0.485	0.053	0.101
2,500	0.0652	0.490	0.054	0.132
3,000	0.0652	0.495	0.073	0.170
4,000	0.0652	0.498	0.200	0.335
5,000	0.0652	0.500	0.505	0.518
6,500	0.0652	0.500	1.340	1.390

*Across laminate
**Along cloth fibers (warp)

Table 14-34. FM-5039 Asbestos Phenolic Thermal Properties

Temperature °F	Density lbs/in.3	Specific Heat Btu/lb-°F	Thermal Conductivity Btu/in.-sec-°F (x 10^4)	
			*	**
0	0.0630	0.16	0.041	0.135
300	0.0620	0.255	0.070	0.176
600	0.0605	0.300	0.078	0.165
900	0.0558	0.300	0.066	0.142
1,200	0.0484	0.300	0.064	0.141
1,500	0.0422	0.315	0.065	0.141
1,800	0.0413	0.330	0.068	0.142
2,500	0.0412	0.385	0.075	0.147
3,000	0.0412	0.418	0.079	0.150
4,000	0.0412	0.481	0.089	0.159
5,000	0.0412	0.542	0.099	0.168
6,000	0.0412	0.601	0.141	0.215
6,500	0.0412	0.630	0.240	0.328

*Across broadgoods laminate
**Along broadgoods sheet

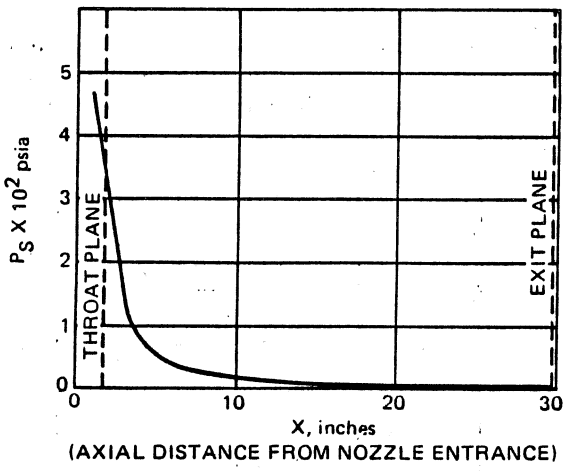

Figure 14-143. TE-364-4 Nozzle Pressure

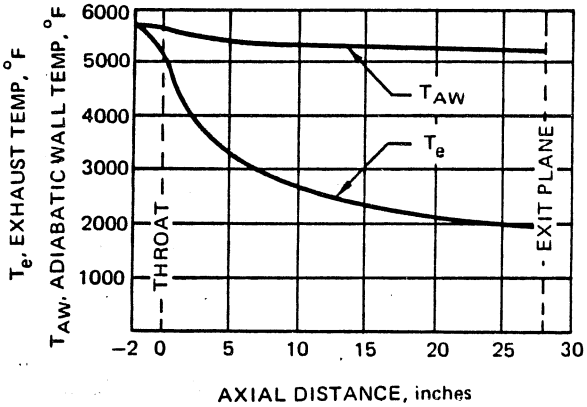

Figure 14-144. TE-364-4 Nozzle Temperature Profiles

where:

V = Volume of the region

S = Surface of the region's boundary

$\underset{\approx}{k} \equiv \underset{\approx}{k}(x^i)$ = Conductivity tensor for an anisotropic material

$c \equiv c(x^i)$ = Specific heat

$\rho \equiv \rho(x^i)$ = Density

$Q \equiv Q(x^i)$ = Internal heat source density

$\underset{\sim}{q} \equiv \underset{\sim}{q}(x^i)$ = Heat flux vector across a boundary

$n \equiv n(x^i)$ = Unit normal vector

$u \equiv u(x^i,t)$ = Temperature

$\dot{u} \equiv \dot{u}(x^i,t)$ = Time derivative of temperature

$\underset{\sim}{\nabla} u$ = Gradient of u

x^i = Coordinates

It was shown in Rohm and Haas Company Technical Report S-198 *Heat Conduction and Stress Analysis of Solid Propellant Rocket Motor Nozzle* by J.T. Brisbane, February 1969 that the functional $\pi(u,\dot{u})$ when extremized, satisfies the field and boundary equations of transient heat conduction in an anisotropic body, i.e., $\underset{\sim}{\nabla} \cdot \underset{\approx}{k} \underset{\sim}{\nabla} u = \rho c \dot{u} - Q$ in the volume of the region and $\underset{\sim}{n} \cdot \underset{\approx}{k} \underset{\sim}{\nabla} u = \underset{\sim}{n} \cdot \underset{\sim}{q}$ on the surface of the region. The former is the Fourier heat conduction equation and the latter is the heat flux $\underset{\sim}{q}$ at the surface of the body. Since there was no internal heat source within the nozzle, Q became zero in this problem and the only contribution to q was the convective heat transfer to the nozzle surfaces from the hot gases.

The AMG065 program is a heat conduction program which does not take into account the radiation interchange between the nozzle surface and the exhaust gases. However, the lack of radiation heating to the nozzle was partly offset by a conservative approach in treating the heat transfer coefficients.

The AMG065 program was chosen over other MDAC heat transfer programs, such as JA03 or JA26, because it has built-in grid-generation features (and a capacity of 1,500 nodal points) that materially reduce the time required to set up the nozzle finite element grid for the heat transfer solution. Also, this same grid was used in the finite element stress analysis program SAASII which computed the structural margins of the nozzle using the thermal output from the AMG065 program.

The JA03 and JA26 programs are based on the finite difference method and have a relatively limited number of grids (300 nodes). Further, the output temperature distributions from these programs must be reprocessed before they can be used in the stress program.

The MDAC Computer Program F586, described in MDAC Report SM-45735, was used to calculate the convective boundary heat transfer parameters as part of the input to the AMG065 program. The F586 program is specifically designed for solid rocket nozzle applications. It computes the extended boundary layer solutions of Mayer for the analysis of convective heat transfer in rocket nozzle.

The basic equation for this heat transfer to the boundary surface is:

$$h_c(s) = \frac{0.296\beta^{5/4}\, pr^{-2/3}\, \rho_\infty c_p U_\infty}{\left[\int_0^s \beta^{5/4}\, \rho_\infty U_\infty \mu_\infty^{-1}\, ds\right]^{1/s}} \qquad (345)$$

where:

$$\beta = \left(\frac{T}{T^*}\right)^{0.67} \text{ for solid propellant gases} \qquad (346)$$

$$Pr = \mu c_p/k$$

$$T^* = 0.5(T_W + T_\infty) + 0.22(T_{AW} - T_\infty) \qquad (347)$$

The computed h_c values along the nozzle wall for various reference wall temperatures are shown in Figures 14-145 and 14-146. The higher h_c values were used in the nozzle thermal analysis in order to compensate for the lack of radiation heating effect in the AMG065 program.

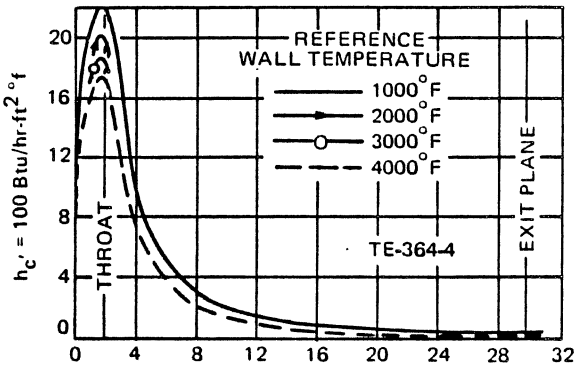

Figure 14-145. Nozzle Convective Heat Transfer Coefficients (h_c)

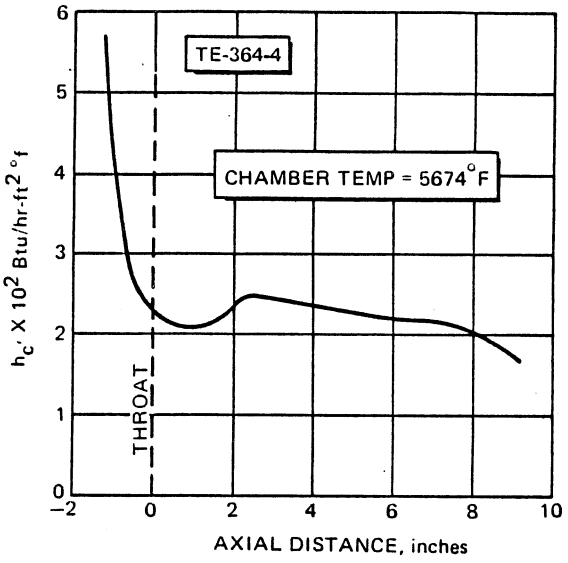

Figure 14-146. Nozzle Backside Convective Heat Transfer Coefficient Profile

The finite element modeling of the nozzle is shown in Figure 14-147. The number of each element is designated by the number of the lowest bounding node (I, J), where I denotes the row, and J denotes the column. The grid structure is laid out so that the grid lines normally fall on the natural material boundaries. A maximum of 1500 nodal points can be used for arbitrary-shaped axisymmetric or plane bodies.

14-9.4.6 Calculations

Computer runs were made on nozzle configurations as modeled in Figure 14-146A, first with a graphite tape and then with a carbon tape exit cone liner. Typical temperature distributions through the nozzle wall near the end of motor operation time (45 seconds after motor ignition) are shown in Figure 14-146A for both graphite tape and carbon tape liner configurations. The steeper temperature gradient within the carbon tape liner is primarily because the carbon tape has a lower thermal conductivity than the graphite tape.

For the same reason, the axial thermal profiles at the exit-cone liner/glass-cloth phenolic interface, shown in Figure 14-146B, indicate significantly lower temperatures for the carbon tape liner than for the graphite tape liner. These results indicated that the carbon tape liner provides better thermal protection for the glass cloth phenolic structure, although the graphite tape liner design is considered adequate.

Firings of TE-364-4 motors with graphite tape and carbon tape liners confirmed that nozzle external surface temperatures were lower, and char depth was shallower on the carbon tape nozzle. Therefore, the carbon tape liner was chosen for the flight motor nozzle design.

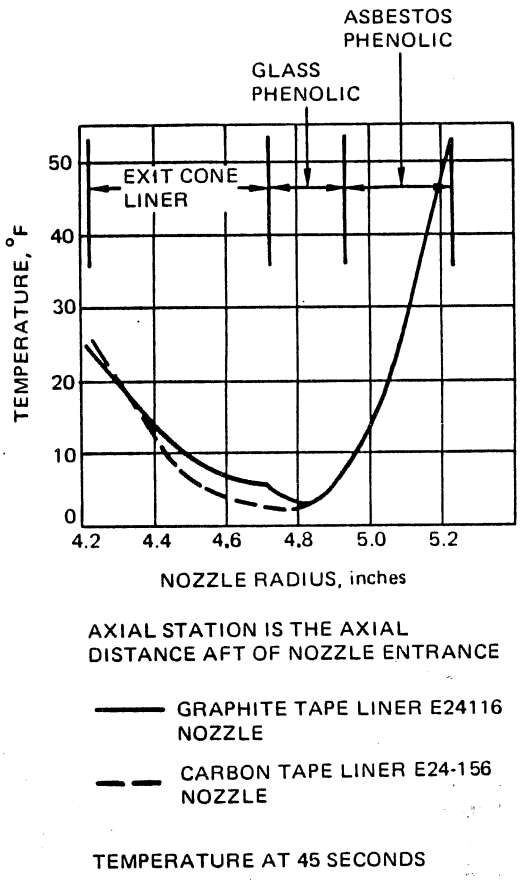

Figure 14-146A. Nozzle Temperature Distribution at Axial Station 7.1

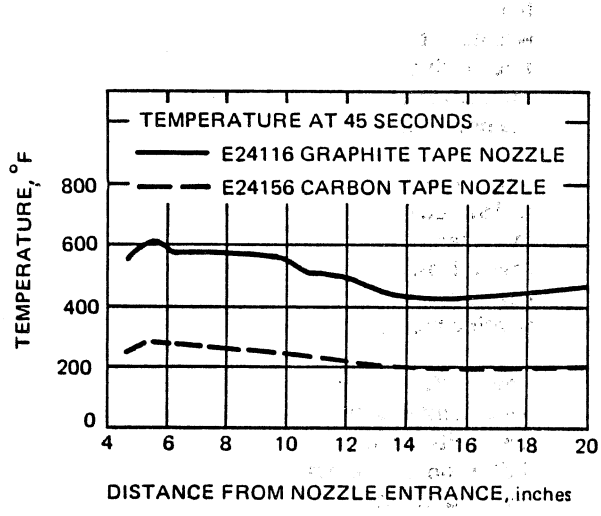

Figure 14-146B. Predicted Nozzle Liner – Glass Phenolic Interface Temperatures

STRESS MATERIAL CODE:	THERMAL MATERIAL CODE:	
②	①	GRAPH-I-TITE
②	②	CARBON CLOTH PHENOLIC
③	③	GLASS CLOTH PHENOLIC FM 5045 FM 5046
④	④	GRAPHITE CLOTH PHENOLIC
⑤	⑤	GLASS CLOTH PHENOLIC FM 5044
⑥	⑥	ASBESTOS PHENOLIC
①	⑦	TITANIUM
③	⑧	FIBERGLASS EPOXY

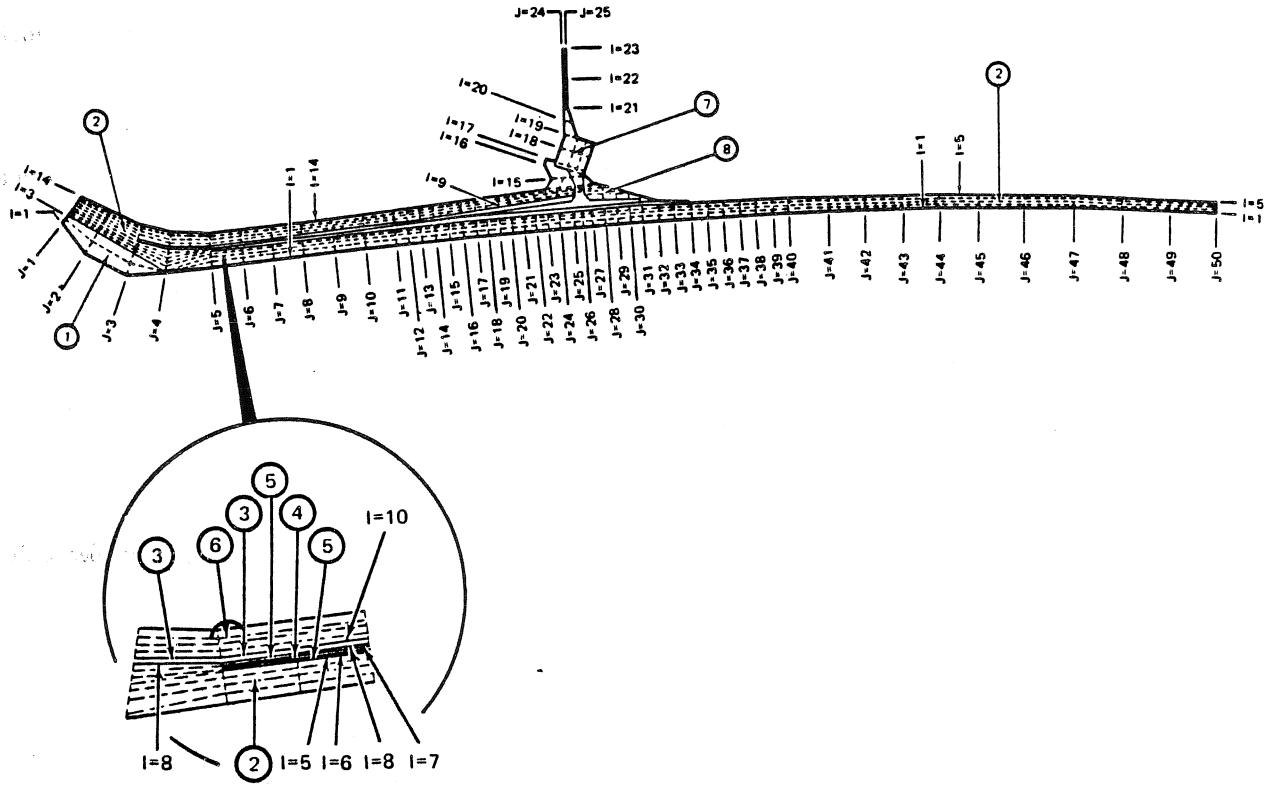

Figure 14-147. Nozzle Finite Element Model for Thermal Analysis

14-10 NOMENCLATURE

LETTER SYMBOLS

a = Velocity of sound, ft/sec

a = Thermal diffusivity - $k/\rho c$, ft^2/hr

A = Area, ft^2

b = Breadth or width, ft

C = Hourly heat capacity, Btu/hr-°R

C_A = Concentration of component A, lb-moles/ft^3

c = Specific heat: c_p specific heat at constant pressure; c_v, specific heat at constant volume, Btu/lb-°R

C_e = Electrical capacitance, farads

C_f = Skin friction coefficient

D = Diameter, ft

D_H = Hydraulic diameter = $4r_H$, ft

D_V = Mass diffusivity, ft^2/hr

e = Base of natural or Napierian logarithm

$\dot{e}$ = Energy transport rate, Btu/hr-ft^2

E = Electric potential, volt

E = Emissive power of a radiating body, Btu/hr-ft^2

ϵ = Heat exchanger effectiveness

f = Fanning friction coefficient

f = frequency, 1/sec

F = Geometric shape factor

$\mathcal{F}$ = Geometric shape and emissivity factor

g = Acceleration of gravity, ft/sec^2 or ft/hr^2

g_c = Dimensional conversion factor, 32.2 ft-lb/lb-sec^2 or 4.18×10^8 ft-lb/lb-hr^2

G = Mass velocity or flow rate per unit area = ρV, lb/hr-ft^2

G = Irradiation incident upon unit surface in unit time, Btu/hr-ft^2

h = Hour angle of the sun, deg

h = Unit-surface conductance (heat-transfer coefficient), Btu/hr-ft^2-°R

h_{fg} = Latent heat of vaporization, Btu/lb

H_{eff} = Effective heat of ablation, Btu/lb

i = Electric current flow rate, amp

i = Enthalpy of gas, Btu/lb

I = Intensity of radiation, Btu/hr-unit solid angle

J = Mechanical equivalent of heat = 778 ft-lb/Btu

J = Radiosity, Btu/hr-ft^2

k = Thermal conductivity, Btu/hr-ft-°R

k_G = Mass-transfer coefficient for the gas phase, lb-moles/hr-ft^2-atm

k_L = Mass-transfer coefficient for the liquid phase, lb-moles/hr-ft^2 (lb-moles/ft^3)

ℓ = Length, general, ft

L = Length along a heat flow path or characteristic length of a body, ft

m = molecular weight, lb/lb-mole

p = pressure, lb/ft^2

P = Wetted perimeter, ft

P = Total pressure, lb/ft^2

q = Rate of heat flow, Btu/hr

$\dot{q}$ = Rate of heat generation per unit volume, Btu/hr-ft^3

Q = Quantity of heat, Btu

r = radius, ft

r_H = Hydraulic radius = flow cross-section area/wetted perimeter, ft

R = Thermal resistance, hr-°R/Btu

R = Gas constant, lb-ft/lb-°R

Re = Electrical resistance, ohm

$\mathcal{R}$ = Universal gas constant = 1545.4 ft-lb/lb-mole-°R

S = Shape factor for conduction heat flow

t = time, hr or sec

T = Temperature, °R

u = Velocity in x direction, ft/sec

U = Overall unit conductance (heat-transfer coefficient), Btu/hr-ft^2-°R

v = Velocity in y direction, ft/sec

v = Specific volume, ft^3/lb

V = Average velocity, ft/sec

V = Volume, ft^3

$\dot{w}$ = Weight flow rate, lb/sec

X = Coordinate

x = Distance from leading edge, ft

X = Quality

Y = Coordinate

y = Distance from solid boundary measured in direction normal to surface, ft

Y = Absolute humidity, lb/lb

Z = Height of mass-transfer equipment, ft

z = Coordinate

GREEK SYMBOL

α = Absorptivity for radiation

α' = Thermal accommodation coefficient

β = Coefficient of thermal expansion, 1/°R

β' = Temperature coefficient of thermal conductivity, 1/°R

γ = Specific heat ratio = c_p/c_v

Γ_c = Mass rate of flow of condensate per unit breadth, lb/hr-ft

δ = Boundary layer thickness, ft

δ = Solar declination, deg

Δ = Difference between values

ϵ = Emissivity for radiation

θ = Time, hr or sec

λ = Wave length, micron

λ = Latent heat of vaporization, Btu/hr

λ = Molecular mean free path, ft

μ = Absolute viscosity, lb/ft-hr or lb/ft-sec

υ = Kinematic viscosity = μ/ρ, ft^2/hr or ft^2/sec

ρ = Mass density, lb/ft^3

ρ = Reflectivity of radiation

τ = Shearing stress, lb/ft^2

τ = Transmissivity for radiation

σ = Stefan-Boltzmann constant = 0.1714×10^{-8} Btu/hr-ft^2-°R^4

σ = Surface tension, lb/ft

ϕ = Latitude of location, deg

ψ = Inclination from horizontal, deg

ω = Angular velocity, 1/sec

ω = Solid angle, steradian

SUBSCRIPTS

AW = Adiabatic wall

b = Bulk or black body

C = Convection

c or cr = Critical

e = Electrical

f = Film

g = Gray body

i = Inner

K = Conduction

L = Liquid

max = Maximum

min = Minimum

o = Outer

R = Radiation

s = Surface or solid

sat = Saturation

v = Vapor

w = Wall

λ = Wavelength

o = Stagnation condition

∞ = Far removed from surface (free stream condition)

14-11 BIBLIOGRAPHY

1. Bird, R. B., Stewart, W. E. and Lightfoot, E. N., *Transport Phenomena,* John Wiley and Sons, Inc., 1960.

2. Boelter, L. M. K., Cherry, V. H., Johnson, H. A. and Martinelli, R. C., *Heat Transfer Notes,* University of California Press, 1948 Berkeley.

3. Brentari, E. G., Giarratano, P. J. and Smith, R. V., *Boiling Heat Transfer for Oxygen, Nitrogen, Hydrogen and Helium,* NBS Tech Note 317, 1965.

4. Carslaw, H. S. and Jaejer, J. C., *Conduction of Heat in Solids,* Oxford Univeristy Press, 2nd Edition, 1959.

5. Catchpole, J. P. and Fulford, G. D., *Dimensionless Groups,* Industrial and Engineering Chemistry, Vol. 58, No. 3, 1966.

6. Eckert, E. R. G., *Introduction to the Transfer of Heat and Mass,* McGraw-Hill Book Co., Inc., 1950.

7. Eckert, E. R. G. and Drake, R. M. Jr., *Heat and Mass Transfer,* McGraw-Hill, New York, 1959.

8. Gebhart, B., *Heat Transfer,* McGraw-Hill Book Co., Inc., 1961.

9. Gubareff, G. G., Janssen, J. E. and Torborg, R. H., *Thermal Radiation Properties Survey,* 2nd Edition, Honeywell, 1960, Minneapolis, Minnesota.

10. Hill, P. G. and Peterson, C. R., *Mechanics and Thermodynamics of Propulsion,* Addison-Wesley Publishing Co., 1965.

11. Holman, J. P., *Heat Transfer,* McGraw-Hill Book Co., Inc., 1963.

12. Howell, J. R. and Siegel, R., *Thermal Radiation Heat Transfer,* NASA SP164 Vol. II, 1969.

13. Jakob, M., *Heat Transfer,* John Wiley & Sons, Inc., Vol. I, 1949, Vol. II, 1957.

14. Johnson, F. S., *Satellite Environment Handbook,* Stanford Press, 1961, Stanford, California.

15. Kays, W. M. and London, A. L., *Compact Heat Exchangers,* National Press, 1955.

16. Kern, D. Q., *Process Heat Transfer,* McGraw-Hill, New York, 1st Edition, 1950.

17. Klinkenberg, A. and Mooy, H. H., *Dimensionless Groups in Fluid Friction, Heat, and Material Transfer,* Chemical Engineering Progress, Vol. 44, No. 1, 1948.

18. Kreith, F., *Principles of Heat Transfer,* International Textbook Co., 2nd Edition, 1965.

19. Kutateladze, S. S., *Handbook on Heat Transfer English Translation,* Clearinghouse of the U.S. Department of Commerce, Aug 1962.

20. Laver, B. E., *Heat Transfer,* The Oil and Gas Journal, 1955.

21. McAdams, W. H., *Heat Transmission,* McGraw-Hill Book Co., Inc., 3rd Edition, 1954.

22. Montgomery, A. D., *Computer Program JA03 Three-Dimensional Heat Transfer User's Manual,* MDAC-West, Aug 1971.

23. Moon, Parry, *The Scientific Basis of Illuminating Engineering,* Dover, 1961, New York.

24. Proceedings, *General Discussion on Heat Transfer,* Institution of Mechanical Engineers, 1951, London.

25. Ritter, J., *A Graphical Aid for Evaluating Convective Heat Transfer Coefficients in Rocket Motor Nozzles,* Douglas Report No. SM-52339, April 1966.

26. Rohsenow, W. M. and Choi, H. Y., *Heat Mass, and Momentum Transfer,* Prentice-Hall, Inc., 1961.

27. Schneider, P. J., *Conduction Heat Transfer,* Addison Wesley Publishing Co., Reading Massachusetts, 1955.

28. Schneider, P. J., *Temperature Response Charts,* John Wiley and Sons, 1963, New York.

29. Seader, J. D., *Boiling Heat Transfer for Cryogenics,* NASA CR-243, 1965.

30. Siegel, R. and Howell, J. R., *Thermal Radiation Heat Transfer,* NASA SP164 Vol. I, 1968.

31. Sparrow, E. M. and Cess, R. D., *Radiation Heat Transfer,* Brooks/Cole Publishing Co., Belmont, California, 1966.

32. Tong, L. S., *Boiling Heat Transfer and Two-Phase Flow,* John Wiley & Sons, Inc., 1965.

33. Treybal, R. E., *Mass-Transfer Operations,* McGraw-Hill Book Co., Inc., 1955.

34. University of Michigan, *Heat Transfer Symposium,* Engineering Research Institute, 1953, Ann Arbor.

35. Valley, S.L., *Handbook of Geophysics and Space Environments,* McGraw-Hill, 1965, New York.

36. Weibelt, J. A., *Engineering Radiation Heat Transfer,* Holt, Rinehart, and Winston, New York, 1966.

37. Wilson, D. G., *The Design and Performance Analysis of Compact Heat Exchangers,* Northern Research and Engineering Corporation, Report No. 1095-1, 5 Volumes, 1965.

38. Zijl, H., *Large Size Perfect Diffusors,* 2nd Edition, Phillips, 1960, Eindhoven (Netherlands).

39. Zuber, N. and Fried, E., *Two-Phase Flow and Boiling Heat Transfer To Cryogenic Liquids,* ARS Propellants, Combustion and Liquid Rockets Conference, 1961.